INL/EXT-15-36682
Revision 2

SSHAC Level 1 Probabilistic Seismic Hazard Analysis for the Idaho National Laboratory

INL SSHAC Level 1 Team

September 2016

The INL is a U.S. Department of Energy National Laboratory
operated by Battelle Energy Alliance

INL/EXT-15-36682
Revision 2

SSHAC Level 1 Probabilistic Seismic Hazard Analysis for the Idaho National Laboratory

INL SSHAC Level 1 Team

Suzette Payne (Project Technical Integrator)
Ryan Coppersmith
Kevin Coppersmith
Adrian Rodriguez-Marek
Valentina Montaldo Falero
Robert Youngs

September 2016

Idaho National Laboratory
Applied Engineering Department
Idaho Falls, Idaho 83415

http://www.inl.gov

Prepared for the
U.S. Department of Energy
Office of Nuclear Energy, Science and Technology
Under DOE Idaho Operations Office
Contract DE-AC07-05ID14517

EXECUTIVE SUMMARY

A Probabilistic Seismic Hazard Analysis (PSHA) was completed for the Materials and Fuels Complex (MFC), Advanced Test Reactor (ATR), and Naval Reactors Facility (NRF) at the Idaho National Laboratory (INL). The PSHA followed the approaches and procedures for Senior Seismic Hazard Analysis Committee (SSHAC) Level 1 study and included a Participatory Peer Review Panel (PPRP) to provide the confident technical basis and mean-centered estimates of the ground motions. A new risk-informed methodology for evaluating the need for an update of an existing PSHA was developed as part of the Seismic Risk Assessment (SRA) project. To develop and implement the new methodology, the SRA project elected to perform two SSHAC Level 1 PSHAs. The first was for the Fuel Manufacturing Facility (FMF), which is classified as a Seismic Design Category (SDC) 3 nuclear facility. The second was for the ATR Complex, which has facilities classified as SDC-4. The new methodology requires defensible estimates of ground motion levels (mean and full distribution of uncertainty) for its criteria and evaluation process. The INL SSHAC Level 1 PSHA demonstrates the use of the PPRP, evaluation and integration through utilization of a small team with multiple roles and responsibilities (four team members and one specialty contractor), and the feasibility of a short duration schedule (10 months). Additionally, a SSHAC Level 1 PSHA was conducted for NRF to provide guidance on the potential use of a design margin above rock hazard levels for the Spent Fuel Handling Recapitalization Project (SFHP) process facility.

The technical foundation for the INL PSHA was developed through a Work Plan for the SSHAC Level 1 processes of *evaluation* and *integration*. The *evaluation* phase of the project entailed the identification, compilation, and review of data, models, and methods that exist within the larger technical community. During the *integration* phase of the project, the Technical Integration (TI) Teams developed their Seismic Source Characterization (SSC) and Ground Motion Characterization (GMC) models that represent the center, body, and range of technically defensible interpretations. The evaluation phase of the INL PSHA entailed gathering and reviewing existing literature and data sets, evaluating any new data and information for key SSC and GMC issues, and assembling the 1850-2014 earthquake catalog for the region. Data compilation began at the time of project authorization and continued to the point at which the final SSC and GMC models were developed. The data compiled by the project team included references from the literature, publicly available information developed by other agencies, and INL and other hazard related studies.

As part of the evaluation activity, data focused on specific technical issues of interest were presented at the kickoff meeting, and alternative models and methods that were potentially applicable to the INL PSHA were presented and discussed during the kickoff meeting and subsequent team webinars. As the project progressed, the database development activity included preparation of maps and products that are directly applicable to the PSHA (e.g., seismicity and fault maps).

The INL is located in the Eastern Snake River Plain (ESRP), which is the eastern part of the Snake River Plain (SRP). The SRP is a large physiographic region (~90 km wide and 560 km long) covered by basaltic lava flows and sediments. The SRP's low-relief transects and sharply contrasts with the surrounding mountainous country of the Basin and Range, Yellowstone Plateau, and Idaho batholith. The SRP and surrounding region have a geologic history of extension and volcanism, which gives rise to contemporary earthquake sources associated with normal faulting, volcanic processes, and zones of seismicity. The 1850-2014 catalog, with over 20,000 events of magnitude >2.0, shows epicenters form a distinct parabolic seismic zone in the Basin and Range region around the ESRP. Seismicity within the boundaries of the Seismic Parabola is coincident with Quaternary normal faults that have ruptured in Holocene and historic time. The 1959 moment magnitude (**M**) 7.3 Hebgen Lake, Montana and 1983 **M** 6.9 Borah Peak, Idaho earthquakes are the largest normal faulting events to occur near or within the Seismic Parabola. With the exception of the 1905 Shoshone earthquake, the ESRP lacks earthquakes (**M**>2.5) and has Quaternary volcanic vents concentrated in NW-trending volcanic rift zones, three of which cross the INL. The NE-trending Axial Volcanic Zone intersects with the three VRZs and also crosses the INL. Due to uncertainty in its location, the 1905 local magnitude 5.5±0.5 earthquake may or may not have occurred in the ESRP.

Modifications to the ESRP's crust due to Yellowstone Hotspot volcanism also contribute effects that impact ground motions. Hotspot-related, large-scale intrusions, melting, and volcanism significantly modified the crust of the ESRP and caused subsidence that has allowed infilling of the ESRP by basalt lava flows and sediments. Surface soil deposits overlie basalt lava flows interbedded with sediment layers, which overlie rhyolitic rocks as shown by a 3-km deep borehole on INL.

The SSC component of the INL PSHA entailed the compilation and review of a wide range of data and information that exist within the technical community. Data sources included available information from professional literature; and data held in the public domain, such as past INL seismic hazard studies. To the extent possible, mapped information was compiled in geographic information system (GIS) formats that allowed the TI Team to superimpose various combinations of data layers for use in interpretations and developing the SSC model. In addition to the GIS database, a comprehensive bibliography of literature was compiled for use by the TI Team.

Like all seismic hazard analyses, the earthquake catalog (1850-2014) provided an essential database needed in the development of an SSC model. The process of homogenizing the magnitudes to a uniform moment magnitude measure and calculating unbiased earthquake counts to be used in recurrence analysis allowed for proper treatment of the uncertainty in the magnitude estimates and in the magnitude conversions. For earthquake recurrence assessments, the catalog was declustered to remove all foreshocks and aftershocks, the completeness of the catalog is assessed as a function of location, time, and earthquake size.

The GMC database included three types of data for GMC model development: 1) Ground Motion Prediction Equations (GMPEs) based on the Southwestern United States (SWUS) GMC model; 2) recorded data that was used to constrain the applicability of the GMPEs to the MFC, FMF, SFHP, and ATR site conditions; and 3) characterization of the representative near-surface geological profiles that defined the target site conditions to which the prediction equations were adjusted to. For this effort no new data were collected. Analyses were performed using existing earthquake data recorded and shear-wave velocities measurements at MFC, NRF, and ATR.

The SSC model in the PSHA defined the seismogenic potential, locations, sizes, and rates of future earthquakes. The SSC model-building process for the INL PSHA began with the identification of criteria that would be used by the TI Team to define seismic sources. These criteria were identified based on consideration of the extensional regime, the types of seismic sources that might be present (e.g., fault sources and source zones), and precedent from past INL and other seismic hazard analyses and recent SSC models developed for similar tectonic environments and for nuclear facilities. The SSC model included eleven tectonic and six volcanic seismic sources and thirteen regional and three local fault sources. Based on these considerations, seismic tectonic and volcanic sources were defined to account for distinct spatial differences in the following criteria: earthquake recurrence rate, maximum earthquake magnitude (Mmax), expected future earthquake characteristics (e.g., style of faulting, rupture orientation, seismogenic thickness), and probability that a source is seismogenic. Based on their availability of data, the characterization of the regional fault sources included fault geometry, slip rate, and recency of faulting resulting in much simpler logic trees. Based on detailed paleoseismic data, the three local fault sources have more complex logic trees for fault geometry, slip rate, and recency of faulting.

The SWUS Ground Motion Model (GMM) for Greater Arizona sources was adopted for use in characterizing the ground motions produced by shallow crustal earthquakes in the region surrounding the INL sites. Under a SSHAC Level 3 study, the SWUS GMM for the Greater Arizona sources was developed using a new approach for characterizing the epistemic uncertainty in median ground motions. The approach used in the SWUS project is to treat the available relevant GMPEs as a sample of possible GMPEs appropriate for assessing ground motion hazard at the site. The statistics of the GMPE parameters are then used to define a distribution for the space of possible models for median ground motions. This distribution is then discretized to produce a manageable number of ground motion models for use in hazard analysis that capture the center, body, and range of the ground motion model space.

The SWUS GMC for the Greater Arizona sources provides ground motion values at the surface of a reference rock velocity profile with a shear wave velocity in the top 30 m (V_{S30}) value of 760 m/s and site kappa values in the range of 0.037 to 0.045s. Transfer functions from the reference rock profile for the SWUS GMM to the MFC, FMF, SFHP (at NRF), and ATR site profiles were developed by the process of relative site response analysis using the point source stochastic model to represent input earthquake ground motions and one-dimensional site response to model crustal and soil amplification. Updated kappa distributions calculated using earthquake records at recording sites at MFC (0.011 to 0.030s), NRF (0.022 to 0.062s), and ATR (0.012 to 0.035s) were used in the point the source model. The adjustment from the reference rock hazard to the site-specific hazard is performed using NUREG/CR-6728 Approach 3 for hazard consistent soil hazard calculations.

The seismic hazard was calculated for MFC rock, FMF site-specific, SFHP rock, SFHP soil, ATR rock, and ATR soil conditions using the comprehensive seismic hazard model developed for SSHAC Level 1 process. The seismic hazard was calculated for SWUS reference site conditions at MFC, SFHP, and ATR. The results include total mean seismic hazard curves for SWUS reference site conditions for Peak Ground Acceleration (PGA) and spectral acceleration at ground motion frequencies: 50, 33.3, 20, 13.3, 10, 6.67, 5, 3.33, 2.5, 2, 1, 0.5, 0.33, 0.2, 0.13, and 0.1 Hz (structural periods of 0.02, 0.03, 0.05, 0.07, 0.1, 0.15, 0.2, 0.3, 0.4, 0.5, 1, 2, 3.3, 5, 7.7, and 10 s). The contributions of individual sources or groups of sources, as well as the sensitivity to particular elements of the seismic hazard model and deaggregation of the mean hazard in terms of magnitude and distance, are also presented for spectral frequencies, 0.1, 0.5, 1, 2, and 10 Hz.

Using Approach 3 and the site transfer functions, site-specific hazard results were obtained for MFC, SFHP, and ATR rock conditions and FMF, SFHP, and ATR soil conditions. For each site, tables of the mean site-specific hazard results for PGA and the ground motion frequencies are presented. Fractiles were also calculated for PGA, 2 or 10 Hz spectral acceleration depending on the site. Uniform Hazard Spectra Response (UHRS) were obtained from the mean hazard curves for return periods of 2,500, 10,000, 25,000 and 100,000 yr, and were used to develop the site-specific, performance-based, Ground Motion Response Spectrum (GMRS) using the performance based approach discussed in American Society of Civil Engineers/Structural Engineers Institute Standard 43-05.

For MFC rock conditions, comparison of seismic hazard curves at PGA, 10 Hz and 1 Hz spectral acceleration show that at high frequency the results of the 1996 INL PSHA produce higher hazard for short return periods (Annual Exceedance Frequency – AEF of 10^{-3} or 10^{-4}), while at long return periods the opposite is observed. The differences between the 1996 and 2015 hazard results are attributed to changes in methods used to calculate recurrence rates of source zones and changes to the recurrence models of the Lost River and Lemhi faults, and the addition of the regional faults. At 1 Hz, the 2015 hazard at MFC is consistently lower than 1996 and is likely due to a combination of lower median motions from the adjusted SWUS GMPEs compared to the 1996 set of median models, and lower effective total sigma (combined aleatory and epistemic) than the ergodic sigmas used in the 1996 PSHA.

The 2015 SSHAC Level 1 PSHA results are compared to hazard curves and UHS from the 1996 INL PSHA for rock conditions at MFC, the 2006 MFC rock DBE spectrum, and to the 2006 FMF DBGM, which is defined as the MFC 2,500 yr site-specific DBE 5% damped spectrum for one soil layer. The comparison of the 2015 MFC rock UHS, 2015 MFC rock GMRS for SDC-3, and 2006 MFC rock DBE spectrum at AEF $4x10^{-4}$ and $4x10^{-5}$ shows that although the GMRS is shifted towards high frequency motions, the spectrum is enveloped by the 2006 MFC rock DBE spectrum. Because the soil thickness varies across the footprint of FMF, the GMRS is calculated from the envelope of the AEF $4x10^{-4}$ UHS and the envelope of the AEF $4x10^{-5}$ UHS obtained for the two soil thicknesses. In general the UHS calculated for 15 ft of soil is higher than the UHS for 5 ft of soil. The comparison of the 2015 FMF site-specific UHS, 2015 FMF site-specific GMRS for SDC-3, and the 2006 FMF site-specific DBGM spectrum at $4x10^{-4}$ and $4x10^{-5}$ AEFs, shows that 2006 FMF site-specific DBGM spectrum fully encompasses the 2015 FMF site-specific GMRS for SDC-3.

Hazard sensitivities were evaluated for the SSHAC Level 1 hazard at SFHP. For rock conditions, comparison of seismic hazard curves at PGA, 10 Hz and 1 Hz spectral acceleration show that the tectonic source zones control the high-frequency hazard (PGA and spectral frequencies greater than 10 Hz). The fault sources are the primary contributors for low-frequency hazard (5 Hz and lower). The Cascadia interface contribution becomes noticeable only for spectral frequencies of 1 Hz or less. Deaggregation of the total mean seismic hazard shows that the largest contribution to the total hazard comes from the fault sources, particularly the closest fault (Lemhi) to SFHP. The Cascadia Subduction interface source shows a contribution of approximately 5% to the total hazard.

From the SSHAC Level 1 PSHA UHRS were obtained for SFHP rock and two soil thicknesses of 20 and 40 ft UHRS, obtained for return periods of 2,500, 10,000, 25,000 and 100,000 yr, were used to develop site-specific, performance-based, GMRS for SDC-3, SDC-4, and SDC-5 per ASCE/SEI 43-05. Comparison of the GMRS to the broadened Design Response Spectra (BDRS) for rock conditions being used for the SFHP process facilty shows that for all three SDC levels, the existing BDRS envelops the GMRS computed from the results of the SSHAC Level 1 study. Additionally, UHRS for the SFHP soil depths of 20 ft and 40 ft were computed using generic and site-specific sets of material curves. The UHRS produced by the two sets of material curves are similar. GMRS for soil thickness of 20 and 40 ft were also computed and presented for the SDC-3, SDC-4, and SDC-5 levels.

Hazard sensitivities were evaluated for the ATR SSHAC Level 1 hazard. For rock conditions, fault sources contribute more to the hazard at spectral frequencies <5 Hz at AEF of $<1x10^{-4}$. Source zones control the hazard at PGA and spectral frequencies >5 Hz for AEF of $>1x10^{-4}$. Deaggregation of the total mean seismic hazard at 10 Hz (0.1-sec) and 2 Hz (0.5-sec) spectral accelerations for AEFs of $4x10^{-4}$ and $1x10^{-4}$ reflect slightly higher contributions from the faults at 2 Hz and that the source zones are important contributors to the hazard at both frequencies. ATR is on the hanging wall side of the Big Lost fault. Sensitivity tests to its seismogenic probability (p[S] 0.3, 0.65, and 1.0) and style of faulting (normal vs. strike-slip) based on new data still show that it only contributes to the hazard at AEF$<10^{-5}$ mainly due to its low slip rate. Comparisons of ATR rock hazard curves at PGA, 10 Hz (0.1-sec), and 1 Hz (1-sec), between the SSHAC

Level 1 and 2000 INL PSHA show similar differences as observed for MFC and for the same reasons discussed above. At high frequency (>10 Hz) the 2000 INL PSHA produces higher hazard for short return periods (AEFs of 10^{-3} or 10^{-4}), while at long return periods the SSHAC Level 1 produces higher hazard at ATR. At 1 Hz, hazard from SSHAC Level 1 is lower than the 2000 hazard at ATR.

The 2016 SSHAC Level 1 PSHA results for ATR include rock and soil conditions specific to ATR buildings and firewater piping areas classified at SDC-4, which is associated with the return period of 2,500 yr. Results of this study are compared the 2002 ATR Rock DBE spectrum, which is the DBGM for ATR rock sites, and to the 2006 ATR Soil DBE spectrum, which is the DBGM for ATR soil sites; both defined at the 10,000-yr return period. At ATR, the hazard was computed using two shear wave velocity profiles, one with and one without interbeds at ~40 m depth. Because this interbed is intermittently observed in boreholes across ATR and its presence impacts spectral acceleration levels, both responses were enveloped to produce the rock response. Due to the highly variable soil thickness above basalt bedrock, three soil depth cases (20 ft, 40 ft, and 60 ft) were used to capture the site responses. Site-specific responses were produced by enveloping the responses of the individual soil depth cases that covered the range of soil depth variability at a site of interest. Based on borehole data, the buildings and firewater piping areas were grouped into three sets of soil depth ranges (20-40 ft, 40-60 ft, and 20-60 ft) for which UHRS and GMRS were developed. Comparisons of the 2016 ATR UHRS and SDC-4 GMRS for rock and soil conditions with their respective DBGMs show that all of the 2016 spectra are completely enveloped by their respective DBGMs primarily due to the difference in return periods.

An evaluation of recent datasets of ground motions from the Next Generation Attenuation (NGA) project was made to recommend vertical to horizontal (V/H) ratios for use at MFC, FMF, SFHP, and ATR. Four models for V/H were selected for each site based on magnitude, distance, style of faulting, and site conditions as parameterized by V_{S30}. The V/H ratios for both the MFC site and the FMF can be represented by a value of 2/3 (0.667) with increases in ratios for lower frequencies to values of approximately 0.85 for the MFC site (rock) and 0.82 for the FMF site (soil). The SFHP have V/H ratios as low as 0.6 and 0.55 and as high as 0.85 and 0.8 for rock and soil sites, respectively. The V/H ratios for ATR rock are as low as 0.6 and as high as 0.85. For soil, three sets of V/H ratios were developed for the soil depths of 20-ft, 40-ft, and 60-ft since differences across these soil depths were significant. In general, the V/H ratios have lows of 0.52, 0.50, and 0.50 and highs of 0.83, 0.77, and 0.75 for the 20-ft, 40-ft, and 60-ft soil depths, respectively.

FOREWARD

This report contains results of a probabilistic seismic hazard analysis for the Materials and Fuels Complex (MFC) and the Naval Reactors Facility (NRF) at the Idaho National Laboratory. The probabilistic seismic hazard analysis (PSHA) was performed under Senior Seismic Hazard Analysis Committee (SSHAC) Level 1 processes and procedures. Results of the SSHAC Level 1 probabilistic seismic hazard analysis are intended for development of a new risk-informed methodology and should not be used for updating design basis earthquake levels for any INL facility. Note that the appendices to this report are in a separate document under the same report number.

This report has a revision history that includes the addition of SSHAC Level 1 PSHAs for multiple INL facility areas. The original issue in October 2015 (Revision 0) only included the SSHAC Level 1 PSHA for MFC as part of the development of the new risk-informed methodology. Revision 1 issued in February 2016 includes the SSHAC Level 1 PSHA for NRF to provide guidance on the potential use of a design margin for a proposed new facility, and Appendix I, which supports implementation of the new risk-informed methodology. Revision 2 issued September 2016 includes the SSHAC Level 1 PSHA for facilities at the ATR Complex. The ATR study was completed to provide inputs to the application of the new risk-informed methodology for a Seismic Design Category (SDC) 4 nuclear reactor whereas the MFC study provided inputs for an SDC-3 nuclear storage facility.

ACKNOWLEDGEMENTS

We appreciate the guidance and support from members of Battelle Energy Alliance's Seismic Risk Assessment project team: Justin Coleman, Mark Russell, Richard Yorg, Bentley Harwood, Lannie Workman, Paul Henslee, Mark Cox, and Evert Mouser. We also appreciate the assistance of Dan Stout (BEA) with subcontracts. We also thank Gary Anderson (Spent Fuel Handling Project) for his help and support of the analyses for Naval Reactors Facility. The U. S. Department of Energy (DOE), Office of Nuclear Energy, Science, and Technology funded this work under DOE Idaho Field Office Contract DE-AC07-05ID14517.

CONTENTS

ACRONYMS

ACR	Active Crustal Region
AEF	Annual Exceedance Frequency
AIC	Akaike Information Criterion
ANSI/ANS	American National Standards Institute/American Nuclear Society
ANSS	Advanced National Seismic System
ASCE/SEI	American Society of Civil Engineers/Structural Engineers Institute
ASME	American Society of Mechanical Engineers
ASTM	American Society for Testing and Materials
ATR	Advanced Test Reactor
AVZ	Axial Volcanic Zone
BB	Broadband
BEA	Battelle Energy Alliance
BIC	Bayesian Information Criterion
BLT	Big Lost Trough
CBR	Center, Body, and Range
CEUS	Central and Eastern United States
CFA	Central Facilities Area
COM	Craters of the Moon National Monument
CSZ	Centennial Shear Zone
CTB	Centennial Tectonic Belt
C_u	Coefficient of Uniformity
CV	Coefficient of Variation
DBE	Design Basis Earthquake
DBGM	Design Basis Ground Motion

DF	Design Factor
DMIN	Minimum Distance
DOE	U.S. Department of Energy
DRS	Design Response Spectrum
EFIS	Emergency Firewater Injection System
EPRI	Electric Power Research Institute
EPRI/SOG	Electric Power Research Institute Seismic Owners Group
ERZ	Vertical Standard Error
ESRP	Eastern Snake River Plain
ETS	Episodic Tremor and Slip
FAS	Fourier Amplitude Spectrum
FMC	Forearc Mantle Corner
FMF	Fuels Manufacturing Facility
G	Shear Modulus
GIS	Geographical Information System
GMC	Ground Motion Characterization
GMM	Ground Motion Model
GMPE	Ground Motion Prediction Equation
GMT	Greenwich Mean Time
GPE	Gravitational Potential Energy
GRMS	Ground Motion Response Spectrum
HID	Hazard Input Document
INL	Idaho National Laboratory
INTEC	Idaho Nuclear Technology and Engineering Center
ISB	Intermountain Seismic Belt
ISFSI	Independent Spent Fuel Storage Installation

ISRMIP	INL Seismic Risk-Informed Methodology Independent Panel
IWTU	Integrated Waste Treatment Unit
MFC	Materials and Fuels Complex
MFD	Magnitude Frequency Distribution
NE	Nuclear Energy
NEHRP	National Earthquake Hazards Reduction Program
NGA	Next Generation Attenuation
NQA	Nuclear Quality Assurance
NRC	U.S. Nuclear Regulatory Commission
NRF	Naval Reactors Facility
PEER	Pacific Earthquake Engineering Research Center
PGA	Peak Ground Acceleration
PI	Plasticity Index
PNNL	Pacific Northwest National Laboratory
PPRP	Participatory Peer Review Panel
PSA	Peak Spectral Acceleration
PSHA	Probabilistic Seismic Hazard Analysis
PVNGS	Palo Verde Nuclear Generating Station
RLME	Repeated Large-Magnitude Earthquake
RMS	Root Mean Square Error
RESORCE	Reference Database of Seismic Ground Motion in Europe
RWMC	Radioactive Waste Management Complex
QA	Quality Assurance
SA	Spectral Acceleration
SAEP	Seismic Assessment Evaluation Project
SDC	Seismic Design Category

SET	Seismic Evaluation Team
SFHP	Spent Fuel Handling Recapitalization Project
SHPRM	Seismic Hazard Periodic Review Methodology
SP	Short Period
SPS	Samples Per Second
SRP	Snake River Plain
SSC	Seismic Source Characterization
SSHAC	Senior Seismic Hazard Analysis Committee
SPRA	Seismic Performance Risk Assessment
SRA	Seismic Risk Assessment
SWUS	Southwestern United States
SZ	Subduction Zone
TA	Transportable Array
TAN	Test Area North
TDI	Technically Defensible Interpretations
TI	Technical Integration
UHRS	Uniform Hazard Response Spectrum
UHS	Uniform Hazard Spectrum
V/H	Vertical/Horizontal
V_P	Compression Wave Velocity
VRZ	Volcanic Rift Zone
V_S	Shear Wave Velocity
WNA	Western North America
WSRP	Western Snake River Plain

SSHAC Level 1 Probabilistic Seismic Hazard Analysis at the Idaho National Laboratory

1. Introduction

A Probabilistic Seismic Hazard Analysis (PSHA) was completed for the Materials and Fuels Complex (MFC), Naval Reactors Facility (NRF), and the Advanced Test Reactor (ATR) at Idaho National Laboratory (INL) (Figure 1-1). The PSHA followed the approaches and procedures appropriate for a Study Level 1 provided in the guidance advanced by the Senior Seismic Hazard Analysis Committee (SSHAC) in U.S. Nuclear Regulatory Commission (NRC) NUREG/CR-6372 and NUREG-2117 (NRC, 1997; 2012a). The SSHAC Level 1 PSHAs for MFC and ATR were conducted as part of the Seismic Risk Assessment (SRA) project (INL Project number 31287) to develop and apply a new-risk informed methodology, respectively. The SSHAC Level 1 PSHA was conducted for NRF to provide guidance on the potential use of a design margin above rock hazard levels.

The SRA project is developing a new risk-informed methodology that will provide a systematic approach for evaluating the need for an update of an existing PSHA. The new methodology proposes criteria to be employed at specific analysis, decision, or comparison points in its evaluation process. The first four of seven criteria address changes in inputs and results of the PSHA and are given in U.S. Department of Energy (DOE) Standard, DOE-STD-1020-2012 (DOE, 2012a) and American National Standards Institute/American Nuclear Society (ANSI/ANS) 2.29 (ANS, 2008a). The last three criteria address evaluation of quantitative hazard and risk-focused information of an existing nuclear facility. The seven criteria and decision points are applied to Seismic Design Category (SDC) 3, 4, and 5, which are defined in American Society of Civil Engineers/Structural Engineers Institute (ASCE/SEI) 43-05 (ASCE, 2005). The application of the criteria and decision points could lead to an update or could determine that such update is not necessary.

To develop and implement the new methodology, the SRA project elected to perform a SSHAC Level 1 PSHA for an initial candidate nuclear facility at INL. The methodology requires defensible estimates of ground motion levels (mean and full distribution of uncertainty) for its criteria and evaluation process. It proposes using a SSHAC Level 1 or 2 PSHA with a Participatory Peer Review Panel (PPRP) to provide the confident technical basis and mean-centered estimates of the ground motions. During development of the new methodology, the SRA project chose to demonstrate implementation at the SDC-3 level utilizing a SSHAC Level 1 PSHA to produce the mean-centered ground motion estimates for the Fuels Manufacturing Facility (FMF) at MFC. The FMF is classified as SDC-3, which per ASCE/SEI 43-05 (ASCE, 2005) is associated with a hazard exceedence probability of $4x10^{-4}$ (or return period of 2,500 yr). As discussed in this report, the SSHAC Level 1 PSHA follows the SSHAC processes (NUREG/CR-6372 and NUREG-2117; NRC, 1997; 2012a) and demonstrates the use of the PPRP, evaluation and integration through utilization of a small team, and the feasibility of a short duration schedule (10 months from January to October 2015).

The SRA project also chose to demonstrate the application of the new risk-informed methodology at another nuclear facility. The SSHAC Level 1 PSHA for ATR Complex produced mean-centered ground motion estimates for the nuclear test reactor at ATR or building TRA-670. TRA-670 is classified as SDC-4 which is associated with the hazard exceedence probability of $4x10^{-4}$ (or return period of 2,500 yr) as per ASCE/SEI 43-05 (ASCE, 2005). To fully evaluate TRA-670, its six supporting building and the region covered by fire-water piping, all classified as SDC-4, are also included in the ATR SSHAC Level 1 PSHA.

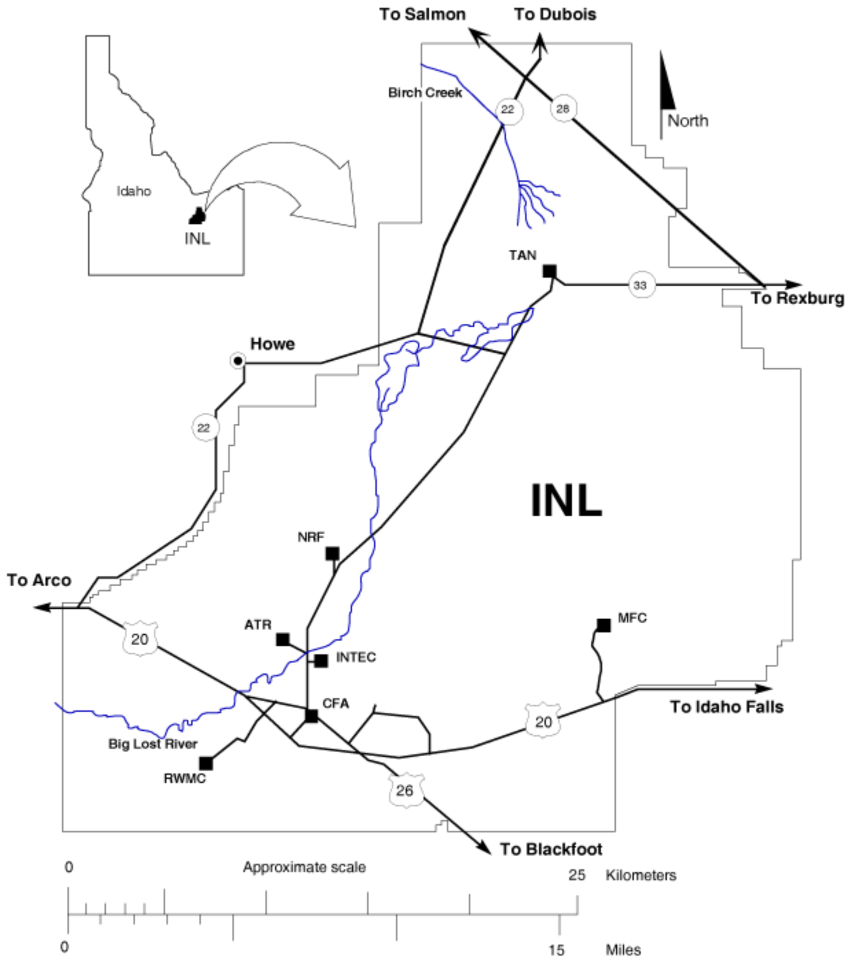

Figure 1-1. Map of the facility areas at the Idaho National Laboratory (INL). Facility areas include: Materials and Fuels Complex (MFC), Advanced Test Reactor (ATR), Naval Reactors Facility (NRF), Idaho Nuclear Technology and Engineering Center (INTEC), Central Facilities Area (CFA), Radioactive Waste Management Complex (RWMC), and Test Area North (TAN).

The SSHAC Level 1 PSHA for NRF began after completion of the PSHAs for MFC and FMF. The Spent Fuel Handling Recapitalization Project (SFHP) at NRF is performing an evaluation of the proposed design margin for the new SFHP process facility. The evaluation involves using a mean-centered definition of the seismic hazard at NRF to provide guidance on an appropriate design margin. The SFHP process facility contains structural elements classified as SDC-5 and SDC-3 as defined by ANSI/ANS 2.26 (ANS, R2010), which correspond to hazard exceedence probabilities of 1×10^{-4} and 4×10^{-4} (return periods of 10,000 and 2,500 yr) as per ASCE/SEI 43-05 (ASCE, 2005).

1.1 Background

1.1.1 Previous Seismic Hazard Analyses at INL

Results of two PSHAs form the basis of the current Design Basis Earthquake (DBE) levels for INL facilities. The first PSHA was completed in 1996 and included mean Uniform Hazard Spectra (UHS) for MFC along with several other INL facility areas (Woodward-Clyde Federal Services et al., 1996). Since the 1996 PSHA predated NUREG/CR-6372 (NRC, 1997), SSHAC was not applied. The 1996 PSHA included regional source zones, volcanic zones, and fault-specific sources in its Seismic Source Characterization (SSC) model and 1980's vintage empirical ground motion prediction equations (GMPEs) for its Ground Motion Characterization (GMC) model. Since MFC was under the direction of a different DOE office than the other facility areas, rock DBE spectra were developed in 1998 based on the SSC and GMC models of the 1996 PSHA (Woodward-Clyde Federal Services, 1998). Following reviews by the NRC for a license to operate an independent spent fuel storage installation (ISFSI) at INL and reviews by the State of Idaho, recomputations of the INL PSHA were completed in 1999 and 2000, for all other INL sites except MFC. The 1999 and 2000 recomputations were performed using the 1996 SSC model and an updated GMC model that included empirical GMPEs for extensional environments (URS Greiner Woodward-Clyde Federal Services et al., 1999; 2000). In 2006, updated rock DBE levels at the 2,500 yr and 10,000 yr return periods were developed for MFC using adjustments to 1998 rock design UHS to account for changes to the ground motion models used in the 2000 PSHA for the other INL sites (Payne, 2006a). Additionally, site response analyses were performed for the range of soil thicknesses above bedrock at MFC, which were then used to develop the MFC DBE soil spectra at the 2,500 yr and 10,000 yr return periods (Payne, 2006a).

In 2010, the Seismic Assessment Evaluation Project (SAEP) performed seismic hazard sensitivity analyses as recommended by its Seismic Evaluation Team (SET) (Seismic Evaluation Team, 2010). The 2010 sensitivity analysis evaluated impacts to probabilistic seismic hazard levels by isolating effects of changes in GMC and SSC models. The sensitivity analyses were performed for a subsurface geology representative of the ATR Complex, which has basalt and sedimentary interbeds. The sensitivity analyses used state-of-the-art methods and incorporated aleatory and epistemic uncertainties different from those used in previous INL PSHAs. The results of the 2010 sensitivity analyses revealed the potential for significant impacts to seismic hazard levels at ATR from changes in the source zonation model and GMPEs. Later in 2012 and 2013, additional hazard sensitivity analyses were conducted for NRF to provide information to the SFHP. These analyses revealed the potential for impacts to seismic hazard levels at NRF from changes to GMPEs and fault-specific sources (AMEC, 2011; 2013).

Despite the various site response analyses and sensitivity analyses conducted over the past 19 yr, the basic underlying PSHA model has not been systematically re-evaluated since the 1996 INL PSHA. That is, the SSC and GMC models have not been subject to systematic updates that would consider new data, models, and methods that currently exist within the larger technical community. Likewise, the SSC and GMC models have not been re-assessed such that they represent the center, body, and range (CBR) of technically defensible interpretations (TDI) given the current state of knowledge. As a result, a defensible mean-centered estimate of the seismic hazard at MFC and ATR do not exist currently. The SSHAC Level 1 process implemented for the SRA project provides those estimates, such that evaluation of the criteria and risk analyses can be conducted for purposes of methodology development. Also, this study provides the systematic identification and evaluation of new data, models, and methods, as well as the development of new SSC and GMC models that capture the center, body, and range of technically defensible interpretations.

1.1.2 Fuels Manufacturing Facility (FMF) and Seismic Design

The FMF is located near the southern end of the MFC (Figure 1-2). FMF is on thin soil deposits of 1.5 to 4.6 m (5 to 15 ft) thick overlying subsurface bedrock composed of predominantly basalt with very few sedimentary interbeds. Surficial sediments at MFC are from wind-blown surface soils and local drainage. The sediments are composed of silty loam with basalt cobbles and cinders (Argonne National Laboratory, 1985). For the SRA project, rock surface motions for MFC and site-specific surface motions for FMF are computed by the SSAHC Level 1 PSHA.

The FMF was constructed in 1986 to house fuel manufacturing equipment in support of an operational reactor. The reactor is no longer operational and now the FMF houses research and development activities related to fuel fabrication. The FMF is a one-story structure covered by an earthen berm. A two-story support wing is attached to FMF on its west side, and FMF is directly adjacent to another facility on its south side. The FMF is classified as SDC-3 and its authorization basis earthquake is the horizontal MFC 2,500 yr soil DBE 5% damped spectrum for one soil layer (Payne, 2006a). For the implementation of the methodology, the Design Basis Ground Motion (DBGM) is defined as the authorization basis earthquake for FMF. This study it will be referred to as the “2006 FMF site-specific DBGM.”

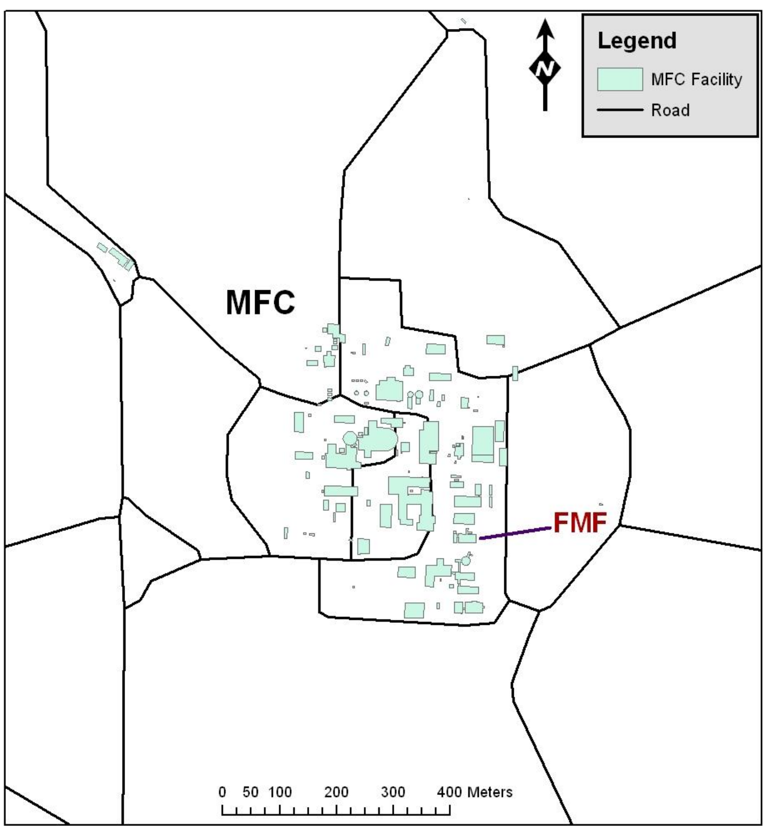

Figure 1-2. Map showing the location of the Fuels and Manufacturing Facility (FMF) at the Materials and Fuels Complex (MFC).

1.1.3 Spent Fuel Handling Recapitalization Project (SFHP) Process Facility and Seismic Design

NRF is located in the south central part of INL within the Big Lost River flood plain (Figure 1-1). Within the NRF complex, the SFHP process facility is located on the northeast corner (Figure 1-3). The SFHP process facility area is underlain by Big Lost River alluvial deposits. The deposits are composed of a near surface layer with sand, clay, and gravel, which overlie a layer of predominantly gravel with sand. Below the gravel layer is a finer grained layer of clay loess (clay, sand, and silt). The alluvial deposits overlie basalt and have a thickness range from 4.6 to 13.7 m (15 to 45 ft) (North Wind Resource Consulting and Rizzo Associates, 2015). For the SSHAC Level 1 PSHA at NRF, rock surface motions and site-specific soil surface motions are computed for the SFHP.

The SFHP process facility is being constructed to handle and process Naval Spent Nuclear Fuel. The SFHP process facility is a steel framed high bay structure, 216 m (710 ft) long (north-south) by 64.6 m (212 ft) wide (east-west), and 32 m (105 ft) tall with insulated metal panels for the siding and roofing. The main high bay area houses two primary water pools interconnected by a narrow canal (3.3 m by 9.1 m deep (11 ft wide by 30 ft deep) in an H-like configuration; each leg (or pool) of the H is 70 m by 15 m (or 230 ft long by 50 ft wide) for processing two types of fuel containers. An exam annex is connected to the process facility on the east side, providing another high bay with overhead crane and central water pool, which is interconnected to the two primary pools (Jacobs Team, 2013).

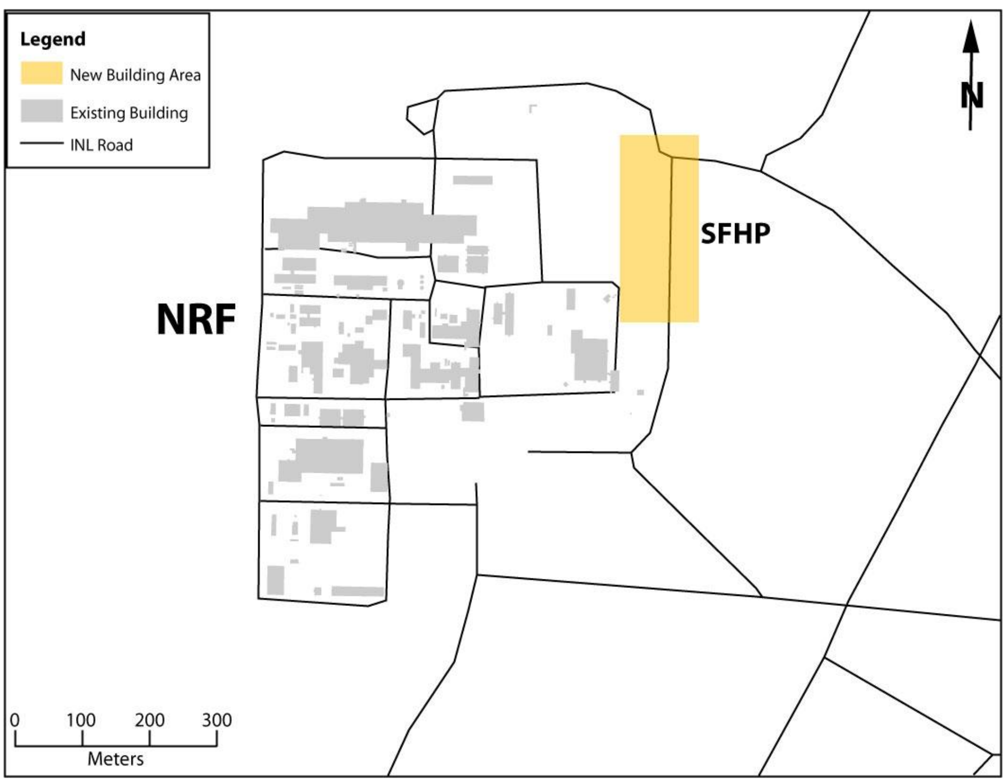

Figure 1-3. Map showing the location of the new Spent Fuel Handling Recapitalization Project (SFHP) process facility area at the Naval Reactors Facility (NRF).

The SFHP process facility and support structures have two safety-related categorizations. The two water pools are embedded pool structures categorized as SDC-5. The high bay structural steel process facility is categorized as safety significant and designed to SDC-3 requirements but designed to prevent system interaction with the SDC-5 pools. The base of the pools and high bay columns will be tied to rock and other support structures will be on soil (Jacobs Team, 2013). For comparisons discussed in Section 10, the SFHP provided "design" rock spectra being used for analysis and design of the new facility. The design rock spectra are based on the 2000 INL PSHA rock hazard levels (URS Greiner Woodward-Clyde Federal Services et al., 2000) and adjustments presented in Payne et al. (2002).

1.1.4 Advanced Test Reactor (ATR) Complex and Seismic Design

The ATR Complex is located in the south central part of INL within the western edge of the Big Lost River alluvial deposits (Figure 1-1). Within the ATR Complex, the alluvial soil deposits above bedrock range in thickness from 6.1 to 18.3 m (20 to 60 ft). The mainstream alluvium is composed predominantly of sand and gravel which overlies a layer of sandy clay or silts. The finer grained layers are more often found just above basalt near the base of thicker alluvial deposits >12 m (40 ft) (Ebasco Services, Inc., 1961a; Redpath Geophysical, Inc., 2001; TRA, 2001).

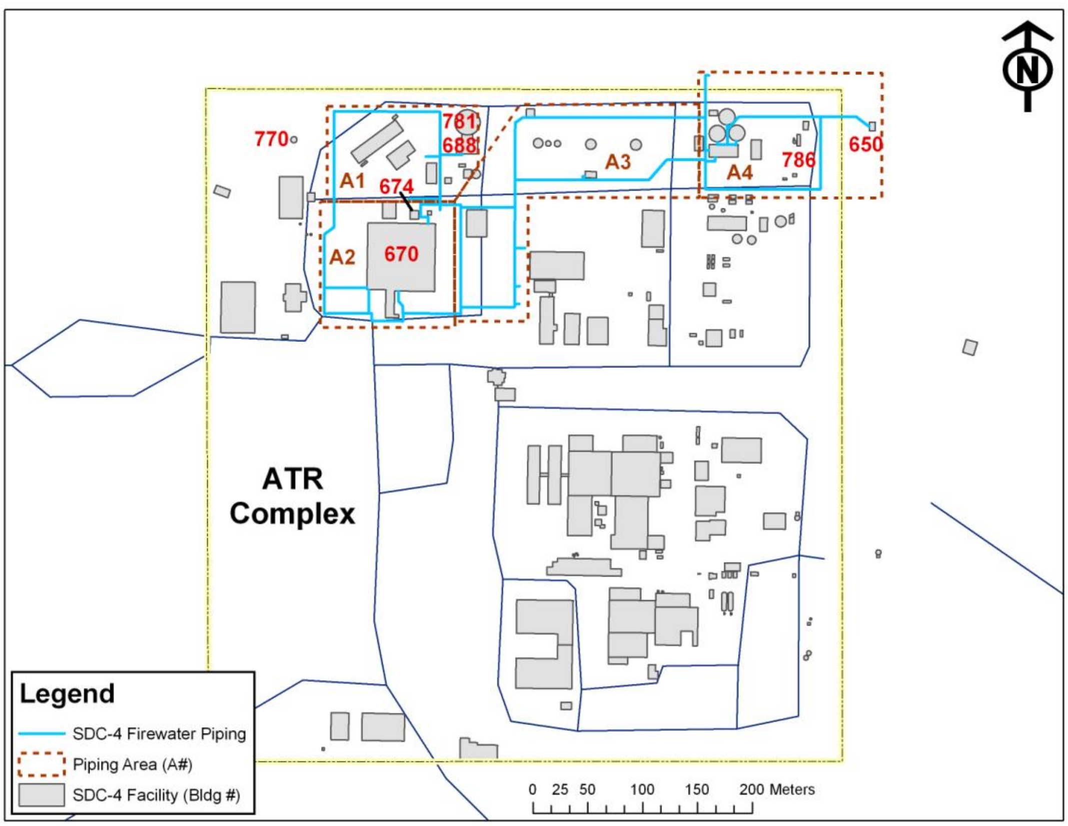

Figure 1-4. Map showing locations of the SDC-4 ATR reactor, support buildings, and sections of firewater piping at the ATR Complex. Firewater piping areas (A#) show sections that are analyzed together in Seismic Probabilistic Risk Assessments (SPRAs).

The ATR Complex houses the ATR reactor, buildings that support reactor operations, and firewater piping, which comprises the Emergency Firewater Injection System (EFIS). The ATR reactor has been in operation since 1969, and is a 250-MW nuclear test reactor designed to study the effects of intense irradiation on samples of reactor materials. The building houses the ATR reactor, primary systems, and operational control equipment. The ATR reactor building's subgrade foundation is supported on rock and drilled piers due to the variable depths to bedrock, 7.3 to 17.4 m (24 to 57 ft). Two-thirds of the foundation footprint is supported directly on basalt bedrock. One-third of the foundation footprint overlies ~6.1 m (20 ft) of sediments and is supported by 1.2-1.8 m (4-6 ft) diameter piers that are embedded 4 ft into rock (Table 1-1).

The ATR reactor (TRA-670) has six support buildings, TRA-770, TRA-781, TRA-688, TRA-674, TRA-786, and TRA-650 that are located in the northern region of the ATR Complex. Firewater piping is interconnected among all of these buildings except TRA-770 which is a vent stack (Figure 1-4). With the exception of TRA-670, all six buildings and firewater piping are founded on or in soil deposits that range in thickness from 6.1 to 18.3 m (20 to 60 ft) above basalt bedrock. Table 1-1 lists the building names and a short description of the buildings including its purpose and relationship to the ATR reactor.

Table 1-1. Description and seismic design basis for SDC-4 structures at ATR.

Name	Building Description	1st Mode Natural Frequency (Hz)	Design Basis Ground Motion (DBGM)
TRA-670	The ATR reactor is a 250-MW reactor designed to study the effects of intense irradiation on samples of reactor materials. The ATR Reactor is a 4,087 m^2 (44,000 ft^2) building with an above grade super-structure and double basement substructure. The super-structure is composed of steel and aluminum weather panels that provide containment. The reactor cavity and heat exchanger pit extend below the second basement to 17.6 m (58 ft). Two-thirds of the foundation is supported directly on basalt bedrock. One-third of the foundation overlies 6.1 m (20 ft) of sediments and is supported by 1.2-1.8 m (4-6 ft) diameter piers that are embedded 1.2 m into rock.	8.4 (substructure) 2.3 (super-structure)	ATR 10,000-yr Rock DBE (Payne et al., 2002) referred to as "2002 ATR rock DBE" in this study
TRA-770	ATR Vent Stack provides a seal and an elevated release point for TRA-670 exhaust. The stack is a concrete structure 76 m (250 ft) high with a 5.7 m (19 ft) diameter at the base and 1.9 m (6 ft) at the top. The stack sits on a concrete base mat that is 10.3 m (34 ft) in diameter and with 2.1 m (7 ft) thickness with its bottom ~2.4 m (8 ft) below grade.	0.5	ATR/INTEC 10,000-yr Soil DBE (Payne, 2006b) referred to as "2006 ATR soil DBE" in this study
TRA-674	The Diesel Building is a 65 m^2 (700 ft^2) slab on grade steel and aluminum paneled structure, which provides weather protection for the emergency diesel generator 674-M-6. The diesel generator provides power to TRA-670 and several other support buildings if there is a loss of commercial power.	4.3	

Table 1-1. Continued.

Name	Building Description	1st Mode Natural Frequency (Hz)	Design Basis Ground Motion (DBGM)
TRA-781	Firewater Storage Tank is a ground-level water storage tank that is a steel circular structure ~23 m (75 ft) in diameter, ~11 m (37 ft) high, and sits on ground surface. It provides a dedicated water source to the Emergency Firewater Injection System (EFIS) pumps located in TRA-688. EFIS provides emergency water injection to TRA-670 should the primary pressure boundary break or develop a leak larger than normal makeup systems can provide.	0.2 (convective) 75.6 (impulsive)	ATR/INTEC 10,000-yr Soil DBE (Payne, 2006b) referred to as "2006 ATR soil DBE" in this study
TRA-688	Firewater Pumphouse is an environmental enclosure to protect two diesel driven EFIS pumps. It is a 234 m^2 (2,520 ft^2) slab on grade, steel structure that butts up against TRA-781. EFIS provides emergency water injection to TRA-670 should the primary pressure boundary break or develop a leak larger than normal makeup systems can provide.	4.4	
TRA-786	The TRA-786 Diesel Power System is dedicated to powering Deep Well #3 in TRA-650. The power system ensures water from Deep Well #3 is available through "critical firewater" paths to TRA-670, thus ensuring long term water is available should commercial power not be recovered before the water in TRA-781 is exhausted. The power system is housed in a trailer setting on ground surface. The diesel fuel tank sits directly on the ground and the electrical switchgear associated with the diesel generator are located on a concrete slab.	2.8	
TRA-650	Deep Well #3 Pumphouse is a ~40 m^2 (427 ft^2) one-story concrete steel frame structure that houses the pump to provide long term water through a "critical firewater" path to TRA-670 should commercial power not be recovered. It can be powered directly from the diesel generator system in TRA-786.	4.5	
Piping Areas (A1 - A4)	Fire-water Piping is a piping system covering ~47,600 m^2 (51,230 ft^2) and buried 2.4 m (8 ft) below the surface that provides water to TRA-670 support facilities, which are located in the northern area of the ATR Complex. In an emergency valves (L-2 and L-7) are closed to ensure that the TRA-670 is given priority over other firewater needs (e.g., includes supply to the low pressure demineralizer system, potable, and fire suppression water).	~0.5	

The ATR reactor (TRA-670), support buildings, and firewater piping are classified as SDC-4 and their respective DBGM are defined for either rock or soil conditions. The DBGMs defined in this study are the authorization basis earthquakes that are identified in the ATR reactor's facility safety analysis report. Table 1-1 lists the DBGMs and the first mode natural frequency for each of the ATR buildings and piping. The DBGM for the ATR reactor is the ATR rock DBE at the 10,000-yr -return period from Payne et al. (2002) and is referred to as "2002 ATR Rock DBE" for this study. Payne et al. (2002) developed a broadened DBE spectrum for rock based on the 2000 INL PSHA UHS for ATR and other nearby facility areas (INTEC, RWMC, and PBF). The DBGM for the six support buildings (TRA-770, TRA-781, TRA-688, TRA-674, TRA-786, and TRA-650) and piping is the ATR/INTEC soil DBE at the 10,000-yr return period from Payne (2006b) and is referred to as "2006 ATR Soil DBE" for this study. Payne (2006b) developed a generic broadened soil DBE spectrum based on site response analyses using time histories compatible with the broadened DBE rock spectrum (Payne et al., 2002) and included soil profiles and properties applicable to both ATR and INTEC.

For the SSHAC Level 1 PSHA, rock surface motions are computed for the ATR reactor building (TRA-670) and site-specific soil surface motions are computed for the six support buildings and firewater piping. To develop site-specific motions for the firewater piping, the region covered by the SDC-4 sections of piping were subdivided into four areas (A1, A2, A3, and A4 in Figure 1-4). The areas are representative of four piping sections that are analyzed together as part of the Seismic Probabilistic Risk Assessments (SPRAs) for the ATR reactor (Pers. Comm. B. Harwood, 2016).

1.2 SSHAC Level 1 Scope and Objectives

The SSHAC Level 1 PSHA for INL is conducted with the scope and objectives to provide input to the risk-informed methodology and to demonstrate the use of SSHAC Level 1 for defining defensible, mean-centered, and well-documented ground motion estimates. Within the context of the risk-informed methodology, the SSHAC Level 1 PSHA provides a defensible, well-documented basis to make comparisons with the existing technical underpinnings of the current seismic design for FMF.

1.2.1 SSHAC Level 1 Framework for the PSHA

The scope of the SSHAC Level 1 PSHA at INL is designed to fully express the uncertainties of the SSC and GMC models to achieve the mean-centered hazard results with adequate technical justification for MFC, FMF, SFHP, and structures at the ATR Complex. A work plan was developed at the beginning and then implemented for the SSHAC Level 1 PSHA prior to each specific study. The work plan was modified to include the ATR buildings and piping areas (see Appendix C).

The SSHAC Level 1 PSHA for INL implemented the "*Evaluation*" and "*Integration*" processes that are essential for a SSHAC study as defined in NUREG-2117 (NRC, 2012a). The SSC and GMC models are developed from compilations of existing data, information from literature, existing studies, and other seismic hazard analyses that have had the benefits of an informed technical community. Where applicable, the SSC and GMC model developments built upon previous INL seismic hazard analyses including the 1996 PSHA at MFC (Woodward-Clyde Federal Services et al., 1996), 2000 PSHA at NRF and ATR (URS Greiner Woodward-Clyde Federal Services et al., 2000), 2006 site response analyses at MFC and ATR (Payne, 2006a; 2006b, respectively), 2010 sensitivity analyses at ATR (Seismic Evaluation Team, 2010), 2011-2013 sensitivity analyses at NRF (AMEC, 2011; 2013), and the Southwestern Unites States (SWUS) SSHAC Level 3 GMC model (GeoPentech, 2015). The *Integration* process included the development of SSC and GMC models that represent the CBR of TDI. Section 2 more fully discusses the implementation of the SSHAC Level 1 process.

The PPRP was integral to the SSHAC Level 1 process providing both *procedural* and *technical* reviews from start to finish. The PPRP performed technical reviews that ensured the full range of data, models, and methods were duly considered by the Technical Integration (TI) Team and all technical decisions were adequately justified and documented. The PPRP performed process reviews that ensured the SSHAC Level 1 PSHA conformed with the requirements of the SSHAC process and to the work plan. Collectively, these two reviews by the PPRP provided oversight and assurance that the *Evaluation* and *Integration* processes of the SSC and GMC model developments in the PSHA logic-tree framework for the SSHAC Level 1 were performed appropriately (see Appendix B for closure letter).

1.2.2 SSHAC Level 1 Hazard Outputs

The hazard outputs were selected to provide inputs to the risk-informed methodology, provide information for SFHP, and be consistent with the SSHAC process. The SSHAC Level 1 PSHA generated both preliminary and final hazard products. The preliminary hazard products included dissection of hazard uncertainty contributions which evaluated sensitivities to the hazard for the SSC and GMC models. The preliminary hazard products included mean seismic hazard curves at Peak Ground Acceleration (PGA) and accelerations at spectral periods of 0.5, 0.2, and 0.1 seconds (or 2, 5, 10 Hz) for MFC rock and FMF soil conditions.

Although not the primary purpose, the SSHAC Level 1 study also provides data, information and recommendations that can be used in a future update of the INL PSHA. Under the SSHAC process, Hazard Input Documents (HIDs) for the GMC and SSC models, and an SSC data summary table were developed (see Appendices G and H, respectively). Methods and models that were considered but not included in the PSHA were also documented (Appendix E).

1.2.2.1 Final Hazard Products for Risk-informed Methodology

The final hazard products included MFC rock and FMF soil conditions in the form of mean seismic hazard curves and Uniform Hazard Response Spectra (UHRS) at PGA and at spectral periods of 0.02, 0.03, 0.05, 0.1, 0.2, 0.3, 0.5, 1, and 2 seconds (5% damping). Seismic hazard curves were computed for annual exceedance frequencies (AEFs) between ~10^{-1} and ~10^{-9} and larger, consistent with the inputs needed for SPRAs. Spectral accelerations defining mean UHRS for return periods of 2,500, 10,000, 25,000 and 100,000 yr were produced to allow calculation of seismic design factors for SDC-3, SDC-4, and SDC-5 per ASCE/SEI 43-05 (ASCE, 2005). These UHRS are then used calculate the Ground Motion Response Spectrum (GMRS) (also referred to as the *DRS* – Design Response Spectrum in ASCE/SEI 43-05). At 10 Hz and PGA, rock and soil seismic hazard curves were computed at the 5th, 15th, 50th, 85th, and 95th percentiles. Also, vertical to horizontal spectral ratio model are provided for rock and soil conditions.

1.2.2.2 Final Hazard Products for Naval Reactors Facility

The final hazard products for NRF included rock and soil conditions specific to the SFHP area in the form of mean seismic hazard curves and UHRS at PGA and at spectral periods of 0.02, 0.03, 0.05, 0.1, 0.2, 0.3, 0.5, 1, 0.15, 3, 5, 7.5, and 10 seconds (5% damping). Seismic hazard curves were computed for AEFs between ~10^{-1} and ~10^{-9} and larger. Spectral accelerations defining mean UHRS for return periods of 2,500, 10,000, 25,000 and 100,000 yr were produced to allow calculation of seismic design factors for SDC-3, SDC-4, and SDC-5 to then calculate the GMRS as per ASCE/SEI 43-05 (ASCE, 2005). Rock and soil seismic hazard curves were also computed at the 5th, 15th, 50th, 85th, and 95th percentiles, and vertical to horizontal spectral ratio model are provided for rock and soil conditions.

1.2.2.3 Fina Hazard Products for Advanced Test Reactor

The final hazard products for ATR included rock and soil results in the form of mean seismic hazard curves and UHRS. Spectral periods for the seismic hazard curves included PGA, 0.02, 0.03, 0.05, 0.075, 0.1, 0.15, 0.2, 0.3, 0.4, 0.5, 1, and 2 seconds. The seismic hazard curves were computed for AEFs between ~10^{-1} and ~10^{-9}. Spectral accelerations defining UHRS were provided at return periods of 2,500, 10,000, 25,000 and 100,000 yr to calculate the GMRS at SDC-4 as per ASCE/SEI 43-05 (ASCE, 2005). Seismic hazard curves were computed at the 5^{th}, 15^{th}, 50^{th}, 85^{th}, and 95^{th} percentiles for PGA. Vertical to horizontal spectral ratio model are provided for both rock and soil conditions.

1.2.3 SSHAC Level 1 Inputs to the Risk-informed Methodology

The primary objective of the SSHAC Level 1 PSHA at MFC, FMF, and ATR is to provide results for six of seven Evaluation Criteria that the Seismic Hazard Periodic Review Methodology (SHPRM) proposes to use for evaluating the need for an update of an existing PSHA (see Appendix I). The SHPRM was developed by the INL Seismic Risk-Informed Methodology Independent Panel (or ISRMIP, 2015). Appendix I only identifies changes and compares results which are then considered inputs to the SHPRM. The evaluations of any identified changes for the criteria and their significance that would support or negate the need for an update is beyond the scope of this report. The evaluation and implementation of the methodology at FMF is documented in Cox et al. (2016). The evaluation and implementation of the methodology at ATR will occur after completion of the SSHAC Level 1 PSHA and will be documented in a separate report.

For the SHPRM, Evaluation Criteria 1 through 4 are related to the seismic hazard analysis. Consistent with DOE-STD-1020-2012 (DOE, 2012a) and ANSI/ANS 2.29 (ANS, 2008a) these Evaluation Criteria are used to evaluate changes in: 1) data, methods, and models; 2) inputs to the hazard such as SSC models, GMC models, treatment of aleatory and epistemic uncertainties, or site response analysis; 3) technical bases or justification; and 4) mean hazard as seen by comparisons of the existing hazard with the new hazard. For input to these four criteria, Appendix I presents a systematic approach for identifying qualitative and quantitative changes and lists these changes to the SSHAC Level 1 PSHA relative to the 1996 and 2000 PSHAs (Woodward-Clyde Federal Services et al., 1996; URS Greiner Woodward-Clyde Federal Services et al., 1999; 2000). Under Evaluation Criterion 4 for quantitative changes, the SSHAC Level 1 PSHA UHRS for MFC rock at 2,500 yr is referred to as “2015 MFC rock UHRS”, and the MFC 2,500 yr rock DBE spectrum from Payne (2006a) is referred to as “2006 MFC rock DBE”. Quantitative comparisons of the 2015 MFC rock UHRS and 2006 MFC rock DBE spectrum are presented and discussed in Section 10.

Evaluation Criteria 5 and 6 relate to facility risk and are used to evaluate the existing seismic design basis relative to target performance goals listed in ASCE/SEI 43-05 (ASCE, 2005). In the initial implementation of the risk-informed methodology, the SSHAC Level 1 FMF soil surface ground motion estimates at the target performance goals for SDC-3 are compared to the DBGM for FMF. For Evaluation Criterion 5, the SSHAC Level 1 FMF soil UHRS at the 2,500 yr return period (referred to as “2015 FMF site-specific UHRS”) is compared with the 2006 FMF soil DBGM spectrum (defined in Section 1.1.2). For Evaluation Criterion 6, design factors as specified in ASCE/SEI 43-05 are applied to the FMF soil UHRS to produce the “2015 FMF site-specific GMRS” which is then compared to the 2015 FMF soil DBGM spectrum. These comparisons are presented and discussed in Section 10.

Evaluation Criterion 7 is related to evaluations of facility-specific risk. Results of implementing Evaluation Criteria 1 through 6 for FMF may lead to a follow-on SPRA including analysis of fragilities of structures, systems, and components, as well as systems models. The 2015 FMF site-specific GMRS and FMF soil hazard curves will be used as inputs to those analyses (Section 10).

For implementation of the methodology at ATR, inputs for Evaluation Criteria 1 through 6 were developed in a similar manner as for MFC and FMF. For Evaluation Criteria 1 through 4, the qualitative changes to the hazard are the same as those identified for MFC and FMF since they are predominantly changes between the SSHAC Level 1 PSHA and previous INL PSHAs. For Criterion 4, the quantitative changes are presented in comparisons of 2016 SSHAC Level 1 hazard curves with the previous hazard curves from the 2000 INL PSHA for rock conditions (URS Greiner Woodward-Clyde Federal Services et al., 2000). For Evaluation Criterion 5, the 2016 SSHAC Level 1 rock and site-specific UHRS are compared with the DBGMs for the 2002 ATR Rock DBE and the 2006 ATR Soil DBE spectra. For Evaluation Criterion 6, the 2016 ATR rock and site-specific GMRS are compared with the DBGMs (2002 ATR Rock DBE and the 2006 ATR Soil DBE spectra). All comparisons are presented in Section 10. If results of implementing Evaluation Criteria 1 through 6 for ATR lead to a follow-on SPRA, the applicable 2016 SSHAC Level 1 results in Section 10 will be used as inputs to those analyses.

1.3 Report Contents and Organization

The report contains sections specific to the SSHAC Level 1 PSHA and supplemental information in appendices. The next two sections complete the general introduction and overview of the SSHAC Level 1 PSHA. Section 2 describes the organization of, processes used in, and participants involved in the SSHAC Level 1 study. Section 3 discusses the key tasks and activities performed for the PSHA. The remaining sections describe the SSHAC Level 1 PSHA outputs derived from the tasks and activities. The supporting data and information are included in the tectonic setting (Section 4), SSC database of geologic and geodetic data (Section 5), the earthquake catalog (Section 6), and GMC databases consisting of the site velocity profiles, regional recordings, kappa and Q estimates, and selected GMPEs (Section 7). The respective SSC and GMC models and their technical bases are presented in Sections 8 and 9. The hazard calculations, sensitivity analyses, and results are presented in Section 10. Finally, Section 11 lists the references for the report.

Appendices A through I contain information supporting various aspects of the SSHAC Level 1 PSHA. Appendix A lists the biographies of the SSHAC Level 1 participants. Appendix B has the PPRP closure letter. A copy of the work plan is included in Appendix C for completeness even though it was issued as a separate report. Appendix D expands upon development of the earthquake catalog beyond the summary provided in Section 6. Appendix E discusses methods and models considered but not used in the PSHA. Appendix F has the index of electronic files for the report, including the SSC summary data table. The GMC and SSC HID are in Appendices G and H, respectively. Appendix I includes the approach for identifying changes and a detailed table listing the changes to the hazard for Evaluation Criteria 1 through 4 of the SHPRM.

2. SSHAC Level 1 Process

The SSHAC Level 1 PSHA was initiated as an activity under the SRA project and was implemented consistent with SSHAC guidance NUREG/CR-6372 (NRC, 1997) and NUREG-2117 (NRC, 2012a). The SRA project was performed by Battelle Energy Alliance (BEA) for the DOE Nuclear Energy (NE) office. The SRA project is under the auspices of BEA's INL Director, Office of Nuclear Assurance and Safety, who will receive the SRA project deliverables. The SSHAC Level 1 PSHA is one of three activities being performed for the SRA project. BEA's Project Technical Performer will provide the outputs from the SSHAC Level 1 PSHA which will then be inputs to the "Seismic Risk Methodology" and "Fragilities & PRA" activities (Figure 2-1). The SRA selected the SSHAC Level 1 PSHA as part of the development of a new risk-informed methodology (Section 1).

2.1 Implementation of the SSHAC Level 1 Process

As with any SSHAC process, including the SSHAC Level 1 PSHA at INL, the fundamental goal is to carry out properly and document completely the activities of evaluation and integration, defined as follows:

- *Evaluation*: The consideration of the data, models, and methods proposed by the larger technical community that are relevant to the hazard analysis.
- *Integration*: Representing the center, body, and range of technically defensible interpretations in light of the evaluation process.

These two activities were carried out by adhering to the work plan, "*Work Plan for the SSHAC Level 1 Probabilistic Seismic Hazard Analysis at MFC*," which was developed as the first step in the SSHAC Level 1 process. The work plan was developed at an initial kick-off meeting held February 23-25, 2015 at INL. The work plan identifies the SSHAC work flow processes, communications, roles and responsibilities of participants, key tasks and activities, and schedule. The work plan is reproduced in Appendix C and its implementation is summarized here in Section 2.

Per the work plan, the *Evaluation* and *Integration* activities were conducted in the SSHAC Level 1 PSHA by implementing the steps shown in Figure 2-2. The work plan identified the existing data and models to be compiled for the SSC and GMC models and housed within the SSHAC Level 1 PSHA database by the Data Base Manager (Section 2.2.5). It also identified the key tasks and activities (Section 3) to be completed as part of the Evaluation and Integration activities. These two activities were carried out by expert evaluators and integrators which comprised the TI Team. The TI Teams performed the responsibilities of evaluators and integrators (Section 2.2.1) to develop the SSC and GMC models and logic tree structure for the PSHA. At times, some members of the TI Teams took on the role of resource expert or proponent expert (Section 2.2.2). A Specialty Subcontractor used existing data to calculate some of the model components for the GMC model (Section 2.2.4). The TI Teams developed the SSC and GMC HIDs which were then given to the Hazard Analyst who performed the PSHA calculations (2.2.4). The SSHAC Level 1 PSHA at INL is completely documented though this report and associated appendices, which also include the data summary table for SSC. The PPRP provided *procedural* and *technical* reviews throughout the SSHAC Level 1 PSHA (Section 2.2.6).

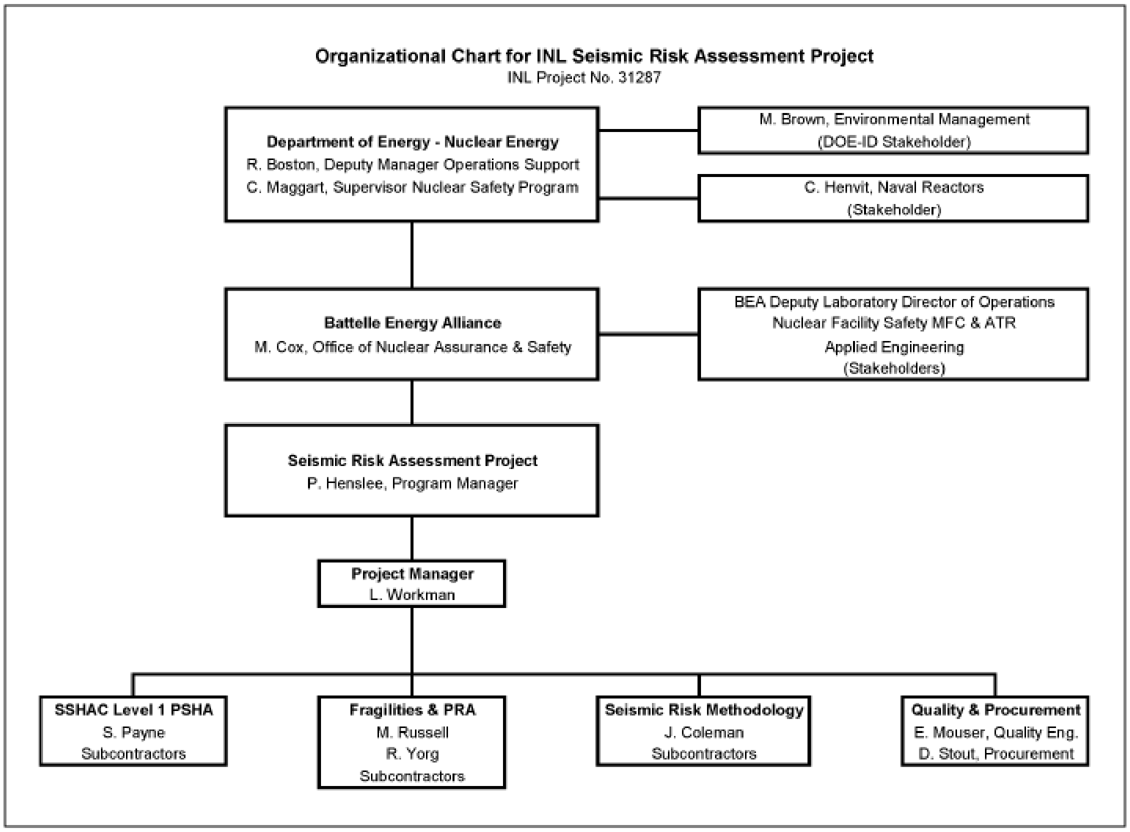

Figure 2-1. Organizational chart for INL Seismic Risk Assessment Project.

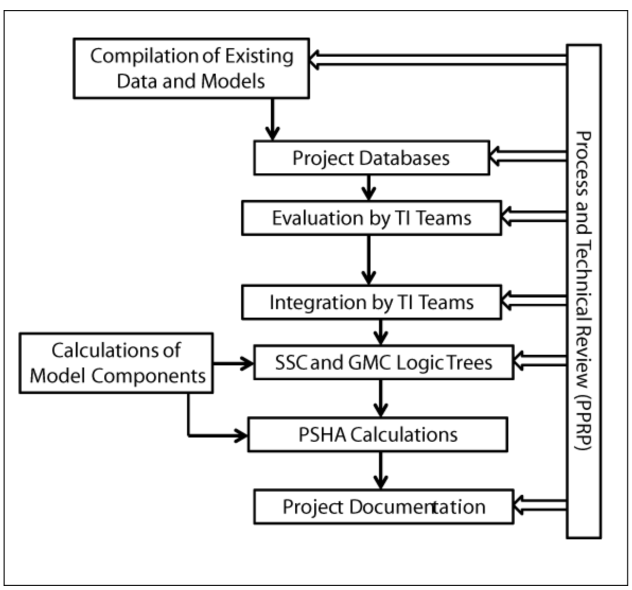

Figure 2-2. Flow chart shows the components and work flow of the SSHAC Level 1 PSHA at INL.

2.2 Roles and Responsibilities

The SSHAC process has defined roles and responsibilities to interface with the SRA project, SFHP point of contact, and conduct the *Evaluation* and *Integration* activities of the SSHAC process. Table 2-1 summarizes the roles of the participants, their names, and their corresponding responsibilities. The SSHAC Level 1 PSHA activity interfaces with the SRA project and SFHP through Suzette Payne who is the Project Technical Performer for BEA (Figure 2-1). In this role, she interfaces with the SRA Project Manager (Lannie Workman), SRA Quality Engineer (Evert Mouser), and NRF's SFHP point of contact (Gary Anderson). Since the SSHAC Level 1 PSHA at INL was staffed by a small number, participants fulfilled responsibilities for more than one role as discussed below for implementation of the SSHAC process.

2.2.1 Technical Integration (TI) Teams

The TI Teams were responsible for developing the SSC and GMC models and logic-trees, which together defined inputs to the SSHAC Level 1 PSHA calculations for MFC and FMF. Four participants, Ryan Coppersmith, Suzette Payne, Robert Youngs, and Valentina Montaldo Falero, fulfilled the roles and responsibilities for the SSC and GMC TI Teams (Table 2-1). Each TI Team member took on the role of *Evaluator Expert* and *Integrator Expert*.

As an *Evaluator* expert, a TI team member objectively examined available data and various models, challenged the technical bases and underlying assumptions of models, and, in some cases, tested models against observations. They also:

- Completed key tasks and activities (Section 3) identified in the work plan
- Identified hazard-significant issues and applicable data to address those issues
- Compiled available data into a SSHAC Level 1 project database
- Evaluated data relative to their quality and relevance for constructing SSC and GMC models
- Identified the full range of data, models, and methods that exist in the technical community.

In light of their evaluations of the data, models, and methods in the professional literature, TI team members as *integrators* built models (logic trees) that captured their assessments of knowledge and uncertainties. They also developed and refined some of their own models and methods. The TI team developed the HIDs for the SSC and GMC models and provided them to the Hazard Analyst.

2.2.2 Resource Experts and Proponent Experts

When applicable, TI team members fulfilled the responsibilities of resource and proponent experts. Since there was limited interaction with Proponent Experts and Resource Experts under a SSHAC Level 1 process, the TI teams relied primarily on available data and literature to make their evaluations. When appropriate, a TI Team member took on the role of a *Resource Expert*, one who presents data in an impartial manner to the TI Team for their use in the evaluation process. For example, Suzette Payne provided site-specific subsurface data for MFC and FMF, INL earthquake data, and geodetic velocity data to the TI Team. A *Proponent Expert* advocates particular models and methods for the consideration by the TI Teams. In this role, Suzette Payne advocated the use of a geodetic rate model to include the geodetically expressed "Centennial Shear Zone" in the SSC model.

2.2.3 Specialty Contractor

A Specialty Contractor performs calculations that support an SSC or GMC model but is not a member of the TI Team since he/she is not involved in the Evaluation or Integration activities. For the SSHAC Level 1 PSHA, Pacific Engineering and Analysis (Walt Silva and Robert Darragh) used existing earthquake data to calculate estimates of kappa and Q and generated amplification models for rock and soil conditions (Table 2-1). These products were provided to the TI Team for evaluation and integration.

2.2.4 Hazard Analyst

The hazard analyst is responsible for executing all PSHA calculations and deaggregations for sensitivity studies according to the HIDs developed by the SSC and GMC TI Teams. Valentina Montaldo Falero performed these responsibilities with support from Robert Youngs for the SSHAC Level 1 PSHA (Table 2-1).

2.2.5 Database Manager

The Database Manager is responsible for establishing and managing the necessary systems to document and compile all data and information collected by the TI Teams. Suzette Payne managed the password-protected web-based portal, SharePoint site on an INL server. The web site held documents (e.g., draft reports, final versions, references, and regulations), data (e.g., seismicity catalog), web links for other resources (e.g., SWUS PSHA), and calendar for the SSHAC Level 1 PSHA. It facilitated the transmittal of data and information among TI Team members and the PPRP. Ryan Coppersmith managed the Geographical Information System (GIS) and compiled various data sets along with their geographical reference points. The GIS database helped the TI Team to evaluate different data sets on maps and ensured consistency among inputs to the SSC and GMC models.

2.2.6 Participatory Peer Review Panel (PPRP)

The PPRP is responsible for *technical* and *procedural* reviews to ensure the SSHAC approach is implemented per regulatory guidance. For the technical reviews, the PPRP ensures that the full range of data, models, and methods have been duly considered in the assessment, and all technical decisions are adequately justified and documented. For the procedural reviews, they ensure that the SSHAC Level 1 PSHA conforms to the requirements of the SSHAC process level. They also ensure adequate oversight and assurance that the *Evaluation* and *Integration* aspects of the TI Teams' assessments have been performed appropriately.

For the SSHAC Level 1 PSHA, the PPRP's participation began at the initial kick-off meeting where they provided input to the development of the work plan. After which they reviewed the draft work plan and provided approval of the final work plan. Throughout the SSHAC process, they participated in all scheduled conference calls and reviewed the preliminary hazard results at the July 7, 2015 on-site meeting at INL. The PPRP addressed concerns of the TI Team, guided selection of sensitivity analysis, reviewed SSC and GMC model development prior to preliminary and final hazard calculations, reviewed the SSC and GMC HIDs, and reviewed PSHA results and sensitivity analyses. They revised the draft report and concurred with the final report (Appendix B).

2.3 Communications and Schedule

The SSHAC Level 1 PSHA participants communicated through the use of web based systems and via conference calls to complete the key tasks and activities (Section 3). INL's "PSHA Doc Center" SharePoint web site served as the reservoir for SSHAC Level 1 PSHA data, files, references, documents, and the SSC and GMC HIDs. It facilitated transmittals of the SSC and GMC inputs from the TI team

Table 2-1. Participants, roles, and responsibilities of the SSHAC Level 1 PSHA.

Role	Participant	Responsibilities
Project Manager	Lannie Workman[1]	Coordinate organizational and administrative aspects of the Seismic Risk Assessment (SRA) Project. Also serves as the project manager for the NRF work.
Project Technical Performer	Suzette Payne[1]	Manage project work and delivery of the products from the SSHAC Level 1 PSHA to the SRA project (Figure 2-1) and to Gary Anderson (NRF).
Quality Engineer	Evert Mouser[1]	Review development and implementation of Quality Assurance requirements of the SRA.
SSC and GMC Technical Integration (TI) Teams	Ryan Coppersmith[2] Suzette Payne Robert Youngs[3] Valentina Montaldo Falero[3]	Develop the SSC and GMC models and logic-trees to define inputs to the PSHA calculations. Perform Evaluation and Integration processes to develop SSC and GMC models. Develop the Hazard Input Documents (HIDs) and provide them to the Hazard Analyst. Fully document the SSHAC Level 1 PSHA study.
Hazard Analyst	Valentina Montaldo Falero Robert Youngs	Execute all PSHA calculations (preliminary and final) and deaggregations for sensitivity studies and documents the final hazard results.
Database Manager	Ryan Coppersmith Suzette Payne	Establish and manage all the data and information collected by the TI Teams.
Specialty Contractor	Walt Silva[4] Robert Darragh[4]	Use data to calculate parameters and associated uncertainties for GMC models at the direction of the GMC TI Team.
Resource and Proponent Experts	Ryan Coppersmith Suzette Payne Robert Youngs Valentina Montaldo Falero	When applicable, fills the responsibilities of resource and proponent experts. As a Resource Expert, present data in an impartial manner to the TI Teams for their use in the evaluation process. As a Proponent Expert, advocate a particular model or method for the consideration by the TI Teams.
Participatory Peer Review Panel (PPRP)	Kevin Coppersmith[2] Adrian Rodriguez Marek[5]	Responsible for *technical* and *process* reviews to ensure the SSHAC approach is implemented per regulatory guidance and the SSHAC Level 1 PSHA work plan. Ensures that the full range of data, models, and methods have been duly considered, the center, body, and range of the technically defensible interpretations have been captured in the integration process, and all technical decisions are adequately justified and documented.
1. Battelle Energy Alliance 2. Coppersmith Consulting 3. AMEC Foster Wheeler 4. Pacific Engineering and Analysis 5. Virginia Tech		

members to the hazard analyst. The TI team communicated with the PPRP via conference calls every 3 to 4 weeks. The calendar on SharePoint contained the schedule for deliverables, milestones, conference calls, targeted dates for completion of tasks and activities, deadlines for documentation, and on-site INL meetings. Table 2-2 shows the schedule used to complete the INL SSHAC Level 1 PSHA. For the SRA project regarding MFC and FMF, the dates of tasks and activities were designed to facilitate presenting preliminary results on July 8, 2015 and completion of the SSHAC Level 1 PSHA by October 29, 2015 (actual date completed). The SSHAC Level 1 PSHA for NRF was completed by March 3, 2016 and for ATR, by September 26, 2016.

2.4 Quality Assurance

The Quality Assurance (QA) requirements for the SSHAC Level 1 PSHA are consistent with BEA's QA program, which is commensurate with American Society of Mechanical Engineers (ASME) Nuclear Quality Assurance (NQA) NQA-1 2008/2009 Addendum. The QA requirements including the applicable regulatory requirements are contained in the work plan (see Appendix C). As applicable to their tasks and activities, all participants in the SSHAC Level 1 PSHA followed and implemented the QA requirements.

2.4.1 Applicable Codes, Regulations, and Guidelines

The following documents provided guidance and requirements for the work performed for the SSHAC Level 1 PSHA:

- DOE O 430.1C, Facility Safety (DOE, 2012b)
- DOE-STD-1020-12, Natural Phenomena Hazards Analysis and Design Criteria for DOE Facilities (DOE, 2012a)
- NUREG-2117, Rev. 1, Practical Implementation Guidelines for SSHAC Level 3 and 4 Hazard Studies (NRC, 2012a)
- NUREG/CR-6728, Technical basis for revision of regulatory guidance on design ground motions: Hazard and risk-consistent ground motion spectra guidelines (NRC, 2001)
- NUREG/CR-6372, SSHAC – Senior Seismic Hazard Analysis Committee (NRC, 1997)
- RG 1.208, A performance-based approach to define the site-specific earthquake ground motion (NRC, 2007)
- ANSI/ANS 2.26, Categorization of nuclear facility structures, systems, and components for seismic design (ANS, 2004; R2010)
- ANSI/ANS 2.27, Criteria for Investigations of Nuclear Facility Sites for Seismic Hazard Assessments (ANS, 2008a)
- ANSI/ANS 2.29, Probabilistic Seismic Hazard Analysis (ANS, 2008b)
- ASCE/SEI 43-05, Seismic design criteria for structures, systems, and components in nuclear facilities (ASCE, 2005)
- ASME NQA-1 2008/2009 Addendum, Quality Assurance Requirements for Nuclear Facilities Applications (ASME, 2009).

Table 2-2. Schedule for the SSHAC Level 1 PSHA.

Task or Activity	Date Completed
SSHAC Level 1 PSHA study initiated by the Seismic Risk Assessment (SRA) project	January 20, 2015
Field trip and work plan meeting at INL	February 23-25, 2015
INL regional earthquake recordings sent to Specialty Contractor	March 18, 2015
Work plan issued	March 20, 2015
1st Conference call and webinar	March 20, 2015
2nd Conference call and webinar	April 10, 2015
Updated earthquake catalog sent to Hazard Analyst	April 23, 2015
3rd Conference call and webinar	May 1, 2015
4th Conference call and webinar	May 29, 2015
5th Conference call and webinar	June 22, 2015
SSC and GMC HIDs sent to Hazard Analyst	June 30, 2015
PPRP review preliminary hazard results and sensitivities at INL	July 7, 2015
Presentation to SRA project at INL	July 8, 2015
6th Conference call and webinar	July 24, 2015
Report outline completed	July 24, 2015
Initiated writing draft sections for the report, first reviews of the sections by the PPRP, and responses to PPRP comments by the TI team	July 27, 2015
SSC models finalized	July 31, 2015
GMC models finalized	August 14, 2015
7th Conference call and webinar	August 18, 2015
Final hazard calculations and sensitivity analyses	August 28, 2015
Conference call to revise work plan for NRF	August 28, 2015
Sections and all reviews completed for draft report	October 5, 2015
Draft final report assembled into BEA's format and transmitted to PPRP	October 19, 2015
Work Plan issued with NRF revisions	October 28, 2015
PPRP Closure Letter with final report	October 25, 2015
Final report (Revision 0) issued and sent to SRA project	October 29, 2015
GMC HID for NRF to Hazard Analyst	November 13, 2015
Final hazard calculations	December 2, 2015
Presentation of hazard results to SFHP at INL	December 10, 2015
Draft report, revision 1 with NRF PSHA	February 17, 2016
Reviews from PPRP; comments resolved; and final report to PPRP	February 25, 2016
Final report (Revision 1) issued with PPRP closure letter	March 3, 2016
Work Plan issued with ATR revisions	April 7, 2016
Changes to SSC HID to Hazard Analyst	May 6, 2016

Table 2-2. Continued.

Task or Activity	Date Completed
GMC HID for ATR to Hazard Analyst	June 30, 2016
Rock hazard results	July 12, 2016
Soil hazard results	August 15, 2016
Draft report, revision 2 with ATR PSHA	September 12, 2016
Reviews from PPRP; comments resolved; and final report to PPRP	September 19, 2016
Final report (Revison 2) issued with PPRP closure letter	September 26, 2016

3. Key Tasks and Activities

3.1 Project Work Plan Summary

The first step of the project was the development of the PSHA work plan for the sites at INL, which identified all of the project activities, roles and responsibilities of project participants, schedules, action items, milestones, and products to be developed. The work plan outlined the sequence of steps for a SSHAC Level 1 project as illustrated in Figure 2-2. The PPRP was put in place early in the project and its two members were present during the initial kick-off meeting that was held to outline the document. Further, the PPRP was provided with the work plan for an early understanding of the manner in which the project would be conducted. The work plan discussed the objectives of the SSHAC Level 1 study for the FMF site along with a convenient working document to guide all participants with a clear and consistent description of the scope, schedule, and products of the PSHA. The work plan remained an active working document throughout the project in order to express any changes to scope, schedule or actions required during the project. The key activities included in the work plan are described in Sections 3.2 to 3.9 and the work plan itself is included as Appendix C of this report.

3.2 Database Development

This task included the compilation of applicable SSC and GMC data and information for use by the TI Teams in their evaluations. The relevant datasets were identified during the kick-off meeting through presentations of existing data and recommendations from the PPRP. As a SSHAC Level 1 study, a focus of the data compilation effort stemmed from existing data used during the 1996 PSHA and recommendations and analyses presented in the 2010 SET study. Further, any new information developed since these studies were considered as part of the database development.

3.2.1 SSC Data

Data compilation began at the time of project authorization and continued to the point at which the final SSC models were developed. To the extent possible, mapped information was compiled in GIS formats that allowed for various combinations of spatial layers. The Database Manager(s) took an active role in compiling data, including the information made available at the kick-off meeting. Data sources included readily available information from the following:

- Professional literature
- GIS data held at INL
- Data held in the public domain
- Unpublished data.

In addition to the GIS database, data summary tables document the data from literature and reports along with the reasoning for including or not including data in a model.

3.2.2 GMC Data

The GMC database includes three types of data for GMC model development: 1) GMPEs based on the SWUS GMC model; 2) data that can be used to constrain the applicability of the GMPEs to the site conditions at MFC, FMF, SFHP (NRF), and ATR; and 3) characterization of the representative near-surface geological profiles that define the target site conditions to which the prediction equations will need to be adjusted. For this effort no new data were collected. Analyses were performed using existing earthquake data recorded at MFC, NRF, and ATR and shear-wave velocities measured for previous projects at MFC, NRF, and ATR. These data were identified at the kick-off meeting for MFC and for revisions to the work plan prior to the start of the NRF and ATR PSHAs. The timely completion of the SWUS GMC models allowed for their inclusion in the SSHAC Level 1 PSHA.

3.3 Identification of Significant Issues

A key task of the PSHA is to identify which elements of the SSC and GMC models have the greatest influence on the hazard results so that the TI teams can focus their efforts on the development of those parts of the hazard input models. This is particularly true in a SSHAC Level 1 study where the hazard significant issues can be tested for sensitivity and documented for future, higher level SSHAC studies. Identifying the greatest contributors to the overall uncertainty allows data-compilation and data-collection efforts to be as focused as possible. To meet these objectives, the TI teams met during a kick-off meeting to identify and begin to compile pertinent datasets through discussion of past studies and visualization of the current state of knowledge. Additionally at the kick-off meeting and during conference calls as the SSHAC Level 1 study progressed, sensitivity analyses were determined as part of the preliminary results.

3.4 SSC and GMC Model Development

For the SSHAC Level 1 study, the SRA project requested that preliminary results be provided prior to the final hazard results. Additionally, the work plan outlined the schedule for the SRA to include preliminary results to examine sensitivities and important contributors to the hazard. For their purposes, the SRA project specified that ground motion estimates at the 2,500 yr return period be provided for soil conditions at the FMF site at four spectral frequencies (PGA, 2, 5, and 10 Hz). As a result, preliminary SSC and GMC models were developed based on the key tasks and activities listed in the work plan. The SSC included models for regional source zones, host zone, geodetic rate zone, volcanic source zones, and fault sources. The GMC model used the SWUS model adjusted for the host zone which includes the MFC rock and FMF soil conditions, and appropriate incorporation of uncertainties. Preliminary hazard results also permitted examination of the SSC and GMC models and their uncertainty contributions to the SSHAC Level 1 PSHA. Following presentation of the preliminary results to the SRA project and evaluations by the PPRP and TI team, final SSC and GMC models were completed.

For the NRF PSHA, only the final hazard results were provided to the SFHP. The hazard included the same SSC model but with the addition of the Cascadia Subduction zone. The SFHP process facility has large water pools which may be impacted by long period motions from very distance large moment magnitude (**M**) earthquakes (**M** 9). The GMC model used the SWUS model adjusted for the host zone and the SFHP rock and soil conditions and included appropriate incorporation of uncertainties.

For the ATR PSHA, only the final hazard results were provided to the SRA project. The hazard included minor modifications to the SSC model for the Centennial Shear Zone and Big Lost fault because new data became available after completion of the NRF SSHAC Level 1 study. The GMC model used the

SWUS model adjusted for the host zone and ATR rock and soil conditions and included appropriate incorporation of uncertainties.

3.5 Development of the Hazard Input Document

According to the definition given in NUREG-2117 (NRC, 2012a), the HID provides the essential elements of the SSC and GMC models that the Hazard Analyst needs to calculate the seismic hazard. The HID is owned by the TI Teams and expresses all details of the models, including logic trees, parameter distributions, and derived parameters, but it does not include any discussion or description of the technical bases for the model elements (which are in Sections 8 and 9). For the SRA project, two rounds of HID development occurred during the course of the project: 1) one following the development of the preliminary SSC and GMC models, and 2) one following the finalization of the SSC and GMC models. The final GMC and SSC HIDs are in Appendices H and G, respectively, for MFC, NRF, and ATR.

3.6 Hazard Calculations

Preliminary and final hazard calculations were performed for the SSHAC Level 1 PSHA. The preliminary hazard calculations for MFC were based on the first draft of the HID and were included in the presentation to the SRA project at a meeting in Idaho Falls on July 8, 2015. After finalization of the SSC and GMC models, the final hazard calculations were conducted for MFC rock and FMF site-specific conditions as specified by the SRA project. Important contributors to the hazard results were assessed through sensitivity analyses for MFC, NRF, and ATR. These analyses identified the SSC and GMC issues of greatest significance to mean hazard at the annual frequencies of interest. Likewise, the key contributors to the uncertainty in the hazard were identified in terms of various annual frequencies of interest and specific response periods.

3.7 Development of Draft and Final Reports

For the SRA project, draft and final reports were prepared of the SSHAC Level 1 PSHA. Due to the accelerated schedule for the SRA project, the draft report was completed after presentation of preliminary results. Draft report sections and appendices were outlined by the TI Team and with concurrence of the PPRP. As sections were completed, the PPRP performed an initial preliminary review. Minor comments were tracked in the electronic documents whereas major comments were provided separately. The TI team addressed the PPRP's comments through documented responses, and changes were made to the report as necessary (see Appendix F). Once all comments were incorporated or resolved, a final draft report containing all sections was provided to the PPRP for final review and preparation of the closure letter. The PPRP's review and closure letter fulfilled the review process for SRA project. The final report as Revision 0 was issued October 29, 2015.

For the SFHP and ATR, draft and final reports were also prepared. The same review steps were followed for development of draft and final reports for Revision 0. Revisions were made to include NRF and ATR in drafts of the SSHAC Level 1 PSHA report. Each draft report was provided to the PPRP for review. Minor comments were tracked electronically in the report, and major PPRP comments were addressed through documented responses (electronic file listed in Appendix F). Changes were made to where necessary to each report and a final review by the PPRP provided concurrence with these changes. The PPRP's review and closure letter fulfilled the review process for SFHP and ATR. The final reports were issued as Revision 1 on March 3, 2016 for the SFHP and as Revision 2 on September 23, 2016.

4. Tectonic and Seismologic Setting of the INL

The INL is located in the Eastern Snake River Plain (ESRP), which is the eastern part of the Snake River Plain (SRP). The SRP is a large physiographic region (~90 km wide and 560 km long) with low-relief and covered by basaltic lava flows and sediments. The SRP extends in a broad arc across southern Idaho from the Yellowstone Plateau in Wyoming on the east to the Oregon-Idaho graben in Oregon on the west. It transects and sharply contrasts with the surrounding mountainous country of the Basin and Range, Yellowstone Plateau, and Idaho batholith (Figure 4-1). The SRP and surrounding region have a geologic history of extension and volcanism since the early Cenozoic which gives rise to contemporary earthquake sources associated with normal faulting, volcanic processes, and zones of seismicity. Modifications to the ESRP's crust due to volcanism also contribute effects that impact ground motions.

This section covers the geologic history and tectonic setting which provide the context for local geology at INL and the present-day zones of active faulting, distributions of seismicity, and stress field orientations. This section also provides the supporting bases for assessing the SSC and GMC models such as the types of seismic sources, the rates of deformation and earthquake occurrence, ranges of earthquake magnitudes, applicable GMPEs, and site-specific subsurface conditions at the site of interest. For magnitudes of selected earthquakes discussed in this section E[**M**] is listed, which represents the expected value of the true moment magnitude (**M**) (see Section 6.1).

4.1 Geologic History and Tectonic Setting

The SRP and surrounding mountainous regions underwent thrust faulting during the Paleozoic and normal faulting during the early Cenozoic to present day. Mountains northwest and southeast of the ESRP have thick sequences of Precambrian through Paleozoic sedimentary strata that are within westward-dipping thrust sheets that formed during east-directed Mesozoic compressional tectonism (Skipp and Hait, 1977; Link et al., 1988; Lewis et al., 2012). Thrust faulting produced the Idaho-Wyoming thrust belt that extends through eastern Idaho. In early Cenozoic time, eastward-directed thrust faults and belts of deformation may have continued uninterrupted from southeast to northwest through the ESRP (Oldow et al., 1989). Also during Mesozoic and early Cenozoic thrusting, large volumes of granitic rock were emplaced by igneous intrusions into the upper crust which produced the Idaho Batholith (54-100 Ma) in central Idaho (Gaschning et al., 2009) (Figure 4-1).

Northwest of the ESRP from ~50 Ma to present day, three episodes of extension occurred with different orientations that were likely associated with changes in the Farallon and North American plate convergence rates (Wernicke et al., 1987; Janecke, 1992). In the Eocene (48-49 Ma), NW-SE oriented extension produced the NE-trending Trans-Challis fault zone located on the east side of the Idaho batholith and northern end of the Lost River fault (McIntyre et al., 1982). It also formed NE-trending normal faults with a few kilometers of offset which are evident within the Lost River, Lemhi, and Beaverhead mountain ranges (Janecke, 1992). At 48-46 Ma, the direction of extension changed to WSW-ENE and SW-NE producing N- to NNW-striking normal faults with >10 km offsets in Idaho and southwestern Montana (Janecke, 1992). Also at this time, Eocene Challis volcanism (40-51 Ma) produced volcanic deposits that covered much of south-central Idaho (McIntyre et al., 1982; Gaschning et al., 2009; Lewis et al., 2012) (Figure 4-1). From 16-17 Ma to present, NE-SW oriented extension forms the three prominent NW-trending normal faults (Lost River, Lemhi, and Beaverhead) and other normal faults within the Centennial Tectonic Belt (CTB) (Anders et al., 1989; Richins et al., 1987; Janecke, 1992; Rodgers et al., 2002). The CTB is defined as a NE-trending zone of Holocene normal faulting and high seismicity along the northwest margin of the ESRP from central Idaho to southwest Montana (Stickney and Bartholomew, 1987) (Figure 4-1).

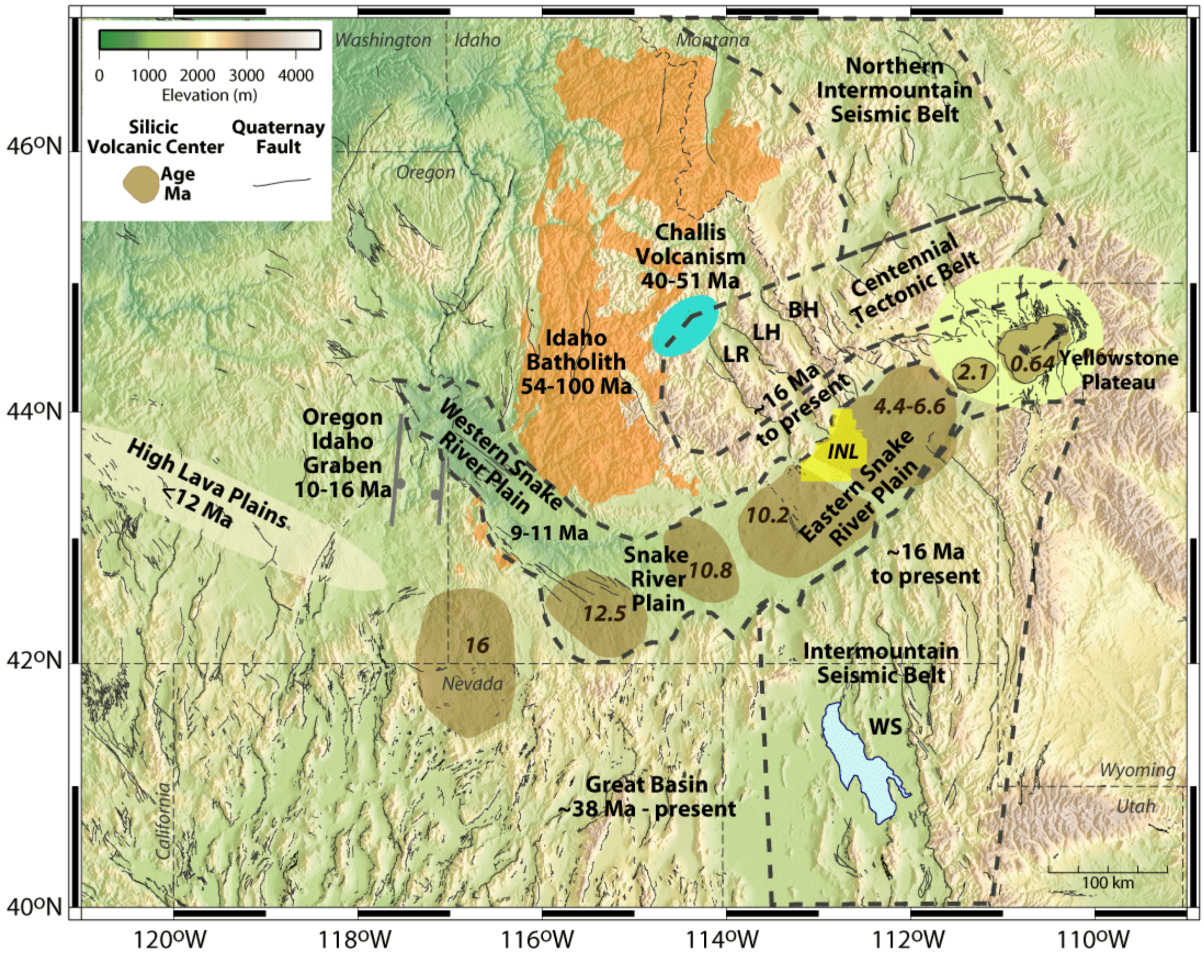

Figure 4-1. Map shows the locations and ages of major geologic features relative to the INL. Normal fault labels are: BH – Beaverhead, LH – Lemhi, LR – Lost River, and WS – Wasatch.

To the south and southeast of the ESRP, the onset of extension in the Great Basin started ~38 Ma and continues to present day (e.g., Wernicke et al., 1987; Ramelli and dePolo, 2011; Hammond et al., 2014). Although extension may have begun earlier, present-day NW- to N-trending normal faults in southeast Idaho began forming ~16 Ma, and their geometries appear to coincide with the earlier formed thrust faults (Rodgers et al., 2002). They are also located within the Intermountain Seismic Belt (ISB) which is a zone of concentrated seismicity marking the eastern boundary of the actively extending Great Basin (e.g. Smith and Sbar, 1974; Smith and Arabasz, 1991) (Figure 4-1). The central part of the ISB extends from the Wasatch fault (in Utah) to the Yellowstone Plateau (in Wyoming). Its northern zone extends north of the CTB into Montana and follows a structural belt of Cenozoic basins bounded by Quaternary faults of diverse trends (Smith and Arabasz, 1991).

In the past 17 Ma, the SRP and nearby regions have undergone extensive bimodal volcanism and crustal modifications associated with the passage of Yellowstone hotspot (Figure 4-1). Volcanic deformation in eastern Oregon and the SRP is accepted by many to have resulted from the interaction of the Yellowstone hotspot or mantle plume with the Earth's crust (e.g., Leeman, 1982; Pierce and Morgan, 1992; 2009; Geist and Richards, 1993; Shervais and Hanan, 2008; Smith et al., 2009). In eastern Oregon, the N-trending, topographically-subdued synvolcanic Oregon-Idaho graben formed from 16 to 10 Ma shortly after eruptions of the largest volumes of flood basalts (Cummings et al., 2000). The western Snake River Plain (WSRP) comprises a NW-trending graben hypothesized to have formed coeval with two different positions of the Yellowstone hotspot. Graben formation is thought to have initiated at 17 Ma in response to crustal tumescence above the Yellowstone plume head and formed between 9 and 11 Ma coeval with the 12.5 Ma silicic volcanism (Wood and Clemmens, 2002; Shervais et al., 2002).

The ESRP region represents the NE-trending track of the Yellowstone hotspot which encompass silicic volcanic centers active from 12 to 4.4 Ma (e.g. Morgan and McIntosh, 2005; Bonnichsen et al., 2008; Pierce and Morgan 1992; 2009; Anders et al., 2014) (Figure 4-1). At each active center, mafic crustal intrusions produced large-volume silicic eruptions that were subsequently covered by basaltic volcanism (e.g., Leeman et al., 2008; McCurry et al., 2008). Following hotspot volcanism, periodic basalt dike intrusions continued into the Pleistocene and Holocene in the SRP and eastern Oregon (Hart et al., 1984; Kuntz et al., 1986; 1992; Cummings et al., 2000; Shoemaker and Hart 2002; Bondre 2006). The most recent basalt volcanism occurred ~2,200 yrs ago in the Great Rift volcanic rift zone south of INL (Kuntz et al., 1986) (Figure 4-2).

The large influxes of basaltic magma and caldera eruptions significantly modified the crust beneath the ESRP and caused subsidence. The crystallization of large volumes of basaltic magma in the mid-crust produced a thick lens of anomalously dense rock referred to as the mid-crustal sill (see Section 4.3 for further discussion). The added weight of this material to the crust, along with the contraction due to

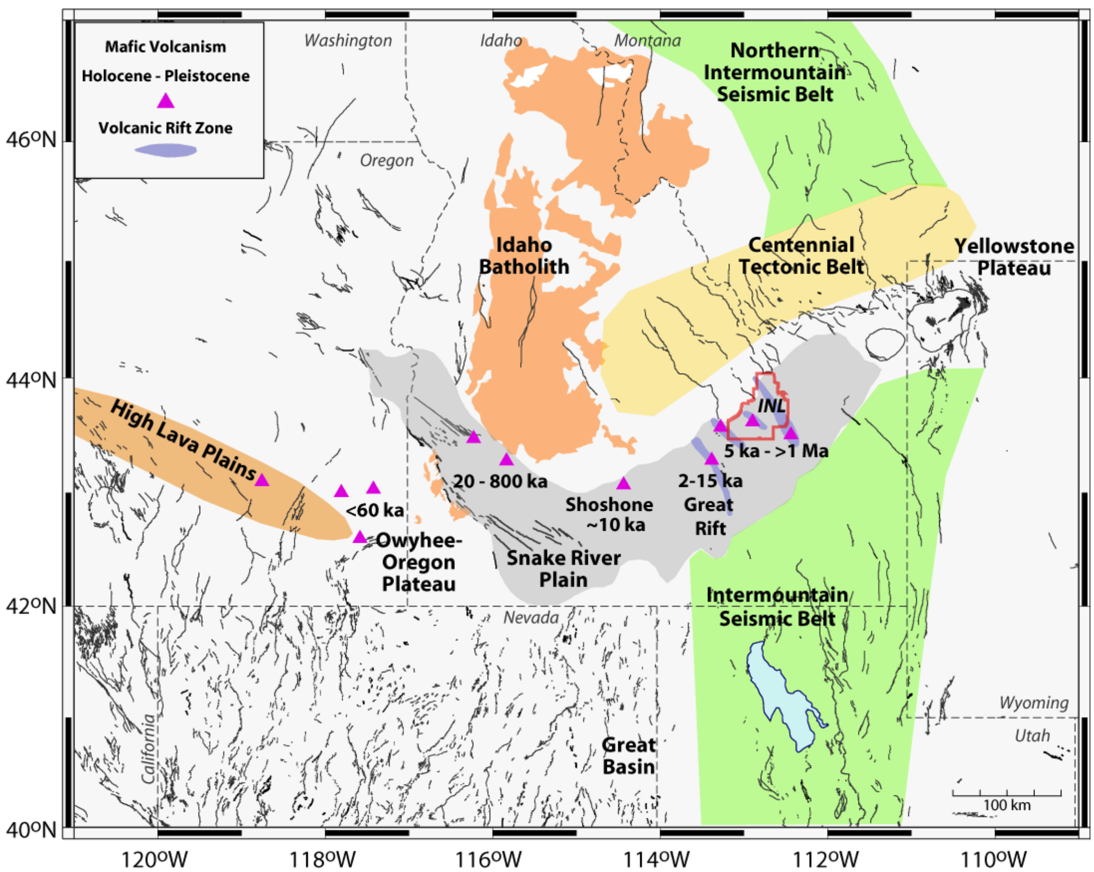

Figure 4-2. Map showing locations of the four volcanic rift zones near INL and ages of recent basalt volcanism (pink triangles).

cooling after passing over the hotspot, has caused the ESRP to subside (Brott et al., 1981; Rodgers et al., 2002). Subsidence of >4 km is estimated to have occurred prior to and coinciding with silicic magmatism before 6 Ma. Subsidence of ~1 km is estimated to have occurred over the last 4 m.y. (Rodgers et al., 2002).

NE-trending normal faults within narrow zones (~30 km) in the mountain ranges along the north and south margins of the ESRP are thought to reflect extension due to crustal flexure (Zentner, 1989; Rodgers et al., 2002; Janecke, 2007). Along the northern margin of the ESRP, surface tilts and 1-20° structural dips of late Cenozoic rocks toward the ESRP are interpreted to be indicative of crustal flexure due to subsidence (McQuarrie and Rodgers, 1998; Rodgers et al., 2002). While no discernable strike-slip offsets in geology have been found along the margins of the ESRP (e.g., Rodgers et al., 2002), geophysical studies reveal subsurface normal faults (presumably NE-trending) at three locations along the northwest margin of the ESRP (Sparlin et al., 1982; Pankratz and Ackerman, 1982; Stanley, 1982; Elbring, 1984; Young and Lucas, 1988) (Figure 4-3).

Recent geodetic studies indicate that at present the ESRP is deforming at a much slower rate than the rapid rate of extension occurring in the CTB (Payne et al., 2008; 2012). The different strain rates are accommodated by right-lateral shear in the Centennial Shear Zone (CSZ) (Payne et al., 2008). The CSZ is defined as a 40-45 km wide zone along the northern margin of the ESRP where differential motion is

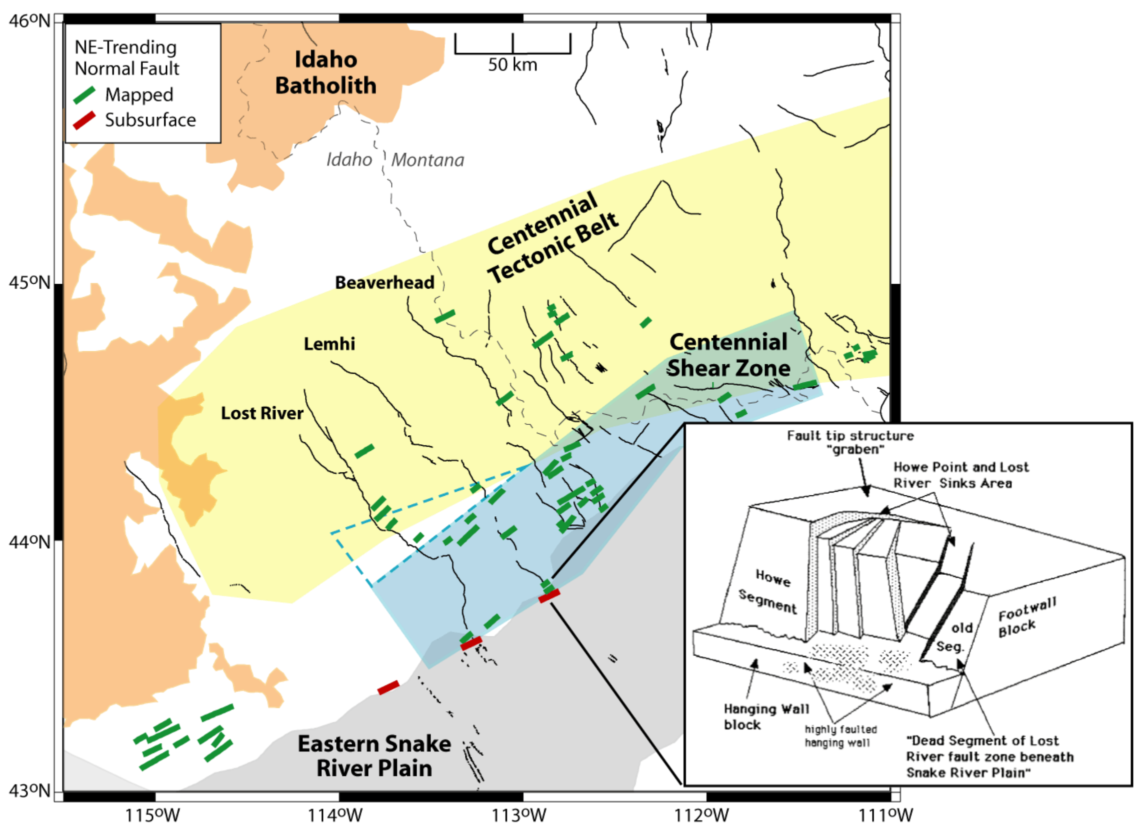

Figure 4-3. Locations of the NE-trending normal faults (shown in green) in the Centennial Tectonic Belt and Centennial Shear Zone northwest of the Eastern Snake River Plain. Inset is from Bruhn et al. (1992).

distributed and may include components of deformation due to strike-slip faulting, distributed simple shear, regional-scale rotation, or some combination of these (Payne et al., 2013). In the CSZ, Payne et al. (2013) hypothesizes that right-lateral strike slip motions may be accommodated on the NE-trending faults (Figure 4-3). As an example, Bruhn et al. (1992) interpreted that NE-striking cross faults associated with an asymmetrical NE-trending graben in the footwall of the Lemhi fault provides a means to accommodate differential motion between the southern end of the Lemhi fault and ESRP over the last 4 m.y. Another example is offered by Parker and Sears (2016) who found a distributed strain across high angle conjugate strike-slip faults in an 800-m thick quartzite comglomerate of Neogene age within the CSZ.

4.2 Surface Geology at INL

The INL is covered by sediments and basalt lava flows (Figure 4-4). Surface sediment deposits are of diverse origins at INL depending on their location relative to the Big Lost River and volcanic zones (e.g., Gianniny et al., 2002; Bestland et al., 2002; Geslin et al., 2002). A wide band of Quaternary fluvial sediments extend along the course of the Big Lost River from the southwestern corner of INL to the Lost River Sinks area near borehole 2-2A (Figure 4-4). The Big Lost River has been flowing to the north across INL for at least the past 2 m.y. (Hodges et al., 2009). Three facility areas located along the Big Lost River, NRF, ATR, Idaho Nuclear Technology and Engineering Center (INTEC) are within alluvial deposits consisting of sands, silts, gravel and clay of <30 m over basalt lava flows (Scott, 1982; Kuntz et al., 1994). At some locations immediately above bedrock and below Big Lost River alluvial deposits is an older alluvium composed of fine-grained sediments of sandy clays, clayey sands, and fine silty sands primarily derived from wind blown loess (e.g., EG&G Idaho Inc., 1984; 1988; Hull, 1989; Golder Associates, 1992). Northern INL areas are covered by lacustrine deposits from Pleistocene Lake Terreton and Holocene to upper Pleistocene eolian sand and wind-blown silt (loess) with varying thickness (Scott, 1982; Kuntz et al., 1994).

At MFC, surface sediments are relatively thin (<14 m). MFC is located within the Axial Volcanic Zone (Figure 4-5); a zone in the central part of the ESRP where more numerous basaltic eruptions formed a topographically higher region that does not receive alluvial stream deposits (Hackett et al., 2002). Consequently, soil deposits originate primarily from wind-blown sediments and localized drainages. The sediments at MFC are composed of silts and sands with a variable underlying layer of silty, sandy gravel. The gravel is composed of weathered basalt cinders and scoria fragments to boulder size, similar to the debris at the top of basalt lava flows (e.g., Dames and Moore, 1965; Argonne National Laboratory, 1985). At FMF, the sediments thicknesses range from 1.5 to 4.6 m (Argonne National Laboratory, 1985).

Surface basalt lava flows at INL range in age from <15 ka to 1.2 Ma (Figure 4-4). Although their vents are not situated on the INL, four Holocene basalt lava fields erupted along the Axial Volcanic Zone (Figure 4-5) between about 5 and 13 ka (Kuntz et al., 1986). In one case, the 13.4 ka Cerro Grande lava field (Qba south of INTEC on Figure 4-4) crosses the southern INL boundary. Quaternary basaltic volcanism on the ESRP has largely involved mild, effusive outpourings of fluid lava flows from eruptive fissures and small, low-lying shield volcanoes (Greely, 1982; Kuntz et al., 1992).

Volcanic vents on the ESRP are concentrated in NW-trending and NE-trending linear belts (Kuntz et al., 1992; Hackett and Smith, 1994; Hackett et al., 2002) (Figure 4-5). The NW-trending belts have associated ground deformation features produced from shallow dike intrusion (<4 km depth) and are referred to as volcanic rift zones (VRZs). ESRP VRZs are polygenetic features that formed through numerous cycles of volcanism. Investigators hypothesize that magma in the form of elongated sills and dikes having dimensions of 10’s of km in length and <1-21 m wide ascend from the upper mantle (~60 km depth) and may pond below or near the base of the mid-crustal sill (23-31 km) before ascending to the surface (e.g., Leeman, 1982; Kuntz, 1992; Hughes et al., 1999; Shervais et al., 2006; Holmes et al., 2008). As a dike ascends and dilates or laterally propagates in the shallow subsurface, ground deformation features form above and ahead of it (Figure 4-6). In the VRZs, ground deformation features generally

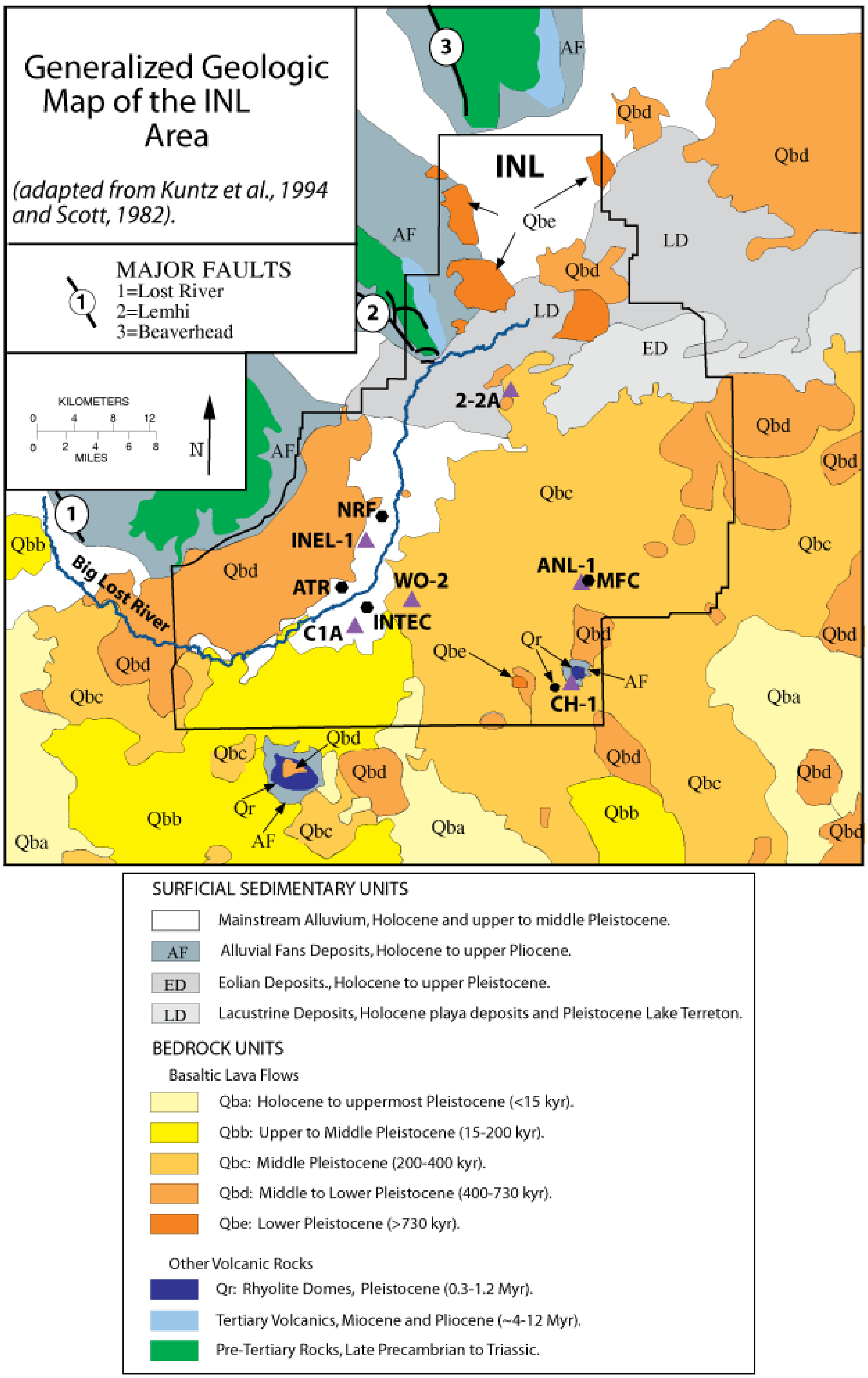

Figure 4-4. Geologic map of the INL. Purple triangles show locations of deep drill holes. See Acronym List for facility area abbreviations.

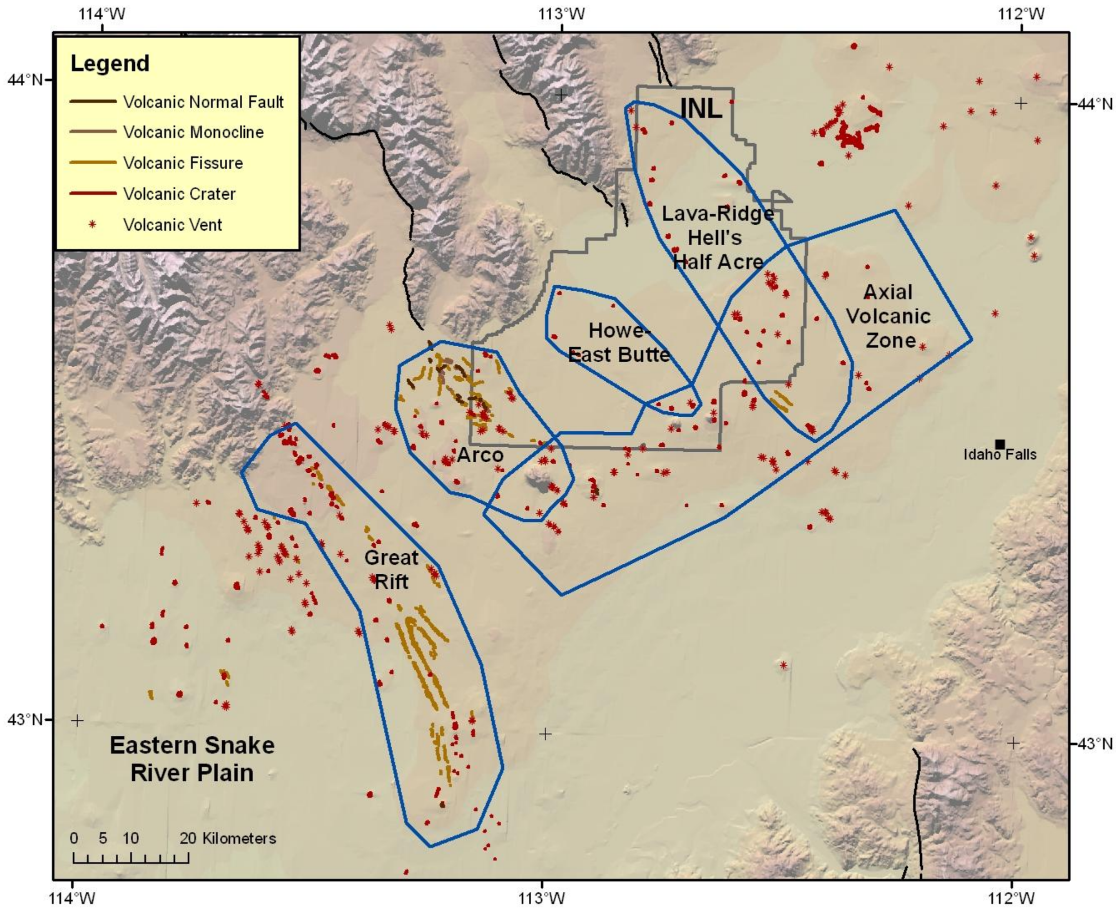

Figure 4-5. Map of the volcanic rift zones and Axial Volcanic Zone based on the boundaries from Hackett et al. (2002).

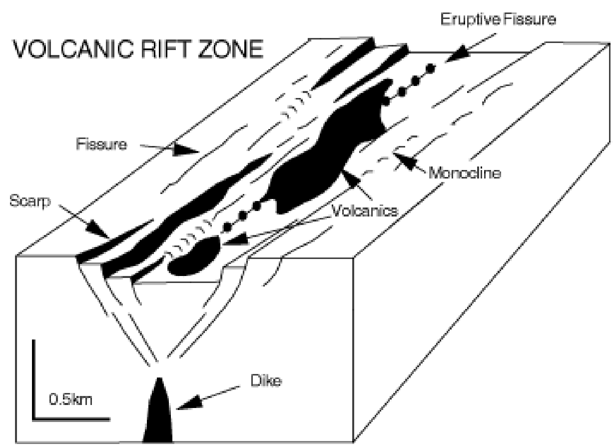

Figure 4-6. Diagram shows ground deformation features in a volcanic rift zone produced by dike-intrusion (Smith et al., 1996).

include fissures, small normal faults, grabens, and monoclines (e.g., Kuntz et al., 1992; Kuntz et al., 1994; Kuntz et al., 2002). They have ages that range from the Holocene to Pleistocene (Kuntz et al., 1994).

Three of the four NW-trending VRZs cross the INL and two VRZs intersect with the NE-trending Axial Volcanic Zone (Hackett et al., 2002) (Figure 4-5). The 80-km-long and 8-10 km-wide Great Rift VRZ is located south of the INL. The Great Rift VRZ has well-developed and aligned basalt volcanic vents and dike-induced deformational features that formed during eight episodes of volcanism over the last 15,000 yr (Kuntz et al., 1988). The Arco VRZ is more diffuse and diachronous, with fissures, monoclines, small normal faults, and vents dispersed across an ~18-km-wide belt that formed by multiple cycles of volcanism during the period 600 ka to 10 ka. The Lava Ridge - Hells Half Acre VRZ is a strongly diachronous feature ~16 km wide; its northern portion is occupied by vents with lavas 1.2 Ma in age, and its southern terminus is marked by vents, dike-induced graben and a 5.2 ka lava field. The Howe-East Butte VRZ is poorly expressed surficially, and is largely covered by fluvial and lacustrine sediments on the central INL (Kuntz et al., 1992). Five vents and several isolated fissures may be associated with a positive, NW-trending aeromagnetic anomaly (Hackett et al., 2002).

The most voluminous and recent volcanism in the INL area occurred during the past 1.2 Ma along the NE-trending Axial Volcanic Zone (AVZ), which is a broad, constructional-volcanic highland consisting of coalesced basaltic shield volcanoes, tephra cones and isolated silicic domes (Hackett et al., 2002). The AVZ forms a topographic divide along the ESRP axis. Basaltic dike-intrusion processes in the AVZ are probably similar to those of VRZs, but increased magma supply along the ESRP axis and the predominance of large shield volcanoes have likely covered most of the dike-induced surface deformation features.

Several small (<7 km^3) rhyolite domes were emplaced during the past 1.2 Ma along the axis of the ESRP. There are two Pleistocene rhyolite domes (~0.6 Ma) located in the southeast corner of INL (Figure 4-4). The Quaternary rhyolitic domes postdate the earlier caldera-related silicic volcanism by about 3 m.y., and they are compositionally dissimilar to the caldera rhyolites, suggesting they are distinct volcanic eruptions (Leeman, 1982; McCurry et al., 2008).

4.3 Subsurface Geology at INL

Hotspot-related, large-scale intrusions, melting, and volcanism significantly modified the crust of the ESRP and caused subsidence that has allowed infilling of the ESRP by basalt lava flows and sediments. Geophysical data reveal a thin layer (<6 km) of volcanic rocks and sediments overlying Paleozoic sediments, a granitic upper crust, and lower crust with partial melt above the mantle (Figure 4-7). At mid- to lower-crustal depths (10-26 km), active and passive seismic studies indicate a 10-16 km thick dense, high-velocity mafic sill beneath the ESRP (e.g. Braile et al., 1982; Sparlin et al., 1982; Peng and Humphreys 1998; Shervais et al., 2006; Stachnik et al., 2008; Yuan et al., 2010). DeNosaquo et al. (2009) used gravity, seismic, thermal, rheological and petrological data to model the density structure of the ESRP crust (42 km thick). Their results indicate a 2-km thick zone of partial melt and 3-km thickened (or underplated) lower crust below the mid-crustal sill. The ESRP’s crust is different from the crust beneath the CTB region northwest of the ESRP. Passive and active seismic studies there show that the crust is unaltered by hotspot volcanism and lacks a mid-crustal sill (Sheriff and Stickney, 1984; Peng and Humphreys, 1998; Stickney, 1997).

The added weight of the mid-crustal sill to the crust, along with the contraction due to cooling after passing over the hotspot, is thought to have caused the ESRP to subside (e.g., Brott et al., 1981; Rodgers et al., 2002). As a result, the ESRP has accumulated 0.6 to ~2 km of basalt lava flows inter-layered with sediments (Doherty et al. 1979; Twining and Bartholomay, 2011). At INL, many shallow boreholes, six deep boreholes, and geophysical investigations show a sequence of alternating layers of basalt lava flows and poorly consolidated sediments extending to depths of 660 to 1,100 m (Figure 4-8). The deep

a)

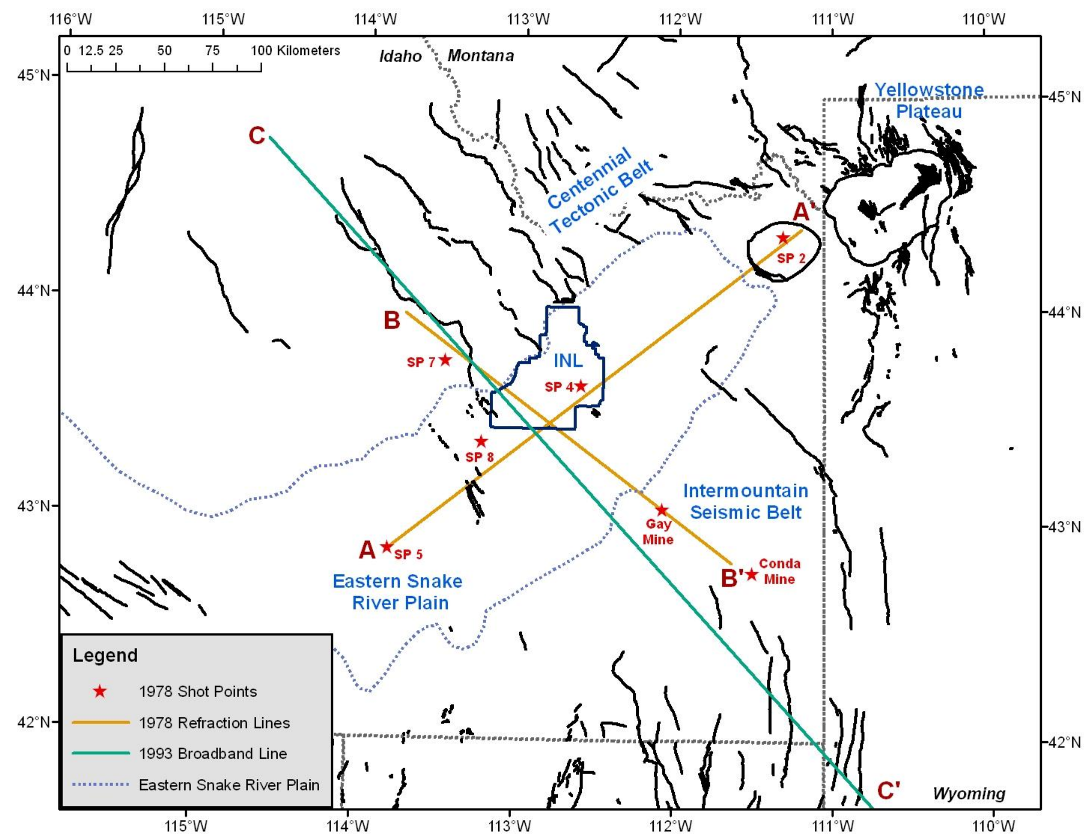

Idaho
Montana
0 12.5 25 50 75 100 Kilometers
Yellowstone Plateau
Centennial Tectonic Belt
INL
Intermountain Seismic Belt
Eastern Snake River Plain
SP 2
SP 4
SP 5
SP 7
SP 8
Gay Mine
Conda Mine
Wyoming
Legend
1978 Shot Points
1978 Refraction Lines
1993 Broadband Line
Eastern Snake River Plain

b)

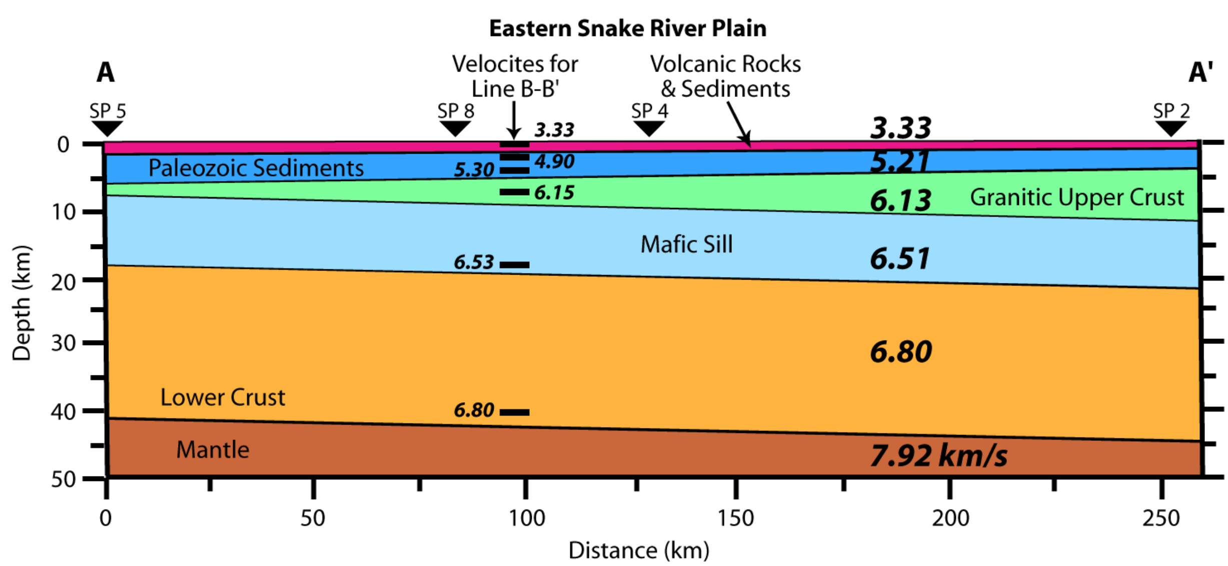

Eastern Snake River Plain
A
A'
Velocites for Line B-B'
Volcanic Rocks & Sediments
SP 5
SP 8
SP 4
SP 2
Paleozoic Sediments
Granitic Upper Crust
Mafic Sill
Lower Crust
Mantle
3.33
4.90
5.30
6.15
6.53
6.80
5.21
6.13
6.51
7.92 km/s
Depth (km)
Distance (km)

c)

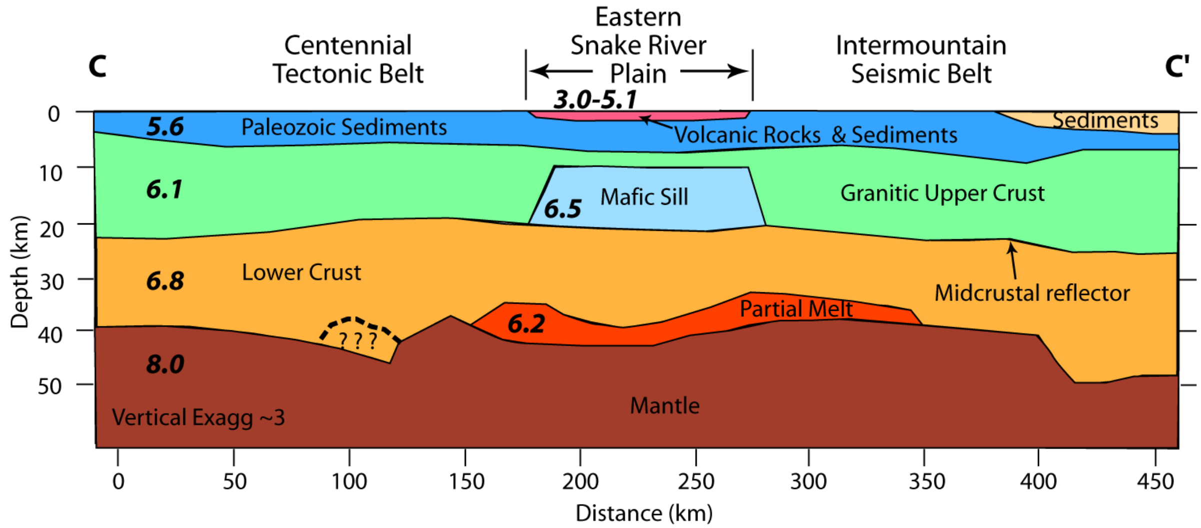

Figure 4-7. (a) Map shows locations of cross sections shown in b and c. (b) Crustal composition and compression-wave velocities (Vp) for cross section A-A’ from the 1978 seismic refraction study are shown in large bold type (Braile et al., 1982). Vp for refraction line B-B’ (not shown) are listed in small bold type with short black line indicating depths for Vp (Sparlin et al., 1982). (c) Crustal composition and Vp for cross section C-C’ from the 1993 teleseismic receiver function study using broadband stations (Peng and Humphreys, 1998).

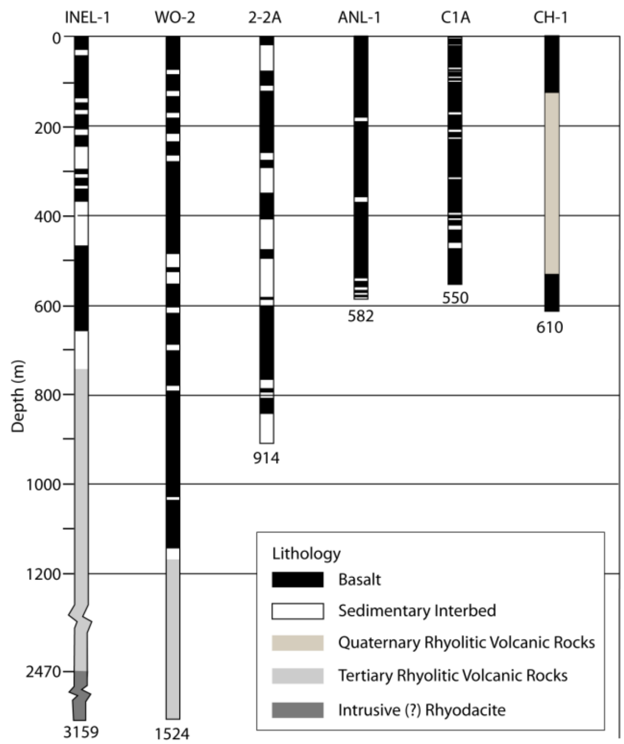

Figure 4-8. Schematic drawing showing the lithology for deep boreholes at INL (see Figure 4-4 for locations).

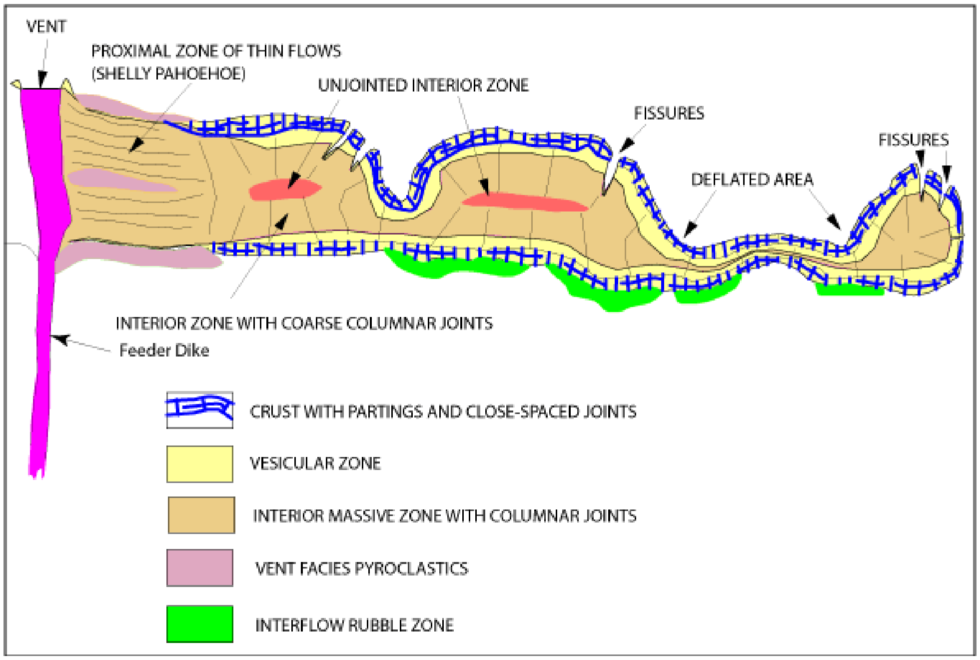

Figure 4-9. Schematic cross section shows the structure of basalt lava flows in the ESRP.

boreholes indicate that the interbedded sequence of basalt and sediments overlies rhyolitic deposits associated with Late Tertiary silicic volcanic centers to at least 3 km depth (Doherty et al. 1979).

Surface basalt lava flows on and near the INL range in age from <15,000 to >730,000 yr (Kuntz et al. 1994). Ages and locations of these flows indicate basalt volcanism has been temporally sporadic and spatially wide-ranging (Figure 4-4). Periods of basaltic volcanic activity produced sequences of multiple lava flows several tens to hundreds of meters thick (Figure 4-8). Depending on the location relative to source vents, repeated volcanic activity produced laterally complex sequences of basalt flows having the different facies. An idealized section in Figure 4-9 shows the distribution of vertical and horizontal facies variation for a typical basalt lava flow. From bottom to top, basalt lava flows are composed of a basal rubble zone, a lower vesicular zone, a massive columnar jointed zone, an upper vesicular and fissured zone, and a cap of platy jointed crust. The near vent structure of a lava flow is typified by thin, vesicular, platy flows (shelly pahoehoe). Also, pyroclastic ash and breccia layers are commonly interwoven within the thin proximal flow layers. With increasing distance from the vent, the shelly pahoehoe flows grade rapidly into the layered facies structure, described above, which typifies the medial and distal portions of the lava flow. For example, borehole INEL-1 is located between the Howe - East Butte and Lava Ridge - Hells Half Acre VRZs and far from the AVZ (Figures 4-4 and 4-5). INEL-1 has basalt flows with more distal facies variations due to the longer distances of flows from the source vents. In contrast, MFC has basalt flows with proximal to medial facies variations indicating closer source vent locations (Figure 4-4).

During long periods of quiescence between volcanic eruptions, sediments accumulated to thicknesses ranging from <1 m to >90 m (Figure 4-8). Since the sedimentary depositional processes operating today likely represent those operating in the geologic past, similar types of sediments are thought to make up the sedimentary interbeds in the basalt sequences of the subsurface. In general, lower percentages of sedimentary interbeds are observed in boreholes to the south near the Arco VRZ (borehole C1A in Figure 4-8) and east near the AVZ (borehole ANL-1 at MFC). Higher percentages of sedimentary interbeds (up to 50%) as well as thicker surficial sediments are observed in boreholes along the western ESRP margin

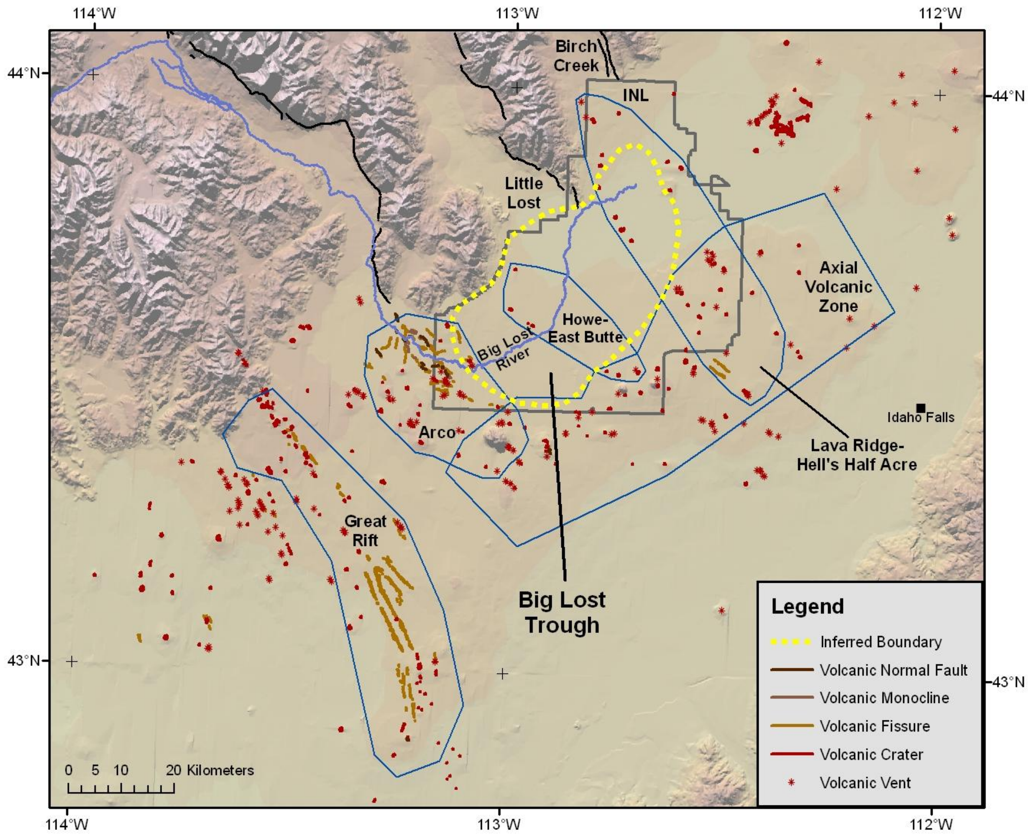

Figure 4-10. Map shows the locations of the Big Lost Trough at INL.

and within the Big Lost River flood plain (boreholes INEL-1 and 2-2A). Thicker sedimentary interbeds occur in the deeper parts of the basalt sections (Figure 4-8).

The western region receives sediments from the Big Lost River, the Little Lost River, and Birch Creek which terminate in sinks and playas within a closed basin referred to as the Big Lost Trough (BLT) (Gianniny et al., 1997; Geslin et al. 1999). The BLT is hypothesized to be a subsiding under filled basin that has been accumulating sediments and basalt lava flows for possibly the last 2.5 m.y. (Blair, 2001; Bestland et al., 2002; Geslin et al., 2002). Boundaries of the BLT include the northwest margin of the ESRP, VRZs on its northern and southern ends, and the AVZ to the east (Figure 4-10). Correlations of sediments and basalt flows within selected boreholes were used to estimate post-depositional elevation changes of 100-200 m over distances of 10-25 km (Blair, 2001; Geslin et al., 2002). Several mechanisms are hypothesized for the post-depositional deformation, including differential subsidence coincident with elevated development of VRZs and the AVZ, flexure from loading by the mid-crustal sill, deposition across an active fault system associated with faulting on buried caldera or Basin and Range normal faults, and rapid sedimentation followed by valley-cutting and subsequent infilling with basalt flows (Blair, 2001; Geslin et al., 2002; Gianniny et al., 2002). Other investigators suggest that subsurface sediment and basalt layers can be correlated differently and in a manner that do not necessarily support a structurally controlled basin for BLT (Geist et al., 2002; Helm-Clark et al., 2006).

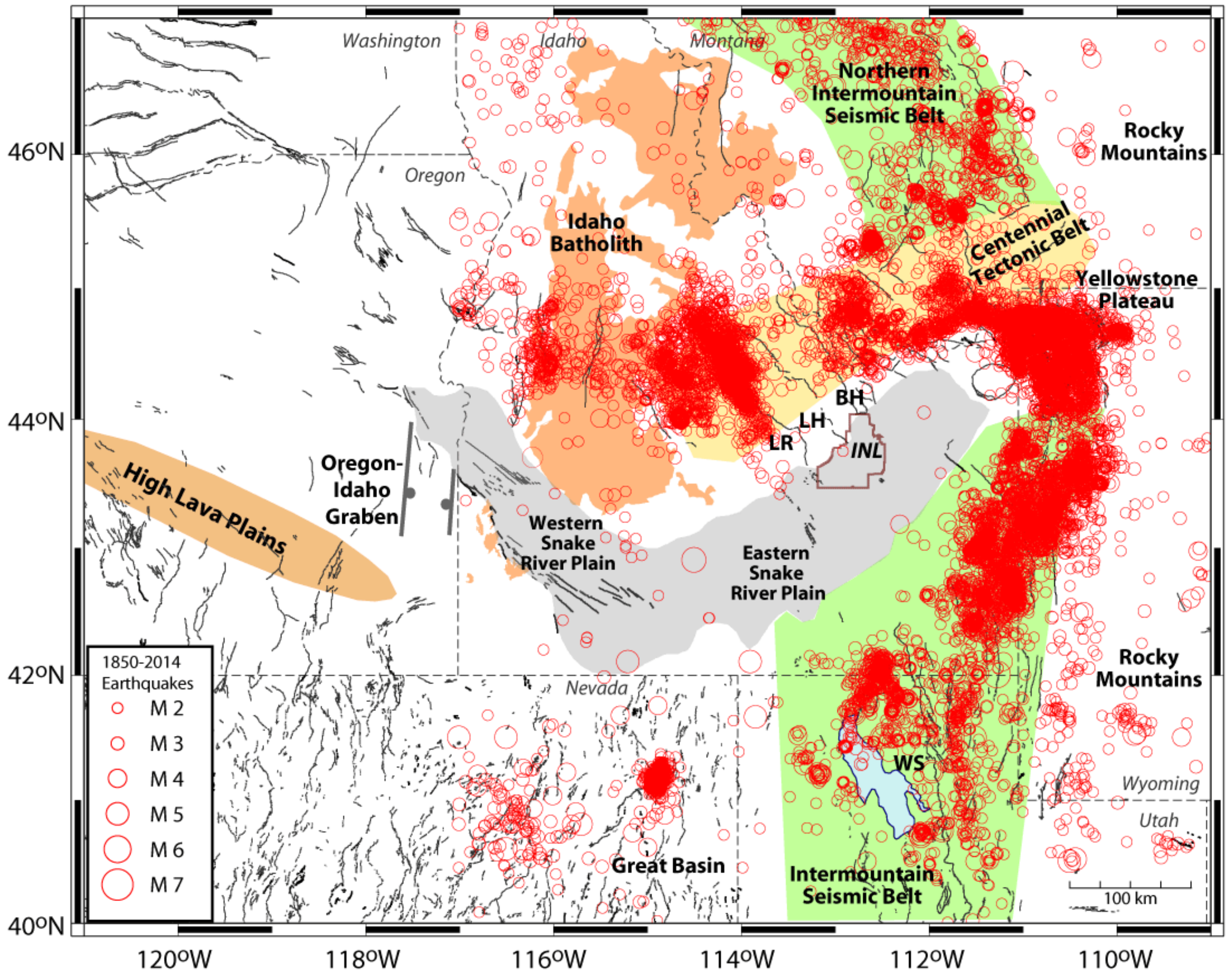

Figure 4-11. Maps shows the epicenters of earthquakes from 1850 to 2014 for magnitudes >2.0.

4.4 Seismicity and Faulting

This section discusses seismicity and Quaternary faults in the surrounding regions outside and within the ESRP. The discussions are divided into subsections by seismic zones, geologic features or geographical regions. The regional earthquake catalog presented here for INL covers the area of 40-47°N and 108-117°W and includes events from 1850 to 2014 with magnitudes >2.0 (see Section 6 for catalog details). This catalog with over 20,000 events shows that epicenters form a distinct parabolic seismic zone around the ESRP, other regions have more diffuse epicenters, and the SRP lacks earthquakes (Figure 4-11).

4.4.1 Seismic Parabola

Many Quaternary normal faults fall within a high seismic region referred to as the Seismic Parabola (after Smith and Braile, 1994). The Seismic Parabola encompasses the CTB which crosses Idaho and southwest Montana and the ISB which extends from the Yellowstone Plateau into northern Utah along the Wasatch fault. At its northeastern apex in the Yellowstone Plateau, earthquakes are closest to the ESRP

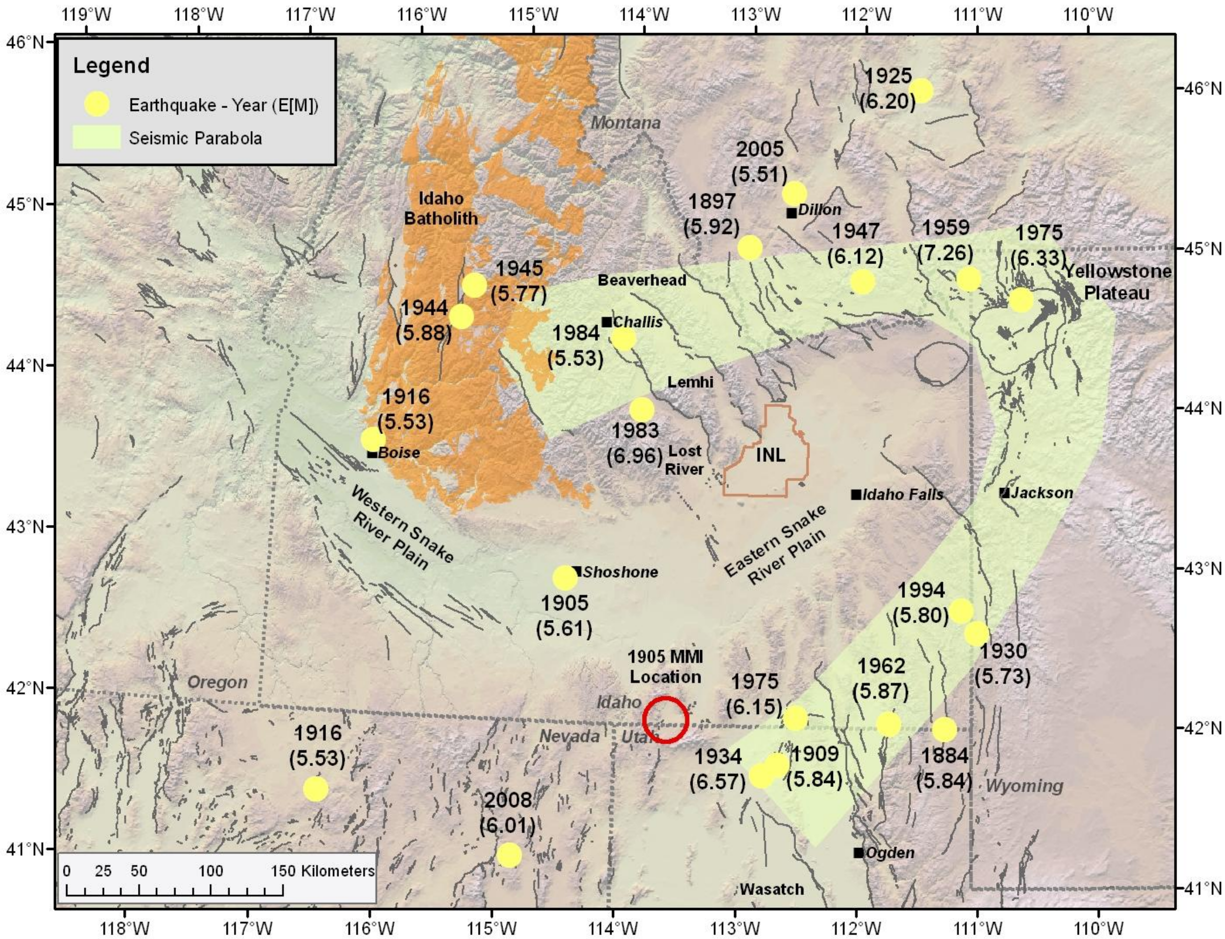

Figure 4-12. Map shows earthquakes from 1850 to 2014 for E[**M**]>5.5. The boundaries of the seismic parabola are based on Smith and Braile (1994). Red circle is the for the 1905 E[**M**] 5.61 Shoshone, Idaho earthquake's Modified Mercalli Intensity (MMI) location as determined by Oaks (1992).

margins, and to the southwest, the distribution of seismicity flares outward away from the margins of the ESRP (Figure 4-11).

Seismicity within the boundaries of the Seismic Parabola is coincident with Quaternary normal faults that have ruptured in Holocene and historic time (Stickney and Bartholomew, 1987; Anders et al., 1989; Pierce and Morgan, 1992; Smith and Braile, 1994) (Figure 4-13). The 1959 E[**M**] 7.26 Hebgen Lake, Montana and 1983 E[**M**] 6.96 Borah Peak, Idaho earthquakes are the largest normal faulting events to occur near or within the Seismic Parabola (Figure 4-12). The 1959 earthquake consisted of two sub-events that ruptured the W-striking, S-dipping (40-60°) Hebgen and Red Canyon normal faults producing maximum vertical displacements of 6.7 m over a surface scarp length of 23 km (Red Canyon) and 6.1 m over 14.5 km (Hebgen) (Myers and Hamilton,1964; Doser, 1985). A 1-m scarp was observed along a 3-km segment of the southern Madison fault which may or may not have been coseismic movement associated with the 1959 earthquake (Witkind, 1964). The 1983 Borah Peak, Idaho earthquake ruptured two central segments of the NW-striking, SW-dipping (40-50°) of Lost River normal fault producing a 36-km long scarp with a maximum vertical displacement of 2.7 m (Richins et al., 1987; Crone et al., 1987). The 1959 and 1983 earthquakes both nucleated at mid-crustal depths (~12-18 km) (Doser, 1985;

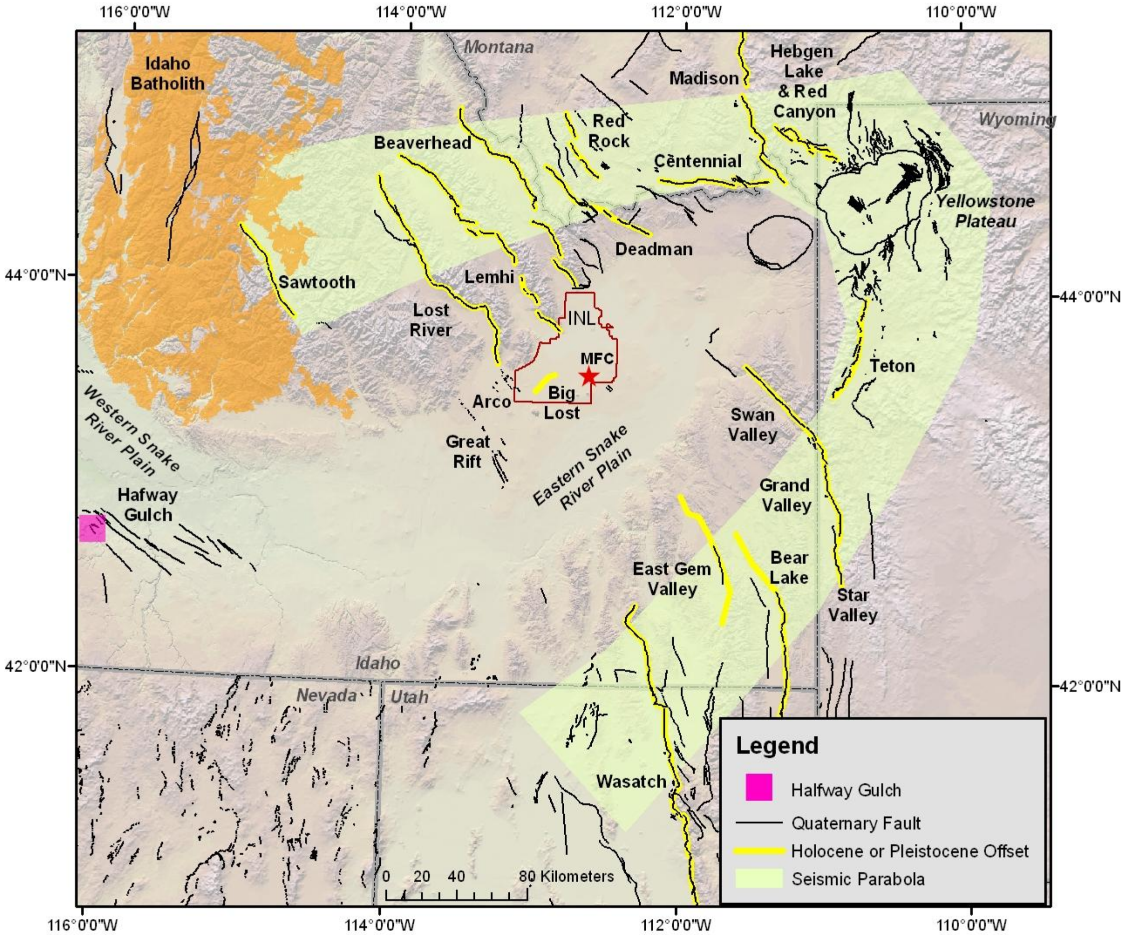

Figure 4-13. Map shows Seismic Parabola (Smith and Braile, 1994) relative to Quaternary normal faults. Normal faults outside the ESRP with most recent offsets in Holocene or Pleistocene times are highlighted in yellow. See text for discussions of the Big Lost fault within the ESRP.

Doser and Smith, 1989). Other normal faults with Holocene offsets within the Seismic Parabola include (Figure 4-13):

- SE-striking, NW-dipping Sawtooth (Thackray et al., 2013)
- Central segments of the NW-striking, SW-dipping Lemhi and Beaverhead (e.g., Stickney and Bartholomew, 1987)
- SE-striking, NE-dipping (Stickney and Lageson, 2002)
- E-striking, N-dipping Centennial (e.g., Petrik, 2008)
- N-striking, W-dipping Madison (e.g., Stickney and Bartholomew, 1987)
- S-striking, E-dipping Teton (e.g., Byrd et al., 1994)
- N-striking, W-dipping Star Valley (McCalpin, 1993)
- N-NW-striking, W-SW-dipping Bear Lake (McCalpin, 2003)
- N-striking, W-dipping Wasatch (e.g., Wong et al., 2002).

The inner regions between the Seismic Parabola and ESRP margins lack earthquakes (Figure 4-11). The inner region (also categorized as Faulting Belt III by Pierce and Morgan, 1992) has normal faults that have had periods of increased rates of faulting coincident the northeast progression of hotspot silicic volcanic centers (Smith and Braile, 1994; Pierce and Morgan, 1992; 2009; Anders et al., 1989; 2009; 2014). These normal faults typically have lower slip rates in recent times and their most recent offsets as early Holocene to Pleistocene. The normal faults include (Figure 4-13): southern segments of the NW-striking, SW-dipping Lost River, Lemhi, and Beaverhead (Olig et al., 1995; Hemphill-Haley et al., 1992; Crone and Haller, 1991, respectively); NW-striking, SW-dipping Deadman (Skipp, 1985); and NW-striking, SW-dipping Swan Valley and Grand Valley (Piety et al., 1986).

4.4.2 Yellowstone Caldera

At the apex of the seismic parabola is the Yellowstone Plateau which resides over the current position of the Yellowstone hotspot (Figure 4-11). The Yellowstone Plateau hosted three silicic volcanic centers that erupted at 2.1, 1.3, and 0.64 Ma; the last eruption produced the Yellowstone caldera (Christiansen, 2001). Seismicity is due to a combination of regional tectonics and local-spatial and temporal variations in stress associated with active volcanic processes (Waite and Smith, 2004). The largest earthquake, 1975 E[**M**] 6.33, occurred on the northern rim of the Yellowstone caldera and is interpreted to be associated with slip along a NW-trending normal fault (Pitt et al., 1979) (Figure 4-12). The Yellowstone caldera has exceptionally high heat flow, abundant hot spring and geyser activity, low seismic velocities at shallow and mid crustal levels, and rapid crustal deformation rates (centimeter-scale inflation and deflation within months to years) of land surface elevations (Fournier, 1989; Smith and Braile, 1994; Blackwell and Richards, 2004; Husen and Smith, 2004; Farrell et al., 2014; Huang et al., 2015). From 2004 to 2006, the Yellowstone caldera underwent uplift due to intrusion and expansion of sill-like magma body at 7-10 km depth (Chang et al., 2010).

4.4.3 Northern Intermountain Seismic Belt

To the north of the CTB, earthquakes are concentrated more in the northern ISB with fewer and scattered epicenters in western Montana and northern Idaho (Figure 4-11). Within the northern ISB, many of the normal faults have diverse trends, offset late Pleistocene deposits, and appear to have longer recurrence intervals (Stickney and Bartholomew, 1987; Smith and Arabasz, 1991). The 1925 E[**M**] 6.20 Clarkston Valley, Montana earthquake occurred in the northern ISB (Figure 4-12) and is interpreted to be associated with oblique normal slip on a northwesterly-dipping plane (Doser, 1989a).

4.4.4 Rocky Mountains

East of the ISB, earthquakes are fewer and more scattered and extend from central Montana south into Utah (Figure 4-11). The earthquakes in this region are of moderate size with the largest event (1950 E[**M**] 5.06) located in Utah about 100 km east of the Wasatch fault (Figure 4-12). This region has very few mapped Quaternary faults (Figure 4-13).

4.4.5 Great Basin in Northeastern Nevada

South of the ESRP and WSRP, the Great Basin in northeastern Nevada has scattered seismicity and a concentration of epicenters associated with the 2008 E[**M**] 6.01 Wells, Nevada earthquake mainshock and aftershocks (Figure 4-11). Prior to the 2008 earthquake, northeast Nevada had broadly scattered earthquakes throughout with a general trend from higher activity in the southwest to lower activity in the northeast (Anderson, 2011). The 2008 earthquake ruptured along a previously unmapped NE-striking, SE-dipping normal fault (Smith et al., 2011); no surface ruptures were found (dePolo, 2011) (Figure 4-12). Slip on several nearby faults range in age from Holocene to middle Quaternary and recurrence times

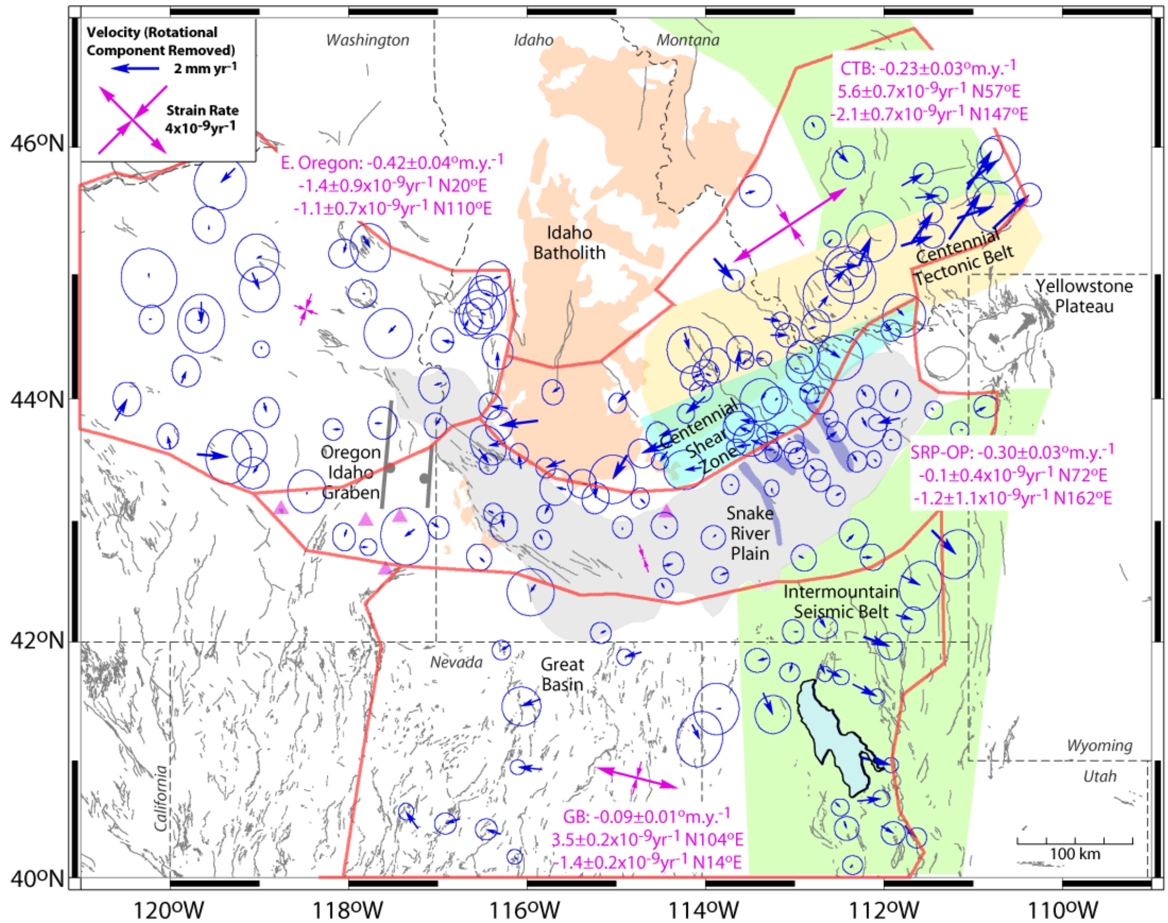

Figure 4-14. Horizontal GPS velocities (blue vectors with 70% confidence ellipses) show remaining gradients after subtracting out their respective rotational components. Horizontal strain rates (pink arrows) and vertical-axis rotation rates were calculated using observed velocities within the regions defined by the orange lines. Labels list tectonic province, clockwise rotation rate, and strain rates for the two principal horizontal axes (pink letters) (Payne et al., 2012).

of large earthquake ruptures are on the order of tens of thousands to hundreds of thousands of years (Ramelli and dePolo, 2011).

4.4.6 Idaho Batholith

North of the WSRP, earthquakes have a diffuse pattern of epicenters in western Idaho and are concentrated near and within the Idaho batholith (Figure 4-11). The Idaho batholith has high rugged topography, is a relatively non-extended region, and lacks late Tertiary and Quaternary volcanism (Bond et al., 1978; Gasching et al., 2009). A zone of seismicity cuts through the southern part of the Idaho batholith (Figure 4-11). Earthquakes within and near edges of the Idaho batholith tend to occur in swarms with the maximum magnitudes between 3.0 and <5.0 (e.g., Pennington et al., 1974; Smith and Sbar, 1974; Dewey, 1987). Two moderate size earthquakes, 1944 E[**M**] 5.88 and 1945 E[**M**] 5.77, occurred within the Idaho batholith and are located near two Quaternary faults (Figure 4-12).

4.4.7 Western Snake River Plain

Within the WSRP there are fewer earthquakes than in the nearby regions to the north and south, and it is bounded by NW-trending normal faults (Figure 4-11). The largest earthquake is the 1916 E[**M**] 5.58, which occurred along the northern margin of the WSRP near Boise, Idaho (Figures 4-11 and 4-12). Wood and Clemens (2002) suggest that during graben development, the NW-trending normal faults had higher slip rates between 9.5 and 11 Ma and, at present, their average long-term slip rates are very low. Episodic reactivation may occur on suitably oriented faults. Four scarps near and on the Halfway Gulch fault, a SE-striking, SE-dipping normal fault, show evidence of Holocene to late Pleistocene movements Beukelman (1997) (Figure 4-13).

4.4.8 Eastern Snake River Plain

The ESRP has far fewer earthquakes than the Seismic Parabola and may have Quaternary faults that are possibly tectonic in origin and others that are associated with dike intrusion (Figure 4-11). Due do the very low seismicity, investigators characterize the ESRP as aseismic relative to the surrounding Basin and Range regions. Several alternative mechanisms have been offered for how extension may be accommodated in the ESRP. These include: aseismic creep in response to high crustal temperatures (Pennington et al., 1974; Smith and Sbar, 1974; Brott et al., 1981); increased crustal strength by mafic densification of the crust which resists fracturing (Anders et al., 1989; Smith and Arabasz, 1991); extension via dike intrusion (Rodgers et al., 1990; Parsons et al., 1998; Rodgers et al., 2002); and lower strain rates within the ESRP (Anders and Sleep, 1992; Homes et al., 2008; Chadwick et al., 2007; Payne et al; 2012; 2015).

Recent geodetic results suggest that at present the ESRP has a much lower strain rate than the surrounding Basin and Range regions (Figure 4-14). Analysis of Global Positioning System (GPS) horizontal velocities for 1994-2010 by Payne et al. (2012) show a NE-oriented extensional strain rate of $5.6 \pm 0.7 \times 10^{-9}$ yr^{-1} in the CTB and an ~E-oriented extensional strain rate of $3.5 \pm 0.2 \times 10^{-9}$ yr^{-1} in the Great Basin. These extensional rates contrast with the very low strain rate of $-0.1 \pm 0.4 \times 10^{-9}$ yr^{-1} (which is indistinguishable from zero) within the 125 km x 650 km region of the SRP and Owyhee-Oregon Plateau. Payne et al. (2012) propose that dike intrusion in ESRP VRZs produces only local dilation of the crust in response to post-hotspot volcanism and does not accommodate regional crustal extension at a rate similar to the adjacent Basin and Range regions. They also suggest that the low strain rate in the SRP may result from greater lithospheric strength due to mafic crustal modifications or lower internal differential stress resulting from lower Gravitational Potential Energy (GPE) variations due to the flat topography coupled with a high-density crustal composition or both.

Historic earthquakes with large epicentral errors have been located within the ESRP. The largest historic earthquake that may have occurred in the ESRP is the 1905 Shoshone, Idaho earthquake (Figure 4-12). The Shoshone earthquake occurred before there was instrumental monitoring in Idaho and, since its epicenter was based on felt reports, it may have an error of 100 km or more. Oaks (1992) conducted a comprehensive investigation of historical records throughout an eight-state region to determine the magnitude and epicenter of the Shoshone earthquake. Using damage reports to assess Modified Mercalli intensities, Oaks (1992) determined the 1905 earthquake to be a local magnitude (M_L) 5.5±0.5 (or E[**M**] 5.61) and its epicenter to be southeast of Shoshone outside the ESRP near the Idaho-Utah border (Figure 4-12). Another earthquake, the 1964 E[**M**] 4.17, is located along the eastern margin of the ESRP north of Pocatello, Idaho (Figure 4-13). With limited seismic station coverage at that time, the event likely has a large epicentral error and may or may not be located within the ESRP. Detailed investigations of this event have not been done.

Detailed seismic monitoring since 1972 by INL has located over 80 microearthquakes of M_L<2.5 within the ESRP and 17 of these are within the INL boundaries (Figure 4-15). The concentration of

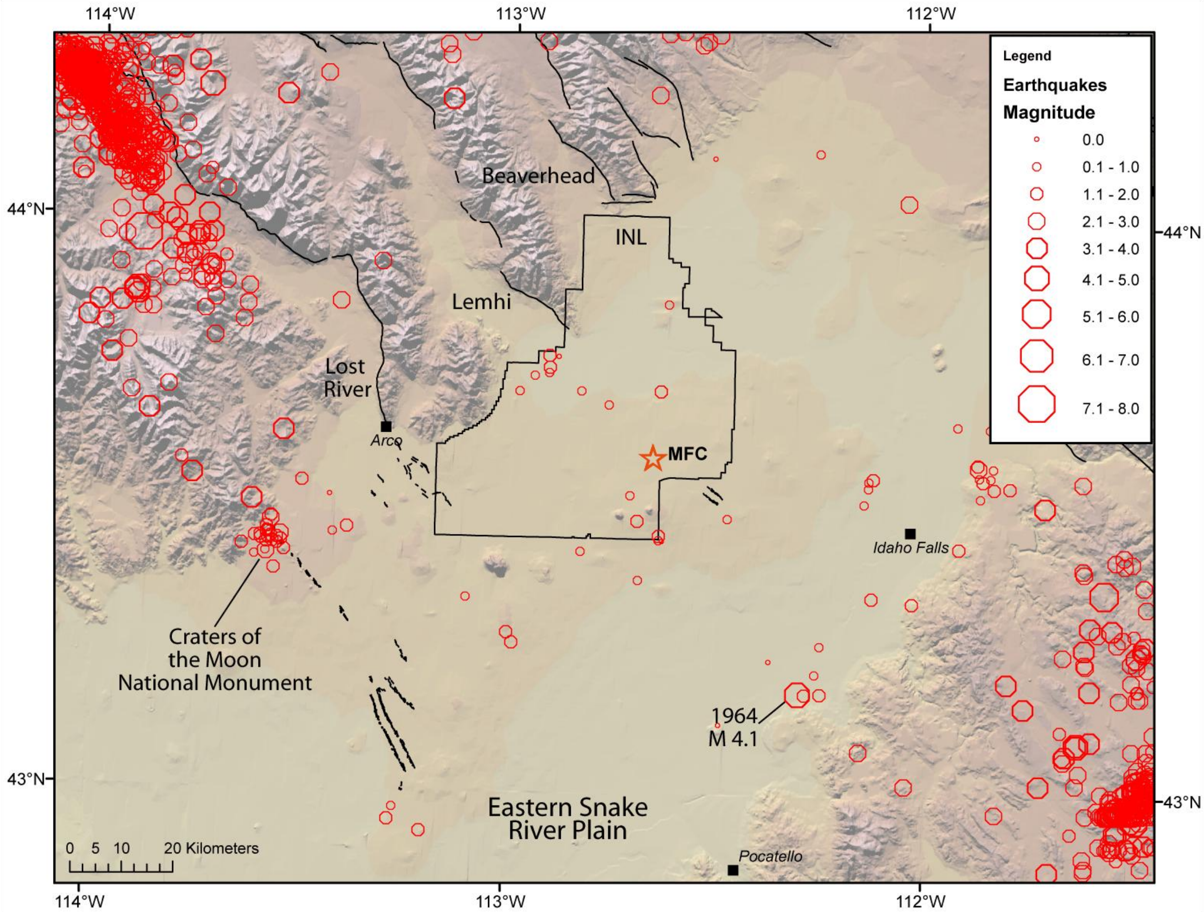

Figure 4-15. All microearthquakes within the ESRP (M<2.5) as detected by the INL seismic stations since 1972. The 1850-2014 M>2.0 catalog is also shown for earthquakes outside the ESRP.

earthquakes at Craters of the Moon National Monument (COM) includes 23 events of M_L<2.5; all but one have been detected since 2007. Eleven of the COM events evaluated by Carpenter and Payne (2009) have hypocenters between 15 and 25 km depth and waveforms with low-frequency content suggesting association with fluid or magma movement. Previous investigators suggested microearthquakes may be the result of subsidence due to cooling and contraction of the ESRP or mass loading of the crust by rhyolite domes (Brott et al., 1981; Pelton et al., 1990). Based on fault plane solutions with NE-SW oriented T-axes (see Section 4.5), Jackson et al. (1993) attributed the occurrence of microearthquakes to small-scale faulting in the shallow crust in response to regional extensional stresses.

With the exception of the Big Lost fault (a newly named fault in this study) and possibly faults in the northern Arco VRZ, normal faults within the ESRP (such as within the Great Rift VRZ) are the products of dike intrusion (see Section 4.2). The Big Lost fault in the south central region of INL is identified by a stratigraphic discontinuity. Wood et al. (2007) recognized that the basalt stratigraphy on the west side of the Big Lost River is very different from that on the east side of the river (Figure 4-16). One possibility is the presence of the Big Lost fault. Wood et al. (2007) show correlations of basalt flows between two of the closest boreholes have a down to the east step with a maximum offset of 309 m that occurs in flows

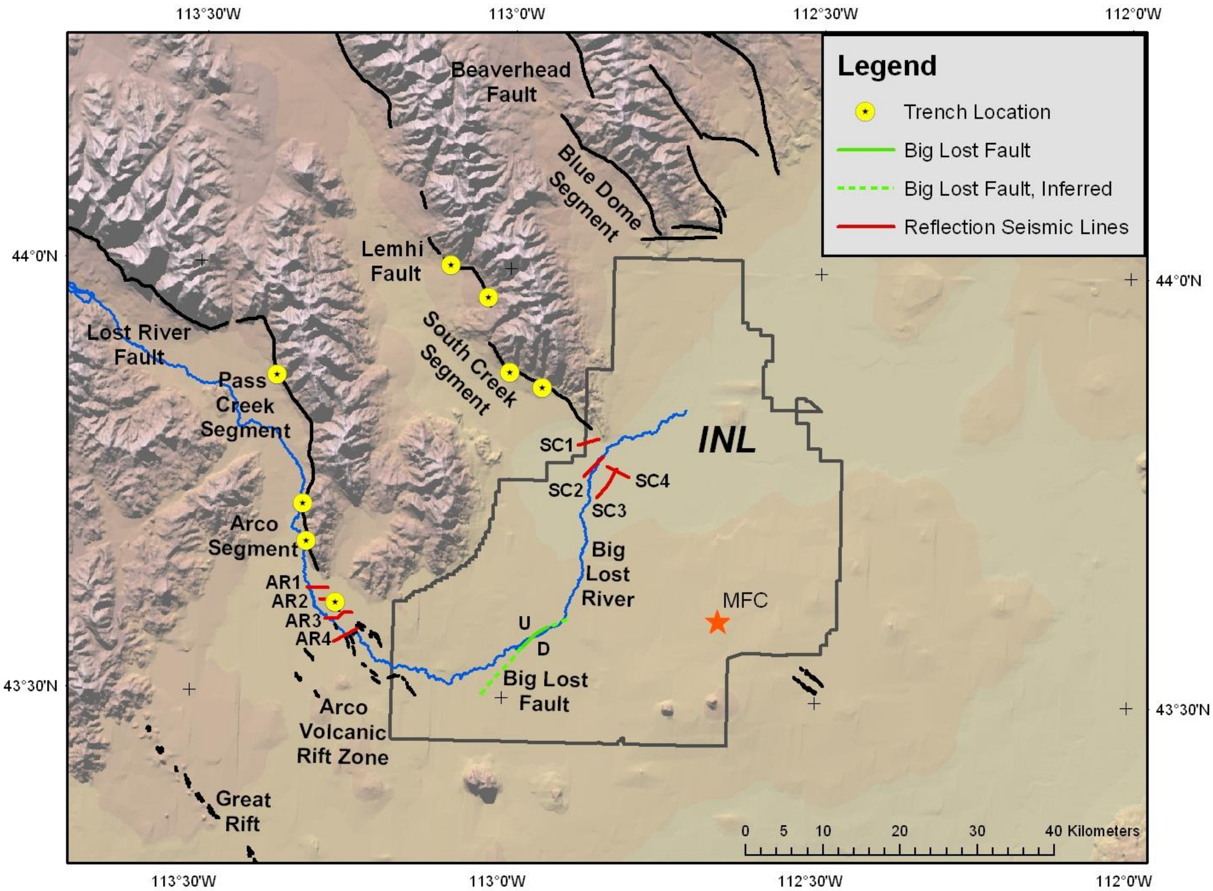

Figure 4-16. Map shows locations of Quaternary faults (black lines), the Big Lost fault (vertical sense of slip: U= Up and D=Down), paleoseismic trench locations, and reflection seismic lines.

with ages from >292 ka to 780 ka. Stratigraphic discontinuities in other nearby wells may support up to a 15 km length and SE-strike for the Big Lost fault (see Section 5.4). Alternatively the stratigraphic differences may be due to a steep fold or NE-trending VRZ. Near-vent facies in other nearby wells could be evidence of a NE-trending set of volcanic vents that is aligned with the Big Lost River floodplain (Helm-Clark et al., 2006; Wood et al., 2007) (Figure 4-16).

The northern end of the Arco VRZ may overlap with the southern termination of the Arco segment of the Lost River fault. Short, NW-trending normal faults and monoclinal flexures expressed within 400-730 ka basalt flows have a generally left-stepping en echelon pattern in a northeast direction from the projection of the Arco segment into the ESRP (Kuntz et al., 1994). Monoclines in the basalt flows could be surface expressions of subsurface normal faults that have not breached the surface and are caused by flexure of the surface above upward-propagating fault tips (Grant and Kattenhorn, 2004). Smith et al. (1996) interpret the short normal faults and monoclines along with nearby fissures and volcanic vents to be of volcanic origin produced by dike intrusion in the Arco VRZ. Alternatively, others interpret the short normal faults and monoclines to be tectonic in origin and related to slip on the Arco segment (Wu and Bruhn, 1994; Kuntz et al. 2002). Jackson et al. (2006) interpreted both west- and east-dipping faults on seismic reflection lines AR2 and AR3 in Figure 4-16 acquired in the Arco VRZ and suggested that the normal faults and monoclines could be products of dike intrusion. They also suggested that the west-dipping faults on lines AR1 and AR2 may be associated with slip on the Arco segment to a distance of 4.6 km south of its mapped location at the end of the Lost River Range (Figure 4-16).

4.4.9 Lost River, Lemhi, and Beaverhead Faults

The Lost River, Lemhi, and Beaverhead normal faults are closest to the INL. All three faults have lengths of ~150 km and extend from the northwest margin of the ESRP into central Idaho (Figure 4-13). The three normal faults are also thought to be segmented with segment lengths from 13 to 45 km (Crone and Haller, 1991; Woodward-Clyde Federal Services et al., 1996). Segment lengths are based on scarp morphology, age of deposits displaced, and range front morphology particularly where pronounced offsets or gaps occur in the continuity of the fault (Crone and Haller, 1991). Each of the faults has southern ends that may terminate at the ends of their respective ranges or may project beneath the basalt flows in the ESRP (Bruhn et al., 1992; Wu and Bruhn, 1994; Rodgers et al., 2002). The southern end of the Lost River fault may terminate in the northern end of the Arco VRZ as discussed in the previous section (Figure 4-16). The Lemhi fault may terminate just south of the Lemhi range (Figure 4-16). Seismic reflection line SC1 shows a southwest dipping fault, which is thought to be the southernmost extent of the Lemhi fault and two the south, lines SC2 and SC3 show flat lying continuous reflections (Jackson et al., 2006). Although limited investigations have been performed, interpretations of regional gravity data suggest the Birch Creek valley may partially extend into the ESRP and that a volcanic vent may be aligned with a splay fault of the Beaverhead fault (Figure 4-10) (Woodward-Clyde Federal Services et al., 1996).

Paleoseismic investigations have been conducted on various segments of the Lost River, Lemhi, and Beaverhead faults. The Lost River and Lemhi faults have paleoseismic trenching (Figure 4-16) and scarp morphology studies and the Beaverhead fault has scarp morphology studies. Excluding the 1983 earthquake, results of the paleoseismic investigations show the central and northern segments of the Lost River (Mackay, Thousand Springs, and Warm Spring) and Lemhi (Falls Creek, Big Gulch, and Warm Creek) faults have Holocene displacements and that only the central segment (Leadore) of the Beaverhead fault ruptured during the Holocene. The southern segments of the Lost River, Lemhi, and Beaverhead have ruptured in the Pleistocene. The most recent offsets on the southern two segments (Pass Creek and Arco) of the Lost River and southernmost segment on the Lemhi (South Creek) faults occurred sometime between 15,000 and 25,000 years ago (Hemphill-Haley et al., 1992; Olig et al., 1995). The most recent offset on southernmost segment of the Beaverhead (Blue Dome) fault could be as young as 30,000 yr or as old as 100,000 yr (Haller, 1988; Crone and Haller, 1991).

Paleoseismic investigations on the Lost River and Lemhi faults also indicate that earthquakes are temporally clustered whereby they have periods of elevated earthquake activity and quiescence over tens of thousands of years (Schwartz, 1989; Hemphill-Haley et al., 1992; Olig et al., 1995). Within clusters of earthquake activity, recurrence intervals range from <1,000 to 10,000 yr, and between clusters of activity, they range from 10,000 to 100,000 yr. Estimated long-term slip rates vary depending on the time period and vertical offsets used in the calculations. For the Lost River fault, the slip rates for the central segments range from 0.15 to 0.3 mm/yr (Vincent, 1985; Hanks and Schwartz, 1987) and for the southern segments from 0.05 to 1.1 mm/yr (Olig et al., 1995). For the central and southern segments of the Lemhi fault, slip rates range from 0.15 to 0.28 mm/yr (Olig et al., 1995; Woodward-Clyde Federal Services et al., 1996).

Each normal fault bounds the southwest side of a mountain range of 2 km relief, producing typical Basin-and-Range half graben basins as much as 3.5 km deep (Rodgers et al., 2002). The three faults are thought to be planar based on the aftershocks and geodetic studies of the 1983 E[**M**] 6.96 Borah Peak earthquake, which show the Lost River fault as planar to mid-crustal depths (Richins et al., 1987; Barrientos et al., 1987). The 1983 earthquake ruptured two central segments (Thousand Springs and

Warm Spring) of the Lost River fault producing a 36-km long scarp and maximum vertical displacement of 2.7 m (Crone et al., 1987). Paleoseismic trench investigations at other locations on the Lost River fault have displacements per event that from range from 0.5 to 2.6 m (Olig et al., 1995). The displacements per event on the Lemhi fault have a greater range from 0.9 to 5 m based on trench measurements and scarp morphology profiling (Baltzer, 1990; Turko and Knuepher, 1991; Hemphill-Haley et al., 1992). For the Beaverhead fault (Nicholia segment), scarps thought to be the product of one faulting event have displacements of 2.2 to 3.7 m (Crone and Haller, 1991).

4.5 Stress Orientation

Fault plane solutions, geologic indicators, and geodetic data are used to assess the style of faulting and stress orientations for the ESRP and surrounding regions. Figure 4-17 shows lower hemisphere fault plane solutions for earthquakes of E[**M**] 3.64 to 7.26 in the CTB, ISB, Idaho Batholith, and Great Basin. In these regions, fault plane solutions are predominately normal faulting and consistent with the strikes of

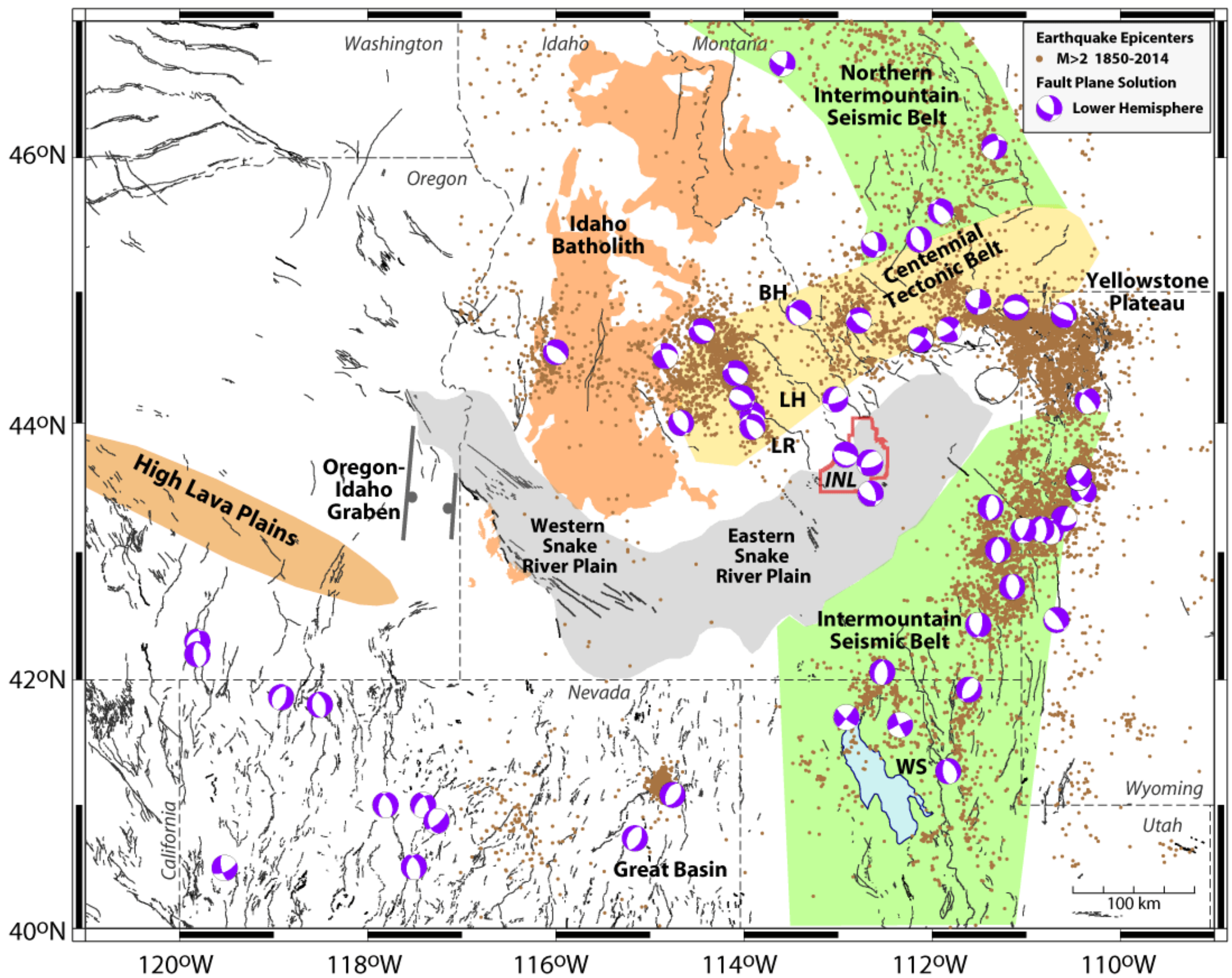

Figure 4-17. Fault plane solutions were compiled from: Zollweg and Richins (1985); Richins et al. (1987); Jackson and Zollweg (1988); Doser (1989a; 1989b); Doser and Smith (1989); Jackson et al. (1993); Pezzopane and Weldon (1993); Stickney (1997; 2007); http://www.seismology.harvard.edu/; and http://www.eas.slu.edu/Earthquake_Center/MECH.NA/index.html.

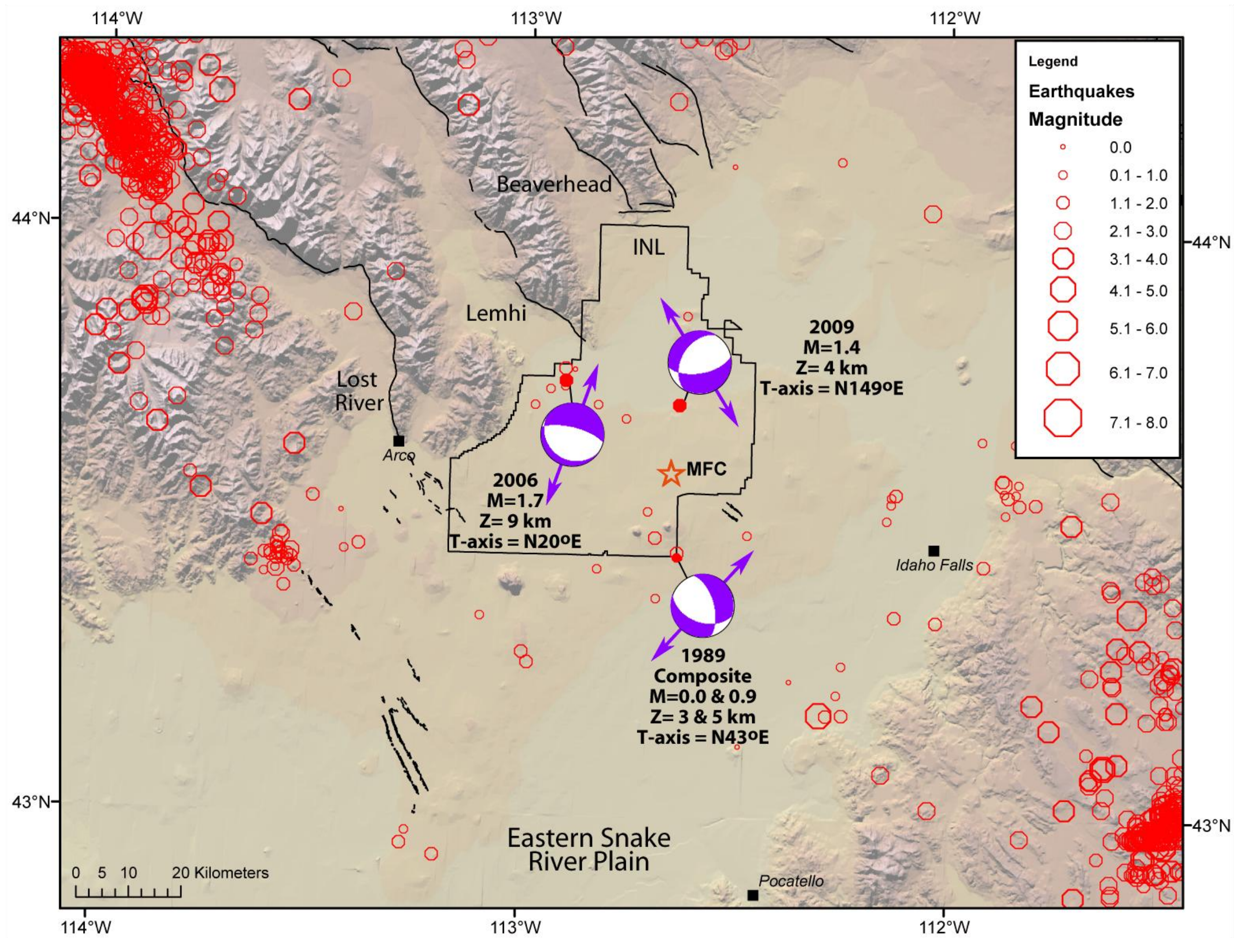

Figure 4-18. Lower hemisphere fault plane solutions (purple and white balls) and T-axis (purple arrows). The 1989 composite solution is from Jackson et al. (1993). Red dots show the locations of the earthquakes for the fault plane solutions. Text includes year, coda magnitude (M), depth, and T-axis orientation.

mapped Quaternary faults. In the ESRP, three fault plane solutions are only available for microearthquakes of coda magnitude (M_D) <1.7, and all events are located within the INL boundaries. The composite fault plane solution for two events in 1989 (Jackson et al., 1993) and for two other microearthquakes, the 2006 coda magnitude (M_D) 1.7 and 2009 M_D 1.4, all show normal faulting with varying components of oblique slip and different nodal plane orientations (Figure 4-17).

In the ISB and CTB, there are some strike-slip fault plane solutions, including the 1934 E[**M**] 6.57 Hansel Valley earthquake (Doser, 1989b) west of the Wasatch fault in the ISB, 2010 E[**M**] 4.81 event east of the Teton fault in the ISB, and 2011 E[**M**] 4.41 event along the Centennial fault in the CSZ (Figure 4-17). Within the ISB, left-lateral strike-slip fault plane solutions for earthquakes are consistent with the right-stepping en echelon pattern of active normal faulting that extends from the Wasatch fault to the Teton fault. They are also consistent with accommodation of left-lateral shear indicated by differences in strain rates between the ESRP and ISB (Payne et al., 2012). North of the ESRP, the right-lateral strike-slip fault plane solution for 2011 E[**M**] 4.41 event is representative of solutions for many smaller

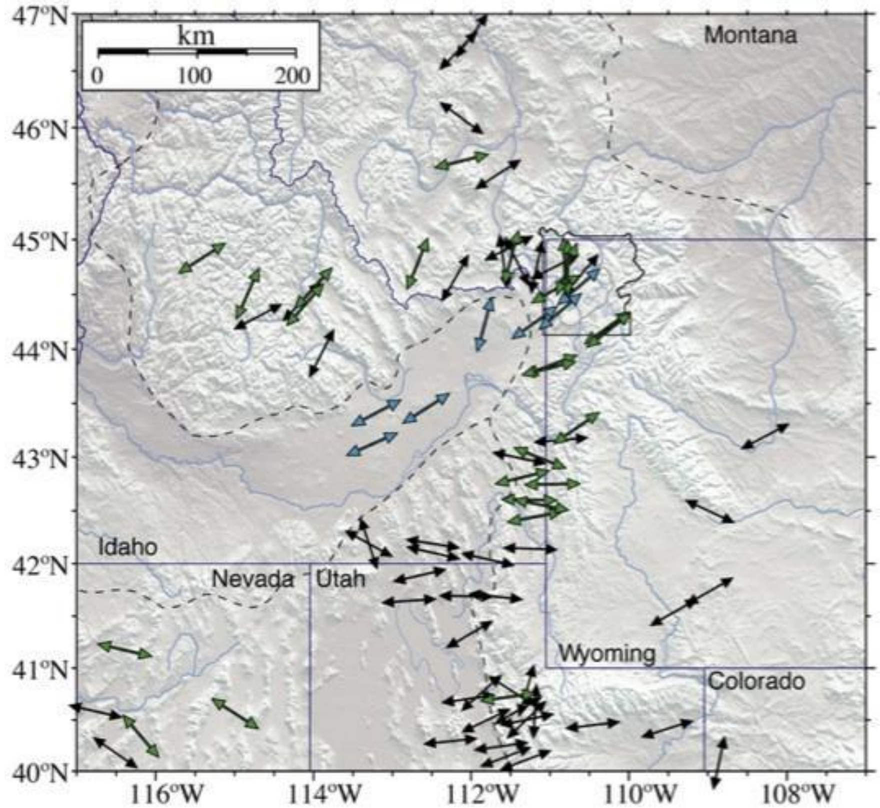

Figure 4-19. Map shows the stress field of Yellowstone and the ESRP. Arrows are directions of tensional stress determined from fault plane solution T-axes (black), maximum tensional stresses (σ_3) (green), slip directions of normal faults (Φ) (black), and volcanic rift zones or volcanic vent alignments (blue). T-axes for fault plane solutions in the ESRP in Figure 4-17 are not included. Map was taken from Smith et al. (2009), which was modified from Waite and Smith (2004).

magnitude events (Stickney, 1997) that are within a NE-trending zone of seismicity near the Centennial normal fault. Here only a small subset of events show normal faulting (Stickney, 2007). The strike-slip earthquakes near the Centennial fault may be accommodating right-lateral shear within the CSZ (Payne et al., 2013), which results from differences in strain rates between the ESRP and CTB (Payne et al., 2012).

Waite and Smith (2004) compiled stress indicators for the ESRP and surrounding regions. The tensional stress indicators include fault plane solution T-axes, maximum tensional stresses (σ_3), slip directions of normal faults (Φ), volcanic rift zones, and volcanic vent alignments. For simplicity, they assumed that the minimum principal stress directions and fault plane solution T-axes are the directions of maximum lithospheric extension. The ESRP, surrounding adjacent regions (CTB, ISB, Great Basin, and Idaho batholith), and central Wyoming are dominated by lithospheric extension (Figure 4-19).

The ESRP has tensional stress orientations of NE-SW based on the VRZz and alignment of volcanic vents (Figure 4-19). Only the 1989 and possibly the 2006 fault plane solutions have T-axes consistent with the volcanic stress indicators. The 2009 event has a T-axes orientation of NW-SE, which is 90° different from the other T-axes (Figure 4-18). Since these earthquakes have very small magnitudes (M_D <1.7) they may or may not be representative of the extensional stress orientations in the ESRP. Recent rock strength measurements of rhyolite core and re-evaluation of well-bore breakouts in the INEL-1 deep borehole suggest that the state of stress at 3.5 km is transitional between normal faulting and strike-slip faulting (Per. Comm. C. Barton, 2016). The variability of fracture trends revealed by the INEL-1 image data indicates there is a well-developed network of existing fractures that include NE-striking, NW- and SW-steeply dipping fractures (Moos and Barton, 1990). However, these fractures may be related to caldera formation, which implies they formed at 8-10 Ma.

The tensional stress orientations change from generally E-W in the ISB to NE-SW in the CTB and the Yellowstone Plateau shows rotation of the extension direction (Figure 4-19). The tensional stress orientations show a mix of N-S, NNE-SSW, and NE-SW to the west of the Yellowstone Plateau, but are more consistently NE-SW within the Yellowstone caldera and to the south. The Idaho batholith has a NE-SW T-axis consistent with the CTB. The northern ISB has varying stress orientations including NE-SW, NNE-SSW and NW-SE. In general, northeastern Nevada has NW-SE orientation of extension. The tensional stress orientations in the CTB and Great Basin (northeast Nevada) are consistent with the extensional principal strain rate axes derived from the 1994-2010 GPS velocities (Figure 4-14).

5. SSC Database: Geologic and Geodetic Data

The INL SSHAC Level 1 PSHA involved compilations of the existing data and evaluations of those data to support development of the SSC model. No new SSC data were collected for the SSHAC Level 1 study. Most geologic, seismologic, volcanic, and geophysical data and analyses of these data that are used in the SSC model are documented in publications. These data are listed in the SSC Data Summary Table (Appendix H). This section discusses compilations of geodetic, geologic, and seismologic data and analyses of these data which are not documented elsewhere. Section 6 discusses compilation of the 1850-2014 earthquake catalog and analyses of the catalog that are used in the SSC model.

5.1 Strain Partitioning in the CSZ

In the SSC model, the CSZ is included as four geodetic subzones, CSZ1, CSZ2, CSZ3, and CSZ4 using geodetic rates (see Sections 8.1.4 and 8.2.8). The CSZ subzones are within the NBR and CTB source zones (Figure 8.1.2). Based on uncertainty in the confidence of the geodetic rates, the SSC logic tree includes branches for when the CSZ exists as a seismic source in the PSHA (weight of [0.5]) and when it does not. When the CSZ exists, the recurrence rate of each subzone is the geodetic rate minus the rate partitioned to any fault sources within the subzones. This section discusses the basis and calculations of the geodetic rates.

The CSZ source zone is a geodetically expressed zone that accommodates differences in strain rates between the slowly deforming ESRP and rapidly extending Basin and Range region in the CTB (Payne et al., 2012). The geodetic rates of deformation within the CSZ are slip rates for right-lateral strike-slip motion to accommodate right-lateral shear (Payne et al., 2013). From inversions of the GPS velocities with their best fit block model (ctb9), Payne et al. (2012) estimated slip rates of right-lateral strike-slip motion that range from 0.1 to 1.4 mm/yr along the boundary between the ESRP and CTB. The highest slip rate is located near the Centennial fault and the lowest is to the southwest near the Sawtooth fault (Figure 9 in Payne et al., 2012).

Payne et al. (2013) proposes that the CSZ is a 40-45 km wide zone where differential motion is distributed and may include components of deformation due to strike-slip faulting, distributed simple shear, regional-scale rotation, or some combination of these. They further suggest that right-lateral shear may be accommodated in the CSZ as right-lateral strike slip motions on optimally aligned NE-trending normal faults or as components of left-lateral oblique slip in localized bookshelf faulting on the southernmost ends of the NW-trending normal faults (Figure 4-3).

The recent work of Parker and Sears (2016) measured and evaluated sedimentary structures and pressure-solution pit dimensions in cobbles of a 365,000 yr old, 800-m thick quartzite comglomerate within the CSZ. From their data, they estimated a maximum horizontal principal stress orientation for σ_1 as 255.8±22.0° (or 75.8±22.0°). This result is similar to the of N78±4°W for the direction of strike-slip derived from the geodetic principal horizontal strain rate (Payne et al., 2013). Parker and Sears (2016) also concluded that the strain was distributed across high-angle strike-slip faults (mean strike of 200±20.0° and dip of N78°W) in a primary deformation zone consistent with the zone proposed by Payne et al. (2013). They further suggest that a localized simple shear stress field (σ_1 horizontal) is superimposed over the regional extensional stress field in the CSZ.

Five normal faults, fault sources in the SSC model, fall within the CSZ subzones. Four NW-trending normal faults, the Lost River, Lemhi, Beaverhead, and Deadman faults, all have southern segments within the CSZ and could have components of oblique slip that may accommodate right-lateral shear. The E-striking Centennial fault is within the CSZ and could have a greater component of oblique slip (e.g., Pierce et al., [2014] observed right-lateral offsets in Pleistocene age glacial moraines). For the SSC model, the recurrence estimates for each of the five normal faults is assumed to already include any component of strike-slip motion. Further, to model the geodetic slip rate in the CSZ subzones, the total rate must first be subtracted by the slip rates of the fault sources to avoid double counting the rates and leading to an unrealistic total rate. As a result, the geodetic rates for the CSZ are partitioned to the five normal faults and the remainder is assumed to be accommodated by the background zone where the geodetic rate is modeled to rupture on NE-striking virtual faults

The calculations for strain partitioning to estimate the remaining background rate of each subzone involves using the CSZ geodetic slip rates, strikes of the normal faults, the orientation of right-lateral strike slip, and normal fault slip rates (Table 5-1):

- The geodetic slip rates are from Payne et al. (2012) for the positions along the block model boundary where they fall in the CSZ subzones.
- The northwest strikes of the normal faults were compiled from the U.S. Geological Survey's Quaternary Fault and Fold Database (Haller et al., 2010a; 2010b; and Seismic Evaluation Team, 2010)
- The N78°W orientation of right-lateral strike-slip is derived by adding 45° to extensional axis orientation, N57°E, of the geodetic principal horizontal strain rate (Figure 4-14) and then taking the opposite orientation or 180° from N102°E

Table 5-1. Strain partitioning of geodetic slip rates onto normal fault sources in the CSZ subzones using a N78°W orientation for right-lateral strike-slip components.

Source Sub-Zone	Geodetic Slip Rate (mm/yr)[1]	Intersected Normal Fault Source and Fault Strike	Weighted Average Fault Slip Rate (mm/yr)[2]	Partitioned to Fault (%)[3]	Slip Rate Partitioned to Fault (mm/yr)[4]	Subzone Geodetic Remaining Slip Rate (mm/yr)[5]
CSZ1	1.1 ± 0.1 [0.2]	Centennial, N90°W	0.950	87	0.83	0.27 [0.2]
	1.2 ± 0.1 [0.6]					0.37 [0.6]
	1.4 ± 0.1 [0.2]					0.57 [0.2]
CSZ2	0.7 ± 0.1 [0.2]	Deadman, N68°W	0.043	89	0.038	0.26 [0.2]
	0.8 ± 0.1 [0.6]	Beaverhead, N27°W	0.940	43	0.40	0.36 [0.6]
	1.0 ± 0.1 [0.2]				Total: 0.44	0.56 [0.2]
CSZ3	0.4 ± 0.1 [0.2]	Lemhi, N34°W	0.185	51	0.094	0.26 [0.2]
	0.5 ± 0.1 [0.6]	Lost River, N22°W	0.116	38	0.044	0.36 [0.6]
	0.6 ± 0.1 [0.2]				Total: 0.14	0.46 [0.2]
CSZ4	0.0	No Faults	None	0	0.00	0.0 [0.2]
	0.1 ± 0.1 [0.6]					0.1 [0.6]
	0.2 ± 0.1 [0.2]					0.2 [0.2]

1. Geodetic slip rates are from Payne et al. (2012); also see text in Section 5.1. Weights for SSC model are shown in brackets.
2. Weighted average slip rates calculated from slip rates and uncertainties in logic trees.
3. Percentage calculated based on fault orientation relative to N78°W direction of right-lateral strike-slip component, assuming 0% is perpendicular and 100% is parallel.
4. Calculated by multiplying the weighted average slip by the percentage portioned to the fault.
5. Weights for SSC are given in brackets.

- The fault slip rates are a weighted average of the characterized fault sources from this study, which takes into account the uncertainty placed on each slip rate in the logic tree.

The amount of strain partitioned is calculated as a percentage of slip imparted to the normal faults. It is calculated by first taking the distribution of geodetic slip rates for each CSZ subzone. The strike-slip orientation of the geodetic strain (N78°W) is compared to the orientation of the fault sources. For strike-slip faulting, it is assumed that the more parallel the two orientations, the more slip rate is partitioned to the fault source. A percentage was applied to each fault source, 0% partitioned to the fault source if perpendicular and 100% would be applied if parallel to the orientation of the geodetic slip rate. The fault slip rate was multiplied by the orientation-based percentage, resulting in a slip rate partitioned to the fault. The remaining amount of geodetic slip rate was considered the background rate for the CSZ subzones. The subzone remaining geodetic slip rates after strain partitioning are listed in Table 5-1. These geodetic rates are used for each CSZ subzone when they exist. In the case where the CSZ zone does not exist, the background rate is calculated using the earthquake recurrence and the fault sources retain their originally assigned slip rates (see Sections 8.1.4 and 8.2.3).

5.2 Focal Depth Distribution for the ESRP

This section discusses the compilation of earthquake focal depths and evaluation to assess the seismogenic depths for the ESRP host zone and VRZs (see Sections 8.2.2 and 8.2.8, respectively). Compilation and evaluation of the 1850-2014 depth-sorted catalog shows that seismogenic thickness of the ESRP is different than that assessed in 1996 INL PSHA. There are 84 microearthquakes within the ESRP and many have well-determined focal depths. By comparison, Jackson et al. (1993) evaluated 19 earthquakes (available at that time) in the ESRP to assess the seismogenic thickness. Additionally the 1850-2014 depth-sorted catalog offers a greater number of earthquakes with well-determined focal depths outside of the ESRP to compare to, more than what was available to Jackson et al. (1993).

The full 1850-2014 earthquake catalog was sorted for well-determined focal depths to assess the seismogenic depths. The full 1850-2014 catalog has 83,799 earthquakes of magnitudes from <1.0 to 7.3 along with other location parameters (see Appendix D). The full 1850-2014 catalog was sorted four times in the order listed below and using the same criteria as Jackson et al. (1993):

1. Azimuth coverage where the station distribution has gaps ≤155°
2. Minimum distance (DMIN) from the earthquake epicenter to the closest station is less than ≤15 km
3. Root mean square error (RMS) is ≤0.25 seconds
4. Vertical standard error (ERZ) is ≤3 km.

Each sort used the output of the previous sort for the above criteria. The catalog sorted for well-determined focal depths resulted in 22,450 earthquakes. Of the 84 ESRP events, 55 did not meet the criteria listed above. Of these, 39 events have ERZ <3 km with gaps >155° or DMIN >15 km and were added back into the depth-sorted catalog for analysis. The other 16 events have ERZ much greater than 3 km and were excluded from the analysis. Figure 5-1 shows the 1850-2014 depth-sorted epicenters and their distributions for the well-determined focal depths including the 39 ESRP events.

A cross section through the 1850-2014 depth-sorted catalog was constructed from the CTB, across the ESRP, and to the ISB, similar to the cross section of Jackson et al. (1993). Earthquakes shown in Figure 5-1 within a ~100 km box on either side of the cross-section line were projected onto the cross section. The large width was used to project all ESRP events onto one cross-section line (Figure 5-2a).

The cross section for the 1850-2014 depth-sorted catalog shows a greater range of focal depths than the cross section of Jackson et al. (1993). For the ESRP, Figure 5-2a shows the 1850-2014 focal depths extend from near the surface to 42 km depth whereas Jackson et al. (1993) show a cutoff at 8 km (Figure 5-2b). The majority of 1850-2014 ESRP earthquakes that extend from 15 to 42 km depth are centered at COM. Eleven events analyzed by Carpenter and Payne (2009) have waveforms with low frequency content and may be associated with magma or fluid movement. Other COM events and possibly two other ESRP deep events may be volcanic related, but their waveforms have not been analyzed. Apart from the COM events and two other deep (~40 km) events, focal depths of the other earthquakes are assumed to be tectonic.

For the SSC model, the focal depth distribution in the ESRP is assumed to reflect the seismogenic thickness potential of the ESRP, which is different from that assessed in the 1996 INL PSHA. For the 1996 INL PSHA, the limited focal depth data presented in Jackson et al. (1993) showed a cutoff earthquake depth of 8 km (Figure 5-2b). Additionally, the heat flow of 100 mW/m^2 (Blackwell, 1989) measured in the INEL-1 borehole was used to estimate the temperature of 350° C at 8 km depth

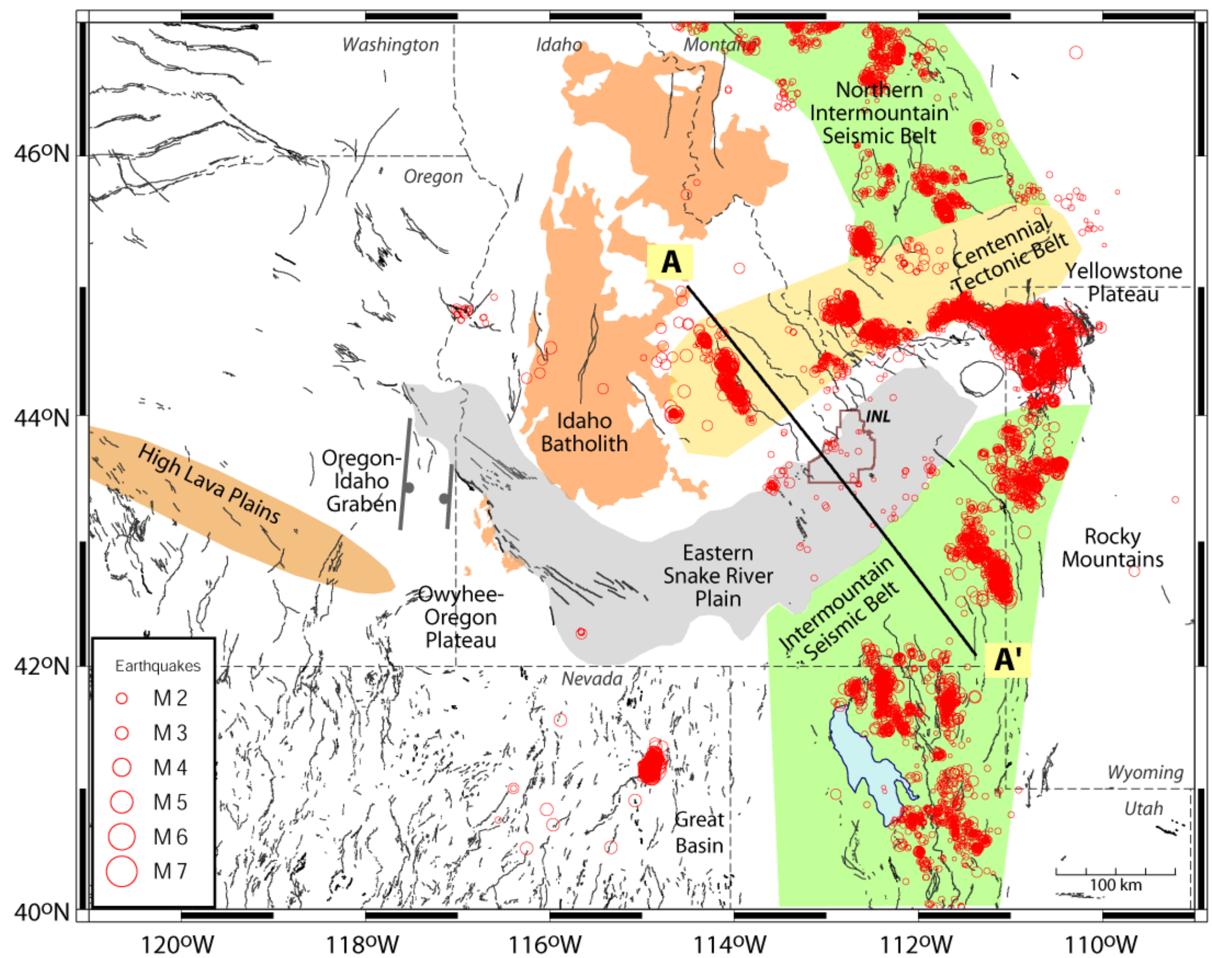

Figure 5-1. Map showing 1850-2014 sorted catalog for well-determined focal depths (see text for sort criteria).

a)

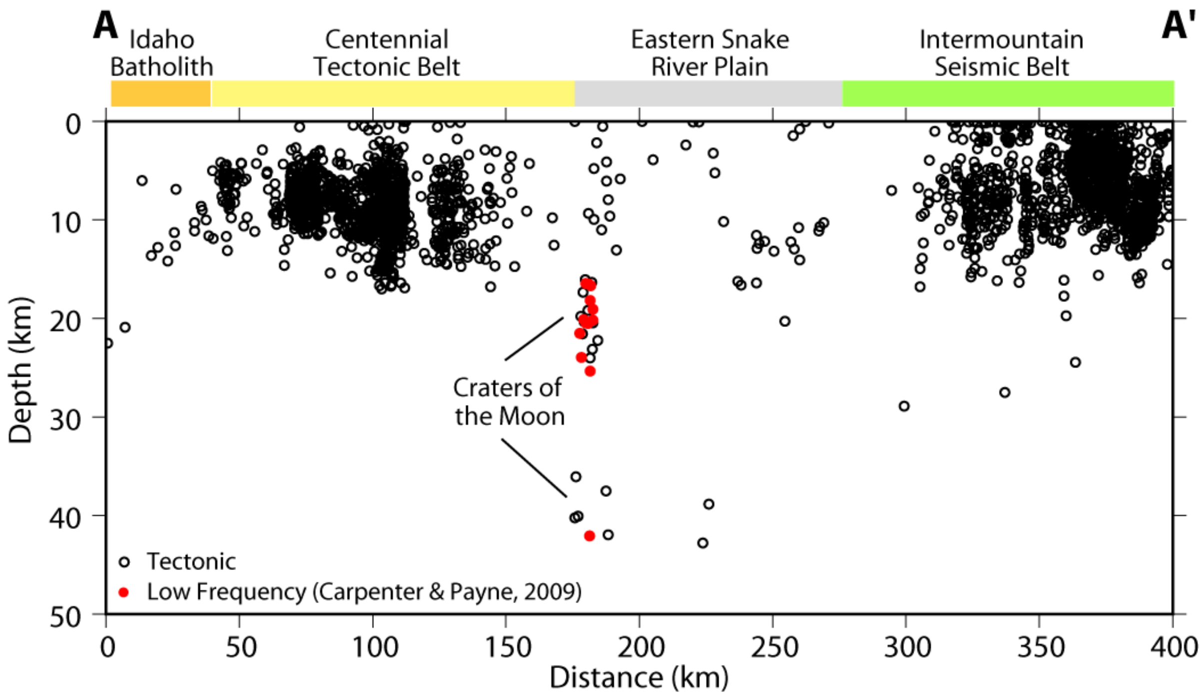

b)

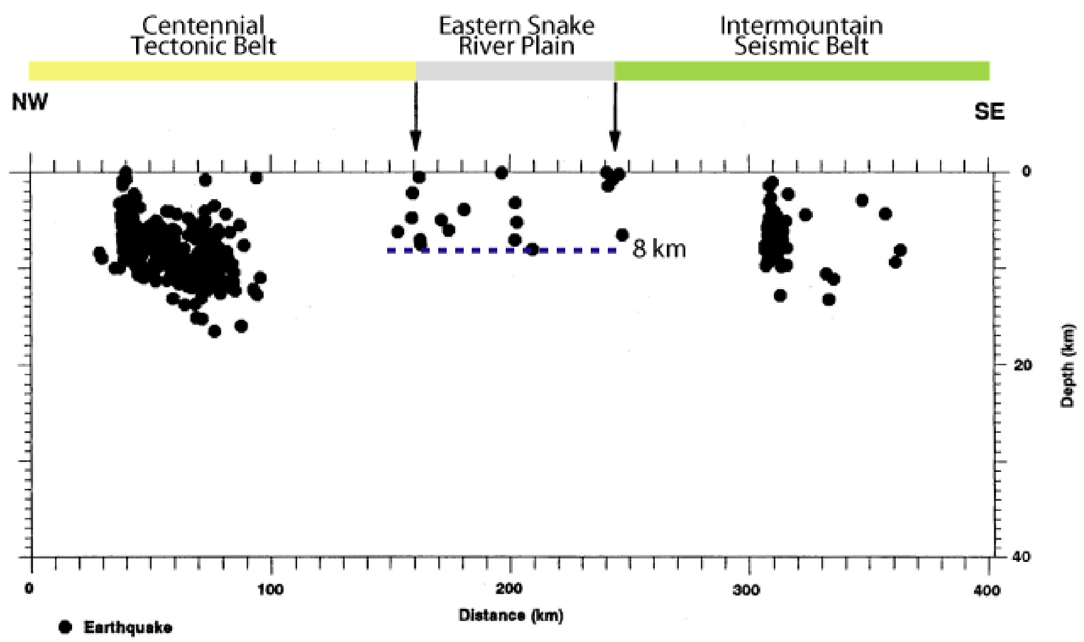

Figure 5-2. Cross sections for: a) 1850-2014 depth-sorted catalog; and b) from Jackson et al. (1993). In (a), earthquakes with deep focal depths (red dots) that have been analyzed by Carpenter and Payne (2009) have waveforms suggesting association with magma or fluid movement. In (b), the dashed blue line shows the proposed cutoff depth of earthquakes at 8 km as assessed by Jackson et al. (1993).

(Woodward-Clyde Federal Services et al., 1996). The correspondence with the cutoff earthquake depth and a temperature 350° C occurring at the same depth of 8 km supported the interpretation that the ESRP could have a shallower brittle crust than the surrounding Basin and Range regions (Jackson et al., 1993; Woodward-Clyde Federal Services et al., 1996). The focal depth distribution of the 1850-2014 depth-sorted catalog to a depth of 20 km is not consistent with this interpretation. Figure 5-2a shows that tectonic earthquakes within the ESRP, CTB, and ISB have focal depths at ≤20 km depth and suggests that the ESRP may have a seismogenic crustal thickness similar to the surrounding regions.

The occurrence of deep earthquakes at COM also suggests that volcanic related earthquakes can occur at depths greater than the depths used in the 1996 INL PSHA for VRZs. In the 1996 INL PSHA, evaluation of dike-induced earthquakes and their intrusion processes suggested volcanic earthquakes would likely occur at shallow depths of <4 km. Magma ascent from its origin at the base of the crust to the surface will likely lead to earthquakes and the possibility of triggering slip on nearby faults close to their yield stress (Payne et al., 2009). For example, at Lake Tahoe, Nevada small-magnitude earthquakes (M 2.2) occurred at depths between 25 and 33 km in association with dike intrusion. The volcanic processes triggered upper crustal seismicity at depths <20 km including the 2004 M_W 4.2 earthquake (Smith et al., 2004; von Seggern et al., 2008). The Lake Tahoe sequence is assumed to be an analog for the ESRP whereby volcanic earthquakes can occur at deep and shallow depths, as is observed at COM in Figure 5-2a. Thus, the seismogenic thickness within the VRZs should be the same as the seismogenic thickness of the ESRP (≤20 km) because slip would occur on the same faults whether due to magmatic or tectonic processes.

5.3 Magnitude Compilations for Seismic Source Zones

This section discusses the earthquake magnitudes compiled and evaluated to assess the maximum magnitude for the ESRP host zone, VRZ source zone, WSRP source zone, and the CSZ source zone. Very few earthquakes have occurred within these source zones to perform an evaluation. As a result, magnitudes of earthquakes assessed to be analogs for these four source zones were compiled from literature and evaluated. The following subsections provide the bases for the compilations of analog earthquake magnitudes and how the maximum magnitude was selected. Where possible E[**M**] is listed, which represents the expected value of the true moment magnitude (**M**) (see Section 6.1). Magnitudes discussed include: local magnitude M_L, coda magnitude M_D, body-wave magnitude m_b, and moment magnitude M_W.

5.3.1 ESRP and VRZs Maximum Magnitudes

Only microearthquakes (M_L<2.5) and the 1905 Shoshone earthquake (M_L 5.5 ± 0.5) are available to characterize the maximum magnitude of earthquakes in the ESRP. Earthquakes in eastern Oregon and those associated with dike intrusion were considered analogs for the ESRP. Since VRZs are located within the ESRP, it is assumed that slip would occur on the same pre-existing faults whether due to magmatic or tectonic processes. Dike intrusion would cause slip on faults close to their yield stress and regional tension would cause slip on these same structures. Thus, the compilation of earthquake magnitudes includes volcanic analogs.

The earthquake magnitudes compiled and considered in the evaluation for the ESRP and VRZs are listed in Table 5-2. The table includes M_L 5.5 ± 0.5 and E[**M**] 5.61 for the 1905 Shoshone, Idaho earthquake. The magnitude M_L 5.5 ± 0.5 was estimated by Oaks (1992) from the areal extent of MMI V isoseismal compiled from historical accounts of damage. Although its MMI epicenter may suggest that the earthquake occurred outside the ESRP (Figure 4-12), it is considered in this compilation. Without instrumental data to allow relocation of the 1905 event, its epicenter remains in the ESRP.

Table 5-2. Observed magnitudes considered in the evaluation of maximum magnitudes for the ESRP and VRZ source zones.

M_W or E[**M**][1]	Observed Magnitude	Location	Comments	Reference
5.61 E[**M**]	M_L 5.5 ± 0.5	Shoshone, Idaho, ESRP	Estimated from the areal extent of MMI V isoseismal compiled from historical accounts of damage.	1
5.79 E[**M**]	M_L 6.1	Milton-Freewater, Oregon	July 15, 1936; calculated M_L 6.1 using 17 stations with the closest at 250 km away. Estimated M_L 6.4 using total felt area developed by Toppozada (1975).	2
4.91 E[**M**]	M_{UK} 5.1	Near Adel, Oregon	Earthquake located east of Lake View near northern Basin and Range faults in eastern Oregon.	3
NA	M 4.2 ± 1.1	Worldwide Observations	Mean and standard deviation for 29 magnitudes of earthquakes associated with dike intrusion (See Table 5-3).	4, This study
5.6	NA	Dabbahu, Afar, Africa	From 2005 to 2010, volcano-tectonic earthquakes in association with dike intrusions and eruptions along a 60-km-long segment of the east African rift system in Afar, Ethiopia. Largest M_W earthquake occurred at the start of the dike intrusion.	5
5.7 - 6.4	NA	Miyakejima Volcano, Izu Islands, Japan	2000 dike intrusion and eruption; magma migrated northwest from Miyakejima volcano along a length of 30 km. M_W 6.2, 5.9, 6.0, 6.4, and 5.7 for five largest earthquakes during the intrusions.	6
6.0	NA	ESRP Source Zone	Assigned maximum M_W for the 1996 PSHA when the earthquake is in the ESRP.	7
5.0 ± 0.5	NA	VRZ Source Zones	Assigned maximum M_W range for the 1996 PSHA based on magnitudes of worldwide dike intrusion events compiled at that time.	7

1. E[**M**] is from the 1850-2014 catalog discussed in Section 6.4; NA – not applicable.
References: 1) Oaks, 1992; 2) Wong and Bott, 1995; 3) Niewendorp-Neuhaus, 2003; 4) Payne et al., 2009; 5) Yirgu et al., 2006; 6) Nishimura et al., 2001; 7) Woodward-Clyde Federal Services et al., 1996.

Table 5-3. Observed earthquake magnitudes, depths, and magma composition associated with dike-intrusion worldwide.[1]

Location	Year	Magnitude	Magnitude Type	Depth or Range (km)	Magma Composition	Reference
Krafla fissure swarm, Iceland	1975-1976	4.5	NA	0-6	Mafic	1
Krafla fissure swarm, Iceland	1977	3.8	NA	0-6	Mafic	2
Krafla fissure swarm, Iceland	1978	4.1	NA	1-4	Mafic	3
Kilauea east rift, Hawaii, USA	1965	4.4	M_L	0-8	Mafic	4
Kilauea east rift, Hawaii, USA	1968	3.3	NA	< 5	Mafic	5
Kilauea east rift, Hawaii, USA	1969	2.9	NA	< 10	Mafic	6
Kilauea east rift, Hawaii, USA	1976-1977	3.8	NA	< 10	Mafic	7
Kilauea east rift, Hawaii, USA	1980, Aug.	3.0	M_c	0.5-3	Mafic	8
Kilauea east rift, Hawaii, USA	1980, Nov.	3.1	M_c	0.7-4	Mafic	8
Kilauea east rift, Hawaii, USA	1982	3.0	M_c	0.5-3	Mafic	8
Kilauea east rift, Hawaii, USA	1999	3.7	NA	ND	Mafic	9
Kilauea southwest rift, Hawaii, USA	1975	3.0	NA	ND	Mafic	7
Kilauea southwest rift, Hawaii, USA	1981	3.4	M_c	1-2	Mafic	8
Asal, Afar, Africa	1978	5.3	m_b	0-6	Mafic	10
Ayelu-Amoissa, Africa	2000	4.6	M_W	< 7	Mafic	11
Dabbahu, Afar, Africa	2005	5.6	M_W	ND	Mafic	12
Nyiragongo, Africa	2002	4.8	m_b	ND	Mafic	13
Dallol, Africa	2004	5.5	M_W	6	Mafic	14
Taupo Volcanic Zone, New Zealand	1964-1965	4.6	NA	4-8	Silicic	15
Ruapehu Volcano, New Zealand	1995	4.8	M_L	5-20	Intermediate	16
Yellowstone Caldera, Wyoming, USA	1985	4.9	M_c	2-10	Mafic ?	17
Lake Tahoe, Nevada, USA	2003	2.2	M_L	29-33	Mafic ?	18
Izu Peninsula, Japan	1989	5.5	M_{JMA}	< 8	Mafic	19
Izu Peninsula, Japan	1997	5.3	M_W	5-10	Mafic	20
Miyake-jima, Japan	2000	6.4	NA	2.3	Intermediate	21
Parícutin Volcano, Mexico	2006	3.7	M_L	<10	Mafic	22

Table 5-3. Continued.

Location	Year	Magnitude	Magnitude Type	Depth or Range (km)	Magma Composition	Reference
Harrat Lunayyir, Saudia Arabia	2009	5.7	M_W	5	Mafic	23
Long Valley Caldera, California, USA	1989-1990	3.4	M_L	7-9	Mafic ?	24
Bardarbunga Volcano, Iceland	2014	5.5	M_W	ND	Mafic	25
		4.2 ± 1.1	Mean and standard deviation			

1. Table from Payne (2009) and updated with additional data for this study.

NA – Not available; ND – Not determined or reported.

References: 1) Einarsson and Bjornsson, 1979; 2) Brandsdottir and Einarsson, 1979; 3) Einarsson and Brandsdottir, 1980; 4) Bosher and Duennebier, 1985; 5) Jackson et al., 1975; 6) Swanson et al., 1976; 7) Dzurisin et al., 1980; 8) Karpin and Thurber, 1987; Nakata et al., 1982; Tanigawa et al., 1981; 1983; 9) Cervelli et al., 2002; 10) Abdallah et al., 1979; Lepine and Hirn, 1992; 11) Ayele et al., 2006; Keir et al., 2011; 12) Yirgu et al., 2006; 13) Kavotha et al., 2002; 14) Nobile et al., 2012; Craig et al., 2011; 15) Grindley and Hull, 1986; 16) Hurst and McGinty, 1999; 17) Waite and Smith, 2002; 18) Smith et al., 2004; 19) Okada and Yamamato, 1991; 20) Aoki et al., 1999; 21) Nishimura et al., 2001; 22) Gardine et al., 2011; 23) Pallister et al., 2010; U.S. Geological Survey, 2013; 24) Hughes, 2011; 25) Gudmundsson et al., 2014.

Eastern Oregon was considered an analog since it is a low-strain rate region that has been impacted by hotspot related volcanism (e.g., Draper, 1991; Shervais and Hanan, 2008). Eastern Oregon displays a very low internal deformation rate (McCaffrey et al., 2013) and may have added crustal strength due to mafic densification (Cox et al., 2011). Two earthquakes, M_L 6.1 and unknown magnitude (M_{UK}) 5.1, in eastern Oregon were included in Table 5-2. For these events E[**M**] 5.79 and E[**M**] 4.91 are also listed.

The volcanic earthquake analogs are those associated with dike intrusion. Table 5-3 lists dike-induced earthquakes from Payne et al. (2009) with six added earthquakes (29 total) which were used to update the estimated mean earthquake magnitude to M 4.2 ± 1.1. Payne et al. (2009) compiled magnitude data for earthquakes involving volcanic processes associated with dike-intrusion, calderas and central volcanoes, tectonic earthquakes triggered by magma intrusion, and tectonic earthquakes that trigger volcanic activity. They used the criteria listed below to distinguish earthquakes related to dike-intrusion and the same criteria were used to update their table. The criteria include:

- Observed to occur in association with an eruptive dike-induced event
- A temporal and spatial pattern indicating dike propagation (e.g., 0.5 m/s; Rubin, 1992)
- Swarm-like seismicity characteristics with a beginning and an end associated with magma movement
- Observed to occur during the formation of extensional ground deformation features in a volcanic rift zone
- Observed to occur concomitantly with geodetic observations indicating dike intrusion
- Dike intrusion occurs external and not within a central volcano or caldera.

Along with the estimated mean magnitude, magnitudes for two dike intrusion sequences were also included in Table 5-2. From 2005 to 2010, volcano-tectonic earthquakes occurred in association with dike intrusions and eruptions along a 60-km-long segment of the east African rift system in Dabbahu, Afar, Ethiopia. Largest earthquake M_W 5.6 occurred at the start of the dike intrusion (Yirgu et al., 2006). The 2000 episode of dike-intrusions and eruptions near the Miyakejima volcano in Izu, Japan had five moderate size earthquakes associated with migration of magma or dikes along a length of 30 km (Nishimura et al., 2001). The earthquakes had M_W 6.2, 5.9, 6.0, 6.4, and 5.7 and the range of 5.7-6.4 is listed in Table 5-2. The Dabbahu, Africa and Miyakejima, Japan dike intrusions, both within extensional regimes (Yirgu et al., 2006; Ida, 2009; respectively), are thought to offer the best analogs for assessing maximum magnitudes associated with dike intrusion.

A maximum of **M** 6.0 ± 0.5 was assessed to be representative of the maximum magnitudes listed in Table 5-2. The range of M_W 5.6 to 6.4 for dike-induced earthquakes includes E[**M**] of 5.61 and 5.79 for the 1905 Shoshone, Idaho and 1936 Milton-Freewater, Oregon earthquakes. The range of the maximum magnitudes M_W 5.5 to 6.5 is higher than maximum magnitudes assessed for the ESRP and VRZ source zones in the 1996 INL PSHA. Table 5-2 lists a maximum of **M** 6.0 for the ESRP source zone and a maximum of **M** 5.5 for the VRZ source zones (Woodward-Clyde Federal Services et al., 1996). By assuming that the same structures will produce earthquakes for either dike-induced or tectonic processes, the compilation of maximum magnitudes for dike-induced earthquake analogs results in increasing the maximum M_W for not only the VRZs but also the ESRP. The maximum of **M** 6.0 ± 0.5 is reasonable for the seismogenic thickness (≤20 km) assessed in Section 5.2.

5.3.2 WSRP Maximum Magnitude

There are few earthquakes located within the WSRP and the largest is the 1916 E[**M**] 5.58 (or M 5.3) earthquake near Boise, Idaho (Figure 4-11). To assess the maximum magnitude for the WSRP, M_W was compiled from two hazard related studies and for the 1916 event. Four scarps near and on the Halfway Gulch fault show evidence of Holocene to late Pleistocene movements. Beukelman (1997) trenched

Table 5-4. Observed magnitudes considered in the evaluation of maximum magnitude for the WSRP source zone.

M_W or E[**M**][1]	Observed Magnitude or Intensity	Location	Comments	Reference
6.7 ± 0.5	NA	Half-way Gulch trench, WSRP	Estimated M_W using maximum displacements of five measurements from 0.5 to 1 m and Wells and Coppersmith (1994).	1
6.0 ± 0.3	NA	Half-way Gulch trench, WSRP	Estimated M_W from surface rupture length 6.2 km and using Wells and Coppersmith (1994).	1
6.5	VIII	Boise Front Fault System, WSRP	Estimated maximum credible earthquake using SEA99 relationships and intensity/acceleration results of Wald et al. (1999), and presumably some relationship to estimate M_W of the fault.	2
5.58 E[**M**]	5.3, VII	Near Boise, WSRP	Earthquake occurred May 13, 1916 with intensity assigned as VII in Boise. Also has an unknown magnitude from Pasadena (PAS). Uses the conversion of MMI to M_W.	3

1. E[**M**] is from the 1850-2014 catalog discussed in Section 6.4; NA – not applicable.
References: 1) Beukelman, 1997; 2) Zollweg, 2005; 3) Stover, 1993.

scarps near the Halfway Gulch fault. Table 5-4 lists M_W of 6.7 ± 0.5 estimated using displacements measured in these trenches and the relationship of Wells and Coppersmith (1994). Beukelman (1997) also estimated M_W of 6.0 ± 0.3 using rupture lengths of the scarps and the Wells and Coppersmith (1994) relations. The M_W of 6.5 estimated by Zollweg (2005) for the Boise Front fault falls within the range of M_W estimated by Beukelmen (1997) using displacements. The estimate M_W of 5.6 for the 1916 event falls below the ranges estimated for paleoseismic investigations. A maximum **M** 6.75 ± 0.25 was assessed for the WSRP based on the range of M_W estimated for displacements, and considering that lengths of the mapped normal faults associated with graben formation in the WSRP exceed those used by to Beukelman (1997) estimate M_W.

5.3.3 CSZ Maximum Magnitude

The maximum magnitude for the CSZ source zone is assessed to be **M** 6.5 ± 0.25 based on analog earthquakes associated with strike-slip faulting in an extensional regime. Magnitudes of three earthquakes were considered; the 1934 M_W Hansel Valley, Utah within the ISB, the 1966 M_L 6.1 with E[**M**] 5.79 Caliente, Nevada, and 2011 E[**M**] 4.41 (or M_W 4.6) Centennial Shear Zone earthquakes (Table 5-5). The 1934 E[**M**] 6.57 (M_W 6.6) Hansel Valley earthquake represents the best analog for maximum magnitude. It occurred in the ISB which has a right-stepping en echelon pattern of active normal faults that extends from the Wasatch fault to the Teton fault. The right-stepping pattern is indicative a region undergoing left-lateral shear. Payne et al. (2012) suggests that earthquakes within the ISB may accommodate left-lateral shear due differences in strain rates between the ESRP and ISB (Payne et al., 2012).

Table 5-5. Observed magnitudes considered in the evaluation of maximum magnitude for the CSZ source zone.

E[**M**][1]	Observed Magnitude	Location	Comments	Reference
6.57	M_W 6.6	Hansel Valley, Utah	The March 12, 1934 M_W 6.6 mainshock and M_W 5.9 aftershock both had left-lateral strike-slip fault plane solutions and are within a zone of right-stepping en echelon pattern of active normal faulting that extends from the Wasatch fault to the Teton fault. The 1934 events occurred within a zone that may accommodate left-lateral shear due to differences in strain rates between the ESRP and ISB.	1
5.79	M_L 6.1	Pahranagat Shear Zone, Nevada	The August 8, 1966 M_L 6 Caliente, NV earthquake was the largest recorded event in the Pahranagat Shear zone, which yielded an almost pure strike-slip fault plane solution, similar to other solutions of many subsequent smaller events. The Pahranagat Shear is a zone of sinistral shear within the Basin and Range domain south of the Wasatch fault necessary to accommodate differences in strain rates from north to south.	2
4.41	M_W 4.6	Centennial Shear Zone, Montana	The April 5, 2011 event is the largest magnitude earthquake of many events which have right-lateral strike-slip fault plane solutions and are located within the CSZ.	3

1. E[**M**] is from the 1850-2014 catalog discussed in Section 6.4; NA – not applicable.
References: 1) Doser, 1989b; Payne et al., 2012; 2) Kreemer et al., 2010; 3) Payne et al., 2013; Stickney, 1997.

5.4 Big Lost Fault Analysis

Wood et al. (2007) recognized that the basalt stratigraphy on the west side of the Big Lost River is very different from that on the east side of the river. They proposed that the discontinuity could be due to a fault (referred to as the Big Lost fault in this study). This section discusses the steps used to estimate the slip rates of the Big Lost fault using the boreholes and correlations of stratigraphic differences presented by Wood et al. (2007). It also discusses the assessment of fault length and strike.

The Big Lost fault is located in the central part of INL (Figure 5-3). The Big Lost fault as interpreted by Wood et al. (2007) relative to nearby boreholes is shown in Figure 5-4. Wood et al. (2007) recognized that the basalt layers in boreholes on the west side of the Big Lost River cannot be correlated with and are different from basalt layers on the east side river. Wood et al. (2007) used U.S. Geological Survey (USGS) boreholes USGS-066 (west) and USGS-043 (east) to assess the stratigraphic differences (Figure 5-5). Further they proposed that the basalt stratigraphy in borehole Middle 2050A has a stratigraphy similar to that on the west side of the Big Lost River and that the placement of this borehole reduces the basalt stratigraphic discontinuities to <300 m. The stratigraphic offsets in the two boreholes indicate the Big Lost fault is an east-dipping normal fault.

Two slip rates were estimated for the maximum offset and most recent offset for the stratigraphic correlations in USGS-066 and USGS-043. First the elevation differences of layers were measured for the correlations interpreted by Wood et al. (2007) and then the ages of those offsets were used to calculate the slip rates. For this study, the elevation differences shown in Figure 5-5 were measured between these two boreholes for the correlations of the ages of basalt layers listed in Table 5-6, and are generally similar to those interpreted by Wood et al. (2007). The elevations differences have a total offset of 309 m (or 309372 mm), which spans 780,000 yrs. The maximum slip rate of 0.40 mm/yr is calculated using the total offset over this time period (Table 5-7). The slip rate of 0.08 mm/yr for the most recent offset is calculated using the elevation difference of 24 m (24384 mm) for the first correlation and the average (321,000 yrs) of the basalt flow ages (292,000 and 350,000 yrs).

Table 5-6. Ages, elevations, and elevation differences of basalt layers in boreholes USGS-066 and USGS-043.

Age of Layer (ka)	West USGS-066 Elevation (ft)	East USGS-043 Elevation (ft)	Elevation Difference (ft)	Elevation Difference (m)	Elevation Difference (mm)
>292 / 350	4860	4780	80	24	24384
461 / 466-543	4800	4605	195	59	59436
643 / 641	4725	4390	335	102	102108
<780 / <759	4645	4240	405	123	123444
				Total Displacement (mm)	309372

Table 5-7. Estimated slip rates for the Big Lost fault.

Type	Offset (mm)	Age (ka)	Slip Rate (mm/yr)
Maximum	309372	780,000	0.40
Most Recent Offset	24384	321,000	0.08

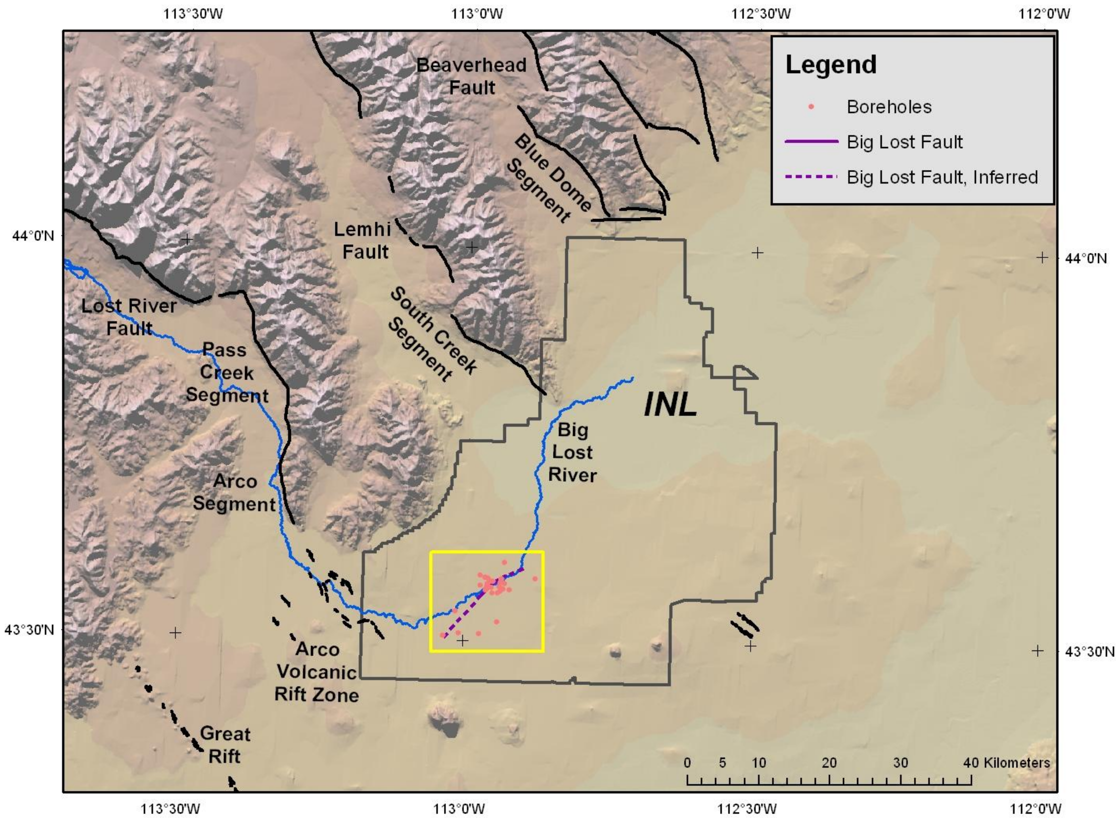

Figure 5-3. Map showing the Big Lost fault at INL and location of the map in shown in Figure 5.4 (yellow box).

The stratigraphic discontinuities in other nearby boreholes may indicate the Big Lost fault has a SE-strike and an estimated length of up to 15 km. Correlations of basalt layers between borehole C1A (west) and boreholes USGS-129, 131, and 132 (east) may indicate an offset <50 m which may be associated with the Big Lost fault or could be due to sloping basalt layers. A similar correlation may be permissible between boreholes USGS-133 and WO-2. Helm-Clark et al. (2006) suggested that near-vent facies in nearby boreholes along the Big Lost River and CIA could be evidence of a NE-trending set of volcanic vents that is aligned with the Big Lost River floodplain. The Big Lost fault could be a dike-induced normal fault associated with formation of the NE-trending set of vents. Extending the fault ends to the southwest to CIA and to the northeast just beyond USGS-133 results in a fault length of 15 km. The southwestern and northeastern ends of the Big Lost fault that extend beyond the 3-km length for the boreholes used by Wood et al. (2007) are highly speculative. Thus, the fault is shown as inferred (dashed lines) on the maps in Figures 5-3 and 5-4.

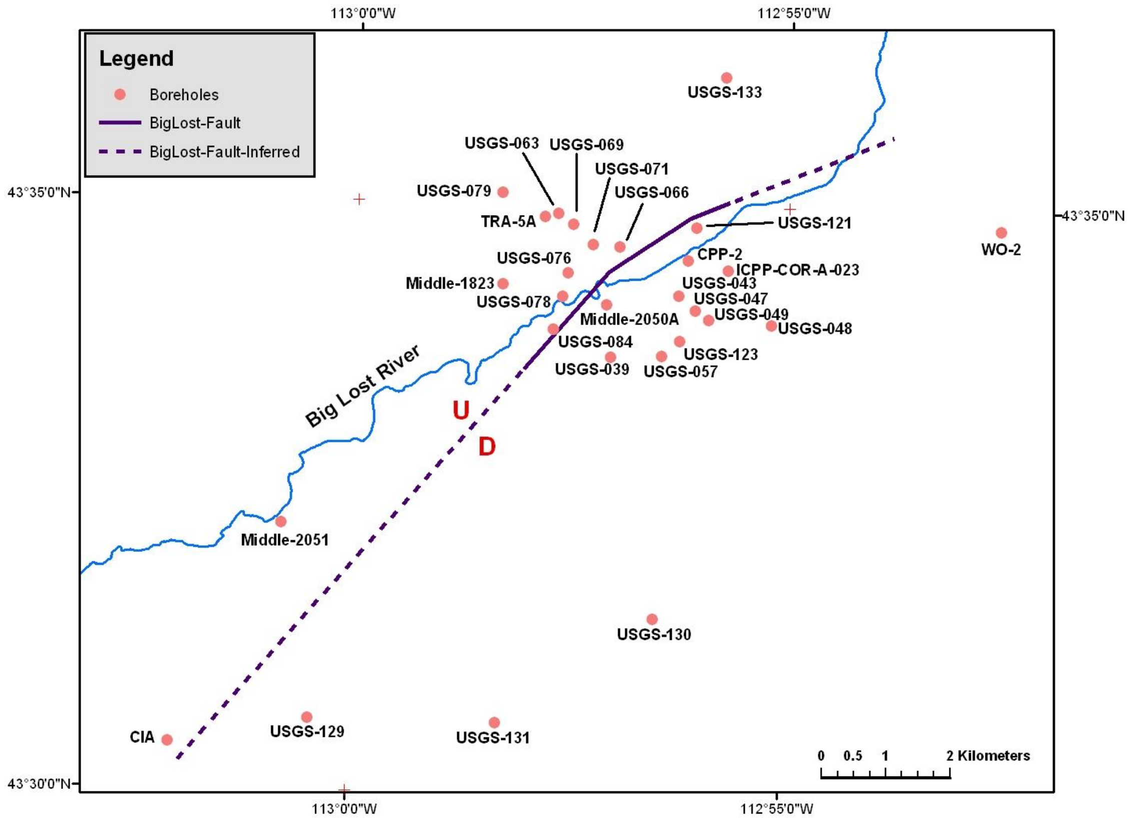

Figure 5-4. Map showing the location of boreholes near the Big Lost fault. The solid line for the Big Lost fault shows the interpretation of the Wood et al. (2007). Stratigraphic correlations across the fault are shown for boreholes USGS-066 and USGS-043 in Figure 5-5. Relative offset of basalt layer is indicated by U for upside and D for downside.

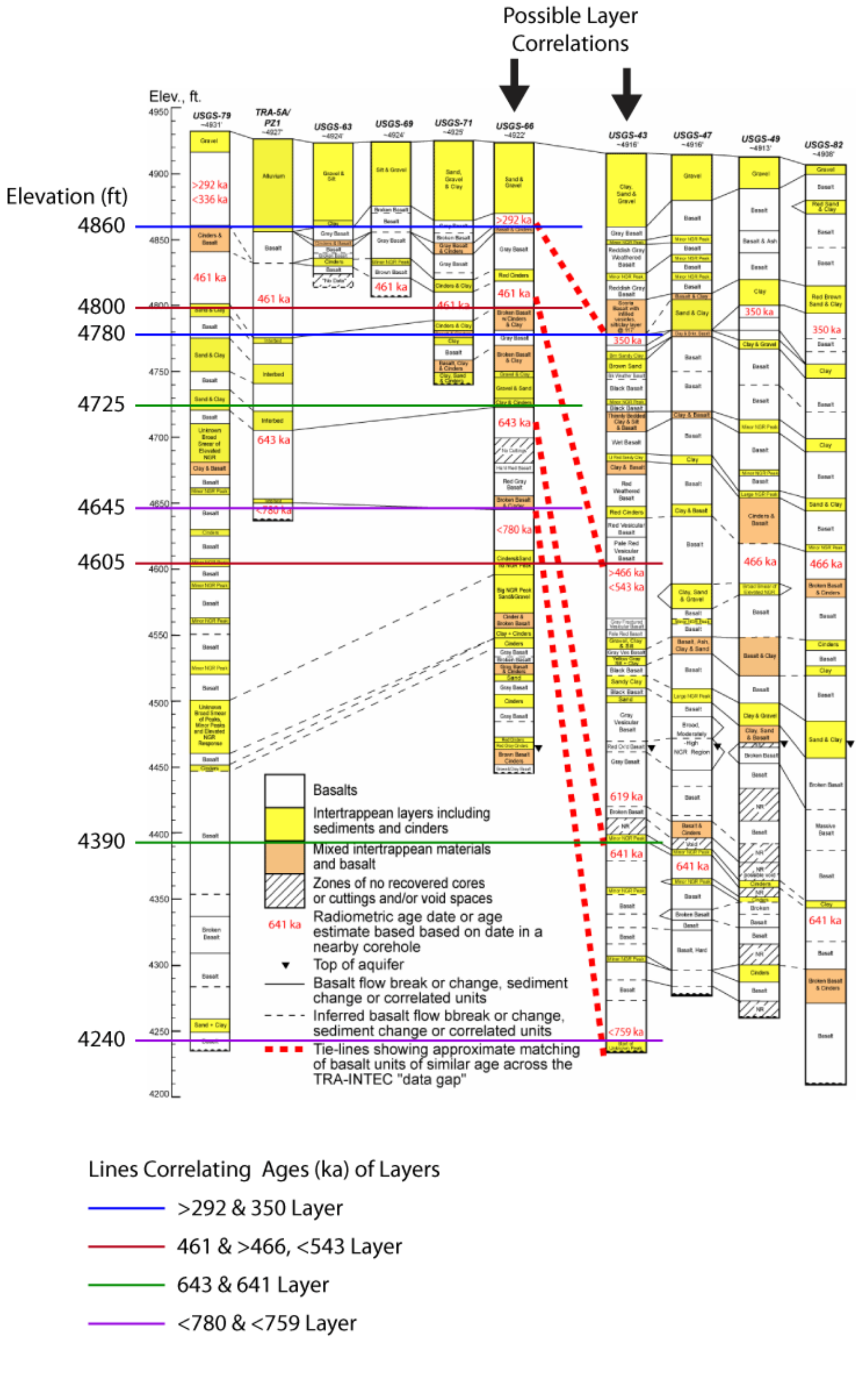

Figure 5-6. Correlations of basalt flows of different ages (dashed red lines) as interpreted by Wood et al. (2007) between boreholes USGS-066 (east) and USGS-043 (west). For this study, different colors lines highlight the elevations for the ages of layers used to estimate offsets of the basalt flows (Table 5-6).

6. SSC Database: Earthquake Catalog

This chapter describes the compilation and analyses of the earthquake catalog for the INL SSHAC Level 1 study. The earthquake catalog developed by Carpenter (2010) for the 2010 sensitivity analysis (Seismic Evaluation Team, 2010) was updated to include earthquakes that occurred from 2008 through the end of 2014. The process of compiling the 1850-2014 catalog follows the approach used by Carpenter (2010). The procedure is similar to that described in the NUREG-2115 (NRC, 2012b), where records from multiple catalogs were merged in an attempt to limit the effect of partial network coverage in time and space, and to obtain a data set of alternative magnitude measures for use in deriving magnitude conversion equations. Section 6.1 summarizes the development of the 1850-2014 catalog and its contents (see Appendix D for details). Section 6.2 describes the process of homogenizing the magnitudes to a uniform moment magnitude measure and the calculation of unbiased earthquake counts to be used in recurrence analysis. This is done by following the procedure developed in NUREG-2115 that allows proper treatment of the uncertainty in the magnitude estimates and in the magnitude conversions. The last two sections describe the declustering process used to remove foreshocks and aftershocks (Section 6.3), and the assessment of the completeness of the catalog as a function of location, time, and earthquake size (Section 6.4).

6.1 1850-2014 Earthquake Catalog

The 1850-2014 earthquake catalog of 84,565 events covers the region of 40.5º-47.0ºN and 109.0º-117.0ºW; the extent which is sufficient to cover the primary sources of seismicity in and around INL. The earthquake catalog covers the time period from the earliest reported earthquake (dated February 22, 1850) to midnight on December 31, 2014. All times are entered as Greenwich Mean Time (GMT). The catalog contains magnitudes of various types (e.g., coda, local, body-wave, surface-wave, and moment magnitudes) from original sources. Some of the pre-instrumental monitoring events have size based on intensity data. The 1850-2014 catalog was used to develop subsequent catalogs discussed in Section 6.2, and for two other evaluations discussed in Section 4 (1850-2014 M>2) and Section 5 (1850-2014 depth-sorted).

The full 1850-2014 catalog was developed as part of this study by compiling earthquakes from 2008 to 2014 and adding them to the 1850-2007 catalog developed by Carpenter (2010). As part of the SET recommendations, an updated 1850-2007 earthquake catalog was developed for use in the 2010 sensitivity analyses. The SET recommended that the 1850-1999 seismicity catalog used in the 2000 INL PSHA be updated to 1850-2007 (Seismic Evaluation Team, 2010). For the 2010 sensitivity analyses, Carpenter (2010) expanded the 1850-1999 catalog to include earthquakes from 1 January 2000 through 31 December 2007 from surrounding seismic monitoring networks. This updated catalog of 75,099 events also included several special-study catalogs which had not been included previously (Appendix D).

The approaches used in this study to compile the 2008-2014 earthquakes follow those used by Carpenter (2010) and are more fully discussed in Appendix D. First, earthquake catalogs were requested from the same seismic monitoring institutions as by Carpenter (2010) and which had data within the region of interest. Second, the earthquake data were reformatted to common format, including date, origin time, location, depth, magnitude, and other location parameters that describe the quality of the computed hypocenter. Third, the different catalogs were merged so that redundant events could be matched and a preferred event selected while the other redundant events were eliminated. The preferred earthquake location was chosen based on its location within an authoritative region specified by the Advanced National Seismic System (ANSS), which is a region generally within the limits of an institution's seismic network. When two or more earthquake locations were within an authoritative region, then a screening process was applied to determine the best located event. In all cases of single entry or multiple earthquake entries, up to six original source magnitudes were retained from an institution's catalog. Over 8,700 earthquakes were compiled for the 2008-2014 catalog and combined with the 1850-2007 catalog to produce the full 1850-2014 catalog.

6.2 Magnitude Homogenization

The 1850-2014 earthquake catalog is used in PSHA to obtain earthquake recurrence parameters for source zones, and it is important that a uniform earthquake size measure is used in the catalog. In modern PSHA studies this measure is chosen to be consistent with the magnitude scale used in the applicable ground motion predictive relationships. The ground motion models used in the INL PSHA are defined in terms of moment magnitude (**M**), so the catalog needs to be uniformly converted to moment magnitude. The approach to calculating a uniform magnitude followed for this study is the same as that described by the NRC in NUREG-2115 (NRC, 2012b) and by the Electric Power Research Institute Seismic Owners Group (EPRI/SOG, 1988), in which the uncertainty in the magnitude is accounted for through a variance-weighted estimate of the expected value of the true moment magnitude (E[**M**]). To correctly incorporate the uncertainty, earthquake records with magnitudes from multiple agencies, including published magnitudes from other studies, were merged into one catalog as described in Section 6.1 and Appendix D. The two approaches presented in NUREG-2115 to obtain uniform magnitudes and the use of N* to obtain unbiased recurrence calculations are used in this study and are described in the following sections.

6.2.1 Target Magnitudes and Available Magnitudes

Based on the discussion above, for the earthquake catalogs to be consistent with the size measure used in the ground motion predictive models, they need to be converted to a uniform estimate of **M**. **M** is available only for a small number of earthquakes (approximately 200) in the 1850-2014 catalog. The earthquake database described in Section 6.1 contains nearly 83,000 records with at least one size measure (magnitude or macroseismic intensity). Most of the earthquake records report M_D or M_L. The remaining data are divided between **M** and M_W, body-wave magnitude (m_b and M_N), surface-wave magnitude (M_S), and macroseismic intensity (I_0). Table 6-1 shows the magnitude types and the ranges of values observed in the1850-2014catalog. Note that **M** indicates the moment magnitudes calculated from seismic moment using the published Hanks and Kanamori (1979) formula.

Table 6-1. Magnitude types and magnitude ranges in the 1850-2014 earthquake catalog.

Magnitude Type	No. Earthquakes	No. Estimates	Time Period	Magnitude Range
M	125	142	1934 to 2014	3.08 to 7.28
M_W	66	172	1962 to 2014	2.51 to 6.14
M_S	20	20	1934 to 2014	3.6 to 7.3
M_L	16,876	19,665	1905 to 2014	-0.5 to 7.7
M_D	72,724	75,889	1901 to 2014	-1.29 to 6.1
m_b	498	540	1934 to 2011	2.8 to 6.6
M_N	7	7	1967 to 1969	4.0 to 4.9
unknown	169	231	1884 to 2014	2.0 to 6.75
I_0[1]	1,674	1,674	1850 to 1979	II to VI
1. These are records with I_0 as the only available earthquake size measure.				

To be able to derive conversion equations it is necessary to have a database of earthquakes with at least one **M** (or M_W) and one other magnitude type. The moment magnitude was consistently calculated for all the earthquakes with a seismic moment (from available literature or catalog) using the Hanks and Kanamori (1979) formula:

$$\mathbf{M}=2/3 \log_{10}(M_0)-10.7 \qquad [6\text{-}1]$$

In cases where multiple values of moment magnitude are available they have been combined in a weighted average using the formulation presented in NUREG-2115, assuming all estimates have equal weight. It should be noted that in the published Hanks and Kanamori (1979) formula the coefficient 10.7 is rounded from 10.73; this different precision determines a 0.03-unit difference between **M** and M_W.

6.2.2 Conversion from M_L, M_D, and Other Magnitude Scales

The following subsections offer details about the empirical magnitude conversion relations derived for the magnitude types represented in the 1850-2014 earthquake catalog.

6.2.2.1 Estimation of E[M] from Moment Magnitude

Following NUREG-2115, the expected value of the true moment magnitude (E[**M**]) can be obtained from the observed moment magnitude ($\hat{\mathbf{M}}$) given its uncertainty $\sigma[\mathbf{M}|\hat{\mathbf{M}}]$ using the following equation:

$$E[\boldsymbol{M}|\widehat{\boldsymbol{M}}] = \widehat{\boldsymbol{M}} - \beta\sigma^2[\boldsymbol{M}|\widehat{\boldsymbol{M}}] \qquad [6\text{-}2]$$

Where β is b*ln(10). Based on a preliminary analysis of the data in the INL catalog, the b value is assumed to be 0.95.

Earthquake catalogs do not typically report the uncertainty in their magnitude estimates, but NUREG-2115 shows that an approximate estimate of σ[**M**] can be obtained from the Harvard CMT catalog. A search was conducted over that catalog to pull all the earthquakes occurred within the space and time windows covered by the 1850-2014 catalog. The resulting dataset contains 14 earthquakes with an average σ[**M**] of 0.09, which is consistent with findings in NUREG-2115 for earthquakes post-1980. Therefore, if σ[**M**] is not specified, it is assumed that $\sigma[\mathbf{M}|\hat{\mathbf{M}}]$ is 0.09.

The catalog contains 68 earthquakes with both **M** (obtained from M_0 using Equation 6.1) and M_W obtained from another source. The data is plotted in Figure 6-1 by open circles, representing earthquakes with only one measure of Mw and **M**, and by black dots, representing earthquakes with more than one estimate of M_W or **M**. Statistical analysis on this data set shows that the best fit is given by an offset model with a coefficient of 0.03 (solid, red curve in Figure 6-1), consistent with the rounding difference in the Hanks and Kanamori (1979) formula discussed in the previous section. This finding confirms that M_W can be converted to **M** by adding 0.03.

6.2.2.2 Estimation of E[M] from Body-Wave Magnitudes

The 1850-2014 earthquake catalog contains over 400 earthquakes with at least one estimate of m_b, and seven earthquakes with M_N, however only 28 of these earthquakes have also at least one estimate of **M**. For the purpose of this study M_N is assumed to be equivalent to m_b, without any further analysis. Figure 6-2 shows 53 data point (obtained from 28 earthquakes) in comparison with the magnitude conversion relation for m_b derived in Pacific Northwest National Laboratory (PNNL, 2014). The

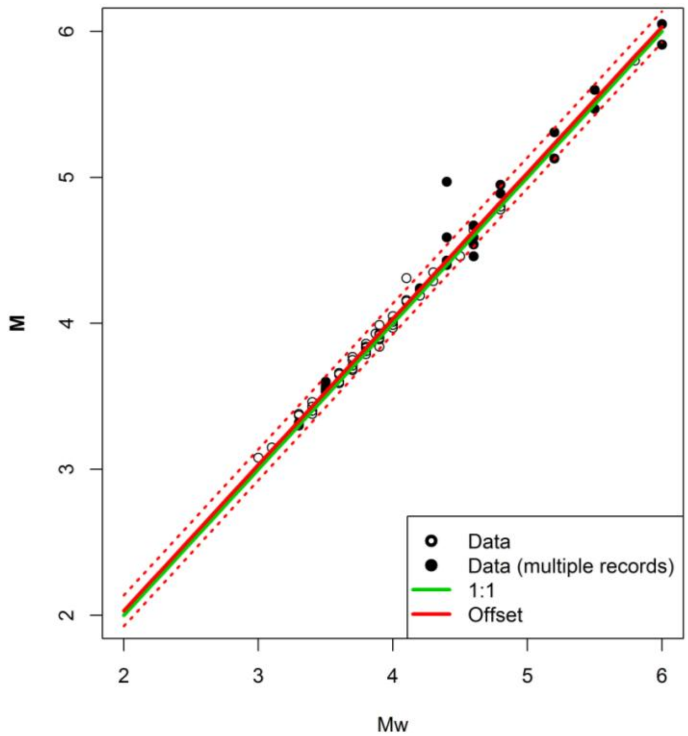

Figure 6-1. Plot of the M_W – **M** regression.

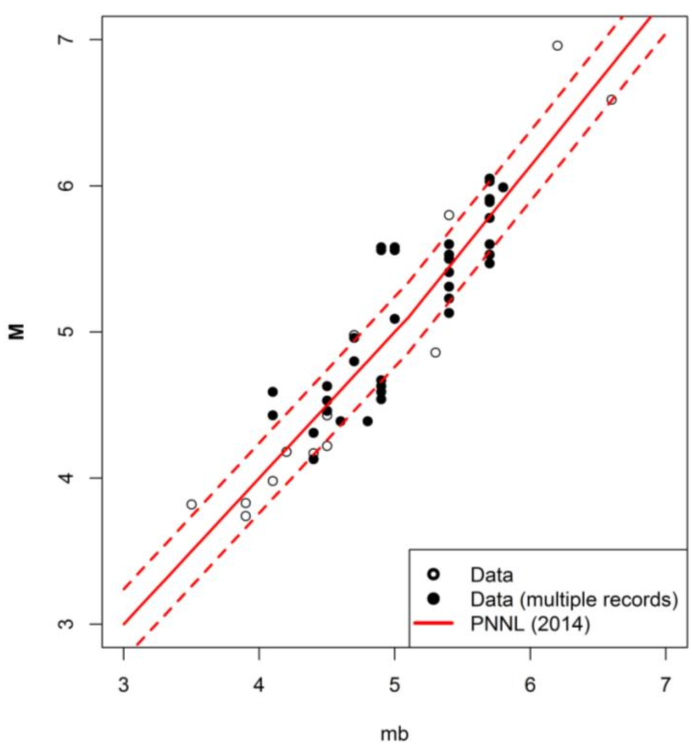

Figure 6-2. Plot of m_b-**M** data in comparison with the Pacific Northwest National Laboratory (PNNL) (2014) conversion relation.

agreement is very good, confirming that the equation can be used to convert the m_b values in the 1850-2014 catalog. Note that the PNNL (2014) conversion relation, although it is not very different from that of Sipkin (2003) used in Seismic Evaluation Team (2010), it is preferable because it was developed following the NUREG-2115 approach to E[**M**].

The magnitude conversion relation is as follows:

$$E[\mathbf{M}] = m_b \qquad \text{for } m_b \leq 5.1 \qquad [6\text{-}3]$$

$$E[\mathbf{M}] = -0.765 + 1.15m_b \qquad \text{for } m_b > 5.1$$

$$\sigma_{\mathbf{M}|mb} = 0.24$$

6.2.2.3 Estimation of E[M] from M_S Magnitudes

The 1850-2014 catalog contains 20 earthquakes with at least one estimate of M_S, but only 17 also have **M** and can be used to derive a magnitude conversion relation. Similarly to what described in the previous section for m_b, PNNL (2014) presents a magnitude conversion relation for M_S. Figure 6-3 shows the comparison between the available data from the 1850-2014 catalog, and the PNNL (2014) relation. The plot shows good agreement, indicating that the quadratic polynomial curve derived in PNNL (2014) can be applied to the 1850-2014 catalog:

$$E[\mathbf{M}] = 2.84 + 0.13M_S + 0.07M_S^2 \qquad [6\text{-}4]$$

$$\sigma_{\mathbf{M}|Ms} = 0.22$$

6.2.2.4 Estimation of E[M] from MD Magnitudes

The 1850-2014 catalog contains tens of thousands of earthquakes with at least one measure of M_D, but only 125 of these have also a measure of **M**. Figure 6-4 shows the data with M_D and M: in the figure, open circles represent earthquakes that only have one M_D and one M, while black circles indicate earthquakes with multiple measures of either M_D or **M**. The figure shows a set of data points represented by magenta circles that appear to be outliers. These were confirmed to be records from the INL catalog (or IE in Figure 6-4) that might have been produced by automatic coda picks by program SEISAN. These earthquakes were removed from the dataset used to derive the magnitude conversion.

The remaining data were fitted by a linear and by an offset model, then statistical test (the AIC (Akaike Information Criterion) and the Bayesian Information Criterion (BIC) are applied to select between the two models. Results indicate a strong preference for the linear model in Equation 6.5:

$$E[\mathbf{M}] = 0.784{*}M_D + 0.904 \qquad [6\text{-}5]$$

$$\sigma_{\mathbf{M}|MD} = 0.14$$

Following NUREG-2115, $\sigma\mathbf{M}|M_D$ is calculated as the difference between the sigma of 0.17 obtained from the regression and the average value of $\sigma[\mathbf{M}|\hat{\mathbf{M}}]$ = 0.1 (rounded from 0.09) for the earthquakes used in this regression. The equation is applicable for $M_D \geq 2.3$.

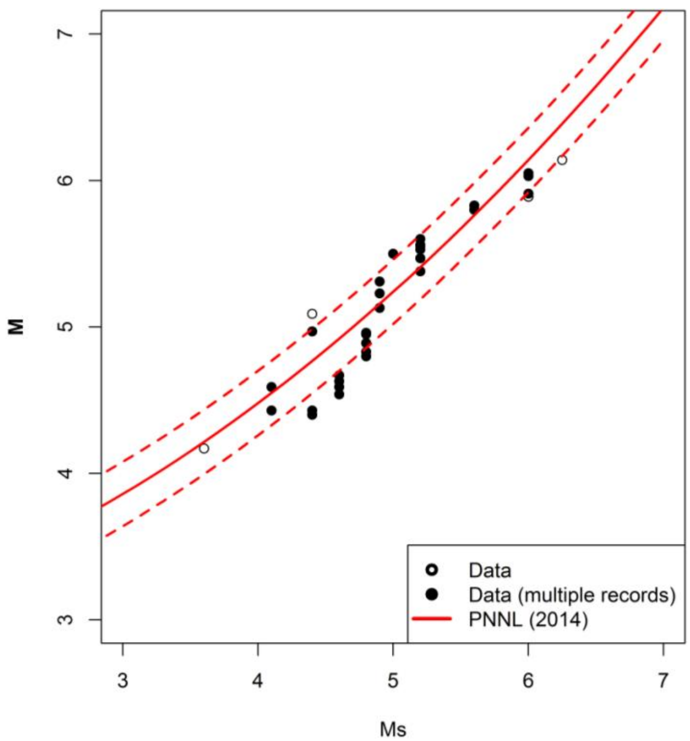

Figure 6-3. Plot of M_S-**M** data in comparison with the Pacific Northwest National Laboratory (PNNL) (2014) conversion.

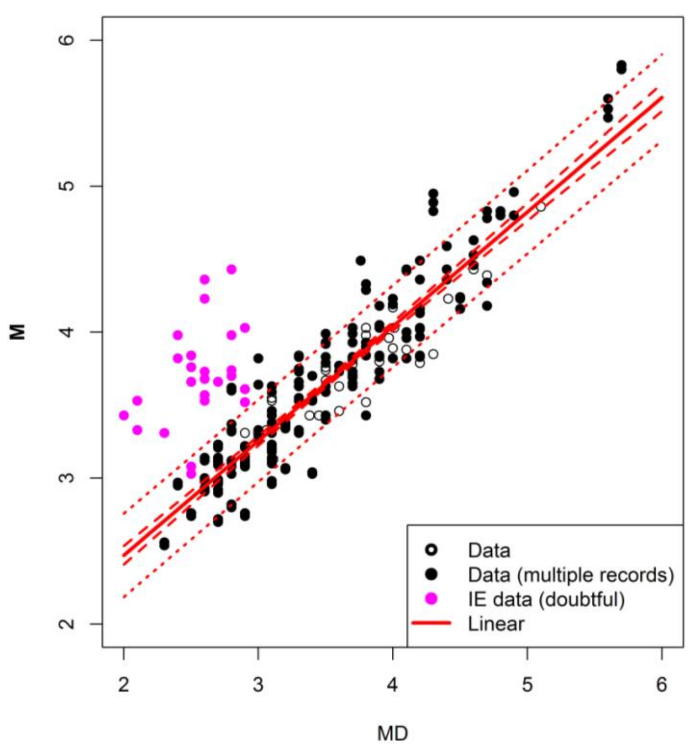

Figure 6-4. Plot of the M_D – **M** regression.

6.2.2.5 *Estimation of E[M] from M_L Magnitudes*

There are 140 earthquakes in the 1850-2014 catalog with one or more M_L and **M**, for a total of 472 data points (see Figure 6-5). The largest earthquake is the August 18, 1959, M_L 7.7 and **M** 7.3 (from Doser and Smith, 1989), which is shown in the Figure 6-5 by a purple dot. Since it is only one earthquake, isolated from the rest of the data set this event is not used to derive conversions.

The data were fit by a linear model and by an offset model, then statistical tests (AIC and BIC) were applied to select between the two models. Results indicate a preference for the linear model, however the offset model seems to capture better the largest magnitudes and it is preferred. The offset model is shown in Equation 6.6:

$$E[\mathbf{M}] = M_L - 0.07 \quad [6\text{-}6]$$

$$\sigma_{\mathbf{M}|MD} = 0.13$$

Following NUREG-2115, $\sigma\mathbf{M}|M_L$ is calculated as the difference between the sigma of 0.16 obtained from the regression and the average value of $\sigma[\mathbf{M}|\hat{\mathbf{M}}]$ = 0.1 (rounded from 0.09) for the earthquakes used in this regression. The equation is applicable for $M_L \geq 3$.

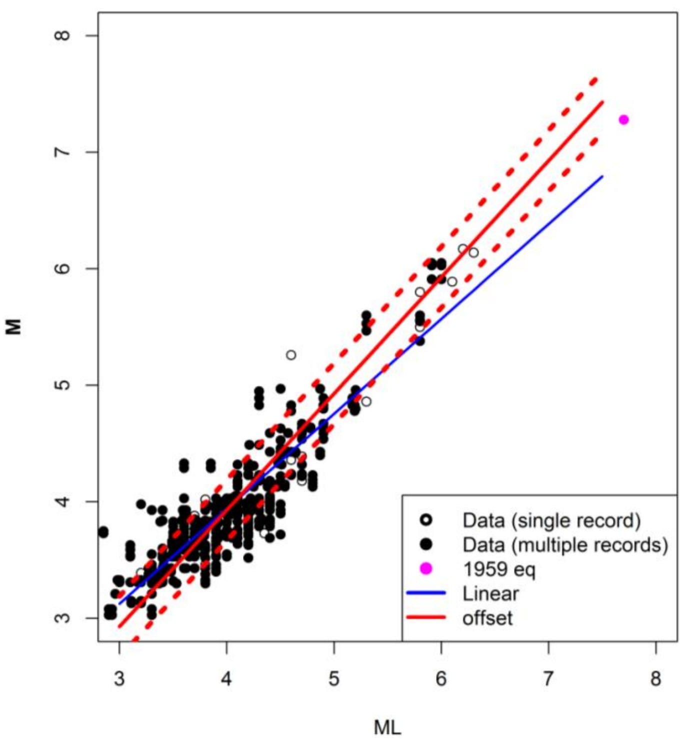

Figure 6-5. Plot of the M_L-**M** regression.

6.2.3 Conversion from Macroseismic Intensities

An attempt to obtain a conversion relation for macroseismic intensities was made using recent records, however the 1850-2014 data set is sparse and does not include a sufficient number of large macroseismic intensities. For this reason it was decided to discard the macroseismic intensities for all earthquakes that have another size measure. Table 6.1 shows that there are1,674 earthquakes for which I_0 is the only available size measure: these have been converted using the Gutenberg relation:

$$E[\mathbf{M}] = 2/3*I_0 + 1 \qquad [6\text{-}7]$$

In this case $\sigma_{\mathbf{M}|I0}$ is assumed to be equal to 0.5.

6.2.4 Treatment of Magnitude Uncertainties in Recurrence Calculations

Earthquake magnitudes are calculated as a statistical average of measurements obtained at a number of seismic stations, and although it is typically not reported in the earthquake catalogs, a certain amount of uncertainty is associated with each reported magnitude. Additional uncertainty is then introduced by using magnitude conversion relations. This uncertainty is symmetrically distributed around the magnitude value. The standard approach to calculating recurrence rates is to obtain earthquake counts for magnitude bins (m_i). Gutenberg and Richter (1944) demonstrate that, in a large region, earthquake magnitudes follow an exponential distribution; that is, the earthquake magnitude bin m_i contains more earthquakes than in the next larger magnitude bin m_{i+1}. As explained in NUREG-2115, the unequal number of earthquakes in adjacent magnitude bins means that more earthquakes are shifted from magnitude bin m_i to the next larger magnitude bin m_{i+1} than from m_{i+1} to m_i, due to the statistical magnitude uncertainty. This bias was studied independently by Tinti and Mulargia (1985) and by EPRI/SOG (1988) and each study proposed an approach to correct the bias: Tinti and Mulargia (1985) approach is to correct the earthquake counts; EPRI/SOG (1988) approach is to correct the magnitudes (M* approach). NUREG-2115 adopts the Tinti and Mulargia (1985) approach to correct the earthquake counts, but applies it to each individual earthquake rather than to the total earthquake counts within a magnitude bin (N* approach). This allows for maintaining the EPRI/SOG (1988) ability to account for differences in magnitude uncertainty for individual earthquakes. The N* approach was recently used for the Hanford site-wide PSHA (PNNL, 2014). Seismic Evaluation Team (2010) used the M* approach to obtain unbiased earthquake counts, however statistical tests described in NUREG-2115 show that for a catalog with variable levels of completeness, such as the 1850-2014 catalog, the N* approach performs better than the M* approach. For this reason the N* approach is followed in this study.

The N* approach can be described as follows:

5. The earthquake catalog is processed to obtain values of E[**M**] and σ[**M**] for each earthquake using the following equations (from EPRI/SOG, 1988):

$$E\left[\mathbf{M} \mid \hat{\mathbf{X}}\right] = \left\{ \sum_i \frac{\sigma^2\left[\mathbf{M} \mid \hat{\mathbf{X}}\right]}{\sigma^2\left[\mathbf{M} \mid \hat{X}_i\right]} \cdot E\left[\mathbf{M} \mid \hat{X}_i\right] \right\} + (R-1)\beta\sigma^2\left[\mathbf{M} \mid \hat{\mathbf{X}}\right] \qquad [6\text{-}8]$$

and

$$\sigma^2\left[\mathbf{M} \mid \hat{\mathbf{X}}\right] = \left\{ \sum_i \frac{1}{\sigma^2\left[\mathbf{M} \mid \hat{X}_i\right]} \right\}^{-1} \qquad [6\text{-}9]$$

Where $\hat{X}_i$ is a single member of $\hat{\mathbf{X}}$.

6. Each earthquake is then assigned an equivalent count N* defined in NUREG-2115 as follows:

$$N^* = \exp\left\{\beta^2\sigma^2[|\mathbf{M}|\hat{\mathbf{M}}]/2\right\}$$

or

$$N^* = \exp\left\{\beta^2\sigma^2[|\mathbf{M}|\mathbf{X}]/2\right\} \quad [6\text{-}10]$$

Where $\hat{\mathbf{M}}$ is the observed moment magnitude.

7. The earthquake rates are computed by summing the effective counts N* within each magnitude bin and dividing it by the period of completeness for that magnitude bin.

Figure 6-6 shows a comparison between the observed annual earthquake rates obtained over the entire area covered by the 1850-2014 catalog using the catalog developed in Seismic Evaluation team (2010) and M* approach, and the rates obtained in using the catalog developed in this study and the N* approach. Since the end of 2007 (last data entry in the Carpenter, 2010 catalog) there have been only 8 earthquakes with E[**M**] ≥ 4.0, but none with E[**M**] ≥ 5. The plot shows that the use of E[**M**] and N* has the effect of reducing the rate of moderate to large earthquakes.

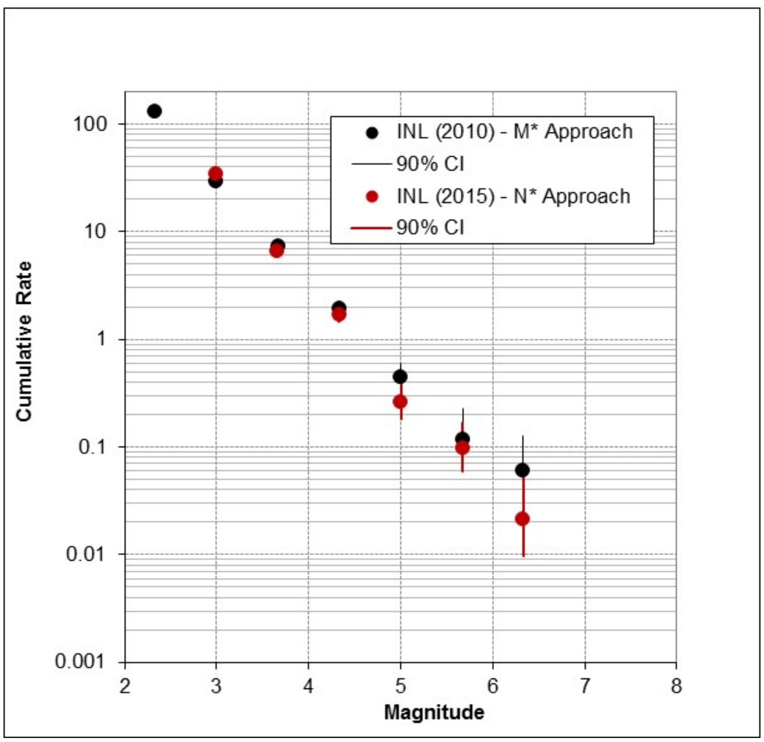

Figure 6-6. Comparison of observed earthquake rates from Seismic Evaluation Team (2010) and this study.

6.2.5 Uniform Moment Magnitude Catalog of E[M] and N* Values

The conversion equations listed in the previous sections were used to convert the available magnitude estimates to a uniform value of the expected moment magnitude (E[**M**]).For earthquakes with an observed M obtained from the seismic moment, E[**M**] is calculated exclusively from this value, based on the assumption that an observed **M** should be preferred to other size measures. The largest earthquake in the catalog is the August 18, 1959 E[**M**] 7.26 earthquake; because of the range of applicability of the magnitude conversion relations used to calculate E[**M**], the minimum magnitude is E[**M**] 2.33. The uniform earthquake catalog is shown in Figure 6-7.

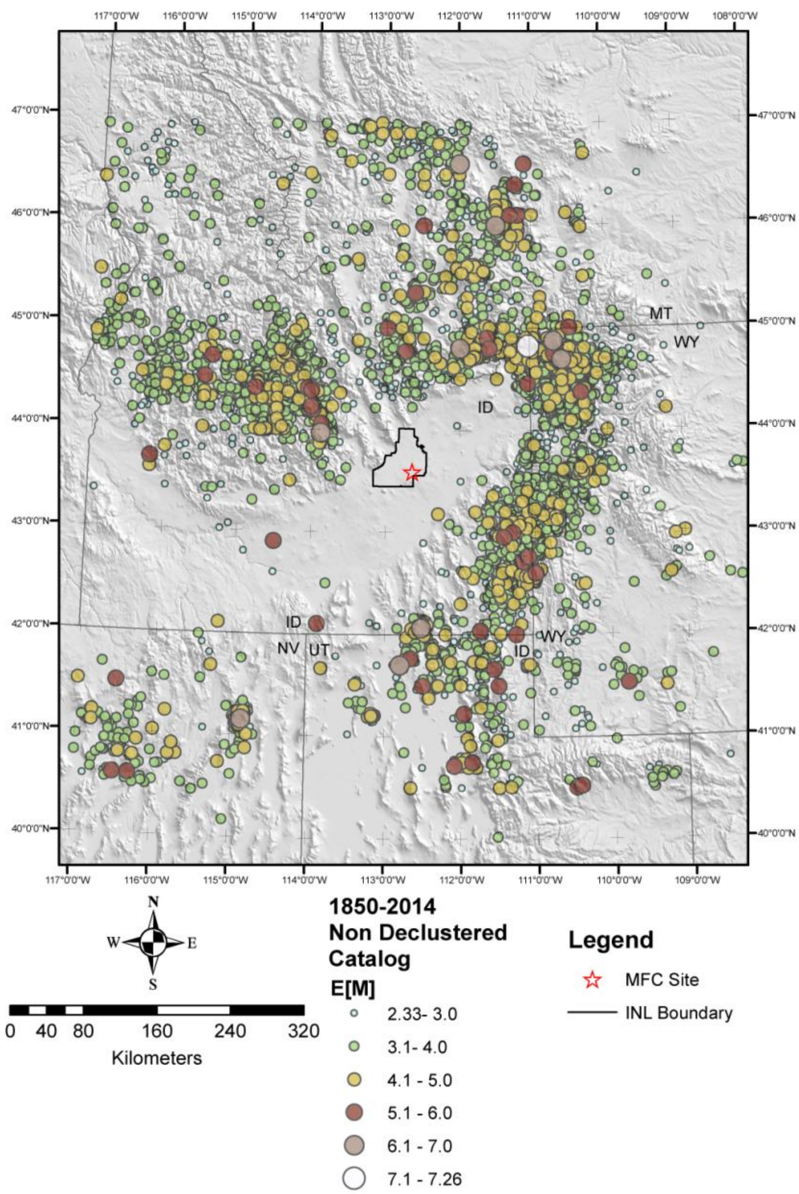

Figure 6-7. Map showing the 1850-2014 earthquake catalog in E[**M**].

6.3 Declustering of the Earthquake Catalogs

Earthquake catalogs typically contain a combination of foreshocks, mainshocks, and aftershocks. In standard PSHA, the mainshocks are assumed to follow a Poisson model in time and are used to estimate the frequency of earthquakes within a source zone. The occurrence of aftershocks, instead, follows the Omori law that predicts the evolution of the aftershock sequence as a function of the magnitude of the mainshock.

The process of identifying and removing aftershocks and foreshocks is called earthquake declustering and various techniques exist that perform this operation. These techniques are typically based on the use of fixed time and distance windows or on the use of statistical analysis.

6.3.1 Alternative Declustering Approaches

Gardner and Knopoff (1974) were the first to develop time and distance windows as a function of earthquake magnitude and to use them in identifying dependent earthquakes. For each large earthquake, the method defines a fixed time window and a fixed distance window whose length is dependent on the magnitude of the large earthquake (mainshock). Every smaller earthquake that occurred within those windows is considered a dependent earthquake. The Gardner and Knopoff (1974) method was originally derived using a catalog of earthquakes in southern California, but has since been applied to other regions, and alternative time and distance windows have been introduced. The Gardner and Knopoff (1974) method and two of its modifications, by Grünthal (1985) and Uhrhammer (1986), were used in this study.

The fourth method used to decluster the 1850-2014 catalog was developed by EPRI/SOG (1988, Vol. 1) and involves the use of statistical testing to identify clusters of earthquakes. The earthquake catalog is ordered from the largest to the smallest earthquake, then the algorithm constructs a local space-time window in the immediate vicinity of the selected earthquake, and a much larger extended window. The null hypothesis used by the algorithm is that, assuming a Poisson process, the seismicity should not be elevated within the local window. If the null hypothesis is rejected, the algorithm keeps testing adjacent space and time windows until none is found that rejects the null hypothesis. The final step in the process is to reduce the earthquake counts in the cluster region to match the background rate in the extended window. The process is repeated a second time, after removing all of the events identified as secondary during the first step. As discussed in NUREG-2115, the advantages of the EPRI/SOG (1988) approach are that it is insensitive to incompleteness because a homogeneous Poisson process is only assumed in proximity to the earthquake sequence being tested and that it does not assume a priori a shape for the clusters.

6.3.2 Application to the 1850-2014 E[M] Catalog

For this study, four alternative techniques were used to identify independent events: three were based on the use of fixed time and distance windows (Gardner and Knopoff, 1974; Grünthal, 1985; Uhrhammer, 1986), and the EPRI/SOG (1988) method based on statistical testing of clusters of earthquakes. Note that these are the same techniques used for the analyses documented in Seismic Evaluation Team (2010).

The earthquake catalog was declustered using the four methods listed above. Results are shown in Figure 6-8 and in Table 6.2, which compares the number of earthquakes inside the magnitude bins used in recurrence calculations obtained from each of the declustered catalog. As expected, the methods differ primarily for small magnitudes (less than E[**M**] 4.33); the method by Grünthal (1985) consistently removes more earthquakes than the other three methods, and the method by Uhrhammer (1986) consistently removes fewer earthquakes than the other methods. The remaining two methods, EPRI-SOG (1988) and Gardner and Knopoff (1974) produce similar results. Note that the first magnitude bin E[**M**] 2.0 to 3.0 is incomplete: following the Gutenberg-Richter relation there should be more earthquakes in

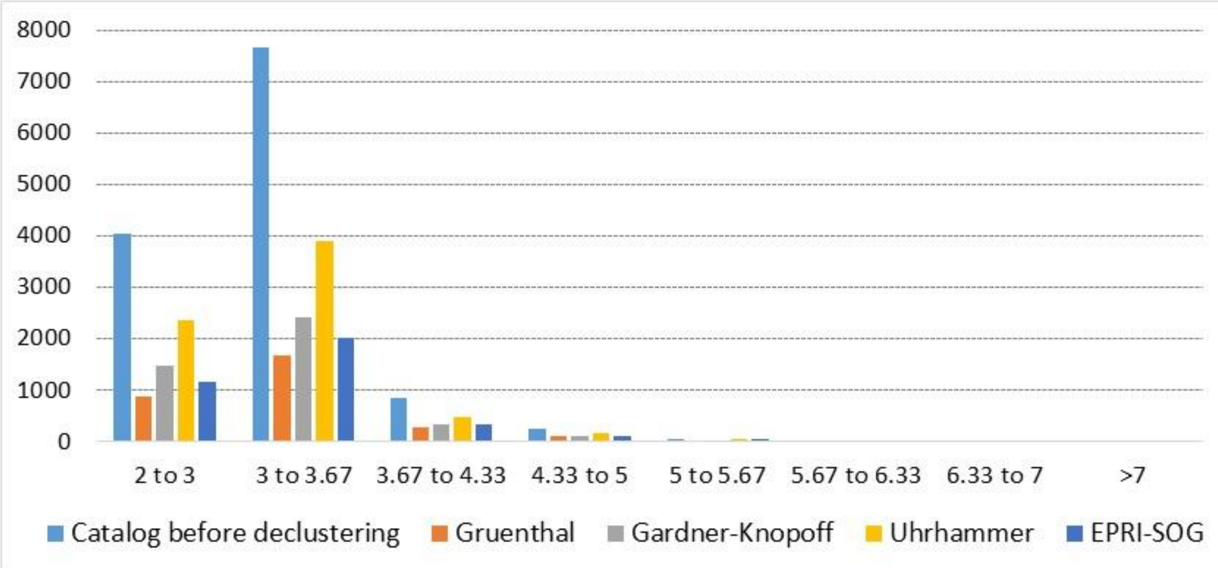

Figure 6-8. Histogram of the number of earthquakes per magnitude bin from alternative declustered catalogs.

Table 6-2. Number of earthquakes per magnitude bin from the alternative declustered catalogs.

E[**M**] Interval	Before Declustering	Grünthal (1985)	Gardner & Knopoff (1974)	Uhrhammer (1986)	EPRI/SOG (1988, Vol. 1)
2.00 to 3.00	4045	879	1479	2376	1157
3.00 to 3.67	7670	1670	2415	3896	2023
3.67 to 4.33	844	291	340	480	336
4.33 to 5.00	246	110	108	151	110
5.00 to 5.67	59	33	34	37	37
5.67 to 6.33	21	13	12	14	12
6.33 to 7.00	3	3	3	3	3
>7.00	1	1	1	1	1
Total	12889	3000	4392	6958	3679

this magnitude bin than there are in the next, smaller bin. This condition is not satisfied by the first bin indicating that the catalog is incomplete in this bin. Only earthquakes with E[**M**] 3.0 are used in all subsequent analyses.

6.4 Catalog Completeness

The procedure to calculate earthquake recurrence rates requires an assessment of the time periods over which independent earthquakes have been completely recorded in the earthquake catalog. In standard PSHAs there are two approaches to the assessment of catalog completeness. The first is the method originally proposed by Stepp (1972).The second is based on the concept of probability of detection, which was introduced by Veneziano and Van Dyck (1985) and evolved in the methodology used in the EPRI/SOG (1988) project (and subsequently in NUREG-2115). The two methods are described in the following sections.

6.4.1 The Stepp Method and the Probability of Detection Method

The Stepp (1972) method defines the completeness for a specific magnitude range by counting the total number of earthquakes in the catalog within that magnitude range, starting from present and moving back in time. Every time an earthquake of that magnitude occurred, the rate was calculated by dividing the number of earthquakes counted from present to that point in time by the corresponding time interval (from present to that point in time). The assumption made in the PSHA is that earthquakes follow a stationary Poisson process in time, so the rate of earthquakes when plotted as a function of time should show a nearly horizontal trend for the complete portion of the catalog, and a downward trending slope for the incomplete part. The point in time where the slope begins is considered the beginning of the complete period.

It is common practice in the PSHA to use only the earthquakes that occurred in the complete portion of the catalog for calculating earthquake recurrence parameters. Earthquake rates are calculated by counting the number of earthquakes within each magnitude bin and completeness time interval and dividing the counts by the length of the complete time interval. Veneziano and Van Dyck (1985) define an equivalent period of completeness (*TE*) such that the rate of earthquake occurrence is equal to the total number of events in the catalog within a given magnitude range, divided by *TE*. The method is based on the assessment of the probability of detection (P^D) as a function of magnitude, time, and completeness region. Under the assumption that seismicity in a region follows a stationary Poisson process in time, the rate of observed earthquakes ν_i for magnitude interval m_{i-1} to m_i is given by:

$$\nu_i = \lambda_i P_i^D(t) \qquad [6\text{-}11]$$

Where λ_i is the true rate of earthquakes in the specified magnitude interval, and $P_i^D(t)$ is the probability of detection of earthquakes in that magnitude bin as a function of time.

If the entire length of the catalog is subdivided into J time periods such that within each j period the probability of detection can be assumed to be relatively constant, the probability of observing the recorded number of earthquakes (n_{ij}) is given by the Poisson distribution:

$$P(N = n_{ij}) = \frac{(\nu_i t_j)^{n_{ij}} e^{-\nu_i t_j}}{n_{ij}!} \qquad [6\text{-}12]$$

Combining Equations 6.11and 6.12, the likelihood of observing the recorded earthquakes in the magnitude interval m_{i-1} to m_i is given by:

$$L(\lambda_i, P_{ij}) = \prod_{j=1}^{J} \frac{(\lambda_i t_j P_{ij})^{n_{ij}} e^{-\lambda_i t_j P_{ij}}}{n_{ij}!} \qquad [6\text{-}13]$$

Where P_{ij} is the probability of detection of events in the *i*-th magnitude interval in the time period *j*.

If it is imposed that the larger magnitudes are complete at present and that P^D decreases monotonically from the present time, Equation 6.13 can be maximized to obtain the parameters most likely to represent the Poisson process that produces the observed earthquake catalog. The equivalent time of completeness *TE* is given by:

$$TE_i = \sum_{j=1}^{J} P_{ij} t_j \qquad [6\text{-}14]$$

6.4.2 Probability of Detection in Space and Time

The assessment of catalog completeness requires the delineation of completeness regions. In Seismic Evaluation Team (2010), two completeness regions were delineated based on the geometry of the source zones, and on the distribution and time of operation of the seismic stations in the area. The geometry of the two regions was modified in this study to conform to the revised boundaries of the source zones. Figure 6-9 shows the 2010 geometries (solid, green lines) and the revised geometries (dashed, red lines) for the 1850-2014 catalog.

The approach to catalog completeness used in Seismic Evaluation Team (2010) was to use probability of detection. The time intervals (t_j in Equations 6.12 through 6.14), within which the probability of detection can be assumed to be relatively constant, were determined in the Seismic Evaluation Team (2010) to be: 1850 to 1900, 1900 to 1925, 1925 to 1963, 1963 to 1974, 1974 to 1987, and 1987 to 2007.The same approach was maintained in this study, with the last time interval extended to the end of 2014.

Table 6.3 shows the resulting probabilities of detection subdivided by completeness region, magnitude and time interval, and the corresponding equivalent time of completeness for use in earthquake recurrence analyses. Note that Table 6.2 shows that there is one earthquake with E[**M**] greater than 7 in the catalog; this is the August 18, 1959 earthquake, which is associated with slip on both the Hebgen Lake and Red Canyon faults and therefore it is not considered in this analysis. The recurrence of earthquakes on these two faults is discussed in Section 8.3.

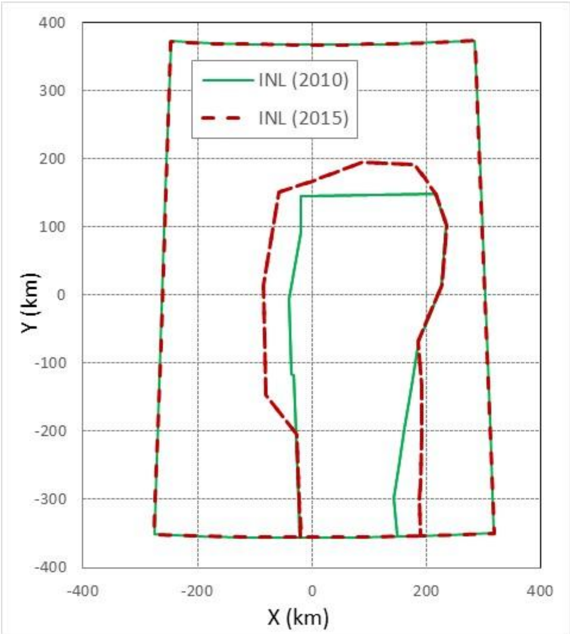

Figure 6-9. Geometry of compeleteness regions used in Seismic Evaluation Team (2010) and in this study.

Table 6-3. P^D by completeness region, magnitude bin, and time intervals.

E[**M**] interval	1850 to 1900	1900 to 1925	1925 to 1963	1863 to 1974	1974 to 1987	1987 to 12/31/2014	*TE*[1]	Beginning of Usable Period
Completeness Region I								
3.00 to 3.67	0.00	0.01	0.01	0.13	0.91	1.00	42.70	1972
3.67 to 4.33	0.03	0.12	0.12	0.63	1.00	1.00	64.76	1950
4.33 to 5.00	0.11	0.39	0.39	0.91	1.00	1.00	83.70	1931
5.00 to 5.67	0.16	0.49	0.49	1.00	1.00	1.00	92.87	1922
5.67 to 6.33	0.29	0.50	0.50	1.00	1.00	1.00	113.48	1902
6.33 to 7.00	0.59	0.91	0.91	1.00	1.00	1.00	142.32	1873
Completeness Region II								
3.00 to 3.67	0.01	0.02	0.15	0.62	0.72	1.00	50.85	1964
3.67 to 4.33	0.02	0.13	0.53	0.87	1.00	1.00	74.95	1940
4.33 to 5.00	0.07	0.27	0.62	1.00	1.00	1.00	86.00	1929
5.00 to 5.67	0.17	0.48	0.87	1.00	1.00	1.00	105.50	1909
5.67 to 6.33	0.33	0.67	1.00	1.00	1.00	1.00	123.17	1892
6.33 to 7.00	0.72	0.77	1.00	1.00	1.00	1.00	145.08	1870

1. *TE* is equivalent time of completeness for use in earthquake recurrence analyses.

7. Ground Motion Characterization (GMC) Databases

The SSHAC Level 1 PSHA involved compilations of data and evaluations of the data to support development of the GMC model. Three types of data were compiled and evaluated as part of this effort. The first related to an evaluation of appropriate GMPEs and their associated models for aleatory variability. The second related to the characterization of the shear wave velocity profiles at the MFC, FMF, and SFHP (NRF) sites. The third type related to characterization of the shallow crustal damping at the MFC and NRF site.

7.1 Relevant Ground Motion Prediction Equations (GMPEs)

As discussed in Section 4, the tectonic setting for the INL is the active extensional northern Basin and Range regime with predominantly normal and normal-oblique faulting. Recently, the SWUS Ground Motion Characterization project (GeoPentech, 2015) performed a SSHAC Level 3 study to develop a GMC for a site in the southern Basin and Range tectonic province. The SWUS study compiled and evaluated all of the available GMPEs for extensional environments and the databases of empirical ground motions compiled recently in both the United States and Europe. The SWUS study used these data and models to develop a complete characterization of median ground motions and their associated aleatory variability for normal and strike slip faulting in an extensional tectonic regime similar to that in which the INL is located. Because the SWUS study was both recent and conducted using a SSHAC Level 3 process, it is considered to be the most relevant database for normal faulting GMPEs for application in the INL SSHAC Level 1 PSHA.

An additional source of seismic hazard considered in this study is ground motions from very large earthquakes occurring on the Cascadia subduction zone interface off the coast of Washington state. The recent PNNL (2014) sitewide PSHA for the Hanford DOE site in south-central Washington state developed a GMC for Cascadia interface earthquake ground motions. The PNNL (2014) study was conducted as a SSHAC Level 3 study in which the development of the Cascadia interface GMC model focused on characterization of ground motions at large distances from the interface source specifically in a source-to-site path orientation that is similar to that from the Cascadia interface to the INL. Because of the similar source-site orientation and because the PNNL (2014) study was conducted as a SSHAC Level 3 study, it is considered to be the most relevant database for subduction zone interface GMPEs for application in the INL SSHAC Level 1 PSHA.

7.2 Shear Wave Velocity (Vs) Profiles for MFC and FMF

Both the SWUS study and the PNNL (2014) study provide GMPEs for a reference site condition significantly different than the site conditions at MFC, FMF, and SFHP (at NRF). Characterization of the shear wave velocity of the shallow crust beneath the INL sites is needed in order to develop the appropriate adjustments of the GMPEs for application in hazard calculations for these INL sites.

7.2.1 MFC Vs Profile

The MFC is located in the eastern part of the INL, far from the Big Lost River and within the AVZ (Figures 4-4 and 4-5). The lithology for nine boreholes at or near MFC (Figure 7-1) shows basalt sequences with few sedimentary interbeds (Figure 7-2). Most of the interbeds are very fine-grained including clay, silt, and some sand. Basalt rubble/cinder layers are interpreted on many of the logs for older boreholes and are thought to reflect layers different from basalt lava flows (Payne et al., 2012). Figure 7-3 shows the measured shear-wave velocity (V_S) values at MFC. The ANL-1 borehole has downhole V_S measurements to a depth of 59 m and suspension logging V_S measurements to a depth of 348 m (Agbabian Associates Inc., 1995). Downhole V_S measurements were obtained in boreholes BH-01,

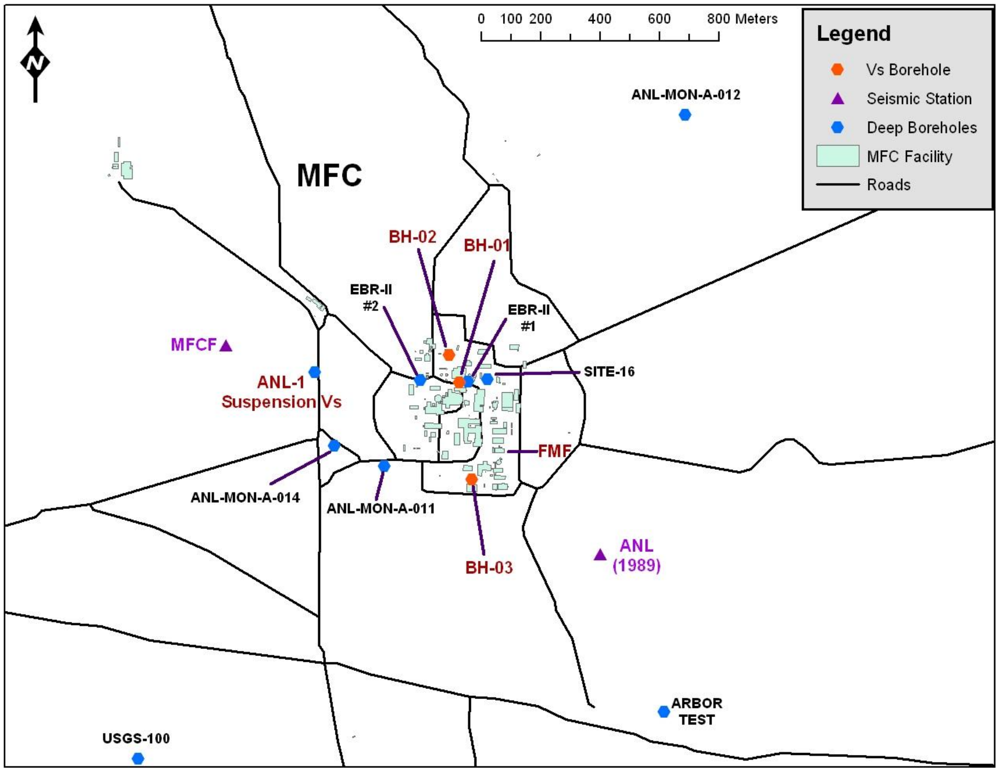

Figure 7-1. Map shows location of boreholes with lithology and Vs measurements in the vicinity of MFC.

BH-02, and BH-03 in the shallow subsurface (depth <13 m) (Redpath, 1997). The low basalt V_S layer at a depth of ~30-35 m in the downhole (and suspension) ANL-1 profile corresponds to a void in the basalts (PC Exploration, Inc. 1995). Another notable feature in the ANL-1 suspension log profile is the overall steep V_S gradient in the basalt from 668 m/s at the surface to 2021 m/s at 38 m depth. This type of gradient is also evident in the downhole V_S shown for the three shallow boreholes (<13 m). Additionally, the ANL-1 downhole velocity profile generally follows the suspension log, which also shows the steep gradient at the top of basalt. The suspension log shows some variability in V_S of the basalt and a slight increase of velocities with depth to 348 m.

Figure 7-3 shows the median base case V_S profile developed for the upper 400 m of the MFC profile. The profile was developed by smoothing the velocity data for the site using a 31-m smoothing window (Payne et al., 2012). Also shown on Figure 7-3 are the lower-range and upper-range V_S profiles for MFC. To accommodate uncertainty in the single measured profile across the facility area, a 10% variation was assumed to reflect 10% and 90% fractiles, based on other velocity measurements at INL. Below the measurement depth of about 300 m, beyond which velocities were based on well log material type and velocity associations, the uncertainty was assumed to increase to 20%.

The median base case V_S profile for the depth range of 348 m to 1,200 m is based on lithology from boring WO-2 and the V_S-depth curve of Payne (2007). For the depth range of 1,200 m to 3,000 m, the median profile is based on lithology and V_S inferred from V_P using the data from boring INEL-1. Because the median profile is based on inferred V_S values, the uncertainty in assigning the lower-range and upper-range V_S values was increased to 20 percent. The appropriate range of uncertainty was informed by

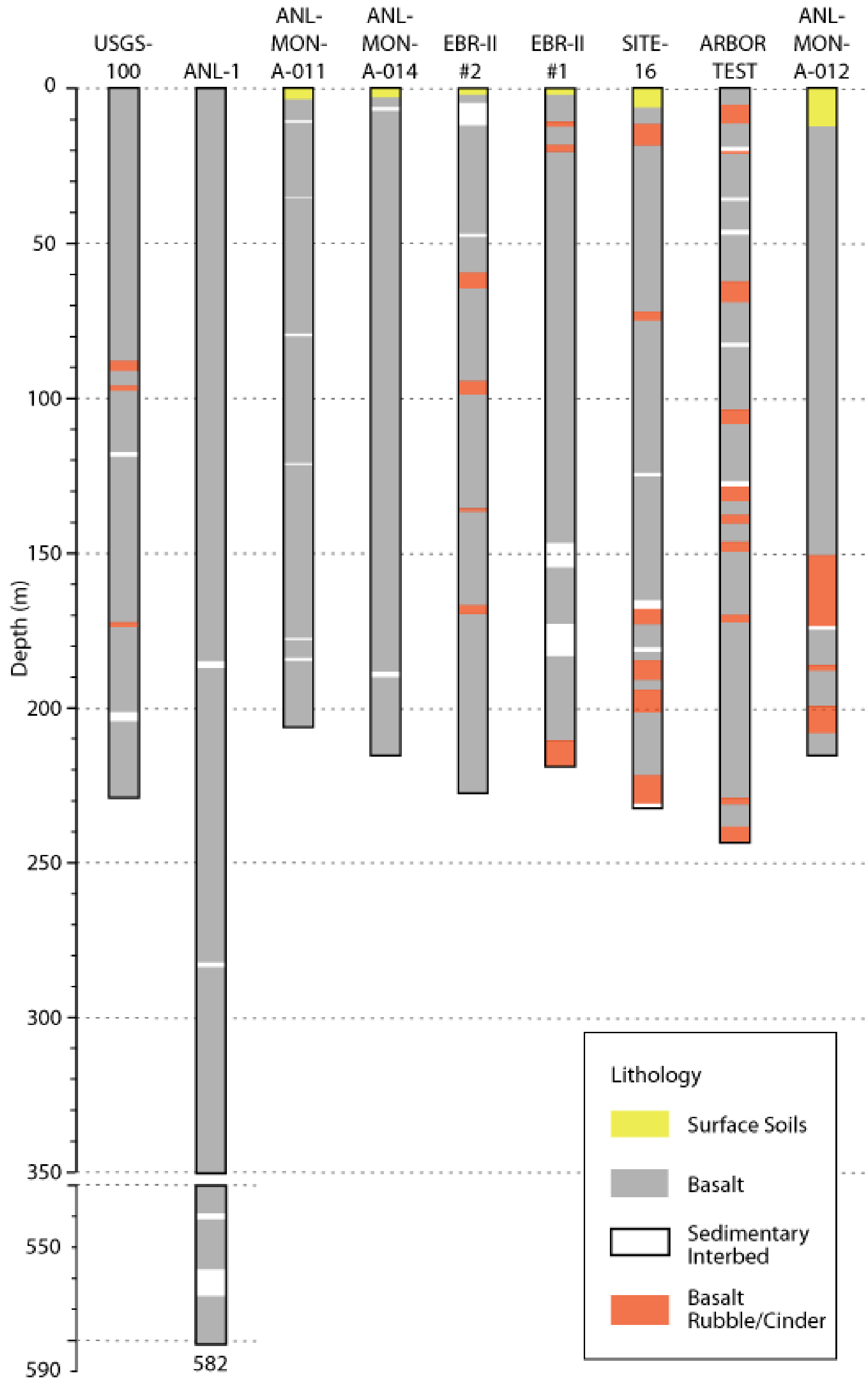

Figure 7-2. Lithology in boreholes at MFC (see Figure 7-1 for borehole locations).

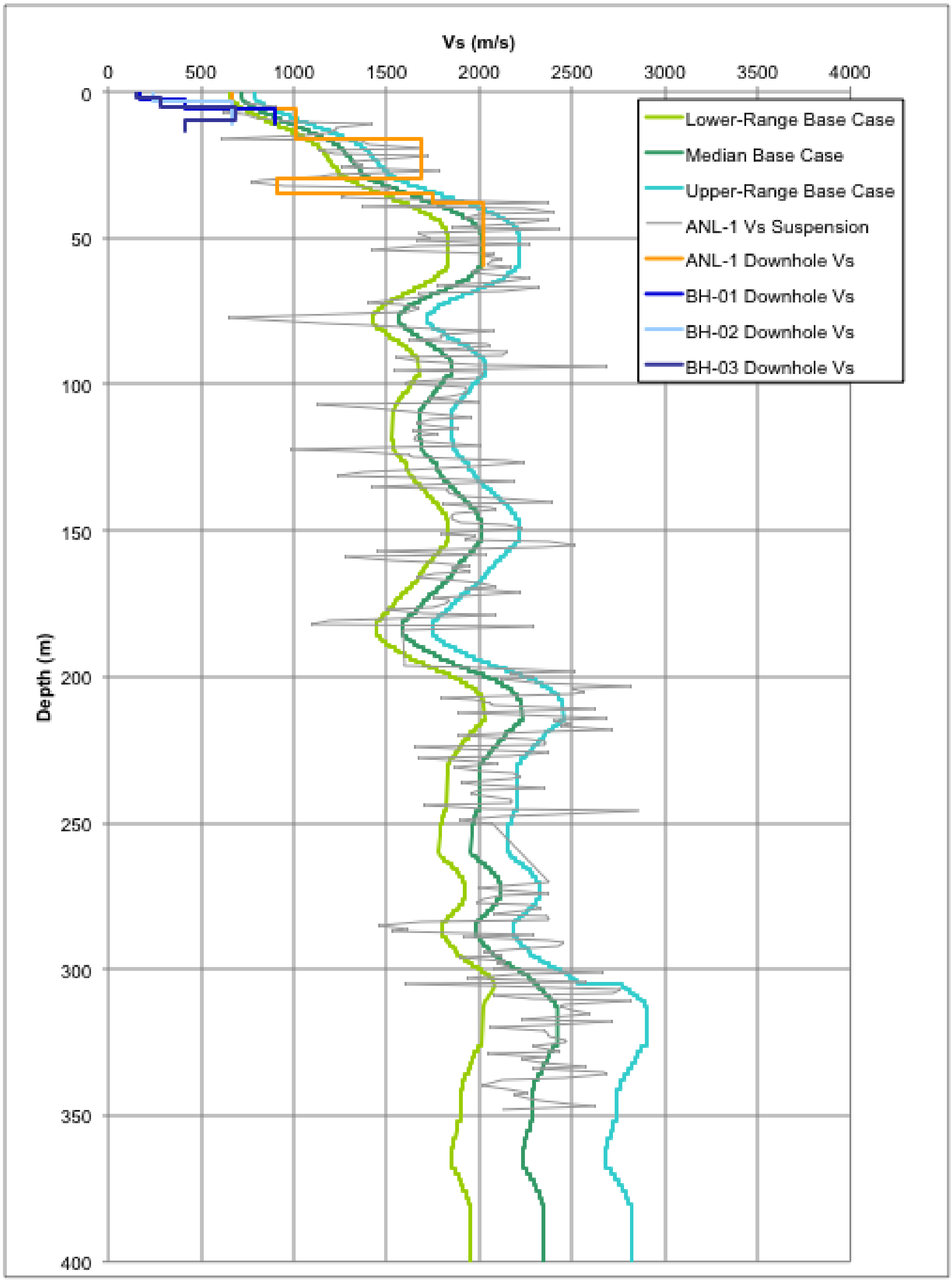

Figure 7-3. Median, lower-range, and upper-range V_S base cases (this study) compared to measured V_S in boreholes at MFC: ANL-1 downhole and suspension (Agbabian Associates Inc., 1995); BH-01, BH-02, and BH-03 downhole (Redpath, 1997).

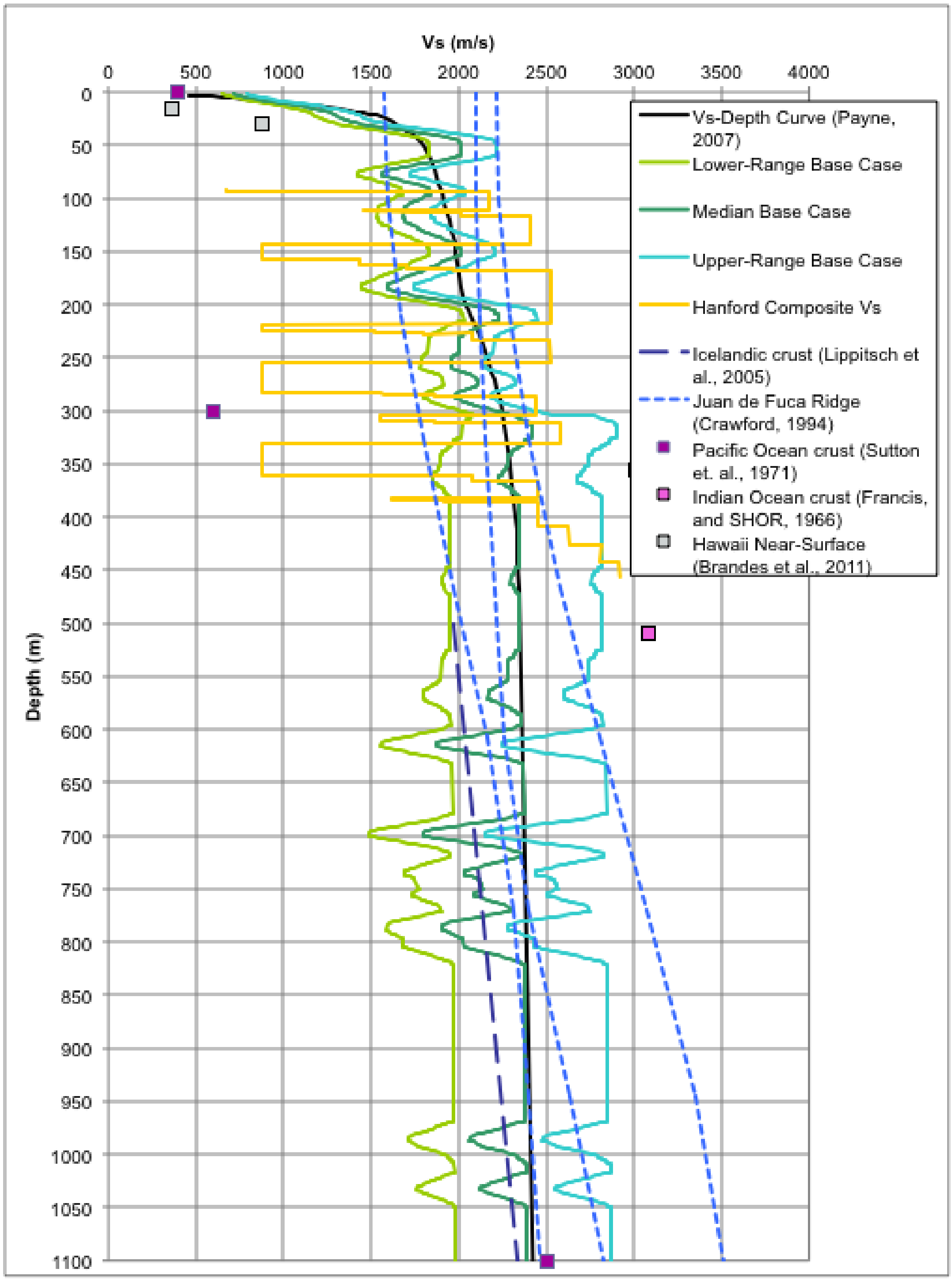

Figure 7-4. Plot of analog Vs data with the MFC lower-range, median, and upper-range base cases (this study). Basalt Vs are shown for: Hanford Washington composite Vs (PNNL, 2014), Icelandic crust (Lippitsch et al., 2005), Juan de Fuca Ridge (Crawford, 1994), Pacific Ocean crust (Sutton et al., 1971), Indian Ocean crust (Francis and Shor, 1966), and Hawaiian near-surface (Brandes et al., 2011). Also shown is the Vs-depth curve for basalt at INL (Payne, 2007).

comparison with analog V_S data from other basaltic regions. Figure 7-4 compares the V_S profile base cases to analog data for V_S of basalts and the Vs velocity-depth relationship (Payne, 2007). The analog basalt V_S data include data for the Icelandic crust (Lippitisch et al., 2005), the Juan de Fuca Ridge (Crawford, 1994), and the Hanford's composite V_S profile (PNNL, 2014). Also shown are measurements at different depths for Pacific Ocean crust (Sutton et al., 1971), Indian Ocean Crust (Francis and Shor, 1966), and Hawaiian near-surface basalt (Brandes et al., 2011). In the depth range from 0 to 500 m, the median, lower-range, and upper-range V_S base cases are within the range of uncertainty of analog V_S. At depths from 500 to 1,200 m, V_S for the Icelandic crust more closely matches the median and lower-range V_S base cases whereas two of the three V_S curves of the Juan de Fuca crust overlap with all three base cases. One of the V_S curves for the Juan de Fuca crust exceeds the V_S of the upper-range base case.

Below a depth of 3,000 m the crustal model of Richins et al. (1987) was used to define the velocities. Table 7-1 lists the Richins et al. crustal model. The base case profiles were merged into the Richins et al. (1987) crustal model by using the second layer as the median base case value and incorporating the approximately 20 percent uncertainty variation for the lower-range and upper-range base cases to provide a smooth transition without unrealistic velocity jumps. Below a depth of 5 km, only the Richins et al. (1987) velocities were used. Figure 7-5 shows the upper 10 km of the three base case profiles. Following the approach given in Appendix B of EPRI (2013), the three profiles were assigned weights of 0.4 for the median base case, profile P1, and 0.3 for the lower-range (P2) and upper-range (P3) profiles. The weighting of the three base case profiles thus approximates a normal distribution for the epistemic uncertainty in V_S, with profiles P2 and P3 representing the 10^{th} percentile and 90^{th} percentile, respectively, of that distribution.

7.2.2 FMF Vs Profile

The shallow V_S measurements at MFC are shown on Figure 7-6. As indicated on Figure 7-1, none of these are obtained near FMF. The soil depth at FMF ranges from 5 to 15 ft (1.5 to 4.5 m). The median V_S profile was developed to represent an approximate average of the shallow V_S measurements in soils. The 10^{th} percentile and 90^{th} percentile V_S values were assessed by applying a depth independent scale factor of 1.34 based on the variability in V_S reported in Payne et al. (2012) for the ATR site where there are a large number of boring. Figure 7-7 compares the three base case V_S profiles for the FMF soils to the shallow V_S data from Figure 7-6. As indicated the range in base case profiles encompasses the measured velocities in soils at MFC. The large velocity values at depth in borehole BH-02 are interpreted to be in the basalt. For the 15 ft soil depth, the V_S profiles shown in Figure 7-7 were attached to the top of the MFC profiles shown on Figure 7-5. For the 5 ft soil depth, the upper 1.5 m of the V_S profiles shown in Figure 7-6 were attached to the top of the MFC profiles shown on Figure 7-5.

Table 7-1. Richins et al. (1987) crustal model.

Thickness (km)	V_S (km/s)	Density (cgs)
2.0	2.74	2.50
4.5	3.23	2.70
11.5	3.55	2.70
22.0	3.93	2.83
	4.62	3.00

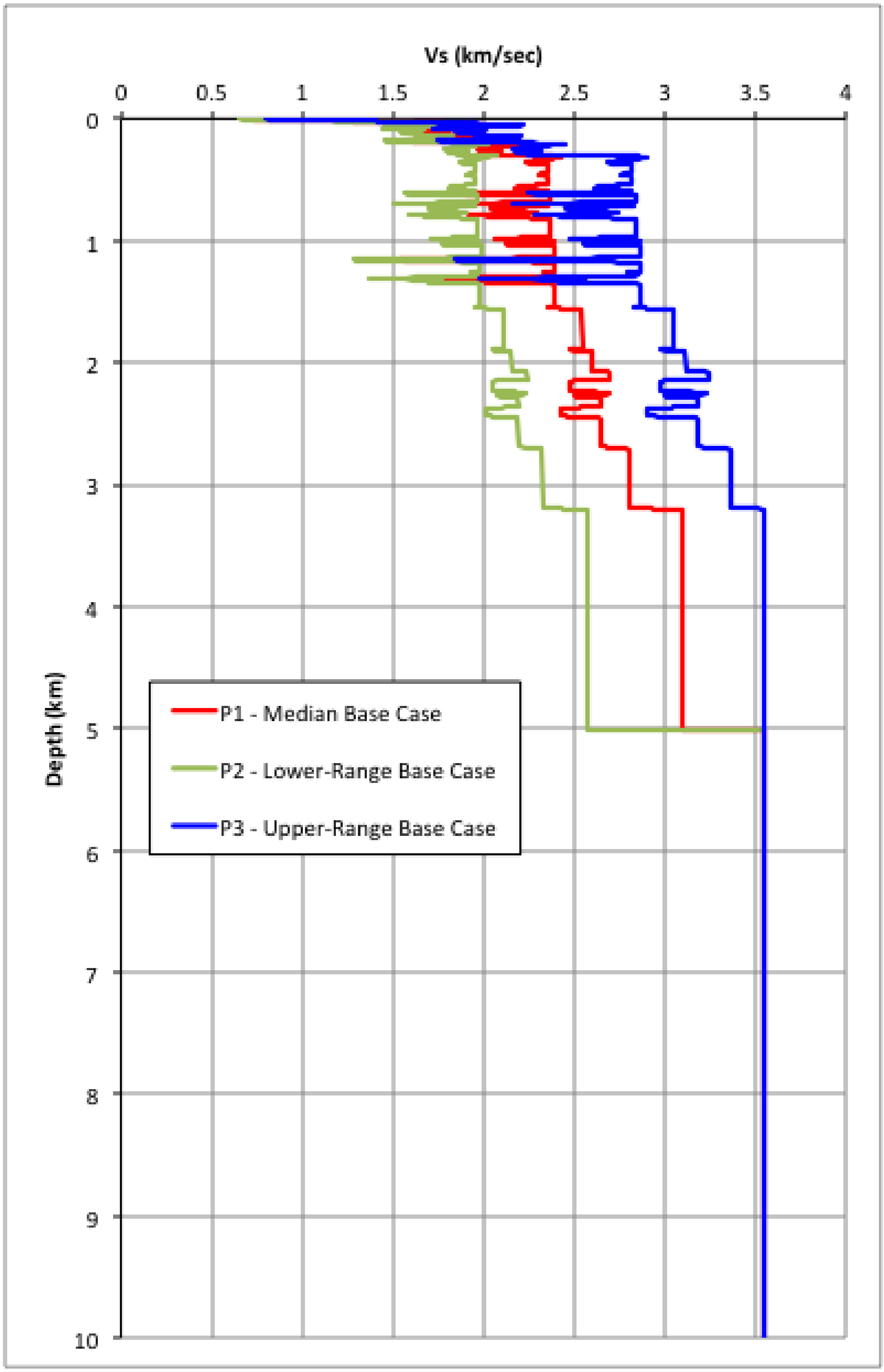

Figure 7-5. Base case V_S profiles for MFC.

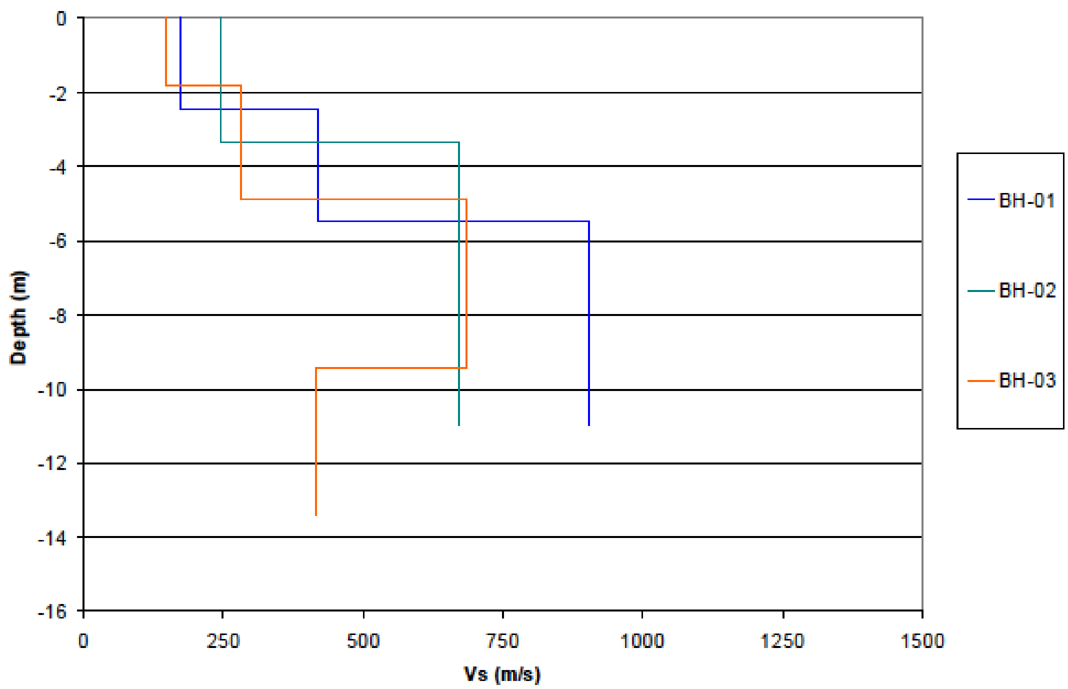

Figure 7-6. Shallow V_S measurements at MFC (from Payne et al., 2012).

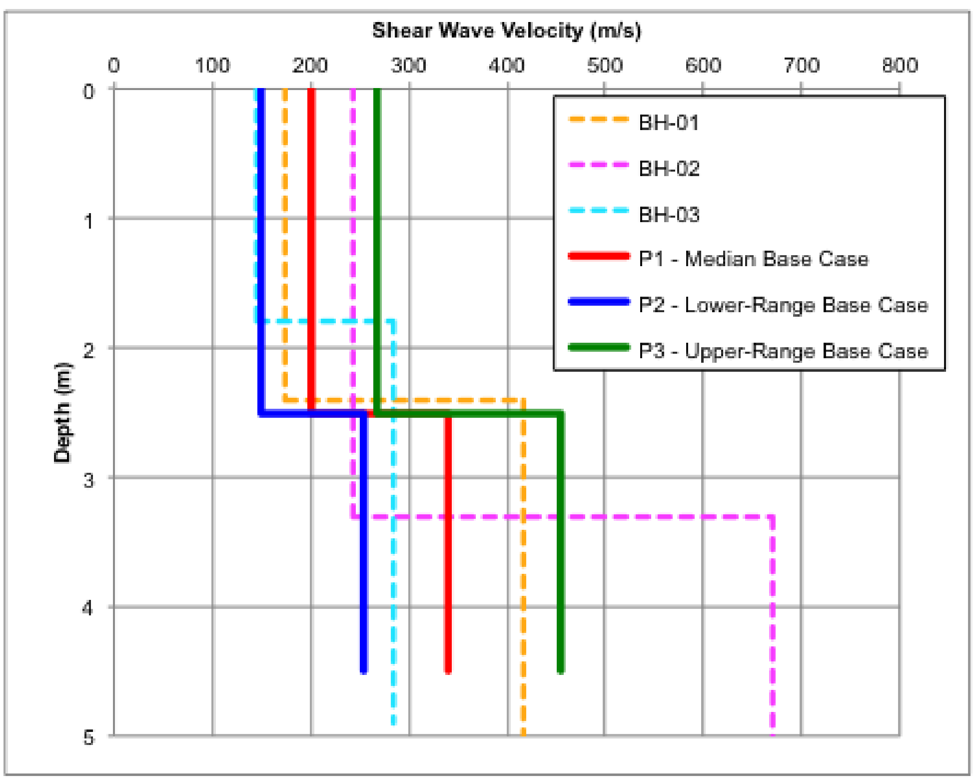

Figure 7-7. Base case V_S profiles for FMF soils.

7.3 Kappa and *Q* for INL Sites and Site Kappa and Soil Dynamic Properties for MFC and FMF

For typical rock and deep soil sites which display an overall increase in stiffness with depth due primarily to increasing confining pressure, the major contribution to energy dissipation at a site occurs over the top 1 to 2 km of the crust (Anderson and Hough, 1984; Silva and Darragh, 1995). This observation was first recognized and subsequently characterized as a site parameter by Anderson and Hough (1984), specifically as parameter kappa at zero epicentral distance, κ_0. Due to geologic processes, for sites which reflect significant departures from an overall increase in stiffness with depth, such as layered basalt and sedimentary soil or rock sequences, significant contributions to kappa may occur at depths well beyond 1 to 2 km and reflect contributions from both intrinsic energy dissipation as well as scattering. This damping appears to be frequency-independent (hysteretic), occurs at low strains, and is the principal site or path parameter controlling the limitation of high-frequency (>5 Hz) strong ground motion at close in (≤50 km) sites. As a result, its value or range of values is important in characterizing strong ground motions for engineering design, particularly in regions of sparse seismicity. Additionally, because it is generally independent of the level of motion at rock or very stiff sites, small local or regional earthquakes may be used to estimate its value or range in values.

The facility areas and seismic stations at the Idaho National Laboratory (INL) are located either on basalt or on shallow soil overlying layered basalts. The basalts have sedimentary interbeds of varying thicknesses and may also include layers of cinders (or basalt rubble) likely over crystalline basement (Woodward-Clyde Federal Services al., 1996). Kappa estimates at ten INL locations, shown on Figure 7-8, have been made to update and expand the earlier kappa estimates (Woodward-Clyde Federal Services al., 1996) at the 1989 temporary stations. Emphasis for this study was to characterize kappa, median estimate and uncertainty in kappa for “Area MFC” (Figure 7-8). Currently Area MFC has a recording site MFCF (Figure 7-8) that has recorded a large number of local and regional earthquakes some 27 of which were selected for analysis. Additionally, about 2 km away from MFCF and located within Area MFC, a temporary station recorded five earthquakes, which were used in the previous analysis, to characterize kappa at specific locations at INL (Woodward-Clyde Federal Services al., 1996). The current study reflects an update of the original analyses augmented with additional regional earthquakes as well as additional recording stations. Figure 7-9 shows the station locations and the locations of the earthquakes used to assess kappa.

7.3.1 Seismic Station Information, Ground Motion Data and Processing

7.3.1.1 Instrumentation

Figure 7-8 shows the location of the temporary stations listed in Table 7-2 that were used in the earlier analyses of site kappa by Woodward-Clyde Federal Services et al. (1996), and the short-period (SP), and broadband (BB) stations listed in Table 7-3 that provided the recent ground motion data from twenty-seven earthquakes recorded from October 2013 to January 2015. The INL broadband and accelerometer stations were installed in September 2013 next to facility areas of interest and one at the INEL-1 deep well location. Note that some stations (e.g., BMO in Table 7-3) are not shown on the map in Figure 7-8 because they are at too great a distance from INL.

7.3.1.2 Shear-Wave Velocity and Linear-Elastic Transfer Function

The subsurface structure including the shear-wave velocity at INL sites have been characterized based on shallow measurements, assumed Poisson ratios, and correlations between geology and velocity

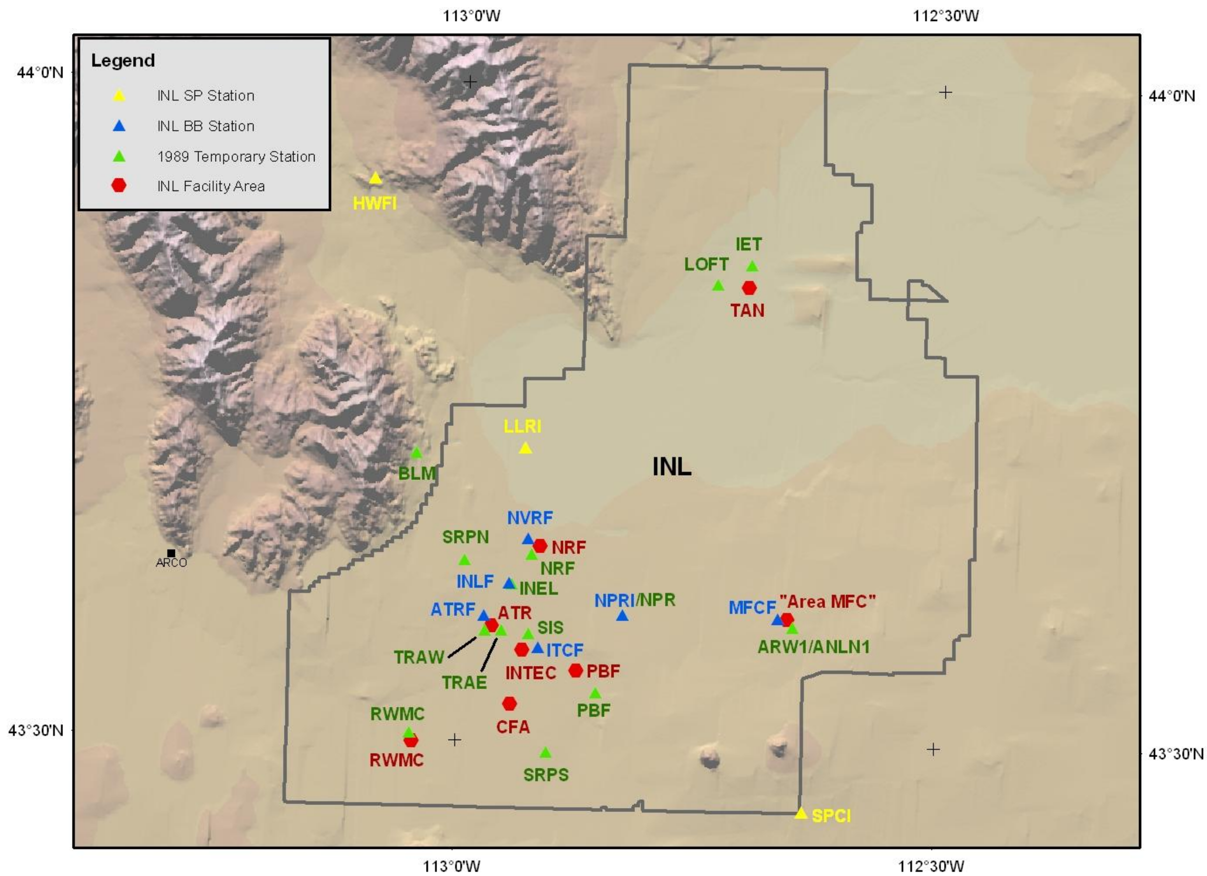

Figure 7-8. Map shows locations of INL facility areas, INL seismic stations with short period (SP) and broadband (BB) seismometers, and 1989 temporary stations.

Table 7-2. Earthquakes and stations used in Woodward-Clyde Federal Services et al. (1996) assessment of kappa at the INL.

Regional Earthquake ID	Number of Stations Used	Earthquake Magnitude	Hypocentral Distance Range (km)	1989 Station Names[1]
Event 11	6	3.0	96 - 134	BLM, IET, INEL, LOFT, NPR, TRAW
Event 12	4	3.5	142 - 172	BLM, INEL, LOFT, NPR
Event 24	6	3.7	154 - 188	ANL, BLM, IET, INEL, LOFT, RWMC
Event 25	6	3.6	154 - 189	ANL, BLM, IET, INEL, LOFT, RWMC
Event 28	5	3.0	194 - 228	ANL, BLM, INEL, LOFT, PBF
Event 29	5	2.9	194 - 230	ANL, BLM, IET, INEL, PBF
Event 31	4	3.1	91 - 121	ANL, BLM, INEL, LOFT
1. All stations recorded at 100 sps.				

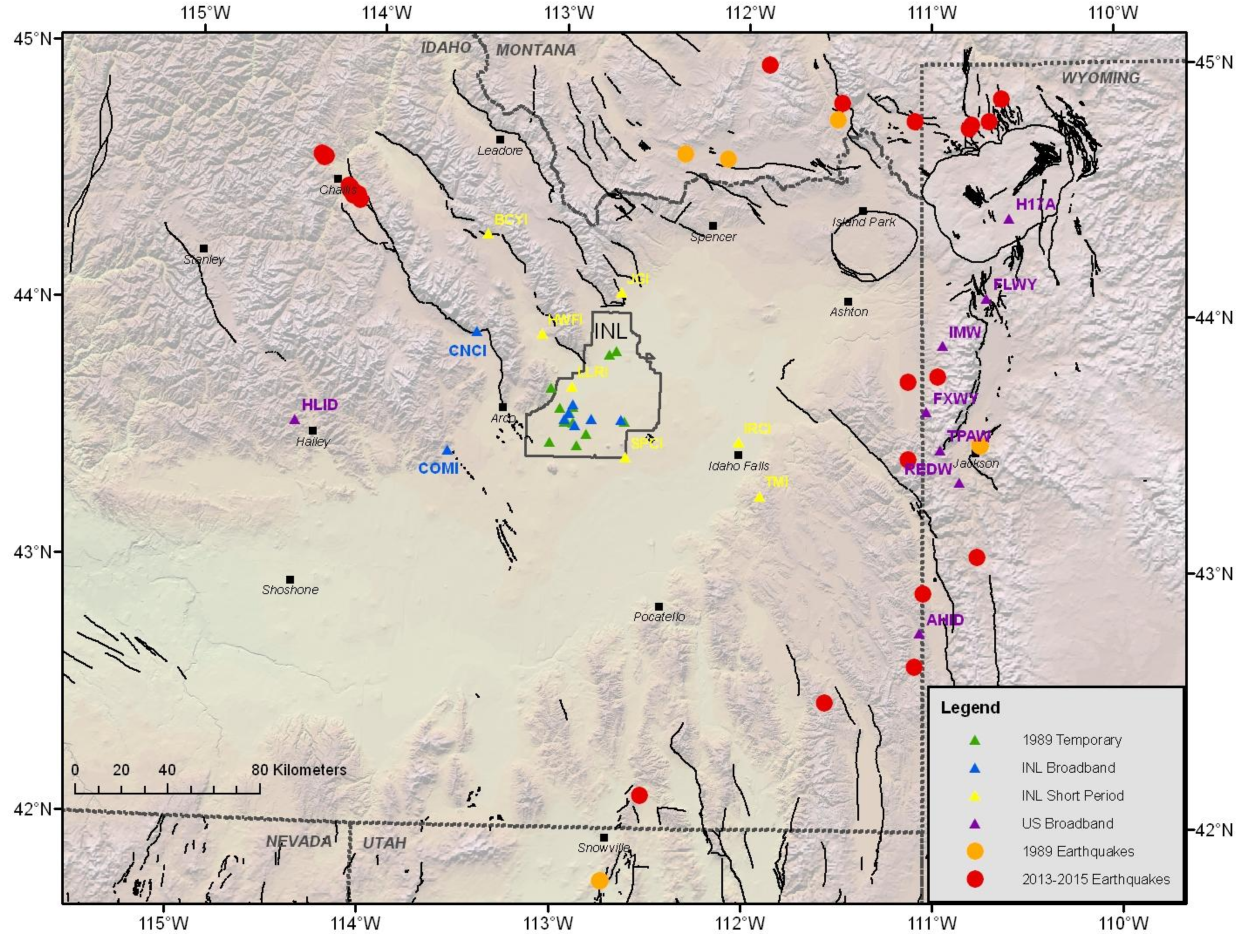

Figure 7-9. Map of seismic stations and regional earthquakes used for kappa estimation (see Figure 7-8 for station codes on INL, Table 7-3 for station information, and Table 7-4 for earthquake list).

(e.g. Woodward-Clyde Federal Services et al., 1996;Seismic Evaluation Team, 2010; Payne et al., 2012). The site-specific velocity profiles have been smoothed as discussed in Woodward-Clyde Federal Services et al. (1996).

Crustal profile amplification factors were estimated from the interpreted and smoothed V_S profiles from source depth to surface. For each site area which had estimated shear-wave velocity profiles through the layered basalt sequence, that profiles replaced the top layer the local profile of the Richins et al. (1987) crustal model (Table 7-1) (Woodward-Clyde Federal Services et al., 1996). The site/area specific linear-elastic transfer functions are shown in Figure 7-10. For sites without shear-wave velocity information, typically regional sites not located within the INL (Figure 7-9) founded on very shallow soil or rock, the amplification from a generic National Earthquake Hazards Reduction Program (NEHRP) B site class was assumed to be appropriate. The generic NEHRP B amplification was based on the $\overline{V_S}$ (30m) profile 1,130m/s and reflected the reference site in Walling et al. (2008). The sites off the INL were included only to add stability to the inversions in constraining the source, propagation (G(R)), and Q(f) parameters.

7.3.1.3 Earthquake Data Recorded at INL

In total the data set included 36 recordings from seven regional earthquakes recorded at the INL temporary stations (Table 7-2) and 513 recordings from twenty-seven regional earthquakes from 2013 to 2015 (Table 7-4). These recent earthquakes were recorded at INL and other near-by stations. Table 7-3 lists the station code, location, instrument type, and seismic recorders information for these sites. The earthquake locations are shown on Figure 7-9.

Table 7-2 lists the 1995 data set, magnitudes, hypocentral distance range and recording station code for the seven regional earthquakes recorded (see Woodward-Clyde Federal Services et al., 1996 for more information). Table 7-4 lists the time, location, magnitude (and type), distance from central INL, depth, number of recordings used in the analyses and hypocentral distance range for the recent twenty-seven earthquakes. The magnitudes range from 3 to 5 (approximate moment magnitude). Several additional regional earthquakes were considered for analyses but eliminated since the time series contained multiple earthquakes.

7.3.1.4 Earthquake Data Processing

Data processing for the time series (1989 and current analyses) generally followed the Next Generation Attenuation (NGA), NGA-West2 procedure as described in Ancheta et al. (2014) and Goulet et al. (2014), and included corrections for the instrument response.

7.3.1.5 Fourier Amplitude Spectra

Shear-wave Fourier amplitude spectra (FAS) and pre-event noise samples were computed from the windowed time series. In total the data set contains 549 vector-averaged horizontal FAS from a total of 34 earthquakes at 31 recording sites. Table 7-3 lists the stations with either broadband velocity (HH) or acceleration instruments (HN) that record ground motion at 100 samples per second (SPS). In addition, the FAS from short-period (EH) recording sites with a sample rate of 100 SPS were also included after correction for instrument response. Finally, several sites have broadband velocity instruments (BH) (e.g. H17A from the TA – Transportable Array) with sampling at 40 SPS and a corresponding high-frequency limit of 18 Hz. Recordings from station SPCI (EH with 25 recordings) were excluded from the analyses due to a gain issue. Also station PLID (BH) only recorded one earthquake so it was also excluded from the kappa analyses. Based on magnitude, record quality, and available bandwidth a subset of 27 earthquakes of the original 34 earthquakes was selected for analyses (Table 7-4).

7.3.2 Inversion of FAS for Kappa and *Q*

An inversion process was used to estimate kappa in which the earthquake source, path, and site parameters were obtained by using a nonlinear least-squares fit to the Fourier Amplitude Spectrum (FAS) using the point-source model (Boore 1983; EPRI 1993). The useable bandwidth for each amplitude spectrum was site and earthquake specific based on a visual examination of the pre-event FAS noise levels compared to the windowed shear-wave FAS and with the maximum frequency constrained by anti-alias filters, generally about 40 Hz for 100 SPS data and 18 Hz for the 40 SPS (BB) data. Typically the inversion bandwidth is magnitude dependent extending to lower frequency as magnitude increases. The inversion scheme treats multiple earthquakes and sites simultaneously with the common crustal path damping parameter $Q(f)$. The parameter covariance matrix was examined to determine which parameters may be resolved for each data set. Asymptotic standard errors were computed at the final iteration. The six parameters that may be determined from the data are kappa (site-specific attenuation), Q_0 (the value of Q for f equal to 1 Hz), and η (frequency-dependent path Q model), $\mathbf{M}$, corner frequency (stress drop), and R_C the transition distance from $1/R$ geometrical attenuation to $1/\sqrt{R}$. The procedure uses the Levenberg-Marquardt algorithm (Press et al., 1986) with the inclusion of the second derivative. Crustal profile

Table 7-3. Station information for 2013-2015 earthquake recordings at the INL.

Station Code[1]	Latitude (N)		Longitude (W)		Elevation (m)	Band Code[2]	Sample Rate (sps)	Sensor Type	Datalogger
	Degrees	Minutes	Degrees	Minutes					
ATRF	43	35.71	112	58.34	1502	HH	100	T120PA	Quanterra Q330SR
BCYI	43	18.65	113	24.31	2194	HN	100	MEMS	NetDAS
COMI	43	27.71	113	35.63	1890	HH	100	T120PH	Quanterra Q330SR
CNCI	43	55.70	113	27.13	1896	HH	100	CMG3T	Quanterra Q330SR
HWFI	43	55.54	113	5.84	1743	EH	100	S-13 - 1Hz	NetDAS
INLF	43	39.25	112	55.67	1476	HH	100	T120PA	Quanterra Q330SR
IRCI	43	30.92	112	2.00	1441	EH	100	S-13 - 1Hz	Quanterra Q330SR
ITCF	43	34.30	112	54.89	1490	HH	100	T120PA	Quanterra Q330SR
JGI	44	5.56	112	40.61	1657	EH	100	S-13 - 1Hz	NetDAS
LLRI	43	0.38	112	55.98	1471	EH	100	S-13 - 1Hz	NetDAS
MFCF	43	35.79	112	39.92	1583	HH	100	T120PA	Quanterra Q330SR
NPRI	43	35.85	112	49.63	1531	HH	100	T120PA	Quanterra Q330SR
NVRF	43	37.24	112	56.80	1489	HH	100	T120PA	Quanterra Q330SR
SPCI	43	27.00	112	38.22	1520	EH	100	S-13 - 1Hz	NetDAS
TMI	43	18.34	111	55.09	2179	EH	100	S-13 - 1Hz	NetDAS
AHID	42	0.92	111	6.02	1960	BH	40	CMG3	Quanterra Q680
BMO	44	51.15	117	18.36	1154	BH	40	STR2-1	Quanterra Q330SR
DLMT	45	21.75	112	35.78	1569	BH	40	CMG3TESP	RT-130-01/6
FLWY	44	4.96	110	41.96	2078	BH	40	CMG3TESP	RT-130-01/6
FXWY	43	38.29	111	1.61	2254	BH	40	CMG3TESP	RT-130-01/6
H17A	44	23.71	110	34.57	2400	BH	40	STR-2	Quanterra Q330
HLID	43	33.75	114	24.38	1772	BH	40	STR2-1	Quanterra Q330SR
IMW	43	53.82	110	56.35	2646	BH	40	CMG3TESP	RT-130-01/6
MFID	43	24.91	115	49.67	1302	BH	40	STR2-1	Quanterra Q330SR
PLID	45	5.26	116	0.01	2164	BH	40	CMG3TESP	RT-130-01/6
REDW	43	21.74	110	51.11	2192	BH	40	CMG3TESP	RT-130-01/6
TPAW	43	29.41	110	57.04	2512	BH	40	CMG3TESP	RT-130-01/6

1. See Figure 7-8 for station locations on INL and Figure 7-9 for regional station locations.

2. Band Codes: HH - Broadband, HN – Accelerometer, and EH - Short Period at 100 sps; and BH - Broadband at 40 sps.

Table 7-4. List of 2013-2015 regional earthquake locations with observed magnitudes, and the number of stations and distance ranges used in the analysis of kappa.

Event ID	Yr-Mo-Dy	Hr:Mn:Sec	Latitude N°	Longitude W°	Depth (km)	Magnitude	Observed Magnitude Type/Source[1]	Location Source[2]	Number of Stations Used	Hypocentral Distance Range (km)
01	2013-10-19	00:05:5	43.4510	-111.1260	5.30	3.8	M_W US	MBMG	20	16-381
02	2013-11-17	13:57:2	42.9277	-111.0448	5.86	3.0	M_L IE	INL	16	51-393
03	2013-11-20	02:32:3	44.8430	-111.4850	7.60	3.1	M_d MB	MBMG	18	88-382
04	2013-11-29	13:45:0	42.6410	-111.0887	10.26	3.0	M_L IE	INL	18	70-326
05	2014-01-01	04:19:5	42.1302	-112.5290	6.80	3.0	M_L IE	UUSS	19	103-359
06	2014-01-06	09:14:1	44.7580	-110.7790	9.50	3.5	M_L UU	MBMG	11	44-261
07	2014-02-11	23:03:1	44.7460	-110.7950	10.80	3.5	M_L UU	MBMG	13	44-259
08	2014-02-15	10:23:5	44.7718	-111.0902	1.58	3.0	M_L UU	INL	14	59-306
09	2014-03-25	16:55:3	44.5910	-114.3040	6.90	3.8	M_L US	MBMG	19	101-387
10	2014-03-30	12:34:4	44.7720	-110.6850	5.60	4.7	M_L UU	MBMG	17	43-308
11	2014-03-30	13:30:5	44.8592	-110.6145	6.06	3.5	M_L UU	INL	12	52-285
12	2014-04-10	12:21:3	44.5910	-114.3210	7.30	4.1	M_L US	MBMG	21	101-388
13	2014-04-13	00:04:4	44.5990	-114.3180	5.40	4.9	m_b US	MBMG	22	102-388
14	2014-04-14	20:16:4	44.6000	-114.3300	7.40	4.4	M_W US	ANSS	22	103-389
15	2014-05-03	08:34:0	44.5882	-114.3130	8.90	3.7	M_W MB	MBMG	21	122-387
16	2014-07-17	23:31:5	43.7560	-111.1237	2.15	3.2	M_L IE	INL	21	15-382
17	2014-08-30	20:09:1	43.7740	-110.9640	7.10	3.9	M_L IE	MBMG	23	16-395
18	2014-10-01	02:34:5	43.0700	-110.7590	4.10	3.5	M_L US	MBMG	19	49-301
19	2014-11-11	15:16:3	42.5017	-111.5643	5.98	3.3	M_L US	INL	20	66-362
20	2014-11-30	22:59:5	44.9890	-111.8860	8.80	3.3	Mc MB	MBMG	20	70-428
21	2014-12-23	13:52:3	44.4467	-114.1198	3.52	3.5	M_L US	INL	21	100-365
22	2014-12-24	04:10:3	44.4280	-114.1090	3.25	3.6	M_L IE	INL	22	77-327
23	2015-01-03	17:44:0	44.4560	-114.1440	11.00	5.0	M_W US	MBMG	20	81-367
24	2015-01-04	06:35:2	44.4450	-114.1490	11.00	4.0	M_L MB	MBMG	22	81-365
25	2015-01-04	07:34:1	44.4790	-114.1760	10.60	4.0	M_L US	MBMG	22	85-371
26	2015-01-04	10:47:5	44.4640	-114.1670	11.60	3.8	M_L MB	MBMG	21	83-369
27	2015-01-04	13:21:5	44.4730	-114.1650	10.50	3.9	M_L IE	MBMG	22	84-370

1. Magnitudes: local magnitude M_L; moment magnitude M_W; body-wave magnitude m_b. Sources: MB – Montana Bureau of Mines and Geology; IE – Idaho National Laboratory; US – U.S. Geological Survey; UU – University of Utah Seismograph Stations.

2. Sources: MBMG – Montana Bureau of Mines and Geology; INL – Idaho National Laboratory; UUSS – University of Utah Seismograph Stations.

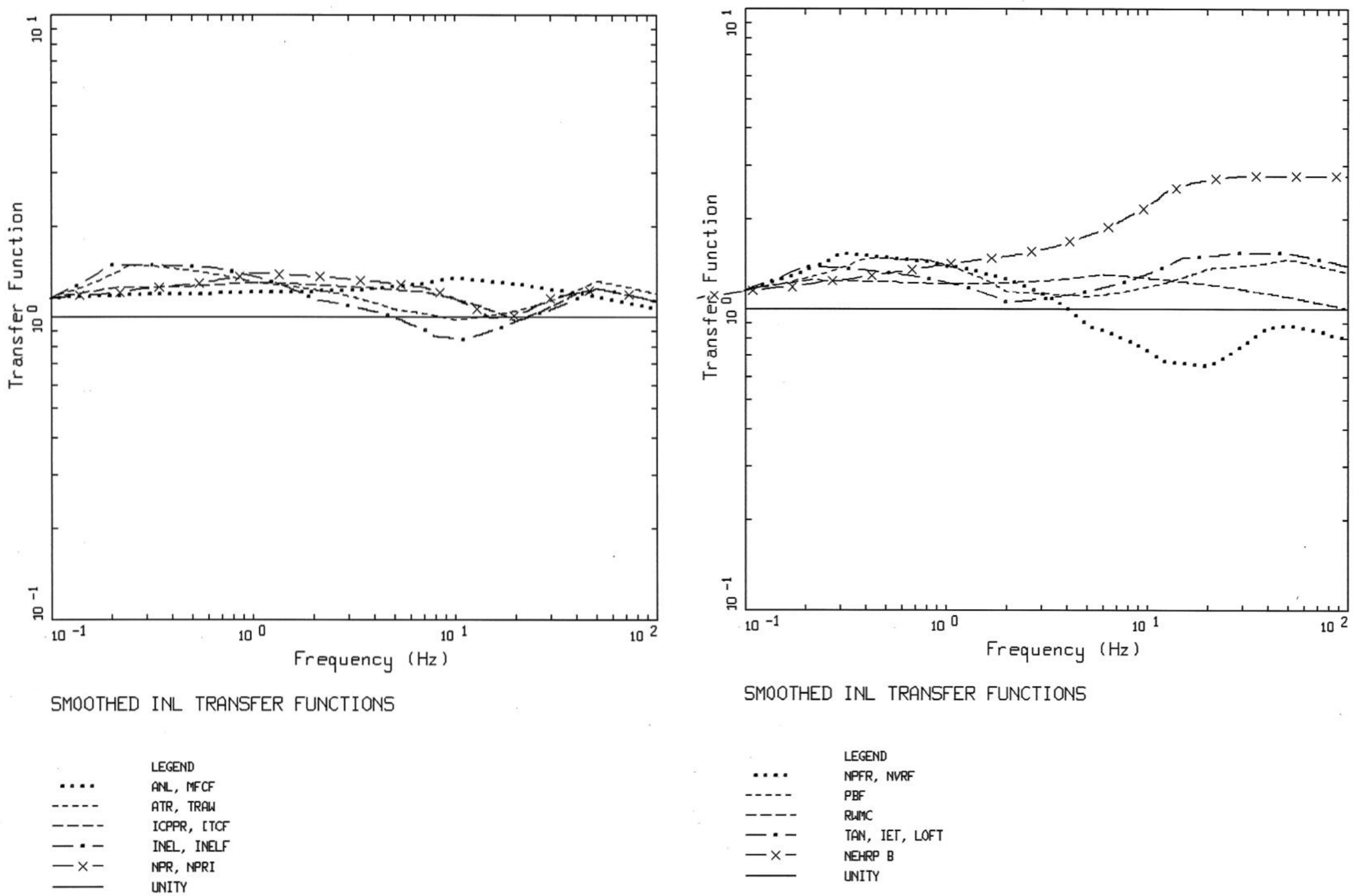

Figure 7-10. Smoothed INL crustal transfer functions. The NEHRP B transfer function was used for shallow soil and rock seismic recording stations off the INL and without shear-wave velocity profiles.

amplification was accommodated in the inversion scheme by incorporating the appropriate transfer functions (source depth to surface) in estimating the point-source surface spectra. These are shown on Figure 7-10.

To reduce the potential for non-uniqueness inherent in inversion results, a suite of starting models was employed. The final set of parameters was selected based upon a visual inspection of the model fit to the Fourier amplitude spectrum, mean squared error, and the parameter covariance matrix. The stress drop was calculated from the moment and corner frequency using the relationship:

$$f_c = \beta \left(\frac{\Delta \sigma}{8.44 \cdot M_o} \right)^{\frac{1}{3}} \qquad [7\text{-}1]$$

The inversions were done on log amplitude spectra (vector average (SRSS) of the two horizontal components), as strong ground motion data appear to be log normally distributed. This is consistent with the model being represented as a product (rather than sum) of models (EPRI, 1993). A feature of the inversion scheme is the flexibility to distinguish between sites for which kappa is determined, and stations for which recordings are available. As a result several stations may share a common site or kappa estimate. This feature permitted analyzing separately the recording sites from the Woodward-Clyde Federal Services et al. (1996) study and the sites in the recent analyses and then grouping near-by sites together to share a common kappa estimate when appropriate (e.g., TRAW and ATRF).

In order to provide stable estimates of kappa for the INL sites and, in particular Area MFC, recordings from the 1996 analyses (Table 7-2) were combined with the current recordings (Table 7-4) to estimate kappa for all of the sites. Unfortunately, with the exception of sites INEL and INLF, it was not possible to place the new sites at the same location as the previous temporary array (Figure 7-8 and Woodward-Clyde Federal Services et al., 1996). In particular, the Area of interest, MFC, has two recording sites: the 1989 temporary array site ARW1/ANLN1 (termed ANL) and the broadband station MFCF (Figure 7-8). To provide an assessment of uncertainty in the kappa estimate for Area MFCF, inversions were done keeping the two sites distinct. The remaining stations in relatively close proximity to each other: TRAW/TRAW, INEL/INLF, and co-located sites NPR/NPRI, had each pair assigned the same kappa. This was done to help stabilize the inversions by reducing the number of free parameters.

The starting model parameters included in Table 7-5 with *Q*(*f*) generally consistent with values for Western North America (WNA) (Erickson et al., 2004). With the limited distance ranges of about 15 km

Table 7-5. Starting values for inversions for kappa.

Parameter and Starting Values
• **M** = Tables 7-2, 7-4
• Q_o = 150
• η = 0.6
• R_C = 40 km
• Source Shear-Wave Velocity = 3.55 km/s (Richins et al., 1987 crustal, model Table 7-1)
• Source Density = 2.70 cgs (Richins et al., 1987 crustal, model Table 7-1)
• $\Delta\sigma$ = 25 bars
• kappa = 0.02s all sites

to about 400 km (Tables 7-2 and 7-4) as well as limited bandwidth of the 40 SPS recordings (Table 7-3), resolution of Q_0, η (frequency dependence of $Q(f)$, Boore, 1983), and R_C was not possible. Initial inversions resulted in R_C close to 90 km, about twice the crustal thickness (Herrmann, 1985) but with strong coupling between Q_0, η, and R_C. Consequently R_C was held fixed at 90 km with the resulting Q_0 and η of 148.08 and 0.54 respectively. These values of Q_0 and η are close to those of active tectonic regions in WNA. The corresponding estimate of the median stress parameter was 80.40 bars with a median kappa across the sites of 0.027s. The suite of inversion parameters is listed in Table 7-5. Figures 7-11 and 7-12 show the inversion fits to the FAS fits for the seven regional earthquakes listed in Table 7-2 with logarithmic axes and linear frequency axes, respectively. Figures 7-13 and 7-14 show the corresponding results for the 27 recent regional earthquakes listed in Table 7-4 again for logarithmic and linear frequency axes, respectively. The site and area specific kappa estimates are listed in Table 7-6.

7.3.3 Estimation of Kappa for Area MFC

The area of interest, MFC, contained two recording stations, the earlier 1989 temporary station ANL (Woodward-Clyde Federal Services et al., 1996) and the BB station MFCF, with the two stations located within Area MFC, separated by about 2 km. To provide an estimate of uncertainty for kappa for Area MFC, the two recording stations were treated as multiple sites but using the same amplification factors. Kappa estimates for the two stations were 0.013s and 0.026s for ANL and MFCF respectively (Table 7-6). The large difference in kappa between the two locations may be related to potential differences in the shallow velocity structure, coupled with the use of the same amplification factors for the two locations. Since neither boreholes reflecting stratigraphy nor velocity measurements were available at the sites, causal mechanisms for the differences remain unknown.

To accommodate the potential uncertainty in kappa across Area MFC, reflected in the two sites, the recommended best estimate of kappa is the median at 0.018s, with lower-range and upper-range base case estimates of 0.011s and 0.030s, respectively. These estimates are considered to reflect 10th percentile to 90th percentile % range and a $\sigma_{\ln\kappa}$ of about 0.4 about the median kappa value of 0.018s.

7.3.4 Application of Alternative Procedures to Estimate Kappa

To assess the stability of the kappa estimates resulting from the inversions (Section 7.3.3), two additional methods for estimating kappa were implemented: 1) measuring the slope of the FAS and 2) peak frequency of response spectral shapes (5% pseudo absolute response spectra PSA/PGA).

7.3.4.1 Slope of the FAS

Measuring kappa based on the slope of FAS on logarithmic amplitude and linear frequency axes was first introduced by Anderson and Hough (1984). In this method, as originally proposed, kappa was comprised of a frequency independent Q and considered to control the observed ground motion at frequencies exceeding the corner frequency in an assumed omega-square source model. At a given site kappa was measured at multiple distances based on recordings from multiple earthquakes and extrapolated to zero distance to provide an estimate of κ_o, assumed to reflect damping directly below the site. This approach resulted in an estimate of κ_o relative to a crustal Q that was independent of frequency. Later observations suggested crustal Q was frequency dependent, increasing rapidly with increasing frequency (EPRI, 1993; Silva et al., 1996) and κ_o was taken to reflect frequency independent damping below the site relative to a frequency dependent crustal Q (EPRI, 1993). To accommodate the update in the kappa model to include a $Q(f)$ while maintaining the FAS slope method, the observed FAS was corrected by the $Q(f)$ resulting from the inversion. This approach then provides consistency with the kappa estimates from the inversion and obviates the necessity to extrapolate to zero distance by providing κ_o directly from the slope of the FAS.

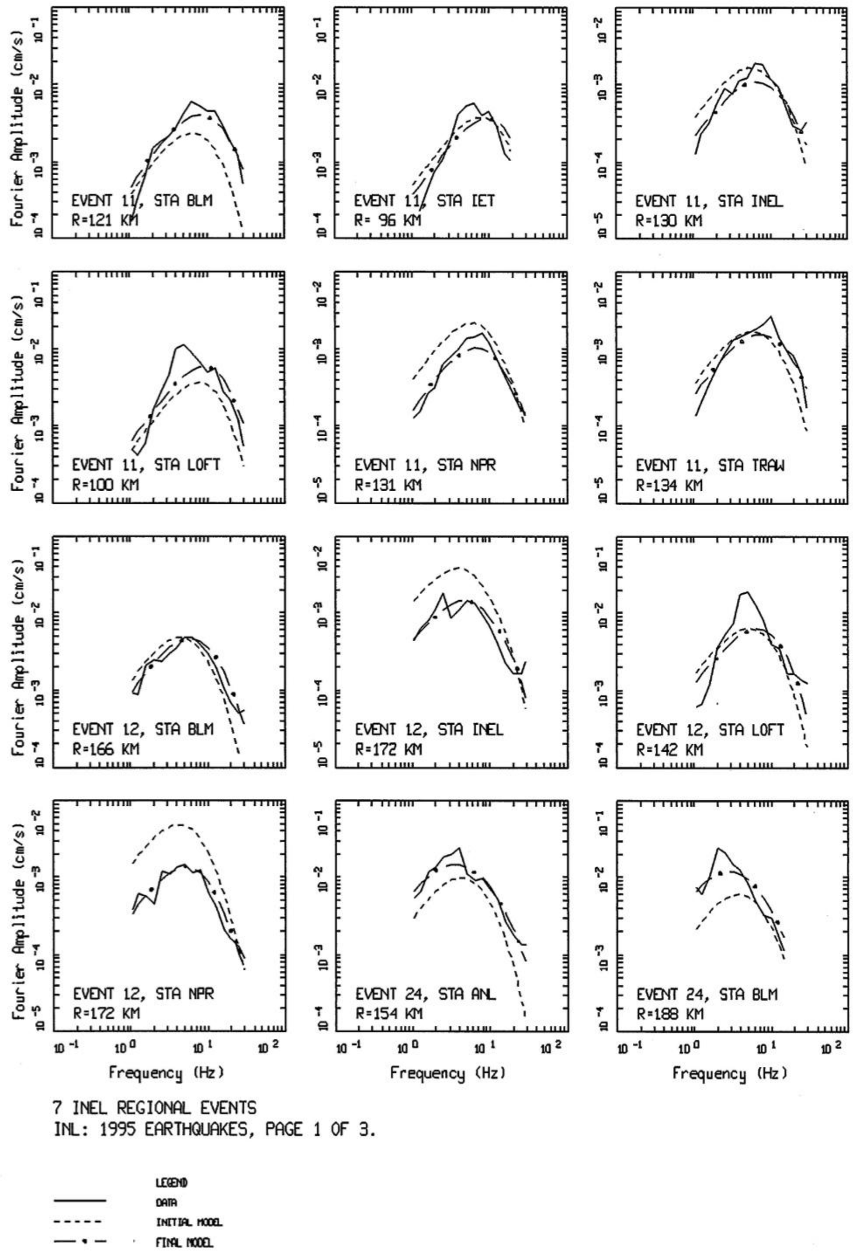

Figure 7-11. Example of FAS spectral fits of Table 7-2 regional earthquakes: logarithmic frequency axes (see Appendix F for all spectral fits).

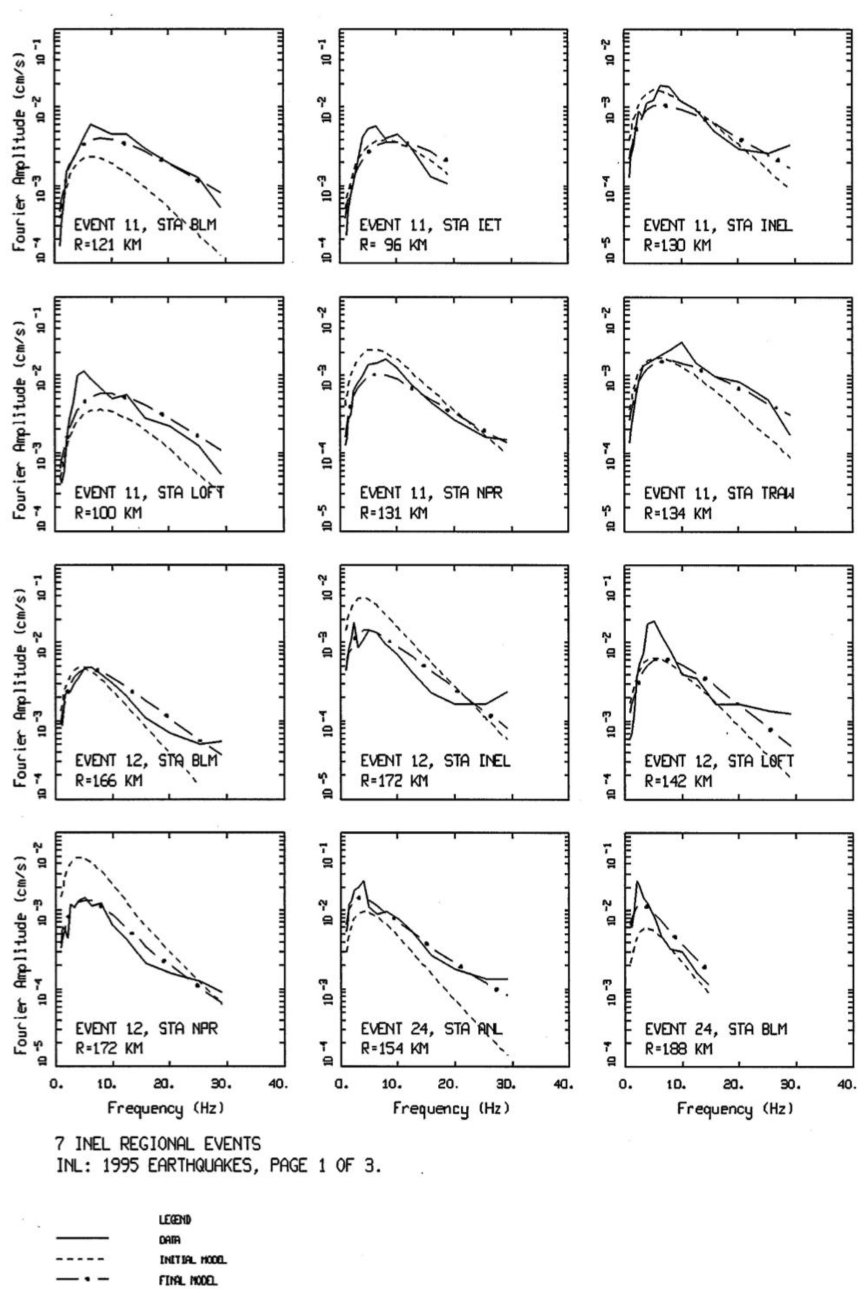

Figure 7-12. Example of FAS spectral fits of Table 7-2 regional earthquakes: linear frequency axes (see Appendix F for all spectral fits).

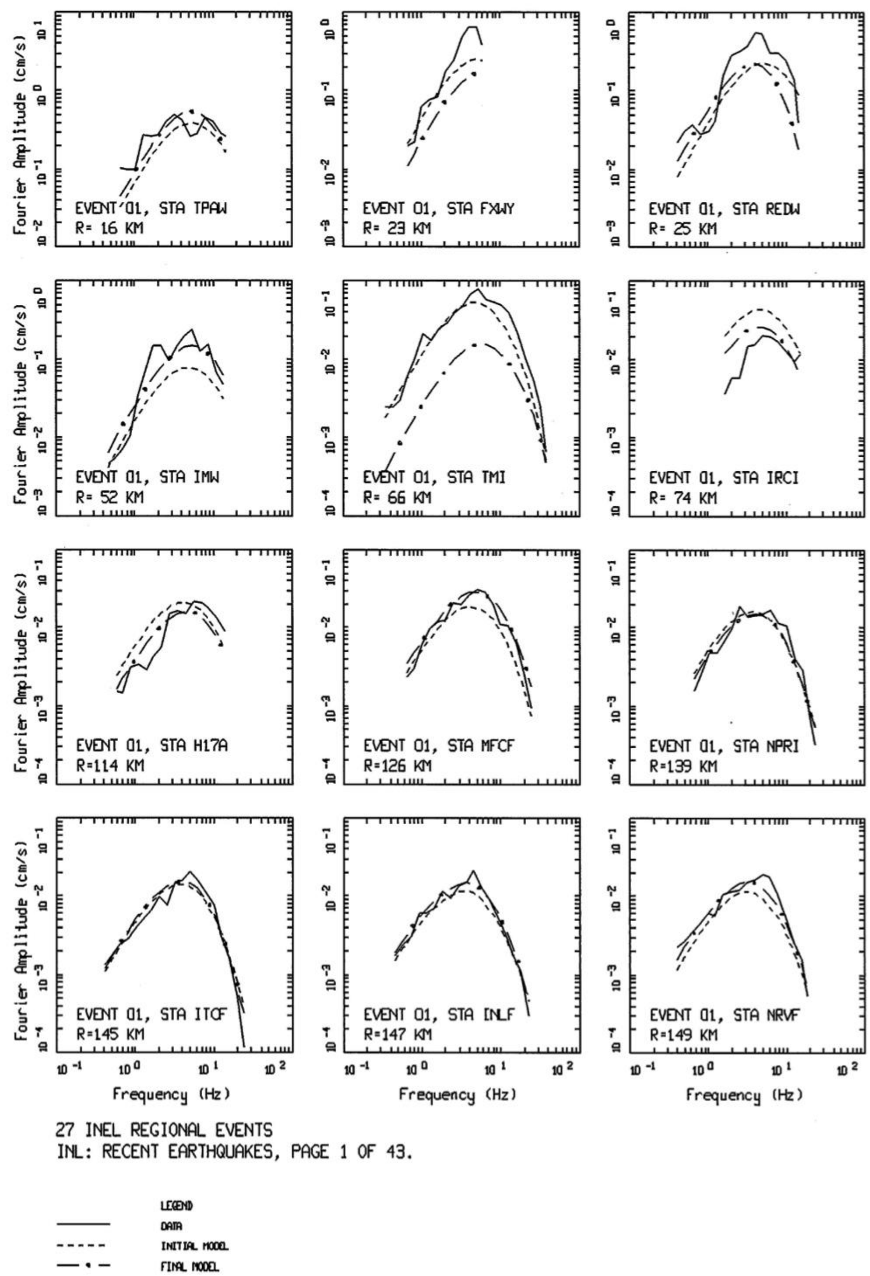

Figure 7-13. Example of FAS spectral fits of Table 7-4 regional earthquakes: logarithmic frequency axes (see Appendix F for all spectral fits).

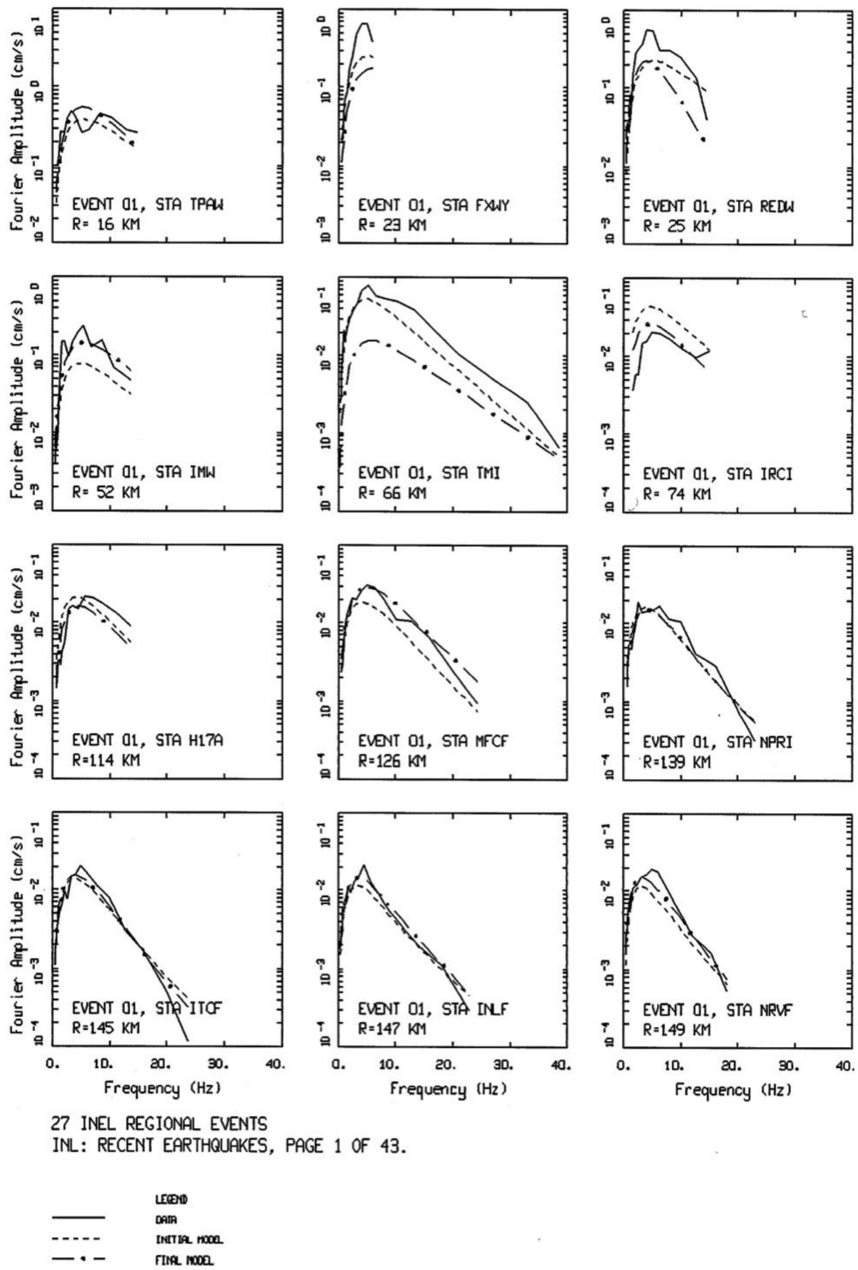

Figure 7-14. Example of FAS spectral fits of Table 7-4 regional earthquakes: linear frequency axes (see Appendix F for all spectral fits).

Table 7-6. Estimates of site kappa from inversions for INL seismic stations.

Station Name (Number of Recordings)	Crustal Amplification (See Figure 7-10)	Site Kappa (κ_0) Earthquakes (Table 7-2)	Site Kappa (κ_0) Combined Earthquakes (Tables 7-2 and 7-4)
ANL (5)		0.012	0.013
MFCF (21)		---	0.026
ANL (5) & MFCF (21)	ANL	---	0.018[1]
TRAW (1)		0.020	---
TRAW (1) & ATRF (21)	ATR	---	0.21[2]
INEL (6)		0.033	---
INEL (6) & INLF (23)	INEL	---	0.036[2]
NPR (2)		0.034	---
NPR (2) & NPRI (25)	NPR	---	0.034[2]
PBF (2)	PBF	0.033	0.032
RWMC (2)	RWMC	0.021	0.015
IET (5)	TAN	0.027	0.029
LOFT (6)	TAN	0.022	0.032
NVRF (23)	NPFR	---	0.037
ITCF (24)	ICPPR	---	0.039
	Median Estimates	0.024	0.027

1. Median kappa estimate of 0.018 s from ANL (0.013 s) and MFCF (0.026 s).
2. Kappa estimate treating the two sets of recordings (stations) as the same site.

Additionally, shear-wave velocity gradients typically result in site amplification with frequency dependencies that may impact the slope of the FAS. To accommodate such effects and provide consistency with the inversions, the recorded FAS were adjusted by the site-specific amplification factors shown on Figure 7-10.

Further considerations in fitting the FAS include the low-frequency limit as approximately twice the corner frequency (Table 7-5) to avoid possible bias in the slope due to the source. Also the high-frequency limit was taken as the filter corner frequency divided by 1.25 to minimize any effects of the low-pass filter, unless the signal-to-noise ratio fell below three. Additionally a minimum bandwidth for estimating a stable slope was set at 8 Hz, based on experience.

The FAS slope method was applied to the recordings at sites ANL and MFCF. Figure 7-15 shows the results for the five earthquakes recorded at ANL (Table 7-2). Of the five recordings only two met the criteria with the fits shown on the plots, resulting in kappa estimates of 0.018s and 0.028s, a median estimate of 0.022s, somewhat larger than 0.013s (Table 7-6) resulting from the current inversion using all five of the recordings. For site MFCF, of the 21 earthquakes recorded at the site, thirteen met the criteria with the fits shown on the plots in Figure 7-16. For this site and suite of earthquakes, kappa estimates ranged from 0.012s to 0.047s with a median estimate of 0.030s, closer to the inversion estimate of 0.026s. While both the FAS slope as well as the inversion methods resulted in higher kappa estimates at MFCF compared to ANL (Table 7-6), both sites reflect higher kappa estimates using the slope method compared to the inversion method. These results suggest the subsets of earthquakes used for the FAS method may be biased to larger kappa values. As such it is not recommended to change either the recommended range in kappa or the relative weights (Section 7.3.3) and the best estimate kappa values for sites ANL and MFCF are further assessed in Section 7.3.4.2 using response spectral shapes.

7.3.4.2 Response Spectral Shapes

For rock sites (V_{S30}≥500m/s) where nonlinear effects are small, response spectral shapes (PSA/PGA) provide a diagnostic tool for assessing site kappa (κ_o). Silva and Darragh (1995) and Laurendeau et al. (2013) show that at close distances (≤ 50 km) and after accounting for magnitude, the frequency at which the peak in the spectral shape occurs as well as the general shape in terms of relative amplitudes at low and high frequencies at close distances may be directly related to kappa. The process used was to group the recordings into bins of similar magnitudes and then compute the statistics of the response spectral shapes. These statistics are then compared to response spectral shapes predicted by a simple point source stochastic model for the average magnitude and distance of the recordings using the assessed value of κ_o for the site and incorporating adjustments for site amplification and *Q*(*f*) (Silva and Darragh, 1995).

For site ANL Figure 7-17 shows spectral shapes computed for an earthquake with **M** = 3 with **M** in the range of **M** 2.9 to **M** 3.1 compared to point-source model predictions with a kappa of 0.013s, the median estimate for the site (Table 7-6). Of note the mean **M** of 3.0 does not fit reflecting a shape too low at longer periods. The model shape at **M** 3.6 provides a much better fit suggesting the regional magnitude scale may require a site correction for these recording sites, which should be addressed in a future analysis. This trend was observed at both sites ANL and MFCF, for **M** below about **M** 3.5 to **M** 4.0. Regarding the fit for **M** 3.6, the median kappa estimate of 0.013s matched the frequency of the peak reasonably well in addition to the entire bandwidth. The mean empirical shape is quite high at its peak, about 3, higher than the typical maximum spectral amplification of about 2.2 to 2.5 (Bozorgnia et al., 2014), possibly reflecting short period amplification due to shallow materials not accommodated in the amplification factors (Figure 7-10). The shapes for other two larger earthquakes recorded at ANL, **M** 3.6 and **M** 3.7 are also shown in Figure 7-17 but do not require as significant increase in magnitude. As with the smaller magnitude recordings the median kappa estimate of 0.013s is consistent with the empirical shape.

Considering site MFCF with a median kappa estimate of 0.026s, Figure 7-18 compares empirical and model shapes for a much larger range in magnitudes: **M** 3.0 to **M** 3.3, **M** 3.5 to **M** 3.8, **M** 3.9 to **M** 4.1, and **M** 4.7 to **M** 5.0. As with site ANL, at lower magnitudes a significantly larger magnitude is required to capture the longer periods and near the peak the empirical shape approaches 3, exceeding the model shape, except for the largest magnitudes. The median kappa estimate of 0.026s (Table 7-6) provides a reasonably good fit throughout the period range including the period range of the peak. The results of the response spectral shapes at both sites, ANL and MFCF, suggest the median kappa estimates of 0.013s and 0.026s, respectively, reflect estimates consistent with those of the inversion (Table 7-6) and are appropriate for characterizing an estimated range in kappa for the facility.

7.3.5 Dynamic Properties of FMF Soils

Site-specific dynamic property curves (G/Gmax and damping) are not available for FMF soils. Therefore, the epistemic uncertainty in G/Gmax and damping are accommodated by using two alternative sets of models following the approach described in Appendix B of EPRI (2013). The two sets are the EPRI (1993) relationships for cohensionless soils and the Peninsular Range set (Silva et al., 1996), which represent a more linear set of G/Gmax and damping relationships. Following EPRI (2013) these two sets are given equal weight in defining the epistemic uncertainty in site response for FMF. Figure 7-19 shows the G/Gmax and damping relationships.

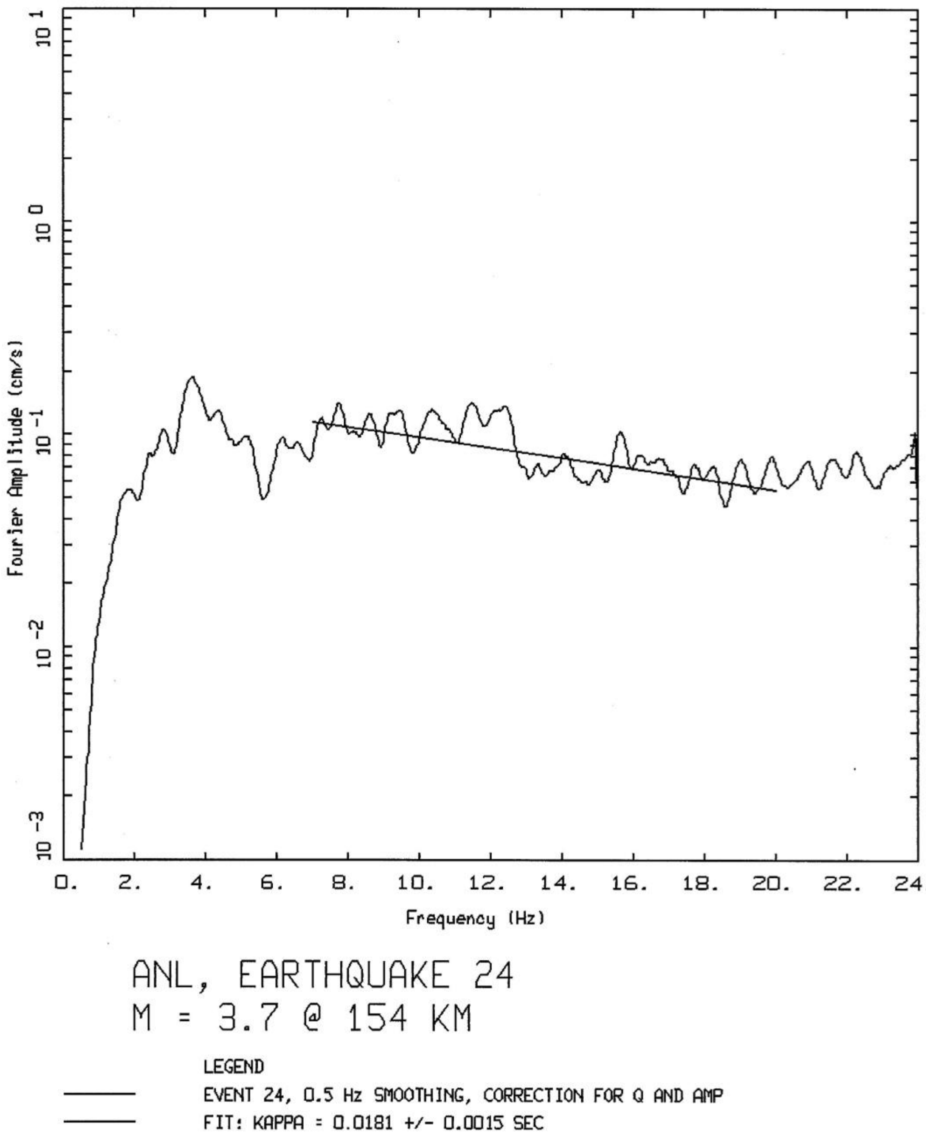

Figure 7-15. Example of the FAS slope fit for Earthquake 24 at ANL (Table 7-2). See Appendix F for the other FAS slope fits at ANL.

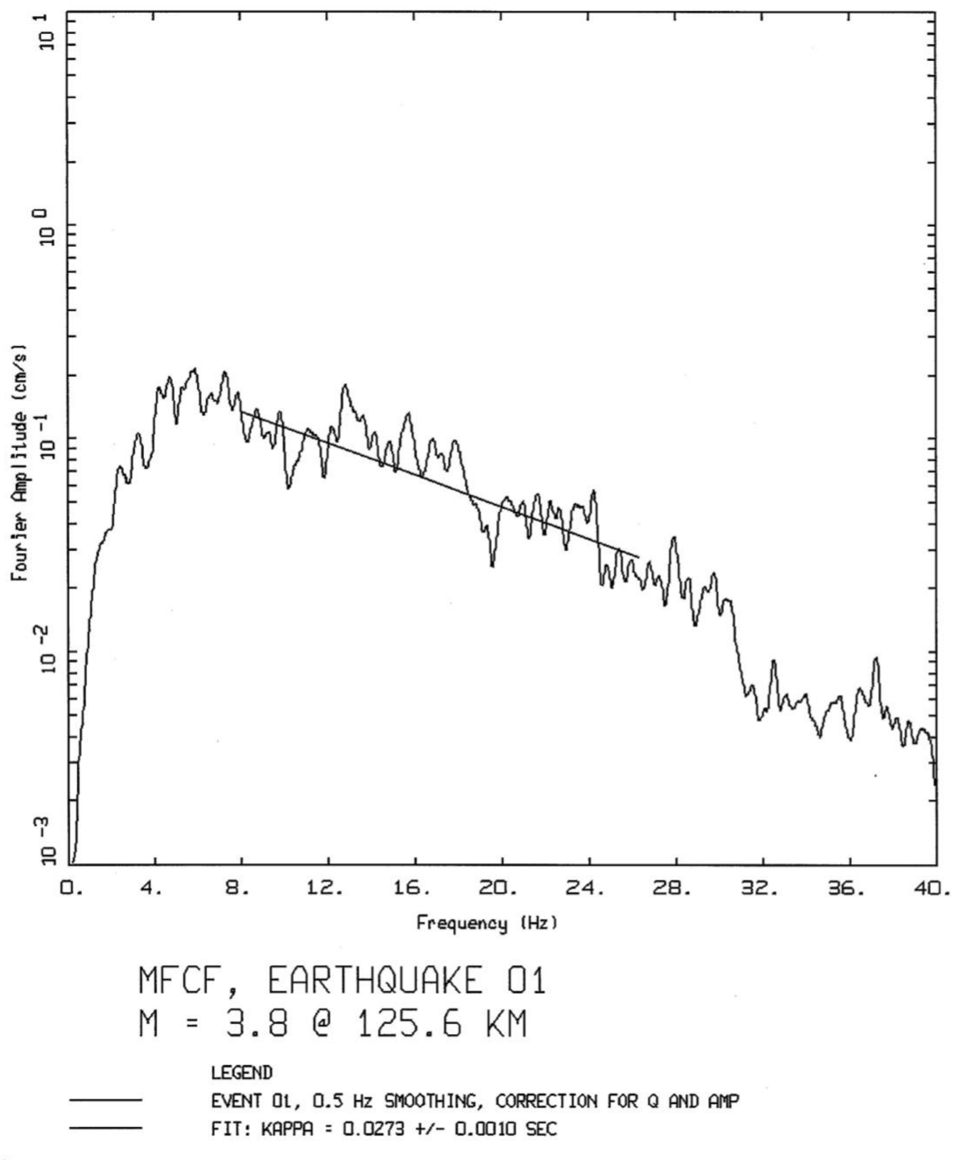

Figure 7-16. Example of the FAS slope fit for Earthquake 01 at MFCF (Table 7-4). See Appendix F for the other FAS slope fits at MFCF.

(a)

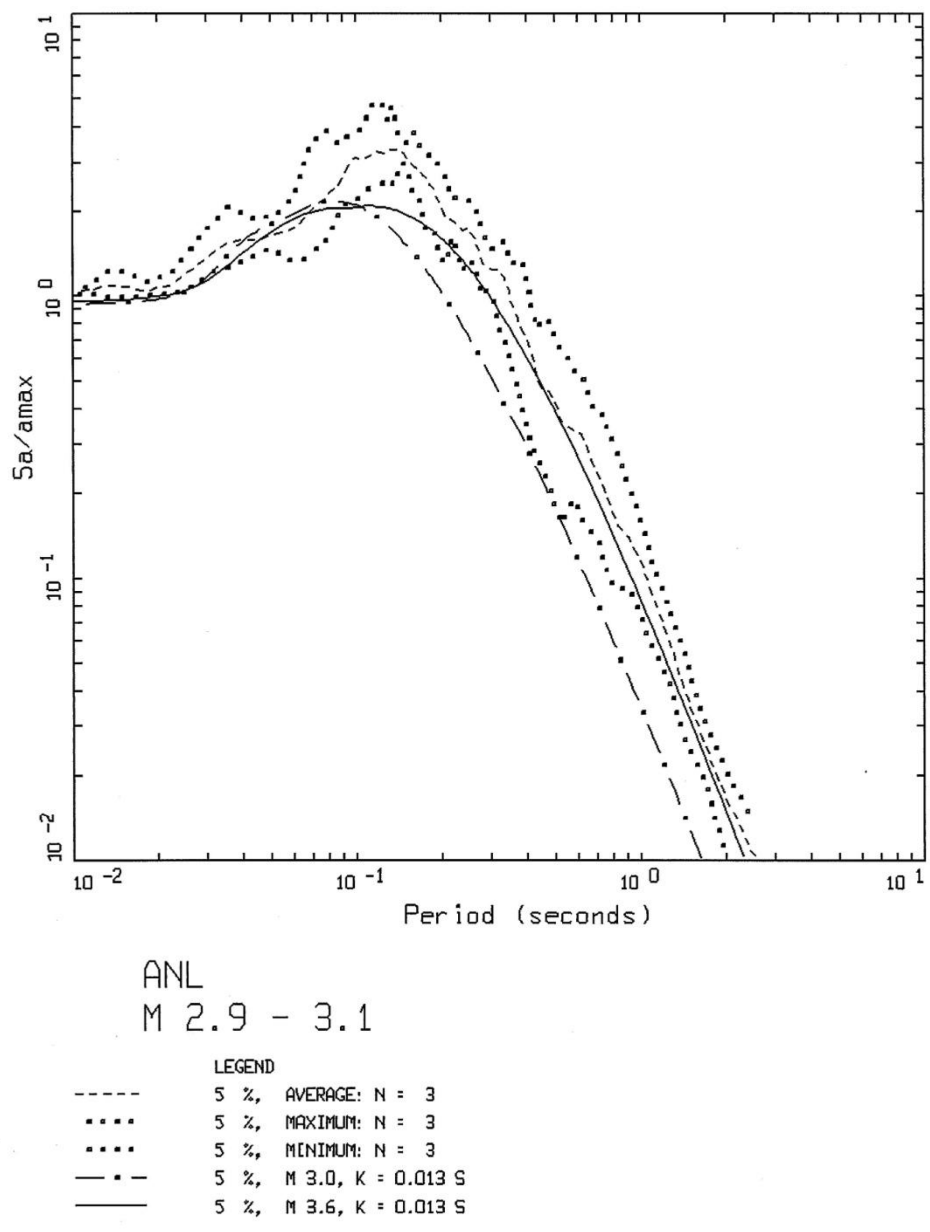

10 1
10 0
10 -1
10 -2
Sa/amax
10 -2
10 -1
10 0
10 1
Period (seconds)
ANL
M 2.9 - 3.1
LEGEND
5 %, AVERAGE: N = 3
5 %, MAXIMUM: N = 3
5 %, MINIMUM: N = 3
5 %, M 3.0, K = 0.013 S
5 %, M 3.6, K = 0.013 S

(b)

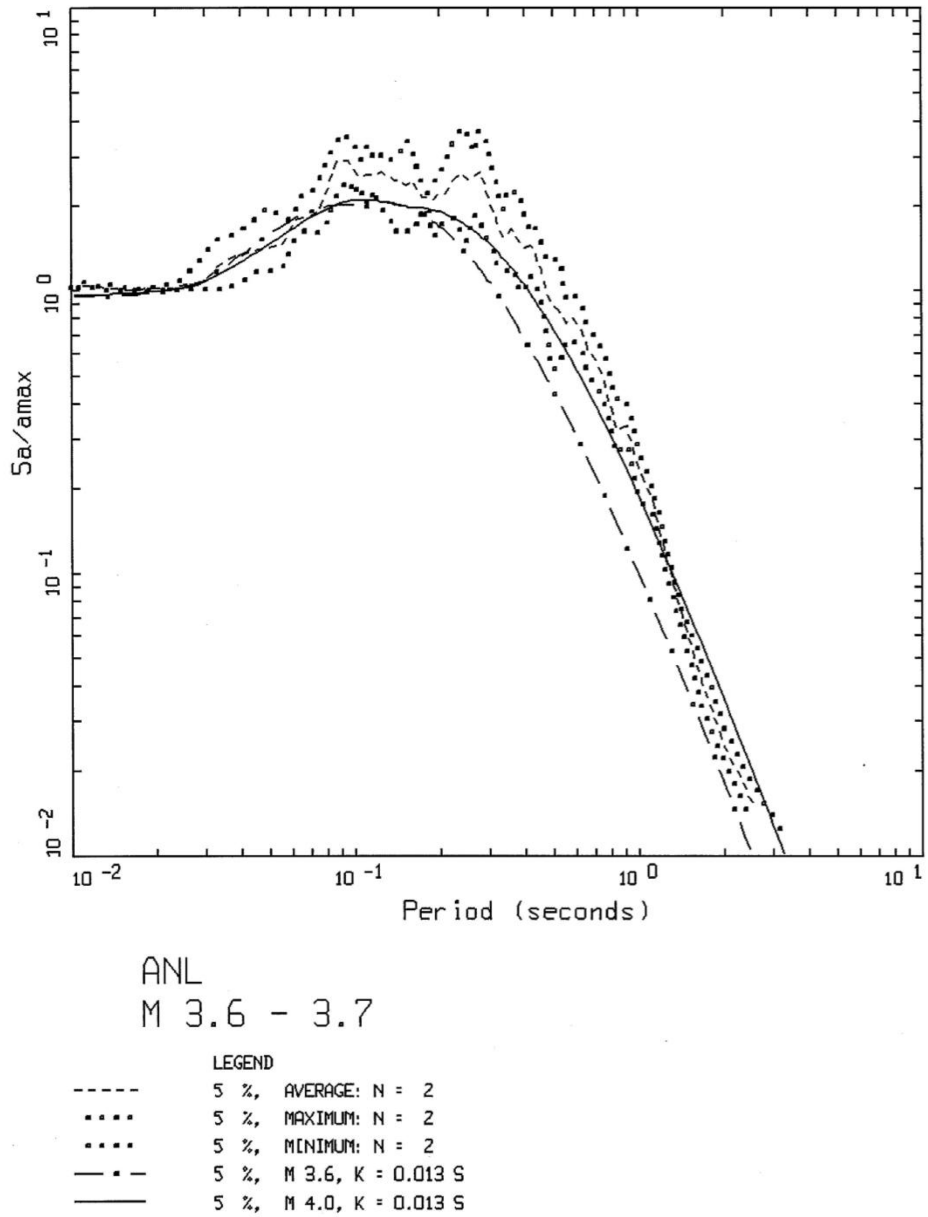

Figure 7-17. Response spectral shape (5% damped PSA/PGA) fits of Table 7-2 regional earthquakes recorded at ANL: a) M 2.9-3.1; and b) M 3.6-3.7.

(a)

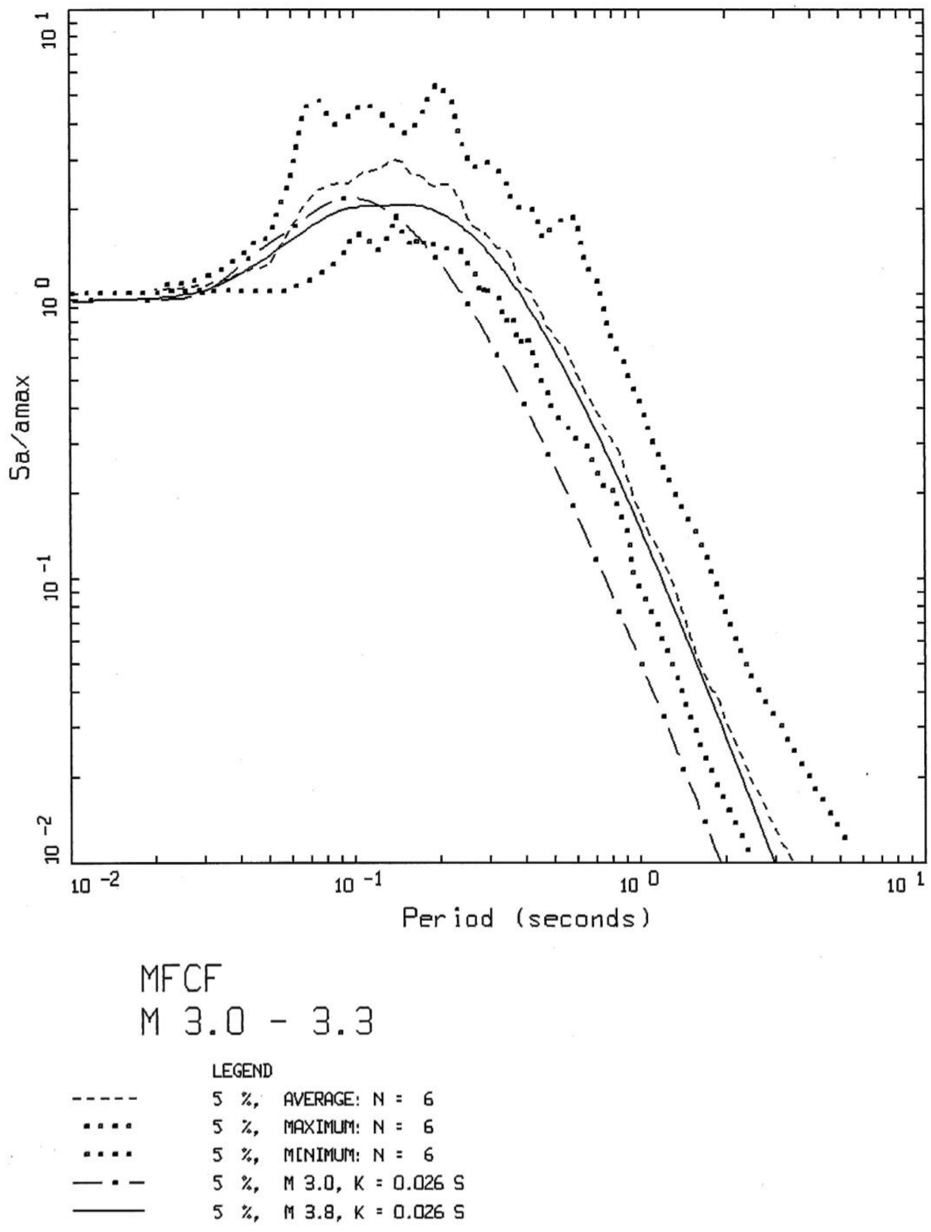

10 1
10 0
10 -1
10 -2
Sa/amax
10 -2
10 -1
10 0
10 1
Period (seconds)
MFCF
M 3.0 - 3.3
LEGEND
5 %, AVERAGE: N = 6
5 %, MAXIMUM: N = 6
5 %, MINIMUM: N = 6
5 %, M 3.0, K = 0.026 S
5 %, M 3.8, K = 0.026 S

(b)

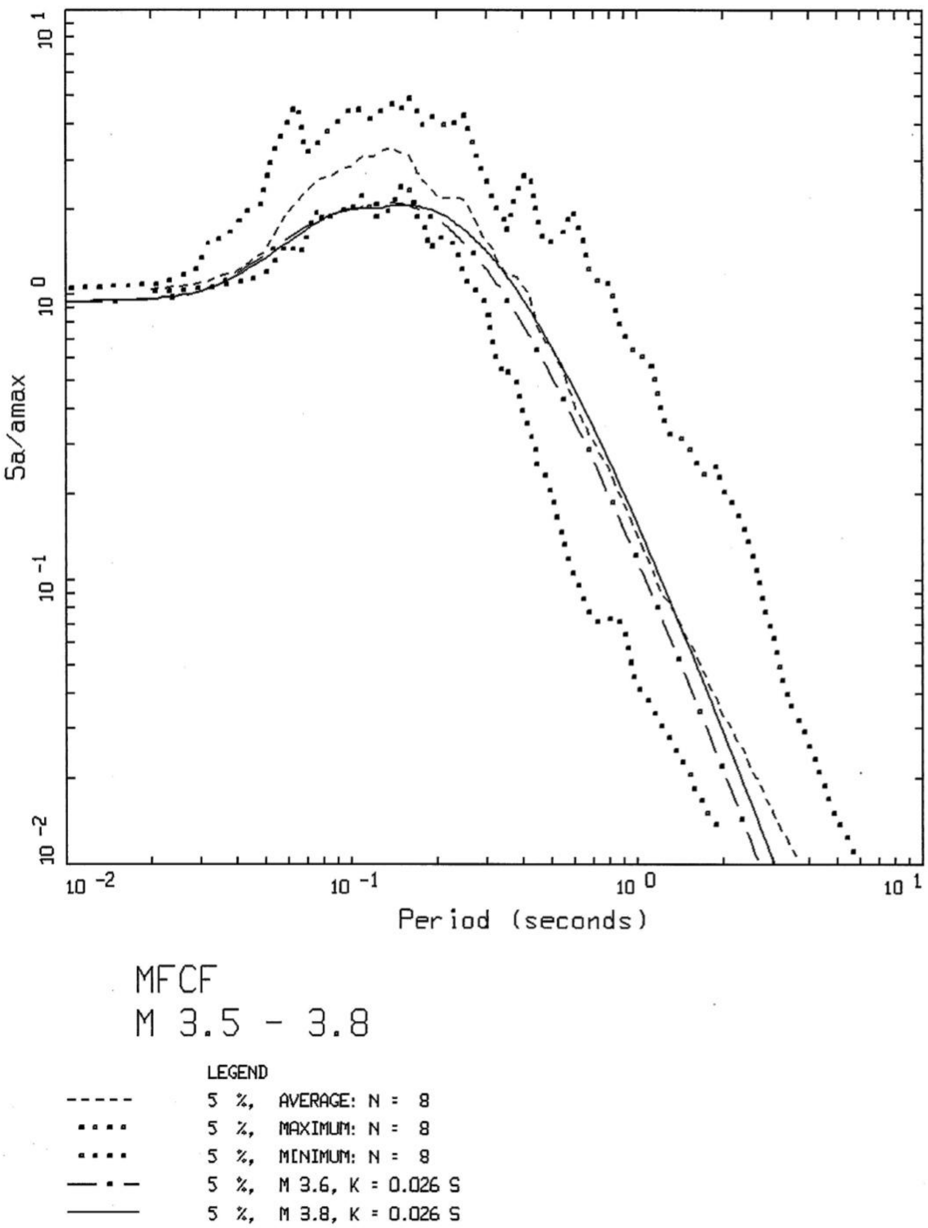

10 1
10 0
10 -1
10 -2
Sa/amax
10 -2
10 -1
10 0
10 1
Period (seconds)

MFCF
M 3.5 - 3.8

LEGEND
5 %, AVERAGE: N = 8
5 %, MAXIMUM: N = 8
5 %, MINIMUM: N = 8
5 %, M 3.6, K = 0.026 S
5 %, M 3.8, K = 0.026 S

(c)

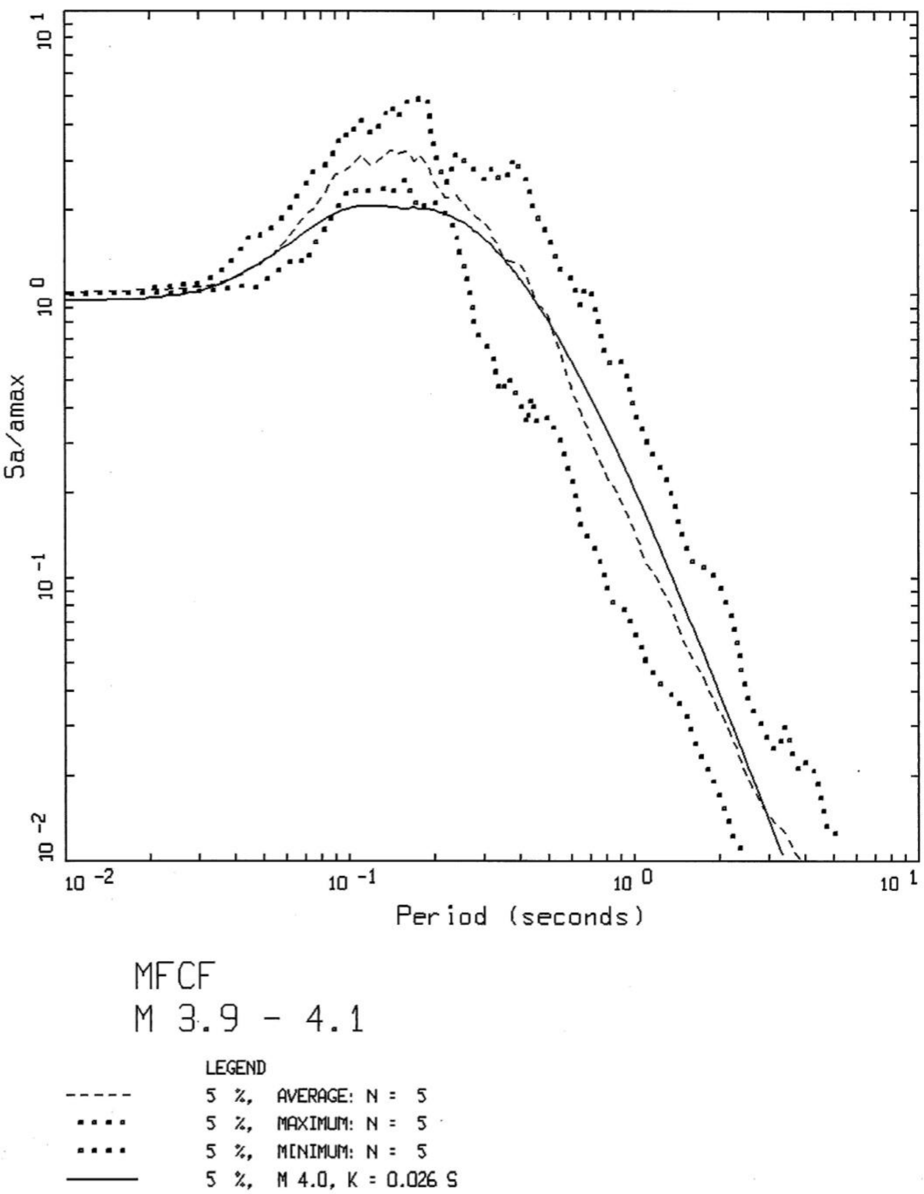
Sa/amax
10 1
10 0
10 −1
10 −2
10 −2
10 −1
10 0
10 1
Period (seconds)
MFCF
M 3.9 − 4.1
LEGEND
5 %, AVERAGE: N = 5
5 %, MAXIMUM: N = 5
5 %, MINIMUM: N = 5
5 %, M 4.0, K = 0.026 S

(d)

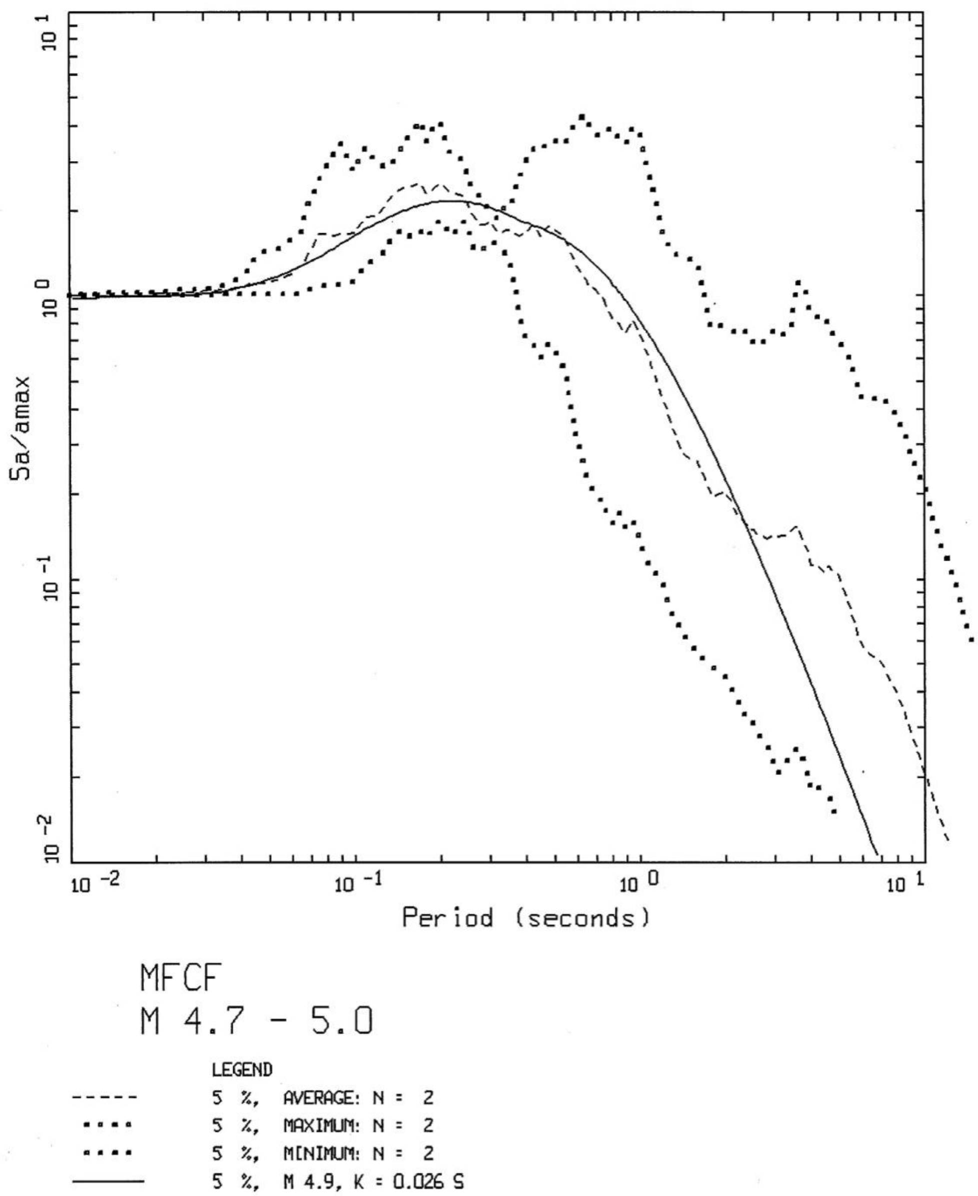

Figure 7-18. Response spectral shape (5% damped PSA/PGA) fits of 2013-2015 regional earthquakes (Table 7-4) recorded at MFCF: a) M 3.0-3.3; b) M 3.5-3.8; c) M 3.9-4.1; d) M 4.7-5.0.

(a)

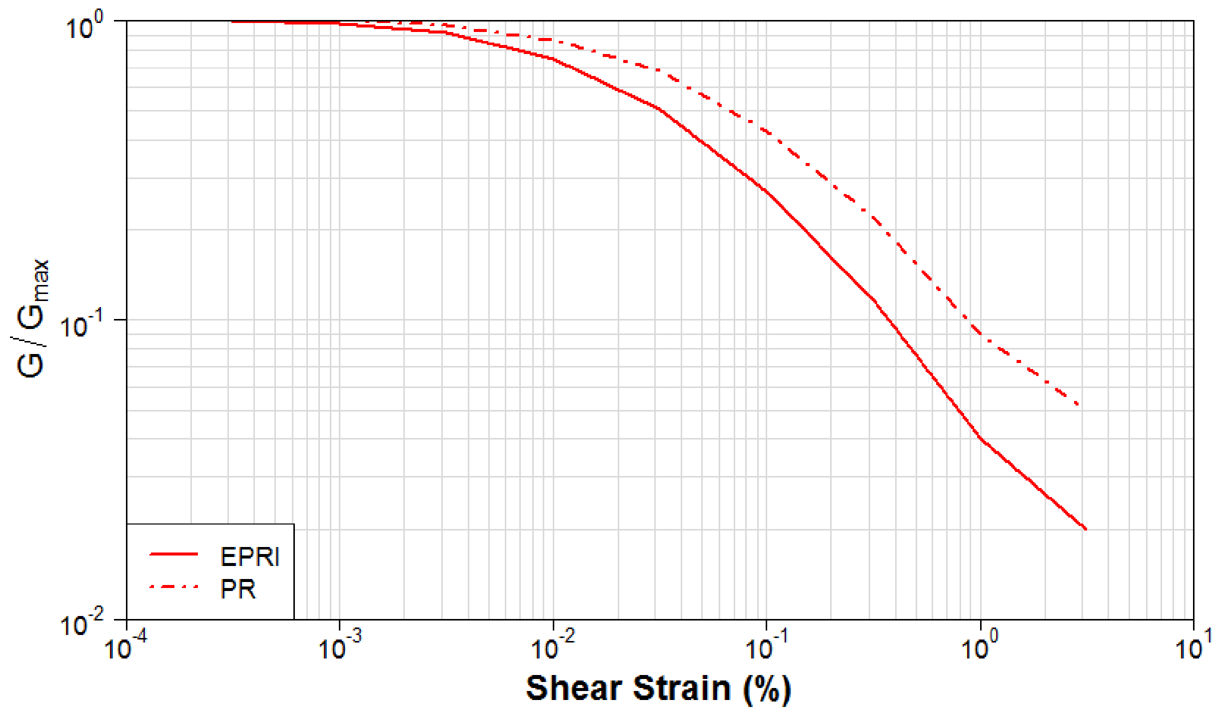

(b)

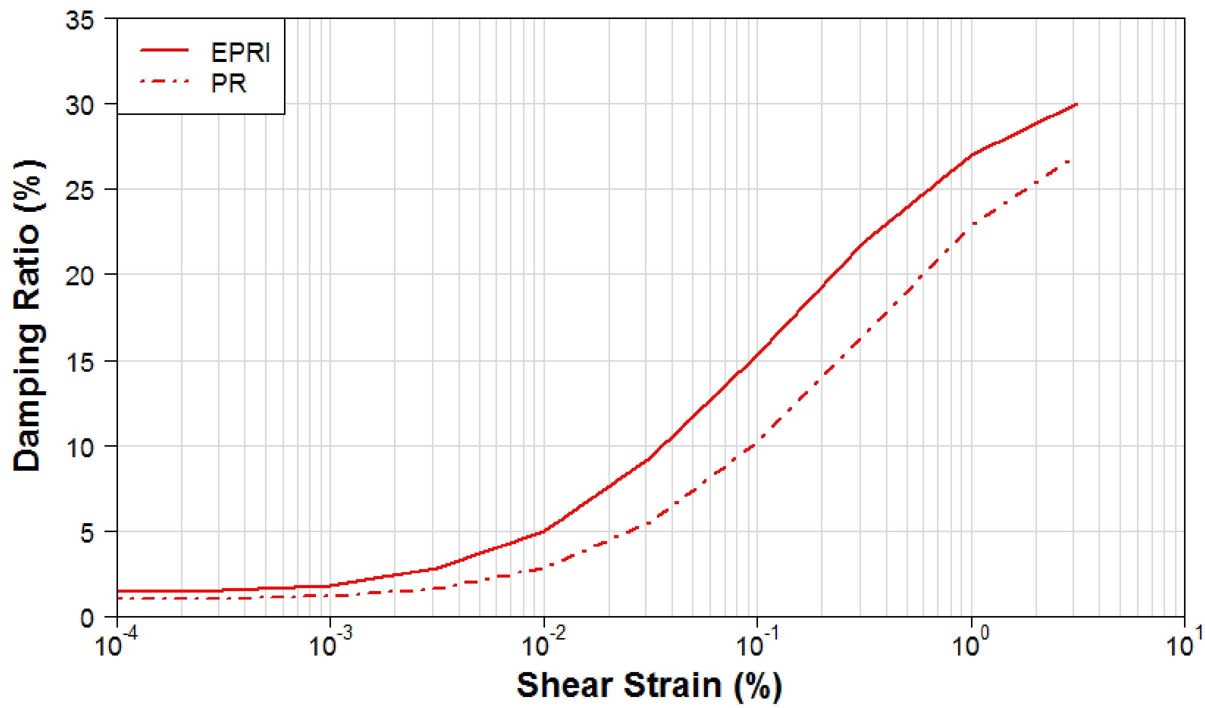

Figure 7-19. Relationships for EPRI (1993) and Peninsular Range (PR): a) G/Gmax; and b) damping ratio used for FMF soils.

7.4 Shear Wave Velocity (Vs) Profiles for NRF and SFHP

As was the case for MFC and FMF, characterization of the shear wave velocity of the shallow crust is needed in order to develop the appropriate adjustments of the GMPEs for application in hazard calculations for NRF and SFHP. The Vs profile for NRF was originally developed in the 1996 INL PSHA. For this study, the Vs profile for NRF is updated.

7.4.1 NRF Vs Profile

NRF is located ~3 km west of the Big Lost River within its flood plain. During Holocene and Pleistocene time, the flood plain of the Big Lost River formed a place where sediments from the river and lava flows originating at higher elevations coalesced and inter-fingered (Helm-Clark et al., 2006). Figure 7-20 shows the locations of borings near NRF with lithology. Figure 7-21 shows the lithology for these boreholes. Eight boreholes near and at NRF show sedimentary interbeds dispersed throughout basalt layers. Six boreholes show that the upper 100 m have fewer thin sedimentary interbeds whereas the S-5-G and USGS-097 boreholes have more. Three boreholes, NRF-15 located 1 km north of NRF, NRF-4 located in center of NRF, and S-5-G located in the southern end of NRF (Figure 7-20), show thicker sedimentary interbeds starting near 140 m depth (Figure 7-21). Thicker interbeds are also located at depths below 200 m with the thickest interbed (159 m) at 365 m depth in the S-5-G borehole (Figure 7-21). The sedimentary interbeds are composed primarily of clay, silt, and sand with an occasional gravel interbed.

For this study, the NRF Vs profile was revised to include only the lithology from the S-5-G borehole, which is the deepest borehole (408 m) within the NRF facility area (Figure 7-21). The 2015 NRF Vs

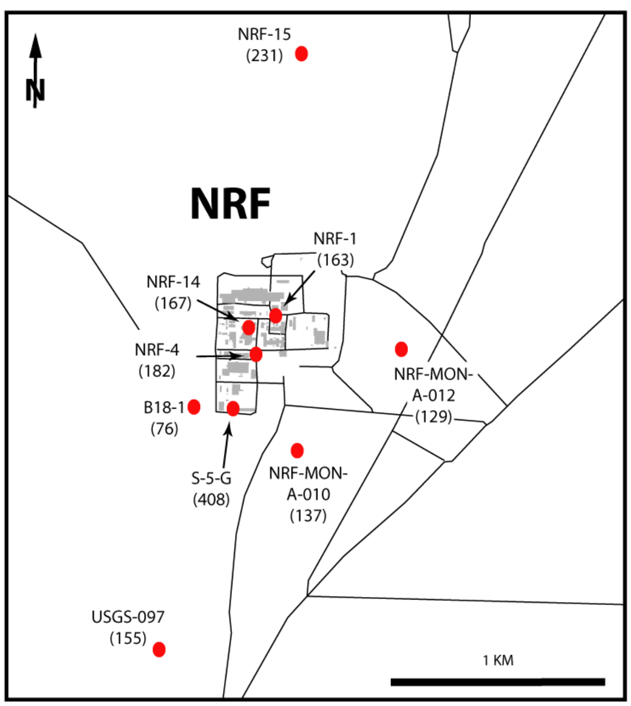

Figure 7-20. Map shows location of boreholes with basalt lithology in the vicinity of NRF. Bottom hole depths in meters are listed in parentheses.

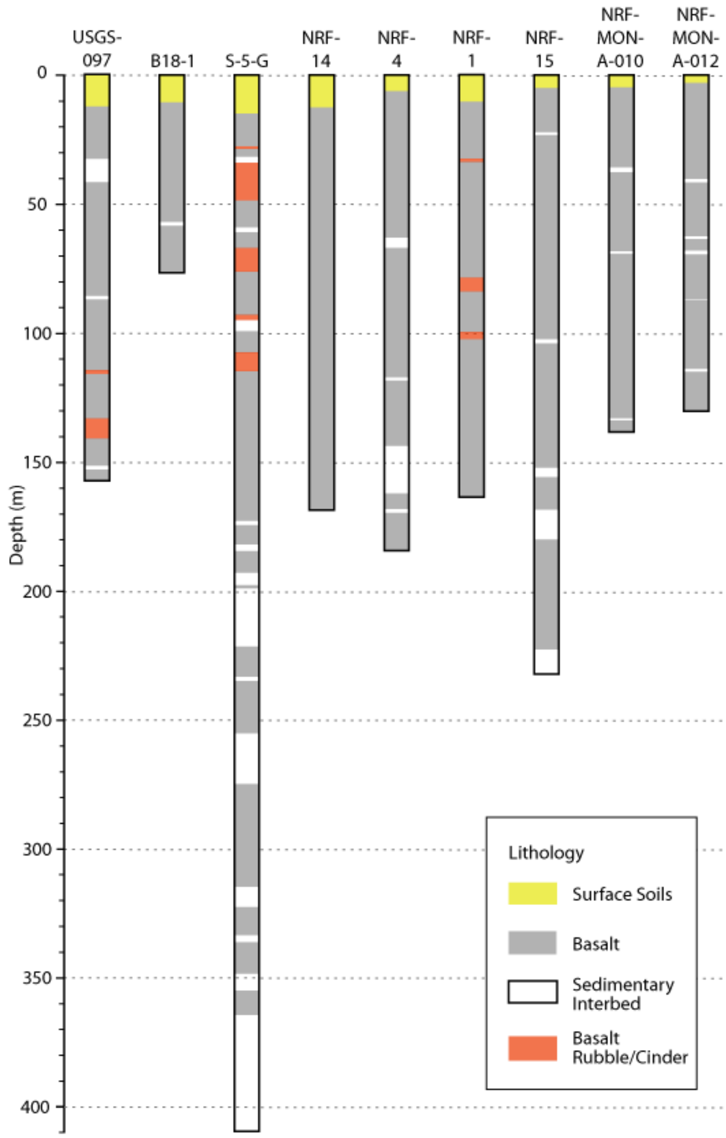

Figure 7-21. Lithology of boreholes at and near NRF (see Figure 7-20 for map locations).

profile was constructed following the approach in Payne (2007), which assumes that lithology and its depth can be used as surrogates to assess Vs of sediments and basalt layers. As per Payne (2007), Vs-depth relationships as a function of depth were developed for sediments and basalts in the upper 1200 m of INL based on available site-wide data. The Vs-depth relationships were used to assign Vs to each sediment or basalt layer at their respective depths for the S-5-G borehole.

Figure 7-22 shows the comparison of the 2015 and 1996 NRF Vs profiles in the upper 450 m. At the time of the 1996 INL PSHA, lithologies from two boreholes, B18-1 and NRF-1 (alias STR-1), were used to construct the lithologic profile to a depth of 163 m for NRF. Lithology from the INEL-1 borehole was appended from 163 to 3000 m since it is located <3 km to the south of NRF (Payne, 2007). The upper 175 m of the 2015 NRF Vs profile shows fewer and thinner sedimentary interbeds than the 1996 NRF Vs profile. From 175 to 360 m, the 2015 NRF Vs profile has more thinner interbeds than 1996 Vs profile, but both profiles have a thick interbed from 360 to 408 m. Below 408 m, the 2015 NRF Vs profile matches INEL-1 Vs profile since the INEL-1 lithology is appended to 3000 m.

The North Wind Resource Consulting and Rizzo Associates (NWRC-RA, 2015) study provided interval velocity data from 10 borings in the vicinity of the proposed SFHP facility. The measurements were made using downhole geophysical surveys using a P-wave and polarized S-wave surface source. The reported interval velocities were based on the difference in wave travel time from the top and bottom points at specific depth intervals. Figure 7-23 shows the boring locations. The borings penetrate to depths up to approximately 30 m below the top of the basalts. In that study, the basalts are grouped into two primary categories:

- B1 to B3 non-vesicular to highly vesicular and wide to closely spaced fractures
- B4 highly fractured or soil interbeds

NWRC-RA (2015) stated that B4 layers are not laterally continuous and are generally thin within the depth range that they investigated. NWRC-RA (2015) provides interval velocity data that have been screened to remove what they considered unrealistic values. The interval velocity data were presented for three sets of measurements (passes) in each boring. These data are shown on Figure 7-24.

NWRC-RA (2015) provides a single average velocity for the basalts computed from the screened data. However, examination of the data indicate that there is statistically significant trend with depth that is slightly stronger using depth below top of basalt compared to depth below the surface. Using t-tests, the shallow basalt data were divided into three depth ranges, as shown on Figure 7-24, and median (mean log) Vs values computed for each depth interval. Figure 7-25 compares the NWRC-RA (2015) data and fitted model from Figure 7-24 to the shallow portion of the Vs data from ANL-1 (at MFC) that was used to develop the NRF Vs profile shown on Figure 7-22.

Additional Vs data for the shallow basalts at the NRF facility are shown on Figure 7-25. STRATA (2010) provided downhole Vs profiles for six borings at NRF. Paul C. Rizzo and Associates (Rizzo, 2008) provided downhole (DH) and suspension logging (PS) velocity profiles for the ECF facility and Rizzo Associates (1994) provides very limited data for the ECF facility. The locations of these borings are shown of Figure 7-23.

The shallow basalt Vs velocity data shown on Figure 7-25 were used to modify the upper 33 m of the NRF basalt Vs profile shown in Figure 7-22. The model fit to the NWRC-RA (2015) data is used as the best estimate model. As indicated above, NWRC-RA (2015) did not find a continuous interbed layer within the upper 30 m of the site. Review of the logs for other borings in the vicinity of NRF did not indicate the presence of a well-defined interbed layer in this depth range. Therefore, the shallowest interbed layer at a depth of about 50 m below the ground surface shown on Figure 7-22 was removed from the final NRF basalt profile. Evidence for the deeper interbeds indicated in the S-5-G boring log was found in the other borings and these interbeds were retained.

The ANL-1 Vs data show a step up to a higher velocity at a depth of about 35 m below the top of basalt. There is no reason not to expect a similar increase at a similar depth below the NRF site. Therefore, the ANL-1 profile is used as a model for the upper basalts at depths below the site-specific data. The harmonic mean of ANL-1 data in depth range 38 to 184 m is used for the next three basalt layers as it provides a better fit to the shallow ANL-1 data than the Payne (2007) Vs model. A constant value for basalt is used over this depth range rather that individual layers as the data show a reverse gradient. The Payne (2007) model is then used for greater depths as it produces velocities consistent with the ANL-1 data. Figure 7-26 shows the resulting best estimate Vs profile for NRF.

For the NRF site, epistemic uncertainty in Vs was assessed to be ±10 percent in the shallow portion where site-specific measurements were available, and increasing to ±20 percent where the velocities were based on well log material type and velocity associations. For the NRF profile, the velocities below 33 m

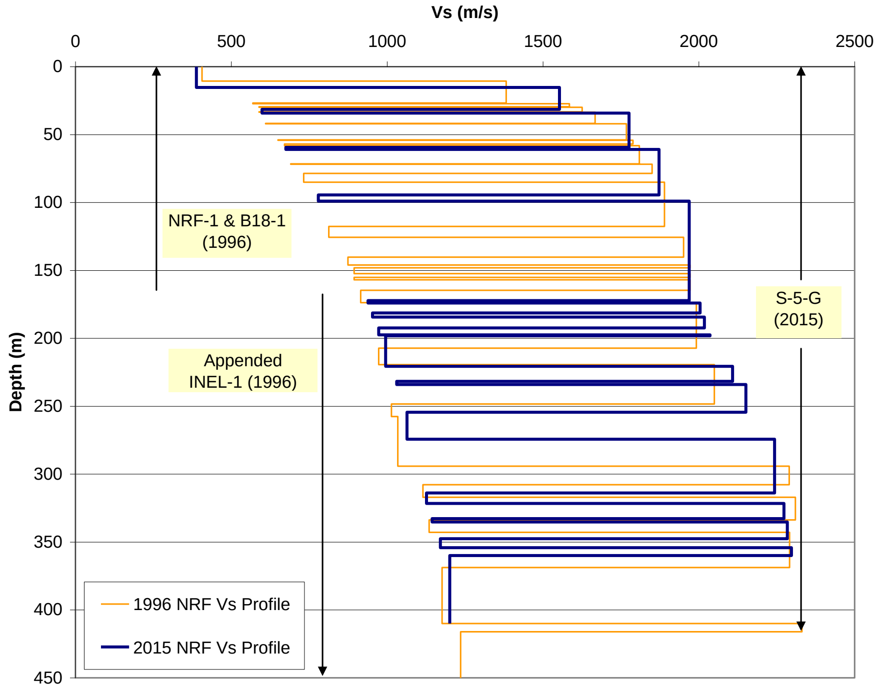

Figure 7-22. Comparison of the 2015 and 1996 NRF Vs profiles as developed using the approach in Payne (2007).

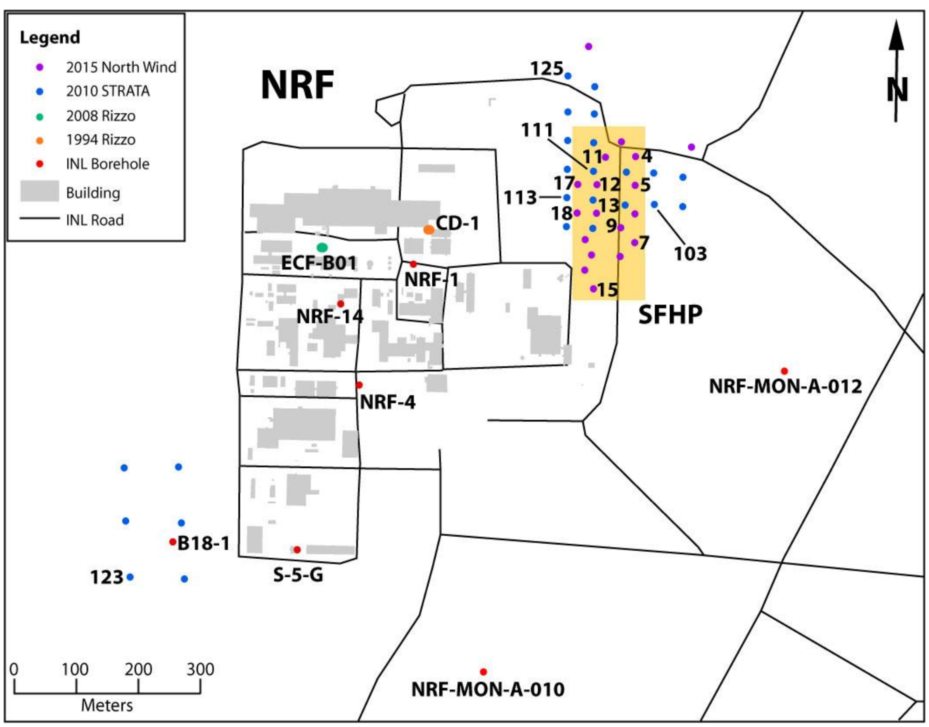

Figure 7-23. Map showing locations of shallow boreholes from the NWRC-RA (2015), STRATA (2010), Rizzo Associates (1994), and Rizzo (2008) studies. The Spent Fuel Handling Project (SFHP) area is shown by the orange box.

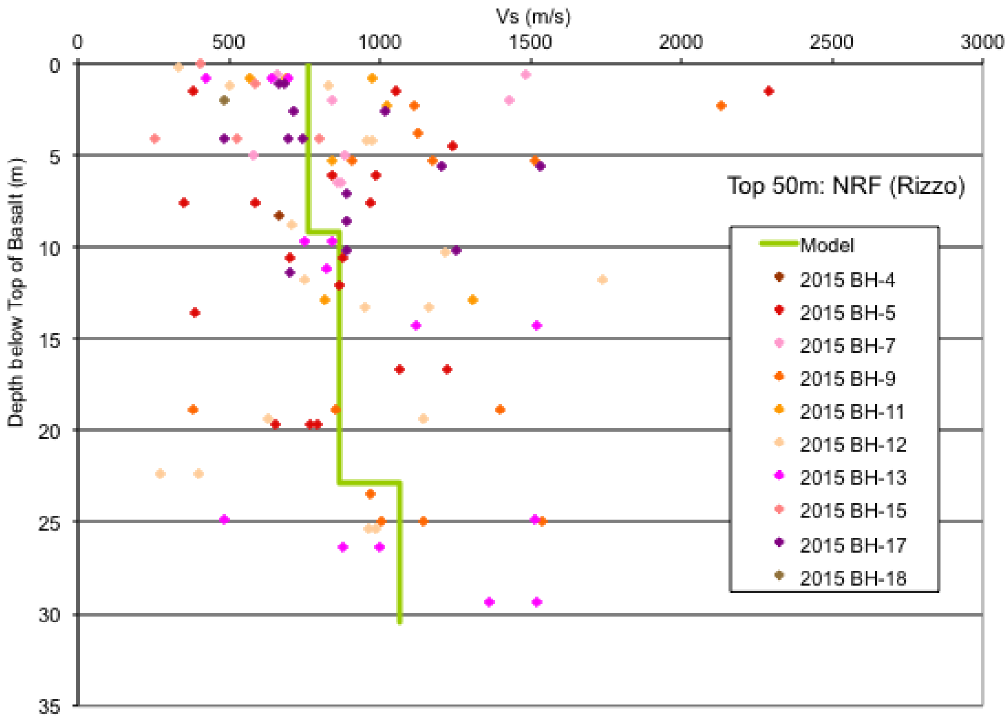

Figure 7-24. Shear wave velocity data from NWRC-RA (2015) and proposed velocity profile.

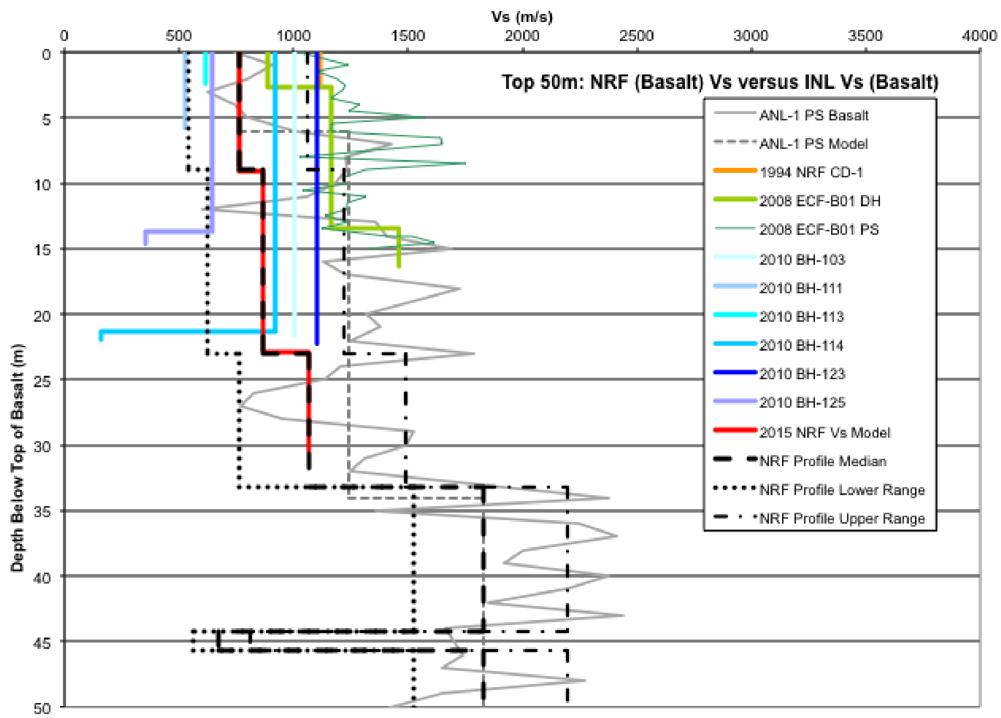

Figure 7-25. Final NRF Vs model (median, lower range, and upper range) compared to measurements in the upper 50 m of basalt.

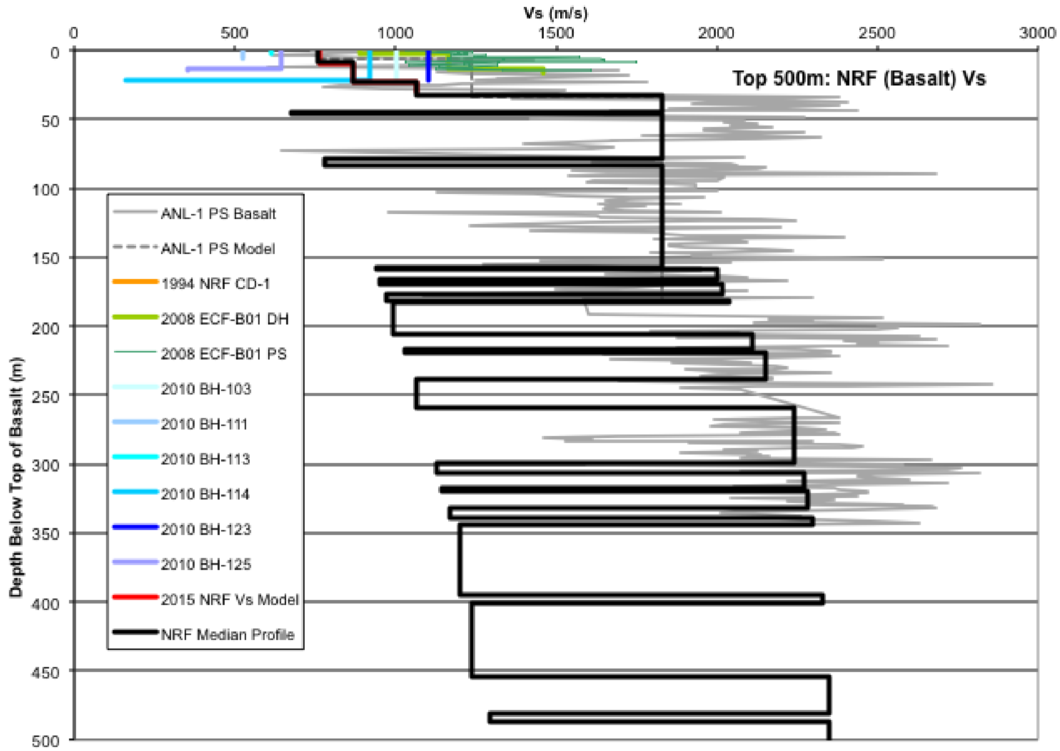

Figure 7-26. Upper 500 m of final NRF Median Vs profile.

are also based the use of lithology and the Payne (2007) model and an epistemic uncertainty ±20 percent is again used. The upper 33 m of the NRF basalt profile is based on site-specific data. However, this data shows a wide range. To encompass the wide variation, the epistemic uncertainty was increased to ±40 percent. Figure 7-25 shows the resulting lower range and upper range profiles. Following the approach used for the MFC profile, the NRF three profiles were assigned weights of 0.4 for the median base case, profile P1, and 0.3 for the lower-range (P2) and upper-range (P3) profiles. The weighting of the three base case profiles thus approximates a normal distribution for the epistemic uncertainty in Vs, with profiles P2 and P3 representing the 10th percentile and 90th percentile, respectively, of that distribution.

7.4.2 SFHP Soil Vs Profile

Two studies were used to assess the Vs soil profile for the SFHP area. NWRC-RA (2015) defines three soil layers for the SFHP site and present interval velocity data computed from down-hole surveys. Table 7-7 summarizes these data. The statistics of the data are provided in two forms. The raw interval data are summarizes in columns 3 and 4 of Table 7-7 and show a large scatter. The addendum to NWRC-RA (2015) indicates that the components of scatter in the raw data includes measurement error, which they attempt to reduce by “stacking” the data, averaging the measurements made for the three passes after removing what they considered to be bad data. The resulting median (mean log) Vs values, listed in column 5 of Table 7-7, differ by less than 5 percent from the median values of raw interval data. Column 6 of Table 7-7 lists the valuesof sigma ln(Vs) for the stacked data from the addendum to NWRC-RA (2015). These values represent the variability among layer averages for the 8 to 10 borings.

The STRATA (2010) report contains downhole Vs values for 8 borings in the SFHP area. The statistics of those data are given in Table 7-8. NWRC-RA (2015) did not use the STRATA (2010) downhole Vs measurements in developing their velocity model for the SFHP site soils, concluding that the differences in average layer Vs in nearby borings between the two studies was "too high". However, the differences in the median Vs values between the two profiles is not that large. For the shallowest soil layer, the difference is 20%, but for the two deeper layers the differences are only 6%. Given the scatter in the measurements within each dataset, two sets are considered generally consistent, and were combined. Table 7-9 lists the combined statistics, taking about the number of borings available for each study.

Epistemic uncertainty in the median soil Vs values was assessed using the statistics of layer velocities. The combined statistics in Table 7-9 indicate a value of sigma ln(Vs) of about 0.2. This value is dominated by the much larger scatter in the NWRC-RA (2015) data compared to the STRATA (2010) data. It us likely that the even the stacked NWRC-RA (2015) measurements still contain a degree of measurement error. Therefore, a reduced standard deviation of 0.15 was used to assess the epistemic uncertainty in the median velocity profile for the SFHRP soils. This value is intermediate between the value of 0.1 computed for the STRATA (2010) data and the value of 0.2 computed for the combined data. Following the guidance in EPRI (2013), the epistemic uncertainty in the median soil shear wave velocities was computed using the 10^{th} and 90^{th} percentiles of a log normal distribution. The velocity scale factor is exp(1.28x0.15) = 1.21. The three profiles (best estimate, lower range, upper range) are weighed 0.4, 0.3, 0.3, respectively, consistent with the basalt profiles.

Table 7-7. SFHP soil Vs statistics from NWRC-RA (2015).

		Interval Data		Stacked Interval Data			
Layer	Depth Range	Vs (fps)	Sigma ln(Vs)	Vs Stacked (fps)	Sigma ln(Vs)	Unit Weight (pcf)	Number of Borings
Surface	0 to 6 ft	440	0.39	437	0.25	110	10
Gravel Alluvium	6 to 24 ft	1155	0.37	1106	0.24	134	10
Clay Loess	24 to 36 ft	1399	0.66	1354	0.24	122	8

Table 7-8. SFHP soil Vs statistics from STRATA (2010).

Layer	Depth Range	Vs (fps)	Sigma ln(Vs)	Number of Borings
Surface	0 to 5 ft	553	0.15	8
Gravel Alluvium	5 to 26 ft	1171	0.11	8
Clay Loess	26 ft to basalt	1289	0.11	5

Table 7-9. Combined Vs statistics for the SFHP soil layers.

Layer	Depth Range	Vs (fps)	Sigma ln(Vs)	Number of Borings
Surface	0 to 6 ft	485	0.24	18
Gravel Alluvium	6 to 25 ft	1134	0.19	18
Clay Loess	25 ft to basalt	1329	0.20	13

7.5 Site Kappa, *Q*, and Soil Dynamic Properties for NRF and SFHP

Section 7.2 presents the general methodology used to assess kappa and Q at the INL sites. This section summarizes the results for the NRF site and presents the available data for shear modulus and damping relationships for the site soils.

7.5.1 Kappa for NRF Site

Twenty-three recording at the broadband station NVRF were used to provide estimates of kappa for NRF. The recordings reflect a range in magnitude from about **M** 3.0 to **M** 4.9 and hypocentral distances of about 140 km to 170 km. Station NVRF is located on basaltapproximately 1.4 km west of the SFHP site. As shown in Table 7-6 the best-estimate kappa value was 0.037s. To characterize uncertainty in the base-case estimate of kappa, it was assumed the range in mean kappa developed for area MFC reflected an appropriate range for area NRF, a factor of 1.5 ($\sigma_\mu \approx 0.4$) about the best-estimate value. Characterizing the uncertainty in kappa with 10th percentile median, and 90th percentile estimates, the estimates are 0.022s, 0.037s, and 0.062s. The appropriateness of the range in kappa, 0.022s to 0.062s was confirmed by comparing response spectral shapes (5% damping) computed from the recordings with model shapes using the two kappa estimates, 0.022 and 0.062s, as illustrated in Figures 7-27 and 7-28. Figure 7-27 shows spectral shapes, average horizontal components over seven earthquakes at similar hypocentral distances (≈ 170 km). For these recordings the frequency range of the peak is representative of a kappa close to the upper-range value of 0.062s. Alternatively, Figure 7-28 illustrates average horizontal component spectral shapes computed for a single earthquake, **M** 4.4 at a hypocentral distance of 155 km. For this recording the frequency range of the peak is representative of a kappa close to the lower-range value of 0.022s. Due to the record-to-record and frequency-to-frequency variability, the data could not support a narrower range in kappa.

The kappa assessments for the NVRF site reported in Table 7-6 were based on site amplification functions developed using the 1996 NRF velocity profile shown in Figure 7-22. Subsequent calculations performed using the updated profile for SFHP shown in Figure 7-26 produce a kappa value approximately 14 percent higher. Given the small difference in the values compared to the broad uncertainty range, the kappa values described above were used to develop the relative amplification functions for the SFHP site.

7.5.2 Dynamic Properties of SFHP Soils

NWRC-RA (2015) developed site-specific dynamic property curves (G/Gmax and damping) for the SFHRP site. Laboratory dynamic test data from samples of the gravel alluvium, clay loess, and shallow basalts were used to develop G/Gmax and damping curves based on the formulation of Darendeli (2001). In addition, NWRC-RA (2015) selected a published relationship for the shallow soil layer. Figures 7-29, 7-30, and 7-31 compare the site-specific G/Gmax and damping relationships recommended by NWRC-RA (2015) for the shallow soils, gravel alluvium, and clay loess, respectively, to the generic models recommended by EPRI (2013) and those used for analysis of the FMF site (Section 7.3.5).

The published relationship for the shallow soils selected by NWRC-RA (2015) are similar to the EPRI (1993) relationships. The site-specific relationships developed for the gravel alluvium and clay loess have similar or greater non-linear behavior to the generic EPRI (1993) and Peninsular Range G/Gmax curves, but exhibit significantly lower damping at higher strains. The test data used to develop the site-specific relationships for the gravel alluvium and clay loess were limited to shear strains less that 0.1 percent and the damping values at higher strains represent extrapolation of the fitted models. To test the sensitivity of the site amplifications for the SFHP soils, two sets of analyses were performed. One set using the site-specific G/Gmax and damping relationships presented by NWRC-RA (2015). A second set of analyses was performed using the EPRI (1993) set and Peninsular Range set (Silva et al., 1996) with equal weights.

NWRC-RA (2015) also developed G/Gmax and damping relationships from tests performed on core samples of the near surface basalts. The fitted relationships are shown in Figure 7-32. These were used to test the sensitivity of site amplification to the incorporation of non-linear behavior in the near surface basalts.

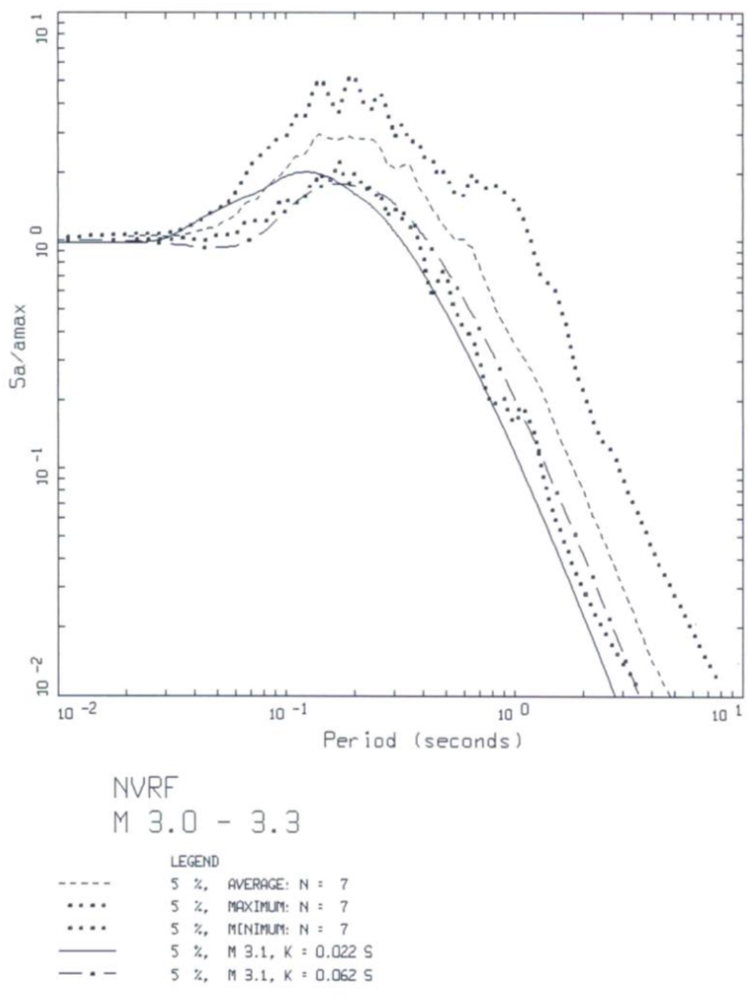

Figure 7-27. Response spectra shapes (5% damping) computed with seven earthquakes (**M** 3.0 to **M** 3.3) at site NVRF compared to model shapes with lower-range and upper-range kappa estimates of 0.022s and 0.062s respectively.

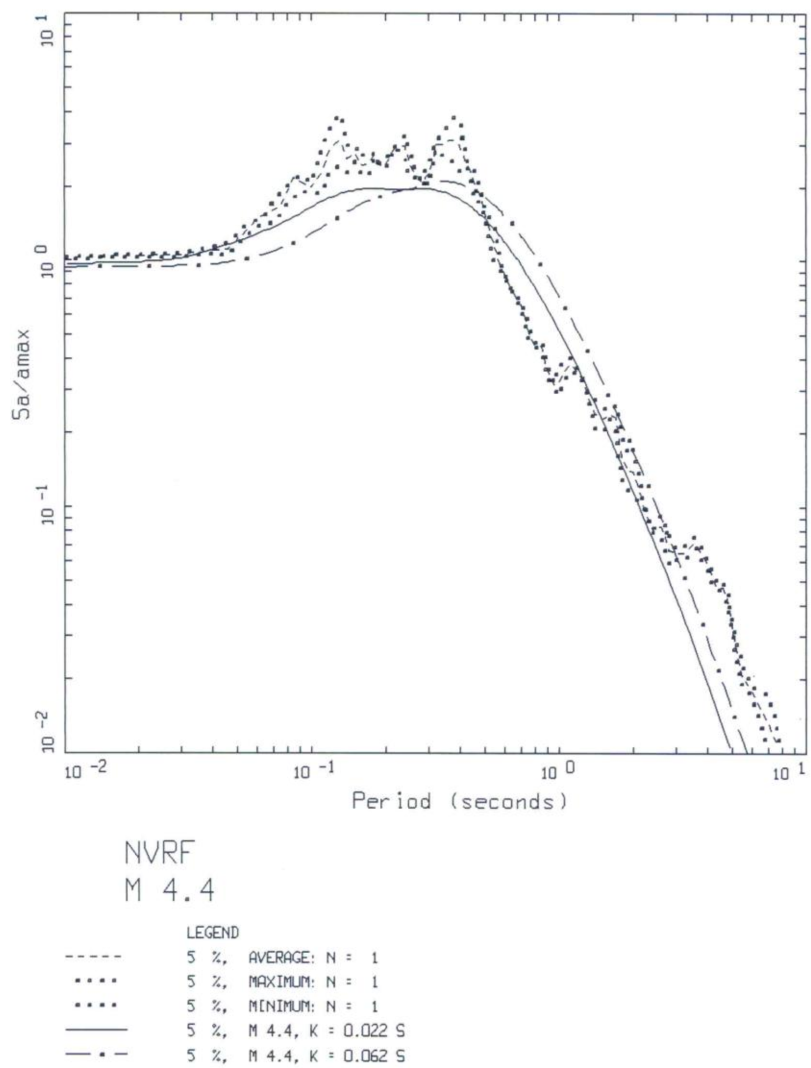

Figure 7-28. Response spectra shapes (5% damping) computed with one earthquake (**M** 4.4) at site NVRF compared to model shapes with lower-range and upper-range kappa estimates of 0.022s and 0.062s respectively.

a)

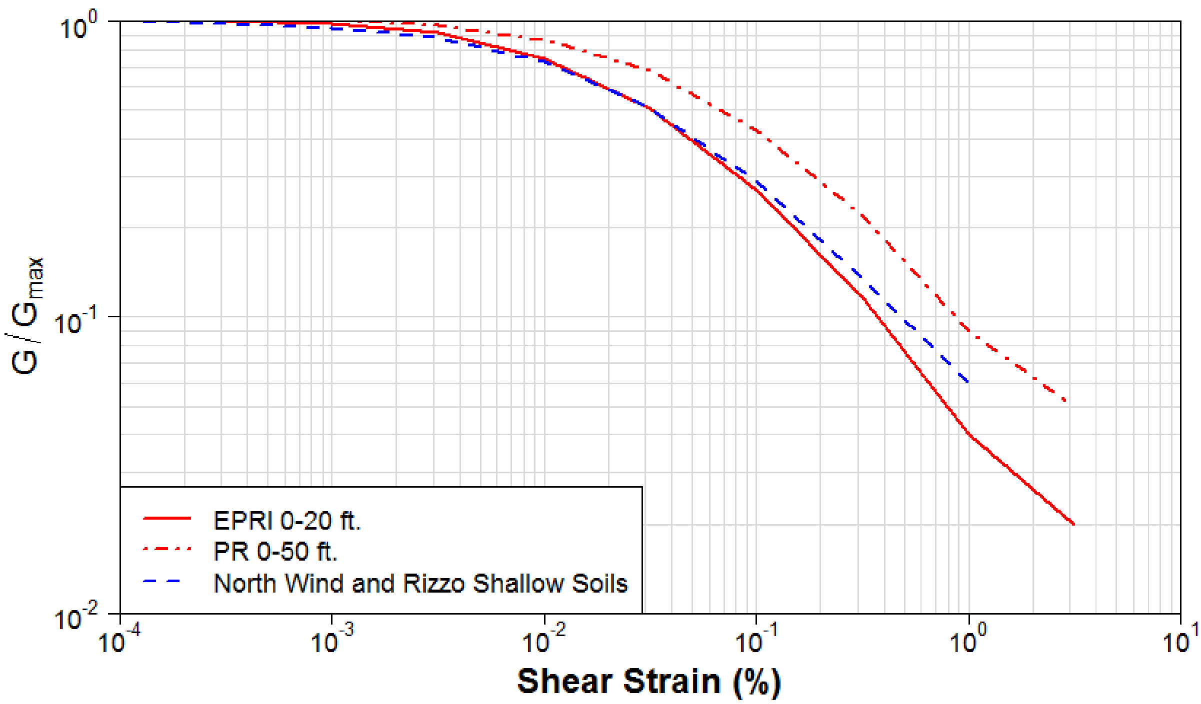

b)

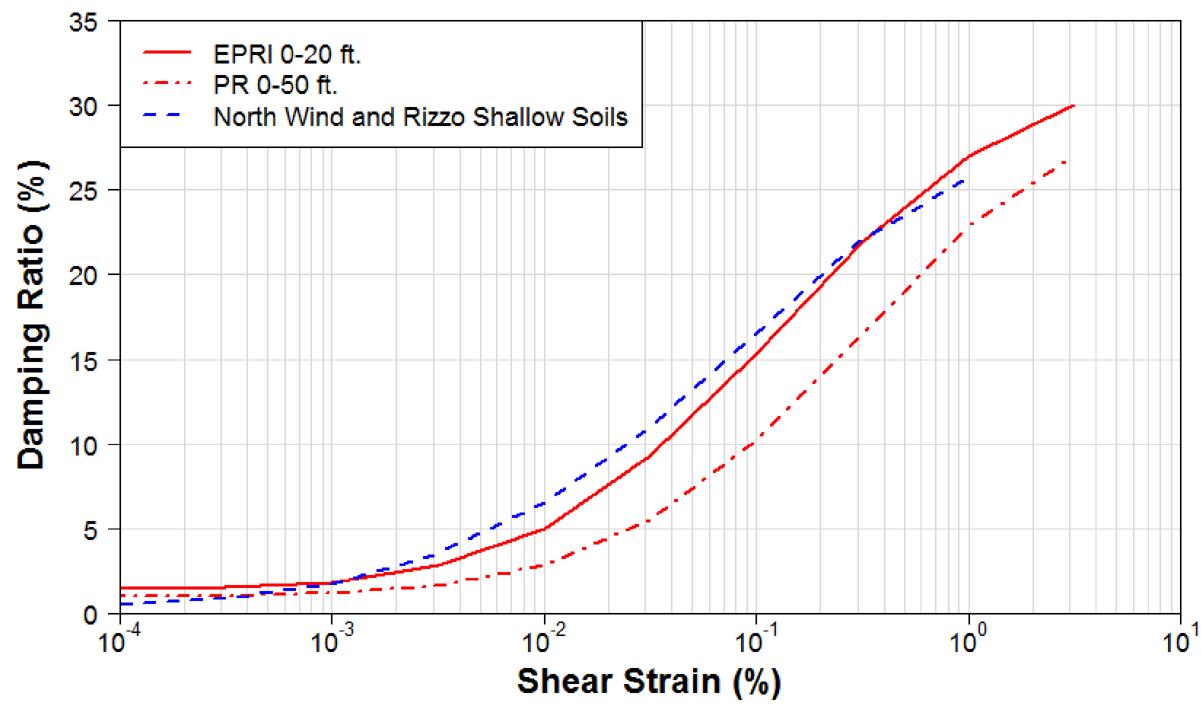

Figure 7-29. a) G/Gmax and b) damping relationships for shallow soils at SFHP.

a)

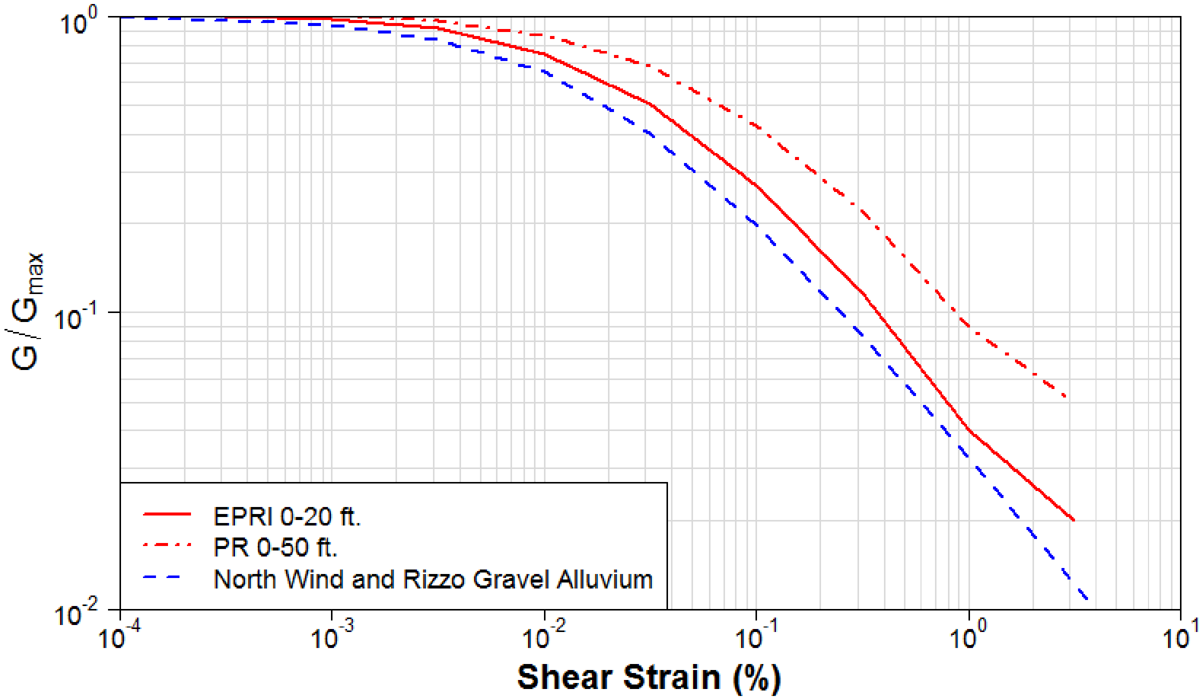

b)

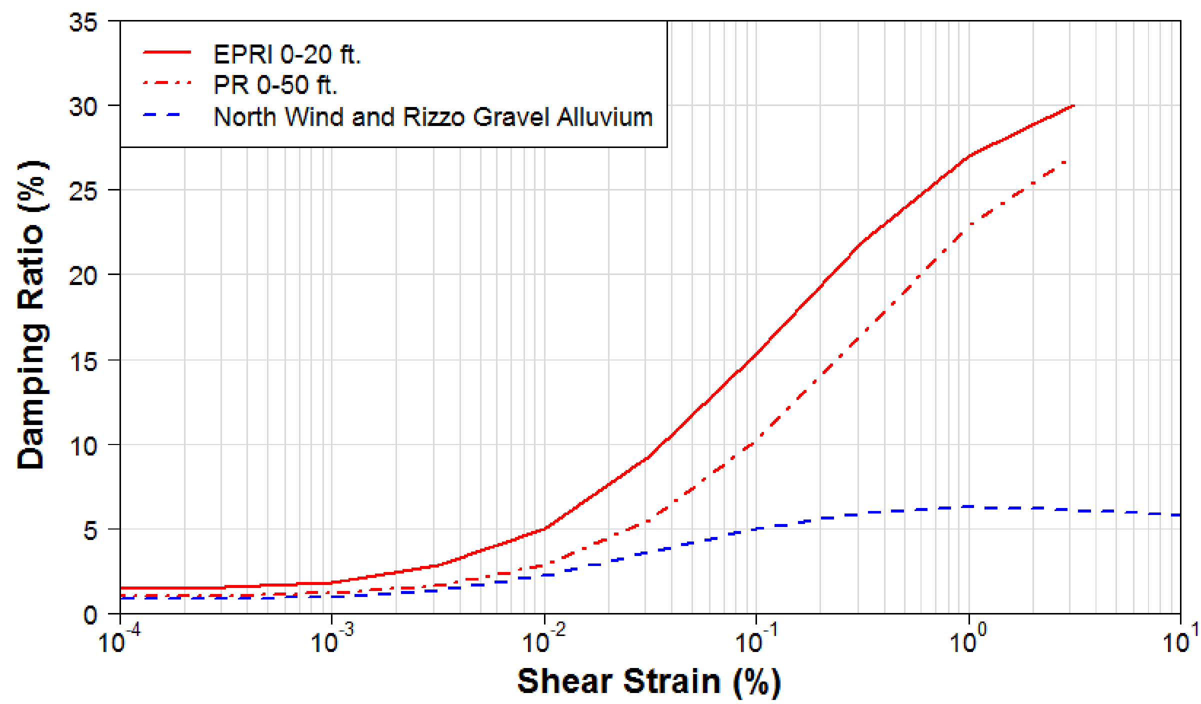

Figure 7-30. a) G/Gmax and b) damping relationships for gravel alluvium at SFHP.

a)

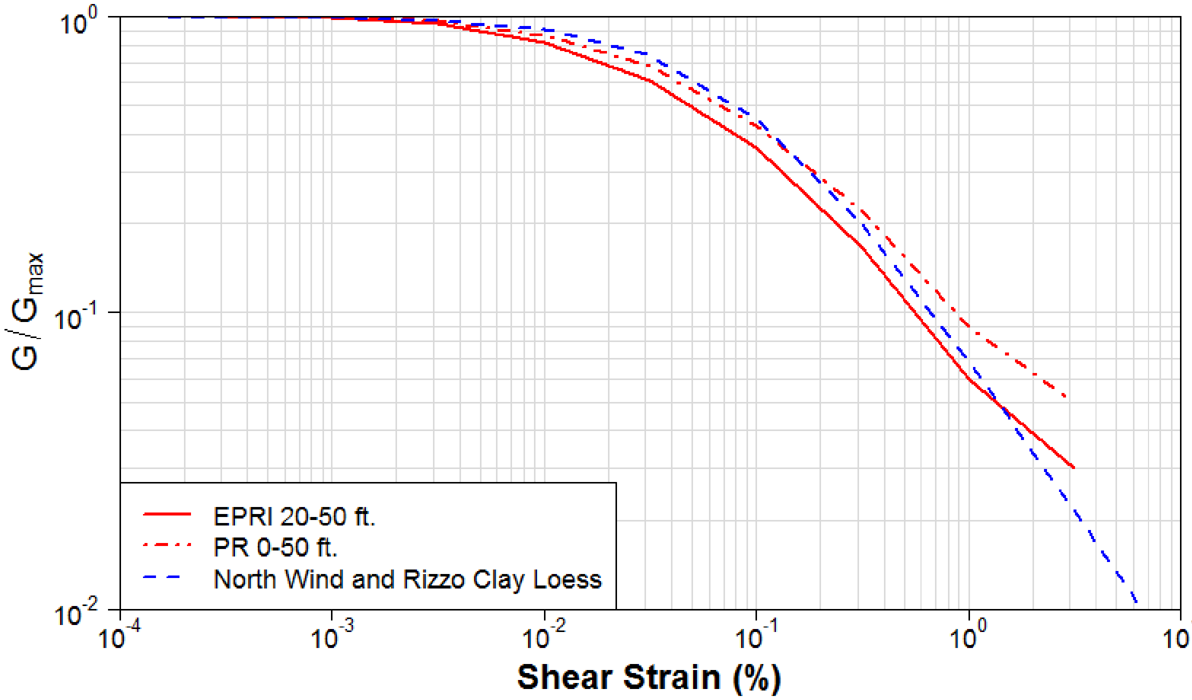

b)

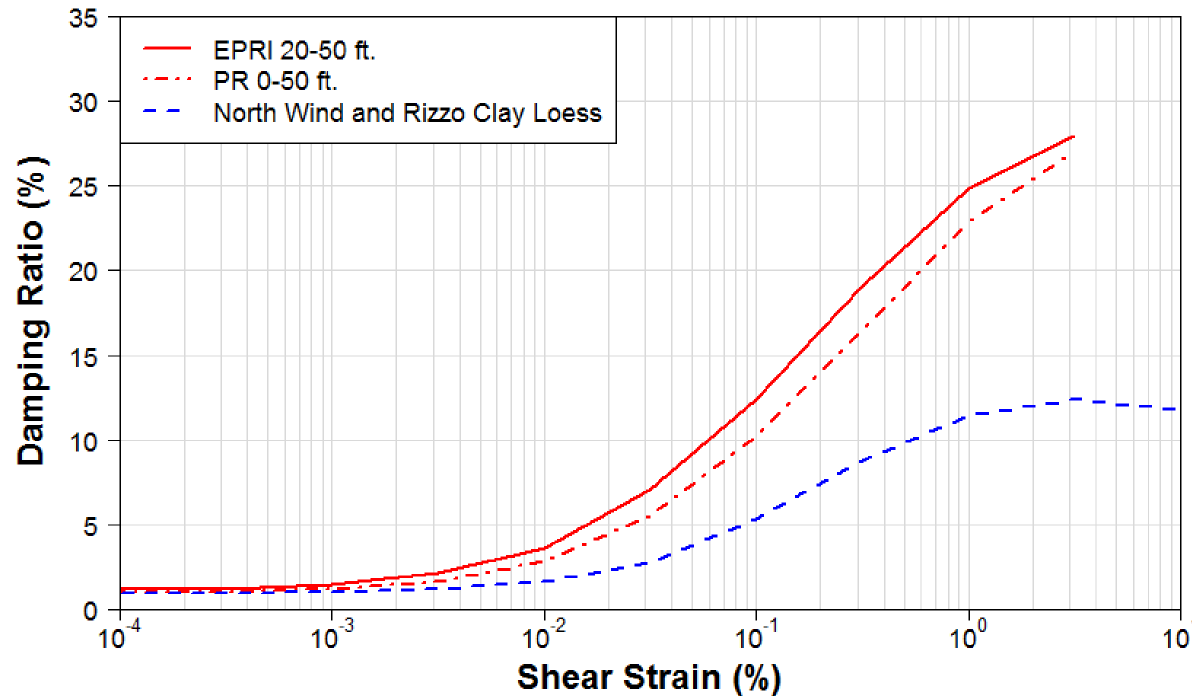

Figure 7-31. a) G/Gmax and b) damping relationships for clay loess at SFHP.

a)

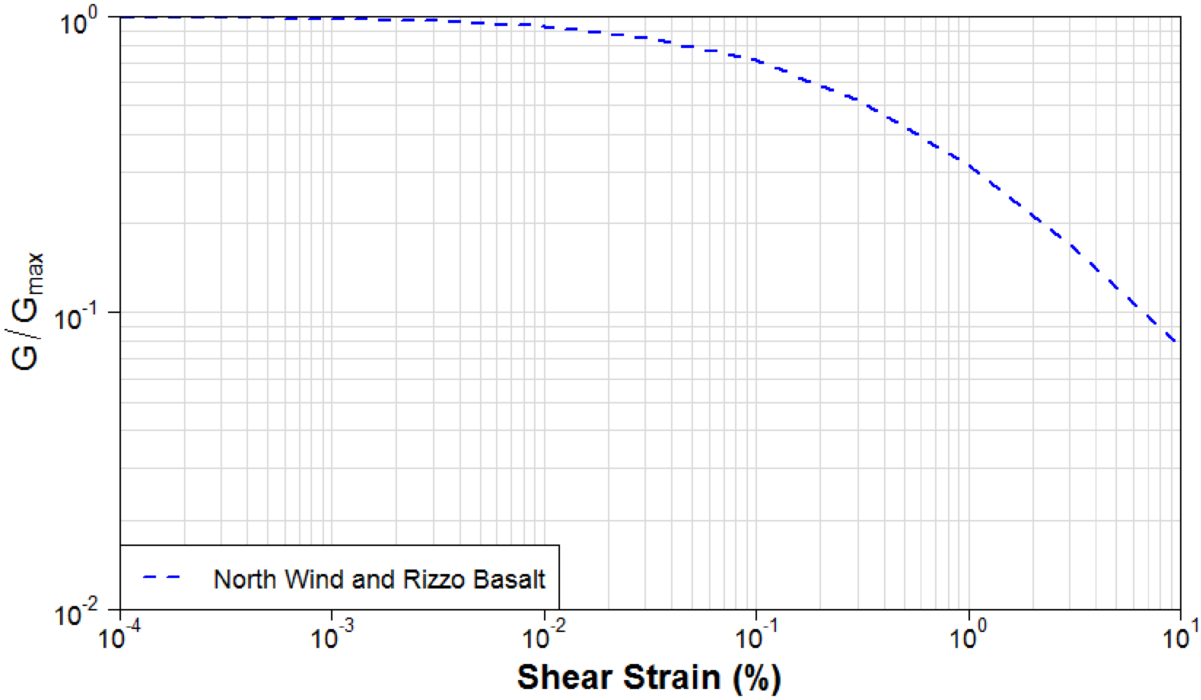

b)

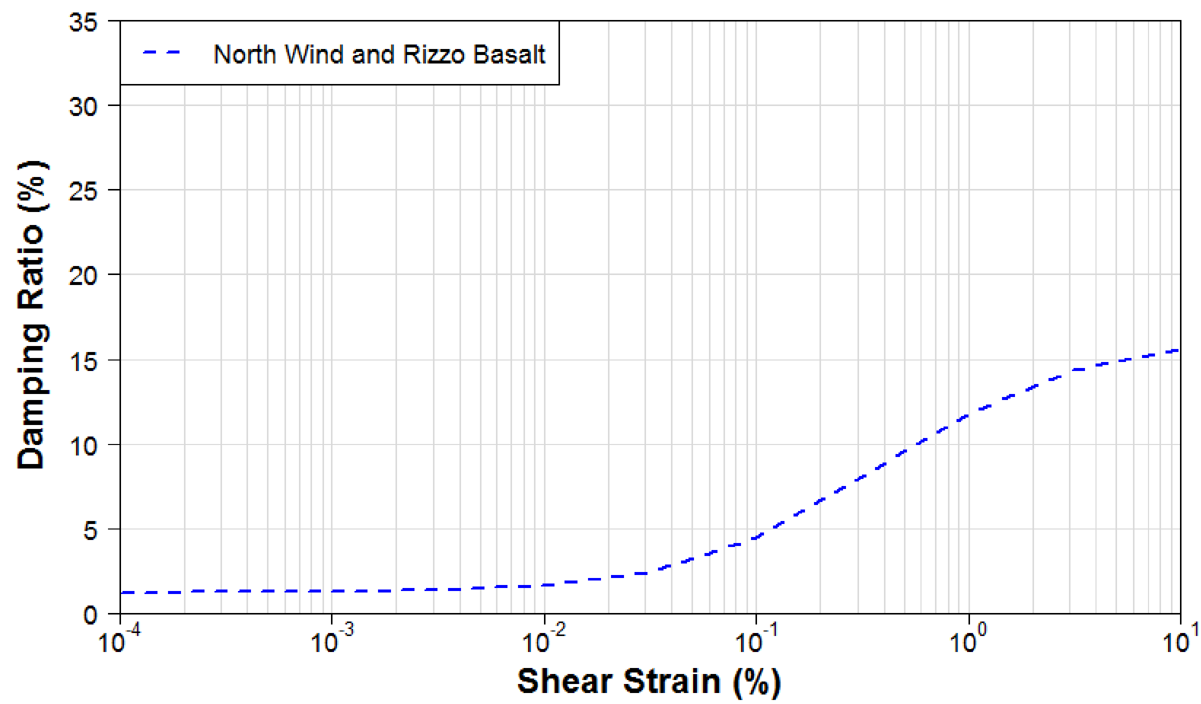

Figure 7-32. a) G/Gmax and b) damping relationships for near-surface basalt at SFHP.

7.6 Shear Wave Velocity Profiles for ATR Rock and Soil Sites

Characterization of the shear wave velocity of the shallow crust was performed to develop the appropriate adjustments of the GMPEs for application in hazard calculations for ATR rock and soil sites. The Vs profile for ATR originally developed in the 1996 INL PSHA was used in this analysis and updated based on new data and re-evaluations of subsurface data. For TRA-670, the ATR Vs profile has ground surface at the top of rock since the facility foundation is supported directly on basalt bedrock. For ATR support facilities (TRA-674, TRA-770, TRA-781, TRA-688, TRA-786, and TRA-650) and firewater piping areas, site-specific ATR Vs profiles were developed which each have ground surface at the top of soil (Section 1.1.4).

7.6.1 ATR Vs Profile

New lithologic data from recently drilled boreholes near ATR were compiled and reported in INL (2011), which correlates sedimentary interbeds in the top 100 m beneath ATR, was evaluated. Additionally, shear wave velocities measured in seven boreholes at ATR were evaluated along with other measurements to assess the ATR Vs profile. The results of the lithologic evaluations supported the use of the ATR Vs profile and an alternative Vs profile that has modifications to the top most sedimentary interbed. Minor modifications were made to the Vs values in the upper 50 m of the profile.

7.6.1.1 Lithology of the ATR Profile

ATR is located west of the Big Lost River within its flood plain (Figure 7-33). As a result, four deep boreholes (TRA-5, TRA-04, Site-19, and USGS-136) at and within 1 km of ATR show sedimentary interbeds dispersed throughout basalt layers to depths of 300 m (Figure 7-34). The upper 100 m of these four boreholes have the majority of sedimentary interbeds. The Middle-1823 borehole, ~2 km south of ATR (Figure 7-33), has sedimentary interbeds that may be correlative with the boreholes within the ATR complex (Figure 7-34). For example, Middle-1823 has a 73 m thick sedimentary interbed between 398 and 475 m depth and this may be correlative with the sedimentary interbed at the base of TRA-5 starting at 365 m depth (Helm-Clark et al., 2005). The sedimentary interbeds are composed primarily of clay, silt, and sand with an occasional gravel or cinder interbed (INL, 2011).

Although additional boreholes have been drilled near ATR (e.g., Middle-1823), the lithology in these boreholes is generally consistent with the lithology in TRA-5, which was used to develop the Vs profile (Payne, 2007). The Vs profile was developed by appending the lithology in INEL-1 to the base of the lithology in TRA-5 at 388 m. TRA-5 has a sedimentary interbed from 365 to 388 m. INEL-1 has a 41 m thick sedimentary interbed from 368 to 409 m. Appending the INEL-1 lithology to the base of TRA-5, results in a 44 m thick interbed from 365 to 409 m in the ATR Vs profile. A sedimentary interbed thickness of 44 m in the ATR Vs profile is consistent with the thicker interbed of 73 m at this depth observed in Middle-1823 (completed in 2003), although it could be thicker.

INL (2011) presents correlations of sedimentary interbeds beneath ATR and beneath the proposed Remote-Handled Low-Level Waste (RHLLW) site which is ~1 km south of ATR (Figure 7-33). An analysis was performed to identify laterally continuous interbeds for predicting advective-dispersive transport and geochemical transformation in the vadose zone and aquifer geostratigraphy beneath the RHLLW. The analysis involved compilation of borehole lithologies and identifying sedimentary units that could be positively correlated over distances spanning at least 20,234 m^2 (5 acres). Geostatistical analyses were used to assess average elevation to the top of the sedimentary unit, depth, and thickness. Kriging was also used to predict the extent of sedimentary units in the area of the proposed RHLLW. The analysis resulted in identification of eight relatively continuous sedimentary units in the top 100 m that could be correlated between the ATR complex and the RHLLW.

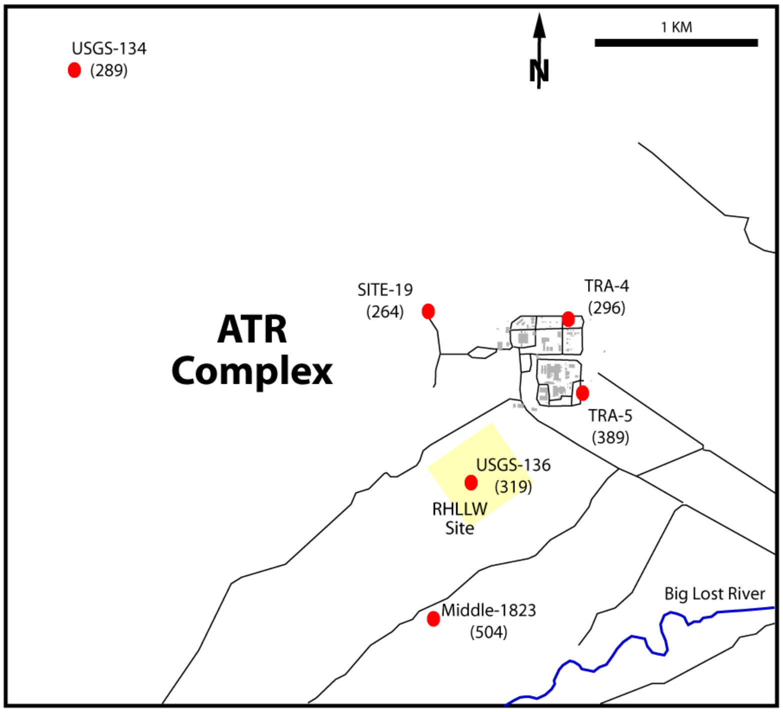

Figure 7-33. Map shows location of boreholes with lithology (shown in Figure 7-34) in the vicinity of ATR Complex and Big Lost River. Bottom-hole depths in meters are listed in parentheses. Yellow box shows the location of the proposed Remote-Handled Low-Level Waste (RHLLW) site.

The depths of the sedimentary interbeds in the boreholes at the ATR Complex and ATR Vs profile were evaluated against the geostatistical results of INL (2011). Seven of the eight sedimentary units identified by INL (2011) in the upper 100 m are observed in two or more of the boreholes in the northern part of ATR and are included in the ATR Vs profile. The first thick interbed represented by a low Vs layer layer starting at a depth of about 40 m is not always present in the boreholes, although the borehole distribution is sparse and some are shallow, <45 m (Figure 7-35). To account for the uncertainty in occurrence of this interbed, two base case profiles were developed from the final ATR Vs model. The median base case P1 includes the low Vs for the first thick interbed (54-68 m) whereas median base case P4 omits the interbed and includes higher Vs for basalt at these same depths. Figure 7-36 shows the upper 200 m of the smoothed velocity profiles for these two base cases.

7.6.1.2 Shear Wave Velocities of the ATR Profile

The shallow basalt Vs velocity data from seven boreholes at ATR were used to adjust the first basalt Vs at 15 m of the ATR Vs profile. Figure 7-37a shows that the measured basalt Vs from 6 to 20 m are generally lower that the Vs of the ATR profile for this depth range. The first basalt layer Vs was adjusted to the average value of the basalt Vs for the seven boreholes. The Vs adjustment was also applied to the Vs for median base cases P1 and P4.

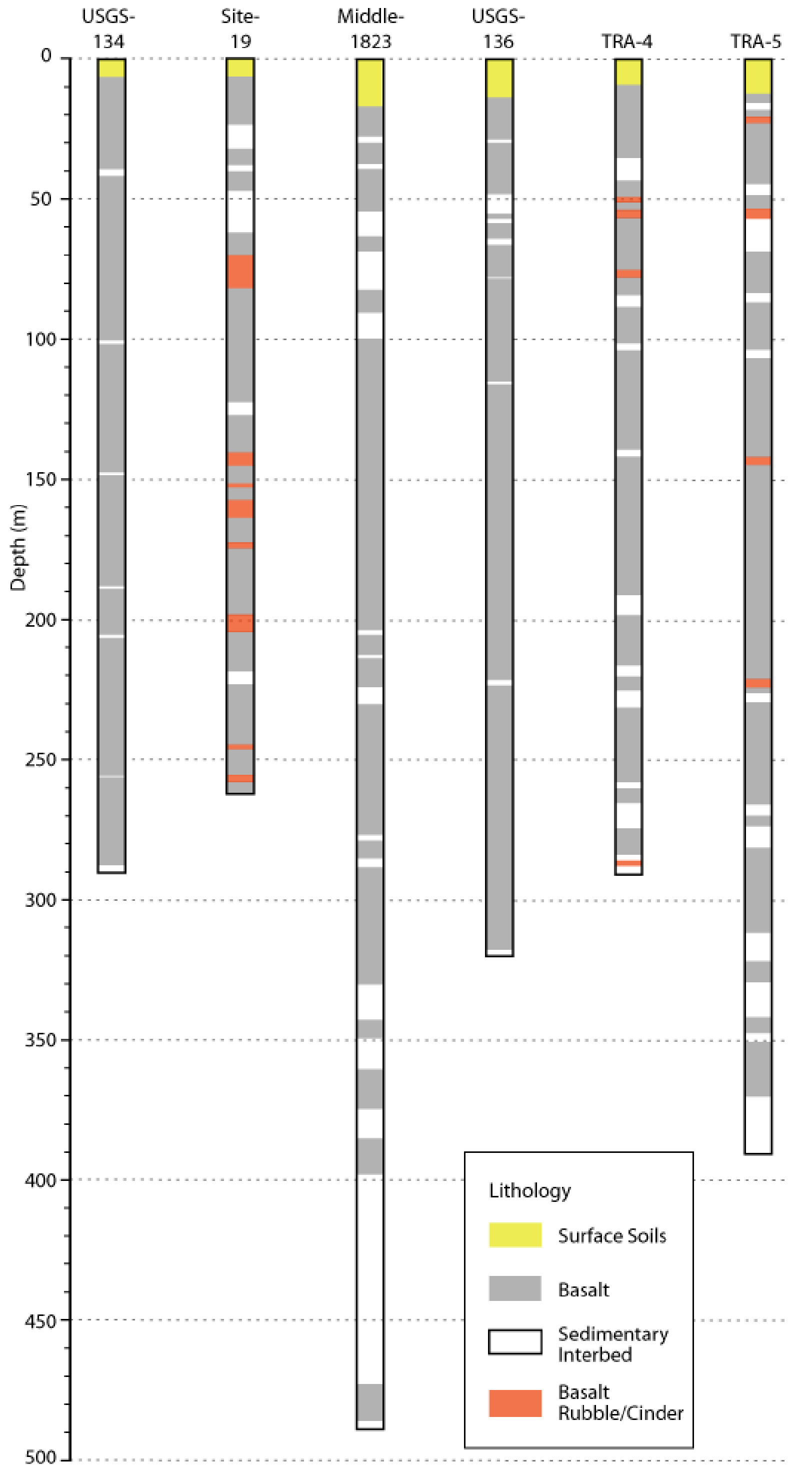

Figure 7-34. Lithology of boreholes at and near ATR (see Figure 7-34 for locations).

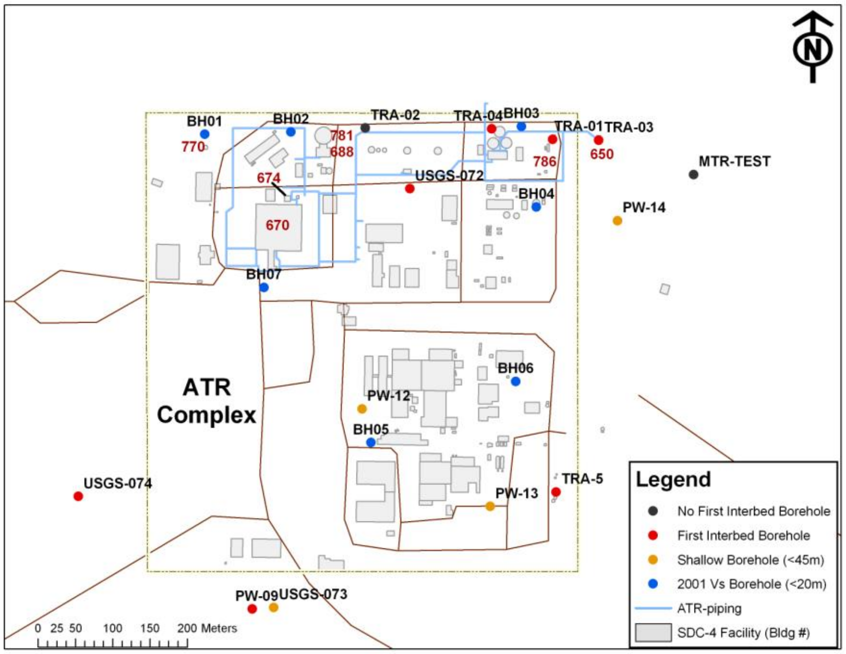

Figure 7-35. Map shows the locations of SDC-4 buildings and firewater piping relative to boreholes with and without the first interbed, and 2001 Vs boreholes. TRA-5 was used to develop the ATR Vs profile.

Figure 7-36. Plot shows the alternative sets of smoothed median base case Vs profiles with lower and upper range cases for the case with the first thick interbed (P1, P2, and P3) and the case where the first interbed is not included (P4, P5, P6).

(a)

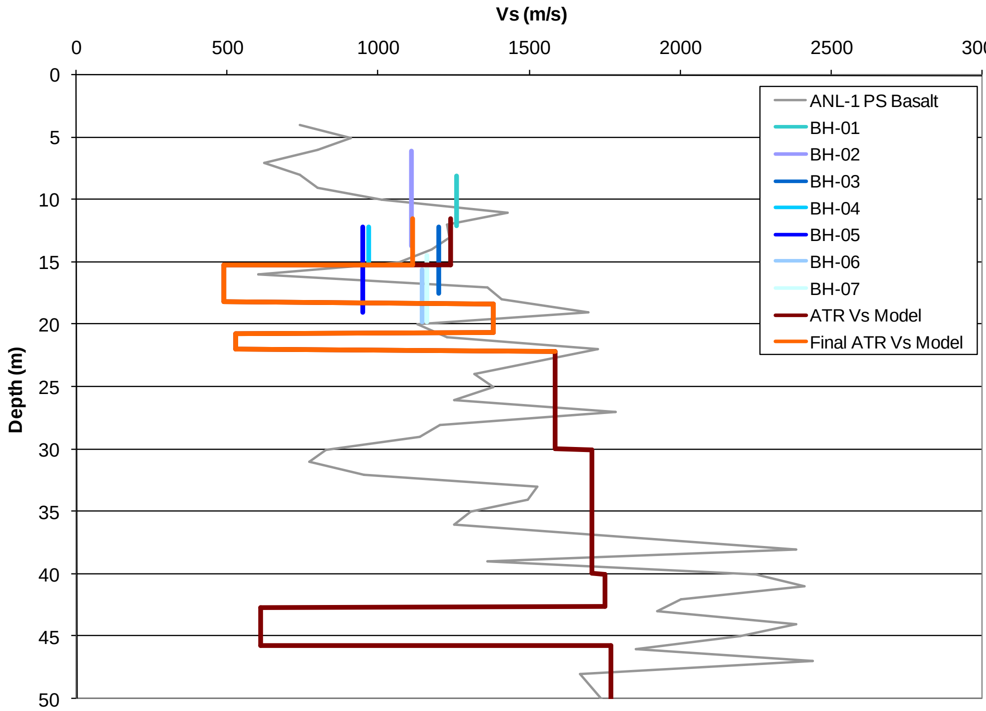

(b)

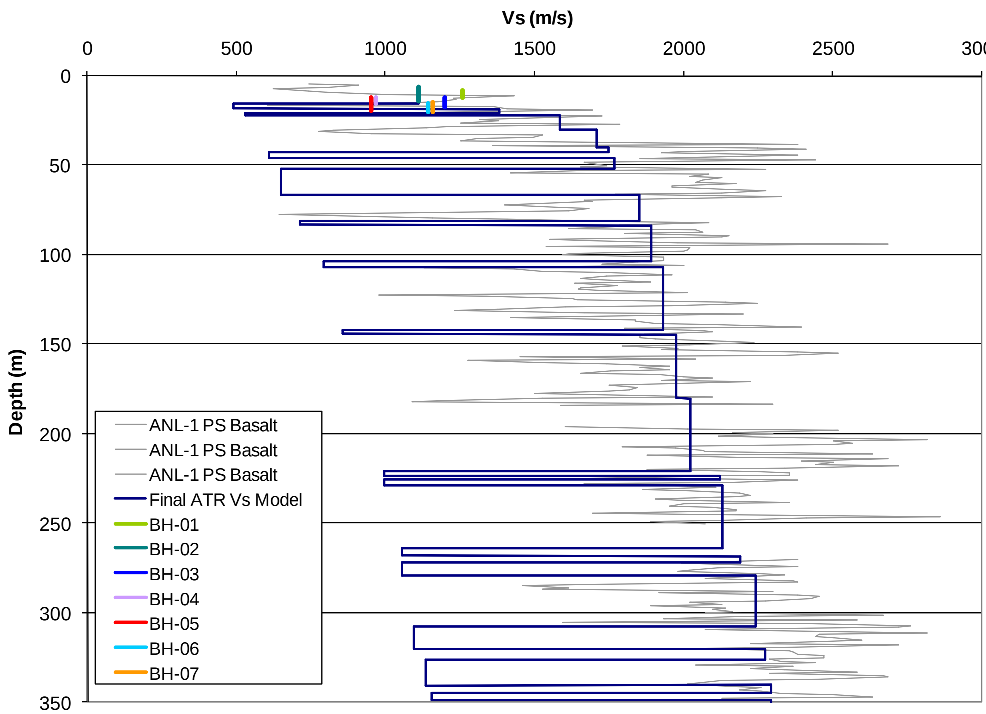

Figure 7-37. Plot of final ATR Vs model compared with the: a) Vs data in the seven ATR boreholes (Redpath Geophysical, Inc., 2001); and b) ANL-1 basalt Vs (Agbabian Associates, Inc., 1997).

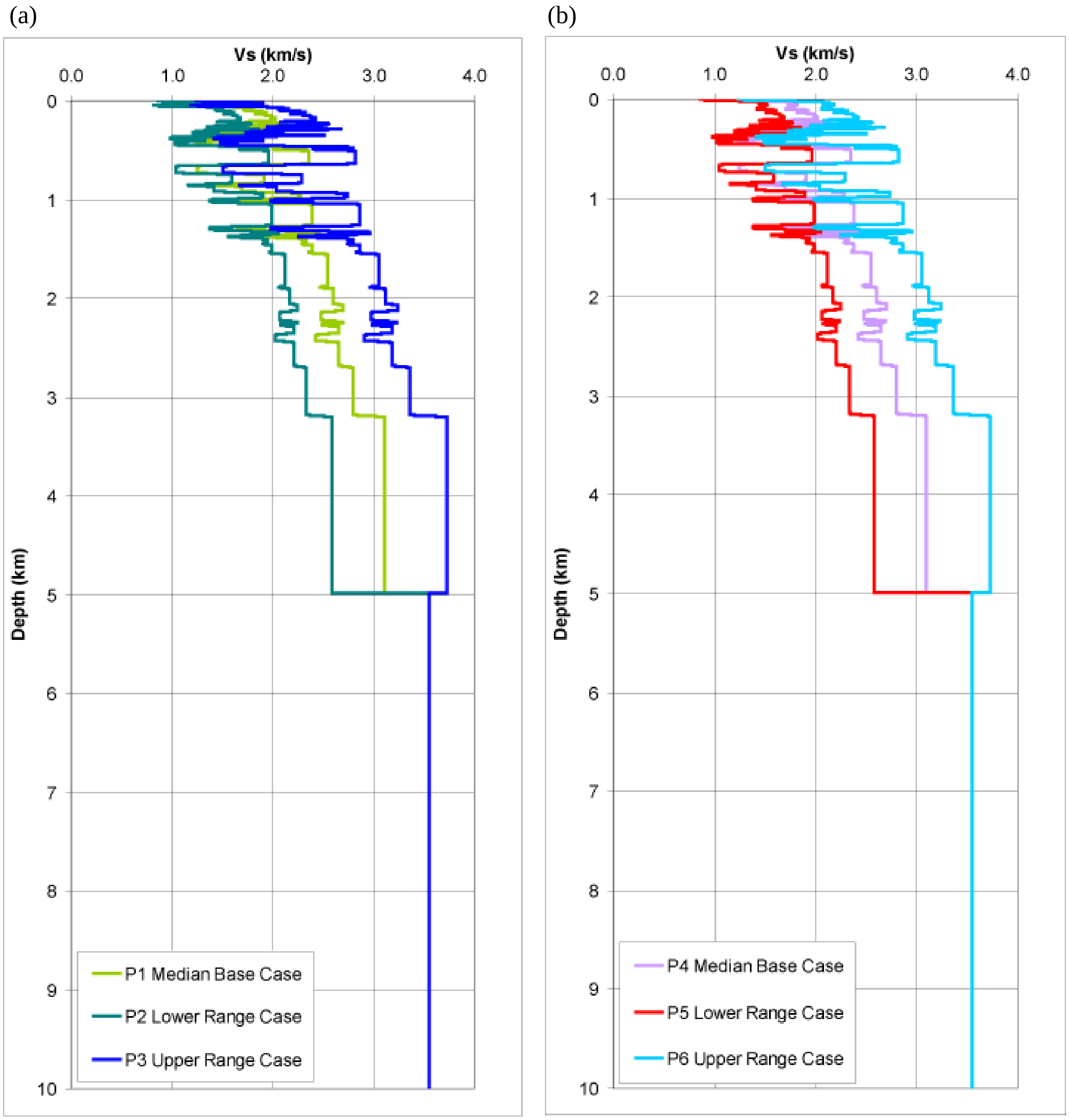

Figure 7-38. Plots show the median base case and lower and upper range cases for the ATR Vs profile: a) includes the first thick interbed; and b) omits the first thick interbed.

The ANL-1 Vs data compare generally well with the final ATR Vs profile from 20 to 350 m with the exception of a step to higher basalt velocity and reverse velocity gradient from 35 to 100 m (Figure 7-37b). At the location of the reverse velocity gradient in the ANL-1 basalt Vs, the final ATR Vs profile has a sedimentary interbed. Thus no changes were necessary to the final ATR Vs model below 20 m and the Vs from 20 to 350 m are consistent with the Payne (2007) model. The upper 200 m of these profiles are also shown in Figure 7-36.

For ATR, epistemic uncertainty in Vs was assessed to be ±20 percent for the entire profile since site-specific measurements are only available at a depth of 15 m and the ATR Vs profile is based on lithology and velocity associations. The epistemic uncertainty was applied to each median base case, P1 and P4, to produce the lower bound (P2 and P5) and upper bound (P3 and P6) cases. Figure 7-38 shows the median base case with the lower and upper range profiles.

The same approach was used at ATR as MFC to assign weights. Each set of three profiles were assigned weights of 0.4 for the median base case (P1 and P4) and 0.3 for the lower-range (P2 and P5) and upper-range (P3 and P6) profiles. The weighting of a set of three base case profiles thus approximates a normal distribution for the epistemic uncertainty in ln(Vs), with profiles for the lower and upper range cases representing the 10^{th} percentile and 90^{th} percentile, respectively, of that distribution. In the PSHA, the hazard using each alternative set of Vs profiles is computed separately and the results are then enveloped to produce the final rock hazard. The envelope of the cases with and without the first interbed is used to address the fact that this interbed may or may not be beneath specific buildings.

7.6.2 Soil Vs Profiles for ATR Buildings and Piping Areas

Site-specific Vs profiles were developed for TRA-770, TRA-771, TRA-688, TRA-674, TRA-786, and TRA-650, and four fire-water piping areas identified as A1, A2, A3, and A4. The ATR buildings and piping areas are founded on soil deposits of the Big Lost River mainstream alluvium that range in thickness from 6.1 to 18.3 m (20 to 60 ft) above basalt bedrock. The soil thickness can also be highly variable beneath the footprint of a building. Thus, the site-specific nature of the Vs profiles includes the number of soil layers and variability of soil thickness above bedrock (or range of soil depths).

In this evaluation, the measured Vs structures in the seven ATR downhole velocity boreholes were used to determine the number of soil layers, which consists of two or three alluvial soil layers above basalt bedrock (Figure 7-39). Previous site response analyses at ATR and INTEC considered one to three soil layers. In some models the deepest soil layer above basalt was modeled as a clay layer with different dynamic properties than those of the alluvial soil layers above (Payne, 2006b; 2008). For the Integrated Waste Treatment Unit (IWTU) at INTEC, the geomechanical model developed from site-specific geotechnical investigations included a 0.4 to 2.4 m (1.2 to 8 ft) thick clay layer. Of the thirty random soil Vs profiles for IWTU, some included the clay layer with a lower Vs than the Vs in the alluvial soil layers above (Payne, 2008). However, Payne (2006b) assessed that a clay or silt layer was only present in 18% of the boreholes, 51 of the total 362 compiled for both the ATR Complex and INTEC. Thus a clay layer was excluded and only Vs profiles with two alluvial soil layers were used in the site response analyses to develop the 2006 ATR soil DBE spectra, which is the DBGM for the SDC-4 buildings and piping areas (Section 1.1.4).

This study found that clayey sands and clay layers are present in the ATR velocity boreholes, two of which (BH03 and BH07) are closest to the ATR buildings and piping areas (Figure 7-40). Figures 7-41 and 7-42 show the types of soils in selected ATR-670 pre-construction boreholes and all seven of the boreholes with downhole Vs, respectively. Velocity boreholes BH03, BH07, and BH06 have relatively thin 0.6 to 0.9 m (2-3 ft) layers classified as clay (CL) based on grain size analyses. Just above basalt (a

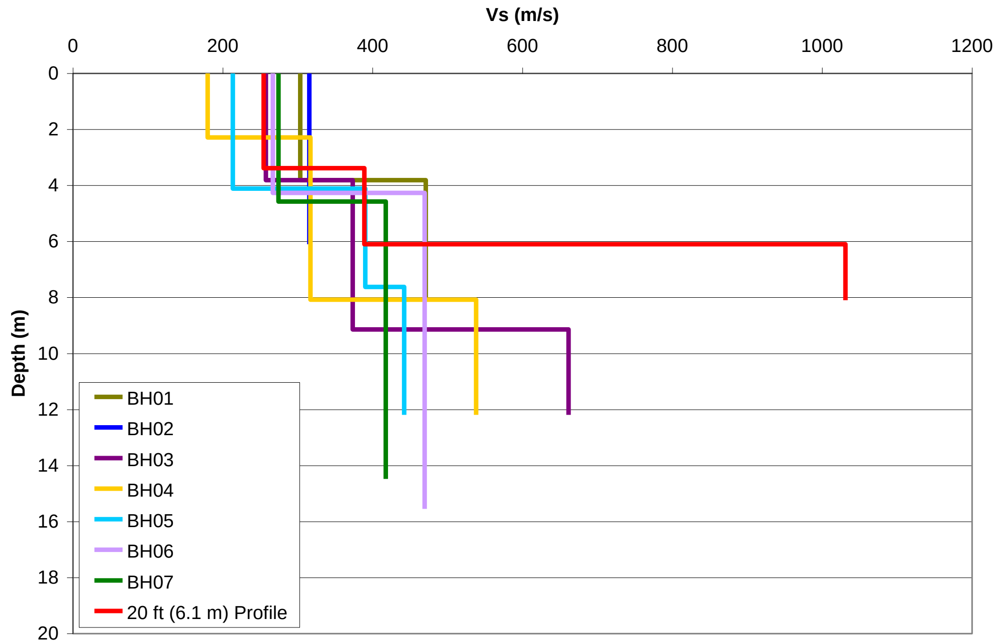

Vs (m/s)
0
200
400
600
800
1000
1200
Depth (m)
0
2
4
6
8
10
12
14
16
18
20
BH01
BH02
BH03
BH04
BH05
BH06
BH07
20 ft (6.1 m) Profile

(b

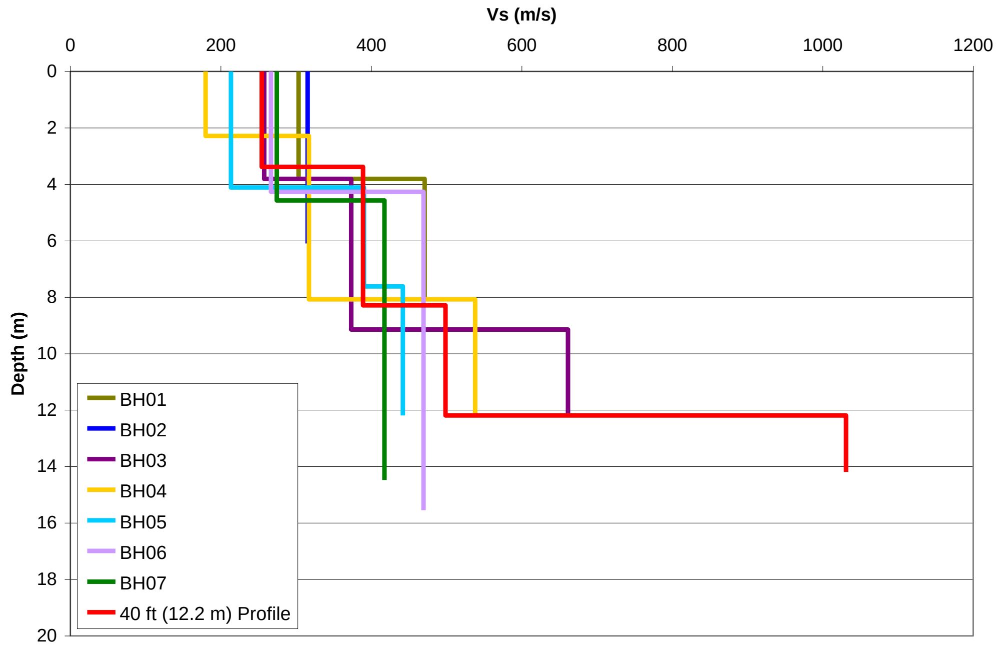

Vs (m/s)
0
200
400
600
800
1000
1200
Depth (m)
0
2
4
6
8
10
12
14
16
18
20
BH01
BH02
BH03
BH04
BH05
BH06
BH07
40 ft (12.2 m) Profile

c)

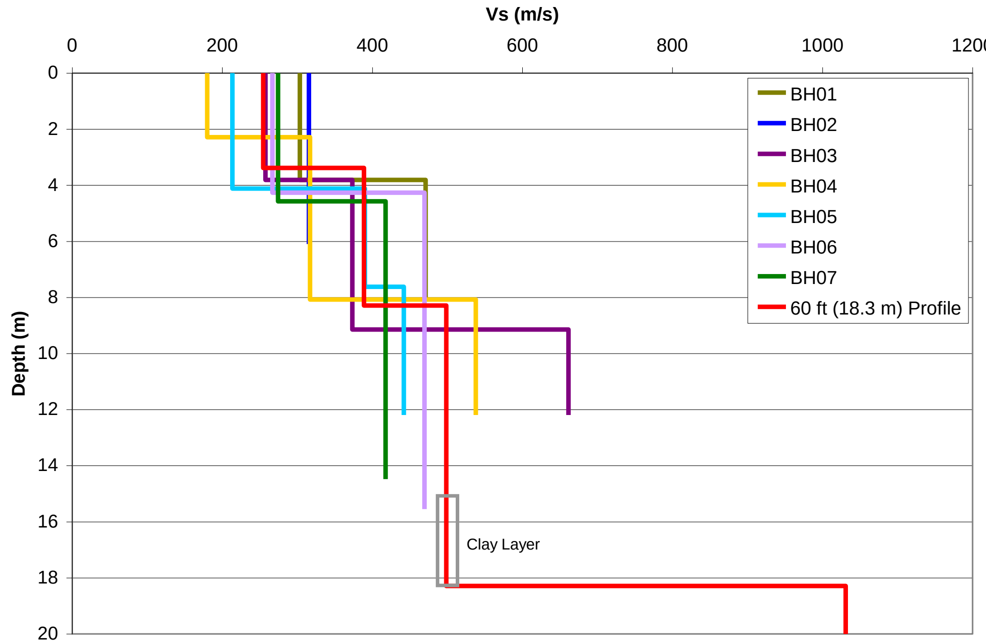

Figure 7-39. Plots of the downhole Vs data for soils at ATR and the Vs profiles for the three soil depth cases: a) 20 ft; b) 40 ft; and c) 60 ft. The top of rock Vs (1,031 m/s) is from the models shown in Figure 7-38.

bedrock, BH06 and BH07 have thicker clayey sand (SC) layers of 1.2 and 2.4 m (4 and 8 ft), respectively (Figure 7-42). Six undisturbed samples obtained from BH06 and BH07 in these two layers at depths from 12.1 to 14.3 m (40 to 47 ft) were subjected to dynamic tests (Stokoe et al., 2002). In each of these boreholes, a uniform Vs was measured in the layer containing both the thin CL and thicker SC layers. Although these two layers are not distinguishable from the overlying gravels in the downhole Vs measurements (Figure 7-42), a separate clay layer with different properties was included in the ATR Vs soil profiles.

Additionally, a review of ATR and IWTU downhole Vs measurements suggest that compacted backfill has the same or higher Vs than undisturbed alluvial soils. All of the ATR velocity boreholes have disturbed soils to at least a 0.9 m (3 ft) depth, and BH02 is located in an area with 2.4 m (8 ft) of backfill associated with installation of the fire-water piping (Pers. Comm. C. Behm, 2013). A review of the shear-wave signals on the BH02 travel time vs. depth plot (Redpath Geophysical, Inc., 2001) supports the interpretation of the 315 m/s (1035-ft/s) uniform Vs to the depth of 6 m (20 ft) (Figure 7-42). Also, Vs measurements in IWTU boreholes of 216 m/s (710 ft/s) to a depth of 4.2 m (14 ft) (B-37) and 274 m/s (900 ft/s) to the depth of 3 m (10 ft) (B-39) are in backfill materials including 1.5 m (5 ft) of urban debris (garbage) in B-37 (Kleinfelder, Inc., 2007). The range of Vs for undisturbed soils in the uppermost layers at ATR is 180 to 303 m/s (590 to 995 ft/s) (without BH02) and at IWTU, 183 to 290 m/s (600 to 950 ft/s) (without B-37 and B-39). A possible reason for the lack of distinction in Vs for backfill and undisturbed alluvium is that INL requires backfill to be composed of well-compacted native alluvial soils (i.e., lifts

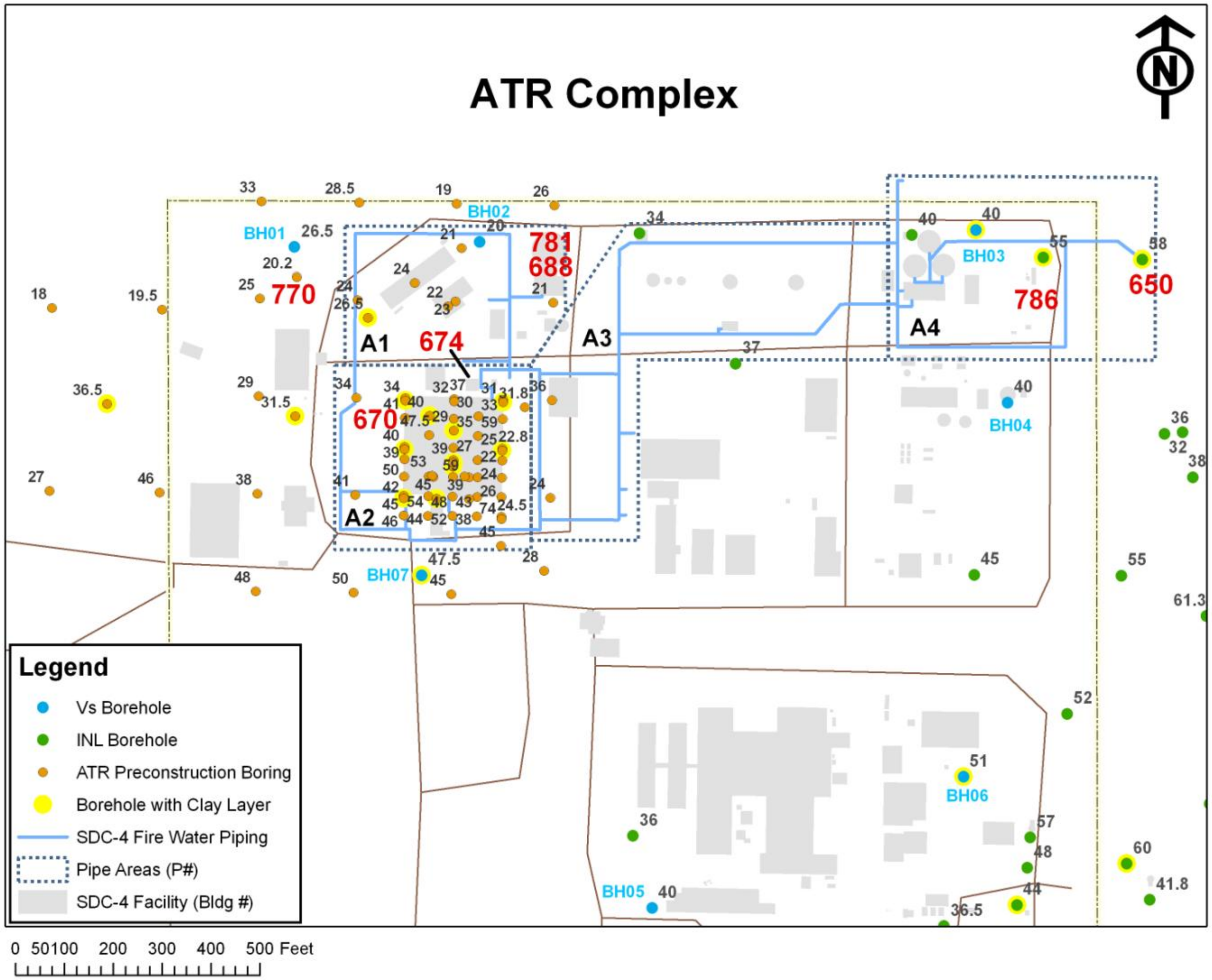

Figure 7-40. Map showing the locations of Vs boreholes (BH0#), INL boreholes and ATR pre-construction borehole annotated with depth of soil (in feet) to the top of basalt. The dashed lines show the fire-water piping areas (A1, A2, A3, and A4) that are grouped together for structural analysis.

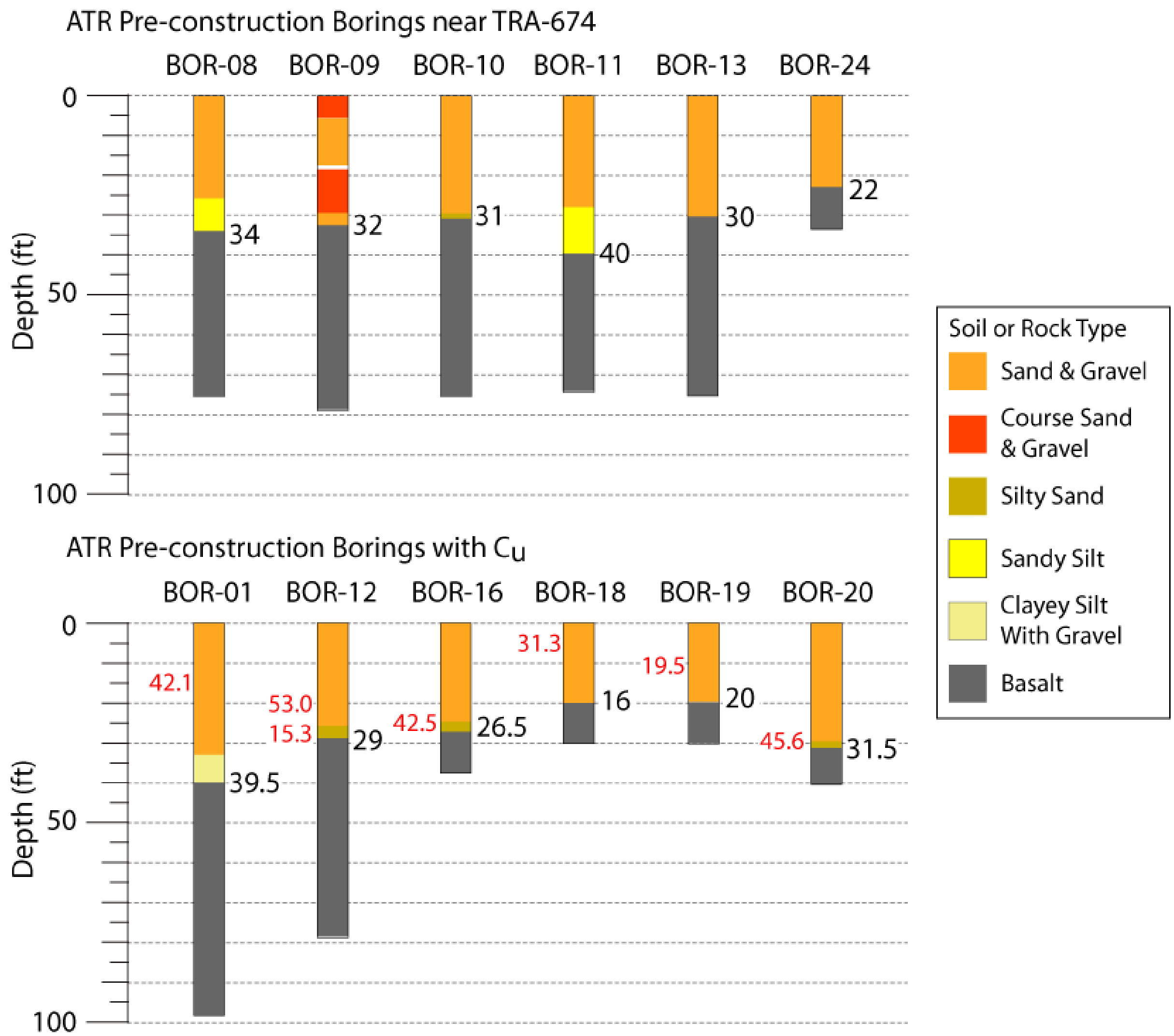

Figure 7-41. Graphic shows soil types, soil particle sizes, and depths to basalt bedrock (black numbers) (Ebasco Services, Inc., 1961a; 1961b) for ATR-670 pre-construction borings. The coefficient of uniformity (C_u) (red numbers) is plotted at the approximate depth of where the soil sample was obtained.

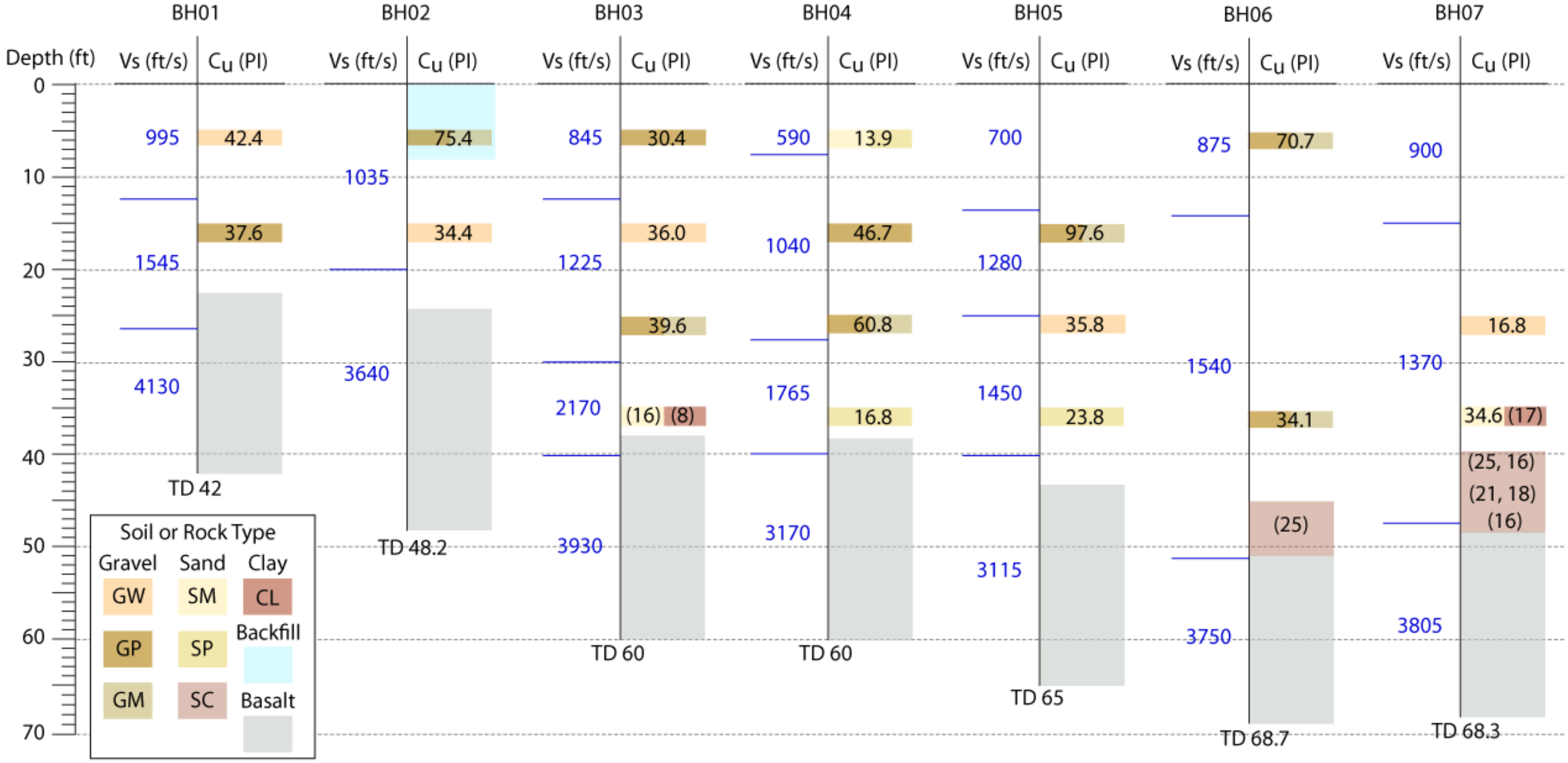

Figure 7-42. Graphic lists the shear-wave velocities (Vs) (Redpath Geophysics, 2001), soil type, coefficient of uniformity (C_u) (TRA, 2000), and Plasticity Index (PI) (Ebasco Services, Inc., 1961a; Stokoe et al., 2002) for the velocity boreholes at the ATR Complex. Soil types, C_u values, and PI values are plotted at the depths where the samples were obtained.

≤15.2 cm or ≤6 inches per lift and compaction to at least 95% of maximum dry density per the Modified Proctor Test in American Society for Testing and Materials, ASTM D1557-70) (EG&G Idaho, Inc., 1984). The 2.4 m (8 ft) of well-compacted native soils in BH02 may explain the lack of a two-layer Vs structure as observed in BH01, only 150 m (492 ft) to the west (Figure 7-40). As result of this evaluation, backfill is assumed to have the same properties as undisturbed alluvium.

7.6.2.1 Layer Median Vs and Variability

The Vs data consists of seven profiles extending into basalt in the ATR Complex (Figure 7-39). The interpretation of the downhole Vs data in three of the boreholes (BH03, BH04, and BH05) indicates three layers, with an average depth to the top of the third layer of 8.3 m (27.2 ft). Interpretation of the velocity data in three of the other profiles indicates only two layers. However, in one of these boreholes (BH01) basalt is encountered at a depth of 8 m (26.5 ft). Thus, only two boreholes (BH06 and BH07) extend to sufficient depth (> ~9 m or 30 ft) such that evidence of an increase in velocity with depth (a 3-layer system) could be observed. The seventh borehole (BH02) is interpreted to have a constant velocity over the depth range from 0 to 6 m (20 ft), were basalt is encountered.

The measured Vs from the seven ATR velocity boreholes were used to calculate the median Vs and its sigma for each model layer (Figure 7-42). The variability in Vs across the seven boreholes was computed for three depth ranges. The first is a depth of 0 to 3.3 m (11.1 ft), which is the average depth to the top of the second velocity layer in BH01, BH03, BH04, BH05, BH06, and BH07. The second is a depth of 3.3 to 8.3 m (11.1 to 27.2 ft) and the third depth is 8.3 m to basalt (Table 7-10).

The velocity results in Table 7-10 indicate that the variability in Vs across the ATR Complex is comparable to that recommended by EPRI (2013) for variability across a footprint. On this basis we interpret that the two deep profiles that do not show a velocity increase with depth represent random variations within a representative three-layer velocity model for the ATR Complex as a whole. Such profiles would then be captured within the randomization about a three layer velocity profile represented by the median velocities in Table 7-10. Therefore, we use only the three-layer velocity model for the ATR soil profiles, with the presence of the third layer determined by profile depth.

The deeper boreholes (depth to basalt ≥ 12 m or 40 ft) generally indicate the presence of sandy clays and silts at the base of the soil column with an average thickness of about 3 m (10 ft). In the boreholes with velocity measurements, these deeper clayey soils have similar velocities to the overlying gravels. However, they are expected to have different modulus reduction and damping behavior, being more linear than gravels. It is important to represent their behavior in the site response analyses because this layer is the first layer above basalt where there is a significant velocity contrast (factor of ~2) such that there is a potential for a strain concentration at the soil-basalt boundary.

7.6.2.2 Site-specific Vs Profiles

The purpose of the site response analysis is to capture the range in amplification for each of the buildings and piping areas at the ATR Complex. Table 7-11 lists the average soil depth and soil depth range assessed for the buildings and piping areas. Although the footprints of the buildings on soil are relatively small, 40 to 234 m^2 (427 to 2,520 ft^2), boreholes near the buildings are relatively sparse and thus greater uncertainty of soil depths is assumed. As an example of the variability, the ATR-670 pre-construction boreholes show the soil depth variability (22 to 59 ft) for a 4,087 m^2 (44,000 ft^2) footprint area (Figure 7-40). For the fire-water piping areas listed in Table 7-11, larger ranges of soil depths were assessed either based on the boreholes within the area (e.g., A2) or because few widely spaced boreholes were available (e.g., A3). Table 7-11 also lists the buildings and fire-water piping areas that were grouped together based on similar soil depths and variability.

Initial sensitivity analyses indicate that variations of ±1.5 m (±5 ft) in the Vs profile soil depth produce only small changes in amplification (generally about 10% or less). In addition, an envelope of the results for the two end-member soil depths envelops the results for the intermediate depth. This suggests that the range in response for soil sites at the ATR Complex can be adequately captured by running a limited set of Vs models with soil depths that span the entire soil depth range from 6.1 to 18.3 m (20 to 60 ft), which encompasses all buildings and piping areas. This limited set consists of three Vs profiles with soil depths of 6.1, 12.1, and 18.3 m (20, 40, and 60 ft). Site-specific responses for each building and piping area are then produced by enveloping the responses for two or three of the Vs profile models that are appropriate for the range of soil depth variability as listed in Table 7-11.

Vs models were developed for each of the three soil depth cases and are listed in Table 7-12. The median Vs and layer depths from Table 7-10 are combined with three soil depths to produce Vs profiles of the three soil depth cases, referred to as 20 ft, 40 ft, and 60 ft. Figure 7-39 shows the comparisons of the Vs models with the downhole Vs data at ATR. The soil depth cases are based on the three-layer velocity model with the assumption that the observed two-layer cases are captured within the randomization.

7.6.2.3 Epistemic Uncertainty in Site-specific Vs Profiles

The ATR velocities are used to assess the epistemic uncertainty of the Vs profiles for the three soil depth cases (20, 40, and 60 ft). Following the guidance in EPRI (2013), the epistemic uncertainty in the median soil Vs was computed using the 10^{th} and 90^{th} percentiles of a log normal distribution. The velocity scale factor is used is $1.28*\sigma\mu$. Dividing the standard deviations in ln(Vs) listed in Table 7-10 by the square root of the number of velocity measurements gives values of $\sigma\mu\ln Vs$ in the range of 0.06 to 0.08, which results in a multiplicative factor of 1.11 to obtain the lower and upper range soil Vs models (Table 7-12).

The three Vs profiles (best estimate, lower range, and upper range) are weighed 0.4, 0.3, and 0.3, respectively, consistent with the basalt Vs profiles. The alternative velocity profiles are then placed at the surface of the alternative rock profiles developed in Section 7.6.1. The best estimate soil velocity profiles for depths of 20 ft, 40 ft, and 60 ft are placed on the best estimate rock profiles P1 (with shallow interbed) and P4 (without shallow interbed). Similarly, the lower range soil profiles are placed on top of the lower range velocity profiles P2 and P5 and the upper range soil profiles are placed on top of the upper range rock profiles P3 and P6. The combined soil and rock profiles are designated P1 through P6 as indicated in Table 7-12.

Table 7-10. Median Vs and sigma for three soil layers based on downhole Vs data at ATR.

Layer #	Depth Range (ft)	Median Vs (ft/s)	Sigma ln(Vs)
1	0 - 11.1	835	0.20
2	11.1 - 27.2	1276	0.17
3	>27.2	1636	0.18

Table 7-11. Soil depths, depth variability, and envelop sets of soil depth cases used to produce site-specific responses for ATR buildings and piping areas.

Building or Area	Depth of Soil Above Bedrock (ft)	Soil Depth Variability (ft)		Envelop Set of Soil Depth Cases for Vs Profiles[1]
		Minimum	Maximum	
TRA-770 TRA-781 TRA-688 Piping Area A1	25	20	30	20 ft and 40 ft
TRA-674	30	25	35	20 ft and 40 ft
TRA-786 TRA-650	55	50	60	40 ft and 60 ft
Piping Area A2	40	25	55	20 ft, 40 ft, and 60 ft
Piping Area A3	35	25	40	20 ft and 40 ft
Piping Area A4	50	40	60	40 ft and 60 ft

1. Table 7-12 lists the Vs profiles for each soil depth case.

Table 7-12. Vs soil profiles and dynamic properties for 20 ft, 40 ft, and 60 ft soil depth cases.

Soil Depth Case Name	Profile Layer	Thickness (ft)	Depth to Base (ft)	Unit Weight (lb/ft^3)[1]	Shear-wave Velocity (ft/s)			Dynamic Property Curves		Lithology
					Median (P1, P4)	10^{th} % (P2, P5)	90^{th} % (P3, P6)	Set M1[2]	Set M2[2]	
20 ft	1	11.1	11.1	122	835	752	927	DM-Cu40 5 ft	Rollins et al. 16^{th}%	Gravelly Alluvium
	2	8.9	20	122	1276	1149	1416	DM-Cu40 25 ft	Rollins et al. median	Gravelly Alluvium
40 ft	1	11.1	11.1	122	835	752	927	DM-Cu40 5 ft	Rollins et al. 16^{th}%	Gravelly Alluvium
	2	16.1	27.2	122	1276	1149	1416	DM-Cu40 25 ft	Rollins et al. median	Gravelly Alluvium
	3	12.8	40	122	1636	1474	1816	DM-Cu40 25 ft	Rollins et al. median	Gravelly Alluvium
60 ft	1	11.1	11.1	122	835	752	927	DM-Cu40 5 ft	Rollins et al. 16^{th}%	Gravelly Alluvium
	2	16.1	27.2	122	1276	1149	1416	DM-Cu40 25 ft	Rollins et al. median	Gravelly Alluvium
	3	22.8	50	122	1636	1474	1816	DM-Cu40 25 ft	Rollins et al. median	Gravelly Alluvium
	4	10.0	60	126	1636	1474	1816	Darendeli PI 18	Vucetic and Dobry PI 15	Clayey Sands and Clay

1. Unit weights obtained from Kleinfelder, Inc. (2007) for IWTU.

2. DM-Cu40, 5 and 25 ft, from Payne (2008); Rollins et al. (1998) for 16^{th}% and median; Darendeli (2001) equations used to calculate Platicity Index (PI) 18; Vucetic and Dobry (1991) for PI 15.

7.7 Site Kappa, Q, and Soil Dynamic Properties for ATR

The general methodology used to assess kappa and Q at the INL sites is presented in Section 7.2. This section summarizes the results of kappa for the ATR Complex; refer to Section 7.2 for Q. This section also presents the available data and evaluations to select the shear modulus and damping relationships for soils at the ATR Complex.

7.7.1 Kappa for the ATR Complex

As indicated in Table 7-6, 21 earthquakes recorded at the broadband station ATRF and one earthquake recorded at the 1989 temporary array site TRAW were used to provide median estimates of kappa for the layered basalt crust at ATR using the methodology described in Section 7.3.2. The recordings reflect a range in magnitude from **M** 3.0 to **M** 5.0 and hypocentral distances of about 130 km to 220 km. The best estimate median kappa value for the ATR Complex is 0.021s (Table 7-6). To characterize epistemic uncertainty in the median kappa estimate, the uncertainty developed for site MFC, $\sigma\mu\ln\kappa = 0.4$ based on multiple recordings at two site locations, was adopted for the ATR Complex. Based on the uncertainty of 0.4, the 10% and 90% kappa estimates are 0.013s and 0.035s, respectively.

7.7.2 Dynamic Properties of ATR Soils

All boreholes at the ATR Complex have similar alluvial soils since they are within the Big Lost River floodplain. ATR pre-construction borings for TRA-670 have alluvial soils above bedrock composed predominantly of sand and gravel (Ebasco Services, Inc., 1961a). For example, particle size analyses performed on samples taken from two pre-construction boreholes are classified as well-graded gravel (BOR-01) and poorly-graded gravel with sand (BOR-12) (Figure 7-41) (Ebasco Services, Inc., 1961b). From particle size analyses (TRA, 2000), Figure 7-42 shows that the seven ATR velocity boreholes have alluvium composed of well-graded gravel or poorly-graded gravel with silt and sand.

Previous site response analyses at ATR and INTEC used two different sets of dynamic property curves for Big Lost River alluvial soils. For ATR, Payne (2006b) used the EPRI (1993) depth-dependent G/Gmax and damping curves; these curves were also used at MFC and NRF (Sections 7.3.5 and 7.5.2). For IWTU at INTEC (~1.6 km east of ATR), Payne (2008) used dynamic property curves developed from the work of Darendeli (2001) and Menq (2003) for a coefficient of uniformity (Cu) of 40, referred to as "Darendeli/Menq Cu 40". The minimum low strain damping was computed from the Darendeli (2001) relationship using a PI of 0. The IWTU site-specific analysis was reviewed by external reviewers (Blue Ribbon Panel) and the Defense Nuclear Facilities Safety Board (DNFSB).

The Darendeli/Menq Cu 40 dynamic property curves are applicable to ATR since INTEC and ATR are both underlain by Big Lost River alluvial soils. The Darendeli/Menq Cu 40 G/Gmax and damping curves were developed to be consistent with grain size curves for alluvial soils at IWTU which have Cu values that range from 30 to 50. Menq (2003) concluded that it is the uniformity of the gradation (or Cu) of gravels that affects their nonlinearity, rather than the particle size. Table 7-13 shows the average and one-sigma Cu are 44 ±20 over depths of 5 to 36 ft for the alluvium at the ATR Complex.

Several dynamic property curves were evaluated for the ATR gravelly alluvium. Figure 7-43 shows the Darendeli/Menq Cu 40 curves developed for a depth of 1.5 m or 5 ft (to be applied to the depth range 0-4.6 m or 0-15 ft) and a depth of 7.6 m or 25 ft (to be applied to a the depth range of >4.6 to 18.3 m or >15 to 60 ft.). The dynamic property curves of Darendeli/Menq Cu 40 were chosen for the gravelly alluvium based the average Cu for site-specific soil data at ATR (Table 7-13). Also shown on Figure 7-43 are other sets of curves that may be considered as alternatives including those developed by Rollins et al. (1998) and the EPRI (1993) cohenionless soil curves. The EPRI (1993) cohenionless curves have been used for a wide variety of materials, The curves from Rollins et al. (1998) were chosen as alternative curves (Table 7-12) because they allow for potentially more linear behavior of the gravelly alluvium. The

16th percentile Rollins et al. (1998) curves were used for the shallowest gravelly soil layers to account for the effects of depth.

For the clay layer above bedrock, dynamic properties of soil samples obtained in the ATR velocity boreholes (BH06 and BH07) were compared to alternative dynamic property curves. Figure 7-44 shows the ATR test data from Stokoe et al. (2002) for the deeper clay layers with: the EPRI (1993) curves for 6-15.5 and 15.5-36.5 m (20-50 and 50-120 ft); Vucetic and Dobry (1991) curves for a Plasticity Index (PI) of 15; and curves computed using the Darendeli (2001) equations for soil at a depth of 16.7 m (55 ft) with a PI of 18 (the average PI of the test data for ATR). The Vucetic and Dobry and the Darendeli curves provide reasonable representations of the G/Gmax data and the lower damping data and are used as the alternative relationships to model nonlinear response of the deep clay layer in the 18.3 m (60 ft) profile (Table 7-12). The damping data do show a large scatter, with some very large damping values at low strain levels. These large damping values are considered to be unrealistic given typical results presented in the literature.

Table 7-13. Coefficient of uniformity for alluvial soils at the ATR Complex.

	Sample Depth (ft)			Results of Sieve Analysis					
Borehole[a]	Top	Bottom	Soil Type[b]	%Gravel	%Sand	%Fines (Clay & Silt)	D_{10} Grains 10% Finer (mm)	D_{60} Grains 60% Finer (mm)	Coefficient of Uniformity (C_u)[c]
BH01	5	6.5	GW	58.8	37.5	3.7	0.25	10.53	42.4
BH01	15	17	GP	63.5	32.3	4.2	0.29	10.80	37.6
BH02	5	7	GP-GM	46.8	44.0	9.2	0.09	6.89	75.4
BH02	15	17	GW	67.9	29.7	2.4	0.41	14.20	34.4
BH03	5	6.5	GP	57.3	40.0	2.7	0.34	10.31	30.4
BH03	15	17	GW	63.0	33.4	3.6	0.33	16.80	36.0
BH03	25	27	GP-GM	52.0	41.6	6.4	0.22	8.90	39.6
BH04	15	17	GP	58.1	37.5	4.4	0.25	16.55	46.7
BH04	25	27	GP-GM	55.8	37.8	6.4	0.17	10.31	60.8
BH05	15	17	GP-GM	70.7	22.6	6.7	0.19	18.12	97.6
BH05	25	27	GW	61.8	34.3	3.9	0.31	16.06	35.8
BH06	5	7	GP-GM	69.4	23.0	7.6	0.16	16.57	70.7
BH06	35	37	GP-GM	51.9	42.7	5.4	0.22	7.55	34.1
BH07	25	27	GW	71.2	25.5	3.3	0.74	12.48	16.8
BOR-18	5	5.7	GW	75.0	21.0	4.0	0.30	10.0	33.3
BOR-19	10	16.5	GP	67.0	30.0	3.0	0.32	8.0	25.0
BOR-01	15	15.5	GW	67.5	33.5	0.0	0.19	8.0	42.1
BOR-12	20	20.8	GP	75.0	25.0	0.0	0.20	10.6	53.0
BOR-12	30	30.8	GP	84.0	16.0	0.0	0.70	10.7	15.3

a. BH0# indicates samples are from TRA (2000) for the ATR velocity boreholes (Redpath Geophysics, Inc., 2001); BOR-# indicates samples are for ATR pre-construction borings (Ebasco Services, Inc., 1961b).
b. Unified Soil Classification System: GW - Well graded gravel with sand; GP - Poorly graded gravel with sand; GM - Poorly graded gravel with silt and sand.
c. $C_u = D_{60}/D_{10}$

(a)

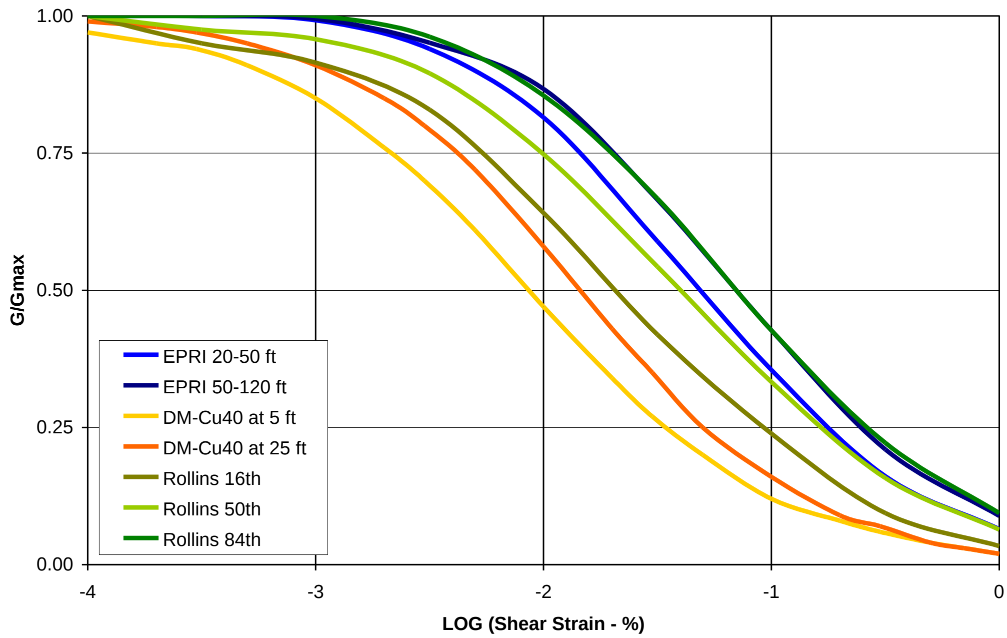

(b)

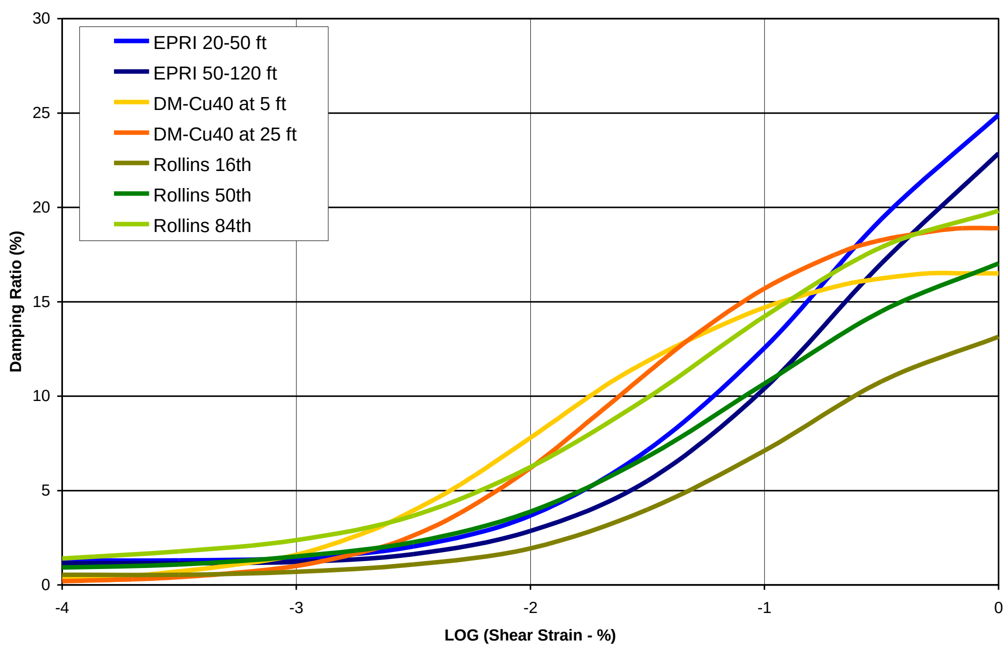

Figure 7-43. Comparisons of dynamic property curves for gravelly alluvium at ATR including EPRI (1993), Rollins et al. (1998), and Darendeli/Menq DM-C_u 40 (Payne, 2008) for: a) G/Gmax; and b) damping.

(a)

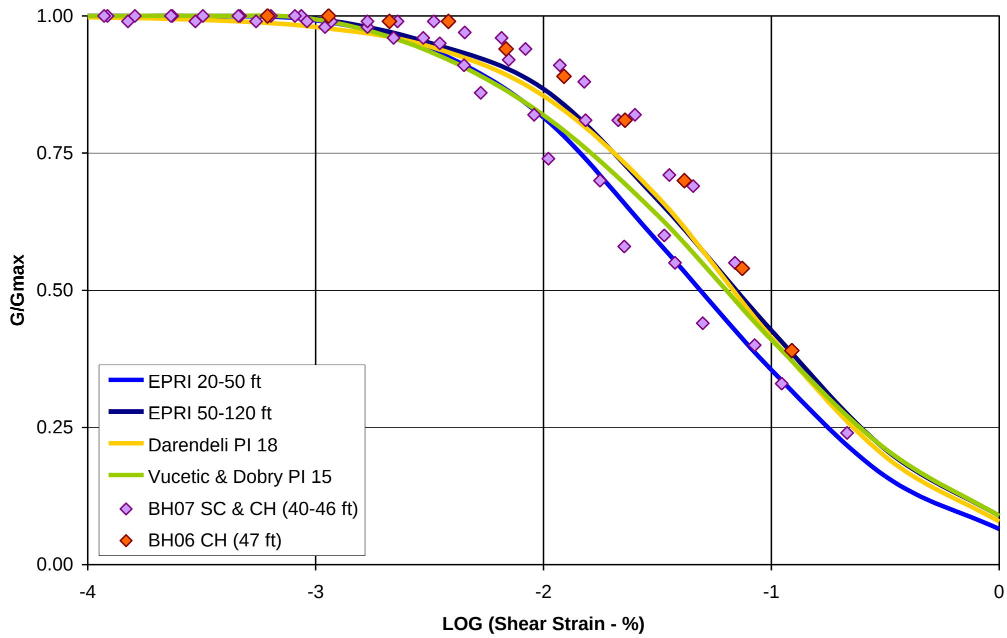

(b)

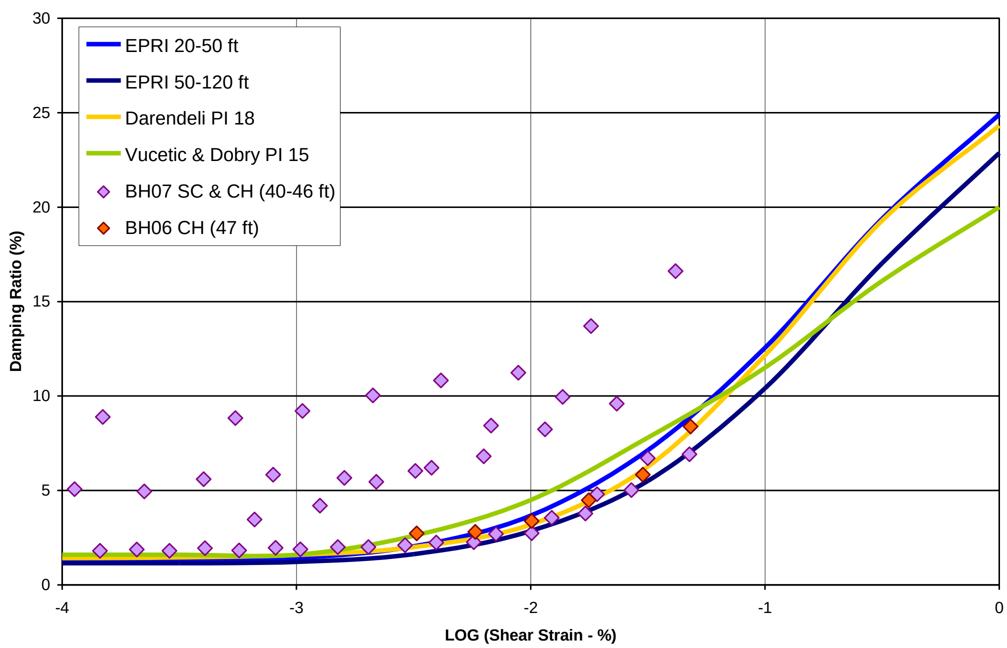

Figure 7-44. Comparison of dynamic test data (Stokoe et al., 2002) for deeper clayey sands (SC) and clay (CH) samples (40-47 ft) at ATR and dynamic property curves including EPRI (1993), Vucetic and Dobry (1991) Plasticity Index (PI) 15, and Darendeli (2001) PI 18 for: a) G/Gmax; and b) damping.

8. Seismic Source Characterization

This section provides a description of the elements of the SSC model that are used as input to the SSHAC Level 1 PSHA. The section begins with an overview of the SSC model and the approach taken to develop the model. This is followed by a detailed description of each element of the model: the characteristics of the crustal seismic source zones, and the fault sources. The goal in this section is to provide the reader with a full understanding of all elements of the SSC model that are included in the HID (hazard input document) provided in Appendix H.

8.1 Building the SSC Model: Overview and Approach

This section describes the conceptual framework for the SSC model, the manner in which data were evaluated by the SSC TI Team, the types of seismic sources that are included in the model, an overview of the sources that are characterized, and the structure of the logic tree that defines the SSC model.

An SSC model in a PSHA defines the seismogenic potential along with the locations, sizes, and rates of future earthquakes. To be useful, the SSC model must include elements that are appropriate to the tectonic environment for which it is developed. For example, the INL site lies within a tectonic environment that is less active than major plate boundaries, but has generally undergone more recent tectonic deformation than the stable continental region to the east. As a result, there are known active faults but there are also regions that lack clear definition of the causative faults giving rise to the observed seismicity, such as the ESRP. Therefore, the SSC methodology should include our knowledge of fault location and behavior as well as seismic source zones to account for the unknown locations of the faults giving rise to the “background” seismicity.

Mindful of the tectonic setting and precedents for methods available to identify and characterize seismic sources within similar tectonic environments, an approach was taken that begins with consideration of hazard-significant technical issues based on previous studies; compilation of available data to address the hazard-significant issues; evaluation of applicable data, models, and methods; identification of seismic sources according to defined criteria; and characterization of each seismic source, including the associated uncertainties using a logic-tree approach. An overview of this approach to developing the SSC model is given in Sections 8.1.1 through 8.1.5.

8.1.1 Criteria for Defining Seismic Sources

The SSC process for the SSHAC Level 1 PSHA began with the identification of criteria that was used by the TI Team to define seismic sources. These criteria were identified based on due consideration of the tectonic regime, the types of seismic sources that might be present (e.g., fault sources and source zones), and precedent from recent SSC models developed for similar tectonic environments and for nuclear facilities. Based on these considerations, unique seismic sources were defined to account for distinct spatial differences in the following criteria:

- Earthquake recurrence rate
- Maximum earthquake magnitude (Mmax)
- Expected future earthquake characteristics (e.g., style of faulting, rupture orientation, seismogenic thickness)
- Probability that a fault is seismogenic.

By “differences,” it is meant that a given potential seismic source differs significantly in one or more of these criteria from its neighbor such that identifying a unique seismic source is justified. It is important to note that, although the criteria are defensible because they are related to seismic source characteristics that can be important to seismic hazard, they do not lead to a unique set of seismic sources. The definition of a source zone boundary, for example, is interpretive and based on the expert judgment of the TI Team given the available data. Therefore, given a particular set of data and a specific set of seismic source criteria, there is no assurance that different experts will identify seismic sources in exactly the same way. The goal is to completely document the criteria that were used to define seismic sources and to document on a source-by-source basis the technical justification for the seismic sources that are included in the SSC model.

Examples assist in illustrating the application of the seismic source criteria for the SSC model. Consider the first criterion of differences in earthquake recurrence rate. The methodologies used to characterize earthquake recurrence for the SSC model are described in Sections 8.2.1.7 and 8.3.8. In general, the record of past earthquakes is obtained from the historical/instrumental catalog and from the paleoseismic record of prehistoric earthquakes. For a fault source such as the Lost River fault, fault slip rate and other paleoseismic evidence are used to define the source's recurrence rate and that is distinct from the seismic source zone within which it lies. Another example of identifying distinct seismic sources based on differences in recurrence is the observed differences in the spatial distribution and density (number of events per unit area) from one region to another. These differences are accounted for either by spatial smoothing of recurrence parameters or by drawing a source boundary between the regions. The choice of either approach is based on the judgment of the TI Team and includes considerations such as uncertainties in the locations of observed epicenters, distance from the source to the site of interest, and the magnitudes of observed seismicity. Because both approaches identify spatial changes in recurrence rates from one region to another, the choice of one approach over the other (or the weights associated with each approach, when both are included as alternatives in the SSC model) should have little hazard significance. One consideration with regard to the decision about whether or not a source boundary is defined, which is described in Section 8.2.1.1, is the spatial homogeneity of epicenters within a seismic source zone (Musson, 2000). Finally, because the observed record of moderate-to-large magnitude earthquakes is typically short relative to the recurrence intervals for those earthquakes, the use of seismotectonic features and boundaries serve as indicators of potential differences in the rates of future earthquakes. Such features provide indications of potential differences in Mmax and/or future earthquake characteristics, as discussed below.

A second criterion for subdividing the region into seismic sources is differences in Mmax. The methodologies used to assess Mmax for the SSC model are described in Sections 8.2.1.6 and 8.3.9. The assessment of Mmax for fault sources is based on consideration of the dimensions of possible future ruptures and models that relate the magnitude of the characteristic earthquake (Mchar) to Mmax. The Mmax for seismic source zones depend on whether or not fault sources are characterized within the boundaries of the seismic source zone of interest. Those source zones that include faults that are not characterized separately have a higher Mmax than those source zones whose faults are characterized separately as sources within the SSC model. Thus, the difference in Mmax between the fault sources and the host zone for those fault sources is a reason for calling out the fault sources specifically in the SSC model.

A third criterion for identifying distinct seismic sources in the INL region is the expected differences in future earthquake characteristics, such as the style of faulting, orientation of earthquake ruptures (strike and dip), seismogenic thickness, and depth distribution. The methodologies used to characterize the future earthquake characteristics for the PSHA seismic source zones are described in Section 8.2.1.4. In seismic hazard models, future earthquakes are modeled as faults having finite dimension, magnitude-dependent rupture dimensions, orientations, and depth extent. This is because these characteristics are important to modern ground motion prediction equations, including those that were selected for this PSHA. In some cases, differences in future earthquake characteristics provided a basis for identifying the boundary between seismic source zones.

A fourth criterion is the identification of particular faults that are assessed to have the potential to localize seismicity; that is, they are assessed to have a seismogenic probability p[S] greater than zero. The criteria for evaluating p[S] are described in Section 8.3.3. If a fault is assessed to be seismogenic, then future earthquakes will be localized on the fault and its source characteristics (e.g., recurrence rate, Mmax, geometry) will be specific to that fault. If the feature has a p[S] less than 1.0, then there is a finite probability, 1–p[S], that the fault is not seismogenic, future earthquakes will not be localized on the fault, and only the seismic source zone within which the fault lies will be the source of seismicity in the vicinity of the fault.

8.1.2 Data Evaluation Process

As defined in NUREG-2117 (NRC, 2012a), the goal of a SSHAC process is the following:

> "The fundamental goal of a SSHAC process is to properly carry out and completely document the activities of evaluation and integration, defined as:
>
> *Evaluation*: The consideration of the complete set of data, models, and methods proposed by the larger technical community that are relevant to the hazard analysis.
>
> *Integration*: Representing the center, body, and range of technically defensible interpretations in light of the evaluation process (i.e., informed by the assessment of existing data, models, and methods)."

Following this paradigm, the activities of the seismic source characterization began the evaluation process by identifying hazard-significant SSC issues, identifying available data applicable to those issues, and evaluating those data for subsequent use in the integration process. Previous INL PSHAs and sensitivity analyses provided an excellent basis for identifying the hazard-significant issues. The MFC site has ground motion estimates from the 1996 INL PSHA for rock conditions (Woodward-Clyde Federal Services et al., 1996) and from 2006 site response analyses for soil conditions (Payne, 2006a; 2006b). Two other sites at INL, ATR and NRF have sensitivity analyses that incorporated state-of-the-art methods and models available in 2010 and 2012, respectively (Seismic Evaluation Team, 2010; AMEC, 2010; 2013). All of these seismic hazard analyses provided a starting framework for the SSC model.

In addition to the INL-specific hazard sensitivity calculations, the SSC TI Team also considered the results of PSHA sensitivity analyses conducted for other sites in similar tectonic regions. For example, other such studies show that the detailed characteristics of nearby faults are often important, while the characteristics of faults that lie at greater distances are not important. Typically, hazard studies also show that the seismic source zone that hosts the site is often a significant contributor to the hazard at annual frequencies of interest for a nuclear plant. In turn, the earthquake recurrence rate of the host zone and those aspects of the SSC model that are important to estimating that recurrence rate (e.g., the earthquake catalog and associated magnitude conversions, catalog completeness) are also important and hazard-significant.

With knowledge of the hazard-significant issues, the TI Team then embarked on the process of data compilation that marks the evaluation part of a SSHAC process. The evaluation process consisted of consideration of the data, models, and methods that have been developed by the larger technical community. Most of the data that are included in the project database consist of reports and professional publications that relate to seismic source characteristics both locally, regionally, and by analogy to other parts of the world. Many of the reports have been developed through the years for various facilities on the INL.

The data that were compiled in the project database were posted on the project Sharepoint site. The data were arranged according to the following topics: INL PSHA references, regulations and guidance, and other references from the scientific literature.

Because the PSHA was conducted following a SSHAC Level 1 process, there was no opportunity to engage resource experts or other representatives from the technical community in workshop settings or through formalized channels. Therefore, the TI Team was responsible for identifying applicable data with the assistance of the PPRP. Fortunately, members of the TI Team have been engaged in seismic hazards studies at the INL for many years as well as comparable studies in other tectonic environments.

An important part of the data evaluation process is the documentation of the data that were considered by the TI Team during the course of the study. For the SSC model, this documentation was accomplished in two ways: in this project report through citations and through the use of data summary tables (described in Section 8.1.2.1 below). The data, models, and methods that were used by the TI Team directly in the development of the SSC model are cited, as appropriate, in the respective parts of this PSHA report that relate to the various aspects of the SSC model. References cited were available to the TI Team through the INL PSHA Sharepoint site.

8.1.2.1 Data Tables

With their introduction under the Central and Eastern United States (CEUS) SSC project (NRC, 2012b), data summary tables have been used to assist in the documentation of the SSC data evaluation process. The data summary tables developed for the SSHAC Level 1 PSHA were designed to provide the information needed to inform the reader regarding the data that were considered during the evaluation process, whether or not the data were used in developing the SSC model, and, if the data were used, the elements of the SSC model that were affected by the data cited. The data summary tables for all data sources include the basic reference information for data that were identified by the TI Team and an identification of the potential relevance of each data source to the SSC model. An indication is then made of whether or not the data were used in the SSC model. For data that were actually used in the construction of the SSC model, additional information is included in the data tables to document which components of the SSC model were affected by the data and which seismic sources (faults or source zones) were affected. The fields in the data summary tables that relate to the components of the SSC model include the following.

SSC Model Components

- Seismotectonic Setting
- Fault Geometry
- Rupture
- Fault Slip Rate
- Recurrence
- Renewal
- Mmax
- Magnitude Distribution
- Boundary

Seismic Source Components

- Lost River Fault
- Lemhi Fault
- Beaverhead Fault
- Big Lost Fault
- Regional Faults
- ESRP Host Zone
- Volcanic Zone
- Regional Zone

8.1.3 Evaluation of Models and Methods

In addition to the compilation and evaluation of data, the SSHAC evaluation process includes consideration of the models and methods that are currently proposed by members of the larger technical community. For this activity to occur within the framework of a SSHAC Level 1 study, the TI Team reviewed the professional literature, drew upon the TI Teams experience from other PSHAs, and sought the advice of the PPRP. This is because the formal inclusion of proponent experts into the project through workshops and other interactions were not performed. Fortunately, however, interactions with members of the larger seismic hazard technical community have occurred in the recent past in association with other INL projects. Although these projects have not been used to formally update the INL PSHA, the PSHA calculations did incorporate new models and methods available at those times and determined the effects that these models and methods have on the hazard. For example, the SET considered new data, models, and methods that had become available subsequent to the 1996 INL PSHA and performed seismic hazard sensitivity analyses at the ATR at INL. This sensitivity analysis revealed the potential for significant impacts to seismic hazard levels at ATR from changes in the source zonation model and ground motion models (Seismic Evaluation Team, 2010). Under a different project, additional sensitivity analyses revealed the potential for impacts to seismic hazard levels at NRF from changes to ground motion models and fault sources (AMEC, 2011; 2013). These sensitivity studies provided the TI Team with significant insights into the relative importance that various SSC and GMC models and methods may have in the seismic hazard at MFC.

The TI Team followed the evaluation process and selected the GMC model from the recently-completed SWUS Ground Motion Characterization Project (GeoPentech, 2015), which was conducted using a SSHAC Level 3 approach. The SWUS GMC model is part of a project that performed a comprehensive evaluation process to consider all applicable data, models, and methods for GMC model. Specifically, the SWUS project focused on ground motion data and information that is applicable to normal-faulting environments of the Basin and Range province, which makes the study directly applicable to the INL PSHA. As a result, the INL SSHAC Level 1 PSHA relies on the evaluation process and results given in the SWUS final report (GeoPentech, 2015).

The recent SSC and GMC sensitivity analyses and availability of the SWUS GMC model enabled the TI Team to focus on those models and methods that have become available in only the last few years. As a result of the large range of data, models, and methods from these other analyses that were reviewed during the evaluation phase of the SSC, the TI Team was well prepared to move into the model-building integration phase of the project.

8.1.4 Types of Seismic Sources Identified and Characterized in the SSC Model

As discussed in Section 8.1.1, a series of criteria were developed and used to define seismic sources. The advantage of identifying the criteria early is that they could then be used to prioritize the data identification process and could be included explicitly in the data evaluation process and the associated documentation in the data tables. As the project moved into the integration phase, the TI Team developed the SSC model by applying the seismic source criteria and arriving at a series of seismic source zones and fault sources. The conceptual bases for identifying these seismic source zones and fault sources are discussed subsequently in this section and the technical details are given in Sections 8.2 and 8.3.

The seismic sources included in the final SSC model consist of both seismic source zones and fault sources. Seismic sources include eleven tectonic and six volcanic seismic source zones (Table 8-1). Tectonic source zones are those whose boundaries and characteristics are defined by differences in tectonic characteristics, including geologic, geophysical, and seismologic properties (Figure 8-1). Volcanic source zones are defined specifically by deformational features produced by volcanic processes and associated with recurrence of volcanic activity (Figure 8-2). Sixteen fault sources are included in the

Table 8-1. Seismic source zones codes, names, and type as included in SSC model.

Code	Name	Type
NISB	Northern Intermountain Seismic Belt	Tectonic
IB	Idaho Batholith	Tectonic
NBR	Northern Basin and Range	Tectonic
CTB	Centennial Tectonic Belt	Tectonic
CSZ	Centennial Shear Zone (with subzones, CSZ1, CSZ2, CSZ3, and CSZ4)	Tectonic
ESRP	Eastern Snake River Plain (Host Zone)	Tectonic
EZ	Eastern Zone	Tectonic
ISB	Intermountain Seismic Belt	Tectonic
CBR	Central Basin and Range	Tectonic
WSRP	Western Snake River Plain	Tectonic
YSC	Yellowstone Caldera	Tectonic
AxVZ	Axial Volcanic Zone	Volcanic
ARC	Arco Volcanic Rift Zone	Volcanic
GRF	Great Rift Volcanic Rift Zone	Volcanic
HEB	Howe-East Butte Volcanic Rift Zone	Volcanic
LCB	Lava Ridge-Hells Half Acre – Circular Butte-Kettle Butte Volcanic Rift Zone	Volcanic
IVRZ	INL Volcanic Regional Zone (combined ARC, HEB, LCB, and AxVZ)	Volcanic

SSC model (Table 8-2 and Figure 8-3). All of the faults included are normal faults, and for the SSC model are divided between regional and local faults primarily related to their significance to the hazard (Figure 8-4).

As discussed in Section 8.1.1, the process of identifying and characterizing seismic sources for the SSC model was hazard-informed such that highest priority would be given to aspects of the model that had the highest potential hazard significance. Likewise, the level of complexity of the SSC model was consistent with current knowledge and importance to hazard. For example, hazard sensitivity analyses at ATR (Seismic Evaluation Team, 2010) and NRF (AMEC, 2011; 2013) showed that the three local faults are the most important fault sources to the mean hazard estimates and, as a result, details of the fault geometries and recurrence behavior are important to the calculated hazard. Accordingly, the local faults (Lost River, Lemhi, and Beaverhead faults, as shown in Figure 8-4) have been characterized in more detail in terms of their behavioral attributes than the regional faults. In addition, some of the regional faults for which detailed paleoseismic evidence exists, such as the Wasatch fault, have also been characterized in light of various identified segments. Likewise, sensitivity analyses show the importance of the host seismic source zone (ESRP zone) to various INL sites, and uncertainties in future earthquake characteristics within the zone, such as the sense of slip and geometries of future ruptures, are included explicitly in the SSC model. Conversely, uncertainties in the detailed characterization of more distant source zones are not included in the SSC model because of the lack of hazard significance.

The region over which the SSC model was developed was designed to extend somewhat beyond the distances that would be expected to contribute significantly to the site hazard. For example, preliminary hazard sensitivity analyses confirmed that the most active Basin and Range regional normal fault, the Wasatch fault, does not contribute significantly to the mean hazard at MFC (see Section 10.2.2.1). The

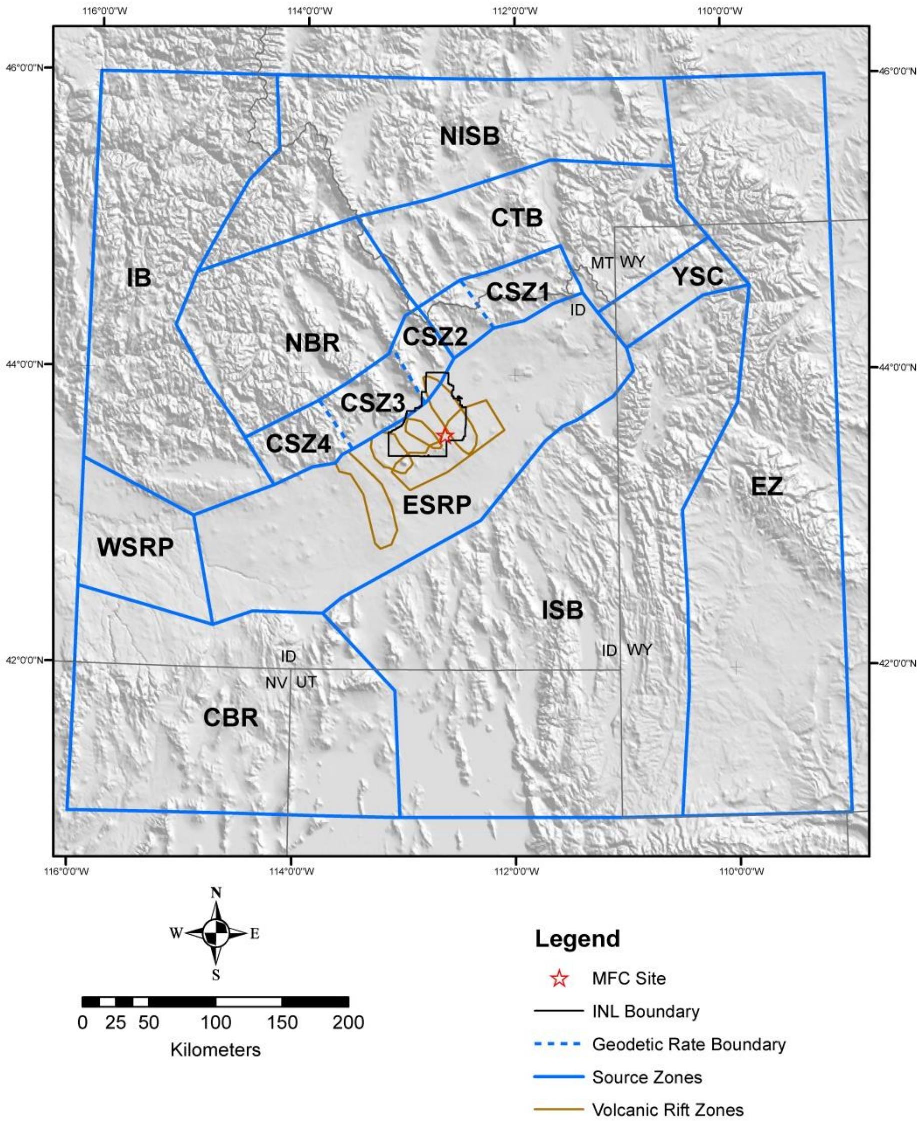

Figure 8-1. Map showing tectonic seismic source zones (blue lines) and volcanic source zones (brown lines) as used in the SSC Model. See Figure 8-2 for codes of volcanic source zones.

SSC model also evaluated contributions from plate interface sources on the Cascadia Subduction Zone (Section 8.4). Sensitivity analyses show that the plate interface does not contribute significantly to the mean hazard at the site, although its contribution increases for long period ground motions (Section 10.2.1).

Consistent with the definition of seismic sources used in other projects (e.g., NRC, 2012b; Jack Benjamin & Associates et al., 2012), the seismic sources identified in the SSC model are judged to have relatively uniform seismic source characteristics within their boundaries relative to adjacent regions. That is, the recurrence rate, Mmax, and future earthquake characteristics within most seismic source zones are judged to be relatively uniform within each source. An exception is the case where the spatial distribution

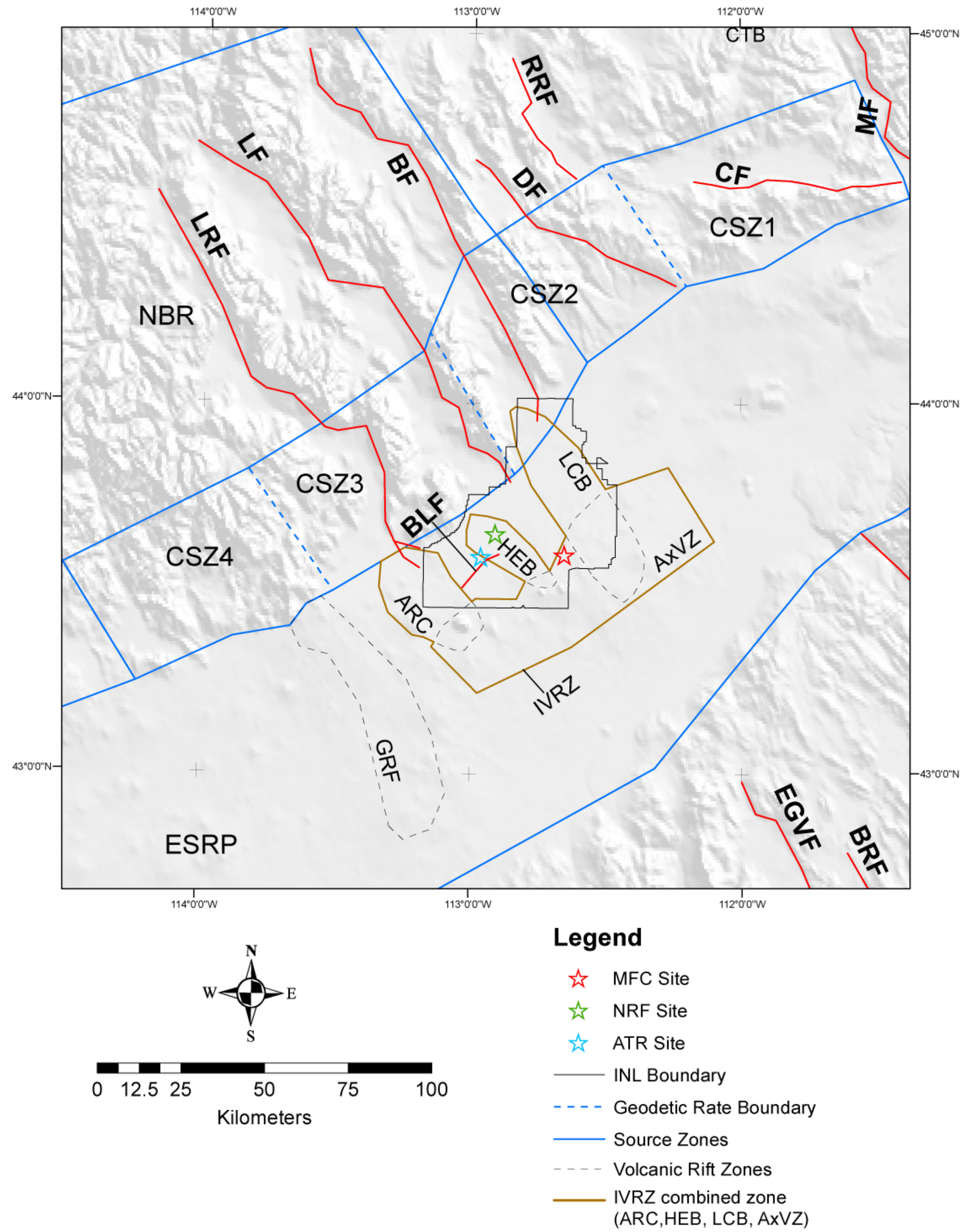

Figure 8-2. Map showing the IVRZ (brown solid lines) and GRF (gray dashed lines) volcanic source zones, tectonic seismic source zones (blue lines), and fault sources (red lines) as used in the SSC model. See Tables 8-1 and 8-2 for codes and names of seismic source zones and fault sources, respectively. Also shown are the locations of INL facility areas (stars) for PSHAs in this study.

Table 8-2. Fault sources, codes, names, and segments as included in the SSC model.

Code	Fault Name	Segment Names (Codes)[1]
BF	Beaverhead	Lemhi (LE) Mollie Gulch (MG) Leadore (L) Baldy Mountain (BM) Nicholia (N) Blue Dome (BD)
BLF	Big Lost	NA
BRF	Bear Lake	NA
CF	Centennial	NA
DF	Deadman	NA
EGVF	East Gem Valley	NA
GVF	Grand Valley	Grand Valley Swan Valley Star Valley
HF	Hebgen Lake	NA
LF	Lemhi	Ellis (E) Falls Creek (FC) Big Gulch (BG) Warm Creek (WC) Badger Creek (BC) South Creek (SC)
LRF	Lost River	Challis (C) Warm Spring (WS) Thousand Springs (TS) Mackay (M) Pass Creek (PC) Arco (A)
MF	Madison	Northern Canyon Southern
RCF	Red Canyon	NA
RRF	Red Rock	NA
STF	Sawtooth	NA
TF	Teton	NA
WF	Wasatch	Malad City Clarkston Collinston Brigham City Weber

1. Codes given for segments used in the SSC model, otherwise names are used to identify segments. NA indicates that no segments were included.

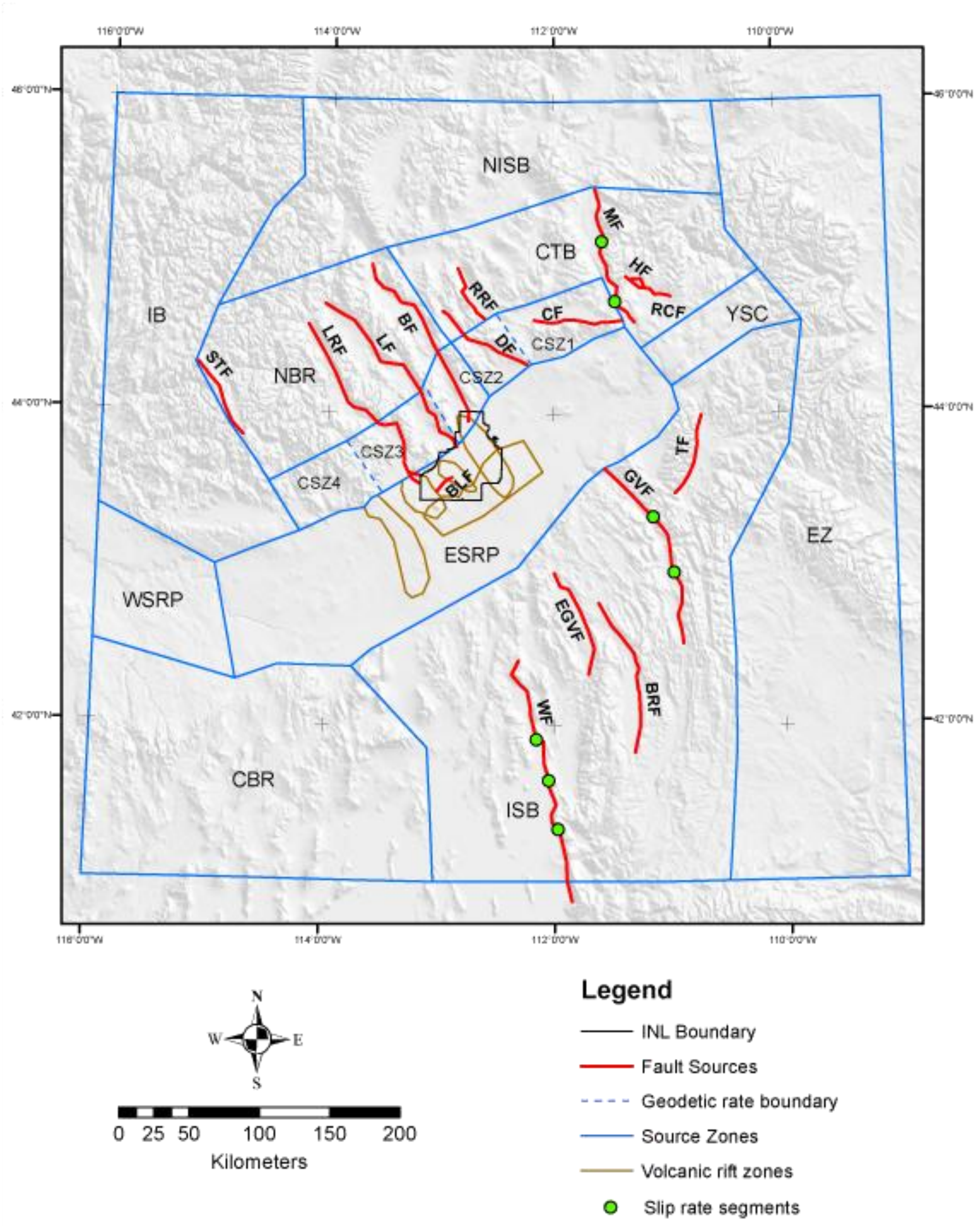

Figure 8-3. Map showing location of fault sources (red lines), tectonic seismic source zones (blue lines), and volcanic source zones (brown lines) as used in the SSC model. See Figure 8-4 for segmentation of the three local faults. See Tables 8-1 and 8-2 for codes and names of seismic source zones and fault sources, respectively.

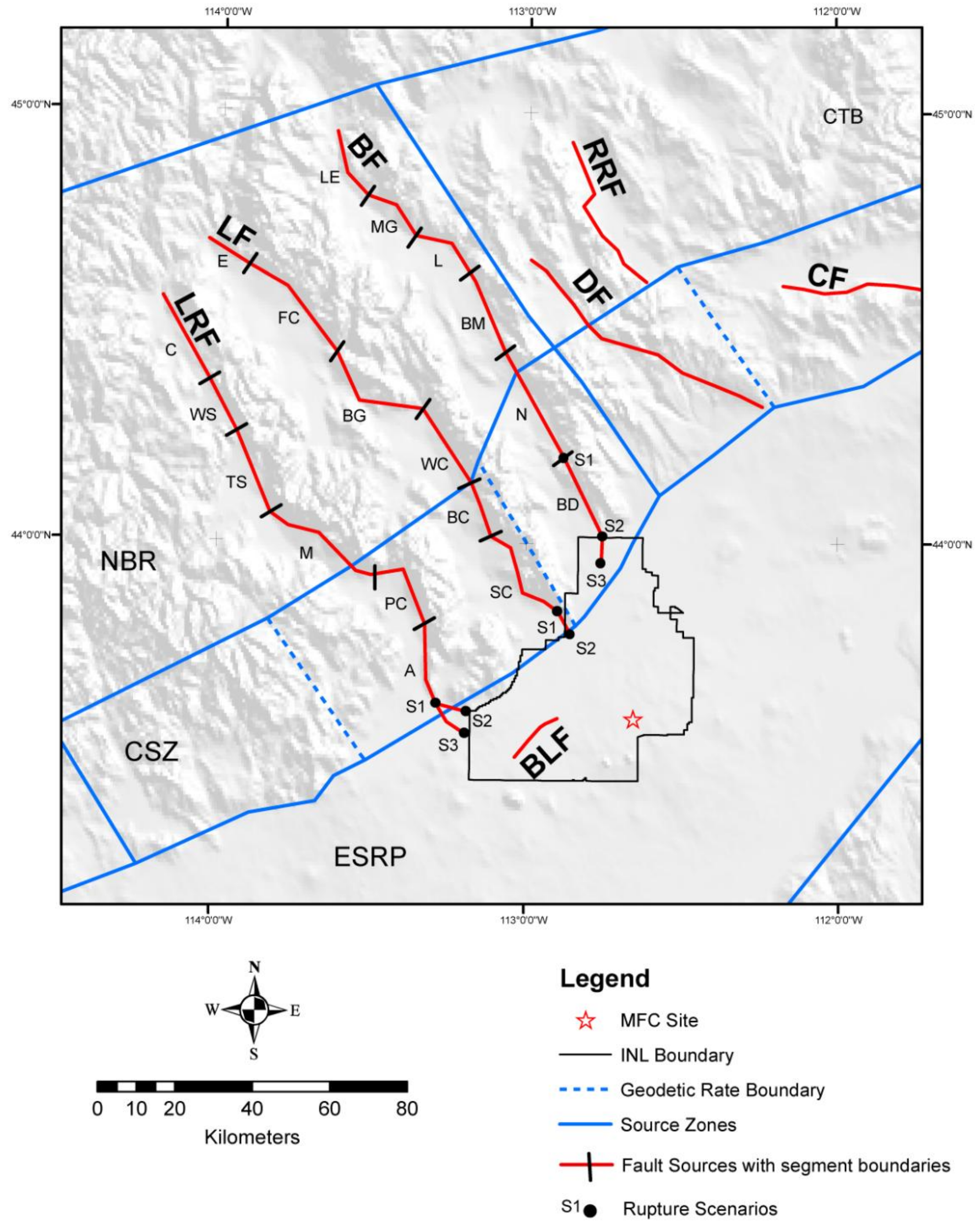

Figure 8-4. Map showing the three local faults sources: Lost River (LRF), Lemhi (LF), and Beaverhead (BF) normal faults and their segments (red lines with black tics). Also shown are the tectonic seismic source zones. See Tables 8-1 and 8-2 for codes and names of seismic source zones and fault sources, respectively.

of recurrence rate is defined by the spatial smoothing of observed seismicity. For fault sources, individual segments of faults are defined by uniform source characteristics (e.g., sense of slip, dip, and slip rate).

8.1.5 Structure of the SSC Model Logic Trees

This section describes the structure of the logic trees that compose the SSC model. The goal is to identify all of the components of the trees, describe the underlying logic for the elements and sequencing of the nodes of the trees, and provide the reader with pointers to where the technical bases for the assessments included in the trees can be located in this report.

A logic tree is a tool for displaying the epistemic uncertainties that are part of the inputs to the PSHA. Each node of the tree represents an element of the model and the alternative branches at each node represent the alternative models or parameter values for that given element. Each branch is assigned a relative weight, treated as a probability in the calculations, which expresses the TI Team's degree of belief that it is a more appropriate model or parameter value. Ideally, epistemic uncertainties can be reduced or even eliminated with additional data and information. The technical assessments that underlie the identification of the nodes of the trees, the alternative branches, and the weights assigned to each branch are included as part of the documentation in Sections 8.2 and 8.3.

Distinct from epistemic uncertainty is aleatory variability, which expresses those aspects of a model that we consider to be random and, at least at the level of our current knowledge, not amenable to reduction with the consideration of additional data and information. For example, the time and size of the next earthquake that will occur on a seismic source have aleatory variability. When multiple states of a model or parameter can both exist then the assessment for purposes of the SSC model is considered to be aleatory. Percentages are assigned to each state to express the relative frequency with which each state is expected to occur. For example, a region is assessed to include both strike slip and normal faulting seismic sources and the styles of faulting can occur randomly with respect to any given future earthquake. In such a case, the seismic source zone may host strike slip and normal faulting earthquakes assessed to have relative frequencies of 80 and 20 percent, respectively. Thus, the future number of strike slip and normal faulting earthquakes is expected to have this relative frequency. Also, aleatory assessments are not typically presented in a logic-tree format because logic trees, by convention, are intended to represent epistemic uncertainties exclusively and the branches are assessed as mutually exclusive alternatives. For clarity in this report, aleatory assessments are clearly indicated and the relative frequencies of aleatory alternatives are indicated as percentages in parentheses (35%). Relative weights used for epistemic alternatives are noted in square brackets [0.35]. This convention is also used in the HID (Appendix H).

The logic tree structure and characteristics are illustrated in Figure 8.5. Following the convention for displaying logic-tree elements, the elements that reflect epistemic uncertainties are indicated by a node (black filled circle) and multiple branches, which represent the alternatives and weights associated with each alternative. The weights associated with all branches at a node sum to 1.0, indicating that the branches represent the "collectively exhaustive" set of options (e.g., 0.2, 0.6, and 0.2 for seismogenic thickness alternatives, Figure 8-5). Likewise, each model or parameter value associated with a branch at a node is "mutually exclusive" of other branches. In some cases a vertical bar without a node is used, which indicates that subsequent elements of the tree are assessed on a source-by-source basis. In general, a logic tree is structured such that more general assessments occur earlier in the tree (i.e., to the left) and more specific assessments, which may be dependent on the general elements, are shown later in the tree (i.e., to the right). For example, alternative conceptual models and their relative weights would occur first in the logic tree, and the parameter values associated with each model would follow in nodes that are conditional on each particular model.

8.1.5.1 Logic Trees for Seismic Source Zones

The tectonic and volcanic seismic source zones in the SSC model are characterized by a number of attributes, some of which are treated as epistemic uncertainties in the logic trees and others are treated as aleatory variabilities. For all source zones the boundaries of the source zones are considered to be “leaky” with respect to future ruptures. That is, all future epicenters fall within the seismic source of interest, but the boundaries will allow ruptures within a source zone to proceed into adjacent sources.

The logic tree for the volcanic source zones is shown in Figure 8-5. The tree is applicable to all of the volcanic zones and the technical bases for the assessments and their relative weights are discussed in Section 8.2. The first assessment is the thickness of the seismogenic crust, then the maximum magnitude and the earthquake recurrence model. As shown, the assessment of earthquake recurrence intervals is a source-zone specific assessment and is related to the number of co-genetic volcanic events identified within each volcanic zone (see Section 8.2.1.7). Also, the spatial variation of recurrence parameters for future earthquakes within the volcanic source zones is assumed to be uniform based on the lack of earthquake information. Aleatory (relative frequency) assessments define the characteristics of future ruptures within the volcanic source zones. The aleatory assessments are not shown in the logic tree because they are not epistemic. The style of faulting is assessed to be normal-faulting (100%) with additional assessments of the strike, dip, and dip direction of future ruptures defined by relative frequencies in the aleatory distribution.

The logic trees for the tectonic seismic source zones differ somewhat depending on the source-specific conditions. The logic tree for the ISB, NISB, IB, EZ, WSRP, and YSC zones includes the assessments of seismogenic thickness, maximum magnitude, and the spatial variation of recurrence parameters (Figure 8-6). The actual values for the assessments and weights are given in the source-specific discussions in Section 8.2. As discussed in Section 8.2.2.3, nodes of the logic tree for the ESRP and CBR source zones also include alternatives related to whether or not the 1905 Shoshone, Idaho earthquake is assessed to be located within either the ESRP or CBR, which affects the assessment of Mmax and earthquake recurrence (Figure 8-7). Note that this implies that the branches of the logic tree for the two zones are correlated and therefore there cannot be a case where the Shoshone earthquake is located in both sources or not located in either source.

Another difference in the logic trees of tectonic seismic source zones is the existence or not of the CSZ. There is uncertainty in whether or not the zone exists and this uncertainty is included in the logic tree. Because the southern parts of the NBR and CTB source zones are spatially coincident with the CSZ source zone, the logic tree for those source zones takes into account whether or not the CSZ zone is assessed to exist (Figure 8-8). As discussed in Section 8.2.3, the geodetic rates of the CSZ subzones take into account the partitioning of slip rates between the source zones and the fault sources that lie within the subzones.

8.1.5.2 Logic Trees for Fault Sources

As discussed in Section 8.3, the fault sources in the SSC model are divided into two types based on their proximity to the site and, as a result, their relative contribution to the site hazard: thirteen “regional” faults are characterized using two logic trees that provide an expression of the knowledge and uncertainties regarding important fault source characteristics; and three “local” faults that are characterized in more detail in a logic tree for each fault source. The characteristics of thirteen normal fault sources are summarized in two logic trees, one for the recurrence approaches (Figure 8-9) and the other for Mchar (Figure 8-10). The normal faults listed in Table 8-2 are characterized by seismogenic thickness, fault geometry (dip, dip direction, length, and characteristic rupture length), seismogenic probability, and recurrence approach (slip rates and recurrence intervals). Fault geometries and recurrence rates are assessed for each fault or fault segment such that variations in these characteristics can occur

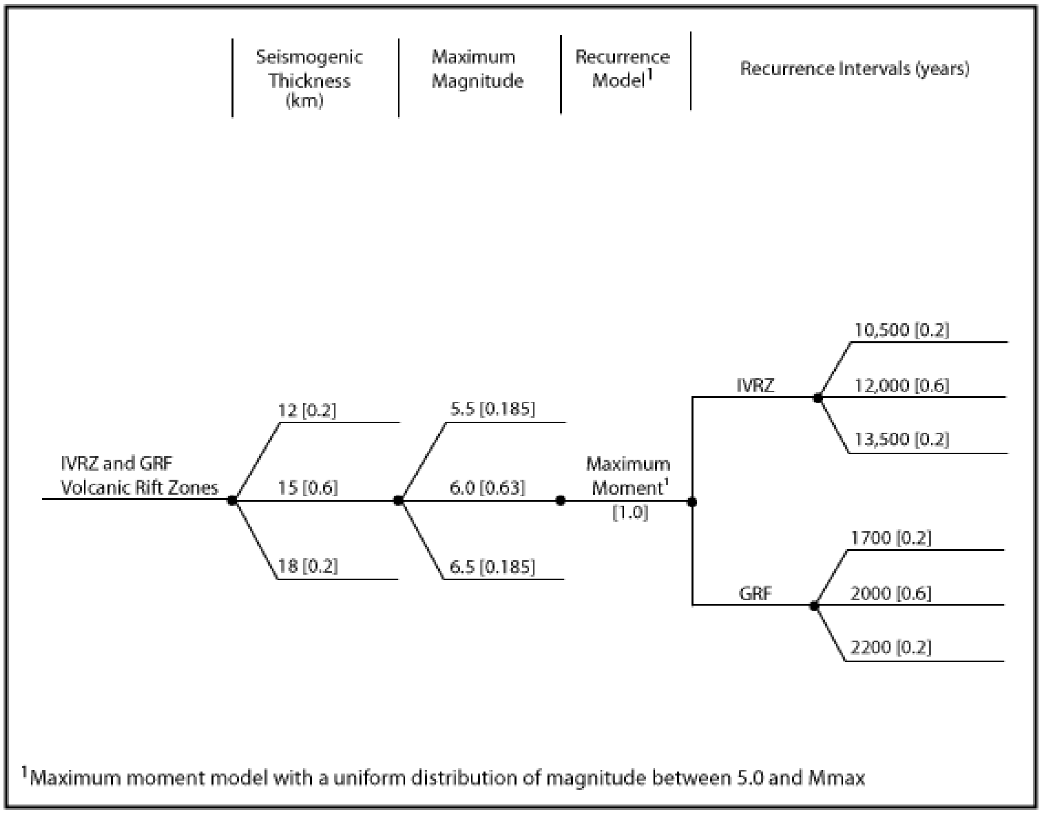

Figure 8-5. Logic tree for IVRZ and GRF volcanic zones. See Table 8-1 for codes and names.

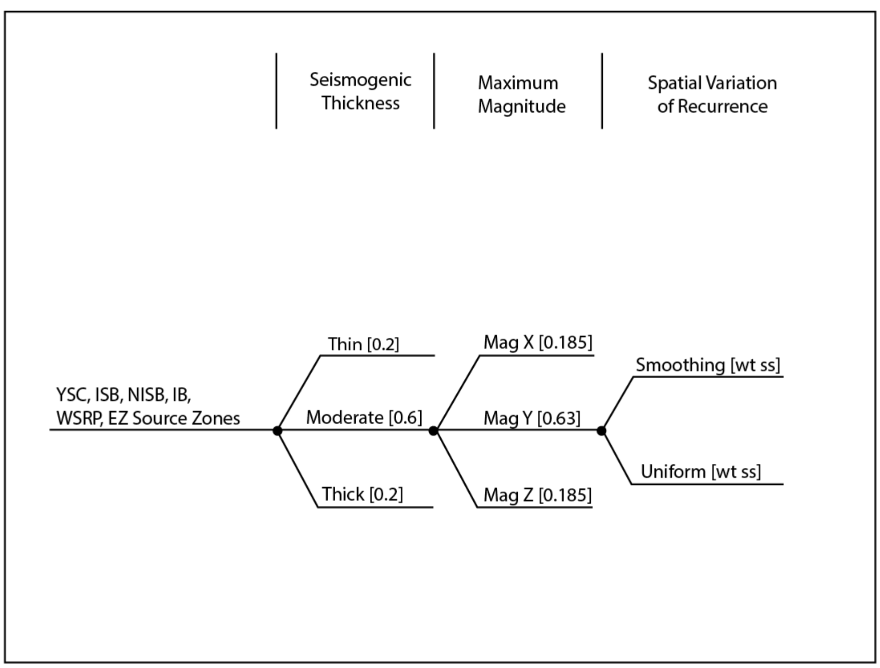

Figure 8-6. Logic tree for tectonic seismic source zones: ISB, NISB, IB, EZ, WSRP, and YSC (see Table 8-1 for codes and names). See Table 8-3 for seismogenic thickness and Mmax.

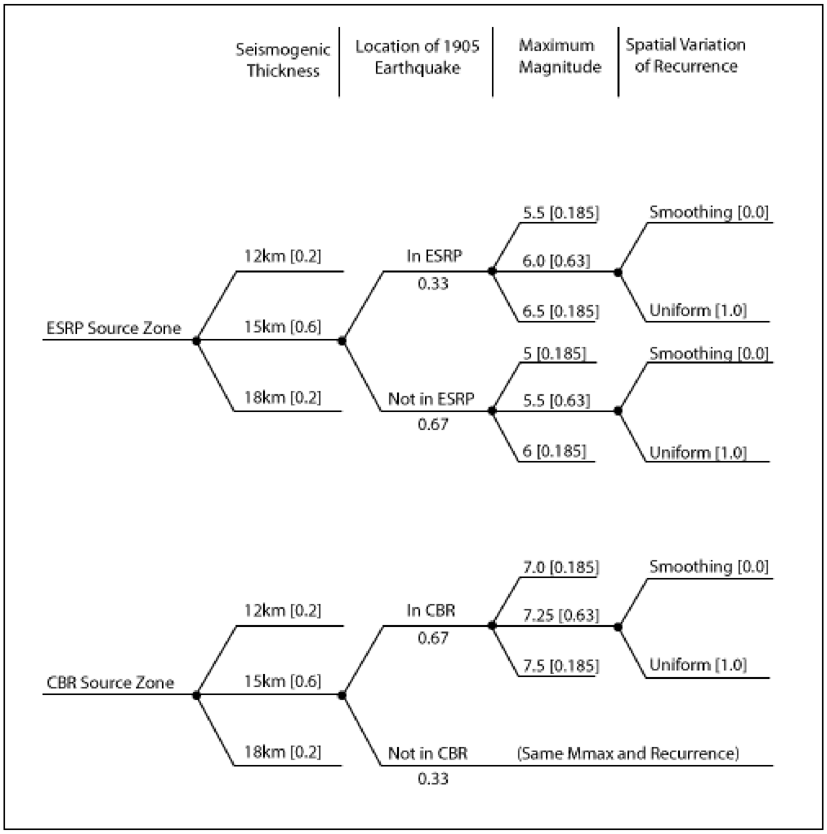

Figure 8-7. Logic trees for the ESRP and CBR source zones and to incorporate the uncertainty in the location of the 1905 Shoshone, Idaho earthquake.

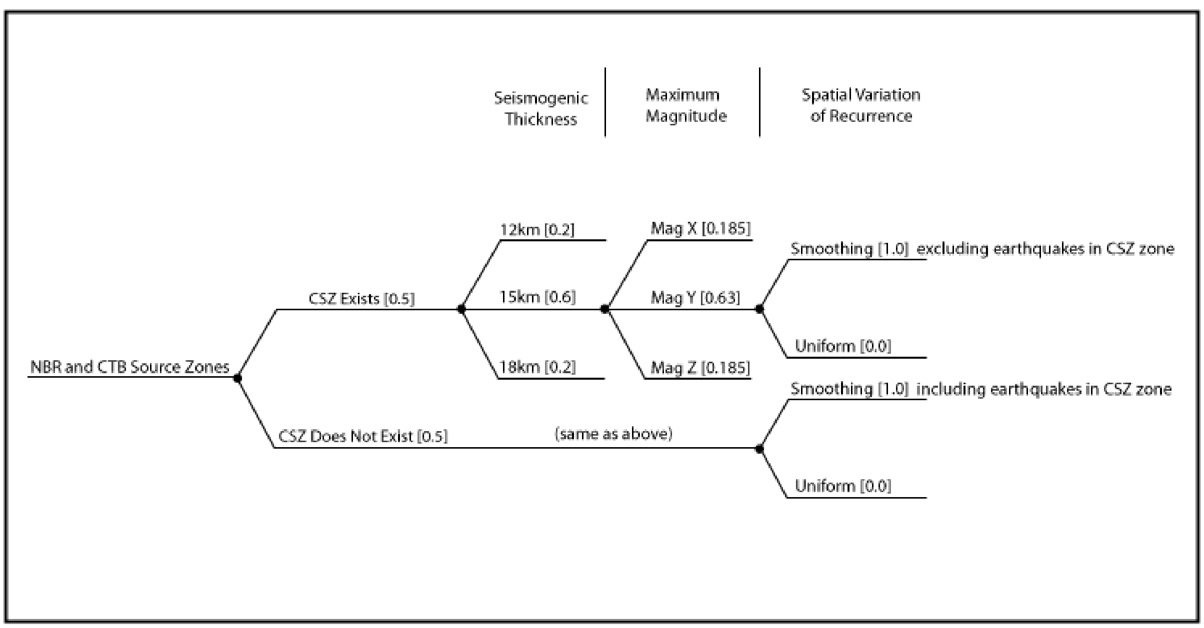

Figure 8-8. Logic tree for the NBR and CTB source zones, which includes the existence or nonexistence of the geodetically expressed CSZ source zone. See Table 8-3 for Mmax.

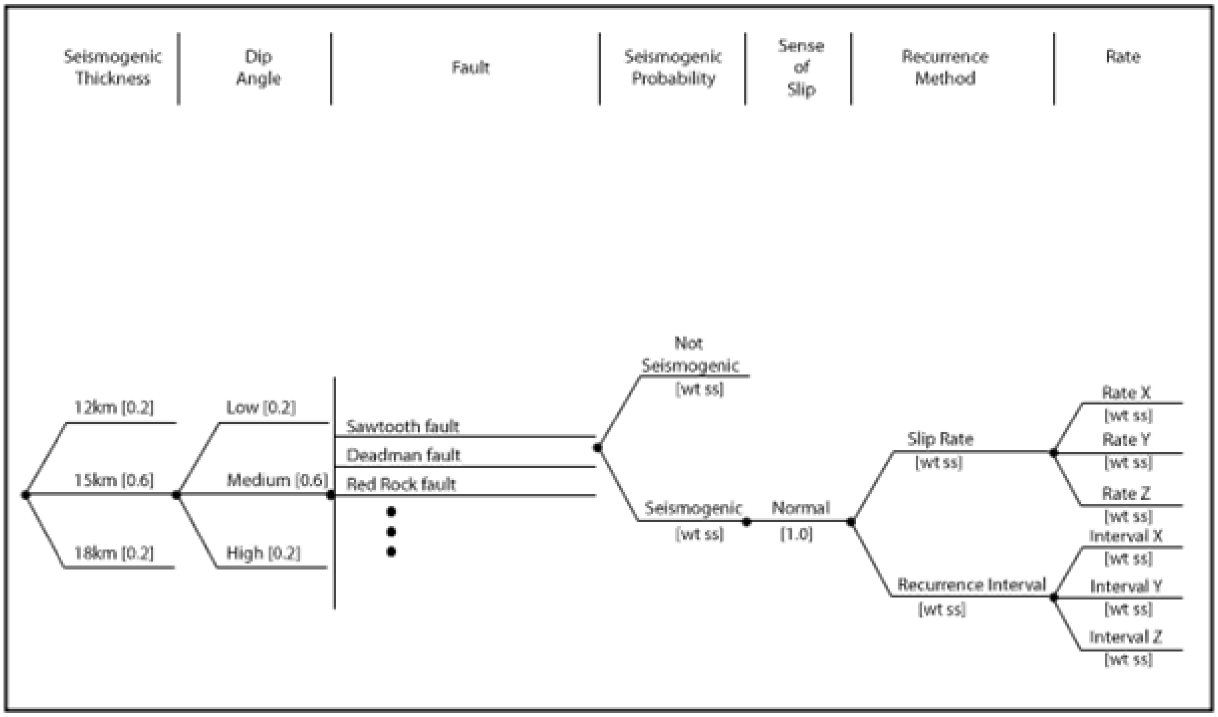

Figure 8-9. Logic tree for the thirteen regional normal fault sources listed in Table 8-2.

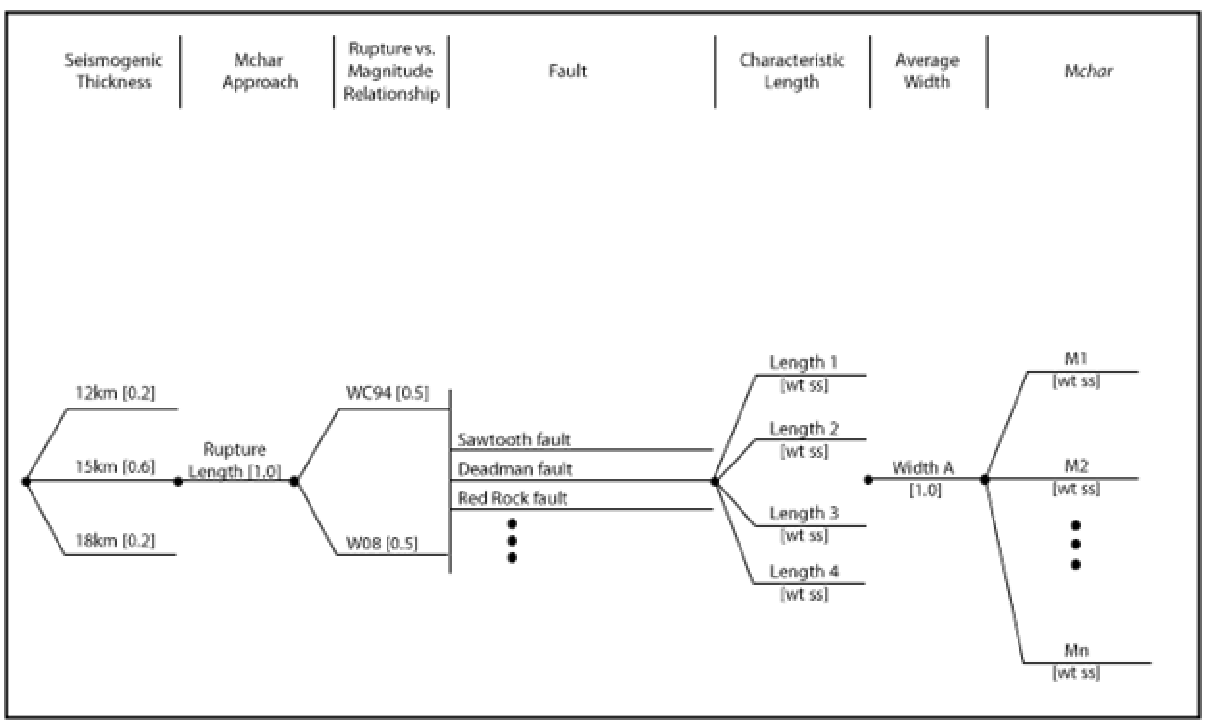

Figure 8-10. Logic tree for the thirteen normal fault sources used to calculate the characteristic magnitudes (Mchar) for each source.

along the lengths of the fault sources. Only those regional faults that have been studied sufficiently to have fault segmentation models published in the literature, have been characterized according to their segmentation behavior.

The logic trees for the local fault sources, which are the Lost River, Lemhi, and Beaverhead faults, have been developed through careful consideration of the full range of geologic, geophysical, and seismologic data covering several decades of investigations. In particular, an extensive re-evaluation of the three local faults was conducted by AMEC (2013) to update the logic trees in light of new data, models, and methods that had become available since the 1996 and 2000 INL PSHAs. As discussed in Section 8.3, the TI Team for the present study reviewed these logic trees in detail and concluded that with a few modifications they continue to represent the center, body, and range of technically defensible interpretations. Where data are available, the epistemic uncertainties captured in the logic trees for the three fault sources include the following:

- Dip
- Depth (seismogenic thickness)
- Southern termination
- Segmentation
- Approach to assessing Mchar
- Rupture dimension versus magnitude empirical relationship
- Displacement per event
- Recurrence model (magnitude frequency distribution)
- Temporal clustering
- Slip rate
- Recurrence interval

8.2 Characterization of Seismic Source Zones

This section provides information regarding the elements of the SSC model that resulted from the TI Team's evaluation of available data, models, and methods and integration process. This discussion is intended to show that the seismic source zones identified are technically defensible and that the center, body, and range of uncertainties included in the model are appropriate. First, the various source zone characteristics and the methods used to assess them are described in Section 8.2.1. Then, the specific seismic source zone characteristics in the SSC model for the source zones are described in Sections 8.2.2 through 8.2.18. Recall the conceptual basis and criteria for identifying seismic sources generally, and for defining source zones specifically, are given in the Section 8.1.

8.2.1 Source Zone Characteristics for the SSC Model

Seismic sources were identified by the TI Team if they exhibited a unique set of characteristics, such as differences in p[S], recurrence, Mmax, or future earthquake characteristics, which indicated they localize seismicity differently from adjacent regions. As a result of applying these criteria, eleven tectonic seismic source zones and six volcanic source zones were developed for the SSC model. The two types of zones differ in the manner by which they were identified and in the characteristics that are used to define their future behavior. Volcanic source zones are defined on the basis of the spatial distribution of mapped volcanic features and the recurrence of earthquakes is based on the recurrence of volcanism.

Tectonic source zone boundaries are defined by geologic, geophysical, and seismologic differences that can give rise to differences in future earthquake characteristics. These characteristics include the seismogenic thickness, style of faulting, Mmax, orientations of future ruptures, etc. The fundamental basis for the assessment of earthquake recurrence within tectonic source zones is the earthquake catalog. The single exception is the CSZ source zone, whose recurrence rate is defined by geodetic slip rates since its existence is implied due to differences in geodetic strain rates. Also, the methods used are applicable to the data that are available for the characterization as well as the tectonic environment of the site region. For example, the characteristics of future earthquakes within the ESRP source zone, such as the style of faulting and orientation of ruptures, are assessed in light of the available geologic and seismologic data within that zone. If uncertainties exist, they are duly incorporated into the model.

It is important to note that the characteristics of the source zones are assessed mindful of the fault sources that may or may not be defined within the source zone of interest. For example, the assessment of the Mmax for the NBR source zone is made in light of the fact that the major faults within that zone have been defined and characterized separately in the SSC model. As a result, the Mmax for the source zone is assessed considering that the dimensions of any additional faults within the zone would be limited and, as a result, the Mmax for the zone would be expected to be lower than the Mmax assessed for the fault sources within the zone. In addition to the relationships between source zones and fault sources, the relationships between alternative source zones have also been defined in the SSC model. For example the existence of the CSZ source zone is uncertain and the characterization of the zones that coincide with the CSZ accounts for the presence or absence of the CSZ zone.

The following subsections include the bases for the seismic source zone boundaries, seismogenic crustal thickness, rupture geometry of future earthquakes, maximum magnitudes, and earthquake recurrence. Consistent with current SSC practice (e.g., NRC, 2012b), seismic source zones are assumed to have a seismogenic probability p[S] = 1 throughout the zone and, unless indicated by source-specific data, the characteristics that define each source are assumed to be uniform throughout the zone. For example, the assessed style of faulting and Mmax distribution would apply to all parts of the zone. As will be discussed in Section 8.2.1.8, one exception is the potential for recurrence parameters to vary spatially within source zones, depending on the spatial characteristics of the observed seismicity within each zone.

8.2.1.1 Source Boundary Locations

Source boundaries specified the three-dimensional location and geometry of a seismic source which is the lateral extend and thickness. Seismic sources are defined by expected differences in earthquake recurrence rate, Mmax, future earthquake characteristics, or p[S]. In the context of source zones, differences in p[S] are not diagnostic because all source zones are assumed to be seismogenic. Differences in earthquake recurrence rate might be defined by distinct differences in the rate density (number of events per unit area) from one domain to another. Those differences might be accommodated either by drawing a source boundary that separates regions having different recurrence rate densities or through the use of a smoothing procedure that accounts for spatial variations in recurrence parameters. Differences in Mmax may be a function of whether or not fault sources have been defined within the source, the number and scale of known faults within the zone, or the size of the largest observed historical or instrumental earthquake. In addition to the observed seismicity record, differences in either recurrence rates or Mmax may also be inferred based on distinct seismotectonic boundaries and features.

Future earthquake characteristics include the seismogenic thickness, style of faulting, and geometry of ruptures. Differences in these characteristics spatially may provide the basis for drawing a source zone boundary. Defining differences in future earthquake characteristics necessitates the consideration of a wide variety of data sets. For example, spatial differences in seismogenic crustal thickness can be identified using earthquake hypocenter depths and by considering major tectonic boundaries. Likewise, expected differences in the geometries of future ruptures can be assessed based on consideration of earthquake focal mechanisms: structural geologic data, seismotectonic features, and geophysical data regarding the orientations of preexisting structures, and kinematic indicators of the orientation of the contemporary tectonic stress regime.

8.2.1.2 Nature of Boundaries with Respect to the Propagation of Future Ruptures

In the hazard calculation procedure, finite fault ruptures nucleate on virtual faults within each source zone. The length and area of rupture for each earthquake are related to the magnitude of the earthquake being modeled. Earthquake ruptures that nucleate near a source zone boundary can either extend across the boundary (a "leaky" boundary) or be terminated at the boundary (a "strict" boundary), depending on the assessed nature of the boundary. In the SSC model, all source zone boundaries are assessed to be leaky to future ruptures. The basis for this assessment is that changes in tectonics, geology, and the seismicity across the zone boundaries are relatively continuous and not sharply delineated. The style of faulting throughout the region is normal faulting and there are no locally and sharply separated regions that have distinctly different rupture strikes or styles of faulting.

8.2.1.3 Seismogenic Crustal Thickness

The thickness of the seismogenic crust defines the depth extent of ruptures that release seismic energy important to ground motions. Seismogenic thickness is typically estimated based on consideration of the depths of earthquake hypocenters and, due to a lack of detailed knowledge of the processes that locally control the thickness at any given point, it is usually assumed that seismogenic thickness varies gradually spatially unless there is clear evidence otherwise. In the SSC model, the uncertainties in seismogenic crustal thickness are included in logic trees for each seismic source zone.

The assessment of seismogenic crustal thickness is based on the focal depth distributions of well-recorded earthquakes, such that hypocentral depth can be determined with a high degree of confidence. Given a well-constrained focal depth distribution, physical considerations given by various researchers suggest that the base of the seismogenic zone is identified as lying near the deepest of the observed focal depths. For example, Scholz (1998) identifies the 300°C isotherm as corresponding to the onset of dislocation creep in quartz, which he interprets to control the seismic/aseismic transition zone. Tanaka (2004) and Tanaka and Ito (2002) compare high-quality thermal measurements and seismicity depth data to examine the concept that temperature is a fundamental parameter for determining the thickness of the seismogenic zone. Their gridded heat flow or geothermal gradient and D_{90}, the depth above which 90% of earthquakes occur, correlated well with each other. The evaluated temperatures for D_{90} range between 250°C and 450°C, which falls within the typical range for defining the seismogenic zone (e.g., Fagereng and Toy, 2011). The TI Team therefore concluded that the approach taken in the CEUS SSC project (NRC, 2012b) of using D_{90} to estimate the depth of the seismogenic crust was appropriate. The hypocenter depth distributions were developed for each seismic source zone using the 1850-2014 catalog with E[**M**]. Epistemic uncertainty associated with the seismogenic thickness is reflected in the logic tree and accounts for uncertainty in the assessment of D_{90} as well as the degree to which D_{90} provides a unique estimate of seismogenic thickness. The assessment of D_{85} and D_{95} was also identified to provide an indication of the uncertainty in seismogenic thickness. The uncertainty in the seismogenic thickness is expressed for each source zone and fault source in their respective source-specific logic trees (Figures 8-5 through 8-9).

The hazard calculations assume that future earthquakes will be associated with finite ruptures whose size is magnitude-dependent. The depth of nucleation (focal depth) of these earthquakes must be specified in the SSC model. The maximum depth is the depth of the seismogenic thickness, but the relative frequency of other focal depths must also be considered. The depth distribution of hypocenters provides valuable information related to the relative frequency of focal depth, but the focal depth data in

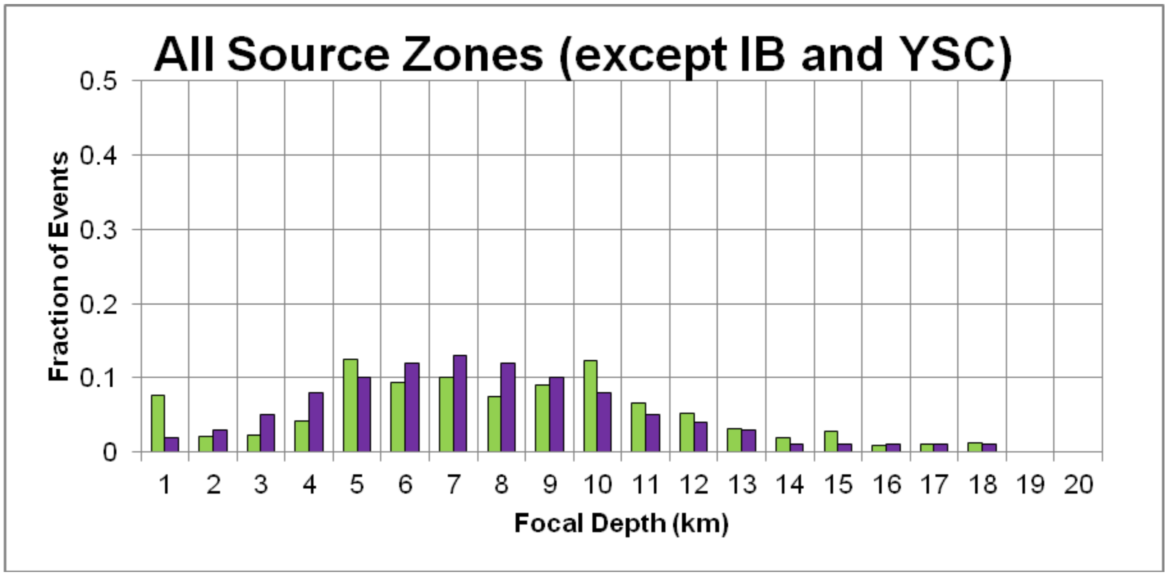

Figure 8-11. Focal depth distribution for earthquakes in all source zones except the IB and YSC source zones where depths were anomalously deep and shallow respectively. The plot shows the actual focal depth histogram with all earthquakes in purple alongside the focal depth distribution for **M**≥3 in green used in the hazard calculations.

the INL region is dominated by small-magnitude (**M**<3) earthquakes. Therefore, consideration must also be given to the observation that the depths of larger magnitude earthquakes commonly occur deeper within the seismogenic crust (e.g., Das and Scholz, 1983; Mori and Abercrombie, 1997).

Within the seismic source zones and along fault sources in the SSC model, the depth distribution of future moderate-to-large earthquake focal depths is defined by a combination of the focal depth distribution for small-magnitude earthquakes and magnitude-dependent models for the location of the hypocenter relative to the rupture for normal faults. The focal depth distribution for all source zones is displayed in Figure 8-11. The focal depth distribution is a starting point for expressing the relative frequency of various nucleation depths of future earthquakes, provided that the observed distribution is judged to be representative of the future depths.

Given the depth distributions and the expected normal style of faulting, the TI Team adopted an approach that would realistically model the downdip rupture of future earthquakes ruptures in the hazard calculations. For each magnitude, rupture area is calculated using the inverse of Hanks and Bakun (2008). For the rupture length-to-width aspect ratio, the model for normal faulting defined in Appendix B of Chiou and Youngs (2008) is used until the width reaches the maximum defined by the crustal thickness and the dip. For each assessed focal depth (defined in 1-km increments beginning at a depth of 1 km), the distribution for the location of the hypocenter with respect to the rupture for normal faults defined in Appendix B of Chiou and Youngs (2008) defines a distribution for how to place the rupture on the hypocenter. If the rupture extends above the surface or below the seismogenic thickness, that case is discarded. Summing the weights for the remaining cases (product of the focal depth frequency and the probability of hypocenter location) and normalizing the results produces a distribution for distance to the top of the rupture (ZTOR) that is a function of magnitude, dip, and thickness.

8.2.1.4 Style of Faulting, Strike, Dip of Future Ruptures

Future earthquakes within the source zones must be described according to the characteristics needed to model them in the GMC model. So, in addition to their depth and rupture area, their style of faulting (also called the sense of slip) and geometry must also be provided. In the case of source zones, these are descriptions that apply to the virtual faults that are modeled in the hazard calculations within each zone.

The assessment of the characteristics of future ruptures comes from a consideration of the tectonic setting, characteristics of nearby fault sources, earthquake focal mechanisms, and other strain indicators including geodetic data. As discussed in Section 4.5, the contemporary tectonic setting in the INL region is extensional as confirmed by historical fault surface ruptures, fault kinematic indicators, earthquake focal mechanisms, and geodetic data. Available earthquake focal mechanisms in the INL region in Figure 4-17 show primarily normal faulting with lesser amounts of strike slip.

The strikes and dips of future earthquakes are assessed based on the orientations and geometries of observed Quaternary faults as well as analogies to other normal faults that have shown coseismic rupture geometries from aftershock sequences. In addition, the assessment of possible strike slip faults within the CSZ source zone is based on a consideration of mapped faults as well as the resolved strains from the geodetic interpretations (Section 8.2.3).

The analyses of the earthquake focal mechanisms are coupled with geologic and tectonic considerations to arrive at aleatory distributions of the styles of faulting, strikes, and dips of future ruptures within each source zone (Table 8-3). The distributions are aleatory and represent the relative frequency of different conditions that are all assessed to be possible within the source zone.

8.2.1.5 Rupture Area Versus Magnitude Relationships for Hazard Analysis

Because future earthquake ruptures within the seismic source zones are modeled as finite faults, their dimensions of rupture must also be modeled. Since they are a function of magnitude as well, the recurrence curves for each seismic source zone will define the relative numbers of earthquakes having particular magnitudes and their associated rupture dimensions. The important assessment here is the relationship between rupture area and moment magnitude. Given a rupture area, the associated length and width are modeled in the hazard calculations.

Alternative rupture area versus magnitude relationships have been proposed in the literature and were considered for application in this study. A common feature of these relationships is that they appear to be insensitive to the style of faulting, such that they can be used for all styles of faulting identified for the source zones in the SSC model. Section 8.3.9 discusses the selection of two alternative relationships for use in assessing the characteristic magnitudes (Mchar) for fault sources appropriate for normal faulting. However, due to the minimal difference in their magnitude ranges of interest and, therefore, minor contribution to uncertainty, only a single rupture area relationship is selected for use in the hazard calculations.

The magnitude dependency for rupture area A is given by the following relationships as given by Hanks and Bakun (2008):

$$\mathbf{M} = \log A + 3.98 \quad \text{for } A \leq 537 \text{ km}^2 \qquad [8\text{-}1]$$

$$\mathbf{M} = 1.33 \log A + 3.07 \quad \text{for } A > 537 \text{ km}^2 \qquad [8\text{-}2]$$

For use in the hazard calculations, a rupture area is needed for a given magnitude, so the inverse of the relationship is used.

8.2.1.6 Maximum Magnitudes

The assessment of maximum magnitudes (Mmax) for seismic source zones usually entails significant uncertainty. Approaches have been developed for use in stable continental regions (Johnston et al., 1994; NRC, 2012b) that rely on a Bayesian procedure, but the INL region does not qualify as a stable continental region, according to the criteria given by Johnston et al. (1994). A common approach to assessing Mmax is to consider the historical record and the largest observed earthquake within the seismic source zone of interest. Accordingly, the largest observed earthquakes within each source zone are given in the summary of source zone characteristics in Table 8-3. In the case of the ESRP source, which hosts the MFC site, the largest observed earthquake is possibly the 1905 Shoshone, Idaho earthquake (E[**M**] 5.61, expected magnitude within the 1850-2014 E[**M**] catalog, see Section 6.2), but it is uncertain if it was located within the ESRP or CBR source zones. As shown in the logic trees for the ESRP and CBR source zones (Figure 8-7), the presence or absence of this earthquake within each zone influences the upper estimate of Mmax for those zones.

An important consideration in assessing Mmax for the source zones in the SSC model is the presence or absence of fault sources within the zone. Fault sources have substantial dimensions (both length and width) and, as a result, are capable of generating larger earthquakes than those parts of the crust lacking through-going faults. Based on this observation, an approach was developed for the NBR and CSZ source zones that accounts for the fact that fault sources within those zones are treated separately in the SSC model. Within the NBR, earthquakes that are associated with the fault sources—particularly the E[**M**] 6.96, 1983 Borah Peak earthquake—have been removed from the source zone earthquake counts for purposes of assessing recurrence. This is because these earthquakes are clearly related to the fault sources and not to the source zone. Also, when the CSZ source zone exists, its geodetic strain rate is used to assess its recurrence rate (see Section 8.2.3) and the component of the slip rate that is resolved onto the faults within the CSZ zone is removed to avoid double-counting the rate from fault slip and from strain within the CSZ zone. Other more distant source zones do not include this consideration of the fault versus the zone seismicity partitioning because of their distance to the site and relative insignificance to site hazard.

The TI Team developed the Mmax distribution for each source zone (Table 8-3) based on one or more of the following considerations:

- Largest observed earthquakes within each zone (used to define the lower limit of the Mmax distribution in all cases)
- Lengths of faults that are not defined as separate fault sources
- Mmax distribution for fault sources within each zone
- Analogues of similar source zones within comparable tectonic environments.

8.2.1.7 Earthquake Recurrence

The assessment of earthquake recurrence within the seismic source zones entails the development of a catalog of earthquakes having a uniform size measure (moment magnitude), removal of dependent events through a declustering process, and correction of the catalog for incompleteness. As discussed in Appendix D, a significant effort was devoted to developing a comprehensive earthquake catalog that includes both historical and instrumental earthquakes merged from various data sources and to converting all earthquakes from their native size measure to **M** (Section 6). There is uncertainty in the magnitudes estimated for each earthquake, which is quantitatively addressed for purposes of recurrence calculations accounting for the bias that is introduced due to the exponential distribution of earthquake magnitudes

Table 8-3. Parameters with values and uncertainties for tectonic seismic source zones.

Parameter	ESRP	CBR	NBR (background)	CTB (background)	CSZ1 (background)	CSZ2, CSZ3, and CSZ4 (background)	ISB (background)	NISB	IB	EZ	YSC	WSRP
Seismogenic Thickness	12km [0.2] 15km [0.6] 18km [0.2]	12km [0.2] 15km [0.6] 18km [0.2]	12km [0.2] 15km [0.6] 18km [0.2]	12km [0.2] 15km [0.6] 18km [0.2]	12km [0.2] 15km [0.6] 18km [0.2]	12km [0.2] 15km [0.6] 18km [0.2]	12km [0.2] 15km [0.6] 18km [0.2]	12km [0.2] 15km [0.6] 18km [0.2]	12km [0.2] 15km [0.6] 20km [0.2]	12km [0.2] 15km [0.6] 18km [0.2]	8km [0.2] 12km [0.6] 15km [0.2]	12km [0.2] 15km [0.6] 18km [0.2]
Style of Faulting	Normal (100%)	Normal (100%)	Normal (100%)	Normal (100%)	Normal (0.2) Oblique-Normal (0.3) Strike-Slip (0.5)	Normal (0.3) Oblique-Normal (0.6) Strike-Slip (0.1)	Normal (90%) Strike-Slip (10%)	Normal (100%)	Normal (100%)	Normal (100%)	Normal (100%)	Normal (100%)
Strike of Ruptures	115° (25%) 140° (50%) 170° (25%)	0° (25%) 30° (50%) 60° (25%)	0° (25%) 330° (50%) 300° (25%)	250 (10%) 270 (10%) 300 (20%) 330 (40%) 360 (20%)	55° (25%) 70° (50%) 100° (25%)	0° (25%)[1] 40° (25%) 60° (25%)[1] 85° (25%)	320° (70%) 0° (20%) 20° (10%)	Uniform Aleatory Distribution	Uniform Aleatory Distribution	Uniform Aleatory Distribution	Uniform Aleatory Distribution	290° (10%) 310° (80%) 330° (10%)
Dip of Ruptures	40° (15%) 55° (75%) 89° (10%)	30° (25%) 55° (50%) 75° (25%)	35° (25%) 50° (50%) 65° (25%)	Normal 30° (20%) 55° (40%) 75° (40%)	Normal and Oblique 65° (25%) 75° (50%) 85° (25%) Strike-Slip 90°	Normal and Oblique 65° (25%) 75° (50%) 85° (25%) Strike-Slip 90°	Normal 30° (10%) 55° (60%) 75° (30%) Strike-Slip 75° (25%) 90° (75%)	30° (25%) 55° (50%) 75° (25%)	30° (25%) 55° (50%) 75° (25%)	30° (25%) 55° (50%) 75° (25%)	30° (25%) 55° (50%) 75° (25%)	50° (25%) 60° (50%) 70° (25%)
Dip Direction	SW (50%) NE (50%)	E (50%) W (50%)	SW (75%) NE (25%)	NE (50%) SW (50%)	NW (50%) SE (50%)	NW (50%) SE (50%)	E (25%) W (75%)	Uniform Aleatory Distribution	Uniform Aleatory Distribution	Uniform Aleatory Distribution	Uniform Aleatory Distribution	NE (100%)
Mmax	5.5 [0.185] 6.0 [0.63] 6.5 [0.185]	7.0 [0.185] 7.25 [0.63] 7.50 [0.185]	6.25 [0.185] 6.5 [0.63] 6.75 [0.185]	6.75 [0.185] 7.0 [0.63] 7.25 [0.185]	6.25 [0.185] 6.5 [0.63] 6.75 [0.185]	6.25 [0.185] 6.5 [0.63] 6.75 [0.185]	7.25 [0.185] 7.5 [0.63] 7.75 [0.185]	6.75 [0.185] 7.0 [0.63] 7.25 [0.185]	6.75 [0.185] 7.0 [0.63] 7.25 [0.185]	5.50 [0.185] 6.0 [0.63] 6.5 [0.185]	6.3 [0.185] 6.6 [0.63] 6.9 [0.185]	6.50 [0.185] 6.75 [0.63] 7.0 [0.185]
Maximum Magnitude Observed Within Zone[2]	E[**M**] 5.61 1905 Shoshone	E[**M**] 6.01 2008	E[**M**] 5.53 1984	1897 M 6.4 E[**M**] 6.12 1947	E[**M**] 5.97 1964	E[**M**] 5.97 1964	E[**M**] 6.57 1934	E[**M**] 6.2 1925	E[**M**] 5.88 1944	E[**M**] 5.2 1995	E[**M**] 6.33 1975	Historical (trench) **M** 6.7 Instrumental **M** 5.6 May 13, 1916
Spatial Variation of Recurrence	Uniform (1.0)	Uniform (1.0)	See Logic Tree in Figure 8-7	See Logic Tree in Figure 8-7	Uniform (1.0)	Uniform (1.0)	Smoothing (1.0)	Smoothing (1.0)	Smoothing (1.0)	Smoothing (1.0)	Uniform (1.0)	Uniform (1.0)

1. In the MFC and NRF PSHAs, the distribution of strike was 40° (25%), 60° (50%), 85° (25%). For the ATR PSHA, based on new data the strike of 0° was included as (25%) and the strike of 60° was reduced from 50% to 25% (see Section 8.2.3.6).
2. Magnitude is the expected magnitude, E[**M**], in the 1850-2014 earthquake catalog unless otherwise described. References for WSRP: trenching from Beukelman (1997); instrumental from Stover (1993).

in a recurrence curve (Section 6.2.4). The results are expressions of the expected magnitude E[**M**] for each earthquake in the catalog and corrected counts N* that account for this uncertainty and bias.

The assessment of recurrence for the source zones containing fault sources is a function of whether or not some of the seismicity within the source zones is assigned to the fault sources or is assessed not to be associated with the fault sources. This study considers seismicity within “capture areas” of the fault sources to be associated with the fault and thus taken out of the recurrence calculation for the source zone. The capture area is defined by the area neighboring a fault source and by projecting the fault dip and seismogenic depth to an area at the surface. See Section 8.2.5.3 in discussion of recurrence curves for individual source zones which show the influence of extracting the fault associated events from the source zone recurrence.

In addition, the earthquake catalog has been declustered to remove dependent earthquakes (foreshocks and aftershocks) using several declustering algorithms (Section 6.3). The resulting catalogs of independent events are appropriate for use in recurrence calculations that are based on the assumption that all earthquakes occur according to a Poisson process. Finally, an analysis of catalog completeness was conducted, which includes the assessment of the probability of detecting earthquakes as a function of time and magnitude in the region of the catalog (Section 6.4). The completeness analysis process used allows for full use of the historical and instrumental catalog.

The calculation of earthquake recurrence for source zones is done assuming an exponential distribution of magnitudes, incorporating the uncertainties in magnitudes, and correcting for the bias in counts due to the exponential distribution (Section 6). Based on the maximum likelihood approach used, the uncertainties in rates for each magnitude bin are a function of the counts within each bin, which are discussed in Section 8.2.5.3. The uncertainties increase with increasing magnitudes and decreasing counts of earthquakes. In the case of all the INL source zones, there are no or very few observed earthquakes in the largest magnitude bins near the maximum magnitude and very few earthquakes in the larger magnitude bins. Because the maximum likelihood approach to recurrence calculation accounts for the numbers of events within each bin (Weichert, 1980), the recurrence curve is not very sensitive to the counts in the largest magnitude bins. This explains why the recurrence curves are either above or below the mean counts in the largest observed magnitude bins.

8.2.1.8 Spatial Variation of Recurrence

One of the criteria for defining seismic sources is differences in earthquake recurrence, which can be expressed as differences in the spatial density of earthquake occurrence defined by the pattern of observed earthquakes. If the observed pattern of spatial density variation is judged to be representative of the future distribution, the spatial pattern can be accounted for in the SSC model by either drawing seismic source boundaries or by spatially smoothing the recurrence parameters. Accordingly, the SSC model is based to a large extent on an assessment that spatial stationarity of seismicity will persist for time periods of interest for the INL PSHA (approximately the next 50 yr). Stationarity in this sense does not mean that future locations and magnitudes of earthquakes will occur exactly where they have occurred in the past, based on the historical and instrumental record. Rather, the degree of spatial stationarity varies as a function of the type of data available to define the seismic source. Fault sources are based on geologic evidence of localized deformation from repeated large-magnitude earthquakes that occur in approximately the same location (i.e., the same fault) over geologic time periods. Uncertainties in the locations and sizes of these events are a function of the types of data available. Because the record that defines the fault sources spans a relatively long time period and records large-magnitude events, repeated events for these sources are expected to occur within a restricted location defined by the fault source.

On the other hand, patterns of seismicity within seismic source zones are defined from generally small- to moderate-magnitude earthquakes that have occurred during a relatively short (i.e., relative to the repeat times of large events) historical and instrumental record. Thus the locations of future earthquakes are not as tightly constrained by the locations of past earthquakes as they are for fault sources. Some recent studies within stable continental regions, such as the CEUS SSC study (NRC, 2012b), have identified very large seismic source zones and have used “spatial smoothing” to express the spatial variation of recurrence rates. In the CEUS SSC study, b-values vary little across the study region and a-values vary at scales judged by the TI Team to reflect the belief that the observed record provides a spatial constraint on rate density variation. Likewise, in that smoothing approach, the recurrence calculation considers weighting of magnitudes in the recurrence rate calculations such that moderate events are assigned more weight than smaller events.

Spatial density models are used to define the future spatial density of earthquakes in the source zones when observed seismicity is used to define earthquake recurrence. The standard assumption is the location of future seismicity within a seismic source zone is spatially homogeneous with equal probability. Musson (2000) notes that this assumption is integral to an acceptable seismic hazard model and proposed that seismic hazard models be tested to verify that observed seismicity within particular source zones conforms to this assumption. Musson (2000) provides approaches for testing how well the observed seismicity pattern in a source zone conforms to the assumption of spatial homogeneity. He notes that a homogeneous pattern of seismicity does not need to necessarily be a uniform pattern, but may be random and not spatially clustered. If the seismicity within a source zone is not spatially homogeneous, then an explanation should be provided for the inhomogeneity (perhaps it has a tectonic explanation), the zone should be subdivided into smaller zones that each are homogeneous, or spatial smoothing should be considered to account for the spatial variations.

The observed seismicity within the seismic source zones in the SSC model shows that nearly all of the earthquakes are small in magnitude (E[**M**]<4) and their epicenters are not uniformly spaced (Figure 8-12). Visual observation of the epicenters shows evidence of spatial clustering in the “seismic parabola” surrounding the ESRP.

As noted by Musson (2000), even random distributions, which are homogeneous, show local evidence of spatial clusters. To test whether or not the seismicity within the seismic sources is spatially homogeneous, the nearest-neighbor analysis given by Musson (2000) was applied to all tectonic source zones. The volcanic source zones were not subject to the analysis because of their small size and extremely low numbers of observed seismicity within the zones. The seismicity within each zone was used after removal of events that were judged to be related to the fault sources and only independent events (not foreshocks or aftershocks, based on the declustering analysis) were used. The nearest neighbor results indicated that the observed seismicity in all tectonic zones is non-random except in the CBR and YSC, which can be considered consistent with a homogeneous distribution. The ESRP and WSRP zones were not subject to the test because of the very low number of observed earthquakes: it is assumed that a homogeneous distribution of the seismicity applies to these zones.

Given the results of these homogeneity tests, the TI Team also considered other key issues that are important in the consideration of spatial stationarity and whether or not spatial smoothing of recurrence parameters was appropriate for the seismic source zones. An important consideration is the fact that although the spatial distribution of observed events is based on smaller-magnitude earthquakes, the spatial smoothing of recurrence parameters would be used in the hazard analysis to describe the spatial variation of moderate-to-large-magnitude earthquakes. Another important consideration is which recurrence parameters are subject to smoothing. The TI Team decided to allow for smoothing of the equivalent number of events, N*, but to consider b-values to be uniform (with appropriate uncertainty) throughout each source zone. This assessment is consistent with the assessments of b-values for the source zones in

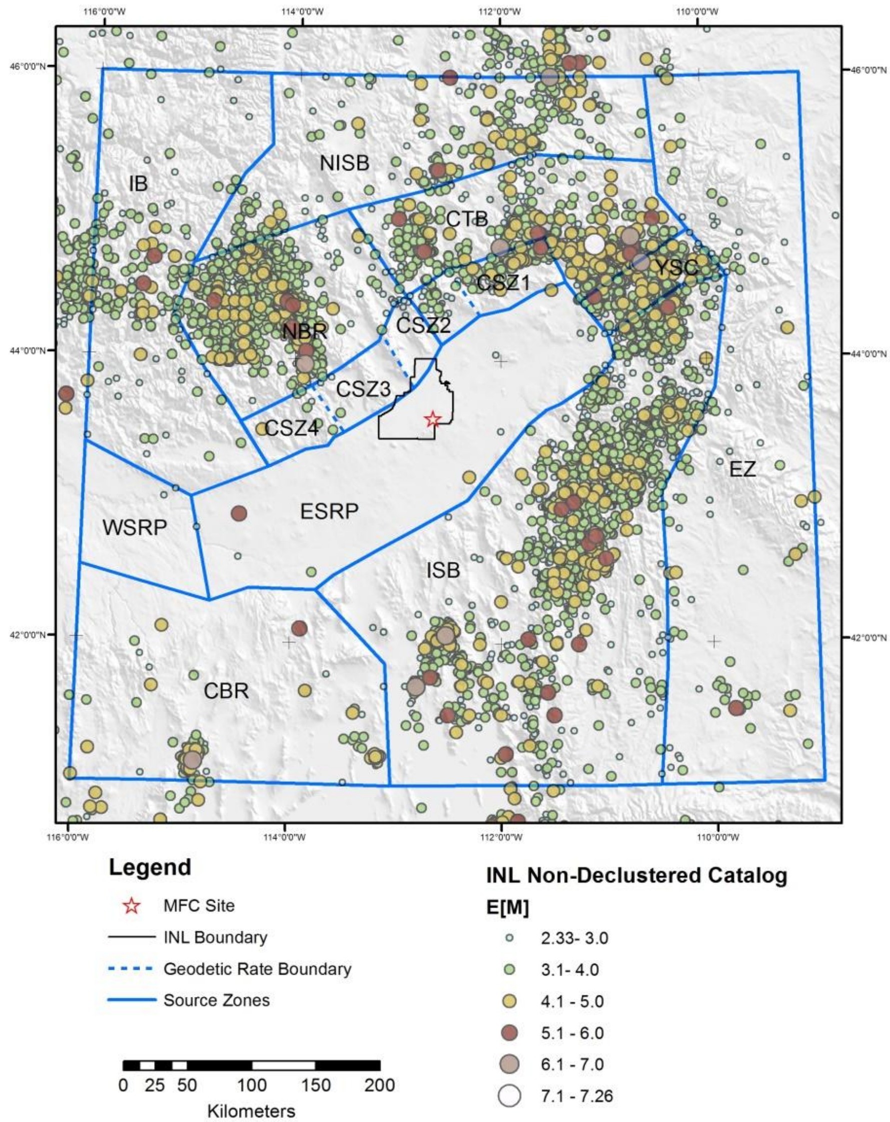

Figure 8-12. Map showing source zones with the 1850-2014 E[**M**] seismicity catalog.

the CEUS SSC project (NRC, 2012b). In that study, the source zones are very large relative to the size of the INL PSHA sources (by more than a factor of 10), yet very little variation in b-values was assessed. This is also consistent with the constant b-values assessed for seismic source zones in the U.S. National Seismic Hazard maps (Petersen et al., 2008). Given the relatively small dimensions of the INL seismic source zones and the absence of tectonic mechanisms that might suggest that spatial variations in b-values might be appropriate (e.g., active volcanic-related seismicity), the TI Team assessed the b-values within each source zone to be uniform.

In light of the various issues defined above, the TI Team decided to conduct spatial smoothing for all tectonic zones except CBR, YSC, ESRP, and WSRP, which were assessed to have a uniform spatial distribution of recurrence parameters. The approach taken for spatial smoothing is the approach recommended by Stock and Smith (2002) as a preferred approach to the fixed smoothing kernel approach because it uses an adaptive kernel (Silverman, 1986). In this approach, the kernel size is adjusted throughout the study region, decreasing in size in areas of higher data density and increasing in size in areas of sparse data. The initial kernel bandwidth (h) was selected for these source zones by testing values of h from 5 to 100 km, in 5-km increments and log-likelihood according to the procedure given by Silverman (1986). The adaptive kernel method was then used to define the final spatial density for the hazard calculations.

8.2.2 Characterization of the Host Zone

The INL resides in the ESRP which makes it the host zone. Characteristics of the ESRP host zone include its p[S], boundaries, seismogenic thickness, earthquake recurrence, Mmax, and future earthquakes. The ESRP lacks seismicity (>80 microearthquakes of **M**<2.5, Section 4.4.8) as compared to the surrounding Basin and Range regions (>83,000). As discussed previously, the E[**M**] 5.61 1905 Shoshone earthquake may be located within or outside the ESRP. Geologic and geophysical data are available to assess its characteristics and along with the limited seismologic data uncertainties are duly incorporated into the model.

As with the other nearby tectonic seismic source zones, the ESRP has a seismogenic probability and leaky boundaries. Based on its limited seismologic data, the ESRP host zone has an assumed seismogenic probability p[S]=1, which is consistent with current SSC practice (e.g., NRC, 2012b). As discussed in Section 8.1.5.1, source zone boundaries in the SSC model are assumed to be leaky. Fault ruptures that originate near a source zone boundary can extend beyond the boundary and are not terminated at the boundary. This is important for the ESRP since the southern terminations of the Lost River, Lemhi, and Beaverhead may extend into the ESRP (Figure 8-4).

8.2.2.1 Source Zone Geometry

The source zone boundary of the ESRP was adopted from the SET evaluation performed for sensitivity analysis regarding the source zonation model and modified in this study. The SET evaluated the boundaries of not only the ESRP, but other tectonic seismic source zones for the purposes of including a seismic parabola source zone (Seismic Evaluation Team, 2010). The SET made minor modifications to the southern boundary of the ESRP where it abuts the CBR seismic source zone for its original boundary model in the 1996 INL PSHA. For this study, the northwestern boundary between the ESRP and the NBR and CTB seismic source zones were modified. The minor modifications are consistent with the boundary proposed by Payne et al. (2013) for the CSZ (Figure 8-3).

8.2.2.2 Seismogenic Thickness

The seismogenic thickness for the ESRP host zone was assessed to be the same as the surrounding tectonic seismic source zones (NBR and ISB). Focal depths of earthquakes within the 1850-2014 depth-sorted catalog and supplemented with 68 well-determined focal depths of ESRP earthquakes were evaluated to assess the seismogenic thickness of the ESRP. The results presented in Section 5.2 showed that focal depths of earthquakes within the ESRP are similar to the range of focal depths in the surrounding NBR and ISB, generally <20 km. Based on these results, the seismogenic depths for the ESRP host zone were chosen to be the same as those assessed for the CTB and ISB using the D_{90} analysis (Sections 8.2.1.3 and 8.2.5.2). The seismogenic depths and weights for the ESRP are 12 km [0.2], 15 km [0.6], and 18 km [0.2] (Table 8-3).

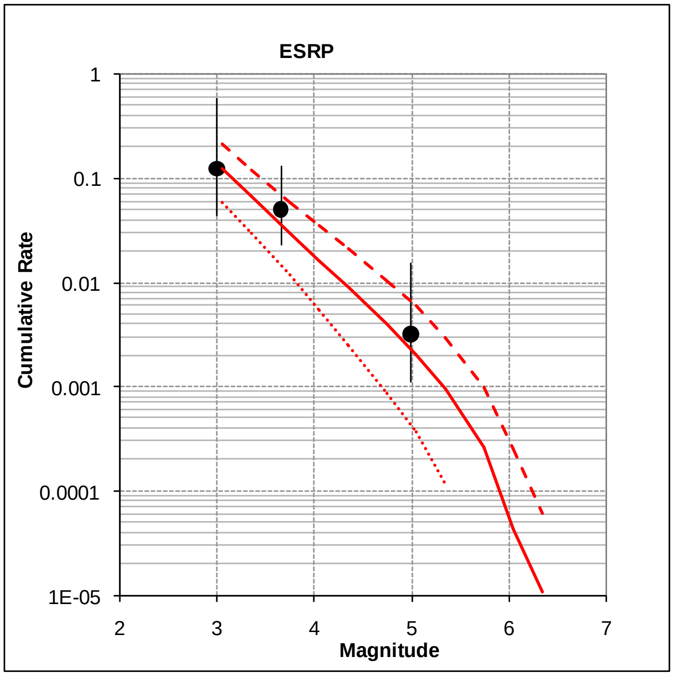

Figure 8-13. Plot shows the earthquake recurrence (cumulative rate versus magnitude) for the ESRP host zone (solid red line). The weighted recurrence is computed using the alternatives for when the 1905 E[**M**] 5.61 earthquake is within the ESRP [0.33] and outside the ESRP [0.67] (see logic tree in Figure 8-7). The observed earthquake rates (black dots) with their 90% confidence limits, and the 5th percentile (dotted red line) and 95th percentile (dashed red line) are also shown.

8.2.2.3 Earthquake Recurrence

The earthquake recurrence for the ESRP host zone was assessed using the four declustered 1850-2014 E[**M**] catalogs (Section 6.3), a correction for completeness (Section 6.4), and the weights assigned to the alternatives for the location of the 1905 Shoshone earthquake, within the ESRP or within the CBR seismic source zones. The resulting catalogs used in the analysis have independent events, which assume that all earthquakes occur according to a Poisson process. The earthquake recurrence method discussed in Section 6.2.4 is used to calculate earthquake recurrence for the ESRP and other tectonic seismic zones (see also Sections 8.2.17 and 8.2.5.3). The earthquake recurrence of the ESRP, shown in Figure 8-13, was used in the SSC model. The uncertainties are shown in Figure 8-13 by the error bars associated with the mean counts. The uncertainties increase with increasing magnitudes and decreasing counts of earthquakes. The recurrence curve is fit to three earthquakes of E[**M**]>3 and takes into account the alternatives for when the E[**M**] 5.61 1905 Shoshone earthquake is located within the ESRP host zone weighted as [0.33] and when it is not at a weight of [0.67] (see logic tree in Figure 8-7). The assigned weights reflect the probability of the 1905 earthquake being in the ESRP due to the uncertainty in its location. Although the assigned weights are assumed, they reflect the observation that the majority of earthquakes occur more often in the surrounding Basin and Range regions than in the ESRP (Figures 4-11 and 4-12).

8.2.2.4 Spatial distribution of Recurrence Parameters

Due to its lack of seismicity, the ESRP seismic source zone was assumed to have a uniform future spatial distribution of recurrence parameters. Figure 8-12 shows the distribution of earthquakes in the 1850-2014 E[**M**] catalog and the ESRP seismic source zone has <20 events within its boundaries.

8.2.2.5 Maximum Magnitude

Two Mmax and their distributions are assessed to the ESRP host zone based on an evaluation of analog earthquakes and consideration of the location of the E[**M**] 5.61 1905 Shoshone earthquake. With the exception of the 1905 earthquake, only microearthquakes of **M**<2.5 have occurred in the ESRP (Figure 4-15). The assessment of Mmax in Section 5.3 considers earthquakes in eastern Oregon and those associated with dike intrusion (see Table 5-2). Eastern Oregon was considered an analog due to its low-strain rate and mafic densification of the crust, similar to the ESRP. Since VRZs are located within the ESRP, slip would occur on the same pre-existing faults whether due to magmatic or tectonic processes. From the evaluation in Section 5.3, a maximum of **M** 6.0 ± 0.5 was assessed to be representative for the ESRP. For the SSC model, Mmax with weights were assigned as **M** 5.5 [0.185], 6.0 [0.63], and 6.5 [0.185] assuming the 1905 Shoshone earthquake is within the ESRP. For when the 1905 earthquake is not in the ESRP, Mmax with weights were assigned as **M** 5.0 [0.185], 5.5 [0.63], and 6.0 [0.185] (Table 8-3). The lower Mmax for when the 1905 Shoshone earthquake is assessed because without the 1905 earthquake, the observed E[**M**] in the ESRP is lower.

8.2.2.6 Properties of Future Earthquake Ruptures

For the ESRP seismic source zone, the properties of future earthquake ruptures include the characterization of the style of faulting, fault strike and fault dip (Section 8.2.1.4). The uncertainty distributions for these properties are given as relative frequency distributions (or percentages) because they are aleatory in nature (Section 8.1.5). Slip on future faults within the ESRP could occur on pre-existing faults produced either by tectonic or magmatic processes. Thus, the future earthquake rupture properties are based on fault plane solutions computed for ESRP microearthquakes, volcanic deformational features produced by dike intrusion, and similarity with Basin and Range normal faults.

Since the ESRP resides in an extensional regime and it has dike-induced deformation exhibited in the Great Rift VRZ (see Sections 4.2 and 4.5), the style of future faulting is assessed to be normal (100%). Normal faulting is also supported by fault plane solutions of three microearthquakes M<1.7 (Figure 4-17) in the ESRP. Future strikes of normal faults (given as orientations from north) are assessed to be 115° (25%), 140° (50%), and 170° (25%). The strikes encompass the range of small normal faults, fissures, and aligned volcanic vents produced by dike intrusion that are evident in the ESRP (Figure 4-18). Future fault dips are assessed to be 40° (15%), 55° (75%), and 89° (89%). The range of future fault dips is consistent with dips assessed for normal fault dips within the Basin and Range region (Table 8-3) and those that may be produced by dike intrusion (Payne et al., 2009). As a result of dike intrusion, the graben bounding normal faults have opposing dips (Figure 4-6). Therefore, dip directions of future faulting are assessed to be both NE (50%) and SW (50%).

8.2.3 Characterization of the Centennial Shear Zone

The CSZ source zone was added to the SSC model for this study. Recent geodetic studies completed since the 2010 SET study reveal that the CSZ may be an accommodation zone between the slowly deforming ESRP and the rapidly deforming CTB (Payne et al., 2012). The different strain rates are accommodated by right-lateral shear in the CSZ (Figure 4-3). Payne et al. (2012) estimated slip rates of right-lateral strike-slip motion that range from 0.1 to 1.4 mm/yr along the boundary between the ESRP and CTB. Results of the geodetic studies combined with geologic data are used to characterize the CSZ source zone including its p[S], boundaries, seismogenic thickness, earthquake recurrence, Mmax, and future earthquakes.

The CSZ is assessed to exist with a probability of [0.5] and, assuming it exists, it is subdivided into four zones (CSZ1, CSZ2, CSZ3, and CSZ4) based on differences in geodetic rates. A probability of 0.5 was chosen since there are alternative hypotheses proposed for CSZ region, such as crustal flexure due to subsidence of the ESRP (McQuarrie and Rodgers, 1998; Rodgers et al., 2002) and reduced strain rates resulting from passage of the Yellowstone hotspot (e.g., Pierce and Morgan, 1992; Anders and Sleep, 1998). Also no discernable strike-slip offsets are evident in the geology along the northwest margin of the ESRP. Finally, geodetic rates of a decade or more may or may not reflect long-term deformation rates in the CSZ.

8.2.3.1 Source Zone Geometry

The CSZ source zone overlaps with the NBR and CTB source zones and is subdivided into smaller zones (Figures 8-1 and 8-2). The CSZ source zone boundaries are from Payne et al. (2013). The CSZ is a 40-45 km wide zone along the northern margin of the ESRP. Payne et al. (2012) estimated slip rates of right-lateral strike-slip motion that range from 1.4 mm/yr near the Centennial fault to 0.1 mm/yr near the Sawtooth fault. Since the slip rates decrease from northeast to southwest, four subzones were created to accommodate these changes (Table 8-4).

8.2.3.2 Seismogenic Thickness

The seismogenic thickness of the CSZ was assessed to be the same as the NBR and CTB source zones. The assessment of seismogenic thickness considered the focal depths calculated from the D_{90} analysis of the 1850-2014 E[**M**] catalog (Section 8.2.1.3) for the CSZ: D_{85}=14.11, D_{90}=16.00, and D_{95}=18.00 km. The range of focal depths within the CSZ is similar to those calculated for the NBR and CTB (Table 8-5). Based on these results and considerations of the seismogenic depths used in previous INL PSHAs, the distribution of seismogenic thickness for CSZ is 12 km [0.2], 15 km [0.6], 18 km [0.2] (Table 8-3).

8.2.3.3 Earthquake Recurrence

The earthquake recurrence for the CSZ source zone was characterized by different geodetic rates in each subzone. The subzone geodetic rates used in the SSC model were calculated and are the geodetic rates remaining after partitioning to the fault sources located within each subzone. Payne et al. (2013) proposed that components of deformation within the CSZ may include strike-slip faulting, distributed simple shear, regional-scale rotation, or some combination of these. There are five fault sources that fall within CSZ subzones: the Centennial fault (CSZ1) and the southern segments of the Deadman (CSZ2), Beaverhead (CSZ2), Lost River (CSZ3), and Lemhi (CSZ3) faults (Figure 8-3). It is assumed that the recurrence estimates for each of the five fault sources already includes any components of strike-slip motion due to right-lateral shear (i.e., distributed simple shear). The starting geodetic rates were obtained from Payne et al. (2012) and were used to calculate the remaining geodetic rate after partitioning. The methods used and calculations of the rate partitioning to the five faults are discussed in detail in Section 5.1; only results are listed in Table 8-4.

In the SSC model, the subzone geodetic rates listed in Table 8-4 were applied assuming the CSZ exists. Assuming it exists, the earthquake recurrence curves for the NBR and CTB were calculated without the earthquakes that fall within the CSZ subzones. When the CSZ does not exist, then the earthquake recurrence curves for the NBR and CTB were calculated using earthquakes that fall within the entire NBR and CTB source zones (Section 8.2.4.3).

Table 8-4. Geodetic rates for CSZ subzones.

Source Subzone	Subzone Geodetic Rate (mm/yr)
CSZ1	0.27 [0.2] 0.37 [0.6] 0.57 [0.2]
CSZ2	0.26 [0.2] 0.36 [0.6] 0.56 [0.2]
CSZ3	0.26 [0.2] 0.36 [0.6] 0.46 [0.2]
CSZ4	0.0 [0.2] 0.1 [0.6] 0.2 [0.2]

8.2.3.4 Spatial distribution of Recurrence Parameters

The future spatial distribution of recurrence parameters is assumed to be uniform in each of the CSZ subzones. This is because the geodetic data do not provide sufficient spatial variation to see spatial variations in rate. CSZ subzones use geodetic rates for earthquake recurrence.

8.2.3.5 Maximum Magnitude

The Mmax distribution for all CSZ subzones is assessed to be **M** 6.25 [0.185], 6.5 [0.63], and 6.75 [0.185] (Table 8-3) based on analog earthquakes associated with strike-slip faulting in an extensional regime. As discussed in Section 5.3.3, the 1934 E[**M**] 6.57 Hansel Valley earthquake represents the best analog for maximum magnitude since it occurred in the ISB. The ISB has a right-stepping en echelon pattern of active normal faults that is indicative of a region undergoing left-lateral shear as proposed by Payne et al. (2012) to accommodate differences in strain rates between the ESRP and ISB.

8.2.3.6 Properties of Future Earthquake Ruptures

For the CSZ subzones, properties of future earthquake ruptures include the characterization of the style of faulting, fault strike, and fault dip (Section 8.2.1.4). The uncertainty distributions for these properties are given as relative frequency distributions (or percentages) since they are aleatory in nature (Section 8.1.5). In the CSZ, Payne et al. (2013) hypothesizes that right-lateral strike slip motions may be accommodated on E- and NE-trending normal faults (Figure 4-3). Thus, the style of faulting in each of the subzones includes normal, oblique-normal, and strike-slip with the highest weights corresponding to the variations in strike orientations of existing faults in that subzone (Table 8-3). Within the CSZ, strikes, dips, and dip directions of NE-trending normal faults from field measurements (Zentner, 1989; Janecke, 1992; Rodgers et al., 2002) and fault plane solutions (Stickney, 1997; 2007) were used to assess the distributions of these parameters listed in Table 8-3 for the SSC model. For the ATR, the strike orientations were revised to include the results of Parker and Sears (2016) who found the strikes of strike-slip faults and related fractures to be 200±20.0°.

8.2.4 Characterization of the Tectonic Seismic Source Zones

This section describes the characterization of the Intermountain Seismic Belt (ISB), Northern Intermountain Seismic Belt (NISB), Northern Basin and Range (NBR), Centennial Tectonic Belt (CTB), Idaho Batholith (IB), Western Snake River Plain (WSRP), Central Basin and Range (CBR), Yellowstone Caldera (YSC), and Eastern Zone (EZ) tectonic seismic source zones (Figure 8-1). These zones represent all of the tectonic seismic source zones in the SSC model with the exceptions of the ESRP and CSZ (Sections 8.2.2 and 8.2.3, respectively). The tectonic seismic source zones vary in location, size, and the number of fault sources contained within the zones (Figure 8-3) as well as in the physiographic province in which they are located. However, they are described together in this section since they have similar characteristics and similar technical basis for assessment in the SSC model.

8.2.4.1 Source Zone Geometry

The tectonic seismic source zone boundaries were adopted and modified from the SET's sensitivity analysis which involved evaluating an alternative source zonation model (Seismic Evaluation Team, 2010). The alternative source zonation model included some of the same tectonic seismic source zones used in this study. In 2010, the SET evaluated and modified the boundaries of the seismic source zonation model originally developed in the 1996 INL PSHA, which was also used without modifications in the 2000 INL PSHA (Woodward-Clyde Federal Services et al., 1996; URS Greiner Woodward Clyde Federal Services et al., 1999; 2000). The modifications to the boundaries of the 1996 zonation model were based on the SET's evaluation of primarily the 1850-2007 seismicity catalog (Carpenter, 2010) and other new data available since completion of the 2000 INL PSHA. In this SSHAC Level 1 PSHA, changes to the boundaries of the tectonic seismic sources take into consideration the SET recommendations (Seismic Evaluation Team, 2010) and new data, models, and methods available since completion of the SET's 2010 evaluation.

The major factors influencing the relative positions of the seismic source zone boundaries are transitions in major physiographic boundaries that surround the SRP. The SRP extends in a broad arc across southern Idaho and is juxtaposed against contrasting provinces that include the Basin and Range, Yellowstone Plateau, and the Idaho Batholith provinces. An overview of the tectonic setting and detailed descriptions of these provinces is discussed in Section 4. A major change across these physiographic provinces is in the relative concentrations of seismicity. The region immediately surrounding the ESRP source zone is known as the Seismic Parabola (after Smith and Braile, 1994) which transects many source zones including the NBR, CTB, YSC, and ISB as seen in Figure 8-12 and Figure 4-11. The concentrations of seismicity dissipates away from the zones in the Seismic Parabola region and therefore lower earthquake recurrence rates are observed in the CBR, WSRP, IB, EZ, and NISB seismic source zones (Figure 8-12).

The changes in relative seismicity concentrations have created challenges in building past SSC models. For comparison to past studies and in order to discuss relative locations of source zone boundaries, Figure 8-14 shows the locations of the source zone boundaries relative to the SET's alternative source zonation model (Seismic Evaluation Team, 2010) and the zonation model used in the 1996 INL PSHA (Woodward-Clyde Federal Services et al., 1996). A summary of the source zone geometries and modifications made in this study are described for each seismic source zone.

Central Basin and Range (CBR). The CBR source zone is positioned in the southwest corner of the study area (Figure 8-14). The locations of the boundaries were adopted directly from the SET's alternative source zonation model, which were changed significantly from the 1996 INL PSHA. The northern boundary of the CBR indicates a physiographic province change from the SRP to the north and the Basin and Range province to the south. The boundary was modified from the 1996 INL PSHA from a straight E-W line that included a portion of the SRP, to its new location that better distinguishes the two

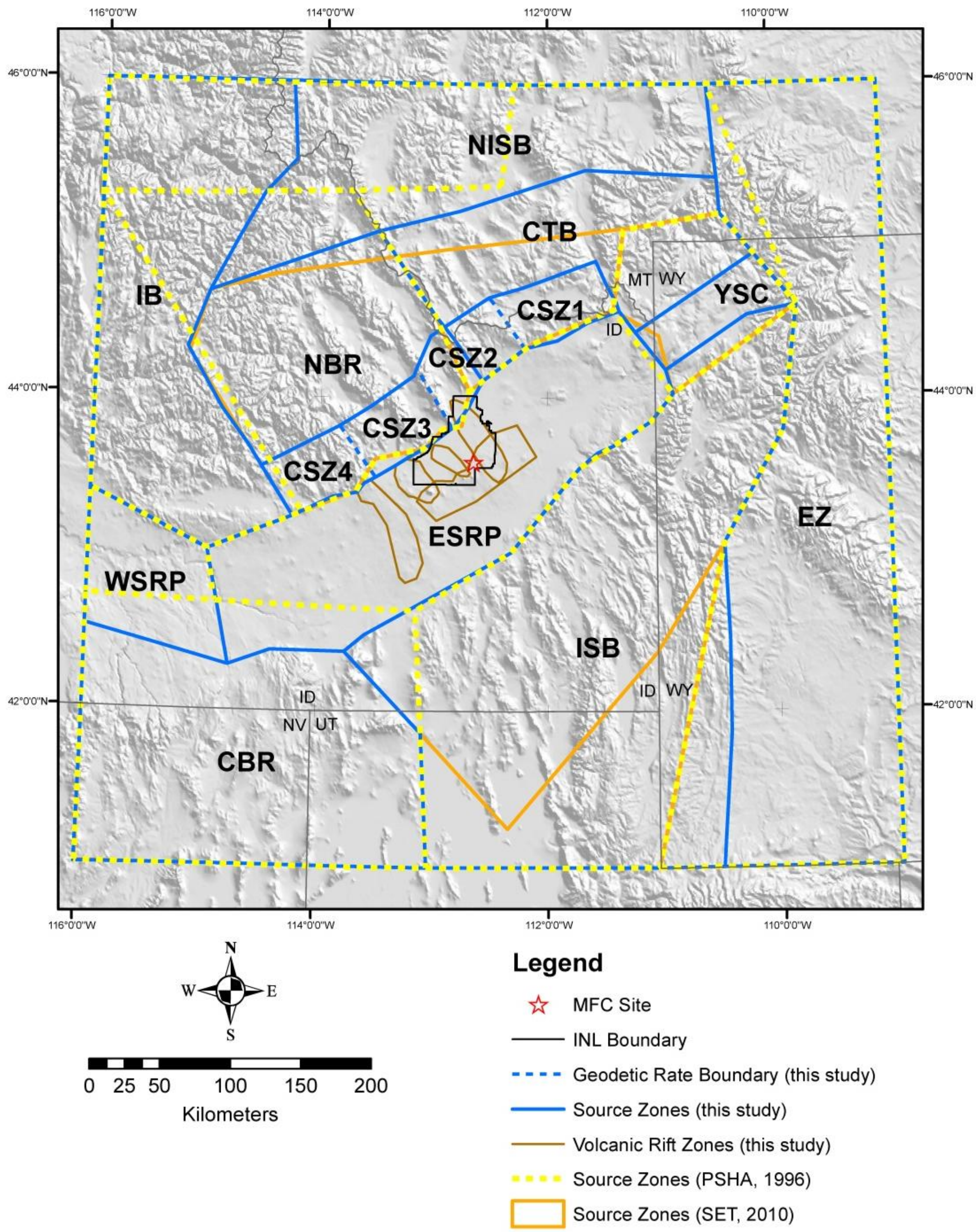

Figure 8-14. Map showing the evolutions of source zone geometries from the 1996 INL PSHA (Woodward-Clyde Federal Services et al., 1996), the SET's 2010 alternative zonation model (Seismic Evaluation Team, 2010), and this study.

provinces. The eastern boundary of the CBR distinguishes a lower level of seismicity in the CBR with a relatively higher concentration of seismicity in the ISB (Figure 8-12). Despite a lower concentration of seismicity, the southern portion of the source zone contains some of the largest historical earthquakes in the Basin and Range province, discussed in more detail for Mmax in Section 8.2.5.5.

Intermountain Seismic Belt (ISB). The ISB source zone is located in the south-central portion of the SSC model (Figure 8-14). The zone encompasses structures of the Basin and Range province and contains five of the fault sources characterized in the SSC model as discussed in Section 8.3. The concentration of seismicity in the ISB zone distinguishes it from the ESRP host zone to the north and the CRB and EZ zones to the west and east, respectively. Section 4.1 provides detailed discussion of the ISB tectonic province in the actively extending Great Basin. The 1996 INL PSHA and 2010 SET studies created two separate source zones within the ISB to account for the seismicity associated with the Seismic Parabola (Section 4.4.1). The Seismic Parabola zone cuts across major faults, such as the Grand Valley, Bear Lake, East Gem Valley, and Wasatch (Figure 8-12). As result of the seismic parabola's extent, the TI team decided to create a single ISB source zone that varied in rate, but had consistent structural grain, future earthquake characteristics, and seismogenic thicknesses, all of which are the main factors that are used in characterizing a seismic source zone. Spatial smoothing was used to honor the varying concentrations of seismicity within the zone as described in Section 8.2.1.7. The eastern boundary of the ISB zone was moved further east than previous studies in order to capture Basin and Range structures consistent with those in the ISB zone.

Eastern Zone (EZ). The EZ source zone is located along the eastern portion of the SSC model (Figure 8-14). The zone encompasses the Rocky Mountain physiographic province. The eastern boundary of the EZ source zone separates an area of high seismicity in the Basin and Range in the west with a relatively low concentration of seismicity to the east. The geometry of the eastern zone follows the pattern of seismicity that is also associated with the eastern edge of the Basin and Range and portions of the Yellowstone Plateau. The southern part of the eastern EZ boundary was modified from past studies to exclude Basin and Range structures associated with the ISB zone.

Yellowstone Caldera (YSC). The YSC source zone is located northeast of the ESRP host zone (Figure 8-14). The source zone is a relatively narrow area of concentrated seismicity that is predominantly associated with a combination of regional tectonics and stress associated with active volcanic processes (Waite and Smith, 2004). The volcanic processes associated with this source zone result in a high concentration of seismicity and a shallower seismogenic crust relative to neighboring source zones. The formation and tectonic history of the Yellowstone Caldera is discussed in Section 4.4.2. The northwest and southeastern zone boundaries are positioned to encompass the structures and seismicity associated with the Yellowstone Caldera. The narrow nature of this zone compared to past studies is a modification based on revised understanding and locations of associated seismicity and to exclude structures of the CTB and ISB zones which are characterized as a separate zone in this study due to differences in seismogenic crust and future earthquake characteristics. The southwest zone boundary has been modified from past studies in order to better demarcate where the SRP ends and the Yellowstone Caldera begins. The northeast boundary is located where the seismicity associated with the Yellowstone Caldera dissipates and the crust thickens in the Rocky Mountain province of the EZ source zone.

Centennial Tectonic Belt (CTB). The CTB source zone is located northeast of the ESRP source zone and neighbors with the YSC and NBR source zones on the east and west, respectively (Figure 8-14). In this study, the northern boundary of the zone was moved further north (than in the 2010 SET study) to include the northern extent of the Madison fault and other Basin and Range structures. It more closely matches the CTB as defined by the NE-trending zone of Holocene normal faulting and high seismicity from central Idaho to southwest Montana (Stickney and Bartholomew, 1987). The active normal faults in the CTB have been characterized as fault sources in this study, and the CTB source zone has been characterized as a background zone relative to these faults. The CTB zone is positioned in the Seismic Parabola and has higher seismicity than that of the NISB source zone to the north. The CSZ is located along the southern CTB seismic zone. Recent geodetic studies indicate that at present the ESRP is deforming at a much slower rate than the extension occurring in the CTB (Payne et al., 2012). The different strain rates are accommodated by right lateral shear in the CSZ source zone, described in detail in Section 4.1. In the SSC model as discussed in Section 8.2.3, the CSZ source zone has a probability of existence of [0.5] (Figure 8-8). When the CSZ exists, the southern boundary of the CTB is moved northward about 40 km and borders the CSZ zone. When the CSZ does not exist, the southern boundary of the CTB shares a boundary with the ESRP source zone.

Northern Basin and Range (NBR). The NBR source zone is located north of the ESRP between the IB and CTB source zones (Figure 8-14). The zone encompasses structures of the Basin and Range Province and three faults sources including the Lost River, Lemhi, and Beaverhead faults. Much like that of the CTB zone, the NBR encompasses high concentrations of seismicity relative to the NISB zone to the north. The main distinction between the CTB zone and the NBR zone is the Mmax that could occur in the zone. The western boundary of the zone separates the Basin and Range province from that of the Idaho Batholith and was also adjusted to include the Sawtooth fault as part of the NBR source zone, which had previously cut across the boundary. Also similar to the CTB zone, the CSZ overlaps with the southern part of the NBR zone. In the SSC model, the CSZ source zone has a probability of existence of [0.5]. Thus, the NBR shares its southern boundary with the CSZ source zone when the CSZ exists and with the ESRP source zone when the CSZ does not exist (Figure 8-8).

Northern Intermountain Seismic Belt (NISB). The NISB source zone is north of the CTB and NBR source zones (Figure 8-14). It is bounded to the west by the IB source zone and to the east by the EZ source zone. There is a lower concentration of seismicity relative to the zones to the south. The NISB is north and outside of the Seismic Parabola (Figure 4-11). Within the NISB, many of the Basin and Range structures have diverse trends and normal faults offset late Pleistocene deposits and appear to have longer recurrence intervals (Section 4.4.3).

Idaho Batholith (IB). The IB source zone is in the northwest corner of the SSC model (Figure 8-14). The Idaho Batholith has high rugged topography and is relatively non-extended compared to neighboring zones to the east and south as described in detail in Section 4.4.6. Lower concentrations of seismicity occur in the IB source zone but are most concentrated in the center portion of the zone. Whereas the Idaho Batholith geologic boundaries have been well mapped, the source zone boundaries that encompass this region have evolved significantly since the 1996 INL PSHA. The 2010 SET study recommended adjusting the boundaries to be more compatible with the geologic mapped units (Worl et al., 1991). This study accommodates this recommendation and in addition shifts the eastern boundary slightly to the west in order to keep the Sawtooth fault within the NBR source zone.

Western Snake River Plain (WSRP). The WSRP is located in the western part of the SSC model between the IB and CBR source zones. The WSRP eastern boundary is the ESRP source zone (Figure 8-14). The WSRP source zone contains fewer earthquakes than in the nearby regions to the north and south as described in Section 4.1 and 4.4.7. The source zone encompasses the southeast sliver of the larger WSRP province, an area of extension that is thought to have formed as part of the Yellowstone hotstpot volcanism at 9-11 Ma. Within the WSRP source zone, no fault sources have been characterized, but paleoseismic investigations have been conducted to the west of the zone on graben bounding normal faults of the WSRP (Figure 4-13 and Section 5.3.4).

8.2.4.2 Seismogenic Thickness

In the SSC model, seismogenic thickness is estimated based on the depth distributions of earthquake hypocenters and is assumed to smoothly vary spatially across the zone. As discussed in Section 8.2.1.3, the assessment of seismogenic thickness is assessed based on consideration of the D_{90} analysis results (Table 8-5). Further, the thicknesses from the 1996 INL PSHA and 2010 SET studies were also considered in determining the full range of thicknesses. It is assumed that all zones are perfectly correlated such that the shallowest seismogenic thickness for a zone in the hazard calculation would imply that the other zones are modeled with the shallowest thickness also for that particular hazard run.

For CBR, ISB, EZ, YSC, CTB, NBR, NISB, IB, and WSRP source zones, seismogenic thickness and uncertainties are summarized in Table 8-5. Due to the lack of seismicity, the seismogenic thickness distribution for the WSRP is assumed to be similar to the surrounding regions based on results of paleoseismic investigations on WSRP normal faults with ~1 m offsets (Section 5.3.4). For the other source zones, the assessed depth distributions for the SSC model are relatively consistent with the exceptions of the YSC and IB. The YSC source zone contains active volcanic processes that give rise to a warmer, thinner crust whereas the thicker seismogenic crust in the IB source zone is due to the lack of extended crust in the batholith (see Sections 4.4.2 and 4.4.6, respectively).

8.2.4.3 Earthquake Recurrence

Earthquake recurrence relations for the ISB, NISB, YSC, EZ, IB, WSRP, CBR, NBR, and CTB source zones are calculated in the same manner as the ESRP host zone (Section 8.1.4.3). The earthquake recurrence was derived by using the four declustered 1850-2014 E[**M**] catalogs (Section 6.3), a correction for completeness (Section 6.4), and any weights assigned to the alternatives. For the SSC model, earthquake recurrence curves with the 5^{th} and 95^{th} percentiles for the ISB, NISB, YSC, EZ, IB, and WSRP are shown in Figures 8-15 to 8-17. Each plot also shows the observed earthquake in the catalog with their 90% confidence intervals (black dots and vertical black bars). As discussed in Section 8.2.17, seismicity within capture areas (calculated using a 3 km buffer width, fault dip, and seismogenic depth to the surface) of a fault source was removed. For the ISB, the impacts of extracting fault-related events from the source zone recurrence are shown by the red dots and vertical red bars in Figure 8-15a.

Table 8-5. Results of the D_{90} analysis and seismogenic thickness distributions assessed for tectonic seismic source zones in the SSC model.

<table>
<tr><th rowspan="2">Seismic Source Zone Code[1]</th><th colspan="3">Focal Depth Distribution (km)[2]</th><th rowspan="2">Assessed Seismogenic Thickness (km) With [Weights]</th></tr>
<tr><th>D_{85}</th><th>D_{90}</th><th>D_{95}</th></tr>
<tr><td>CBR</td><td>11.81</td><td>13.08</td><td>14.39</td><td rowspan="8">12 km [0.2]
15 km [0.6]
18 km [0.6]</td></tr>
<tr><td>CSZ</td><td>14.11</td><td>16.00</td><td>18.00</td></tr>
<tr><td>CTB</td><td>12.00</td><td>12.78</td><td>15.95</td></tr>
<tr><td>EZ</td><td>10.97</td><td>15.51</td><td>31.27</td></tr>
<tr><td>ISB</td><td>11.07</td><td>12.24</td><td>13.87</td></tr>
<tr><td>NBR</td><td>16.30</td><td>18.50</td><td>21.00</td></tr>
<tr><td>NISB</td><td>13.34</td><td>14.10</td><td>15.50</td></tr>
<tr><td>WSRP</td><td>NA</td><td>NA</td><td>NA</td></tr>
<tr><td>YSC</td><td>12.02</td><td>13.99</td><td>17.24</td><td>8 km [0.2]
12 km [0.6]
15 km [0.6]</td></tr>
<tr><td>IB</td><td>15.01</td><td>16.62</td><td>21.95</td><td>12 km [0.2]
15 km [0.6]
20 km [0.6]</td></tr>
<tr><td colspan="5">1. See Table 8-1 for names and codes.
2. Results from D_{90} analysis where D_{85}, D_{90}, and D_{95} are the depths above which 85%, 90% and 95%, respectively, of earthquakes occur. D_{85} and D_{95} represent range of depth uncertainty. NA indicates too few earthquakes available for analysis.</td></tr>
</table>

(a)

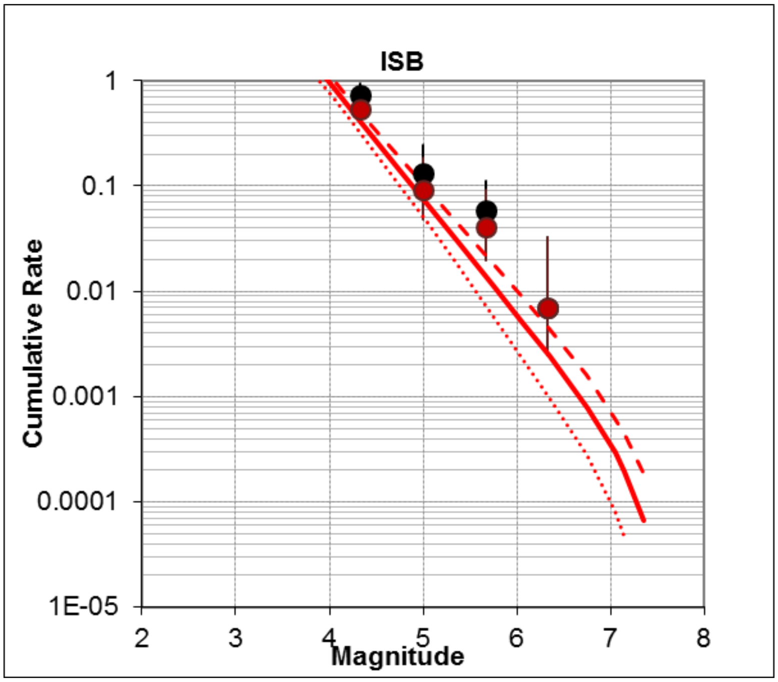

(b)

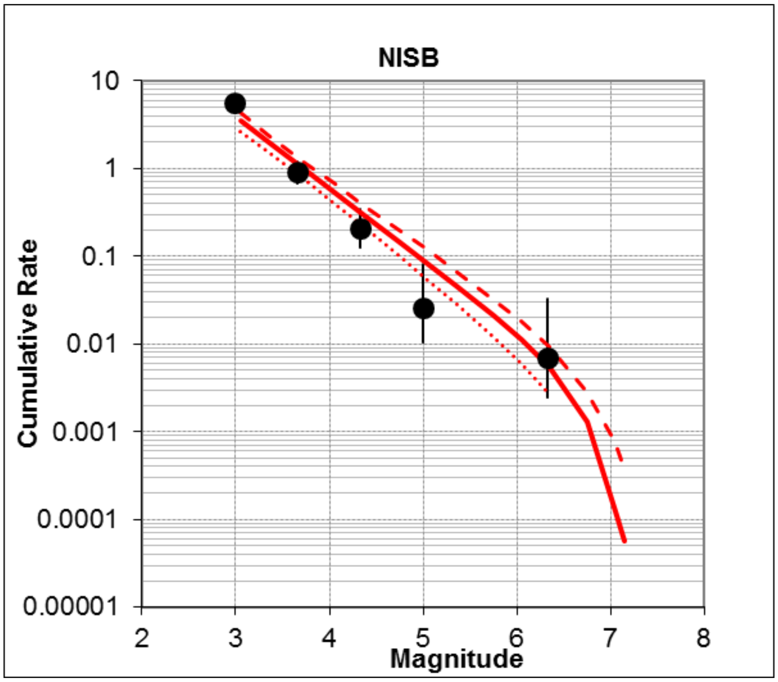

Figure 8-15. Plots of earthquake recurrence curves (cumulative rate versus magnitude) shown by solid red lines for: a) ISB; and b) NISB. Also shown are the 5th percentile (dotted red line) and 95th percentile (dashed red line) curves, and observed earthquakes in the catalog (black dots) with their 90% confidence limits (black vertical bars). In (a), the observed earthquakes without fault-source-related events are shown by the red dots and vertical bars.

(a)

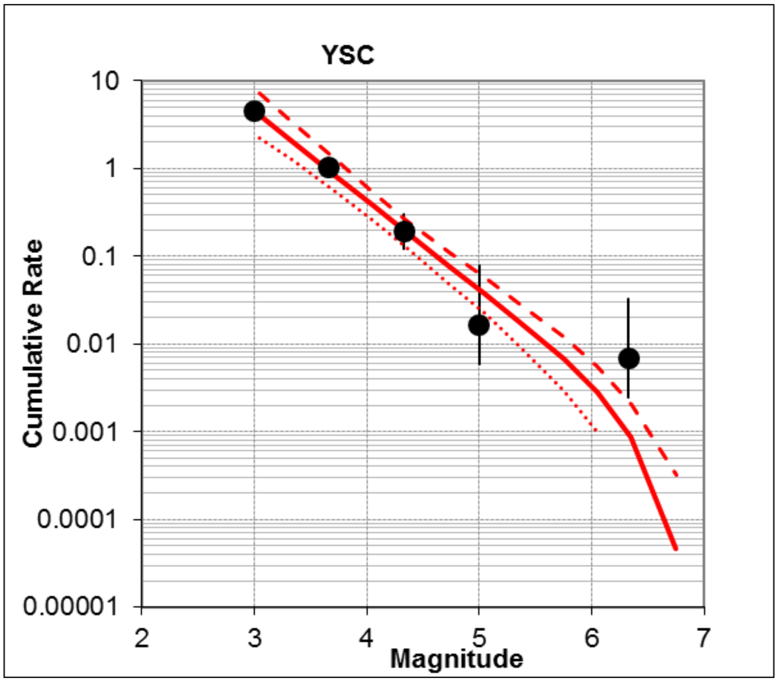

(b)

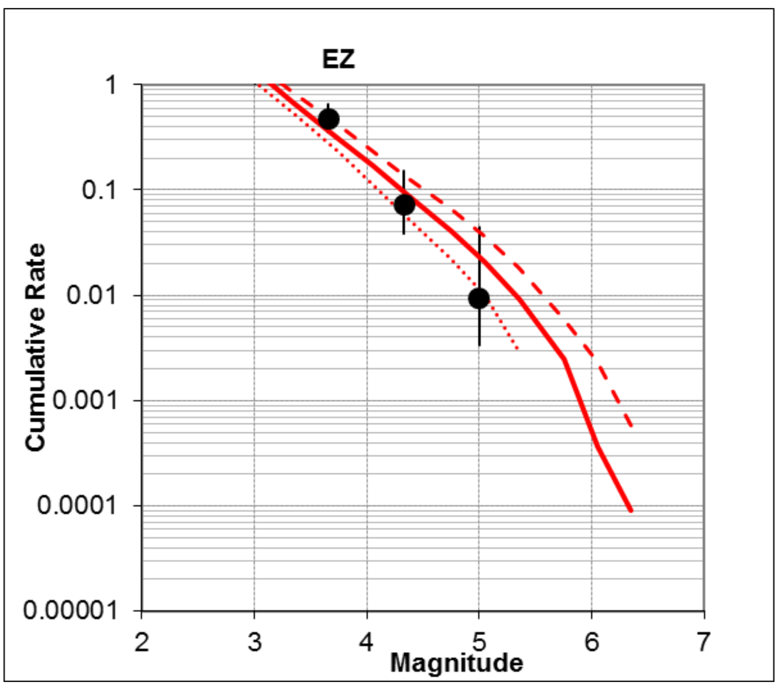

Figure 8-16. Plots of earthquake recurrence curves (cumulative rate versus magnitude) shown by solid red lines for: a) YSC; and b) EZ. Also shown are the 5th percentile (dotted red line) and 95th percentile (dashed red line) curves, and observed earthquakes in the catalog (black dots) with their 90% confidence limits (black vertical bars).

(a)

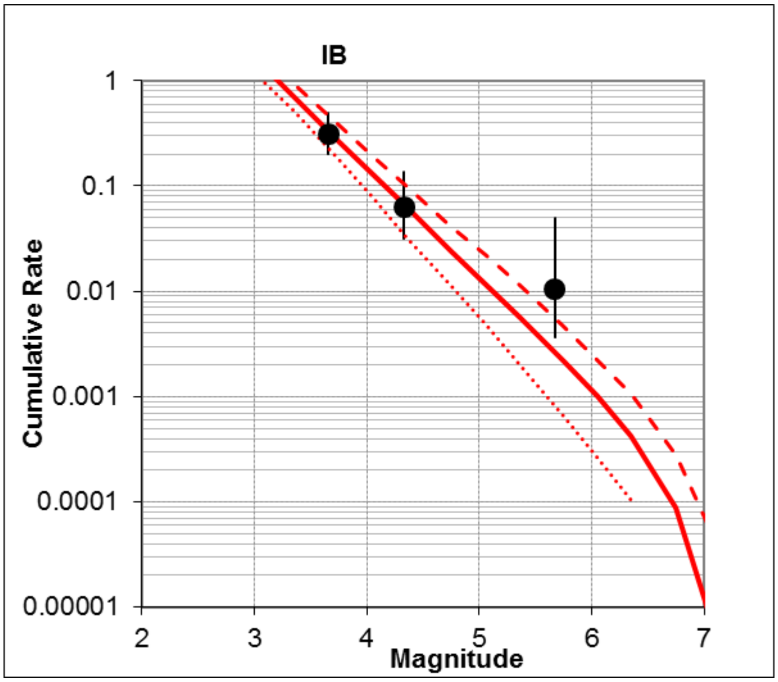

(b)

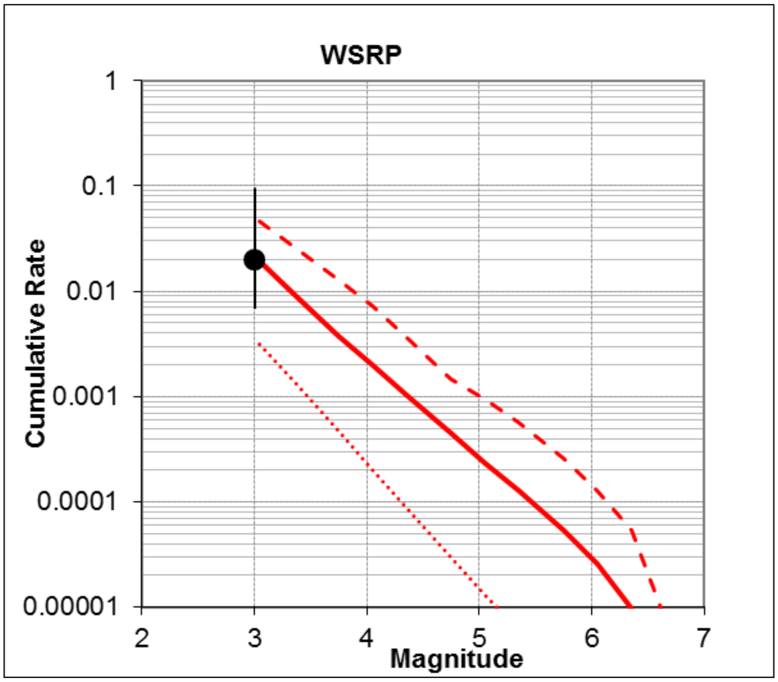

Figure 8-17. Plots of earthquake recurrence curves (cumulative rate versus magnitude) shown by solid red lines for: a) IB; and b) WSRP. Also shown are the 5th percentile (dotted red line) and 95th percentile (dashed red line) curves, and observed earthquakes in the catalog (black dots) with their 90% confidence limits (black vertical bars).

(a)

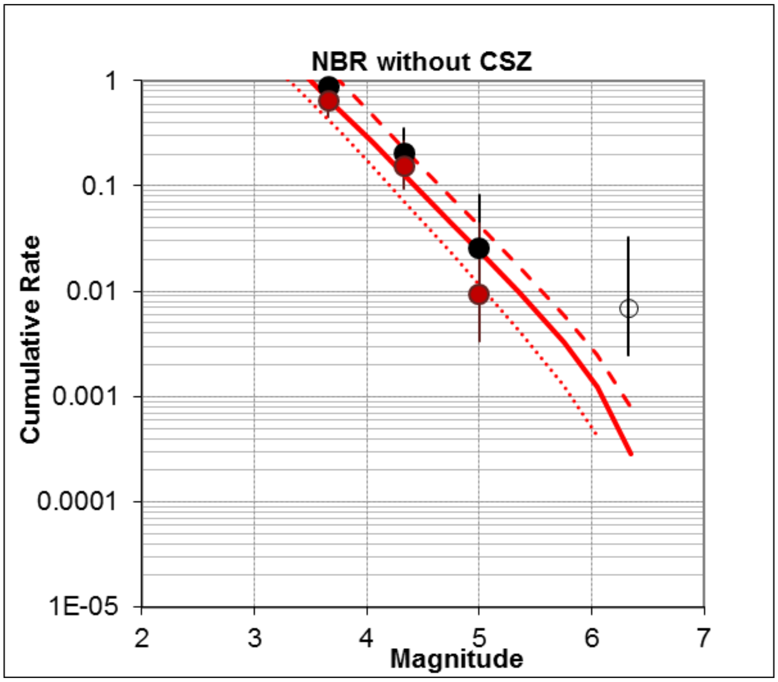

(b)

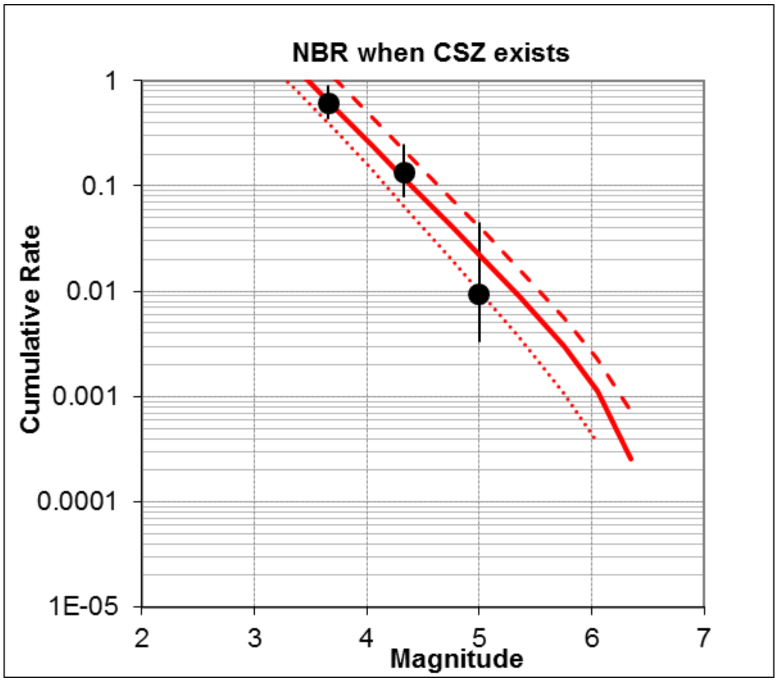

Figure 8-18. Plots of earthquake recurrence curves (cumulative rate versus magnitude) shown by solid red lines for: a) NBR; and b) NBR when CSZ exists. Also shown are the 5th percentile (dotted red line) and 95th percentile (dashed red line) curves, and observed earthquakes in the catalog (black dots) with their 90% confidence limits (black vertical bars). In (a), the observed earthquakes without fault-source-related events are shown by the red dots and vertical bars.

(a)

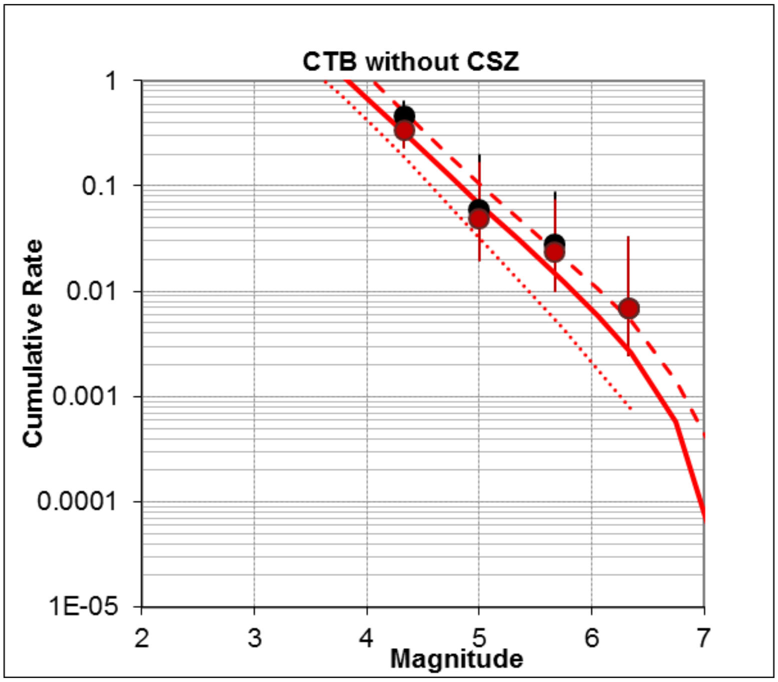

(b)

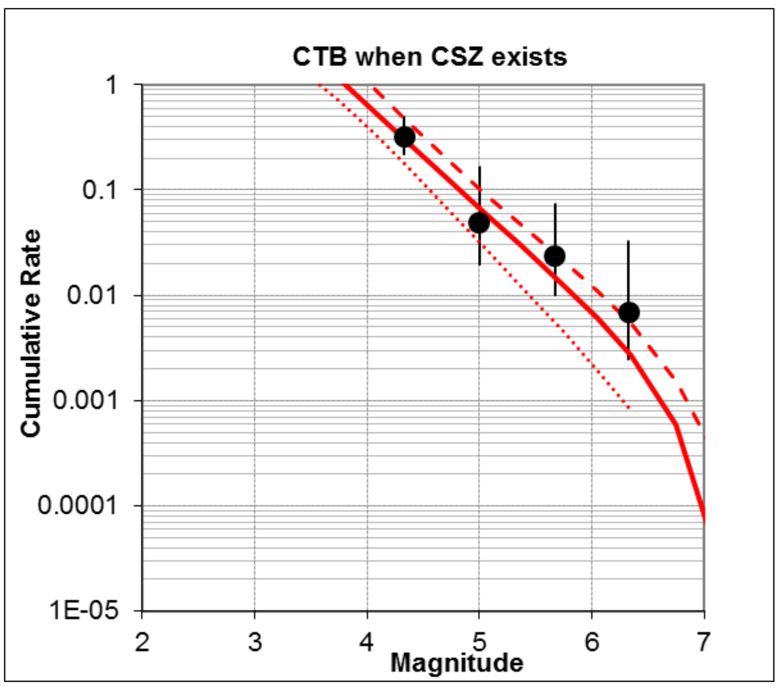

Figure 8-19. Plots of earthquake recurrence curves (cumulative rate versus magnitude) shown by solid red lines for: a) CTB; and b) CTB when CSZ exists. Also shown are the 5th percentile (dotted red line) and 95th percentile (dashed red line) curves, and observed earthquakes in the catalog (black dots) with their 90% confidence limits (black vertical bars). In (a), the observed earthquakes without fault-source-related events are shown by the red dots and vertical bars.

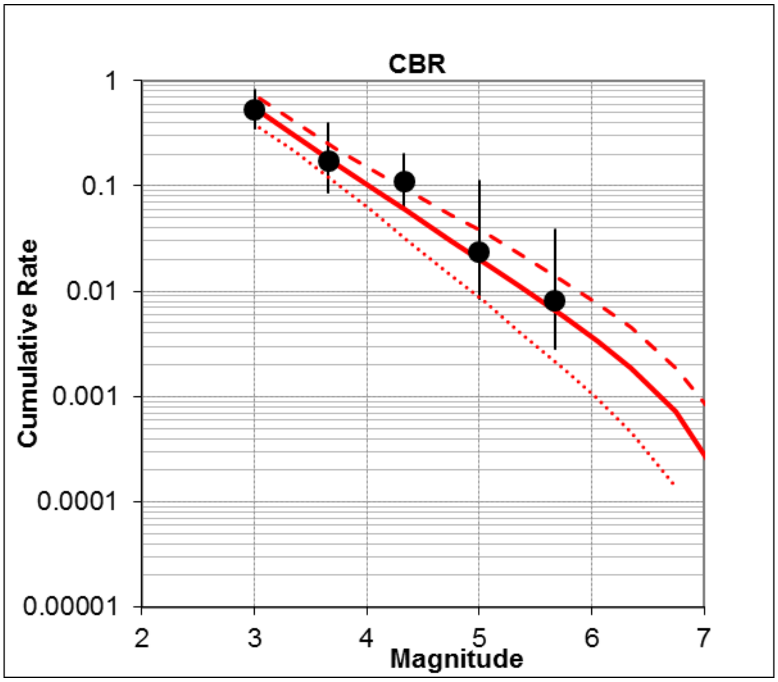

Figure 8-20. Plots of earthquake recurrence curves (cumulative rate versus magnitude) shown by solid red lines for the CBR source zone. The recurrence is computed using the alternatives for when the 1905 E[**M**] 5.61 earthquake is within the CBR [0.67] and outside the CBR [0.33] (see logic tree in Figure 8-7). Also shown are the 5th percentile (dotted red line) and 95th percentile (dashed red line) curves, and observed earthquakes in the catalog (black dots) with their 90% confidence limits (black vertical bars).

The NBR, CTB, and CBR source zones have earthquake recurrences that are dependent on alternatives associated with other source zones. For the NBR and CTB source zones, two recurrence curves are calculated for each zone depending on whether or not the CSZ exists (Figure 8-8). All seismicity in each of the NBR and CTB sources zones are used to calculate the earthquake recurrence assuming the CSZ does not exist (Figure 8-18a and 8-19a, respectively). Also shown are the impacts of removing fault-source-related earthquakes (i.e., red dots and vertical red bars). Assuming the CSZ exists, seismicity within the CSZ zone is removed from each of the NBR and CTB source zones to calculate earthquake recurrence (Figure 8-18b and 8-19b). With regard to the CBR source zone, the logic tree for the CBR and ESRP source zones shows alternatives for the location of the 1905 Shoshone earthquake. When the E[**M**] 5.61 1905 Shoshone earthquake is located within the CBR source zone the weight is [0.67] and, if it is not, the weight is [0.33] (Figure 8-7). The CBR earthquake recurrence curve shown in Figure 8-20 includes these two alternatives.

8.2.4.4 Spatial distribution of Recurrence Parameters

Spatial density models are used to define the future spatial density of earthquakes in the seismic source zones when observed seismicity is used to define earthquake recurrence (Section 8.2.1.7). Using tests described by Musson (2002), the CBR, ISB, EZ, YSC, NBR, CTB, NISB, IB, and WSRP source zones were examined for how well the observed seismicity conformed to the assumption of spatial homogeneity. The observed seismicity within the four seismic source zones in the SSC model is shown in Figure 8-13.

Based on the nearest-neighbor analysis given by Musson (2000) the seismicity in the CBR, YSC, and WSRP source zones were assigned a uniform distribution with a weight of [1.0]. The nearest neighbor test showed that the spatial distribution of earthquakes in the CBR and YSC are effectively random. In the CBR this happens because there are only a few earthquakes which are sparsely located, whereas in the YSC, because there are too many earthquakes. There are not enough earthquakes in WSRP to do nearest-neighbor test, so a uniform distribution is assumed.

The distributions of seismicity in the ISB, NISB, NBR, CTB and IB source zones were determined to have a non-homogeneous distribution based on the analysis. Therefore based on the results of the nearest neighbor analysis, the TI team implemented spatial smoothing for these source zones with a weight of [1.0].

8.2.4.5 Maximum Magnitude

Estimates of Mmax for the CBR, ISB, EZ, YSC, NBR, CTB, NISB, IB, and WSRP source zones were made with considerations of the largest observed magnitudes within each source zone and possible presence of faults that might have significant dimensions. For the source zones containing fault sources, the fault source characterization for Mmax was done separately from the source zone. In these cases, the Mmax for the source zone is considered the largest event that could occur without the faults sources.

The distributions of Mmax and respective weights for the CBR, ISB, EZ, YSC, NBR, CTB, NISB, IB, and WSRP source zones are listed in Table 8-3. Mmax and their distributions were derived by considering the following:

- Observed earthquake maximum magnitudes in each source zone, such as 1934 E[**M**] 6.57 (ISB), 1975 E[**M**] 6.33 (YSC), 2008 E[**M**] 6.01 (CBR) (Table 8-3)
- Mmax from the 1996 INL PSHA and 2010 SET studies
- Potential magnitudes of virtual faults that would fit within a source zone, which were derived by using magnitude-length relationships by Wells and Coppersmith (1994) and Wesnousky (2008) with fault dimensions
- Compilation and evaluation of paleoseismic and other seismic hazard studies such as for the WSRP (Section 5.3.2).

8.2.4.6 Properties of Future Earthquake Ruptures

As discussed in Section 8.2.1.4, characterization of source zones includes properties of future earthquake ruptures including style of faulting, strike and dip. The uncertainty distributions of these properties are given as relative frequency distributions since they are aleatory in nature. A summary of the future earthquake characteristics for these source zones are in Table 8-3.

The style of faulting is predominantly normal faulting throughout the SSC model. This is based on multiple studies and predominant structures that are well understood in the region (see discussion in Section 4.1). The style of faulting for future earthquake ruptures is modeled as Normal (100%) for the CBR, NBR, CTB, NISB, IB, EZ, YSC, and WSRP source zones. Focal mechanisms in the region shown in Figure 4-17 indicate that there are some strike-slip earthquake ruptures that occur within the ISB source zone. For this reason, the ISB source zone is modeled as Normal (90%) and Strike-Slip (10%).

8.2.5 Characterization of the Volcanic Source Zones

Two volcanic source zones, GRF and IVRZ, were characterized for the SSC model. The volcanic source zones are located within the ESRP host zone; the GRF volcanic source zone is located south of INL whereas the IVRZ volcanic source zone encompasses most of the INL (Figure 8-2). While the GRF volcanic source zone is similar to models used previously, the IVRZ source zone represents a change from how volcanic source zones were modeled in previous INL PSHAs. In the 1996 and 2000 PSHAs, the VRZs and Axial Volcanic Zone (AxVZ) that cross INL were modeled as independent volcanic source zones each with different volcanic recurrence estimates (Woodward-Clyde Federal Services et al., 1996; URS Greiner Woodward Clyde Federal Services et al. 1999; 2000). Results of the 1996 INL PSHA showed that the contribution of INL volcanic zones had very small impacts to hazard levels primarily due to their long recurrence estimates (Woodward-Clyde Federal Services et al., 1996).

The TI Team chose to use a simplified alternative approach to model and assess recurrence estimates of volcanic source zones. The alternative approach was not only applied to avoid double counting of cogenetic vent/fissure groups as was done by Hackett et al. (2002), but also to assess the impacts of shorter recurrence estimates for volcanic sources on hazard levels at INL. Thus for this study, the IVRZ combines the three VRZs and AxVZ into one volcanic source zone and estimates the recurrence interval based on the total number of individual cogenetic vent/fissure groups and oldest age of volcanism within the IVRZ.

Underlying the use of volcanic seismic source zones is the assumption that future dike intrusions within the ESRP will produce earthquakes with a recurrence estimate based on the timing of basalt volcanism. Such an assumption is based on observations of earthquakes associated with volcanic dike-induced processes worldwide (Payne et al., 2009). The volcanic source zones in the ESRP have diagnostic deformational features that are produced by dike intrusion processes and associated with various ages of basalt lava flows. While no basalt dike intrusion events have been observed in historical time, geologic, volcanic, seismologic and geophysical data at analog VRZs worldwide and in the ESRP are used to characterize boundaries, seismogenic thickness, earthquake recurrence, Mmax, and future earthquakes for the volcanic source zones.

As with the other nearby tectonic seismic source zones, the IVRZ and GRF have a seismogenic probability and leaky boundaries. The two volcanic source zones each has an assumed seismogenic probability p[S]=1, which is consistent with current SSC practice for sources zones (e.g., NRC, 2012b). As discussed in Section 8.1.5.1, source zone boundaries in the SSC model are assumed to be leaky. Fault ruptures that originate near a source zone boundary can extend beyond the boundary and are not terminated at the boundary. For example, the Big Lost fault and the southern terminations of the Lost River and Beaverhead may extend into the IVRZ (Figure 8-2).

8.2.5.1 Source Zone Geometry

Boundaries for the GRF and IVRZ volcanic source zones were developed for this study and are different from previous hazard analyses. The GRF boundaries were broadened slightly from those used in the 1996 INL PSHA. The broadening allowed for inclusion of vents with ages <15,000 yr that are associated with the eight episodes of volcanism in the Great Rift VRZ (Kuntz et al., 1986; Kuntz et al., 2007).

The IVRZ source zone represents a change in number and boundaries from the volcanic source zones used in previous INL PSHAs. In the 1996 and 2000 PSHAs, the VRZs and AxVZ were independent volcanic source zones each with different volcanic recurrence estimates. Due to the issues with how recurrence was calculated for the independent zones (i.e., the same cogenetic vent/fissure groups were counted in more than one zone), this study took a simplified approach that combines the three VRZs and AxVZ that cross INL into one volcanic source zone (Figure 8-2) with one distribution of recurrence estimates (Section 8.2.5.3). Boundaries of the three VRZs (Arco – ARC, Lava Ridge-Hell's Half Acre – LCB, and Howe-East Butte – HEB) and AxVZ were adopted from Hackett et al. (2002).

8.2.5.2 Seismogenic Thickness

The distribution of seismogenic thickness of the GRF and IVRZ volcanic source zones was assessed to be the same as the ESRP tectonic seismic source zone. The assessment is based on the evaluation of focal depths in the ESRP, magma intrusive processes, and consideration of dike-induced related volcanic earthquake depths at other VRZs worldwide. The cross section of ESRP focal depths in Figure 5-2a shows that earthquakes occur at depths from 0 to 42 km (Section 5.2). This cross section shows volcanic related earthquakes at COM can occur at depths greater than the assumed seismogenic thickness (<4 km) used in the 1996 INL PSHA for VRZs (Woodward-Clyde Federal Services et al., 1996). Worldwide analogs compiled in Table 5-3 show focal depths of earthquakes (0-33 km) associated with dike intrusion are similar to the depth range observed in the ESRP (Figure 5-2a). Magma ascent from the base of the crust to the surface will lead to earthquakes and the possibility of triggering slip on nearby faults close to their yield stress (Payne et al., 2009). As discussed in Section 5.2, the Lake Tahoe, Nevada volcanic earthquake sequence is assumed to be an analog for the ESRP whereby volcanic earthquakes can occur at deep (25-33 km) and shallow depths (<20 km), as is observed at COM in the ESRP (Figure 5-2a). Thus, the distribution of seismogenic thickness within the VRZs is assessed to be the same as the ESRP, 12 km [0.2], 15 km [0.6], 18 km [0.2].

8.2.5.3 Earthquake Recurrence

As discussed in Section 8.2.5, the TI Team chose to use an alternative approach to model and assess recurrence estimates of the IVRZ volcanic source zone, and to also update the recurrence estimates for the GRF volcanic source zone. Combining the volcanic sources into one volcanic source zone (IVRZ) has the advantage of assessing how shorter recurrence estimates for volcanic sources impact hazard levels at INL.

For the IVRZ, the number of individual cogenetic vent/fissure groups for the entire IVRZ source zone and the oldest age of volcanism were used to estimate the recurrence interval. This simplified approach was taken to avoid double counting of cogenetic vent/fissure groups as was done by Hackett et al. (2002) for two VRZs and the AxVZ. This study counted the total number of individual cogenetic vent/fissure groups in the three VRZs, the AxVZ, and two boreholes at INL as 102 (Table 3 in Hackett et al., 2002). A recurrence estimate of 12,000 yrs was calculated by using the oldest age of volcanism in the IVRZ of 1.2 m.y. and dividing by 102. This calculation assumes that cogenetic vent/fissure groups can be used to represent discrete dike intrusions that have occurred over the last 1.2 m.y. The 12,000 yr recurrence estimate is the shortest recurrence when compared to the range from 16,000 to 100,000 yrs for recurrence estimates of individual VRZs and the AxVZ (Woodward-Clyde Federal Services et al., 1996; Hackett et al., 2002). Additionally the uncertainty about this recurrence estimate was assessed by assuming ±13 cogenetic vent/fissure groups in the counts, which is somewhat less than the numbers (16 and 17) of overlapping vent/fissures groups used by Hackett et al (2002). The distribution of the recurrence estimates for the IVRZ is listed in Table 8-6.

Updated recurrence estimates were assessed for the GRF volcanic source zone. For the 1996 INL PSHA, volcanic recurrence estimates were assessed using counts of individual vents and fissures and

Table 8-6. Distribution of recurrence intervals for the IVRZ and GRF volcanic source zones used in the SSC model.

Volcanic Source Zone	Recurrence Interval (yr)		
	Weight [0.2]	Weight [0.6]	Weight [0.2]
IVRZ	10,500	12,000	13,500
GRF	1,700	2,000	2,200

cogenetic vents/fissure groups (as Hackett et al., 2002). Using counts of individual vents and fissures produced the shortest recurrence estimate of 150 yr for the GRF volcanic source zone in the 1996 INL PSHA. The chronology of basalt flow ages and geologic relations were distinguished by Kuntz et al. (1986) to identify eight major episodes of basalt volcanism in the Great Rift VRZ. In this study, the preferred approach was to calculate the recurrence estimates using basalt flow ages and episodes of volcanism (Table 1 in Kuntz et al., 1986). The following calculations were used to estimate the distribution of recurrence estimates for the GRF volcanic source zone listed in Table 8-6.

- The recurrence estimate of 1,700 yrs is derived from using the ages of lava flows categorized in each eruptive episode to calculate the average time interval between each eruptive episode (Episodes A though G and ages listed in Table 1 of Kuntz et al., 1986).
- The recurrence estimate of 2,000 yrs was obtained from Hackett et al. (2002), which is calculated for 8 episodes of volcanism in 15,000 yrs.
- The recurrence estimate of 2,200 yrs is calculated from using 7 episodes of volcanism in 15,000 yrs (i.e., omits counting Episode C that only has one dated basalt flow and assumes the age of this flow is part of Episode D).

8.2.5.4 Spatial distribution of Recurrence Parameters

The spatial variation of recurrence parameters for future earthquakes within the volcanic source zones is assumed to be uniform based very low levels of earthquake data within the ESRP.

8.2.5.5 Maximum Magnitude

The distribution of Mmax is supported by the evaluation of maximum magnitudes of earthquakes associated with dike intrusion discussed in Section 5.3.1. Table 5-3 lists an update of maximum magnitudes of dike-induced earthquakes compiled by Payne et al. (2009). From this table, two earthquake sequences that occurred in extensional regimes provided the best analogs of maximum magnitudes for future dike intrusion in the ESRP. The episode of dike-intrusions and eruptions near the Miyakejima volcano in Izu, Japan in 2000 had five moderate size earthquakes (**M** 6.2, 5.9, 6.0, 6.4, and 5.7) associated with migration of intruding dikes along a length of 30 km (Nishimura et al., 2001). From 2005 to 2010, volcano-tectonic earthquakes, the largest **M** 5.6, occurred in association with dike intrusions and eruptions along a 60-km-long segment of the east African rift system in Dabbahu, Afar, Ethiopia (Yirgu et al., 2006). Based on these analogs, the distribution of maximum magnitudes for dike-induced earthquakes is assessed to be **M** 5.5 [0.185], 6.0 [0.63], and 6.5 [0.185] (Section 5.3.1).

The distribution of Mmax for the IVRZ and GRF volcanic source zones was also applied to ESRP tectonic seismic source zone. The consistency of Mmax among the volcanic and tectonic source zones is based on the assumption that slip will occur on the same pre-existing faults whether due to magmatic or tectonic processes. Worldwide, dike intrusion is observed to cause slip on nearby faults close to their yield stress (Payne et al., 2009), and regional tension would presumably cause slip on these same structures in the ESRP.

The maximum moment model with a uniform distribution of magnitude between **M** 5 and Mmax is used in the SSC model (Figure 8-21). Use of the maximum moment model is supported by worldwide observations of earthquakes associated with the initial dike intrusion having generally the larger magnitude event. It is assumed that dike-induced earthquakes of **M**<5 do not occur more frequently.

8.2.5.6 Properties of Future Earthquake Ruptures

The properties of future earthquake ruptures for the IVRZ and GRF include the characterization of the styles of faulting, fault strikes and fault dips. Due to the aleatory nature of these future properties, the uncertainty distributions are assigned as relative frequency distributions (or percentages) (Section 8.1.5).

Properties of future earthquake ruptures in volcanic source zones are assessed to be the same as for the ESRP. Since dike intrusion is observed to cause slip on nearby faults close to their yield stress (Payne et al., 2009), slip on future faults within volcanic source zones could occur on pre-existing faults produced either by magmatic or tectonic processes. Section 8.2.3.6 discusses the assessment which considered volcanic deformational features produced by dike intrusion along fault plane solutions computed for ESRP microearthquakes and geometries of Basin and Range normal faults. Thus, the properties of future earthquake ruptures in the ESRP were also assigned to the volcanic source zones: style of future faulting is normal (100%); strikes of normal faults and their uncertainties are 115° (25%), 140° (50%), and 170° (25%); dips and their uncertainties are 40° (15%), 55° (75%), and 89° (89%); and dip directions of future faulting include both NE (50%) and SW (50%).

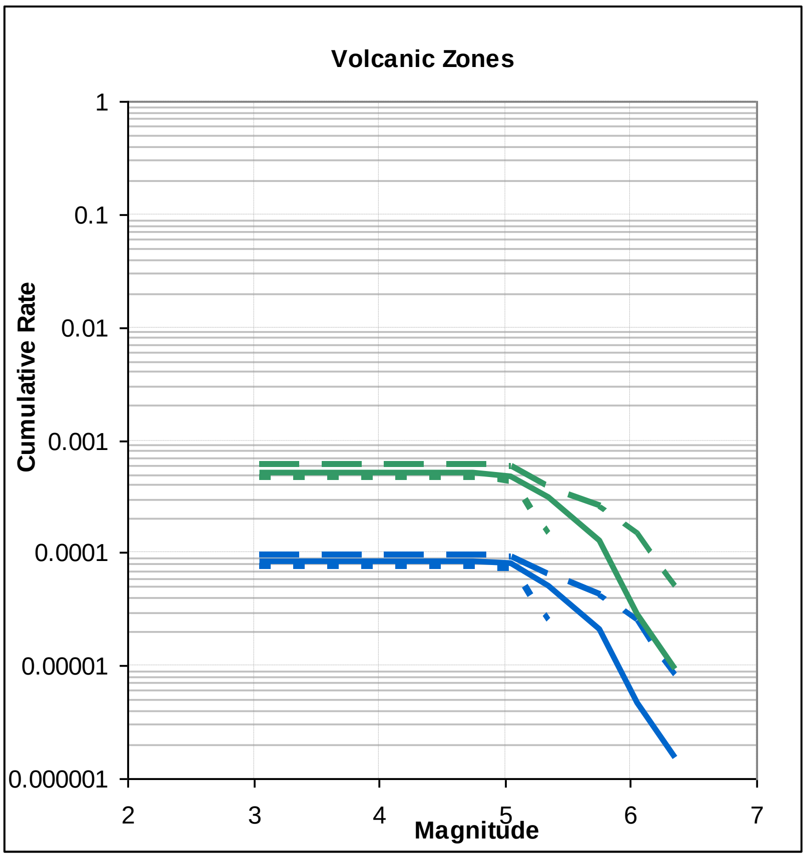

Figure 8-21. Plot of the earthquake recurrence curves (cumulative rate versus magnitude) for the GRF (solid green line) and IVRZ (solid blue line) volcanic source zones. Also shown are the 5th percentile (long dotted lines) and 95th percentile (short dashed lines) curves. The maximum moment model is used with a uniform distribution of magnitude between **M** 5 and Mmax.

8.3 Fault Sources

Sixteen fault sources are included in the SSC model all of which are normal faults (Table 8-2). Fifteen of the fault sources have been included in previous hazard analyses at INL and one regional fault (Big Lost) was added in this study. For this section, the fault sources are grouped as thirteen regional fault sources and three local fault sources (Lost River, Lemhi, and Beaverhead). Primary reason for the grouping is based on the detailed information available to model the faults and their significance to hazard levels at INL. The southern segments of the three local fault sources are in close proximity (<30 km) to INL (Figure 8-3) and have greater impacts to INL hazard levels than many of the more distant regional faults (AMEC, 2013).

The regional fault sources were first characterized for sensitivity analyses conducted in 2013 (AMEC, 2013). The primary purpose of including these faults was to address the change in DOE-STD-1020-2012, which requires assessing any sources that contribute more than 1% to the total mean hazard (DOE, 2012a). The characterization of the regional fault sources includes fault geometry, slip rate, and recency of faulting resulting in much simpler logic trees.

The Lost River, Lemhi, and Beaverhead fault sources were first characterized in the 1996 INL PSHA (Woodward-Clyde Federal Services et al., 1996) and were included without modifications in the 2000 INL PSHA (URS Greiner Woodward Clyde Federal Services et al. 1999; 2000) and 2010 SET sensitivity analysis (Seismic Evaluation Team, 2010). Some modifications occurred in the characterization of the Lost River and Lemhi fault sources in the 2013 sensitivity analysis (AMEC, 2013). Due to their hazard significance, paleoseismic data along with other geologic and seismologic data and investigations are available for the three local faults sources. Since the 1983 E[**M**] 6.96 Borah Peak earthquake ruptured segments of the Lost River fault, it has even more data and investigations than the other two local fault sources. As a result, the local fault sources have complex logic trees for fault geometry, slip rate, and recency of faulting.

This section discusses the SSC model of the regional and local fault sources. The characterization of both regional and local fault sources is included in the following subsections.

8.3.1 Seismogenic Probability

Attributes are used to assess the seismogenic probability of fault sources. A seismogenic fault is defined as having all of the following attributes:

- Actively involved in the contemporary tectonic environment
- Capable of generating moderate-to-large (M>5) earthquakes
- Localizes moderate-to-large earthquakes on a fault source in the PSHA.

These attributes give rise to the types of criteria that are useful in identifying seismogenic faults as well as the manner in which seismogenic faults are included in the hazard analysis. Faults that are not identified as being seismogenic are represented by virtual faults within source zones, which are defined by random locations with given rupture orientations, styles of faulting, dips, depths, and magnitude-dependent rupture dimensions (see Section 8.2.1). In this sense, all seismic source zones are assumed to be seismogenic. However, any individual mapped fault is either seismogenic or not seismogenic from the standpoint of the PSHA; the uncertainty in this assessment is expressed as the p[S]. A fault assessed to have a p[S]>0 is modeled in the PSHA as a localizer of future seismicity and the fault source is characterized by fault-specific attributes that define the style of faulting, three-dimensional geometry, Mchar, Mmax, and earthquake recurrence.

For this study, the p[S] is an assessment of whether the fault source should be included in the SSC model. The assessment of p[S] for any particular fault is a judgment made by the TI Team taking into consideration available data for the fault. The TI Team applied the criteria below to assess p[S] for fault sources included in this study. All faults listed in Table 8-2 and shown in Figure 8-3 have a p[S]=1.0 except for the Big Lost fault, which has a p[S]=0.3. The seismogenic probability for regional faults is included in the logic tree as shown in Figure 8-22a. The application of the criteria listed below considered the types and quality of the data available. Criteria for assessing p[S] range from more diagnostic (top of the list) to less diagnostic (bottom of the list) are as follows:

- Causal association with an M>5 historical earthquake
- Geologic evidence for coseismic displacement(s) during late Quaternary to Holocene
- Geologic evidence for Quaternary displacement
- Geologic evidence for displacements that is consistent with the contemporary tectonic environment, but inconsistent with previous environments
- Spatial association with M>5 earthquake.

With regard to the Big Lost fault, the p[S] of 0.3 is assigned to the Big Lost fault to account for uncertainty in interpretations of the subsurface basalt discontinuity and overall lack of evidence for Quaternary displacement. A discontinuity in basalt stratigraphy could be due to a fault or alternatively, evidence of aligned volcanic vents. In the ATR PSHA, p[S] of 0.65 and 1.0 were included as a sensitivity to determine the hazard significance of the Big Lost fault, particularly to nearby facility areas such as the ATR Complex. The sensitivity was also added because of new rock strength data and re-evaluation of existing borehole breakout data. See section 4.4.8 which describes the studies and associated uncertainties.

8.3.2 Approach to Fault Segmentation and Future Ruptures

Fault sources in the SSC model are characterized as being capable of generating a range of magnitudes up to a fault-specific Mmax. Studies of historical surface ruptures show that moderate-to-large-magnitude earthquakes occur on preexisting faults, and that the dimensions of rupture are correlated with earthquake magnitude. Further, paleoseismic studies of faults have provided estimates of the lengths of prehistoric ruptures and the amount of displacement associated with those ruptures at multiple locations along the fault length. These studies and comparisons with historical rupture characteristics (e.g., Wesnousky, 2008) have allowed estimates to be made of potential future rupture segments that could occur on a fault of interest. Estimates of such potential rupture segments can allow estimates to be made of the magnitudes of future earthquakes associated with the segments (e.g., Wells and Coppersmith, 1994). Accordingly, geologic information related to possible segmentation of the regional and local faults in the SSC model were reviewed and assessed for purposes of evaluating the earthquake magnitudes that faults are capable of generating (Section 8.3.9).

Most studies of fault segmentation have been focused on “behavioral” evidence for segmentation (e.g., differences in the timing of the most recent earthquake along strike, slip-rate differences) or “geometric” evidence (e.g., discontinuities in the mapped fault trace, cross structures). There is general consensus that behavioral segments are more definitive of future ruptures than geometric segmentation evidence (e.g., McCalpin, 2009), but both types of information are often used to develop a segmentation model for a fault of interest.

For this study, the information related to segmentation differs between the local faults and the regional faults. The local faults have been subjected to detailed geologic and paleoseismic investigations such that behavioral information is used to define the segment boundaries (Figure 8-4). The segment

(a)

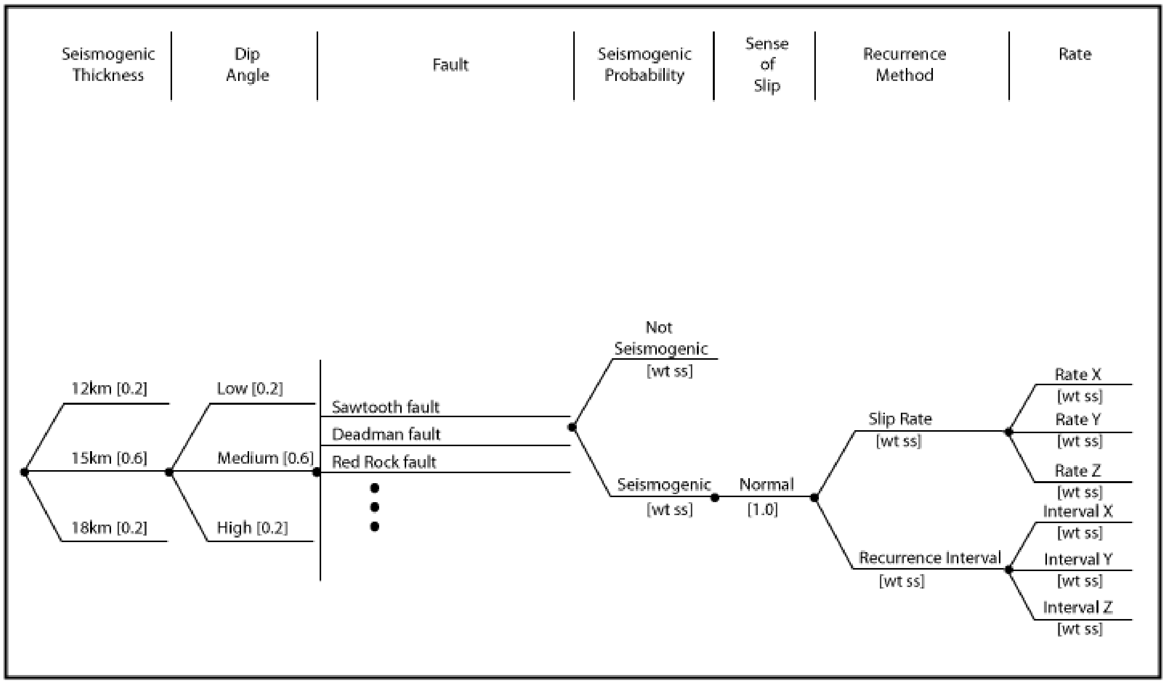

(b)

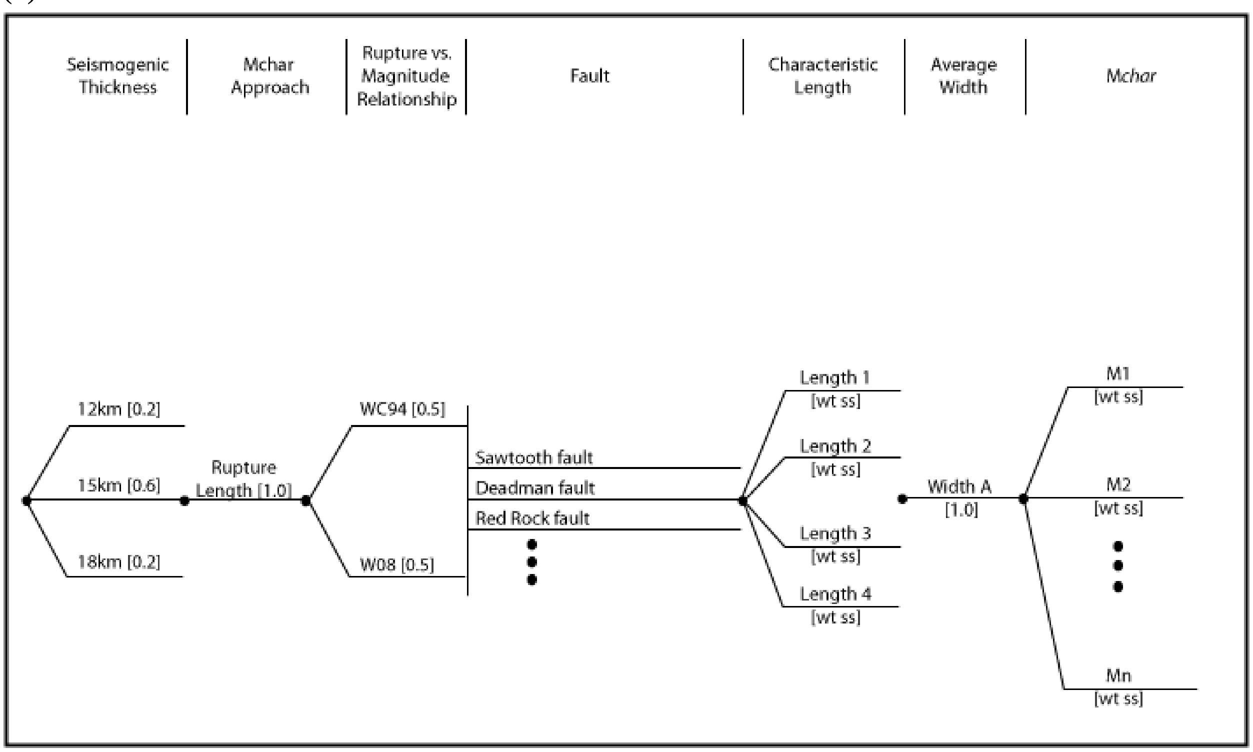

Figure 8-22. Logic trees used in the SSC model for each of thirteen faults sources listed in Table 8-2 for: a) fault geometry, seismogenic probability, and recurrence; and b) characteristic magnitudes. See Table 8-7 for parameter values.

Table 8-7. Parameters for the thirteen regional normal fault sources.

Fault Name	Dip[1] (Degree)	Dip Direction	Seismogenic Thickness (km)	Total Fault Length (km)	Characteristic Rupture Length (km)	Seismogenic Probability	Slip Rate[2] (mm/yr)	Recurrence Interval[2] (yr)
Sawtooth	30 [0.2] 55 [0.6] 70 [0.2]	NE	12 [0.2] 15 [0.6] 18 [0.2]	60	30 [0.2] 40 [0.4] 60 [0.4]	1.0	0.2 [0.4] 0.48 [0.4] 0.72 [0.2]	
Deadman	30 [0.2] 55 [0.6] 70 [0.2]	SW	12 [0.2] 15 [0.6] 18 [0.2]	73	30 [0.3] 45 [0.3] 70 [0.4]	1.0	0.005 [0.2] 0.03 [0.6] 0.12 [0.2]	
Red Rock	30 [0.2] 55 [0.6] 70 [0.2]	NE	12 [0.2] 15 [0.6] 18 [0.2]	45	10 [0.3] 20 [0.6] 45 [0.1]	1.0	0.05 [0.2] 0.2 [0.6] 0.6 [0.2]	
Centennial	30 [0.2] 55 [0.6] 70 [0.2]	N	12 [0.2] 15 [0.6] 18 [0.2]	63	15 [0.2] 20 [0.6] 40 [0.2]	1.0	0.3 [0.2] 0.4 [0.1] 1.0 [0.4] 1.5 [0.3]	
Madison Northern Segment	30 [0.2] 55 [0.6] 70 [0.2]	W	12 [0.2] 15 [0.6] 18 [0.2]	40	15 [0.2] 30 [0.4] 40 [0.3] 55 [0.1]	1.0	0.01 [0.2] 0.3 [0.65] 2.0 [0.15]	
Madison Canyon Segment	30 [0.2] 55 [0.6] 70 [0.2]	W	12 [0.2] 15 [0.6] 18 [0.2]	47	15 [0.2] 30 [0.4] 40 [0.3] 55 [0.1]	1.0	0.03 [0.2] 0.3 [0.35] 0.4 [0.35] 3.0 [0.1]	
Madison Southern Segment	30 [0.2] 55 [0.6] 70 [0.2]	W	12 [0.2] 15 [0.6] 18 [0.2]	20	15 [0.2] 30 [0.4] 40 [0.3] 55 [0.1]	1.0	0.01 [0.2] 0.3 [0.65] 2.0 [0.15]	
Hebgen	40 [0.2] 60 [0.6] 75 [0.2]	S	12 [0.2] 15 [0.6] 18 [0.2]	14	12 [0.2] 14 [0.6] 16 [0.2]	1.0	0.2 [0.2] 0.6 [0.6] 1.0 [0.2]	
Red Canyon	55 [0.2] 70 [0.6] 85 [0.2]	S	12 [0.2] 15 [0.6] 18 [0.2]	34	10 [0.2] 20 [0.6] 30 [0.2]	1.0	0.2 [0.2] 0.6 [0.6] 1.0 [0.2]	

Table 8-7. Continued.

Fault Name	Dip[1] (Degree)	Dip Direction	Seismogenic Thickness (km)	Total Fault Length (km)	Characteristic Rupture Length (km)	Seismogenic Probability	Slip Rate[2] (mm/yr)	Recurrence Interval[2] (yr)
Teton[2]	45 [0.2] 60 [0.6] 75 [0.2]	E	12 [0.2] 15 [0.6] 18 [0.2]	60	20 [0.2] 40 [0.6] 60 [0.2]	1.0	0.5 [0.2] 1.5 [0.4] 2.0 [0.3] 4.0 [0.1]	800 [0.2] 2,000 [0.6] 4,000 [0.2]
Grand Valley Swan Valley Segment	30 [0.2] 55 [0.6] 70 [0.2]	W	12 [0.2] 15 [0.6] 18 [0.2]	49	40 [0.2] 50 [0.6] 60 [0.2]	1.0	0.014 [0.6] 0.30 [0.2] 1.10 [0.2]	
Grand Valley Grand Valley Segment	30 [0.2] 55 [0.6] 70 [0.2]	W	12 [0.2] 15 [0.6] 18 [0.2]	43	40 [0.2] 50 [0.6] 60 [0.2]	1.0	0.014 [0.6] 0.30 [0.2] 1.10 [0.2]	
Grand Valley Star Valley Segment[2]	30 [0.2] 55 [0.6] 70 [0.2]	W	12 [0.2] 15 [0.6] 18 [0.2]	53	40 [0.2] 50 [0.6] 60 [0.2]	1.0	0.6 [0.2] 0.8 [0.6] 1.2 [0.2]	2,500 [0.2] 5,000 [0.6] 15,000 [0.2]
Bear Lake	30 [0.2] 55 [0.6] 70 [0.2]	W	12 [0.2] 15 [0.6] 18 [0.2]	115	25 [0.2] 50 [0.6] 80 [0.2]	1.0	0.4 [0.2] 0.6 [0.6] 1.5 [0.2]	
East Gem Valley	40 [0.2] 50 [0.6] 60 [0.2]	W	12 [0.2] 15 [0.6] 18 [0.2]	80	25 [0.2] 50 [0.6] 80 [0.2]	1.0	0.02 [0.3] 0.05 [0.4] 0.10 [0.3]	
Wasatch Malad City Segment	40 [0.2] 50 [0.6] 60 [0.2]	W	12 [0.2] 15 [0.6] 18 [0.2]	45	20 [0.2] 30 [0.3] 40 [0.3] 50 [0.2]	1.0	0.05 [0.2] 0.10 [0.6] 0.20 [0.2]	Not Constrained
Wasatch Clarkston Segment	30 [0.2] 55 [0.6] 70 [0.2]	W	12 [0.2] 15 [0.6] 18 [0.2]	18	20 [0.2] 30 [0.3] 40 [0.3] 50 [0.2]	1.0	0.10 [0.2] 0.40 [0.6] 0.70 [0.2]	Not Constrained

Table 8-7. Continued.

Fault Name	Dip[1] (Degree)	Dip Direction	Seismogenic Thickness (km)	Total Fault Length (km)	Characteristic Rupture Length (km)	Seismogenic Probability	Slip Rate[2] (mm/yr)	Recurrence Interval[2] (yr)
Wasatch Collinston Segment	30 [0.2] 55 [0.6] 70 [0.2]	W	12 [0.2] 15 [0.6] 18 [0.2]	33	20 [0.2] 30 [0.3] 40 [0.3] 50 [0.2]	1.0	0.05 [0.2] 0.10 [0.6] 0.20 [0.2]	Not Constrained
Wasatch Brigham City Segment[2]	30 [0.2] 55 [0.6] 70 [0.2]	W	12 [0.2] 15 [0.6] 18 [0.2]	39	20 [0.2] 30 [0.3] 40 [0.3] 50 [0.2]	1.0	0.60 [0.2] 1.40 [0.6] 4.50 [0.2]	500 [0.2] 1,300 [0.6] 2,800 [0.2]
Wasatch Weber Segment[2]	30 [0.2] 55 [0.6] 70 [0.2]	W	12 [0.2] 15 [0.6] 18 [0.2]	53	20 [0.2] 30 [0.3] 40 [0.3] 50 [0.2]	1.0	0.6 [0.2] 1.2 [0.6] 4.3 [0.2]	500 [0.2] 1,300 [0.6] 2,800 [0.2][3]
Big Lost	45 [0.2] 55 [0.6] 75 [0.2]	E	12 [0.2] 15 [0.6] 18 [0.2]	15	3 [0.5] 11 [0.3] 15 [0.2]	0.3	0.08 [0.8] 0.4 [0.2]	
Big Lost Sensitivity to Normal Faulting	45 [0.2] 55 [0.6] 75 [0.2]	E	12 [0.2] 15 [0.6] 18 [0.2]	15	3 [0.5] 11 [0.3] 15 [0.2]	0.3[4] 0.65 1.0	0.08 [0.8] 0.4 [0.2]	
Big Lost Sensitivity to Strike-slip Faulting[1]	90 [1.0]		12 [0.2] 15 [0.6] 18 [0.2]	15	3 [0.5] 11 [0.3] 15 [0.2]	0.3	0.08 [0.8] 0.4 [0.2]	

1. All faults have normal sense of slip (weight 1.0), with the exception of sensitivity analyses for the Big Lost fault where a weight of 1.0 is used for strike-slip faulting with the other parameters listed in that row.
2. When recurrence intervals are listed, slip rate branch is weight 0.6 and recurrence interval branch is weight 0.4, otherwise slip rate branch is weight 1.0.
3. The Weber Segment recurrence interval was originally documented as 500 [0.2], 1,400 [0.6], and 2,400 [0.2] but was simplified to match with the Brigham City recurrence interval.
4. Different p[S] scenarios were used in sensitivity analyses for the Big Lost fault involving both normal and strike-slip styles of faulting (Sections 8.3.1 and 8.3.4). In the case for strike-slip faulting, the dip was set at 90º so no dip direction is given.

boundaries for the local faults are defined by historical surface rupture, geomorphic expression of late Quaternary faulting, changes in recency of slip, changes in slip rates, significant discontinuities in the surface trace, changes in fault strike and dip, cross structures, and geologic evidence for discontinuity of stratigraphy across the projection of the fault along strike.

Only the better-studied regional faults, such as the Wasatch, Madison, and Grand Valley faults, have sufficient information to identify segmentation points indicating different slip rate segments for the SSC model (Figure 8-3). Considering the relative distance of the regional faults to the site, slip rate is the most important fault characteristic for purposes of the SSC model. Thus, the variations in fault slip rate are used to define fault slip rate segments and are incorporated into the SSC model for those regional fault sources such supporting data.

The identified segments are important in the characterization of the fault sources in the SSC model. Slip rates, which are based on Quaternary geologic evidence for displacement, fault dip, and style of faulting, are defined for each fault segment or for the entire fault if segments are not identified (Section 8.3.8). This approach is consistent with studies of faults with long-term slip rates that exhibit repeated coseismic slip distributions during multiple earthquakes (e.g., Hecker et al., 2013; Simoes et al., 2014). The combination of slip rate and fault segment downdip geometry defines the seismic moment rate that is used in the recurrence calculation for fault sources. Based on consideration of the segmentation of the various faults and the potential for rupturing one or more segments, characteristic earthquake ruptures associated with Mchar are identified for each fault source (Section 8.3.9) as well as Mmax. Although the segmentation points are important, the TI Team did not conclude that they would invariably be a barrier to rupture. Therefore, the hazard calculations allow for ruptures to propagate across segmentation points along a fault of interest. However, the seismic moment rates of individual segments are maintained (or "balanced") throughout the full range of ruptures that are modeled to occur, based on the recurrence relationships (Section 8.3.10).

It should be noted that all of the coseismic rupture scenarios considered in the SSC model involve the rupture of parts of, or the entire length of, individual faults. Although the simultaneous occurrence of ruptures of multiple fault sources is not precluded due to random chance, there are no coseismic rupture scenarios that specifically entail the "linkage" of multiple fault sources.

Based on consideration of the various lines of evidence, the TI Team identified segmentation points along the lengths of the fault sources, as shown in Figure 8-3 for the regional faults and Figure 8-4 for the local faults. For the regional faults, the uncertainties associated with the potential rupture of single or multiple segments are not expressed explicitly in the SSC model. Rather, uncertainties in rupture lengths are taken from Table 8-7 and generally range from fractions of the total length up to the total length of the fault. For the local faults, the consideration of segmentation for assessing rupture length is more explicit. For these faults, the alternatives of single segment, multiple segment, or unsegmented ruptures (i.e., ruptures without any controls by segmentation) are all included in the logic trees (Figures 8-23 through 8-26). The use of the estimated lengths of potential ruptures leads directly to the assessment of characteristic and maximum magnitudes, as described in Section 8.3.9.

8.3.3 Fault Location

The locations of twelve regional faults and three local normal faults are well understood and have been mapped for many years. The location of the Big Lost fault was assessed in this study and is based on interpretations of possible offsets in boreholes (see Section 5.4). The southern terminations of the three local faults at their juncture with the northwest margin of the ESRP are uncertain (see Sections 4-8 and 4-9). Because of the potential hazard-significance of the proximity of the three local faults to INL, the

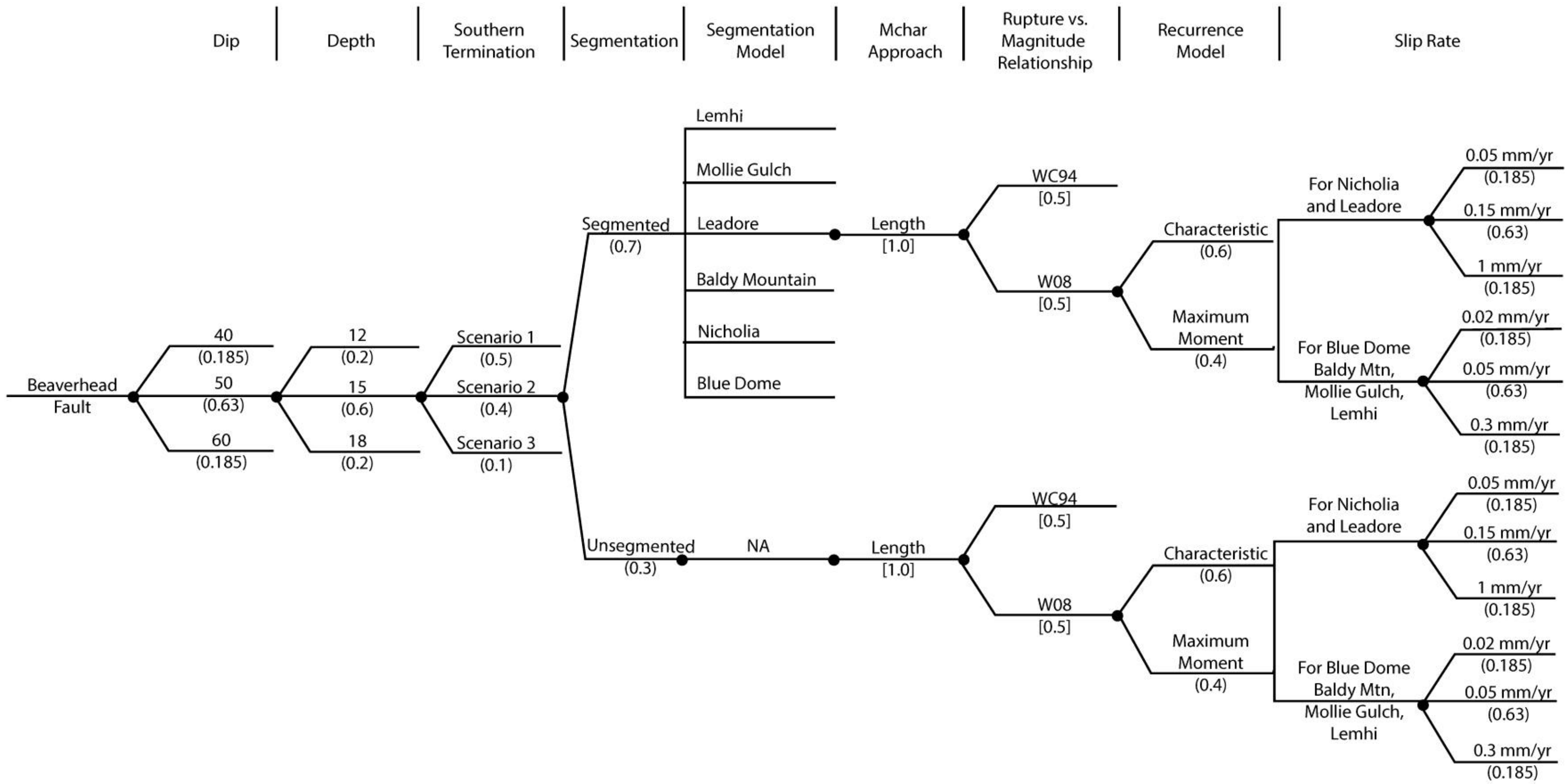

Figure 8-23. Logic tree for the Beaverhead fault as used in the SSC model.

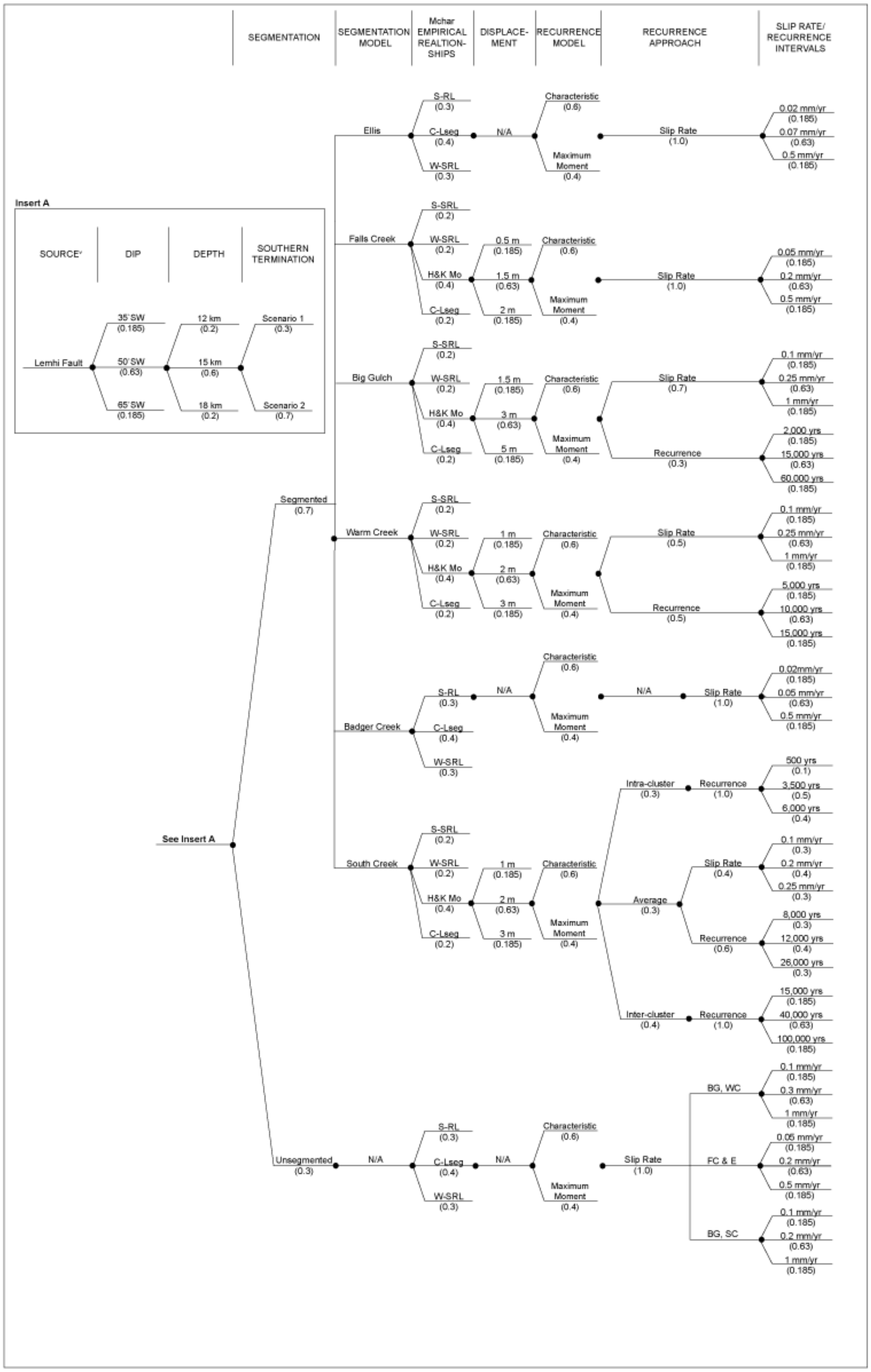

Figure 8-24. Logic tree for the Lemhi fault as used in the SSC model.

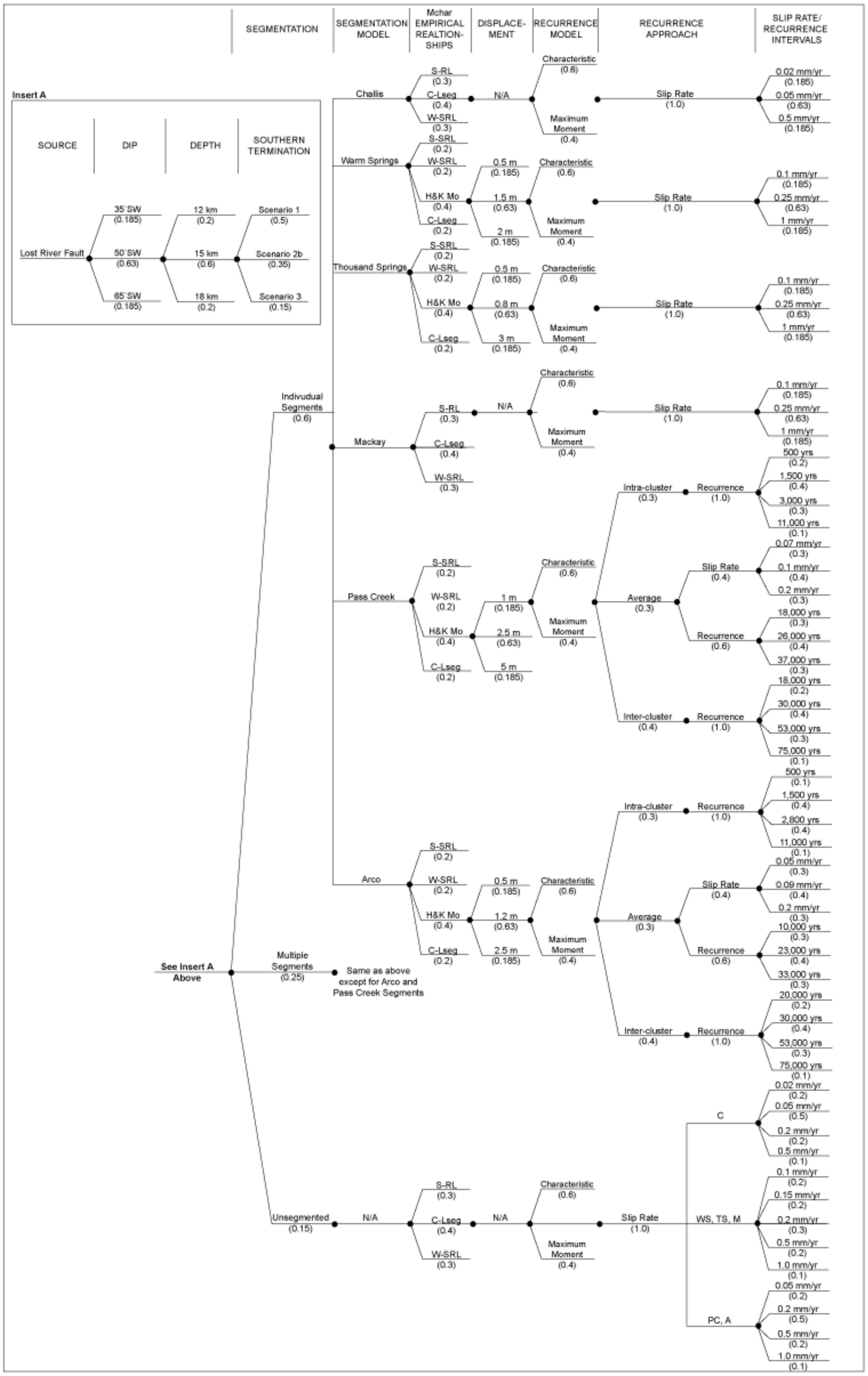

Figure 8-25. Logic tree for the Lost River fault as used in the SSC model. Also see Figure 8-26.

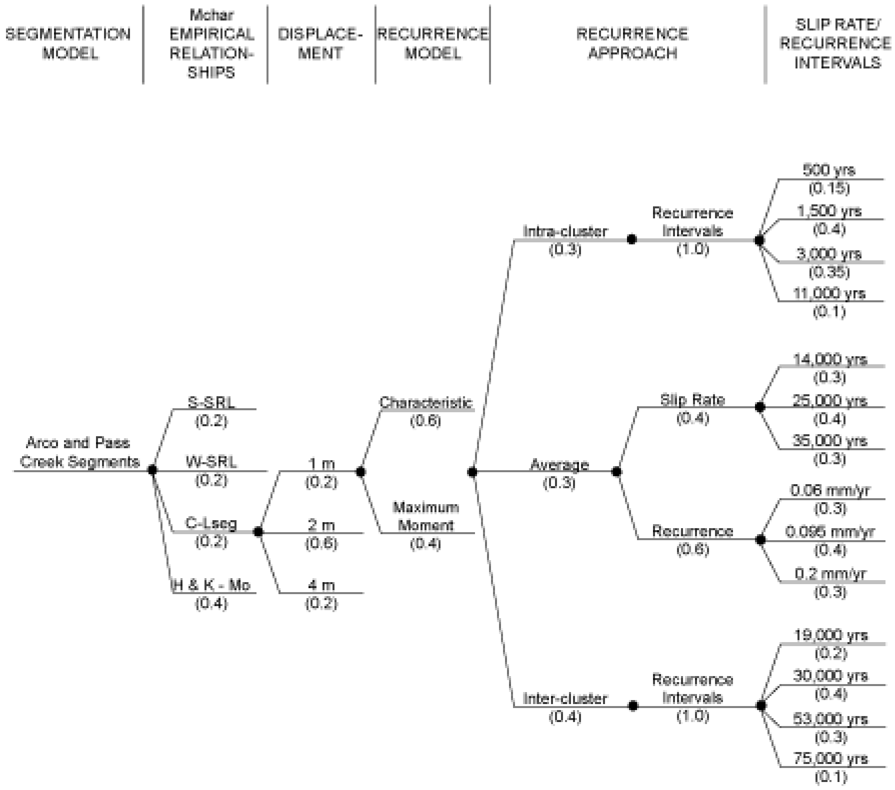

Figure 8-26. Logic tree for the Lost River fault assuming the Arco and Pass Creek segments are combined.

uncertainties of the southern terminations of the Beaverhead, Lemhi, and Lost River faults were included in the logic trees of these faults (Figures 8-23, 8-24, and 8-25, respectively). Two or three locations are possible for the southern terminations of the Lost River, Lemhi and Beaverhead fault sources based on available data. The termination scenarios are shown in Figure 8-4 and their uncertainty distributions are listed in Table 8-8. The supporting basis for the scenarios and weights are also given in Table 8-8.

8.3.4 Style of Faulting

The style of faulting assigned to all fault sources for the PSHA is normal faulting with a weight of [1.0], with the exception of specific sensitivity analyses for the Big Lost fault. The fault sources identified in this study are assessed to be normal faults that accommodate east-west or northeast-southwest extension (Section 4-5). However, new data and evaluations sugesst that the ESRP host zone could have a state of stress that includes normal and strike-slip faulting (Section 4.5). As a result, the sensitivity to strike-slip versus normal faulting was evaluated in the ATR PSHA. A sensitivity test was included by using a weight of [1.0] for strike-slip faulting with p[S]=0.3 (Table 7-8).

Table 8-8. Basis for and assigned weights of fault termination scenarios locations.

Fault	Termination Scenario Map Label In Figure 8-4	Scenario ID for SSC Model [Weights]	Supporting Basis (See Figures 8-4 and 4-16)
Lost River	S1	1 [0.5]	S1 is ~1 km south of the end of the Lost River range coincident with late Pleistocene range-front scarps (1).
	S2	2 [0.35]	S2 is located at the southern end of the Arco Hills near INL boundary based on mapping by and a trench that revealed that scarps are fluvial and the buried faults observed in seismic reflection profiles (AR2 and AR3) have not ruptured to the surface since 30-50 ka (2, 3, 4, 5).
	S3	3 [0.15]	S3 is located in the Arco volcanic rift zone by the INL boundary near dike-induced deformational features that may be interpreted as such or possibly as tectonic and associated with the Arco segment (1, 6, 7, 8).
Lemhi	S1	1 [0.3]	S1 is located near a cross fault that intersects the South Creek segment, and to the south, fault scarps are buried by eolian deposits (1, 9).
	S2	2 [0.7]	S2 is located near the end of the Lemhi range between seismic reflection lines that show a SW-dipping fault on SC1, but only flat lying reflectors on lines SC2 and SC3 (5, 9).
Beaverhead	S1	1 [0.5]	S1 is located at the northern end of the Blue Dome segment because the most recent offsets may be 30-100 k.y. (1, 10).
	S2	2 [0.4]	S2 is located at the southern end of the Blue Dome segment to account for possibility that the segment is nearing the end of a long quiescence period (1).
	S3	3 [0.1]	S3 is located in the ESRP along a possible projection of the Birch Creek valley and alignment with volcanic vents (1).

References: 1) Woodward-Clyde Federal Services et al., 1996; 2) AMEC, 2013; 3) Olig et al., 1997; 4) Olig, 1997; 5) Jackson et al., 2006; 6) Smith et al., 1996; 7) Wu and Bruhn, 1994; 8) Kuntz et al. 2002; 9) Bruhn et al., 1992; 10) Crone and Haller, 1991.

8.3.5 Seismogenic Thickness

The seismogenic thicknesses for the local and regional faults were assessed to be consistent with the tectonic regional zones that they fall within. As discussed in Section 8.2.1.3, the D_{90} analysis was performed using the E[**M**] catalog. This catalog includes the mainshock focal depths of earthquakes that ruptured segments of both regional and local faults such as the 1983 E[**M**] 6.96 Borah Peak earthquake that ruptured the central section of the Lost River fault and 1959 E[**M**] 7.26 Hebgen Lake earthquake that ruptured the Hebgen and Red Canyon faults. Table 8-7 lists the distributions of seismogenic thickness for the regional faults and the logic trees show them for the three local faults (Figures 8-23, 8-24, and 8-25).

8.3.6 Fault Dip

The fault dips for the regional fault sources were derived from previous studies including the AMEC (2013), which compiled and evaluated information primarily from the Wong et al. (2005) and USGS Quaternary Fault and Fold Database (Haller et al., 2010a; 2010b). The distributions of fault dips and directions for the thirteen regional fault sources are listed in Table 8-7.

The dips associated with the local fault sources were derived from previous studies including looking at coseismic ruptures and patterns of aftershocks defining the rupture planes of normal-faulting earthquakes (e.g., 1983 Borah Peak). The distribution of dips and directions for the Beaverhead fault are 40° SW [0.185], 50° SW [0.63], and 60° SW [0.185], and for the Lemhi and Lost River faults are 35° SW [0.185], 50° SW [0.63] and 65° SW [0.185].

8.3.7 Approaches to Assessing Recurrence: Slip Rate and Recurrence Intervals

The logic tree nodes that relate to the assessments of recurrence for fault sources has a node that provides for two alternative approaches for the assessment of earthquake recurrence, which are slip rate and recurrence intervals. All of the fault sources have geologic data that allow for the assessment of slip rate, but only the Lost River and Lemhi faults have sufficient paleoseismic data to allow for the assessment of recurrence intervals along with some of the regional faults that have paleoseismic investigations.

The TI Team’s assessment of the relative weights assigned to the slip-rate approach for recurrence estimation and the paleoseismic recurrence interval approach is a function of the fault-specific data that are available to assess each quantity. In ideal circumstances with abundant paleoseismic data that define with low uncertainties both the presence of individual earthquakes and their timing the recurrence interval approach would be given high weight relative to the slip-rate approach. This is because a slip rate provides the average behavior of a fault over a given time period, but the recurrence interval approach can provide more direct evidence of the actual length of recurrence intervals during the most recent period of activity. Unfortunately, the paleoseismic data that are available for the two local faults have significant uncertainties in both the numbers of paleo-earthquakes present in the geologic record and in the timing of each earthquake. For this SSHAC Level 1 PSHA, in light of a thorough review of these data and their associated uncertainties, the TI Team adopted the assessments of relative weights that were given in AMEC (2013). The characterization of fault sources in AMEC (2013) had the advantage of including data compilation and evaluations involving other experts in the paleoseismic community (i.e., S. Olig and M. Machette), and are consistent with those used in the recent seismic hazard analysis for the state of Montana (Wong et al., 2005).

8.3.8 Characteristic and Maximum Magnitudes

As discussed in detail in Section 8.3.10, the characteristic earthquake magnitude frequency distribution (Youngs and Coppersmith, 1985; denoted as YC85) is adopted as being appropriate for use in defining the shape of earthquake recurrence curves for all of the regional fault sources and has the highest weight for the local fault sources. The alternative distribution for the local faults is the Wesnousky (1986) "maximum moment" model, which is essentially the same as the YC85 model except that it does not have an exponential part in the smaller magnitudes. For this study, it is assumed that the Mchar for the Wesnousky model is identical to that for the YC85 model. The YC85 model requires as input the slip rate and an estimate of the Mchar for the fault of interest. The functional form of the YC85 model expresses the magnitude range of the characteristic earthquake to be a 0.5 magnitude-wide uniform (boxcar) aleatory distribution centered on the mean Mchar for the fault of interest. The distribution is aleatory in the sense that all magnitudes within the distribution are expected to occur and their relative frequency is the same. This means that the maximum magnitude, Mmax, in the YC85 model is 0.25 magnitude units larger than the mean Mchar. This section describes the assessment of Mchar for each of the fault sources and, by definition Mmax is therefore also defined as 0.25 magnitude units larger.

The assessment of characteristic earthquake magnitudes in paleoseismology typically involves consideration of the dimensions of rupture of paleo-earthquakes (e.g., rupture lengths, rupture areas, maximum and average displacement per event). In the case of the regional faults in this study and the Beaverhead fault, displacement per event paleoseismic data and downdip widths were generally not available, but data that can be interpreted to estimate the possible lengths of past ruptures were available. Such data include discontinuities in the surface trace, changes in fault strike, cross-structures, changes in geomorphic expression, changes in cumulative slip or structural relief, large stepovers, and the like. Based on this evidence, characteristic rupture lengths and their uncertainties were assessed by the SSC TI Team for each fault source, as given in Table 8-7.

It should be noted that the characteristic rupture lengths do not necessarily correspond exactly to the lengths of mapped sections along the fault, nor do they uniquely apply to any given section of the fault. Rather, the assessment of characteristic lengths was made in light of all possible segmentation points along the fault, the data quality, and correspondence of multiple lines of evidence for particular segmentation points. Further, the assessed characteristic lengths are judged by the TI Team to be applicable to the entire fault source and to have the potential to occur anywhere along its length. Therefore, ruptures in the hazard calculations are allowed to straddle segmentation points defined from structural relief evidence, but the seismic moment rates of each fault segment are held constant throughout the assumed occurrence of the full range of magnitudes and associated ruptures.

Given the distribution of potential rupture lengths associated with characteristic earthquakes available for each regional fault source and the Beaverhead fault, the next step is to develop estimates of Mchar. This includes the selection of appropriate scaling relationships between magnitude and rupture length, as well as the development of weights for the two alternative approaches. The selection of magnitude-to-rupture-length scaling relationships was made in light of the normal-faulting tectonic environment of the fault sources. After review of the literature, the TI Team concluded that the available scaling relationships relating moment magnitude to rupture length were limited. The TI Team selected two published scaling relationships relating rupture length to moment magnitude and applicable to normal faults. For the regional faults and the Beaverhead fault, Table 8-9 lists the scaling relationships and the weights assessed for the SSC model. Note that the rupture length at depth (RLD) relationship from WC94 was selected based on the fact that the segment lengths and assessed characteristic lengths for the regional faults are estimated without any direct knowledge of the surface rupture lengths of past earthquakes. The W08 relationship provides rupture lengths that are assessed based on a combination of geologic and seismologic (aftershocks) evidence. The two scaling relationships are assigned equal weights of [0.5].

Table 8-9. Magnitude (Mchar) scaling relationships used in the SSC model.

Fault	Parameter	Equation	Relationship Reference and ID for Logic Tree
All Regional Beavehead	Rupture length at depth (RLD)	**M** = 5.08 + 1.16 log RLD	Wells and Coppersmith (1994) WC94
	Rupture length (L)	**M** = 5.30 + 1.12 log L	Wesnousky (2008) W08
Lost River Lemhi	Rupture length (RL)	**M** = 5.88 + 0.80 log RL	Stirling et al. (2002) S-RL
	Paleoseismic segment length (Lseg)	**M** = 5.67 + 0.88 log Lseg	Carpenter et al. (2012) C-Lseg
	Surface rupture length (SRL)	**M** = 5.30 + 1.02 log SRL	Wesnousky (2008) W-SRL
	Displacement (D) [1]	**M** = 2/3 log(Mo) - 10.7; Mo = μAD	Hanks and Kanamori (1979) H&K-Mo
1. Mo = μAD; μ is the rigidity modulus (3×10^{10} Pa), A is fault area, and D is the displacement.			

Because additional information is available for the Lemhi and Lost River faults, this information is used to better define Mchar for these faults. In particular, better information is available relative to the lengths of paleoseismic surface ruptures, thus allowing for the use of relationships that specifically include that information. The rupture length scaling relationships used for the Lemhi and Lost River fault estimates of Mchar included those from Stirling et al. (2002), Carpenter et al. (2012), and Wesnousky (2008) (Table 8-9). In addition to rupture length estimates, some of the segments of the Lemhi and Lost River faults have estimates of the amount of displacement that occurred during individual paleoseismic events. In these cases, the moment magnitude of Mchar is estimated using the relationship of Hanks and Kanamori (1979). The displacement (per event) and fault rupture area (product of rupture length and downdip width) are used to calculate the seismic moment, which is then used in the Hanks and Kanamori (1979) relationship to calculate **M** (Table 8-9). The weights applied to displacement as well as rupture lengths are shown in the logic trees (Figures 8-23, 8-24, and 8-25).

8.3.9 Recurrence Model

Recurrence models or magnitude frequency distributions (MFDs) define the relative frequency of various earthquake magnitudes generated by a fault source. As such, they define the “shape” of the recurrence curve as it expresses the annual frequency of various magnitude earthquakes up to the maximum for a given fault source. Although it is a common observation that the appropriate MFD describing regional recurrence for a large region is an exponential distribution (Gutenberg and Richter, 1956) that is truncated at the Mmax, the appropriate MFD for a fault source has been the subject of research for many years (e.g., Schwartz and Coppersmith, 1984). As part of the evaluation process, the SSC TI Team considered three alternative MFDs for use in defining the recurrence for fault sources: a truncated exponential distribution, the maximum moment model (Wesnousky, 1986), and the characteristic earthquake distribution (Youngs and Coppersmith, 1985). The three alternative models are shown in Figure 8-27 for a hypothetical fault using the same Mmax and seismic moment rate.

Consistent with the SSHAC process, the TI Team evaluated the alternative MFDs that have been proposed for fault sources: a truncated exponential distribution, the maximum moment model, and the characteristic earthquake model (indicated by the notation YC85). This evaluation follows years of consideration of these models by other PSHAs for application in describing fault-specific recurrence. For

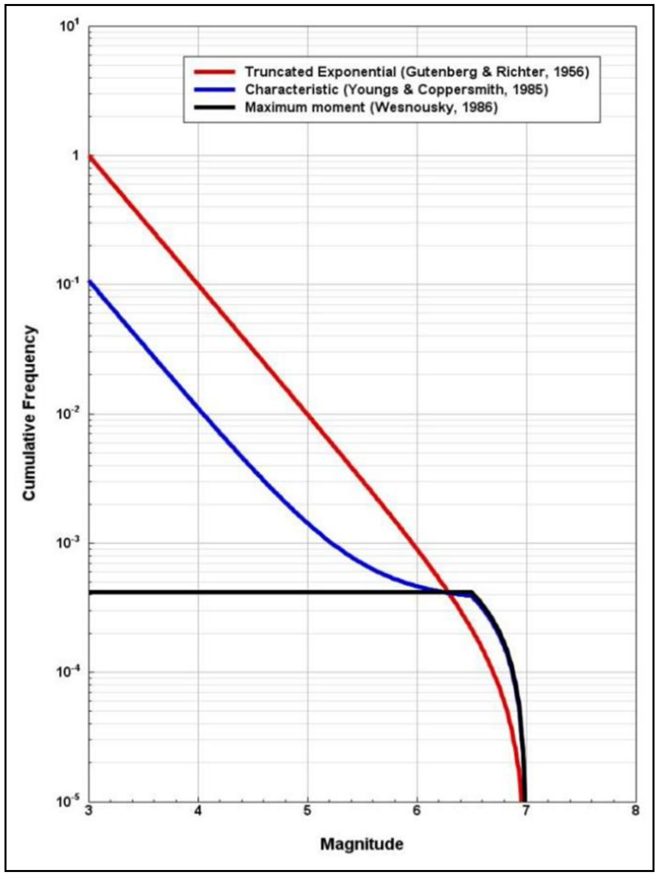

Figure 8-27. Alternative cumulative magnitude frequency distributions of earthquake recurrence for a given Mmax of 7 and for a constant seismic moment rate (modified from Youngs and Coppersmith, 1985).

example, the SSHAC Level 3 BC Hydro PSHA (Jack Benjamin & Associates et al., 2012) conducted a review of these alternatives and concluded that the exponential and maximum moment models (termed the “maximum magnitude” model in that study) should be assigned very low to zero weight. Similarly, the SSHAC Level 3 CEUS SSC project (NRC, 2012b) concluded that the exponential model was not appropriate for fault sources or for repeated large-magnitude earthquake (RLME) sources based on comparisons with observed paleoseismic evidence and historical earthquake recurrence.

Likewise, the Hanford PSHA (PNNL, 2014) concluded that the YC85 model as the most appropriate model for fault-specific recurrence. This was done by comparing of the rates of observed small-magnitude seismicity spatially associated with each fault with the predicted recurrence based on the YC85 model and an exponential model. A number of observed earthquakes can be reasonably associated with each fault and the maximum moment model does not provide for these events. Therefore, the Hanford TI Team concluded that the model is not appropriate for the faults studied and it was assigned zero weight. This observation has been made elsewhere and was one of the first reasons that the characteristic earthquake model was first proposed (e.g., Youngs and Coppersmith, 1985; Youngs et al., 1992). For example, the same type of comparison was made for several major faults in the San Francisco Bay Area between observed seismicity and predicted recurrence using slip rate with the YC85 model and the exponential model. Although the observed seismicity rates are considerably higher and therefore cover a larger range of magnitudes, the exponential model consistently overestimates the recurrence rates based on the observed seismicity record. For comparison, the observed seismicity within the fault plane proximity of the Lemhi, Lost River, and Beaverhead faults were plotted together with the exponential and YC85 recurrence curves (Figure 8-28).

In addition to the comparisons with observed seismicity, the YC85 model is also strongly supported by a recent examination of paleoseismic evidence by Hecker et al. (2013). A key element of the characteristic earthquake concept is the repeated occurrence of essentially the same size earthquake at particular points along a fault, as evidenced by observed multiple displacements in trenches along faults. Hecker et al. (2013) quantified the characteristic earthquake by exploring coefficient of variation (CV) values of surface rupture displacements. The data included 505 slip-at-a-point observations from 171 sites in 20 countries, and the average number of observations per site is about 3. Analysis of the variability of displacement amounts at individual sites in the empirical data showed a range of CVs of 0.40-0.55. The calculated CV for the YC85 model is 0.45-0.46, which is reasonably consistent with the empirical data. But the calculated CV for an exponential distribution, which would be expected to give rise to a wider range of displacement events, is 0.66-0.83. Hecker et al. (2013) conclude that the exponential distribution does not agree with fault-specific paleoseismic observations and that the YC85 model predicts a range of displacements that is reasonably consistent with the observations.

In light of the evaluations described above, the TI Team selected the YC85 model as an appropriate MFD for use in calculations of recurrence for all regional fault sources and is the preferred model for the local fault sources. Although it cannot be eliminated based on the present evidence, lesser weight is given to the maximum moment model for the local faults. In all cases, the exponential model is assigned zero weight as an appropriate MFD for the fault sources.

(a)

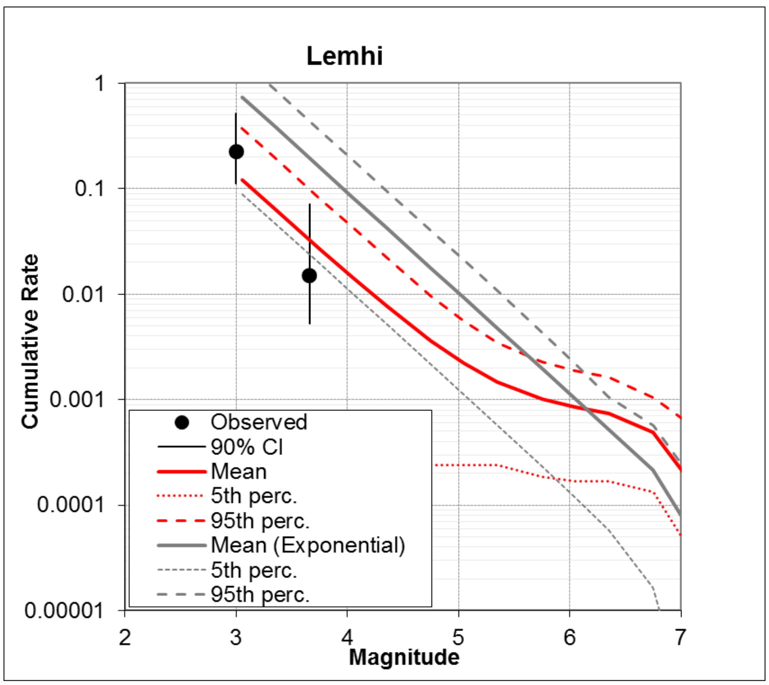

(b)

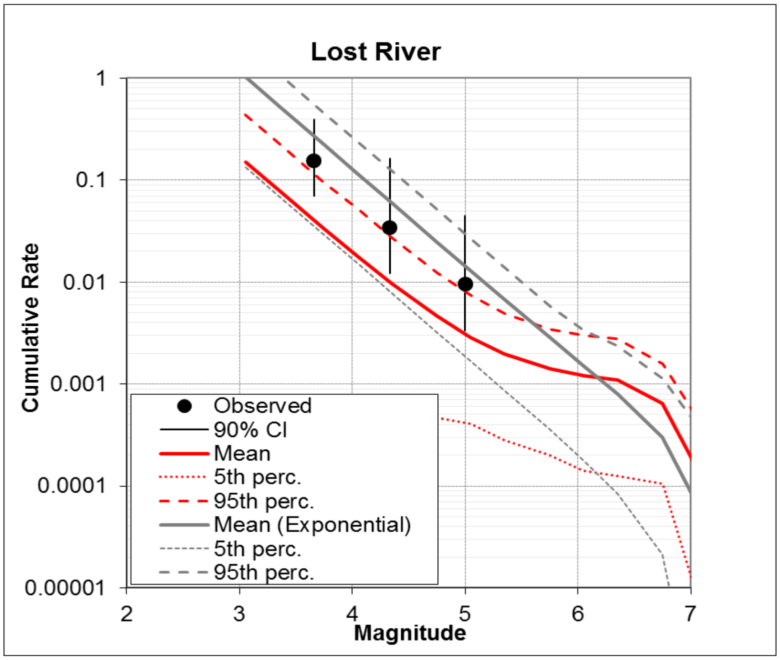

(c)

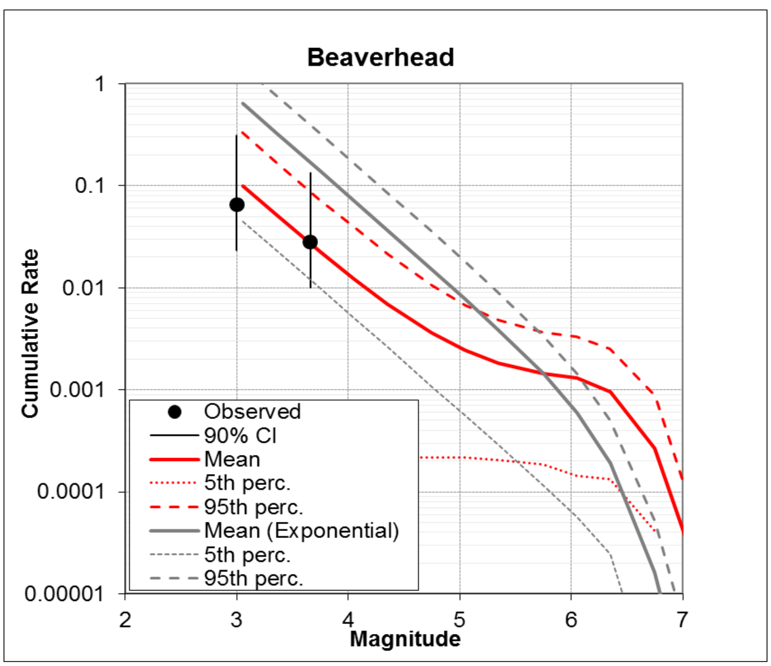

Figure 8-28. Comparison of the YC85 and exponential magnitude frequency distributions (MFDs) with observed seismicity rates for the Lemhi, Lost River, and Beaverhead faults. Seismicity rates are based on observed counts of earthquakes lying within the seismicity capture areas and extended capture areas. The mean recurrence based on the exponential MFD is shown by the brown line and the mean, 5th, and 95th percentile recurrence curves are also shown for the YC85 model.

8.4 Cascadia Plate Interface Source

As shown diagrammatically in Figure 8-29, the seismogenic plate interface is characterized as a fault source in the INL SSHAC Level 1 PSHA. The interface of the Cascadia Subduction Zone is located approximately 900 km from the INL Site (Figure 8-30). Given its tectonic position, its expected style of faulting is reverse and its lateral and downdip dimensions imply the potential to generate very large earthquakes.

The plate interface is different than most subduction zones in its near absence of observed thrust-faulting earthquakes in the instrumental record. However, abundant paleoseismic evidence, both from offshore turbidite sequences and from onshore evidence of coastal subsidence and tsunami deposits, confirms its seismogenic potential in the contemporary tectonic regime. Fortunately, the BC Hydro SSC model (BC Hydro, 2012) included a comprehensive review and evaluation of applicable data, models, and methods at the time the study was being conducted, and the plate interface model includes all pertinent aspects of the source geometry, Mmax, and recurrence characteristics. Sensitivity analyses conducted for the Hanford SSHAC Level 3 PSHA (PNNL, 2014) showed that the most important aspect of the Cascadia Subduction Zone plate interface model is the easternmost extent of the plate interface, thus defining the closest approach of the source to the site. Lesser sensitivity is related to the plate interface Mmax and recurrence rates.

The evaluation phase of the Hanford SSHAC Level 3 PSHA included a comprehensive review of data developed after completion of the BC Hydro model related to the eastern extent of the plate interface, Mmax, and recurrence. This evaluation by the Hanford TI Team led to the need to modify slightly the plate interface logic tree to better represent the uncertainties regarding the eastern extent of the interface, which has been the subject of considerable research in recent years. Other aspects of the model related to Mmax and recurrence were judged to not require updating in light of new information. Due to the recency and thoroughness of the study, the Cascadia Interface source for this study was modeled directly from the

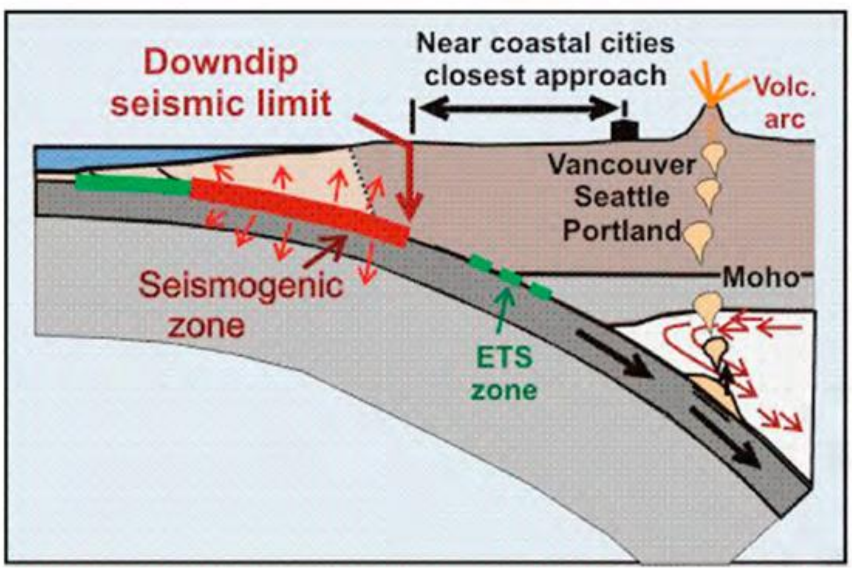

Figure 8-29. Diagrammatic depiction of the seismic sources and other elements related to the Cascadia Subduction Zone (Hyndman, 2013). The plate interface source is shown in red and labeled "seismogenic zone." The landward extent of the plate interface, which is included in the SSC model, is labeled "downdip seismic limit" (Hyndman, 2013).

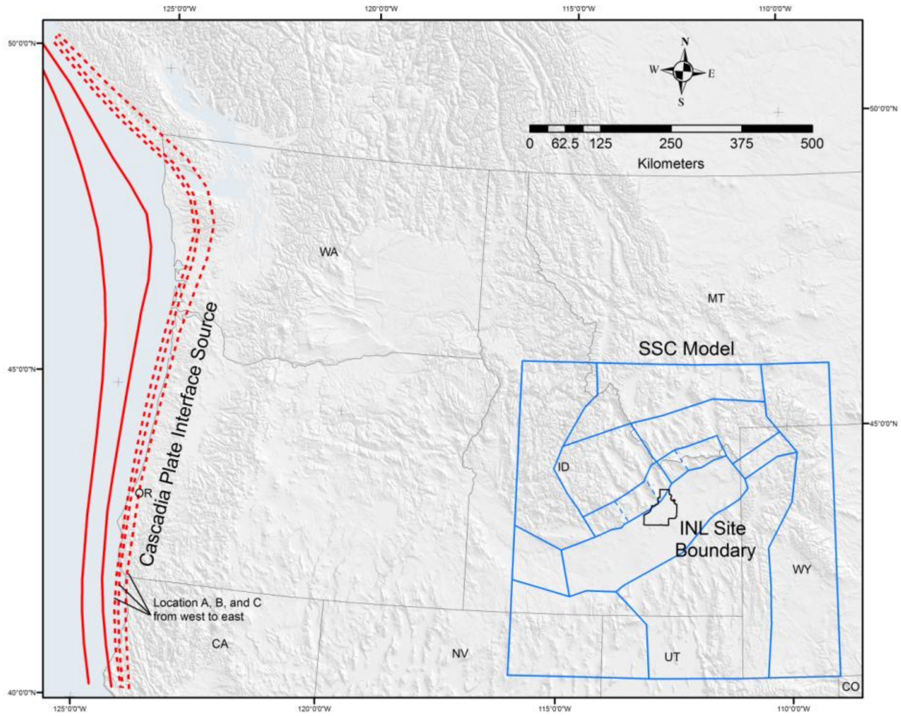

Figure 8-30. Map showing location of the Cascadia Plate Interface fault source relative to INL and the INL SSC model boundaries. INL is located 900 km to the east. Locations of the easternmost boundary of the Cascadia source (dotted red lines) are referred to as Location A, B, and C from west to east, respectively.

methods used in the Hanford SSHAC Level 3 PSHA (refer to Section 8.2.3 of the Hanford SSHAC Level 3 PSHA report; PNNL, 2014). The characteristics and inputs used in this study are based on the Hanford PSHA model and described below.

Given the new data, models, and methods that have become available regarding the landward extent of the plate interface source, the Hanford TI Team considered the characterization given in the logic tree in the BC Hydro SSC model. The logic tree considered three potential locations for the landward-to-downdip extent of the seismogenic plate interface, which are labeled A, B, and C in Figure 8-31. At the time of developing the alternatives, the focus lay on the thermal models and the locations of the "coseismic transition zone." Regardless of the original constraints, the TI Team considered the degree to which the three alternatives capture the range of current interpretations for the location of the downdip limit of seismogenic rupture, based on all available data and interpretations. For example, the westernmost alternative (A) lies at the approximate location of many of the thermal and geodetic models; the easternmost alternative (C) is the approximate location derived from models that conclude the seismogenic interface lies up-dip of the episodic tremor and slip (ETS) events and is close to, but slightly up-dip of, the interpreted location of the forearc mantle corner (FMC); and the central alternative (B) simply lies between the other two alternatives and generally represents the studies that have attempted to integrate all data types. The weights assigned to the alternatives in the BC Hydro study were as follows:

- Location A [0.1]
- Location B [0.7]
- Location C [0.2].

Based on consideration of the new information, the Hanford SSHAC Level 3 study concluded that the three alternatives continue to provide a reasonable and defensible range of interpretations of the downdip extent of the interface. However, the Hanford study also concluded that the relative weights assigned to the alternatives are not a representative description of current knowledge and uncertainties. Additional weight should be assigned to alternative C, which appears to be more consistent with interpretations that consider ETS events and the FMC. The three alternative locations for the easternmost boundary are shown in Figure 8-31 and assessment of weights is listed below:

- Location A [0.1]
- Location B [0.2]
- Location C [0.7].

In addition to the location of the interface, the Hanford SSHAC Level 3 PSHA considered the new information related to the magnitude of Mmax and Mchar, as well as to the timing of paleoseismic earthquakes. For example, Witter et al. (2012) report on interpretations of the size of paleoseismic earthquakes based on the modeled slip of interface events associated with tsunami deposits. The implied magnitudes of the paleo-earthquakes are not well constrained, but lie within the range already included in the BC Hydro logic tree for Mchar and Mmax. No new primary data have been published related to the number and timing of paleoseismic events that would lead to the need to revise the recurrence rates given in the BC Hydro logic tree. Rather, the detailed statistical analyses of the paleoseismic data conducted for the BC Hydro project have now been published (Kulkarni et al., 2013). The Hanford study concluded that the BC Hydro logic-tree elements related to Mchar, Mmax, and recurrence for the plate interface source do not require updating.

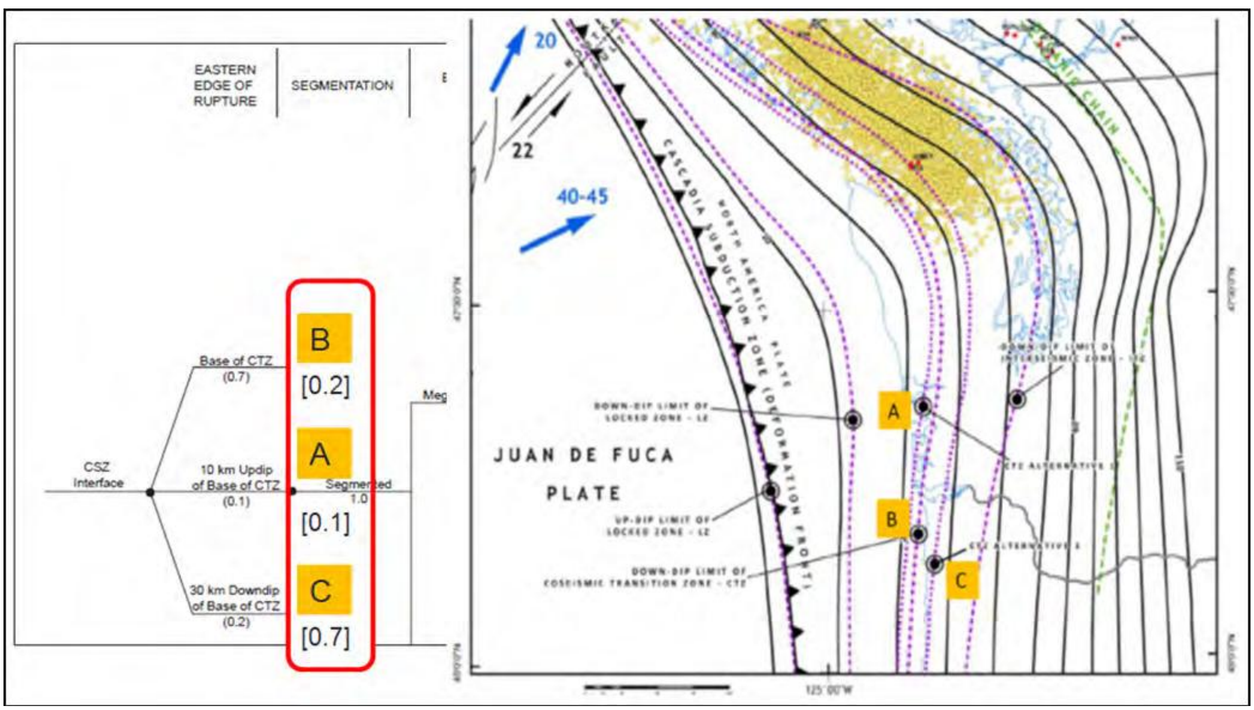

Figure 8-31. Interpretation of the eastern or downdip extent of the seismogenic plate interface in the BC Hydro study (BC Hydro, 2012). The map shows the three alternative locations A, B, and C and associated pink dotted lines. Episodic tremor and slip (ETS) events in the northern part of the Cascadia Subduction Zone (noted as “CSZ Interface”) are shown by the yellow dots. The logic tree for the alternatives is also shown.

9. Ground Motion Characterization (GMC) Model

This section describes the development of the ground motion characterization model used to assess the seismic hazard at the MFC, FMF, SFHP (at NRF), and ATR sites. As described in Section 8, the INL is located in an extensional tectonic regime in which normal faulting earthquakes are the dominant source of seismic hazard. The previous seismic hazard assessments for the INL (Woodward-Clyde Federal Services et al., 1996; URS Greiner Woodward-Clyde Federal Services et al., 1999; 2000) used a mixture of empirical and site-specific GMPEs to characterize the ground motions that may be produced by future earthquakes in the region. The 1996 study used empirical GMPEs for strike slip earthquakes in active tectonic regions (mainly California) without adjustment and the 1999 and 2000 studies used empirical models for strike slip earthquakes applying adjustment factors for normal faulting developed as part of the Yucca Mountain Project (CRWMS M&O, 1998; Stepp et al., 2001). In all three studies the empirical models were not adjusted for INL site conditions. The site-specific GMPEs used in the 1996, 1999, and 2000 studies were based on the point-source stochastic model (e.g., Boore, 1983, 1986; Silva et al., 1996) and utilized parameters specific to the INL sources and site conditions.

Recently, the SWUS Ground Motion Characterization project (GeoPentech, 2015) developed a ground motion model for earthquake sources in the extensional environment of the southern Basin and Range (labeled Greater Arizona sources). The study was conducted as a SSHAC Level 3 study and provided a complete characterization of median ground motions and their aleatory variability. The SWUS study utilized all of the available GMPEs for extensional environments and the extensive databases of empirical ground motions compiled recently in both the US and Europe to develop the SWUS Ground Motion Model (GMM). Because of the much greater amount of empirical data utilized and because the GMM was developed using a formal SSHAC Level 3 process, the SWUS GMC for Greater Arizona was adopted for use in this project to characterize ground motions from shallow crustal seismic sources in the region around the site (within 200 km). Section 9.1 summarizes the SWUS GMM and describes its implementation in this project.

Previous seismic hazard assessments at INL have only considered the contributions from earthquake sources within approximately 200 km of the site. For this study, an additional source, the Cascadia subduction interface source, was also included because of its potential to contribute to the hazard at low to very low ground motion frequencies. Section 9.2 presents the GMPE used to characterize ground motions from this source.

The SWUS Greater Arizona GMM was developed for a generic crustal profile represented by a time averaged shear wave velocity in the upper 30 m (V_{S30}) of 760 m/s, along with a reference level of shallow crustal damping, denoted by parameter kappa. Application of the model to a specific site, such as the INL, requires development of an appropriate transfer function that accounts for the differences in the shallow crustal properties between the site of interest and the reference site. The aleatory variability in ground motions was characterized in terms of a partially non-ergodic standard deviation single station standard deviation (σ_{SS}) that represented the variability of ground motions recorded at a single site. As discussed in GeoPentech (2015), use of σ_{SS} to compute site hazard requires that the epistemic uncertainty in developing the transfer function be incorporated into the hazard assessment. Section 9.3 describes the development of the transfer functions from the SWUS GMM reference site to the MFC and FMF sites for use in computation of the site hazard. Section 9.5 describes the development of a similar set of transfer functions for the SFHP site at NRF. Section 9.7 discusses the development of the transfer functions from the SWUS GMM reference site to rock and soil sites at the ATR Complex. Because the reference site for the PNNL (2014) GMM for Cascadia interface sources is generally similar to that of the SWUS reference site model, the same sets of transfer functions are used for the Cascadia GMM.

Recommendations are also developed for vertical to horizontal (V/H) response spectral ratios to be used to assess vertical response spectra. These are presented in Section 9.4 for the MFC and FMF sites, Section 9.6 for the SFHP site, and Section 9.8 for the ATR Complex.

9.1 Ground Motion Characterization for Shallow Crustal Earthquakes in the Site Region

The SWUS GMM for Greater Arizona sources was adopted for use in characterizing the ground motions produced by shallow crustal earthquakes in the region surrounding the MFC and FMF sites.

9.1.1 Summary of the SWUS GMM

The SWUS GMM for the Greater Arizona sources was developed using a new approach for characterizing the epistemic uncertainty in median ground motions. Typically, a set of GMPEs appropriate for the seismic sources is selected from the literature. These GMPEs are assigned weights in a logic tree format and these weighted alternative GMPEs are assumed to represent the range of epistemic uncertainty in median ground motions. If the GMPEs were developed from regression analysis of empirical data, the epistemic uncertainty may be expanded by considering the epistemic uncertainty in the individual models (e.g., Al Atik and Youngs, 2014). The approach used in the SWUS project is to instead treat the available relevant GMPEs as a sample of possible GMPEs appropriate for assessing ground motion hazard at the site. The statistics of the GMPE parameters are then used to define a distribution for the space of possible models for median ground motions. This distribution is then discretized to produce a manageable number of ground motion models for use in hazard analysis that capture the center, body, and range of the ground motion model space. The steps used in development of the SWUS GMM are as follows.

The literature was reviewed to identify potentially relevant GMPEs. The SWUS project used a set of seven criteria to eliminate GMPEs. The seven criteria are: 1) being superseded by more recent versions; 2) being not relevant to the tectonics of the southern Basin and Range; 3) not extrapolating well beyond the magnitude-distance range over which the models were developed; 4) not clearly separating shallow crustal earthquakes from earthquakes occurring as part of a subduction; 5) models developed as research tools; 6) models developed for a relatively small, specific region different from the one of interest; 7) models that have not been peer reviewed or vetted by the larger scientific community. Table 9-1 is an excerpt from Table 5.5.1-1 of GeoPentech (2015) listing the GMPEs evaluated by the SWUS project for use in modeling median ground motions in active extensional tectonic regions (with focus on sources in the Greater Arizona). The six candidate GMPEs selected are in bold; the reasons given in GeoPentech (2015) for eliminating the other GMPEs are alsolisted.

9.1.2 Selection of Relevant Ground Motion Data

Two databases of recorded ground motions were identified in the SWUS project as being relevant for use in evaluating the candidate GMPEs for the Greater Arizona sources and in developing models for aleatory variability. One was the Pacific Earthquake Engineering Research Center (PEER) NGA-West2 project database (Ancheta et al., 2014) and one was Akkar dataset from the Reference Database of Seismic Ground Motions in Europe (RESORCE) (Akkar et al., 2014c).

9.1.2.1 Development of Model for Median Ground Motions

The SWUS project used a novel approach for characterizing the CBR of the TDI for median ground motions. Rather than just weighting the alternative candidate models listed in Table 9-1, the candidate models were instead considered a sample of possible models for median motions. The range of possible models was developed as follows. Each candidate model was used to predict median ground motions for a

Table 9-1. Candidate GMPEs selected in the SWUS Project to model Basin and Range (Greater Arizona) median ground motions.

GMPE	Comments	Candidate for PVNGS Greater Arizona Sources
Abrahamson et al. (2014)	Update of Abrahamson and Silva (2008)	Abrahamson et al. (2014)
Akkar and Cagnan (2010)	Regional for Turkey	Akkar and Cagnan (2010)
Akkar et al. (2014)	Update of Akkar and Bommer (2010)	Akkar et al. (2014)
Bindi et al. (2014a, 2014b)	Update of Bindi et al. (2011)	Bindi et al. (2014a, 2014b)
Boore et al. (2014)	Update of Boore and Atkinson (2008)	Boore et al. (2014)
Bora et al. (2013)	RESORCE Experimental Model	Bora et al. (2013)
Bradley (2013)	Modification of Chiou et al. (2010) for New Zealand	Bradley (2013)
Campbell and Bozorgnia (2014)	Update of Campbell and Bozorgnia (2008)	Campbell and Bozorgnia (2014)
Chiou and Youngs (2014)	Update of Chiou and Youngs (2008)	Chiou and Youngs (2014)
Derras et al. (2013)	RESORCE Experimental Model	Derras et al. (2013)
Faccioli et al. (2010)	Global data, primarily Japan	Faccioli et al. (2010)
Grazier (2014)	NGA West 1 database plus 2004 Parkfield and 2005 San Simeon	Grazier (2014)
Hermkes et al. (2013)	RESORCE Experimental Model	Hermkes et al. (2013)
Idriss (2014)	Update of Idriss (2008)	Idriss (2014)
Kanno et al. (2006)	Used only depth for separation of event type	Kanno et al. (2006)
McVerry et al. (2006)	Regional for New Zealand	McVerry et al. (2006)
Pankow and Pechmann (2004)	Update of Spudich et al. (2009)	Pankow and Pechmann (2004)
Zhao and Lu (2011)	Proposed change in magnitude scaling above M ~ 7.1	Zhao and Lu (2011)
Zhau et al. (2006)	Mostly Japan data, ACR and SZ with separate factors	Zhau et al. (2006)
Abbreviations: ACR – Active Crustal Region; GMPE – Ground Motion Prediction Equation; NGA – Next Generation Attenuation; PVNGS – Palo Verde Nuclear Generating Station; RESORCE – Reference Database of Seismic Ground Motion in Europe; SZ – Subduction Zone.		

range of magnitude-distance scenarios. These ground motion predictions were then fit by a common functional form, providing one set of possible GMPE parameters. The number of parameter sets was then expanded by interpolating between the various possible pairs of ground motions predicted by the candidate models and fitting the common functional form to these interpolated ground motion predictions.

The next step was to compute a covariance matrix for the parameters of the common function form GMPE using the parameters from the fits to the ground motion predictions from the candidate GMPEs and the parameter fits to the interpolated ground motion predictions. The covariance matrix was then sampled to produce 2000 sets of parameters for the GMPE common form, resulting in 2000 alternative GMPEs.

The SWUS project then used the Sammon's map visualization technique (Sammon, 1969; Scherbaum et al., 2010) to examine the model space created by the 2000 GMPEs. This process involves first computing the Euclidean distance between the ground motion predictions produced by the 2000 GMPEs for the range of scenarios used in the model generation. The resulting distances represent the differences in the ground motion predictions in the high dimensional space represented by the number of alternative scenarios used in the calculations. The Sammon's map technique is then used to calculate a two-dimensional representation of these distances that can be displaced for visual examination. Figure 9-1 shows an example of one such Sammon's map created for the models for PGA (equivalent to spectral acceleration at a period of 0.01 s). The Sammon's map axes have been scaled such that the units represent the standard deviation in natural log units between the ground motion predictions by any two models. The red dots on the figure show the relative positions of the six candidate GMPEs (Table 9-1) used to generate the model space. The Sammon's map technique is devised such that the relative distance between any two points on the map (for example, between any two of the candidate GMPEs) is proportional to the Euclidian distance between the ground motions predicted by the two models over the set of defined earthquake scenarios.

The region outlined on Figure 9-1 defines the envelope of the 2000 models generated by sampling from the covariance matrix of the common form GMPE parameters. As indicated, the GMPE model space has been expanded significantly beyond the range of predictions from the six candidate GMPEs. The magenta and cyan dots show the locations of GMPEs created by applying the epistemic uncertainty models of Al Atik and Youngs (2014) at the plus and minus two sigma level to the candidate GMPEs. This range of uncertainty is also enveloped by the range of the generated GMPEs.

The final step in the development of the GMM for median ground motions is the discrete representation of the GMPE model space for use in PSHA calculations. The shape than encompasses the candidate models and the plus and minus two-sigma epistemic uncertainty about the candidate models (colored dots on Figure 9-1) was approximated by an ellipse. Scaled ellipses with scale factors of 0.5, 1.5, and 2 along with the contour lines for mean errors of ± was then used to divide the model space into a series of cells. A single GMPE was selected to represent each cell by computing the mean hazard from all models within a cell using a simplified seismic source model and identifying the GMPE that produced a hazard curve closest to the mean hazard for the cell. The results produced from 16 to 25 GMPEs to represent the GMPE model space, depending on the spectral frequency. Weights were then assigned to each of the representative models using a combination of the mean residuals computed using the two datasets (NGA-West2 and European), the relative likelihoods computed using the two datasets, and the density of models generated from the sampling of the covariance matrix for the parameters of the common form GMPE.

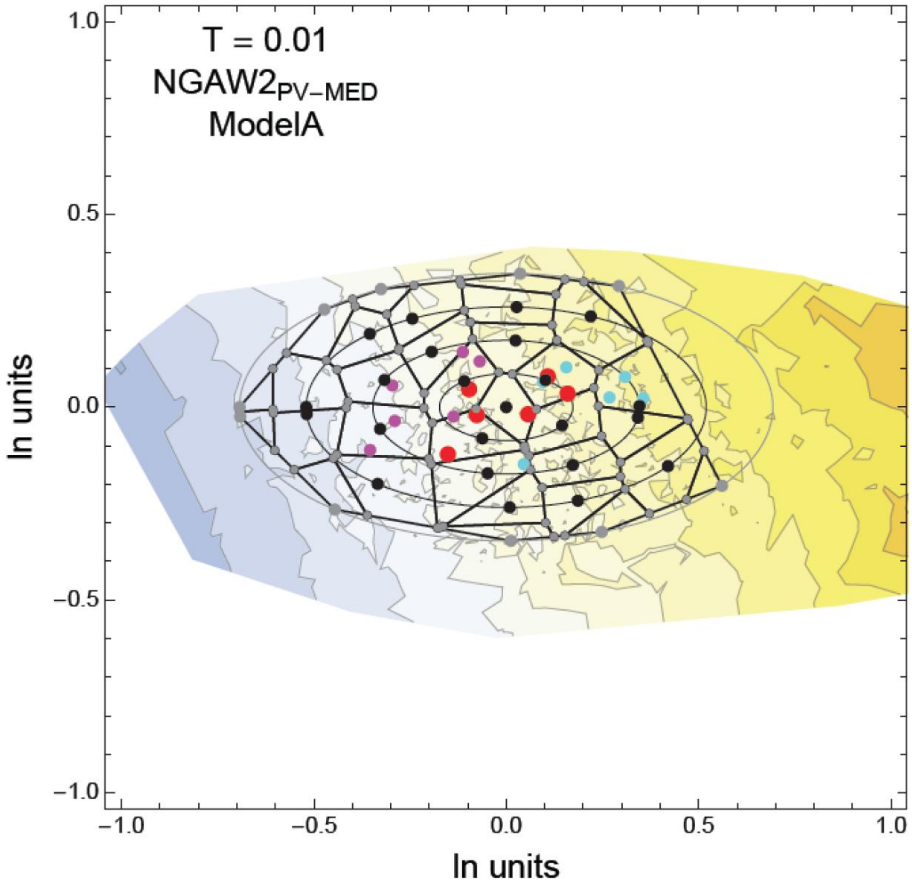

Figure 9-1. Example Sammon's map used in the evaluation of the SWUS GMM. Red dots are candidate GMPE's with their plus/minus uncertainty shown by magenta and cyan dots. Soil lines denote subvisions of model space and black dots the selected models used to represent the model space. Contour lines show mean residuals computed using NGA-West2 dataset (source GeoPentech, 2015).

9.1.2.2 Treatment of Hanging Wall and Directivity Effects

Hanging wall effects for sites above dipping ruptures were addressed in two ways in the SWUS GMC for the Greater Arizona sources. In the SWUS Model A, the distance metric used was rupture distance, R_{RUP}, and a separate hanging wall model was developed based on the hanging wall factors contained in the Abrahamson et al. (2014), Campbell and Bozorgnia (2014), and Chiou and Youngs (2014) GMPEs. These three sets of hanging wall factors were used to develop a distribution of hanging wall models that was then randomly sampled to assign a single hanging wall model to each of the representative GMPEs developed to represent the GMPE model space. In the SWUS Model B, the Joyner-Boore distance metric, RJB, was used on the basis that it captures general hanging wall effects for the range of rupture dips and earthquake depths anticipated from the Greater Arizona sources.

For the seismic hazard calculations at MFC and FMF, only the SWUS Model A set of GMPEs is used. The rationale is that the majority of the hazard in the AEF range of interest comes from sources at some distance from the site and hanging wall effects are not expected to be a major factor in the hazard assessment.

The SWUS Project also assessed models to apply the effects of rupture directivity to ground motions for strike slip and reverse faulting earthquakes. These effects were not applied to the Greater Arizona sources because of the distance (>20 km) of the Palo Verde site from known faults in the southern Basin and Range. The directivity model adopted in the SWUS Project was not applied in the hazard calculations for MFC and FMF for the same reason.

9.1.2.3 Development of Model for Aleatory Variability

The SWUS Project developed a partially non-ergodic aleatory variability model for application with the median GMPEs for the Greater Arizona sources. As discussed in Al Atik et al. (2010), aleatory variability in ground motions can be considered to consist of three main components: event-to-event variability representing differences in the average level of ground motions from earthquake to earthquake, site-to-site variability representing the differences in the average site-specific effects produced by different sites, and the single site (single station) variability representing the variation in ground motions recorded from different earthquake at a site after removal of the average source and systematic site effects. A fully ergodic aleatory model includes all three effects, while a partially non-ergodic model removes the site-to-site variability component under the assumption that the average site-specific effects for a single site can be captured either from repeated observations of ground motions at the site, or more typically through the use of modeling of site response.

The SWUS partially non-ergodic aleatory variability model was developed by separately evaluating the two components, event-to-event variability and single station within-event variability. Event-to-event variability is parameterized by the standard deviation of event terms, denoted by τ. The value of τ was assessed using the five selected candidate models listed in Table 9-2. The central estimate of the τ was taken as the average of the estimates from the five models, accounting for the average magnitude dependence. A frequency-independent model for τ was adopted. Uncertainty in τ was assessed based on the statistical uncertainty in estimating it from the data for an individual model (specifically Chiou and Youngs, 2014) and the model-to-model variability in τ among the five candidate models.

The model for single-station within-event variability, parameterized by the standard deviation ϕ_{SS}, was developed using two different datasets. The first dataset was based on the global NGA-West2 dataset. The specific data consisted of the within-event residuals obtained by Abrahamson et al. (2014), Boore et al. (2014), Campbell and Bozorgnia (2014), and Chiou and Youngs (2014). The data were limited to recording sites for which there were at least three recordings and were combined with within-event residuals from the Lin et al. (2011) dataset. The average of the values of ϕ_{SS} computed from these four datasets was used to develop a magnitude independent, frequency dependent global model for ϕ_{SS}. The second dataset consisted of the within-event residuals from Akkar et al. (2014a, 2014b), again limited to

Table 9-2. Candidate models for event-to-event variability selected in the SWUS Project.

Ground Motion Prediction Equation (GMPE) Reference
• Abrahamson et al. (2014)
• Boore et al. (2014)
• Campbell and Bozorgnia (2014)
• Chiou and Youngs (2014)
• Zhao et al. (2006)

sites with three or more recordings. Uncertainty in ϕ_{SS} was characterized by a coefficient of variation of 0.12 estimated by computing the variability in ϕ_{SS} for individual sites and adjusting for sampling error as a function of number of recordings per site.

Finally, a composite distribution for total single station sigma, σ_{SS}, was developed by combining the uncertainty distributions for τ and ϕ_{SS}. The uncertainty distribution for σ_{SS} was then represented by a discrete three-point distribution for use in hazard calculations. The weights applied to the three alternatives were adjusted from symmetric weights to account for the effects of spatial correlation in within-event residuals (Jayaram and Baker, 2010; Shahi et al., 2015). Because of the magnitude dependence of the τ model and the frequency dependence of the ϕ_{SS} model, the resulting model for σ_{SS} is both magnitude and frequency dependent.

The SWUS Project evaluated the common assumption of a lognormal distribution for aleatory variability in peak ground motion amplitudes. The results indicated that the distribution of within-event residuals tends to be heavy tailed compared to a lognormal distribution. These heavy tailed distributions were found to be adequately modeled by a mixture of two lognormal distributions. Sensitivity results presented in GeoPentech (2015) indicated that the effect of the heavy tailed distribution only became significant at low AEF values, typically less than 10^{-4}. PNNL (2014) also included the same mixture model for aleatory variability and also found that it had only a minor effect on the hazard for AEF values of 10^{-6} and greater. Given the AEF range of interest for the SDC-3 facilities at MFC and FMF is at AEF values of 10^{-5} and greater, the mixture model for aleatory variability in shallow crustal earthquake ground motions was not implemented in this study.

9.1.3 Implementation of the SWUS GMC Model for INL Sites

The GMC logic tree for the implementation of the SWUS median ground motion model for shallow crustal earthquakes for hazard analyses of INL sites is shown on Figure 9-2. The logic tree contains two levels; one representing the alternative distance metrics and the second level contains the alternative median GMPE models. As discussed above, only the R_{RUP} Model A median models are used in this study. The figure shows the number of alternative models for PGA. Table 9-3 lists the number of models for each frequency contained in the SWUS Greater Arizona model. Each median model consists of the coefficients for the common form:

$$\ln(Y) = a_0 + a_7^2 R_{RUP} + a_8^2 Z_{TOR} + a_{10} F_{REV} - a_9^2 F_{NML}$$

$$+\{a_4 + a_5(M-5)\} \times ln\left(\sqrt{R_{RUP}^2 + a_6^2}\right) \qquad [9\text{-}1]$$

$$\begin{array}{ll} -a_1 + a_2(M-5.5) & for\ M < 5.5 \\ a_1(M-6.5) & for\ 5.5 \le M \le 6.5 \\ a_3(M-6.5) & for\ M > 6.5 \end{array}$$

The coefficients a_0 though $a_{10}$for each ground motion frequency are listed in the GMM HID (Appendix G). As discussed in Section 9.1.1.4, a hanging wall model is assigned to each median ground motion model, as indicated on Figure 9-2. The hanging wall factor model is defined by the expression:

$$f_{HW} = C_1 \cos(dip) \times \left[C_2 + (1-C_2) tanh\left(\frac{C_3 R_X}{W\cos(dip)}\right)\right] \qquad for\ R_X \ge 0$$

$$\times (1 + C_4(M-7)) \times \left\{1 - \frac{R_{JB}}{R_{RUP}+0.1}\right\} \times \max\left(0, 1 - \frac{Z_{TOR}}{12}\right)$$

$$f_{HW} = 0 \qquad for\ R_X < 0 \qquad [9\text{-}2]$$

The coefficients C_1 through $C_4$for each of the hanging wall models are listed in Appendix G. The term f_{HW} is added to the mean log ground motions produced by Equation [9-1].

Figures 9-3, 9-4, and 9-5 illustrate the range in median ground motions produced by the SWUS Model A median models for PGA, 10 Hz PSA, and 2 Hz PSA, respectively. Results are shown for three earthquake scenarios, normal fault ruptures with magnitudes of **M** 5, 6, and 7. The predicted ground motions are plotted against the distance parameter R_X, which measures the horizontal distance from the surface projection of the top of rupture, measured perpendicular to the rupture strike. Negative values of R_X denote sites located on the footwall side of the rupture where the hanging wall effect is zero. Also shown on the plots are the 5th, 50th, and 95th percentile ground motions at each distance.

Figure 9-6 shows the logic tree characterizing the epistemic uncertainty in σ_{SS} implemented for hazard assessments at INL sites. As indicated, the SWUS project produces only a magnitude-dependent model for aleatory variability. The value of σ_{SS} is obtained from the expression:

$$\sigma_{SS} = \sigma_1 + \left(\frac{M-5}{2}\right) \times (\sigma_2 - \sigma_1) \quad for\, 5 \le M \le 7$$
$$\sigma_{SS} = \sigma_2 \quad for\, M > 7 \qquad [9\text{-}3]$$

The coefficients σ_1 and σ_2 are listed in Appendix G.

9.2 Ground Motion Characterization for Cascadia Interface Sources

The Cascadia interface source is located approximately 900 km west of the INL and is expected to produce earthquakes of approximately **M** 9. The recent sitewide probabilistic seismic hazard for the Hanford DOE site (PNNL, 2014) developed a GMM to characterize Cascadia interface ground motions at distances of 200 to 300 km. The interface GMM was a refinement of the BC Hydro model developed by Abrahamson et al. (2015). The refinement was focused on extension of the BC Hydro model to the larger

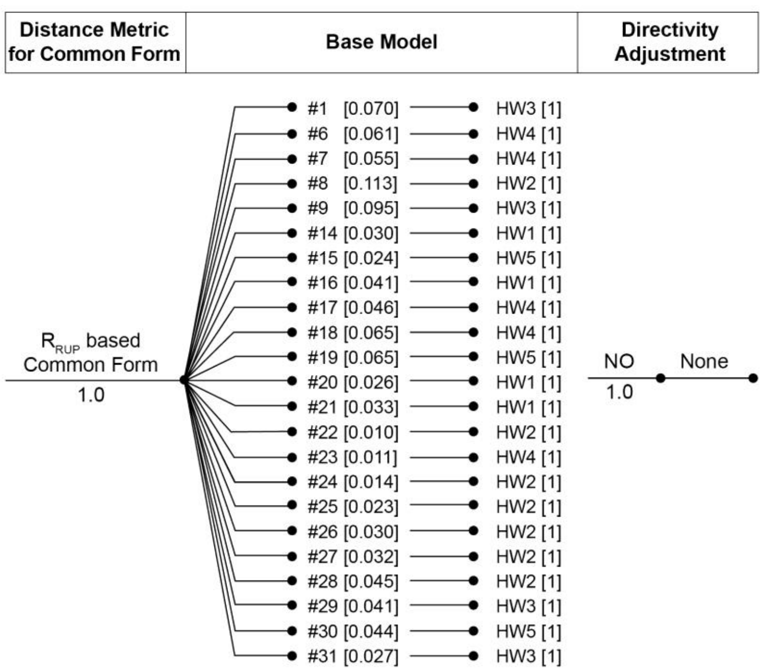

Figure 9-2. Logic tree used in this study for epistemic uncertainty in SWUS median models for Greater Arizona.

Table 9-3. Number of median ground motion models.

Ground Motion Frequency (Hz)	Number of Models
PGA (100)	23
50	25
33.3	25
20	24
13.3	23
10	22
6.67	23
5	23
3.33	22
2.5	23
2	23
1.33	26
1	27
0.667	27
0.5	27
0.333	25
0.25	25
0.2	25
0.133	25
0.1	25

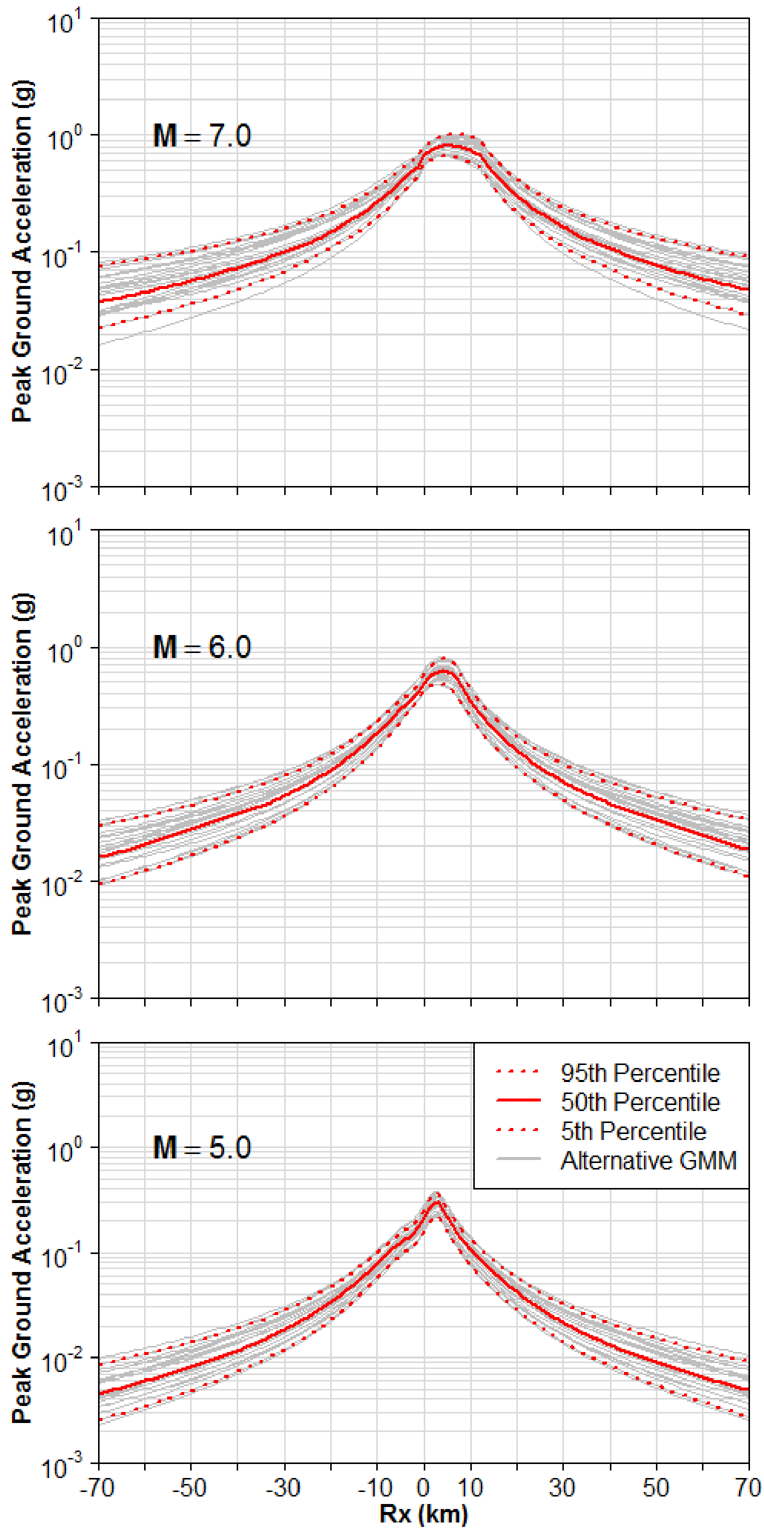

Figure 9-3. Range and distribution of PGA predicted by SWUS median models using R_{RUP}.

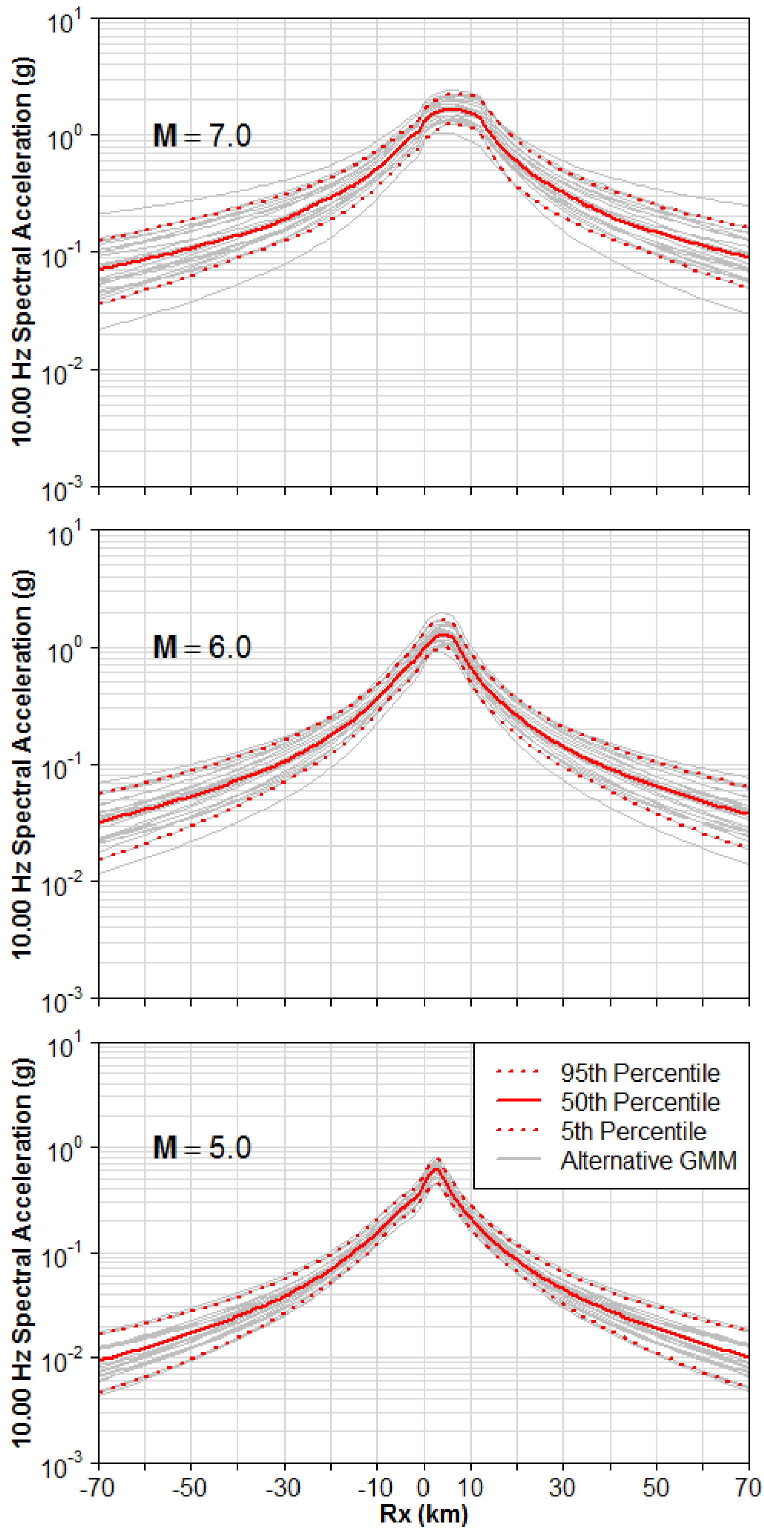

Figure 9-4. Range and distribution of 10 Hz PSA predicted by SWUS median models using R_{RUP}.

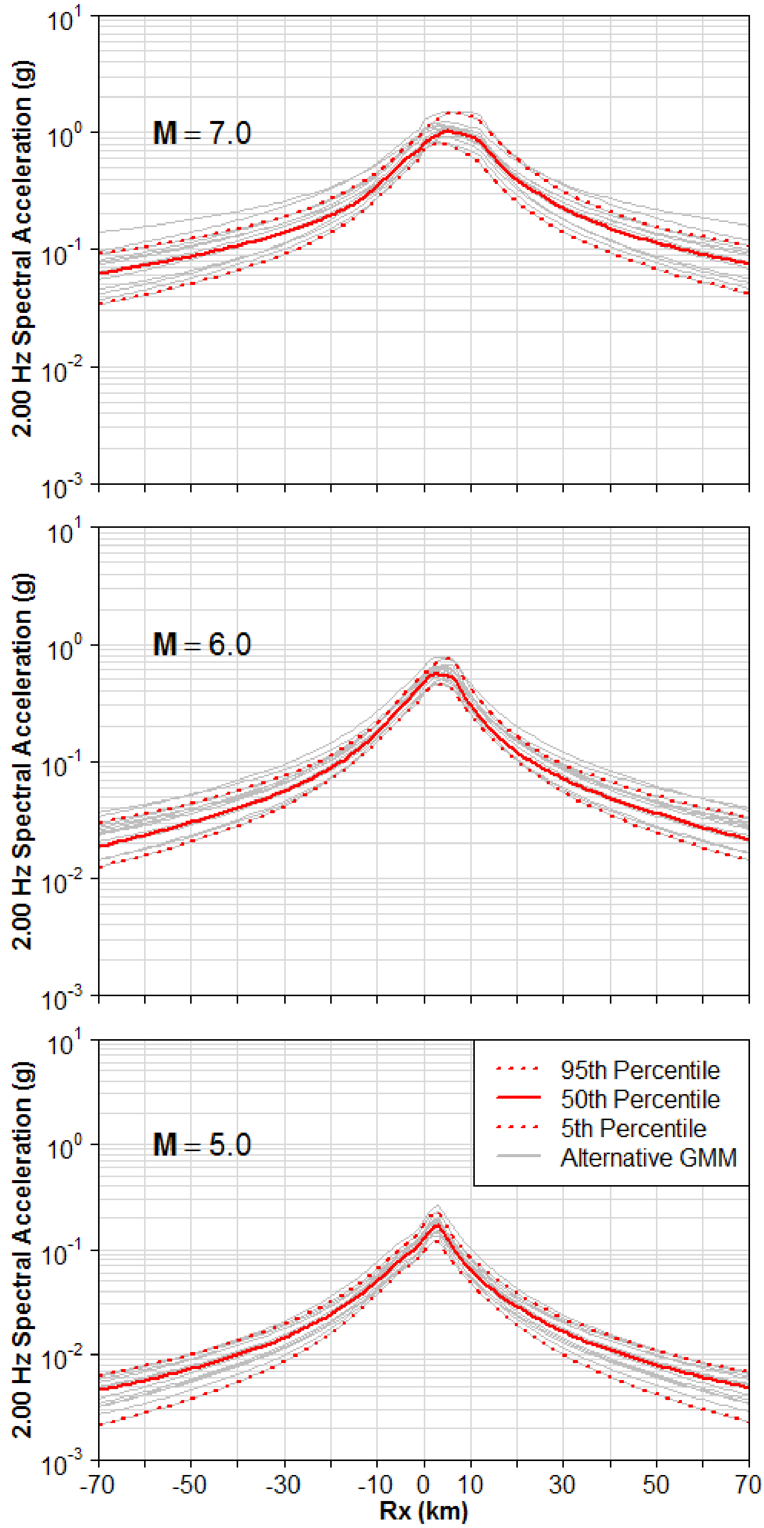

Figure 9-5. Range and distribution of 2 Hz PSA predicted by SWUS median models using R_{RUP}.

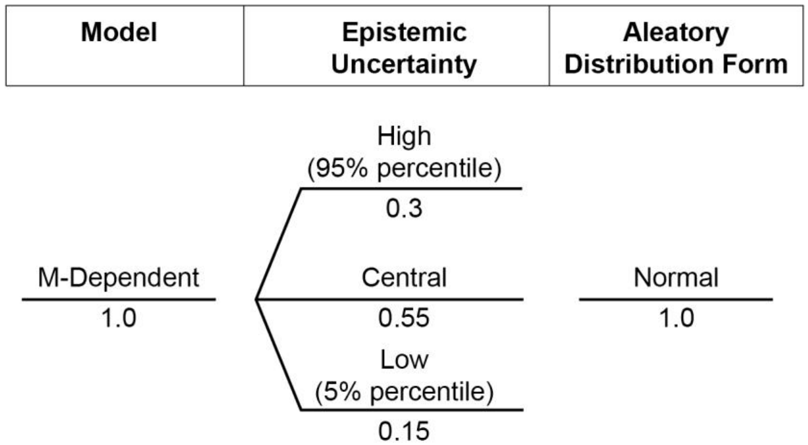

Figure 9-6. Logic tree used in this study for epistemic uncertainty in σ_{SS} from shallow crustal sources.

distances important to the hazard at the Hanford DOE site. Because the INL is located east of the Hanford DOE site on an extension of the same travel path from the interface and because the PNNL (2014) study was conducted as a SSHAC Level 3 study, the model was adopted for use in this study.

9.2.1 Summary of the Cascadia Subduction Interface GMM

9.2.1.1 Model for Median Motions

PNNL (2014) reviewed the available GMPEs for subduction zone earthquakes and concluded that the BC Hydro GMPE (Abrahamson et al., 2015) was the best model available from which to develop the subduction earthquake ground motion characterization. This conclusion was based on the fact that the BC Hydro model was based on a database that combined most of the data from previous investigators and that the model was developed under a SSHAC process. The BC Hydro model contains alternatives for fore arc and back arc ground motions, with back arc being defined as beyond the volcanic chain that marks the arc of the subduction zone. In addition, the BC Hydro model contained explicit treatment of the epistemic uncertainty in the magnitude scaling of ground motions for very large earthquakes, an important aspect for Cascadia, as the expected magnitude for large interface earthquakes is **M** 9.

PNNL (2014) developed refinements to the BC Hydro model for application to the Hanford site. These refinements concentrated on evaluation of ground motions at distances of 200 to 400 km. Additional empirical data at large distances were obtained to expand the BC Hydro database. The BC Hydro formulation was modified slightly and refit to the expanded database, with greater weight applied to the distant data. In addition, an alternative model with a lower rate of anelastic attenuation with distance was incorporated into the formulation. Finally, an epistemic uncertainty factor was defined based on the statistical uncertainty in fitting the data combined with the region to region variation in median ground motions for subduction zone earthquakes. PNNL (2014) designated the model as the Modified BC Hydro model. The modified BC Hydro subduction zone earthquake GMPE was developed for a reference V_{S30} of 760 m/s. PNNL (2014) also developed adjustments from this reference condition to the Hanford site conditions, but these adjustments are not used in this study.

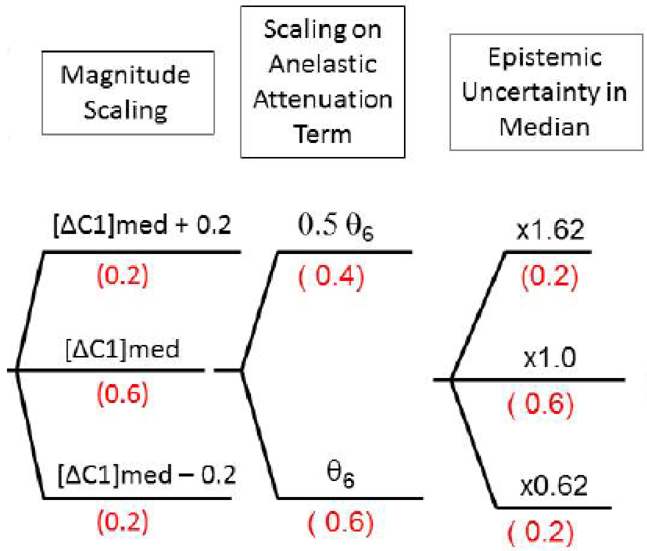

Figure 9-7. Logic tree used in this study for epistemic uncertainty in median ground motions from Cascadia interface source.

9.2.1.2 Model for Aleatory Variability

PNNL (2014) developed a partially non-ergodic single station total aleatory variability model following a similar process to that used in the SWUS model. The σ_{SS} model for subduction zone earthquakes is magnitude and frequency independent. Similar to the SWUS project, PNNL (2014) evaluated the assumption of a lognormal distribution for aleatory variability in peak ground motion amplitudes and reached the same conclusion that the distribution of within-event residuals tends to be heavy tailed compared to a lognormal distribution. PNNL also model the heavy tailed distributions by a mixture of two lognormal distributions. Because of the large distance from the Cascadia interface source to INL, it is expected that the characterization of the tails of the aleatory distribution may have an impact on the hazard assessment from this source. Therefore, the mixture model for aleatory variability for the Cascadia interface source was implemented in this study.

9.2.2 Implementation of the Modified BC Hydro Subduction Interface GMC Model for INL Sites

The GMC logic tree for the implementation of the Modified BC Hydro median ground motion model for the Cascadia interface source for hazard analyses at INL is shown on Figure 9-7. Similar to the PNNL (2014) application for the Hanford DOE site, only the back arc model is used for INL hazard analyses. The logic tree contains three levels. The first level contains the epistemic uncertainty in magnitude scaling for very large earthquakes developed by Abrahamson et al. (2015). The second level contains the epistemic uncertainty in anelastic attenuation. The third level contains the epistemic uncertainty in the median level of the ground motions. The form for the median subduction interface model is given by:

$$\ln(Y) = \theta_1 + \theta_4 \Delta C_1 + (\theta_2 + \theta_3 (M - 7.8)) \ln\{R_{RUP} + C_4 \exp[\theta_9 (M-6)]\}$$
$$+\theta_6 R_{RUP} + \theta_{16} \ln\left[\frac{\max(R_{RUP}, 40)}{40}\right] + f_{Mag}(M) + f_{site}(PGA_{1000}, V_{S30}) \qquad [9\text{-}4]$$

The term $f_{Mag}(M)$ is given by:

$$f_{Mag}(M) = \begin{cases} \theta_4 (M - (7.8 + \Delta C_1) + \theta_{13} (10 - M)^2 & for\ M \leq 7.8 + \Delta C_1 \\ \theta_5 (M - (7.8 + \Delta C_1) + \theta_{13} (10 - M)^2 & for\ M > 7.8 + \Delta C_1 \end{cases} \qquad [9\text{-}5]$$

The term $f_{site}(PGA_{1000}, V_{S30})$ is given by:

$$f_{site}(PGA_{1000}, V_{S30}) =$$
$$\begin{cases} \theta_{12} \cdot \ln\left(\frac{V_S^*}{V_{lin}}\right) - b \cdot \ln(PGA_{1000} + c) + b \cdot \ln\left(PGA_{1000} + c\left(\frac{V_S^*}{V_{lin}}\right)^n\right) & for\ V_{S30} < V_{lin} \\ \theta_{12} \cdot \ln\left(\frac{V_S^*}{V_{lin}}\right) + b \cdot n \cdot \ln\left(\frac{V_S^*}{V_{lin}}\right) & for\ V_{S30} \geq V_{lin} \end{cases} \qquad [9\text{-}6]$$

where PGA_{1000} is the median PGA for V_{S30} = 1000 m/s and V_S* equals V_{S30} for $V_{S30} \leq$ 1000 m/s. The coefficients θ_i for each ground motion frequency are listed in Appendix G.

Figure 9-8 illustrates the range in median ground motions produced by the modified BC Hydro model for an interface **M** 9 earthquake for 1 Hz and 0.1 Hz PSA. Also shown on the plots are the 5th, 50th, and 95th percentile ground motions at each distance.

Figure 9-9 shows the logic tree characterizing the epistemic uncertainty in σ_{SS} for subduction interface earthquakes implemented for hazard assessments at INL sites. For the mixture model, the conditional probability of ground motion parameter Z exceeding a value z is given by:

$$P(Z > z) = w_{Mix1}\left\{1 - \Phi\left[\frac{\ln(z) - \mu}{\sigma_{Mix1}}\right]\right\} + w_{Mix2}\left\{1 - \Phi\left[\frac{\ln(z) - \mu}{\sigma_{Mix2}}\right]\right\} \qquad [9\text{-}7]$$

where Φ[] is the cumulative normal and $w_{Mix1} = w_{Mix2} = 0.5$. The values for σ_{Mix1} and σ_{Mix2}along with σ_{SS} for the normal case are listed in the GMM HID (Appendix G).

9.3 Development of Transfer Functions for the MFC and FMF Sites

As described in Section 15.1 of GeoPentech (2015), the SWUS GMC for the Greater Arizona sources provides ground motion values at the surface of a reference rock velocity profile with a V_{S30} value of 760 m/s and site kappa values in the range of 0.037 to 0.045s. The reference velocity profile is taken from Kamai et al. (2013) and is given in Appendix M of GeoPentech (2015). Use of the SWUS GMC for this project requires the development of transfer functions that account for the difference in crustal amplification for the SWUS reference site compared to that for the MFC and FMF sites. As discussed in Section 15.4 of GeoPentech (2015), consideration of epistemic uncertainty in the kappa of the target site should be considered in the development of the transfer function.

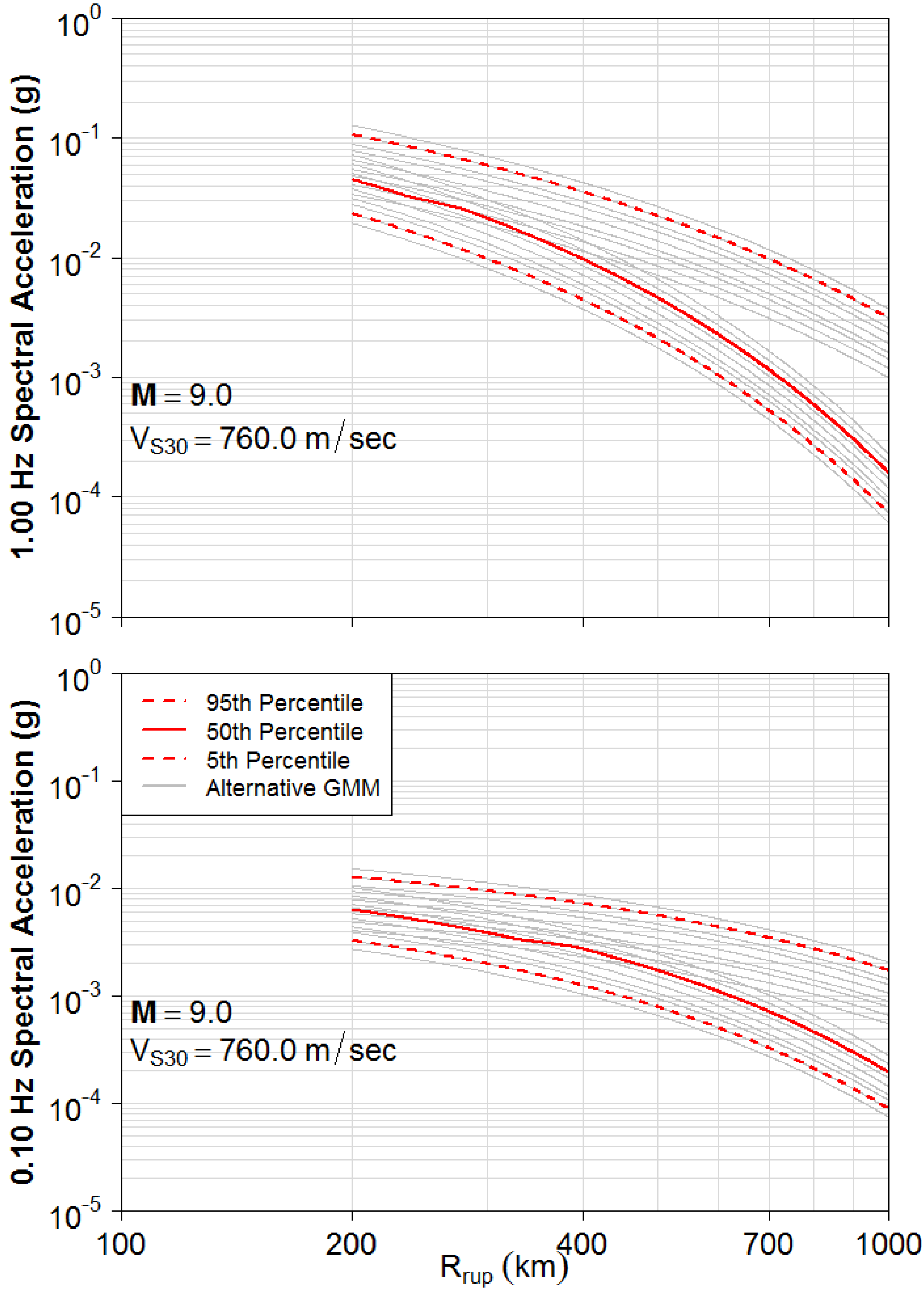

Figure 9-8. Median ground motions from Cascadia interface source.

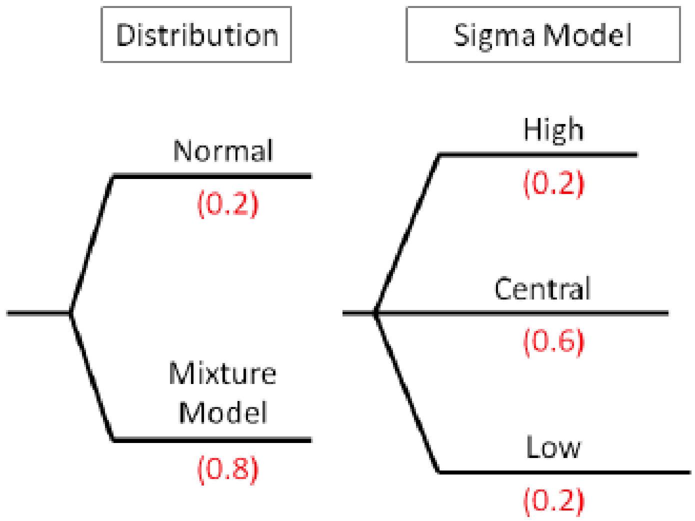

Figure 9-9. Logic tree used in this study for epistemic uncertainty in σ_{SS} from subduction interface sources.

9.3.1 Approach for Transfer Function Development

The transfer functions from the reference rock profile for the SWUS GMM to the MFC and FMF site profiles are developed by the process of relative site response analysis using the point source stochastic model to represent input earthquake ground motions and one-dimensional site response to model crustal and soil amplification. The basic formulation for this process is described in Silva and Lee (1987), Schneider et al. (1993), and Silva et al. (1996). Stochastic point source models of the earthquake source placed at a range of distances from the site are used to represent a range of input ground motion levels.

Two alternative models are used to represent the shape of the earthquake source Fourier spectrum. One is the single corner Brune source spectrum (Brune, 1970, 1971) and the second is the WUS double corner spectrum of Atkinson and Silva (2000) modified to have the same high frequency level as the single corner Brune spectrum. Because the MFC site is a rock site with linear analyses assumed and there is only a limited amount of soil (5 to 15 ft) at the FMF site, the effect of earthquake magnitude on relative site amplification is expected to be small, and the earthquake source spectra are created for a single earthquake magnitude. Previous analyses of hazard at the INL sites have indicated that the local faults northwest of the ESRP are a major contributor to the hazard and these faults have characteristic magnitudes near **M** 7. Therefore, an **M** 7 earthquake with a high frequency source parameter of 50 bars was used to generate the source spectra for the relative site response analyses. The 50-bar source parameter represents a generic value for large magnitude active tectonic region earthquakes (Boore, 1986) and is similar to values obtained from inversions of the NGA GMPEs (Silva, pers. comm., 2015).The frequency dependent quality factor Q(*f*) estimated for the INL region (Section 7.3) is similar to values for California. Therefore, adjustment for differences in Q(*f*) between the SWUS model and the INL region are not needed.

The site response analyses were conducted following the general approach described in Appendix B of EPRI (2013). Thirty sets of dynamic properties were developed for the reference and thirty sets were developed for each target profile for MFC and FMF using the process described in EPRI (2013). Each randomized profile is subjected to the range in input ground motions described above. For each input ground motion, the response spectrum for motions computed at the top of one of the target profiles is divided by the response spectrum for motions computed at the top of the SWUS reference profile. This response spectral ratio defines one estimate of the transfer function from the SWUS reference profile to the MFC or FMF target profiles. The process is repeated for all 30 profiles, producing 30 spectral ratios. The statistics of the natural logarithm of the spectral ratios are then used to define the median (mean log) and standard deviation of ln(amplification) for 301 spectral frequencies for the specified input ground motion level. These calculations are repeated for each ground motion level to produce transfer functions for each frequency.

9.3.2 Transfer Functions for MFC for Shallow Crustal Earthquakes

The epistemic uncertainty in the dynamic properties of the MFC site is characterized by three alternative velocity profiles, P1 (median), P2 (lower-range), and P3 (upper-range) (Section 7.2), and three alternative values of kappa, k1 – 0.018s, k2 – 0.030s, and k3 – 0.011s (Section 7.3). Figure 9-10 compares the three velocity profiles to the reference V_S profile for the SWUS GMM. Figure 9-11 shows the upper two km of these velocity profiles. The V_S values for the SWUS and MFC profiles become similar below a depth of 5 km. The MFC profiles quickly rise to V_S values of approximately 2 km/s and greater compared to the more gradual velocity increase for the SWUS reference profile. Figures 9-12 and 9-13 show the randomized velocity profiles for MFC profile P1. The correlation model has a depth dependent σ_{ln} of 0.33 over the top 15 m and 0.15 below (Toro, as appears in Silva et al., 1996).

Figure 9-14 shows the effect of the alternative MFC velocity profiles on the transfer functions for four levels of input motion. The designation "1C" and "2C" refer to the two different earthquake source spectra shapes used to define the input motions. As shown on the figure, the three MFC velocity profiles produce similar transfer functions. In addition, there is very little difference in the transfer functions computed using the one-corner and two-corner earthquake source spectra.

Figure 9-15 shows the effect of the alternative values for kappa on the transfer functions for four levels of input motion. The alternative values of kappa result in differences in the transfer functions for frequencies above 2 Hz, with the differences becoming large for frequencies above 10 Hz.

Figures 9-16 and 9-17 show the effect of input ground motion amplitude on the transfer functions for the three profiles (Figure 9-16) and for the three kappa values (Figure 9-17). The upward curvature of the transfer functions at large ground motion amplitudes reflects the effect of modeled nonlinearity in the reference SWUS profile, while linear response was assumed for the MFC profile.

9.3.3 Transfer Functions for FMF for Shallow Crustal Earthquakes

As described in Section 7.2, the FMF site consists of 5 to 15 ft of soil on top of the MFC profiles. The epistemic uncertainty in the dynamic properties of the FMF site is characterized again by three alternative velocity profiles, P1 (median), P2 (lower-range), and P3 (upper-range) and three alternative values of kappa, k1 – 0.018s, k2 – 0.030s, and k3 – 0.011s. Additionally two alternative sets of G/Gmax and damping relationships are used to model the nonlinear behavior of the soils. Figure 9-18 compares the three velocity profiles to the reference V_S profile for the SWUS GMM. Figure 9-19 shows the randomized velocity profiles for FMF profile P1 for 15 ft of soil. For the FMF site, the G/Gmax and damping relationships are also randomized following the approach described in Appendix B of EPRI (2013). Figures 9-20 and 9-21 show the randomized G/Gmax and damping relationships for material set M1 and M2, respectively. The randomized damping relationships are capped at a maximum damping ratio of 15 percent following guidance given in NRC (2013).

Figures 9-22 and 9-23 shows the effect of the alternative FMF velocity profiles on the transfer functions for four levels of input motion for soil depths of 15 ft and 5 ft respectively. The alternative

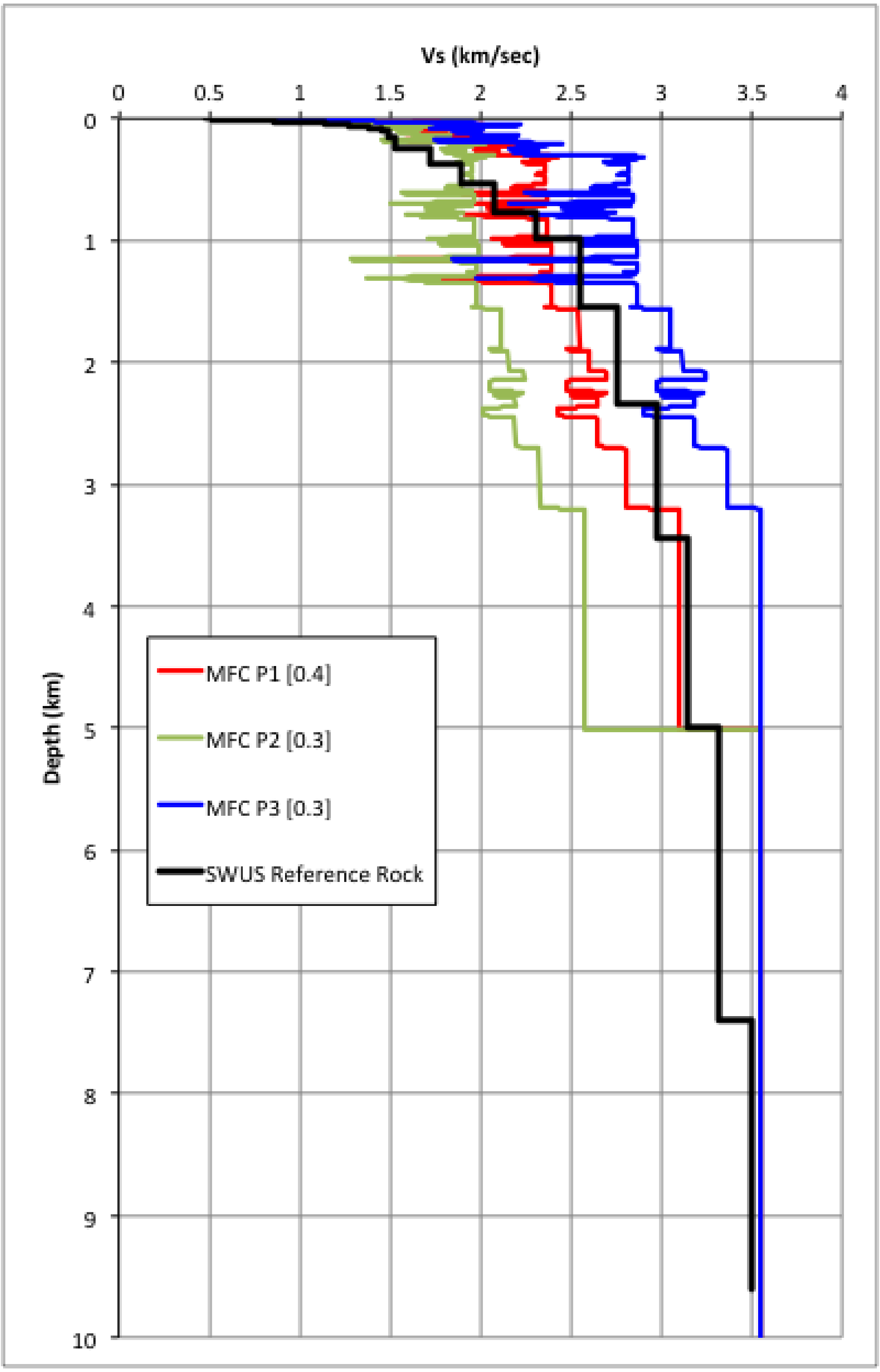

Figure 9-10. Comparison of SWUS reference rock V_S profile with MFC profiles.

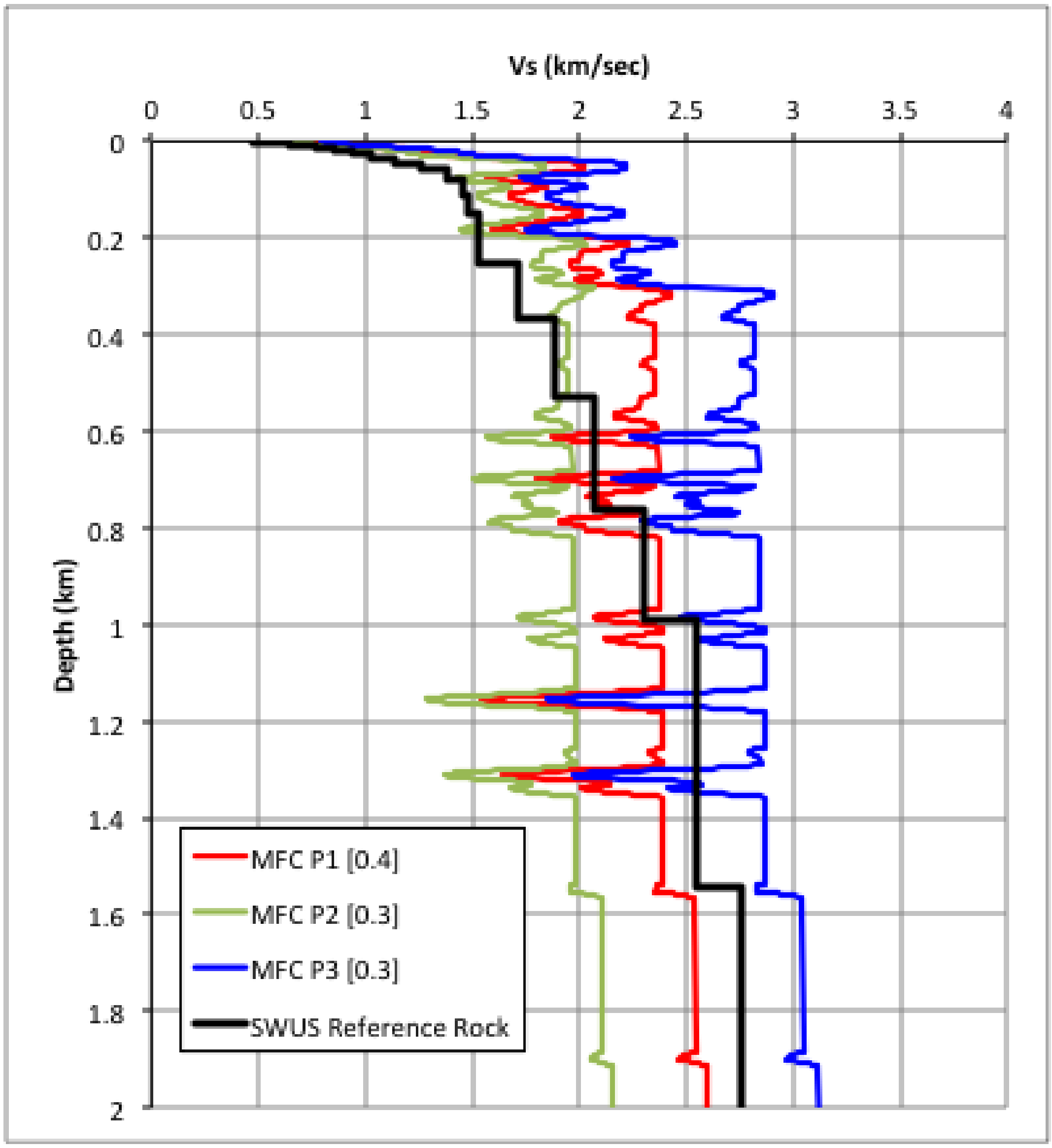

Figure 9-11. Comparison of top 2 km of SWUS reference rock V_S profile with MFC profiles.

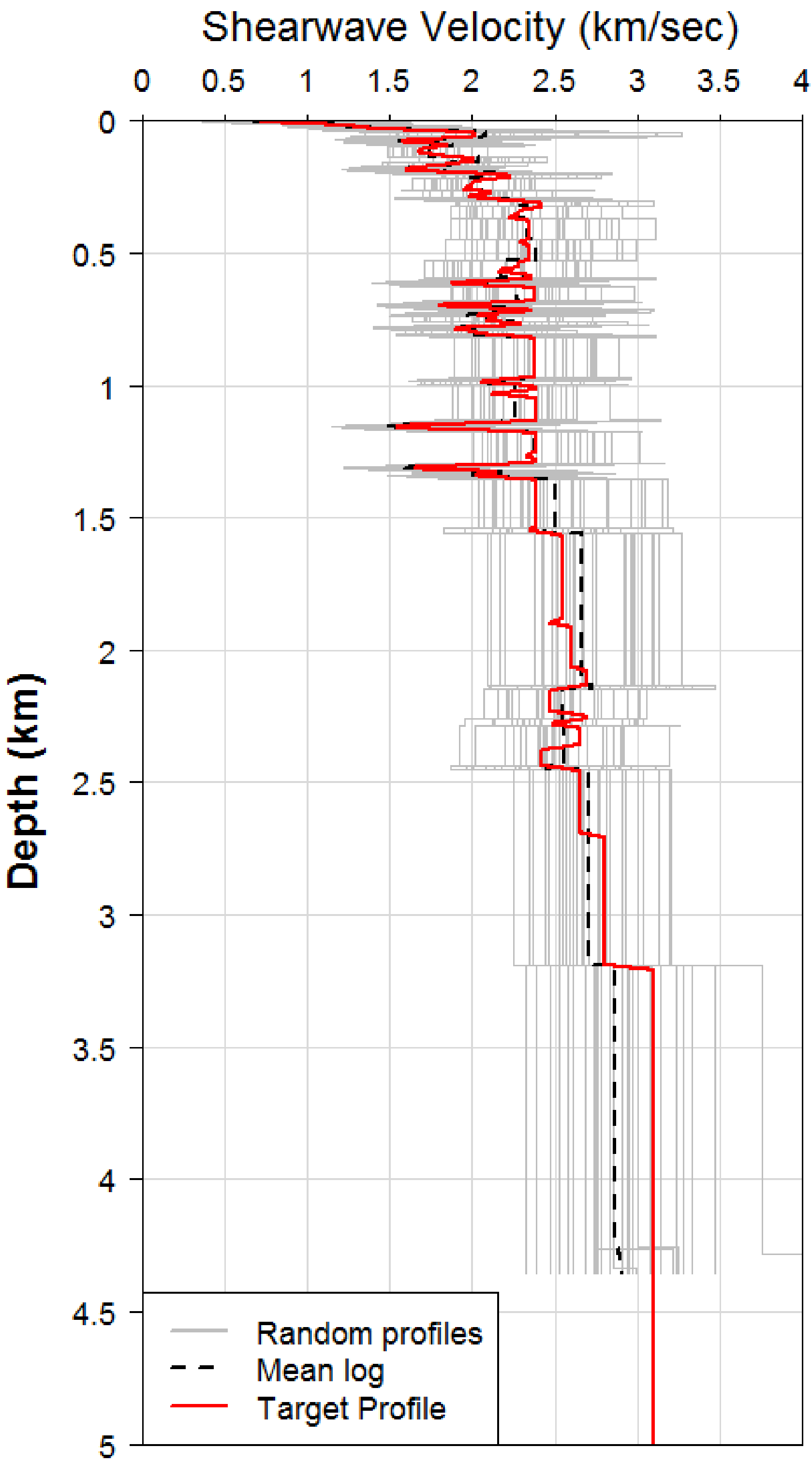

Figure 9-12. Randomized V_S profiles for MFC profile P1.

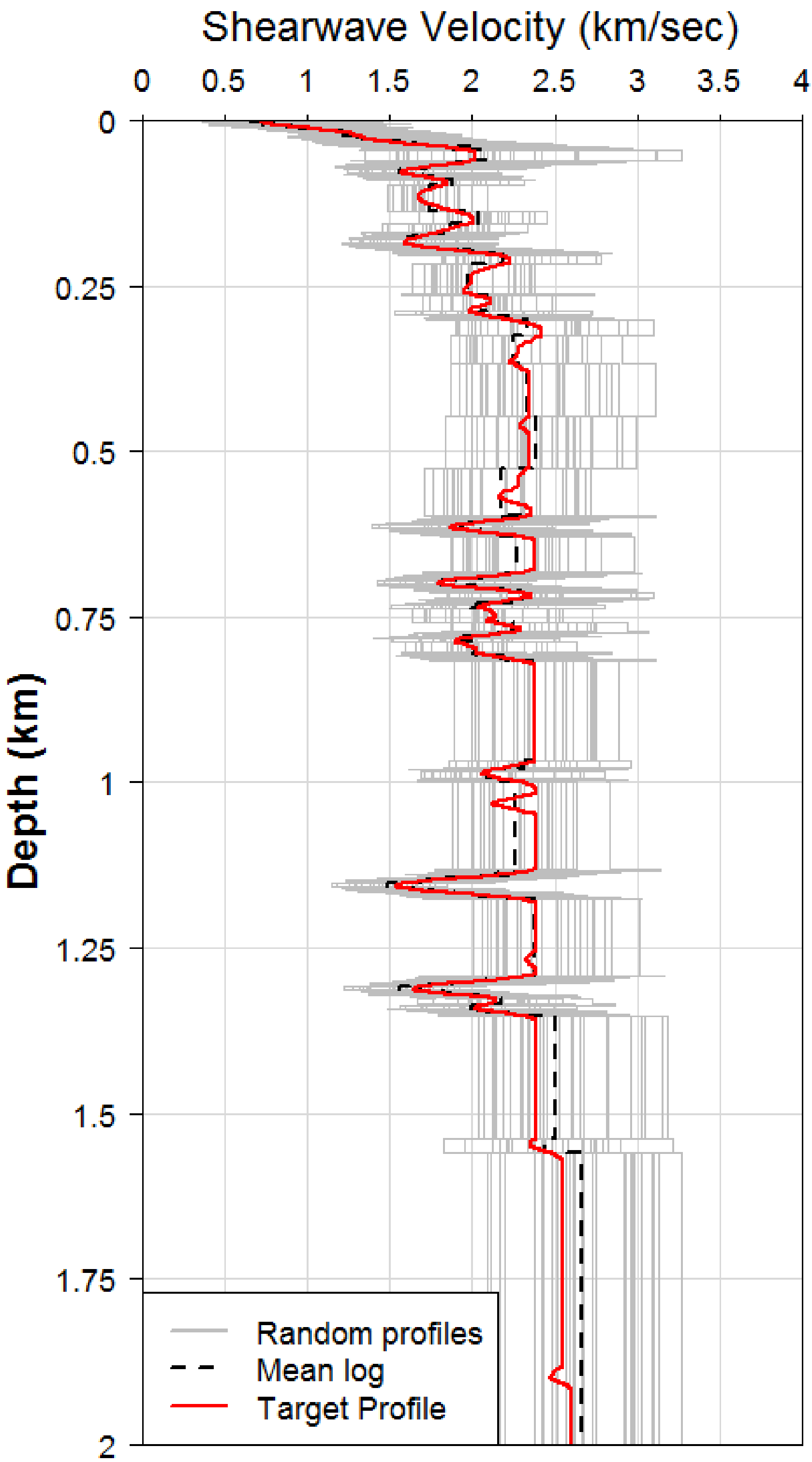

Figure 9-13. Top 2 km of randomized V_S profiles for MFC profile P1.

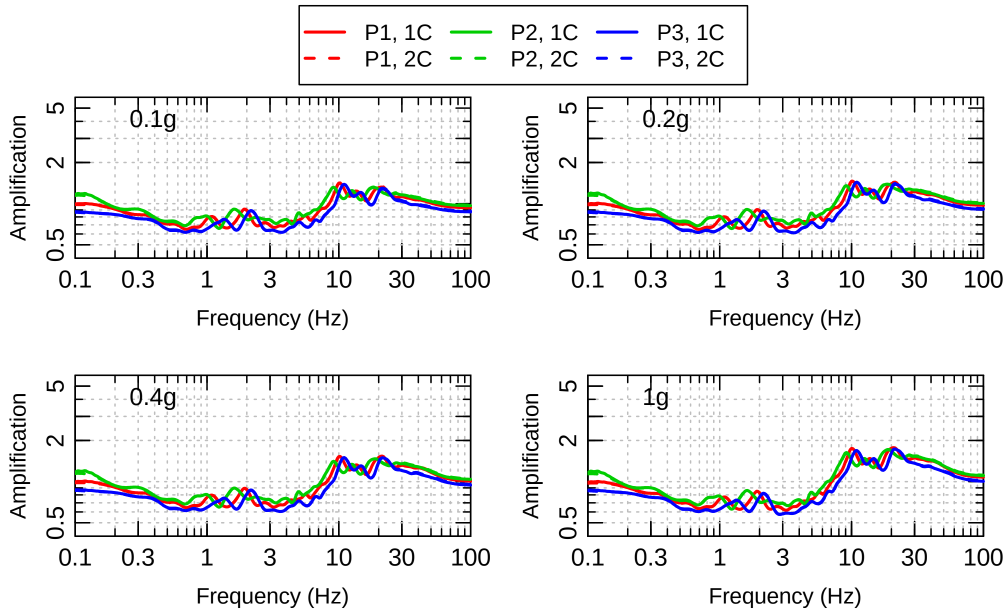

Figure 9-14. Effect of VS profile on MFC transfer function (kappa = 0.018s).

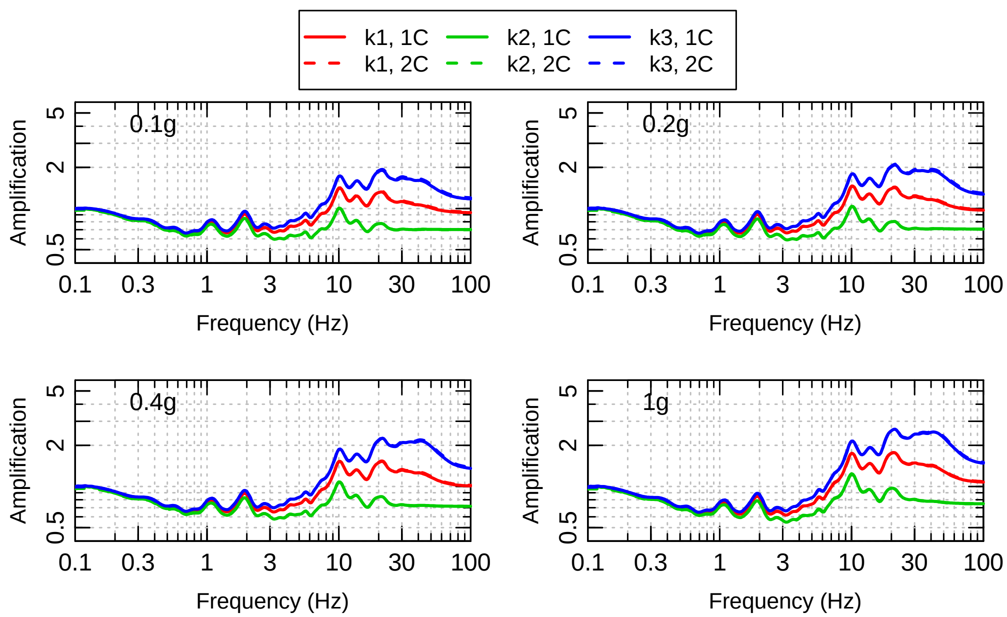

Figure 9-15. Effect of kappa on MFC transfer function (V_S profile P1).

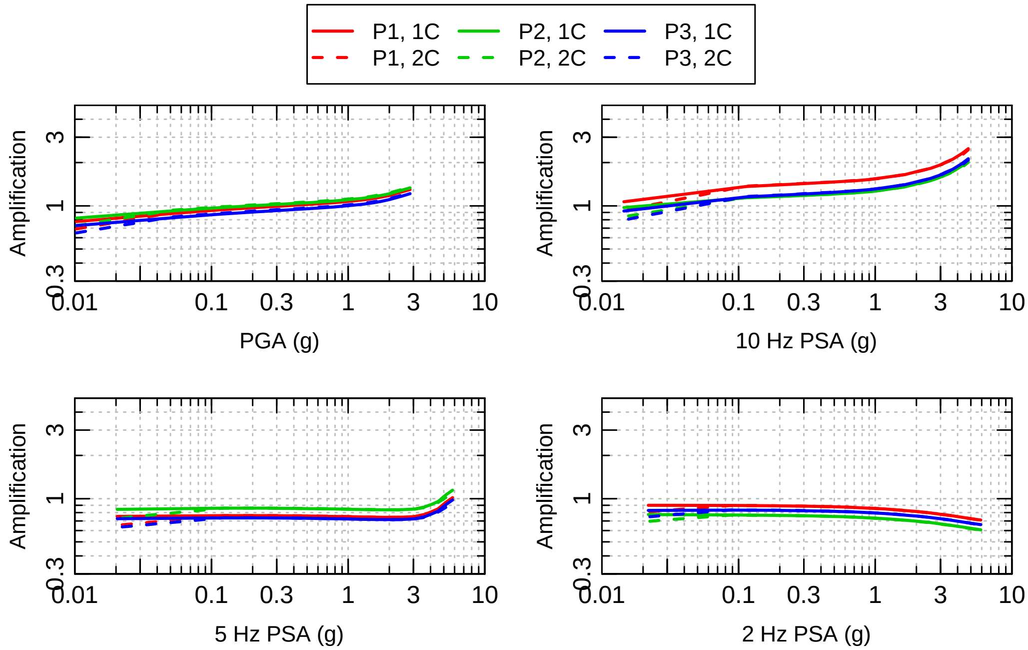

Figure 9-16. Effect of amplitude of input ground motions on MFC transfer function (kappa = 0.018s).

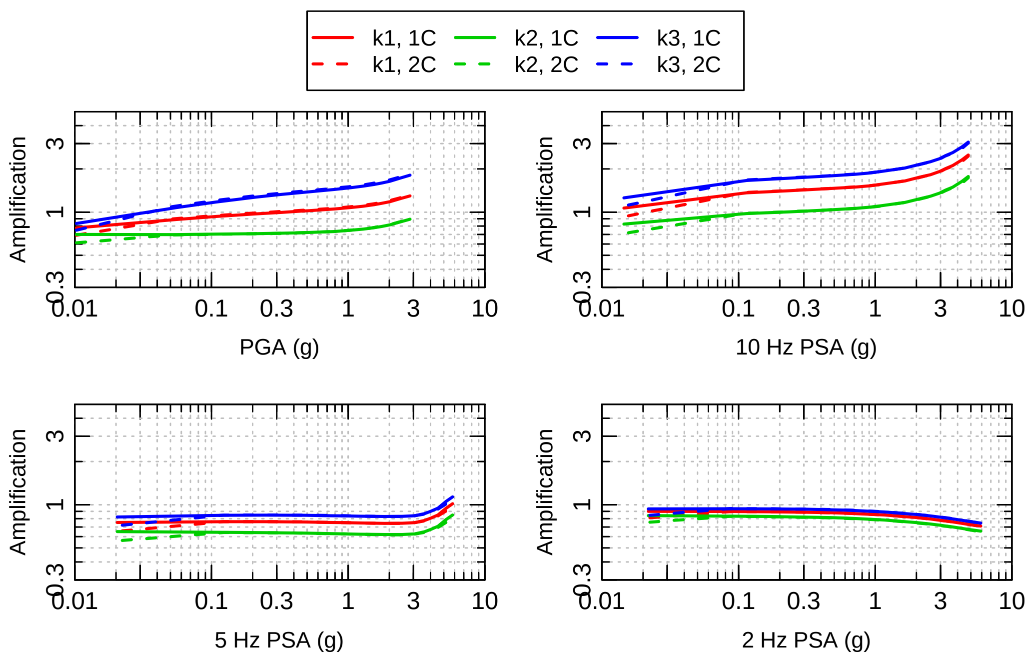

Figure 9-17. Effect of amplitude of input ground motions on MFC transfer function (V_S profile P1).

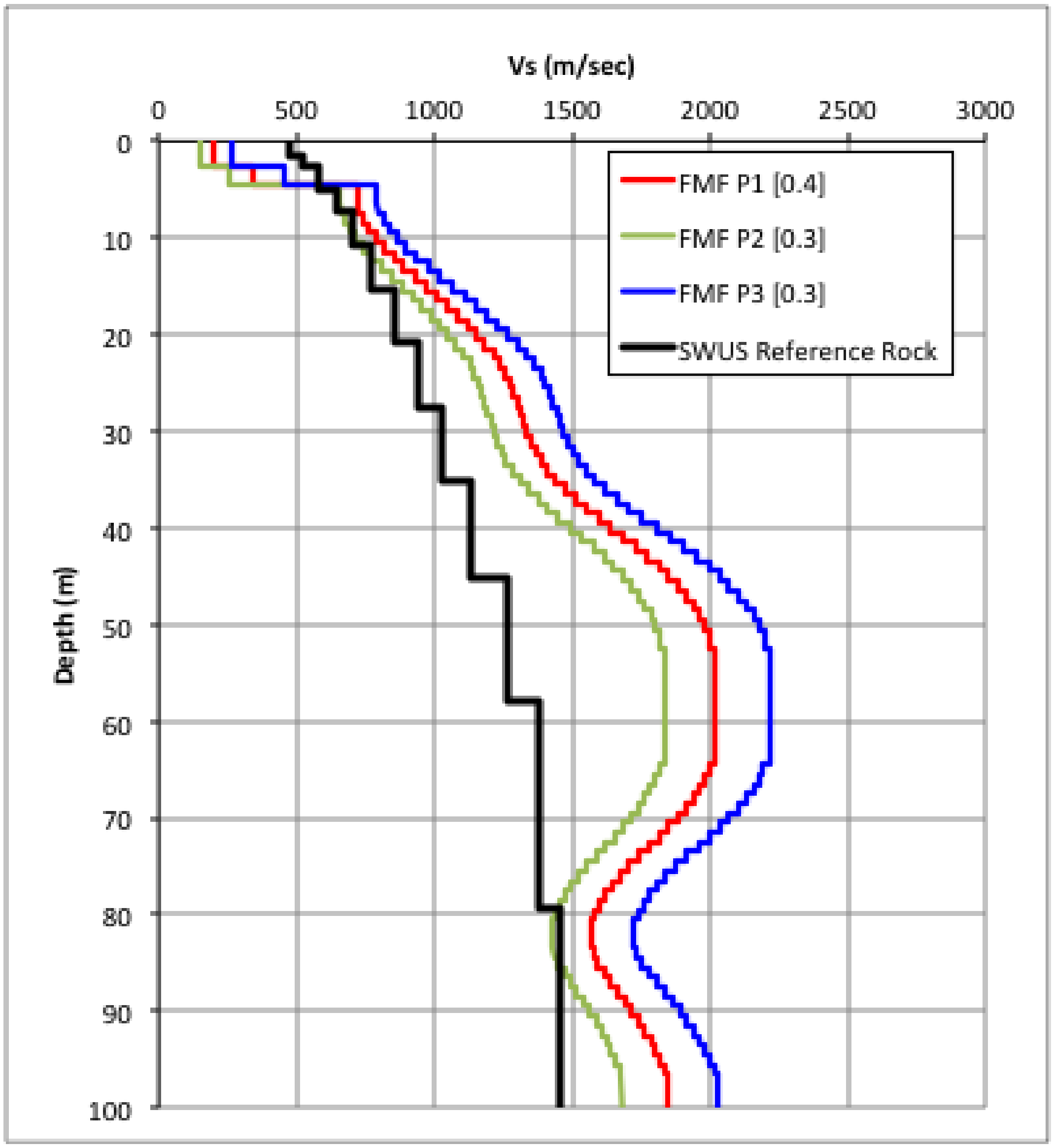

Figure 9-18. Comparison of SWUS reference rock V_S profile with FMF profiles for 15 ft of soil.

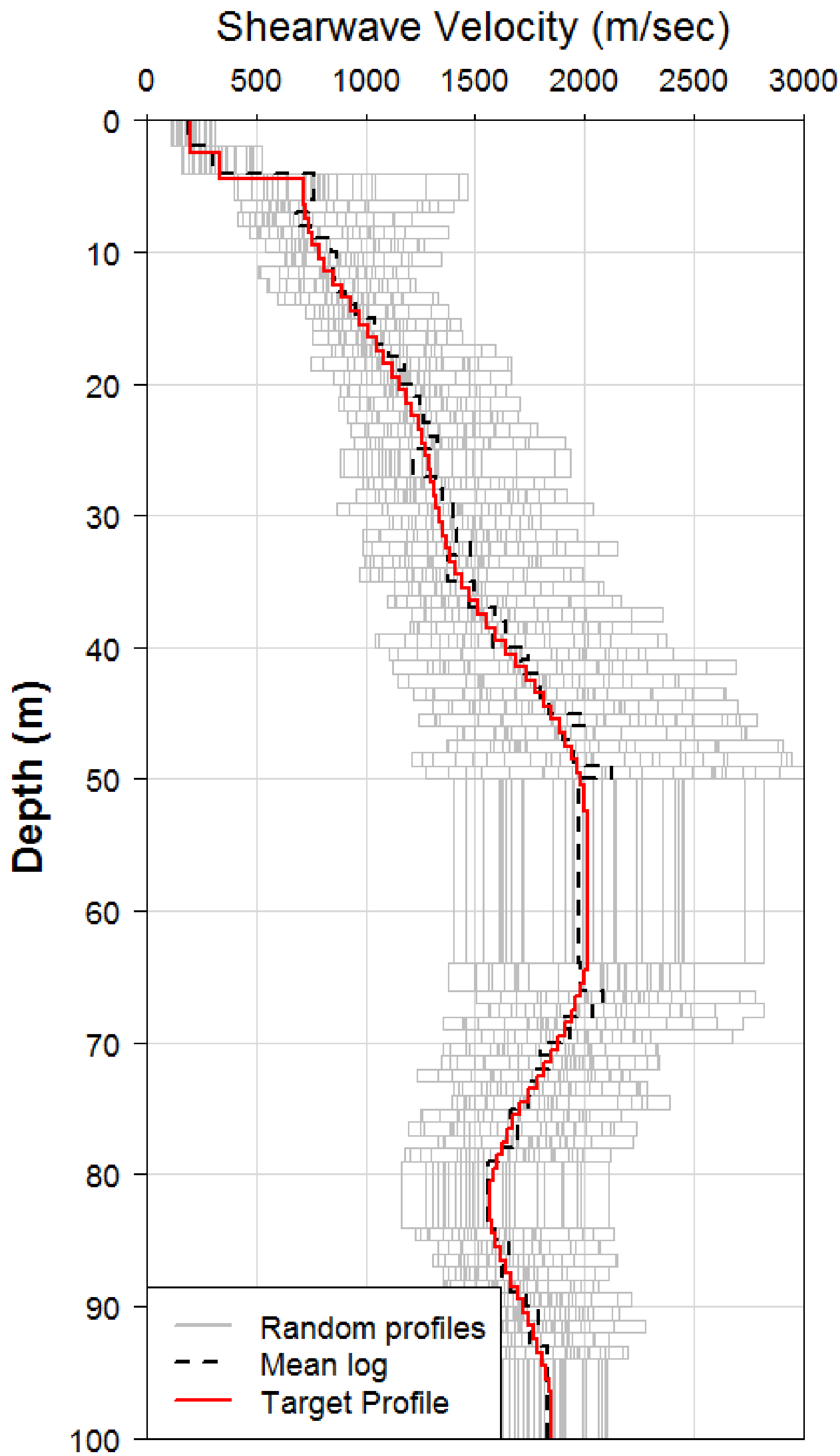

Figure 9-19. Randomized V_S profiles for FMF profile P1, 15 ft of soil.

(a)

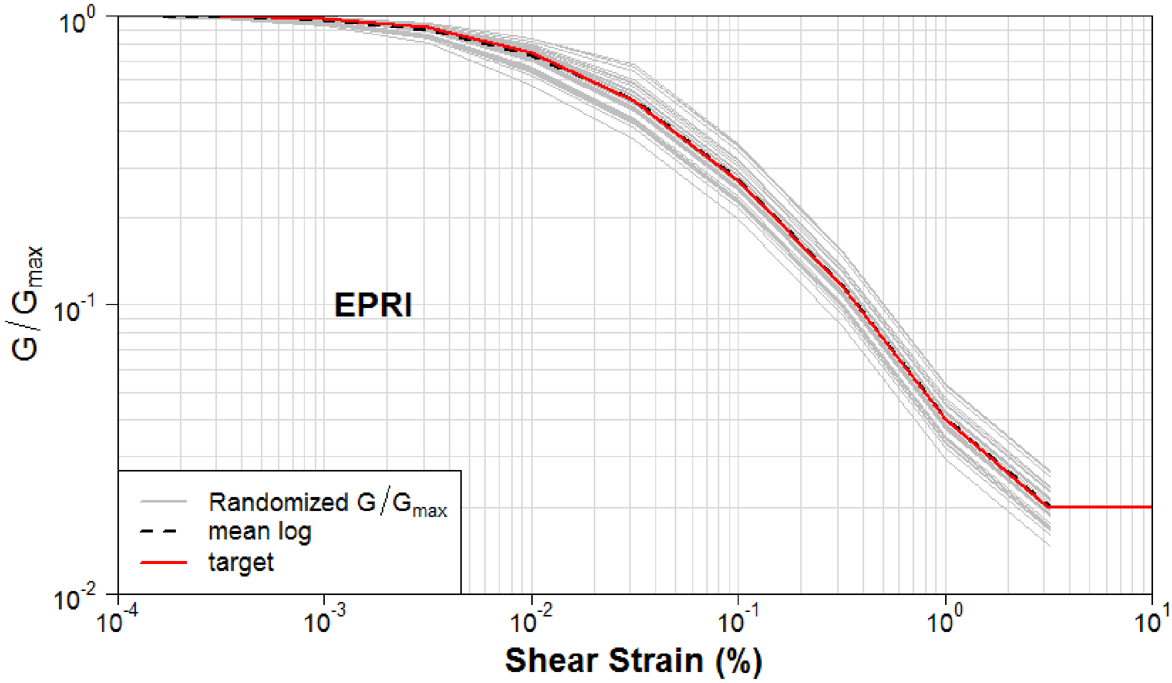

(b)

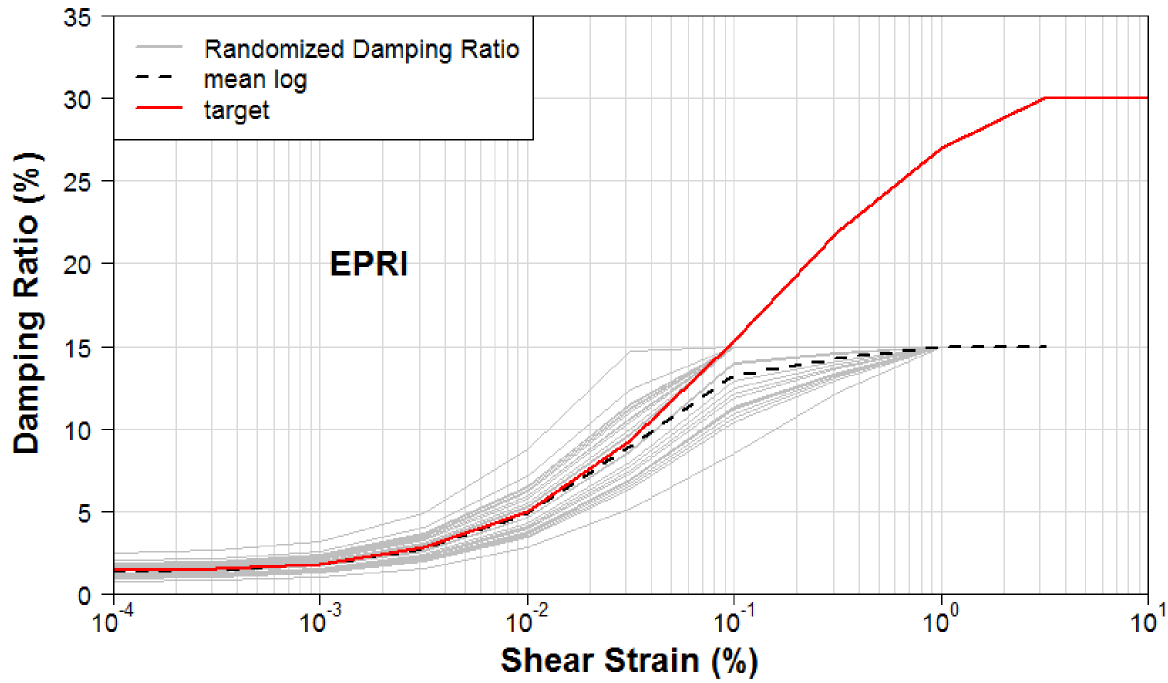

Figure 9-20. Randomized: a) G/Gmax and b) damping ratio for soil material set M1 (EPRI).

(a)

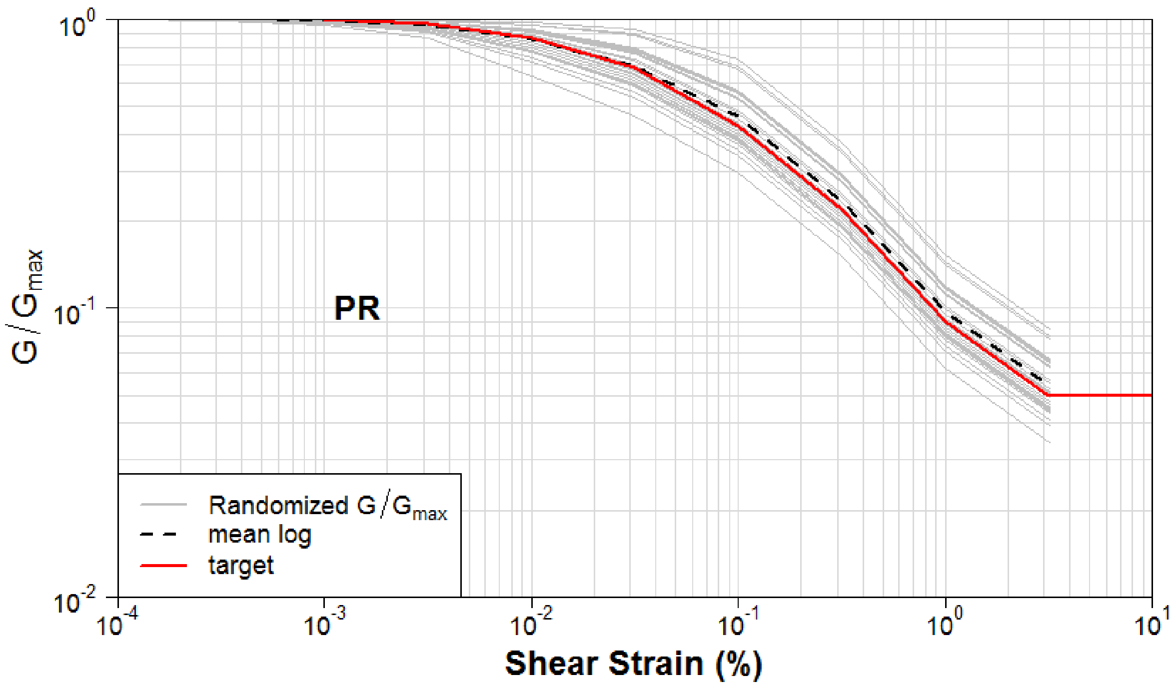

(b)

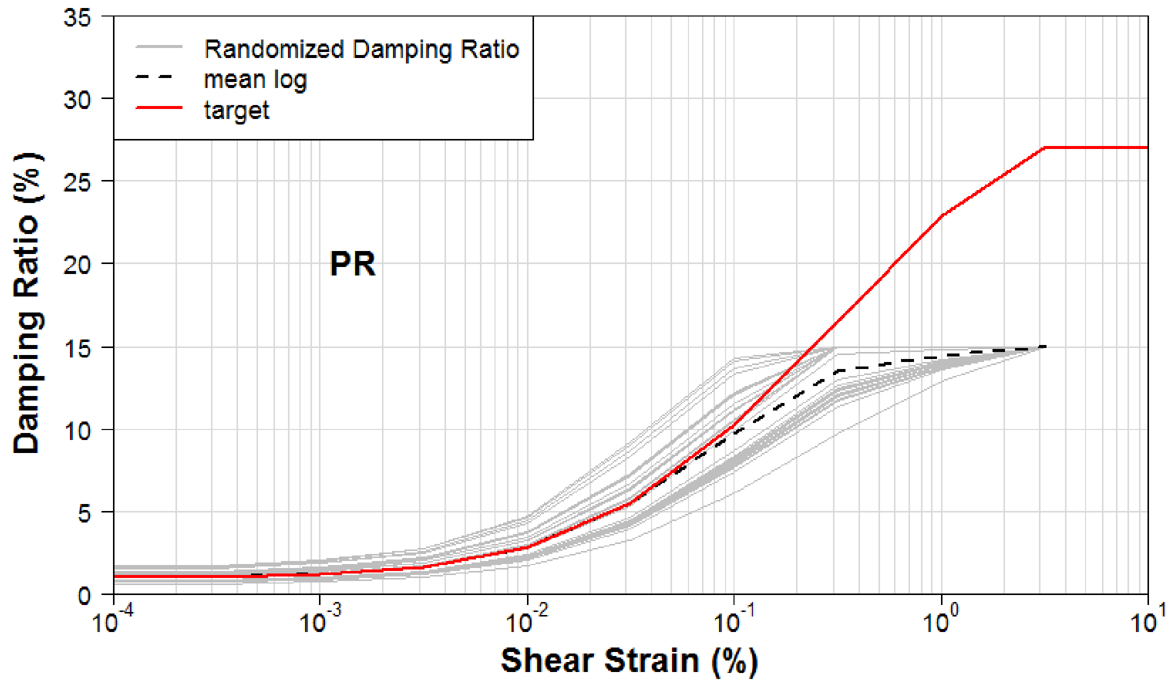

Figure 9-21. Randomized: a) G/Gmax and b) damping ratio for soil material set M2 (PR-Peninsular Range).

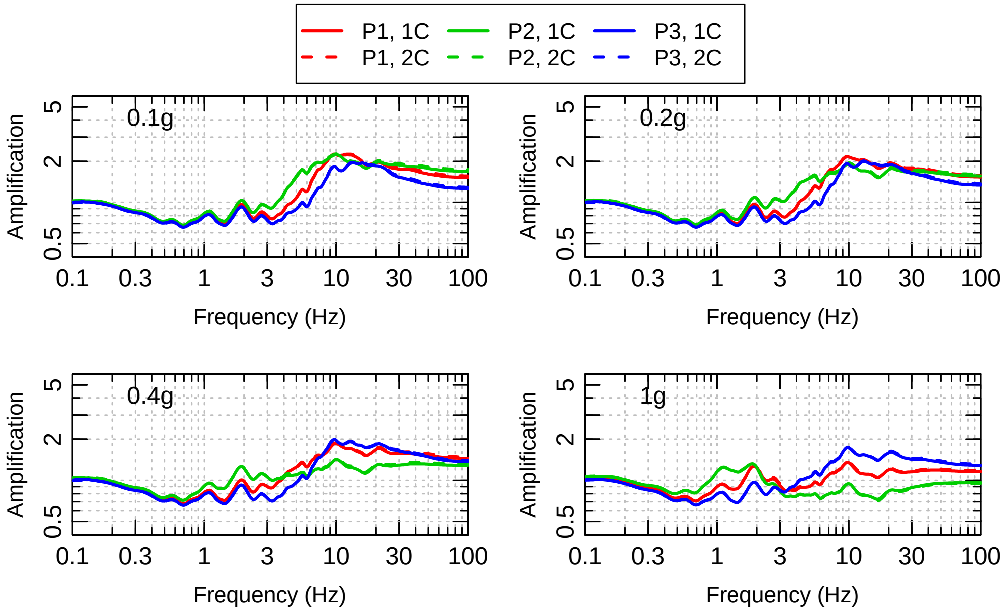

Figure 9-22. Effect of V_S profile on FMF transfer function (kappa = 0.018s, soil depth 15 ft, soil material set M1).

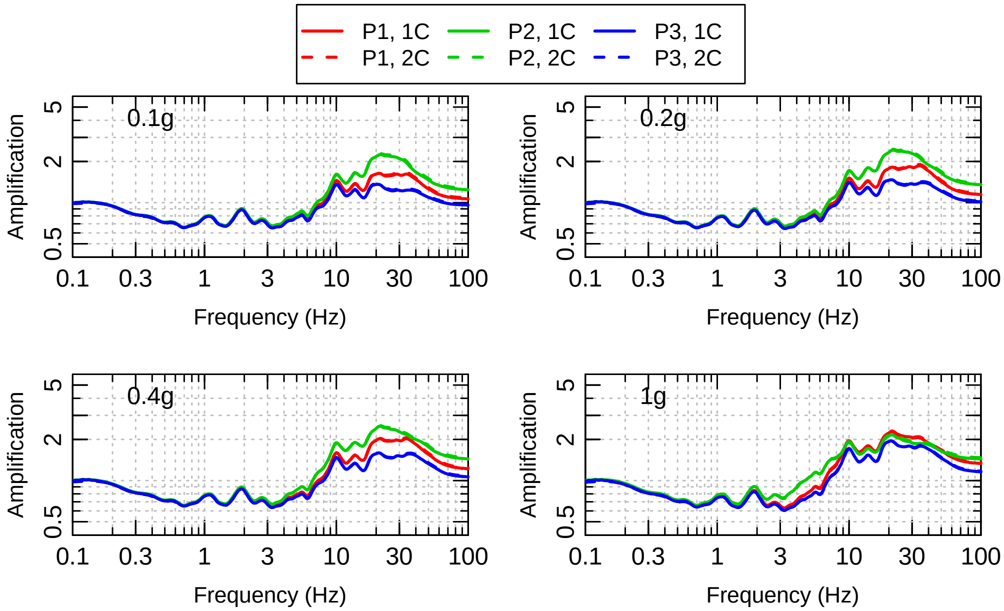

Figure 9-23. Effect of V_S profile on FMF transfer function (kappa = 0.018s, soil depth 5 ft, soil material set M1).

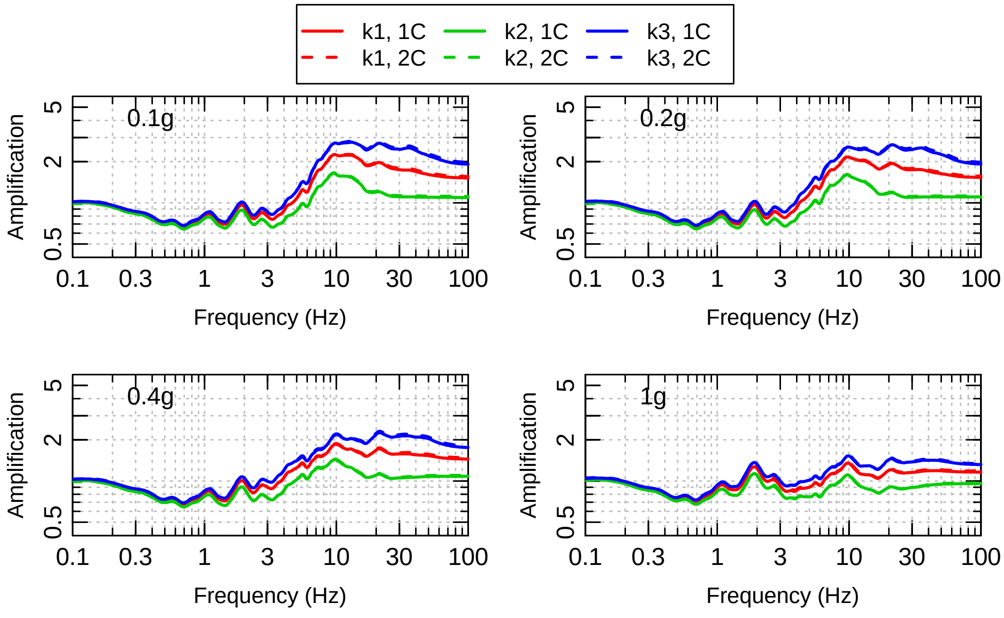

Figure 9-24. Effect of kappa on FMF transfer function (VS profile P1, soil depth 15 ft, soil material set M1).

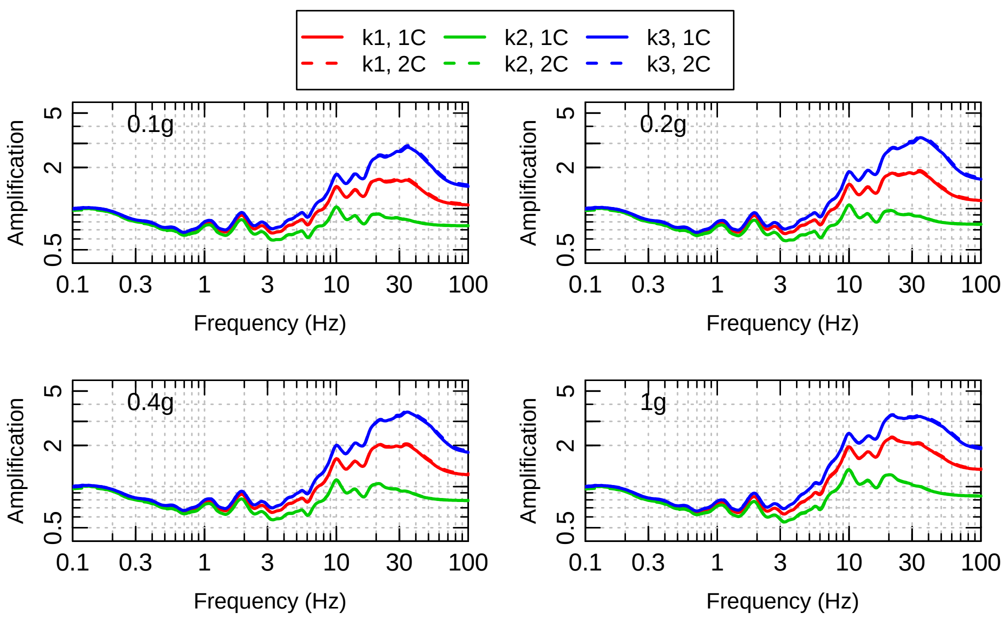

Figure 9-25. Effect of kappa on FMF transfer function (V_S profile P1, soil depth 5 ft, soil material set M1).

profiles produce greater differences in the transfer functions for FMF than for MFC. This reflects the influence of the shallow soil deposits on the transfer functions. The effects of the alternative velocity profiles extend to lower frequencies for the 15 ft soil depth than for the 5 ft soil depth. As was the case for the MFC site, there is very little difference in the transfer functions computed using the one-corner and two-corner earthquake source spectra.

Figures 9-24 and 9-25 show the effect of the alternative values for kappa on the transfer functions for four levels of input motion for soil depths of 15 ft and 5 ft, respectively. The kappa effects for FMF are generally similar to those for MFC. For the 15 ft soil depth, the kappa effects become somewhat smaller at high loading levels because the transfer function is being influenced by the soil nonlinearity. The kappa effects are larger for the 5 ft soil profile than for the 15 ft soil profile. This is likely due to the fact that the 15 ft profile develops greater shear strains in response to high loading levels, and thus greater damping levels that counter balance the effects of the larger ground motions for the low kappa case.

Figures 9-26 and 9-27 show the effect of the alternative sets of G/Gmax and damping relationships on the transfer functions for the three profiles for the 15 ft and 5 ft soil depths, respectively. For the 15 ft soil depth, use of soil material set M1 (EPRI curves) produces lower motions at high frequencies than the soil material set M2 (Peninsular Range curves) because of the greater nonlinearity and corresponding larger damping as the loading level increases. Use of the M1 curves also produces somewhat higher motions at intermediate frequencies due to a reduction in the fundamental period of the soil profile at higher loading levels. These effects are much smaller for the 5 ft soil depth as only limited strains are developed in the thin soil layer. Figure 9-28 compares the transfer functions for the 15 ft and 5 ft soil depths and the two sets of soil G/Gmax and damping curves. The 15 ft soil depth produces higher motions than the 5 ft soil depth except at frequencies above 10 Hz at the higher loading levels.

Figures 9-29 and 9-30 show the effect of loading level on the FMF transfer functions for the 15 ft soil depth and the 5 ft soil depth, respectively. For the 15 ft soil depth, the trend with amplitude is affected by both the site profile and the choice of the soil G/Gmax and damping relationships. At low ground motion levels, the highest level of motion is produced by the lowest velocity profile (P2) as this produces the greatest crustal amplification among the three profiles. As the loading level increases, the greater nonlinearity of the M1 (EPRI) material curves leads to increased damping in the soil and a reduction in the level of motion. The trends seen in the transfer functions for the 15 ft soil depth are much weaker for the 5 ft soil depth.

9.3.4 Transfer Functions for Cascadia Interface Earthquakes

The reference profile for the modified BC Hydro GMM for a V_{S30} of 760 m/s has gross characteristics similar to that of the SWUS GMM. Furthermore, the V_S adjustment factors developed by PNNL (2014) for shallow crustal earthquakes and subduction zone earthquakes are very similar for ground motion frequencies of 1 Hz or less, the frequency range where the Cascadia interface source contributes to the hazard at MFC and FMF. Therefore, the transfer functions developed for shallow crustal earthquake ground motions were applied to the subduction zone earthquake ground motions.

9.3.5 Epistemic Uncertainty in Transfer Functions

Figure 9-31 shows the logic tree for the epistemic uncertainty in the inputs to the transfer function calculations for MFC and FMF. Note that the alternative soil material curve sets apply only to the FMF site. The alternative transfer functions obtained for each end branch define the epistemic uncertainty in adjusting from the reference rock profile to the site profiles for MFC and FMF.

The transfer functions were computed using 1-dimensional site response. Figure 9-32 shows an assessment of the modeling uncertainty in this calculation (W. Silva, pers. com., 2015). Shown on the

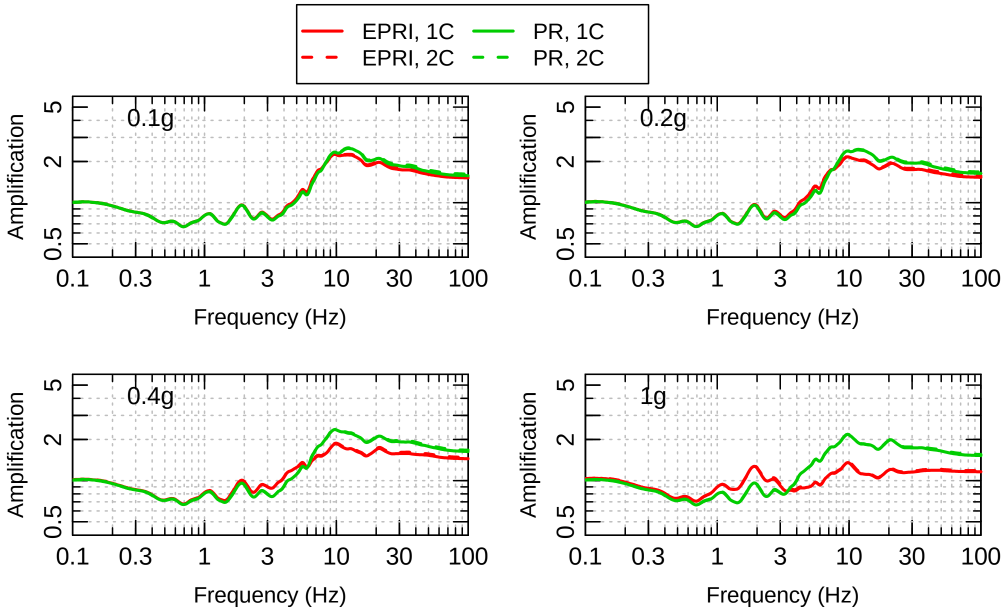

Figure 9-26. Effect of G/Gmax and damping curves on FMF transfer function (kappa = 0.018s, V_S profile P1, soil depth 15 ft).

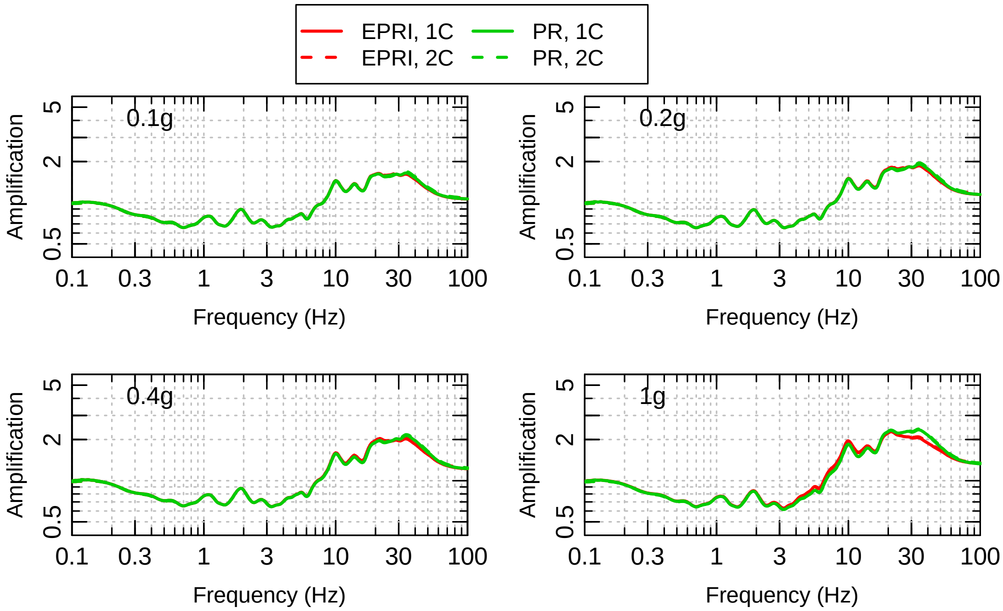

Figure 9-27. Effect of G/Gmax and damping curves on FMF transfer function (kappa = 0.018s, V_S profile P1, soil depth 5 ft).

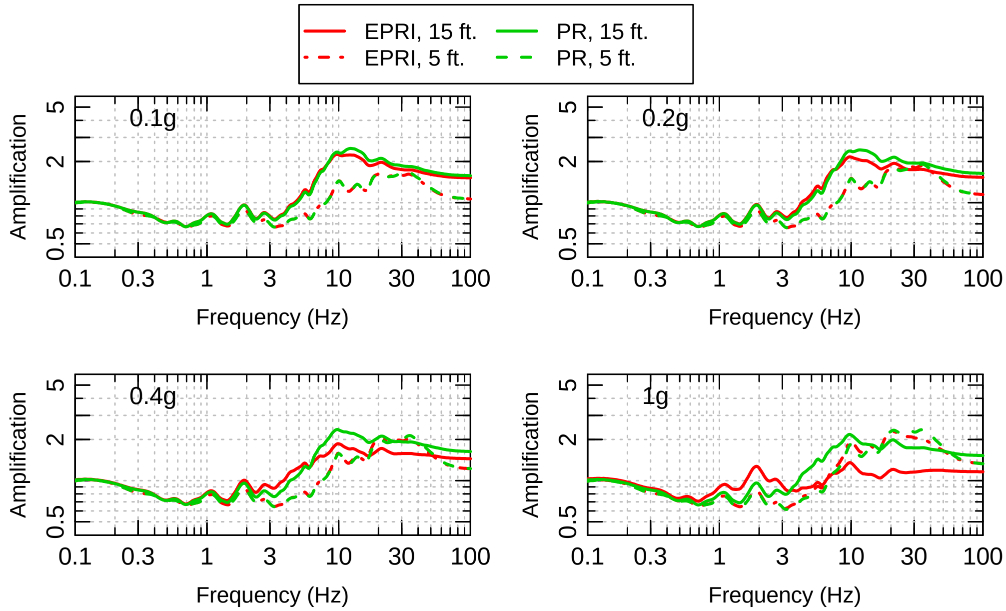

Figure 9-28. Effect of soil depth on FMF transfer function (kappa = 0.018s, V_S profile P1, soil material set M1).

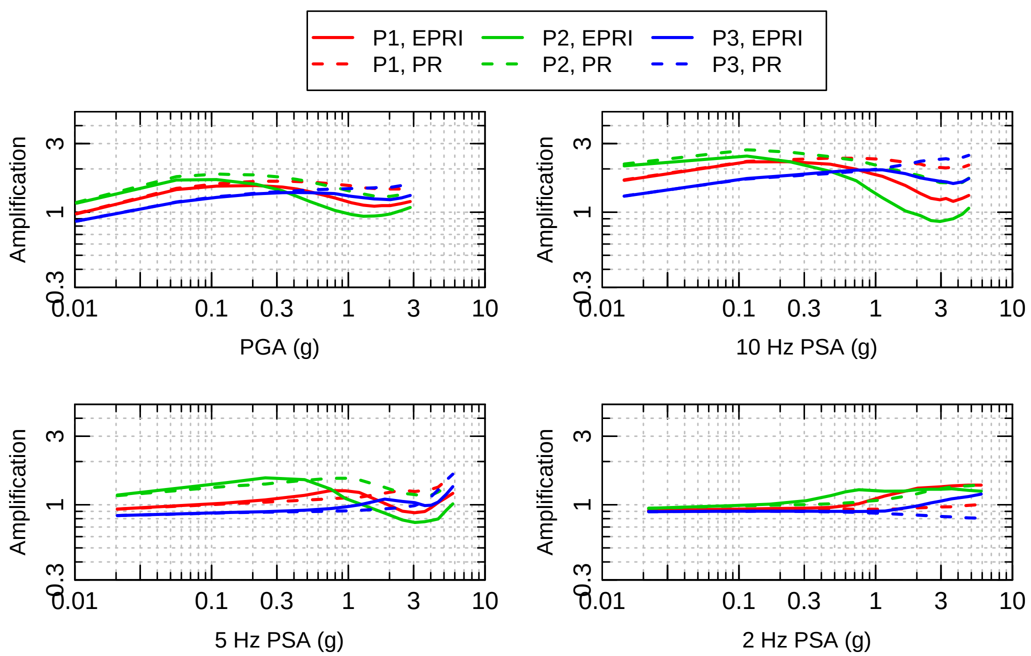

Figure 9-29. Effect of amplitude of input ground motions on FMF transfer function (kappa = 0.018s, soil depth 15 ft).

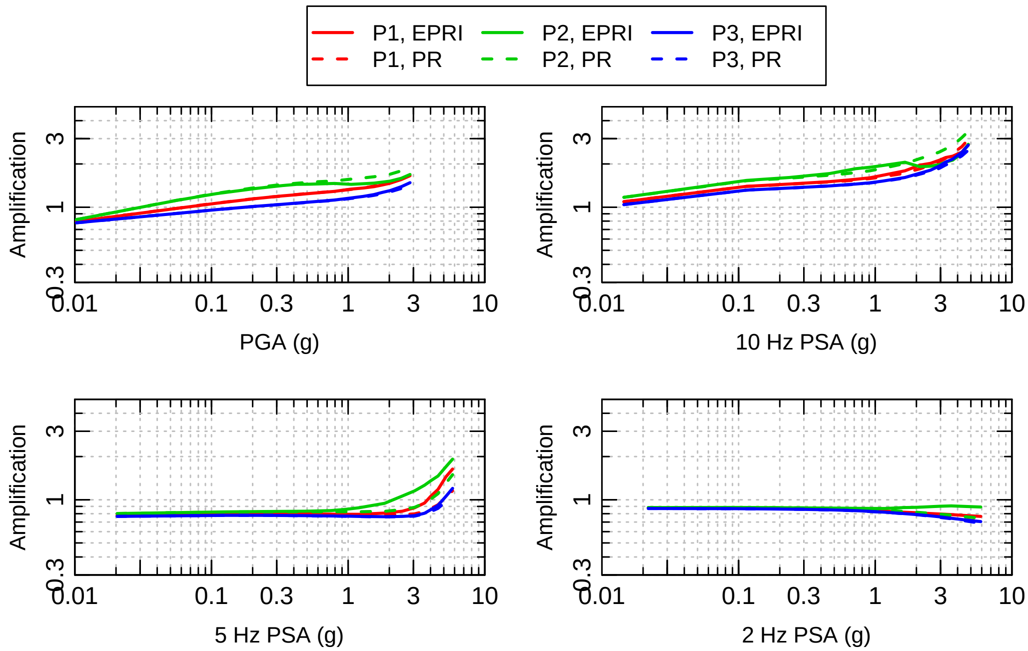

Figure 9-30. Effect of amplitude of input ground motions on FMF transfer function (kappa = 0.018s, soil depth 5 ft).

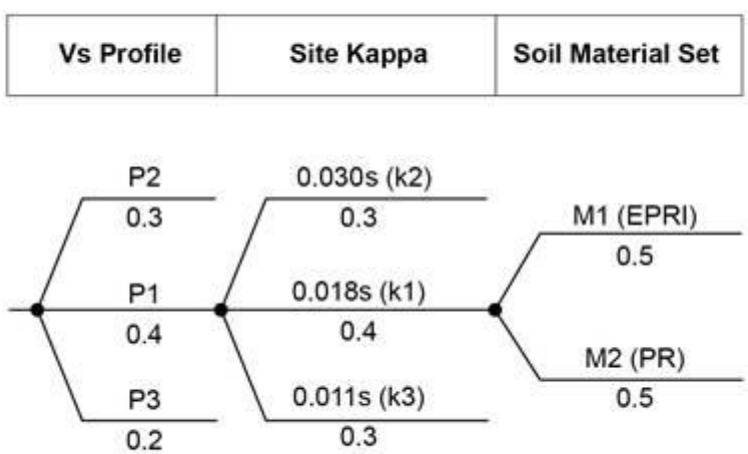

Figure 9-31. Logic tree for characterizing epistemic uncertainties in inputs to transfer function calculations for MFC (V_S and kappa only) and FMF (V_S, kappa, and Soil Material Set).

figure are calculations performed using ground motions recorded in seven downhole arrays during 37 earthquakes. The process involved using the motions recorded at depth as input to 1-dimensional site response calculations to compute surface motions. The computed surface motions were then compared to the recorded surface motions. The standard deviation of the natural logarithm of the ratio of observed over predicted represents the standard deviation of the modeling uncertainty.

Using the results of the transfer function calculations, the epistemic standard deviation in the transfer functions was computed as a function of frequency. The modeling uncertainty shown on the bottom panel of Figure 9-32 was incorporated by summing variances. The results are shown on Figure 9-33 for the MFC site and on Figures 9-34 and 9-35 for the FMF site for soil depths of 15 ft and 5 ft, respectively. The logic tree plus modeling epistemic uncertainty is shown for two levels of reference rock motions corresponding to return periods of 2,500 yrs. and 10,000 yrs. The resulting values are largest for frequencies above 10 Hz, the frequency range where the uncertainty in site kappa has the greatest effect on the transfer functions.

The adjustment from the reference rock hazard to the site-specific hazard is performed using Approach 3 for hazard consistent soil hazard calculations presented in NUREG/CR-6728 (NRC, 2001) as implemented in Appendix B of EPRI (2013). The formulation is discussed in Section 10.3. The process involves convolving the mean rock hazard with the site transfer function defined by a median (mean log) amplification and a standard deviation of ln(amplification). As discussed in Appendix B of EPRI (2013), the standard deviation in ln(amplification) can contain both epistemic and aleatory components. The basic process of the calculations produces the aleatory component from the randomization. If one considered that the alternative transfer functions defined by the end branches of the logic tree shown on Figure 9-31 represent all of the epistemic uncertainty, then one can compute a conditional mean hazard for each transfer function using the aleatory variability for each case in an Approach 3 calculation. The conditional mean hazard curves are then combined using the weights defined on the logic tree to produce the final site-specific mean hazard curves. The alternative described in Appendix B of EPRI (2013) is to combine the aleatory and epistemic uncertainties by summing variances to produce a composite standard deviation in ln(amplification). The composite standard deviation is then used in Approach 3 to compute the site-specific mean hazard curves from the reference rock hazard curves.

The approach used in this study to compute the site-specific mean soil hazard is a combination of these two approaches. Separate soil hazard calculations are performed for each transfer function defined by the end branches of the logic tree shown on Figure 9-31 to produce conditional mean hazard curves that are then combined using the logic tree weights to produce the site-specific mean hazard curves. In the calculation of each conditional mean hazard curve, the aleatory variability standard deviation is combined with the modeling uncertainty standard deviation from Figure 9-32 in order to incorporate the modeling uncertainty into the process.

The above process is based on the assumption that the components of the logic tree shown on Figure 9-31 combined with the modeling uncertainty shown in the bottom panel of Figure 9-32 captures all significant epistemic uncertainty in the transfer functions. PNNL (2014) discuss this issue and conclude that at ground motion frequencies smaller than the fundamental frequency of the site profile being analyzed, uncertainty in 1-dimensional site response analyses results may under estimate the epistemic uncertainty.

To address this potential underestimation, PNNL (2014) developed a minimum level of epistemic uncertainty that transitioned from zero at high frequencies (≥ 5 Hz) to a fully ergodic site-to-site variability at very low frequencies, ϕ_{S2S}. The ergodic ϕ_{S2S} was assessed based on empirical data derived from the analyses of residuals for the NGA-West2 GMPEs. Shown on Figures 9-33 through 9-35 are the Global ϕ_{S2S} values presented in PNNL (2014). These were used along with data from subduction zone earthquakes to set a minimum epistemic uncertainty at very low frequencies of $\phi_{S2S} = 0.45$. These values were based on a global data set where for many sites the only site parameter is an estimate of V_{S30} and where there may be a wide range of crustal structures. PNNL (2014) also present ϕ_{S2S} calculated from the Chiou and Youngs (2014) residuals for California earthquake data where many sites have the additional site parameter of depth to V_S of 1 km/s, Z1.0, and for which the crustal structure may be more uniform. It might be argued that the California results are more appropriate for establishing a possible minimum level of epistemic uncertainty at low frequencies because more aspects of site characterization are included. Another possible assessment of an appropriate ϕ_{S2S} is provided by Rodriguez-Marek et al. (2011) who found a value of ϕ_{S2S} of approximately 0.22 for borehole recordings at rock sites in Japan.

The approach used by PNNL (2014) for a transition from zero minimum epistemic uncertainty at high frequencies to empirical ϕ_{S2S} as the minimum epistemic uncertainty at low frequencies was based on the frequency range represented in site response. For the MFC and FMF calculations, the relative site response calculations used to develop the transfer functions employ the full crustal profile, and thus have very low fundamental frequencies (< 0.2 Hz). Therefore, this argument cannot be used to provide a basis for a transition frequency. Given these uncertainties, two alternative end members of a range of possibilities are employed for defining the minimum epistemic uncertainty. The first, Option A, is to use the modeling uncertainty from Figure 9-32. The second, Option B, is to use the ϕ_{S2S} values for the California data for **M**> 5 shown on Figures 9-33 through 9-35, after removing the variance in the computed transfer functions defined by the logic tree shown on Figure 9-31. A weighted combination is used to develop the final mean hazard. Option A is favored slightly (weight 0.6) over Option B (weight 0.4) because the transfer calculations make use of the full crustal profile. This combination produces an effective weighted minimum epistemic uncertainty that is approximately the same as the borehole ϕ_{S2S} reported by Rodriguez-Marek et al. (2011). The final transfer functions are tabulated in the GMM HID (Appendix G).

9.4 Relationships for Vertical Motions for MFC and FMF

The common approach to development of design response spectra for vertical motions is to multiply the horizontal design spectral by appropriate vertical to horizontal (V/H) response spectral ratios. For probabilistically determined design spectra, the V/H ratios should be chosen based on the dominant earthquakes contributing to the horizontal hazard.

The recent NGA (Power et al., 2008) and NGA-West2 (Bozorgnia et al., 2014) projects produced extensive datasets of ground motions for use in development of V/H ratios. Gülerce and Abrahamson (2011) developed a model for V/H based on data from the NGA project. More recently, Stewart et al. (2015) and Bozorgnia and Campbell (2015) have developed GMPEs for vertical ground motions as part of the NGA-West2 project. These models can be used in conjunction with their companion GMPEs for horizontal motions, Boore et al. (2014) and Campbell and Bozorgnia (2014), respectively, to produce V/H spectra ratios. All of these models characterize vertical motions or V/H ratios as a function of magnitude, distance, style of faulting, and site conditions as parameterized by V_{S30}. In addition, Bommer et al. (2011) have developed a model for V/H using data from active tectonic regions in Europe and the Middle East.

The reference rock hazard results for the MFC and FMF site presented in Section 10.2 indicate that the mean magnitude and distance for earthquakes contributing to the hazard at return periods near 2,500 years range from approximately **M** 6.4 and R_{RUP} of 45 km for ground motion frequencies ≥ 5 Hz to approximately **M** 6.9 and R_{RUP} of 75 km at a ground motion frequency of 1 Hz. The V_{S30} for the MFC site is 1030 m/s and the V_{S30} for the FMF site is 678 m/s for a soil depth of 15 ft and 844 m/s for a soil depth of 5 ft Figure 9-36 shows the V/H ratios for the MFC site. Figure 9-37 shows the V/H ratios for the FMF site for the high frequency controlling earthquakes and Figure 9-38 shows the V/H ratios the FMF site for low frequency controlling earthquakes. The plotted V/H ratios are Gülerce and Abrahamson (2011) – GK11, Stewart et al. (2015) over Boore et al. (2014) – SBSA15/BSSA14, Bozorgnia and Campbell (2015) over Campbell and Bozorgnia (2014) – BC15/CB14, and Bommer et al. (2011) – BSK11.Normal faulting V/H ratios are computed for all relationships. The average of the four V/H ratios is also shown on each figure.

Figure 9-39 shows the average high frequency and low frequency V/H ratios for the MFC site and the envelopes of the average high frequency earthquake and average low frequency earthquake V/H ratios for the two soil depths for the FMF site. As shown, at frequencies of 2 Hz and greater, the V/H ratios for both the MFC site and the FMF can be represented by a value of 2/3. The V/H ratios increase for lower frequencies to values of approximately 0.85 for the MFC site (rock) and 0.82 for the FMF site (soil). The sharp peak at a frequency of 0.133 Hz is smoothed through as there is no reason to expect such a sharp peak at a low frequency. The recommended V/H ratios are listed in Table 9-4.

Table 9-4. Recommended V/H ratios for MFC and FMF at the return period of approximately 2,500 yrs.

Ground Motion Frequency (Hz)	Vertical to Horizontal (V/H) Ratio	
	MFC (Rock)	FMF (Site-Specific)
PGA (100)	0.667	0.667
50	0.667	0.667
33.3	0.667	0.667
20	0.667	0.667
10	0.667	0.667
5	0.667	0.667
3.33	0.667	0.667
2	0.667	0.667
1	0.759	0.744
0.5	0.850	0.820

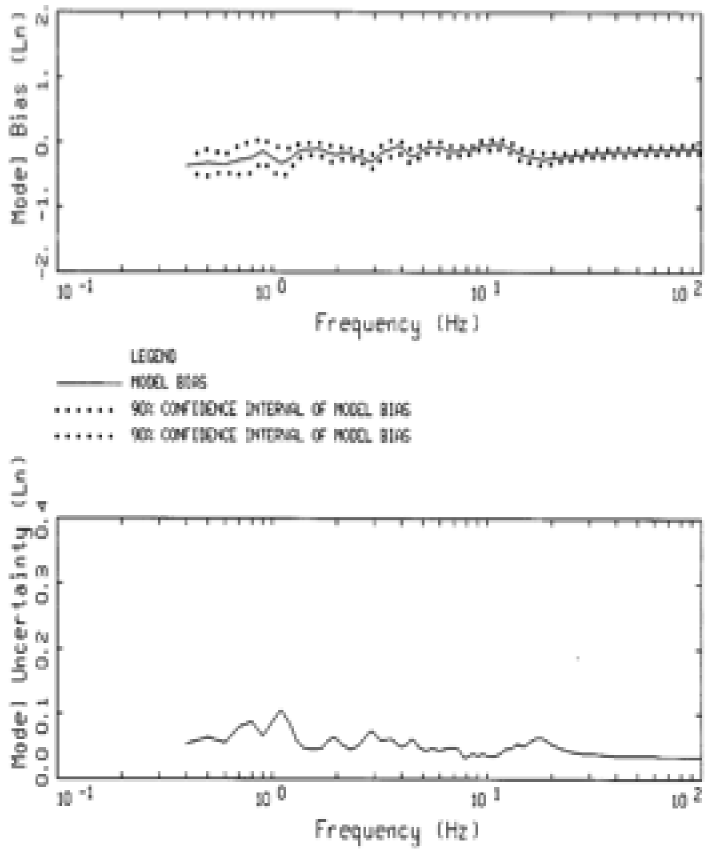

Figure 9-32. Modeling uncertainty in 1-Dimensional site response (W. Silva, pers. comm., 2015).

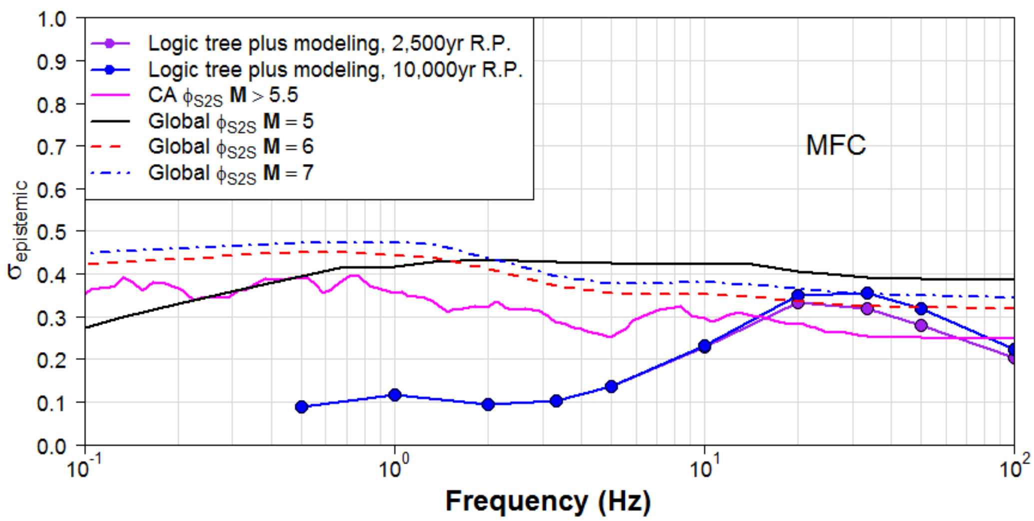

Figure 9-33. Epistemic uncertainty in the transfer function for MFC.

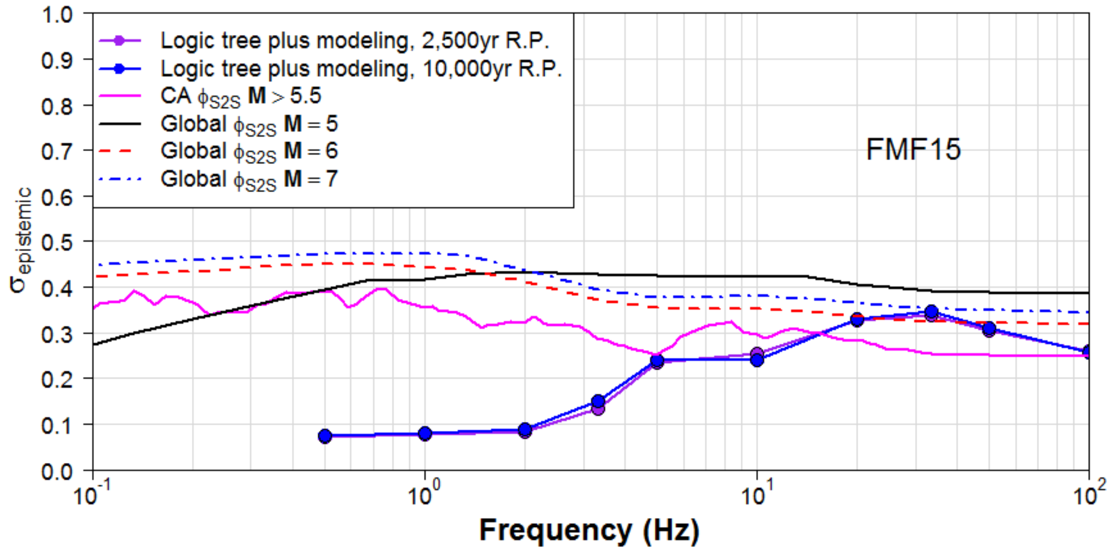

Figure 9-34. Epistemic uncertainty in the transfer function for FMF (15 ft of soil).

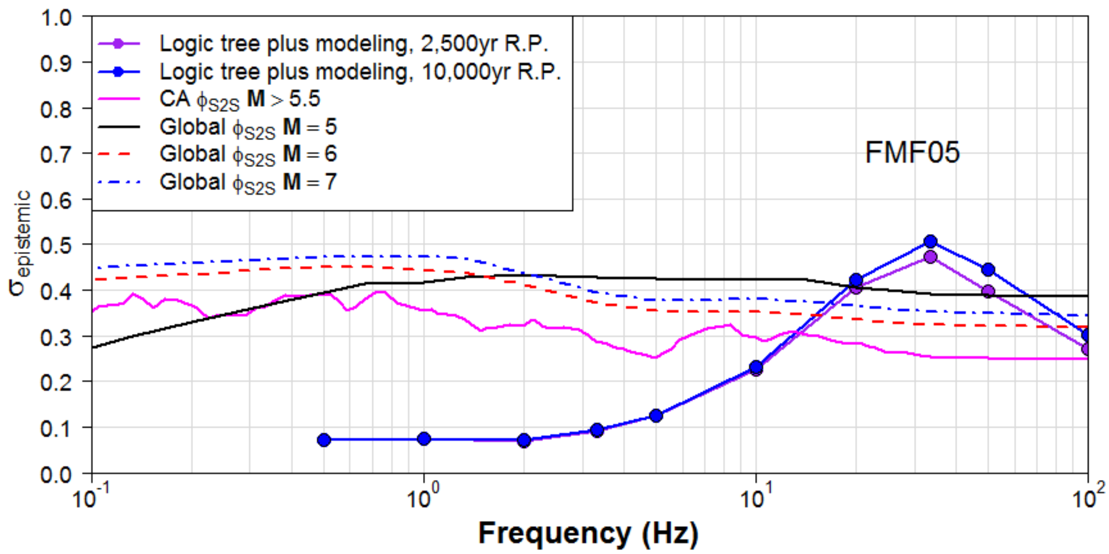

Figure 9-35. Epistemic uncertainty in the transfer function for FMF (5 ft of soil).

(a)

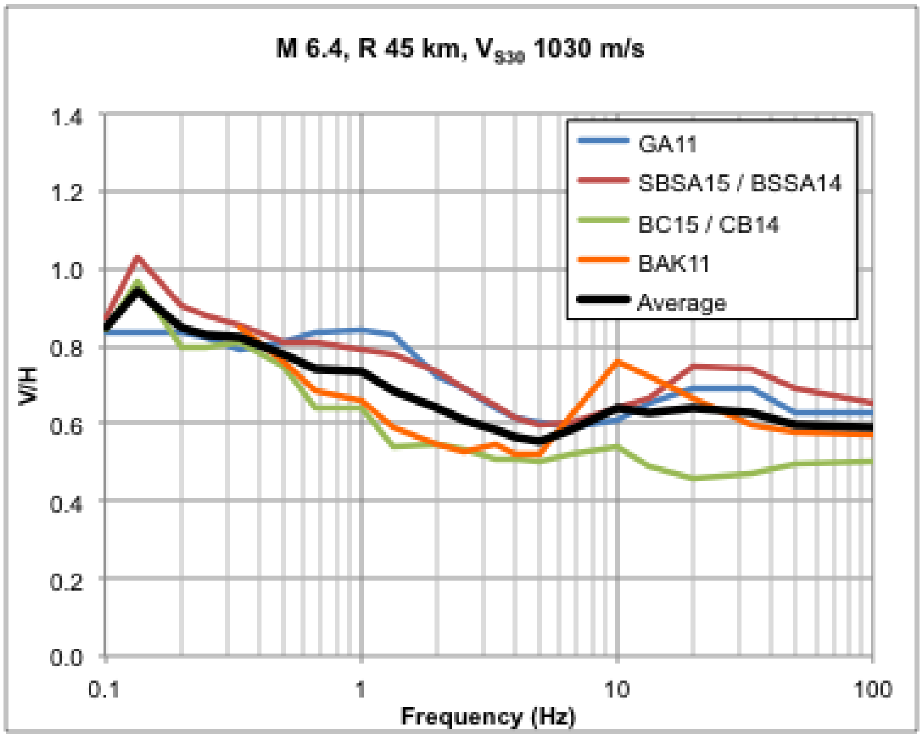

(b)

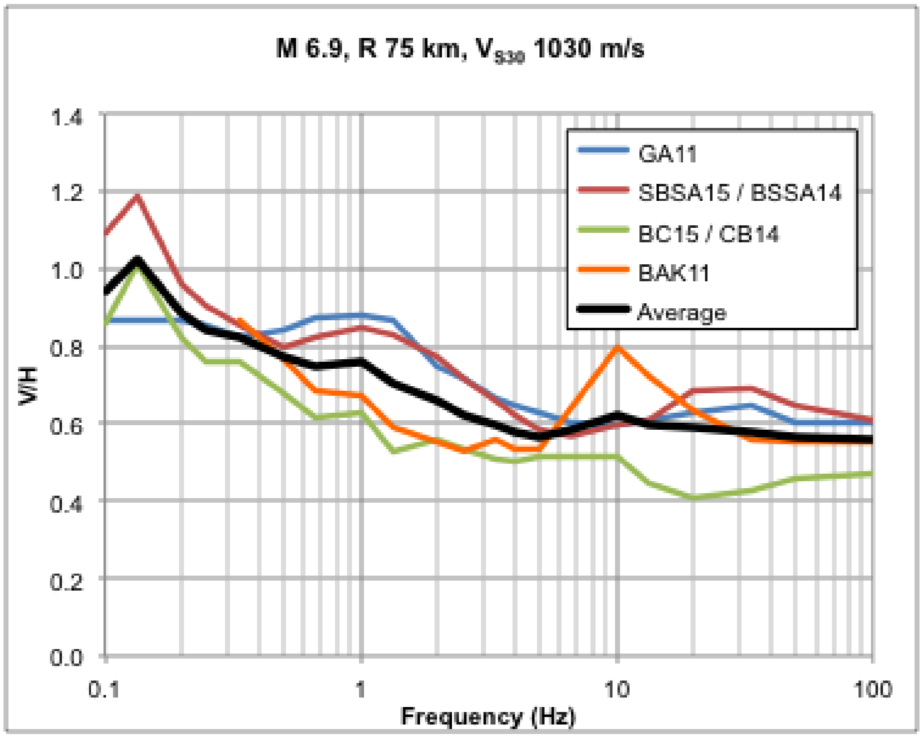

Figure 9-36. V/H ratios for MFC: a) high frequency controlling earthquake; and b) low frequency controlling earthquake.

(a)

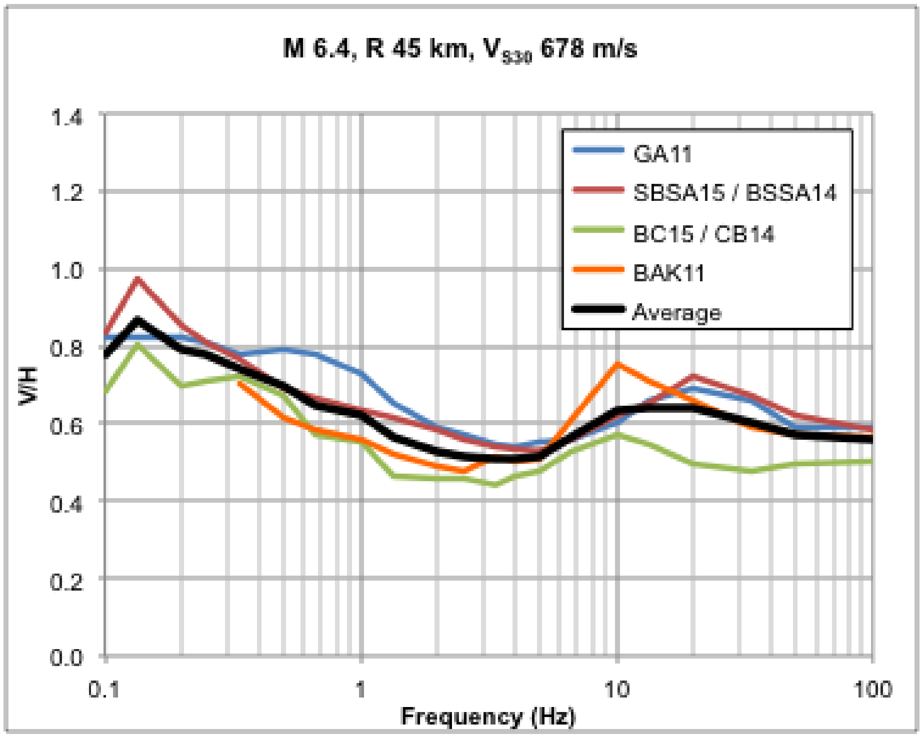

(b)

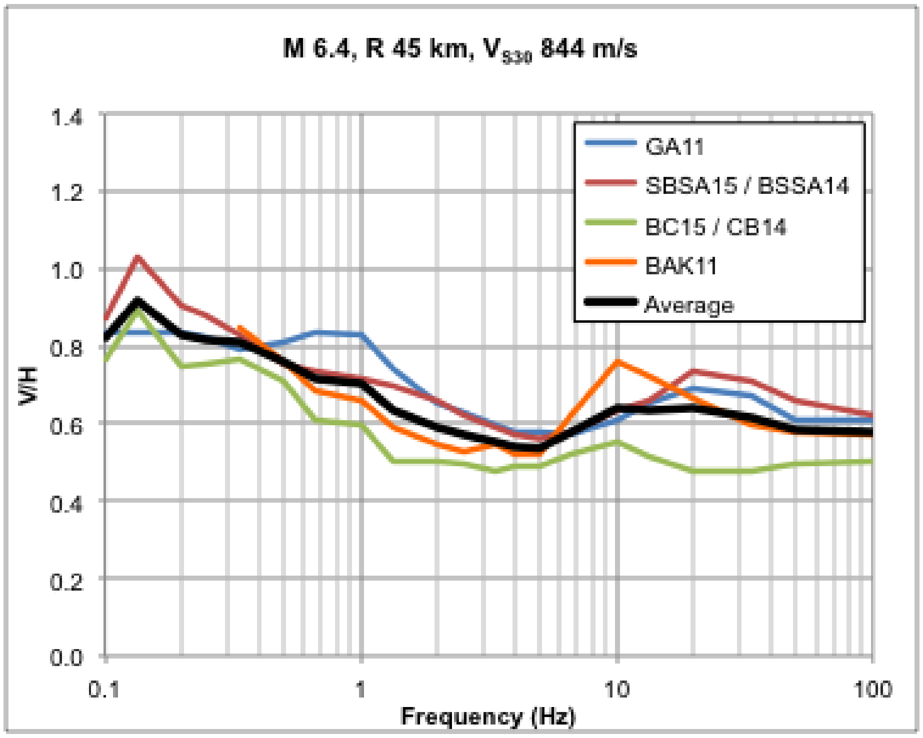

Figure 9-37. V/H ratios for FMF: a) high frequency controlling earthquake, 15 ft soil depth; and b) 5 ft soil depth.

(a)

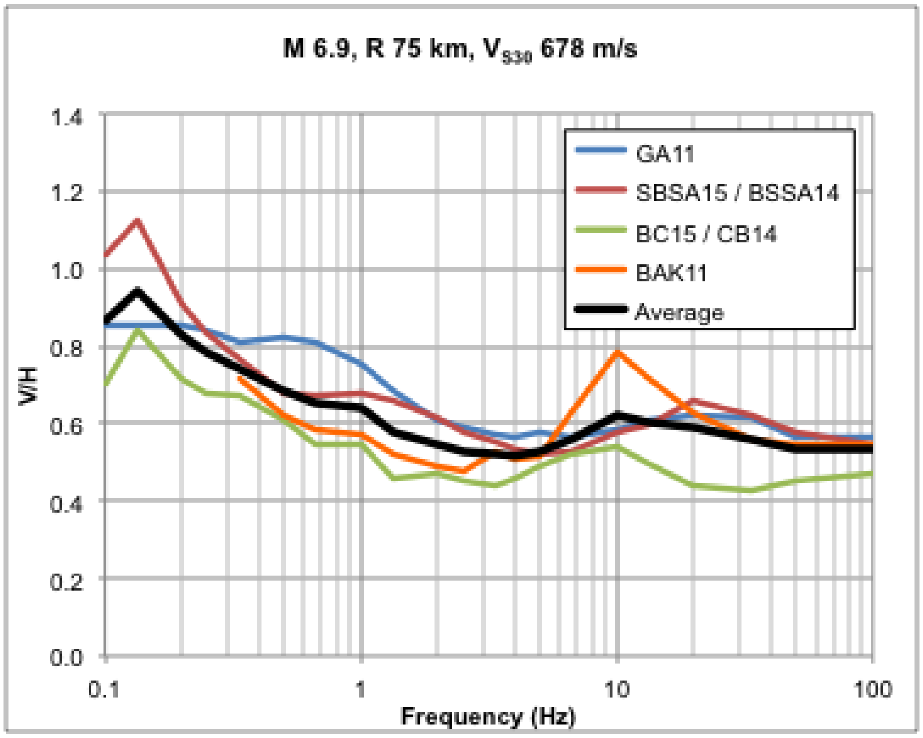

(b)

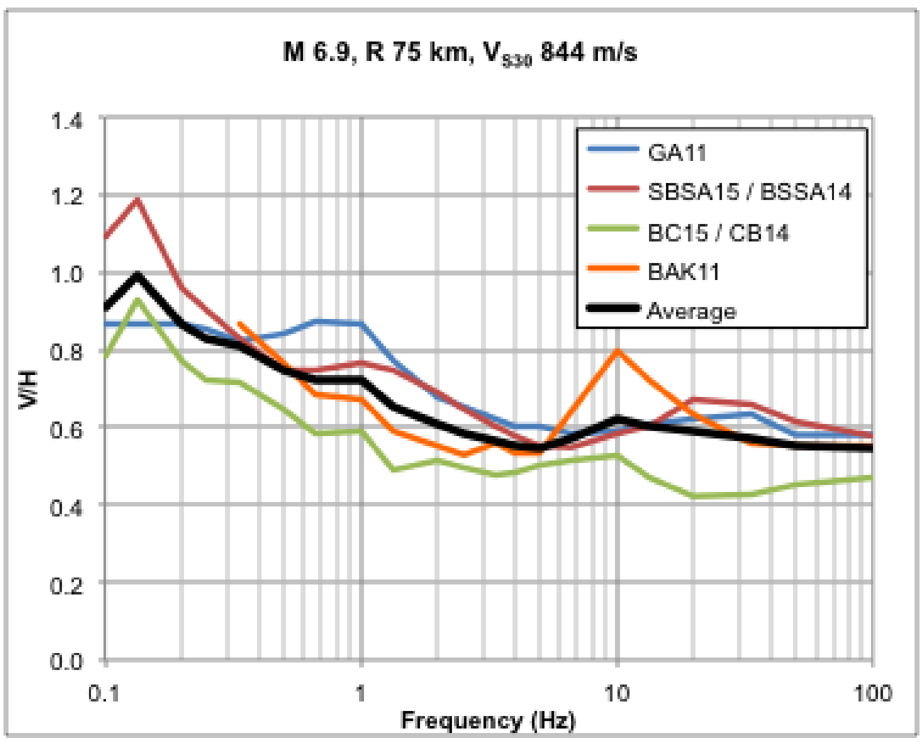

Figure 9-38. V/H ratios for FMF: a) low frequency controlling earthquake, 15 ft soil depth; and b) 5 ft soil depth.

(a)

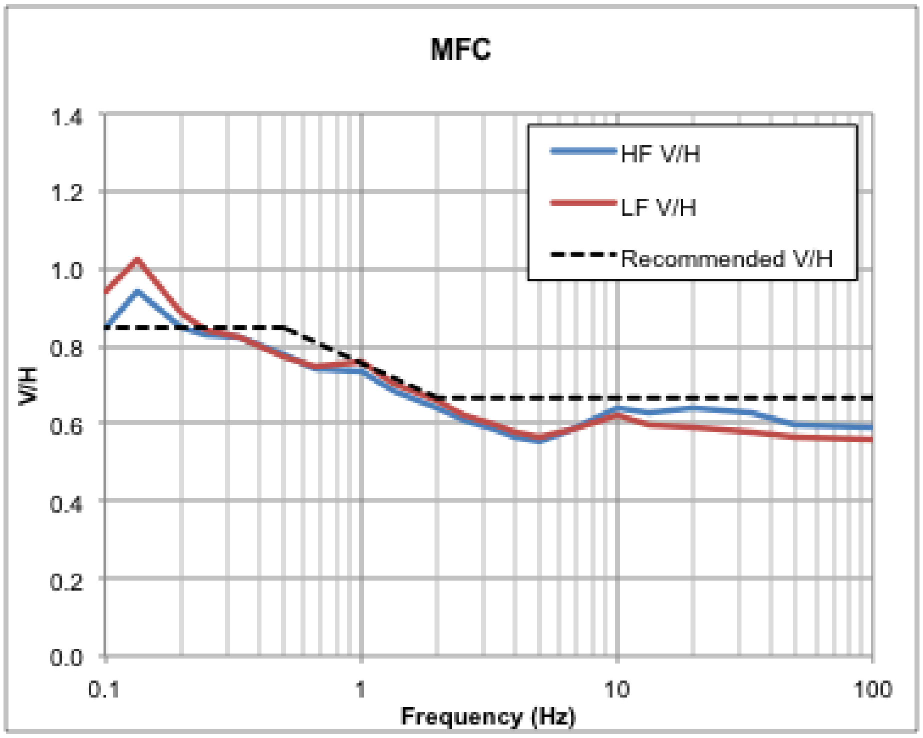

(b)

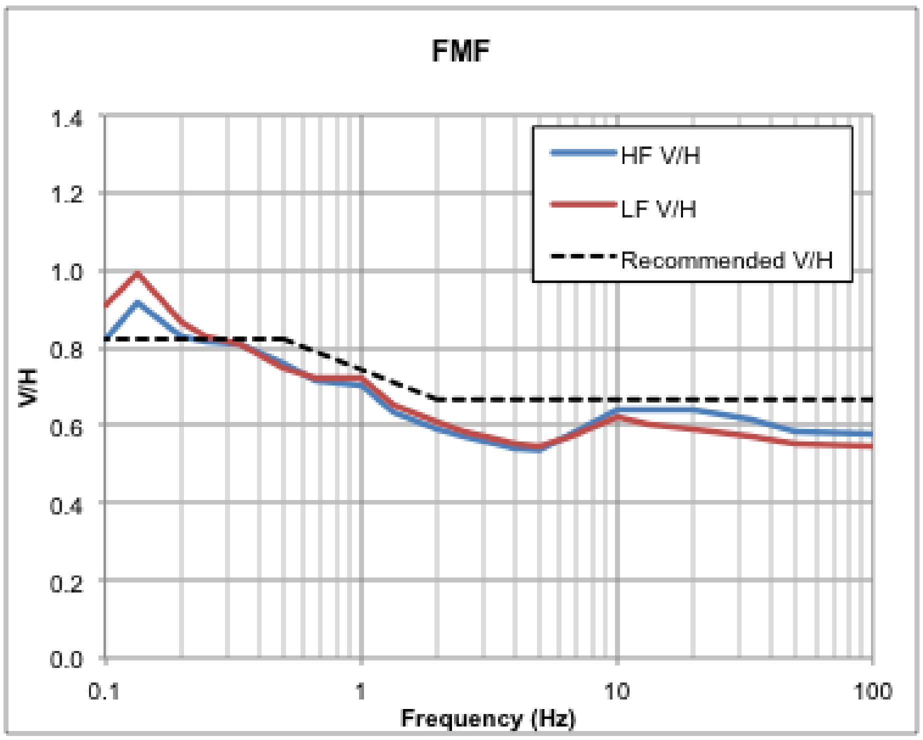

Figure 9-39. Recommended V/H ratios for (a) MFC (rock) and (b) FMF (site-specific) at the return period of approximately 2,500 yrs.

9.5 Development of Transfer Functions for the SFHP at the NRF Site

The methodology described in Section 9.3 was used to develop transfer functions from the SWUS reference rock profile to the SFHP rock and soil profiles. Recall from Section 7.4.1 that the V_S profile for NRF was modified using site-specific V_S data for basalt at the SFHP area.

9.5.1 Transfer Functions for SFHP Rock for Shallow Crustal Earthquakes

The epistemic uncertainty in the dynamic properties of the SFHP Rock site is characterized by three alternative velocity profiles, P1 (median), P2 (lower-range), and P3 (upper-range) (Section 7.4), and three alternative values of kappa, k1 – 0.037s, k2 – 0.062s, and k3 – 0.022s (Section 7.5). Figure 9-40 compares the three velocity profiles to the reference V_S profile for the SWUS GMM. Figure 9-41 shows the upper two kilometers of these velocity profiles. The V_S values for the SWUS and SFHP Rock profiles become similar below a depth of 5 km. The SFHP Rock profiles quickly rise to V_S values of approximately 2 km/s and greater compared to the more gradual velocity increase for the SWUS reference profile. The SFHP Rock profiles also contain a number of low velocity zones representing the soil interbeds.

The SWUS to SFHP Rock transfer function calculations utilized randomized velocity profiles in the same manner as the computations for MFC. The same correlation model was used for both sites. The correlation model has a depth dependent σln of 0.33 over the top 15 m and 0.15 below (Toro, as appears in Silva et al., 1996).

Figure 9-42 shows the transfer functions developed for the three alternative SFHP Rock velocity profiles for four levels of input motion. The designation “1C” and “2C” refer to the two different earthquake source spectra shapes used to define the input motions. The three SFHP Rock velocity profiles produce differences in the transfer functions in terms of the locations of peaks and troughsin the frequency range of 1 to 6 Hz and in the level of the transfer function at higher frequencies. Effect of epistemic uncertainty on the median velocity profile for SFHP Rock is greater than that obtained for the MFC site. As was the case for the MFC site, there is very little difference in the transfer functions computed using the one-corner and two-corner earthquake source spectra.

Figure 9-43 shows the effect of the alternative values for kappa on the transfer functions for four levels of input motion. The alternative values of kappa result in differences in the transfer functions for frequencies above 2 Hz, with the differences becoming large for frequencies above 6 Hz.

The transfer functions for SFHP Rock profiles shown on Figures 9-42 and 9-43 show lower relative amplification than those developed for the MFC rock profiles (Figures 9-14 and 9-15). These lower motions for the SFHP Rock site are attributed to two effects, the higher kappa for the SFHP Rock site compared to the MFC site and the presence of the interbeds in the SFHP Rock profile.

The SFHP Rock transfer functions shown on Figures 9-42 and 9-43 were computed assuming that the basalts remain linear under seismic loading. NWRC-RA (2015) present strain-dependent shear modulus reduction (G/Gmax) and damping relationships for the shallow basalts (Figure 7-32). Sensitivity analyses were performed to evaluate the impact of considering non-linear behavior in the upper portions of the SFHP Rock basalts. Two sensitivity cases were analyzed. The first case modeled non-linear behavior in the upper 30 m of the basalts. This is the region where lower basalt Vs values were obtained (Figure 7-25). The second case modeled non-linear behavior in the top 500 ft (140 m) of the basalt profile. This is the range in which non-linear behavior is typically assumed to occur (EPRI, 2013). In both cases, the low strain damping from the damping curves (Figure 7-32) was used to compute the equivalent kappa in the non-linear portion of the profile and this value was removed from the kappa assigned to the deeper layers in order to maintain the level of total kappa assigned to the SFHP Rock profile. Figure 9-44 shows the results of the sensitivity analyses. Including non-linear behavior in the shallow basalts produces slightly lower transfer functions than obtained assuming linear behavior.

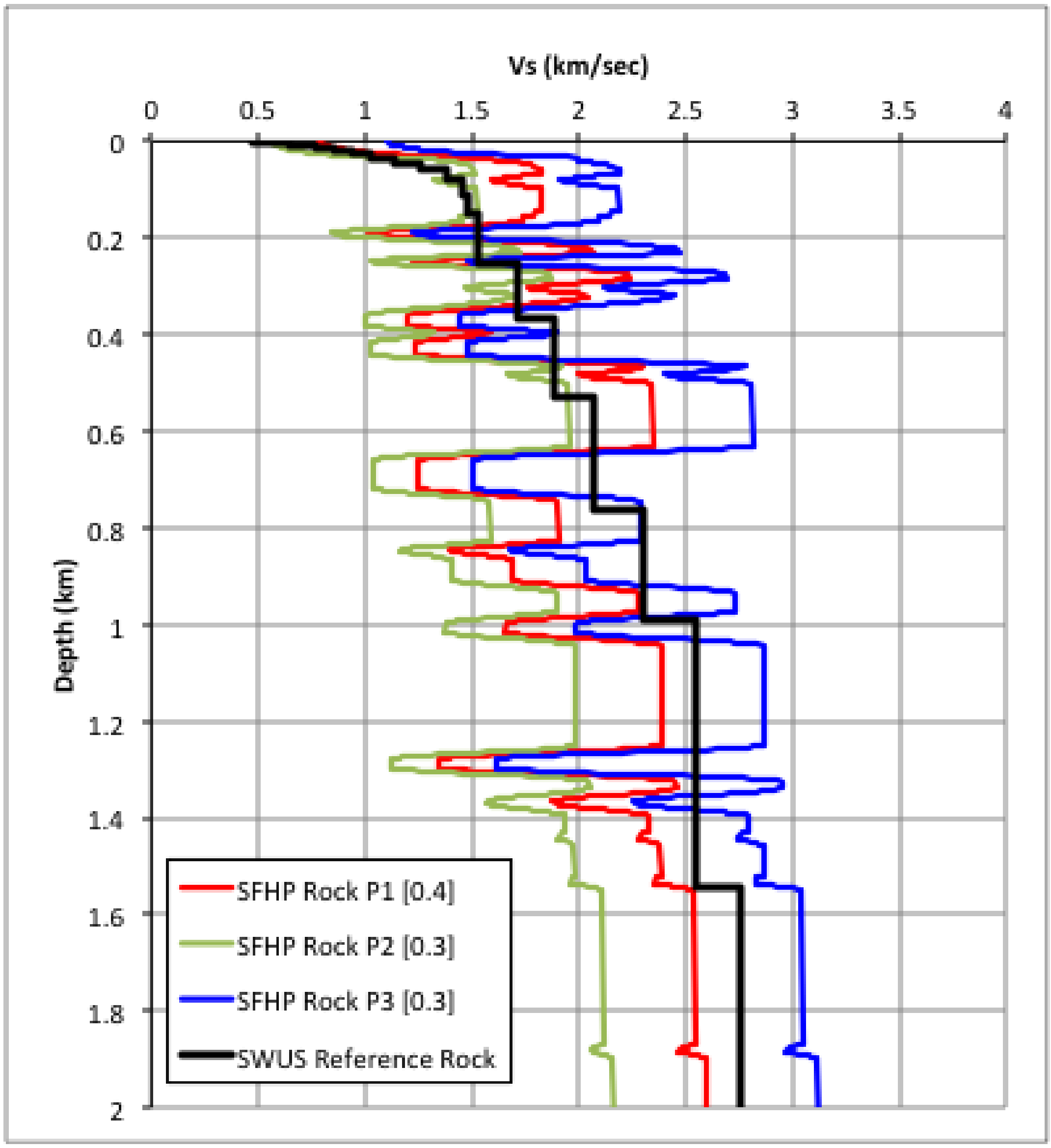

Figure 9-40. Comparison of SWUS reference rock V_S profile with SFHP Rock profiles.

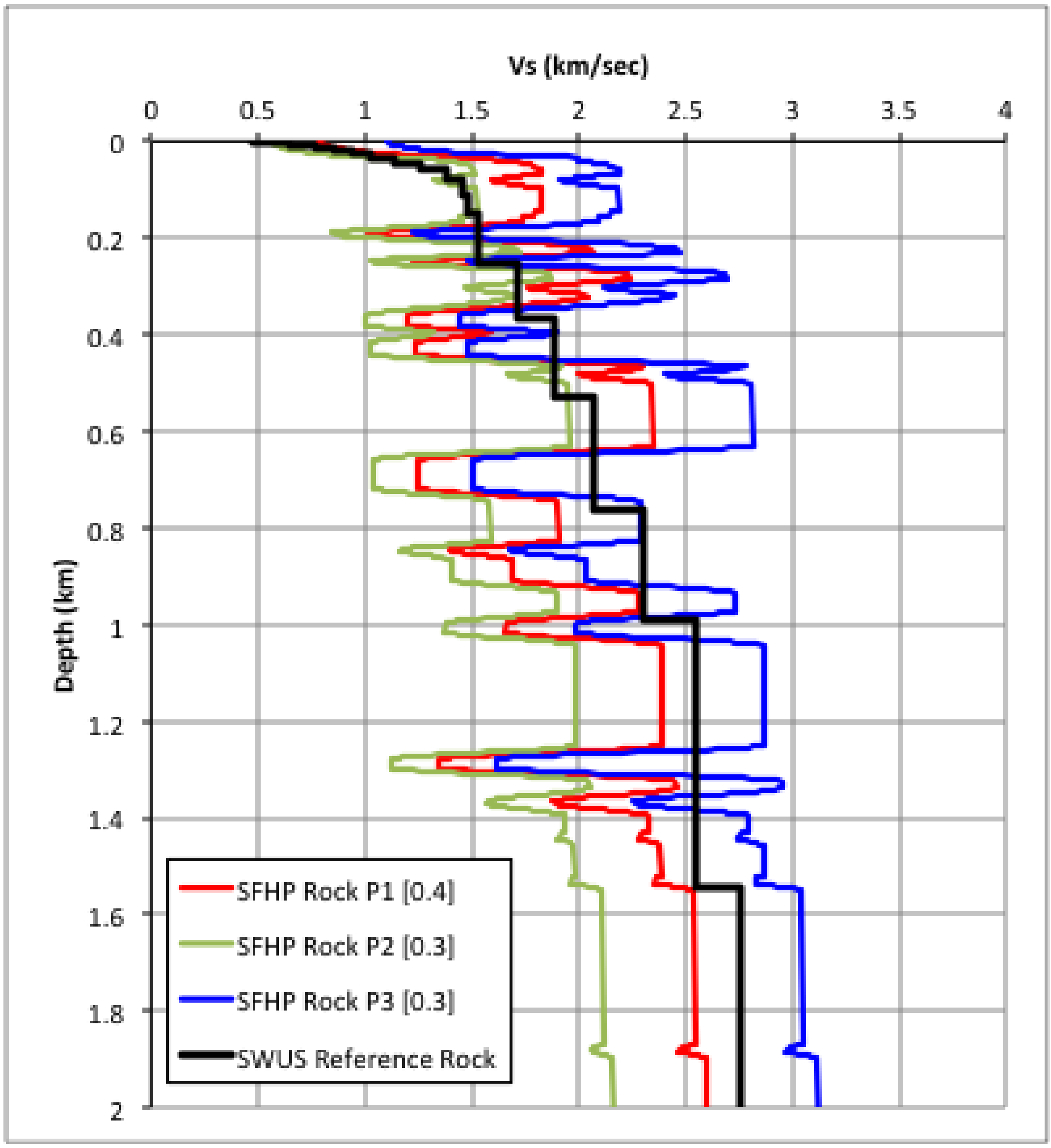

Figure 9-41. Comparison of top 2 km of SWUS reference rock V_S profile with SFHP Rock profiles.

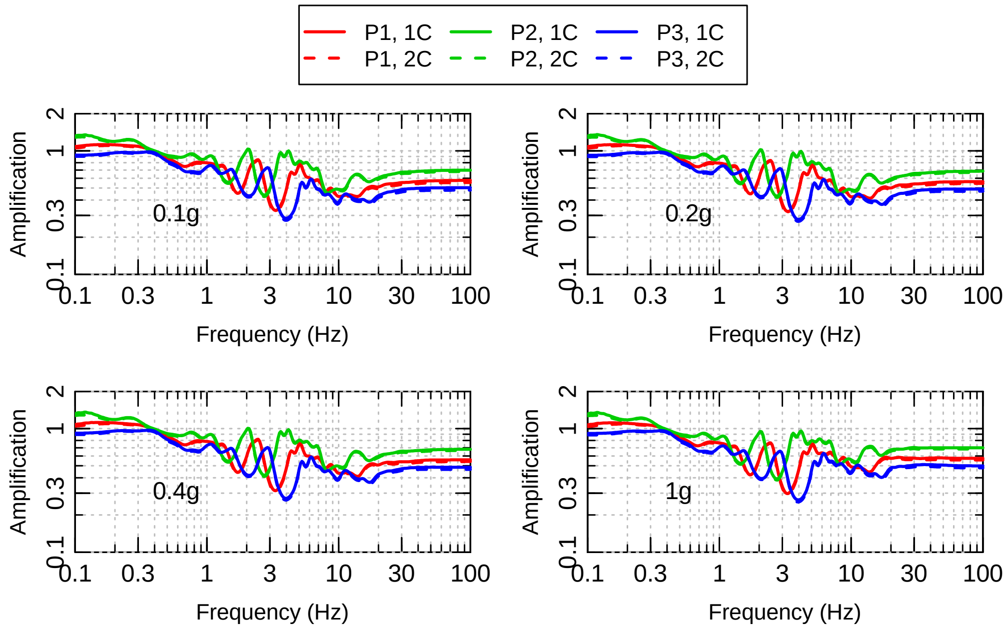

Figure 9-42. Effect of Vs profile on SFHP Rock transfer function (kappa = 0.037s).

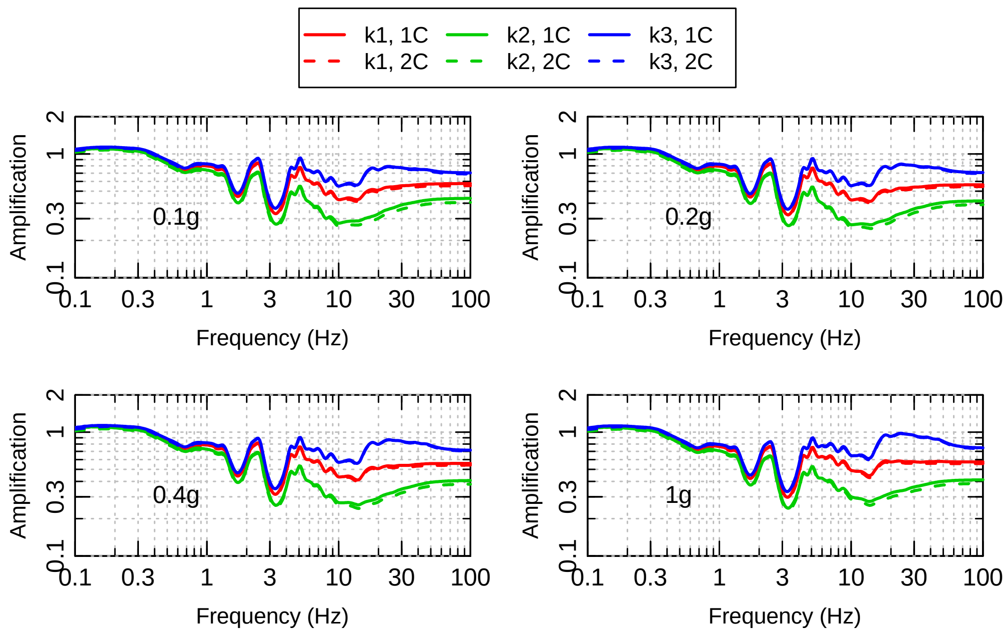

Figure 9-43. Effect of kappa on SFHP Rock transfer function (V_S profile P1).

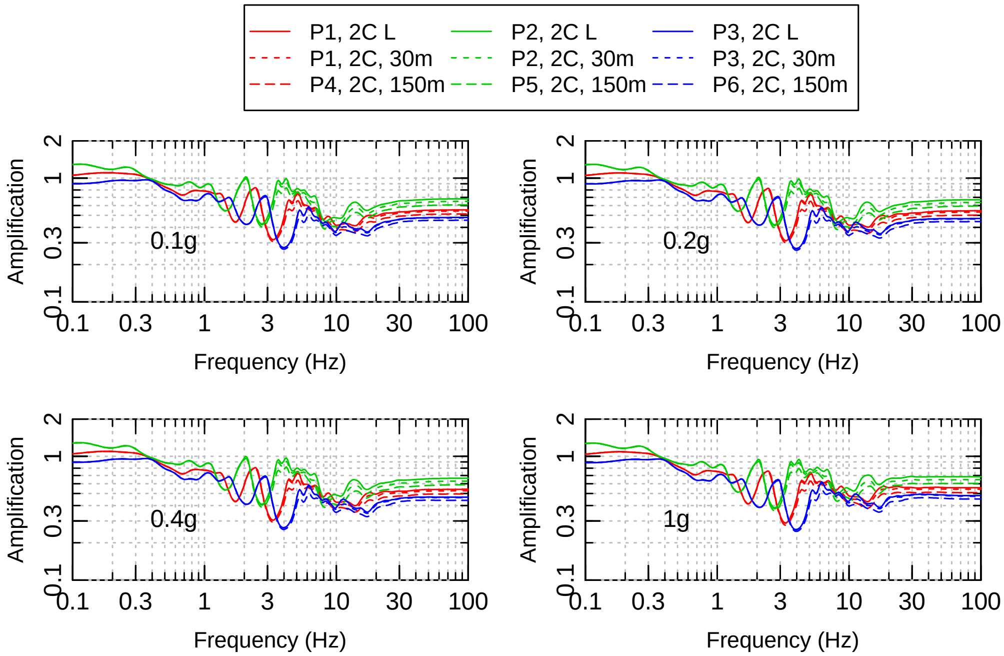

Figure 9-44. Effect of considering non-linear behavior in the SFHP site shallow basalt layers. (kappa = 0.037s).

9.5.2 Transfer Functions for SFHP Soil Sites for Shallow Crustal Earthquakes

As described in Section 7.4, the SHFP soil sites contain up to approximately 45 ft of soils. Transfer functions are developed for two soil depths, 20 and 40 ft, to represent the variability in soil depth across the site. The epistemic uncertainty in the dynamic properties of the SFHP soil sites is characterized again by three alternative velocity profiles, P1 (median), P2 (lower-range), and P3 (upper-range) for the 20-ft soil depth case, P4 (median), P5 (lower-range), and P6 (upper-range) for the 40-ft soil depth case, and three alternative values of kappa, k1 – 0.037s, k2 – 0.062s, and k3 – 0.022s. The soil profiles consist of the three basalt profiles P1, P2, and P3 for the SFHP rock site case with the addition of either 20 ft of soil (for P1, P2, and P3) or 40 ft of soil (for P4, P5, and P6). The values of kappa are applied to the basalt profiles below the soil layers. Additionally three sets of G/Gmax and damping relationships are used to model the nonlinear behavior of the soils. Set M1 is the generic EPRI (1993) curves, set M2 is the generic Peninsular Range curves (Silva et al., 1996), and set M3 is the site-specific curves developed by NWRC-RA (2015). Figure 9-45 compares the three velocity profiles for the 20-ft soil depth to the reference VS profile for the SWUS GMM and Figure 9-46 compares the profiles for the 40 ft soil depth. For the 20-ft soil depth, the soil layers consist of the surface soils and gravel alluvium overlying basalt. For the 40-ft soil depth, the material below a depth of 25 ft consisted of clay loess.

The randomization of the velocity profiles and G/Gmax damping relationships for the SFHP soil sites was conducted in the same manner as for the FMF site. In addition, variability in soil depth was addressed by computing transfer functions for soil depths of 15 and 25 ft and for 35 and 45 ft.

Figures 9-47 and 9-48 shows the effect of the alternative SFHP velocity profiles on the transfer functions for four levels of input motion for soil depths of 20 ft and 40 ft respectively. In contrast to the results observed for the MFC and FMF sites (Section 9.3), the alternative velocity profiles produce similar differences in the transfer functions for the SFHP Rock and Soil sites. As is the case for the results for other sites, there is very little difference in the transfer functions computed using the one-corner and two-corner earthquake source spectra.

Figures 9-49 and 9-50 show the effect of the alternative values for kappa on the transfer functions for four levels of input motion for soil depths of 20 ft and 40 ft, respectively. The kappa effects for SFHP soil are generally similar to those for SFHP rock. For the 20 ft soil depth, the kappa effects become somewhat smaller at high loading levels because the transfer function is being influenced by the soil nonlinearity. The kappa effects are larger for the 20 ft soil profile than for the 40 ft soil profile. This is likely due to the fact that the 40 ft profile develops greater shear strains in response to high loading levels, and thus greater damping levels that counter balance the effects of the larger ground motions for the low kappa case.

Figures 9-51 and 9-52 show the effect of the alternative sets of G/Gmax and damping relationships on the transfer functions for the three profiles for the 20 ft and 40 ft soil depths, respectively. For both depths, the alternative material curves produce relatively small differences in relative amplification compared to what was observed for the FMF site. This smaller difference is attributed to the overall lower level of motion for the SFHP site due to the higher level of kappa and the presence of the interbeds. The lower levels of motion lead to lower strains, and thus lower impact on the differences in nonlinearity and damping at higher strains. The basis for this assessment is shown on Figures 9-53 and 9-54 in which the effect of the alternative material curves is shown for the lower kappa value of 0.022s. The greater level of motion resulting from the lower kappa value result in greater differences in relative response among the three sets of material curves.

Figures 9-55 and 9-56 show the effect of loading level on the SFHP Soil transfer functions for the 20 ft soil depth and the 40 ft soil depth, respectively. The effect of loading level is less than exhibited for the FMF site due again to the lower level of motion transmitted to the surface as a result of the effects of the interbeds and the larger kappa for the SFHP site compared to the FMF site.

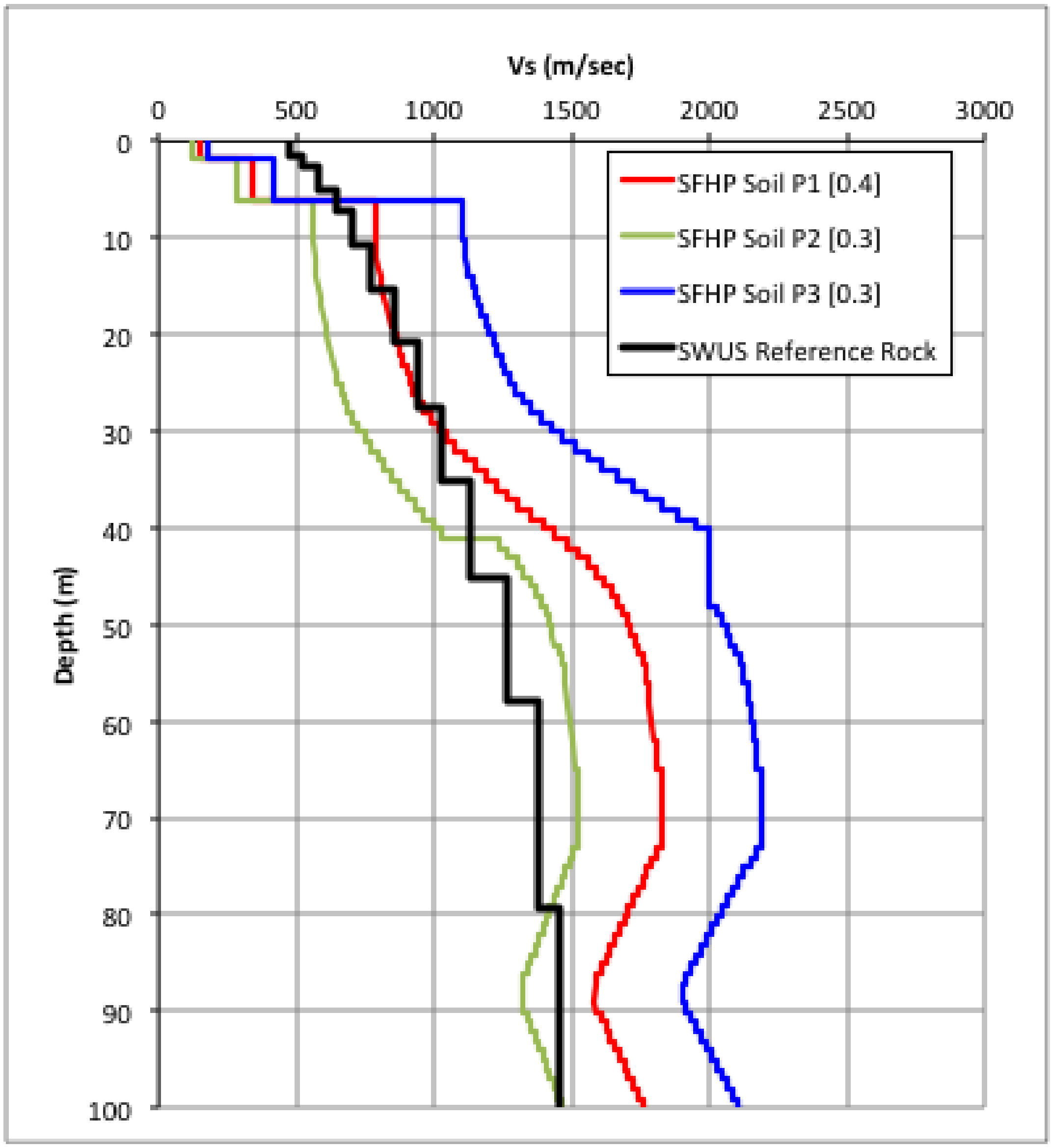

Figure 9-45. Comparison of SWUS reference rock V_S profile with SFHP profiles for 20 ft of soil.

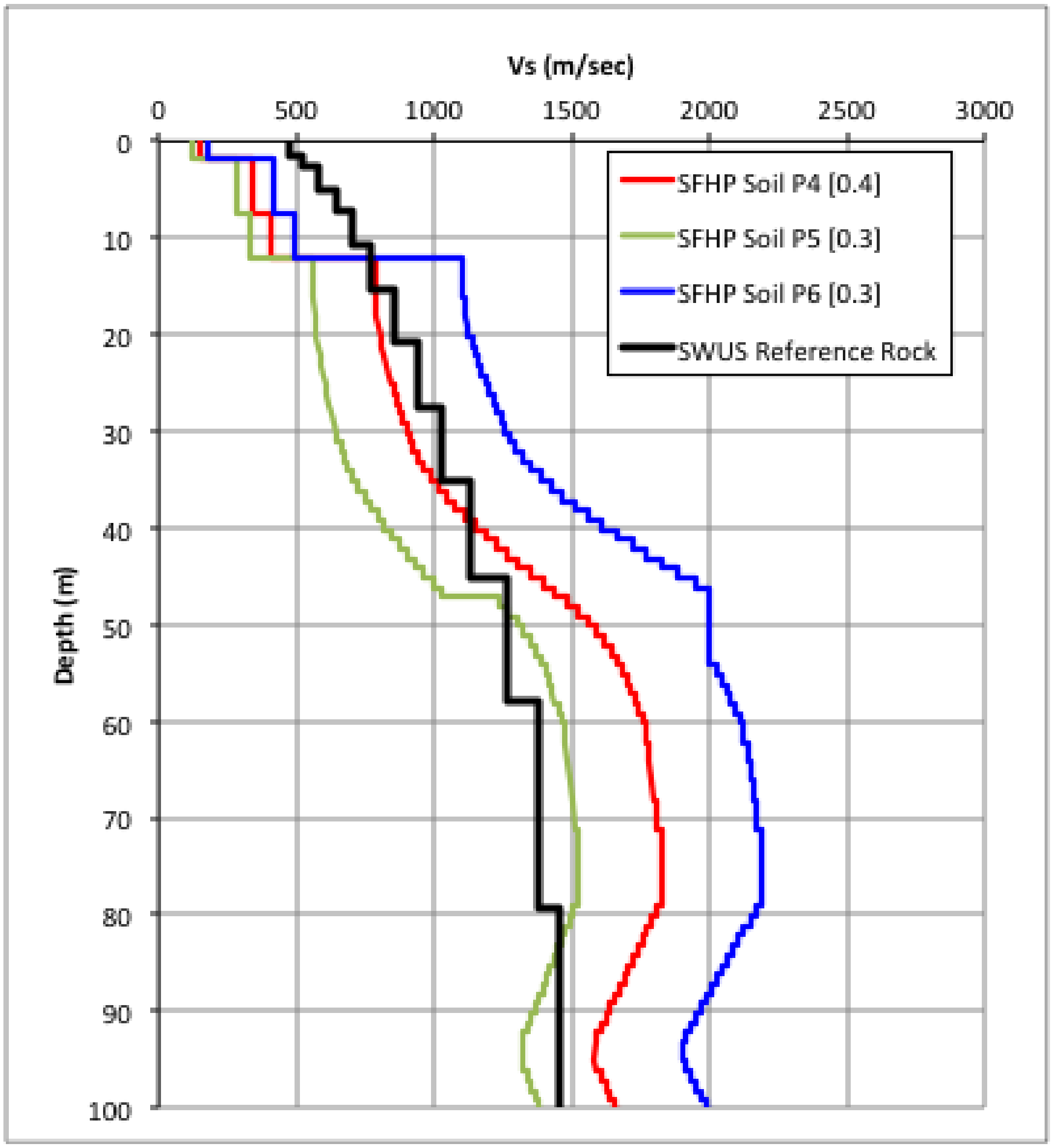

Figure 9-46. Comparison of SWUS reference rock V_S profile with SFHP profiles for 40 ft of soil.

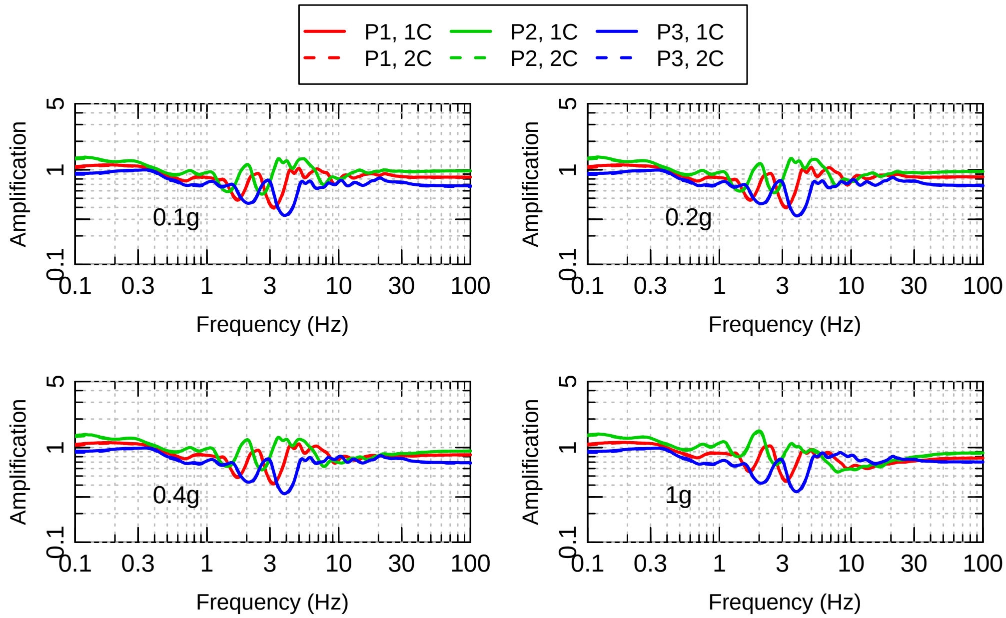

Figure 9-47. Effect of V_S profile on SFHP transfer function (kappa = 0.037s, soil depth 20 ft, soil material set M1).

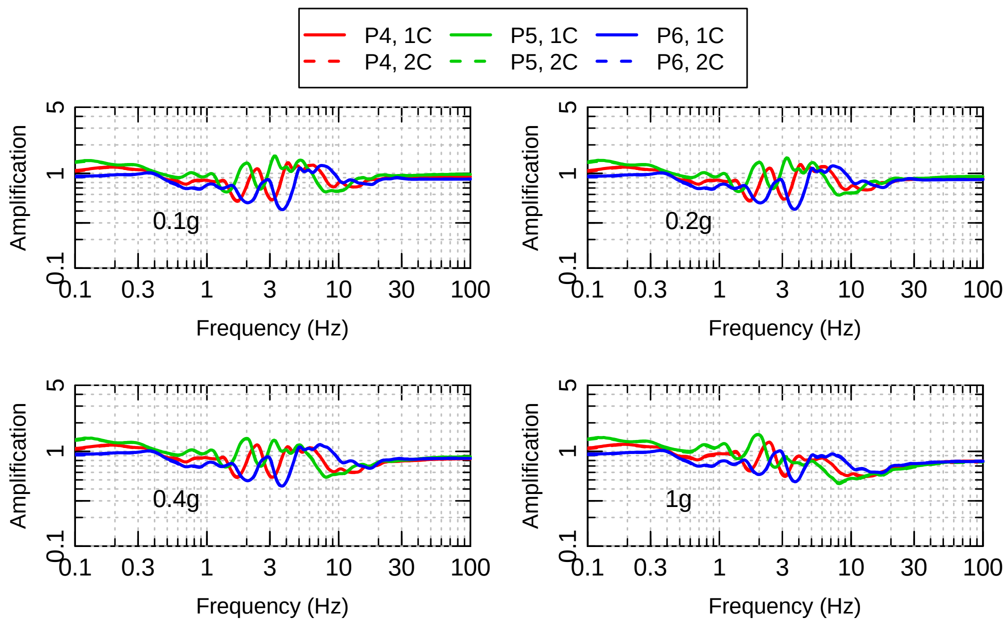

Figure 9-48. Effect of V_S profile on SFHP transfer function (kappa = 0.037s, soil depth 40 ft, soil material set M1).

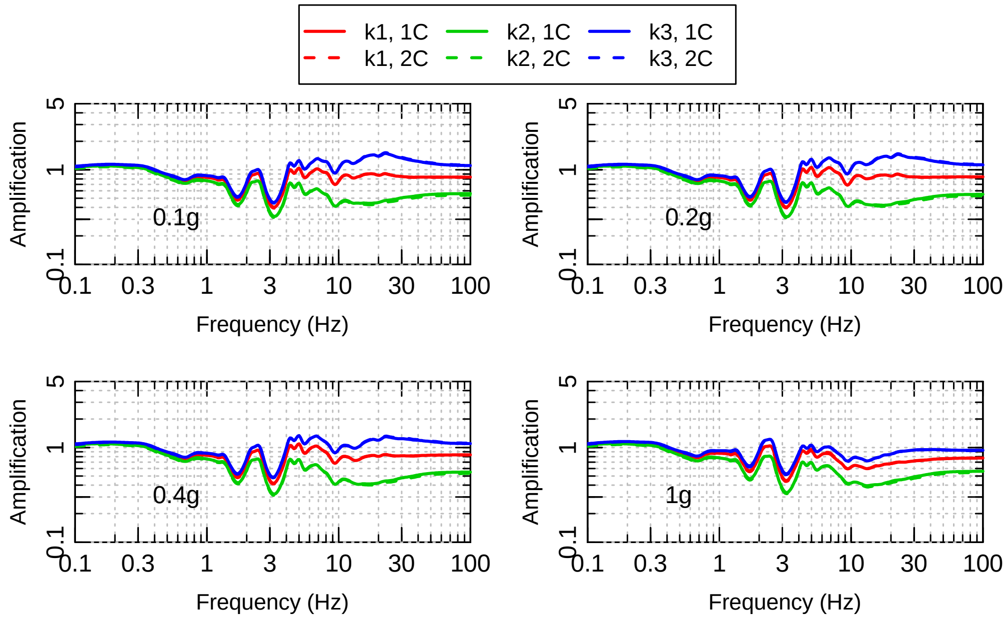

Figure 9-49. Effect of kappa on SFHP transfer function (V_S profile P1, soil depth 20 ft, soil material set M1).

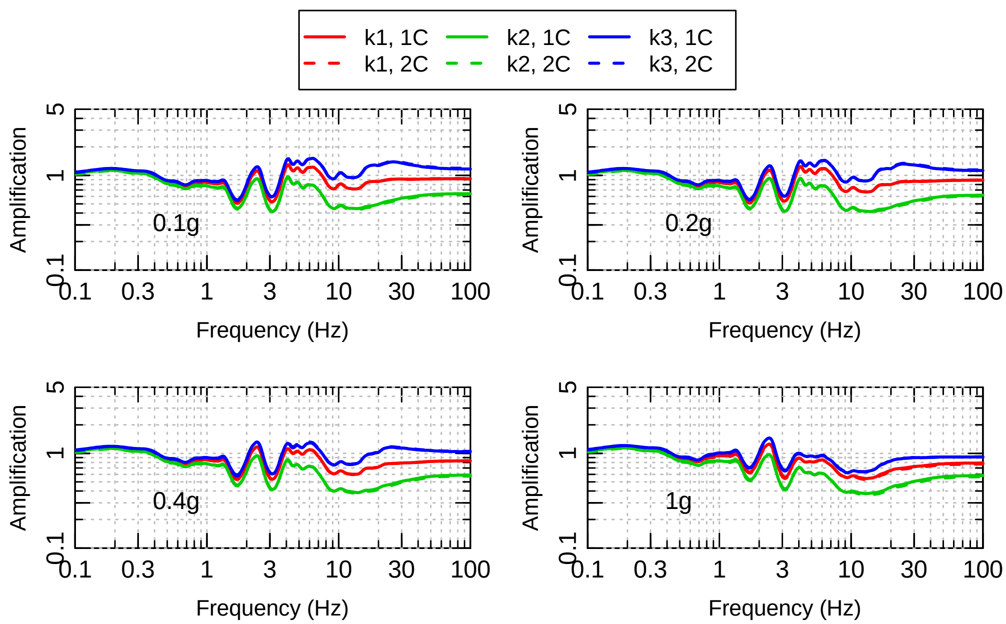

Figure 9-50. Effect of kappa on SFHP transfer function (V_S profile P4, soil depth 40 ft, soil material set M1).

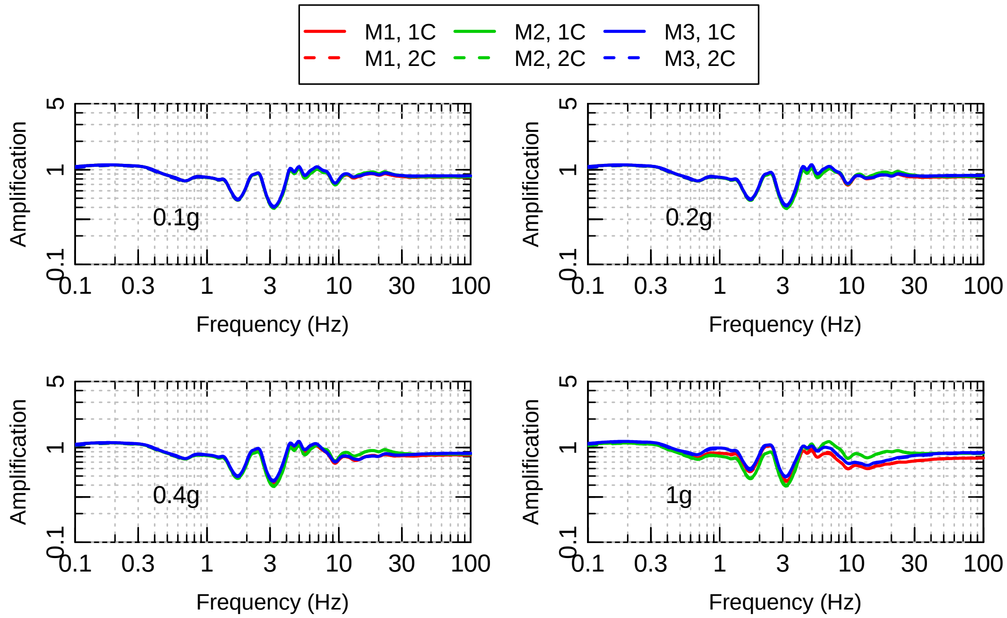

Figure 9-51. Effect of G/Gmax and damping curves on SFHP transfer function (kappa = 0.037s, V_S profile P1, soil depth 20 ft).

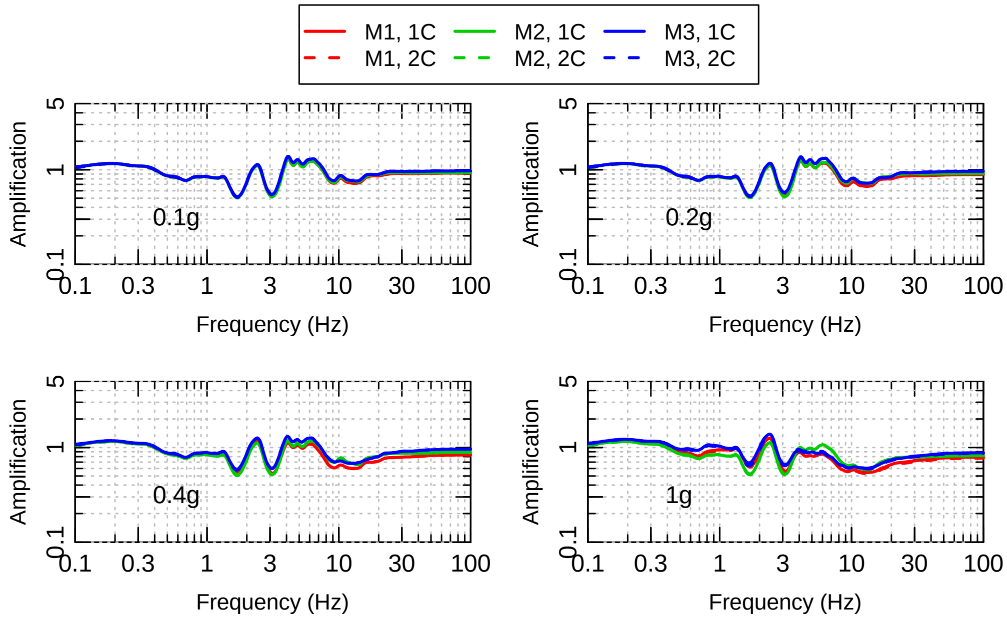

Figure 9-52. Effect of G/Gmax and damping curves on SFHP transfer function (kappa = 0.037s, V_S profile P4, soil depth 40 ft).

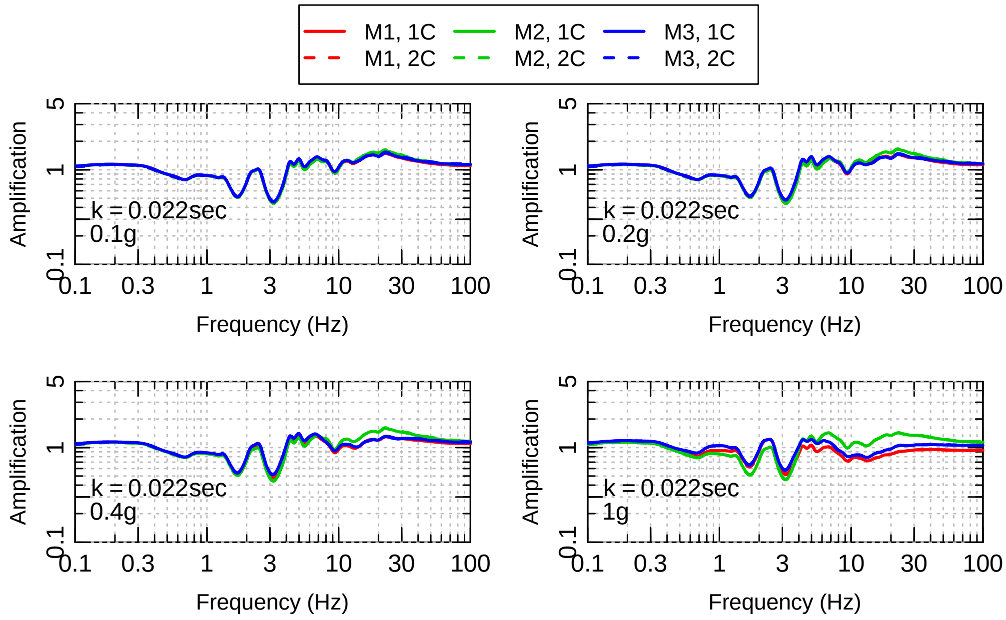

Figure 9-53. Effect of G/Gmax and damping curves on SFHP transfer function (kappa = 0.022s, V_S profile P1, soil depth 20 ft).

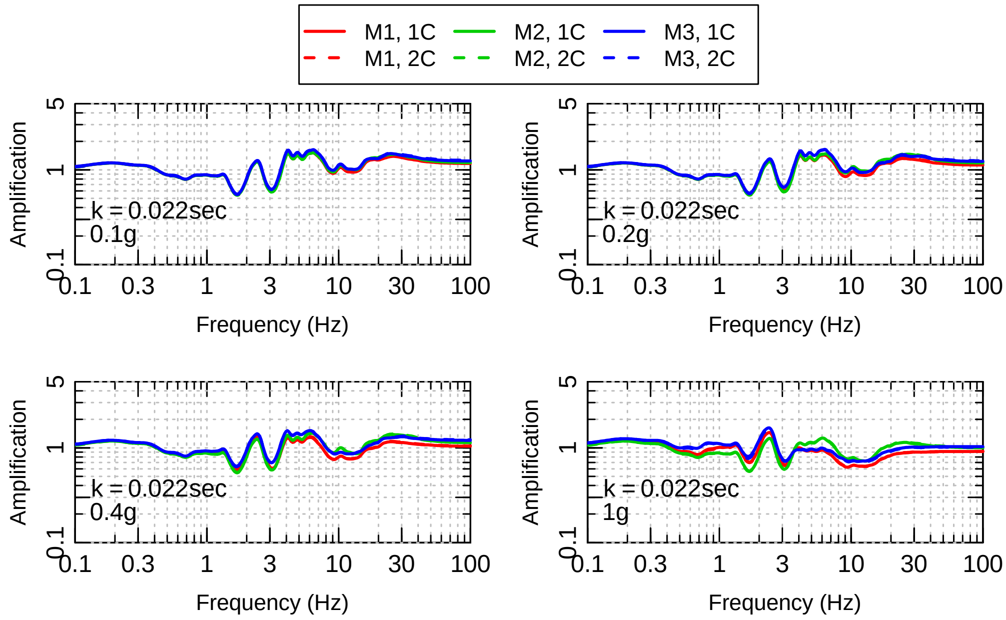

Figure 9-54. Effect of G/Gmax and damping curves on SFHP transfer function (kappa = 0.022s, V_S profile P4, soil depth 40 ft).

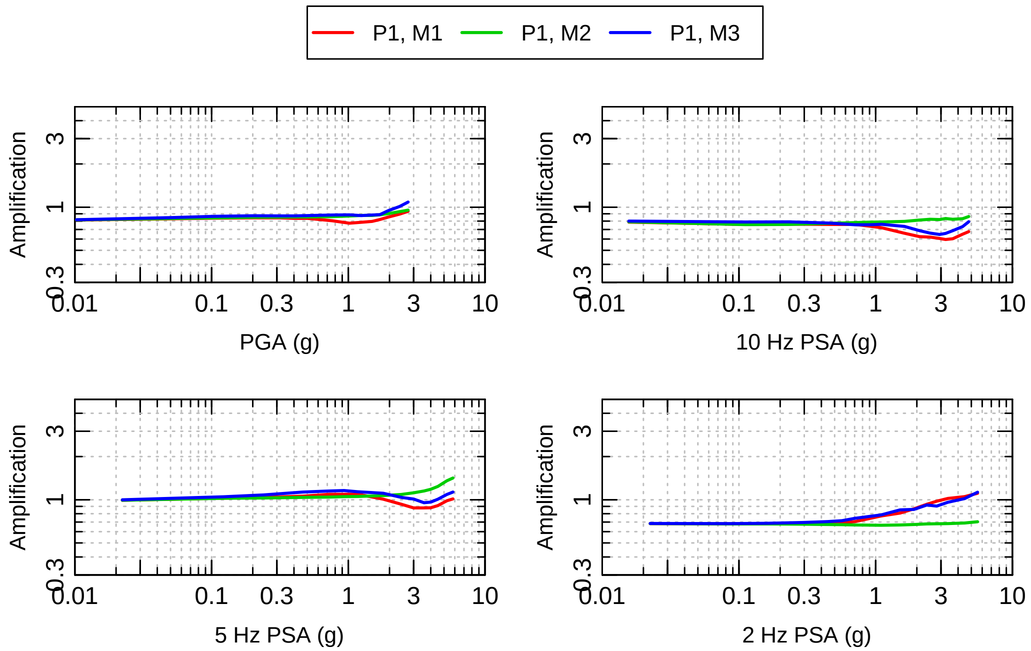

Figure 9-55. Effect of amplitude of input ground motions on SFHP transfer function (kappa = 0.037s, Vs Profile P1, soil depth 20 ft).

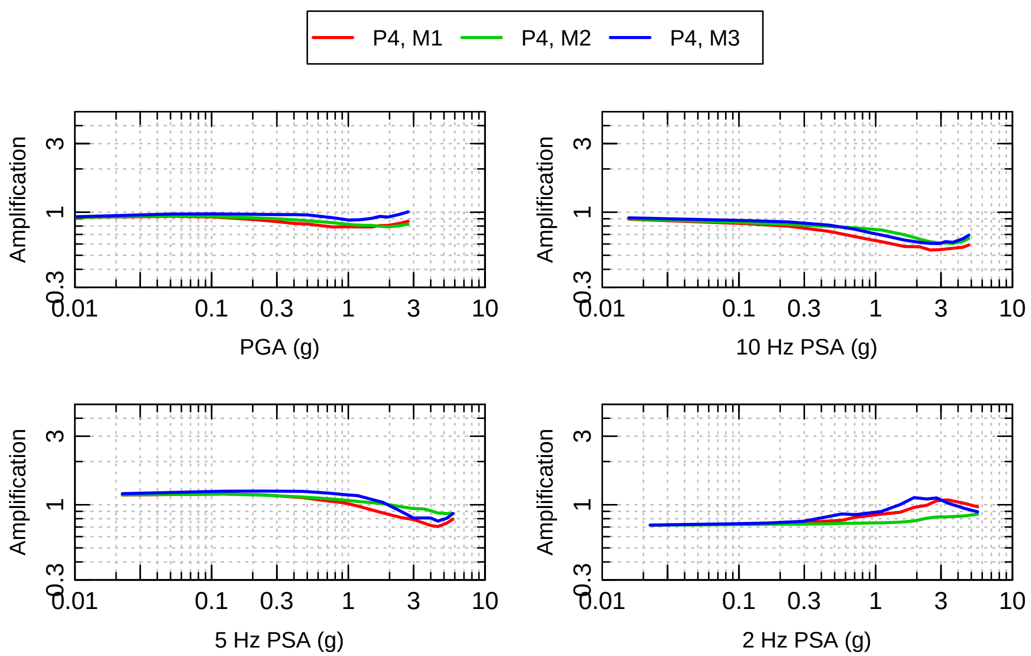

Figure 9-56. Effect of amplitude of input ground motions on SFHP transfer function (kappa = 0.037s, Vs Profile P4, soil depth 40 ft).

9.5.3 Transfer Functions for Cascadia Interface Earthquakes

The reference profile for the modified BC Hydro GMM for a V_{S30} of 760 m/s has gross characteristics similar to that of the SWUS GMM. Furthermore, the V_S adjustment factors developed by PNNL (2014) for shallow crustal earthquakes and subduction zone earthquakes are very similar for ground motion frequencies of 1 Hz or less, the frequency range where the Cascadia interface source contributes to the hazard at the SFHP site. Therefore, the transfer functions developed for shallow crustal earthquake ground motions were applied to the subduction zone earthquake ground motions.

9.5.4 Epistemic Uncertainty in Transfer Functions

Figures 9-57 and 9-58 show the logic trees for the epistemic uncertainty in the inputs to the transfer function calculations for the SFHP site. Note that the alternative soil material curve sets apply only to the soil sites. The alternative transfer functions obtained for each end branch define the epistemic uncertainty in adjusting from the reference rock profile to the site profiles for the SFHP. Two cases are analyzed for the soil sites, one using the generic material curve sets M1 and M2 defined in EPRI (2013), Figure 9-57; and one using the site-specific set M3 developed by NWRC-RA (2015), Figure 9-58. In addition, a sensitivity analysis is performed for the SFHP Rock case using an alternative set of weights on kappa. The range of kappa values developed for the NRF site in Section 7.5.1 is broad and the upper range value of 0.062s is rather higher than would be expected for a rock site. As discussed in Section 7.5.1, the available data for NRF are not sufficient to support a narrower range for kappa. However, a sensitivity analysis was performed using an alternative weighting scheme that favors lower values of kappa typically expected for rock sites. The alternative weighting on kappa tested was 0.022s [0.45], 0.037s [0.5], 0.062s [0.05].

Following the approach described for the MFC and FMF sites in Section 9.3.4, the epistemic standard deviation in the transfer functions was computed as a function of frequency. The modeling uncertainty shown on the bottom panel of Figure 9-32 was incorporated by summing variances. The results are shown on Figure 9-59 for the SFHP Rock site; on Figure 9-60 for the SFHP Rock site with the alternative kappa weighting; on Figures 9-61 and 9-62 for the SFHP soil site and the generic material curves for soil depths of 20 ft and 40 ft, respectively; and on Figures 9-63 and 9-64 for the SFHP soil site and the site-specific material curves for soil depths of 20 ft and 40 ft, respectively. The logic tree plus modeling epistemic uncertainty is shown for two levels of reference rock motions corresponding to return periods of 2,500 yrs. and 10,000 yrs. The resulting values are largest for frequencies above 10 Hz, the frequency range where the uncertainty in site kappa has the greatest effect on the transfer functions.

As discussed above in Section 9.3.4 for the MFC and FMF sites, the concept of a minimum level of epistemic uncertainty (PNNL, 2014) was used to compute the hazard for the SFHP sites. As was done for the MFC and FMF sites, two alternative approaches were used to define the minimum epistemic uncertainty to use in computing the site-specific hazard. The first, Option A, is to use the modeling uncertainty from Figure 9-32. The second, Option B, is to use the ϕ_{S2S} values for the California data for $\mathbf{M}> 5$ shown on Figures 9-59 through 9-64, after removing the variance in the computed transfer functions defined by the logic trees shown on Figures 9-57 or 9-58. A weighted combination is used to develop the final mean hazard. Option A is favored slightly (weight 0.6) over Option B (weight 0.4) because the transfer calculations make use of the full crustal profile. This combination produces an effective weighted minimum epistemic uncertainty that is approximately the same as the borehole ϕ_{S2S} reported by Rodriguez-Marek et al. (2011). The final transfer functions are tabulated in the GMM HID (Appendix G).

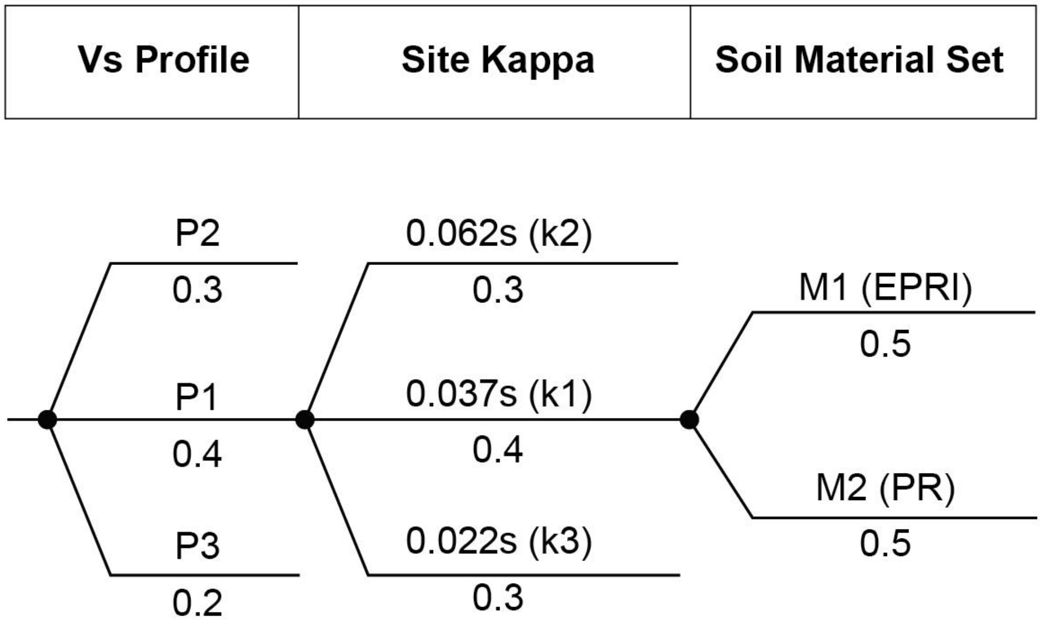

Figure 9-57. Logic trees for characterizing epistemic uncertainties in inputs to transfer function calculations for SFHP Rock (V_S and kappa only) and Soil using (V_S, kappa, and Soil Material Set) for the case using generic material property curves.

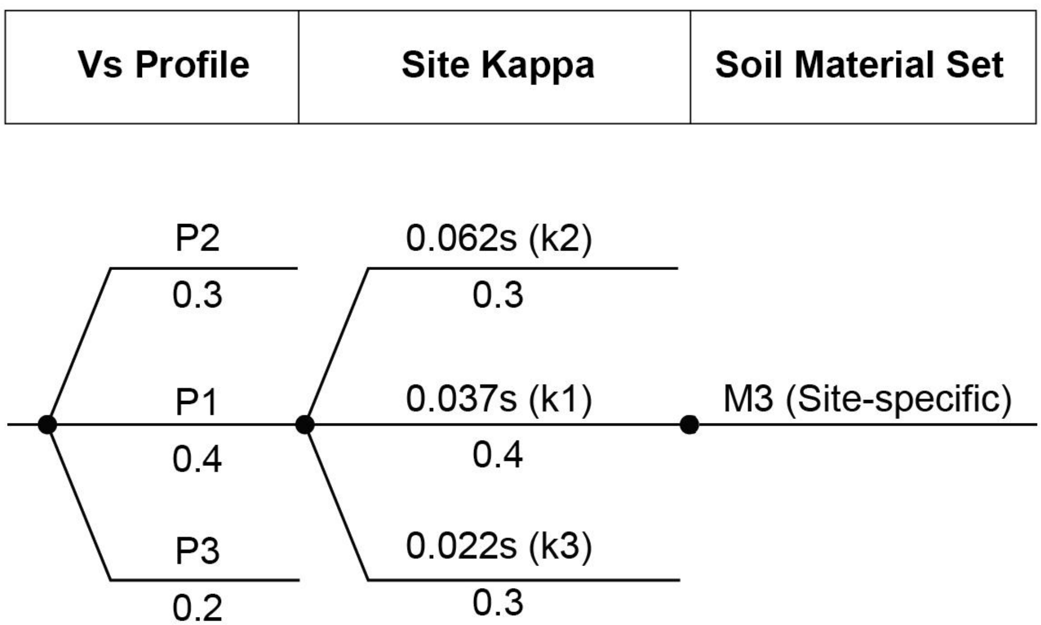

Figure 9-58. Logic trees for characterizing epistemic uncertainties in inputs to transfer function calculations for SFHP Rock (V_S and kappa only) and Soil using (V_S, kappa, and Soil Material Set) for the case using site-specific property curves.

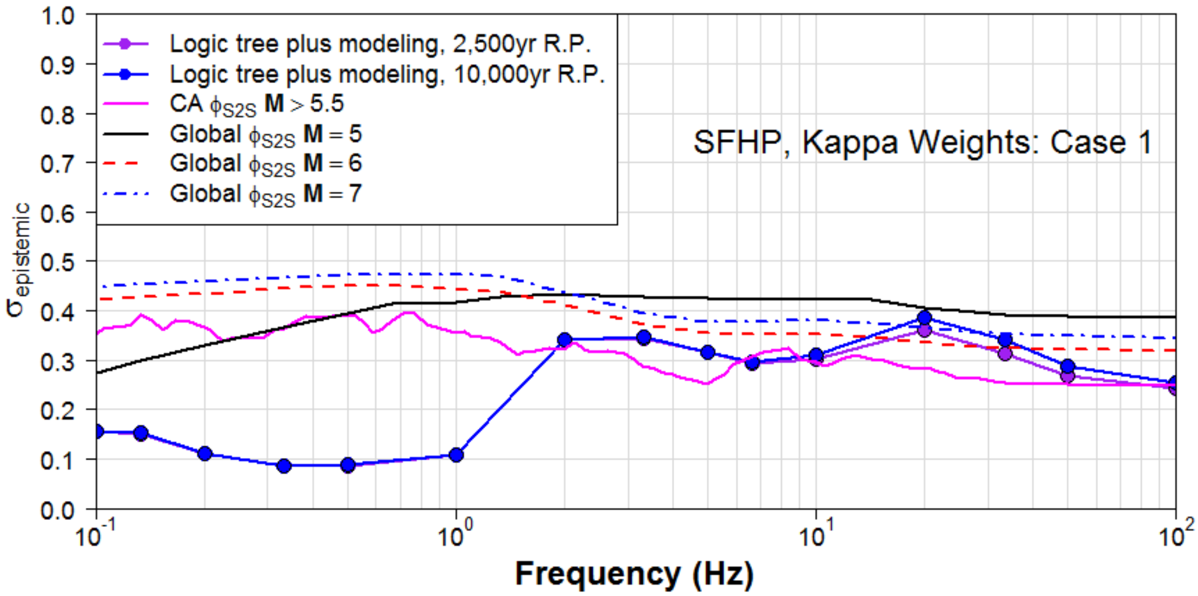

Figure 9-59. Epistemic uncertainty in the transfer function for SFHP Rock using the assigned weights on kappa.

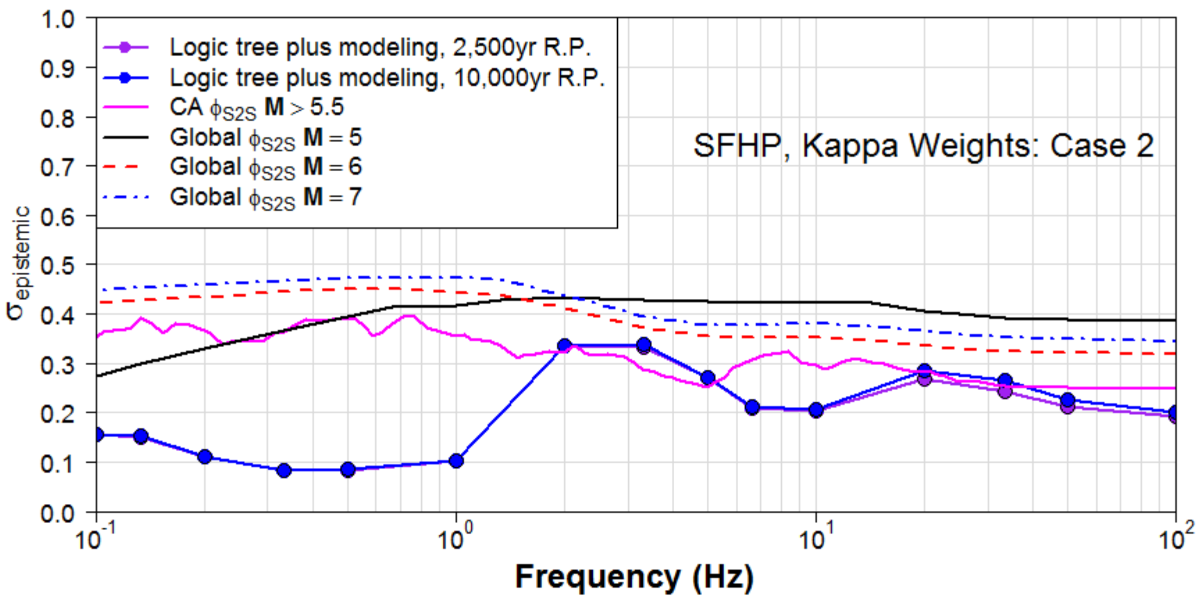

Figure 9-60. Epistemic uncertainty in the transfer function for SFHP Rock using the sensitivity weights on kappa.

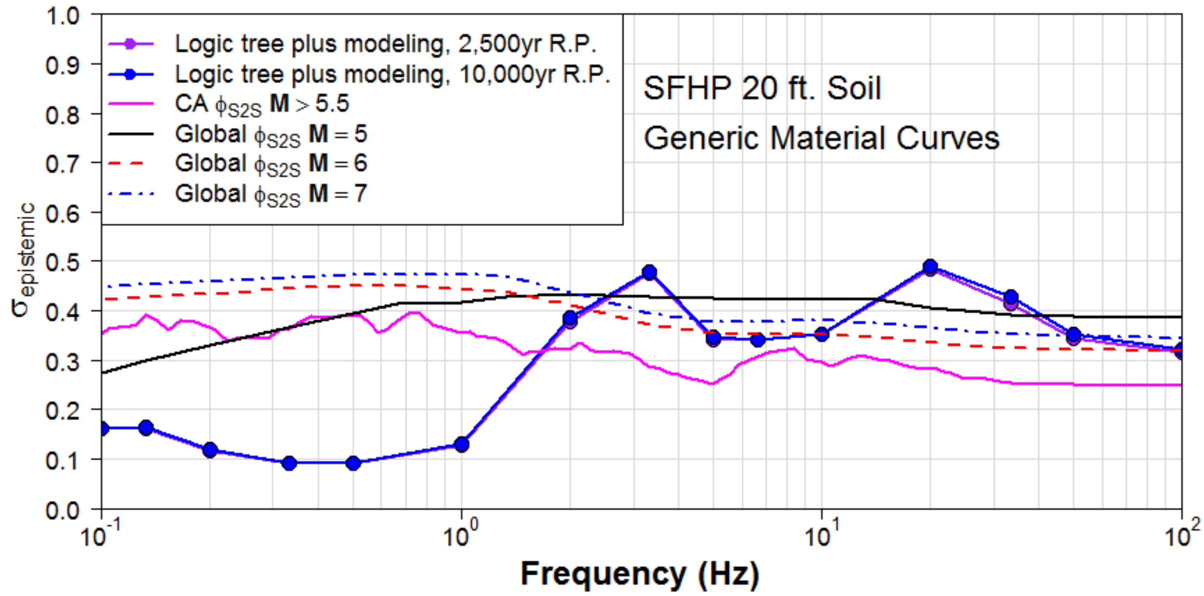

Figure 9-61. Epistemic uncertainty in the transfer function for SFHP Soil (20 ft of soil) using generic material curves.

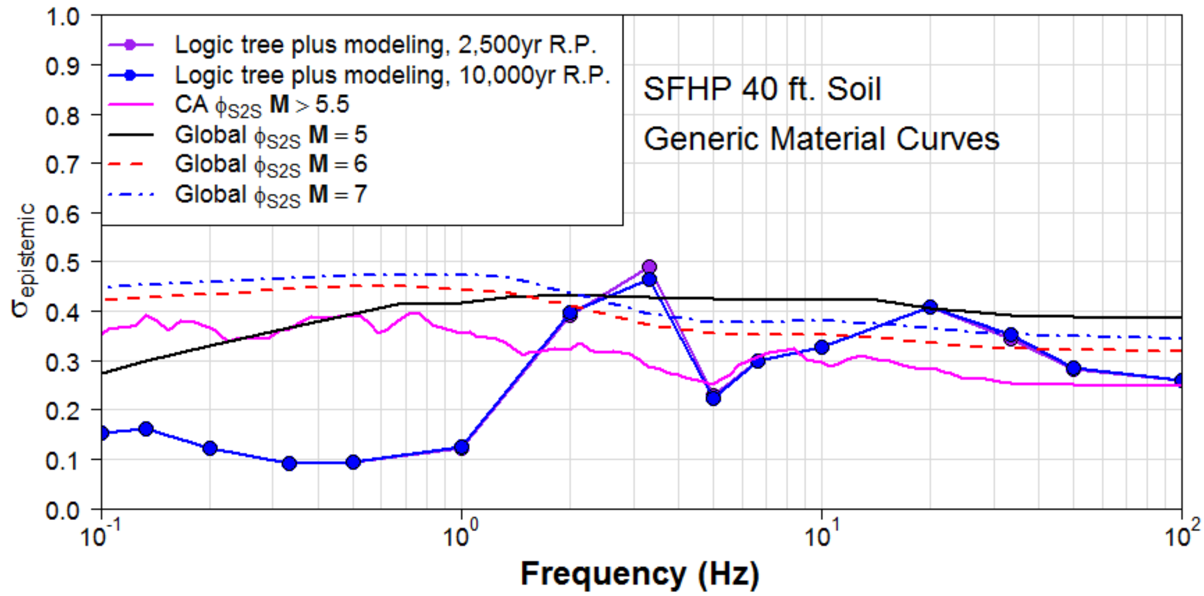

Figure 9-62. Epistemic uncertainty in the transfer function for SFHP Soil (40 ft of soil) using generic material curves.

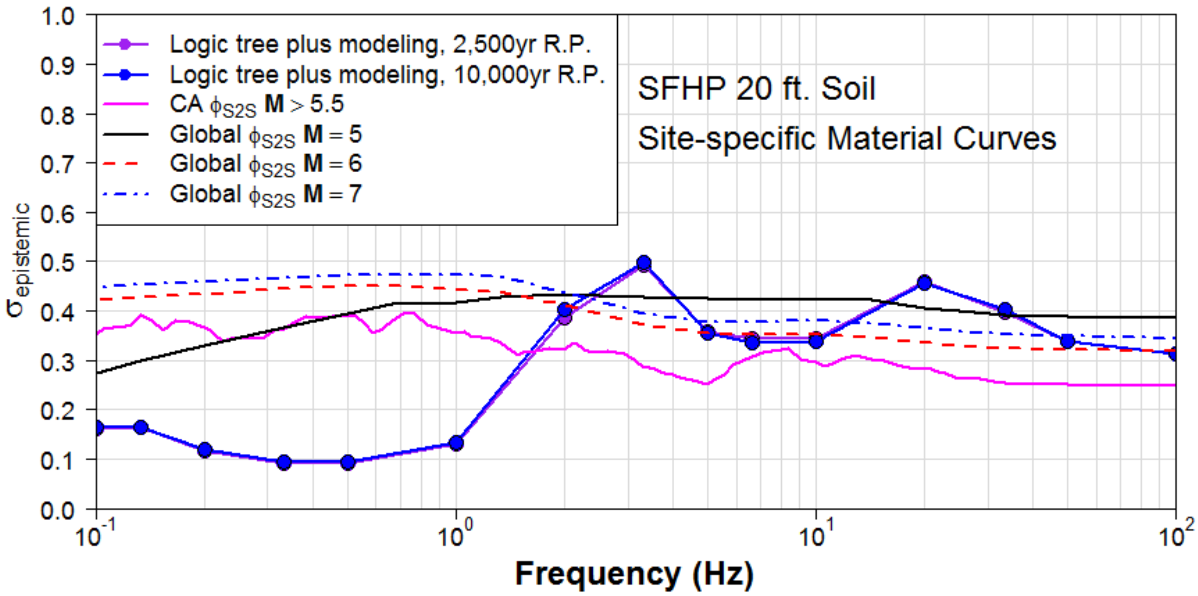

Figure 9-63. Epistemic uncertainty in the transfer function for SFHP Soil (20 ft of soil) using site-specific material curves.

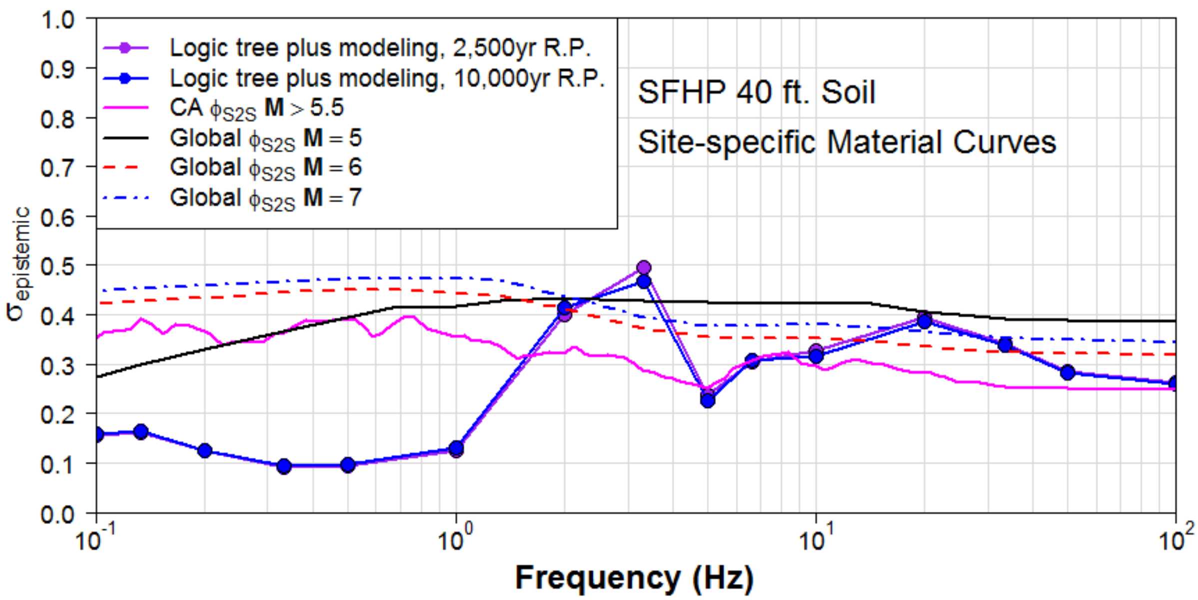

Figure 9-64. Epistemic uncertainty in the transfer function for SFHP Soil (40 ft of soil) using site-specific material curves.

9.6 Relationships for Vertical Motions for SFHP

The approach used in Section 9.4 for the MFC and FMF sites was used to develop V/H ratios for the SFHP Rock and Soil sites. The reference rock hazard results for the SFHP site presented in Section 10.5 indicate that the mean magnitude and distance for earthquakes contributing to the hazard at return periods near 2,500 years range from approximately **M** 6.2 and R_{RUP} of 24 km for ground motion frequencies ≥ 5 Hz to approximately **M** 6.9 and R_{RUP} of 55 km for ground motion frequencies of 1 Hz and less. For a return period near 10,000 years, the mean magnitudes and distances change slightly to **M** 6.4 and R_{RUP} of 20 km for ground motion frequencies ≥ 5 Hz and approximately **M** 7.0 and R_{RUP} of 40 km for ground motion frequencies of 1 Hz and less. The V_{S30} for the SFHP Rock site is 898 m/s and the V_{S30} for the SFHP soil site is 569 m/s for a soil depth of 20 ft and 484 m/s for a soil depth of 40 ft. Figures 9-65 and 9-66 show the V/H ratios for the SFHP site for rock conditions using the controlling earthquakes corresponding to return periods of 2,500 and 10,000 years, respectively. Figures 9-67 and 9-68 show the V/H ratios for 20 ft of soil at the two return periods, and Figures 9-69 and 9-70 show the V/H ratios for 40 ft of soil. The plotted V/H ratios are Gülerce and Abrahamson (2011) – GK11, Stewart et al. (2015) over Boore et al. (2014) – SBSA15/BSSA14, Bozorgnia and Campbell (2015) over Campbell and Bozorgnia (2014) – BC15/CB14, and Bommer et al. (2011) – BSK11. Normal faulting V/H ratios are computed for all relationships. The average of the four V/H ratios is also shown on each figure.

Figure 9-71 shows the average high frequency and low frequency V/H ratios for the SFHP Rock and Soil site conditions. The results for the two return periods are very similar, with a slightly higher peak in the V/H ratios for the 10,000-year return period. The V/H ratios for the two soil depths are also similar. On each plot, enveloping V/H ratios are shown for use in developing vertical spectra for the two site conditions. The recommended V/H ratios are listed in Table 9-5.

Table 9-5. Recommended V/H ratios for SFHP Site for return periods of 2,500 to 10,000 yrs.

Ground Motion Frequency (Hz)	Vertical to Horizontal (V/H) Ratio	
	SFHP Rock	SFHP Soil
PGA (100)	0.650	0.650
50	0.650	0.650
33.3	0.700	0.700
20	0.750	0.800
13.3	0.720	0.770
10	0.700	0.710
6.67	0.642	0.617
5	0.600	0.550
4	0.600	0.550
3.33	0.600	0.550
2.5	0.600	0.550
2	0.624	0.550
1.33	0.669	0.579
1	0.700	0.600
0.667	0.758	0.641
0.5	0.800	0.670
0.333	0.829	0.717
0.25	0.850	0.750
0.2	0.850	0.750
0.133	0.850	0.750
0.1	0.850	0.750

(a)

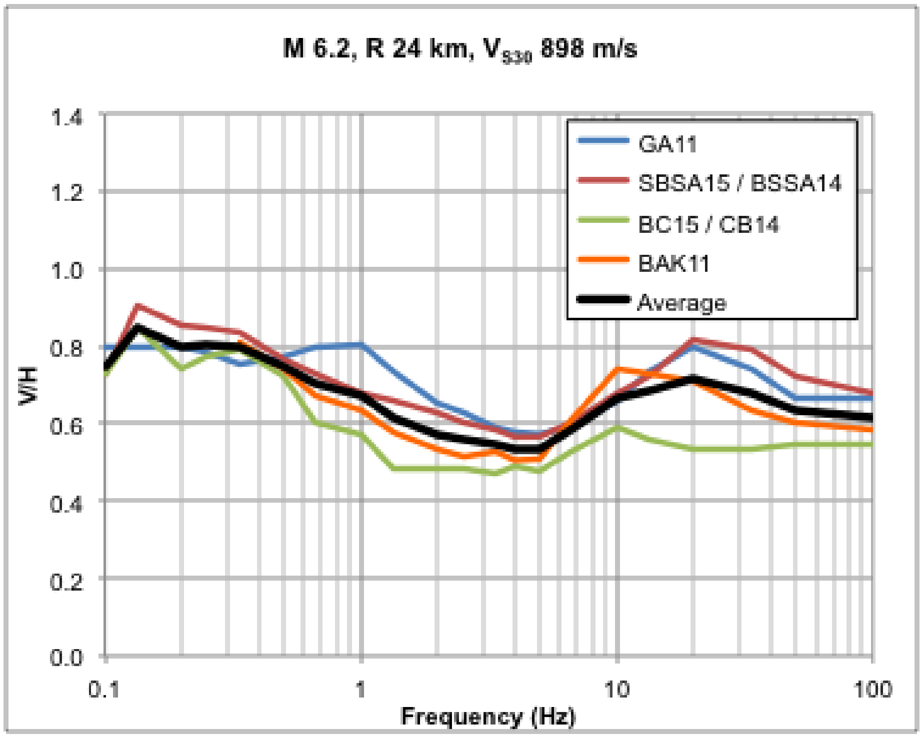

(b)

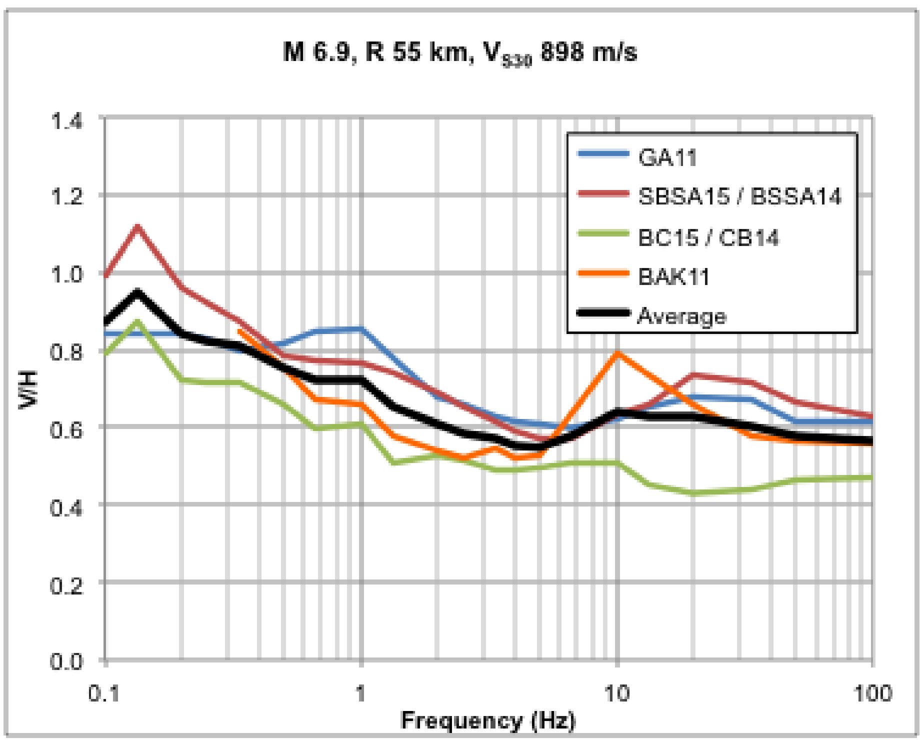

Figure 9-65. V/H ratios for SFHP Rock for 2,500-year Return Period: a) high frequency controlling earthquake; and b) low frequency controlling earthquake.

(a)

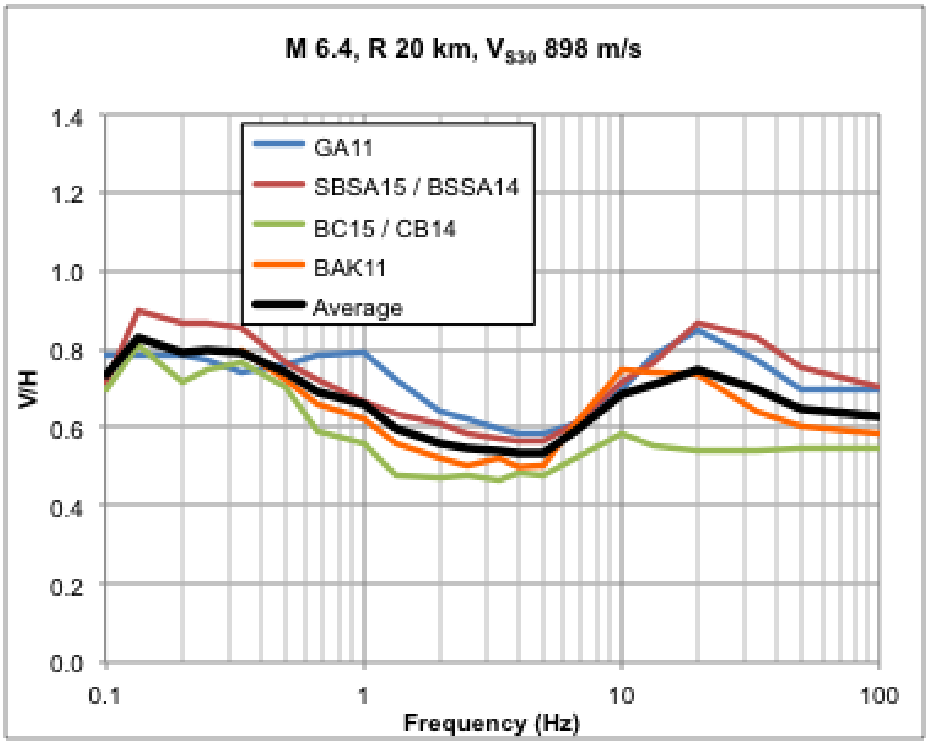

(b)

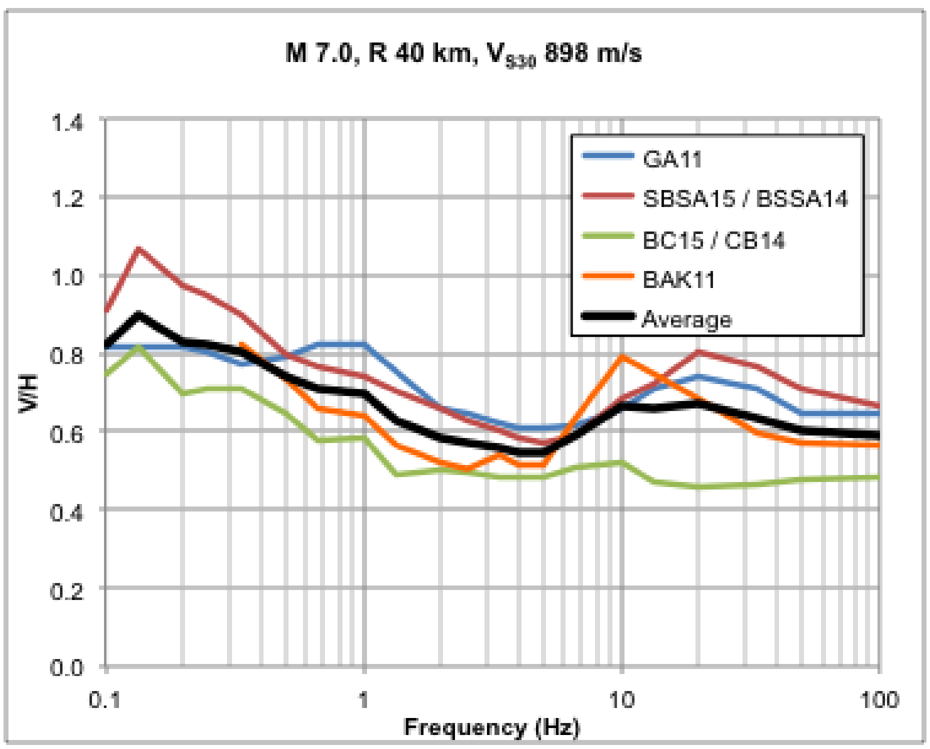

Figure 9-66. V/H ratios for SFHP Rock for 10,000-year Return Period: a) high frequency controlling earthquake; and b) low frequency controlling earthquake.

(a)

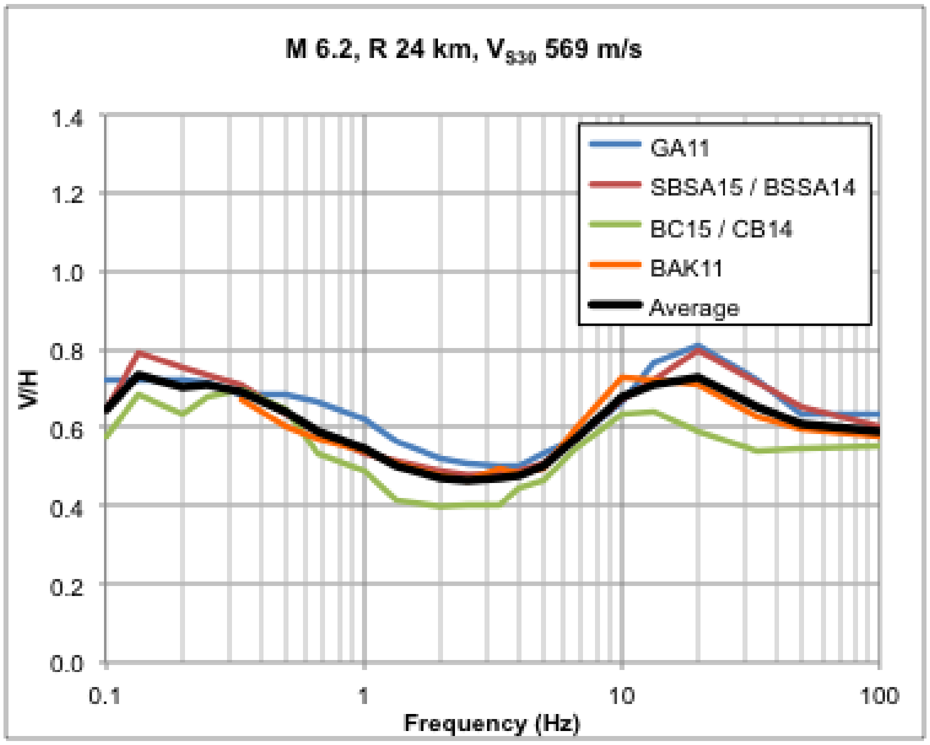

(b)

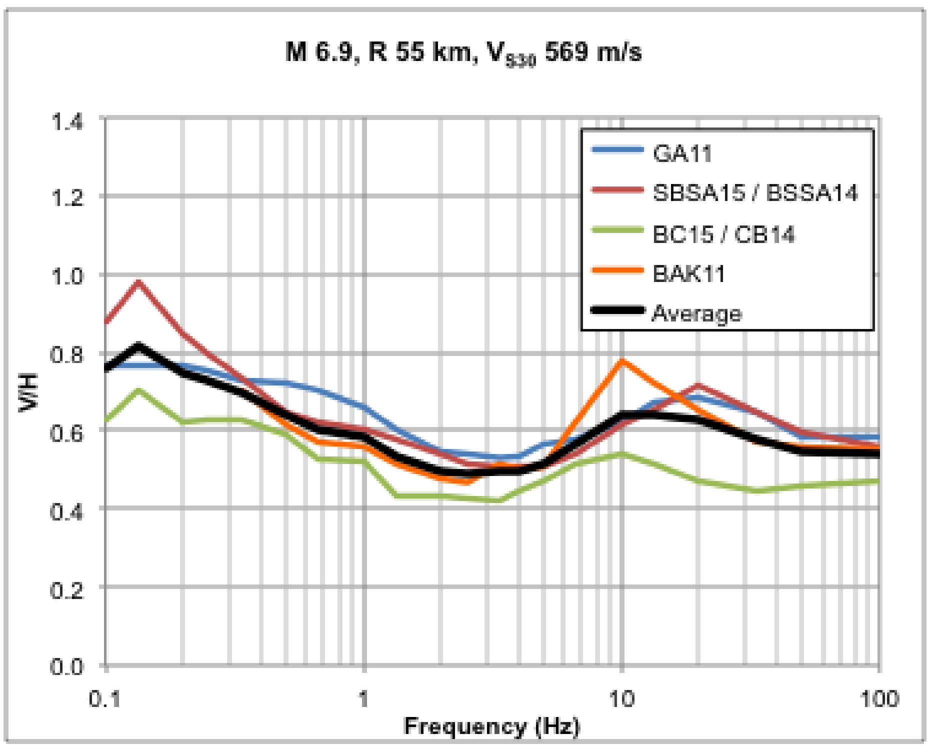

Figure 9-67. V/H ratios for SFHP 20 ft of Soil for 2,500-year Return Period: a) high frequency controlling earthquake; and b) low frequency controlling earthquake.

(a)

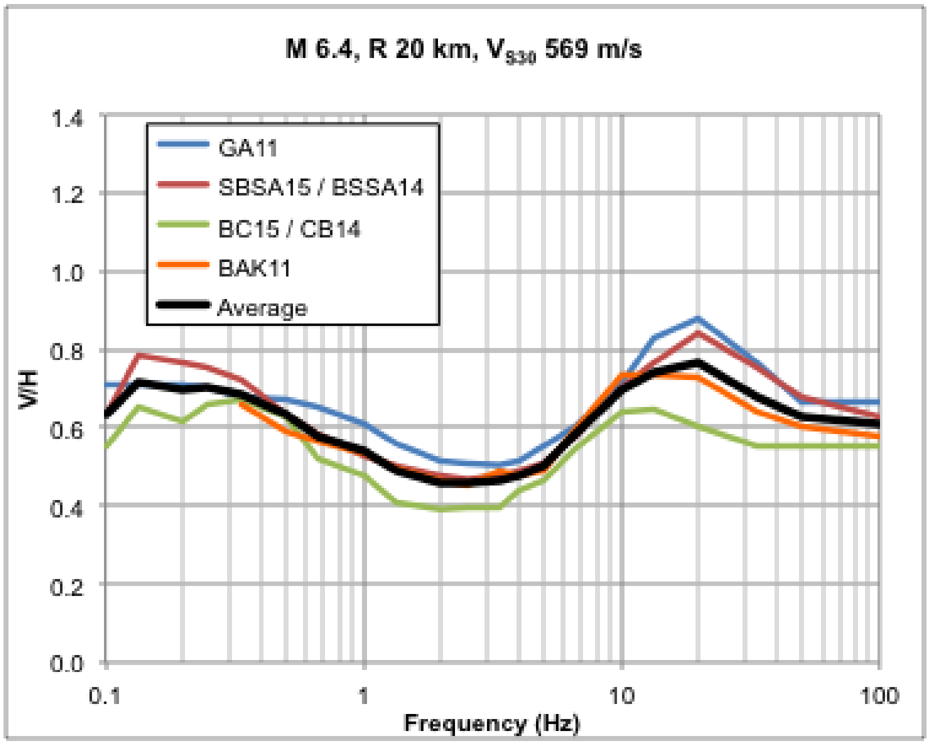

(b)

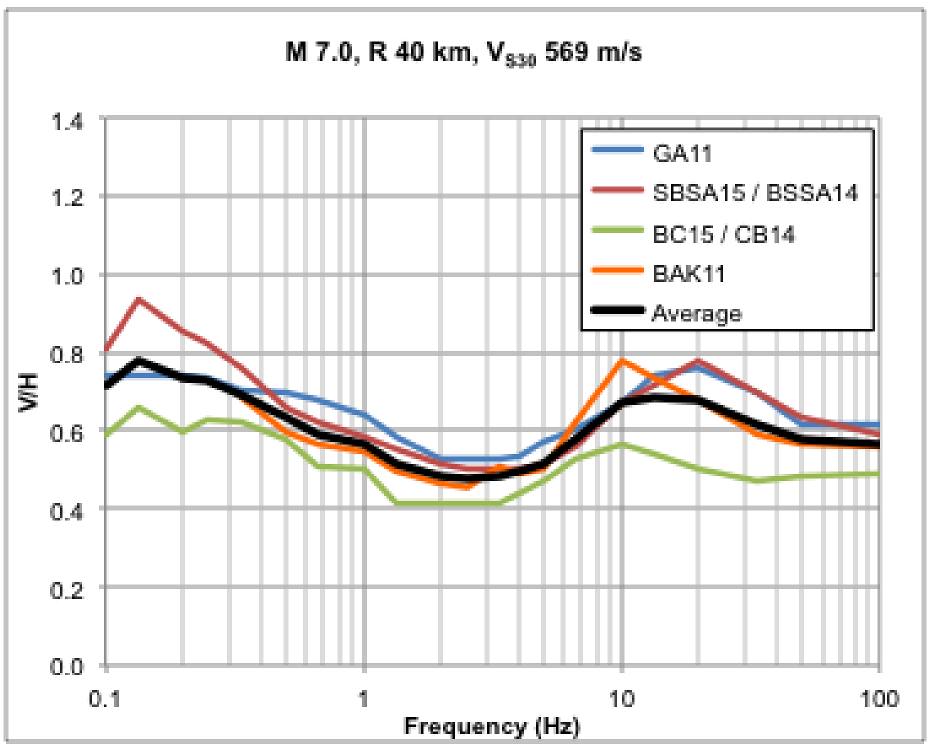

Figure 9-68. V/H ratios for SFHP 20 ft of Soil for 10,000-year Return Period: a) high frequency controlling earthquake; and b) low frequency controlling earthquake.

(a)

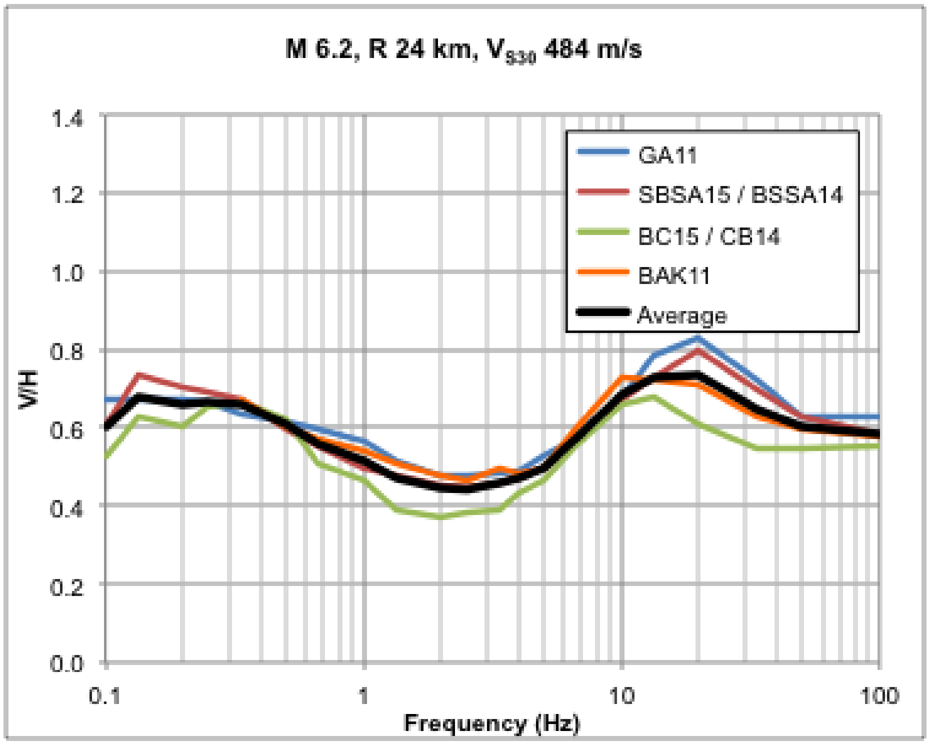

(b)

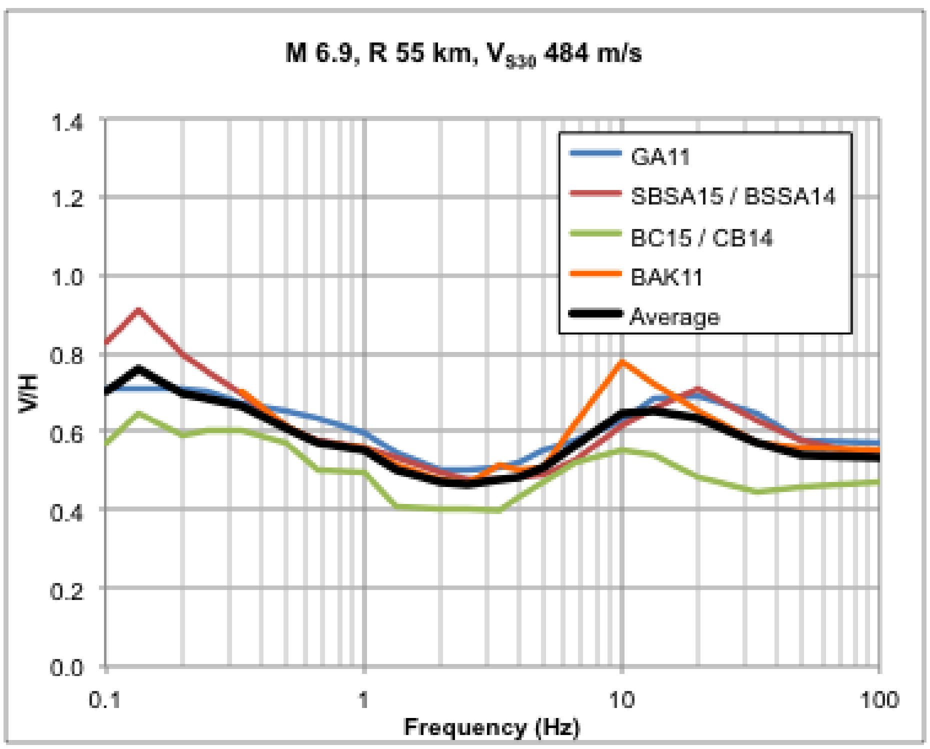

Figure 9-69. V/H ratios for SFHP 40 ft of Soil for 2,500-year Return Period: a) high frequency controlling earthquake; and b) low frequency controlling earthquake.

(a)

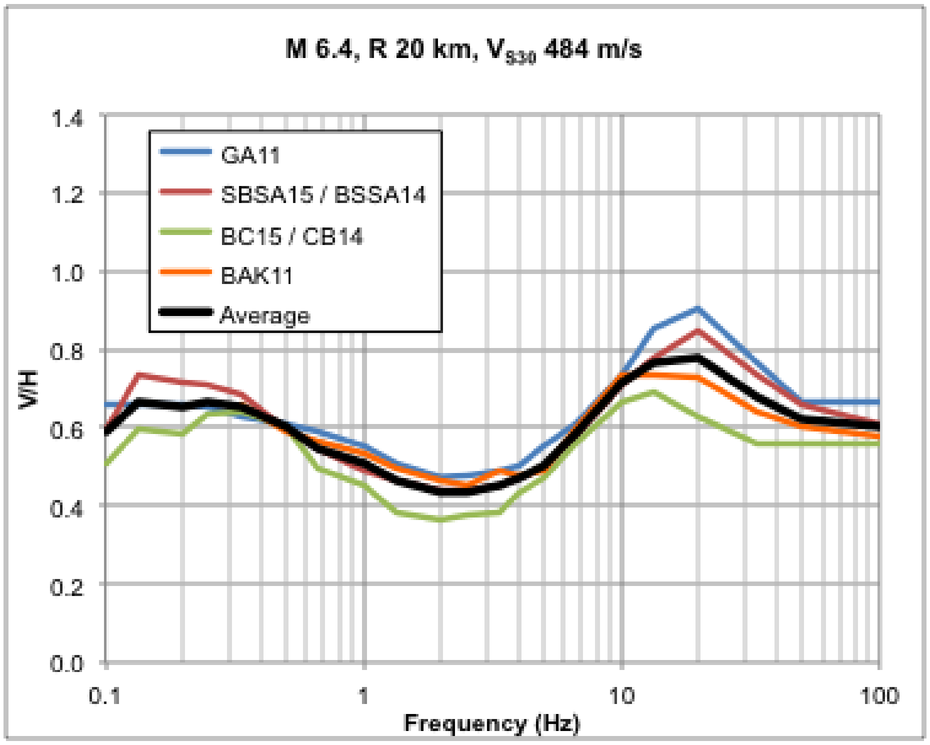

(b)

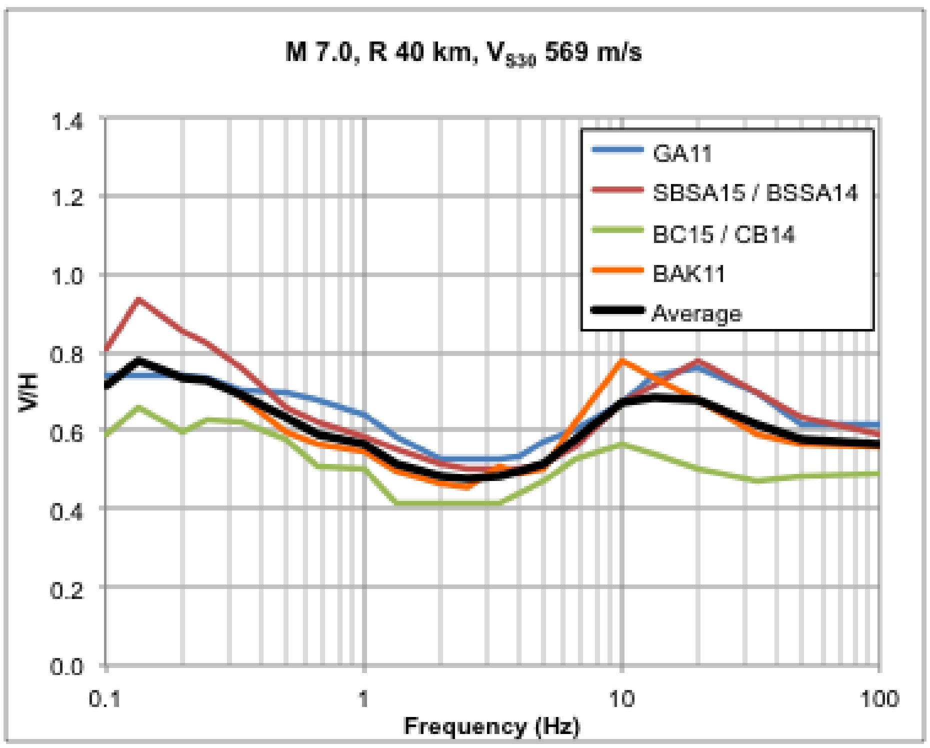

Figure 9-70. V/H ratios for SFHP 40 ft of Soil for 10,000-year Return Period: a) high frequency controlling earthquake; and b) low frequency controlling earthquake.

(a)

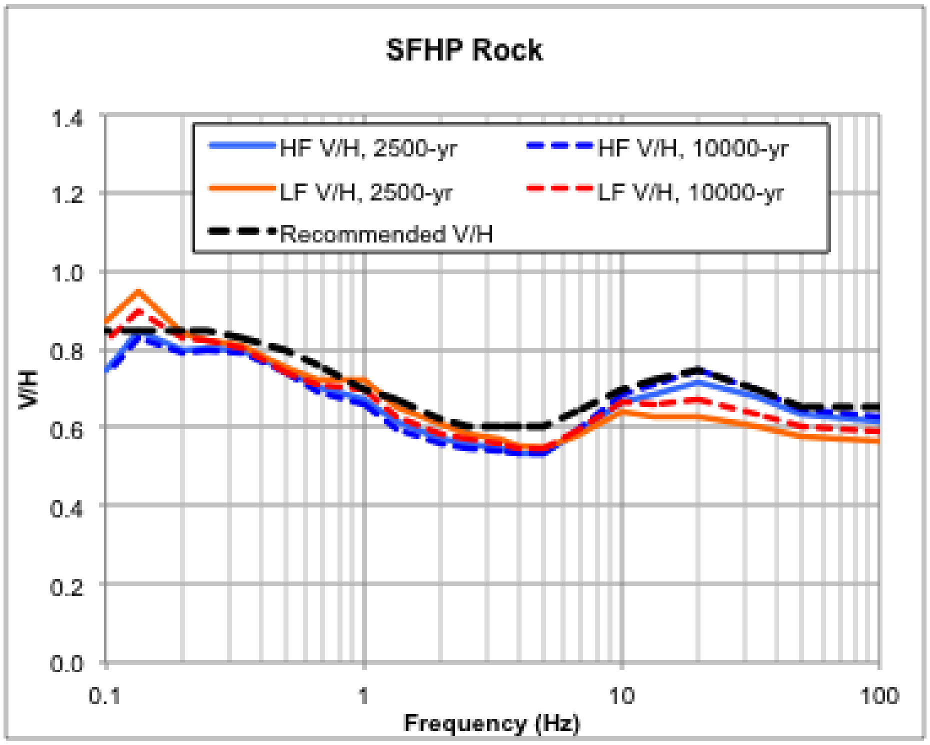

(b)

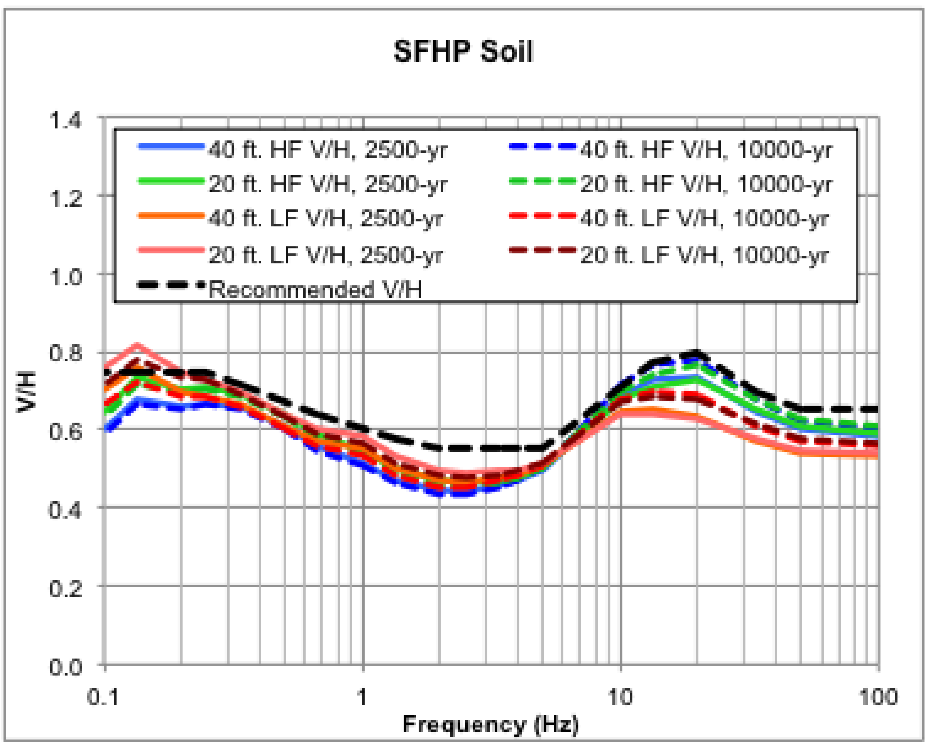

Figure 9-71. Recommended V/H ratios for: a) SFHP Rock; and b) SPHP Soil.

9.7 Development of Transfer Functions for the ATR Complex

This section presents the transfer functions for rock and soil sites at the ATR Complex. The methodology described in Section 9.3 was used to develop transfer functions from the SWUS reference rock profile to the ATR rock and soil profiles.

9.7.1 Transfer Functions for ATR Rock

The epistemic uncertainty in the dynamic properties of the ATR Rock site is characterized by six alternative velocity profiles, P1 (median), P2 (lower-range), and P3 (upper-range) with a shallow interbed at ~40 m, and P4 (median), P5 (lower-range), and P6 (upper-range) without a shallow interbed at ~40 m (Section 7.6), and three alternative values of kappa, k1 – 0.021s, k2 – 0.035s, and k3 – 0.013s (Section 7.7). Figure 9-72 compares the six velocity profiles to the reference V_S profile for the SWUS GMM. Figure 9-73 shows the upper two kilometers of these velocity profiles and Figure 9-74 shows the upper 200 m. The V_S values for the SWUS and ATR Rock profiles become similar below a depth of 5 km. The ATR Rock Vs profiles quickly rise to V_S values of approximately 2 km/s and greater compared to the more gradual velocity increase for the SWUS reference profile. The ATR Rock profiles also contain a number of low velocity zones representing the soil interbeds.

The SWUS to ATR Rock transfer function calculations utilized randomized velocity profiles in the same manner as the computations for MFC. The same correlation model was used for both sites. The correlation model has a depth dependent $\sigma \ln Vs$ of 0.33 over the top 15 m and 0.15 below (Toro, as appears in Silva et al., 1996).

Figure 9-75 shows the transfer functions developed for the six ATR Rock velocity profiles for four levels of input motion. The designation “1C” and “2C” refer to the two different earthquake source spectral shapes used to define the input motions. The six ATR Rock velocity profiles produce differences in the transfer functions in terms of the locations of peaks and troughs in the frequency range of 1 to 6 Hz and in the level of the transfer function at higher frequencies, especially near 10 Hz. Effect of epistemic uncertainty on the median velocity profile for ATR Rock is greater than that obtained for the MFC site. As was the case for the MFC site, there is very little difference in the transfer functions computed using the one-corner and two-corner earthquake source spectra.

Figure 9-76 shows the effect of the alternative values for kappa on the transfer functions for four levels of input motion. The alternative values of kappa result in differences in the transfer functions for frequencies above 2 Hz, with the differences becoming large for frequencies above 6 Hz. The effect of kappa is similar for profiles P1 and P4.

The transfer functions for ATR Rock profiles shown on Figures 9-75 and 9-76 show similar relative amplification to those developed for the SFHP rock site at frequencies below about 10 Hz. At higher frequencies, the relative amplification is higher than obtained for the SFHP Rock site, but lower than that for the MFC site. These lower motions for ATR compared to MFC are attributed to the presence of two effects: 1) the higher kappa for the SFHP Rock site compared to the MFC rock site; and 2) the presence of thicker interbeds in the ATR Rock profile. The lower kappa for the ATR Rock site compared to that for the SFHP Rock site produces greater amplification for frequencies above about 10 Hz.

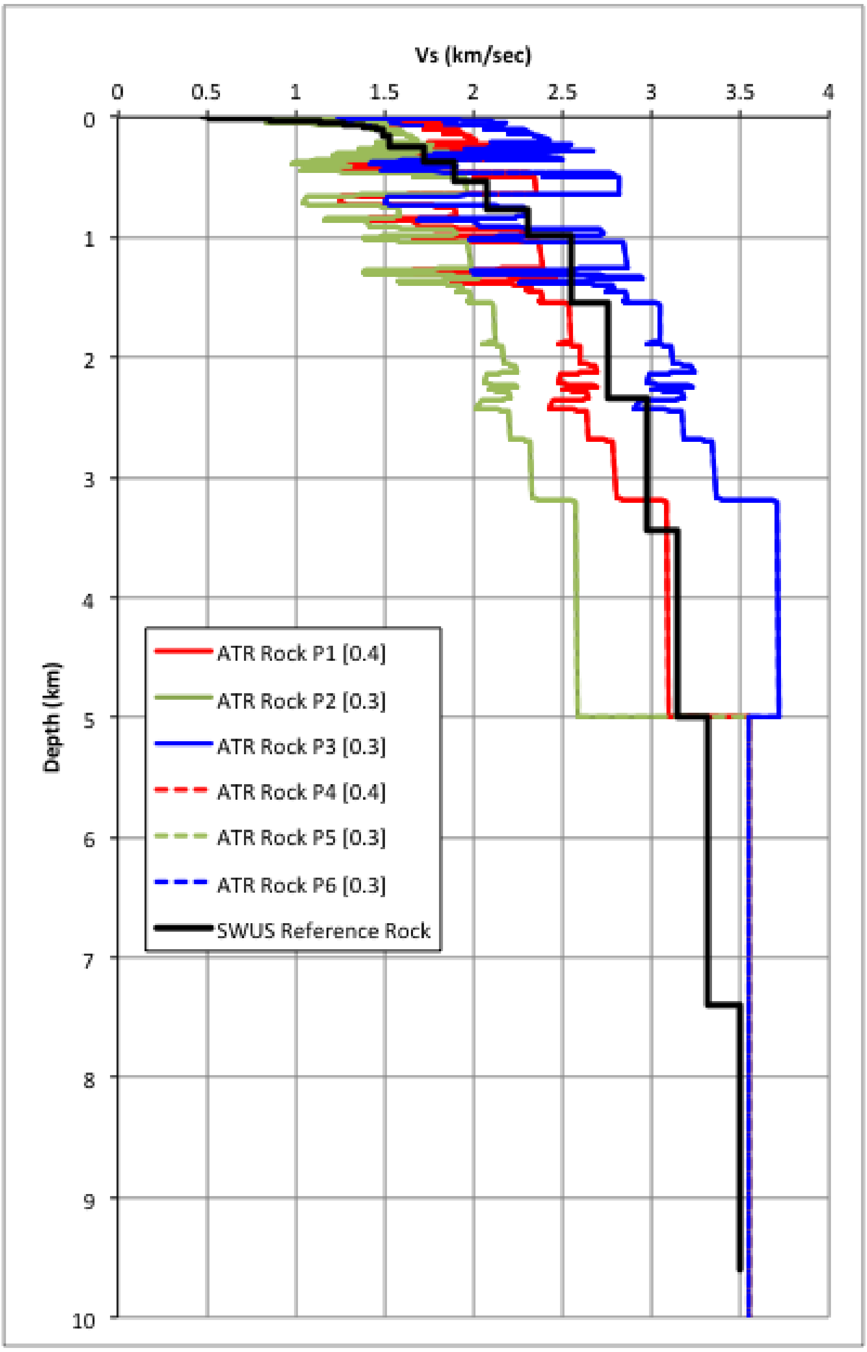

Figure 9-72. Comparison of SWUS reference rock V_S profile with ATR Rock profiles.

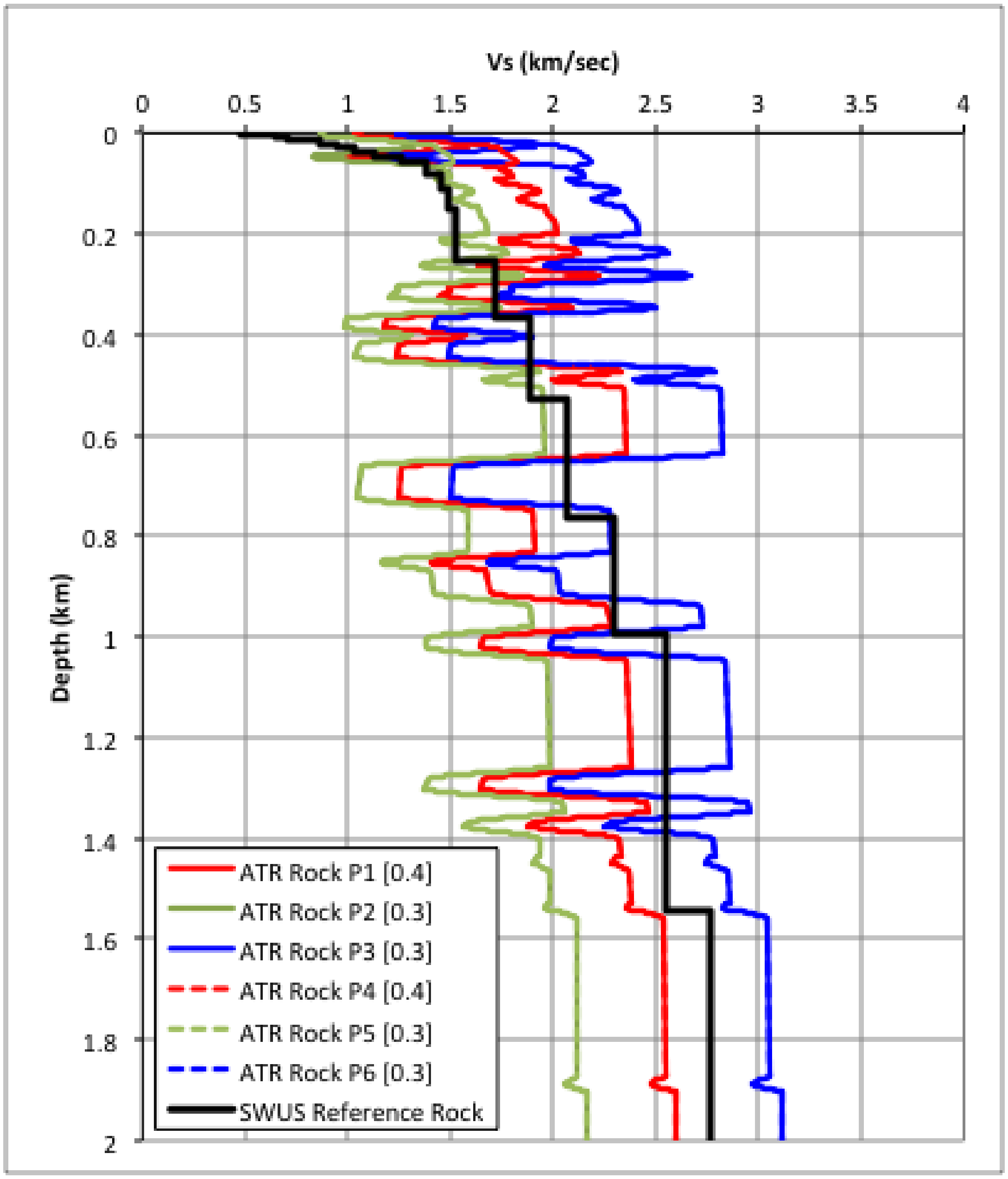

Figure 9-73. Comparison of top 2 km of SWUS reference rock V_S profile with ATR Rock profiles.

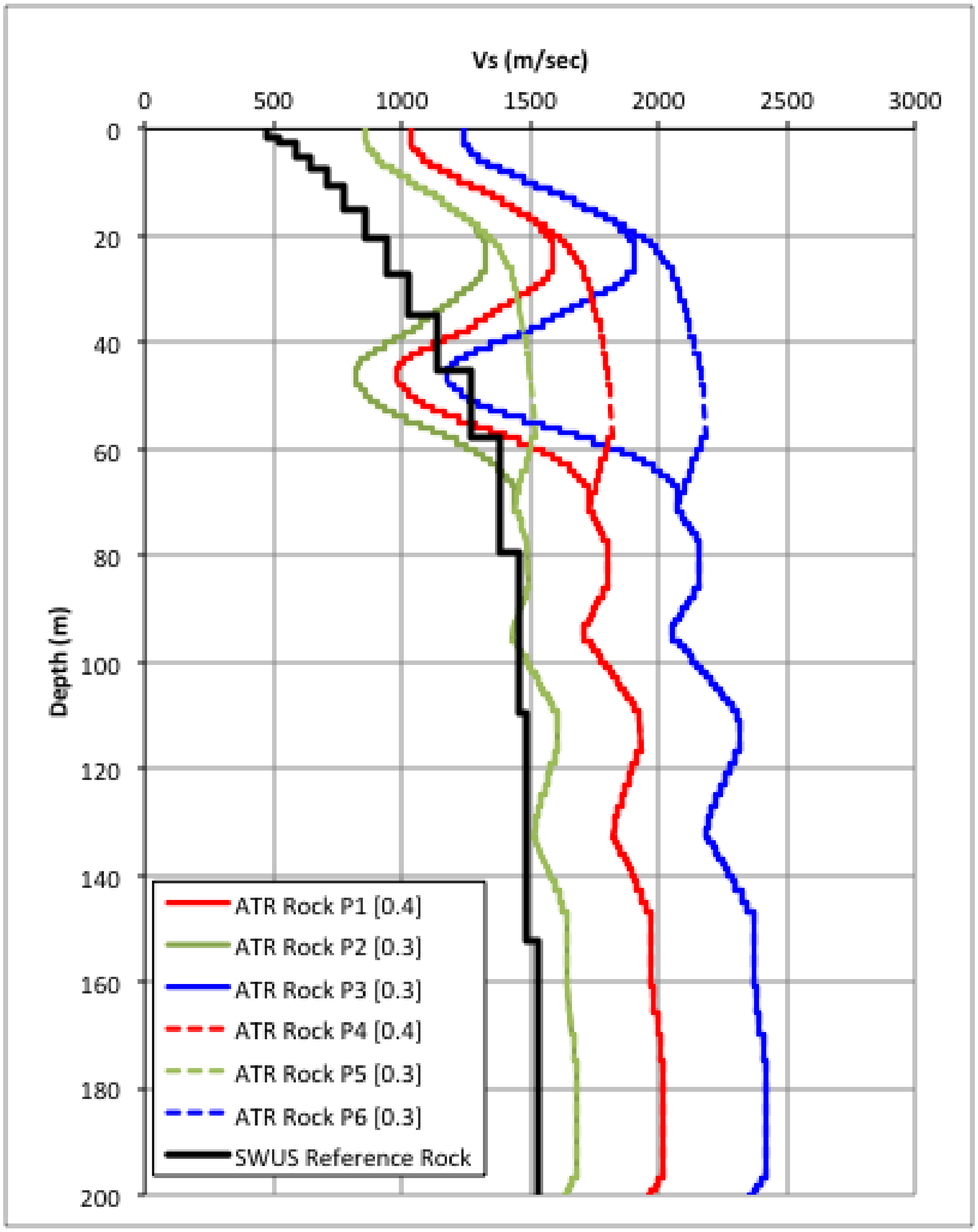

Figure 9-74. Comparison of top 200 m of SWUS reference rock V_S profile with ATR Rock profiles.

a)

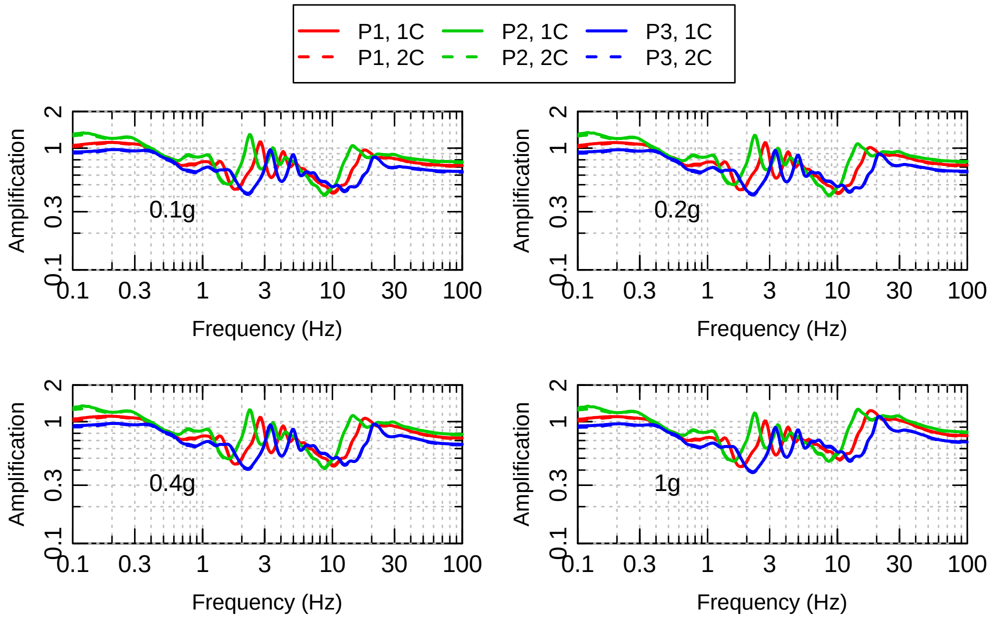

b)

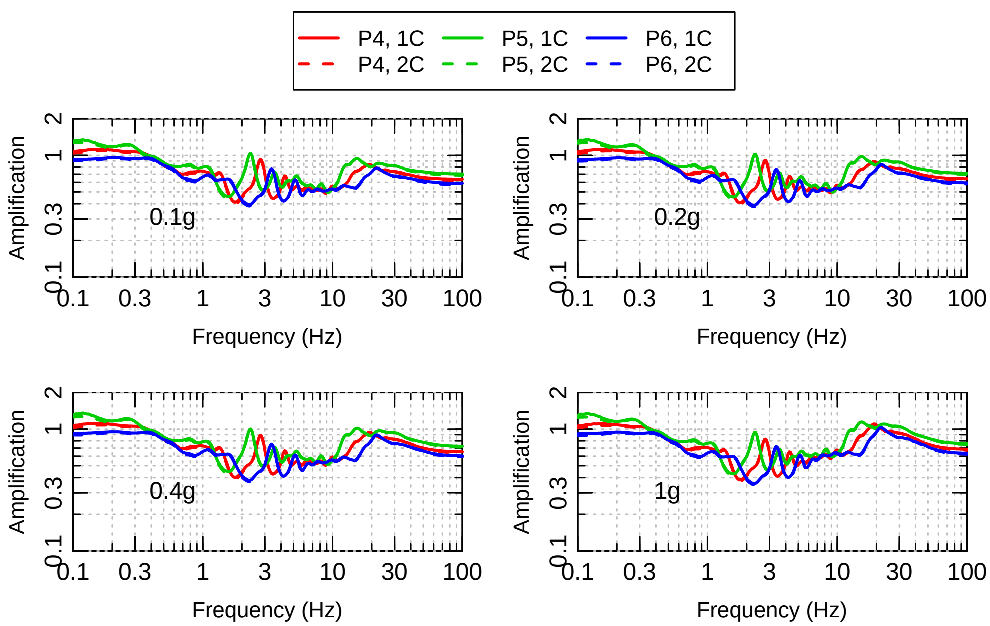

Figure 9-75. Effect of Vs profile on ATR Rock transfer functions (kappa = 0.021s) with different source spectra (C1 and C2) for median base cases: a) P1 (with the interbed at ~40 m); and b) P4 (without the interbed at ~40 m).

a)

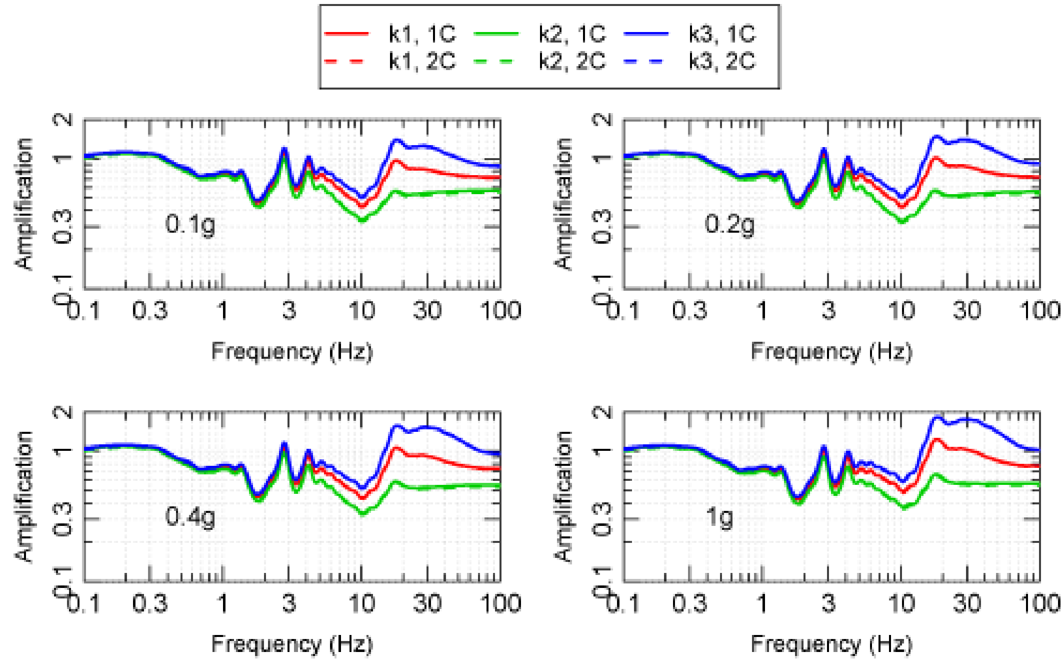

b)

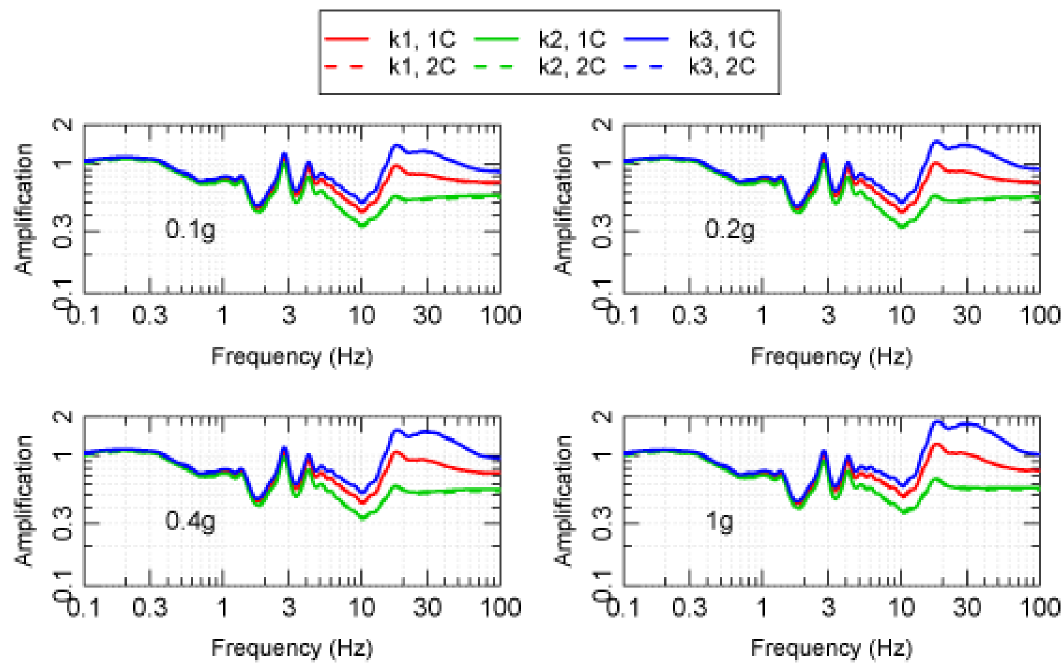

Figure 9-76. Effect of kappa on ATR Rock transfer functions for median base cases: a) P1 (with the interbed at ~40 m); and b) P4 (without the interbed at ~40 m).

9.7.2 Transfer Functions for ATR Soil Sites

As described in Section 7.6, the ATR soil sites contain up to approximately 60 ft of soils. Transfer functions are developed for three soil depths, 20, 40, and 60 ft, to represent the variability in soil depth across the site. The epistemic uncertainty in the dynamic properties of the ATR soil sites is characterized again by six alternative velocity profiles and three alternative values of kappa. In Section 7.6, three alternative values of soil velocity, median, lower-range, and upper-range were developed for the 20-ft, 40-ft, and 60-ft soil depth cases (Table 7-12). These are attached to the respective median, lower-range, and upper-range velocity profiles for the basalts and interbeds. Figures 9-77, 9-78, and 9-79 show the resulting velocity profiles.

As was done for the ATR rock case, the three alternative values of kappa, k1 – 0.021s, k2 – 0.035s, and k3 – 0.013s, were applied to each of the basalt profiles below the soil layers. Additionally, two sets of G/Gmax and damping relationships are used to model the nonlinear behavior of the soils. Set M1 consists of the Darendeli-Menq gravel and Darendeli clay curves and set M2 consists of the Rollins et al. (1998) gravel and Vucetic and Dobry (1991) clay curves. Table 7-12 indicates how the various G/Gmax and damping curves are assigned to the individual soil layers.

The randomization of the velocity profiles and G/Gmax damping relationships for the ATR soil sites was conducted in the same manner as for the FMF site. Variability in soil depth was addressed by computing transfer functions for soil depths of 20, 40, and 60 ft and then enveloping the hazard results for the soil depths that represent the variability at each building or piping area as listed in Table 7-11.

Figures 9-80, 9-81, and 9-82 shows the effect of the alternative ATR soil velocity profiles on the transfer functions for four levels of input motion for soil depths of 20 ft, 40 ft, and 60 ft, respectively. In contrast to the results observed for the MFC and FMF sites (Section 9.3), the alternative velocity profiles produce similar differences in the transfer functions as for the SFHP Rock and Soil sites. As is the case for the results for other sites, there is very little difference in the transfer functions computed using the one-corner and two-corner earthquake source spectra.

Figures 9-83, 9-84, and 9-85 show the effect of the alternative values for kappa on the transfer functions for four levels of input motion for soil depths of 20 ft, 40 ft, and 60 ft, respectively. The kappa effects for ATR soil are generally similar to those for ATR rock. The kappa effects diminish at higher loading levels as the effects of soil nonlinearity become more important in defining the level of high frequency ground motions.

Figures 9-86, 9-87, and 9-88 show the effect of the alternative sets of G/Gmax and damping relationships on the transfer functions for the three profiles for the 20 ft, 40 ft, and 60 ft soil depths, respectively. For all depths, the alternative material curves produce similar relative amplifications at low loading levels. At higher loading levels, the two sets of material curves produce differences in amplification, with the more linear set M2 producing higher high frequency motions and lower low frequency motions. The greater nonlinearity of set M2 results in greater strains at higher loading levels, producing larger soil damping which lowers high frequency motion amplification, and lower soil shear wave velocities, which produces greater low frequency motion amplification.

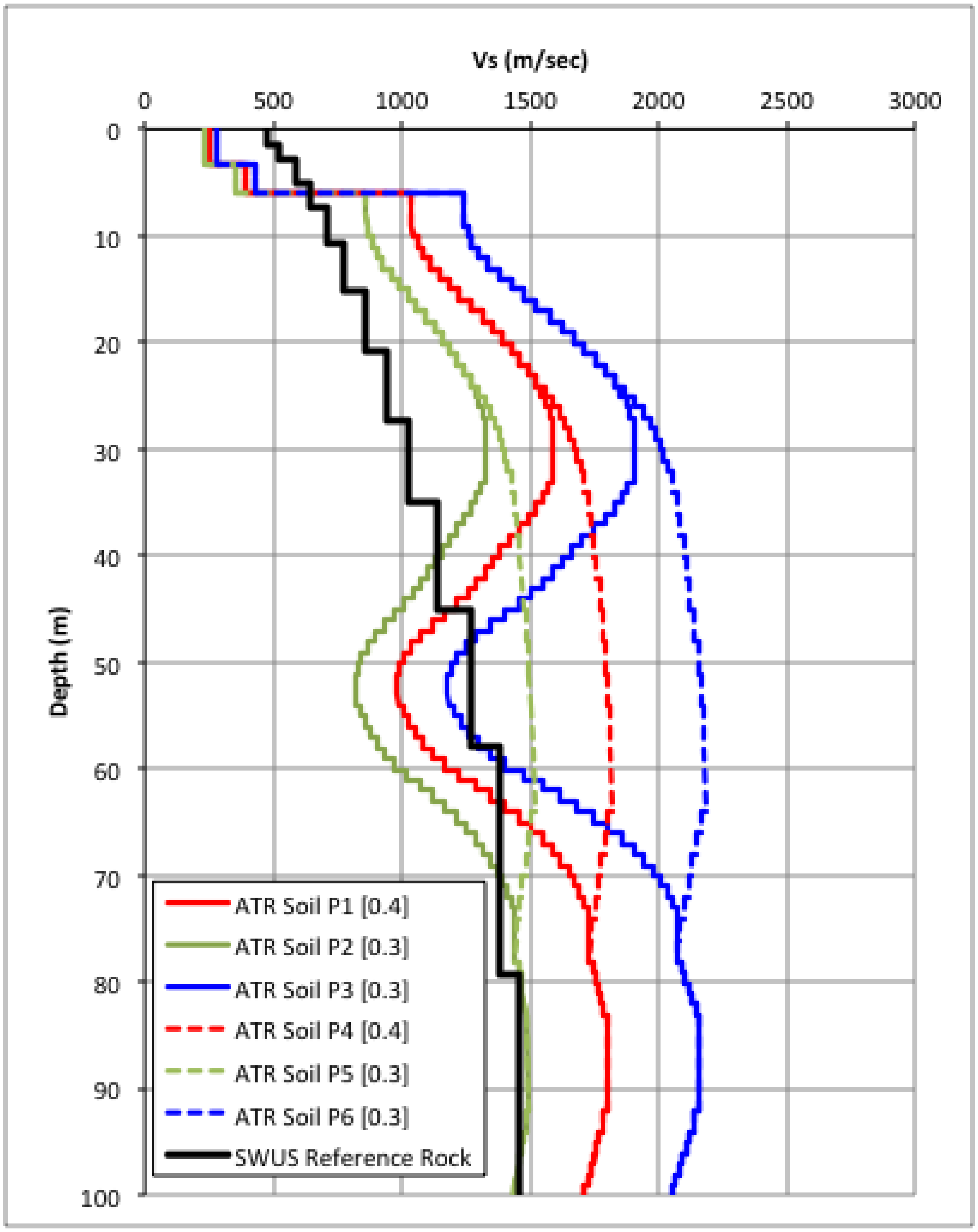

Figure 9-77. Comparison of SWUS reference rock V_S profile with ATR profiles for 20 ft of soil.

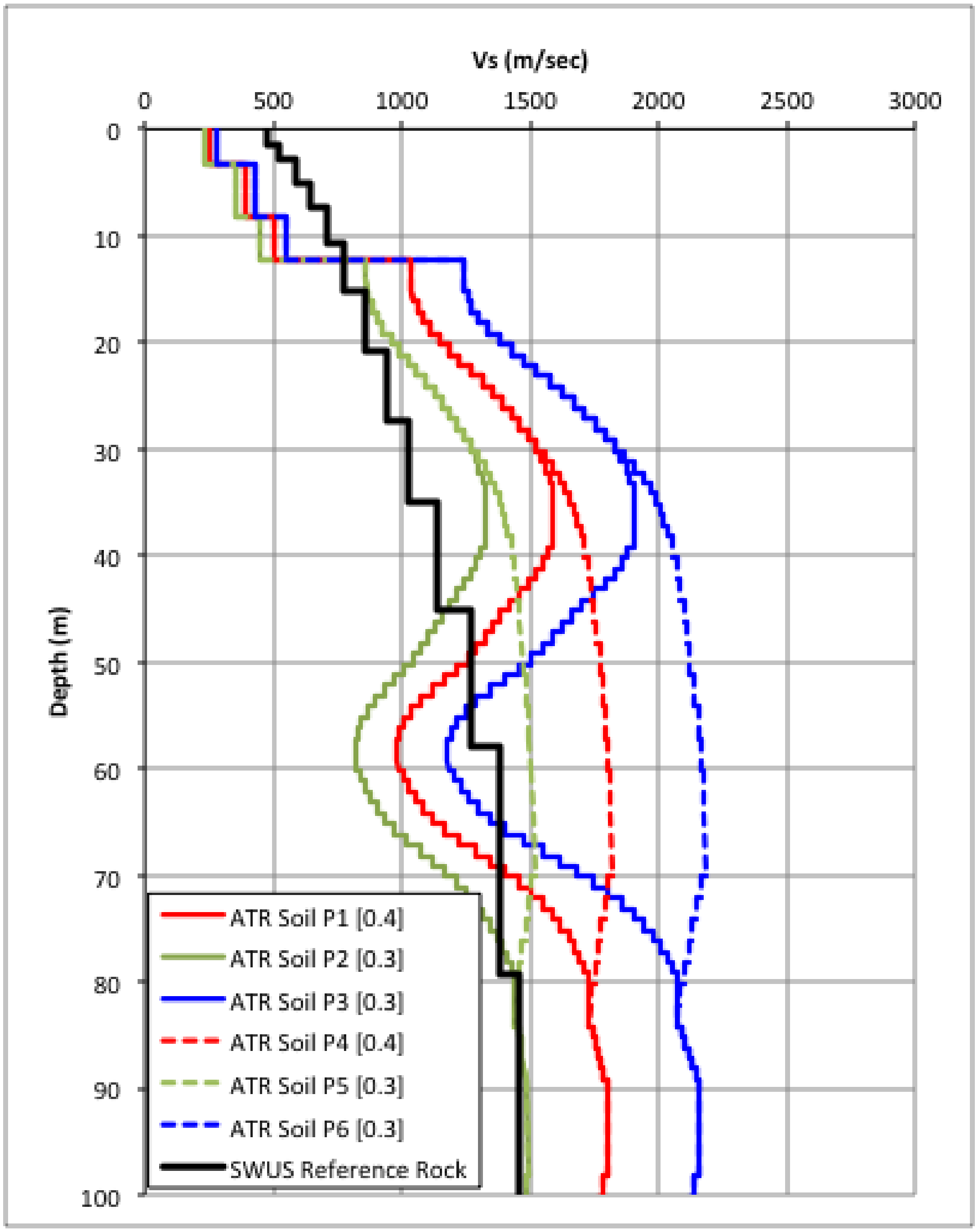

Figure 9-78. Comparison of SWUS reference rock V_S profile with ATR profiles for 40 ft of soil.

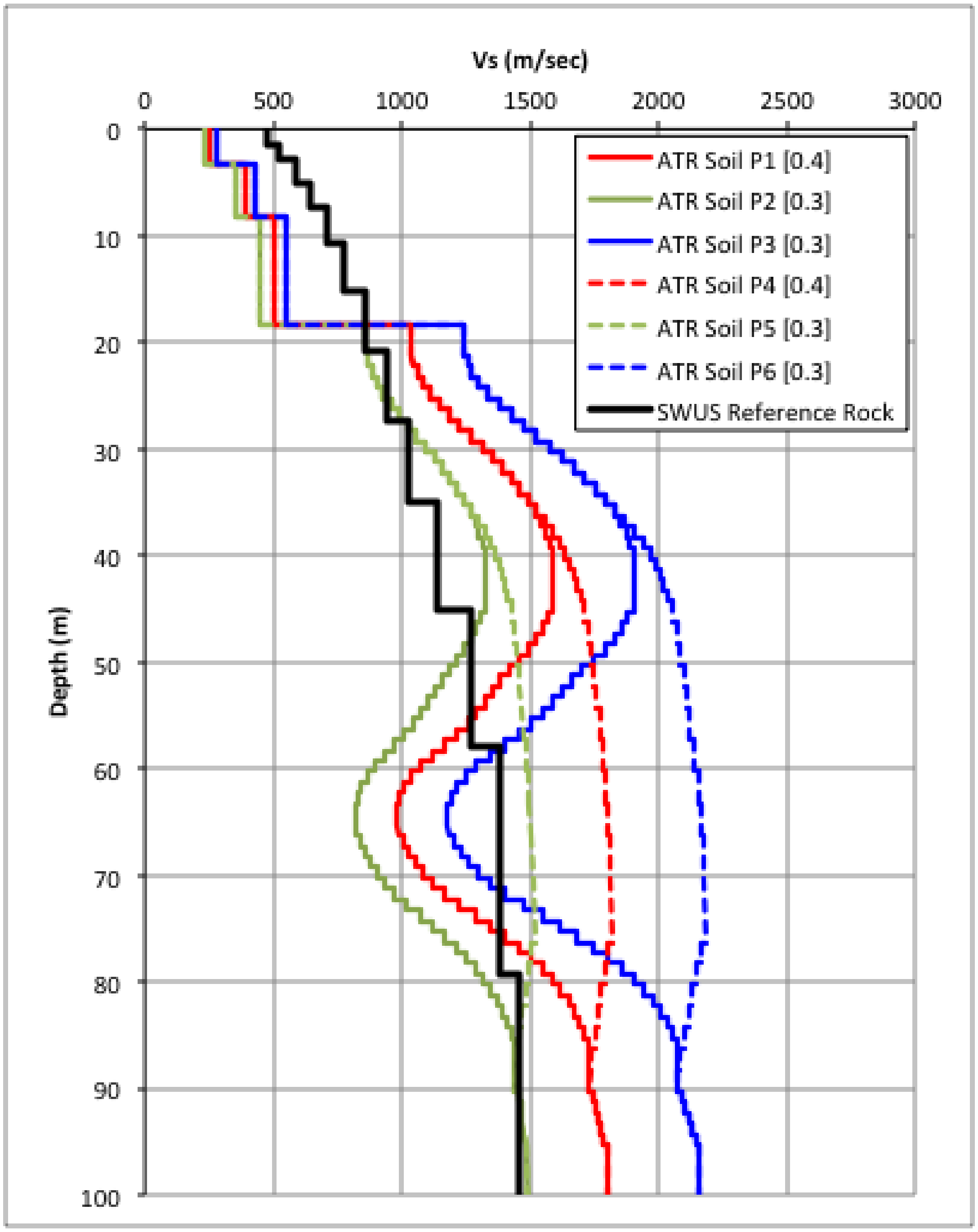

Figure 9-79. Comparison of SWUS reference rock V_S profile with ATR profiles for 60 ft of soil.

a)

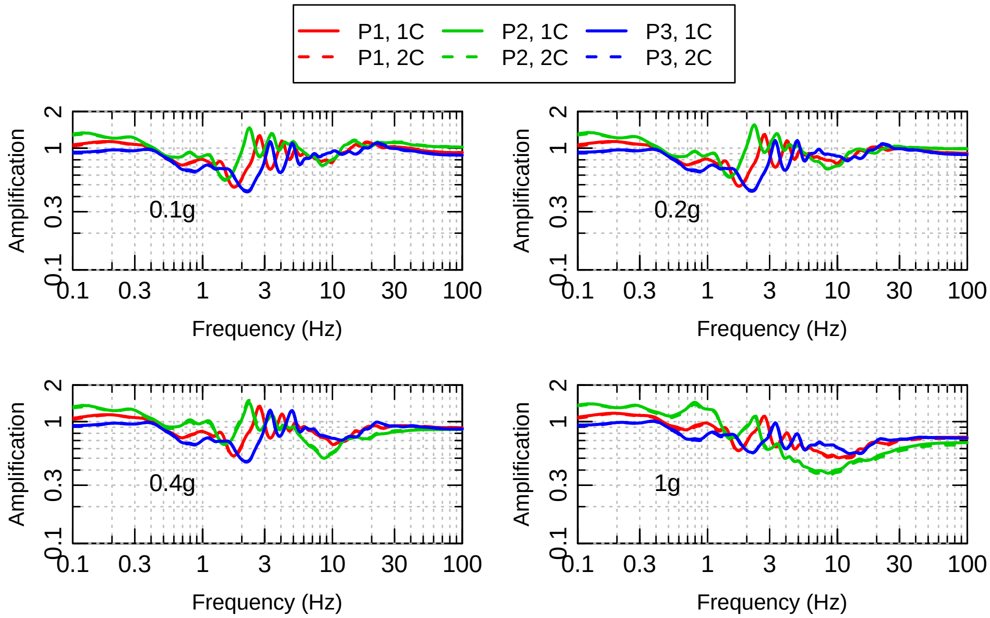

b)

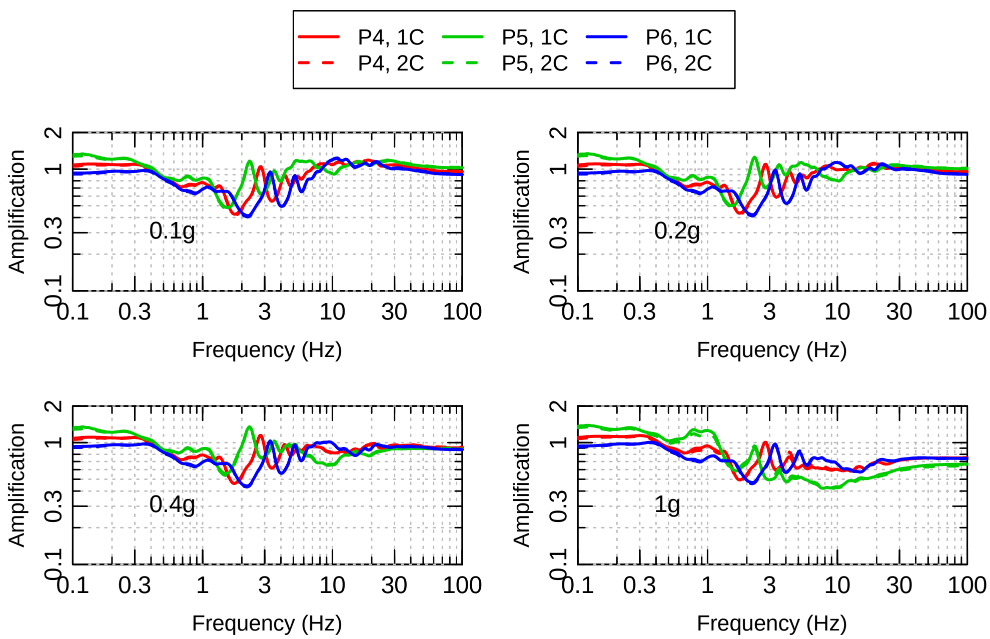

Figure 9-80. Effect of Vs profile on ATR soil transfer function (kappa = 0.021s, soil depth 20 ft, soil material set M1). Designations for the median Vs profiles for rock are: a) P1 (with the interbed at ~40 m); and b) P4 (without the interbed at ~40 m).

a)

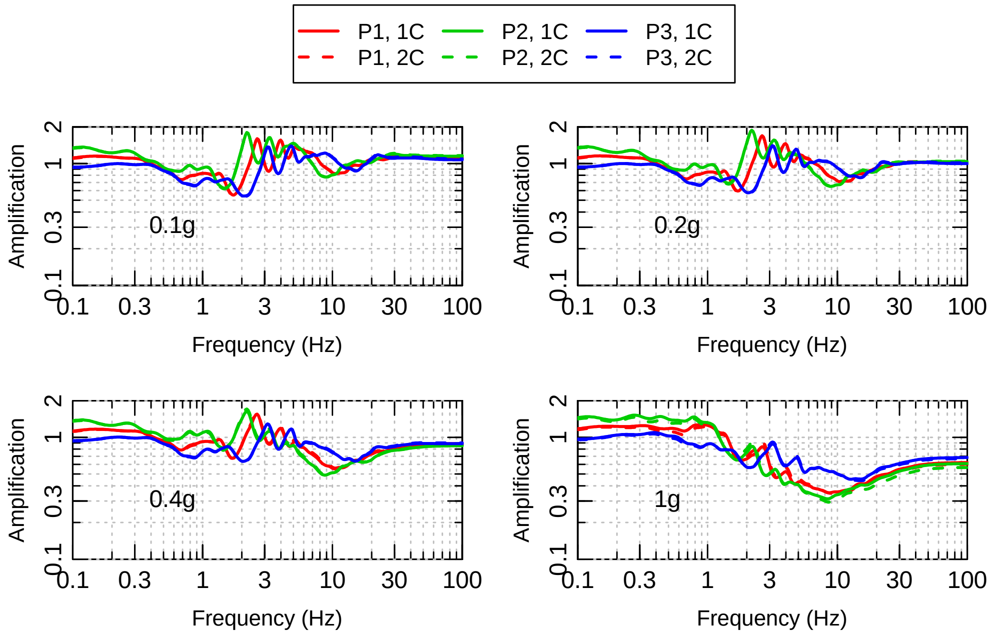

b)

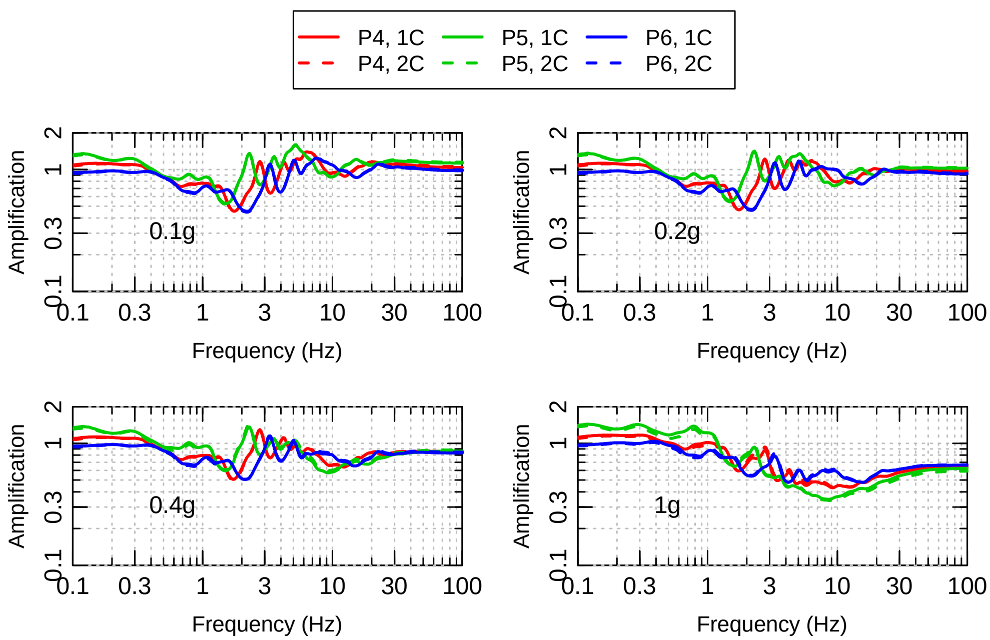

Figure 9-81. Effect of V_S profile on ATR soil transfer function (kappa = 0.021s, soil depth 40 ft, soil material set M1). Designations for the median Vs profiles for rock are: a) P1 (with the interbed at ~40 m); and b) P4 (without the interbed at ~40 m).

a)

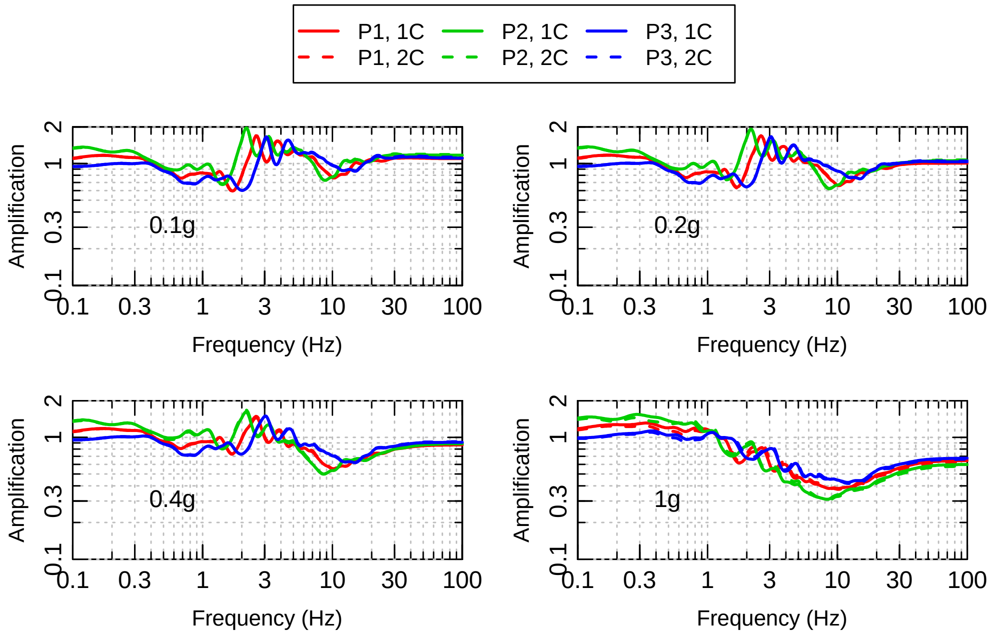

b)

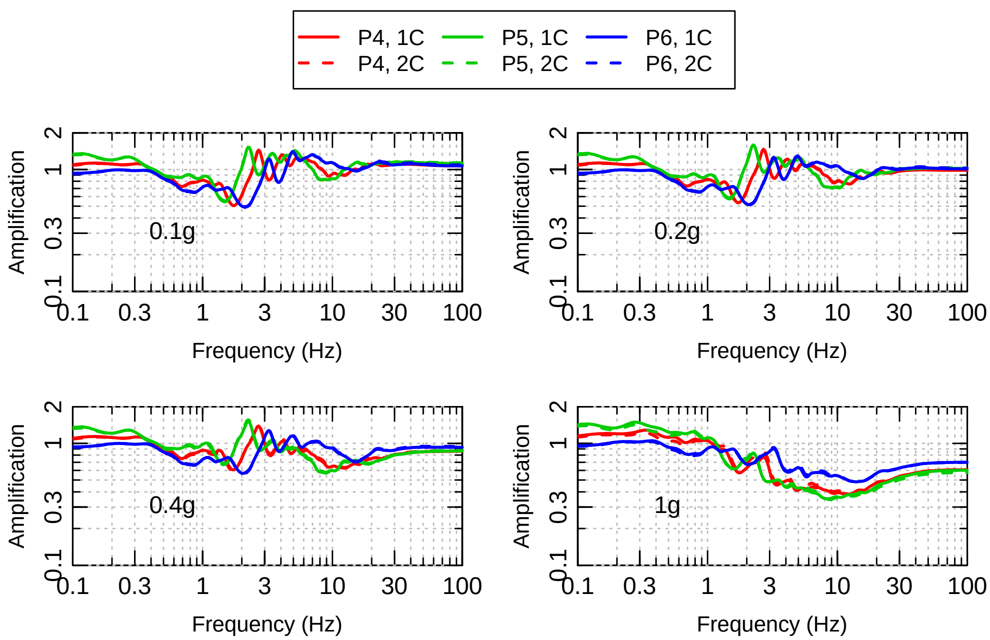

Figure 9-82. Effect of V_S profile on ATR soil transfer function (kappa = 0.021s, soil depth 60 ft, soil material set M1). Designations for the median Vs profiles for rock are: a) P1 (with the interbed at ~40 m); and b) P4 (without the interbed at ~40 m).

a)

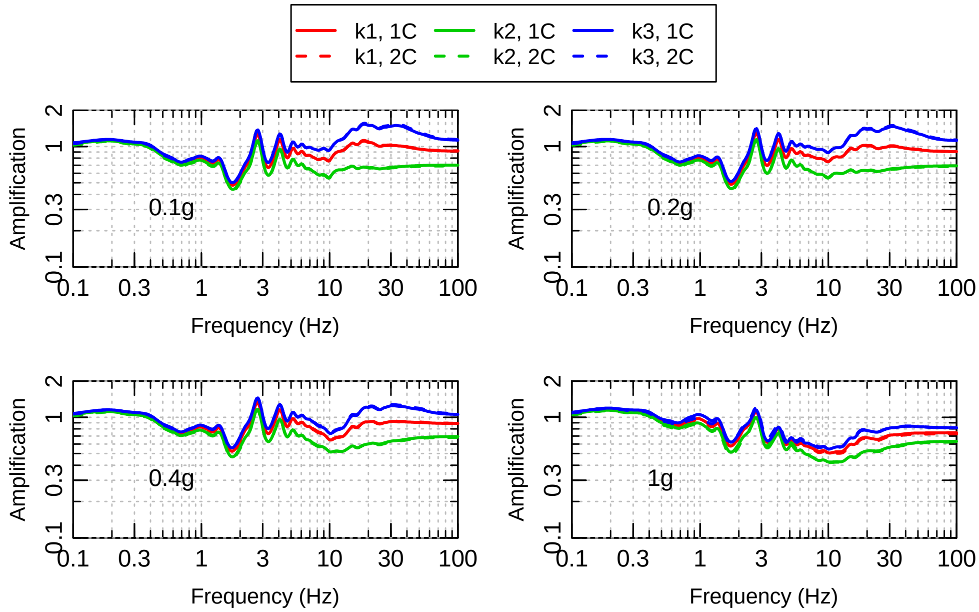

b)

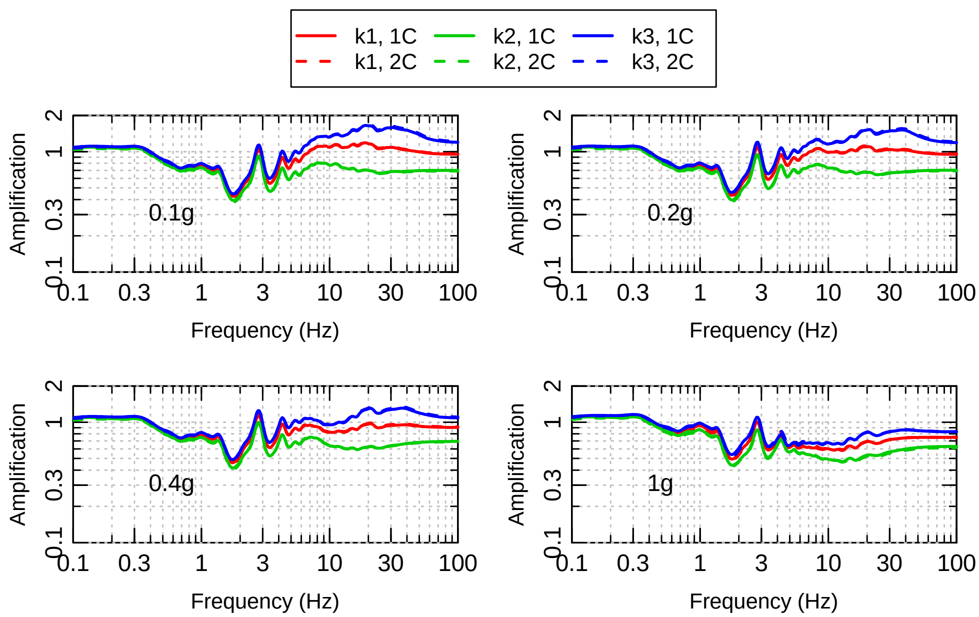

Figure 9-83. Effect of kappa on ATR soil transfer function with soil depth 20 ft, soil material set M1, and median Vs rock profiles: a) P1 (with the interbed at ~40 m); and b) P4 (without the interbed at ~40 m).

a)

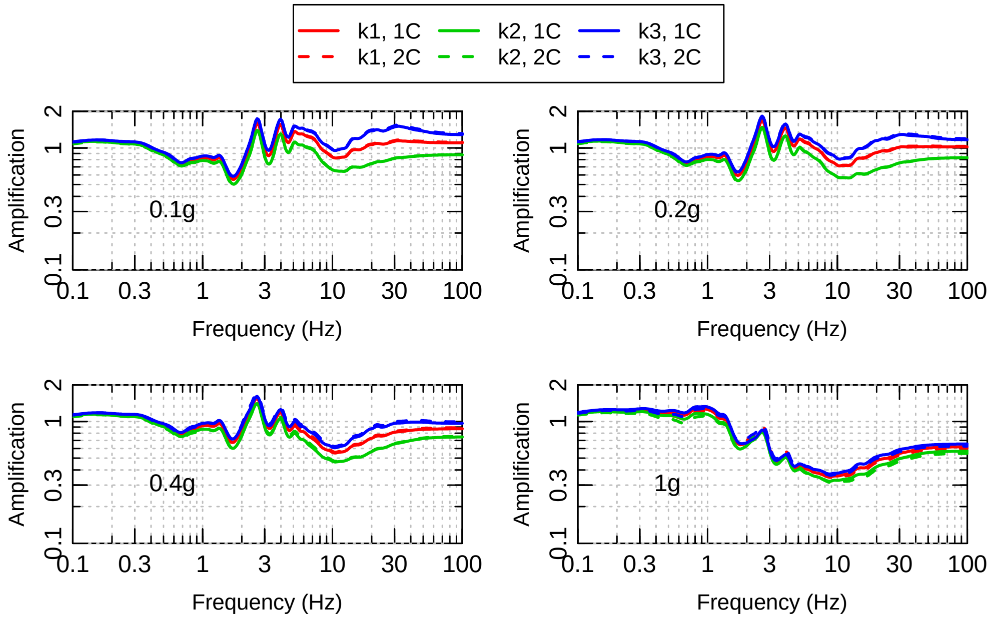

b)

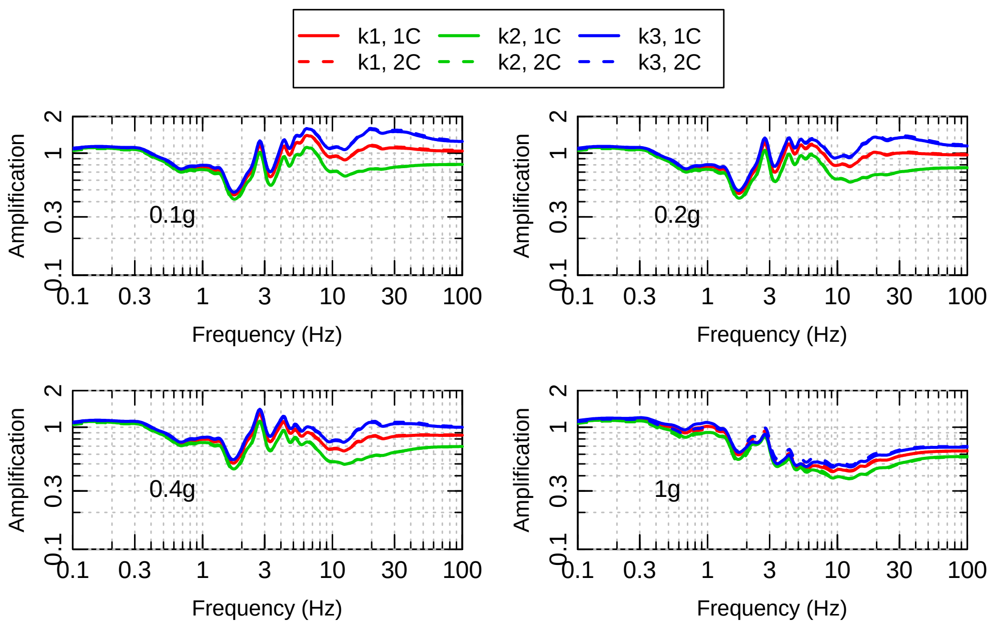

Figure 9-84. Effect of kappa on ATR soil transfer function with soil depth 40 ft, soil material set M1, and median Vs rock profiles: a) P1 (with the interbed at ~40 m); and b) P4 (without the interbed at ~40 m).

a)

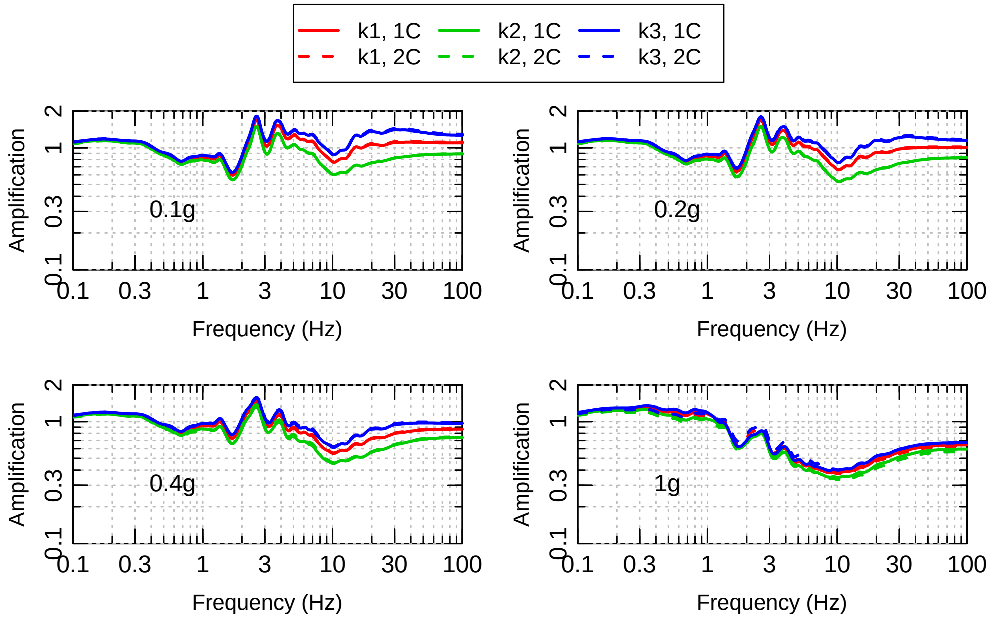

b)

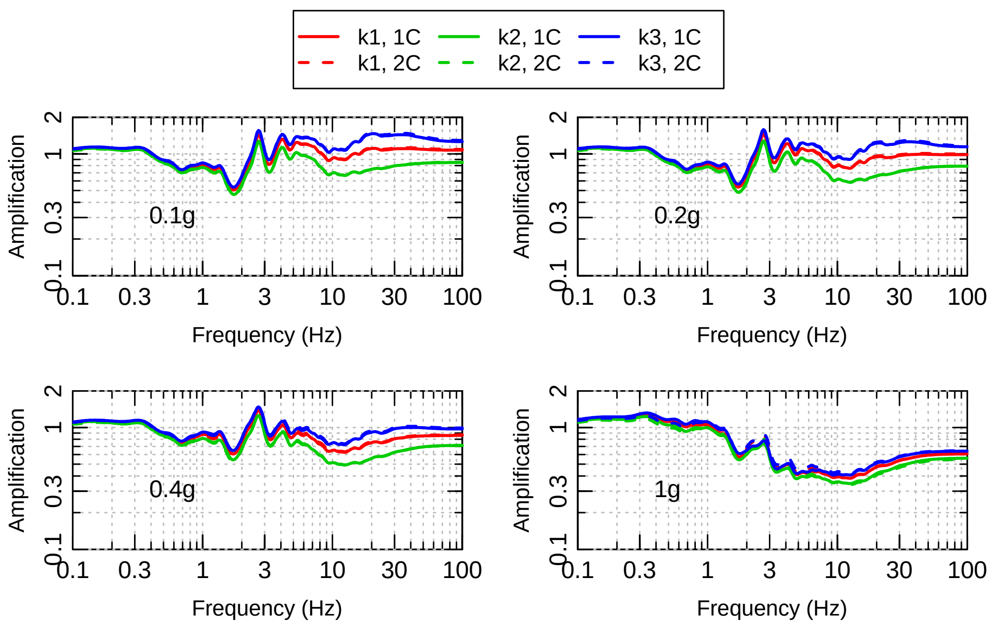

Figure 9-85. Effect of kappa on ATR soil transfer function with soil depth 60 ft, soil material set M1, and median Vs rock profiles: a) P1 (with the interbed at ~40 m); and b) P4 (without the interbed at ~40 m).

a)

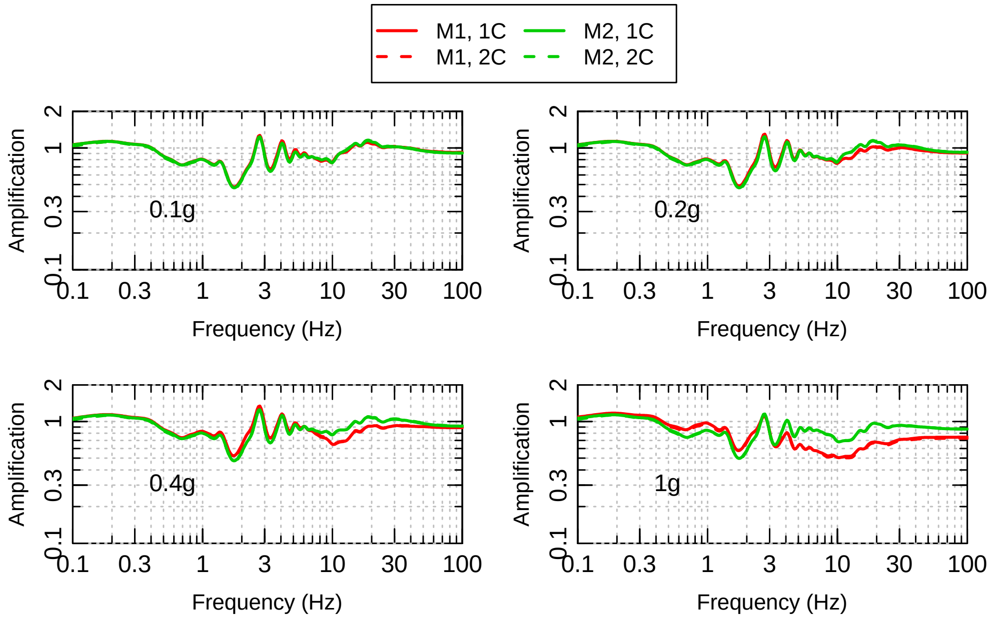

b)

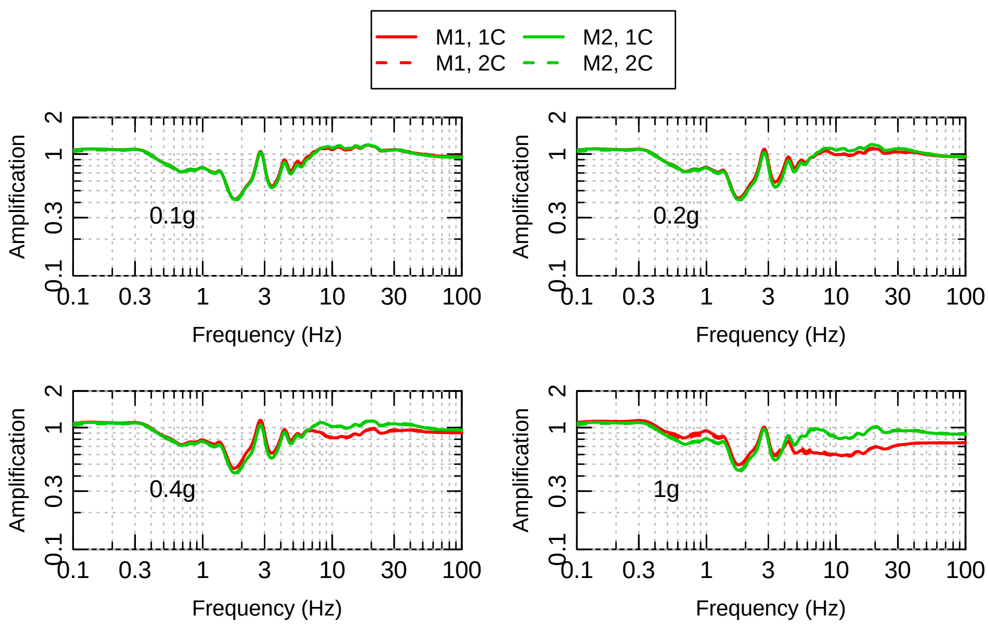

Figure 9-86. Effect of G/Gmax and damping curves on ATR soil transfer functions with kappa= 0.021s, soil depth 20 ft, and median Vs rock profiles: a) P1 (with the interbed at ~40 m); and b) P4 (without the interbed at ~40 m).

a)

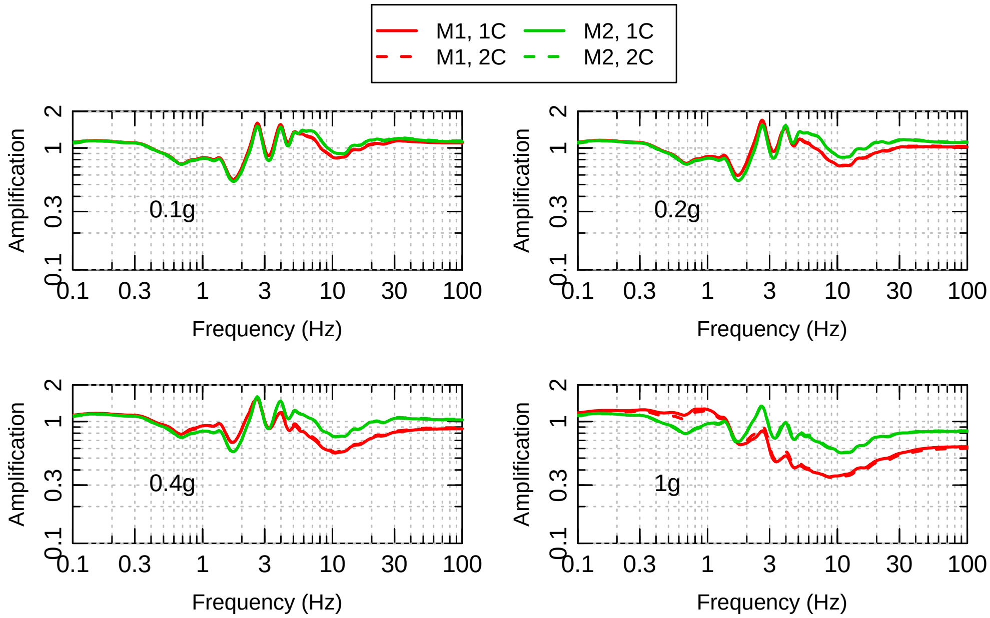

b)

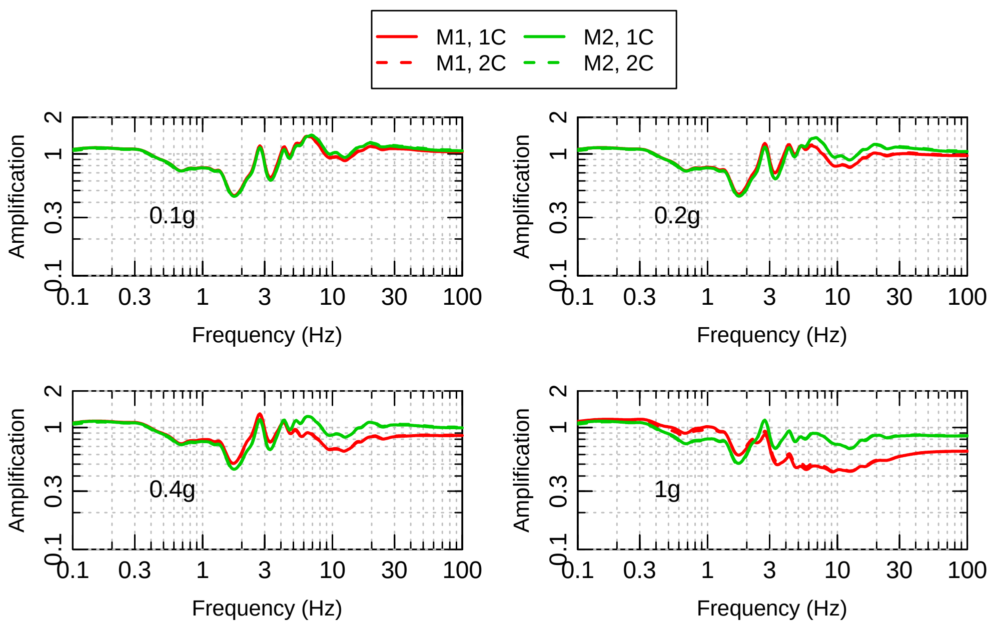

Figure 9-87. Effect Effect of G/Gmax and damping curves on ATR soil transfer functions with kappa= 0.021s, soil depth 40 ft, and median Vs rock profiles: a) P1 (with the interbed at ~40 m); and b) P4 (without the interbed at ~40 m).

a)

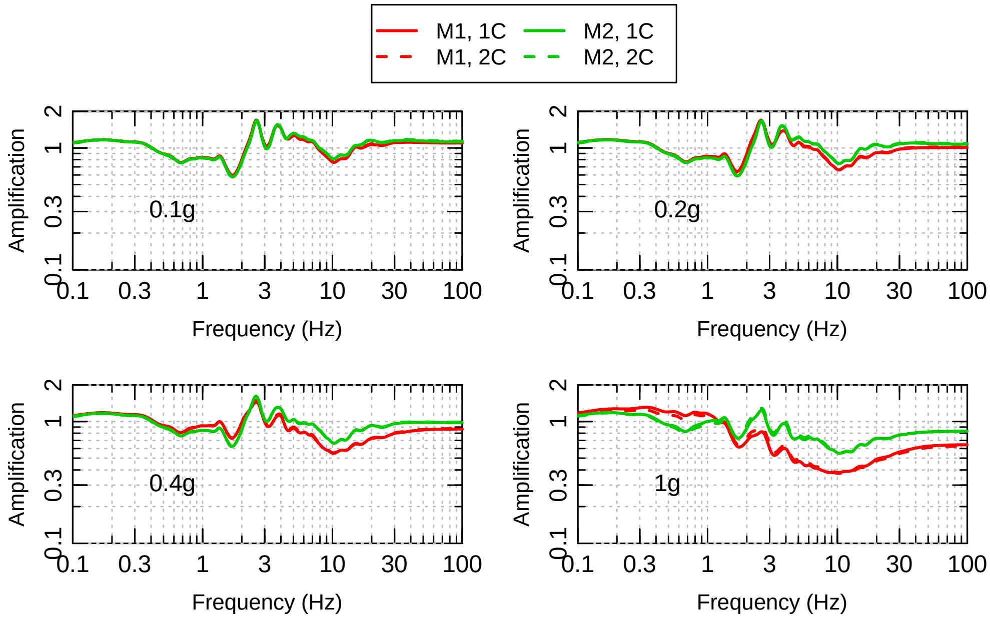

b)

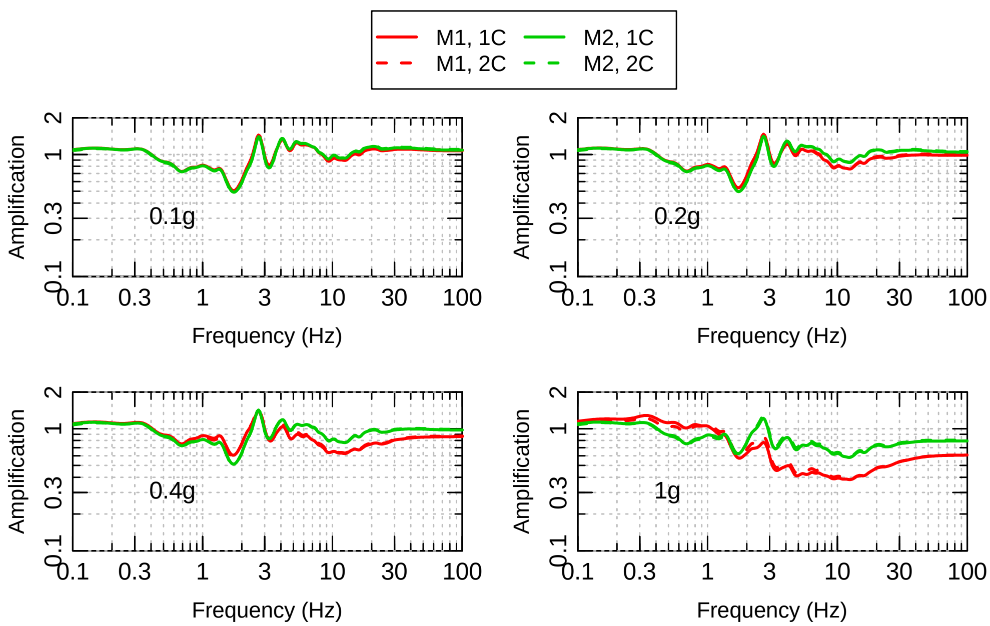

Figure 9-88. Effect of G/Gmax and damping curves on ATR soil transfer functions with kappa= 0.021s, soil depth 60 ft, and median Vs rock profiles: a) P1 (with the interbed at ~40 m); and b) P4 (without the interbed at ~40 m).

9.7.3 Epistemic Uncertainty in Transfer Functions

Epistemic uncertainties were assessed for the transfer functions at ATR rock and soil sites. Figure 9-89 shows the logic tree for the epistemic uncertainty in the inputs to the transfer function calculations for the ATR site. Note that the alternative soil material curve sets apply only to the soil sites. The alternative transfer functions obtained for each end branch define the epistemic uncertainty in adjusting from the reference rock profile to the site profiles for the ATR sites. The epistemic uncertainty in the Vs profile is represented by the alternatives P1, P2, and P3 for the case with an interbed at a depth of ~40 m and alternatives P4, P5, and P6 for the case without an interbed at a depth of ~ 40 m.

Following the approach described for the MFC and FMF sites in Section 9.3.4, the epistemic standard deviation in the transfer functions was computed as a function of frequency. The modeling uncertainty shown on the bottom panel of Figure 9-32 was incorporated by summing variances. The results are shown on Figure 9-90 for the ATR Rock site and on Figures 9-91, 9-92, and 9-93 for the ATR soil sites. The logic tree plus modeling epistemic uncertainty is shown for two levels of reference rock motions corresponding to return periods of 2,500 yrs. and 10,000 yrs. The resulting values are largest for frequencies above 10 Hz, the frequency range where the uncertainty in site kappa has the greatest effect on the transfer functions.

As discussed above in Section 9.3.4 for the MFC and FMF sites, the concept of a minimum level of epistemic uncertainty (PNNL, 2014) was used to compute the hazard for the ATR sites. As was done for the MFC and FMF sites, two alternative approaches were used to define the minimum epistemic uncertainty to use in computing the site-specific hazard. The first, Option A, is to use the modeling uncertainty from Figure 9-32. The second, Option B, is to use the ϕ_{S2S} values for the California data for **M**> 5 shown on Figures 9-90 through 9-93, after removing the variance in the computed transfer functions defined by the logic tree shown on Figure 9-89. A weighted combination is used to develop the final mean hazard. Option A is favored slightly (weight 0.6) over Option B (weight 0.4) because the transfer calculations make use of the full crustal profile. This combination produces an effective weighted minimum epistemic uncertainty that is approximately the same as the borehole ϕ_{S2S} reported by Rodriguez-Marek et al. (2011). The final transfer functions are tabulated in the GMM HID (Appendix G).

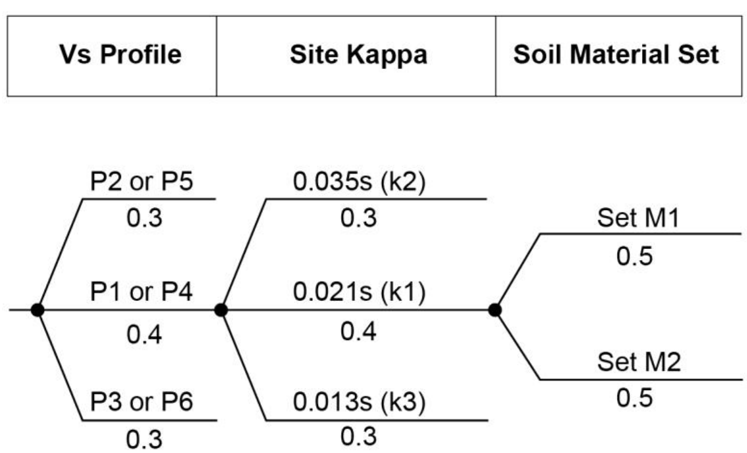

Figure 9-89. Logic trees for characterizing epistemic uncertainties in inputs to transfer function calculations for ATR Rock (V_S and kappa only) and ATR Soil using (V_S, kappa, and Soil Material Set).

(a)

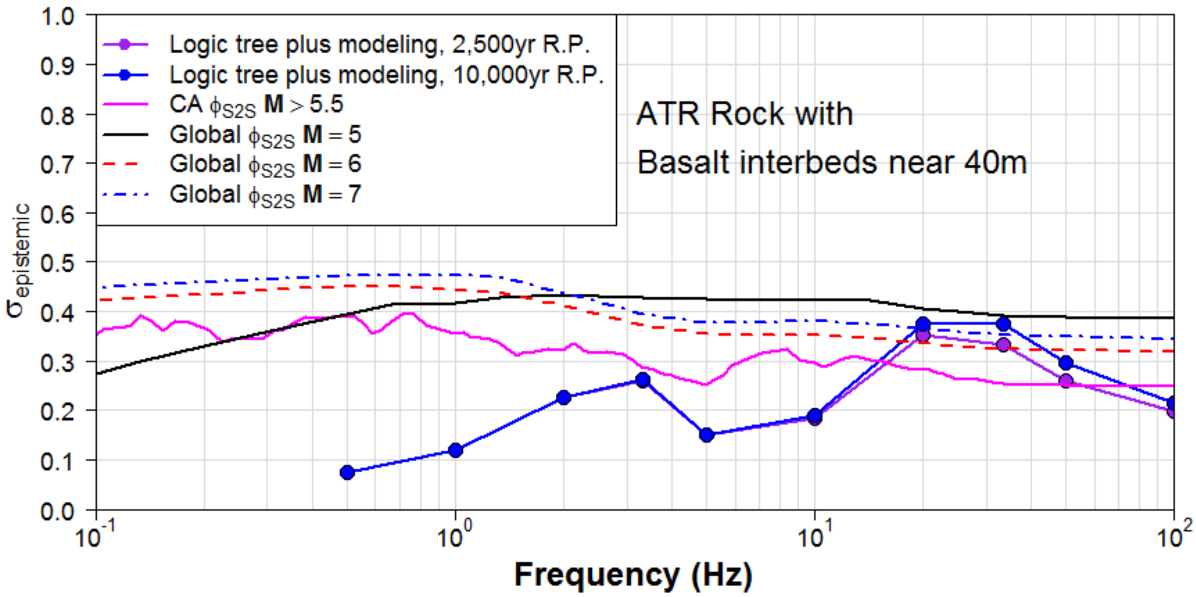

(b)

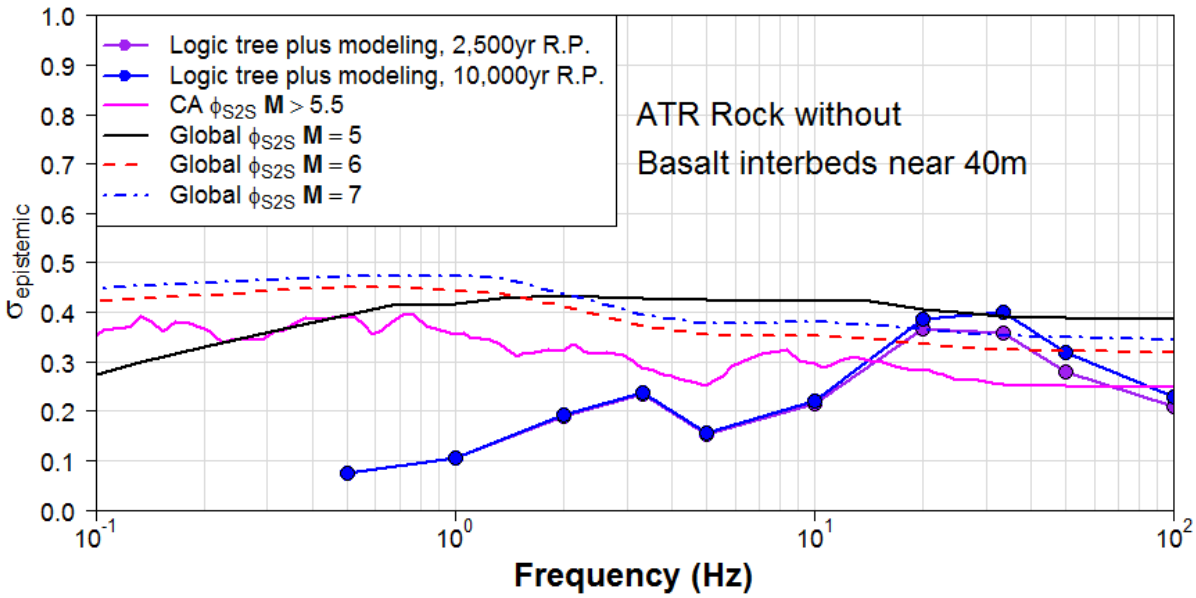

Figure 9-90. Epistemic uncertainty in the transfer function for ATR Rock: (a) with interbed at ~40 m depth, (b) without interbed at ~40 m depth.

(a)

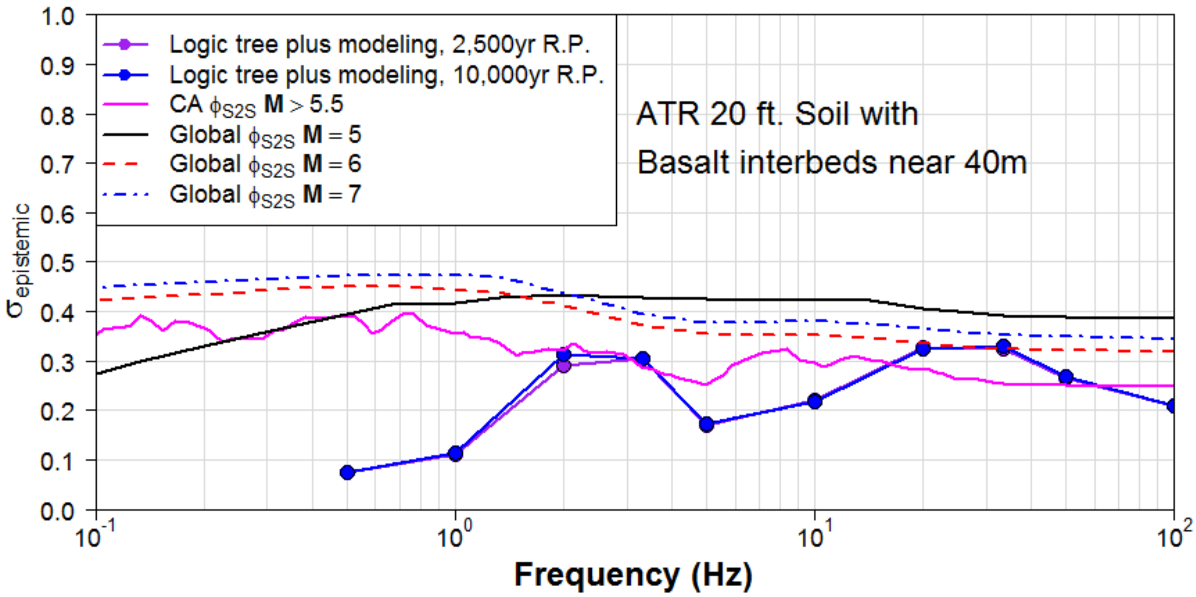

(b)

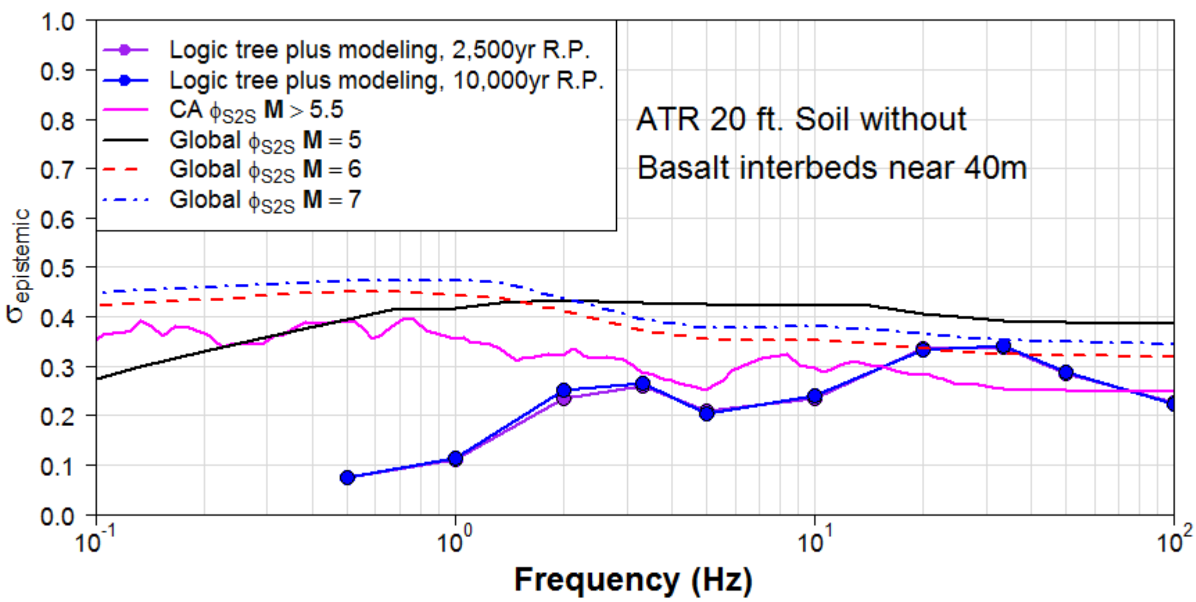

Figure 9-91. Epistemic uncertainty in the transfer function for ATR Soil, 20 ft depth: (a) with interbed at ~ 40 m depth, (b) without interbed at ~40 m depth.

(a)

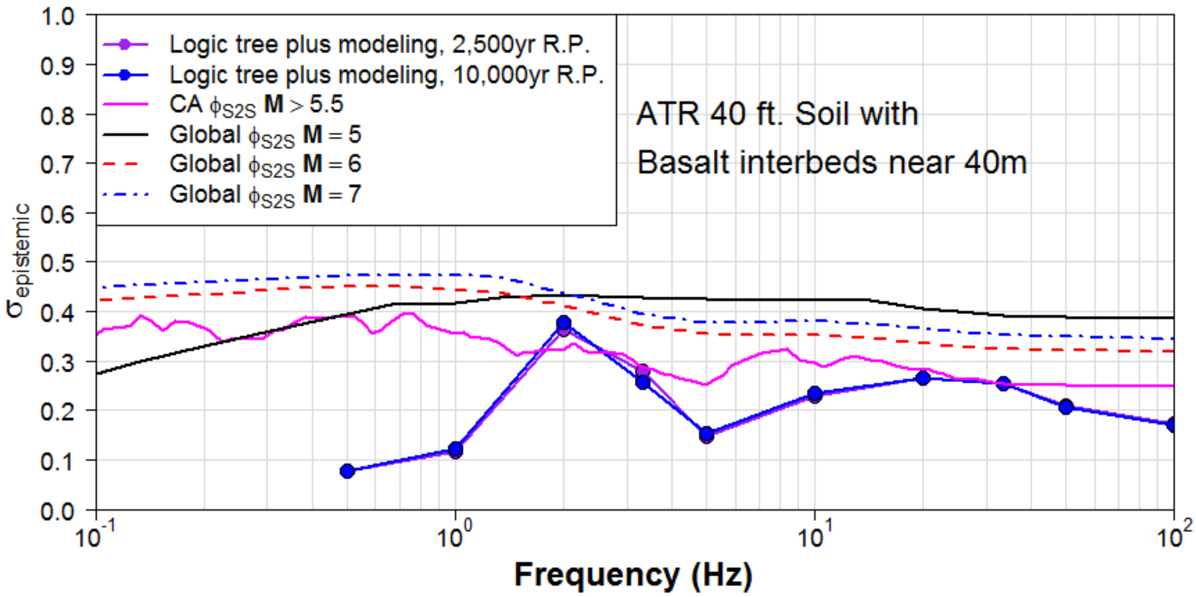

(b)

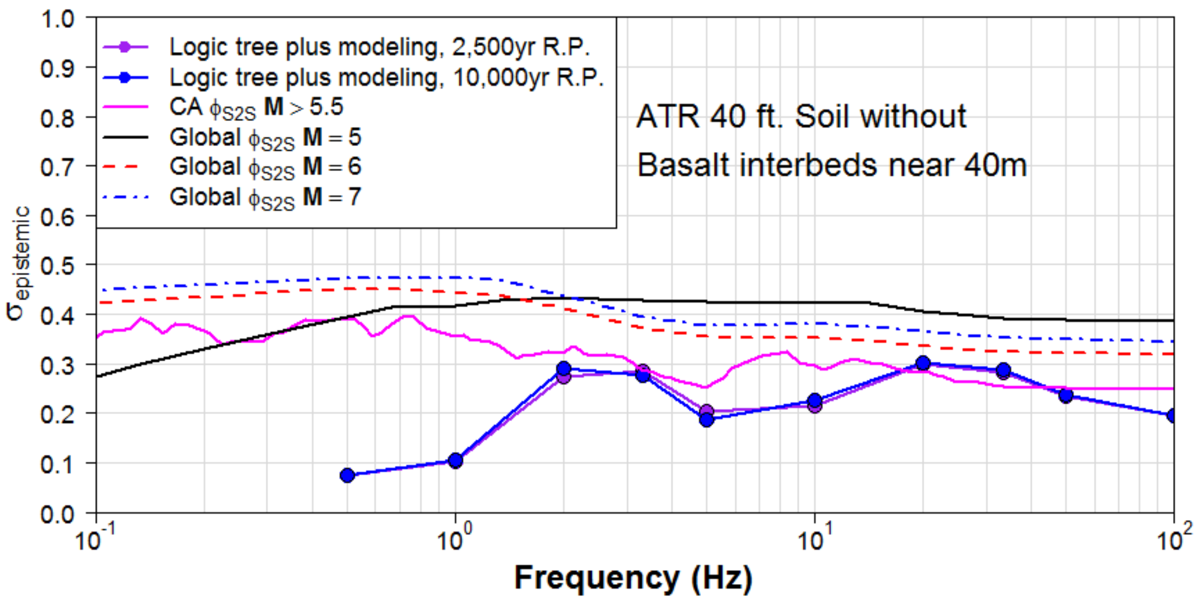

Figure 9-92. Epistemic uncertainty in the transfer function for ATR Soil, 40 ft depth: (a) with interbed at ~ 40 m depth, (b) without interbed at ~40 m depth.

(a)

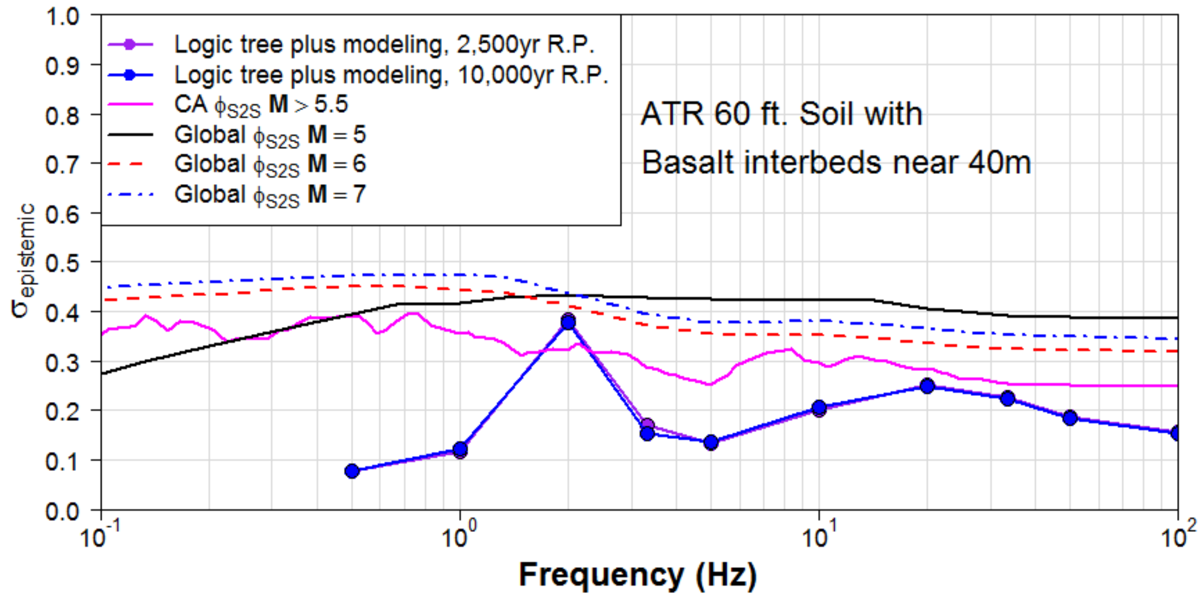

(b)

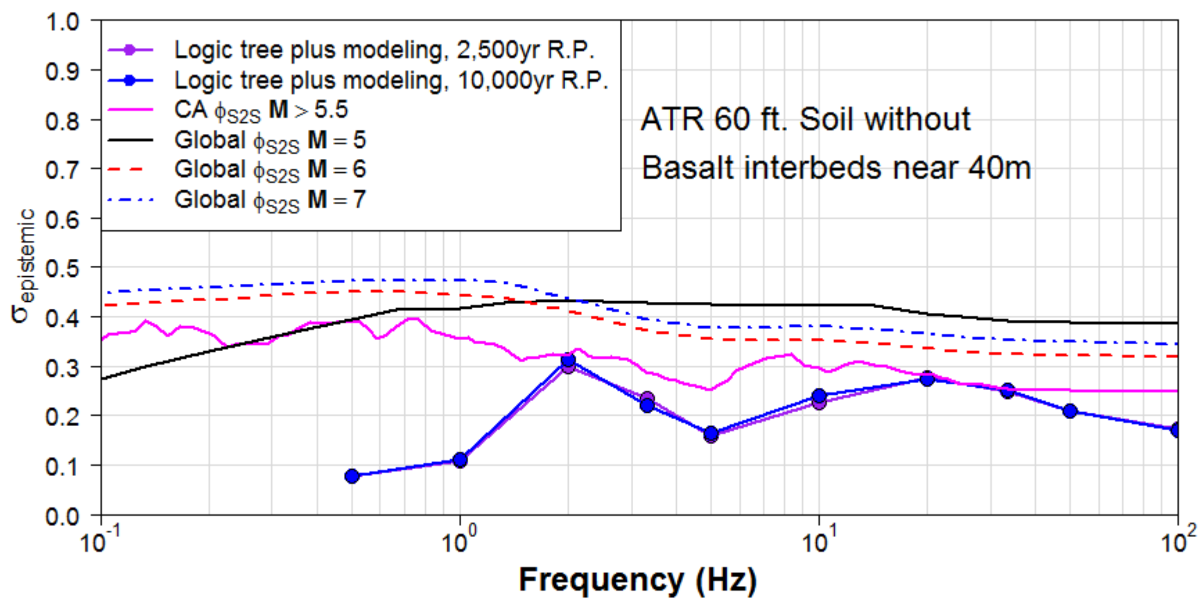

Figure 9-93. Epistemic uncertainty in the transfer function for ATR Soil, 60 ft depth: (a) with interbed at ~ 40 m depth, (b) without interbed at ~40 m depth.

9.8 Relationships for Vertical Motions for the ATR Complex

The approach used in Section 9.4 for the MFC and FMF sites was used to develop V/H ratios for the ATR Rock and Soil sites. The reference rock hazard results for the ATR site presented in Section 10.7 indicate that the mean magnitude and distance for earthquakes contributing to the hazard at return periods near 2,500 years range from approximately **M** 6.3 and R_{RUP} of 27 km for ground motion frequencies ≥ 5 Hz to approximately **M** 6.8 and R_{RUP} of 48 km for ground motion frequencies of 1 Hz and less. For a return period near 10,000 years, the mean magnitudes and distances change slightly to **M** 6.4 and R_{RUP} of 22 km for ground motion frequencies ≥ 5 Hz and approximately **M** 6.9 and R_{RUP} of 37 km for ground motion frequencies of 1 Hz and less. The V_{S30} for the ATR Rock site is 1,458 m/s and the V_{S30} for the ATR soil sites is 805 m/s for a soil depth of 20 ft, 636 m/s for a soil depth of 40 ft, and 540 m/s for a soil depth of 60 ft. Figures 9-94 and 9-95 show the V/H ratios for the ATR site for rock conditions using the controlling earthquakes corresponding to return periods of 2,500 and 10,000 years, respectively. Figures 9-96 and 9-97 show the V/H ratios for 20 ft of soil at the two return periods, Figures 9-98 and 9-99 show the V/H ratios for 40 ft of soil at the two return periods, and Figures 9-100 and 9-101 show the V/H ratios for 60 ft of soil. The plotted V/H ratios are Gülerce and Abrahamson (2011) – GK11, Stewart et al. (2015) over Boore et al. (2014) – SBSA15/BSSA14, Bozorgnia and Campbell (2015) over Campbell and Bozorgnia (2014) – BC15/CB14, and Bommer et al. (2011) – BSK11. Normal faulting V/H ratios are computed for all relationships. The average of the four V/H ratios is also shown on each figure.

Figure 9-102a shows the average V/H ratios for the ATR Rock site conditions. The results for the two return periods are very similar, with a slightly higher peak in the V/H ratios for the 10,000-year return period. The black curve indicates the recommended V/H ratio. Figures 9-102b, 9-103a, and 9-103b show the average V/H ratios for ATR soil depths of 20, 40, and 60 ft, respectively. The V/H ratios for each soil depth are also similar for the two return periods and a single recommended curve is developed for each soil depth. The differences in the V/H ratios across the three soil depths are significant enough that a single soil relationship was not developed as was done for the SFHP site. The recommended V/H ratios are listed in Table 9-6.

Table 9-6. Recommended V/H ratios for ATR Site for return periods of 2,500 to 10,000 yrs.

Ground Motion Frequency (Hz)	Vertical to Horizontal (V/H) Ratio			
	ATR Rock	ATR Soil Depth 20 ft	ATR Soil Depth 40 ft	ATR Soil Depth 60 ft
PGA (100)	0.650	0.620	0.600	0.600
50	0.680	0.635	0.610	0.610
33.3	0.710	0.680	0.660	0.660
20	0.740	0.735	0.750	0.750
13.3	0.710	0.710	0.730	0.730
10	0.690	0.680	0.690	0.690
6.67	0.637	0.580	0.580	0.580
5	0.600	0.525	0.520	0.510
4	0.600	0.530	0.510	0.500
3.33	0.630	0.540	0.500	0.500
2.5	0.660	0.560	0.500	0.500
2	0.680	0.575	0.510	0.500
1.33	0.700	0.620	0.550	0.510
1	0.730	0.680	0.600	0.560
0.667	0.750	0.705	0.630	0.590
0.5	0.770	0.740	0.670	0.630
0.333	0.817	0.790	0.720	0.690
0.25	0.850	0.810	0.760	0.710
0.2	0.850	0.830	0.770	0.725
0.133	0.850	0.830	0.770	0.725
0.1	0.850	0.830	0.770	0.725

a)

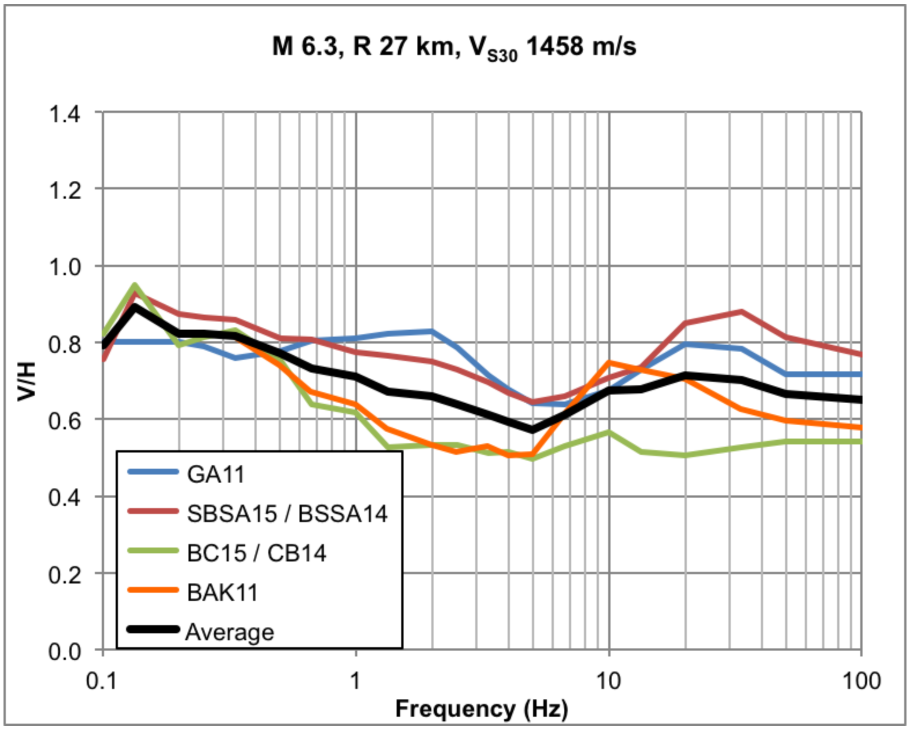

b)

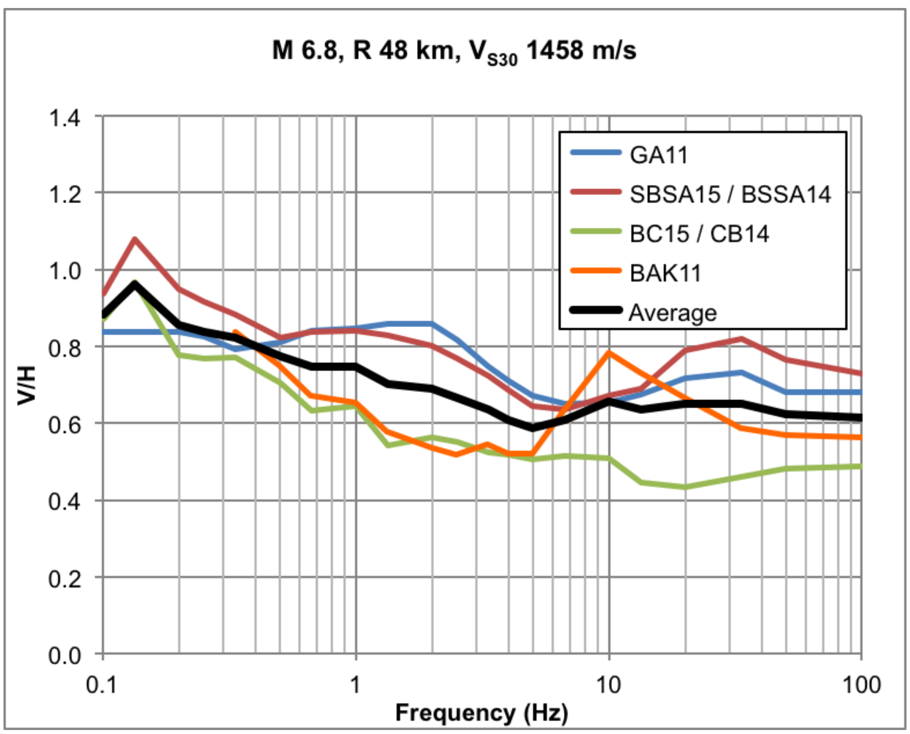

Figure 9-94. V/H ratios for ATR Rock for 2,500-year return period: a) high frequency controlling earthquake; and b) low frequency controlling earthquake.

a)

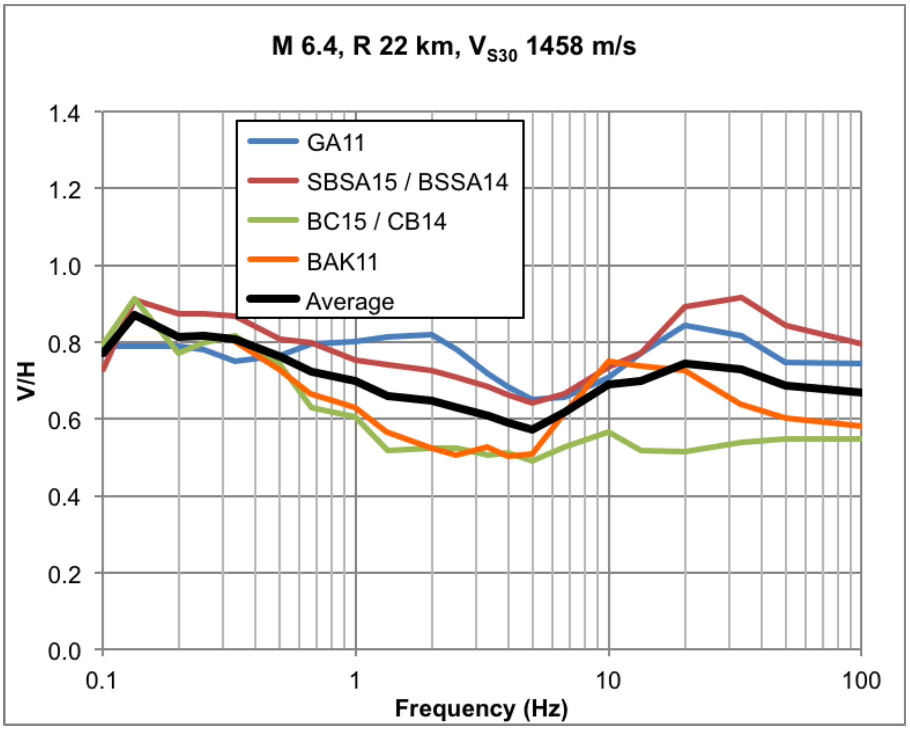

b)

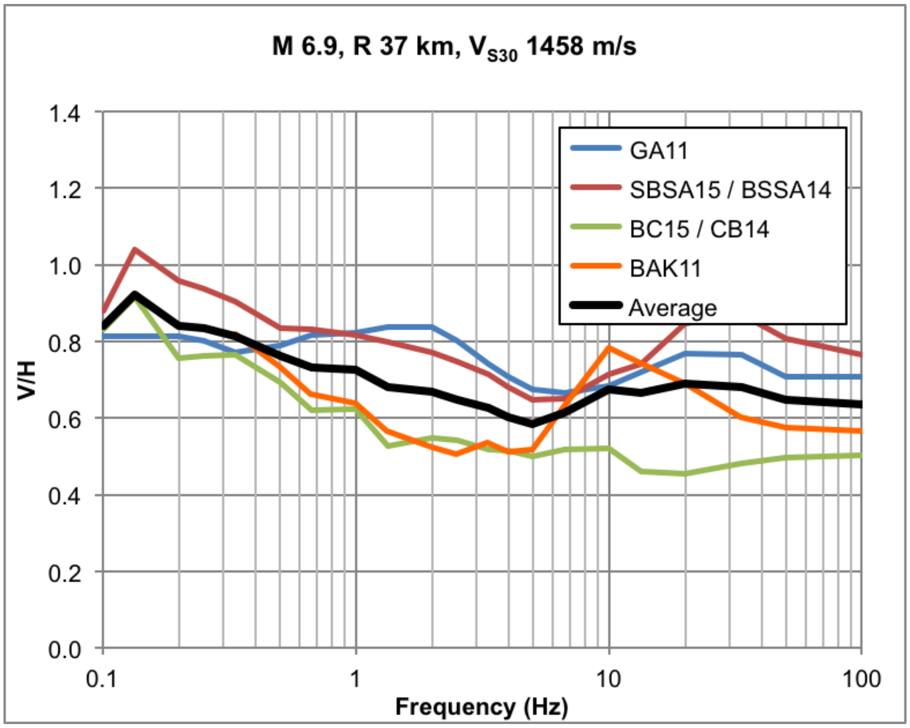

Figure 9-95. V/H ratios for ATR Rock for 10,000-year return period: a) high frequency controlling earthquake; and b) low frequency controlling earthquake.

a)

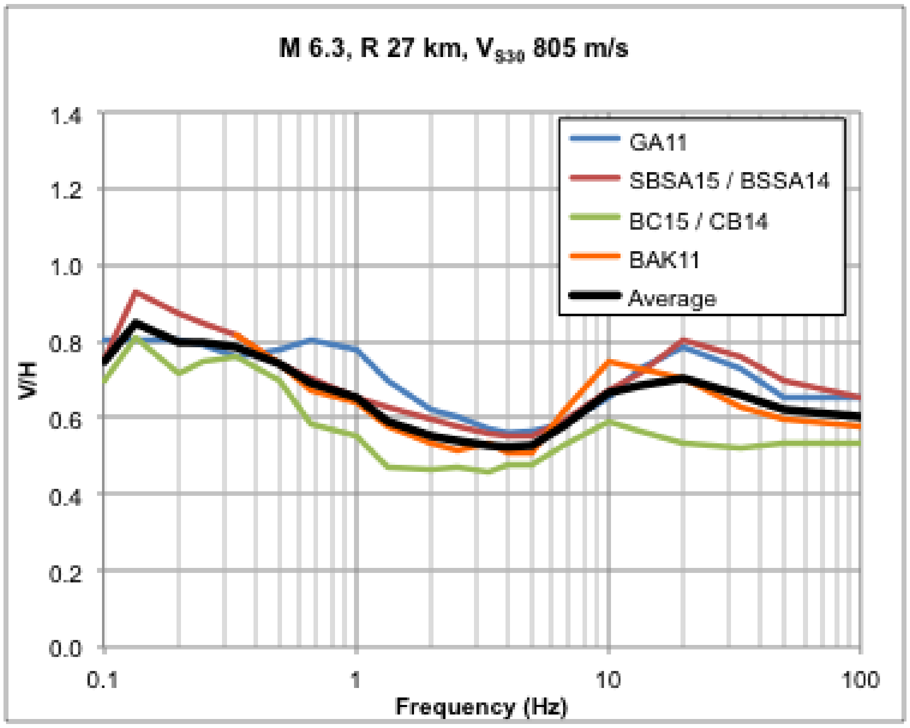

b)

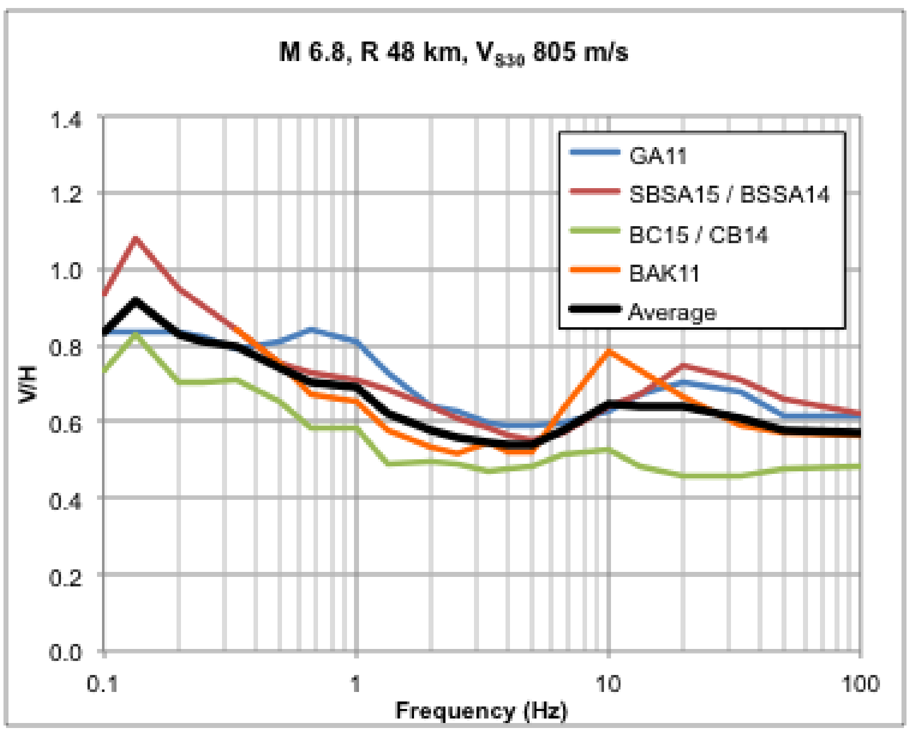

Figure 9-96. V/H ratios for ATR 20-ft Soil Depth for 2,500-year return period: a) high frequency controlling earthquake; and b) low frequency controlling earthquake.

a)

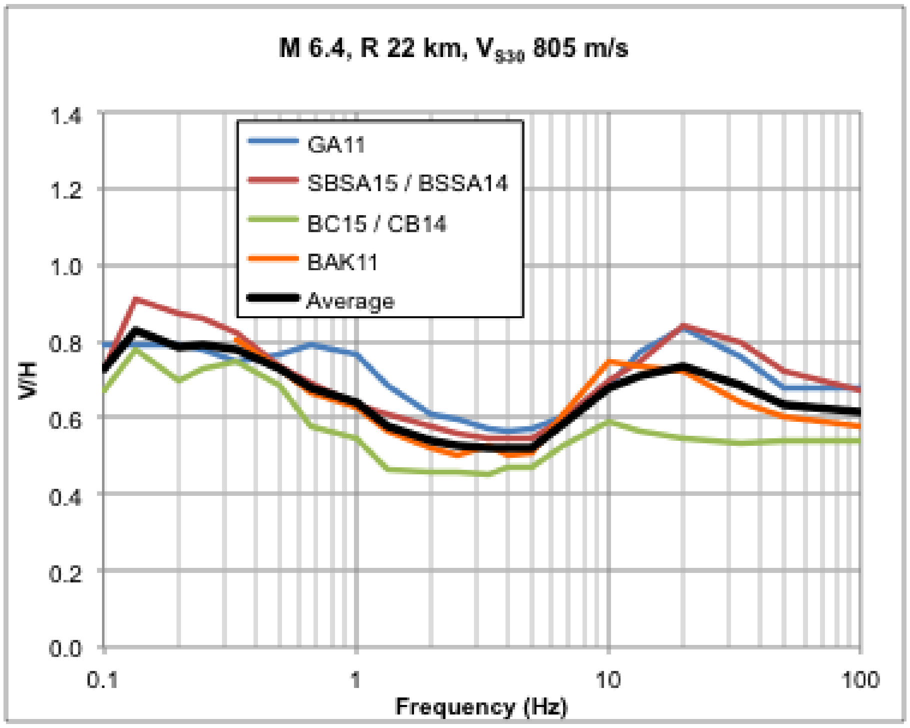

b)

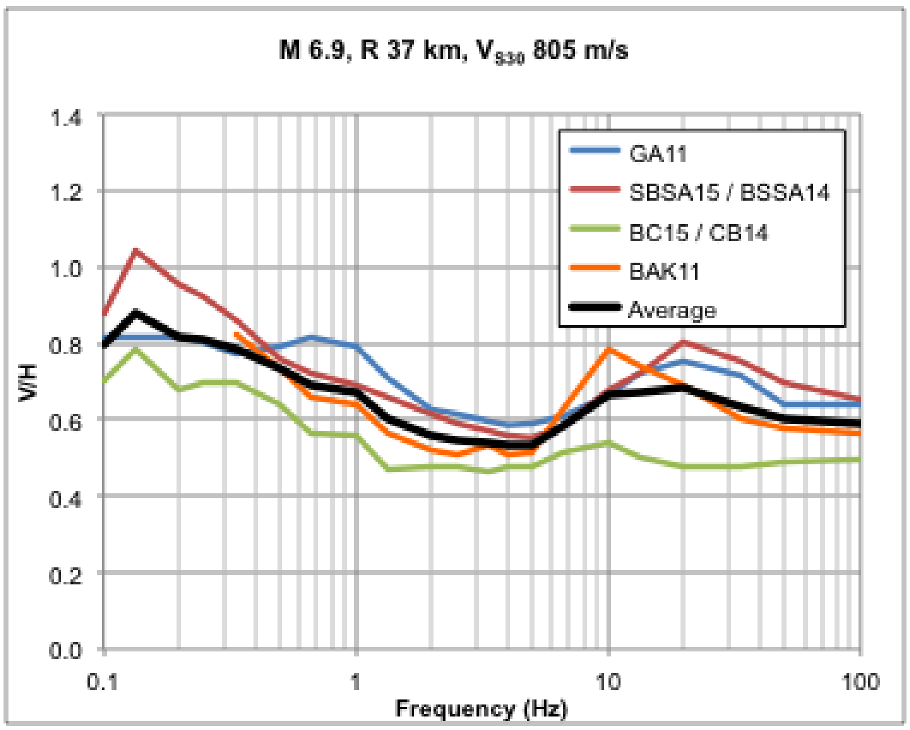

Figure 9-97. V/H ratios for ATR 20-ft Soil Depth for 10,000-year return period: a) high frequency controlling earthquake; and b) low frequency controlling earthquake.

a)

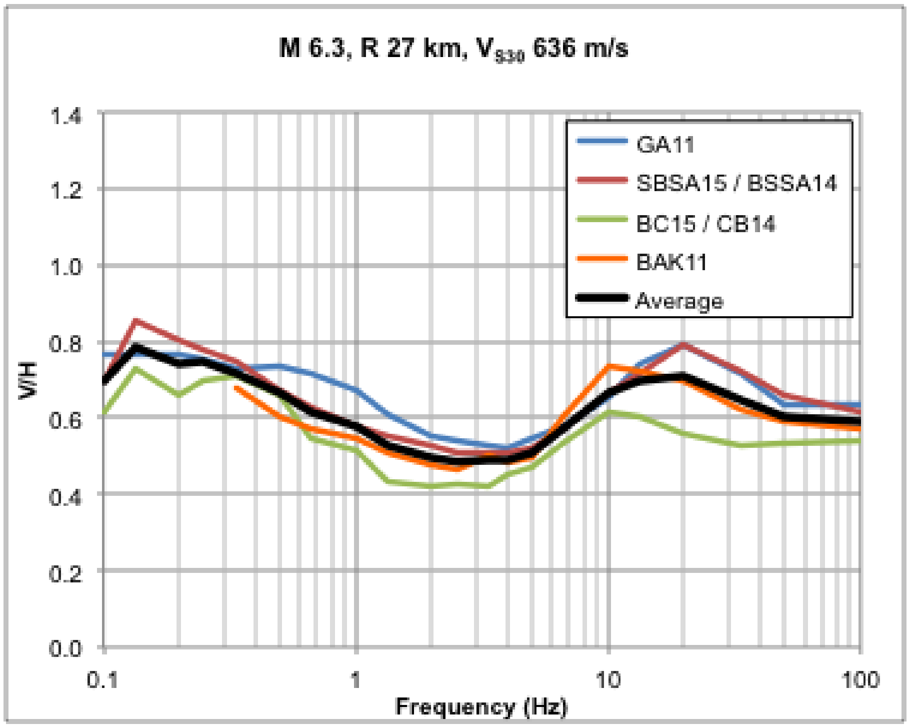

b)

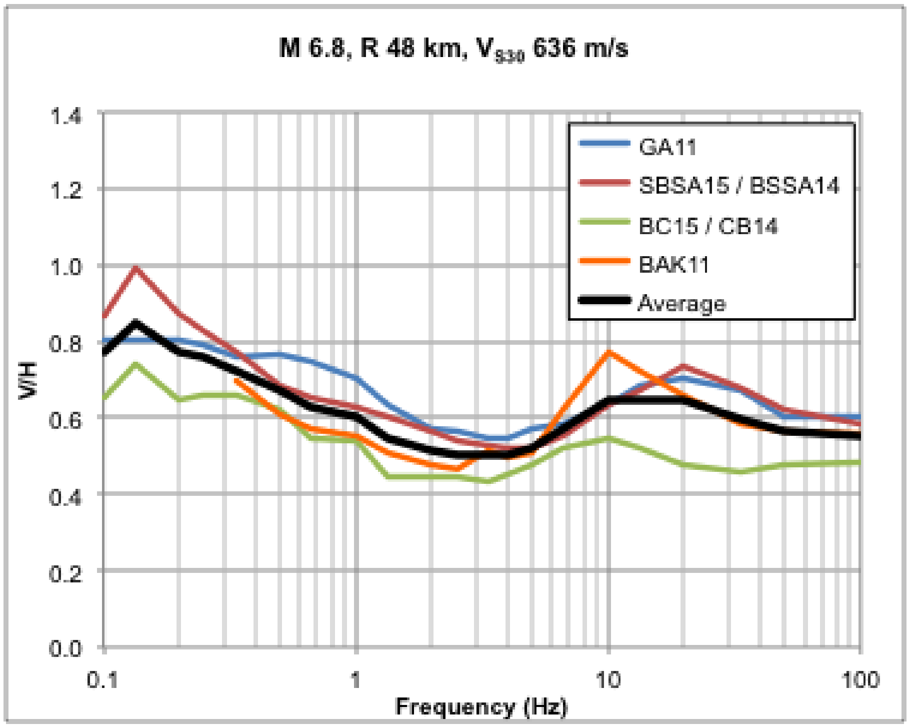

Figure 9-98. V/H ratios for ATR 40-ft Soil Depth for 2,500-year return period: a) high frequency controlling earthquake; and b) low frequency controlling earthquake.

a)

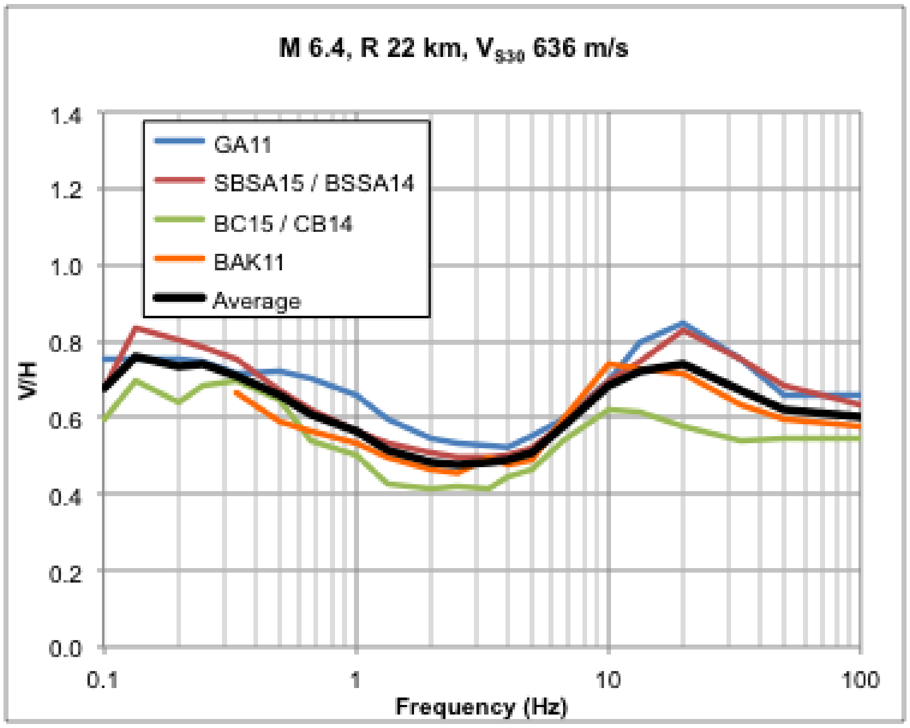

b)

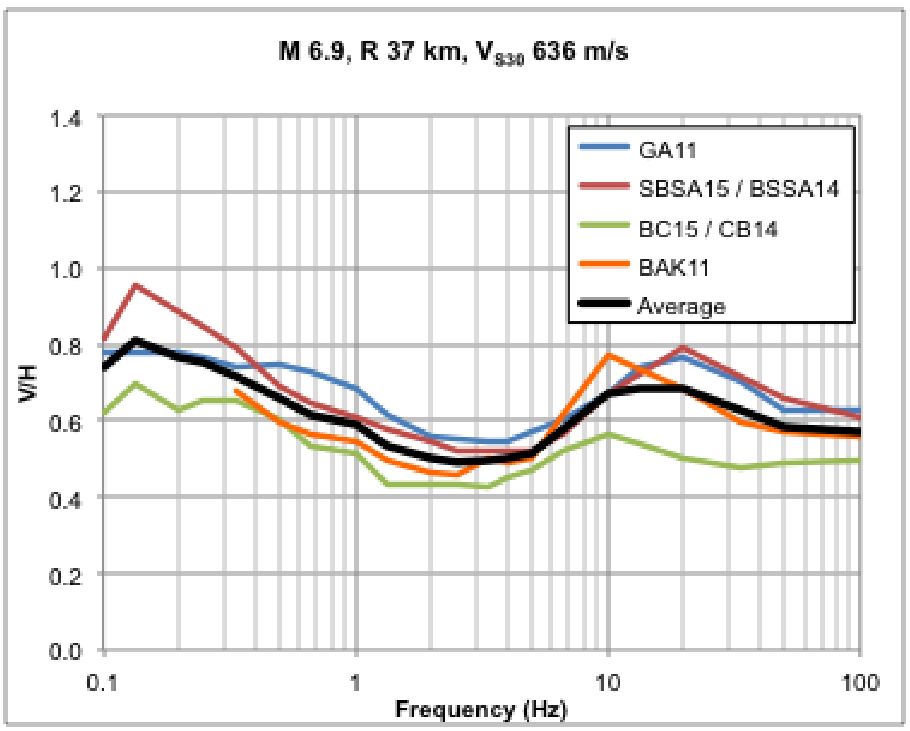

Figure 9-99. V/H ratios for ATR 40-ft Soil Depth for 10,000-year return period: a) high frequency controlling earthquake; and b) low frequency controlling earthquake.

a)

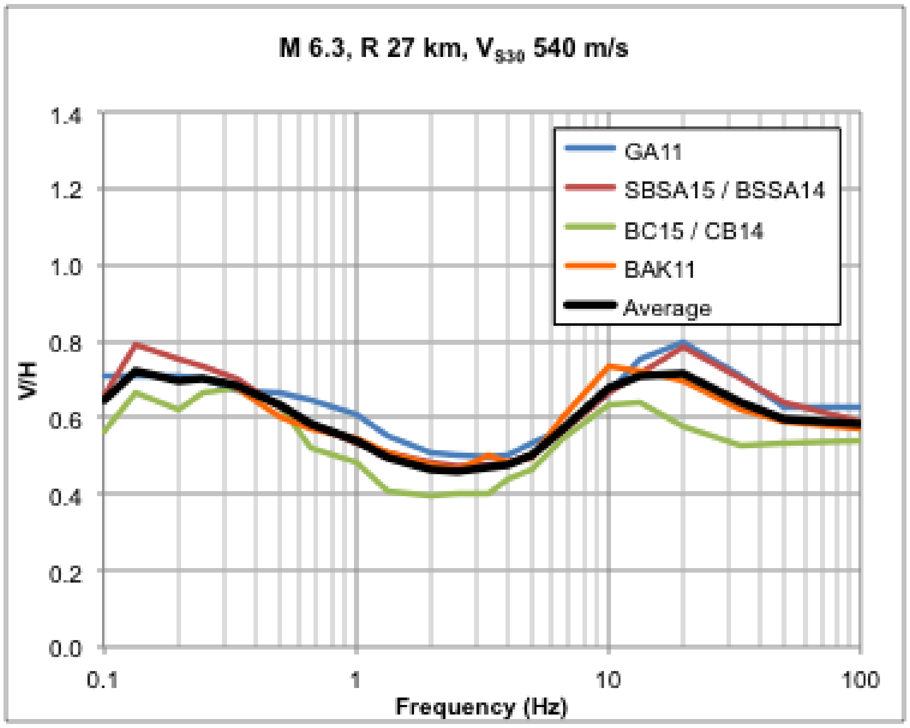

b)

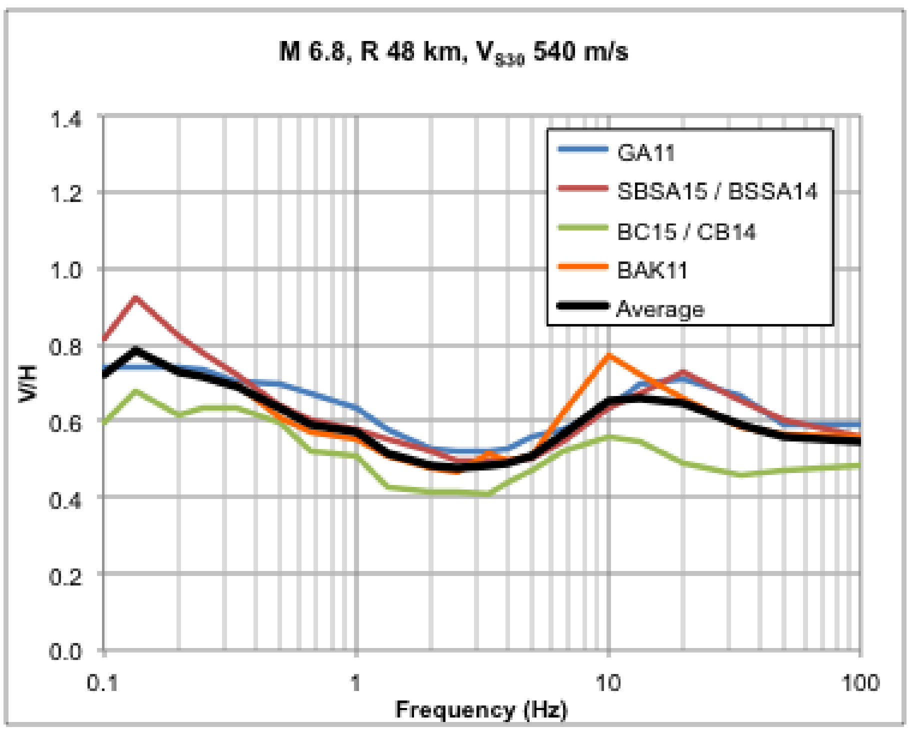

Figure 9-100. V/H ratios for ATR 60-ft Soil Depth for 2,500-year return period: a) high frequency controlling earthquake; and b) low frequency controlling earthquake.

a)

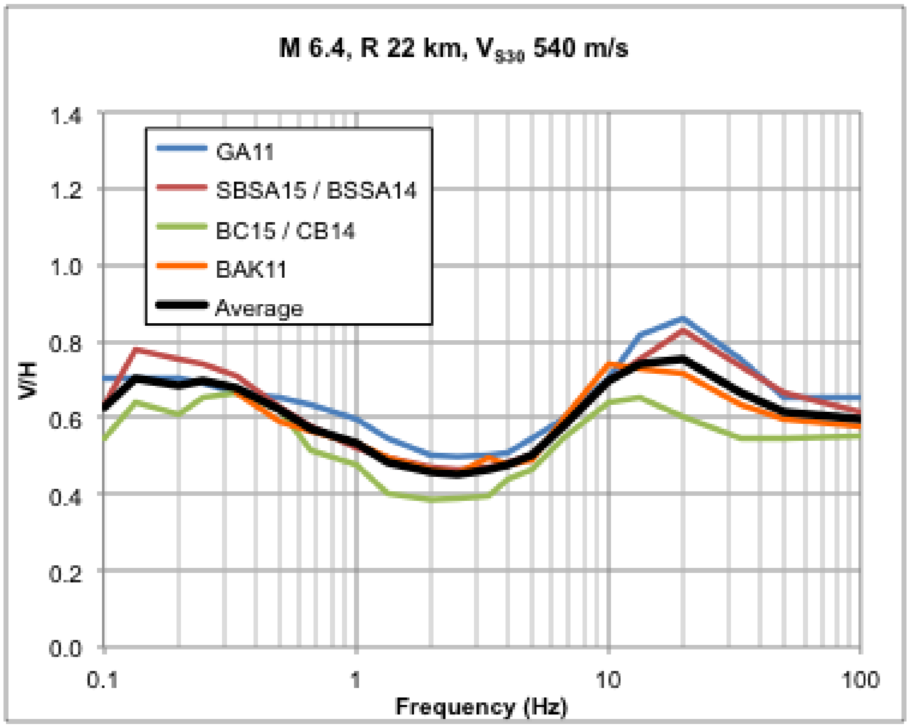

b)

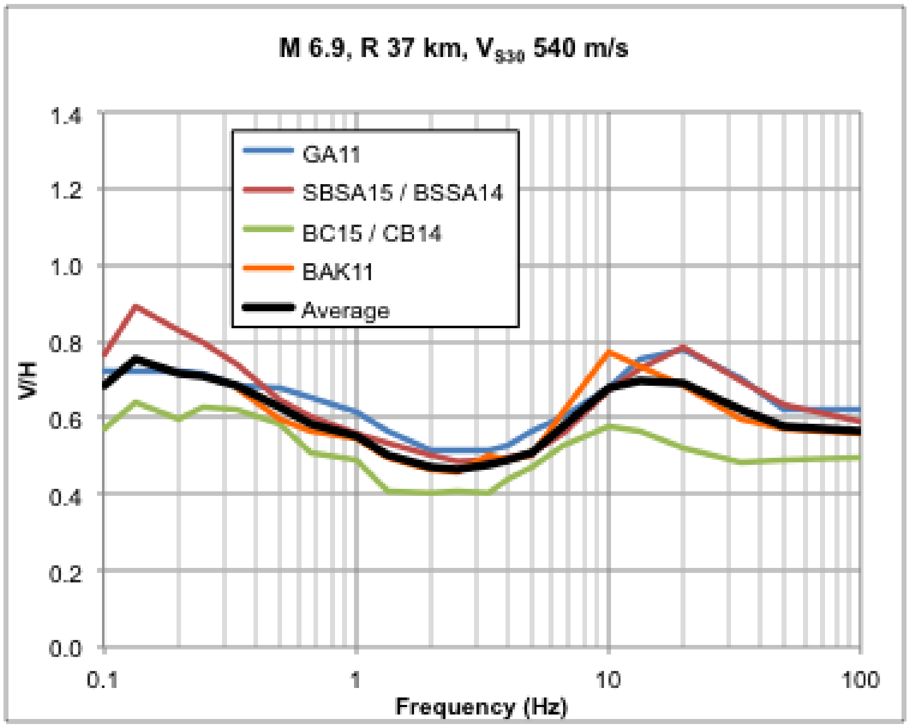

Figure 9-101. V/H ratios for ATR 60-ft Soil Depth for 10,000-year return period: a) high frequency controlling earthquake; and b) low frequency controlling earthquake.

a)

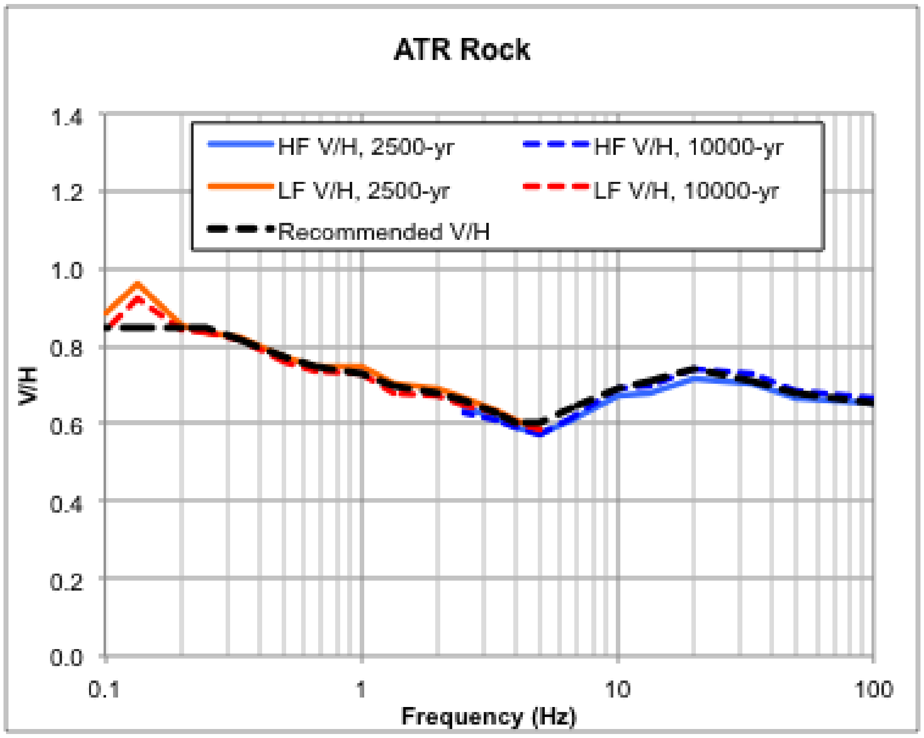

b)

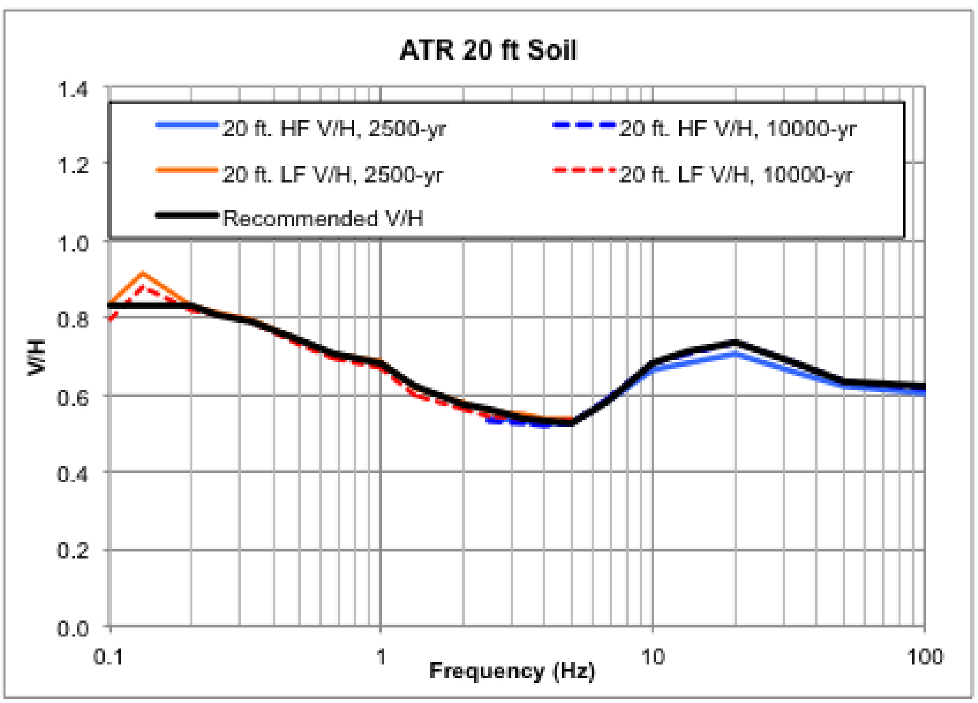

Figure 9-102. Recommended V/H ratios for: a) ATR Rock; and b) ATR 20-ft Soil Depth.

a)

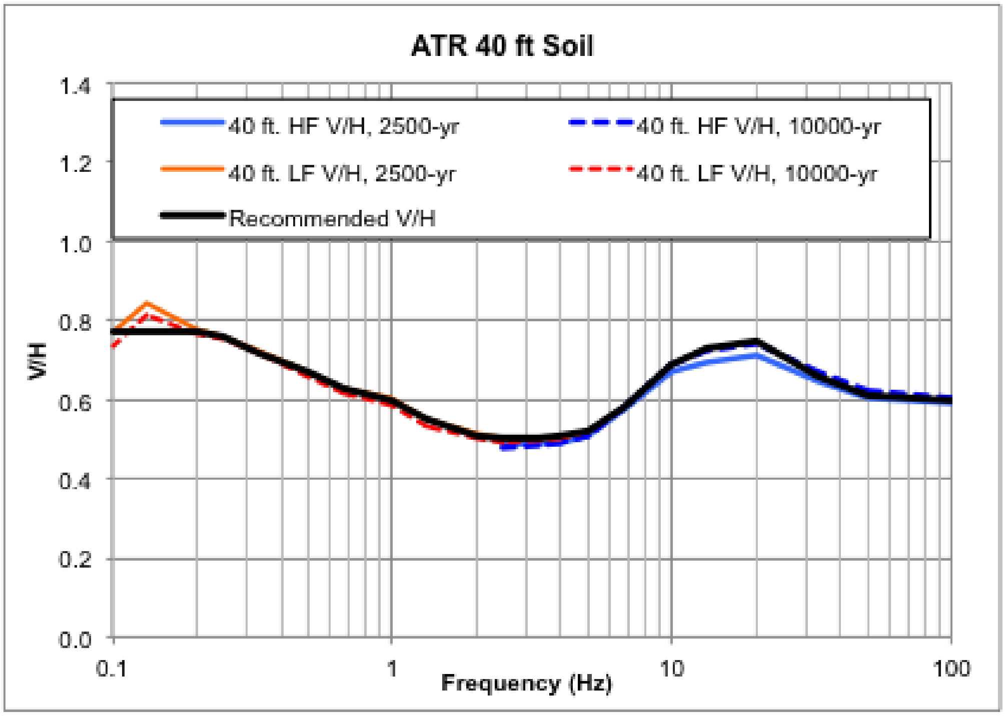

b)

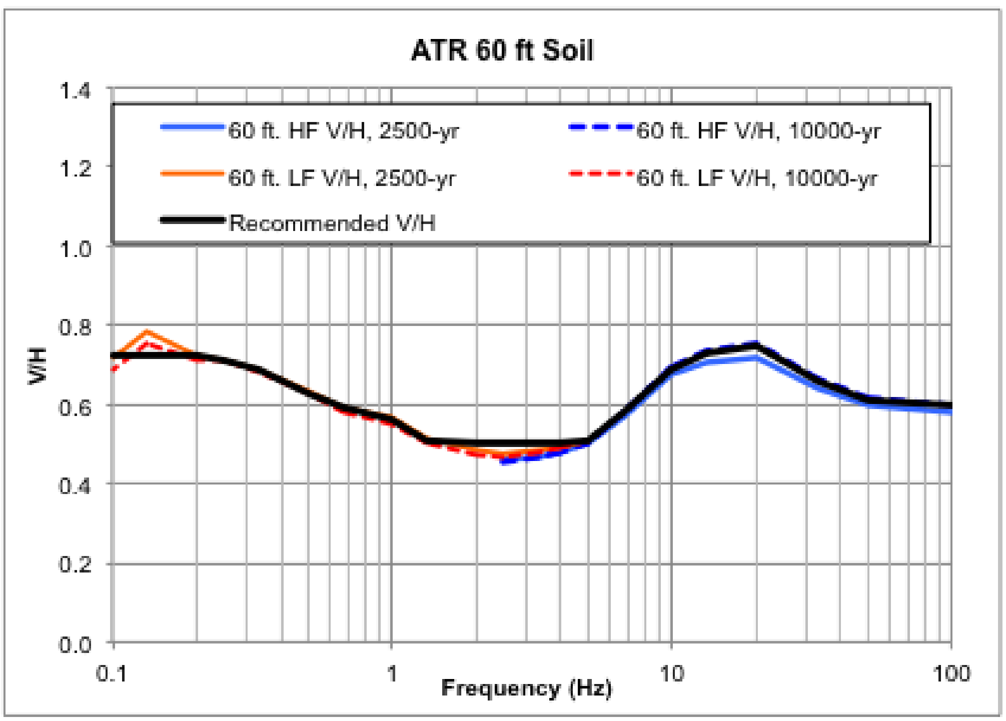

Figure 9-103. Recommended V/H ratios for: a) ATR 40-ft Soil Depth; and b) ATR 60-ft Soil Depth.

10. Hazard Calculations and Results

This section describes the seismic hazard calculations resulting from the implementation of the comprehensive seismic hazard model described in the previous chapters. The results shown in this section are based on hazard calculations performed for PGA and spectral acceleration at ground motion frequencies including: 50, 33.3, 20, 13.3 10, 6.67, 5, 3.33, 2.5, 2, 1, 0.5, and 0.1 Hz (structural periods of 0.02, 0.03, 0.05, 0.075, 0.1, 0.15, 0.2, 0.3, 0.4, 0.5, 1, 2, and 10 seconds). PGA is plotted at 100 Hz (0.01-sec) on all response spectra plots. Hazard results are provided for AEFs in the range of 10^{-2} to 10^{-8}. Section 10.1 describes the methodology used to calculate the seismic hazard, and offers details on the implementation of the seismic hazard model for INL.

For MFC and FMF, Section 10.2 presents the seismic hazard results for SWUS reference site condition at the MFC site. Results include mean and 5^{th}, 15^{th}, 50^{th}, 85^{th}, 95^{th} percentiles seismic hazard curves; source contributions; sensitivity analyses of various elements of the GMC and SSC inputs based on results at 10 Hz (0.1-sec), and 2 Hz (0.5-sec) spectral accelerations; and deaggregation of the mean hazard in terms of magnitude and distance. Sections 10.3 and 10.4 present the approach to obtain site-specific hazard and the results for MFC (rock) and FMF (soil). Site specific results include: mean and 5^{th}, 15^{th}, 50^{th}, 85^{th}, 95^{th} percentiles seismic hazard curves, UHS developed from the mean and fractile hazard curves for return periods of 2,500, 10,000, 25,000 and 100,000 yr, and the design GMRS. The fractiles of the site-specific hazard for MFC and FMF represent the uncertainty in the hazard resulting from the uncertainty in the transfer functions from the SWUS reference site conditions. The results are compared to hazard curves and UHS from the 1996 INL PSHA (Woodward-Clyde Federal Services et al., 1996) for rock conditions at MFC, and to the FMF DBGM, which is defined as the horizontal MFC 2,500 yr site-specific DBE 5% damped spectrum modified to account for the effects of one soil layer (Sections 1.1.2 and 1.2.2).

For the SFHP at NRF, Section 10.5 presents the seismic hazard results and sensitivity for SWUS reference site condition at the SFHP site. Results include mean and 5^{th}, 15^{th}, 50^{th}, 85^{th}, 95^{th} percentiles seismic hazard curves; source contributions; sensitivity analyses of various elements of the GMC and SSC inputs based on results at 10 Hz (0.1-sec), and 1 Hz (1-sec) spectral accelerations; and deaggregation of the mean hazard in terms of magnitude and distance. Section 10.6 presents the approach to obtain site-specific hazard and the results for SFHP Rock and SFHP Soil (20 and 40 ft). Site specific results include: mean and 5^{th}, 15^{th}, 50^{th}, 85^{th}, 95^{th} percentiles seismic hazard curves, UHS developed from the mean and fractile hazard curves for return periods of 2,500, 10,000, 25,000 and 100,000 yr, and the design GMRS. The fractiles of the site-specific hazard for SFHP represent the uncertainty in the hazard resulting from the uncertainty in the transfer functions from the SWUS reference site conditions. The hazard results are compared with the design spectrum for the SFHP process facility.

For ATR Complex, Section 10.7 presents the seismic hazard results and sensitivity for SWUS reference site condition at the ATR Complex. Results include mean and 5^{th}, 15^{th}, 50^{th}, 85^{th}, 95^{th} percentiles seismic hazard curves; source contributions; sensitivity analyses of various elements of the GMC and SSC inputs based on results at 10 Hz (0.1-sec), and 2 Hz (0.5-sec) spectral accelerations; and deaggregation of the mean hazard in terms of magnitude and distance. Section 10.8 discusses the approaches used to obtain site-specific hazard and the results for rock and soil sites at the ATR Complex. Site specific results include: mean and 5^{th}, 15^{th}, 50^{th}, 85^{th}, 95^{th} percentiles seismic hazard curves, UHS developed from the mean and fractile hazard curves for return periods of 2,500, 10,000, 25,000 and 100,000 yr, and the design GMRS. The fractiles of the site-specific hazard for ATR rock and soil sites represent the uncertainty in the hazard resulting from the uncertainty in the transfer functions from the SWUS reference site conditions. The results are compared to the DBGMs for rock and soil sites at ATR (defined in Section 1.1.4).

10.1 Hazard Software and Hazard Runs

In probabilistic terms, seismic hazard is defined as the likelihood that various levels of ground motion will be exceeded at a site during a specified time period. It is commonly assumed that the occurrence of individual earthquake mainshocks can be represented as a Poisson process. Following the approach developed by Cornell and Van Marke (1969) and Cornell (1971), the probability that at a given site a ground motion parameter, *Z*, will exceed a specified level, *z*, during a specified time period, *T*, is given by the following expression:

$$P(Z > z) = 1 - exp\{-\nu(z)T\} \leq \nu(z)T \qquad [10\text{-}1]$$

where $\nu(z)$ is the average frequency during time period *T* at which the level of ground motion parameter *Z* exceeds level *z* at the site resulting from earthquakes on all sources in the region.

The inequality at the right of Equation (10-1) is valid regardless of the appropriate probability model for earthquake occurrence, and $\nu(z) \cdot T$ provides an accurate and slightly conservative estimate of the hazard for probabilities of 0.1 or less, provided $\nu(z)$ is the appropriate value for the time period of interest.

The frequency of exceedance, $\nu(z)$, is a function of the uncertainty in the time, size, and location of future earthquakes and the uncertainty in the level of ground motions they may produce at the site. It is computed by the following expression:

$$\nu(z) = \sum_{n=1}^{N} \alpha_n(m^0) \int_{m=m^0}^{m^u} f_n(m) \left[\int_{r=0}^{\infty} f_n(r|m) \cdot P(Z > z|m,r)dr \right] dm \qquad [10\text{-}2]$$

where $\alpha_n(m^0)$ = is the frequency of earthquakes on source *n* above a minimum magnitude of engineering significance, m^0;

$f_n(m)$ = is the probability density function for event size on source *n* between m^0 and a maximum event size for the source, m^u;

$f_n(r|m)$ = is the probability density function for distance to earthquake rupture on source *n*, which is usually conditional on the earthquake size; and

$P(Z>z|m,r)$ = is the probability that, given a magnitude *m* earthquake at a distance *r* from the site, the ground motion exceeds level *z*.

In the AMECFW computer codes, the double integral in Equation (10-2) is replaced by a double summation with the density functions $f_n(m)$ and $f_n(r|m)$ replaced by discretizations of their corresponding cumulative functions in the following expression:

$$\nu(z) = \sum_{n=1}^{N} \sum_{m_i=m^0}^{m_i=m^u} \lambda_n(m_i) \cdot \left[\sum_{r_j=r_{min}}^{r_j=r_{max}} P(R = r_j|m_i) \cdot P(Z > z|m_i, r_j) \right] \qquad [10\text{-}3]$$

where $\lambda_n(m_i)$ = is the frequency of earthquakes of magnitude *i*on source *n*;

$P(R=r_j|m_i)$ = is the probability that a given magnitude m_i will occur at distance *j*.

The relative frequency of various magnitude earthquakes is allowed to take on a number of forms for the complementary cumulative function $N(m)$, the frequency of events with magnitude $\geq m$. The forms used in the INL seismic hazard model are described in the earthquake recurrence subsections of Section 8.The minimum magnitude m^0 is set to magnitude 5 in the hazard calculations.

The conditional probability distribution for distance from the earthquake rupture to the site, $P(R=r_j \mid m_i)$, is computed numerically. The basic computational procedure is to construct earthquake rupture polygons and then place these on the earthquake source. At each rupture location the program calculates the distance measures used by the GMPE. Details about the calculation of $P(R=r_j \mid m_i)$ for the types of sources in the hazard model are given below.

Fault sources are modeled as segmented planar surfaces. Earthquake ruptures are modeled as rectangular shapes. Following the discussion in Section 8.2.1.5 and in the SSC HID, the relationship between the logarithm of rupture area (RA) and magnitude is defined as follows:

$$\begin{cases} \ln(RA) = C_{3a} + C_{4a} m & for\ m \leq m_c \\ \ln(RA) = C_{3b} + C_{4b} m & for\ m > m_c \end{cases} \qquad [10\text{-}4]$$

and the relationship between magnitude and the logarithm of aspect ratio as follows:

$$\log_{10}(AR) = ar_1 \left[max(m-4,0)\right]^{ar_2} \qquad [10\text{-}5]$$

where aspect ratio (AR) is defined as rupture length (RL) divided by rupture width (RW).

The program limits ruptures to the defined fault plane: if the calculated value for RW exceeds the fault width, it is set equal to the fault width and the value of rupture length is computed by dividing the rupture area from (Equation 10-4) by the fault width. The resulting value of RL is limited to the total length of the fault. In the hazard calculations, earthquake ruptures are moved along the fault plane surface using a 1-km increment, and ruptures are assumed to have equal probability of location along the strike of the fault. For each earthquake magnitude, a distribution for the downdip location of ruptures is computed by convolving a distribution for focal depth with a distribution for location of the hypocenter within the ruptures. This model is applied to all fault sources except Madison, Grand Valley, and Wasatch faults.

As described in Section 8.3.9 and in the SSC HID, the Madison, Grand Valley and Wasatch fault sources consist of multiple fault segments where the segment boundaries are not boundaries to ruptures, but represent changes in the slip rate and/or dip of the fault along the fault length. The difference from the previous, simpler, model is that each fault panel is characterized by a slip-rate factor, which is used to adjust the relative likelihood of ruptures at each location, so that segments with higher slip rates will have more likelihood of ruptures than segments with lower slip rates. The fault is again represented by a series of trapezoid panels, with the top and bottom edges parallel to the ground surface but the panels may have differing dips, and thus differing widths. The fault surface is divided into quadrilateral rupture cells of approximately equal area. Each earthquake rupture is composed of the number of cells for which the sum of the cell area most closely matches the rupture area given by Equation (10-4). Rupture locations are again incrementally placed along the length of the fault, and at each location along strike, the slip-rate factor and fault width are averaged over the rupture length. The product of these two values is a measure of the relative moment release rate at that rupture location. The process is repeated at each possible location along strike and the resulting values are normalized to sum to 1.0 to provide the distribution for rupture location along strike. The distribution for downdip location is computed as described above, using a distance increment of 1 km for all faults.

The calculation of $P(R=r_j \mid m_i)$ for the tectonic and volcanic source zones uses a grid of equally spaced points. For each source zone the fraction of earthquake ruptures that occur at each grid point is specified along the reference depth for the grid point as either a uniform spatial density or a kernel density according to the directions provided in the SSC HID. The kernel density is specified using a Gaussian density function with relative shape parameters specified in each case. The technique applied in this project is the adaptive kernel smoothing presented by Stock and Smith (2002), in which the kernel size is adjusted throughout the region so that the smoothing distance *h* is small in areas where there is a higher number of earthquake epicenters per unit area, and large in areas of sparse seismicity. The starting value of *h* was selected based on the optimum kernel size determined from seismicity data (e.g., Silverman 1986). The starting values of *h* for each combination of source zone and earthquake catalog are summarized in Table 10-1. As discussed in Section 6, the crustal earthquake catalog is declustered using four alternative methods, so for each of the source zones that require smoothing, four grids are produced. In the hazard calculations, the smoothed grids are paired to the recurrence rates obtained using the same declustered catalog.

In the preliminary phase of the PSHA, an exploratory analysis was conducted to determine the effect of uncertainty in the kernel smoothing on the hazard at the site. The test was done for zone ISB, which shows the highest contribution to the total seismic hazard at the site among the zones that have been smoothed. In the test nine alternative catalogs were simulated by randomly sampling nine points within each kernel. The nine points represent alternative epicentral locations for the same earthquake. The resulting nine catalogs were then smoothed using the adaptive kernel technique and the seismic hazard was calculated for each alternative. Results showed that the contribution of epistemic uncertainty in the kernel size is not a significant source of uncertainty in the hazard. The reason is that the zone has many earthquakes and they are closely located: the kernel size is, therefore, rather small and the alternative kernels are not very different from the original ones. Based on these results it was decided not to include the epistemic uncertainty on the kernel size as a node of the logic tree for the tectonic source zones.

The Cascadia interface is a large curved surface that does not have constant depth at the top or bottom. This surface is represented by a set of contiguous quadrilaterals, and is then divided into a grid of quadrilateral cells of approximately 1 km^2 in size. Earthquake ruptures are modeled as quasi-rectangular areas by combining sufficient cells to closely approximate the target magnitude-dependent rupture area and approximately represent the target magnitude-dependent aspect ratio. The relative likelihood of ruptures at each location is computed from the ratio of the average interface width along the rupture length compared to the overall average rupture width. This approximates the assumption of uniform likelihood over the area of the interface, with wider locations along strike having more likelihood of ruptures than narrower locations. The closest distance to the site is obtained as the minimum value for the cells that make up the rupture.

The PSHA calculations were performed using AMECFW software programs, which are verified by running test cases to assure that results of the software matched the anticipated results obtained with alternative calculations.

10.2 Seismic Hazard Results and Sensitivity for SWUS Reference Site Condition at at MFC and FMF

This section describes the seismic hazard results and the results of the sensitivity analyses conducted for the reference site condition of the SWUS ground motion models. From Section 9.0, the reference site condition for the SWUS models is a generic crustal profile represented by a time averaged shear wave velocity in the upper 30 m (V_{S30}) of 760 m/s, along with a reference level of shallow crustal damping, denoted by parameter kappa in the range of 0.037 to 0.045 sec (Section 9.3). Note that the reference site hazard computed at MFC is also valid at FMF because the distance between the sites is less than 1 km. Site-specific hazard results are presented in Section 10.4.

Results are presented in terms of seismic hazard curves showing the mean total hazard and the contribution of groups of sources (background zones, faults, volcanic zones, and the Cascadia intraslab source) to the total hazard. Individual source contribution plots are shown to help identify the zone(s) and fault(s) that contribute the most to the hazard; as discussed earlier, sensitivity analyses will be presented only for two spectral periods to provide the reader with an understanding of the key results.

Deaggregation analysis is used to identify the combination of magnitude and distance pairs that contribute the most to the total seismic hazard at the site. Results of the deaggregation are represented by histograms and are calculated at the same AEF as the UHS. Variance contribution histograms are used to show the relative contribution to the total epistemic variance in ground motions at a given AEF introduced by each element of the seismic hazard model logic tree. For a description of how these histograms are generated refer to the discussion in PNNL (2014), which also includes an example calculation.

10.2.1 Probabilistic Seismic Hazard at MFC for Reference Site Condition

The MFC site resides in the IVRZ volcanic source zone which is within the ESRP seismic source zone (see Figure 8-2). The coordinates of the site are listed in Table 10-2. Figures 10-1 through Figure 10-10 show the seismic hazard results at each of the 10 spectral periods analyzed. In each figure the top part shows the total mean and the 5th, 16th, 50th, 84th, and 95th percentile seismic hazard curves; the plot on the bottom part of the figure compares the total mean hazard with the mean hazard produced by the tectonic source zones (blue curve), the volcanic source zones (red curve), the fault sources (green curve), and the Cascadia interface source (purple curve). The tectonic source zones control the high-frequency hazard (PGA and spectral frequencies greater than 10 Hz). The fault sources are the primary contributors for low-frequency hazard (5 Hz and lower). The Cascadia interface contribution becomes noticeable only for spectral frequencies of 1 Hz or less.

Deaggregation of the total mean seismic hazard is shown in Figure 10-11 through Figure 10-14 for spectral frequencies at 10 Hz and 2 Hz (corresponding to spectral periods of 0.1- and 0.5-sec).Each figure contains histograms representing the percent contribution to the total mean seismic hazard from different magnitude-distance bins. Each histogram represents one AEF level: $4x10^{-4}$, 10^{-4}, $4x10^{-4}$, and10^{-5}. The deaggregation plots for 10 Hz (0.1-sec) spectral acceleration at the $4x10^{-4}$ and 10^{-4}AEF levels are similar, showing equal contribution to the total hazard from the Centennial Shear Zone (CSZ, small magnitudes at distance of 30 to 50 km) and from the faults (magnitudes of about 7 at distance of 30 to 50 km). At AEF of $4x10^{-5}$, and 10^{-5} the background seismicity from the ESRP host zone (small magnitudes at 0 to 20 km) and the contribution from fault sources within 50 km of the site are predominant. At these spectral frequencies the contribution of the Cascadia interface is negligible. Figure 10-15 shows the deaggregation plots for 0.5 Hz (2-sec) at two AEFs: $4x10^{-4}$ and $4x10^{-5}$. The largest contribution to the total hazard comes from the fault sources; the Cascadia interface shows only a small contribution at 2,500 yr return period ($4x10^{-4}$AEF).Sensitivity tests conducted in the preliminary phases of the analysis show that the Cascadia interface is an important contributor (approximately 10% contribution) to the seismic hazard for very long spectral periods, e.g., 0.1 Hz (10-sec) spectral acceleration.

Table 10-1. Values of the initial smoothing distance (*h*) used for the crustal background sources and each of four declustered catalogs.

Source Zone	Initial Smoothing Distance, *h* (km)			
	Catalog 1	Catalog 2	Catalog 3	Catalog 4
CTB	10	5	5	5
EZ	20	20	20	20
IB	20	20	20	20
ISB	10	10	5	10
NBR	10	10	5	10
NISB	10	10	10	10
CTB	10	5	5	5
CTB	10	5	5	5
EZ	20	20	20	20
IB	20	20	20	20

Table 10-2. Coordinates of the MFC and FMF sites.

Site	Latitude N (Degrees)	Longitude W (Degrees)
MFC	43.594172	-112.655228
FMF	43.593603	-112.653775

(a)

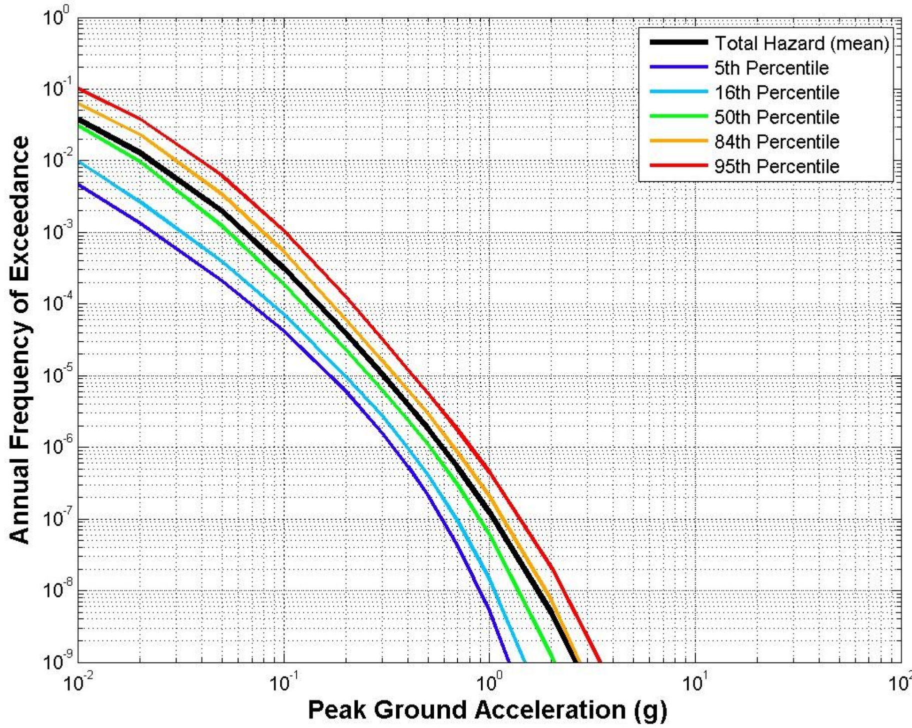

(b)

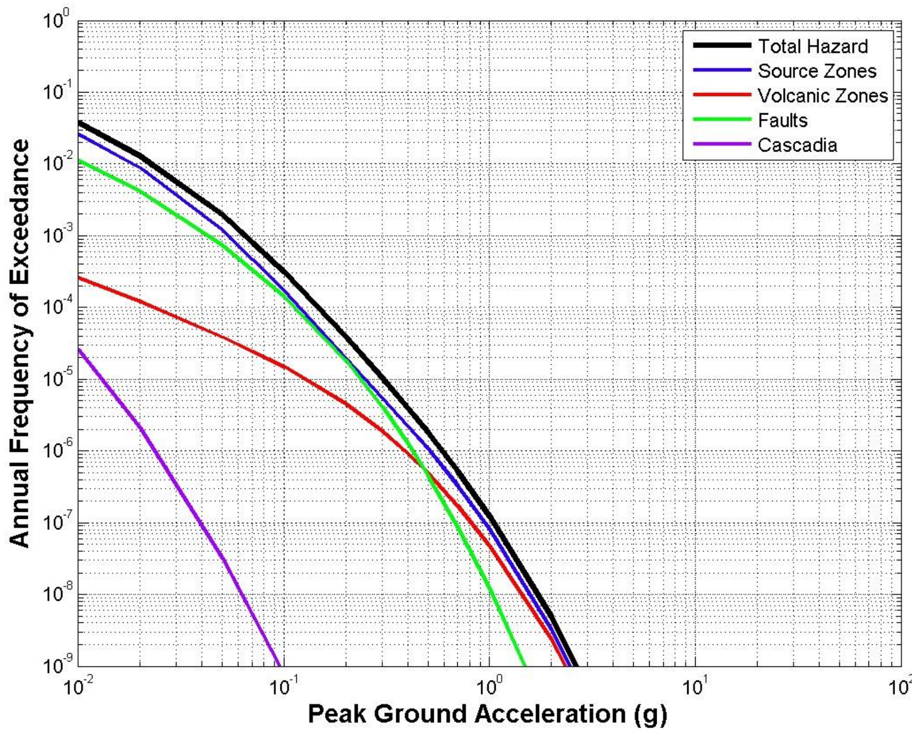

Figure 10-1. Seismic hazard results at MFC for SWUS reference site condition at PGA: a) total mean hazard and fractiles; and b) comparison between the total mean seismic hazard and the contribution of tectonic source zones, volcanic source zones, fault sources, and the Cascadia interface source.

(a)

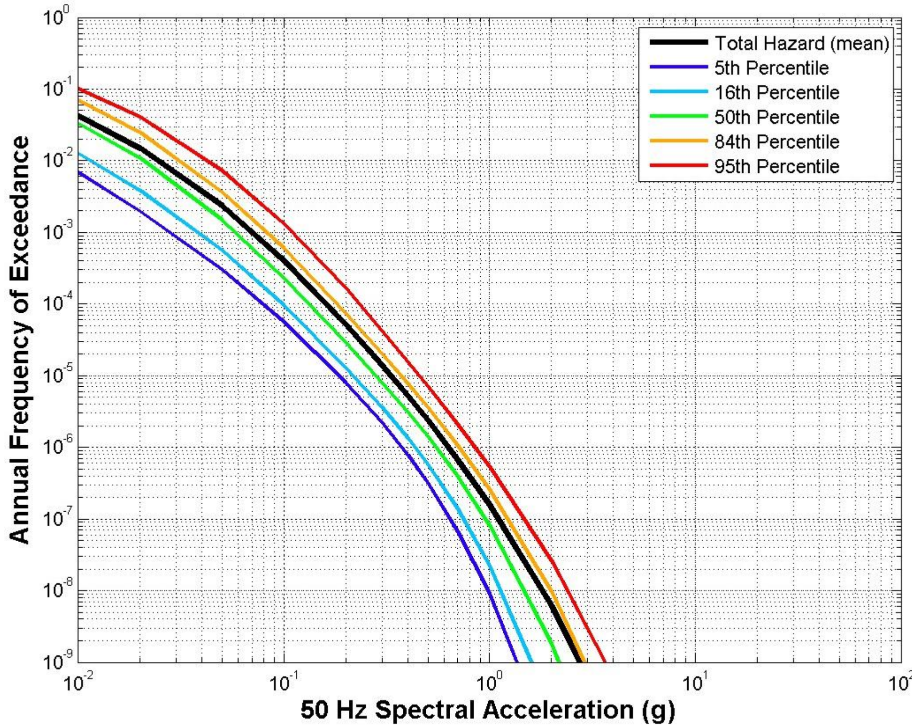

(b)

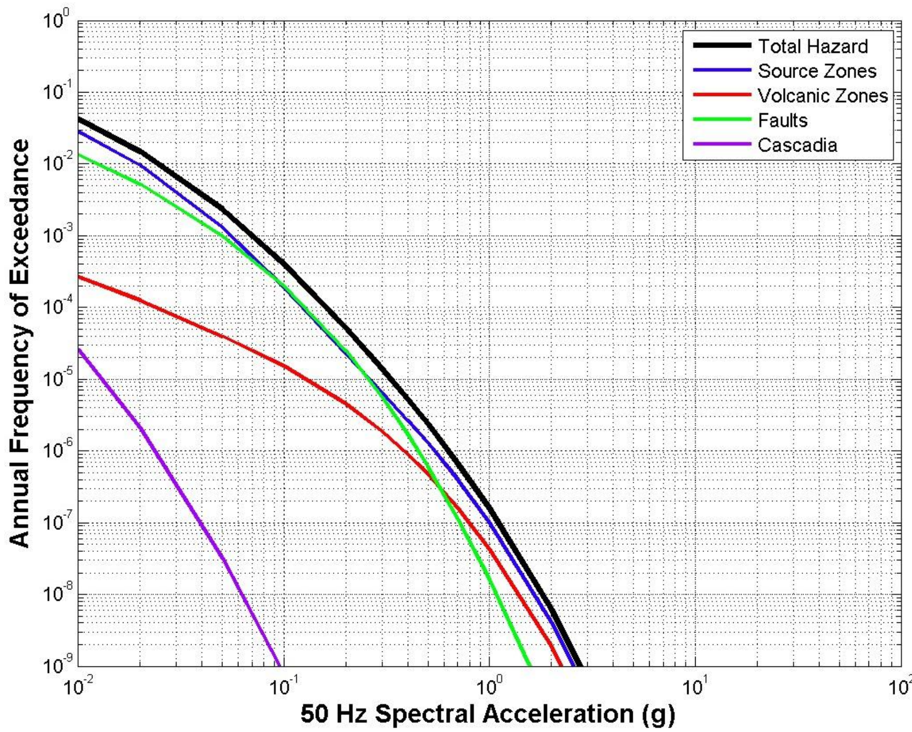

Figure 10-2. Seismic hazard results at MFC for SWUS reference site condition at 50 Hz (0.02-sec) spectral acceleration: a) total mean hazard and fractiles; and b) comparison between the total mean seismic hazard and the contribution of tectonic source zones, volcanic source zones, fault sources, and the Cascadia interface source.

(a)

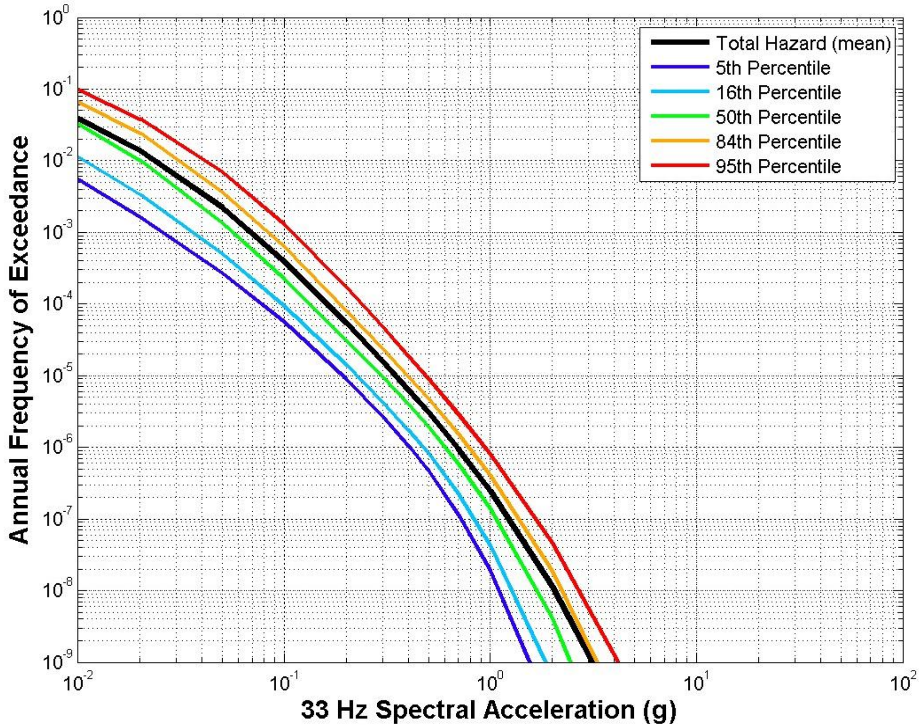

(b)

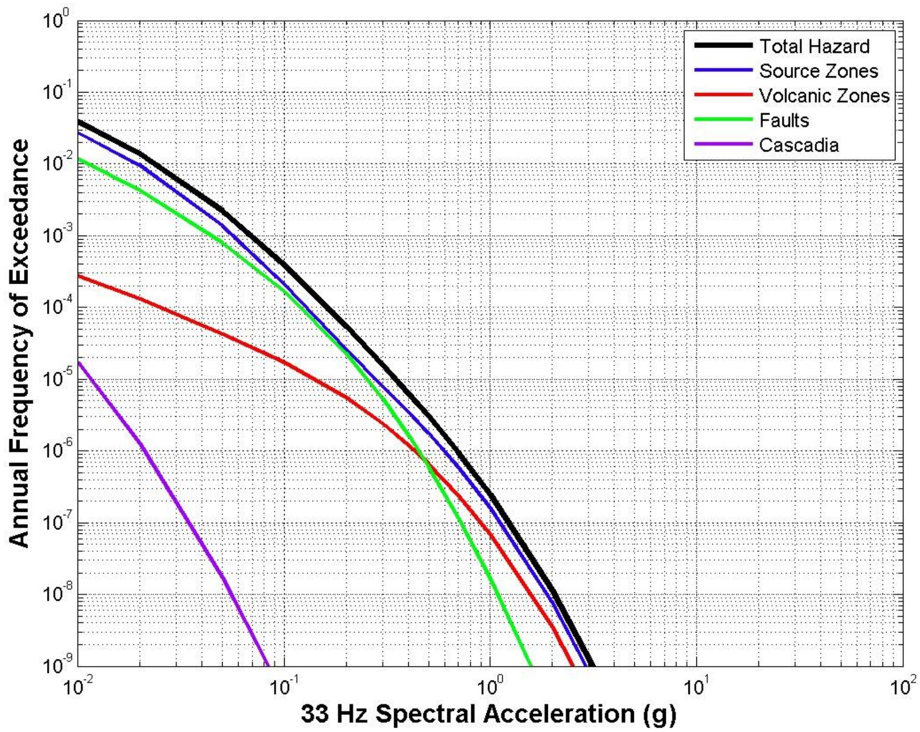

Figure 10-3. Seismic hazard results at MFC for SWUS reference site condition at 33 Hz (0.03-sec) spectral acceleration: a) total mean hazard and fractiles; and b) comparison between the total mean seismic hazard and the contribution of tectonic source zones, volcanic source zones, fault sources, and the Cascadia interface source.

(a)

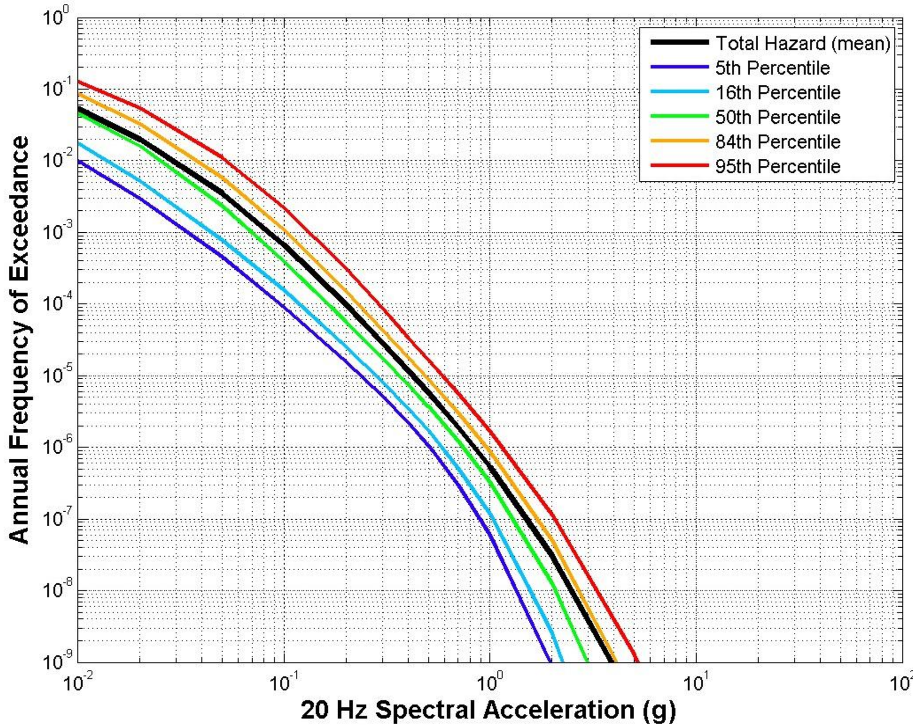

(b)

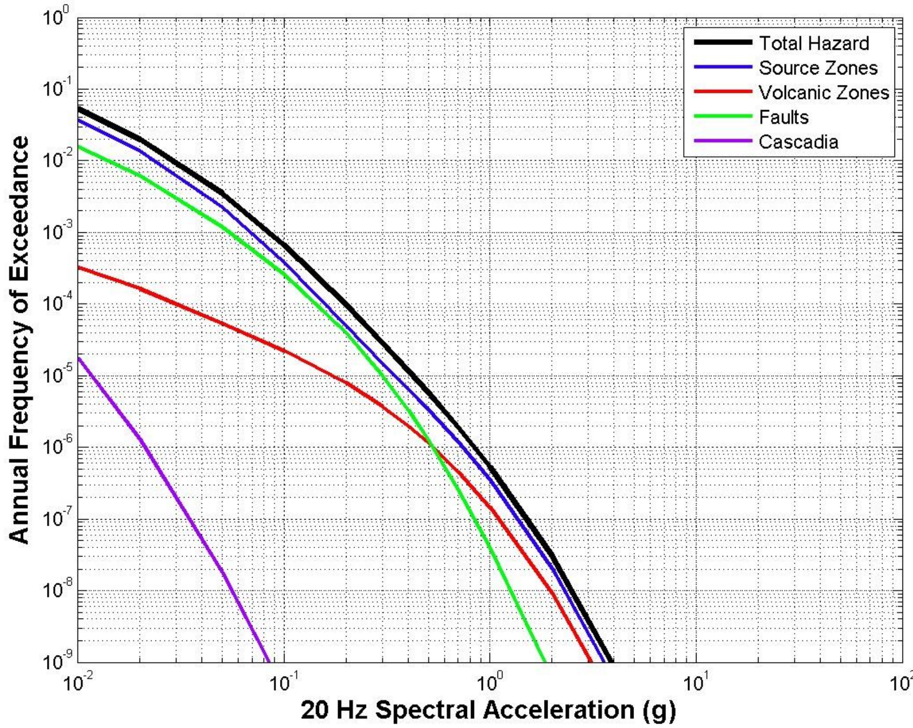

Figure 10-4. Seismic hazard results at MFC for SWUS reference site condition at 20 Hz (0.05-sec) spectral acceleration: a) total mean hazard and fractiles; and b) comparison between the total mean seismic hazard and the contribution of tectonic source zones, volcanic source zones, fault sources, and the Cascadia interface source.

(a)

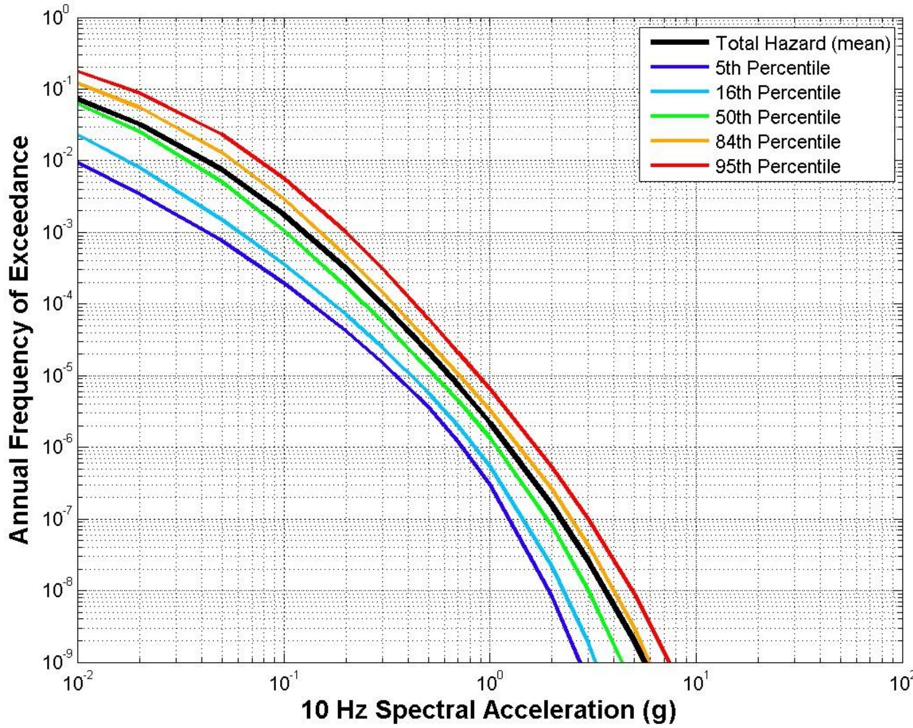

(b)

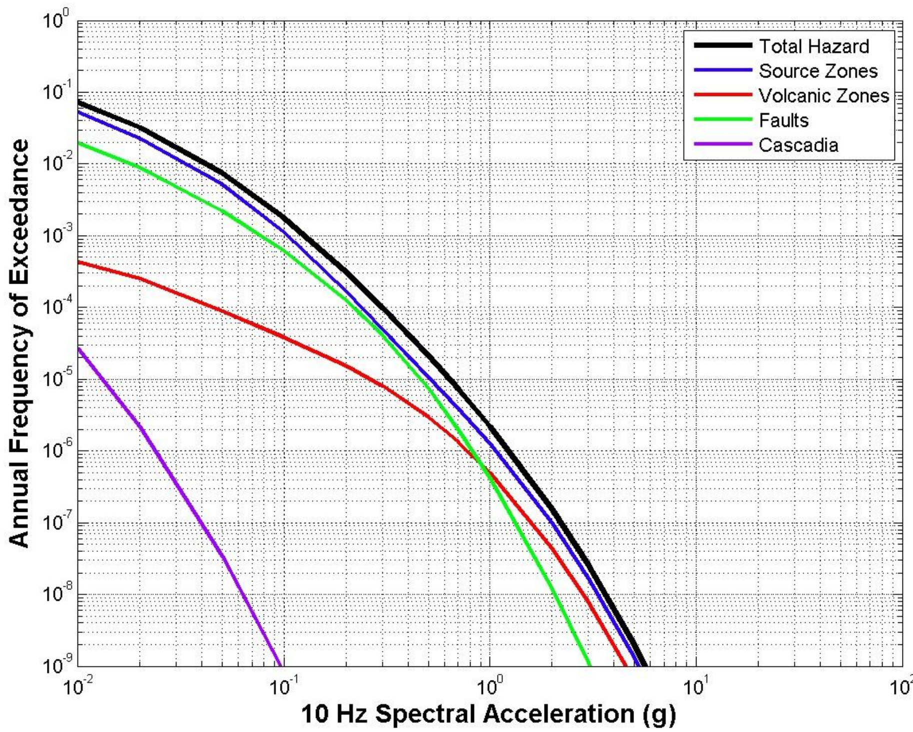

Figure 10-5. Seismic hazard results at MFC for SWUS reference site condition at 10 Hz (0.1-sec) spectral acceleration: a) total mean hazard and fractiles; and b) comparison between the total mean seismic hazard and the contribution of tectonic source zones, volcanic source zones, fault sources, and the Cascadia interface source.

(a)

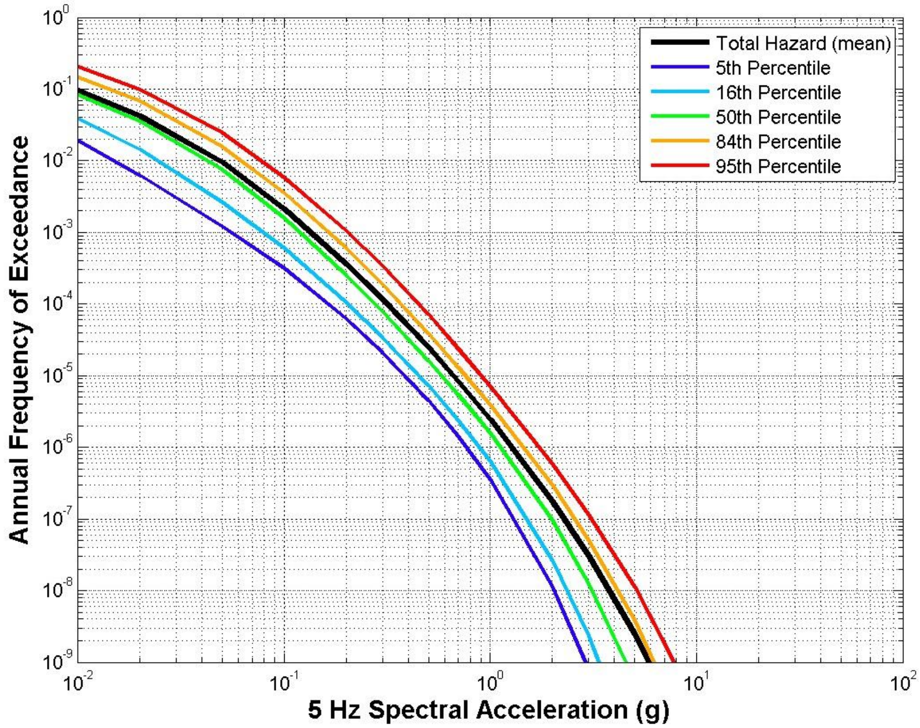

(b)

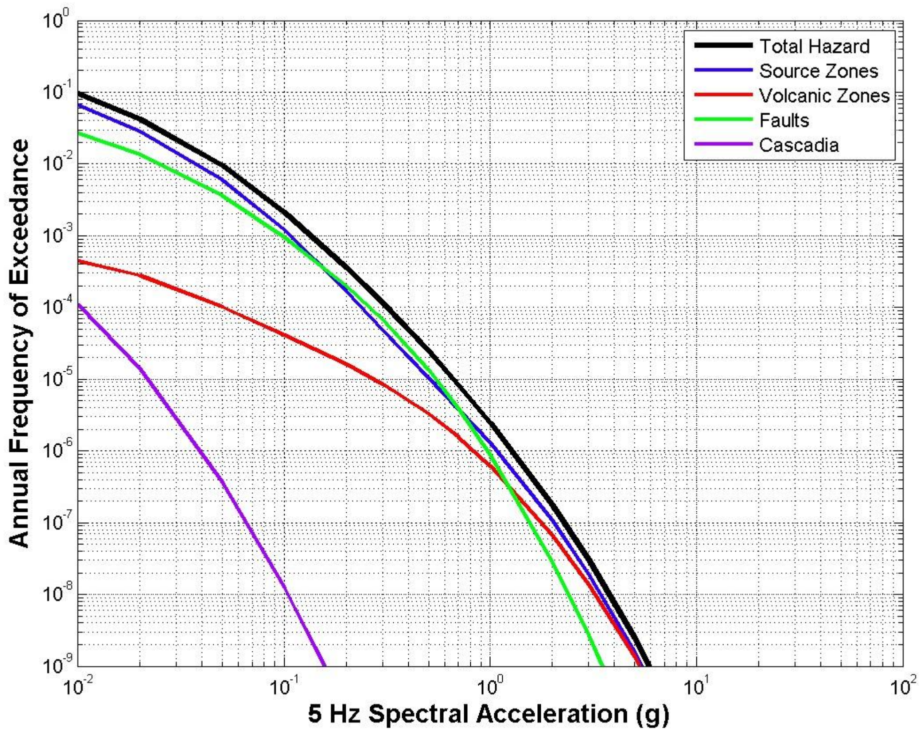

Figure 10-6. Seismic hazard results at MFC for SWUS reference site condition at 5 Hz (0.2-sec) spectral acceleration: a) total mean hazard and fractiles; and b) comparison between the total mean seismic hazard and the contribution of tectonic source zones, volcanic source zones, fault sources, and the Cascadia interface source.

(a)

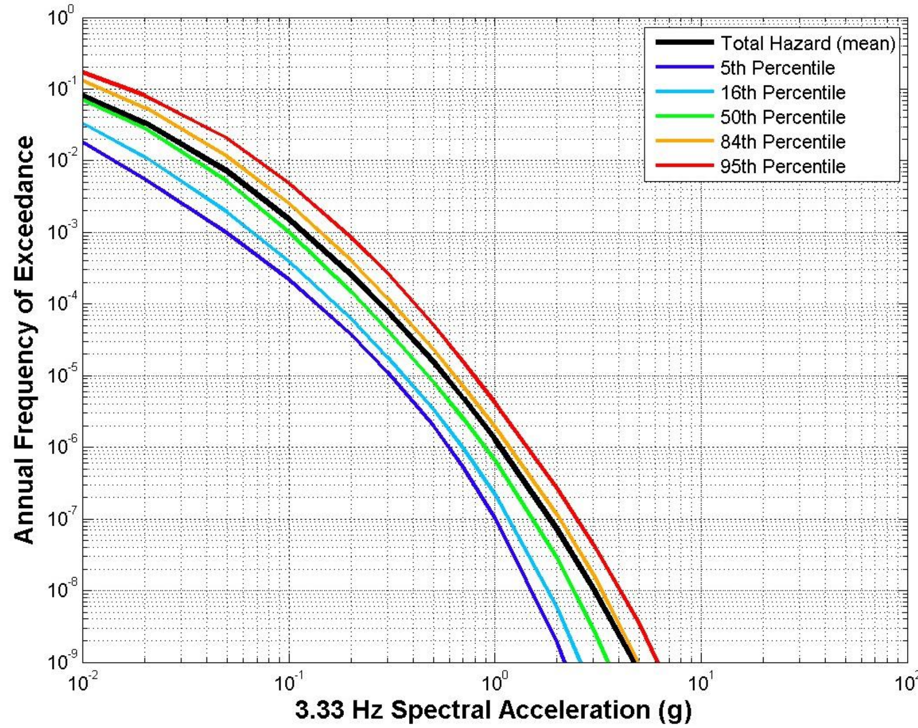

(b)

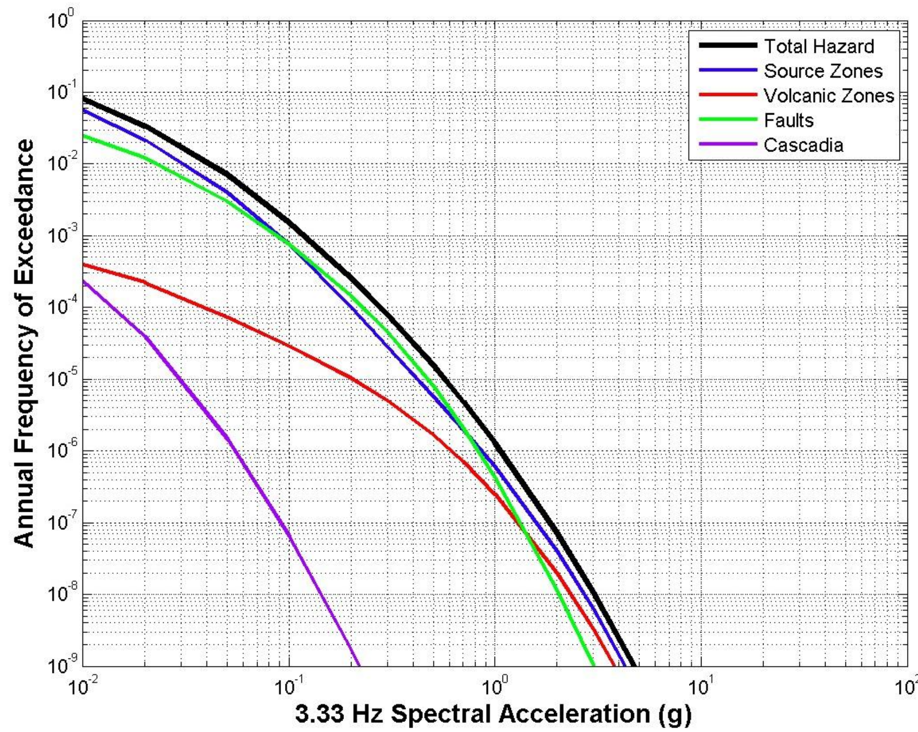

Figure 10-7. Seismic hazard resultsat MFC for SWUS reference site condition at 3.3 Hz (0.3-sec) spectral acceleration: a) total mean hazard and fractiles; and b) comparison between the total mean seismic hazard and the contribution of tectonic source zones, volcanic source zones, fault sources, and the Cascadia interface sources.

(a)

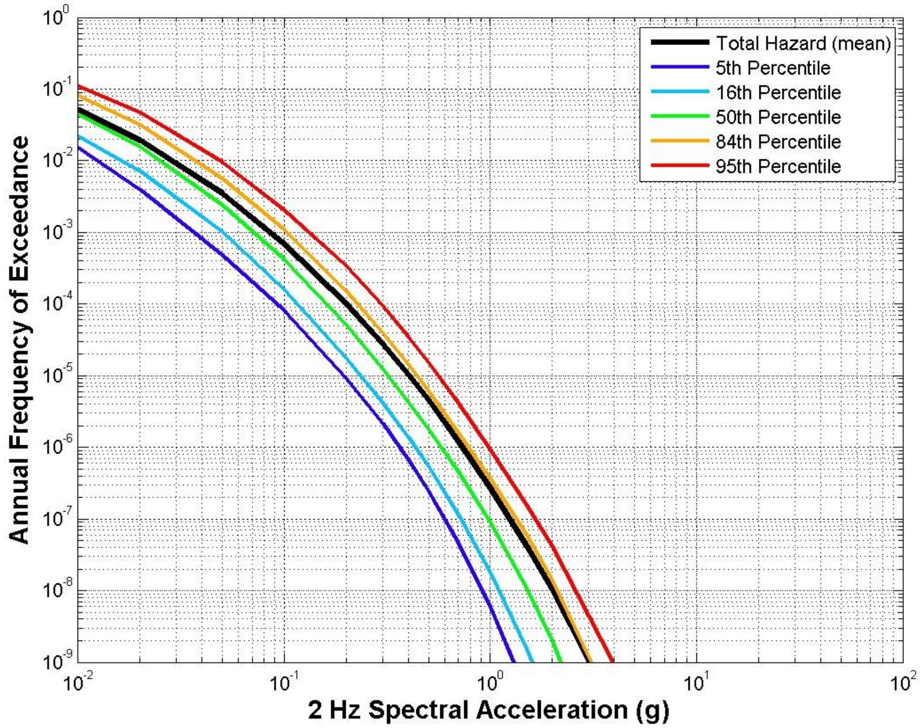

(b)

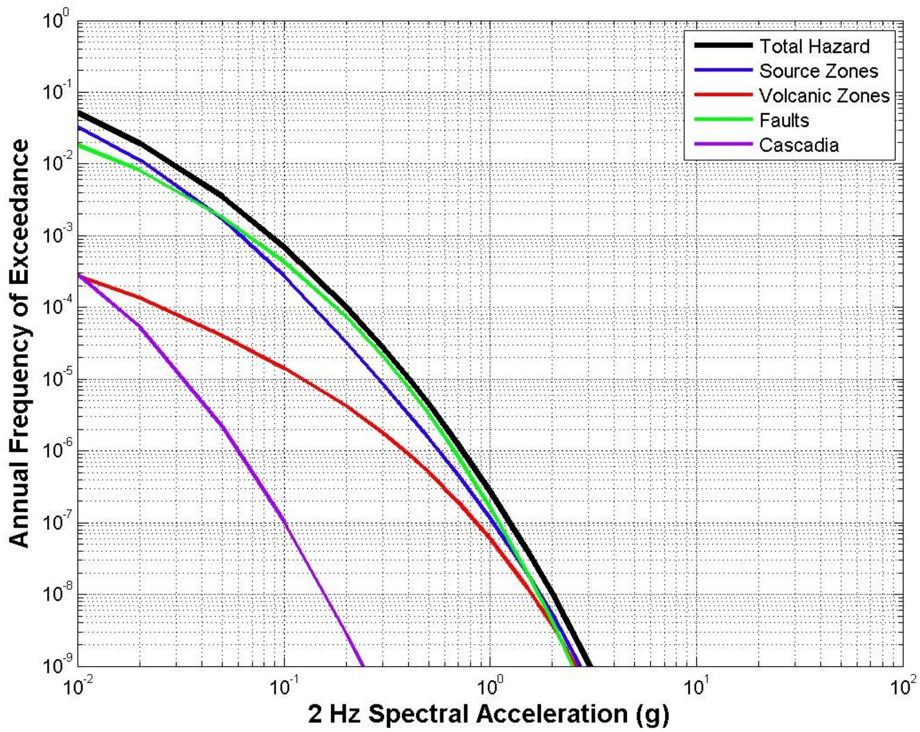

Figure 10-8. Seismic hazard results at MFC for SWUS reference site condition at 2 Hz (0.5-sec) spectral acceleration: a) total mean hazard and fractiles; and b) comparison between the total mean seismic hazard and the contribution of tectonic source zones, volcanic source zones, fault sources, and the Cascadia interface source.

(a)

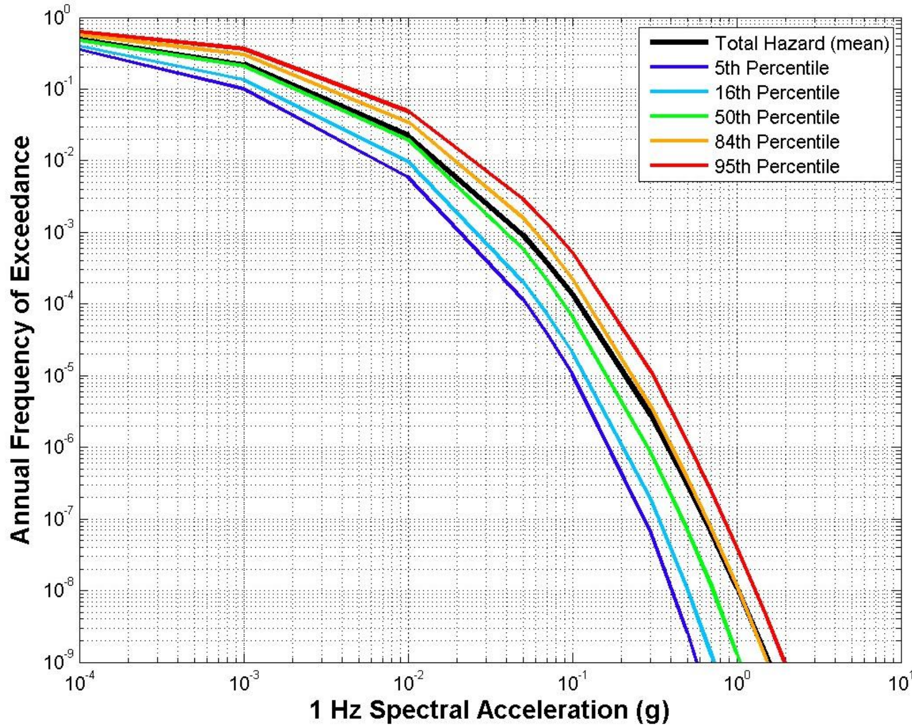

(b)

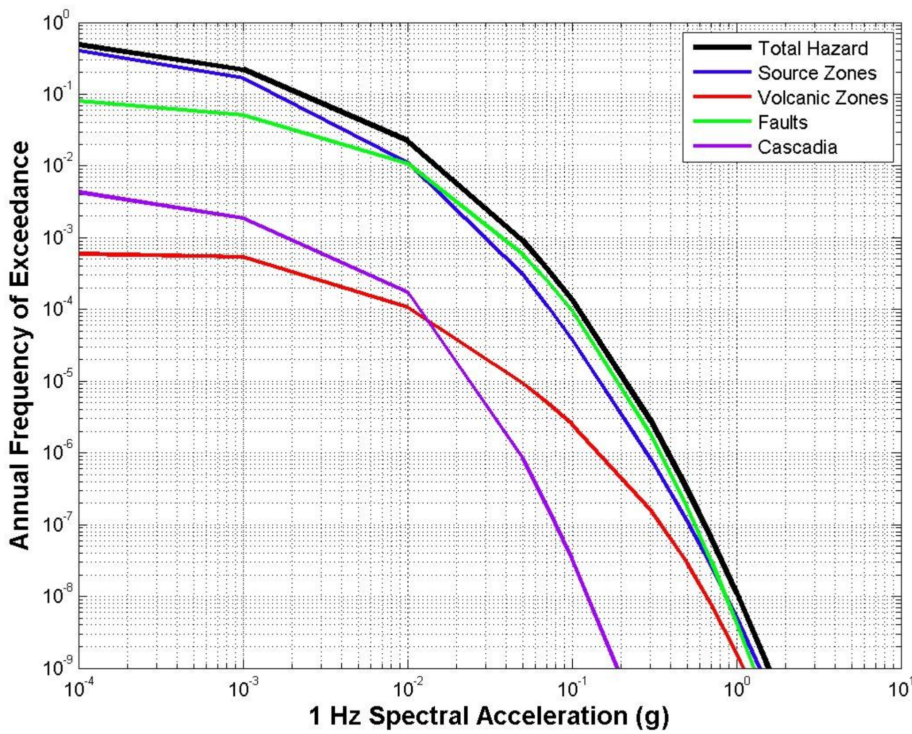

Figure 10-9. Seismic hazard results at MFC for SWUS reference site condition at 1 Hz (1.0-sec) spectral acceleration: a) total mean hazard and fractiles; and b) comparison between the total mean seismic hazard and the contribution of tectonic source zones, volcanic source zones, fault sources, and the Cascadia interface source.

(a)

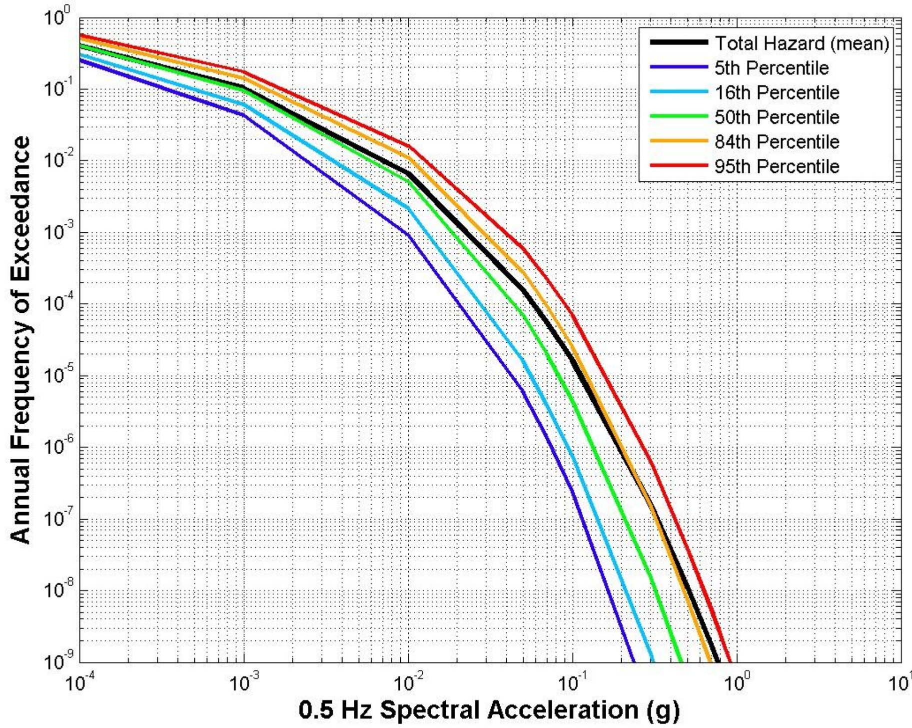

(b)

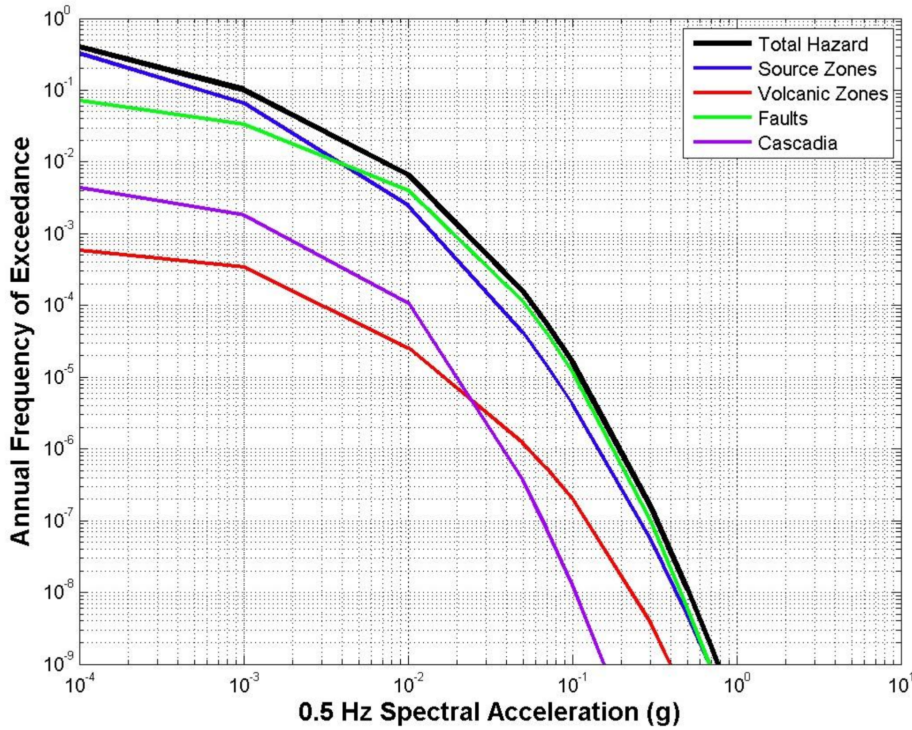

Figure 10-10. Seismic hazard results at MFC for SWUS reference site condition at 0.5 Hz (2.0-sec) spectral acceleration: a) total mean hazard and fractiles; and b) comparison between the total mean seismic hazard and the contribution of tectonic source zones, volcanic source zones, fault sources, and the Cascadia interface source.

(a)

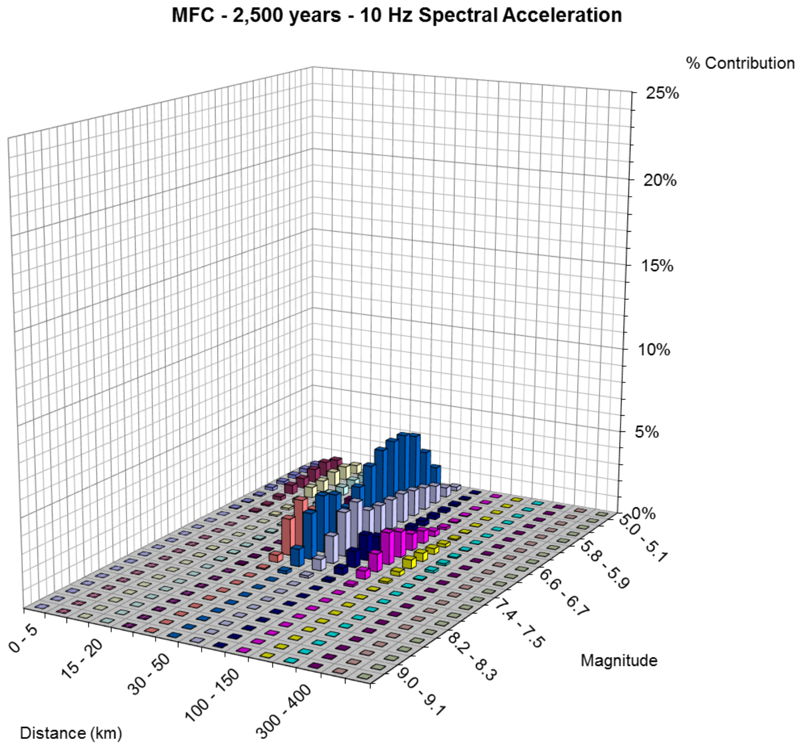

(b)

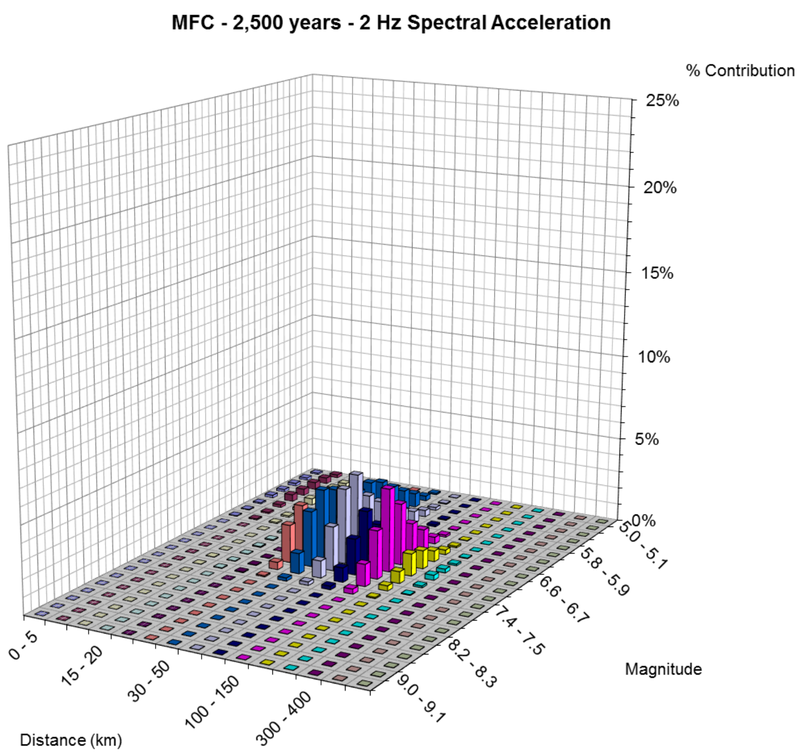

Figure 10-11. Magnitude-distance deaggregation for: a) 10 Hz; and b) 2 Hz at the 2,500 yr return period.

(a)

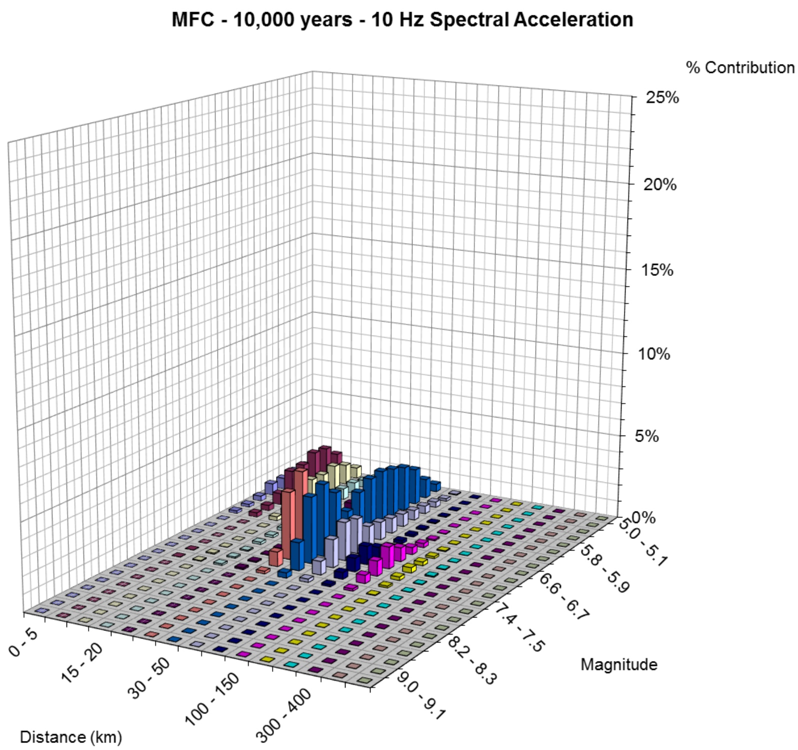

(b)

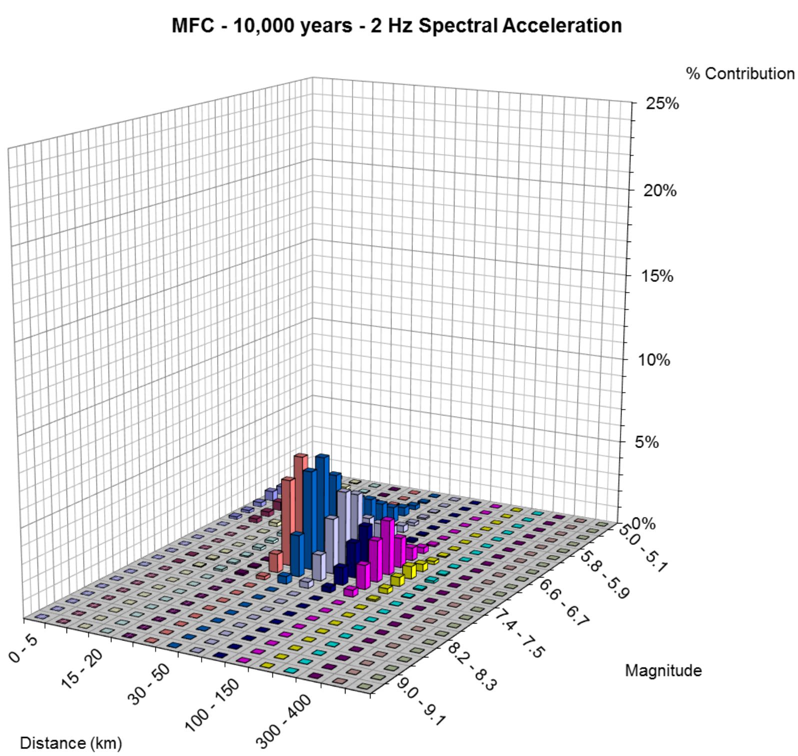

Figure 10-12. Magnitude-distance deaggregation for: a) 10 Hz; and b) 2 Hz at the 10,000 yr return period.

(a)

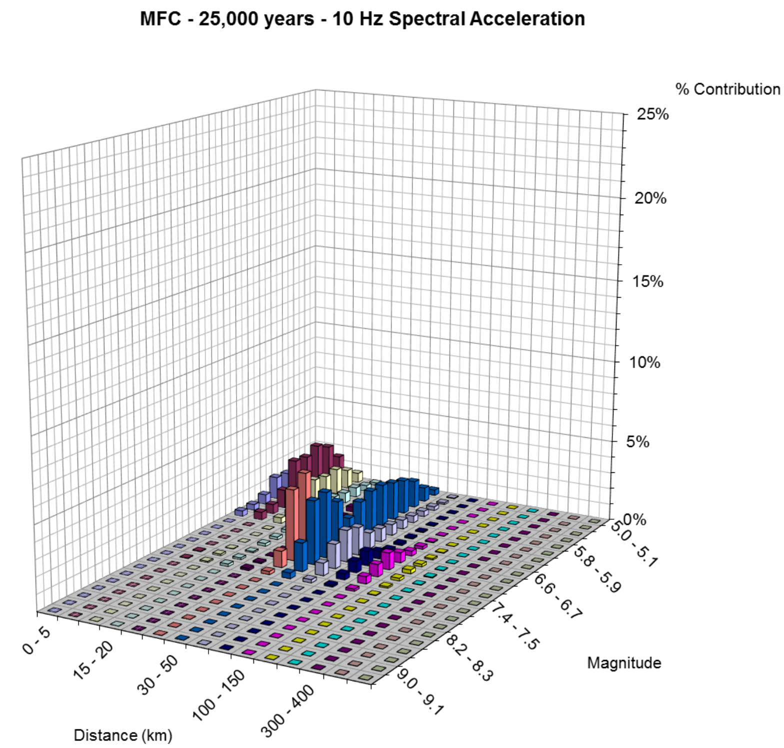

(b)

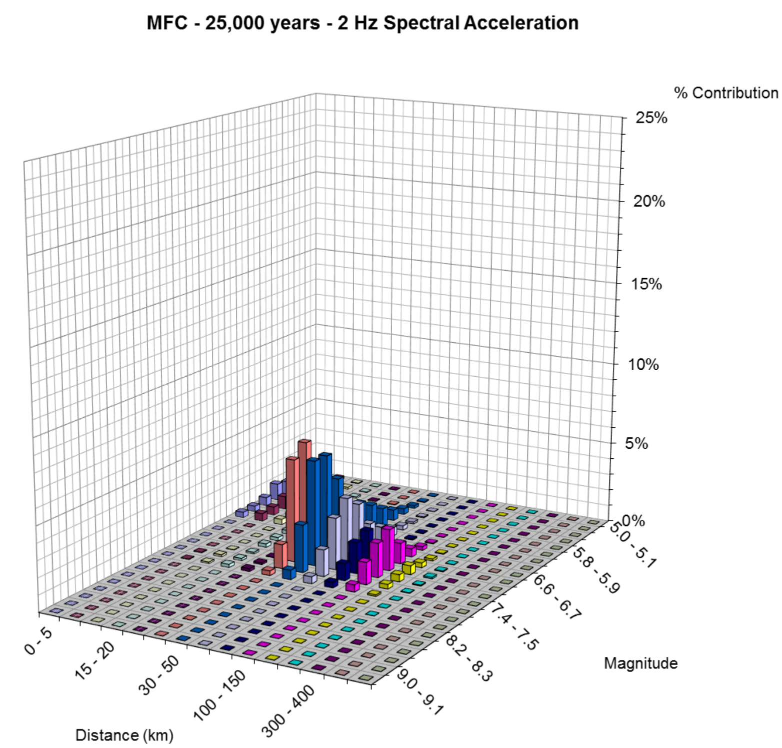

Figure 10-13. Magnitude-distance deaggregation for: a) 10 Hz; and b) 2 Hz at the 25,000 yr return period.

(a)

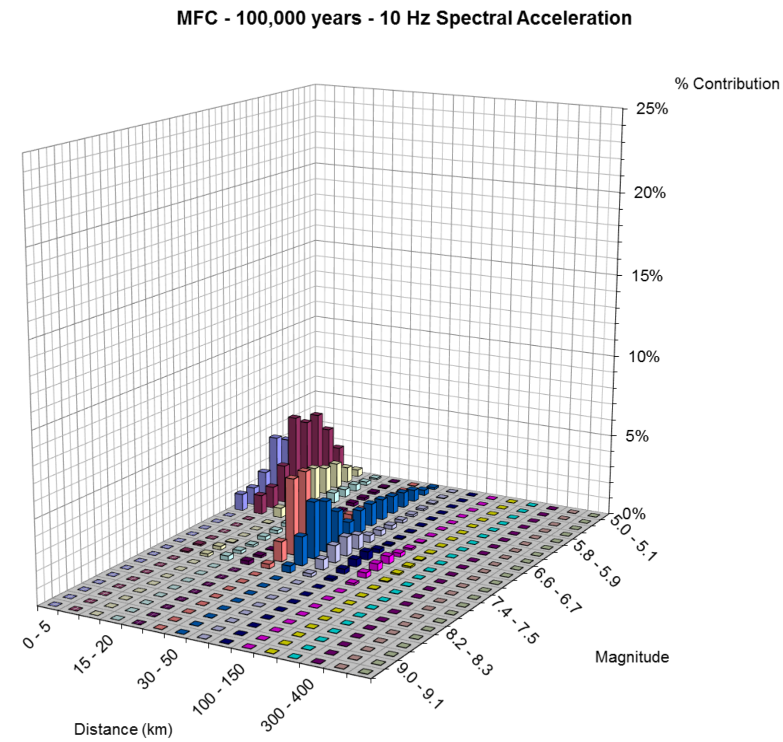

(b)

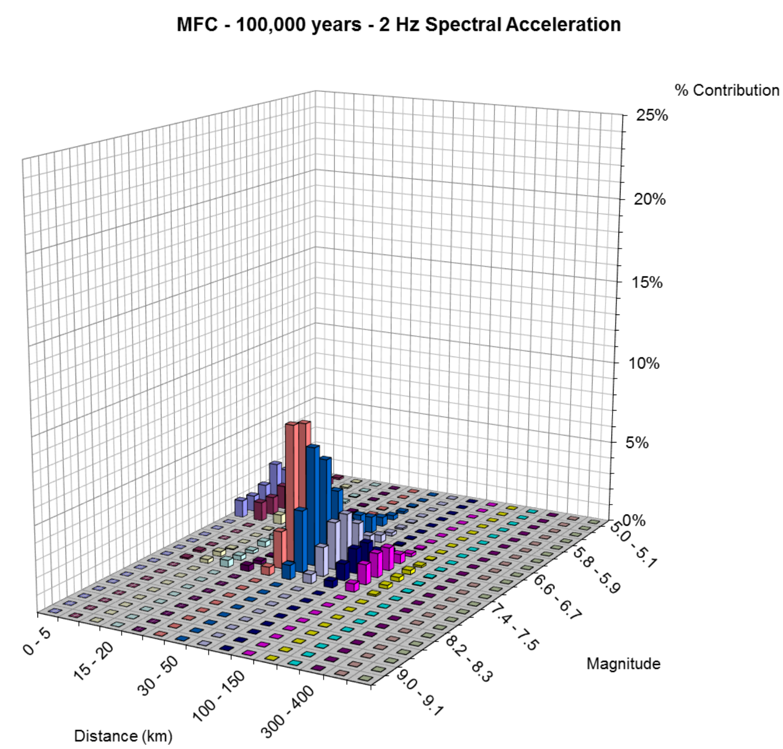

Figure 10-14. Magnitude-distance deaggregation for: a) 10 Hz; and b) 2 Hz at the 100,000 yr return period.

(a)

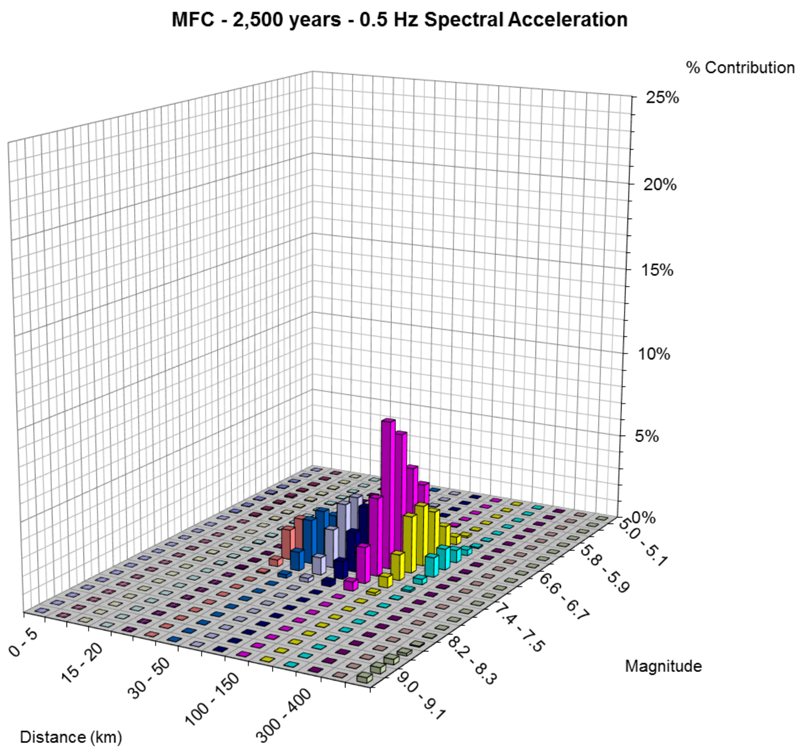

(b)

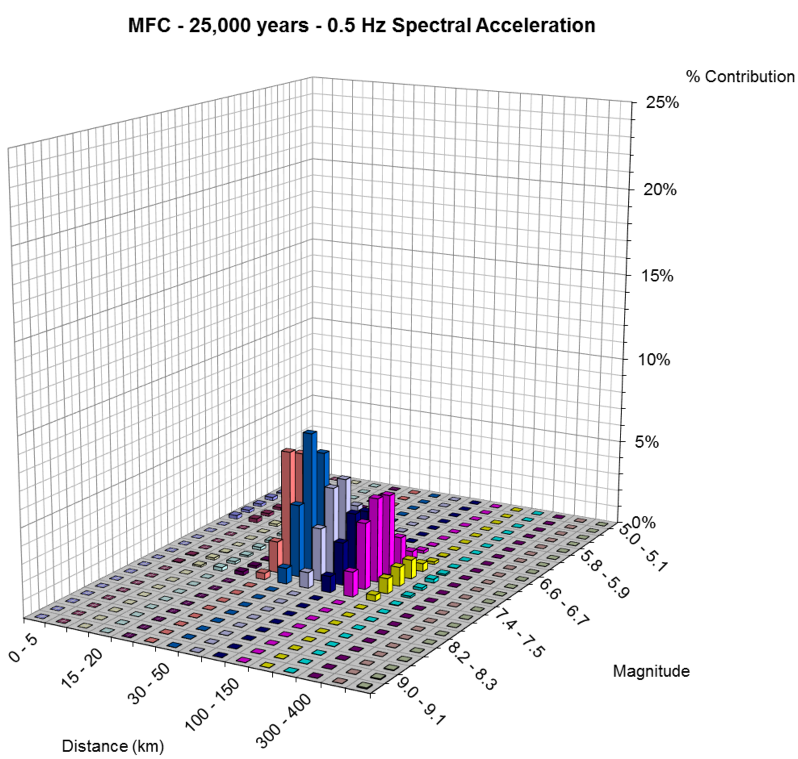

Figure 10-15. Magnitude-distance deaggregation for 0.5 Hz spectral acceleration at return periods of: a) 2,500 yr; and b) 25,000 yr.

10.2.2 Sensitivity Analyses

This section presents a series of seismic hazard curves that illustrate the effect of individual elements of the logic tree on the seismic hazard. For a particular node of the logic tree, the sensitivity analyses are conducted by assigning full weight alternatively to each of the branches that represent epistemic uncertainty. The elements of the SSC model that were tested include testing the contribution of individual source zones and fault sources, and the effect of including the CSZ source zone in the seismic hazard. For the GMC model, sensitivity analyses were conducted to show the effect of alternative ground motion models and of alternative epistemic uncertainty in the mean.

10.2.2.1 Elements of the SSC Model

This section describes the hazard sensitivity at MFC that is related to various elements of the SSC model. Figure 10-16 compares the total mean hazard curve with the mean hazard curves obtained from each individual seismotectonic source zone. Results are shown for 10 Hz (0.1-sec) and 2 Hz (0.5-sec) spectral accelerations: the main contribution at AEFs greater than 10^{-4} comes from the CSZ source zone because of its proximity to the site and its high predicted rate of earthquakes, while for smaller AEFs ISB source and the ESRP host zones produce the highest hazard. Figure 10-17 compares the total mean hazard curve with the mean hazard curves obtained from each fault sources at 10 Hz (0.1-sec) and 2 Hz (0.5-sec) spectral accelerations. The Lemhi and Lost River fault sources are the largest contributors to the hazard at the site for AEFs of 10^{-3} or lower; these faults are the closest to MFC. At very short return periods (AEF of 10^{-2}), the main contribution is from the Centennial fault source.

The next figure (Figure 10-18) illustrates the effect of including or not the CSZ source zone in the model. The total mean hazard is shown by the black curve. Shown in red is the hazard obtained assigning a weight of 1 to the model that includes the CSZ, while in blue is the hazard obtained without the CSZ source zone. There is a significant difference between the results at AEFs greater than 10^{-4} indicating that the hazard results are sensitive to this element of the model.

10.2.2.2 Elements of the GMC Model

This section describes the hazard sensitivity at MFC that is related to various elements of the GMC model. Figure 10-19 shows comparisons of the total mean hazard curve (in red) with the suite of SWUS alternative median ground motion models. Results are presented for 10 Hz (0.1-sec) and 2 Hz (0.5-sec) spectral accelerations. The figure shows that the variability in the results obtained from the range in median models is large. Figure 10-20 compares the total mean hazard curve with the three alternative models (in black) representing the epistemic uncertainty on sigma. The effect of this uncertainty is significant at nearly all AEF levels.

10.2.2.3 Variance Contribution Plots

Variance contribution histograms are used to show the relative contribution that various input uncertainties make to the total variance in the hazard results. Figures 10-21 and 10-22 present the results for 10 Hz (0.1-sec) and 2 Hz (0.5-sec) spectral accelerations, respectively.Each figure contains histograms of the total variance calculated at four return periods: 2,500 yr (AEF of $4x10^{-4}$), 10,000 yr (AEF of 10^{-4}), 25,000 yr (AEF of $4x10^{-4}$), and100,000 yr (AEF of 10^{-5}). The figures show that most of the total variance comes from the epistemic uncertainty in the ground motion models for median motions and in aleatory variability (sigma). Other significant contributions to the total variance come from the uncertainty in the recurrence rates for the fault sources, as expressed by the combination of the uncertainty in the approach (slip rate versus recurrence intervals) and the uncertainty in the slip rate (category labeled “Recurrence Rates” in the histograms), and by the CSZ source zone. The relative contributions of other elements of the model that are much smaller include: use of alternative earthquake catalogs (“Location of 1905 eq”), use of alternative declustering techniques, the southern termination of the Lost River and Lemhi fault sources, and the seismogenic probability of the Big Lost fault source.

(a)

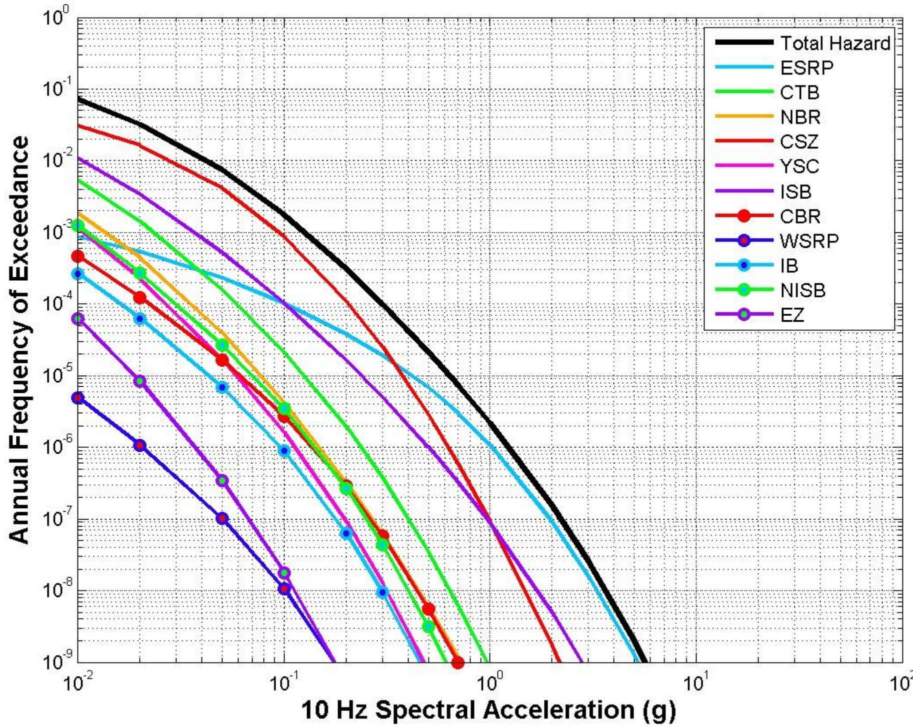

(b)

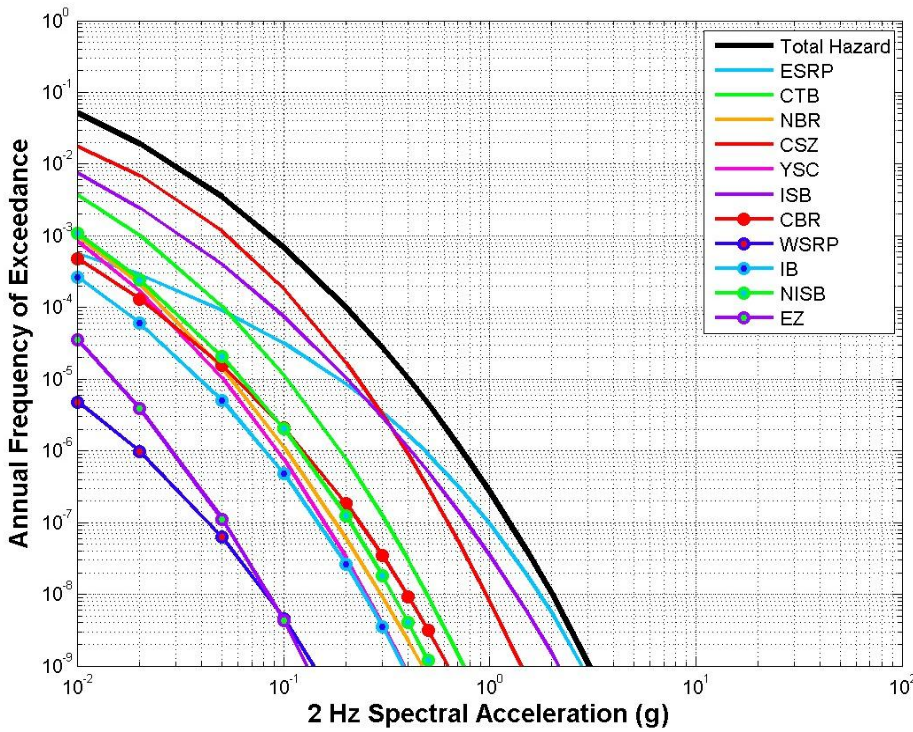

Figure 10-16. Contribution of individual tectonic source zones to the total seismic hazard for reference rock conditions: a) 10 Hz (0.1-sec) spectral acceleration; and b) 2 Hz (0.5-sec) spectral acceleration.

(a)

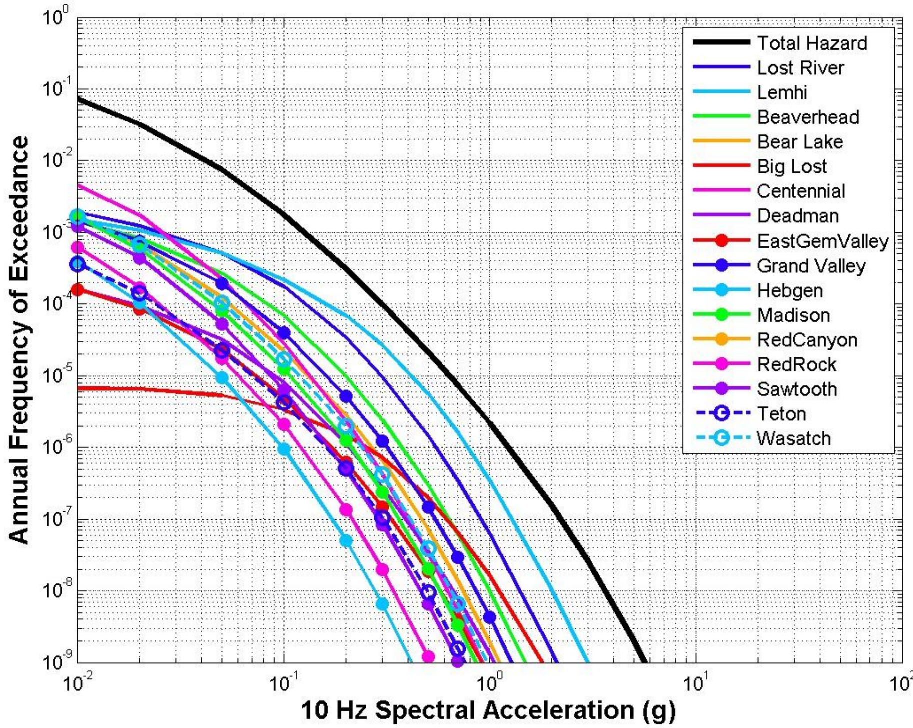

(b)

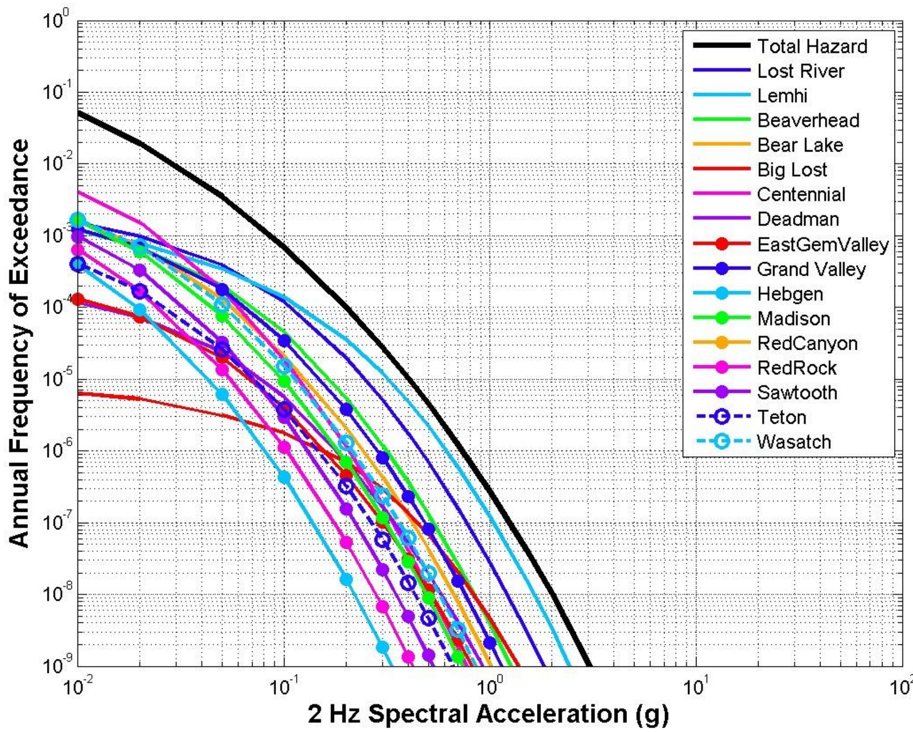

Figure 10-17. Contribution of individual fault sources to the total seismic hazard for reference rock conditions: a) 10 Hz (0.1-sec) spectral acceleration; and b) 2 Hz (0.5-sec) spectral acceleration.

(a)

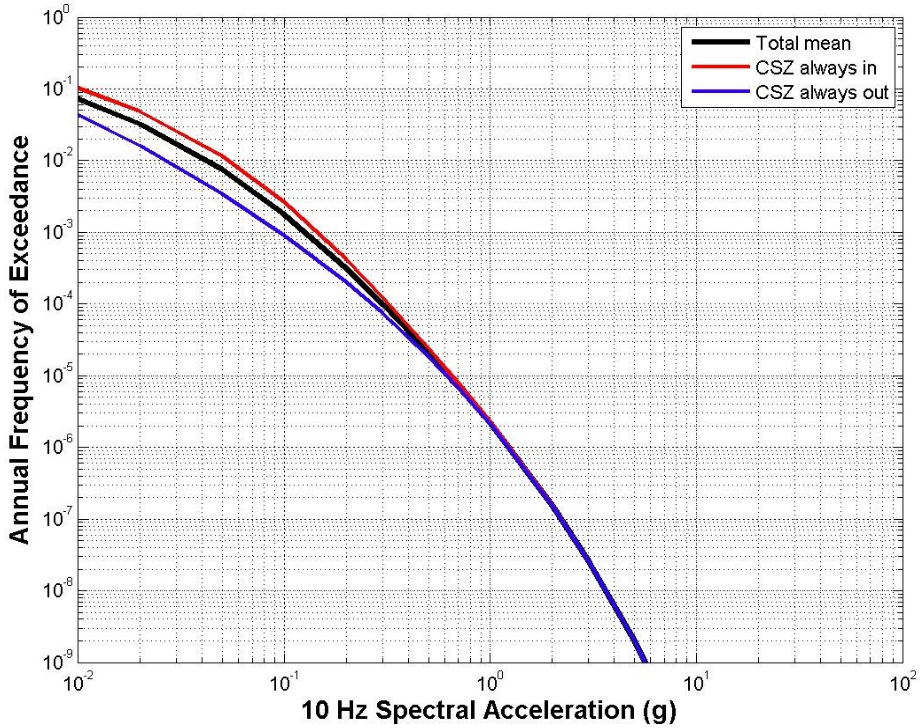

(b)

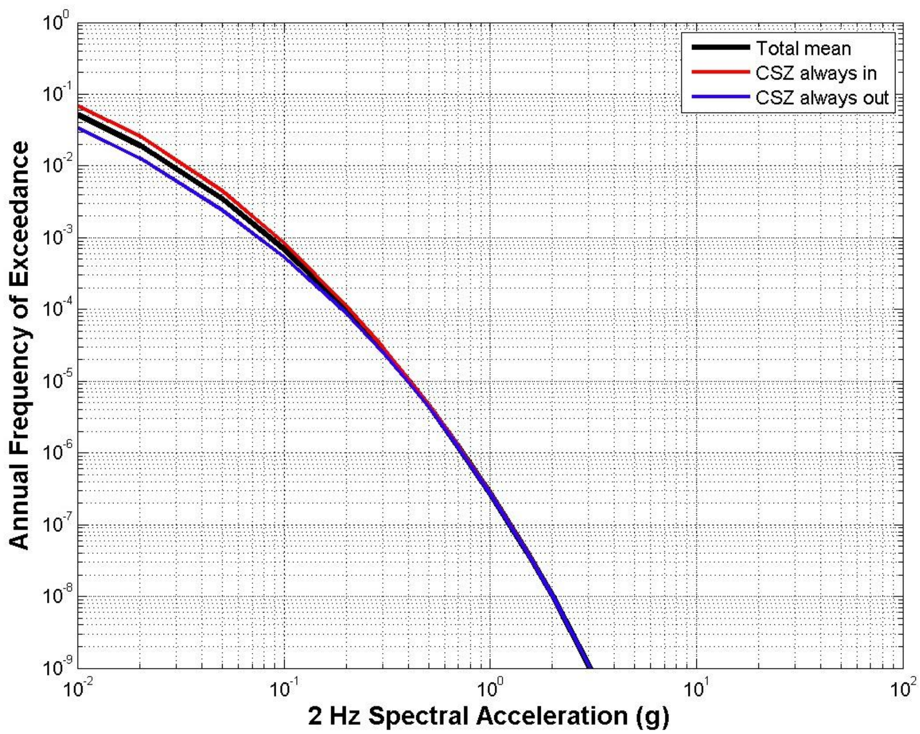

Figure 10-18. Sensitivity to the inclusion of the Centennial Shear Zone (CSZ) source zone: a) 10 Hz (0.1-sec) spectral acceleration; and b) 2 Hz (0.5-sec) spectral acceleration.

(a)

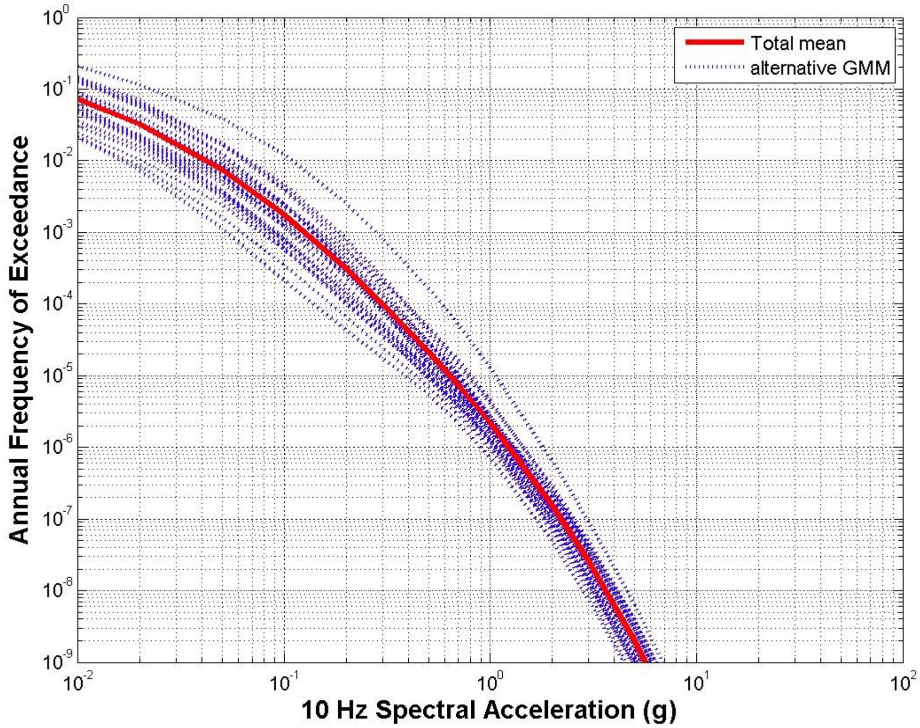

(b)

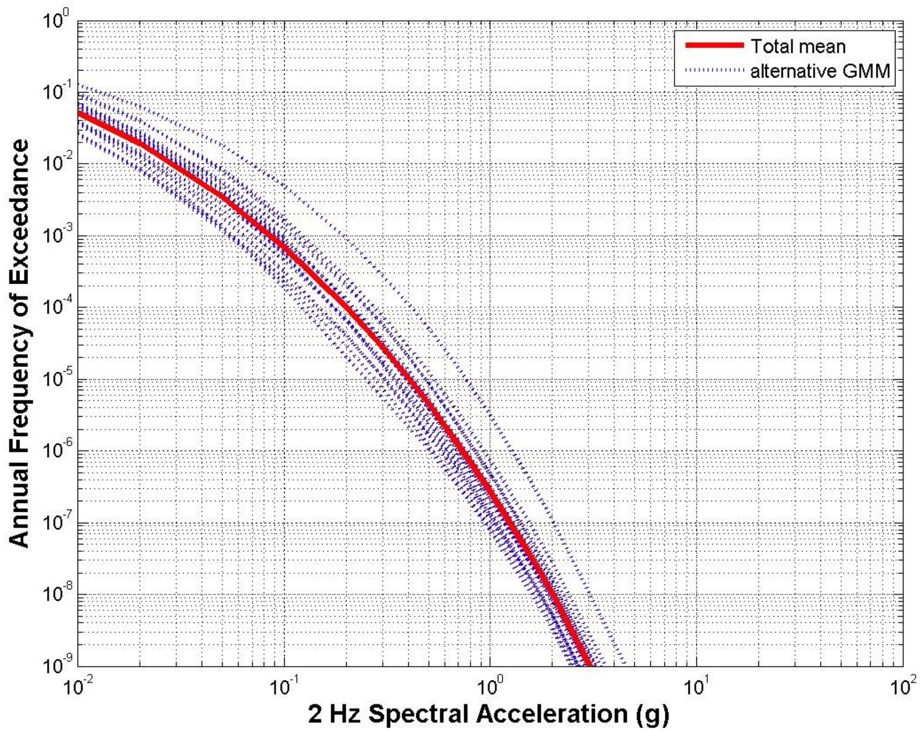

Figure 10-19. Sensitivity to alternative SWUS ground motion models (GMM): a) 10 Hz (0.1-sec) spectral acceleration; and b) 2 Hz (0.5-sec) spectral acceleration.

(a)

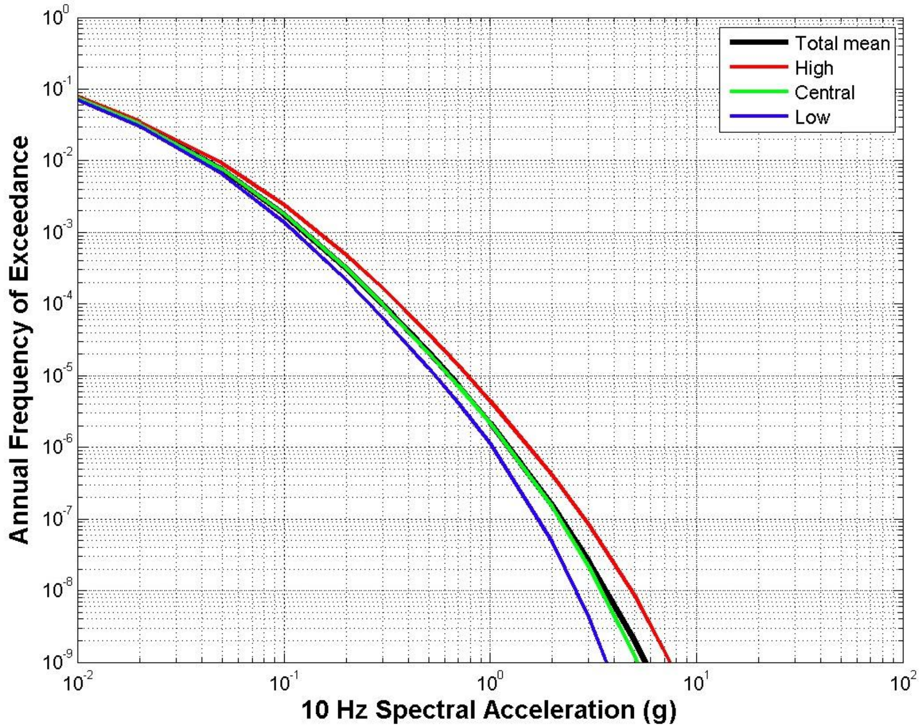

(b)

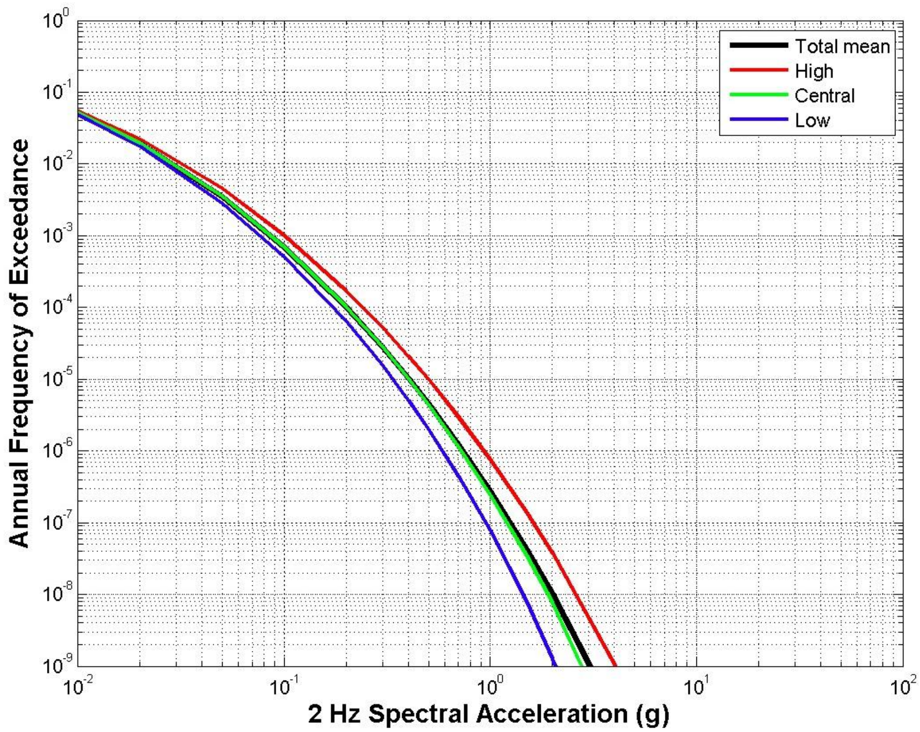

Figure 10-20. Sensitivity to the epistemic uncertainty on the sigma (high, central, and low): a) 10 Hz (0.1-sec) spectral acceleration; and b) 2 Hz (0.5-sec) spectral acceleration.

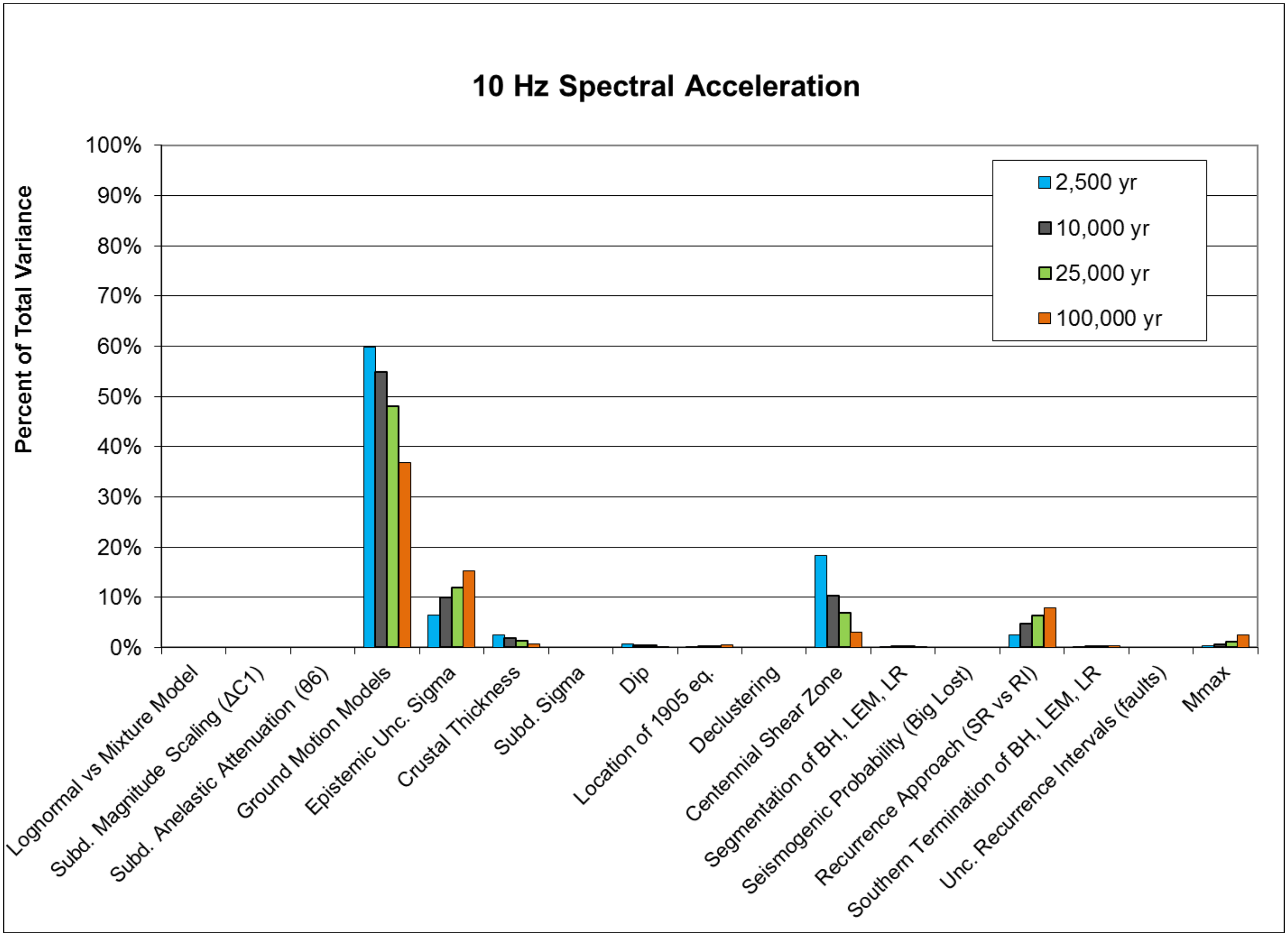

Figure 10-21. Contributions to the variance in the 10 Hz (0.1-sec) hazard for return periods of 2,500, 10,000, 25,000, and 100,000 yr.

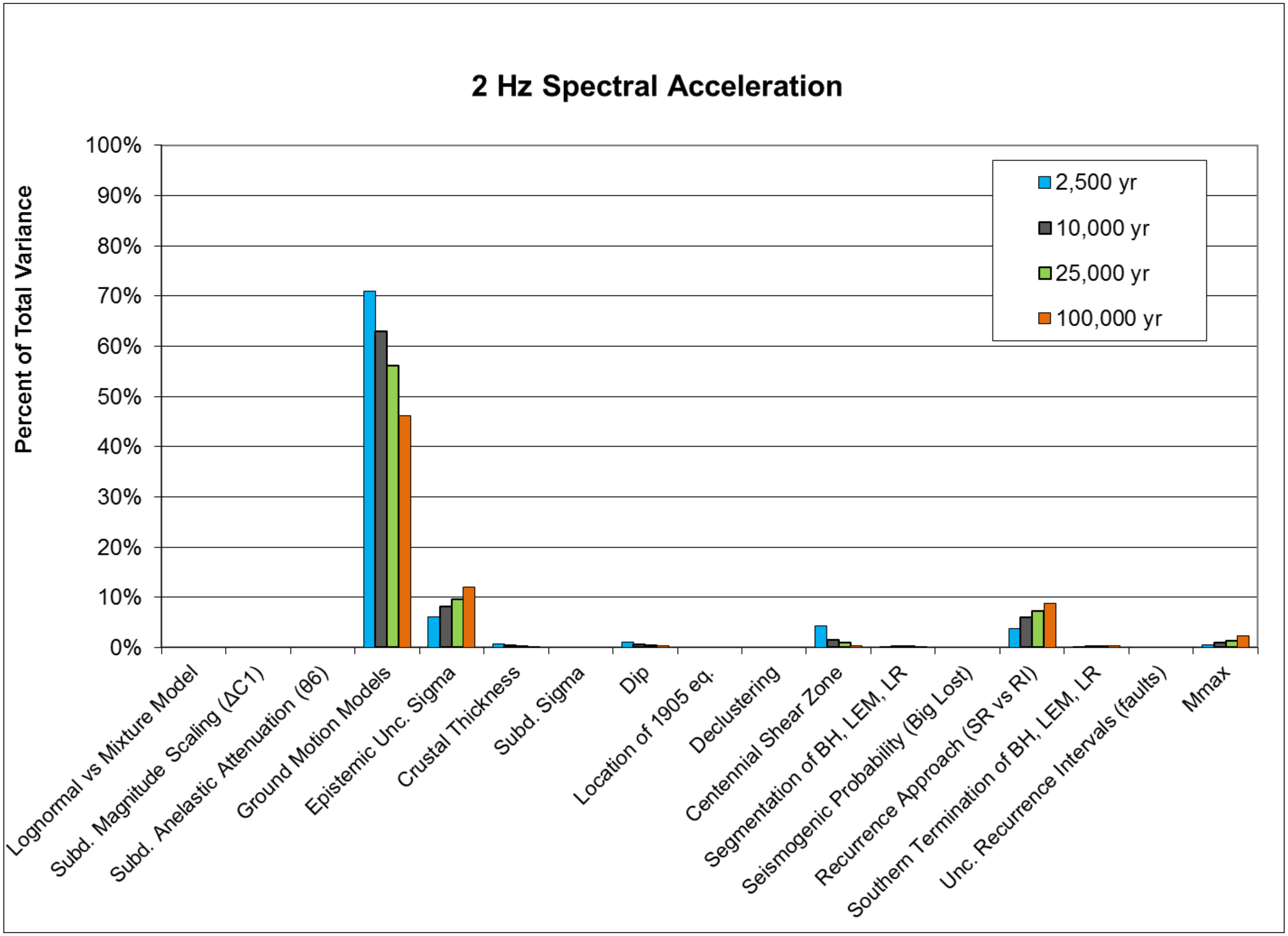

Figure 10-22. Contributions to the variance in the 2 Hz (0.5-sec) hazard for return periods of 2,500, 10,000, 25,000, and 100,000 yr.

10.3 Approach to Site-Specific Hazard

The development of the site-specific hazard curves and GMRS for ground surface in this calculation follows Approach 3 defined in NUREG/CR-6728 (NRC, 2001) and Appendix B of EPRI (2013). The basic concept of Approach 3 is to convolve a probabilistic representation of site response with the probabilistic seismic hazard results for the base rock to produce probabilistic seismic hazard results at the desired horizon within the soil column. As discussed in NUREG/CR-6728 (NRC, 2001), Approach 3 can be applied in various ways depending on the specification of the probabilistic site amplification. The approach used in this calculation follows that outlined in Appendix B of EPRI (2013) in which the site amplification functions are convolved with the mean hard rock hazard curves to produce mean site-specific hazard curves. The formulation is given by Equation 10-6:

$$G_z(z_j) = \sum_i P\left(Y \geq \frac{z_j}{x_i}\middle| x_i\right) p_X(x_i) \qquad [10\text{-}6]$$

where $G_Z(z_j)$ is the site-specific hazard curve giving the annual frequency of exceeding ground motion level z_j,

$p_x(x_i)$ is the discretized rock hazard curve giving the annual frequency of ground motions on rock of level x_i,

$P\ (Y \geq z_j/x_i \mid x_i)$ the probability that the site amplification, Y, is greater than or equal to z_j/x_i given hard rock ground motions of level x_i.

Following EPRI (2013), the site amplification Y is assumed to be log normally distributed, giving:

$$P\left(Y \geq \frac{z_j}{x_i}\middle| x_i\right) = 1 - \Phi\left[\frac{\ln\left(\frac{z_j}{x_i}\right) - \overline{\ln Y|x_i}}{\sigma_{\ln Y|x_i}}\right] \qquad [10\text{-}7]$$

where $\ln(z_j/x_i)$ is the mean value of $\ln Y$ evaluated at x_i

$\sigma_{\ln Y \backslash xi}$ is the standard deviation of $\ln Y$ evaluated at x_i

$\Phi[\ ]$ is the cumulative normal distribution function.

Equation 10-6 provides the basis for developing a site-specific hazard curve incorporating a probabilistic representation of site response. As described in Section 9.5, the site response analysis for the MFC site includes two modeling approaches (1-corner frequency or 2-corner frequencies), three Vs profiles, three kappa values, and two models for $\sigma_{\text{epistemic}}$; while for FMF there are two material types in addition to the logic tree elements already listed. As a result there are36 alternative models used to develop probabilistic representations of site amplification for MFC, and 72 for FMF. In addition, for FMF the amplification functions were derived for two soil thicknesses: 5 and 15 ft.

In applying Approach 3 the epistemic uncertainty in the site dynamic properties is incorporated into the analysis in the same manner as epistemic uncertainties in all of the other inputs to the site hazard calculation are incorporated. Each set of dynamic properties is used to develop mean site-specific hazard curves using Equation 10-6 for the ten frequencies at which the hard rock hazard is computed (PGA and spectral accelerations at 50, 33, 20, 10, 5, 3.33, 2, 1, and 0.5 Hz). The resulting 36 or 72 site-specific hazard curves for each frequency are assigned weights based on the weights assigned to the alternative sets of properties. Composite mean site-specific hazard curves for each frequency are then computed and used to develop the site-specific, performance-based, GMRS using the performance based approach discussed in ASCE Standard 43-05 (ASCE, 2005).

The process is as follows: using the reference-rock hazard at the site described in the previous subsections, and the alternative transfer functions presented in Section 9.3, alternative site-specific hazard curves are calculated by applying Equation 10-6. A combined mean site-specific hazard curve for each ground motion frequency is calculated as the weighed mean of the site-specific hazard curves for the alternative site amplification function, following the logic tree shown in Figure 9.31. The mean site-specific hazard curves are then interpolated to obtain the UHS at the ground surface for the AEF of $4x10^{-4}$, 10^{-4}, $4x10^{-5}$, and 10^{-5}. The GMRS is developed using the performance based method for defining a risk-consistent *DRS* given in ASCE (2005). The *DRS* is obtained from the site-specific UHS using the expression:

$$DRS(f) = DF(f) \times UHRS(f) \qquad [10\text{-}8]$$

For SDC-3 structures, such as MFC and FMF, the UHS(*f*) value at each spectral frequency corresponds to the ground motions with a mean $4x10^{-4}$ AEF, obtained from the site-specific hazard. The Design Factor, *DF*(*f*) is defined based on the ratio of the ground motions for AEFs of $4x10^{-4}$ and $4x10^{-5}$. The procedure for computing the *DRS* is as follows. For each spectral frequency at which the UHS is defined, a slope factor A_R is determined from:

$$A_R = \frac{SA_{(0.1H_D)}}{SA_{(H_D)}} \qquad [10\text{-}9]$$

where $SA(H_D)$ is the spectral acceleration (SA) at the target mean UHS exceedance frequency H_D (i.e., $4x10^{-4}$) and $SA(0.1H_D)$ is the spectral acceleration at $0.1H_D$ (i.e., $4x10^{-5}$).

Then the *DF*(*f*) at this spectral frequency is given by:

$$DF(f) = \text{Maximum}\ (DF_1, DF_2) \qquad [10\text{-}10]$$

For SDC-3 structures ASCE/SEI Standard 43-05specifies that:

$$DF_1 = 0.8 \qquad [10\text{-}11]$$

and

$$DF_2 = 0.6(A_R)^{0.40} \qquad [10\text{-}12]$$

The minimum value of DRS PGA for SDC-3 structures at the foundation level is specified in ASCE/SEI Standard 43-05 to be 0.06g.

For Seismic Design Categories 4 and 5 (SDC-4 and SDC-5), ASCE/SEI Standard 43-05 specifies H_D of 4×10^{-4} and 10^{-4}, respectively, DF_1 of 1.0 and α (the exponent in Equation 10-12) of 0.8 (ASCE, 2005). The minimum value of DRS PGA for SDC-4 and SDC-5 is 0.08g and 0.1g, respectively.

10.4 Site-Specific Hazard at MFC and FMF

Figure 10-23 shows the site-specific mean hazard curves for MFC (in blue) in comparison with the corresponding site-specific hazard curves calculated in the 1996 INL PSHA study (red curves) by Woodward Clyde Federal Services et al. (1996). The plots show the results for PGA, 10 Hz and 1 Hz spectral acceleration. At high frequency the results of the 1996 INL PSHA produce higher hazard for short return periods (AEFs of 10^{-3} or 10^{-4}), while at long return periods the opposite is observed. This is

(a)

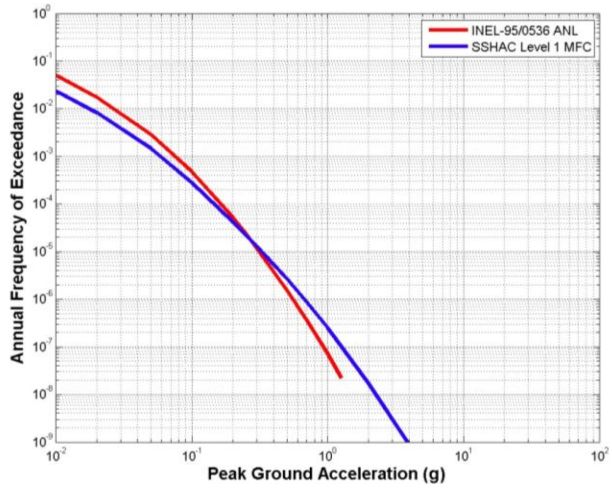

(b)

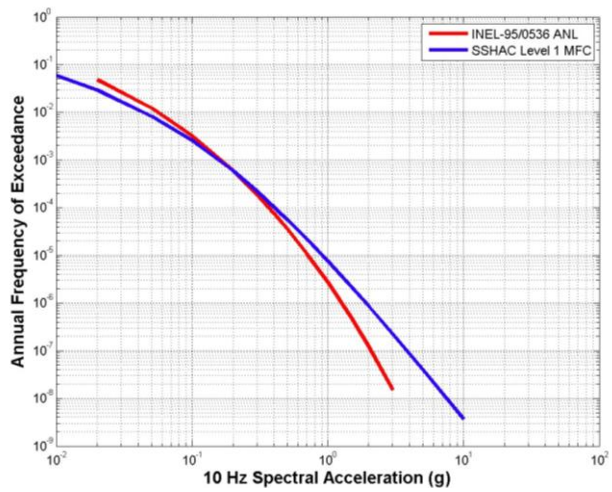

(c)

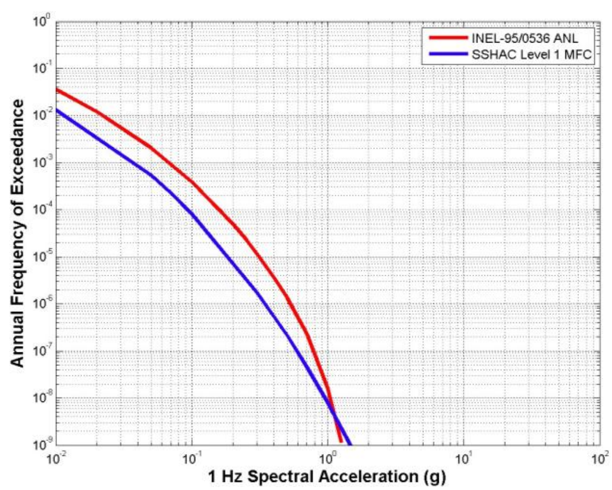

Figure 10-23. Comparison of the mean site-specific hazard curves at MFC obtained in this study (SSHAC Level 1 MFC, blue curves) with the corresponding curves from Woodward Clyde Federal Services et al. (1996, INEL-95/0536 ANL, red curves), for: a) PGA; b) 10 Hz; and c) 1 Hz spectral accelerations.

likely caused by the use of E[**M**] in the earthquake catalog and the N* approach, which would have an effect on the recurrence rates of the source zones. At long return periods, changes to the recurrence models of the Lost River and Lemhi faults, and the addition of the regional faults may be responsible for the higher hazard predicted in this study versus the 1996 PSHA results. At 1 Hz, the results of the SSHAC Level 1 PSHA are consistently lower than what was calculated in 1996 INL PSHA. The lower hazard is likely due to a combination of lower median motions from the adjusted SWUS GMPEs compared to the 1996 set of median models, and lower effective total sigma (combined aleatory and epistemic) than the ergodic sigmas used in the 1996 PSHA.

Figure 10-24 shows the mean and the 5th, 15th, 50th, 85th, and 95th fractiles for PGA, 10 Hz and 2 Hz spectral acceleration at MFC that illustrate the variability introduced in the site-specific hazard by the alternative site amplification functions. The mean site-specific hazard curves at MFC are listed in Table10-3; the fractile hazard curves at PGA, 10 Hz and 2 Hz are listed in Tables 10-4.

There are two sets of results for FMF: one for a soil thickness of 5 ft, and the other for a soil thickness of 15 ft The site-specific hazard curves at FMF, including fractiles for PGA and 10 Hz are listed in Tables 10-5 and 10-6 for a soil thickness of 5 ft, and Tables 10-7 and 10-8 for a soil thickness of 15 ft As was the case for MFC, these fractiles represent only the epistemic uncertainty in the transfer function from the SWUS reference profile to the FMF profiles. The mean site-specific hazard curve and its fractiles for PGA and 10 Hz are also shown in Figures 10-25 and 10-26 for soil thickness of 5 and 15 ft, respectively.

10.4.1 Sensitivity Analyses

This section presents the hazard sensitivity at the MFC and FMF sites with respect to the various parameters used to generate alternative site-amplification functions. Additionally, this section presents hazard sensitivity with respect to the two alternative models for $\sigma_{\text{epistemic}}$ described in section 9.3.4. As described in section 10.2.2, for a particular node of the logic tree, the sensitivity analyses are conducted by assigning full weight alternatively to each of the branches that represent epistemic uncertainty.

10.4.1.1 MFC Site

Alternatives of four different parameters (three alternative kappa values, three alternative velocity profiles, two alternative $\sigma_{\text{epistemic}}$ models, and two alternative earthquake source spectra) were used to capture the uncertainty in the site-amplification functions for MFC, which provided 36 alternative hazard curves at each frequency of spectral acceleration.

Figure 10-27 compares the conditional-mean hazard for a given kappa (red curves) with the total mean hazard at 2 Hz and 10 Hz spectral acceleration for MFC (blue curve); results for the individual 36 possible outcomes of the logic tree for MFC are shown by the grey curves. Kappa has a non-negligible effect on the ground motion level at all AEF less than $1x10^{-2}$ for spectral acceleration at high frequencies. In the AEF range of interest ($4x10^{-4}$ to 10^{-4}) the ground motion level differs by approximately a factor of 2 between the upper and lower bounds of kappa (0.011-0.030 sec). For spectral acceleration at low frequencies kappa has small effect on the ground motion level at all levels of AEF. Further, kappa = 0.011sec produces hazard curves above those of kappa = 0.018sec and kappa = 0.030sec consistently across all frequencies of spectral acceleration.

The three alternative velocity profiles produce a small variation in the ground motion level at all levels of AEF and all frequencies of spectral acceleration. This is shown in Figure 10-28, where the conditional-mean hazard for a given profile (red curves) is compared with the total mean hazard at 2 Hz and 10 Hz spectral accelerations for MFC (blue curve), and with the individual results of the 36 logic tree branches (grey curves). Additionally, there is not one profile that consistently produces larger hazard

Table 10-3. Mean site-specific hazard curves at MFC (rock conditions).

PGA	AEF	50 Hz SA	AEF	33.3 Hz SA	AEF	20 Hz SA	AEF	10 Hz SA	AEF
0.01	2.32E-02	0.01	2.68E-02	0.01	2.51E-02	0.01	3.63E-02	0.01	5.98E-02
0.02	8.06E-03	0.02	9.84E-03	0.02	9.60E-03	0.02	1.53E-02	0.02	2.87E-02
0.05	1.41E-03	0.05	1.91E-03	0.05	2.03E-03	0.05	3.72E-03	0.05	8.12E-03
0.1	2.66E-04	0.1	4.30E-04	0.1	5.07E-04	0.1	1.07E-03	0.1	2.48E-03
0.2	4.00E-05	0.2	8.24E-05	0.2	1.06E-04	0.2	2.34E-04	0.2	5.77E-04
0.3	1.22E-05	0.3	2.92E-05	0.3	3.94E-05	0.3	8.58E-05	0.3	2.12E-04
0.4	5.04E-06	0.4	1.36E-05	0.4	1.90E-05	0.4	4.07E-05	0.5	5.33E-05
0.5	2.49E-06	0.5	7.35E-06	0.5	1.06E-05	0.5	2.23E-05	0.7	2.03E-05
0.7	8.20E-07	0.7	2.79E-06	0.7	4.21E-06	0.7	8.74E-06	1	7.04E-06
1	2.34E-07	1	9.46E-07	1	1.52E-06	1	3.13E-06	2	7.95E-07
2	1.56E-08	2	9.51E-08	2	1.75E-07	2	3.84E-07	3	2.09E-07
5	2.94E-10	5	2.97E-09	5	6.85E-09	5	1.90E-08	5	3.74E-08
10	5.50E-12	10	1.53E-10	10	4.53E-10	10	1.67E-09	10	3.44E-09
5 Hz SA	AEF	3.33 Hz SA	AEF	2 Hz SA	AEF	1 Hz SA	AEF	0.5 Hz SA	AEF
0.01	6.20E-02	0.01	4.54E-02	0.01	3.69E-02	0.0001	4.30E-01	0.0001	3.16E-01
0.02	2.46E-02	0.02	1.62E-02	0.02	1.34E-02	0.001	1.58E-01	0.001	6.58E-02
0.05	5.22E-03	0.05	2.95E-03	0.05	2.41E-03	0.01	1.21E-02	0.01	2.97E-03
0.1	1.16E-03	0.1	5.86E-04	0.1	4.80E-04	0.05	4.57E-04	0.05	6.04E-05
0.2	1.93E-04	0.2	8.78E-05	0.2	6.91E-05	0.07	1.85E-04	0.07	2.07E-05
0.3	5.97E-05	0.3	2.48E-05	0.3	1.88E-05	0.1	6.13E-05	0.1	5.60E-06
0.5	1.21E-05	0.5	4.31E-06	0.4	6.85E-06	0.3	1.18E-06	0.3	5.24E-08
0.7	3.90E-06	0.7	1.20E-06	0.5	2.96E-06	0.5	1.33E-07	0.5	4.20E-09
1	1.07E-06	1	2.73E-07	0.7	7.65E-07	0.7	2.70E-08	0.7	6.85E-10
2	7.11E-08	2	1.16E-08	1	1.61E-07	1	4.36E-09	1	8.77E-11
3	1.34E-08	3	1.54E-09	1.5	2.31E-08	1.5	4.61E-10	1.5	7.19E-12
5	2.12E-09	5	1.26E-10	2	5.05E-09	2	8.20E-11	2	1.10E-12
10	8.78E-11	10	1.15E-12	5	1.33E-11	5	1.54E-13	5	1.57E-15
PGA- Peak Ground Acceleration (g); AEF – Annual Exceedance Frequency; SA – Spectral Acceleration (g).									

Table 10-4. Site-specific hazard fractiles at MFC (rock conditions) for PGA and 10 Hz.

	Annual Exceedance Frequency at Fractiles:				
PGA (g)	5th	15th	50th	85th	95th
0.01	1.79E-02	1.91E-02	2.31E-02	2.72E-02	2.84E-02
0.02	5.17E-03	5.48E-03	7.94E-03	1.01E-02	1.09E-02
0.05	6.19E-04	7.39E-04	1.42E-03	2.10E-03	2.25E-03
0.10	8.76E-05	1.07E-04	2.57E-04	4.47E-04	4.80E-04
0.20	1.02E-05	1.27E-05	3.62E-05	7.46E-05	7.97E-05
0.30	2.66E-06	3.35E-06	1.05E-05	2.42E-05	2.58E-05
0.40	9.80E-07	1.24E-06	4.21E-06	1.03E-05	1.10E-05
0.50	4.38E-07	5.62E-07	2.02E-06	5.23E-06	5.59E-06
0.70	1.21E-07	1.58E-07	6.34E-07	1.80E-06	1.92E-06
1.00	2.71E-08	3.59E-08	1.70E-07	5.38E-07	5.77E-07
2.00	1.48E-09	1.99E-09	1.01E-08	3.81E-08	4.15E-08
5.00	8.39E-12	1.31E-11	1.33E-10	8.19E-10	9.04E-10
10.00	1.39E-15	2.27E-14	1.68E-12	1.71E-11	1.89E-11
10 Hz (g)					
0.01	4.37E-02	4.79E-02	6.26E-02	6.91E-02	6.97E-02
0.02	1.82E-02	2.08E-02	3.02E-02	3.62E-02	4.11E-02
0.05	4.39E-03	4.79E-03	7.96E-03	1.04E-02	1.26E-02
0.10	1.11E-03	1.18E-03	2.29E-03	3.24E-03	4.25E-03
0.20	1.95E-04	2.13E-04	4.98E-04	8.04E-04	1.13E-03
0.30	6.32E-05	7.10E-05	1.80E-04	3.03E-04	4.29E-04
0.50	1.42E-05	1.63E-05	4.42E-05	7.87E-05	1.14E-04
0.70	5.06E-06	5.90E-06	1.67E-05	3.04E-05	4.41E-05
1.00	1.64E-06	1.93E-06	5.73E-06	1.07E-05	1.57E-05
2.00	1.67E-07	1.97E-07	6.26E-07	1.25E-06	1.85E-06
3.00	4.11E-08	4.98E-08	1.65E-07	3.29E-07	4.83E-07
5.00	7.22E-09	8.53E-09	2.87E-08	5.97E-08	9.00E-08
10.00	4.00E-10	5.64E-10	2.63E-09	5.49E-09	8.32E-09

Table 10-5. Mean site-specific hazard curves at FMF, assuming a soil thickness of 5 ft.

PGA	AEF	50 Hz SA	AEF	33.3 Hz SA	AEF	20 Hz SA	AEF	10 Hz SA	AEF
0.01	2.61E-02	0.01	3.04E-02	0.01	2.92E-02	0.01	4.22E-02	0.01	6.59E-02
0.02	9.64E-03	0.02	1.22E-02	0.02	1.26E-02	0.02	1.95E-02	0.02	3.59E-02
0.05	1.85E-03	0.05	2.76E-03	0.05	3.37E-03	0.05	5.42E-03	0.05	1.04E-02
0.1	4.20E-04	0.1	7.83E-04	0.1	1.14E-03	0.1	1.82E-03	0.1	3.29E-03
0.2	7.77E-05	0.2	1.91E-04	0.2	3.36E-04	0.2	5.07E-04	0.2	8.03E-04
0.3	2.63E-05	0.3	7.75E-05	0.3	1.49E-04	0.3	2.14E-04	0.3	3.06E-04
0.4	1.18E-05	0.4	3.88E-05	0.4	8.03E-05	0.4	1.10E-04	0.5	8.13E-05
0.5	6.16E-06	0.5	2.24E-05	0.5	4.83E-05	0.5	6.42E-05	0.7	3.21E-05
0.7	2.20E-06	0.7	9.35E-06	0.7	2.15E-05	0.7	2.74E-05	1	1.17E-05
1	6.65E-07	1	3.35E-06	1	8.55E-06	1	1.05E-05	2	1.52E-06
2	4.84E-08	2	3.38E-07	2	1.12E-06	2	1.43E-06	3	4.32E-07
5	9.56E-10	5	7.78E-09	5	3.99E-08	5	6.89E-08	5	8.44E-08
10	2.65E-11	10	2.70E-10	10	2.03E-09	10	5.63E-09	10	8.73E-09
5 Hz SA	AEF	3.33 Hz SA	AEF	2 Hz SA	AEF	1 Hz SA	AEF	0.5 Hz SA	AEF
0.01	6.79E-02	0.01	4.78E-02	0.01	4.10E-02	0.0001	4.41E-01	0.0001	3.26E-01
0.02	2.76E-02	0.02	1.71E-02	0.02	1.56E-02	0.001	1.70E-01	0.001	7.00E-02
0.05	5.72E-03	0.05	2.96E-03	0.05	2.75E-03	0.01	1.40E-02	0.01	3.25E-03
0.1	1.23E-03	0.1	5.65E-04	0.1	5.40E-04	0.05	5.07E-04	0.05	6.44E-05
0.2	2.06E-04	0.2	8.42E-05	0.2	7.93E-05	0.07	2.07E-04	0.07	2.23E-05
0.3	6.44E-05	0.3	2.38E-05	0.3	2.20E-05	0.1	6.96E-05	0.1	6.09E-06
0.5	1.33E-05	0.5	4.15E-06	0.4	8.12E-06	0.3	1.39E-06	0.3	5.89E-08
0.7	4.38E-06	0.7	1.17E-06	0.5	3.56E-06	0.5	1.62E-07	0.5	4.84E-09
1	1.26E-06	1	2.77E-07	0.7	9.44E-07	0.7	3.38E-08	0.7	8.09E-10
2	1.06E-07	2	1.51E-08	1	2.06E-07	1	5.67E-09	1	1.06E-10
3	2.66E-08	3	2.91E-09	1.5	3.17E-08	1.5	6.36E-10	1.5	9.07E-12
5	5.89E-09	5	4.26E-10	2	7.56E-09	2	1.19E-10	2	1.42E-12
10	8.05E-10	10	2.60E-11	5	3.61E-11	5	2.78E-13	5	2.20E-15
PGA- Peak Ground Acceleration (g); AEF – Annual Exceedance Frequency; SA – Spectral Acceleration (g).									

Table 10-6. Site-specific hazard fractiles at FMF, assuming a soil thickness of 5 ft.

	Annual Exceedance Frequency at Fractiles:				
PGA (g)	5th	15th	50th	85th	95th
0.01	2.09E-02	2.11E-02	2.62E-02	2.95E-02	3.13E-02
0.02	5.98E-03	6.31E-03	9.51E-03	1.23E-02	1.38E-02
0.05	7.49E-04	8.54E-04	1.74E-03	2.67E-03	3.38E-03
0.10	1.10E-04	1.34E-04	3.52E-04	6.81E-04	9.98E-04
0.20	1.33E-05	1.70E-05	5.65E-05	1.40E-04	2.27E-04
0.30	3.55E-06	4.70E-06	1.79E-05	5.03E-05	8.33E-05
0.40	1.34E-06	1.81E-06	7.60E-06	2.35E-05	3.90E-05
0.50	6.10E-07	8.42E-07	3.83E-06	1.26E-05	2.06E-05
0.70	1.75E-07	2.50E-07	1.30E-06	4.71E-06	7.43E-06
1.00	4.12E-08	6.23E-08	3.77E-07	1.47E-06	2.10E-06
2.00	2.61E-09	3.92E-09	2.51E-08	1.10E-07	1.42E-07
5.00	2.87E-11	4.55E-11	5.50E-10	2.18E-09	2.99E-09
10.00	2.25E-13	4.51E-13	1.15E-11	6.88E-11	8.72E-11
10 Hz (g)					
0.01	5.60E-02	5.76E-02	6.90E-02	6.99E-02	7.00E-02
0.02	2.41E-02	2.57E-02	3.58E-02	4.33E-02	4.67E-02
0.05	5.92E-03	6.52E-03	1.04E-02	1.35E-02	1.51E-02
0.10	1.51E-03	1.72E-03	3.27E-03	4.64E-03	5.44E-03
0.20	2.85E-04	3.34E-04	7.62E-04	1.22E-03	1.52E-03
0.30	9.60E-05	1.15E-04	2.85E-04	4.72E-04	6.08E-04
0.50	2.22E-05	2.69E-05	7.27E-05	1.29E-04	1.78E-04
0.70	8.11E-06	1.00E-05	2.80E-05	5.13E-05	7.31E-05
1.00	2.70E-06	3.39E-06	9.95E-06	1.87E-05	2.72E-05
2.00	2.81E-07	3.81E-07	1.22E-06	2.43E-06	3.77E-06
3.00	7.42E-08	1.03E-07	3.27E-07	6.64E-07	1.18E-06
5.00	1.36E-08	1.88E-08	6.27E-08	1.31E-07	2.41E-07
10.00	1.36E-09	1.87E-09	7.16E-09	1.51E-08	2.15E-08

Table 10-7. Mean site-specific hazard curves at FMF, assuming a soil thickness of 15 ft.

PGA	AEF	50 Hz SA	AEF	33.3 Hz SA	AEF	20 Hz SA	AEF	10 Hz SA	AEF
0.01	3.25E-02	0.01	3.71E-02	0.01	3.46E-02	0.01	4.84E-02	0.01	6.94E-02
0.02	1.52E-02	0.02	1.80E-02	0.02	1.72E-02	0.02	2.69E-02	0.02	5.44E-02
0.05	3.59E-03	0.05	4.56E-03	0.05	4.62E-03	0.05	7.93E-03	0.05	2.00E-02
0.1	9.77E-04	0.1	1.35E-03	0.1	1.46E-03	0.1	2.69E-03	0.1	7.31E-03
0.2	1.75E-04	0.2	2.80E-04	0.2	3.39E-04	0.2	7.07E-04	0.2	2.16E-03
0.3	5.30E-05	0.3	9.44E-05	0.3	1.24E-04	0.3	2.69E-04	0.3	9.29E-04
0.4	2.14E-05	0.4	4.07E-05	0.4	5.67E-05	0.4	1.26E-04	0.5	2.66E-04
0.5	1.01E-05	0.5	2.06E-05	0.5	3.00E-05	0.5	6.73E-05	0.7	1.04E-04
0.7	3.01E-06	0.7	6.73E-06	0.7	1.08E-05	0.7	2.49E-05	1	3.55E-05
1	7.53E-07	1	1.85E-06	1	3.28E-06	1	8.00E-06	2	3.57E-06
2	3.45E-08	2	1.02E-07	2	2.27E-07	2	6.97E-07	3	8.09E-07
5	3.23E-10	5	9.60E-10	5	3.18E-09	5	1.65E-08	5	1.12E-07
10	5.71E-12	10	1.57E-11	10	6.61E-11	10	6.72E-10	10	6.39E-09
5 Hz SA	AEF	3.33 Hz SA	AEF	2 Hz SA	AEF	1 Hz SA	AEF	0.5 Hz SA	AEF
0.01	8.00E-02	0.01	5.34E-02	0.01	4.30E-02	0.0001	4.44E-01	0.0001	3.23E-01
0.02	3.85E-02	0.02	2.00E-02	0.02	1.69E-02	0.001	1.73E-01	0.001	6.88E-02
0.05	9.53E-03	0.05	3.82E-03	0.05	3.13E-03	0.01	1.45E-02	0.01	3.17E-03
0.1	2.59E-03	0.1	8.03E-04	0.1	6.50E-04	0.05	5.51E-04	0.05	6.48E-05
0.2	5.69E-04	0.2	1.38E-04	0.2	1.02E-04	0.07	2.30E-04	0.07	2.26E-05
0.3	2.18E-04	0.3	4.54E-05	0.3	3.04E-05	0.1	7.95E-05	0.1	6.26E-06
0.5	5.92E-05	0.5	1.04E-05	0.4	1.21E-05	0.3	1.76E-06	0.3	6.59E-08
0.7	2.33E-05	0.7	3.71E-06	0.5	5.72E-06	0.5	2.38E-07	0.5	5.86E-09
1	7.94E-06	1	1.15E-06	0.7	1.80E-06	0.7	5.96E-08	0.7	1.05E-09
2	7.68E-07	2	9.14E-08	1	5.16E-07	1	1.32E-08	1	1.49E-10
3	1.66E-07	3	1.84E-08	1.5	1.19E-07	1.5	2.27E-09	1.5	1.40E-11
5	2.02E-08	5	2.25E-09	2	3.95E-08	2	6.26E-10	2	2.36E-12
10	1.17E-09	10	1.01E-10	5	8.57E-10	5	6.83E-12	5	4.39E-15

PGA- Peak Ground Acceleration (g); AEF – Annual Exceedance Frequency; SA – Spectral Acceleration (g).

Table 10-8. Site-specific hazard fractiles at FMF, assuming a soil thickness of 15 ft.

	Annual Exceedance Frequency at Fractiles:				
PGA (g)	5th	15th	50th	85th	95th
0.01	2.44E-02	2.83E-02	3.35E-02	3.56E-02	3.59E-02
0.02	8.31E-03	1.07E-02	1.48E-02	1.93E-02	2.22E-02
0.05	1.38E-03	2.07E-03	3.44E-03	5.06E-03	6.33E-03
0.10	2.45E-04	4.24E-04	9.36E-04	1.54E-03	2.02E-03
0.20	3.39E-05	5.91E-05	1.57E-04	3.03E-04	3.63E-04
0.30	9.76E-06	1.60E-05	4.59E-05	9.22E-05	1.17E-04
0.40	3.87E-06	5.89E-06	1.68E-05	3.51E-05	5.11E-05
0.50	1.82E-06	2.46E-06	7.34E-06	1.61E-05	2.58E-05
0.70	5.40E-07	6.08E-07	2.06E-06	4.86E-06	8.56E-06
1.00	1.19E-07	1.33E-07	4.62E-07	1.17E-06	2.27E-06
2.00	4.97E-09	5.19E-09	1.91E-08	5.46E-08	1.15E-07
5.00	4.62E-11	4.94E-11	1.92E-10	5.46E-10	1.23E-09
10.00	4.79E-13	4.99E-13	2.86E-12	8.93E-12	2.23E-11
10 Hz (g)					
0.01	6.62E-02	6.86E-02	6.99E-02	7.00E-02	7.00E-02
0.02	3.25E-02	4.17E-02	5.60E-02	6.63E-02	6.91E-02
0.05	8.90E-03	1.28E-02	1.90E-02	2.75E-02	3.36E-02
0.10	2.59E-03	4.31E-03	6.79E-03	1.04E-02	1.31E-02
0.20	5.72E-04	1.12E-03	1.95E-03	3.30E-03	4.10E-03
0.30	2.12E-04	4.25E-04	8.24E-04	1.50E-03	1.80E-03
0.50	5.47E-05	1.03E-04	2.46E-04	4.39E-04	5.07E-04
0.70	2.14E-05	3.55E-05	9.46E-05	1.70E-04	2.05E-04
1.00	7.58E-06	1.03E-05	3.01E-05	5.63E-05	7.61E-05
2.00	7.69E-07	8.11E-07	2.54E-06	5.15E-06	9.17E-06
3.00	1.38E-07	1.92E-07	6.30E-07	1.25E-06	2.21E-06
5.00	2.01E-08	2.80E-08	9.27E-08	1.83E-07	2.86E-07
10.00	6.46E-10	8.61E-10	5.34E-09	1.19E-08	2.14E-08

(a)

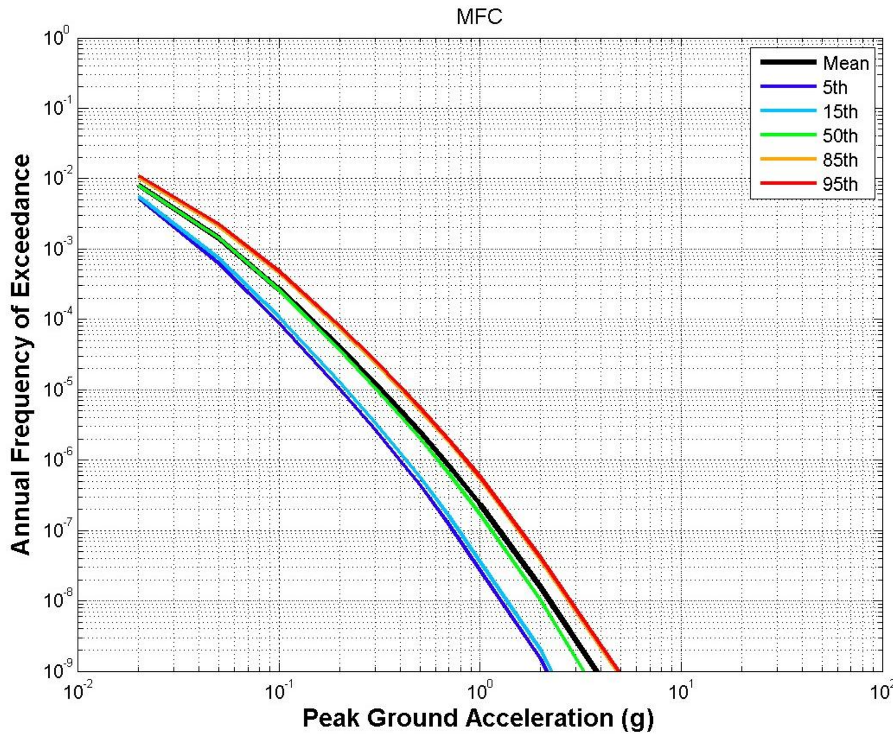

(b)

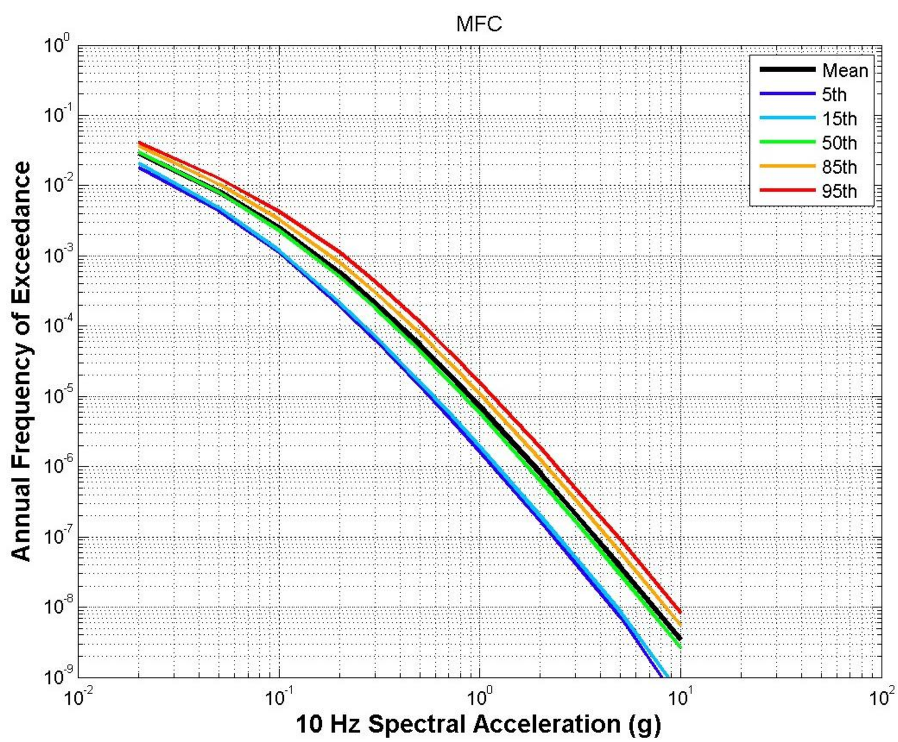

Figure 10-24. Total mean site-specific hazard and fractiles at MFC for: a) PGA; and b) 10 Hz spectral acceleration.

(a)

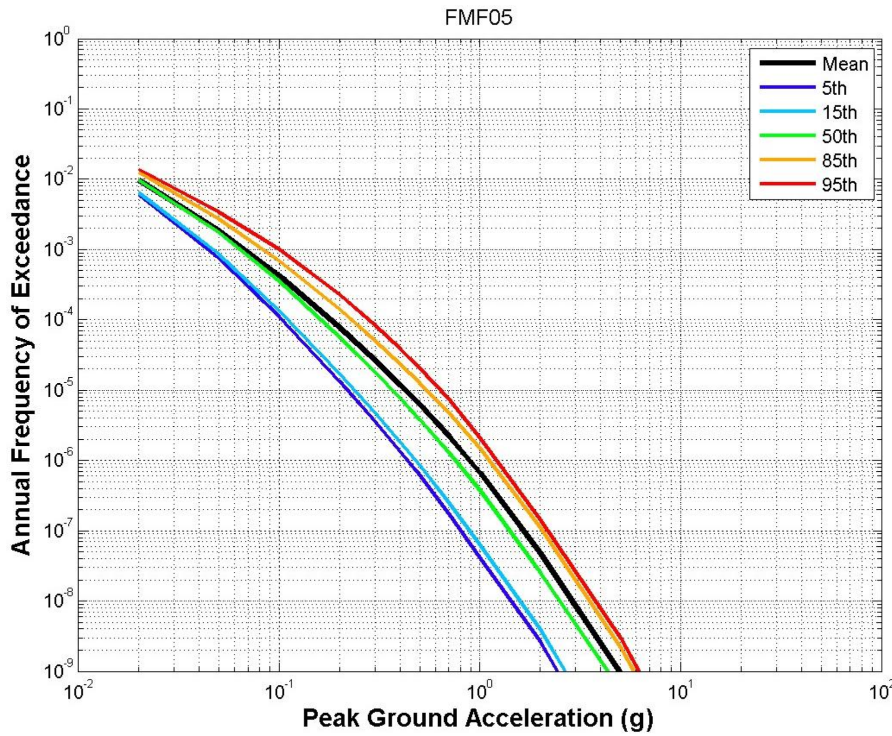

(b)

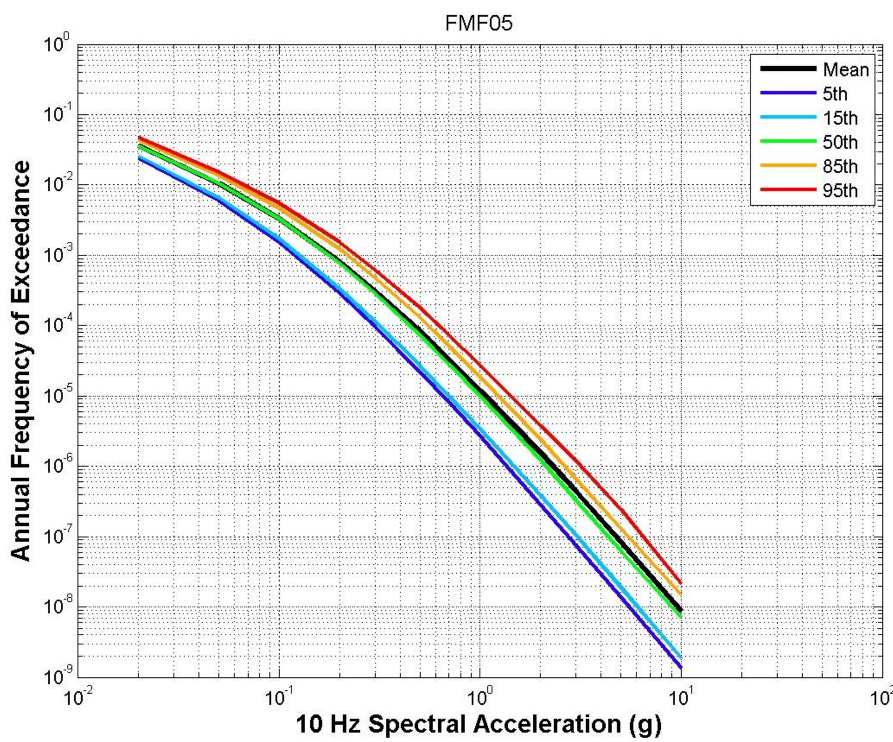

Figure 10-25. Total mean site-specific hazard and fractiles at FMF, assuming a soil thickness of 5 ft, for: a) PGA; and b) 10 Hz spectral acceleration.

(a)

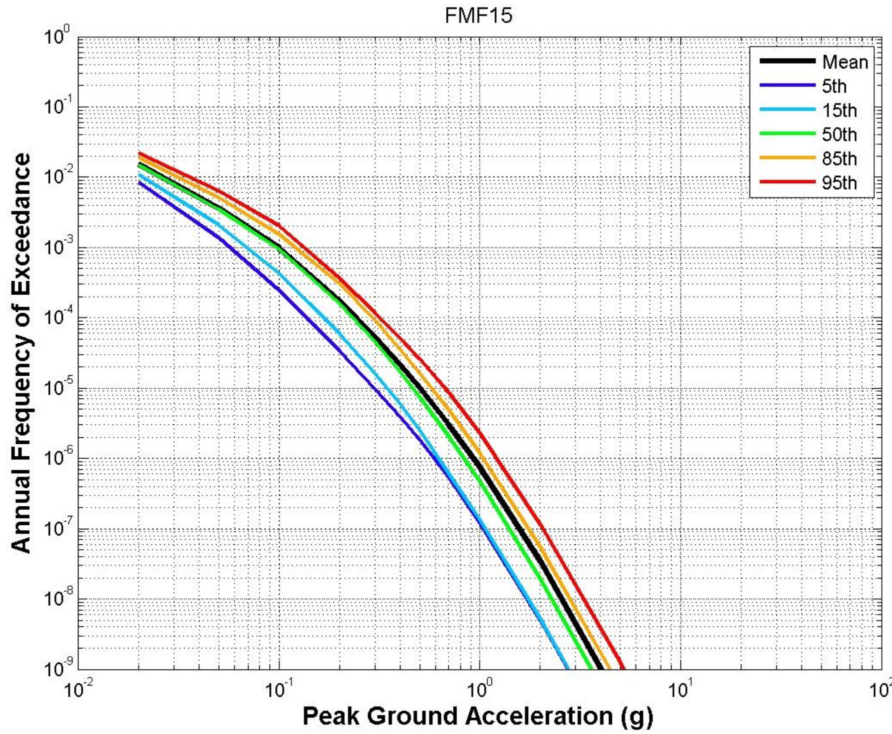

(b)

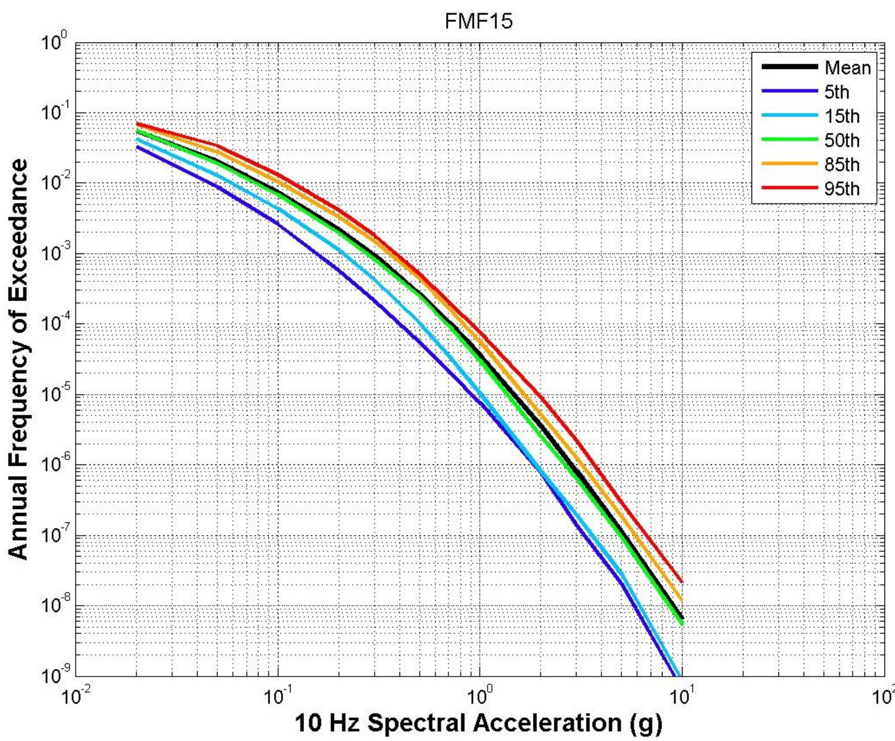

Figure 10-26. Total mean site-specific hazard and fractiles at FMF, assuming a soil thickness of 15 feet, for: a) PGA; and b) 10 Hz spectral acceleration.

(a)

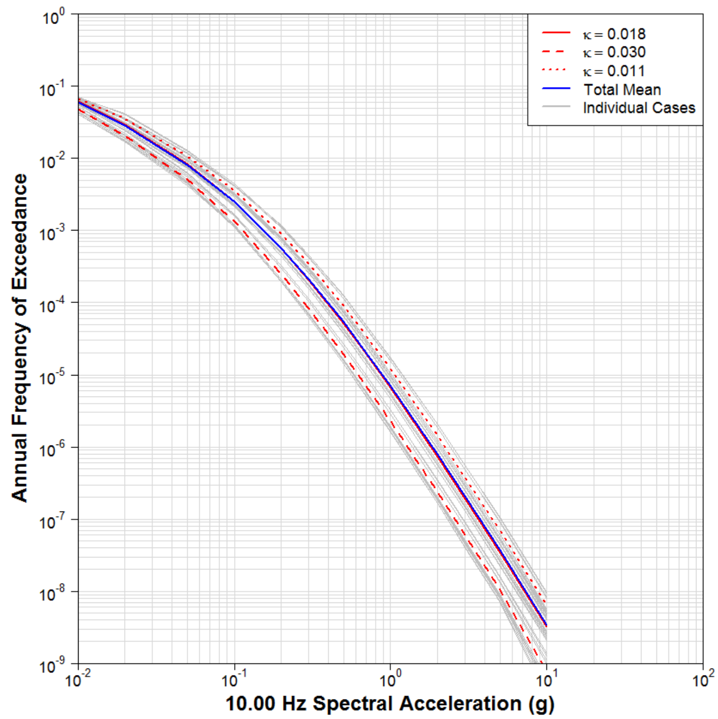

(b)

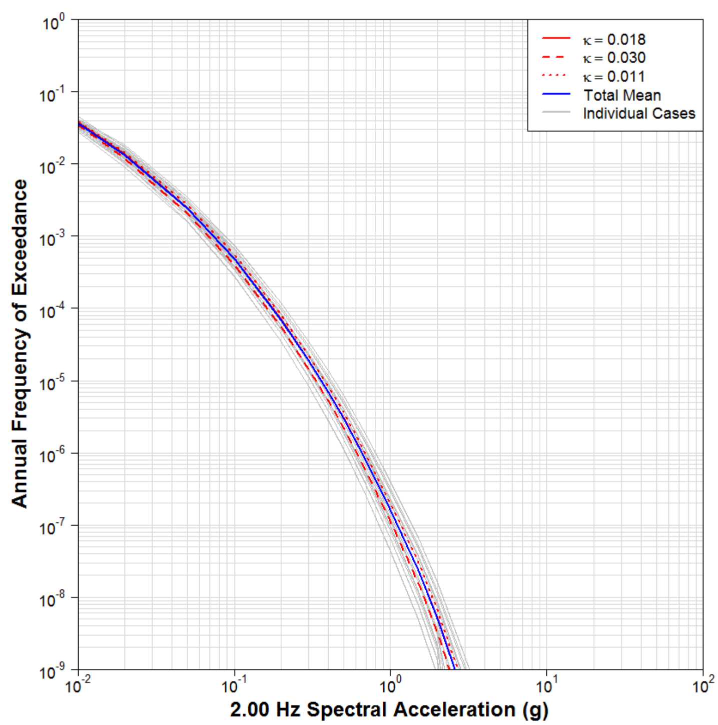

Figure 10-27. Sensitivity of hazard at MFC with respect to kappa at : a) 10 Hz (0.1-sec); and b) 2 Hz (0.5-sec) spectral accelerations.

(a)

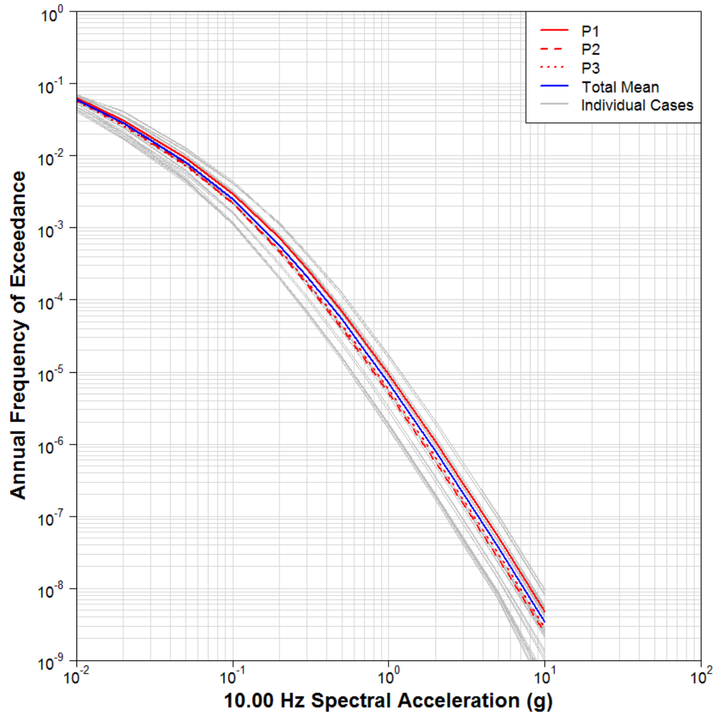

(b)

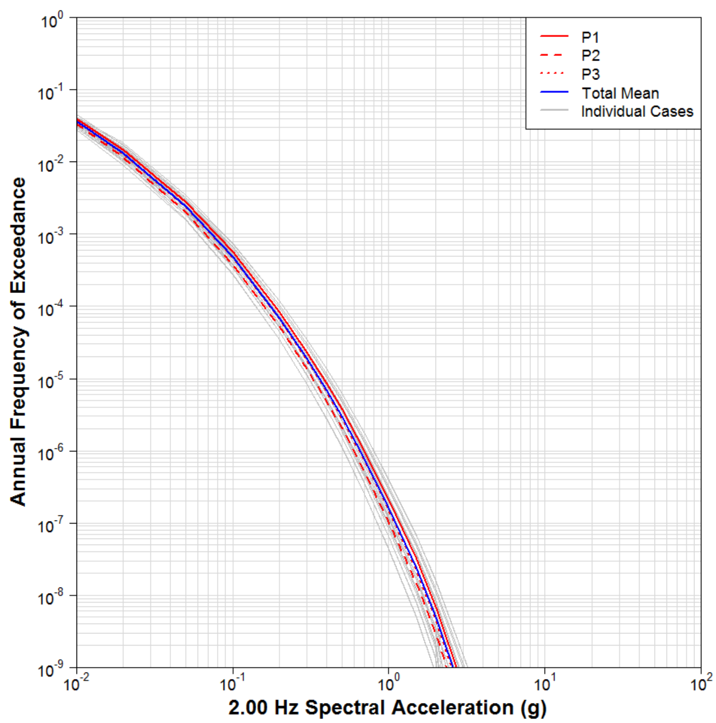

Figure 10-28. Sensitivity of hazard at MFC with respect to velocity profile at: 10 Hz (0.1-sec); and b) 2 Hz (0.5-sec) spectral accelerations.

(a)

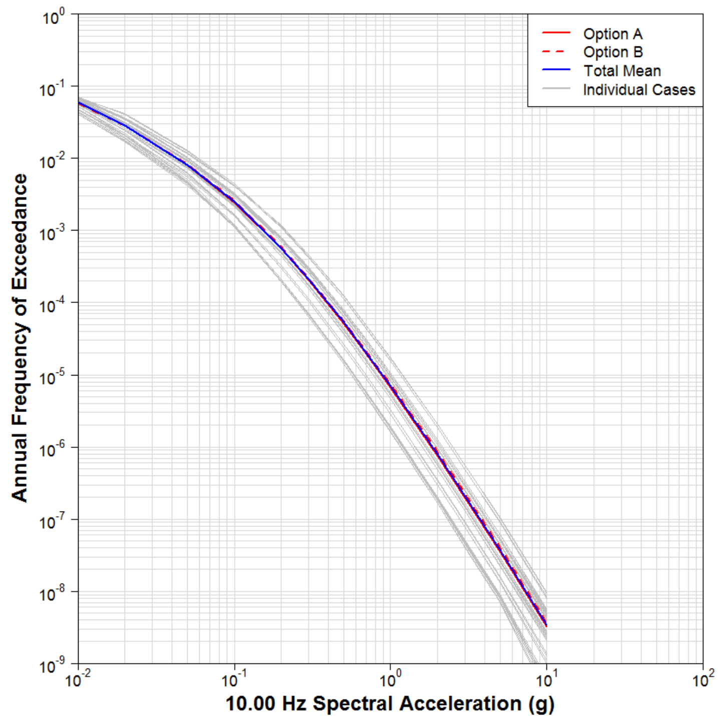

(b)

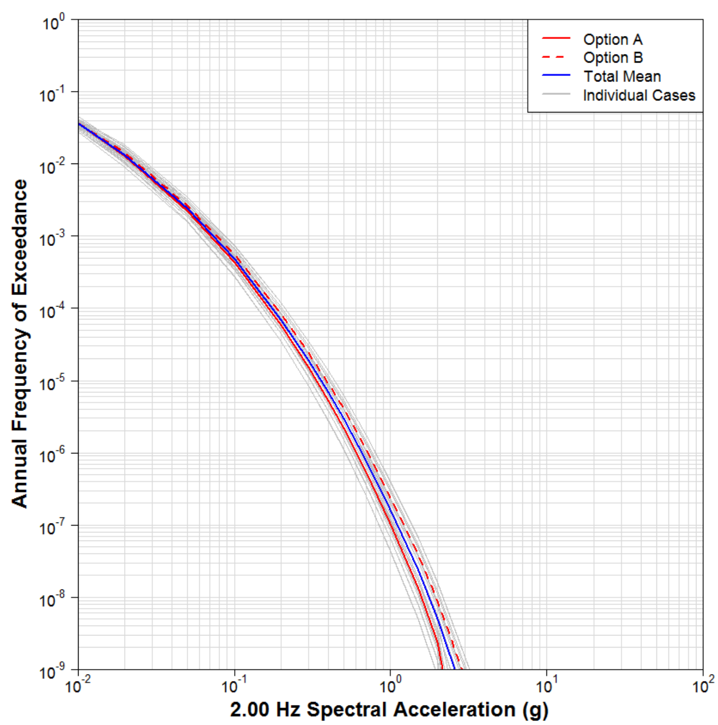

Figure 10-29. Sensitivity of hazard at MFC with respect to $\sigma_{epistemic}$ model at: a) 10 Hz (0.1-sec); and b) 2 Hz (0.5-sec) spectral accelerations.

relative to the remaining across all frequencies of spectral acceleration. These two observations are a result of the relative similarity in the amplitude of the amplification between the three profiles combined with slight phase shifts in the locations of resonant peaks.

The two alternative $\sigma_{\text{epistemic}}$ models, produce similar mean hazard at 5 Hz spectral acceleration and higher. At spectral accelerations lower than 5 Hz the conditional mean hazard of the alternatives begins to deviate, with the deviation increasing as frequency of spectral acceleration and AEF decrease. In the AEF range of interest ($1\text{x}10^{-4}$-$4\text{x}10^{-4}$) the two models differ by factors up to 1.25 for frequencies of spectral acceleration from 0.5-10 Hz (with Option B having a higher hazard for the given frequency range). The observations of hazard sensitivity are consistent with the difference in the two $\sigma_{\text{epistemic}}$ models. Figure 10-29 compares the conditional-mean hazard for a given $\sigma_{\text{epistemic}}$ model (red curves) with the total mean hazard at 2 Hz and 10 Hz spectral acceleration for MFC (blue curve), and with the individual results of the 36 logic tree branches (grey curves). The hazard at MFC is not sensitive to the selection of the model for the earthquake source spectrum used in generating site-amplification functions.

10.4.1.2 FMF Site

Alternatives of five different parameters (the 4 sets of parameters used at MFC with the addition of two alternative material models) were used to capture the uncertainty in the site-amplification functions for FMF, which provided 72 alternative hazard curves at each frequency of spectral acceleration. In addition, two alternative soil thicknesses were considered: 5 and 15 ft; in the following discussion these alternatives are named FMF05 and FMF15, respectively.

The hazard for both, FMF05and FMF15, is only slightly less sensitive to alternative kappa values than MFC but follows the same trends. The hazard for FMF05 shows similar sensitivity with respect to variation in velocity profile as MFC because the soil thickness is not large enough to have a strong influence on the results. The hazard sensitivity with respect to variation in velocity profile for FMF15 is not consistent with the sensitivity observed at MFC and FMF05. At FMF15 the soil thickness is beginning to have an influence on the hazard. In the AEF range of interest profile 2 consistently produces the largest ground motions and profile 3 consistently produces the lowest. At lower AEF values (less than approximately $1\text{x}10^{-6}$) and high frequencies of spectral acceleration (greater than 10 Hz) the conditional-mean hazard curves begin to cross and profile 2 produces a lower ground motion for a given level of hazard. Figures 10-30 and 10-31 compare the conditional-mean hazard for a given velocity profile with the total mean hazard at 2 Hz and 10 Hz spectral acceleration for FMF05 and FMF15, respectively. The hazard at both FMF05 and FMF15 shows similar sensitivity with respect to $\sigma_{\text{epistemic}}$ models as is observed for MFC, with FMF15 showing slightly less sensitivity in the frequency band of 3.33–20 Hz spectral acceleration. The hazard at FMF05 and FMF15 is not sensitive to the selection of source spectrum used in generating site-amplification functions.

For both FMF05 and FMF15 additional epistemic uncertainty in the transfer functions was included through the two alternative soil material property models: the EPRI (1993) set, and the Peninsular Range set. Figures 10-32 and 10-33 compare the conditional-mean hazard for a given material property model with the total mean hazard at 2 Hz and 10 Hz spectral acceleration for FMF05 and FMF15, respectively. Soil nonlinearity has two effects on site amplification. First, the soil shear wave velocity decreases with increasing loading level. As site amplification is inversely proportional to the square root of the near-surface average shear wave velocity compared to the shear wave velocity at depth, the result is an increase in site amplification. At the same time, the level of damping in the soils increases, tending to reduce the soil motions. The effect of increased damping on soil response is greater at high frequencies than at low frequencies. In combination, one typically observes different sensitivities to the degree of soil nonlinearity at high and low frequencies, with more nonlinear soil curves tending to produce large motions at low frequencies where the effects of velocity differences dominate, and more nonlinear curves tending to produce lower response at high frequencies where the effects of increased damping become

(a)

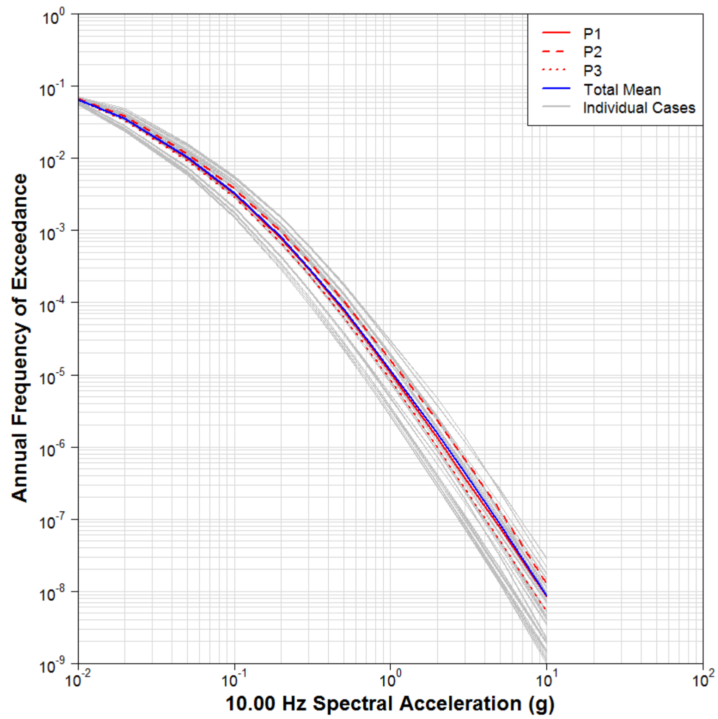

(b)

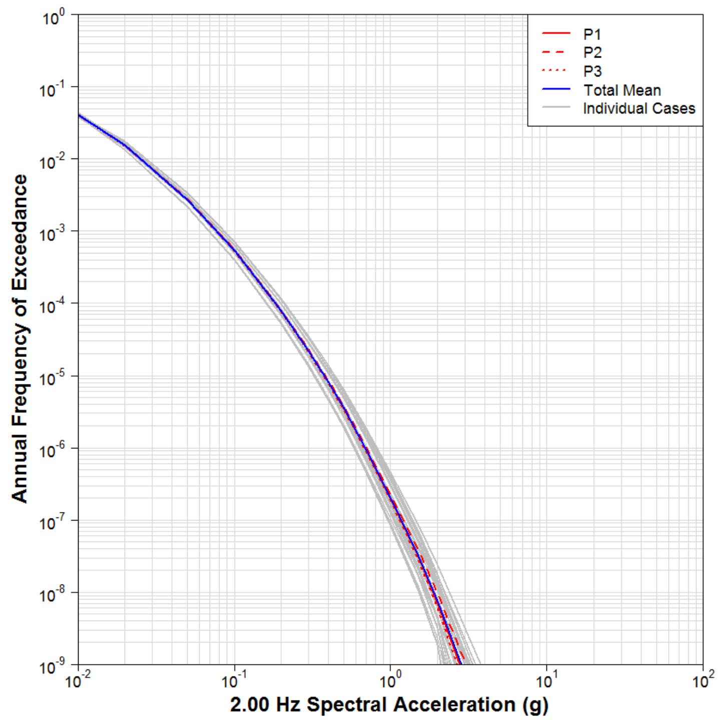

Figure 10-30. Sensitivity of the hazard at FMF05 with respect to velocity profile at: 10 Hz (0.1-sec); and b) 2 Hz (0.5-sec) spectral accelerations.

(a)

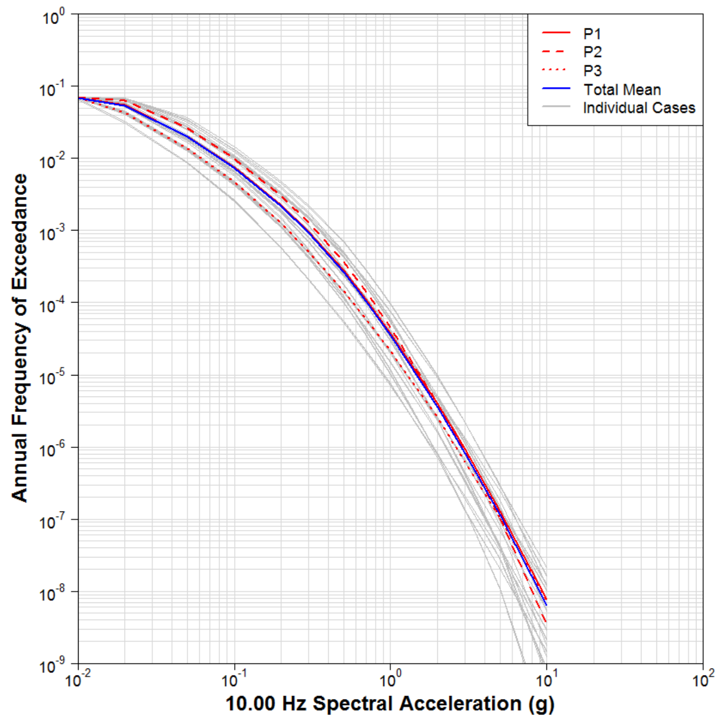

(b)

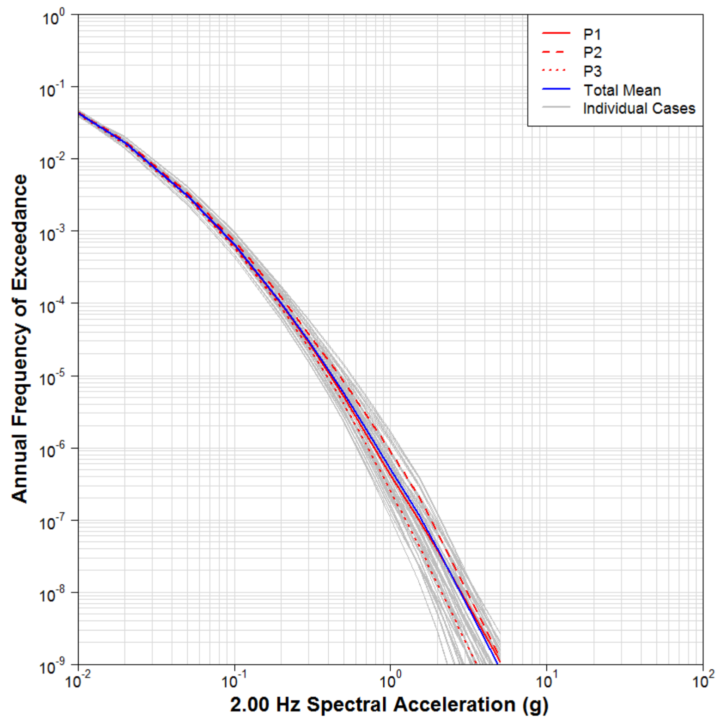

Figure 10-31. Sensitivity of the hazard at FMF15 with respect to velocity profile at: a) 10 Hz (0.1-sec); and b) 2 Hz (0.5-sec) spectral accelerations.

(a)

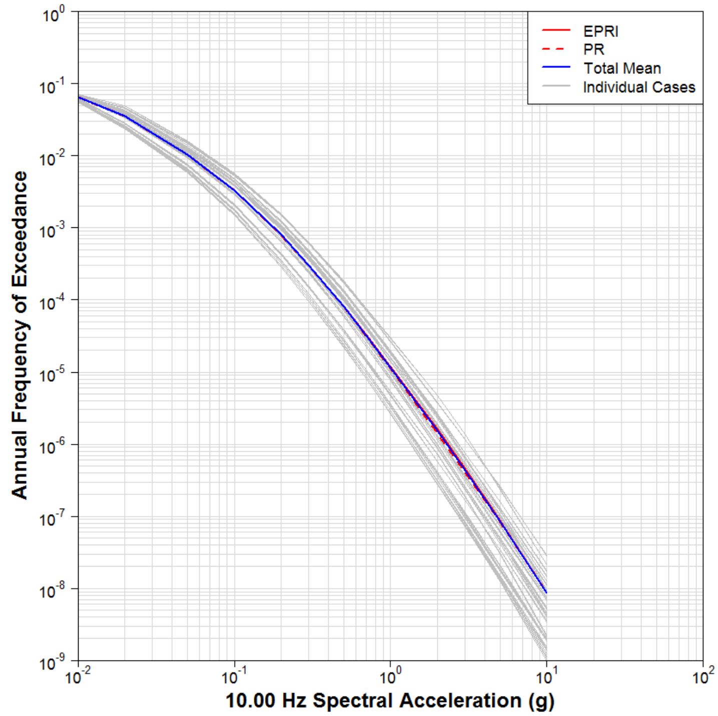

(b)

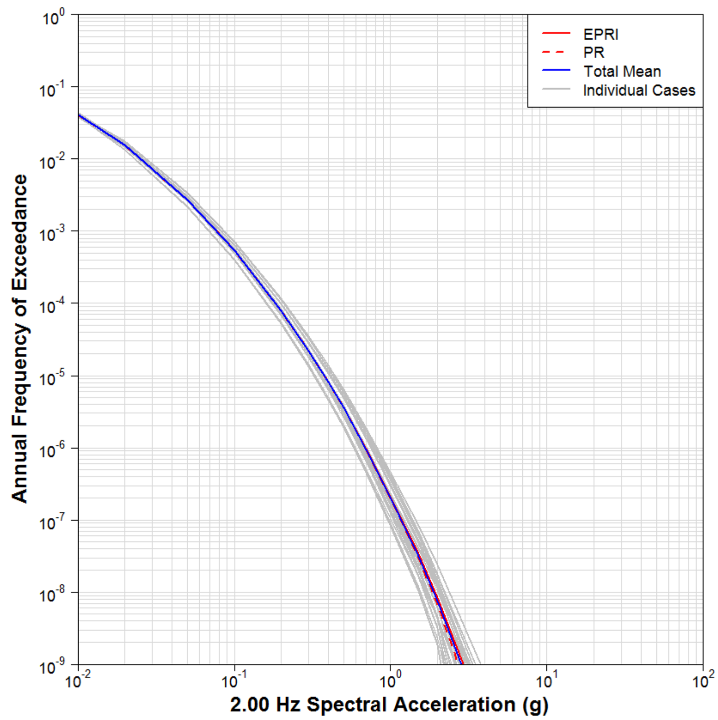

Figure 10-32. Sensitivity of the hazard at FMF05 with respect to material property model at: a) 10 Hz (0.1-sec); and b) 2 Hz (0.5-sec) spectral accelerations.

(a)

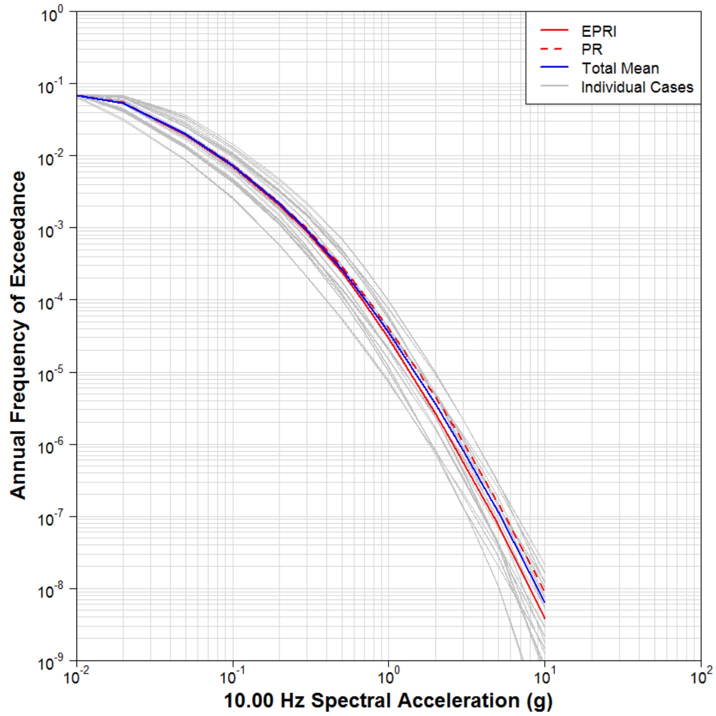

(b)

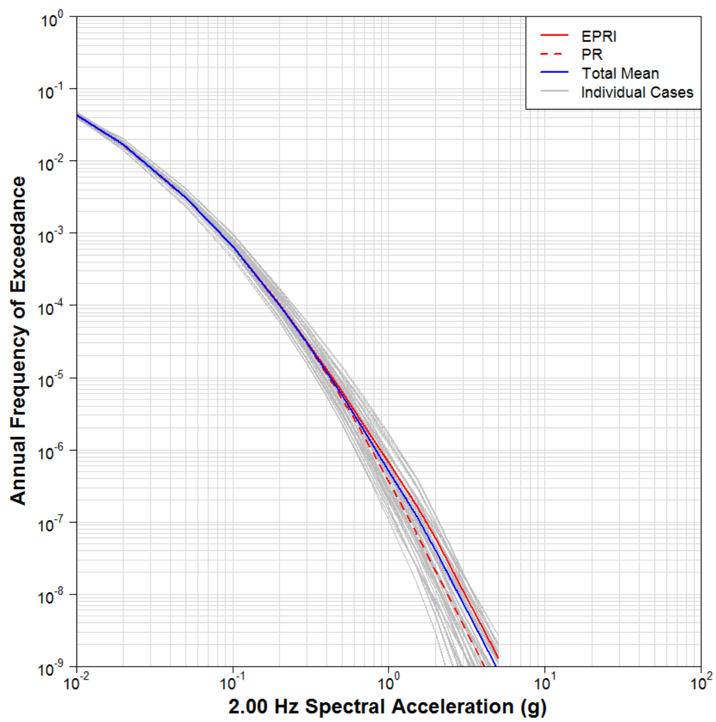

Figure 10-33. Sensitivity of the hazard at FMF15 with respect to material property model at: a) 10 Hz (0.1-sec); and b) 2 Hz (0.5-sec) spectral accelerations.

dominant. These differing effects are evident in the sensitivity results for FMF15 (Figure 10-33), where higher 10 Hz hazard results from using the more linear Peninsular Range curves and higher 2 Hz hazard results from using the more nonlinear EPRI curves. The trends are the same in the sensitivity for FMF05 (Figure 10-32) but the differences are much smaller because of the very limited soil depth.

10.4.1.3 Horizontal UHRS and GMRS for MFC and FMF

Uniform hazard response spectra (UHRS) are computed for the MFC and FMF site by interpolating the mean hazard curves for the individual spectral frequencies. Figure 10-34 shows a comparison of the 2015 MFC rock UHRS, 2015 MFC rock GMRS for SDC-3, and 2006 MFC rock DBE spectrum at $4x10^{-4}$ and $4x10^{-5}$. The results show that although the GMRS is shifted towards high frequency motions, the spectrum is enveloped by the 2006 MFC rock DBE (Payne, 2006a). The $4x10^{-4}$ and $4x10^{-5}$MFC rock UHRS and GMRS are listed in Table 10-9.

Figure 10-35 compares the 2015 FMF site-specific horizontal UHRS, 2015 FMF site-specific GMRS for SDC-3, and the 2006 FMF site-specific DBGM spectrum at $4x10^{-4}$ and $4x10^{-5}$AEFs. Because the soil thickness varies across the footprint of FMF, the GMRS is calculated from the envelope of the $4x10^{-4}$ UHRS and the envelope of the $4x10^{-5}$ UHRS obtained for the two soil thicknesses. In general the UHRS calculated for 15 ft. of soil is higher than the UHRS for 5 ft. of soil. The 2006 FMF site-specific DBGM is from Payne (2006a), see Section 1.1.2. Similar to the MFC rock results, the 2006 FMF site-specific DBGM spectrum (from Payne, 2006a) fully encompasses the 2015 FMF site-specific GMRS for SDC-3. The 15-ft and 5-ft site-specific horizontal UHRS at $4x10^{-4}$ and at $4x10^{-5}$AEF are listed in Table 10-10. Table 10-11 lists the 2015 FMF site-specific horizontal UHRS, 2015 FMF site-specific GMRS for SDC-3 at $4x10^{-4}$ and at $4x10^{-5}$AEF.

10.4.1.4 Vertical UHRS and GMRS for MFC and FMF

Table 9.4 contains the V/H ratios recommended for use at MFC and FMF. The ratio is applied to the horizontal 2015 site-specific UHRS for AEF of $4x10^{-4}$ and to the horizontal 2015 site-specific GMRS to obtain the corresponding vertical 2015 site-specific UHRS for AEF of $4x10^{-4}$ and GMRS as shown in Tables 10-12 (MFC) and 10-13 (FMF). The vertical 2015 UHS and GMRS are compared in Figures 10-36 (MFC) and 10-37 (FMF) to the corresponding vertical 2006 DBGM.

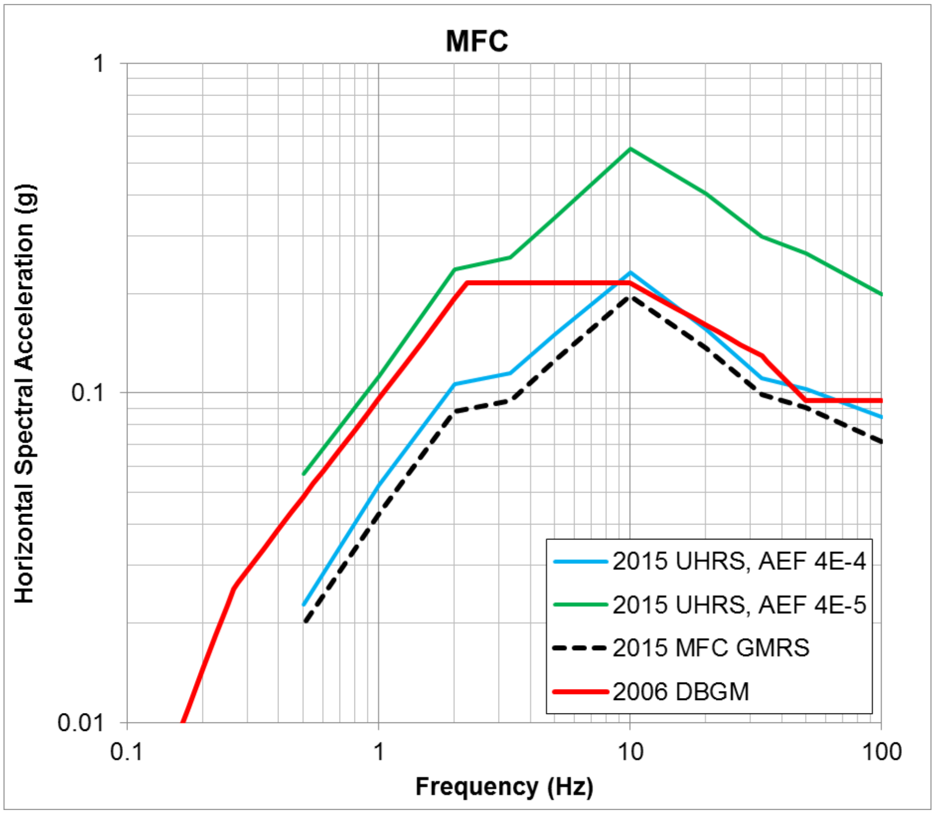

Figure 10-34. Comparison of the 2015 MFC rock horizontal UHRS at 4×10^{-4}AEF (2,500 yr return period) and 4×10^{5}AEF (25,000 yr return period) (blue and green curves, respectively), the 2015 MFC rock GMRS for SDC-3 (dashed, black curve), and the 2006 MFC rock DBE spectrum (red curve) at 5% damping.

Table 10-9. Values of the 2015 MFC rock horizontal UHRS (5% damping) at 4x10-4AEF (2,500 yr return period) and 4x10-5AEF (25,000 yr return period), the 2015 MFC rock GMRS for SDC-3, and Design Factors.

Period (sec)	Frequency (Hz)	AEF 4×10^{-4} UHRS (g)	AEF 4×10^{-5} UHRS (g)	DF_2	MFC Rock GMRS (g)[1]
0.01	100	8.44E-02	2.00E-01	8.47E-01	7.15E-02
0.02	50	1.03E-01	2.65E-01	8.76E-01	9.03E-02
0.03	33.33	1.11E-01	2.98E-01	8.91E-01	9.89E-02
0.05	20	1.57E-01	4.02E-01	8.75E-01	1.37E-01
0.1	10	2.32E-01	5.53E-01	8.49E-01	1.97E-01
0.2	5	1.51E-01	3.41E-01	8.31E-01	1.25E-01
0.3	3.33	1.15E-01	2.57E-01	8.28E-01	9.52E-02
0.5	2	1.07E-01	2.37E-01	8.26E-01	8.82E-02
1	1	5.25E-02	1.13E-01	8.14E-01	4.28E-02
2	0.5	2.29E-02	5.69E-02	8.64E-01	1.98E-02
1. The Design Factor (DF) used to calculate the GMRS is the larger of 0.8 and DF_2 (see Equation 10-10).					

Table 10-10. Values of the 2015 FMF site-specific UHRS (5% damping) at $4x10^{-4}$AEF (2,500 yr return period) and $4x10^{-5}$AEF (25,000 yr return period) for soil thicknesses of 5 and 15 ft.

Period (sec)	Frequency (Hz)	Spectral Acceleration (g)			
		FMF UHRS (5 ft Soil)		FMF UHRS (15 ft Soil)	
		AEF $4x10^{-4}$	AEF $4x10^{-5}$	AEF $4x10^{-4}$	AEF $4x10^{-5}$
0.01	100	1.02E-01	2.56E-01	1.43E-01	3.28E-01
0.02	50	1.39E-01	3.95E-01	1.71E-01	4.02E-01
0.03	33.3	1.81E-01	5.41E-01	1.85E-01	4.52E-01
0.05	20	2.23E-01	6.03E-01	2.54E-01	5.96E-01
0.1	10	2.68E-01	6.46E-01	4.23E-01	9.61E-01
0.2	5	1.55E-01	3.50E-01	2.32E-01	5.76E-01
0.3	3.33	1.13E-01	2.54E-01	1.32E-01	3.14E-01
0.5	2	1.11E-01	2.48E-01	1.20E-01	2.74E-01
1	1	5.47E-02	1.17E-01	5.66E-02	1.22E-01
2	0.5	2.36E-02	5.81E-02	2.35E-02	5.83E-02

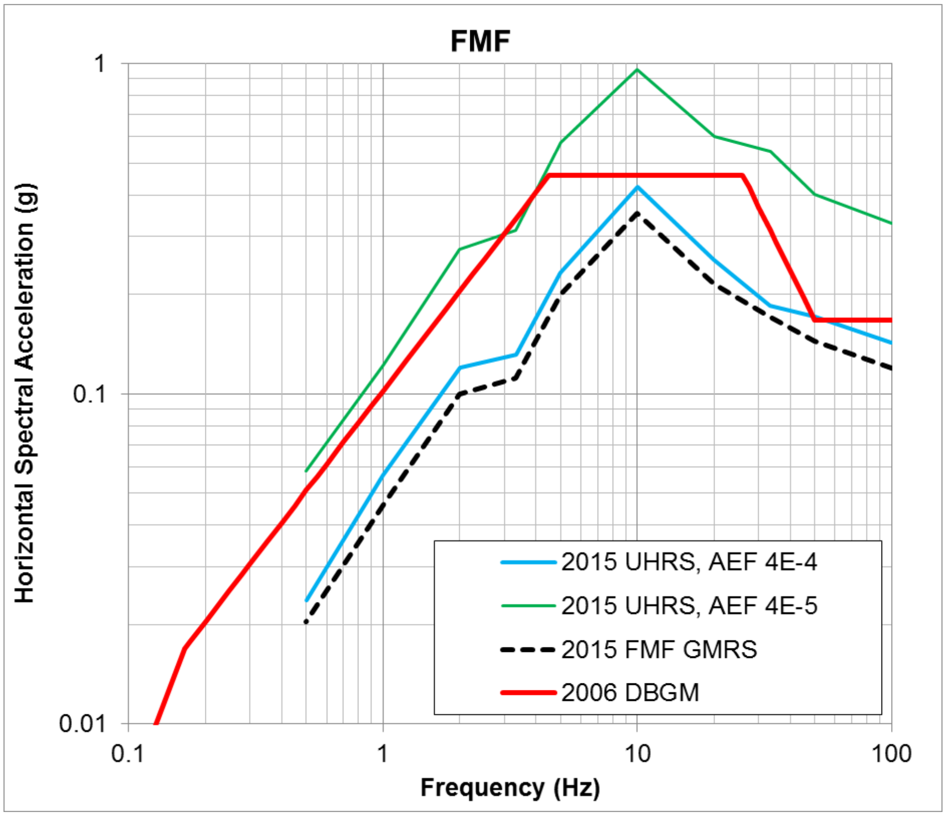

Figure 10-35. Comparison of the 2015 FMF site-specific UHS at $4x10^{-4}$AEF (2,500 yr return period) and $4x10^{-5}$AEF (25,000 yr return period) (blue and green curves, respectively), the 2015 FMF site-specific GMRS for SDC-3(dashed, black curve), and the 2006 FMF site-specific DBGM spectrum (red curve) at 5% damping.

Table 10-11. Values of the 2015 FMF site-specific UHRS at $4x10^{-4}$AEF (2,500 yr return period) and $4x10^{-5}$AEF (25,000 yr return period), 2015 FMF site-specific GMRS for SDC-3, and Design Factors.

Period (sec)	Frequency (Hz)	AEF $4x10^{-4}$ UHRS (g)	AEF $4x10^{-5}$ UHRS (g)	DF_2	FMF Site-specific GMRS (g)[1]
0.01	100	1.43E-01	3.28E-01	8.36E-01	1.20E-01
0.02	50	1.71E-01	4.02E-01	8.45E-01	1.44E-01
0.03	33.3	1.85E-01	5.41E-01	9.22E-01	1.70E-01
0.05	20	2.54E-01	6.03E-01	8.48E-01	2.15E-01
0.1	10	4.23E-01	9.61E-01	8.33E-01	3.53E-01
0.2	5	2.32E-01	5.76E-01	8.63E-01	2.00E-01
0.3	3.33	1.32E-01	3.14E-01	8.49E-01	1.12E-01
0.5	2	1.20E-01	2.74E-01	8.34E-01	1.00E-01
1	1	5.66E-02	1.22E-01	8.16E-01	4.61E-02
2	0.5	2.36E-02	5.83E-02	8.61E-01	2.04E-02

1. The Design Factor (DF) used to calculate the GMRS is the larger of 0.8 and DF_2 (see Equation 10-10).

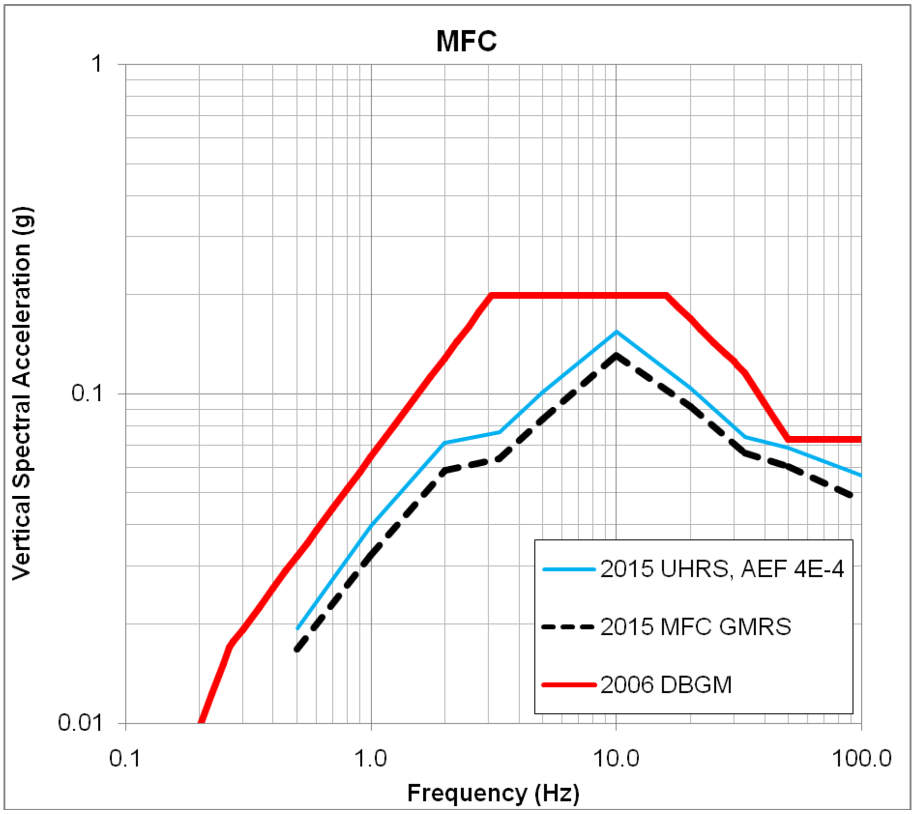

Figure 10-36. Comparison of the vertical 2015 MFC rock UHRS at 4×10^{-4}AEF (2,500 yr return period) (green curve), the vertical 2015 MFC rock GMRS for SDC-3(dashed black curve), and the vertical 2006 MFC rock DBGM spectrum (red curve) at 5% damping.

Table 10-12. Spectral accelerations for the vertical 2015 rock UHRS for AEF of 4×10^{-4} and the 2015 vertical rock GMRS at MFC for SDC-3.

Period (sec)	Frequency (Hz)	Spectral Acceleration (g)	
		4×10^{-4} AEF UHRS	MFC GRMS
0.01	100	5.63E-02	4.77E-02
0.02	50	6.88E-02	6.02E-02
0.03	33.3	7.41E-02	6.60E-02
0.05	20	1.05E-01	9.14E-02
0.1	10	1.55E-01	1.31E-01
0.2	5	1.01E-01	8.37E-02
0.3	3.33	7.67E-02	6.35E-02
0.5	2	7.12E-02	5.88E-02
1	1	3.99E-02	3.25E-02
2	0.5	1.95E-02	1.68E-02

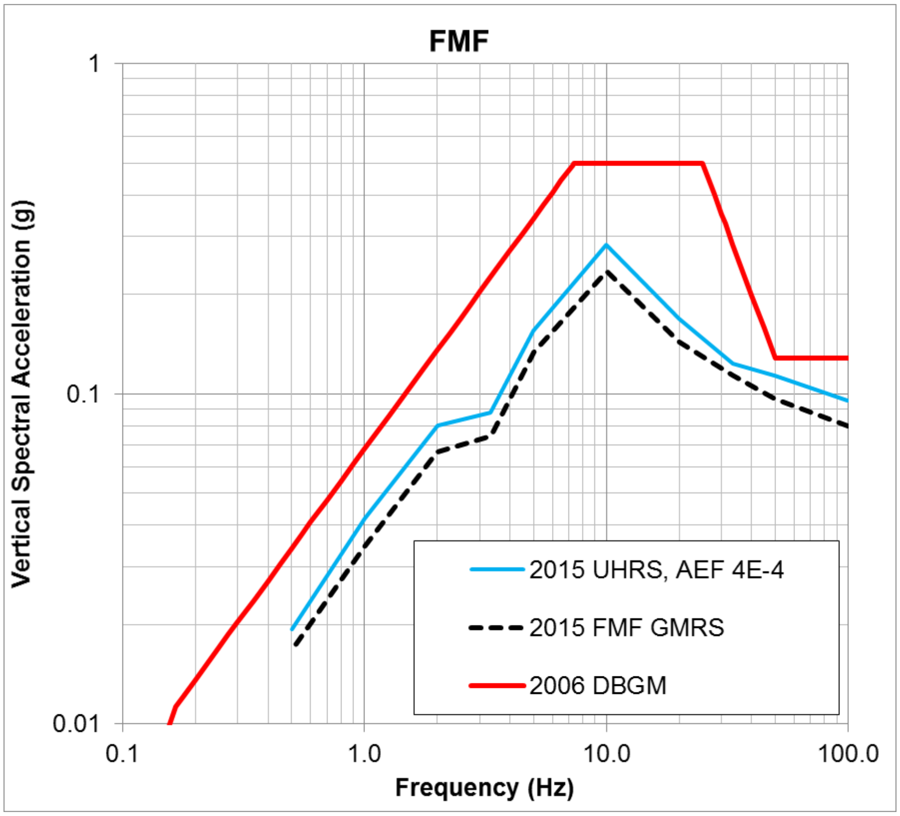

Figure 10-37. Comparison of the vertical 2015 FMF site-specific UHRS at $4x10^{-4}$AEF (2,500 yr return period) (green curve), the vertical 2015 FMF site-specific GMRS for SDC-3(dashed black curve), and the vertical 2006 MFC site-specific DBGM spectrum (red curve) at 5% damping.

Table 10-13. Spectral accelerations for the vertical 2015 site-specific UHRS for AEF of $4x10^{-4}$ and the 2015 vertical site-specific GMRS at FMF for SDC-3.

Period (sec)	Frequency (Hz)	Spectral Acceleration (g)	
		$4x10^{-4}$ AEF UHRS	FMF GMRS
0.01	100	9.56E-02	7.99E-02
0.02	50	1.14E-01	9.63E-02
0.03	33.3	1.23E-01	1.14E-01
0.05	20	1.69E-01	1.44E-01
0.1	10	2.82E-01	2.35E-01
0.2	5	1.55E-01	1.34E-01
0.3	3.33	8.78E-02	7.45E-02
0.5	2	8.00E-02	6.68E-02
1	1	4.21E-02	3.43E-02
2	0.5	1.94E-02	1.67E-02

10.5 Seismic Hazard Results and Sensitivity for SWUS Reference Site Condition at SFHP

The SFHP is located within NRF and resides in the IVRZ volcanic source zone and in the ESRP seismic source zone (see Figure 8-2). The coordinates of the SFHP site are 43.650437341°N; -112.912103520°E. Figures 10-38 through Figure 10-52 show the seismic hazard results at each of the 15 spectral periods analyzed. In each figure the top part shows the total mean and the 5^{th}, 16^{th}, 50^{th}, 84^{th}, and 95^{th} percentile seismic hazard curves; the plot on the bottom part of the figure compares the total mean hazard with the mean hazard produced by the tectonic source zones (blue curve), the volcanic source zones (red curve), the fault sources (green curve), and the Cascadia interface source (purple curve). The tectonic source zones control the high-frequency hazard (PGA and spectral frequencies greater than 10 Hz). The fault sources are the primary contributors for low-frequency hazard (5 Hz and lower). The Cascadia interface contribution becomes noticeable only for spectral frequencies of 1 Hz or less.

Deaggregation of the total mean seismic hazard is shown in Figure 10-53 through Figure 10-56 for spectral frequencies at 10 Hz and 1 Hz (corresponding to spectral periods of 0.1- and 1-sec). Each figure contains histograms representing the percent contribution to the total mean seismic hazard from different magnitude-distance bins. Each histogram represents one AEF level: $4x10^{-4}$, 10^{-4}, $4x10^{-5}$, and10^{-5}. The deaggregation plots for 10 Hz (0.1-sec) and 1 Hz (1-sec) spectral acceleration at the $4x10^{-4}$ and 10^{-4}AEF levels are similar, showing equal contribution to the total hazard from the Centennial Shear Zone (CSZ, small magnitudes at distance of 30 to 50 km) and from the faults (magnitudes of about 7 at distance of 30 to 50 km). At AEF of $4x10^{-5}$, and 10^{-5} the background seismicity from the ESRP host zone (small magnitudes at 0 to 20 km) and the contribution from fault sources within 50 km of the site are predominant. At these spectral frequencies the contribution of the Cascadia interface is negligible. Figure 10-57 shows the deaggregation plots for 0.1 Hz (10-sec) at AEFs of $4x10^{-4}$. The largest contribution to the total hazard comes from the fault sources, particularly the Lemhi fault, which is the closest to SFHP; the Cascadia interface shows a contribution of approximately 5% to the total hazard.

(a)

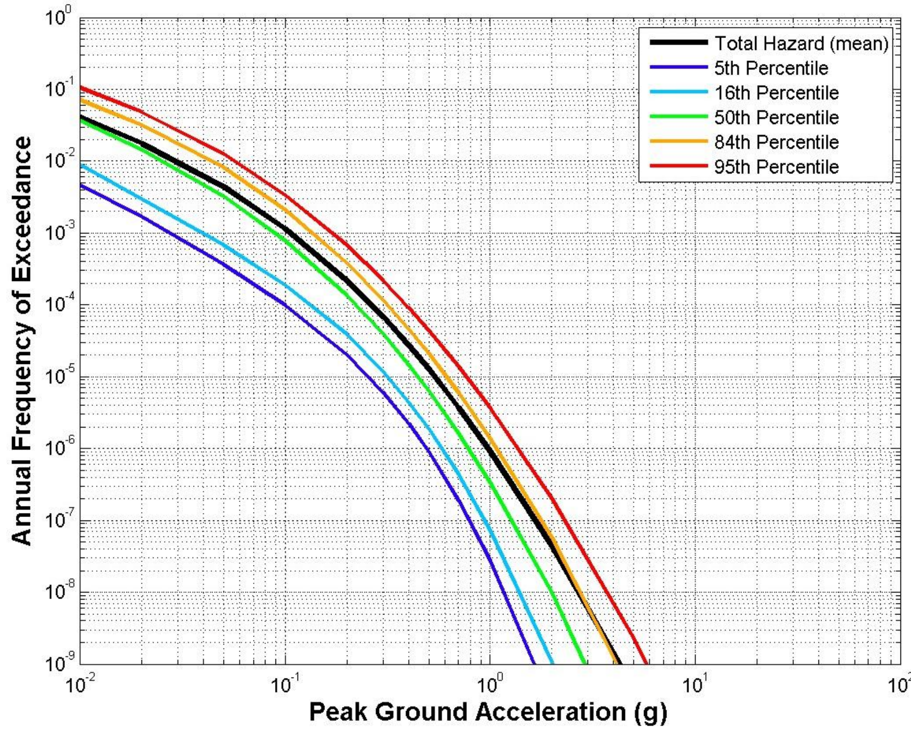

(b)

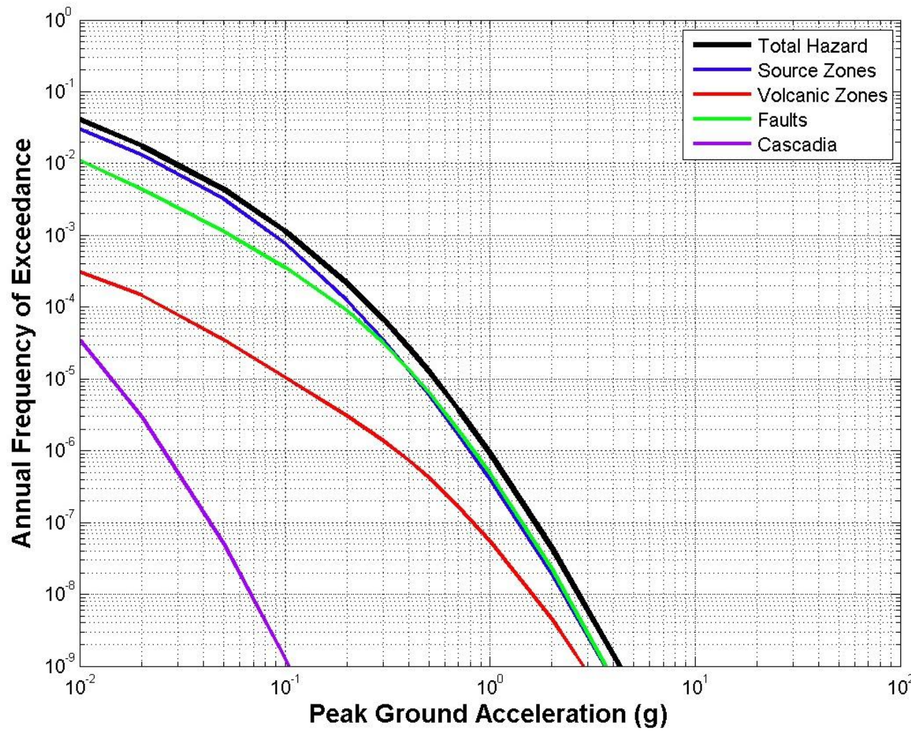

Figure 10-38. Seismic hazard results at SFHP for SWUS reference site condition at PGA: a) total mean hazard and fractiles; and b) comparison between the total mean seismic hazard and the contribution of tectonic source zones, volcanic source zones, faultsources, and the Cascadia interface source.

(a)

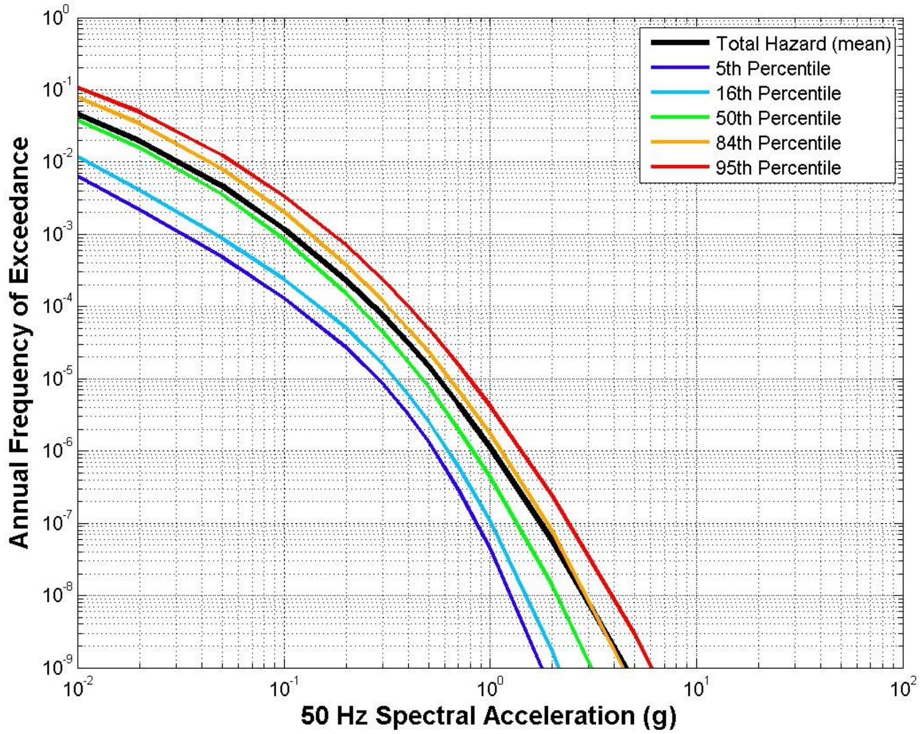

(b)

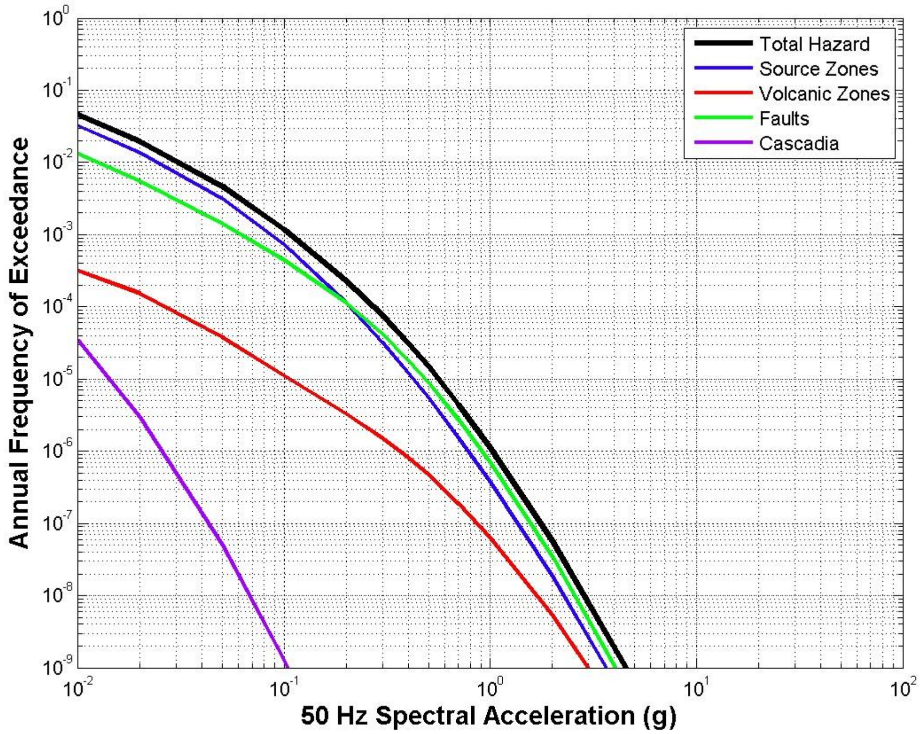

Figure 10-39. Seismic hazard results at SFHP for SWUS reference site condition at 50 Hz (0.02-sec) spectral acceleration: a) total mean hazard and fractiles; and b) comparison between the total mean seismic hazard and the contribution of tectonic source zones, volcanic source zones, faultsources, and the Cascadia interface source.

(a)

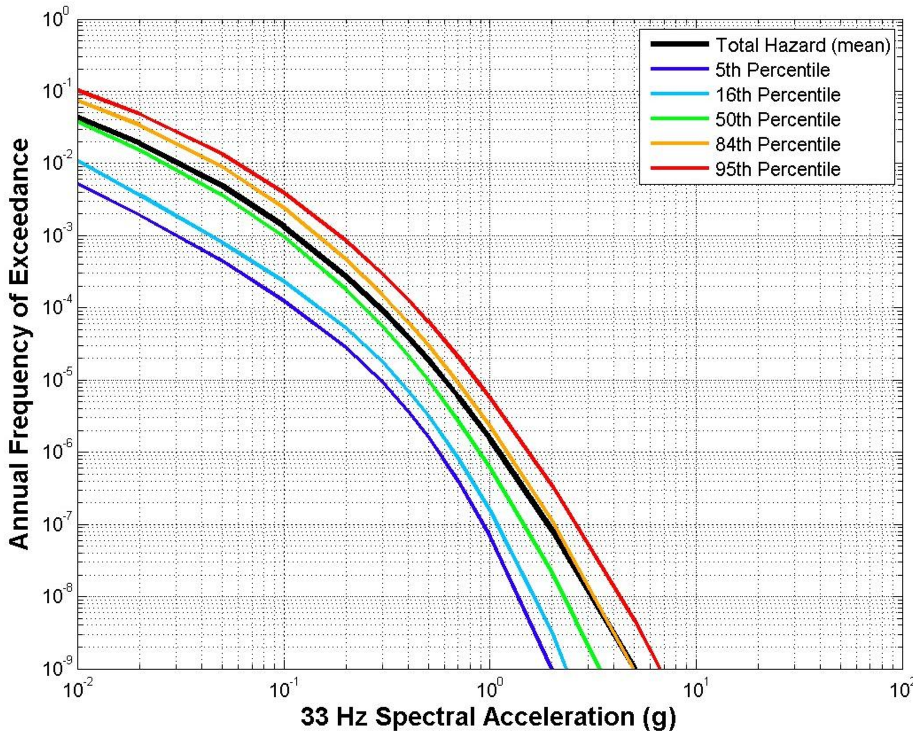

(b)

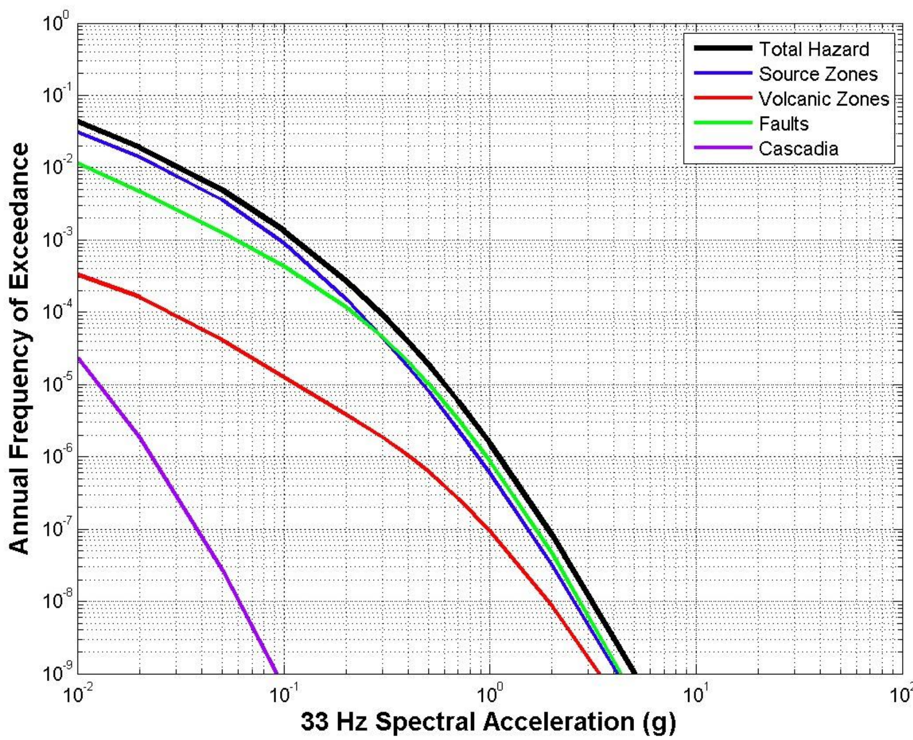

Figure 10-40. Seismic hazard results at SFHP for SWUS reference site condition at 33 Hz (0.03-sec) spectral acceleration: a) total mean hazard and fractiles; and b) comparison between the total mean seismic hazard and the contribution of tectonic source zones, volcanic source zones, faultsources, and the Cascadia interface source.

(a)

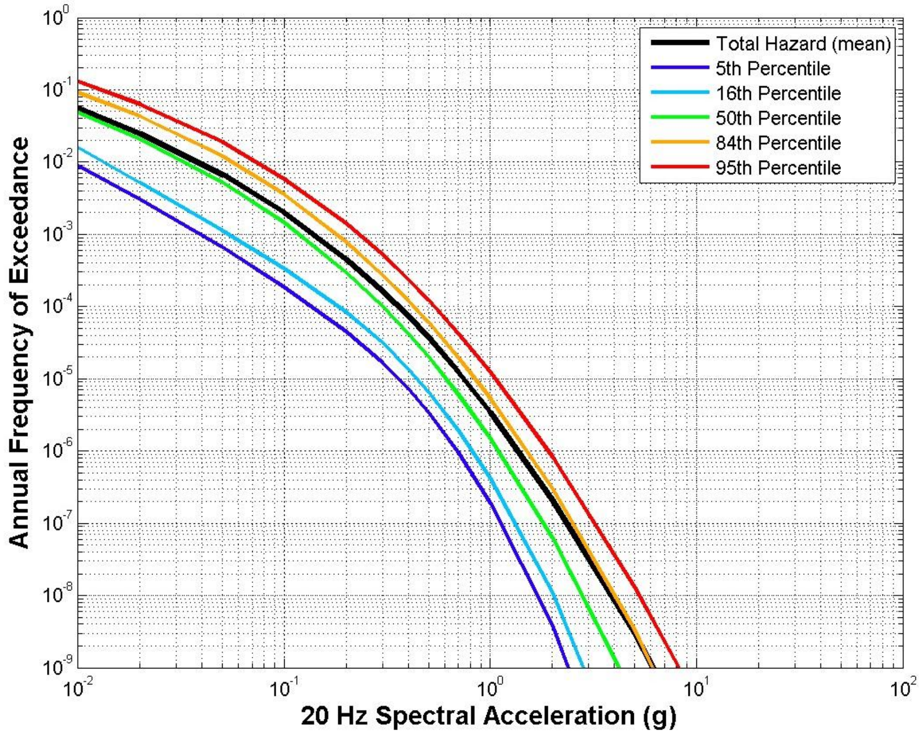

(b)

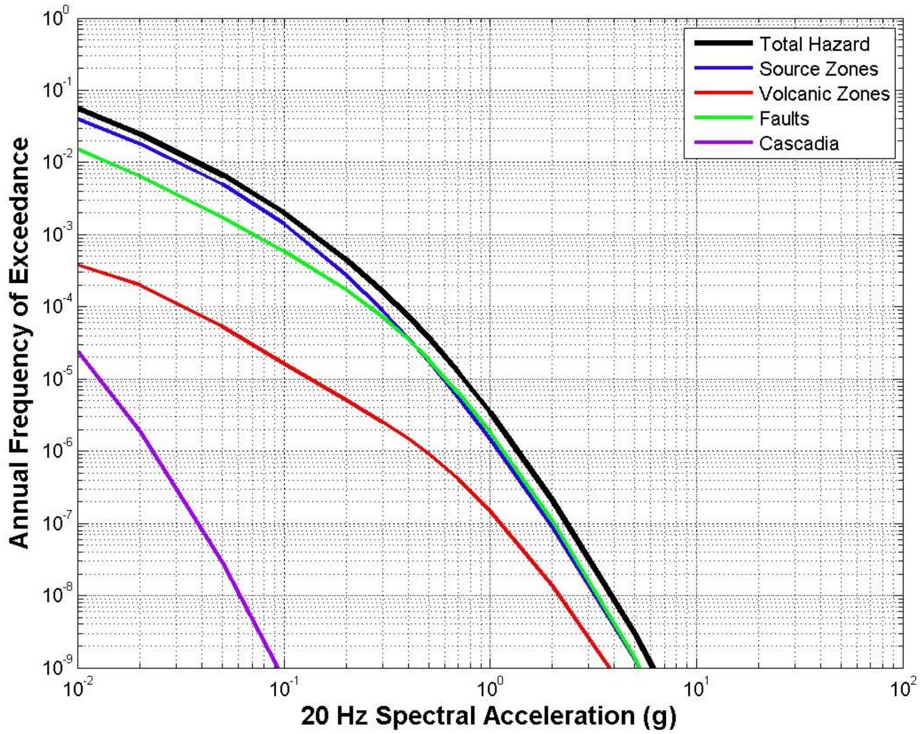

Figure 10-41. Seismic hazard results at SFHP for SWUS reference site condition at 20 Hz (0.05-sec) spectral acceleration: a) total mean hazard and fractiles; and b) comparison between the total mean seismic hazard and the contribution of tectonic source zones, volcanic source zones, faultsources, and the Cascadia interface source.

(a)

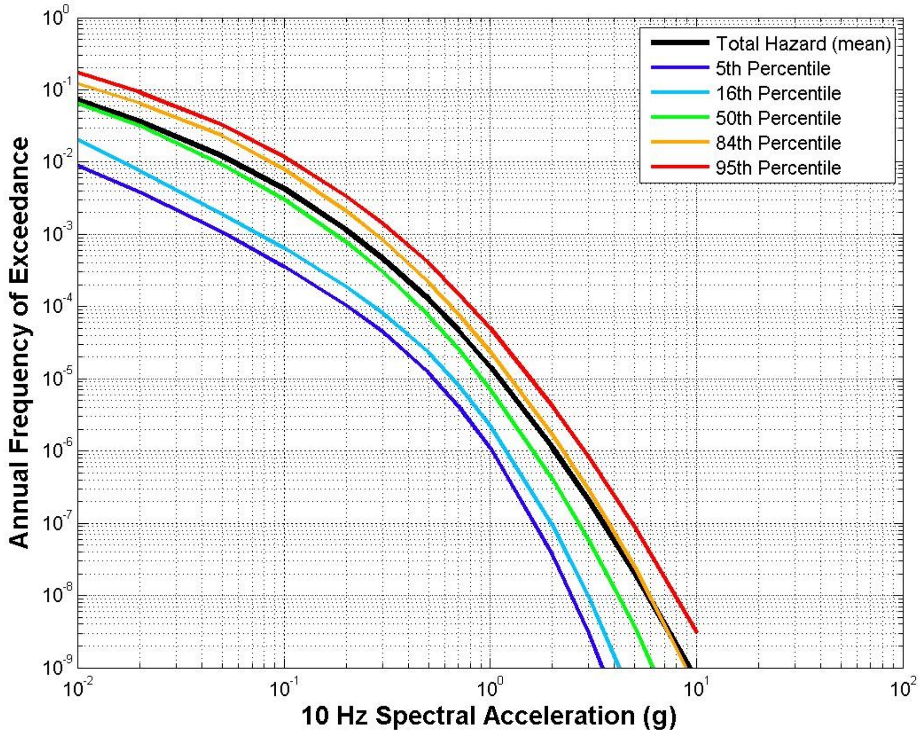

(b)

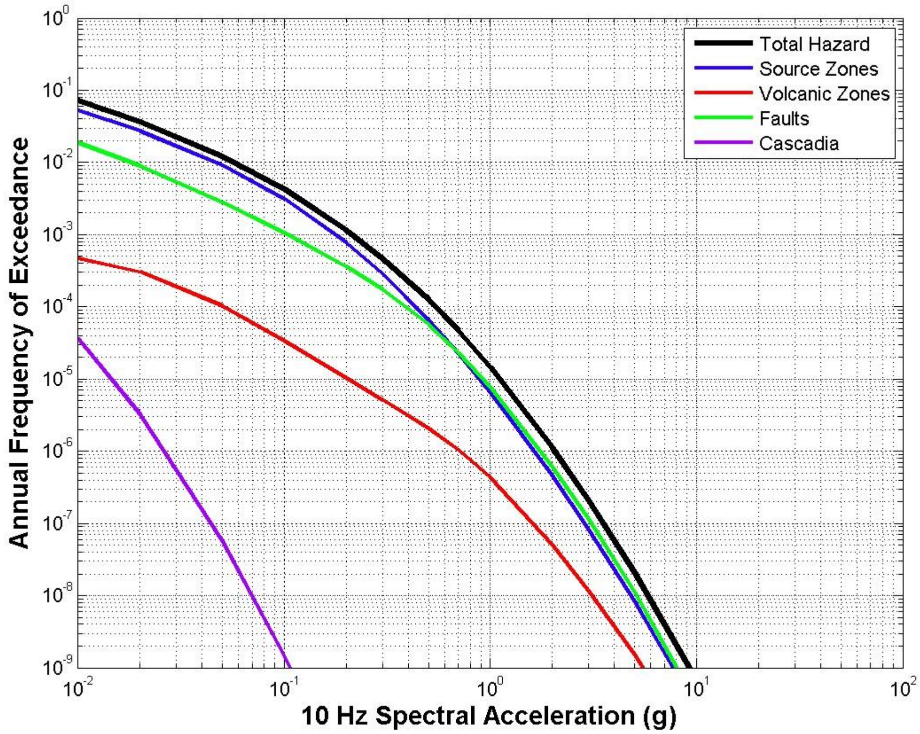

Figure 10-42. Seismic hazard results at SFHP for SWUS reference site condition at 10 Hz (0.1-sec) spectral acceleration: a) total mean hazard and fractiles; and b) comparison between the total mean seismic hazard and the contribution of tectonic source zones, volcanic source zones, faultsources, and the Cascadia interface source.

(a)

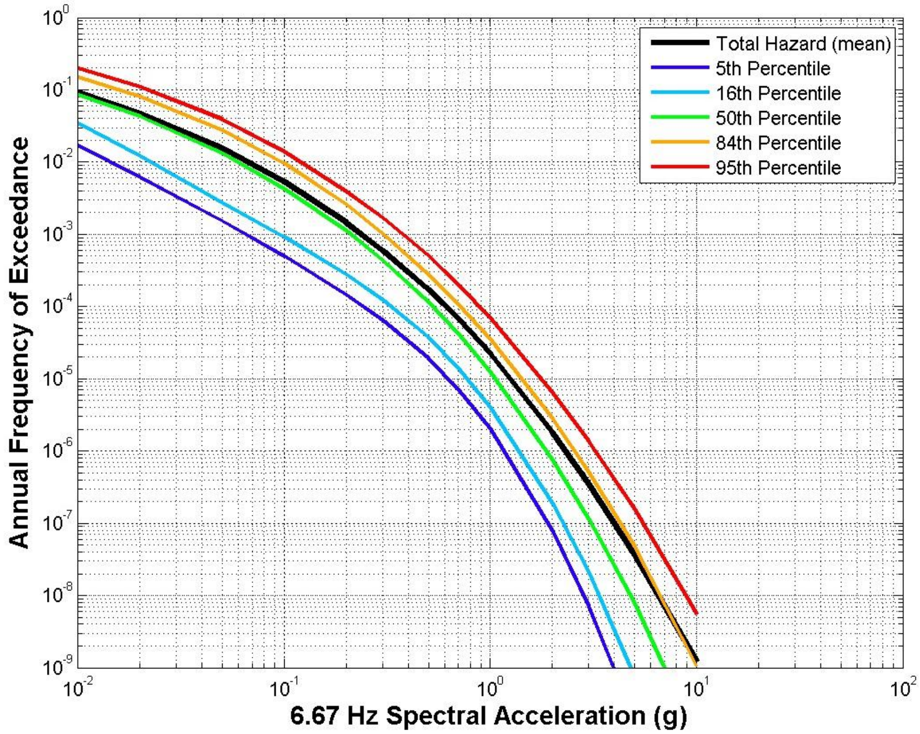

(b)

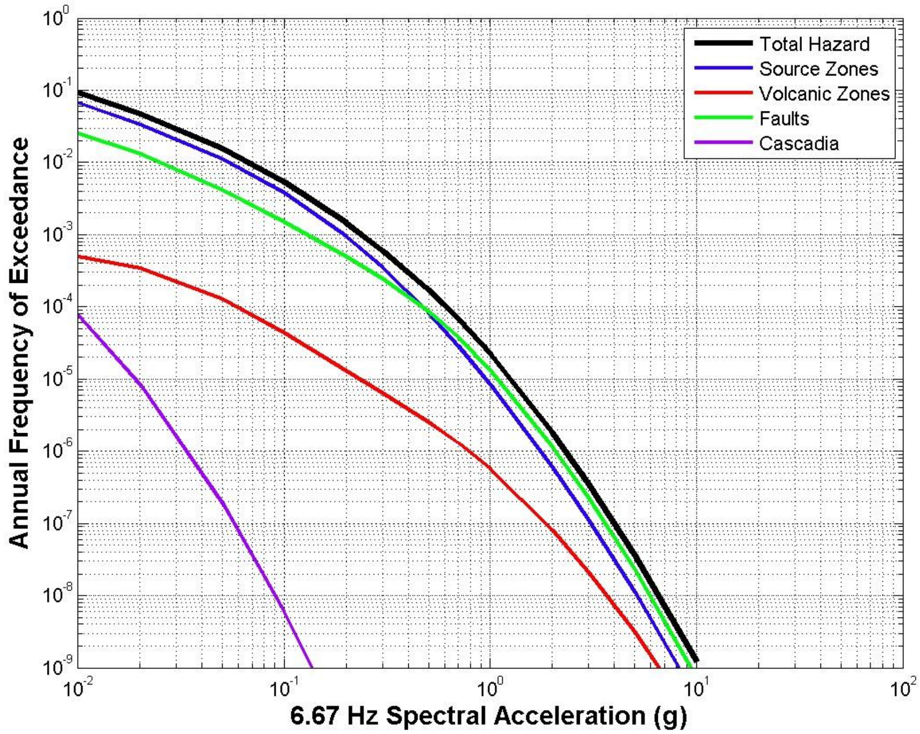

Figure 10-43. Seismic hazard results at SFHP for SWUS reference site condition at 6.67 Hz (0.15-sec) spectral acceleration: a) total mean hazard and fractiles; and b) comparison between the total mean seismic hazard and the contribution of tectonic source zones, volcanic source zones, faultsources, and the Cascadia interface source.

(a)

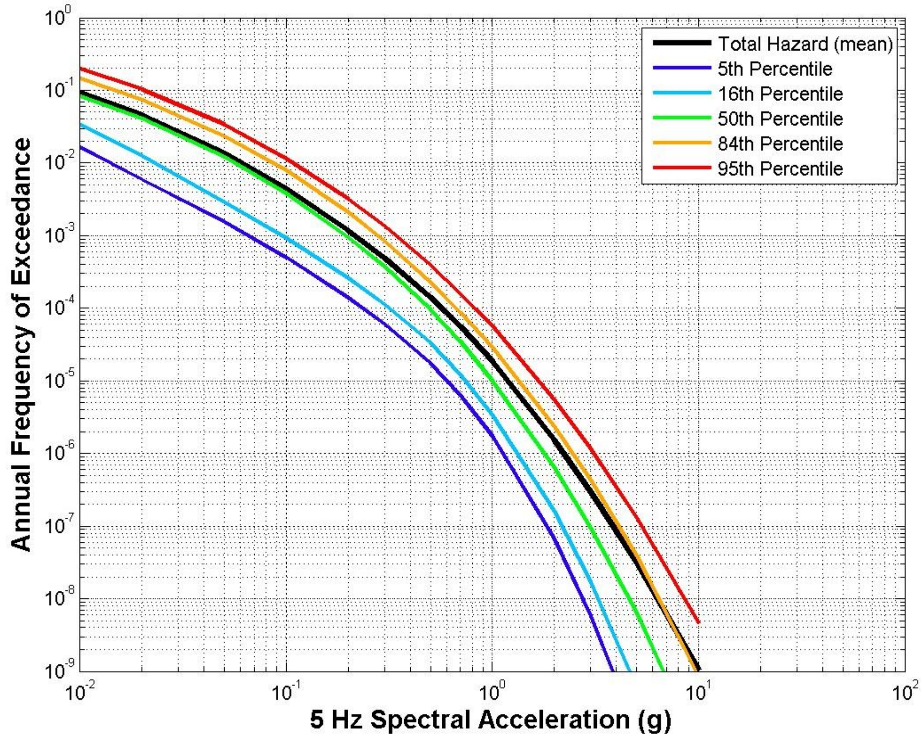

(b)

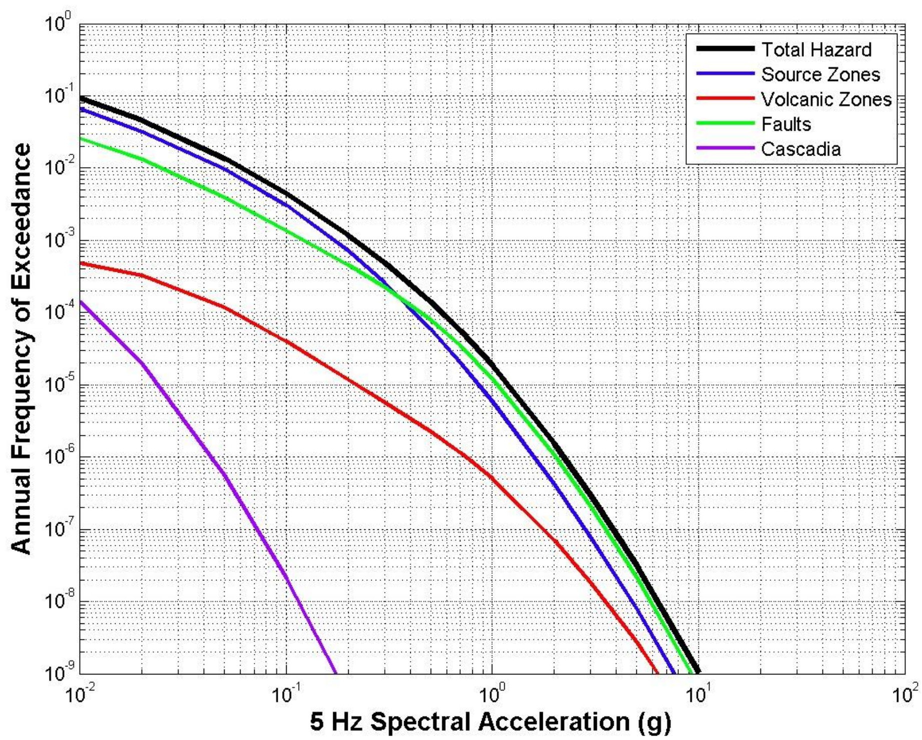

Figure 10-44. Seismic hazard results at SFHP for SWUS reference site condition at 5 Hz (0.2-sec) spectral acceleration: a) total mean hazard and fractiles; and b) comparison between the total mean seismic hazard and the contribution of tectonic source zones, volcanic source zones, faultsources, and the Cascadia interface source.

(a)

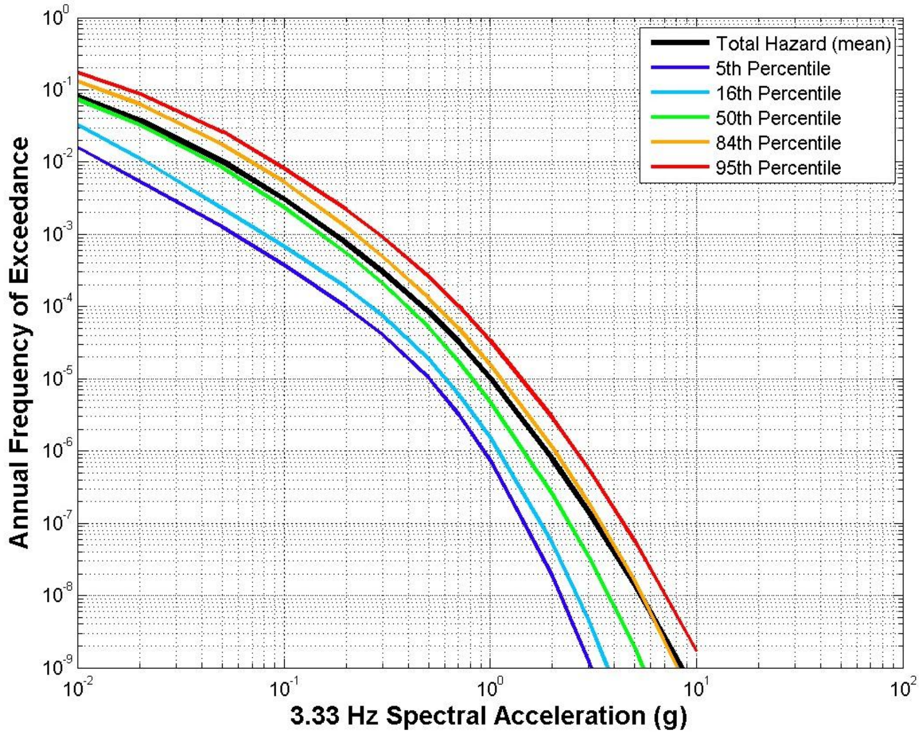

(b)

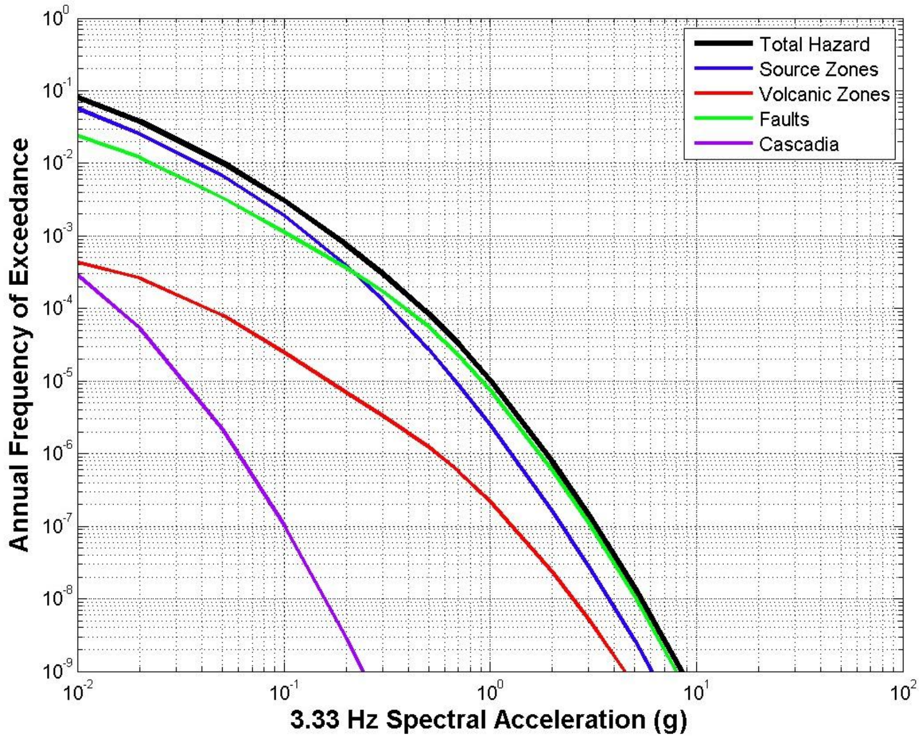

Figure 10-45. Seismic hazard results at SFHP for SWUS reference site condition at 3.3 Hz (0.3-sec) spectral acceleration: a) total mean hazard and fractiles; and b) comparison between the total mean seismic hazard and the contribution of tectonic source zones, volcanic source zones, faultsources, and the Cascadia interface sources.

(a)

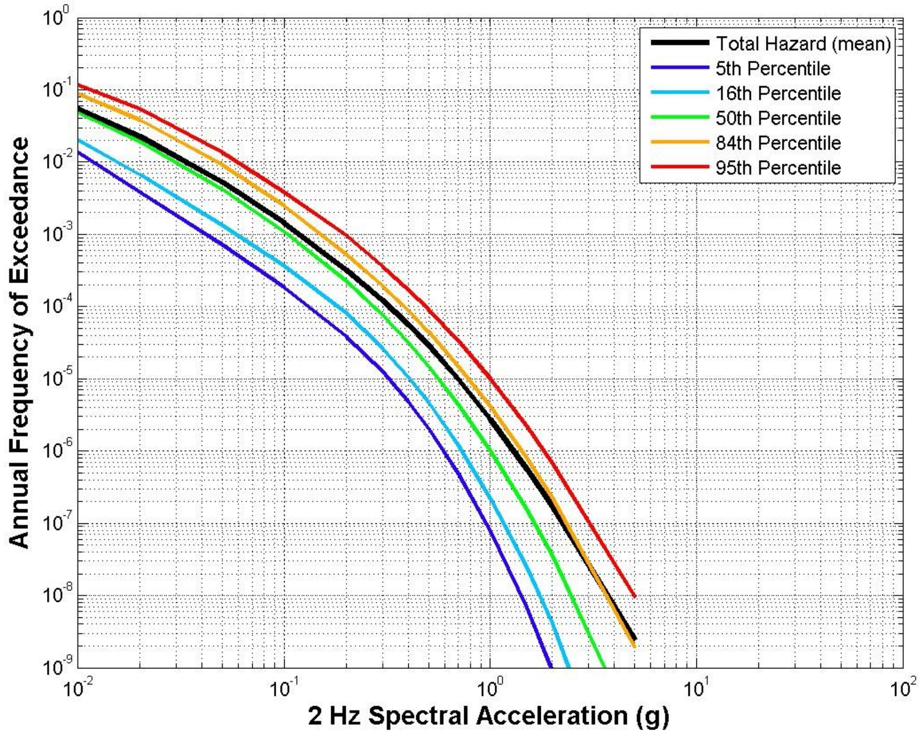

(b)

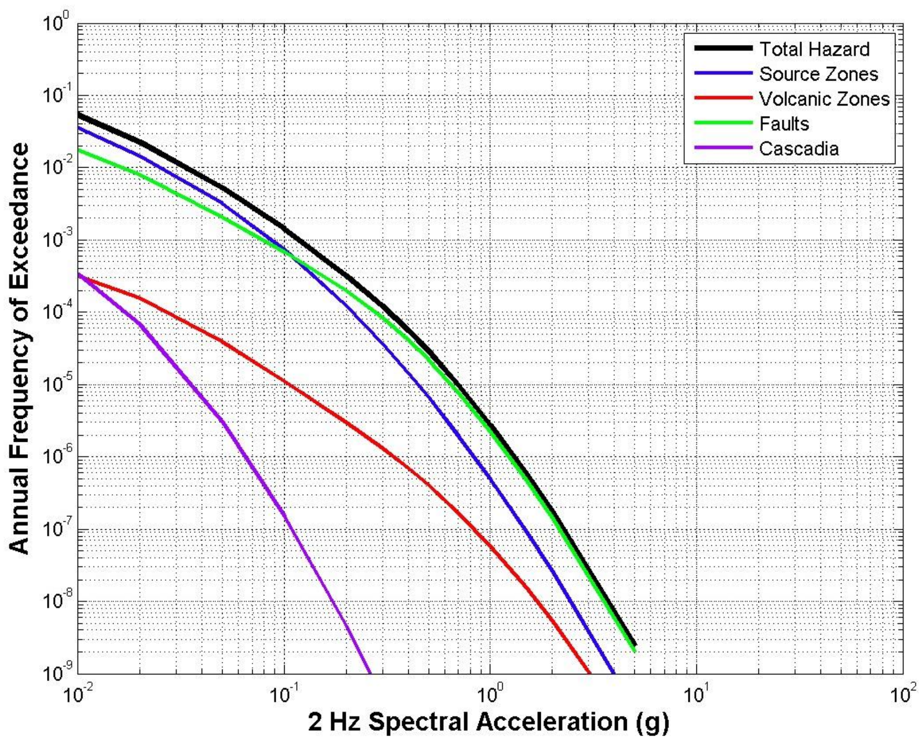

Figure 10-46. Seismic hazard results at SFHP for SWUS reference site condition at 2 Hz (0.5-sec) spectral acceleration: a) total mean hazard and fractiles; and b) comparison between the total mean seismic hazard and the contribution of tectonic source zones, volcanic source zones, faultsources, and the Cascadia interface source.

(a)

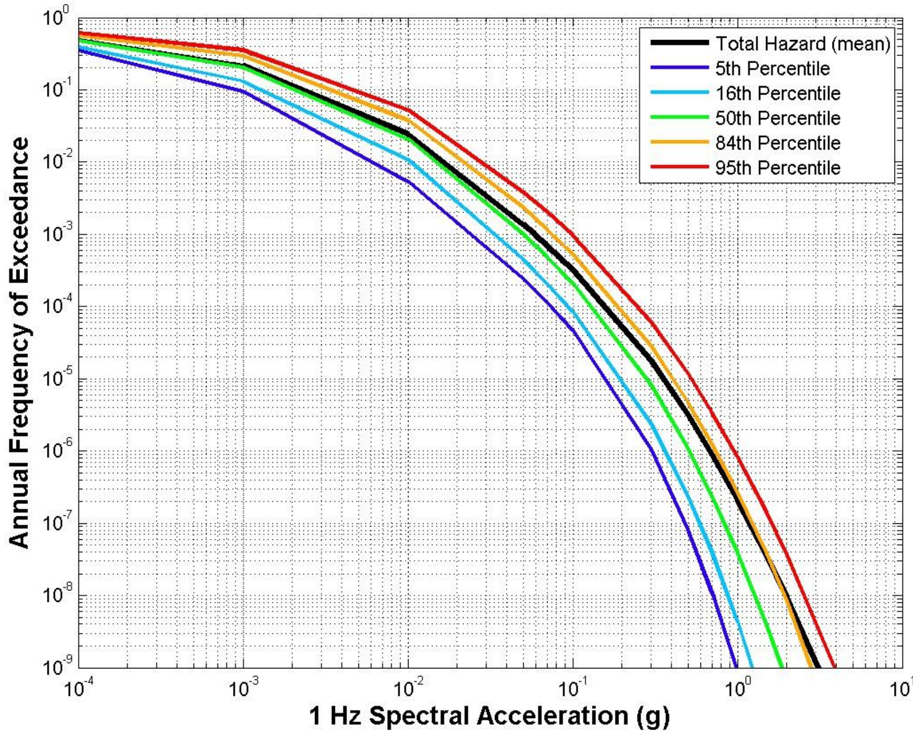

(b)

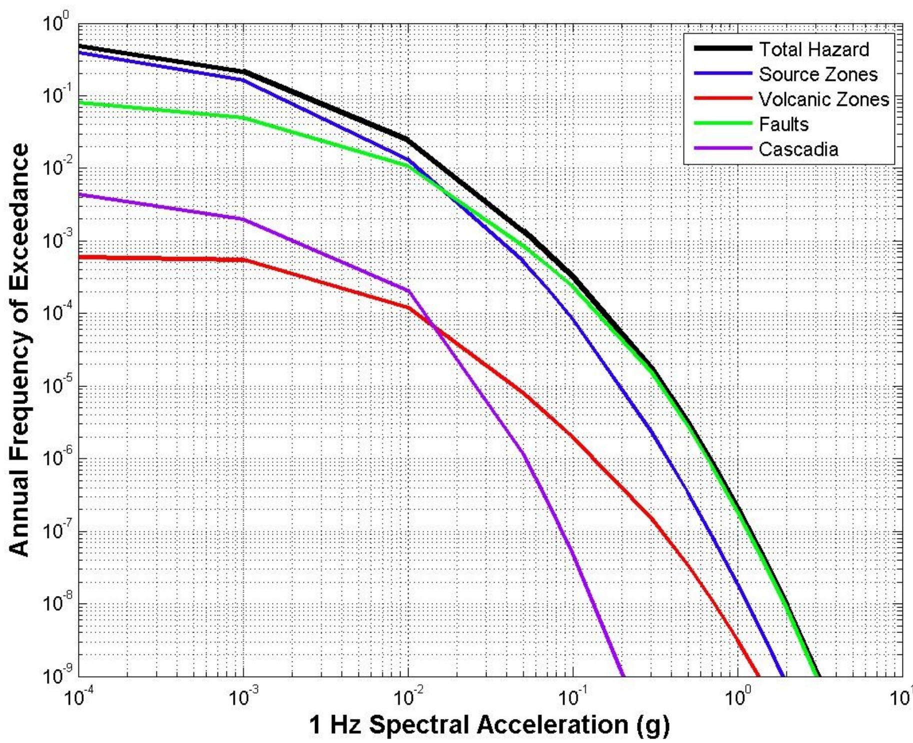

Figure 10-47. Seismic hazard results at SFHP for SWUS reference site condition at 1 Hz (1.0-sec) spectral acceleration: a) total mean hazard and fractiles; and b) comparison between the total mean seismic hazard and the contribution of tectonic source zones, volcanic source zones, faultsources, and the Cascadia interface source.

(a)

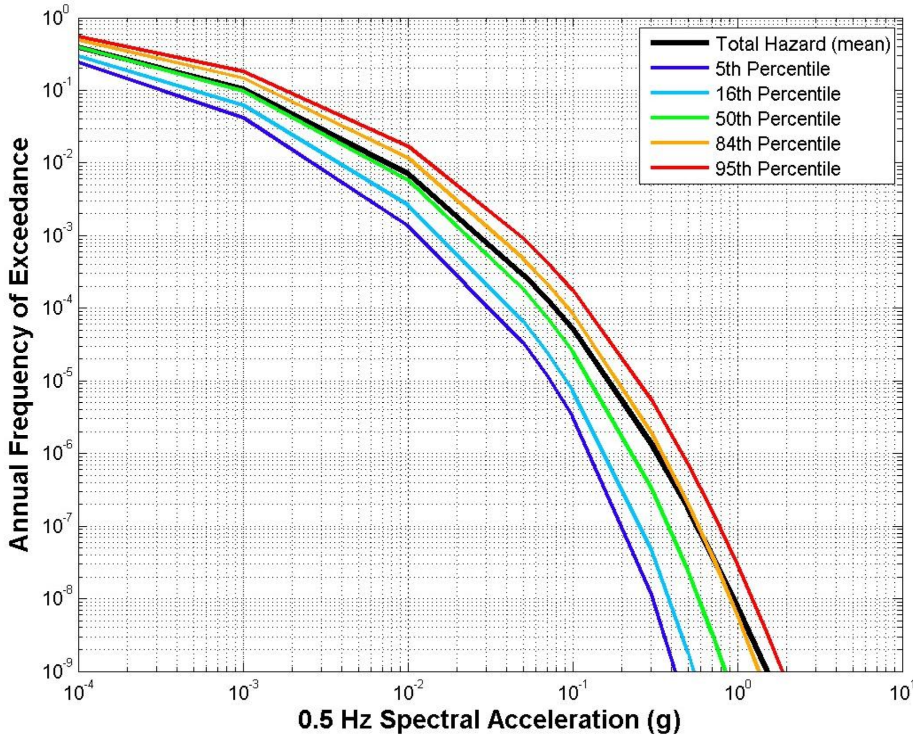

(b)

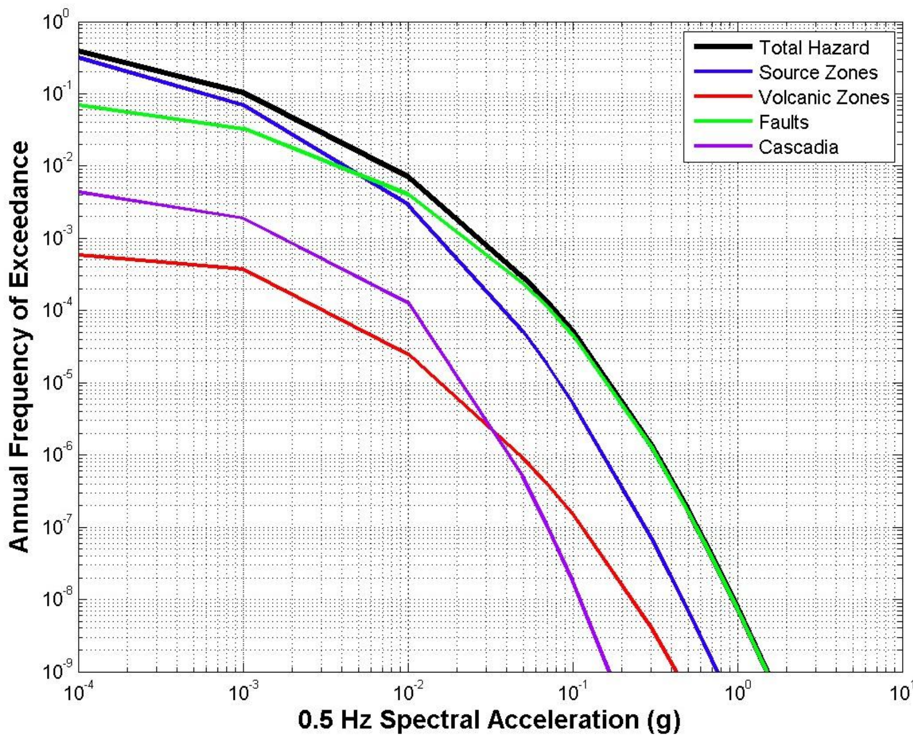

Figure 10-48. Seismic hazard results at SFHP for SWUS reference site condition at 0.5 Hz (2.0-sec) spectral acceleration: a) total mean hazard and fractiles; and b) comparison between the total mean seismic hazard and the contribution of tectonic source zones, volcanic source zones, faultsources, and the Cascadia interface source.

(a)

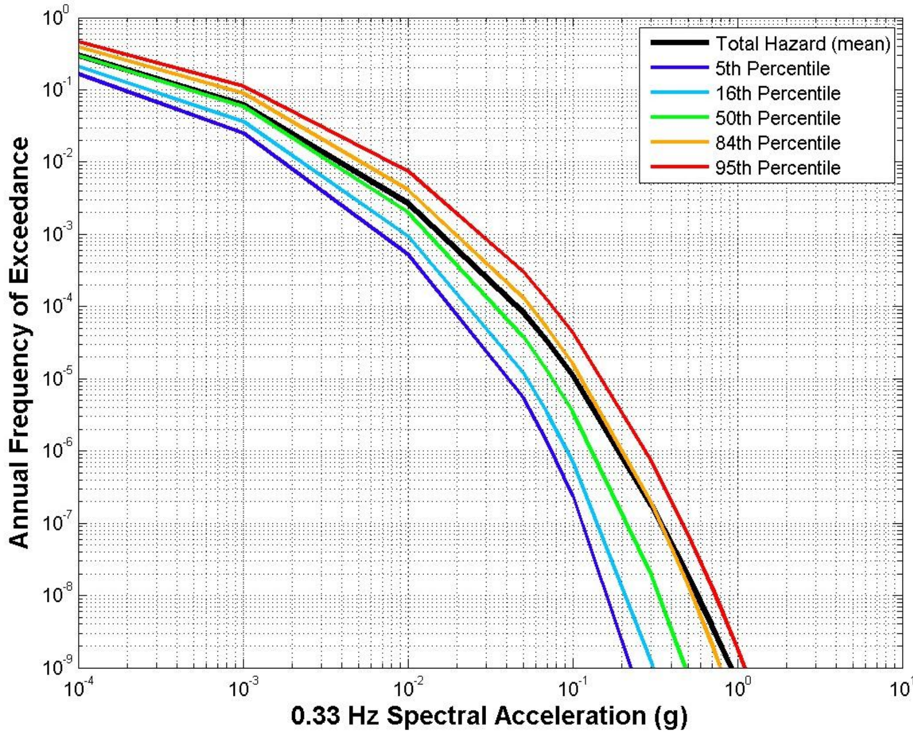

(b)

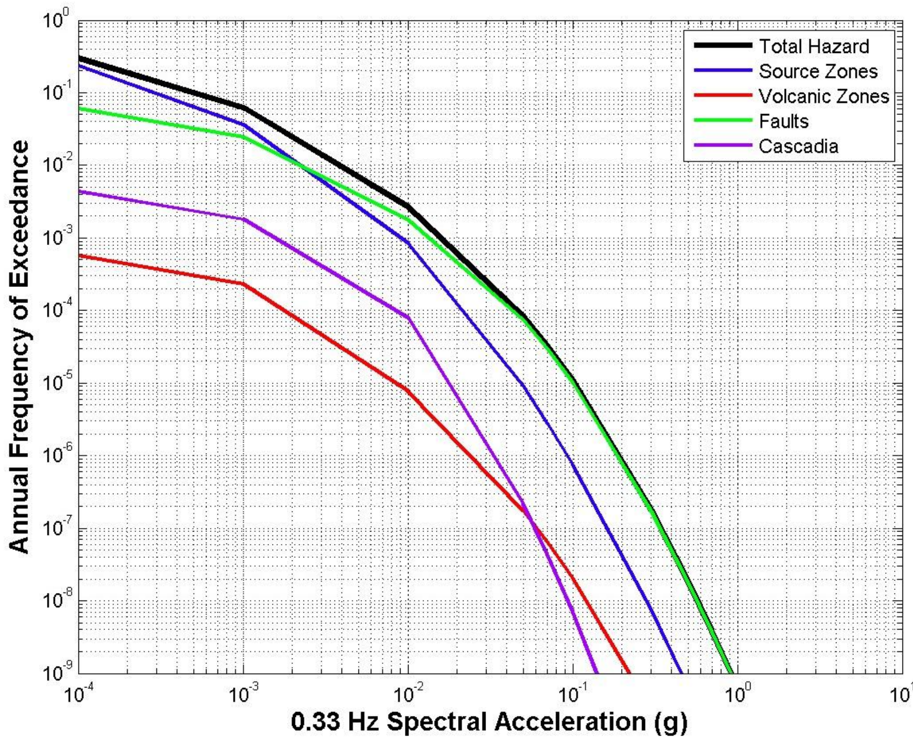

Figure 10-49. Seismic hazard results at SFHP for SWUS reference site condition at 0.33 Hz (3.0-sec) spectral acceleration: a) total mean hazard and fractiles; and b) comparison between the total mean seismic hazard and the contribution of tectonic source zones, volcanic source zones, faultsources, and the Cascadia interface source.

(a)

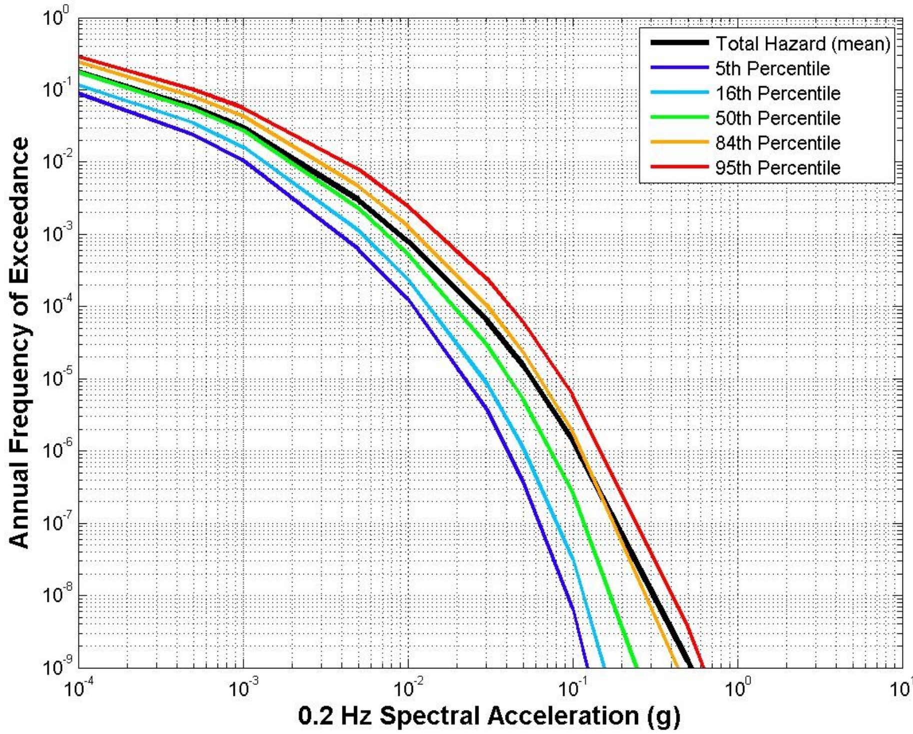

(b)

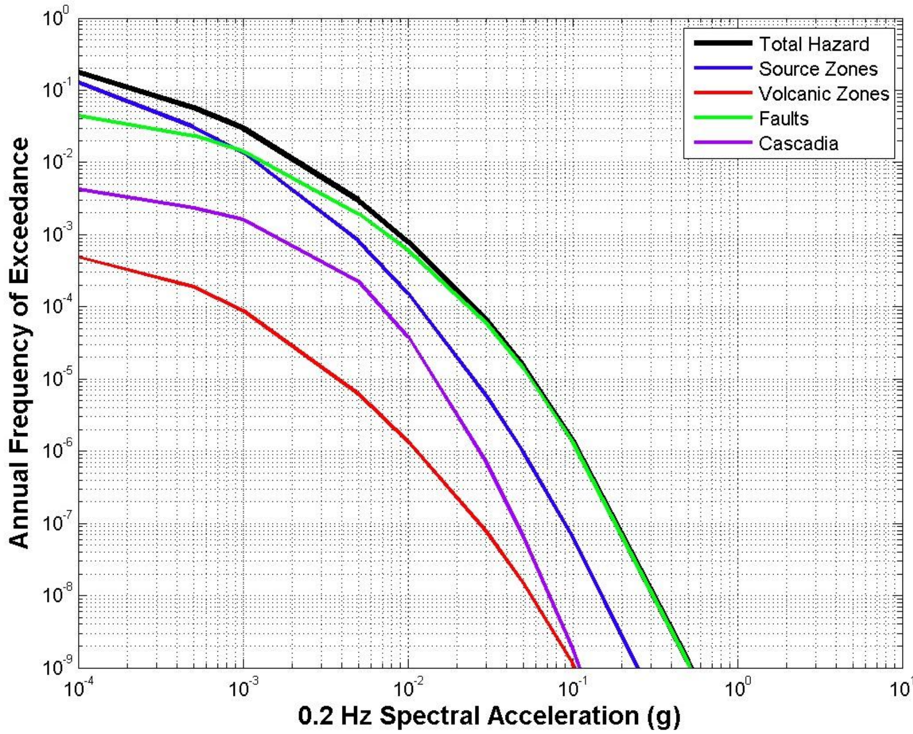

Figure 10-50. Seismic hazard results at SFHP for SWUS reference site condition at 0.2 Hz (5.0-sec) spectral acceleration: a) total mean hazard and fractiles; and b) comparison between the total mean seismic hazard and the contribution of tectonic source zones, volcanic source zones, faultsources, and the Cascadia interface source.

(a)

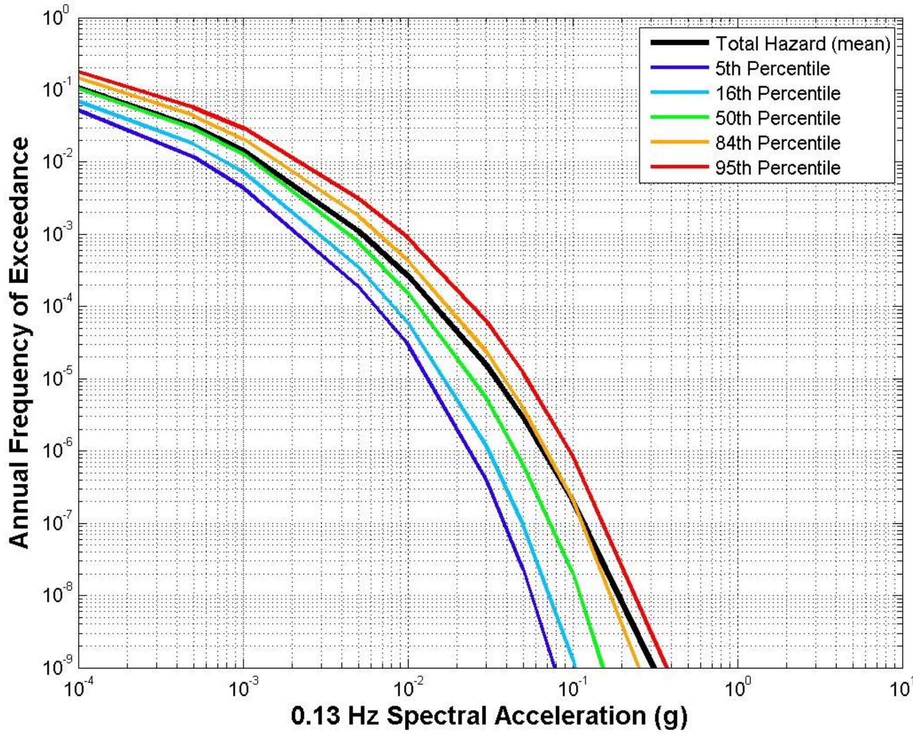

(b)

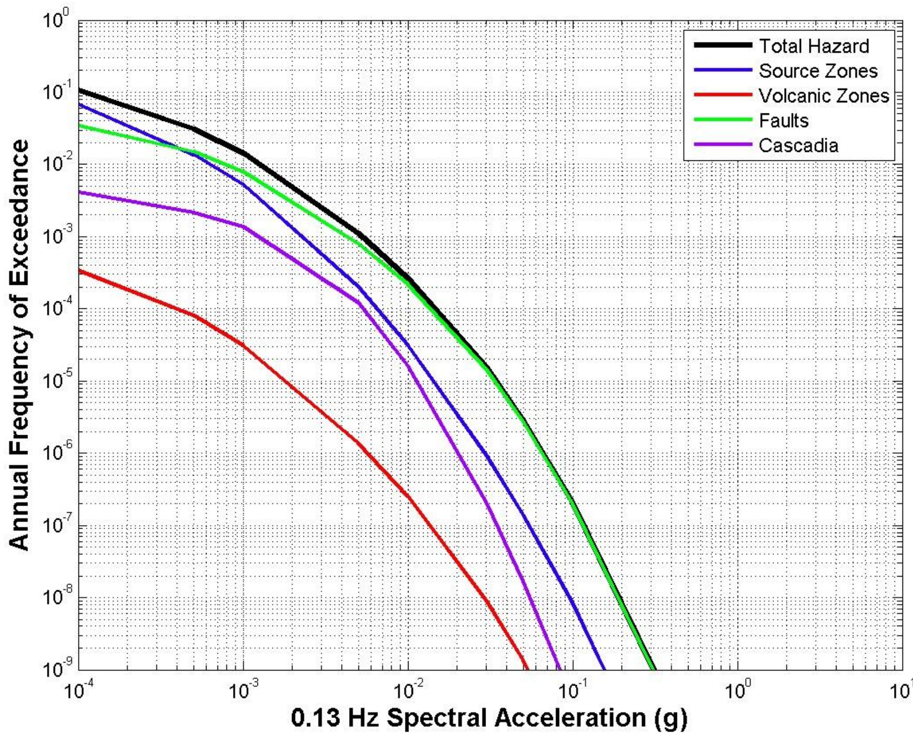

Figure 10-51. Seismic hazard results at SFHP for SWUS reference site condition at 0.13 Hz (7.5-sec) spectral acceleration: a) total mean hazard and fractiles; and b) comparison between the total mean seismic hazard and the contribution of tectonic source zones, volcanic source zones, faultsources, and the Cascadia interface source.

(a)

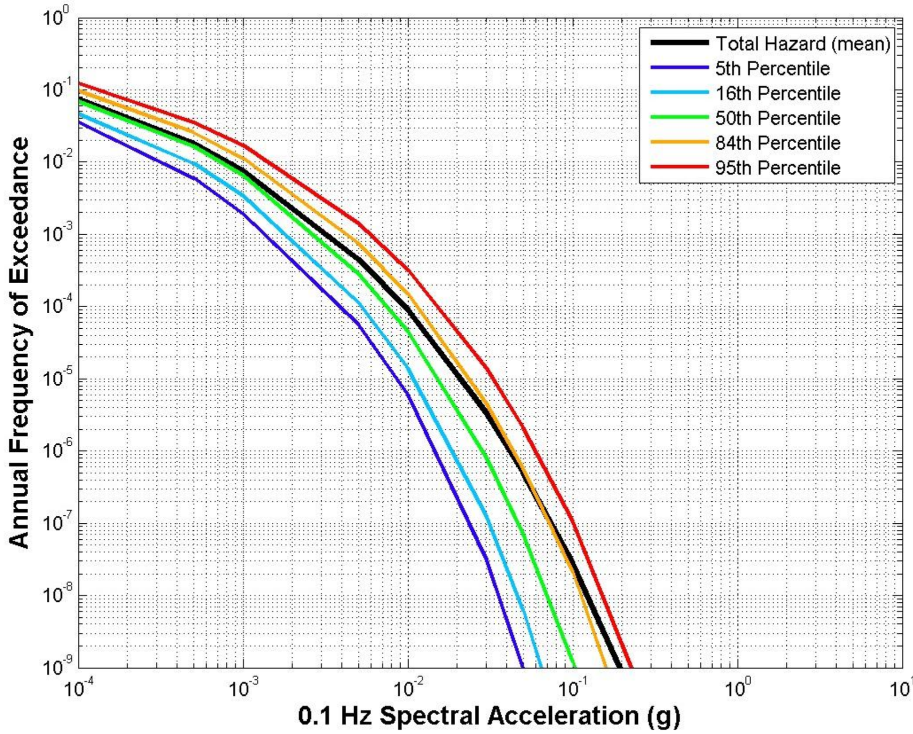

(b)

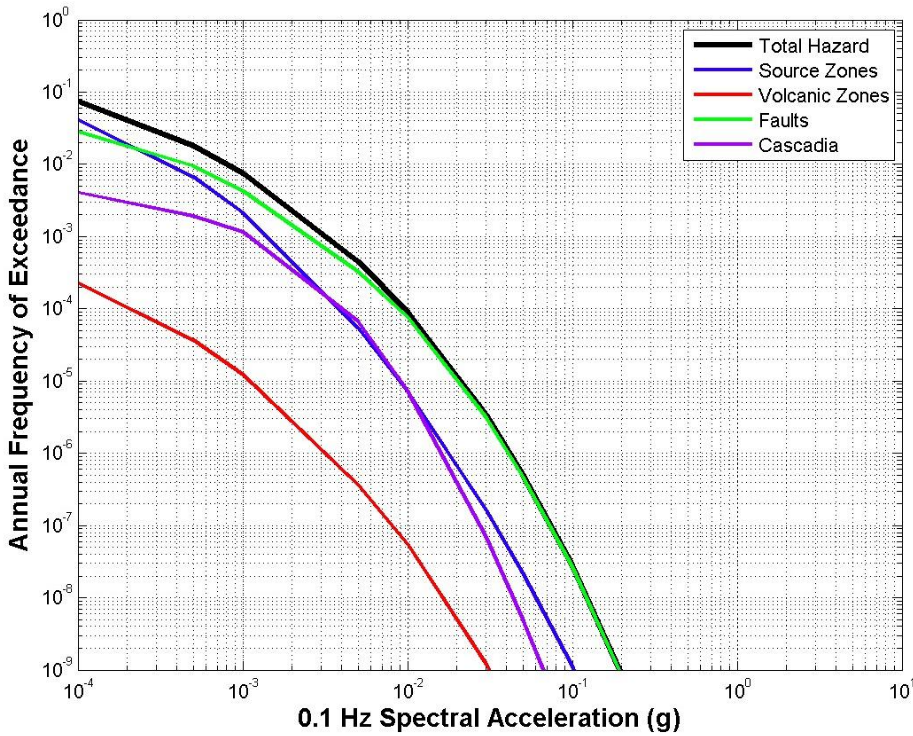

Figure 10-52. Seismic hazard results at SFHP for SWUS reference site condition at 0.1 Hz (10-sec) spectral acceleration: a) total mean hazard and fractiles; and b) comparison between the total mean seismic hazard and the contribution of tectonic source zones, volcanic source zones, faultsources, and the Cascadia interface source.

(a)

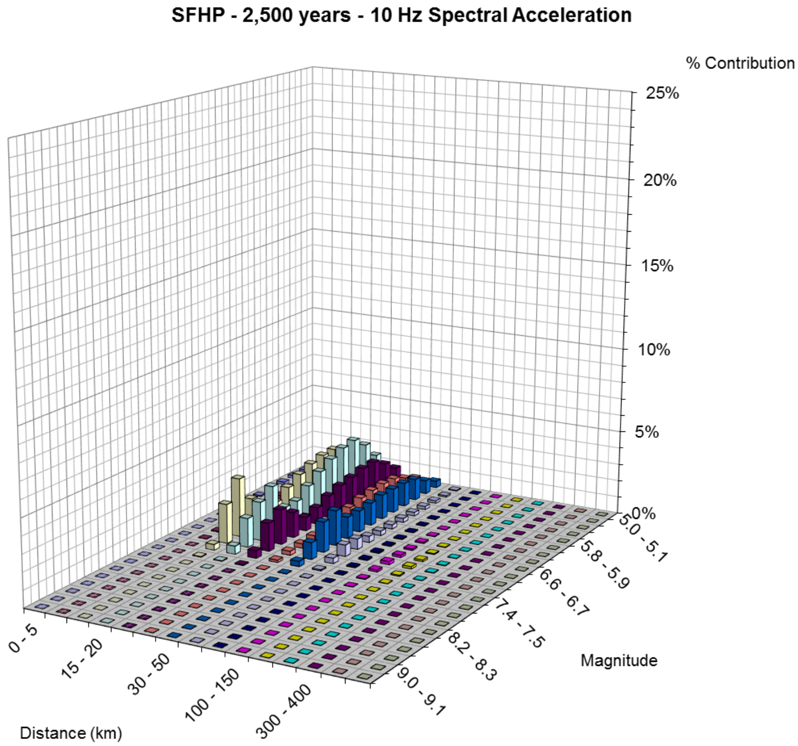

(b)

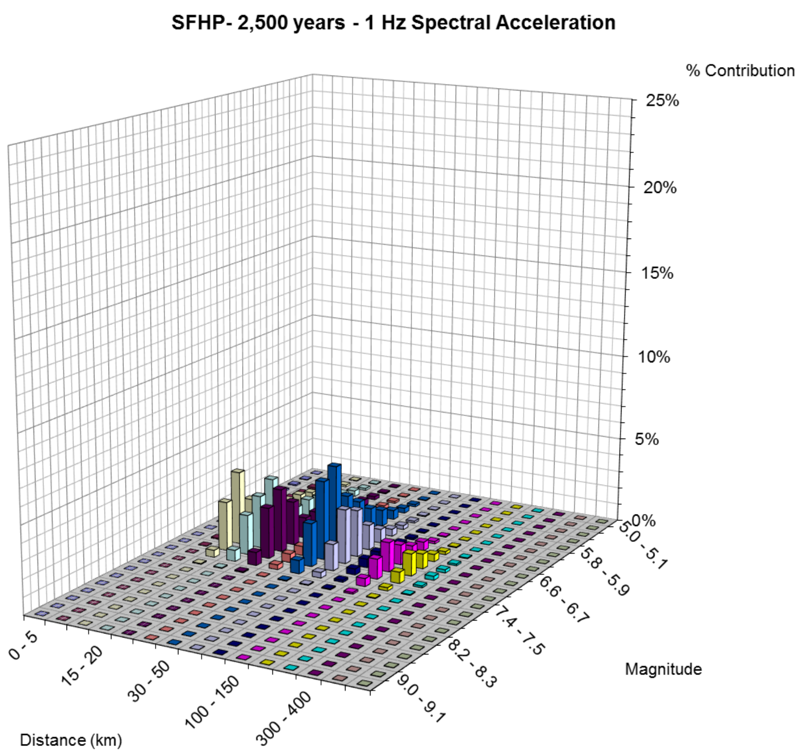

Figure 10-53. Magnitude-distance deaggregation for: a) 10 Hz; and b) 1 Hz at the 2,500 yr return period.

(a)

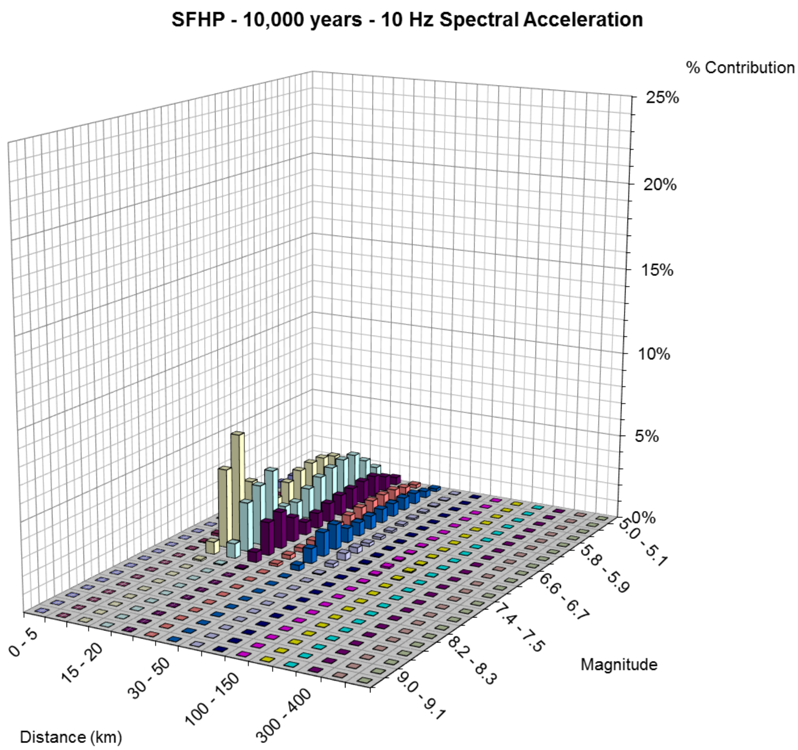

(b)

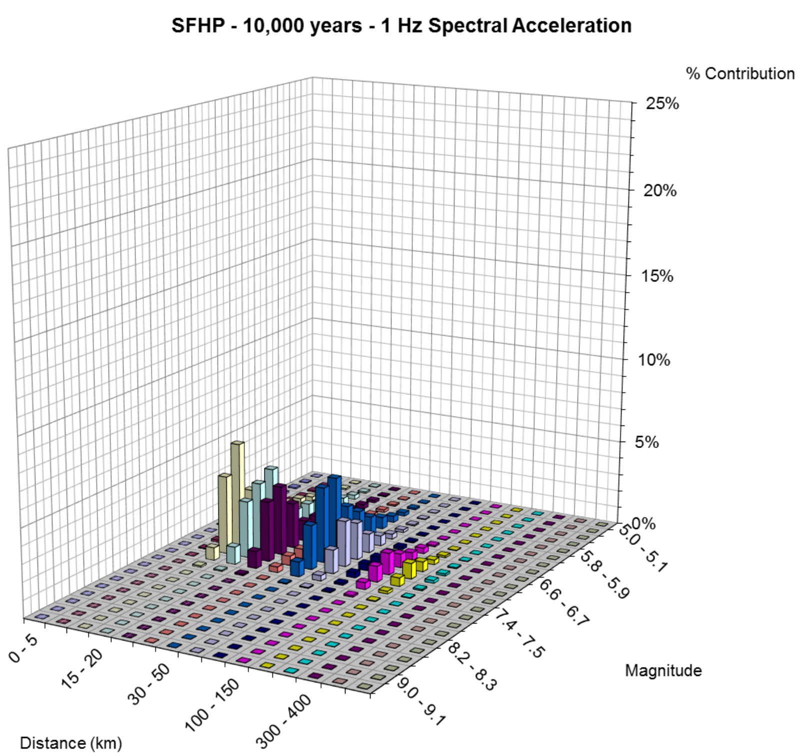

Figure 10-54. Magnitude-distance deaggregation for: a) 10 Hz; and b) 1 Hz at the 10,000 yr return period.

(a)

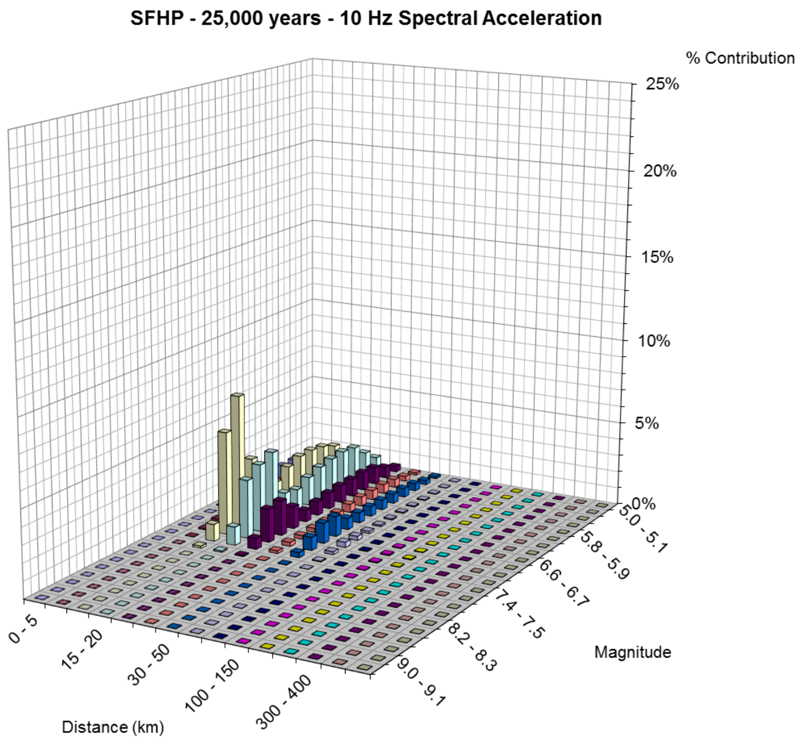

(b)

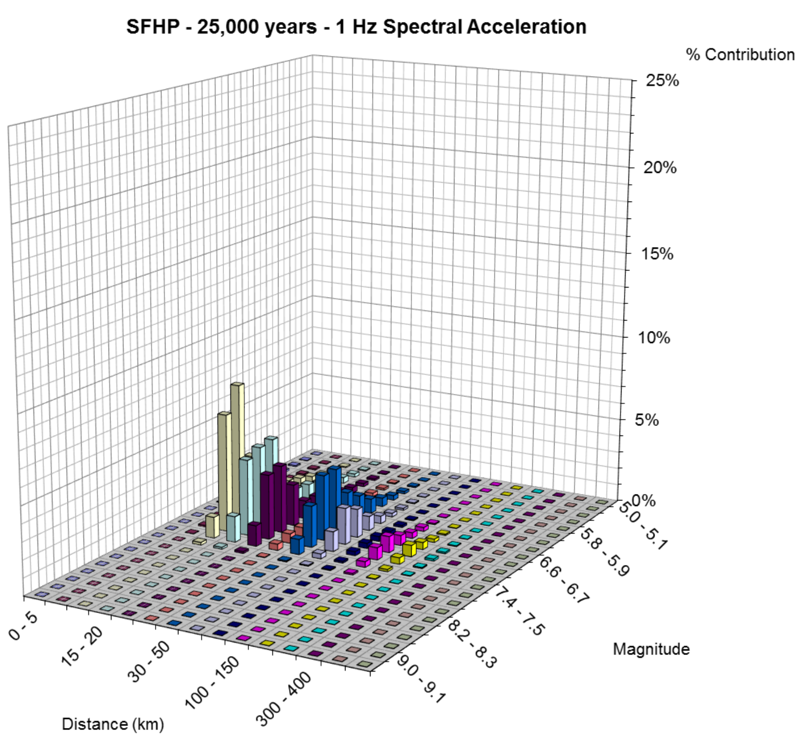

Figure 10-55. Magnitude-distance deaggregation for: a) 10 Hz; and b) 1 Hz at the 25,000 yr return period.

(a)

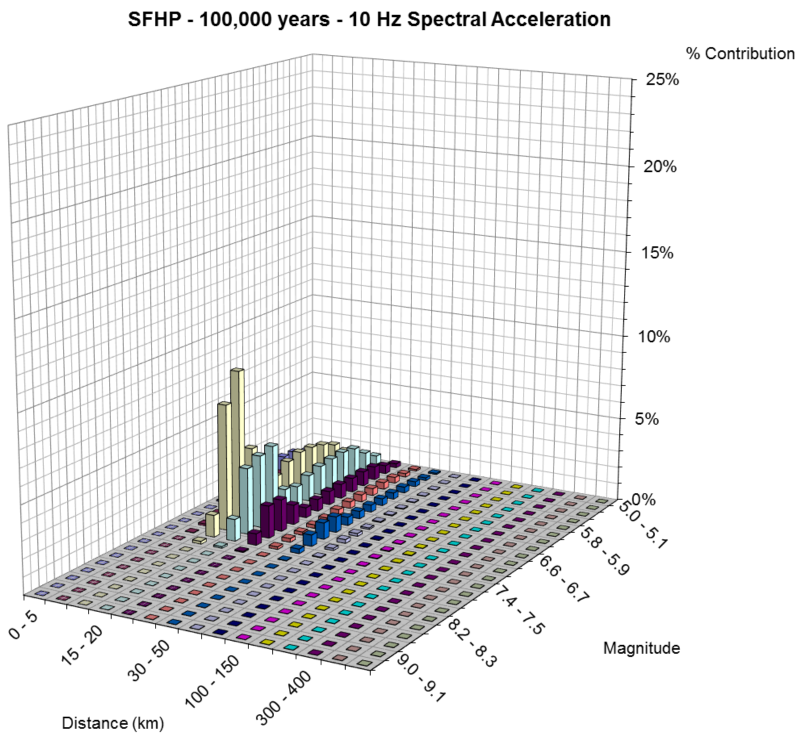

(b)

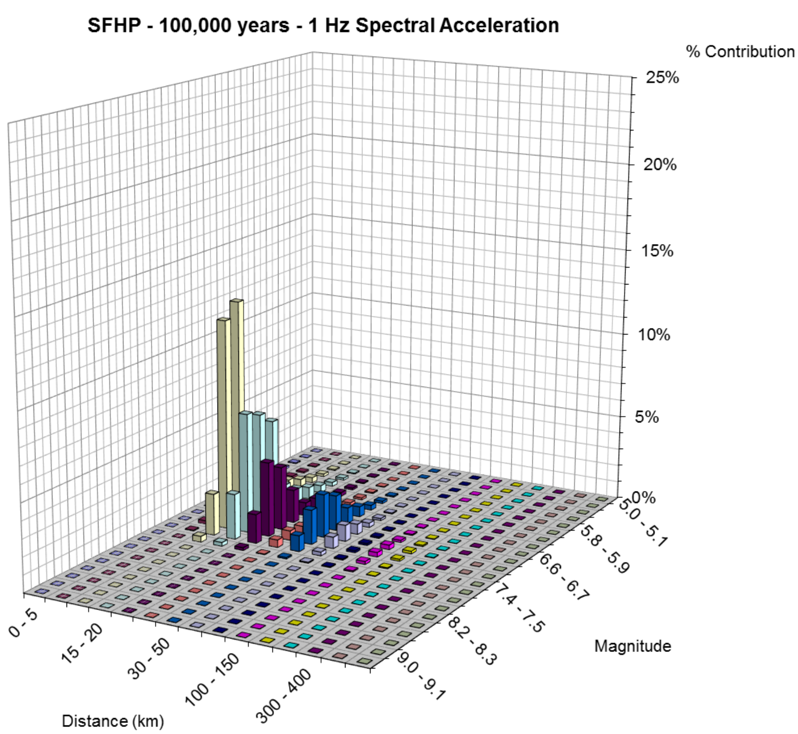

Figure 10-56. Magnitude-distance deaggregation for: a) 10 Hz; and b) 1 Hz at the 100,000 yr return period.

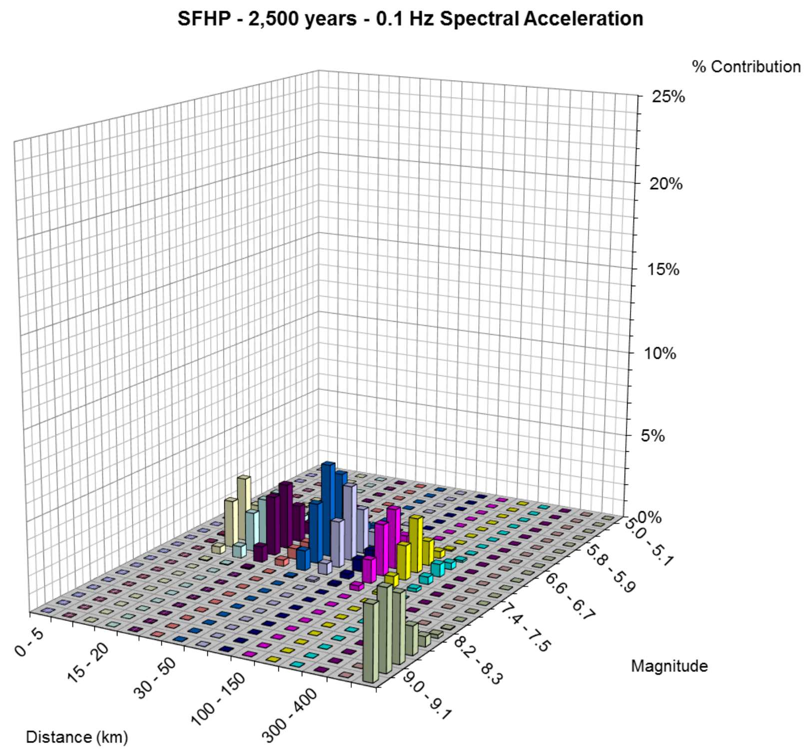

Figure 10-57. Magnitude-distance deaggregation for 0.1 Hz spectral acceleration at return periods of 2,500 yr.

10.5.1 Sensitivity Analyses for SFHP

The sensitivity analyses described in Section 10.2.2 focus on elements of the model that are common to MFC, FMF, and SFHP. This section presents results of additional tests performed for the SFHP site.

10.5.1.1 Elements of the SSC Model

Figures 10-58 and 10-59 show the contribution to the total mean hazard at SFHP by the individual faults and tectonic sources, respectively, in the SSC model. The dominant contributors are the Lemhi fault and the Centennial Shear Zone, due to their proximity to the site and high seismicity rates.

10.5.1.2 Elements of the GMC Model

As discussed in Section 9, the effect of the heavy tailed distribution only became significant at low AEF values, typically less than 10^{-4}. In the PSHA calculations for MFC and FMF, only the lognormal model was used because the return periods of interest were less than 10,000 years, but for SFHP, the return periods of interest range between 2,500 and 100,000 years. Figure 10-60 compares the total mean hazard curve (in black) with the two alternative models (lognormal in blue, and mixture in red). The hazard curves obtained with the mixture and lognormal models begin diverging at AEF of 10^{-4}.

10.5.1.3 Variance Contribution Plots

Variance contribution histograms shown in Figures 10-61, 10-62 and 10-63 for 10 Hz (0.1-sec), 1 Hz (1-sec) and 0.1 Hz (10-sec) spectral accelerations, respectively. Each figure contains histograms of the total variance calculated at four return periods: 2,500 yr (AEF of $4x10^{-4}$), 10,000 yr (AEF of 10^{-4}), 25,000 yr (AEF of $4x10^{-4}$), and 100,000yr (AEF of 10^{-5}). The figures show that most of the total variance comes from the epistemic uncertainty in the ground motion models for median motions and in aleatory variability (sigma). Other significant contributions to the total variance come from the uncertainty in the recurrence rates for the fault sources, as expressed by the combination of the uncertainty in the approach (slip rate versus recurrence intervals) and the uncertainty in the slip rate (category labeled “Recurrence Rates” in the histograms), and by the CSZ source zone. The relative contributions of other elements of the model that are much smaller include, among others, the anelastic attenuation parameter used in the subduction ground motion models applied to the Cascadia subduction zone. Its small contribution is visible at 10-sec.

(a)

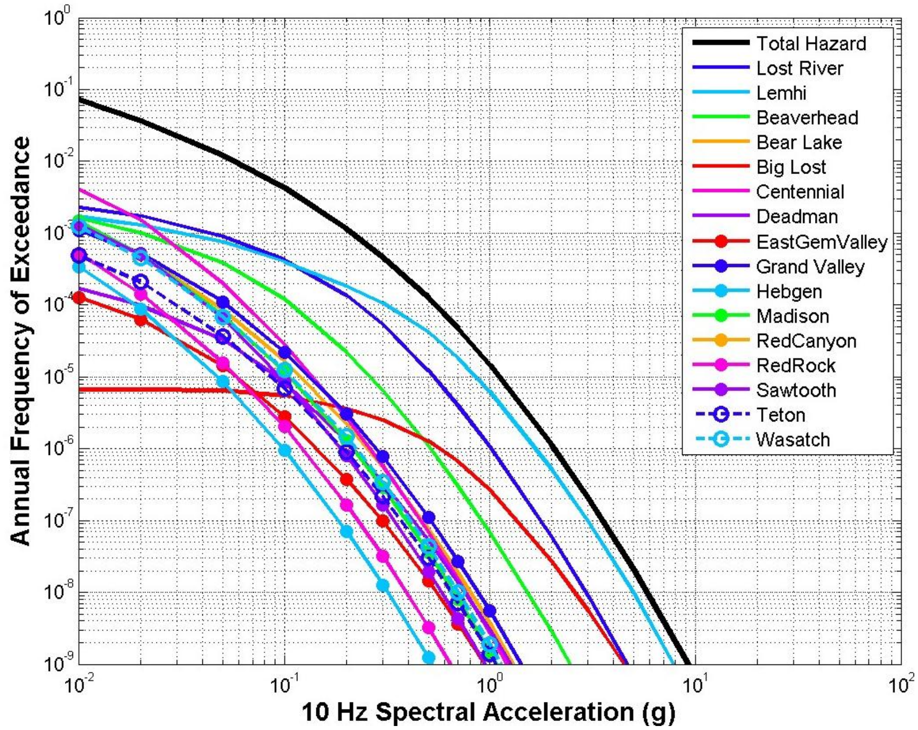

(b)

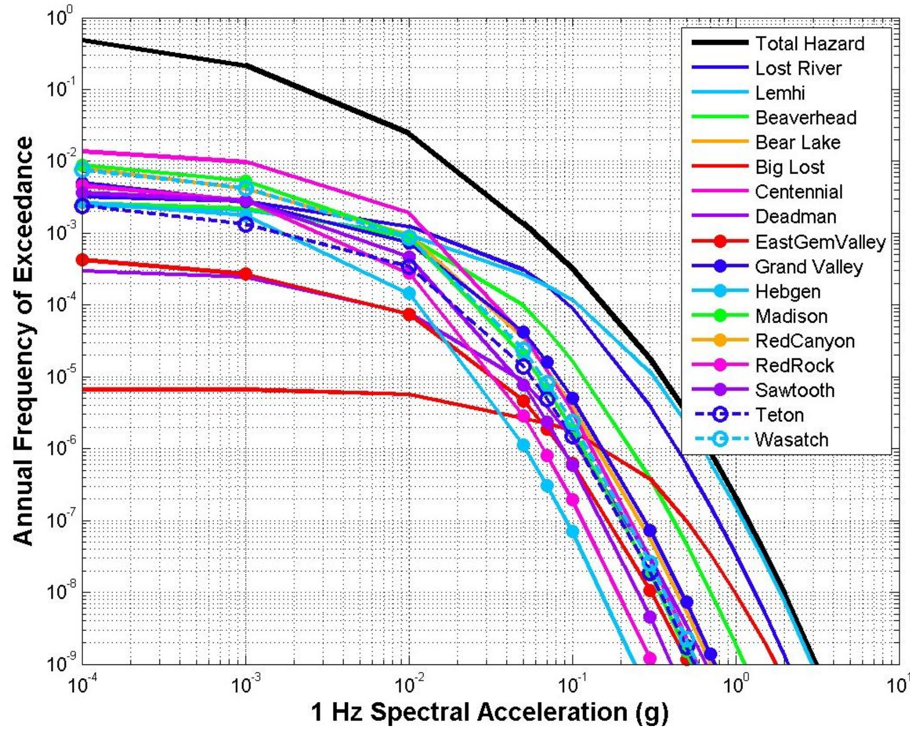

Figure 10-58. Contribution of individual fault sources to the total seismic hazard for reference rock conditions: a) 10 Hz (0.1-sec) spectral acceleration; and b) 1 Hz (1-sec) spectral acceleration.

(a)

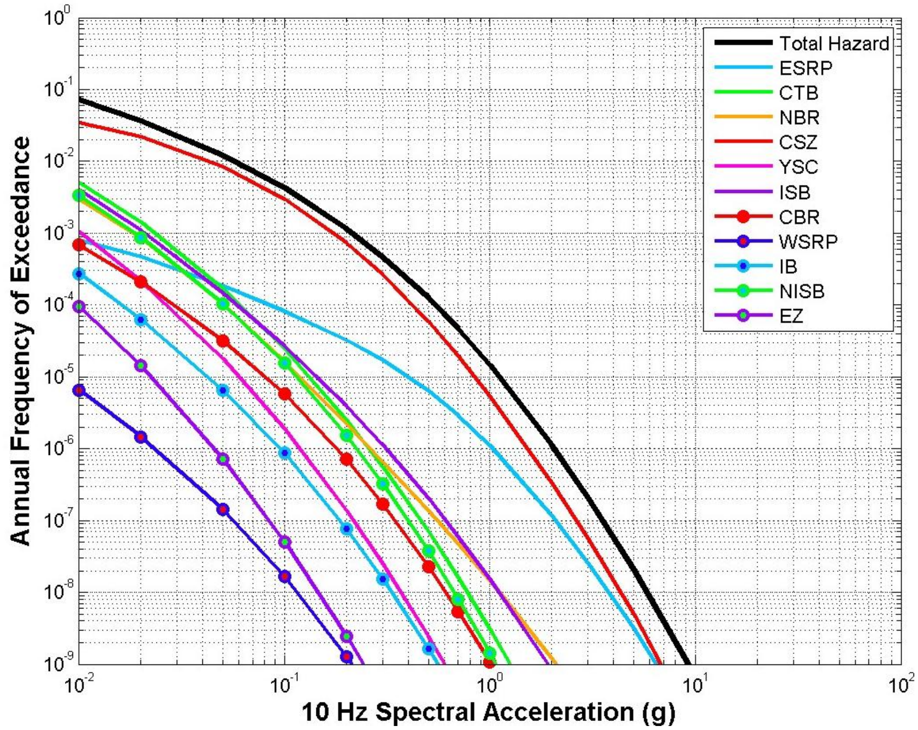

(b)

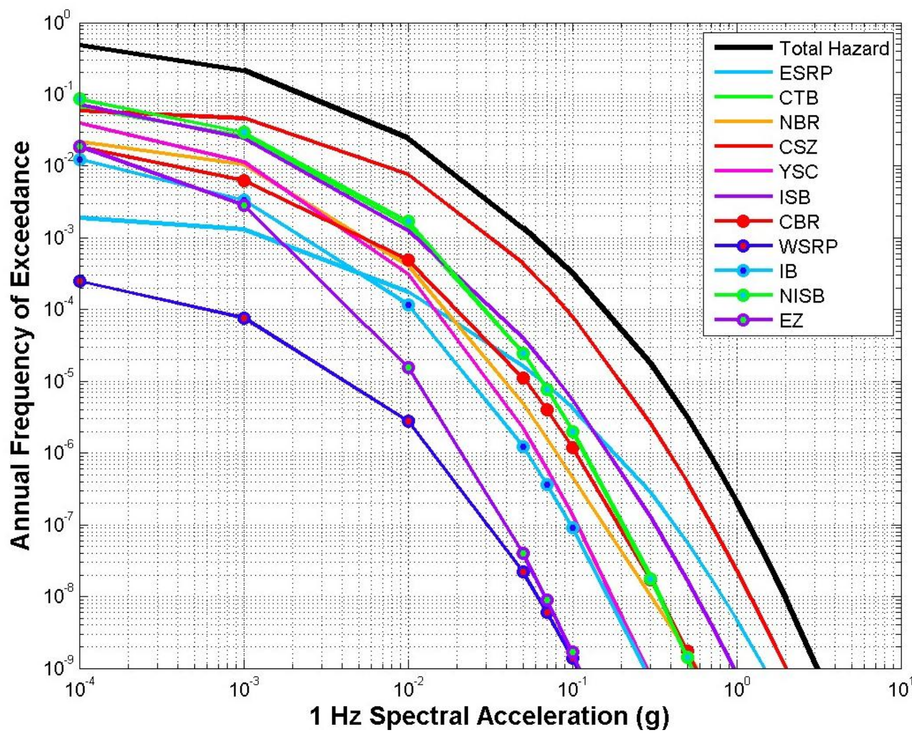

Figure 10-59. Contributions of individual tectonic sources to the total seismic hazard for reference rock conditions: a) 10 Hz (0.1-sec) spectral acceleration; and b) 1 Hz (1-sec) spectral acceleration.

(a)

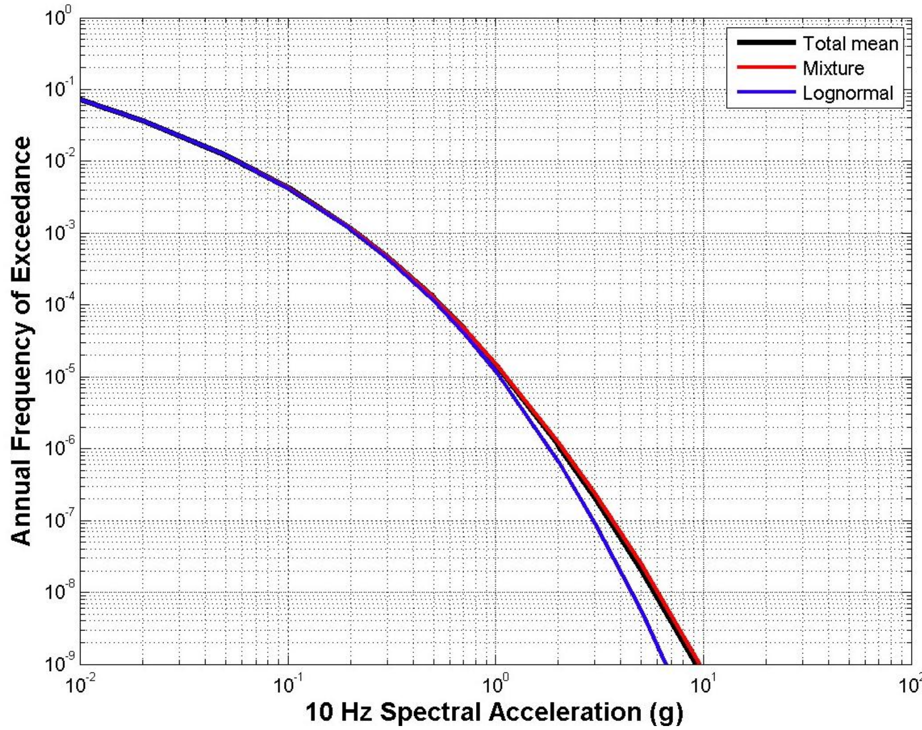

(b)

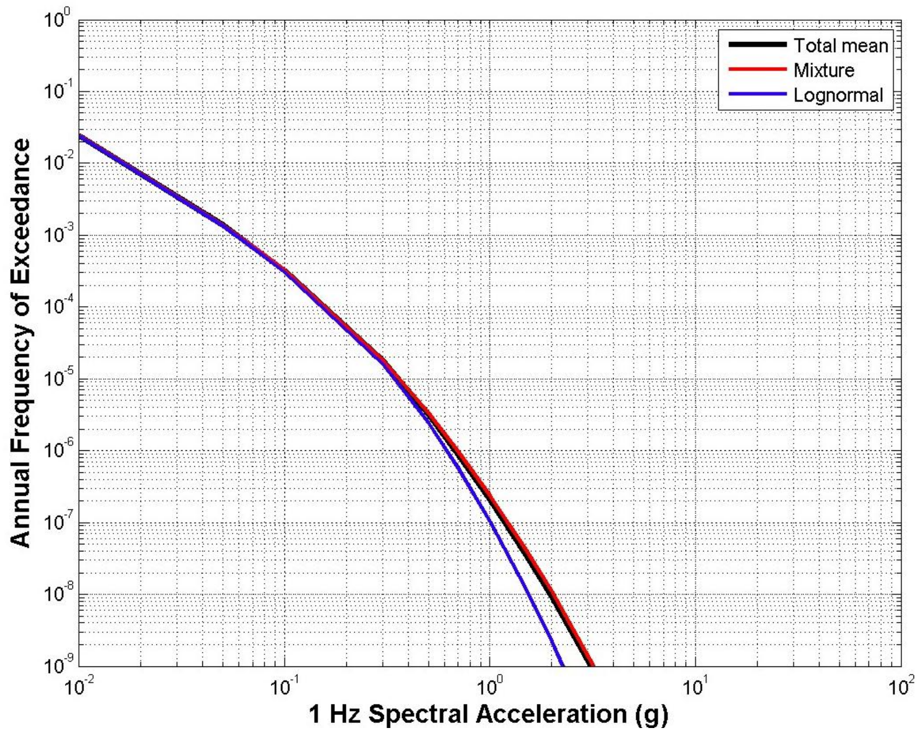

Figure 10-60. Sensitivity to lognormal and mixture models: a) 10 Hz (0.1-sec) spectral acceleration; and b) 1 Hz (1-sec) spectral acceleration.

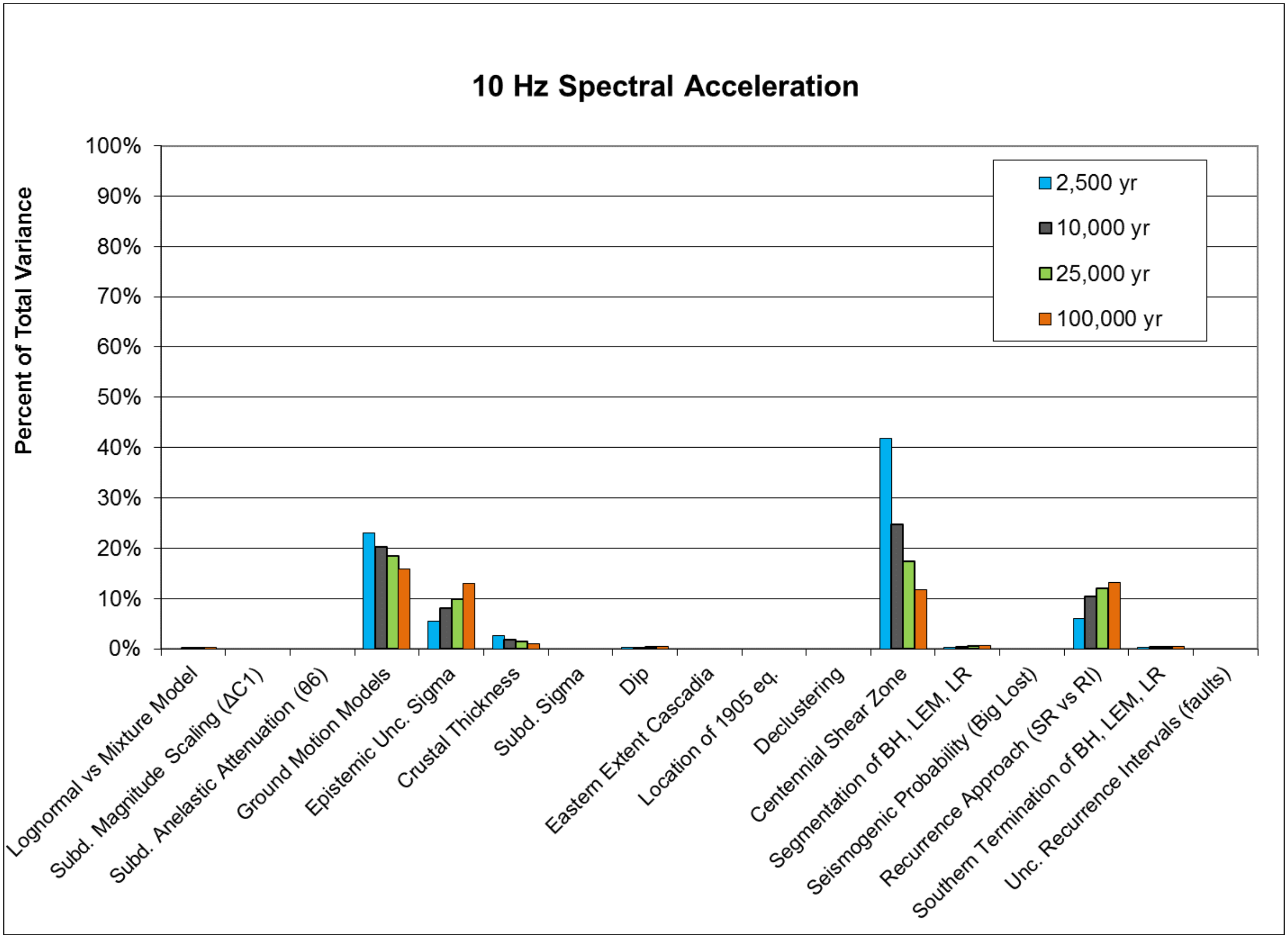

Figure 10-61. Contributions to the variance in the 10 Hz (0.1-sec) hazard for return periods of 2,500, 10,000, 25,000, and 100,000 yr.

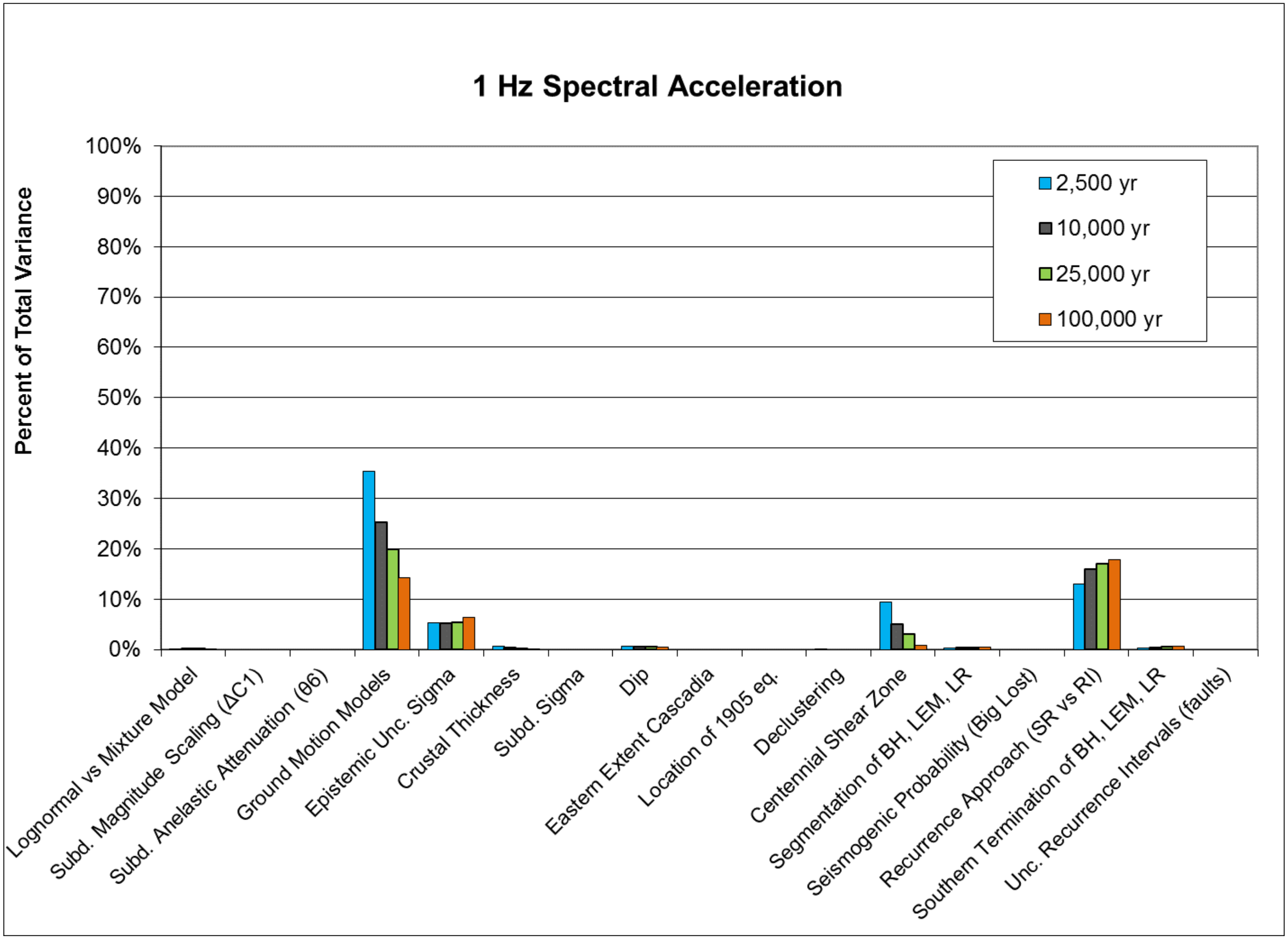

Figure 10-62. Contributions to the variance in the 1 Hz (1-sec) hazard for return periods of 2,500, 10,000, 25,000, and 100,000 yr.

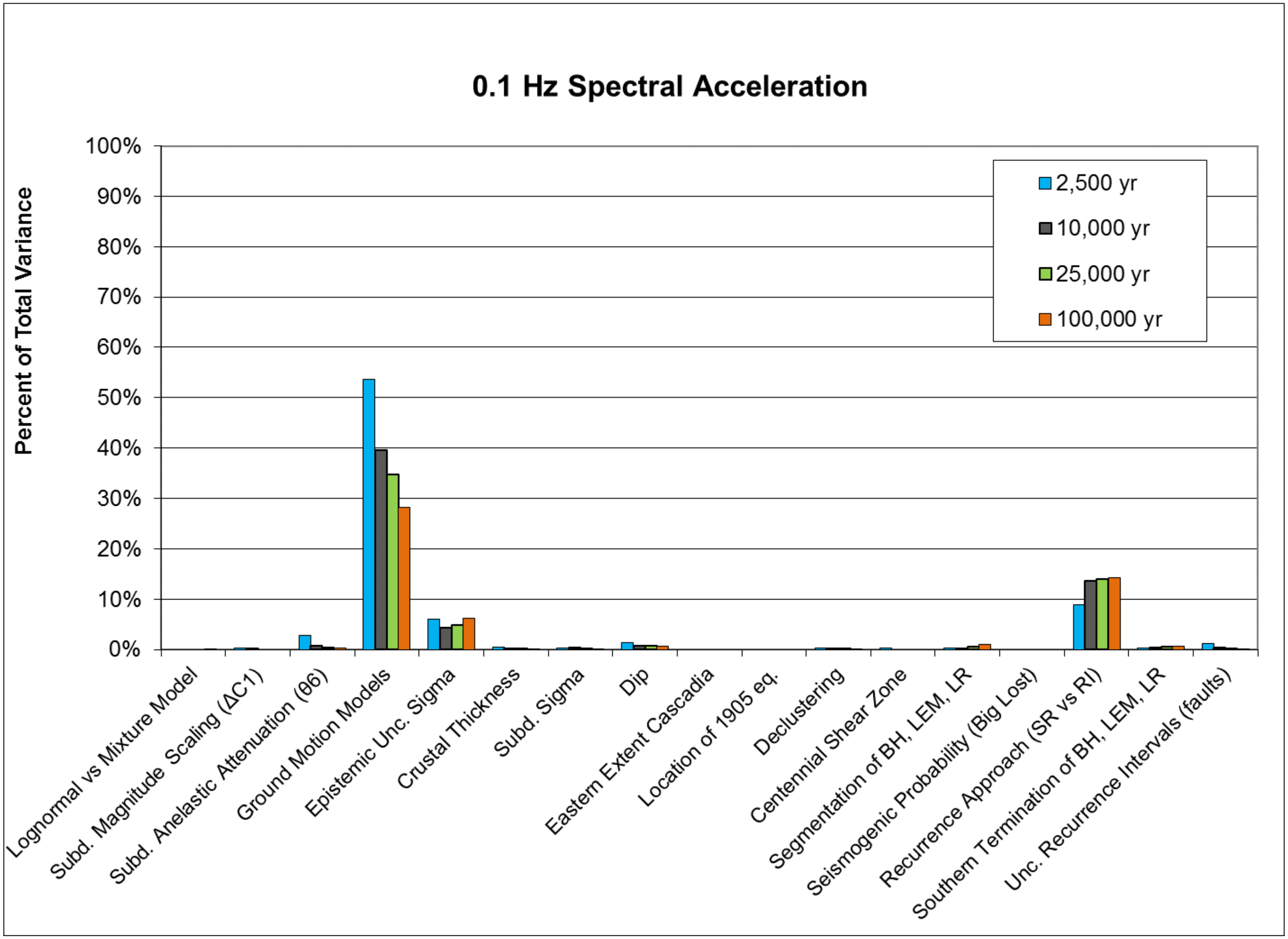

Figure 10-63. Contributions to the variance in the 0.1 Hz (10-sec) hazard for return periods of 2,500, 10,000, 25,000, and 100,000 yr.

10.6 Site-Specific Hazard at SFHP

Figure 10-64 shows the site-specific mean hazard curves for SFHP rock conditions (in blue) in comparison with the corresponding site-specific hazard curves calculated in the 2000 INL PSHA study (red curves) by URS Greiner Woodward-Clyde Federal Services et al. (2000). The plots show the results for PGA, 10 Hz and 1 Hz spectral accelerations. For PGA and 10 Hz spectral acceleration, the results of the SSHAC Level 1 study are lower than those from the 2000 INL PSHA for a wider range of ground motion levels than the results shown on Figure 10-23 for the MFC site. This is likely due to the difference in site characterization as the updated characterization of kappa at the NRF facility produced a best estimate value that is approximately 50 percent higher than the value used in the 2000 INL PSHA. At 1 Hz, the results of the SSHAC Level 1 PSHA are consistently lower than the results obtained in the 2000 INL PSHA, similar to the results shown on Figure 10-23 for MFC. The lower hazard is likely due to a combination of lower median motions from the adjusted SWUS GMPEs compared to the 2000 set of median models, and lower effective total sigma (combined aleatory and epistemic) than the ergodic sigmas used in the 2000 PSHA.

Figure 10-65 shows the mean and the 5th, 15th, 50th, 85th, and 95th fractiles for 10 Hz and 2 Hz spectral accelerations at SFHP for rock site conditions that illustrate the variability introduced in the site-specific hazard by the alternative site amplification functions. The mean site-specific hazard curves at SFHP for rock site conditions are listed in Table 10-14; the fractile hazard curves for 10 Hz and 2 Hz are listed in Tables 10-15.

There are two sets of results for SFHP for soil site conditions: one for a soil thickness of 20 ft ±5 ft, and the other for a soil thickness of 40 ft ±5 ft. The site-specific hazard curves at SFHP soil sites, including fractiles for 10 Hz and 2 Hz are listed in Tables 10-16, 10-17, and 10-18 for a soil thickness of 20 ft, and Tables 10-19, 10-20, and 10-21 for a soil thickness of 40 ft. For 20 ft soil thickness, Tables 10-16 and 10-17 list the generic (EPRI and Peninsular Range) and site-specific (NWRC-RA, 2015) material curves, respectively. For 40 ft, Tables 10-19 and 10-20 list the generic and site-specific material curves, respectively.

The mean soil hazard curves listed represent the envelope of the results obtained over the ±5 ft range. As will be shown below, the variability in hazard results due to the ±5 ft variability in depth is small. As was the case for MFC, the fractiles listed in Tables 10-18 (20 ft) and 10-21 (40 ft) represent only the epistemic uncertainty in the transfer function from the SWUS reference profile to the SFHP profiles. The mean site-specific hazard curve and its fractiles for 10 Hz and 2 Hz are also shown in Figures 10-66 and 10-67for soil thickness of 20 and 40 ft, respectively.

(a)

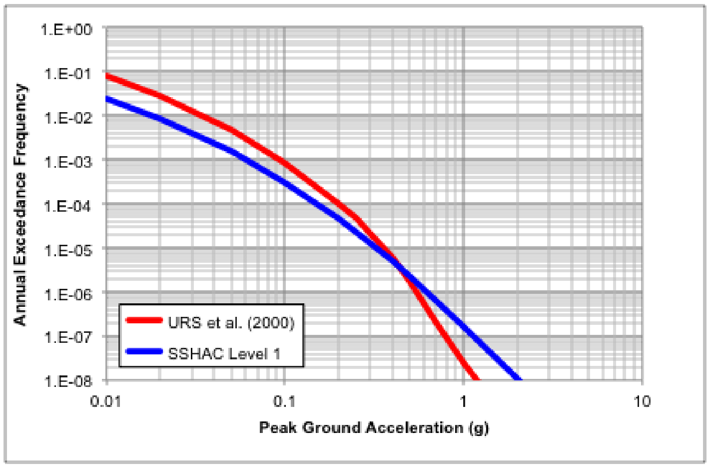

(b)

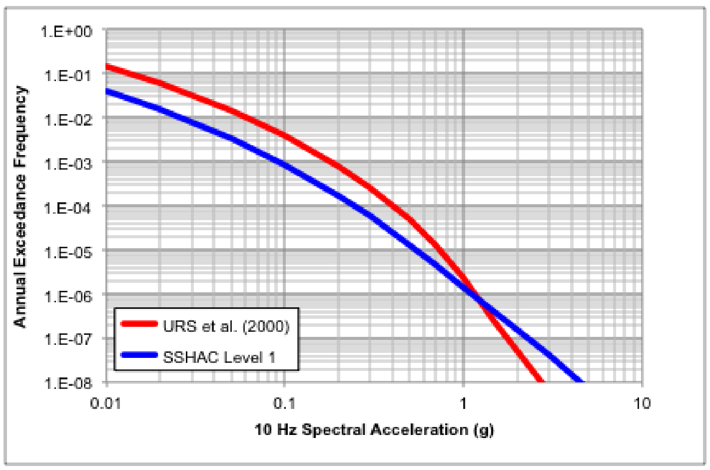

(c)

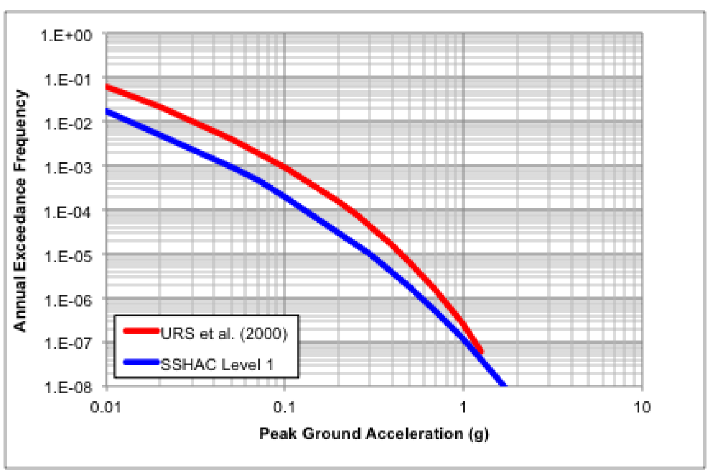

Figure 10-64. Comparison of the mean site-specific hazard curves at SFHP for rock conditions obtained in this study (SSHAC Level 1) with the corresponding curves from URS Greiner Woodward Clyde Federal Services et al. (2000), for: a) PGA; b) 10 Hz; and c) 1 Hz spectral accelerations.

(a)

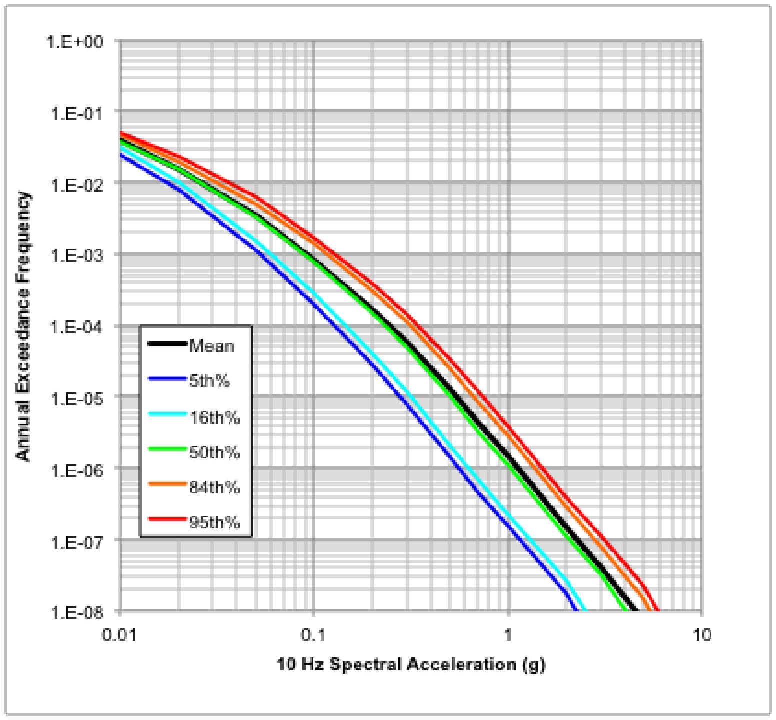

(b)

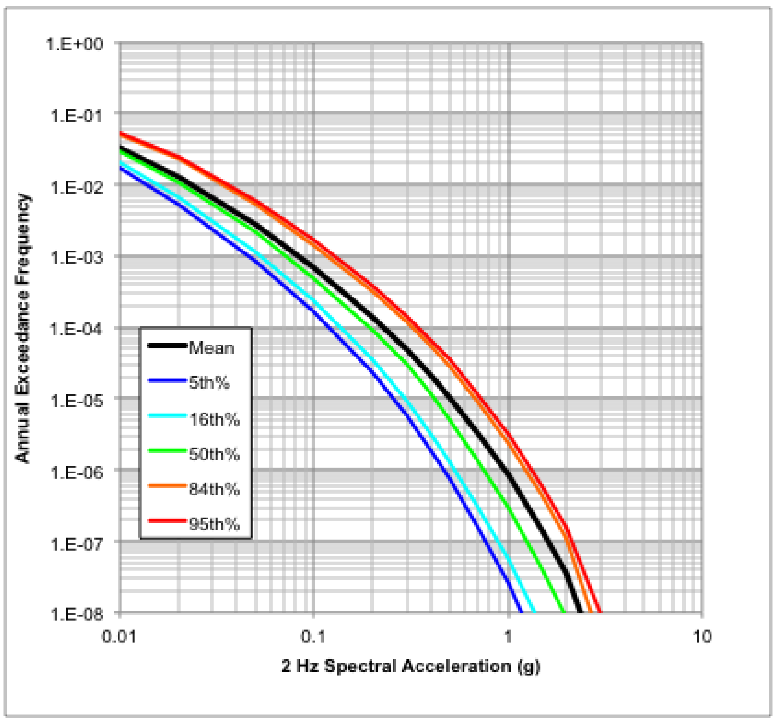

Figure 10-65. Total mean site-specific hazard and fractiles at SFHP for rock conditions for: a) 10 Hz spectral acceleration; and b) 2 Hz spectral acceleration.

Table 10-14. Mean site-specific hazard curves at SFHP for rock conditions.

PGA	AEF	50 Hz SA	AEF	33.3 Hz SA	AEF	20 Hz SA	AEF
0.01	2.46E-02	0.01	2.71E-02	0.01	2.56E-02	0.01	3.21E-02
0.02	8.49E-03	0.02	9.20E-03	0.02	9.18E-03	0.02	1.14E-02
0.05	1.56E-03	0.05	1.66E-03	0.05	1.81E-03	0.05	2.29E-03
0.1	3.21E-04	0.1	3.54E-04	0.1	4.15E-04	0.1	5.48E-04
0.2	4.86E-05	0.2	5.88E-05	0.2	7.54E-05	0.2	1.06E-04
0.3	1.35E-05	0.3	1.76E-05	0.3	2.43E-05	0.3	3.55E-05
0.4	5.03E-06	0.4	6.98E-06	0.4	1.02E-05	0.4	1.54E-05
0.5	2.26E-06	0.5	3.28E-06	0.5	5.03E-06	0.5	7.83E-06
0.7	6.42E-07	0.7	9.97E-07	0.7	1.65E-06	0.7	2.72E-06
1	1.61E-07	1	2.68E-07	1	4.84E-07	1	8.58E-07
2	1.09E-08	2	2.01E-08	2	4.25E-08	2	9.04E-08
5	1.35E-10	5	3.34E-10	5	1.22E-09	5	4.08E-09
10	1.25E-12	10	5.53E-12	10	3.20E-11	10	1.52E-10
10 Hz SA	AEF	6.67 Hz SA	AEF	5 Hz SA	AEF	3.33 Hz SA	AEF
0.01	3.87E-02	0.01	5.72E-02	0.01	6.24E-02	0.01	3.55E-02
0.02	1.53E-02	0.02	2.59E-02	0.02	2.83E-02	0.02	1.34E-02
0.05	3.37E-03	0.05	7.07E-03	0.05	7.74E-03	0.05	2.81E-03
0.1	8.58E-04	0.1	2.10E-03	0.1	2.35E-03	0.1	7.13E-04
0.2	1.71E-04	0.2	5.01E-04	0.2	5.78E-04	0.2	1.47E-04
0.3	5.84E-05	0.3	1.90E-04	0.3	2.26E-04	0.3	5.13E-05
0.5	1.30E-05	0.5	4.85E-05	0.5	5.95E-05	0.5	1.14E-05
0.7	4.51E-06	0.7	1.77E-05	0.7	2.19E-05	0.7	3.69E-06
1	1.42E-06	1	5.60E-06	1	6.74E-06	1	9.85E-07
2	1.53E-07	2	5.46E-07	2	5.26E-07	2	5.82E-08
3	4.23E-08	3	1.45E-07	3	1.14E-07	3	9.84E-09
5	7.26E-09	5	3.05E-08	5	2.06E-08	5	1.03E-09
10	1.66E-10	10	2.16E-09	10	1.27E-09	10	1.46E-11
2 Hz SA	AEF	1 Hz SA	AEF	0.5 Hz SA	AEF	0.333 Hz	AEF
0.01	3.24E-02	0.0001	4.44E-01	0.0001	3.56E-01	0.0001	2.90E-01
0.02	1.27E-02	0.001	1.76E-01	0.001	8.97E-02	0.001	6.45E-02
0.05	2.70E-03	0.01	1.74E-02	0.01	5.76E-03	0.01	2.97E-03
0.1	6.82E-04	0.05	9.59E-04	0.05	2.33E-04	0.05	1.00E-04
0.2	1.41E-04	0.07	4.73E-04	0.07	1.05E-04	0.07	4.25E-05
0.3	4.88E-05	0.1	2.05E-04	0.1	4.03E-05	0.1	1.52E-05
0.4	2.12E-05	0.3	1.04E-05	0.3	1.14E-06	0.3	3.05E-07
0.5	1.05E-05	0.5	1.82E-06	0.5	1.61E-07	0.5	3.76E-08
0.7	3.26E-06	0.7	5.01E-07	0.7	3.95E-08	0.7	8.49E-09
1	8.27E-07	1	1.13E-07	1	7.98E-09	1	1.59E-09
1.5	1.47E-07	1.5	1.78E-08	1.5	1.15E-09	1.5	2.10E-10
2	3.76E-08	2	4.22E-09	2	2.67E-10	2	4.65E-11
5	3.87E-11	5	1.93E-11	5	1.51E-12	5	2.32E-13

Table 10-14. Continued.

0.2 Hz SA	AEF	0.133 Hz SA	AEF	0.1 Hz SA	AEF		
0.000001	4.98E-01	0.000001	4.93E-01	0.000001	4.82E-01		
0.00001	4.50E-01	0.00001	3.63E-01	0.00001	2.84E-01		
0.00005	2.70E-01	0.00005	1.74E-01	0.00005	1.22E-01		
0.0001	1.89E-01	0.0001	1.15E-01	0.0001	7.84E-02		
0.0005	6.16E-02	0.0005	3.39E-02	0.0005	1.98E-02		
0.001	3.30E-02	0.001	1.67E-02	0.001	8.78E-03		
0.005	3.63E-03	0.005	1.40E-03	0.005	5.55E-04		
0.01	1.05E-03	0.01	3.69E-04	0.01	1.24E-04		
0.03	9.14E-05	0.03	2.50E-05	0.03	5.48E-06		
0.05	2.37E-05	0.05	5.63E-06	0.05	9.83E-07		
0.1	2.61E-06	0.1	5.08E-07	0.1	6.54E-08		
0.5	3.24E-09	0.5	4.21E-10	0.5	2.87E-11		
1	1.12E-10	1	1.30E-11	1	6.54E-13		
PGA- Peak Ground Acceleration (g); AEF – Annual Exceedance Frequency; SA – Spectral Acceleration (g).							

Table 10-15. Site-specific hazard fractiles at SFHP for rock conditions for 2 Hz and 10 Hz.

Spectral Acceleration (g)	SFHP Rock Annual Exceedance Frequency at Fractiles				
	5th	15th	50th	85th	95th
10 Hz					
0.01	2.53E-02	3.07E-02	3.75E-02	4.81E-02	5.17E-02
0.02	7.89E-03	9.87E-03	1.49E-02	1.98E-02	2.29E-02
0.05	1.14E-03	1.47E-03	3.23E-03	5.04E-03	6.10E-03
0.10	2.06E-04	2.82E-04	8.03E-04	1.40E-03	1.72E-03
0.20	2.80E-05	4.03E-05	1.50E-04	3.03E-04	3.89E-04
0.30	7.63E-06	1.13E-05	4.90E-05	1.08E-04	1.41E-04
0.40	1.43E-06	2.07E-06	1.02E-05	2.50E-05	3.38E-05
0.50	4.74E-07	7.00E-07	3.40E-06	8.71E-06	1.20E-05
0.70	1.51E-07	2.18E-07	1.08E-06	2.74E-06	3.79E-06
1.00	1.74E-08	2.65E-08	1.15E-07	2.92E-07	4.03E-07
2.00	2.57E-09	4.62E-09	3.29E-08	8.08E-08	1.10E-07
5.00	1.58E-11	1.10E-10	4.21E-09	1.54E-08	2.22E-08
10.00	1.34E-22	1.02E-19	1.33E-11	3.90E-10	7.95E-10
2 Hz					
0.01	1.69E-02	2.04E-02	2.93E-02	5.12E-02	5.25E-02
0.02	5.28E-03	6.53E-03	1.05E-02	2.27E-02	2.48E-02
0.05	8.26E-04	1.10E-03	2.11E-03	5.33E-03	5.97E-03
0.10	1.67E-04	2.34E-04	4.99E-04	1.44E-03	1.65E-03
0.20	2.33E-05	3.59E-05	9.44E-05	3.22E-04	3.78E-04
0.30	5.69E-06	9.40E-06	2.93E-05	1.19E-04	1.43E-04
0.50	1.87E-06	3.23E-06	1.14E-05	5.44E-05	6.67E-05
0.70	7.40E-07	1.32E-06	5.12E-06	2.78E-05	3.48E-05
1.00	1.63E-07	3.10E-07	1.38E-06	9.03E-06	1.16E-05
2.00	2.60E-08	5.39E-08	2.99E-07	2.38E-06	3.16E-06
3.00	2.19E-09	6.14E-09	4.09E-08	4.39E-07	6.03E-07
5.00	8.55E-13	1.47E-10	8.79E-09	1.15E-07	1.64E-07
10.00	1.00E-20	1.00E-20	2.59E-17	6.71E-11	3.01E-10

(a)

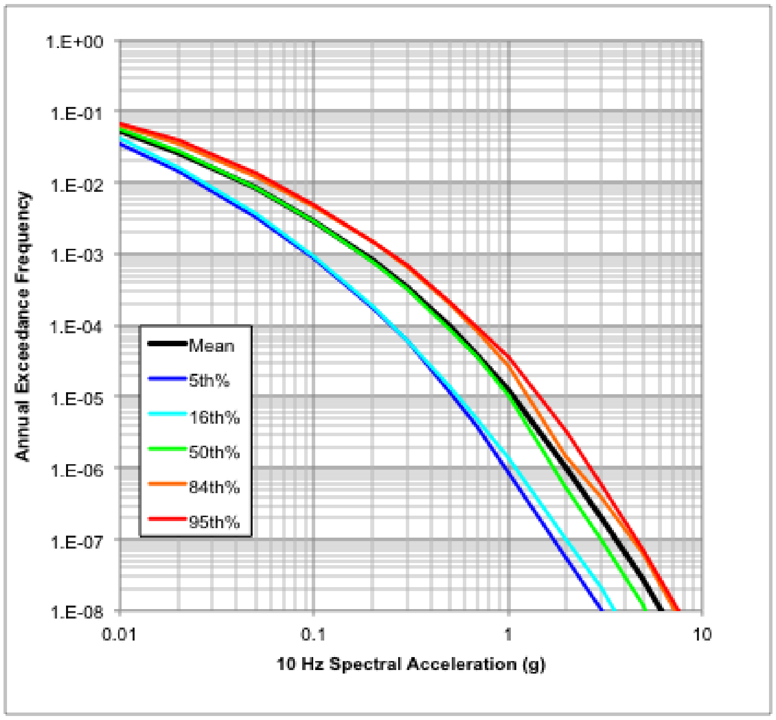

(b)

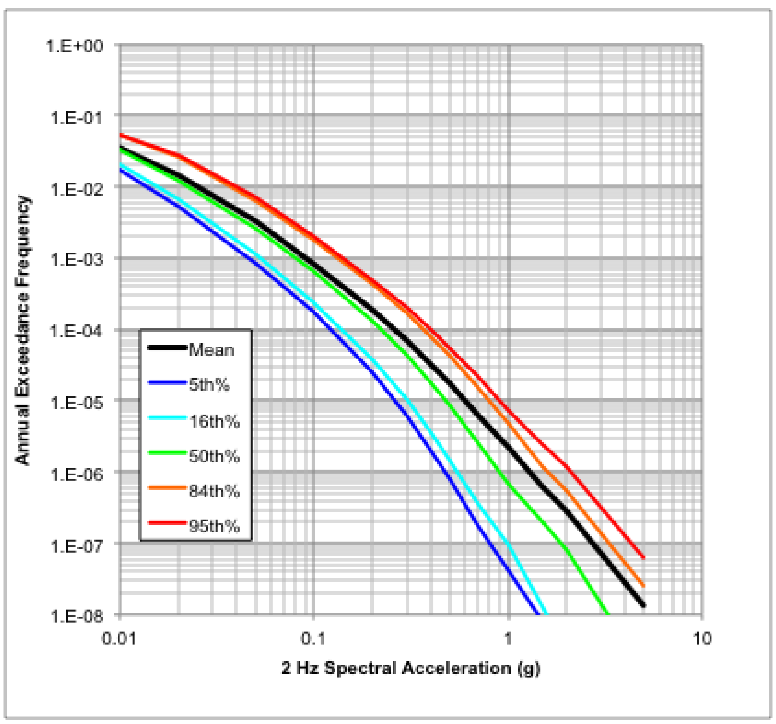

Figure 10-66. Total mean site-specific hazard and fractiles at SFHP, assuming a soil thickness of 20 ft, for: a) 10 Hz spectral acceleration; and b) 2 Hz spectral acceleration.

(a)

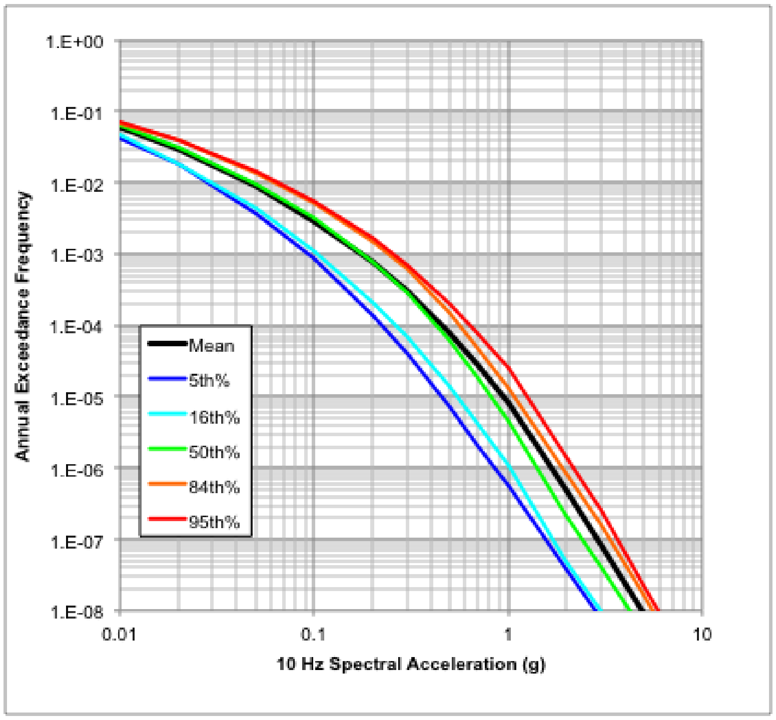

(b)

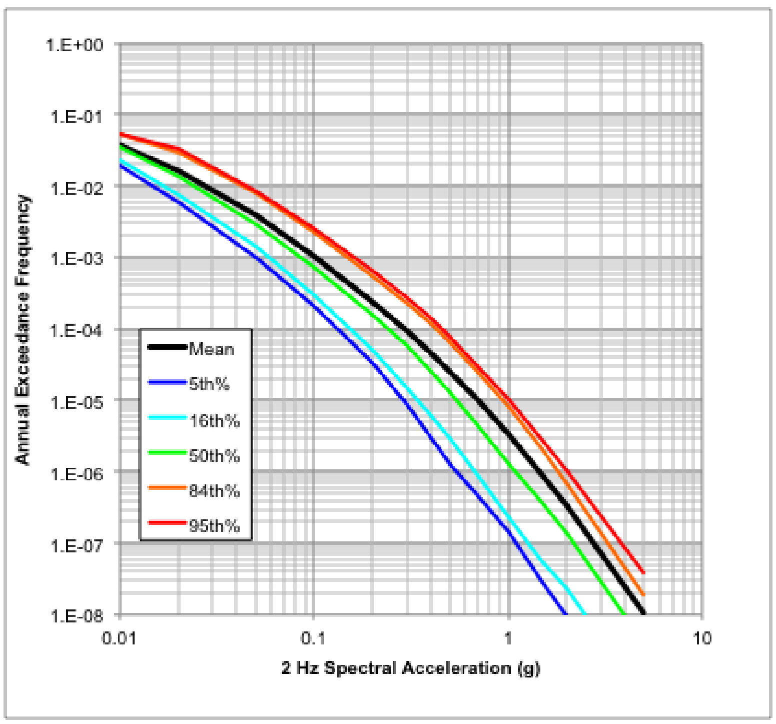

Figure 10-67. Total mean site-specific hazard and fractiles at SFHP, assuming a soil thickness of 40 ft, for: a) 10 Hz spectral acceleration; and b) 2 Hz spectral acceleration.

Table 10-16. Envelope of mean site-specific hazard curves at SFHP, assuming a soil thickness of 20±5 ft computed using generic material curves.

PGA	AEF	50 Hz SA	AEF	33.3 Hz SA	AEF	20 Hz SA	AEF
0.01	3.14E-02	0.01	3.48E-02	0.01	3.29E-02	0.01	4.28E-02
0.02	1.33E-02	0.02	1.46E-02	0.02	1.45E-02	0.02	1.96E-02
0.05	3.28E-03	0.05	3.54E-03	0.05	3.88E-03	0.05	5.64E-03
0.1	8.72E-04	0.1	9.46E-04	0.1	1.14E-03	0.1	1.88E-03
0.2	1.69E-04	0.2	1.92E-04	0.2	2.56E-04	0.2	4.91E-04
0.3	5.43E-05	0.3	6.48E-05	0.3	9.52E-05	0.3	1.96E-04
0.4	2.16E-05	0.4	2.68E-05	0.4	4.27E-05	0.4	9.51E-05
0.5	9.62E-06	0.5	1.26E-05	0.5	2.15E-05	0.5	5.16E-05
0.7	2.60E-06	0.7	3.58E-06	0.7	7.02E-06	0.7	1.87E-05
1	6.11E-07	1	8.57E-07	1	1.82E-06	1	5.64E-06
2	3.40E-08	2	4.96E-08	2	1.10E-07	2	4.08E-07
5	5.47E-10	5	8.13E-10	5	1.71E-09	5	9.01E-09
10	1.05E-11	10	1.69E-11	10	4.41E-11	10	3.33E-10
10 Hz SA	AEF	6.67 Hz SA	AEF	5 Hz SA	AEF	3.33 Hz SA	AEF
0.01	5.62E-02	0.01	7.48E-02	0.01	7.84E-02	0.01	4.64E-02
0.02	2.85E-02	0.02	4.13E-02	0.02	4.37E-02	0.02	2.27E-02
0.05	9.12E-03	0.05	1.36E-02	0.05	1.38E-02	0.05	6.04E-03
0.1	3.23E-03	0.1	4.84E-03	0.1	4.84E-03	0.1	1.87E-03
0.2	9.19E-04	0.2	1.41E-03	0.2	1.41E-03	0.2	4.88E-04
0.3	3.84E-04	0.3	6.18E-04	0.3	6.23E-04	0.3	2.05E-04
0.5	1.06E-04	0.5	1.91E-04	0.5	2.00E-04	0.5	6.21E-05
0.7	3.96E-05	0.7	8.08E-05	0.7	8.75E-05	0.7	2.63E-05
1	1.25E-05	1	2.90E-05	1	3.34E-05	1	9.69E-06
2	9.87E-07	2	2.59E-06	2	3.21E-06	2	8.50E-07
3	2.05E-07	3	5.99E-07	3	6.62E-07	3	1.76E-07
5	2.71E-08	5	9.26E-08	5	8.78E-08	5	2.09E-08
10	1.18E-09	10	6.71E-09	10	7.28E-09	10	1.07E-09
2 Hz SA	AEF	1 Hz SA	AEF	0.5 Hz SA	AEF	0.333 Hz	AEF
0.01	3.52E-02	0.0001	4.48E-01	0.0001	3.55E-01	0.0001	2.92E-01
0.02	1.48E-02	0.001	1.80E-01	0.001	8.90E-02	0.001	6.56E-02
0.05	3.35E-03	0.01	1.82E-02	0.01	5.68E-03	0.01	3.06E-03
0.1	8.93E-04	0.05	1.04E-03	0.05	2.33E-04	0.05	1.06E-04
0.2	1.98E-04	0.07	5.19E-04	0.07	1.06E-04	0.07	4.58E-05
0.3	7.43E-05	0.1	2.29E-04	0.1	4.08E-05	0.1	1.66E-05
0.4	3.47E-05	0.3	1.24E-05	0.3	1.20E-06	0.3	3.64E-07
0.5	1.85E-05	0.5	2.36E-06	0.5	1.82E-07	0.5	4.85E-08
0.7	6.85E-06	0.7	7.33E-07	0.7	4.82E-08	0.7	1.17E-08
1	2.39E-06	1	2.04E-07	1	1.09E-08	1	2.37E-09
1.5	7.63E-07	1.5	4.69E-08	1.5	1.81E-09	1.5	3.41E-10
2	3.34E-07	2	1.68E-08	2	4.66E-10	2	7.93E-11
5	1.57E-08	5	5.67E-10	5	3.51E-12	5	4.55E-13

Table 10-16. Continued.

0.2 Hz SA	AEF	0.133 Hz SA	AEF	0.1 Hz SA	AEF		
0.000001	4.99E-01	0.000001	4.93E-01	0.000001	4.82E-01		
0.00001	4.51E-01	0.00001	3.63E-01	0.00001	2.84E-01		
0.00005	2.71E-01	0.00005	1.74E-01	0.00005	1.22E-01		
0.0001	1.90E-01	0.0001	1.16E-01	0.0001	7.83E-02		
0.0005	6.21E-02	0.0005	3.39E-02	0.0005	1.98E-02		
0.001	3.35E-02	0.001	1.67E-02	0.001	8.76E-03		
0.005	3.71E-03	0.005	1.42E-03	0.005	5.61E-04		
0.01	1.08E-03	0.01	3.76E-04	0.01	1.27E-04		
0.03	9.63E-05	0.03	2.59E-05	0.03	5.78E-06		
0.05	2.55E-05	0.05	5.92E-06	0.05	1.09E-06		
0.1	2.91E-06	0.1	5.61E-07	0.1	7.90E-08		
0.5	4.42E-09	0.5	5.51E-10	0.5	3.86E-11		
1	1.73E-10	1	1.79E-11	1	9.25E-13		
PGA- Peak Ground Acceleration (g); AEF – Annual Exceedance Frequency; SA – Spectral Acceleration (g).							

Table 10-17. Envelope of mean site-specific hazard curves at SFHP, assuming a soil thickness of 20±5 ft computed using site-specific material curves.

PGA	AEF	50 Hz SA	AEF	33.3 Hz SA	AEF	20 Hz SA	AEF
0.01	3.16E-02	0.01	3.51E-02	0.01	3.32E-02	0.01	4.32E-02
0.02	1.37E-02	0.02	1.50E-02	0.02	1.49E-02	0.02	1.99E-02
0.05	3.45E-03	0.05	3.71E-03	0.05	4.03E-03	0.05	5.77E-03
0.1	9.37E-04	0.1	1.01E-03	0.1	1.19E-03	0.1	1.90E-03
0.2	1.81E-04	0.2	2.01E-04	0.2	2.60E-04	0.2	4.59E-04
0.3	5.79E-05	0.3	6.68E-05	0.3	9.31E-05	0.3	1.77E-04
0.4	2.35E-05	0.4	2.80E-05	0.4	4.03E-05	0.4	8.30E-05
0.5	1.10E-05	0.5	1.33E-05	0.5	1.99E-05	0.5	4.34E-05
0.7	3.03E-06	0.7	3.81E-06	0.7	6.01E-06	0.7	1.48E-05
1	7.03E-07	1	9.17E-07	1	1.48E-06	1	4.12E-06
2	4.57E-08	2	5.94E-08	2	8.89E-08	2	2.59E-07
5	1.07E-09	5	1.37E-09	5	1.91E-09	5	4.40E-09
10	2.44E-11	10	3.23E-11	10	4.79E-11	10	1.15E-10
10 Hz SA	AEF	6.67 Hz SA	AEF	5 Hz SA	AEF	3.33 Hz SA	AEF
0.01	5.69E-02	0.01	7.54E-02	0.01	7.87E-02	0.01	4.66E-02
0.02	2.94E-02	0.02	4.22E-02	0.02	4.45E-02	0.02	2.31E-02
0.05	9.53E-03	0.05	1.41E-02	0.05	1.44E-02	0.05	6.28E-03
0.1	3.41E-03	0.1	5.17E-03	0.1	5.19E-03	0.1	2.03E-03
0.2	9.66E-04	0.2	1.54E-03	0.2	1.58E-03	0.2	5.72E-04
0.3	3.98E-04	0.3	6.74E-04	0.3	7.24E-04	0.3	2.53E-04
0.5	1.08E-04	0.5	2.05E-04	0.5	2.38E-04	0.5	8.04E-05
0.7	4.03E-05	0.7	8.60E-05	0.7	1.03E-04	0.7	3.40E-05
1	1.23E-05	1	3.12E-05	1	4.07E-05	1	1.21E-05
2	9.71E-07	2	3.14E-06	2	4.34E-06	2	1.44E-06
3	2.16E-07	3	7.75E-07	3	9.77E-07	3	2.98E-07
5	2.60E-08	5	1.20E-07	5	1.20E-07	5	3.40E-08
10	8.27E-10	10	9.62E-09	10	8.57E-09	10	1.07E-09
2 Hz SA	AEF	1 Hz SA	AEF	0.5 Hz SA	AEF	0.333 Hz	AEF
0.01	3.52E-02	0.0001	4.48E-01	0.0001	3.55E-01	0.0001	2.92E-01
0.02	1.49E-02	0.001	1.80E-01	0.001	8.91E-02	0.001	6.56E-02
0.05	3.39E-03	0.01	1.82E-02	0.01	5.69E-03	0.01	3.06E-03
0.1	9.20E-04	0.05	1.05E-03	0.05	2.35E-04	0.05	1.07E-04
0.2	2.14E-04	0.07	5.23E-04	0.07	1.07E-04	0.07	4.65E-05
0.3	8.58E-05	0.1	2.33E-04	0.1	4.16E-05	0.1	1.70E-05
0.4	4.39E-05	0.3	1.36E-05	0.3	1.48E-06	0.3	4.43E-07
0.5	2.55E-05	0.5	3.21E-06	0.5	2.97E-07	0.5	7.28E-08
0.7	1.07E-05	0.7	1.23E-06	0.7	1.00E-07	0.7	2.01E-08
1	4.07E-06	1	4.58E-07	1	2.99E-08	1	4.58E-09
1.5	1.19E-06	1.5	1.62E-07	1.5	6.73E-09	1.5	7.22E-10
2	5.20E-07	2	7.88E-08	2	2.08E-09	2	1.77E-10
5	1.65E-08	5	5.52E-09	5	2.36E-11	5	1.18E-12

Table 10-17. Continued.

0.2 Hz SA	AEF	0.133 Hz SA	AEF	0.1 Hz SA	AEF		
0.000001	4.99E-01	0.000001	4.93E-01	0.000001	4.82E-01		
0.00001	4.51E-01	0.00001	3.63E-01	0.00001	2.84E-01		
0.00005	2.71E-01	0.00005	1.74E-01	0.00005	1.22E-01		
0.0001	1.90E-01	0.0001	1.16E-01	0.0001	7.83E-02		
0.0005	6.21E-02	0.0005	3.39E-02	0.0005	1.98E-02		
0.001	3.35E-02	0.001	1.67E-02	0.001	8.76E-03		
0.005	3.71E-03	0.005	1.42E-03	0.005	5.63E-04		
0.01	1.09E-03	0.01	3.77E-04	0.01	1.28E-04		
0.03	9.73E-05	0.03	2.65E-05	0.03	6.36E-06		
0.05	2.61E-05	0.05	6.33E-06	0.05	1.32E-06		
0.1	3.18E-06	0.1	6.69E-07	0.1	1.10E-07		
0.5	6.67E-09	0.5	8.53E-10	0.5	6.20E-11		
1	2.97E-10	1	2.96E-11	1	1.58E-12		
PGA- Peak Ground Acceleration (g); AEF – Annual Exceedance Frequency; SA – Spectral Acceleration (g).							

Table 10-18. Site-specific hazard fractiles at SFHP, assuming a soil thickness of 20 ft.

Spectral Acceleration (g)	SFHP Soil 20 ft Annual Exceedance Frequency at Fractiles				
	5th	15th	50th	85th	95th
10 Hz					
0.01	3.60E-02	4.11E-02	5.55E-02	6.39E-02	6.75E-02
0.02	1.44E-02	1.64E-02	2.70E-02	3.51E-02	3.96E-02
0.05	3.26E-03	3.66E-03	8.46E-03	1.22E-02	1.36E-02
0.10	8.60E-04	9.45E-04	2.86E-03	4.71E-03	5.10E-03
0.20	1.76E-04	1.90E-04	7.79E-04	1.47E-03	1.53E-03
0.30	6.00E-05	6.24E-05	3.15E-04	6.47E-04	6.91E-04
0.40	1.19E-05	1.39E-05	8.93E-05	2.03E-04	2.16E-04
0.50	3.66E-06	4.74E-06	3.51E-05	8.09E-05	9.34E-05
0.70	8.39E-07	1.39E-06	1.04E-05	2.58E-05	3.49E-05
1.00	5.37E-08	9.94E-08	5.41E-07	1.48E-06	3.36E-06
2.00	1.05E-08	2.11E-08	1.02E-07	3.85E-07	5.91E-07
5.00	6.77E-10	2.02E-09	1.16E-08	6.21E-08	6.91E-08
10.00	9.06E-15	1.10E-12	1.18E-10	2.02E-09	2.67E-09
2 Hz					
0.01	1.72E-02	2.07E-02	3.29E-02	5.28E-02	5.33E-02
0.02	5.37E-03	6.66E-03	1.22E-02	2.58E-02	2.81E-02
0.05	8.49E-04	1.14E-03	2.58E-03	6.35E-03	7.08E-03
0.10	1.73E-04	2.45E-04	6.39E-04	1.80E-03	2.05E-03
0.20	2.45E-05	3.84E-05	1.30E-04	4.21E-04	4.95E-04
0.30	6.04E-06	1.02E-05	4.34E-05	1.64E-04	1.98E-04
0.50	2.01E-06	3.55E-06	1.79E-05	7.89E-05	9.71E-05
0.70	7.97E-07	1.47E-06	8.54E-06	4.26E-05	5.35E-05
1.00	1.80E-07	3.76E-07	2.58E-06	1.53E-05	2.16E-05
2.00	4.10E-08	9.44E-08	6.84E-07	4.82E-06	7.26E-06
3.00	8.06E-09	1.35E-08	2.08E-07	1.23E-06	2.49E-06
5.00	1.30E-09	3.14E-09	8.33E-08	5.53E-07	1.23E-06
10.00	5.47E-19	3.77E-12	1.63E-09	2.55E-08	6.34E-08

Table 10-19. Envelope of mean site-specific hazard curves at SFHP, assuming a soil thickness of 40±5 ft computed using generic material curves.

PGA	AEF	50 Hz SA	AEF	33.3 Hz SA	AEF	20 Hz SA	AEF
0.01	3.53E-02	0.01	3.92E-02	0.01	3.67E-02	0.01	4.70E-02
0.02	1.59E-02	0.02	1.75E-02	0.02	1.70E-02	0.02	2.22E-02
0.05	3.96E-03	0.05	4.24E-03	0.05	4.52E-03	0.05	6.14E-03
0.1	1.03E-03	0.1	1.10E-03	0.1	1.28E-03	0.1	1.93E-03
0.2	1.86E-04	0.2	2.07E-04	0.2	2.67E-04	0.2	4.63E-04
0.3	5.69E-05	0.3	6.61E-05	0.3	9.20E-05	0.3	1.73E-04
0.4	2.19E-05	0.4	2.64E-05	0.4	3.86E-05	0.4	7.89E-05
0.5	9.64E-06	0.5	1.20E-05	0.5	1.84E-05	0.5	4.05E-05
0.7	2.46E-06	0.7	3.17E-06	0.7	5.22E-06	0.7	1.32E-05
1	5.37E-07	1	7.07E-07	1	1.19E-06	1	3.44E-06
2	3.03E-08	2	3.88E-08	2	6.08E-08	2	1.91E-07
5	4.17E-10	5	5.48E-10	5	8.20E-10	5	2.37E-09
10	7.20E-12	10	9.73E-12	10	1.66E-11	10	5.03E-11
10 Hz SA	AEF	6.67 Hz SA	AEF	5 Hz SA	AEF	3.33 Hz SA	AEF
0.01	5.94E-02	0.01	8.23E-02	0.01	8.69E-02	0.01	5.70E-02
0.02	2.96E-02	0.02	4.85E-02	0.02	5.53E-02	0.02	3.21E-02
0.05	8.98E-03	0.05	1.63E-02	0.05	1.83E-02	0.05	9.24E-03
0.1	3.00E-03	0.1	5.95E-03	0.1	6.56E-03	0.1	2.91E-03
0.2	7.75E-04	0.2	1.75E-03	0.2	1.91E-03	0.2	7.50E-04
0.3	3.03E-04	0.3	7.62E-04	0.3	8.30E-04	0.3	3.02E-04
0.5	7.66E-05	0.5	2.29E-04	0.5	2.53E-04	0.5	8.58E-05
0.7	2.76E-05	0.7	9.36E-05	0.7	1.07E-04	0.7	3.40E-05
1	8.32E-06	1	3.24E-05	1	3.76E-05	1	1.12E-05
2	6.71E-07	2	2.93E-06	2	3.23E-06	2	8.37E-07
3	1.35E-07	3	5.68E-07	3	6.24E-07	3	1.52E-07
5	1.36E-08	5	7.42E-08	5	7.53E-08	5	1.49E-08
10	2.91E-10	10	4.32E-09	10	4.78E-09	10	5.31E-10
2 Hz SA	AEF	1 Hz SA	AEF	0.5 Hz SA	AEF	0.333 Hz	AEF
0.01	3.75E-02	0.0001	4.50E-01	0.0001	3.56E-01	0.0001	2.92E-01
0.02	1.72E-02	0.001	1.83E-01	0.001	8.97E-02	0.001	6.58E-02
0.05	4.08E-03	0.01	1.87E-02	0.01	5.77E-03	0.01	3.10E-03
0.1	1.14E-03	0.05	1.09E-03	0.05	2.41E-04	0.05	1.10E-04
0.2	2.68E-04	0.07	5.49E-04	0.07	1.10E-04	0.07	4.77E-05
0.3	1.06E-04	0.1	2.45E-04	0.1	4.28E-05	0.1	1.74E-05
0.4	5.21E-05	0.3	1.38E-05	0.3	1.30E-06	0.3	3.91E-07
0.5	2.91E-05	0.5	2.84E-06	0.5	2.06E-07	0.5	5.50E-08
0.7	1.13E-05	0.7	9.29E-07	0.7	5.72E-08	0.7	1.40E-08
1	4.00E-06	1	2.77E-07	1	1.40E-08	1	2.99E-09
1.5	1.16E-06	1.5	7.12E-08	1.5	2.66E-09	1.5	4.55E-10
2	4.62E-07	2	2.77E-08	2	7.60E-10	2	1.09E-10
5	1.49E-08	5	1.01E-09	5	7.44E-12	5	6.76E-13

Table 10-19. Continued.

0.2 Hz SA	AEF	0.133 Hz SA	AEF	0.1 Hz SA	AEF		
0.000001	4.99E-01	0.000001	4.93E-01	0.000001	4.83E-01		
0.00001	4.51E-01	0.00001	3.64E-01	0.00001	2.84E-01		
0.00005	2.72E-01	0.00005	1.75E-01	0.00005	1.22E-01		
0.0001	1.91E-01	0.0001	1.16E-01	0.0001	7.84E-02		
0.0005	6.24E-02	0.0005	3.42E-02	0.0005	1.98E-02		
0.001	3.36E-02	0.001	1.69E-02	0.001	8.79E-03		
0.005	3.73E-03	0.005	1.45E-03	0.005	5.67E-04		
0.01	1.10E-03	0.01	3.87E-04	0.01	1.28E-04		
0.03	9.85E-05	0.03	2.69E-05	0.03	5.94E-06		
0.05	2.62E-05	0.05	6.20E-06	0.05	1.13E-06		
0.1	3.03E-06	0.1	6.01E-07	0.1	8.50E-08		
0.5	4.98E-09	0.5	6.40E-10	0.5	4.38E-11		
1	2.05E-10	1	2.13E-11	1	1.07E-12		
PGA- Peak Ground Acceleration (g); AEF – Annual Exceedance Frequency; SA – Spectral Acceleration (g).							

Table 10-20. Envelope of mean site-specific hazard curves at SFHP, assuming a soil thickness of 40±5 ft computed using site-specific material curves.

PGA	AEF	50 Hz SA	AEF	33.3 Hz SA	AEF	20 Hz SA	AEF
0.01	3.56E-02	0.01	3.95E-02	0.01	3.70E-02	0.01	4.74E-02
0.02	1.65E-02	0.02	1.81E-02	0.02	1.76E-02	0.02	2.28E-02
0.05	4.24E-03	0.05	4.54E-03	0.05	4.79E-03	0.05	6.41E-03
0.1	1.16E-03	0.1	1.23E-03	0.1	1.41E-03	0.1	2.03E-03
0.2	2.25E-04	0.2	2.45E-04	0.2	3.04E-04	0.2	4.75E-04
0.3	7.16E-05	0.3	8.06E-05	0.3	1.05E-04	0.3	1.74E-04
0.4	2.83E-05	0.4	3.28E-05	0.4	4.42E-05	0.4	7.70E-05
0.5	1.27E-05	0.5	1.50E-05	0.5	2.09E-05	0.5	3.82E-05
0.7	3.41E-06	0.7	4.13E-06	0.7	5.93E-06	0.7	1.17E-05
1	7.76E-07	1	9.43E-07	1	1.32E-06	1	2.92E-06
2	4.30E-08	2	5.18E-08	2	6.39E-08	2	1.58E-07
5	8.52E-10	5	1.07E-09	5	1.41E-09	5	2.55E-09
10	1.90E-11	10	2.44E-11	10	3.31E-11	10	5.26E-11
10 Hz SA	AEF	6.67 Hz SA	AEF	5 Hz SA	AEF	3.33 Hz SA	AEF
0.01	6.01E-02	0.01	8.28E-02	0.01	8.72E-02	0.01	5.75E-02
0.02	3.04E-02	0.02	4.95E-02	0.02	5.66E-02	0.02	3.29E-02
0.05	9.38E-03	0.05	1.69E-02	0.05	1.90E-02	0.05	9.72E-03
0.1	3.16E-03	0.1	6.32E-03	0.1	7.03E-03	0.1	3.17E-03
0.2	8.41E-04	0.2	1.92E-03	0.2	2.13E-03	0.2	8.57E-04
0.3	3.38E-04	0.3	8.59E-04	0.3	9.55E-04	0.3	3.60E-04
0.5	8.68E-05	0.5	2.73E-04	0.5	3.04E-04	0.5	1.06E-04
0.7	3.06E-05	0.7	1.15E-04	0.7	1.31E-04	0.7	4.54E-05
1	8.77E-06	1	4.09E-05	1	4.78E-05	1	1.67E-05
2	5.90E-07	2	3.60E-06	2	3.89E-06	2	1.23E-06
3	1.24E-07	3	6.54E-07	3	7.28E-07	3	1.82E-07
5	1.54E-08	5	6.40E-08	5	8.30E-08	5	1.40E-08
10	3.90E-10	10	4.16E-09	10	4.34E-09	10	5.28E-10
2 Hz SA	AEF	1 Hz SA	AEF	0.5 Hz SA	AEF	0.333 Hz	AEF
0.01	3.75E-02	0.0001	4.51E-01	0.0001	3.56E-01	0.0001	2.92E-01
0.02	1.73E-02	0.001	1.83E-01	0.001	8.98E-02	0.001	6.59E-02
0.05	4.16E-03	0.01	1.88E-02	0.01	5.77E-03	0.01	3.11E-03
0.1	1.19E-03	0.05	1.10E-03	0.05	2.44E-04	0.05	1.12E-04
0.2	2.91E-04	0.07	5.55E-04	0.07	1.12E-04	0.07	4.90E-05
0.3	1.25E-04	0.1	2.50E-04	0.1	4.42E-05	0.1	1.83E-05
0.4	6.76E-05	0.3	1.59E-05	0.3	1.74E-06	0.3	5.20E-07
0.5	4.00E-05	0.5	4.09E-06	0.5	3.69E-07	0.5	9.07E-08
0.7	1.60E-05	0.7	1.46E-06	0.7	1.31E-07	0.7	2.67E-08
1	5.90E-06	1	5.23E-07	1	4.34E-08	1	6.43E-09
1.5	1.91E-06	1.5	1.73E-07	1.5	1.21E-08	1.5	1.12E-09
2	7.68E-07	2	8.40E-08	2	4.78E-09	2	2.92E-10
5	2.02E-08	5	7.20E-09	5	1.30E-10	5	2.24E-12

Table 10-20. Continued.

0.2 Hz SA	AEF	0.133 Hz SA	AEF	0.1 Hz SA	AEF		
0.000001	4.99E-01	0.000001	4.93E-01	0.000001	4.83E-01		
0.00001	4.51E-01	0.00001	3.64E-01	0.00001	2.84E-01		
0.00005	2.72E-01	0.00005	1.75E-01	0.00005	1.22E-01		
0.0001	1.91E-01	0.0001	1.16E-01	0.0001	7.84E-02		
0.0005	6.24E-02	0.0005	3.43E-02	0.0005	1.98E-02		
0.001	3.36E-02	0.001	1.69E-02	0.001	8.80E-03		
0.005	3.74E-03	0.005	1.45E-03	0.005	5.71E-04		
0.01	1.10E-03	0.01	3.90E-04	0.01	1.31E-04		
0.03	1.00E-04	0.03	2.81E-05	0.03	6.68E-06		
0.05	2.75E-05	0.05	6.87E-06	0.05	1.43E-06		
0.1	3.48E-06	0.1	7.61E-07	0.1	1.19E-07		
0.5	8.08E-09	0.5	9.84E-10	0.5	6.80E-11		
1	3.60E-10	1	3.43E-11	1	1.75E-12		
PGA- Peak Ground Acceleration (g); AEF – Annual Exceedance Frequency; SA – Spectral Acceleration (g).							

Table 10-21. Site-specific hazard fractiles at SFHP, assuming a soil thickness of 40 ft.

Spectral Acceleration (g)	SFHP Soil 40 ft Annual Exceedance Frequency at Fractiles				
	5th	15th	50th	85th	95th
10 Hz					
0.01	4.29E-02	4.59E-02	6.27E-02	6.93E-02	6.97E-02
0.02	1.78E-02	1.83E-02	3.12E-02	3.94E-02	4.06E-02
0.05	3.79E-03	4.37E-03	9.75E-03	1.37E-02	1.44E-02
0.10	8.62E-04	1.14E-03	3.24E-03	5.17E-03	5.56E-03
0.20	1.41E-04	2.12E-04	8.06E-04	1.50E-03	1.66E-03
0.30	4.12E-05	6.85E-05	2.92E-04	6.10E-04	7.05E-04
0.40	7.24E-06	1.36E-05	6.14E-05	1.49E-04	2.01E-04
0.50	2.12E-06	4.22E-06	1.84E-05	4.88E-05	7.90E-05
0.70	5.58E-07	1.08E-06	4.47E-06	1.30E-05	2.56E-05
1.00	3.82E-08	4.93E-08	2.18E-07	8.43E-07	1.48E-06
2.00	8.01E-09	1.02E-08	4.17E-08	1.62E-07	2.58E-07
5.00	5.10E-10	6.55E-10	5.09E-09	1.67E-08	2.24E-08
10.00	4.64E-14	1.71E-13	5.86E-11	6.15E-10	8.80E-10
2 Hz					
0.01	1.90E-02	2.28E-02	3.54E-02	5.34E-02	5.35E-02
0.02	6.08E-03	7.56E-03	1.35E-02	3.03E-02	3.29E-02
0.05	1.01E-03	1.38E-03	2.96E-03	7.76E-03	8.65E-03
0.10	2.15E-04	3.08E-04	7.58E-04	2.30E-03	2.63E-03
0.20	3.29E-05	5.23E-05	1.61E-04	5.64E-04	6.62E-04
0.30	8.62E-06	1.51E-05	5.68E-05	2.30E-04	2.74E-04
0.50	3.02E-06	5.91E-06	2.50E-05	1.14E-04	1.39E-04
0.70	1.32E-06	3.03E-06	1.28E-05	6.39E-05	7.86E-05
1.00	4.72E-07	9.05E-07	4.43E-06	2.44E-05	3.08E-05
2.00	1.47E-07	2.29E-07	1.29E-06	8.00E-06	1.04E-05
3.00	2.92E-08	5.61E-08	3.71E-07	2.03E-06	2.74E-06
5.00	9.83E-09	2.37E-08	1.41E-07	6.94E-07	1.11E-06
10.00	6.78E-11	6.83E-10	4.15E-09	1.86E-08	3.84E-08

10.6.1 Sensitivity Analyses

This section presents the hazard sensitivity at the SFHP sites with respect to the various parameters used to generate alternative site-amplification functions. Additionally, this section presents hazard sensitivity with respect to the two alternative models for $\sigma_{\text{epistemic}}$ described in section 9.3.4. As described in section 10.2.2, for a particular node of the logic tree, the sensitivity analyses are conducted by assigning full weight alternatively to each of the branches that represent epistemic uncertainty.

10.6.1.1 SFHP Rock Site

Alternatives of four different parameters (three alternative kappa values, three alternative velocity profiles, two alternative $\sigma_{\text{epistemic}}$ models, and two alternative earthquake source spectra) were used to capture the uncertainty in the site-amplification functions for the SFHP rock site conditions, which provided 36 alternative hazard curves at each frequency of spectral acceleration.

Figure 10-68 compares the conditional-mean hazard for a given kappa (red curves) with the total mean hazard at 2 Hz and 10 Hz spectral acceleration for SFHP Rock (blue curve); results for the individual 36 possible outcomes of the logic tree for SFHP Rock are shown by the grey curves. Kappa has a non-negligible effect on the ground motion level at all AEF less than 1×10^{-2} for spectral acceleration at high frequencies. In the AEF range of interest (4×10^{-4} to 10^{-4}) the ground motion level differs by approximately a factor of 2 between the upper and lower bounds of kappa (0.022-0.062 sec). For spectral acceleration at low frequencies kappa has small effect on the ground motion level at all levels of AEF. Further, kappa = 0.022 sec produces hazard curves above those of kappa = 0.037sec and kappa = 0.062sec consistently across all frequencies of spectral acceleration.

The three alternative velocity profiles produce a small variation in the ground motion level at all levels of AEF and all frequencies of spectral acceleration. This is shown in Figure 10-69, where the conditional-mean hazard for a given profile (red curves) is compared with the total mean hazard at 2 Hz and 10 Hz spectral accelerations for SFHP Rock (blue curve), and with the individual results of the 36 logic tree branches (grey curves). Additionally, there is not one profile that consistently produces larger hazard relative to the remaining across all frequencies of spectral acceleration. These two observations are a result of the relative similarity in the amplitude of the amplification between the three profiles combined with slight phase shifts in the locations of resonant peaks.

The two alternative $\sigma_{\text{epistemic}}$ models, produce similar mean hazard at 2 Hz spectral acceleration and higher. At spectral accelerations lower than 2 Hz the conditional mean hazard of the alternatives begins to deviate, with the deviation increasing as frequency of spectral acceleration and AEF decrease. In the AEF range of interest (1×10^{-4}- 4×10^{-4}) the two models differ by factors up to 1.25 for frequencies of spectral acceleration from 0.5-10 Hz (with Option B having a higher hazard for the given frequency range). The observations of hazard sensitivity are consistent with the difference in the two $\sigma_{\text{epistemic}}$ models. Figure 10-70 compares the conditional-mean hazard for a given $\sigma_{\text{epistemic}}$ model (red curves) with the total mean hazard at 1 Hz and 10 Hz spectral acceleration for SFHP Rock (blue curve), and with the individual results of the 36 logic tree branches (grey curves). The hazard at SFHP Rock is not sensitive to the selection of the model for the earthquake source spectrum used in generating site-amplification functions.

10.6.1.2 SFHP Soil Site

Alternatives of five different parameters (the 4 sets of parameters used at SFHP Rock with the addition of alternative soil material models) were used to capture the uncertainty in the site-amplification functions for SFHP soil sites. For the soil material models, two alternative cases were assessed. One used the site-specific curves developed by NWRC-RA (2015) (referred to as NWR), and one used the generic set of equally weighted EPRI and Peninsular Range curves. Use of the generic set produces 72 alternative hazard curves at each frequency of spectral acceleration. In addition, two alternative soil thicknesses were considered: 20 ft and 40 ft.

The hazard for the SFHP Soil sites is only slightly less sensitive to alternative kappa values than the SFHP Rock site but follows the same trends. The sensitivity to velocity profile is shown on Figures 10-71 and 10-72 for 20 ft and 40 ft of soil, respectively. For both depths the higher range velocity profiles (P3 and P6) tend to produce higher 10 Hz hazard and the lower range velocity profiles (P2 and P5) tend to produce higher 2 Hz hazard. The hazard for both soil depths shows similar sensitivity with respect to $\sigma_{\text{epistemic}}$ models as is observed for the SFHP Rock site. The hazard at the SFHP Soil sites is not sensitive to the selection of source spectrum used in generating site-amplification functions.

Figures 10-73 and 10-74 compare the conditional-mean hazard for a given material property model with the total mean hazard at 2 Hz and 10 Hz spectral accelerations for soil depths of 20 ft and 40 ft, respectively. As was the case for the FMF soil sites, the more linear PR material curves produce higher motions at 10 Hz and the more nonlinear EPRI curves produce higher motion at 2 Hz. The NWR (NWRC-RA, 2015) curves tend to produce results intermediate between the EPRI and PR curves at 10 Hz and slightly higher than the EPRI curves at 2 Hz. The NWR curves have similar to slightly less non-linearity to the EPRI curves, but lower damping than either, especially at higher strains.

(a)

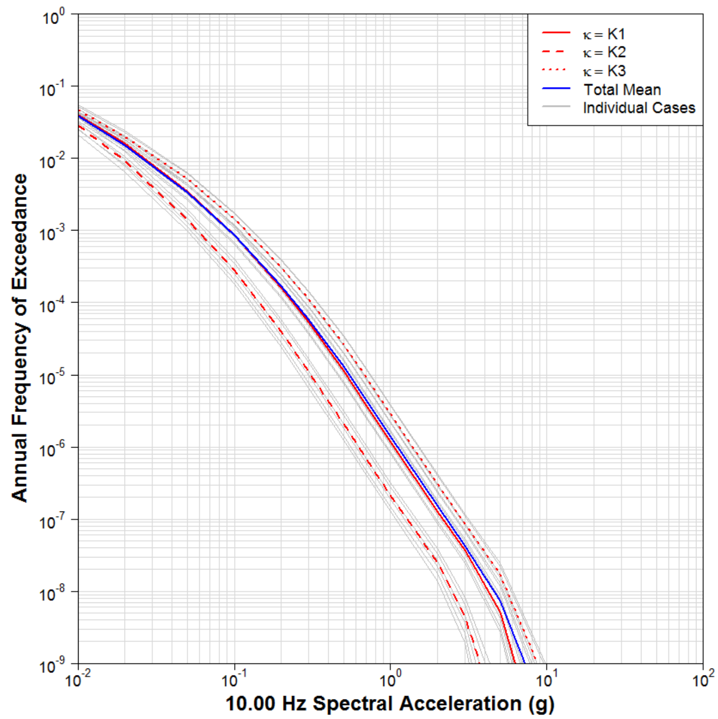

(b)

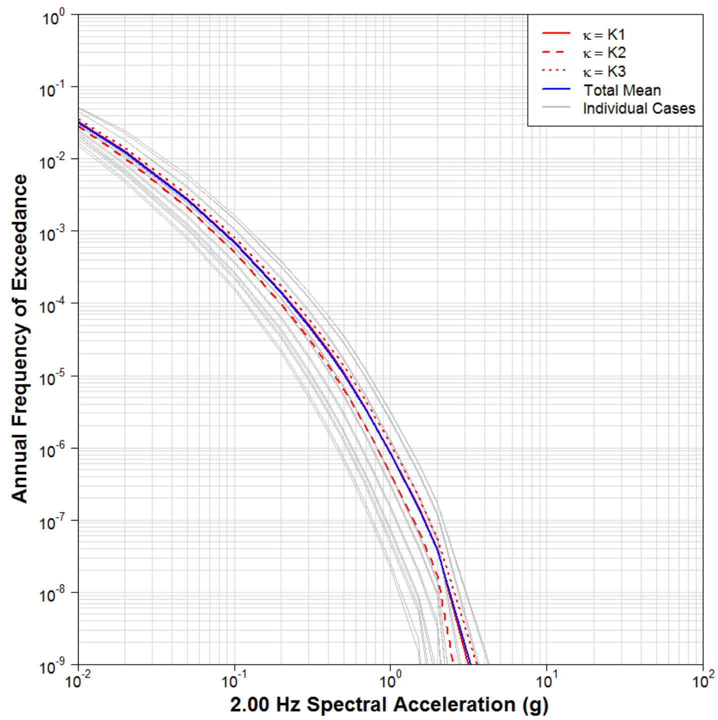

Figure 10-68. Sensitivity of hazard at SFPH Rock with respect to kappa at: a) 10 Hz (0.1-sec); and b) 2 Hz (0.5-sec) spectral accelerations (K1 = 0.037s, K2=0.062s, K3=0.022s).

(a)

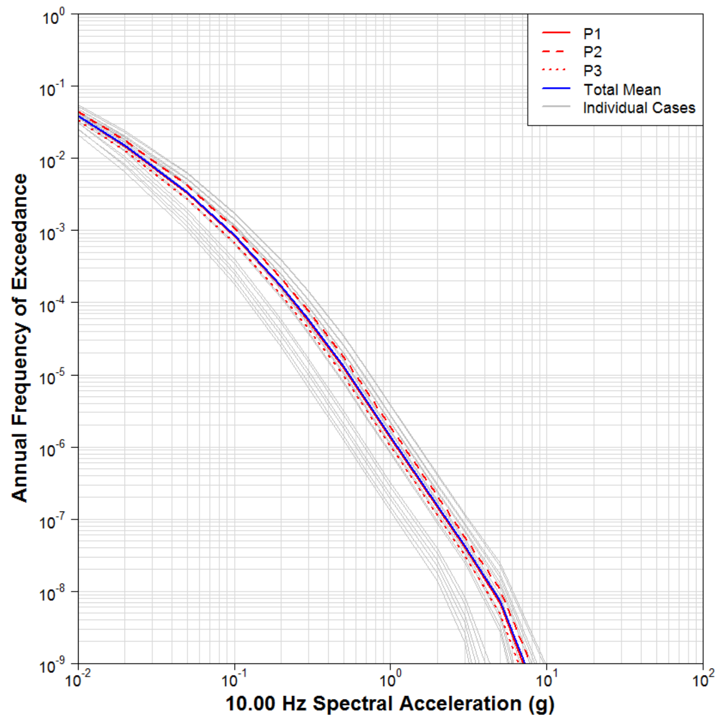

(b)

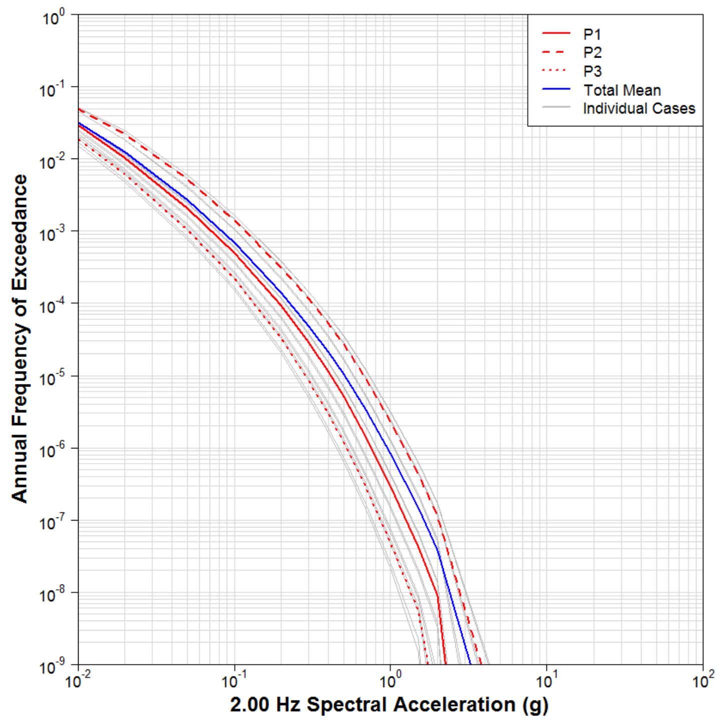

Figure 10-69. Sensitivity of hazard at SFPH Rock with respect to velocity profile at: 10 Hz (0.1-sec); and b) 2 Hz (0.5-sec) spectral accelerations.

(a)

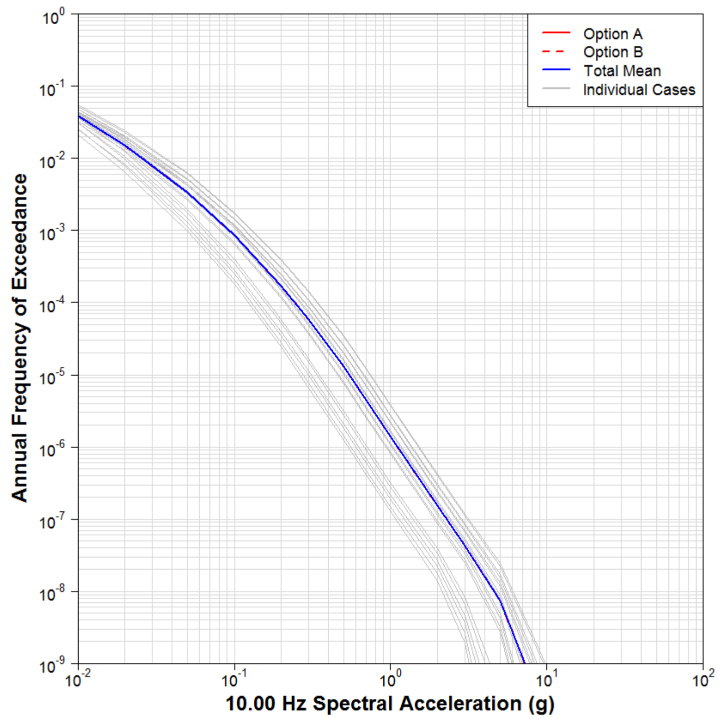

(b)

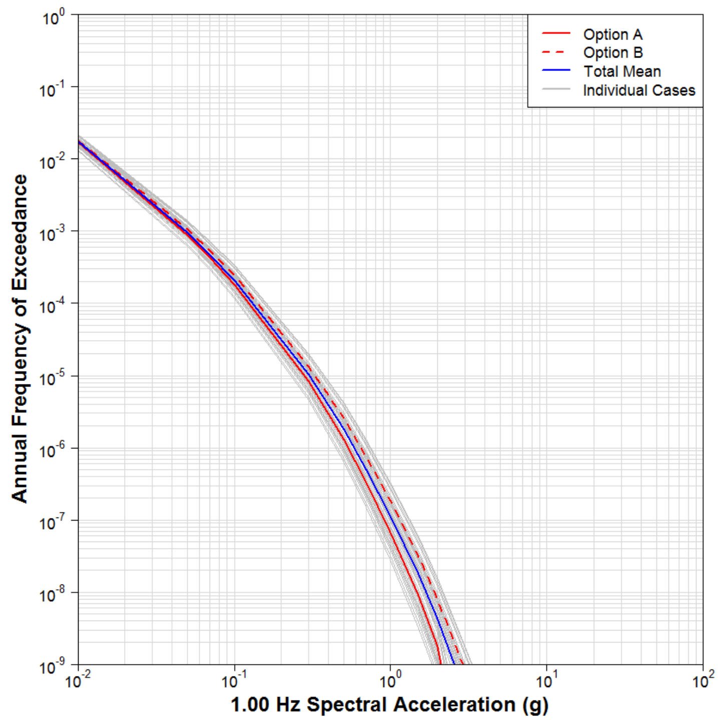

Figure 10-70. Sensitivity of hazard at SFHP Rock with respect to $\sigma_{epistemic}$ model at: a) 10 Hz (0.1-sec); and b) 1 Hz (1-sec) spectral accelerations.

(a)

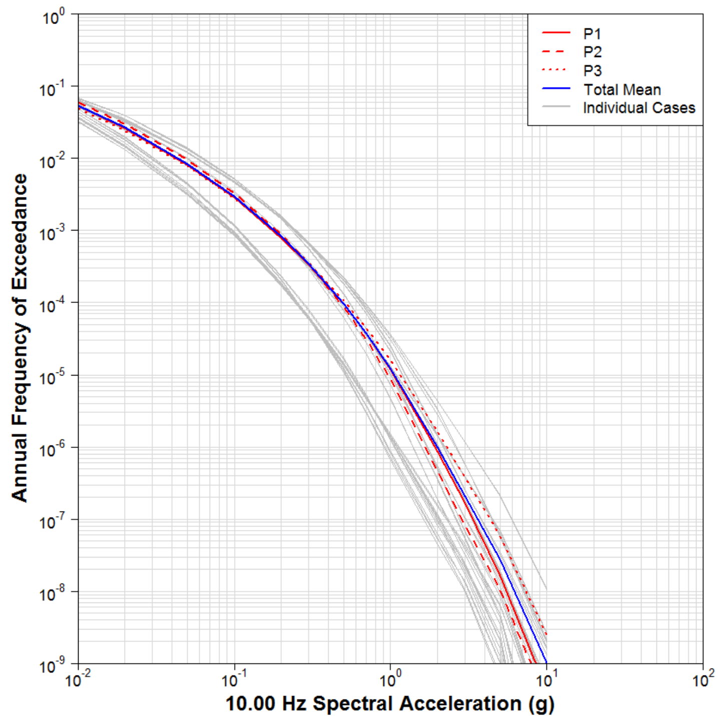

(b)

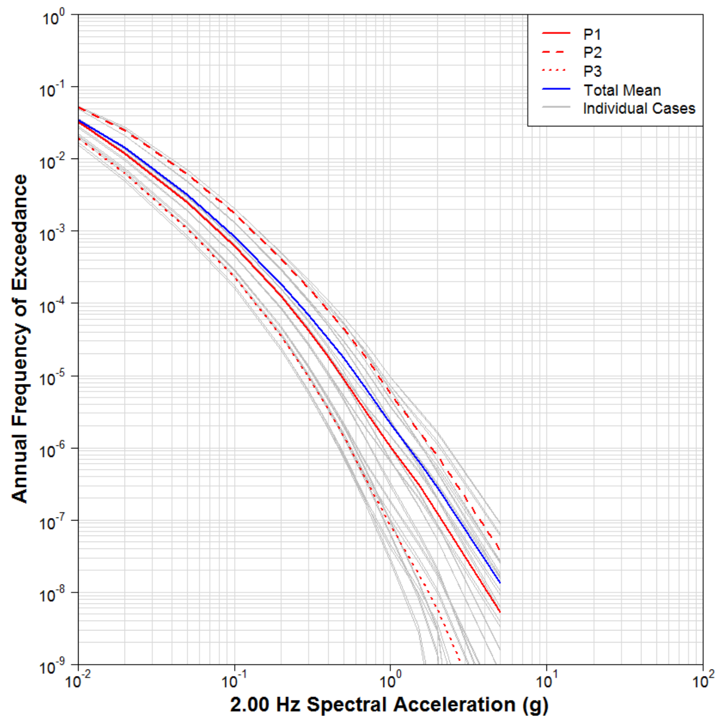

Figure 10-71. Sensitivity of the hazard at SFHP for 20 ft of soil with respect to velocity profile at: 10 Hz (0.1-sec); and b) 2 Hz (0.5-sec) spectral accelerations.

(a)

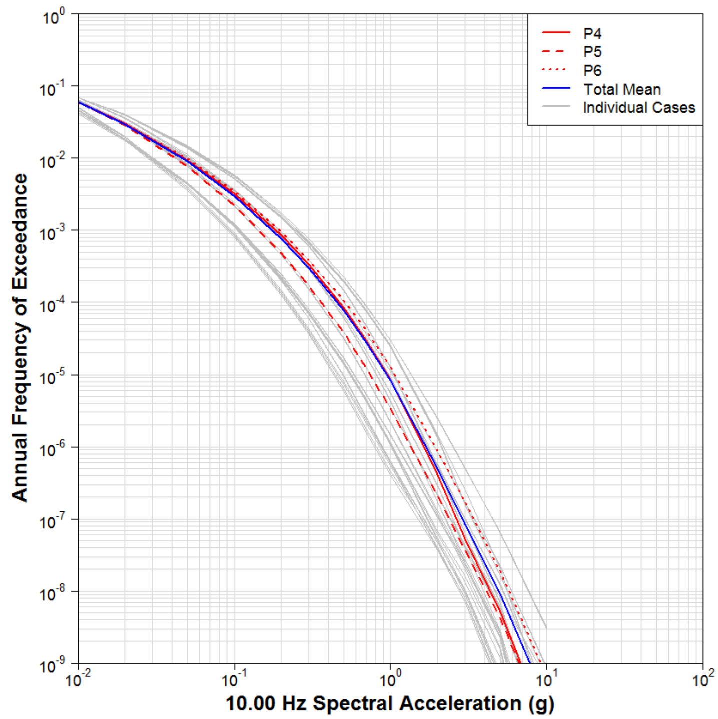

(b)

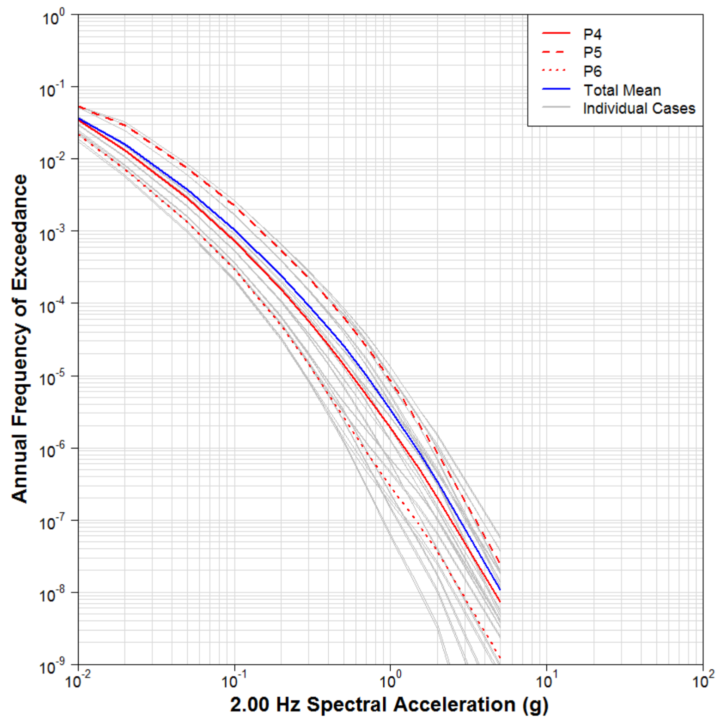

Figure 10-72. Sensitivity of the hazard at SFHP for 40 ft of soil with respect to velocity profile at: a) 10 Hz (0.1-sec); and b) 2 Hz (0.5-sec) spectral accelerations.

(a)

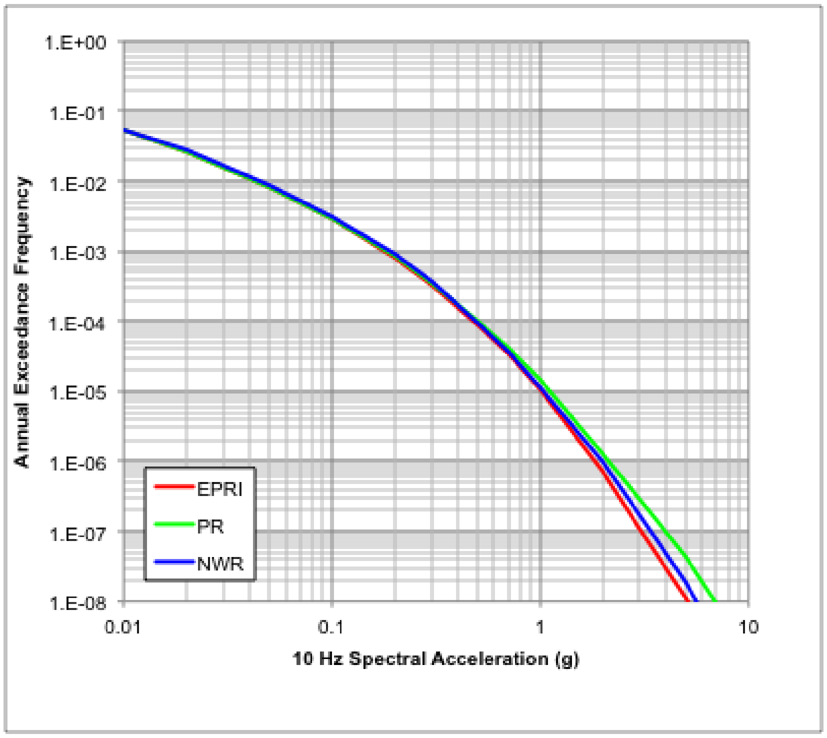

(b)

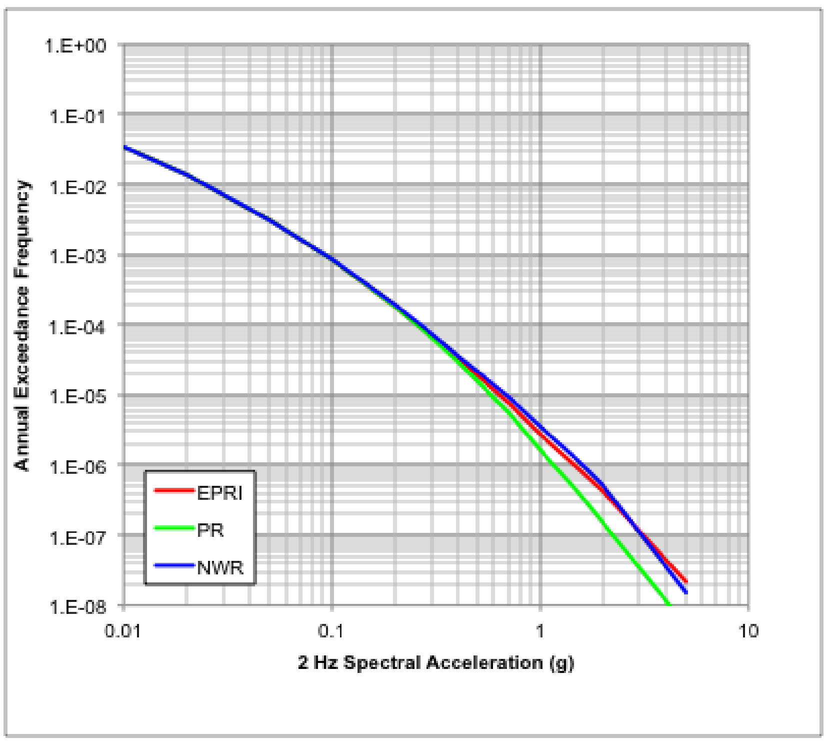

Figure 10-73. Sensitivity of the hazard at SFHP for 20 ft of soil with respect to material property model at: a) 10 Hz (0.1-sec); and b) 2 Hz (0.5-sec) spectral accelerations.

(a)

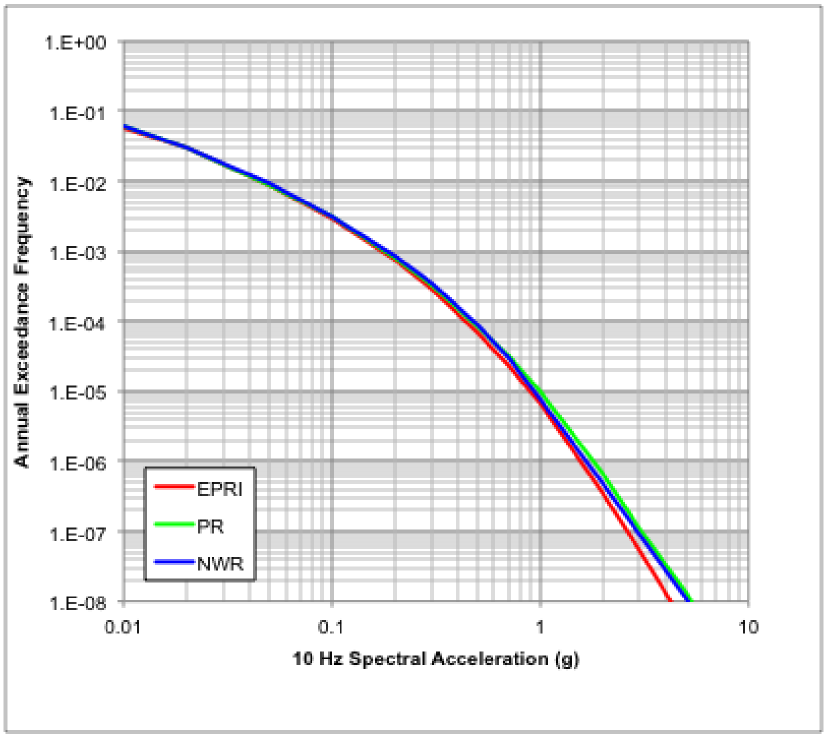

(b)

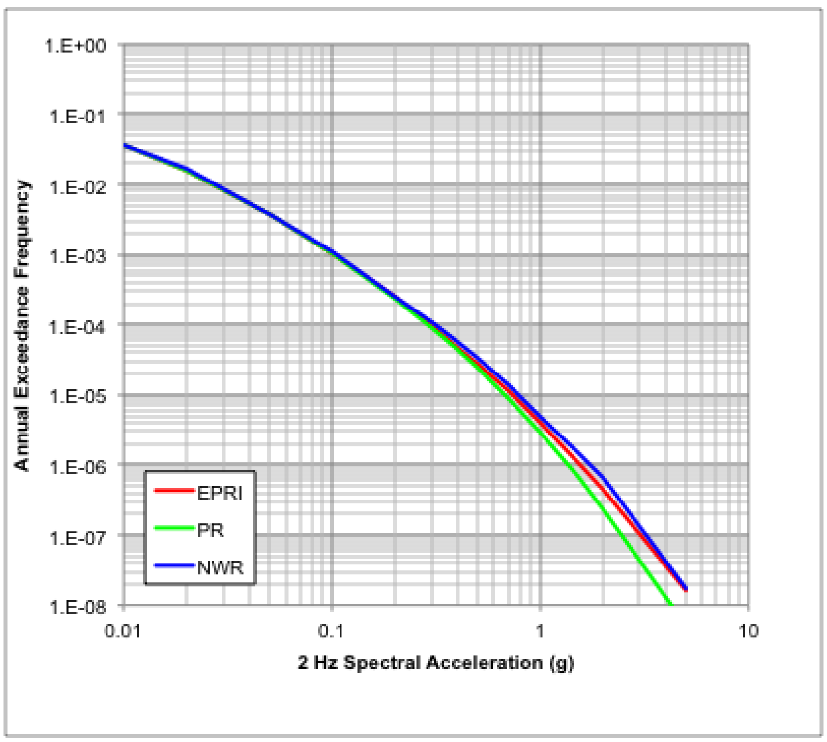

Figure 10-74. Sensitivity of the hazard at SFHP for 40 ft of soil with respect to material property model at: a) 10 Hz (0.1-sec); and b) 2 Hz (0.5-sec) spectral accelerations.

10.6.2 Horizontal UHRS and GMRS for SFHP

The UHRS are computed for the SFHP sites by interpolating the mean hazard curves for the individual spectral frequencies. Figure 10-75 shows the resulting horizontal UHRS for return periods of $4x10^{-4}$, $1x10^{-4}$, $4x10^{-5}$, and $1x10^{-5}$ years. The solid curves are based on the logic tree weights shown in Figure 9-57 in which equal weight is given to the upper and lower values of the epistemic uncertainty in kappa (Case 1). As discussed in Section 9.5.4, a sensitivity analysis was performed using an alternative weighting on kappa that down-weighted the high value at 0.062 sec in favor of a lower value. The resulting UHRS for this sensitivity case, Case 2, are shown on Figure 10-75. As indicated, the alternative weighting produces an increase in the level of motions at high frequencies. However, as discussed in Section 7.5.1, the available data do not provide a basis for rejecting the results for Case 1. Case 2 is provided to indicate the effect of assuming that lower kappa values are more appropriate based on typical values for other sites on INL. The results shown on Figure 10-75 do not include the effect of considering nonlinearity in the shallow basalt layers. As shown on Figure 9-44, incorporation of nonlinear behavior in the shallow basalts would result in slightly lower motions than those shown on Figure 10-75.

Figures 10-76, 10-77, and 10-78 compare the existing DRS and broadened Design Response Spectra (BDRS) for rock conditions being used for the SFHP (AECOM, 2015) to GMRS developed from the UHRS shown on Figure 10-74 for SDC-3, SDC-4, and SDC-5, respectively. For all three SDC levels, the existing BDRS envelops the GMRS computed from the results of the SSHAC Level 1 study for both the base case (Case 1) and the kappa weighting sensitivity case (Case 2). Table 10-22 lists the SDC-3, SDC-4, and SDC-5 horizontal GMRS computed from the SSHAC Level 1 study for Case 1, the base case results for this study.

Figures 10-79 and 10-80 compare the UHRS for the SFHP soil depths of 20 ft and 40 ft, respectively computed using the two sets of material curves, the generic set of equally weighted EPRI and PR set and the site-specific set developed by NWRC-RA (2015). As indicated the UHRS produced by the two sets are similar.

Figures 10-81 and 10-82 compare the UHRS for the ±5-ft depth range for the SFHP soil depths of 20 ft and 40 ft, respectively, computed using the generic set of equally weighted EPRI and PR material curves and Figures 10-83 and 10-84 compare the UHRS for the ±5-ft depth range for the SFHP soil depths of 20 ft and 40 ft, respectively, computed using the site-specific NWRC-RA (2015) (NWR) curves. In all cases, the effect of the ±5-ft depth variability on the UHRS is small. Therefore, for the purpose of reporting the results of the SSHAC Level 1 study, the envelopes of the UHRS for each depth range are used. The envelope UHRS are shown on the figures.

Using the envelope UHRS shown on Figures 10-81 through 10-84, horizontal GMRS were computed for the SDC-3, SDC-4, and SDC-5 levels. These spectra are compared on Figures 10-85 and 10-86 for 20-ft and 40-ft soil depths, respectively, and are listed in Tables 10-23 and 10-24.

10.6.3 Vertical UHRS and GMRS for MFC and FMF

Table 9-5 contains the V/H ratios recommended for use at SFHP rock and soil sites. These ratios are applied to the SDC-3, SDC-4, and SDC-5 horizontal GMRS to obtain the corresponding vertical GMRS based on the results of the SSHAC Level 1 study. The vertical GMRS are shown in Figures 10-87 (SFHP Rock), 10-88 (SFHP 20-ft soil depth) and 10-89 (SFHP 40-ft soil depth) and are listed in Tables 10-25, 10-26, and 10-27, respectively.

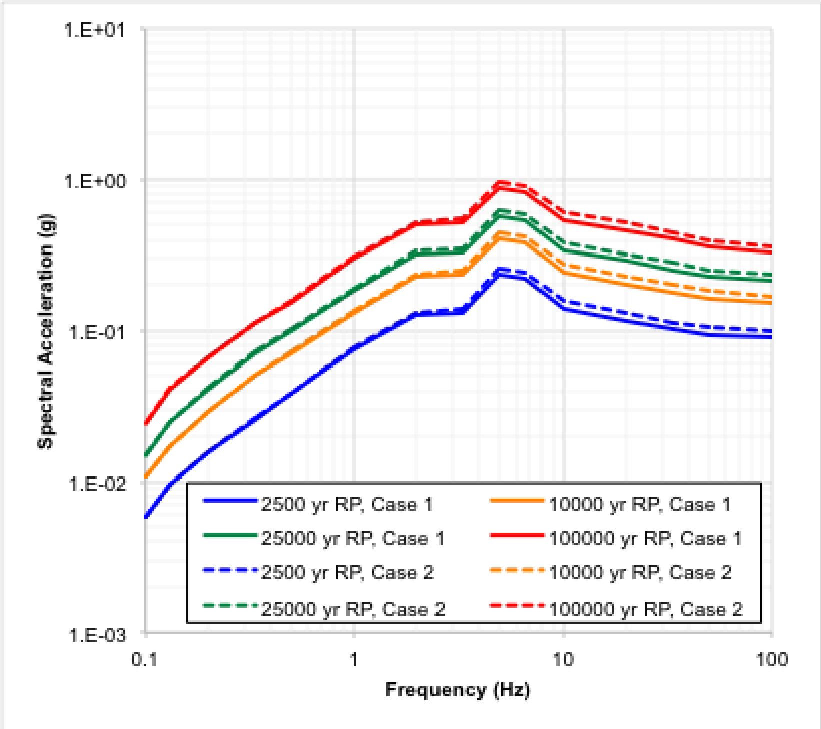

Figure 10-75. SFHP rock horizontal UHRS for Case 1 (base case) and Case 2 (sensitivity to kappa weighting) at 5% damping.

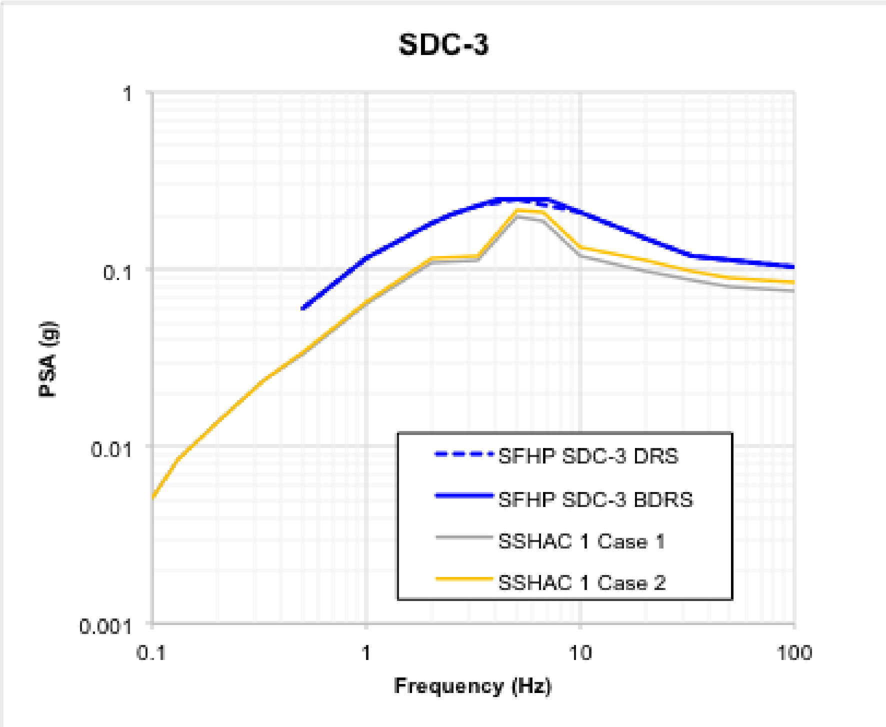

Figure 10-76. Comparison of the SFHP Rock SDC-3 DRS and BDRS (AECOM, 2015) to SDC-3 GMRS computed using the results of the SSHAC Level 1 study at 5% damping.

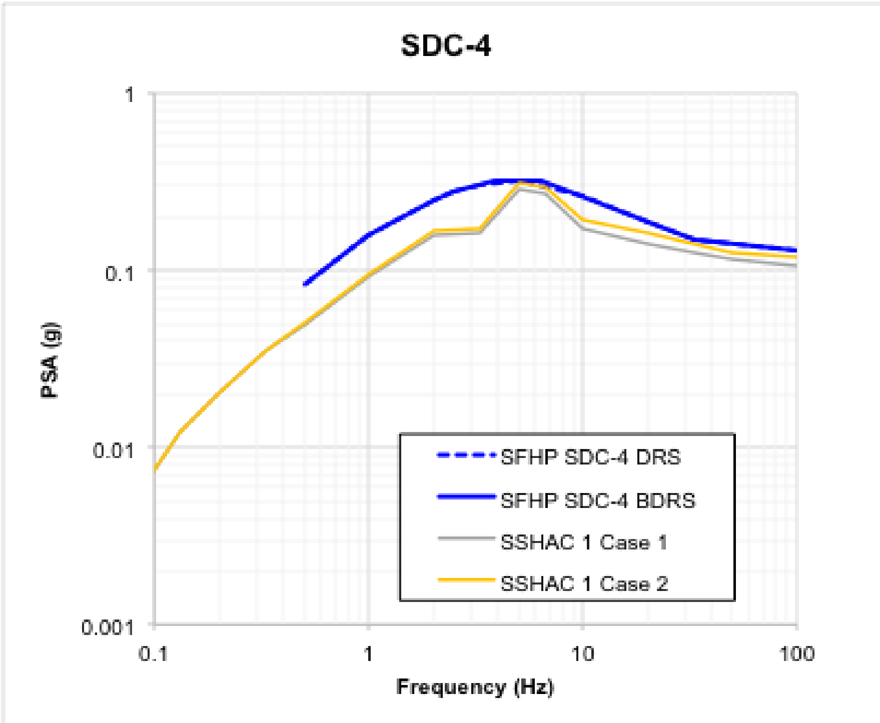

Figure 10-77. Comparison of the SFHP Rock SDC-4 DRS and BDRS (AECOM, 2015) to SDC-4 GMRS computed using the results of the SSHAC Level 1 study at 5% damping.

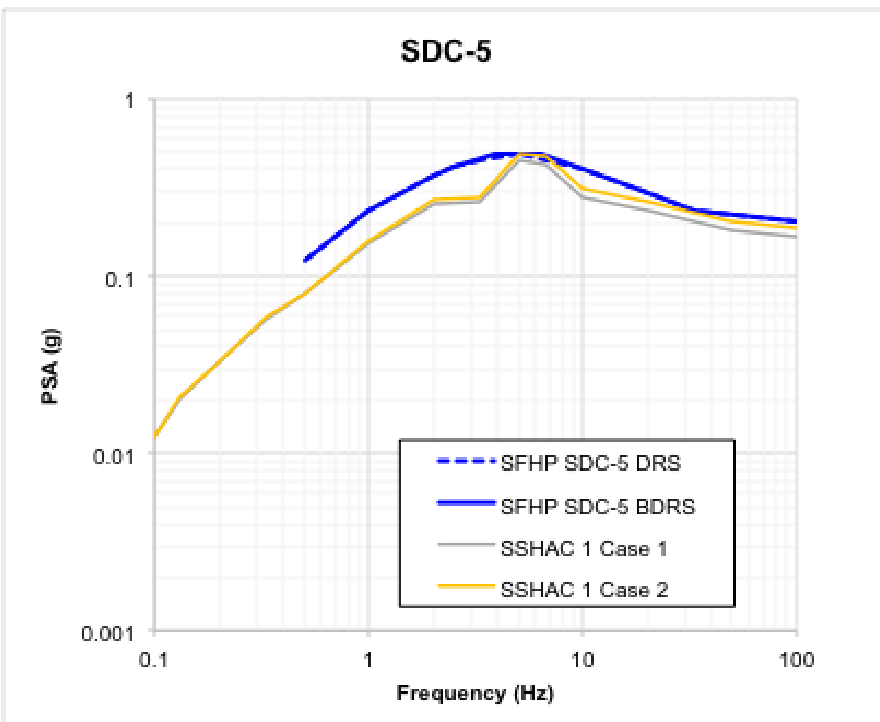

Figure 10-78. Comparison of the SFHP Rock SDC-5 DRS and BDRS (AECOM, 2015) to SDC-5 GMRS computed using the results of the SSHAC Level 1 study at 5% damping.

Table 10-22. Horizontal GMRS for SFHP Rock site conditions computed using the results of the SSHAC Level 1 study.

Period (sec)	Frequency (Hz)	Horizontal SFHP Rock Site Spectral Acceleration (g)		
		SDC-3	SDC-4	SDC-5
0.01	100	7.66E-02	1.08E-01	1.69E-01
0.02	50	8.07E-02	1.15E-01	1.83E-01
0.03	33.3	8.75E-02	1.26E-01	2.05E-01
0.05	20	9.90E-02	1.43E-01	2.35E-01
0.1	10	1.19E-01	1.71E-01	2.78E-01
0.15	6.67	1.88E-01	2.68E-01	4.29E-01
0.2	5	2.01E-01	2.87E-01	4.56E-01
0.3	3.33	1.12E-01	1.63E-01	2.65E-01
0.5	2	1.10E-01	1.60E-01	2.59E-01
1	1	6.43E-02	9.17E-02	1.54E-01
2	0.5	3.37E-02	4.96E-02	7.91E-02
3	0.333	2.33E-02	3.50E-02	5.74E-02
5	0.2	1.37E-02	2.02E-02	3.34E-02
7.5	0.133	8.41E-03	1.23E-02	2.07E-02
10	0.1	5.09E-03	7.41E-03	1.24E-02

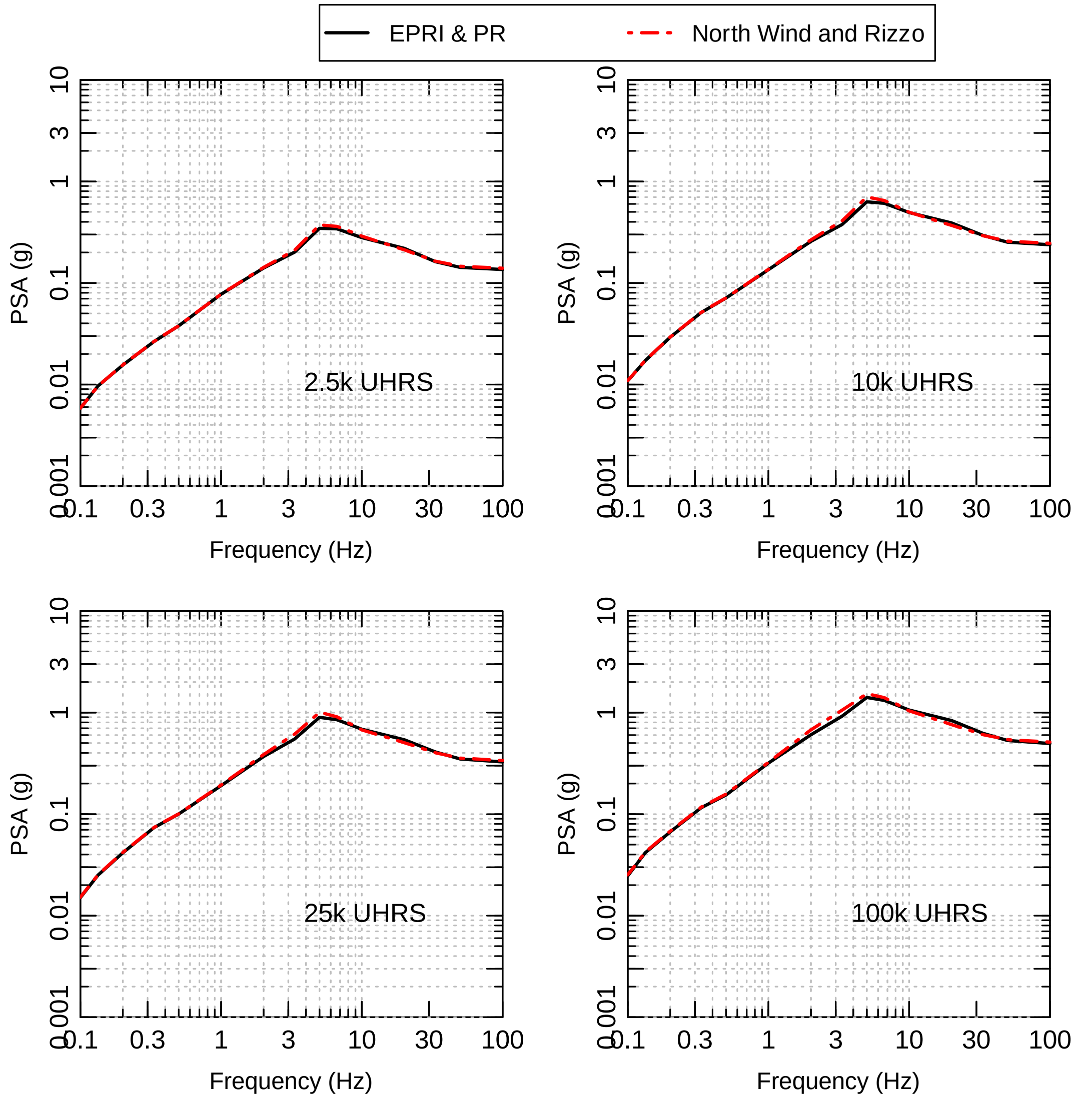

Figure 10-79. Comparison of UHRS for 20 ft. of soil at the SFHP site computed using the generic set of equally weighted EPRI and PR curves to those computed using the site-specific North Wind and Rizzo curves (NWRC-RA, 2015) at 5% damping.

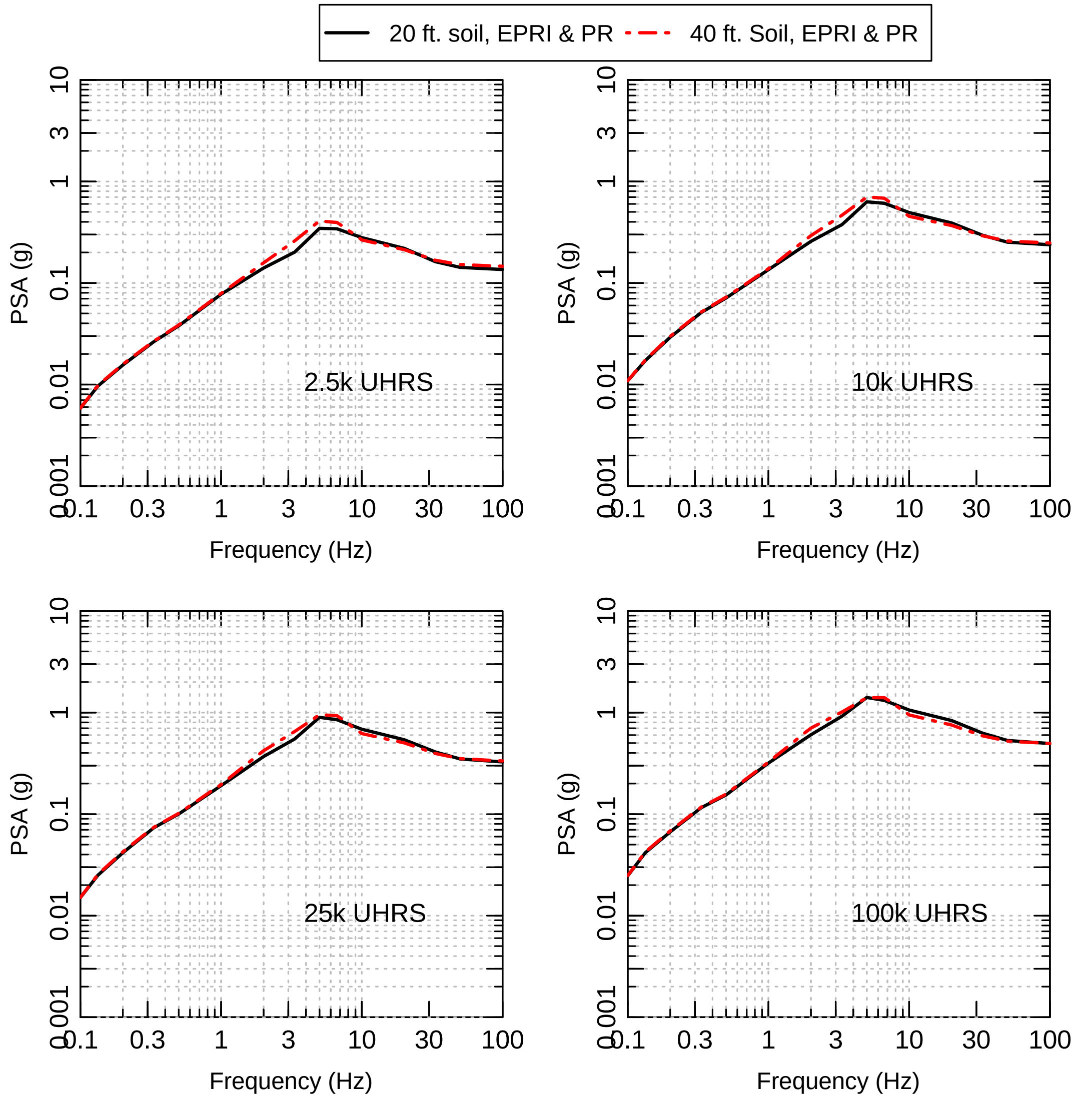

Figure 10-80. Comparison of UHRS for 40 ft of soil at the SFHP site computed using the generic set of equally weighted EPRI and PR curves to those computed using the site-specific North Wind and Rizzo curves (NWRC-RA, 2015) at 5% damping.

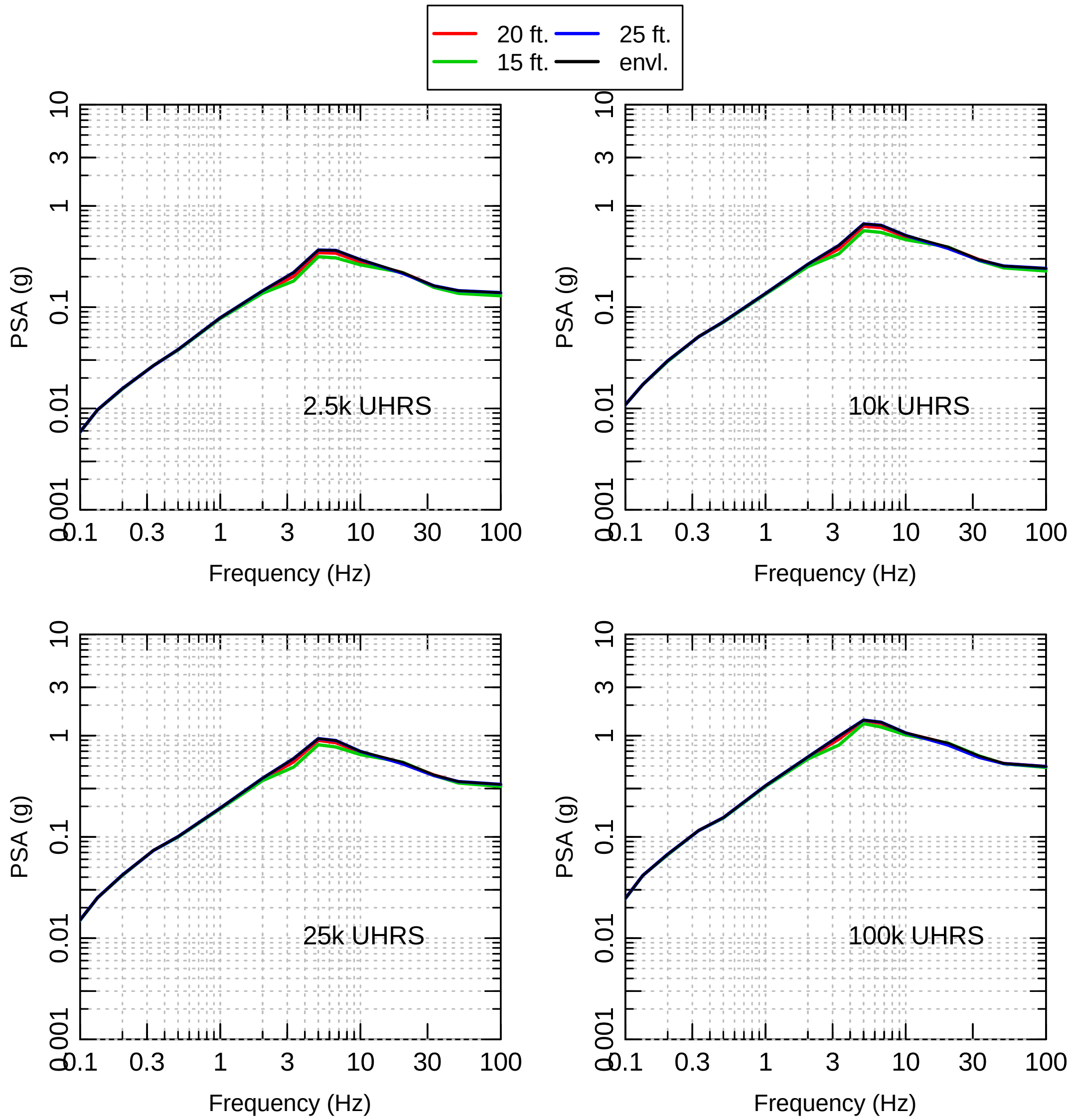

Figure 10-81. Comparison of UHRS for 20±5 ft of soil at the SFHP site computed using the generic set of equally weighted EPRI (EPRI, 1993) and PR (Silva et al., 1996) curves at 5% damping.

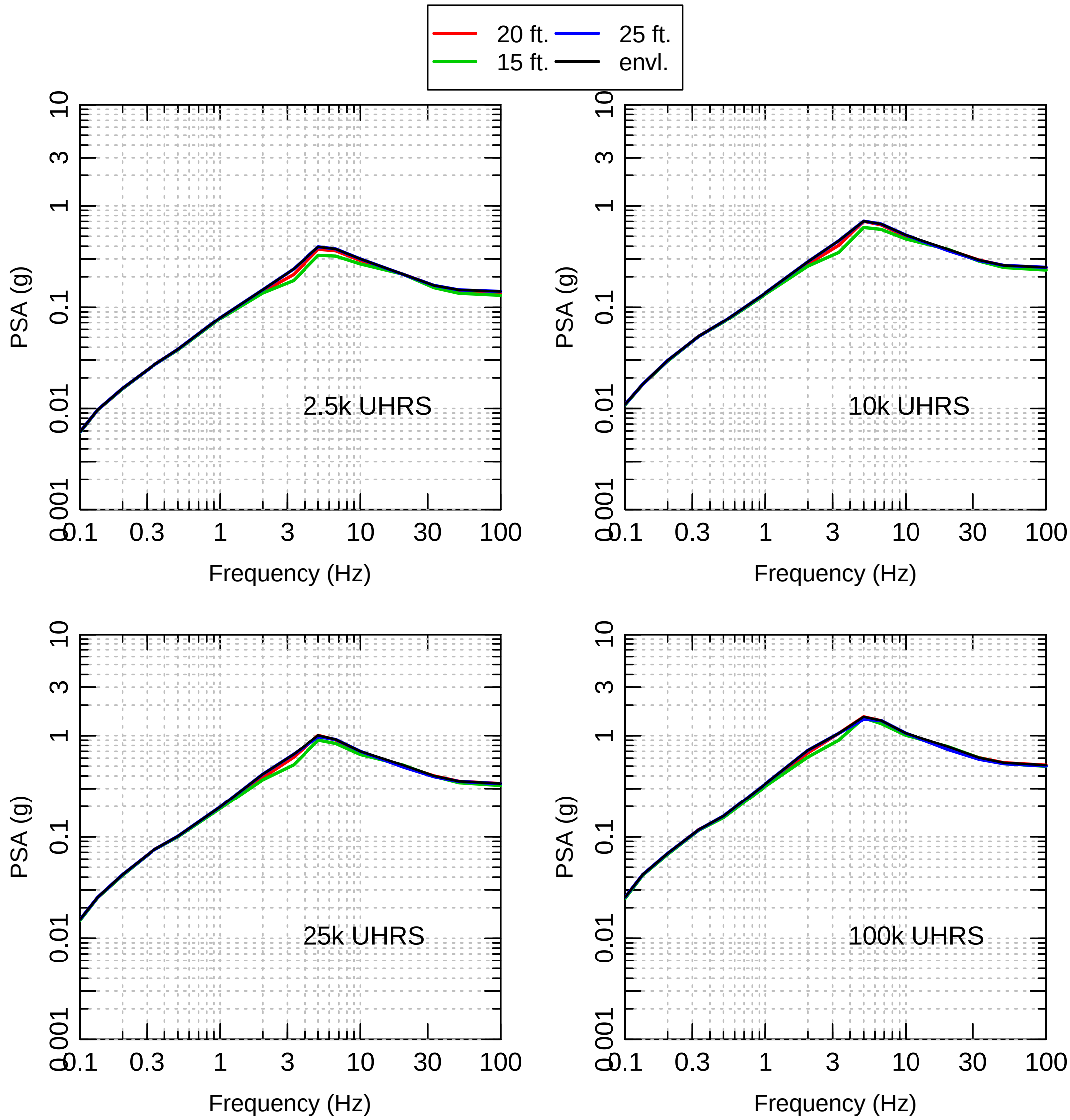

Figure 10-82. Comparison of UHRS for 40±5 ft of soil at the SFHP site computed using the generic set of equally weighted EPRI (EPRI, 1993) and PR (Silva et al., 1996) curves at 5% damping.

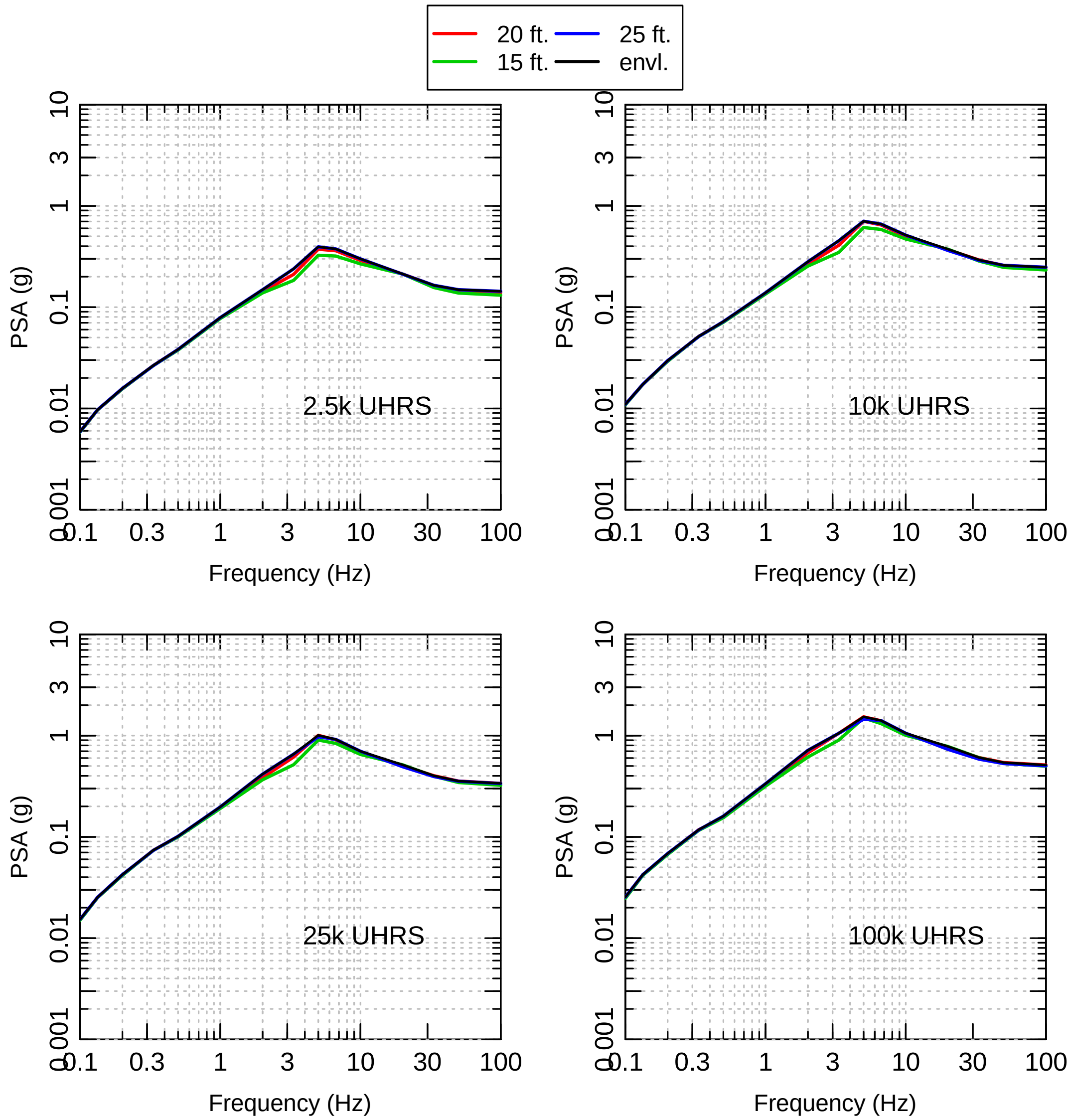

Figure 10-83. Comparison of UHRS for 20±5 ft of soil at the SFHP site computed using the North Wind and Rizzo (NWRC-RA, 2015) site-specific set of curves at 5% damping.

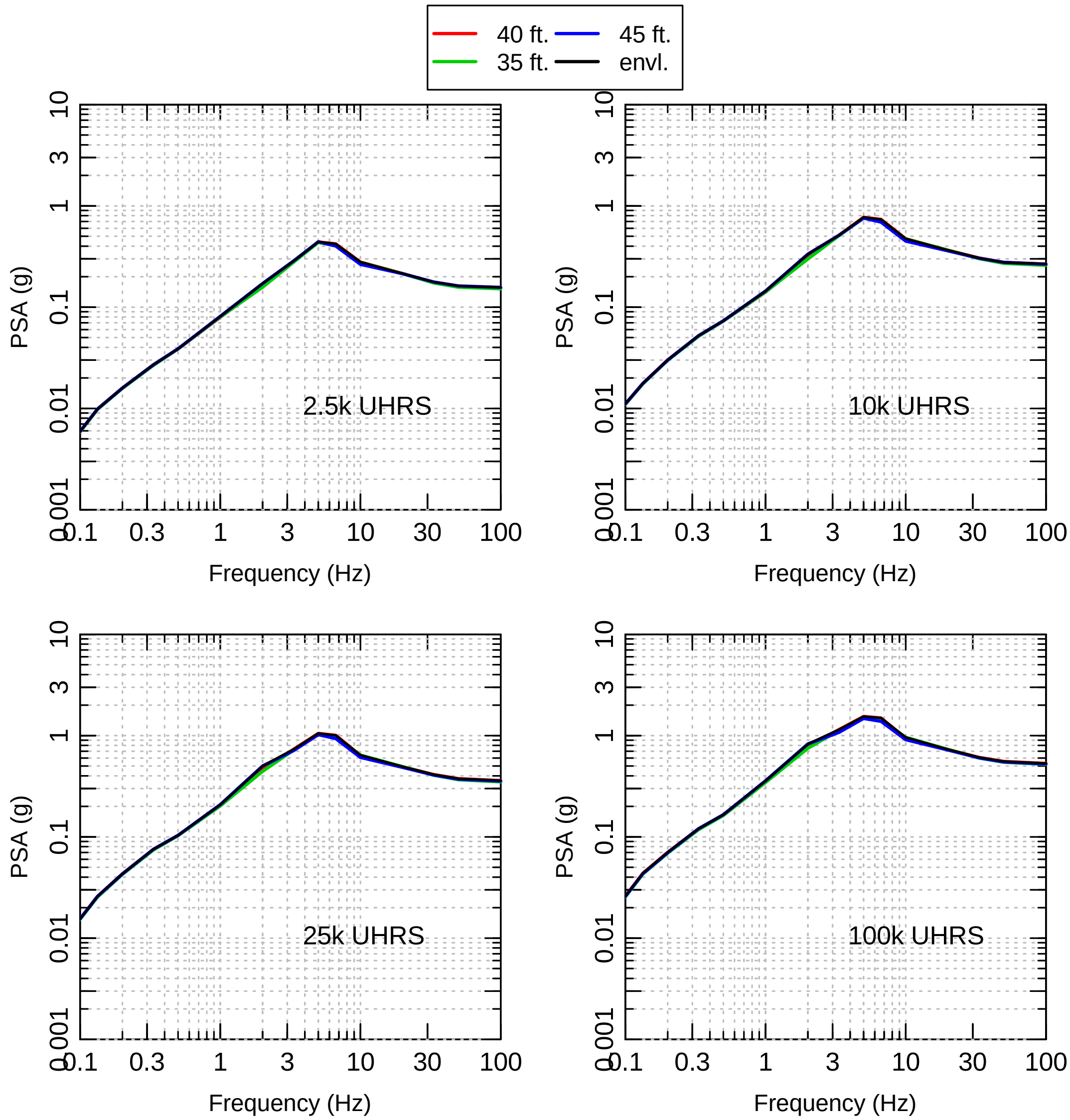

Figure 10-84. Comparison of UHRS for 40±5 ft of soil at the SFHP site computed using the North Wind and Rizzo (NWRC-RA, 2015) site-specific set of curves at 5% damping.

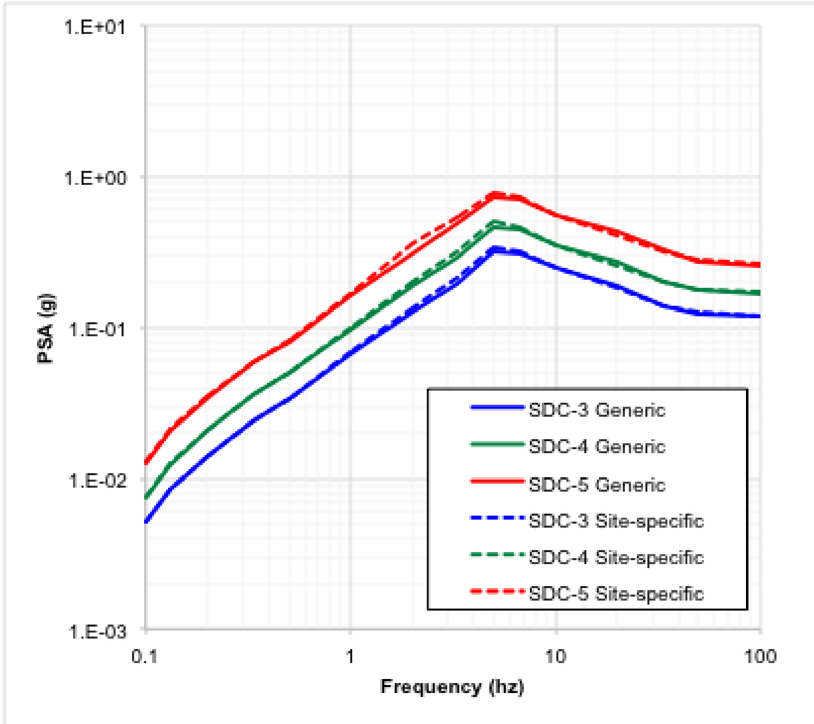

Figure 10-85. Horizontal GMRS for SFHP 20-ft soil depth computed from the envelope UHRS shown on Figures 10-81 and 10-83 at 5% damping.

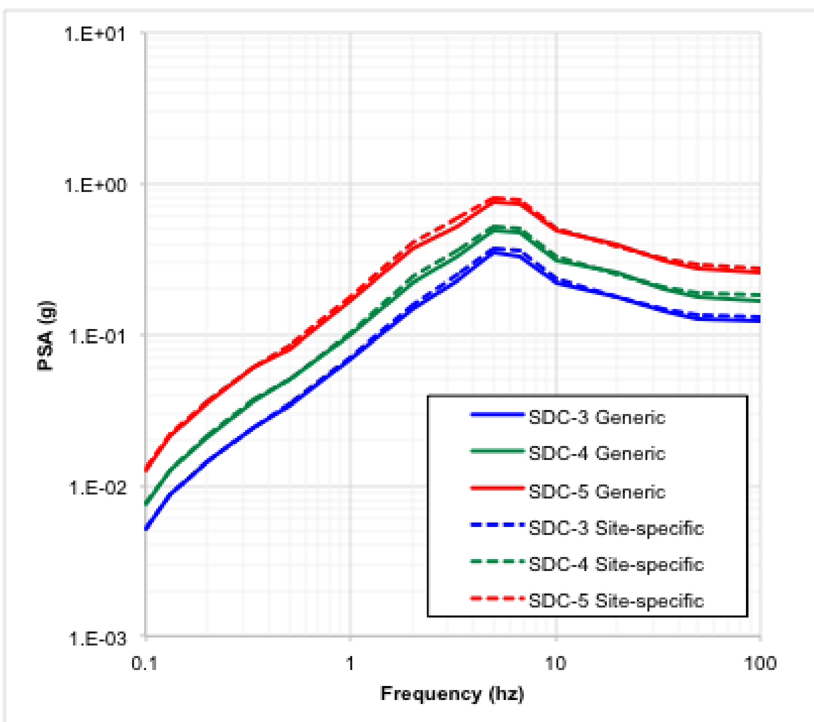

Figure 10-86. Horizontal GMRS for SFHP 40-ft soil depth computed from the envelope UHRS shown on Figures 10-82 and 10-84 at 5% damping.

Table 10-23. Horizontal GMRS for SFHP 20-ft soil depth computed using the results of the SSHAC Level 1 study.

Period (sec)	Frequency (Hz)	Horizontal SFHP Soil 20 ft Site Spectral Acceleration (g)		
		SDC-3	SDC-4	SDC-5
Computed Using Generic Soil Material Properties				
0.01	100	1.18E-01	1.67E-01	2.57E-01
0.02	50	1.24E-01	1.77E-01	2.75E-01
0.03	33.3	1.41E-01	2.04E-01	3.24E-01
0.05	20	1.89E-01	2.72E-01	4.34E-01
0.1	10	2.50E-01	3.52E-01	5.50E-01
0.15	6.67	3.12E-01	4.48E-01	7.02E-01
0.2	5	3.20E-01	4.65E-01	7.32E-01
0.3	3.33	1.96E-01	2.92E-01	4.97E-01
0.5	2	1.28E-01	1.88E-01	3.12E-01
1	1	6.74E-02	9.67E-02	1.62E-01
2	0.5	3.37E-02	4.97E-02	7.97E-02
3	0.333	2.39E-02	3.59E-02	5.90E-02
5	0.2	1.40E-02	2.07E-02	3.43E-02
7.5	0.133	8.50E-03	1.24E-02	2.10E-02
10	0.1	5.13E-03	7.48E-03	1.26E-02
Computed Using Site-specific Soil Properties				
0.01	100	1.21E-01	1.71E-01	2.66E-01
0.02	50	1.27E-01	1.79E-01	2.80E-01
0.03	33.3	1.41E-01	2.01E-01	3.14E-01
0.05	20	1.81E-01	2.58E-01	4.04E-01
0.1	10	2.52E-01	3.55E-01	5.48E-01
0.15	6.67	3.22E-01	4.60E-01	7.25E-01
0.2	5	3.44E-01	5.00E-01	7.88E-01
0.3	3.33	2.15E-01	3.22E-01	5.35E-01
0.5	2	1.34E-01	2.03E-01	3.56E-01
1	1	6.83E-02	9.86E-02	1.68E-01
2	0.5	3.39E-02	5.00E-02	8.17E-02
3	0.333	2.40E-02	3.61E-02	5.96E-02
5	0.2	1.40E-02	2.09E-02	3.48E-02
7.5	0.133	8.54E-03	1.25E-02	2.13E-02
10	0.1	5.17E-03	7.58E-03	1.29E-02

Table 10-24. Horizontal GMRS for SFHP 40-ft soil depth computed using the results of the SSHAC Level 1 study.

Period (sec)	Frequency (Hz)	Horizontal SFHP Soil 40 ft Site Spectral Acceleration (g)		
		SDC-3	SDC-4	SDC-5
Computed Using Generic Soil Material Properties				
0.01	100	1.22E-01	1.70E-01	2.59E-01
0.02	50	1.27E-01	1.78E-01	2.73E-01
0.03	33.3	1.41E-01	2.00E-01	3.07E-01
0.05	20	1.80E-01	2.54E-01	3.91E-01
0.1	10	2.24E-01	3.14E-01	4.90E-01
0.15	6.67	3.34E-01	4.71E-01	7.29E-01
0.2	5	3.48E-01	4.93E-01	7.57E-01
0.3	3.33	2.29E-01	3.30E-01	5.28E-01
0.5	2	1.47E-01	2.18E-01	3.69E-01
1	1	6.95E-02	1.00E-01	1.68E-01
2	0.5	3.42E-02	5.05E-02	8.11E-02
3	0.333	2.42E-02	3.64E-02	5.98E-02
5	0.2	1.41E-02	2.09E-02	3.47E-02
7.5	0.133	8.63E-03	1.26E-02	2.13E-02
10	0.1	5.16E-03	7.53E-03	1.27E-02
Computed Using Site-specific Soil Properties				
0.01	100	1.31E-01	1.83E-01	2.78E-01
0.02	50	1.36E-01	1.90E-01	2.90E-01
0.03	33.3	1.49E-01	2.09E-01	3.18E-01
0.05	20	1.79E-01	2.50E-01	3.81E-01
0.1	10	2.33E-01	3.26E-01	5.02E-01
0.15	6.67	3.58E-01	5.07E-01	7.78E-01
0.2	5	3.75E-01	5.30E-01	8.05E-01
0.3	3.33	2.50E-01	3.64E-01	5.85E-01
0.5	2	1.58E-01	2.42E-01	4.14E-01
1	1	7.09E-02	1.03E-01	1.79E-01
2	0.5	3.45E-02	5.10E-02	8.44E-02
3	0.333	2.44E-02	3.68E-02	6.12E-02
5	0.2	1.42E-02	2.12E-02	3.56E-02
7.5	0.133	8.71E-03	1.28E-02	2.18E-02
10	0.1	5.21E-03	7.66E-03	1.31E-02

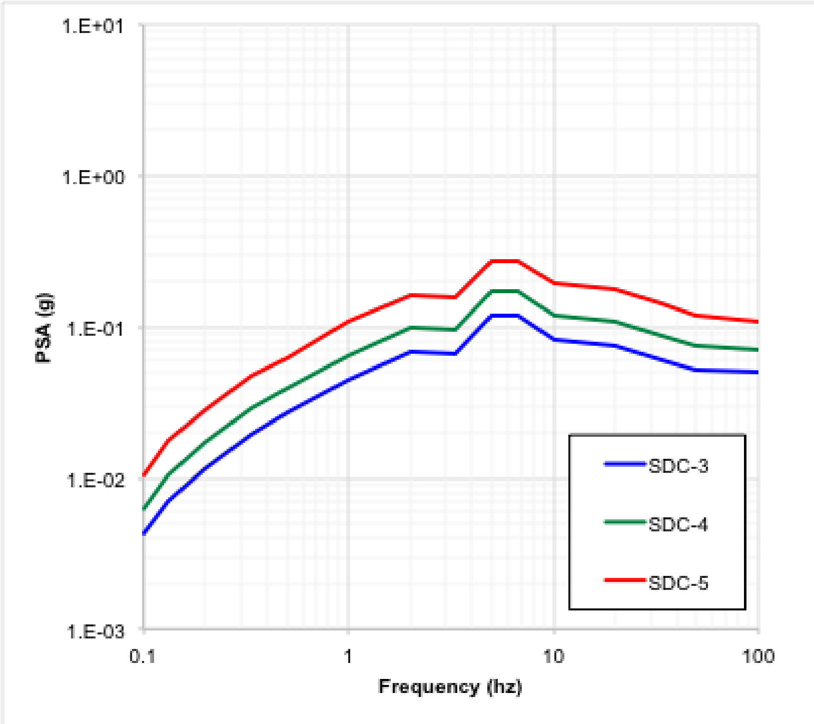

Figure 10-87. Vertical GMRS for SFHP Rock at 5% damping.

Table 10-25. Vertical GMRS for SFHP Rock site conditions computed using the results of the SSHAC Level 1 study.

Period (sec)	Frequency (Hz)	Vertical SFHP Rock Site Spectral Acceleration (g)		
		SDC-3	SDC-4	SDC-5
0.01	100	4.98E-02	7.00E-02	1.10E-01
0.02	50	5.24E-02	7.45E-02	1.19E-01
0.03	33.3	6.12E-02	8.79E-02	1.44E-01
0.05	20	7.42E-02	1.07E-01	1.76E-01
0.1	10	8.35E-02	1.20E-01	1.95E-01
0.15	6.67	1.21E-01	1.72E-01	2.75E-01
0.2	5	1.21E-01	1.72E-01	2.74E-01
0.3	3.33	6.73E-02	9.76E-02	1.59E-01
0.5	2	6.88E-02	9.99E-02	1.62E-01
1	1	4.50E-02	6.42E-02	1.08E-01
2	0.5	2.69E-02	3.96E-02	6.32E-02
3	0.333	1.93E-02	2.90E-02	4.76E-02
5	0.2	1.16E-02	1.72E-02	2.84E-02
7.5	0.133	7.15E-03	1.05E-02	1.76E-02
10	0.1	4.32E-03	6.30E-03	1.05E-02

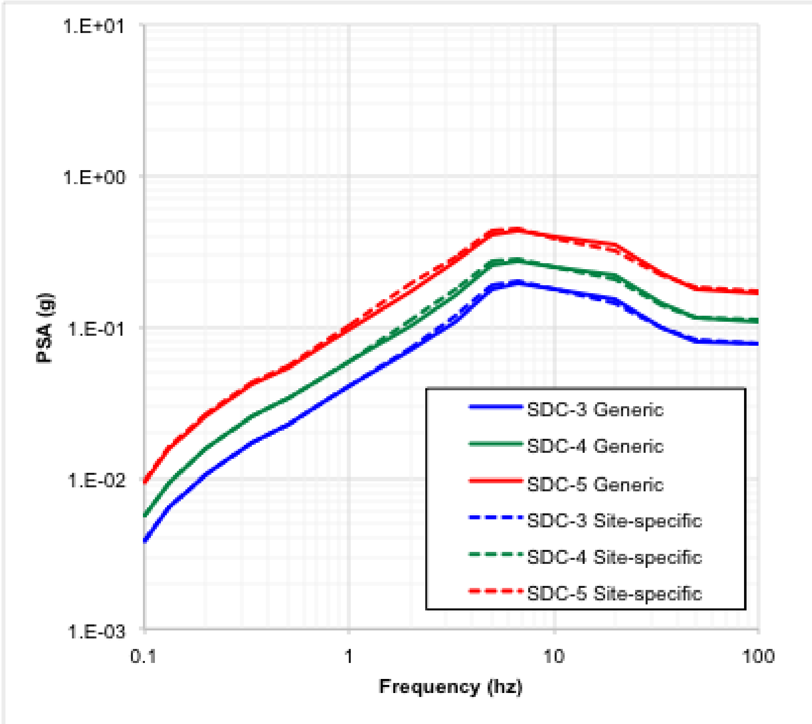

Figure 10-88. Vertical GMRS for SFHP 20-ft soil depth at 5% damping.

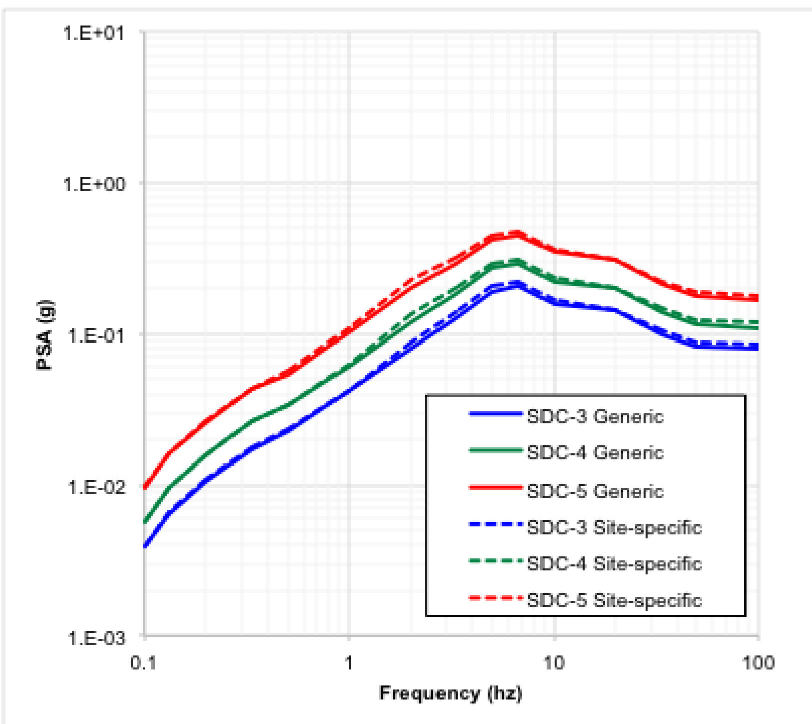

Figure 10-89. Vertical GMRS for SFHP 40-ft soil depth at 5% damping.

Table 10-26. Vertical GMRS for SFHP 20-ft soil depth computed using the results of the SSHAC Level 1 study.

Period (sec)	Frequency (Hz)	Vertical SFHP Soil 20 ft Site Spectral Acceleration (g)		
		SDC-3	SDC-4	SDC-5
Computed Using Generic Soil Material Properties				
0.01	100	7.66E-02	1.08E-01	1.67E-01
0.02	50	8.07E-02	1.15E-01	1.79E-01
0.03	33.3	9.87E-02	1.43E-01	2.27E-01
0.05	20	1.51E-01	2.18E-01	3.47E-01
0.1	10	1.77E-01	2.50E-01	3.91E-01
0.15	6.67	1.92E-01	2.76E-01	4.33E-01
0.2	5	1.76E-01	2.56E-01	4.03E-01
0.3	3.33	1.08E-01	1.61E-01	2.73E-01
0.5	2	7.02E-02	1.03E-01	1.72E-01
1	1	4.05E-02	5.80E-02	9.72E-02
2	0.5	2.26E-02	3.33E-02	5.34E-02
3	0.333	1.71E-02	2.58E-02	4.23E-02
5	0.2	1.05E-02	1.55E-02	2.57E-02
7.5	0.133	6.37E-03	9.33E-03	1.57E-02
10	0.1	3.84E-03	5.61E-03	9.43E-03
Computed Using Site-specific Soil Properties				
0.01	100	7.87E-02	1.11E-01	1.73E-01
0.02	50	8.23E-02	1.16E-01	1.82E-01
0.03	33.3	9.85E-02	1.41E-01	2.20E-01
0.05	20	1.45E-01	2.06E-01	3.23E-01
0.1	10	1.79E-01	2.52E-01	3.89E-01
0.15	6.67	1.98E-01	2.84E-01	4.47E-01
0.2	5	1.89E-01	2.75E-01	4.33E-01
0.3	3.33	1.18E-01	1.77E-01	2.94E-01
0.5	2	7.40E-02	1.12E-01	1.96E-01
1	1	4.10E-02	5.92E-02	1.01E-01
2	0.5	2.27E-02	3.35E-02	5.48E-02
3	0.333	1.72E-02	2.59E-02	4.28E-02
5	0.2	1.05E-02	1.56E-02	2.61E-02
7.5	0.133	6.41E-03	9.40E-03	1.60E-02
10	0.1	3.88E-03	5.69E-03	9.67E-03

Table 10-27. Vertical GMRS for SFHP 40-ft soil depth computed using the results of the SSHAC Level 1 study.

Period (sec)	Frequency (Hz)	Vertical SFHP Soil 40 ft Site Spectral Acceleration (g)		
		SDC-3	SDC-4	SDC-5
Computed Using Generic Soil Material Properties				
0.01	100	7.94E-02	1.10E-01	1.68E-01
0.02	50	8.28E-02	1.16E-01	1.77E-01
0.03	33.3	9.90E-02	1.40E-01	2.15E-01
0.05	20	1.44E-01	2.03E-01	3.13E-01
0.1	10	1.59E-01	2.23E-01	3.48E-01
0.15	6.67	2.06E-01	2.90E-01	4.50E-01
0.2	5	1.91E-01	2.71E-01	4.16E-01
0.3	3.33	1.26E-01	1.81E-01	2.91E-01
0.5	2	8.09E-02	1.20E-01	2.03E-01
1	1	4.17E-02	6.00E-02	1.01E-01
2	0.5	2.29E-02	3.38E-02	5.44E-02
3	0.333	1.74E-02	2.61E-02	4.29E-02
5	0.2	1.06E-02	1.57E-02	2.60E-02
7.5	0.133	6.47E-03	9.47E-03	1.60E-02
10	0.1	3.87E-03	5.65E-03	9.51E-03
Computed Using Site-specific Soil Properties				
0.01	100	8.52E-02	1.19E-01	1.80E-01
0.02	50	8.84E-02	1.24E-01	1.89E-01
0.03	33.3	1.04E-01	1.46E-01	2.23E-01
0.05	20	1.44E-01	2.00E-01	3.05E-01
0.1	10	1.66E-01	2.31E-01	3.56E-01
0.15	6.67	2.21E-01	3.13E-01	4.80E-01
0.2	5	2.06E-01	2.92E-01	4.43E-01
0.3	3.33	1.37E-01	2.00E-01	3.22E-01
0.5	2	8.67E-02	1.33E-01	2.28E-01
1	1	4.25E-02	6.20E-02	1.07E-01
2	0.5	2.31E-02	3.42E-02	5.66E-02
3	0.333	1.75E-02	2.64E-02	4.38E-02
5	0.2	1.07E-02	1.59E-02	2.67E-02
7.5	0.133	6.53E-03	9.60E-03	1.64E-02
10	0.1	3.91E-03	5.75E-03	9.81E-03

10.7 Seismic Hazard Results and Sensitivity for SWUS Reference Site Conditions

The ATR Complex is located within the ESRP seismic source zone and on the southern boundary of IVRZ volcanic source zone and hanging wall side of the Big Lost fault (see Figure 8-2). The coordinates for the reference site conditions are 43.58792°N, -112.96585°W. Figures 10-90 through Figure 10-102 show the seismic hazard results at PGA and each of the 12 spectral periods analyzed. In each figure the top part shows the total mean and the 5^{th}, 16^{th}, 50^{th}, 84^{th}, and 95^{th} percentile seismic hazard curves; the plot on the bottom part of the figure compares the total mean hazard with the mean hazard produced by the tectonic source zones (blue curve), the volcanic source zones (red curve), the fault sources (green curve), and the Cascadia interface source (purple curve). The hazard is dominated by the host and CSZ zones and nearby faults. The source zones control the hazard at PGA and spectral frequencies >5 Hz. The fault sources, primarily Lost River and Lemhi, contribute more to the hazard at spectral frequencies <5 Hz. The contribution from the Cascadia interface source becomes evident at spectral frequencies <1 Hz.

Deaggregation of the total mean seismic hazard is shown in Figure 10-103 through Figure 10-106 for spectral frequencies at 10 Hz and 2 Hz (corresponding to spectral periods of 0.1-sec and 0.5-sec), and Figure 10-107 for spectral frequency of 0.5 Hz (2-sec). Each figure contains histograms representing the percent contribution to the total mean seismic hazard from different magnitude-distance bins. Each histogram represents one AEF level: $4x10^{-4}$, $1x10^{-4}$, $4x10^{-5}$, and $1x10^{-5}$. The deaggregation plots for 10 Hz (0.1-sec) and 2 Hz (0.5-sec) spectral accelerations for AEFs of $4x10^{-4}$ and $1x10^{-4}$ show peaks at ~M 7.5 for distance of 30-50 km that reflect contributions from faults (Figures 10-103 and 10-104). The plots for 2 Hz have slightly higher peaks at M 7.5 and 30-50 km than the 10 Hz plots. For both spectral frequencies, the source zones are also important contributors at M<7.5 and distance of 30-50 km (e.g., CSZ). Figure 10-107 shows peaks at M 7.5 and 30-50 km for $4x10^{-4}$ and $4x10^{-5}$.

10.7.1 Sensitivity Analyses for ATR

The sensitivity analyses described in Section 10.2.2 focus on elements of the model that are common to MFC, FMF, SFHP, and ATR. This section discusses the results of additional sensitivity tests performed for ATR.

10.7.1.1 Elements of the SSC Model

The hazard sensitivity at ATR is shown for the tectonic source zones and faults in the SSC model. Figure 10-107 compares the total mean hazard curve with the mean hazard curves obtained from each individual tectonic source zone and are shown for 10 Hz (0.1-sec) and 2 Hz (0.5-sec) spectral accelerations. At the AEFs of interest (>10^{-5}) the primary contribution is from the CSZ source zone due to its close proximity to the ATR Complex and its high predicted rate of earthquakes. Figure 10-108 compares the total mean hazard curve with the mean hazard curves obtained from individual fault sources at 10 Hz (0.1-sec) and 2 Hz (0.5-sec) spectral accelerations. The Lemhi and Lost River fault sources are the largest contributors to the hazard at ATR for AEFs of interest, 10^{-3} to 10^{-5}, since the two faults are close to ATR. Although ATR is on the hanging wall side of the Big Lost fault, owing to its low slip rate and seismogenic probability p[S] of 0.3 it is a primary contributor to the hazard only at very low AEFs (<10^{-6}).

The SSC model included sensitivity tests that varied the seismogenic probability (p[S] of 0.65 and 1.0) and style of faulting for the Big Lost fault (normal vs. strike-slip). In the case of strike-slip faulting, the fault was assumed to be vertical, whereas for normal faulting the fault has alternative dips of 45º, 55 º, and 75 º. Results of the tests are shown in Figures 10-109 through 10-115, which show contributions to the hazard at PGA and other spectral frequencies. The Big Lost fault, even with the p[S] of 1.0

contributes to the hazard only at AEF<10^{-5}. For high spectral frequencies >1 Hz, strike-slip faulting contributes slightly more to the hazard at ATR than normal faulting (both modeled with p[S] 0.3), while it contributes approximately the same or slightly less than normal faulting at low frequencies.

10.7.1.2 Variance Contribution Plots

Variance contribution histograms show the relative contribution that various input uncertainties make to the total variance in the ATR hazard results. Variance contribution histograms are shown in Figures 10-116, 10-117 and 10-118 for 10 Hz (0.1-sec), 1 Hz (1-sec) and 0.5 Hz (2-sec) spectral accelerations, respectively. Each figure contains histograms of the total variance calculated at four return periods: 2,500 yr (AEF of 4×10^{-4}), 10,000 yr (AEF of 10^{-4}), 25,000 yr (AEF of 4×10^{-4}), and 100,000 yr (AEF of 10^{-5}). At ATR, the dominant contribution to variance at 10 Hz is from choice of GMPE, rate of CSZ, and southern termination of the three main faults. At 2 Hz, the dominant contribution to variance is from choice of GMPE and southern termination of the three main faults while the rate of the CSZ is less important. At 0.5 Hz, the choice of GMPE is the dominant contribution to variance.

(a)

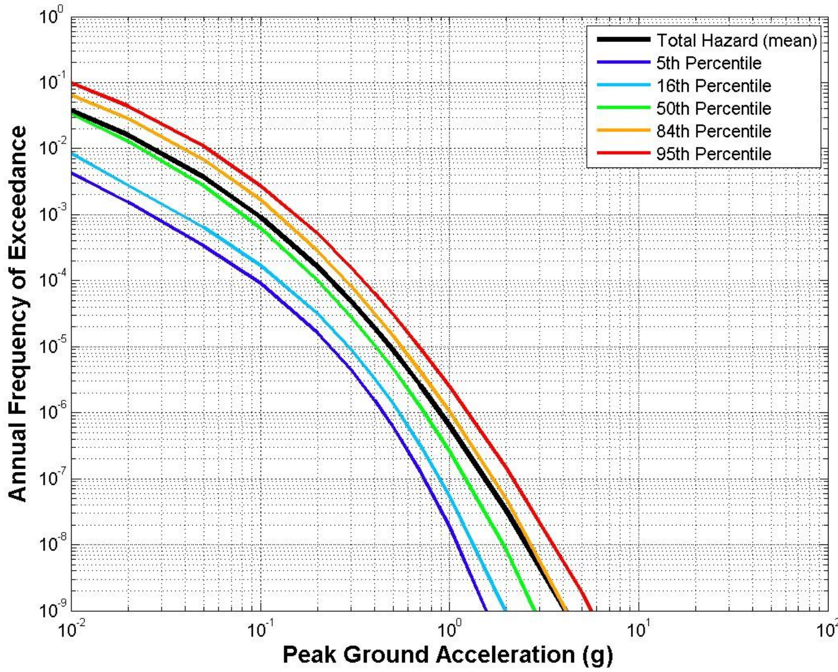

(b)

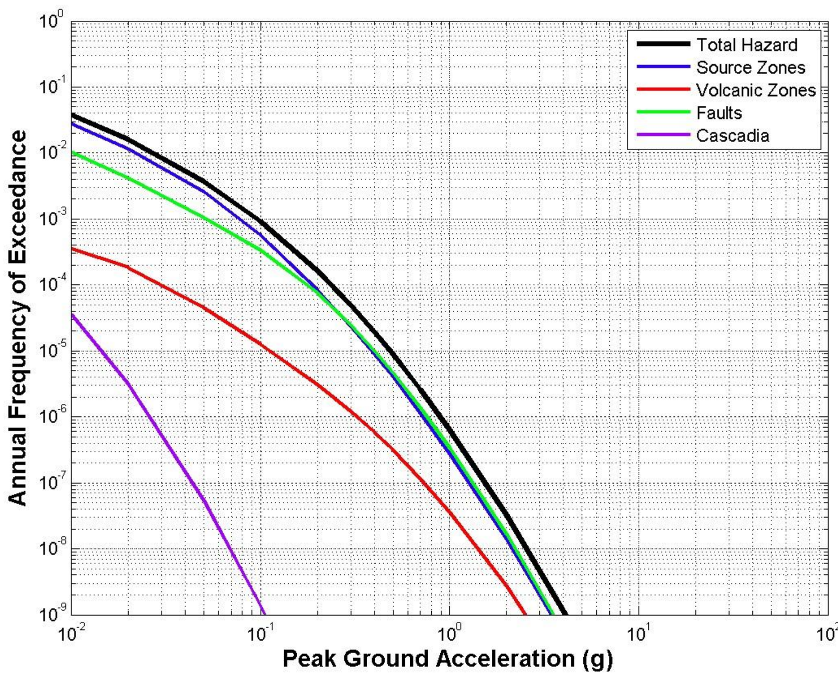

Figure 10-90. Seismic hazard results at ATR for SWUS reference site condition at PGA: a) total mean hazard and fractiles; and b) comparison between the total mean seismic hazard and the contribution of tectonic source zones, volcanic source zones, fault sources, and the Cascadia interface source.

(a)

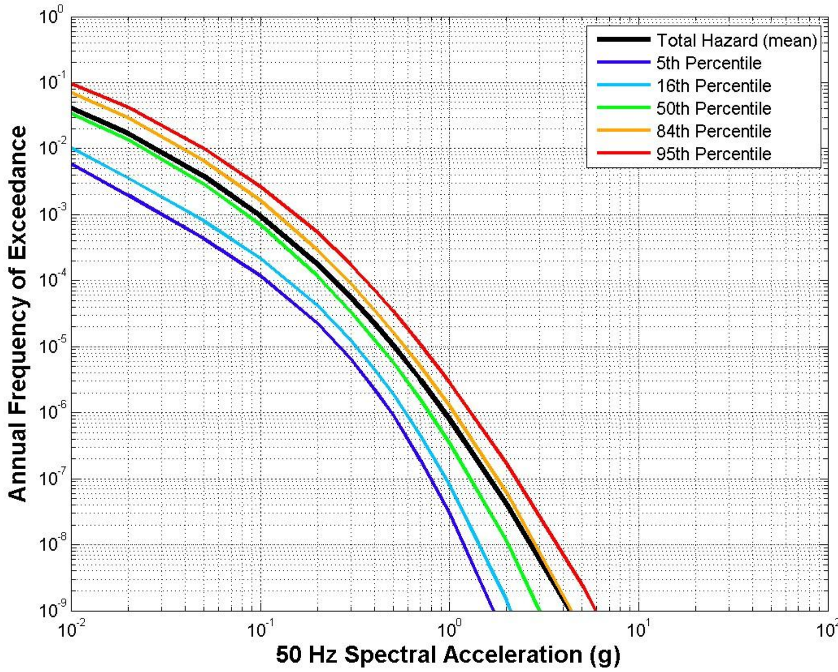

(b)

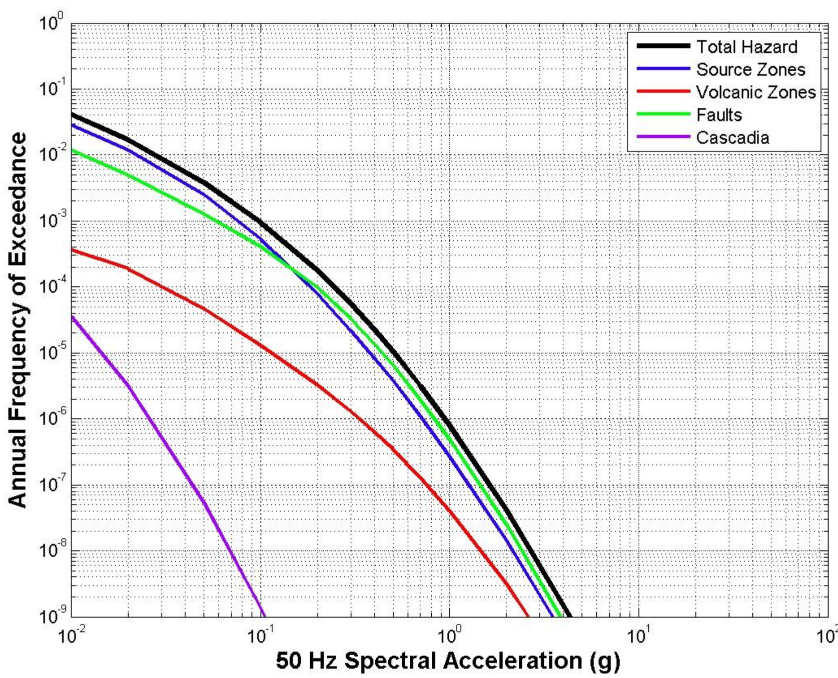

Figure 10-91. Seismic hazard results at ATR for SWUS reference site condition at 50 Hz (0.02-sec) spectral acceleration: a) total mean hazard and fractiles; and b) comparison between the total mean seismic hazard and the contribution of tectonic source zones, volcanic source zones, fault sources, and the Cascadia interface source.

(a)

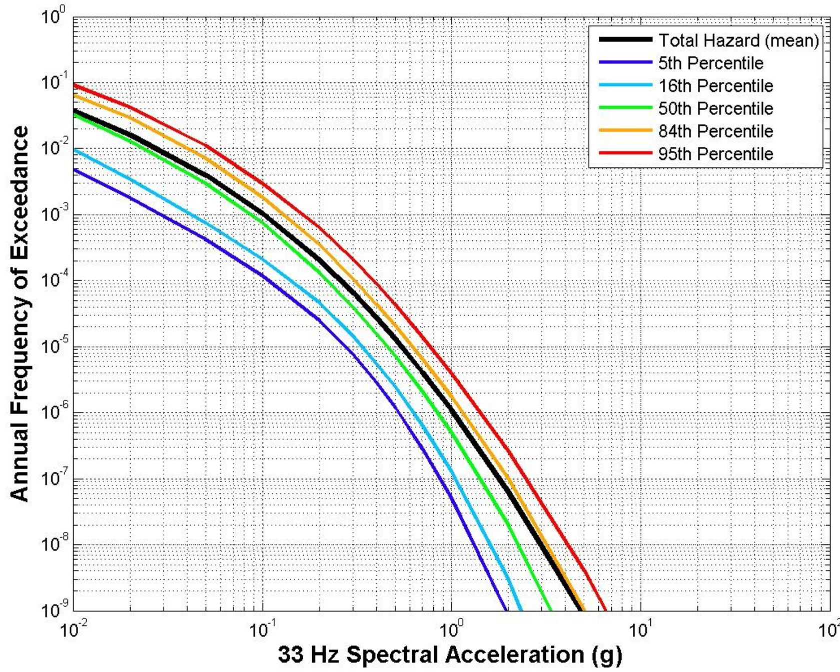

(b)

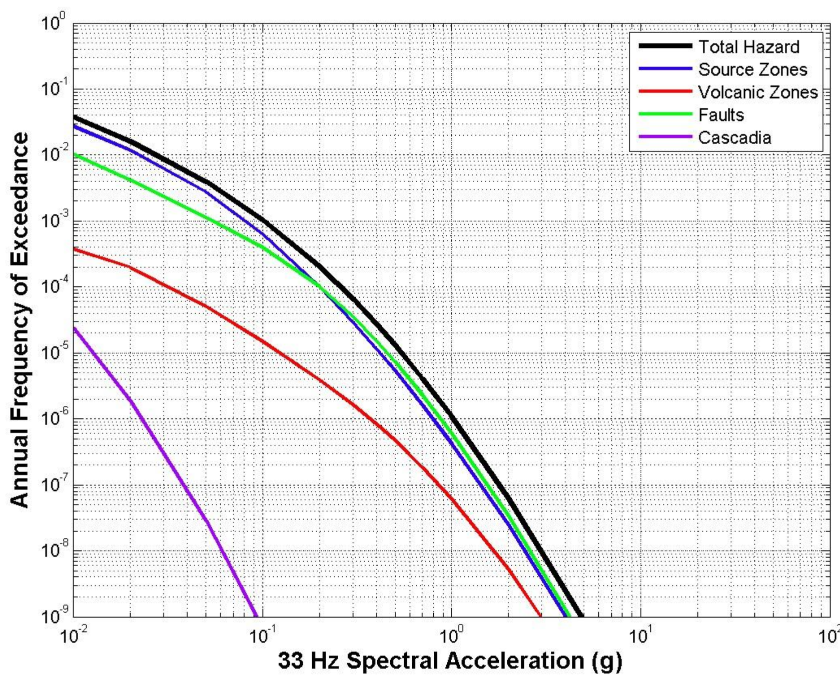

Figure 10-92 Seismic hazard results at ATR for SWUS reference site condition at 33 Hz (0.03-sec) spectral acceleration: a) total mean hazard and fractiles; and b) comparison between the total mean seismic hazard and the contribution of tectonic source zones, volcanic source zones, fault sources, and the Cascadia interface source.

(a)

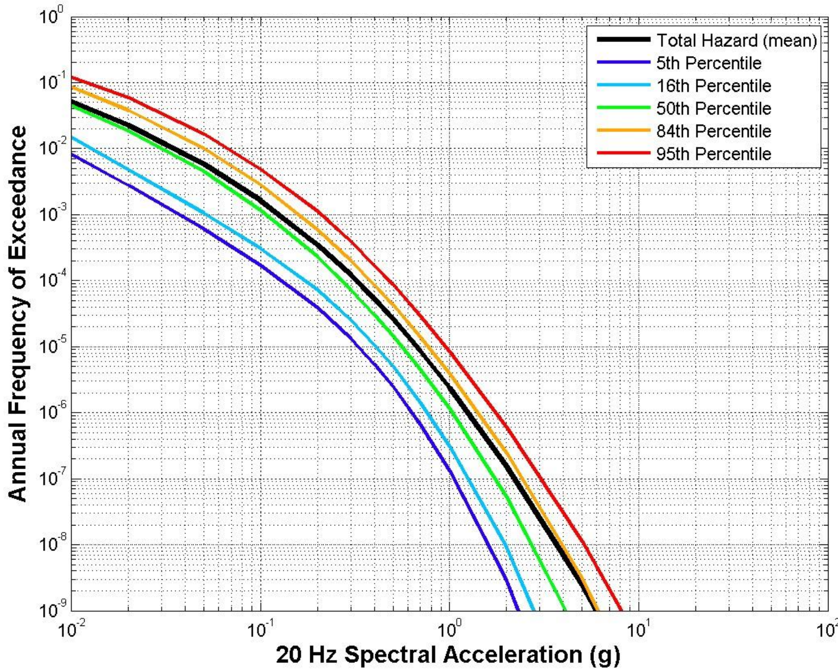

(b)

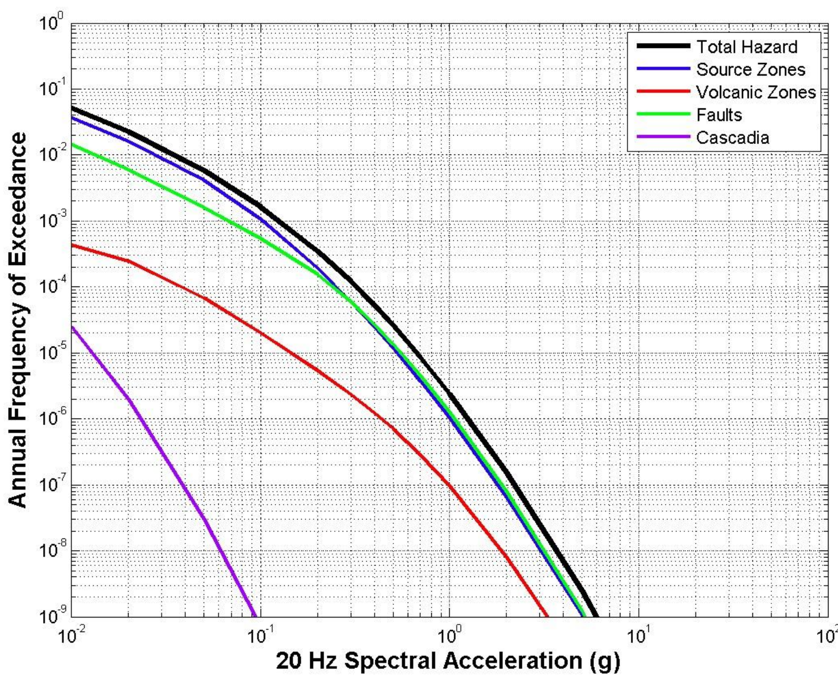

Figure 10-93 Seismic hazard results at ATR for SWUS reference site condition at 20 Hz (0.05-sec) spectral acceleration: a) total mean hazard and fractiles; and b) comparison between the total mean seismic hazard and the contribution of tectonic source zones, volcanic source zones, fault sources, and the Cascadia interface source.

(a)

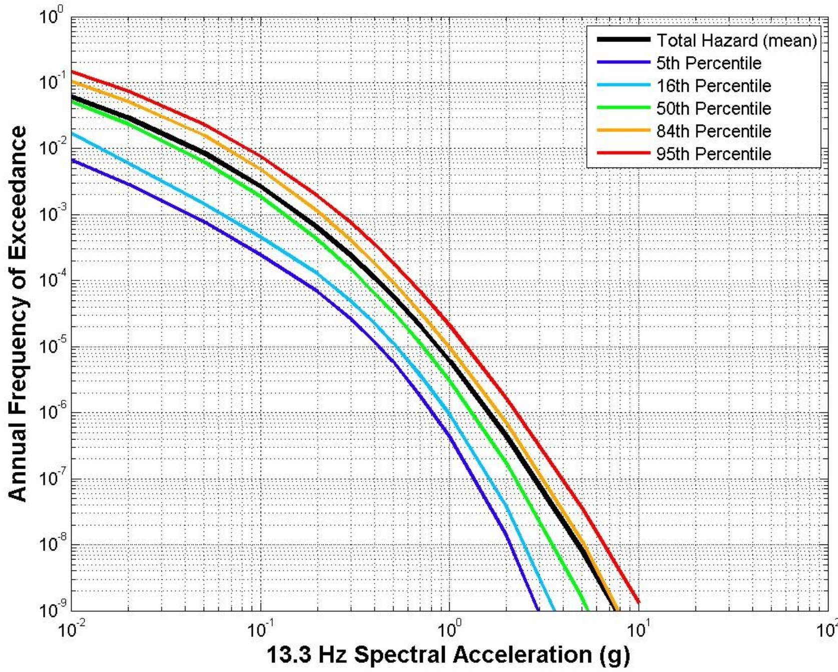

(b)

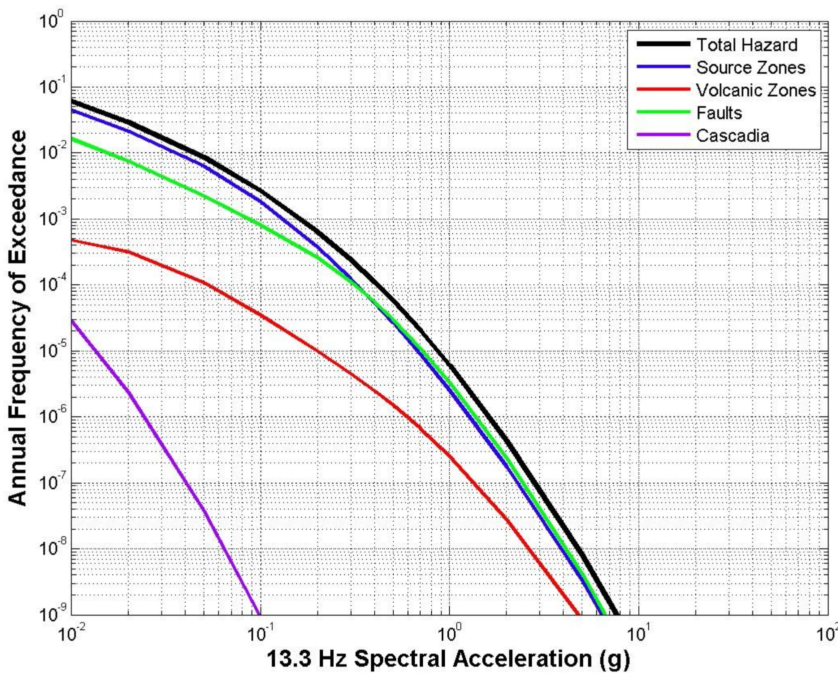

Figure 10-94. Seismic hazard results at ATR for SWUS reference site condition at 13.3 Hz (0.075-sec) spectral acceleration: a) total mean hazard and fractiles; and b) comparison between the total mean seismic hazard and the contribution of tectonic source zones, volcanic source zones, fault sources, and the Cascadia interface source.

(a)

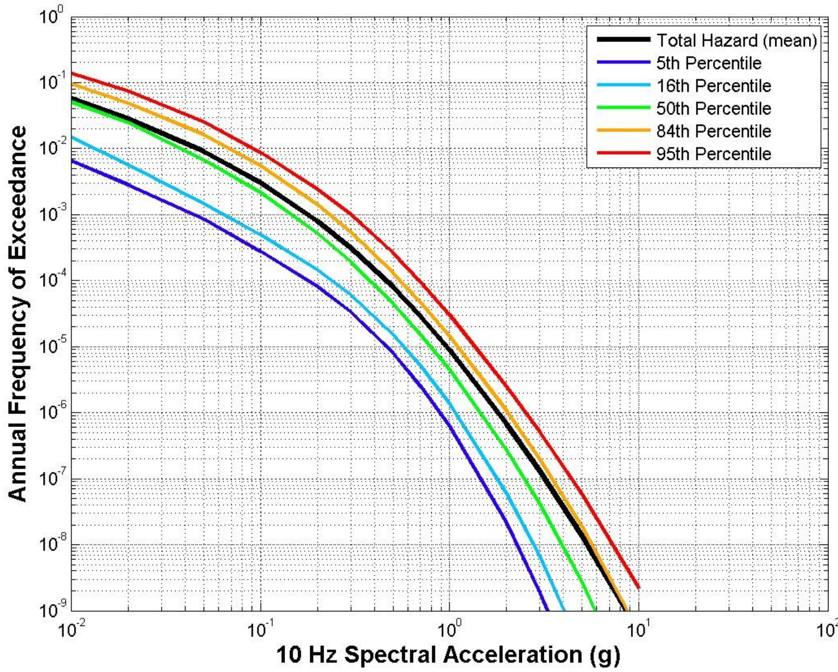

(b)

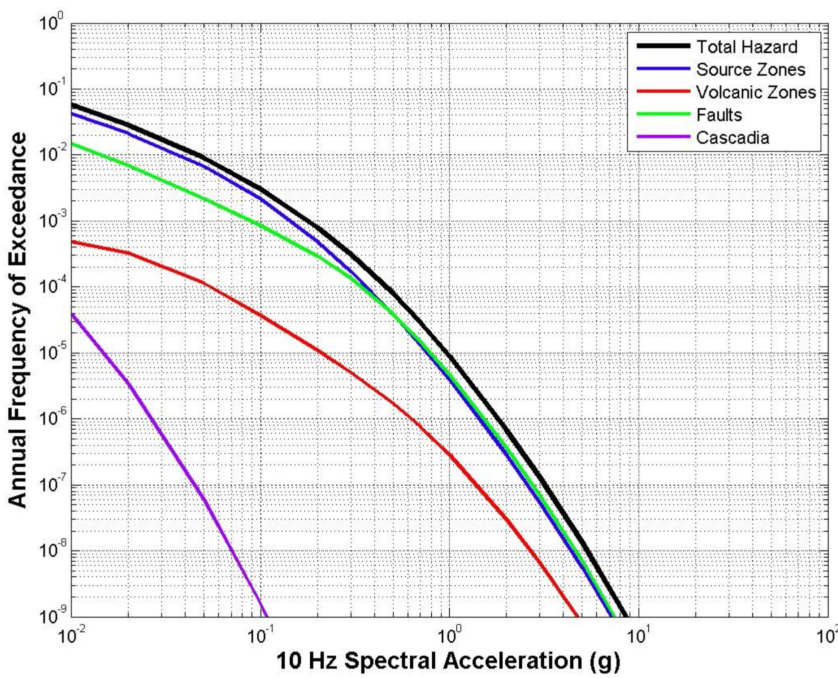

Figure 10-95. Seismic hazard results at ATR for SWUS reference site condition at 10 Hz (0.1-sec) spectral acceleration: a) total mean hazard and fractiles; and b) comparison between the total mean seismic hazard and the contribution of tectonic source zones, volcanic source zones, fault sources, and the Cascadia interface source.

(a)

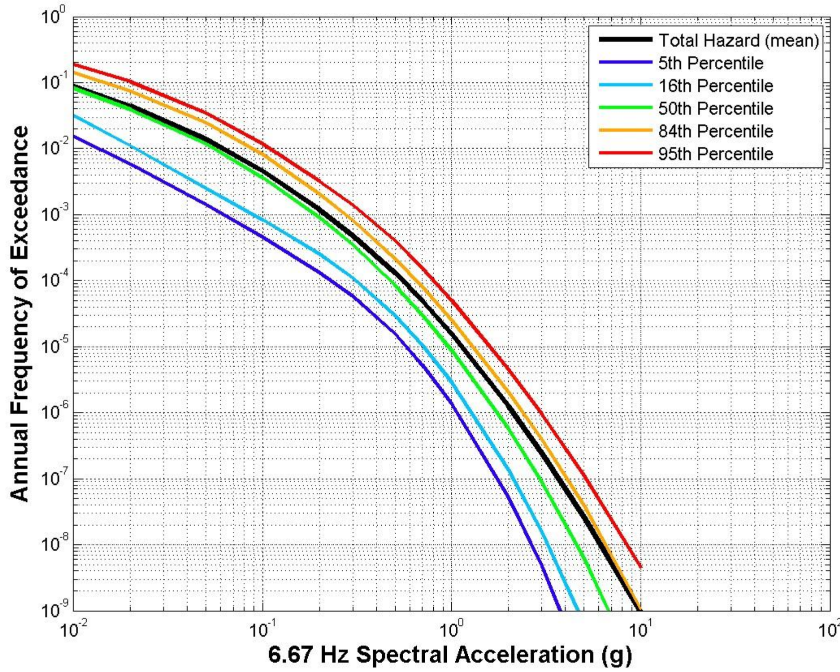

(b)

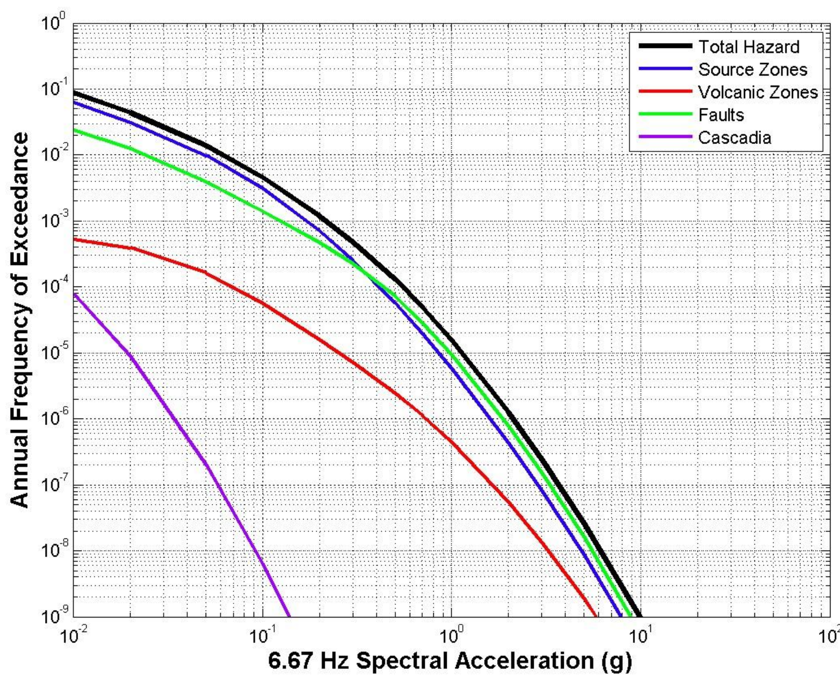

Figure 10-96. Seismic hazard resultsat ATR for SWUS reference site condition at 6.67 Hz (0.15-sec) spectral acceleration: a) total mean hazard and fractiles; and b) comparison between the total mean seismic hazard and the contribution of tectonic source zones, volcanic source zones, fault sources, and the Cascadia interface sources.

(a)

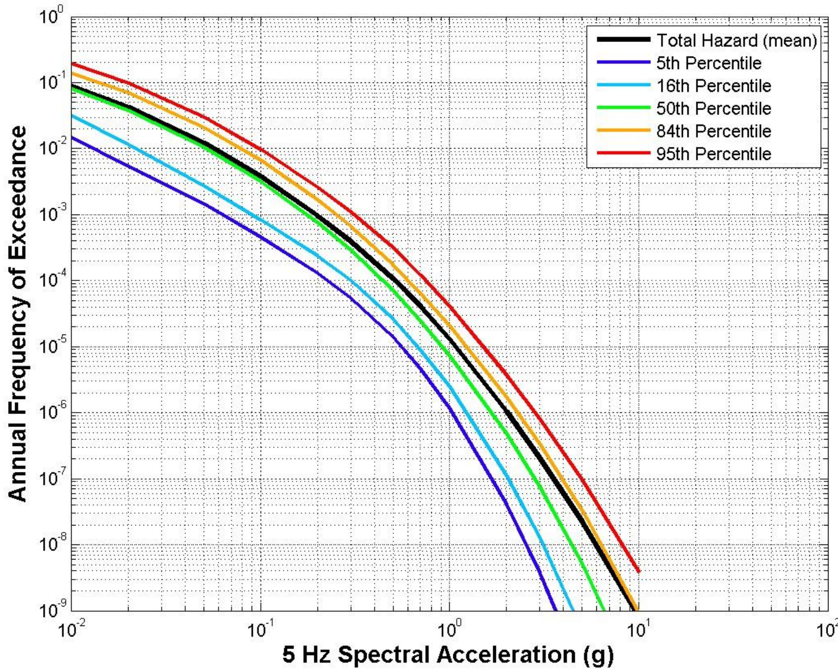

(b)

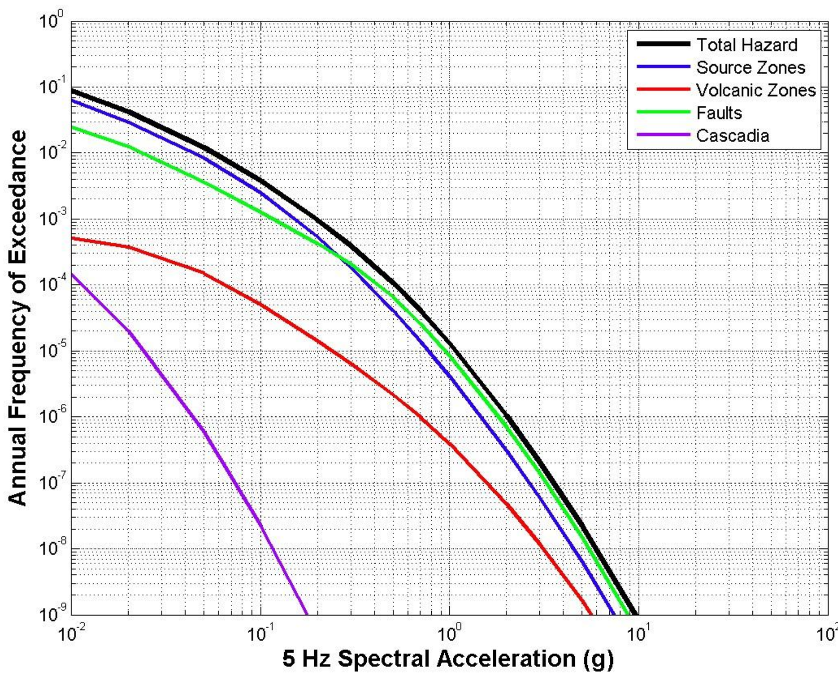

Figure 10-97. Seismic hazard results at ATR for SWUS reference site condition at 5 Hz (0.2-sec) spectral acceleration: a) total mean hazard and fractiles; and b) comparison between the total mean seismic hazard and the contribution of tectonic source zones, volcanic source zones, fault sources, and the Cascadia interface source.

(a)

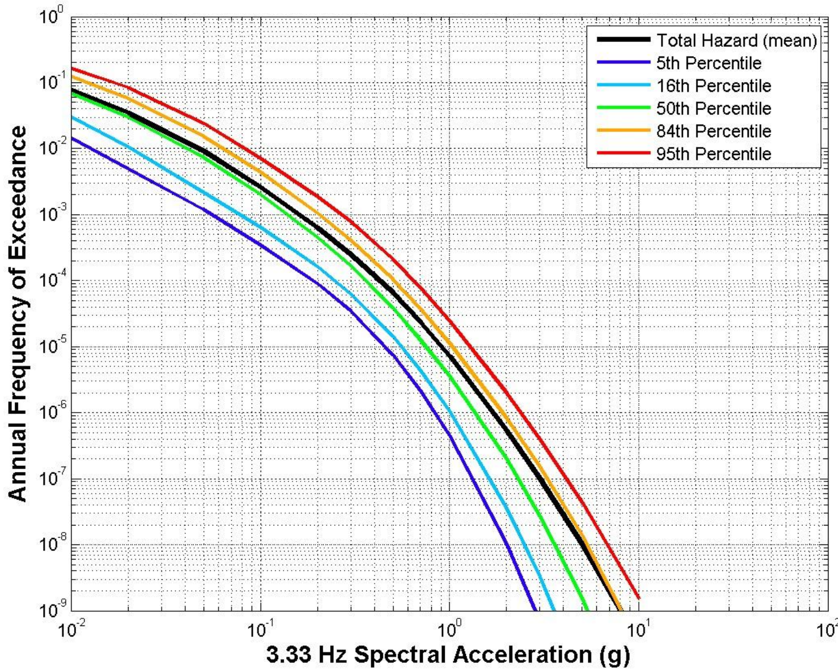

(b)

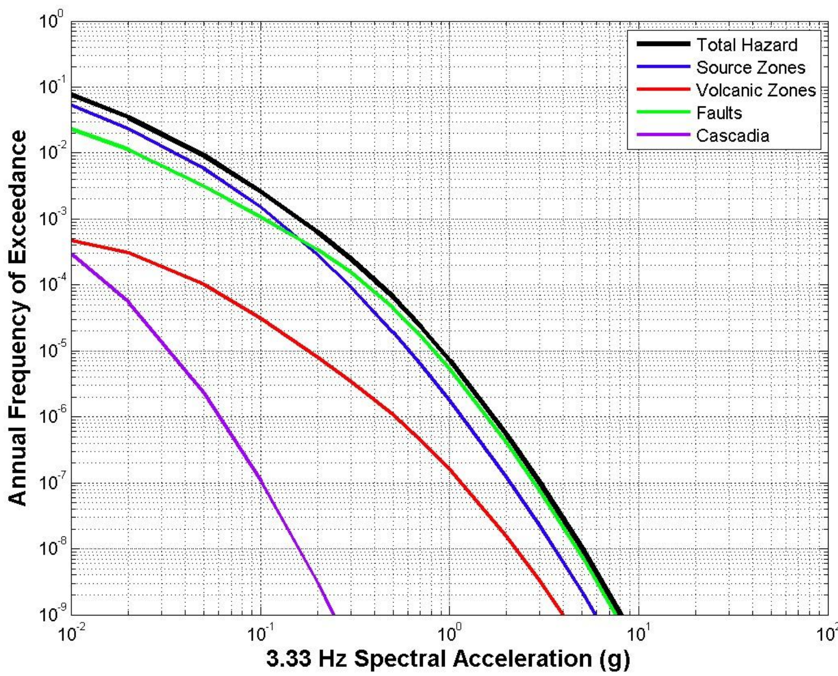

Figure 10-98. Seismic hazard results at ATR for SWUS reference site condition at 3.33 Hz (0.3-sec) spectral acceleration: a) total mean hazard and fractiles; and b) comparison between the total mean seismic hazard and the contribution of tectonic source zones, volcanic source zones, fault sources, and the Cascadia interface source.

(a)

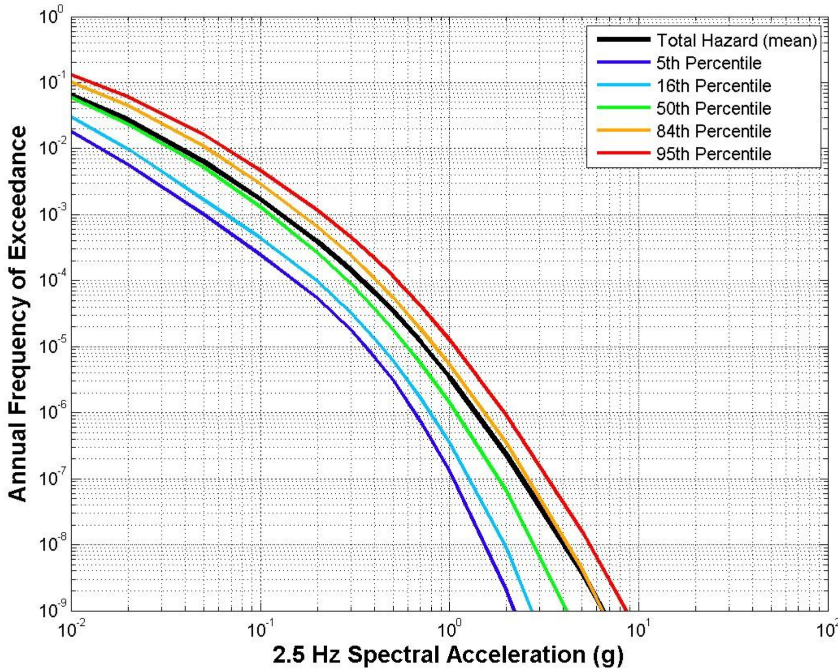

(b)

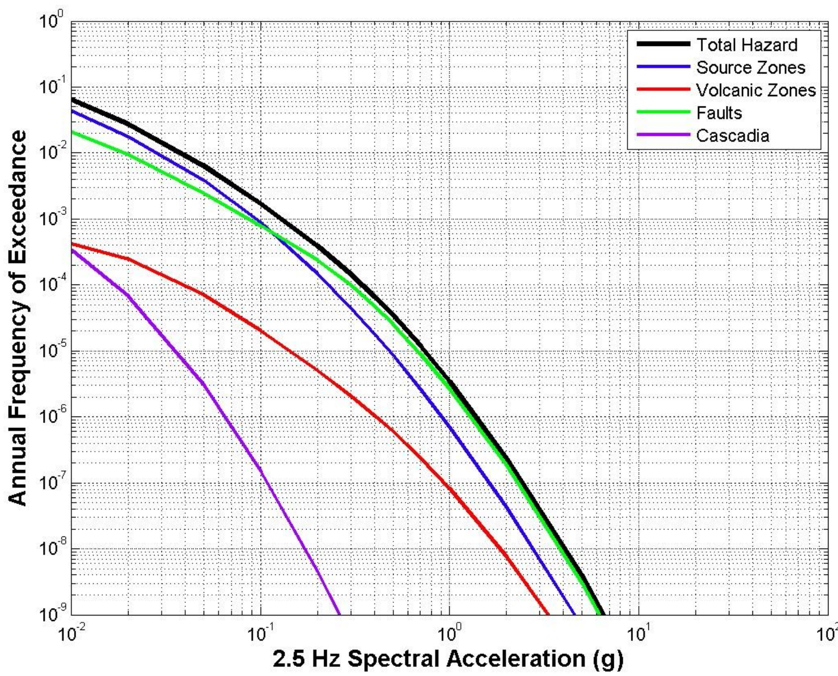

Figure 10-99. Seismic hazard results at ATR for SWUS reference site condition at 2.5 Hz (0.4-sec) spectral acceleration: a) total mean hazard and fractiles; and b) comparison between the total mean seismic hazard and the contribution of tectonic source zones, volcanic source zones, fault sources, and the Cascadia interface source.

(a)

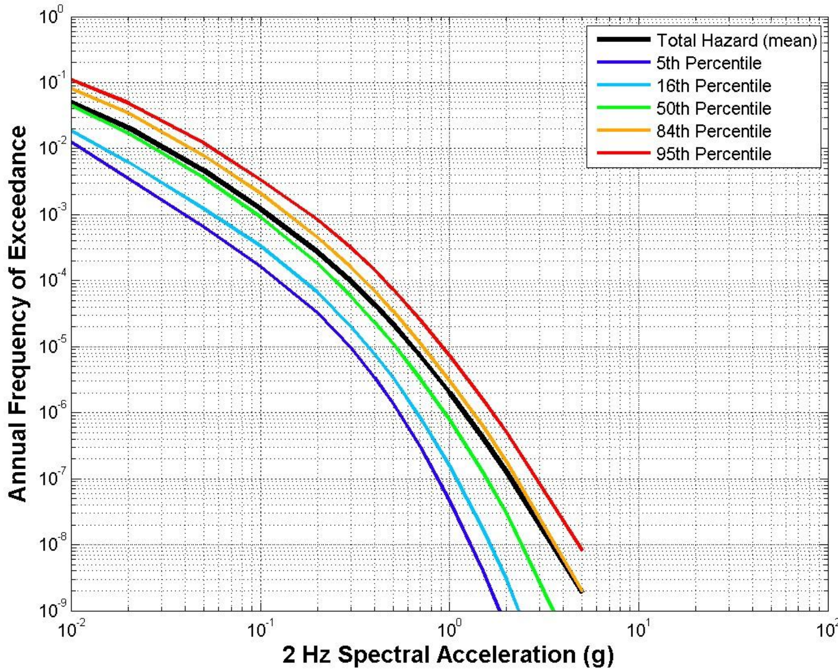

(b)

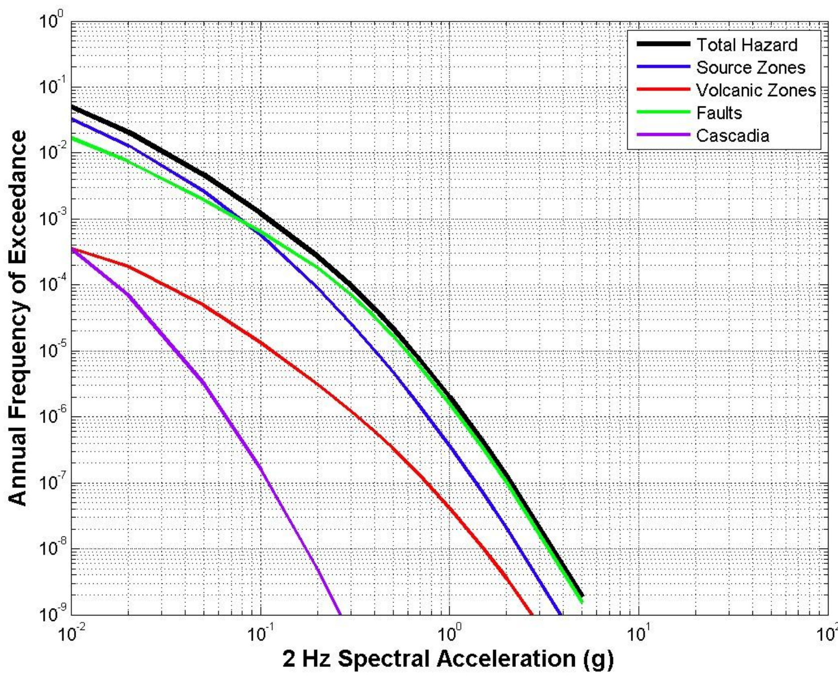

Figure 10-100. Seismic hazard results at ATR for SWUS reference site condition at 2 Hz (0.5-sec) spectral acceleration: a) total mean hazard and fractiles; and b) comparison between the total mean seismic hazard and the contribution of tectonic source zones, volcanic source zones, fault sources, and the Cascadia interface source.

(a)

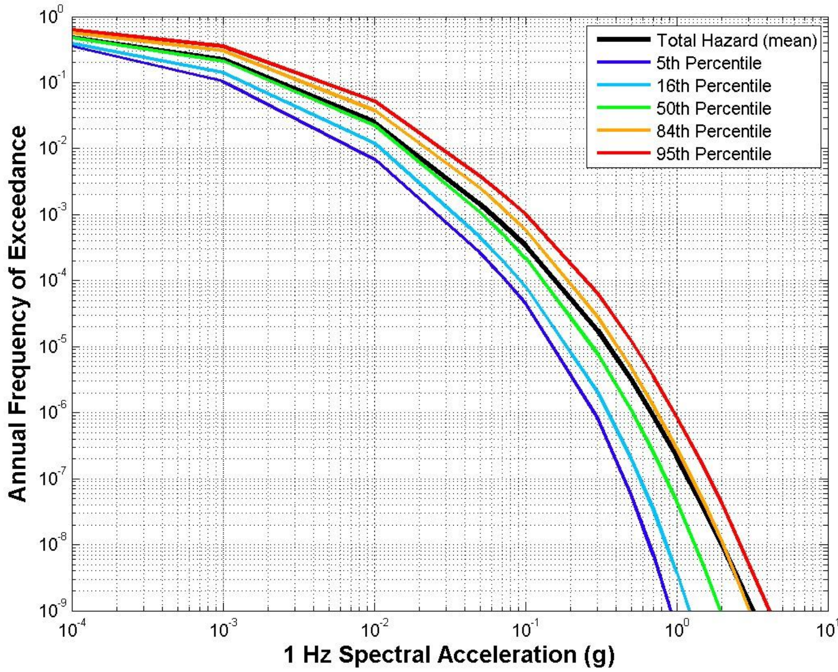

(b)

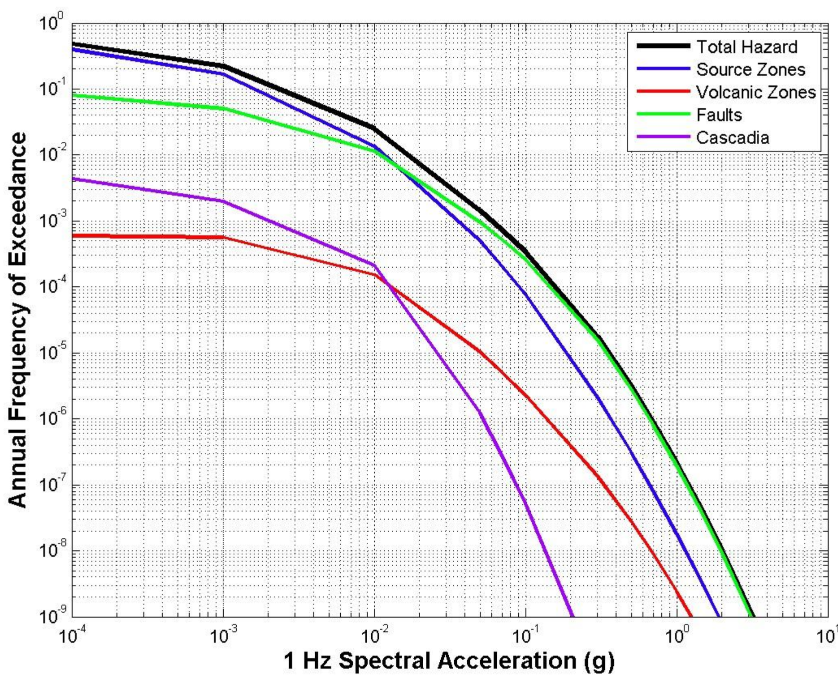

Figure 10-101. Seismic hazard results at ATR for SWUS reference site condition at 1 Hz (1-sec) spectral acceleration: a) total mean hazard and fractiles; and b) comparison between the total mean seismic hazard and the contribution of tectonic source zones, volcanic source zones, fault sources, and the Cascadia interface source.

(a)

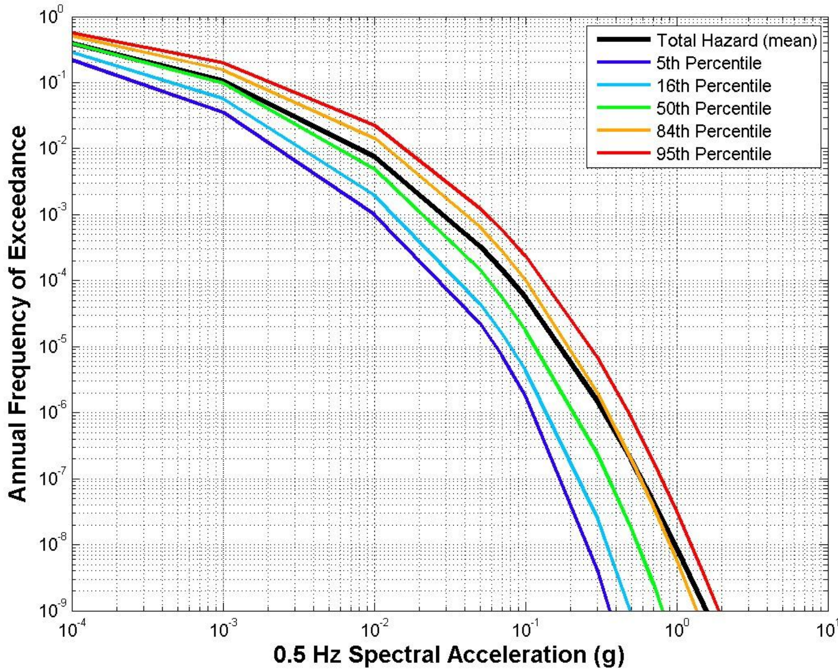

(b)

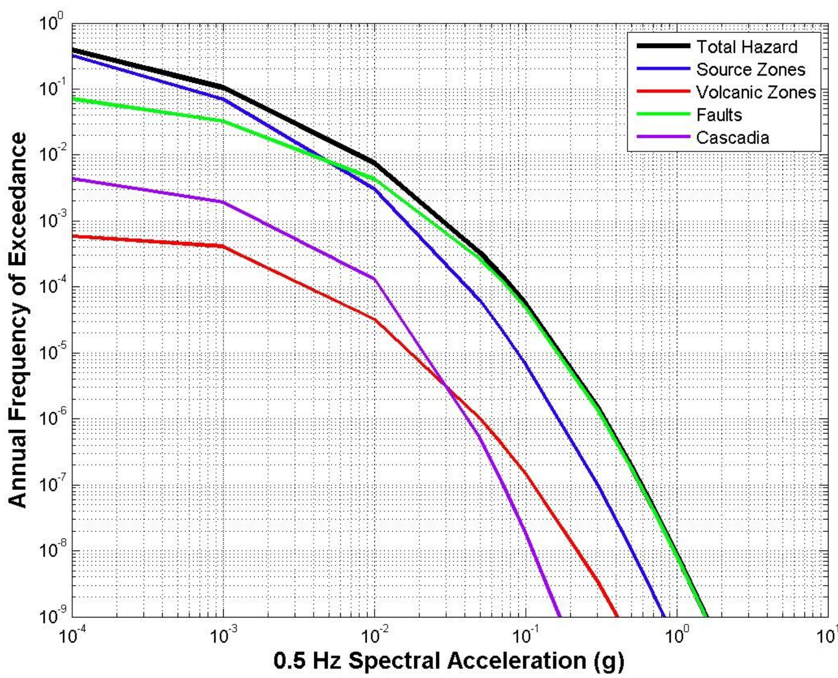

Figure 10-102. Seismic hazard results at ATR for SWUS reference site condition at 0.5 Hz (2-sec) spectral acceleration: a) total mean hazard and fractiles; and b) comparison between the total mean seismic hazard and the contribution of tectonic source zones, volcanic source zones, fault sources, and the Cascadia interface source.

(a)

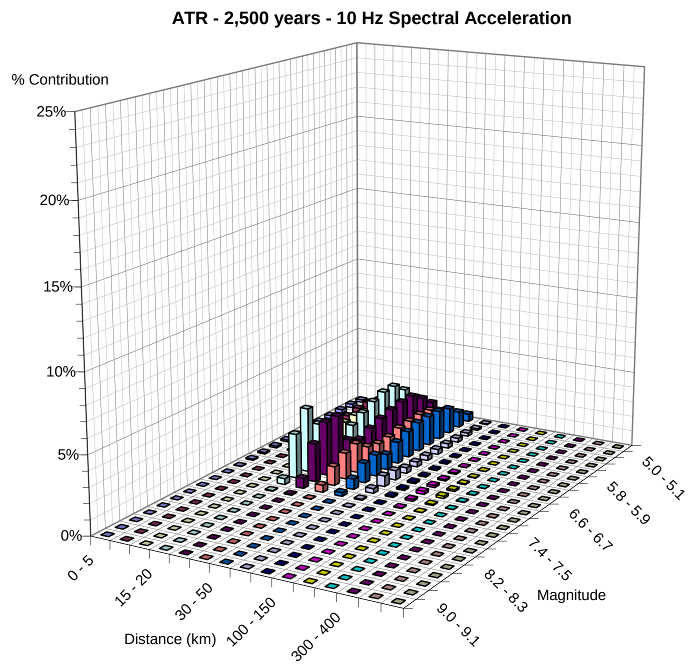

(b)

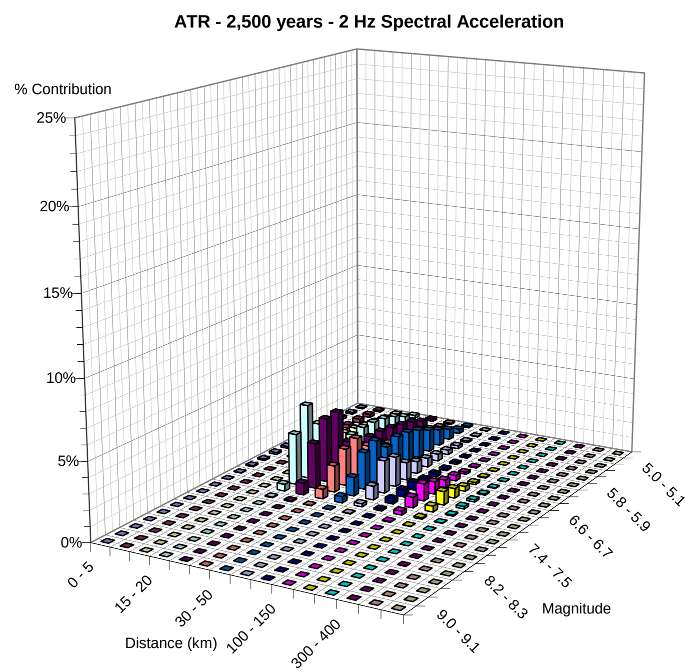

Figure 10-103. Magnitude-distance deaggregation for: a) 10 Hz; and b) 2 Hz at the 2,500 yr return period.

(a)

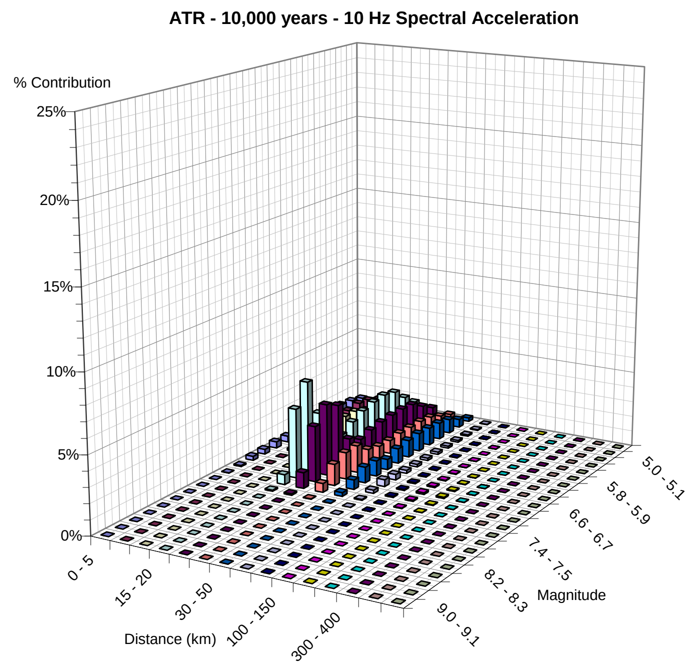

(b)

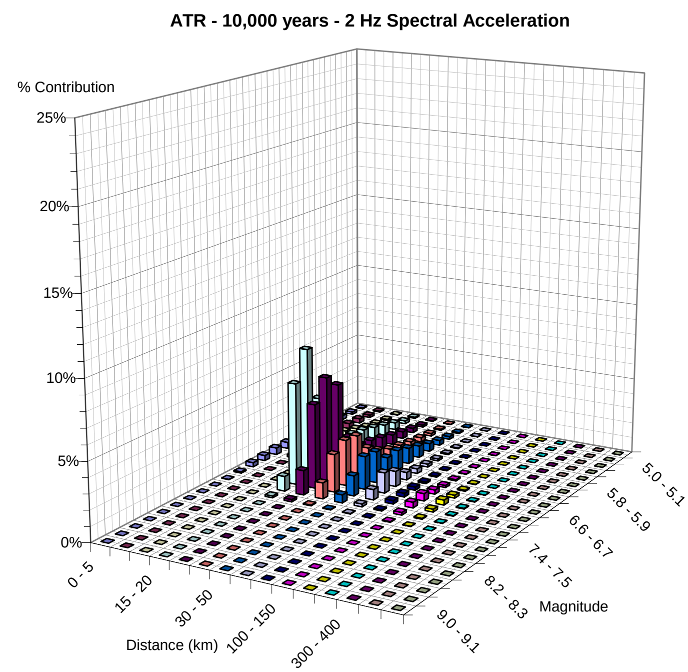

Figure 10-104. Magnitude-distance deaggregation for: a) 10 Hz; and b) 2 Hz at the 10,000 yr return period.

(a)

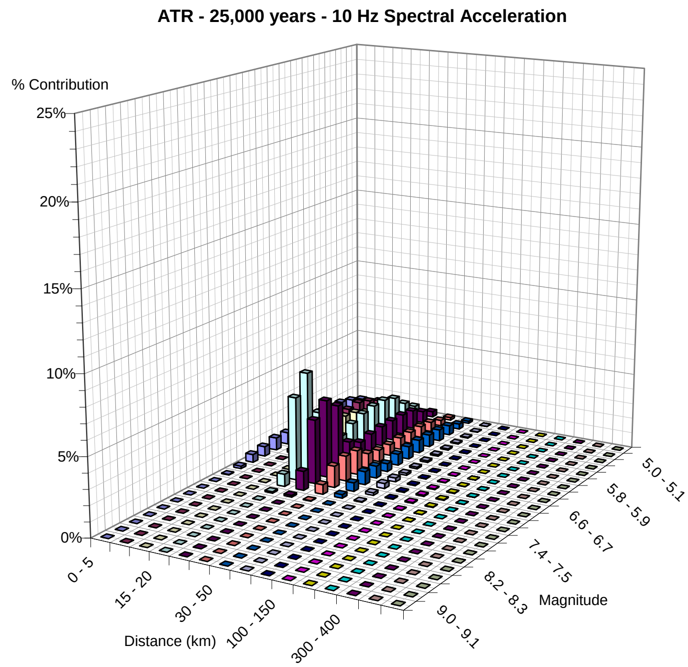

(b)

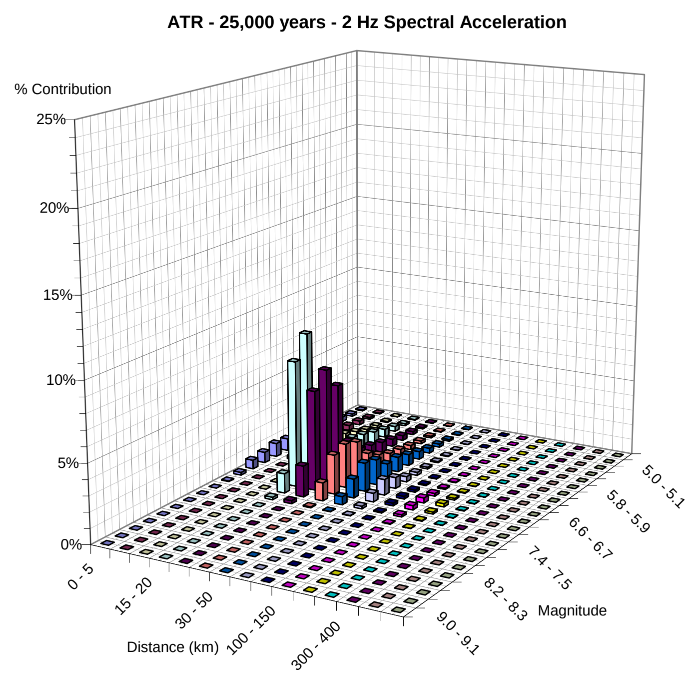

Figure 10-105. Magnitude-distance deaggregation for: a) 10 Hz; and b) 2 Hz at the 25,000 yr return period.

(a)

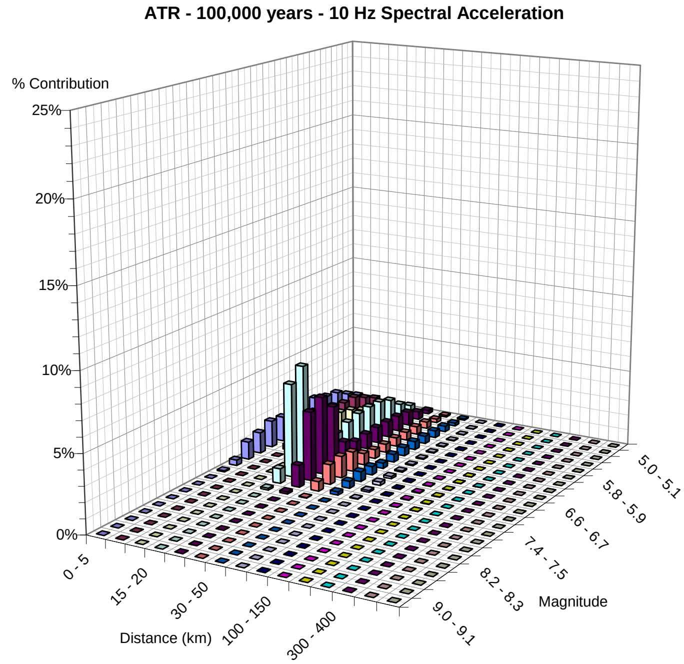

(b)

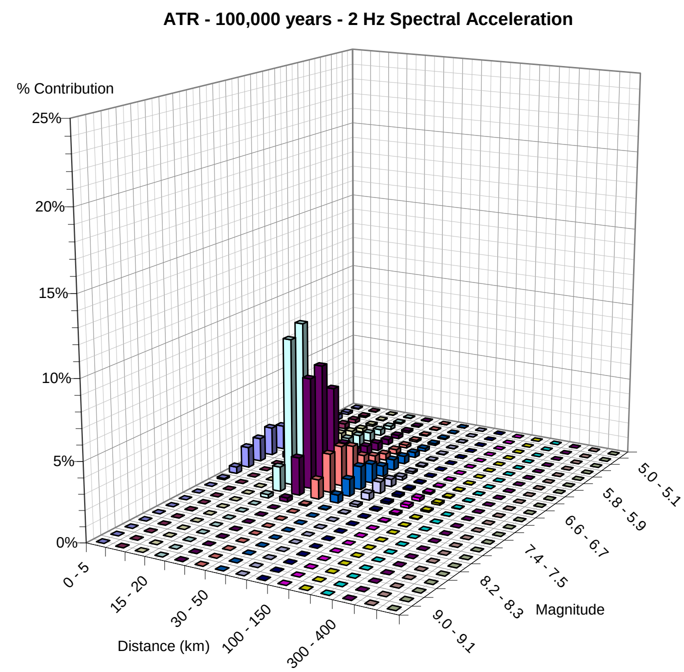

Figure 10-106. Magnitude-distance deaggregation for: a) 10 Hz; and b) 2 Hz at the 100,000 yr return period.

(a)

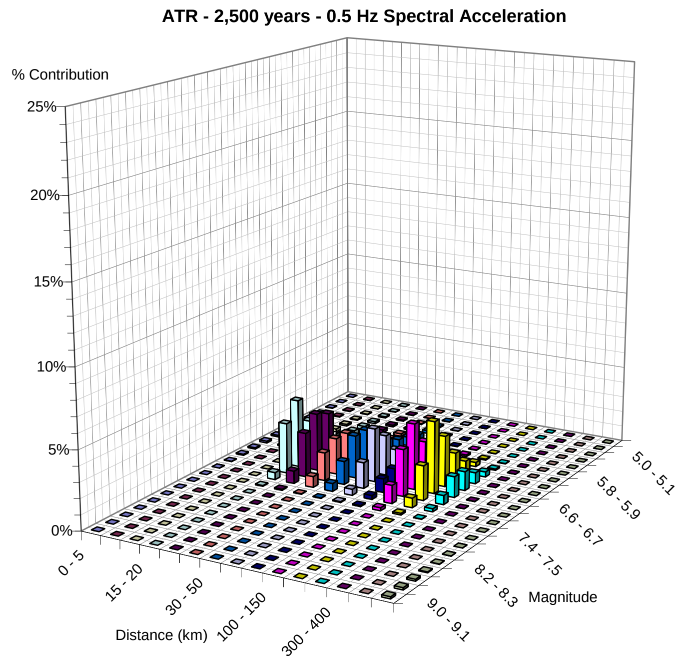

(b)

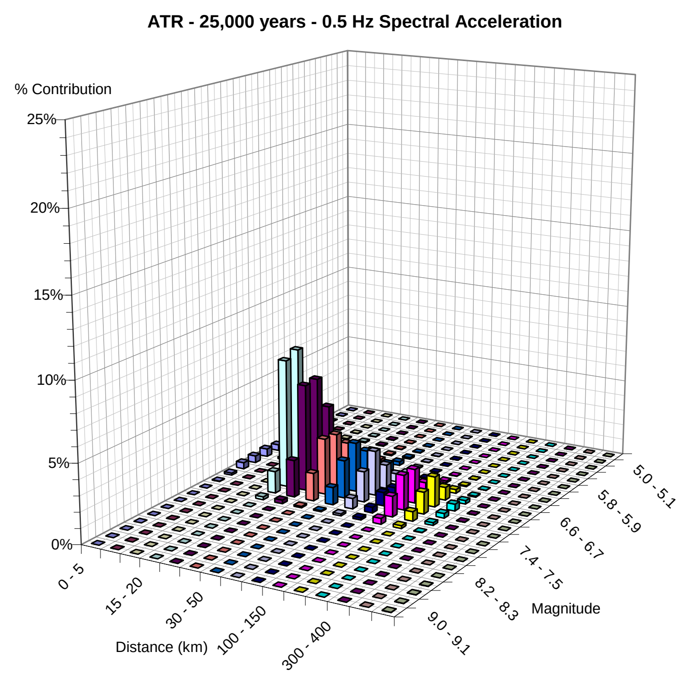

Figure 10-107. Magnitude-distance deaggregation for 0.5 Hz spectral acceleration at return periods of: a) 2,500 yr; and b) 25,000 yr.

(a)

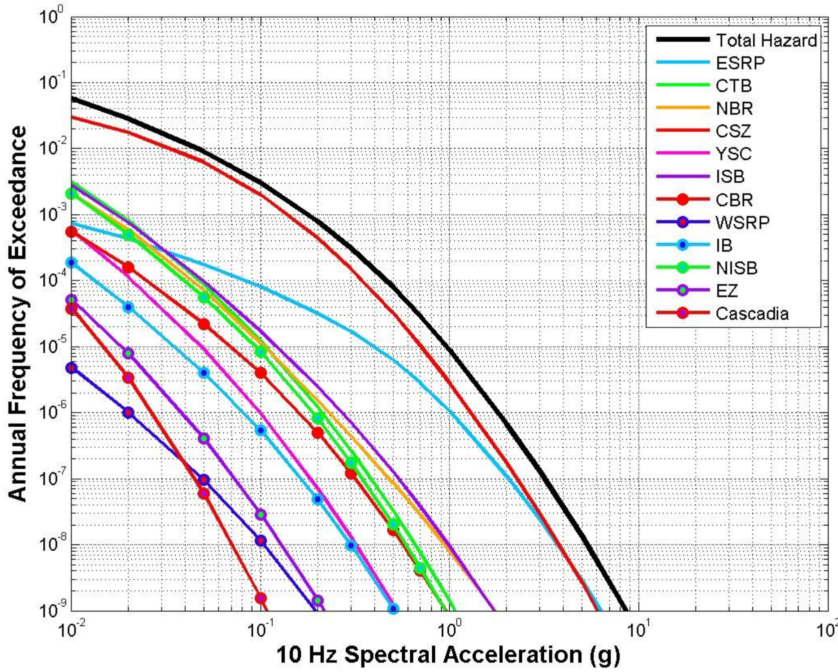

(b)

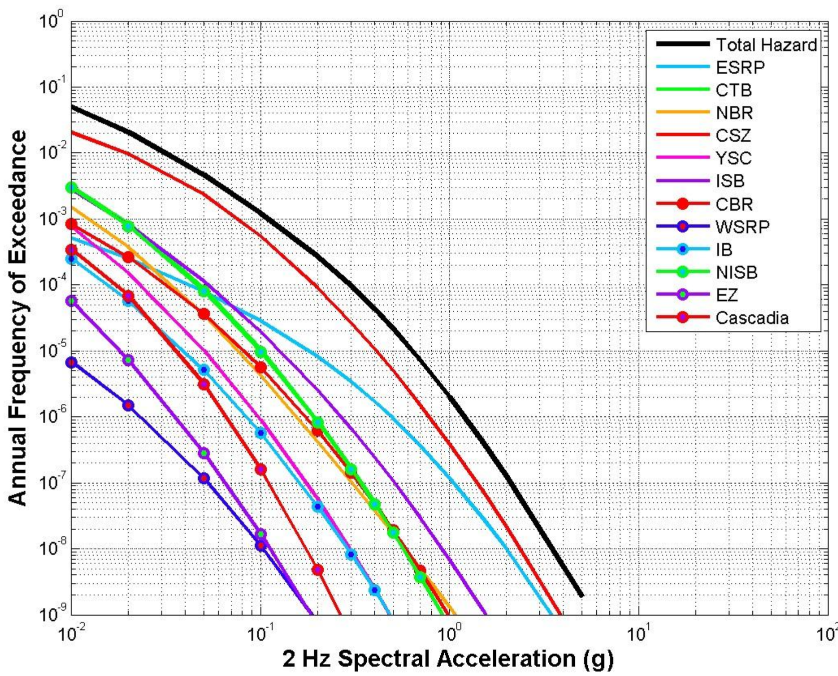

Figure 10-108. Contribution of individual tectonic source zones to the total seismic hazard for reference rock conditions: a) 10 Hz (0.1-sec) spectral acceleration; and b) 2 Hz (0.5-sec) spectral acceleration.

(a)

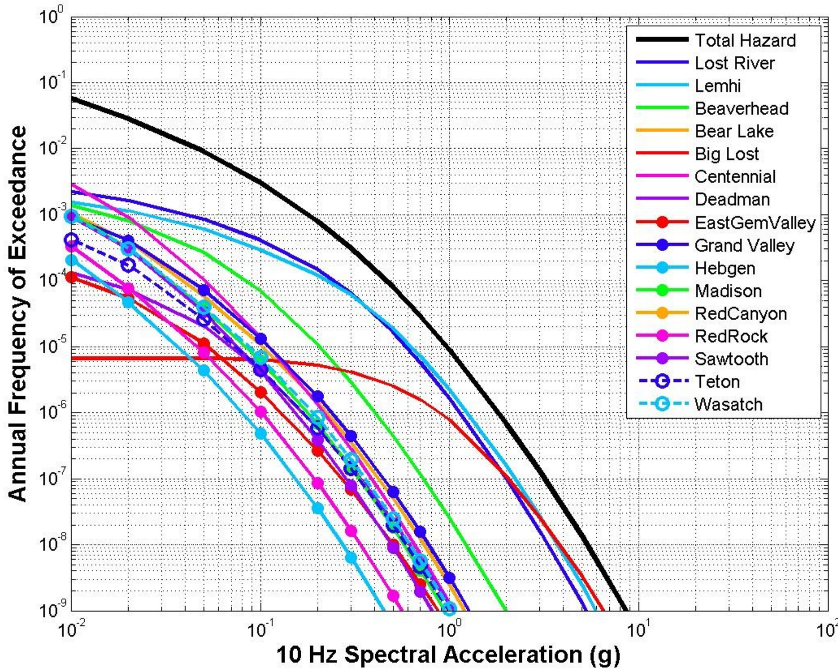

(b)

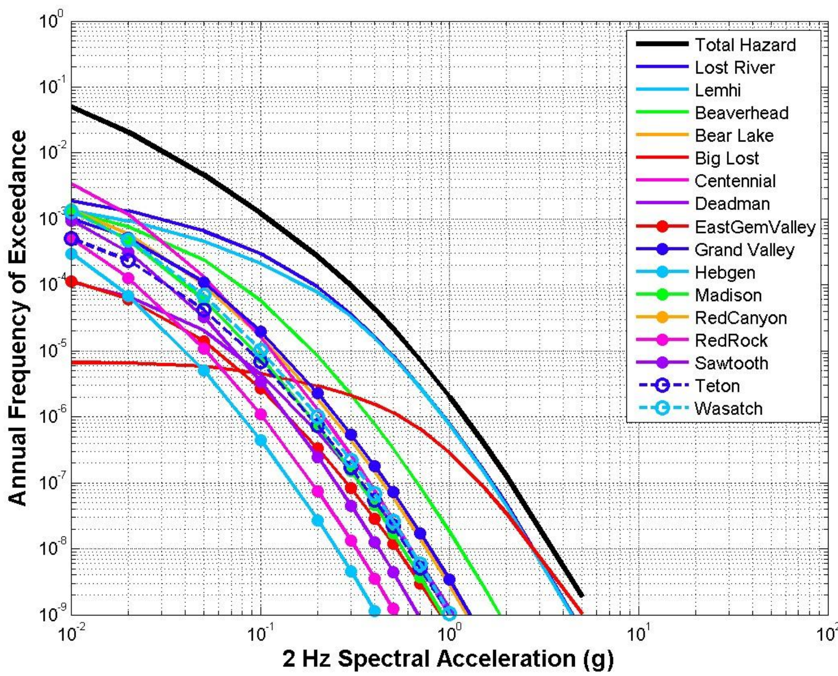

Figure 10-109. Contribution of individual fault sources to the total seismic hazard for reference rock conditions: a) 10 Hz (0.1-sec) spectral acceleration; and b) 2 Hz (0.5-sec) spectral acceleration.

(a)

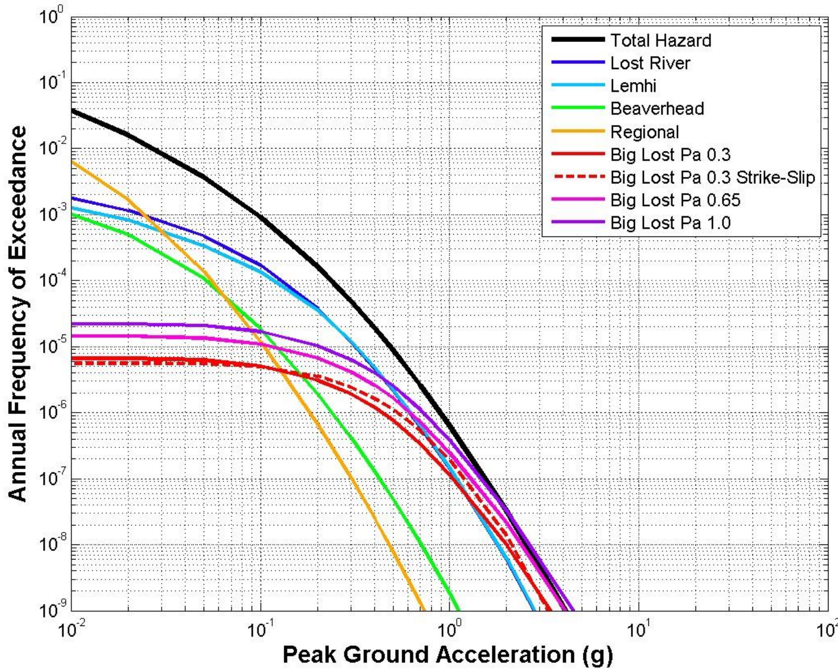

(b)

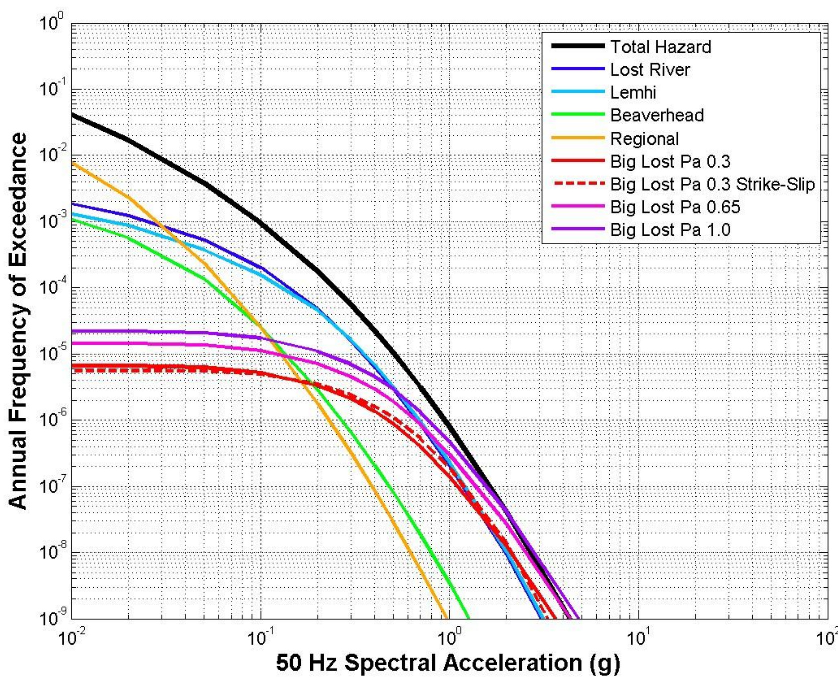

Figure 10-110. Results of sensitivity tests for the Big Lost fault with different seismogenic probabilities and styles of faulting showing the contribution of to the total seismic hazard for reference rock conditions: a) PGA; and b) 50 Hz (0.02-sec) spectral acceleration.

(a)

(b)

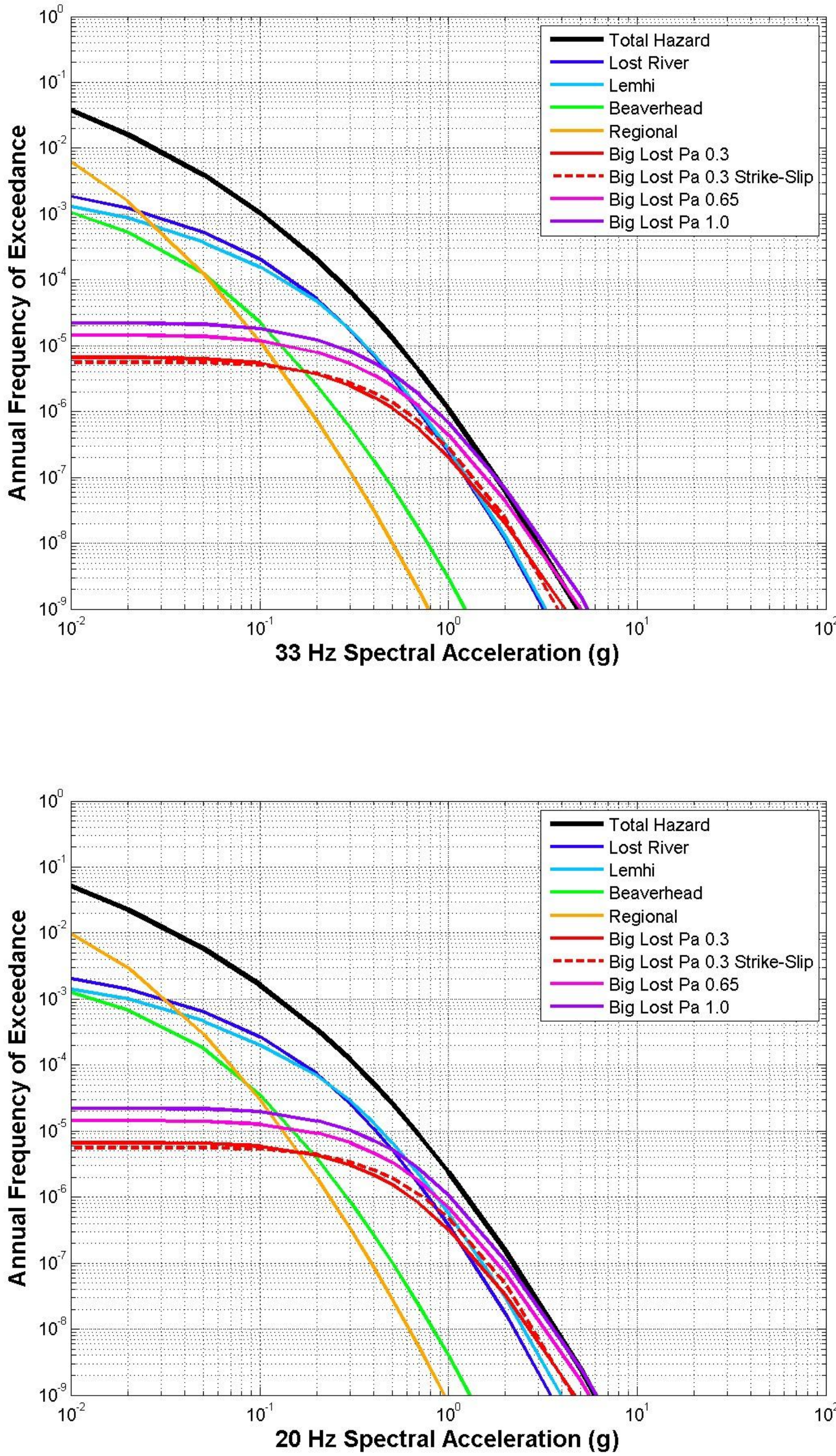

Figure 10-111. Results of sensitivity tests for the Big Lost fault with different seismogenic probabilities and styles of faulting showing the contribution of to the total seismic hazard for reference rock conditions: a) 33 Hz (0.03-sec) spectral acceleration; and b) 20 Hz (0.05-sec) spectral acceleration.

(a)

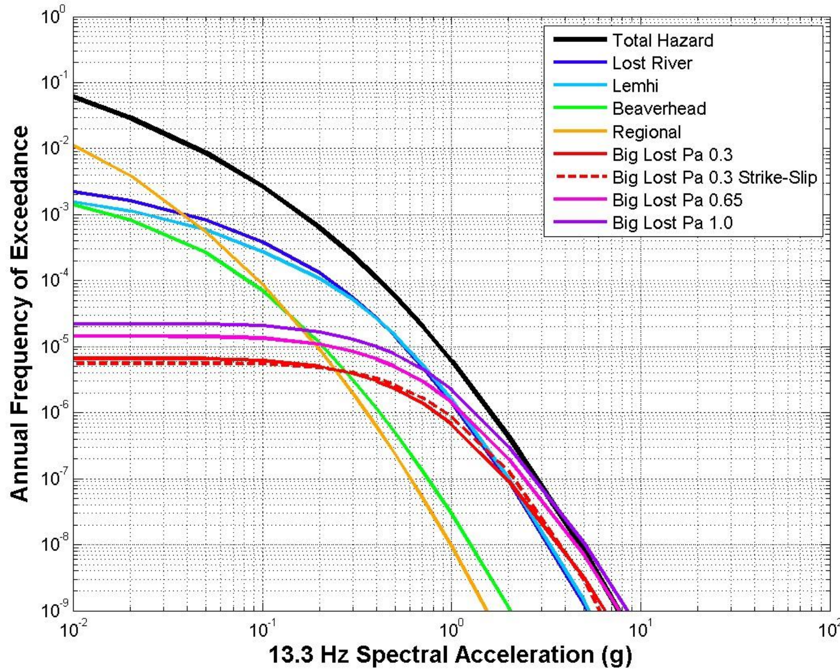

(b)

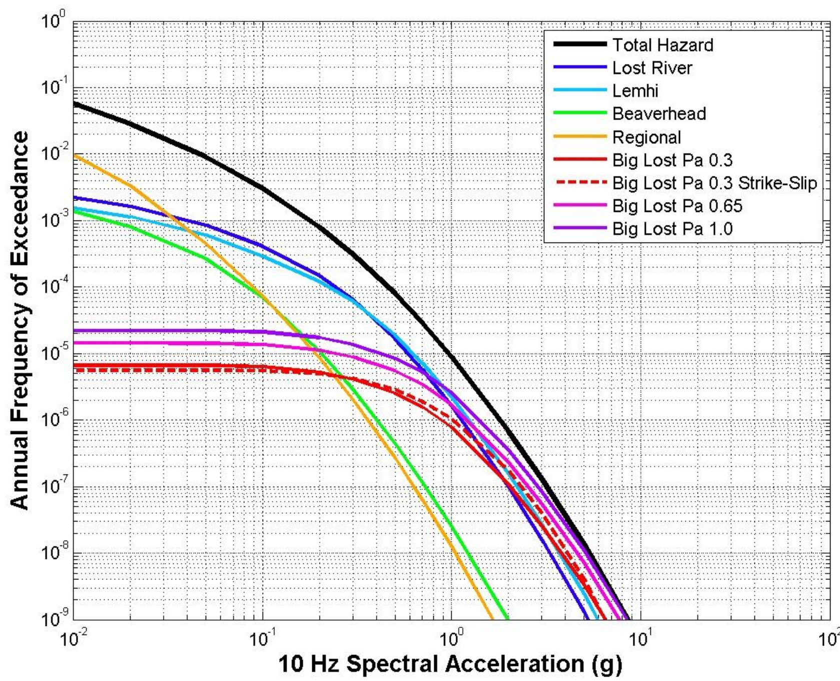

Figure 10-112. Results of sensitivity tests for the Big Lost fault with different seismogenic probabilities and styles of faulting showing the contribution of to the total seismic hazard for reference rock conditions: a) 13.3 Hz (0.075-sec) spectral acceleration; and b) 10 Hz (0.1-sec) spectral acceleration.

(a)

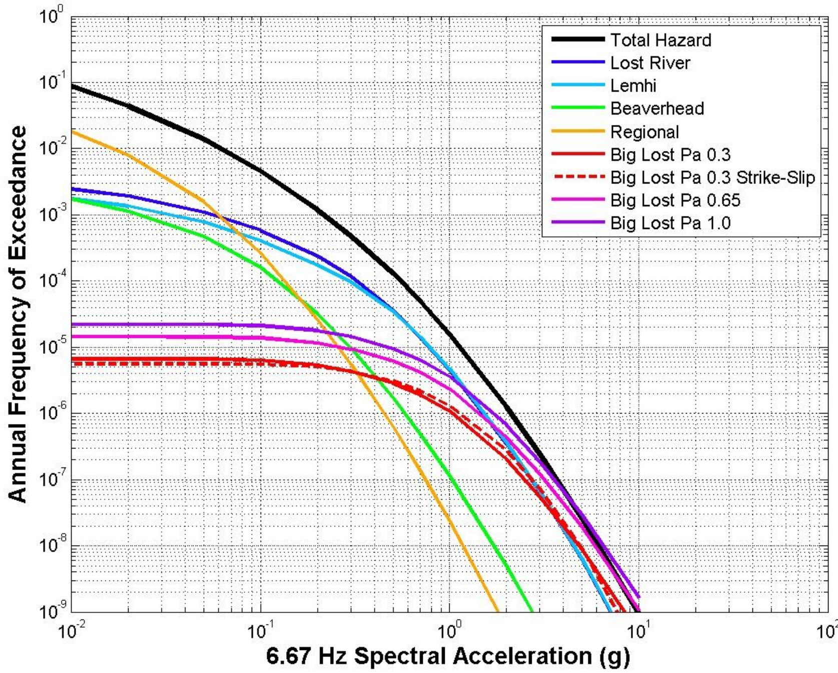

(b)

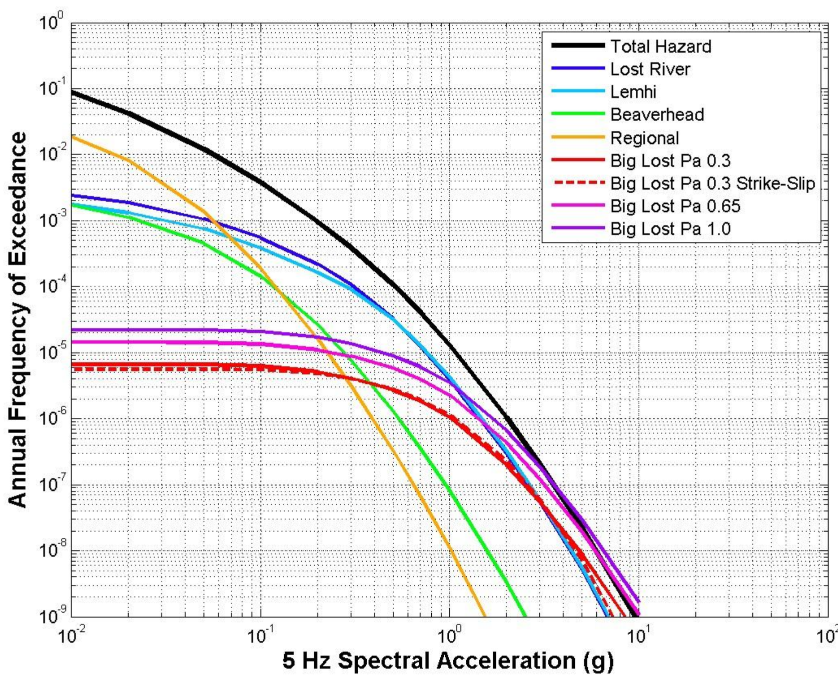

Figure 10-113. Results of sensitivity tests for the Big Lost fault with different seismogenic probabilities and styles of faulting showing the contribution of to the total seismic hazard for reference rock conditions: a) 6.67 Hz (0.15-sec) spectral acceleration; and b) 5 Hz (0.2-sec) spectral acceleration.

(a)

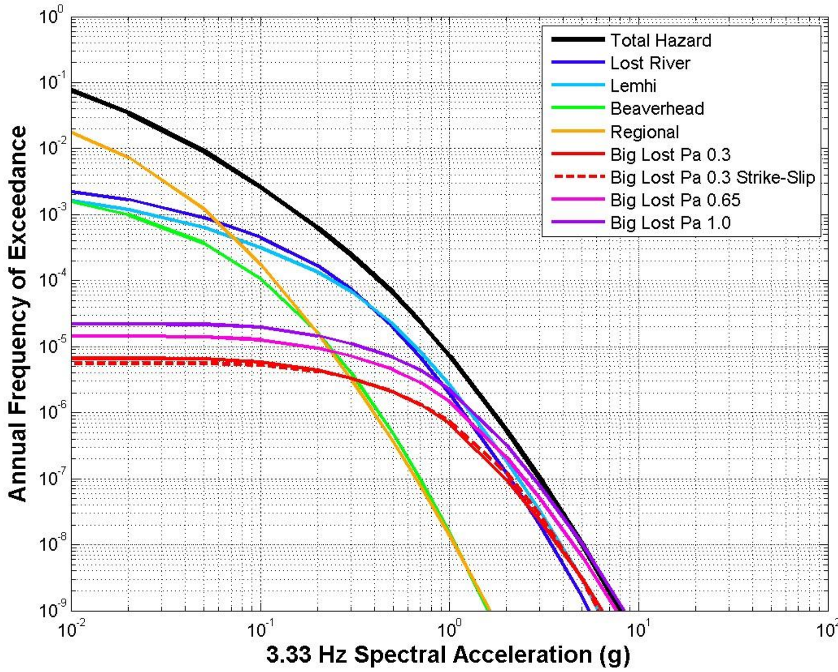

(b)

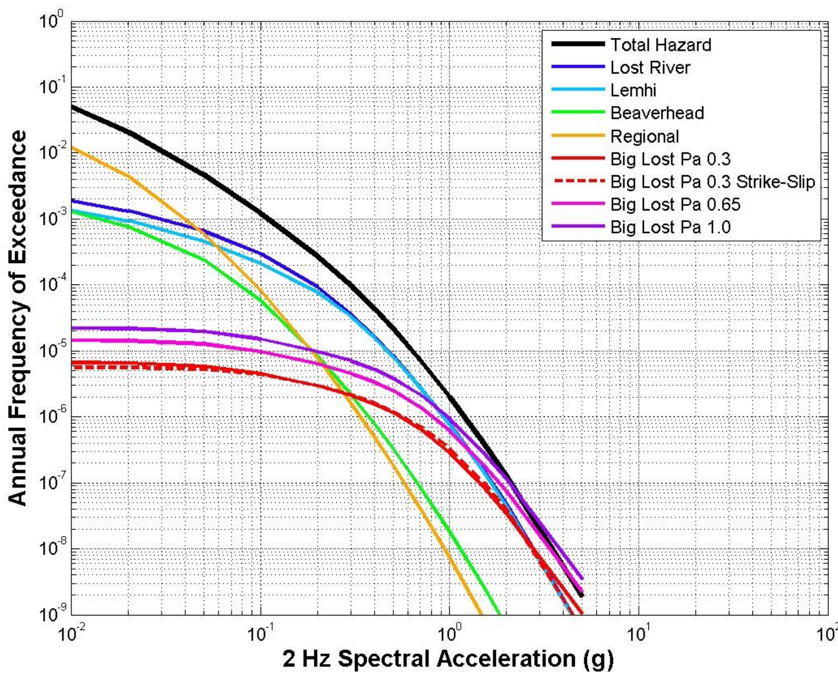

Figure 10-114. Results of sensitivity tests for the Big Lost fault with different seismogenic probabilities and styles of faulting showing the contribution of to the total seismic hazard for reference rock conditions: a) 3.33 Hz (0.3-sec) spectral acceleration; and b) 2 Hz (0.5-sec) spectral acceleration.

(a)

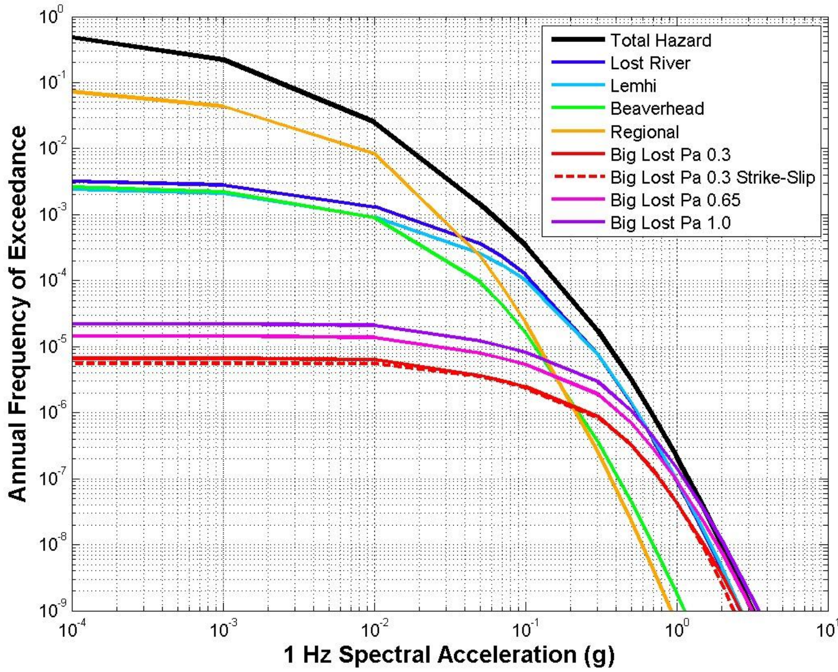

(b)

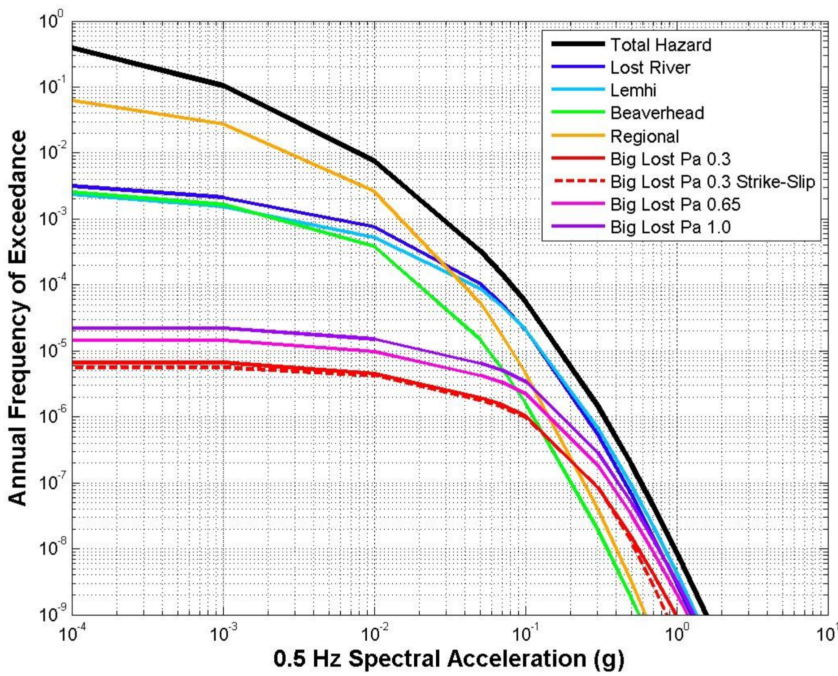

Figure 10-115. Results of sensitivity tests for the Big Lost fault with different seismogenic probabilities and styles of faulting showing the contribution of to the total seismic hazard for reference rock conditions: a) 1 Hz (1-sec) spectral acceleration; and b) 0.5 Hz (2-sec) spectral acceleration.

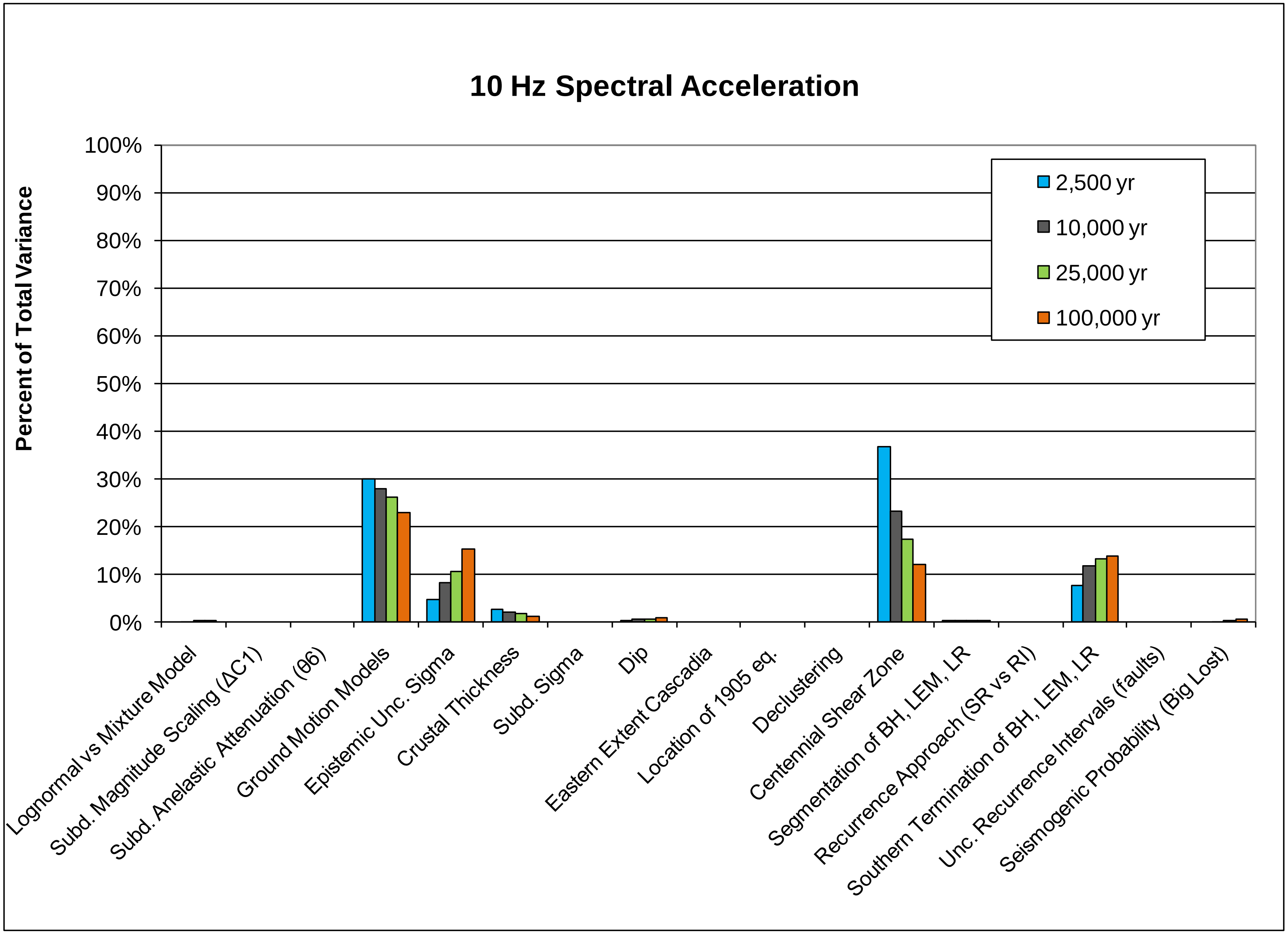

Figure 10-116. Contributions to the variance in the 10 Hz (0.1-sec) hazard for return periods of 2,500, 10,000, 25,000, and 100,000 yr.

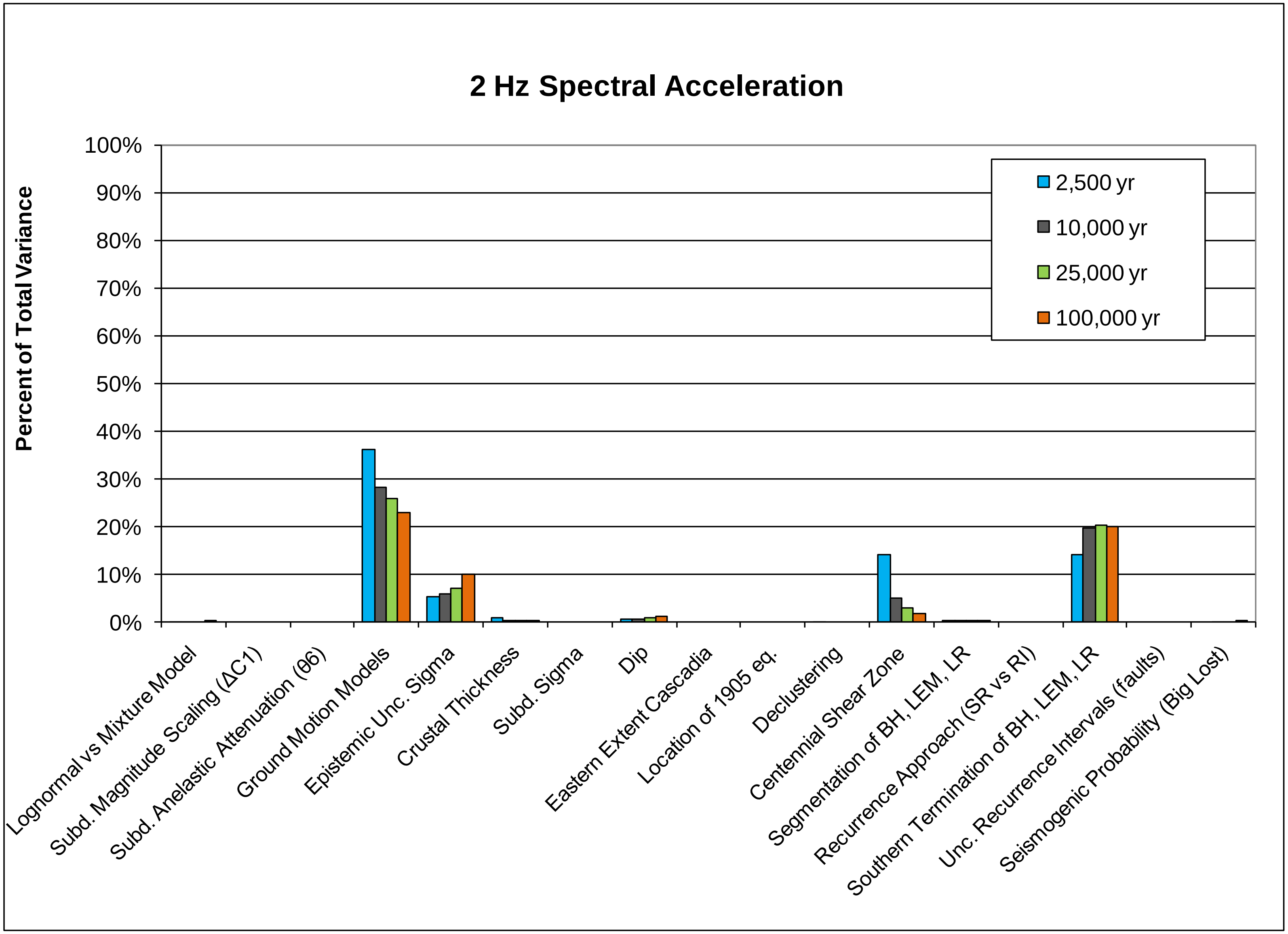

Figure 10-117. Contributions to the variance in the 2 Hz (0.5-sec) hazard for return periods of 2,500, 10,000, 25,000, and 100,000 yr.

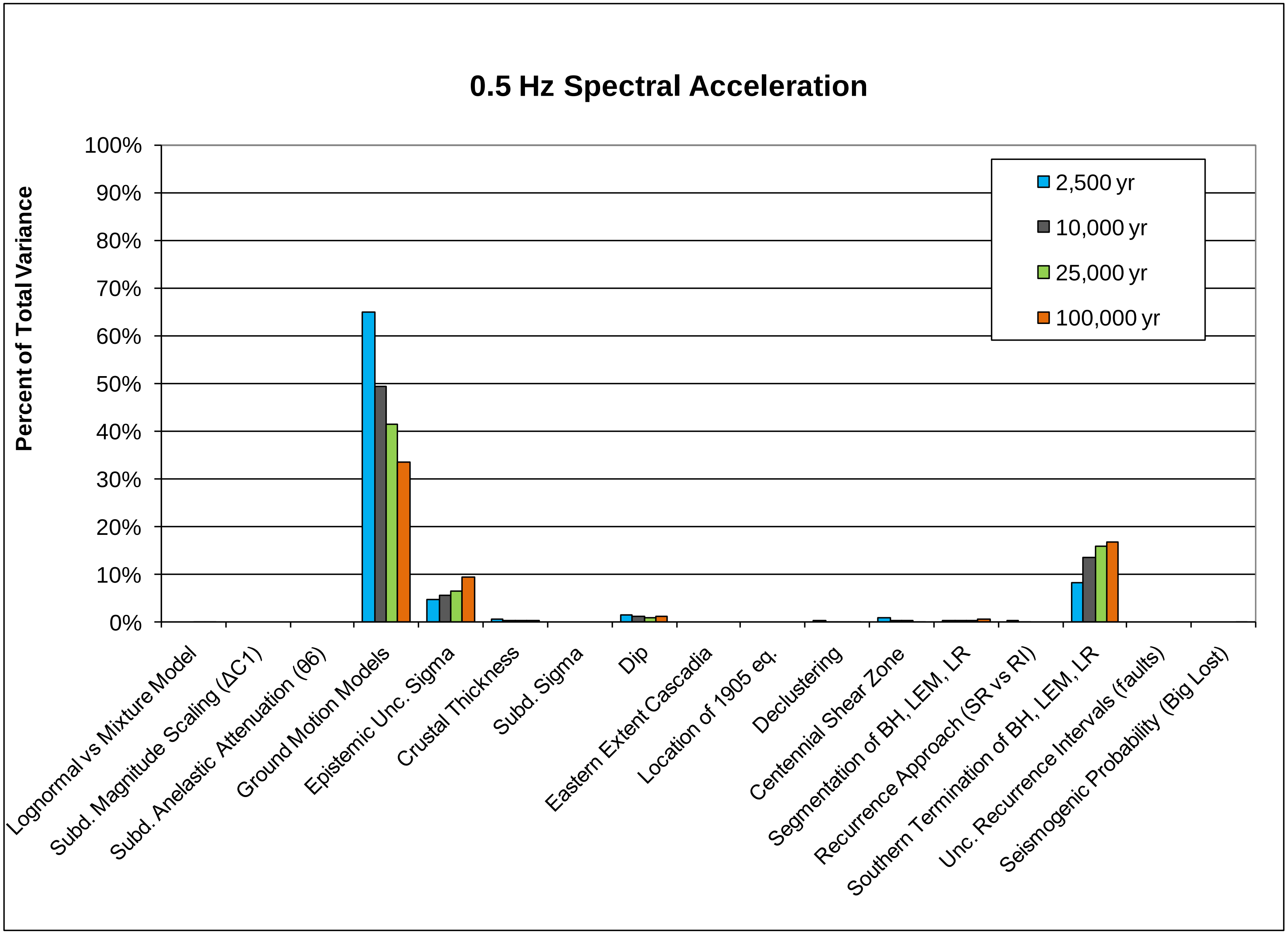

Figure 10-118. Contributions to the variance in the 0.5 Hz (2-sec) hazard for return periods of 2,500, 10,000, 25,000, and 100,000 yr.

10.8 Site-specific Hazard at the ATR Complex

This section presents the site-specific hazard results at the ATR Complex. The section includes comparison of the ATR SSHAC Level 1 PSHA with the 2000 PSHA at ATR for rock site conditions. It also includes the hazard sensitivity to rock and soil sites with respect to the various parameters used to generate alternative site-amplification functions. Comparisons of the GMRS with the DBGMs are also presented for ATR buildings and firewater piping areas classified as SDC-4 per ASCE 43-05 (ASCE, 2005).

10.8.1 Site-specific Rock and Soil Hazard Curves

Figure 10-119 shows the site-specific mean hazard curves for ATR rock conditions (in blue) in comparison with the corresponding site-specific hazard curves calculated in the 2000 INL PSHA study (red curves) by URS Greiner Woodward-Clyde Federal Services et al. (2000). The plots show the results for PGA, 10 Hz and 1 Hz spectral accelerations. For PGA and 1 Hz spectral acceleration, the differences between the results of the SSHAC Level 1 study and 2000 INL PSHA are similar to those shown on Figure 10-23 for the MFC site and are likely caused by the same reasons. For 10 Hz spectral acceleration, the difference between the 2016 SSHAC Level 1 PSHA results and the 2000 INL PSHA results is greater for the ATR site than for the MFC site shown on Figure 10-23. This is likely due the fact that the amplification functions for the MFC rock site show amplifications near or slightly greater than 1 at 10 Hz (Figures 9-14 and 9-15), while those for the ATR rock site show amplifications less than 1 for motions near 10 Hz (Figures 9-75 and 9-76). In the 2000 INL PSHA, differences in site amplification were applied only to the site-specific ground motion models (weighted 0.6) and the empirical rock models (weighted 0.4) were applied to all sites without adjustments.

Figure 10-120 shows the mean and the 5th, 15th, 50th, 85th, and 95th conditional fractiles for 10 Hz and 2 Hz spectral accelerations at ATR for rock site conditions that illustrate the variability introduced in the site-specific hazard by the alternative site amplification functions. The fractiles do not include the uncertainty in the reference condition hazard, and are thus referred to as conditional fractiles. Mean and conditional fractiles are presented for results from two sets of shear-wave velocity profiles: with basalt interbeds at a depth ~40 m, and without the basalt interbeds at ~40 m depth. These two cases are explicitly accounted for because the areal extent of ATR buildings and firewater piping areas covers both site conditions. The mean site-specific hazard curves at ATR for rock site conditions are listed in Tables 10-28 and 10-29; the conditional fractile hazard curves for 10 Hz and 2 Hz are listed in Tables 10-30 and 10-31.

There are three sets of results for ATR soil site conditions: one for a soil thickness of 20 ft., one for a soil thickness of 40 ft., and one for a soil thickness of 60ft. Within each set are two subsets of results, one for shear-wave velocity profiles with basalt interbeds at a depth ~40m, and the other for shear-wave velocity profiles without basalt interbeds at a depth ~40 m. The site-specific hazard curves at ATR soil sites, including conditional fractiles for 10 Hz and 2 Hz are listed in:

- Tables 10-32 through 10-35 for a soil thickness of 20 ft
- Tables 10-36 through 10-39 for a soil thickness of 40 ft
- Tables 10-40 through 10-43 for a soil thickness of 60 ft.

As was the case for ATR rock, the conditional fractiles listed in Tables 10-34, 10-35, 10-38, 10-39, 10-42, and 10-43 represent only the epistemic uncertainty in the transfer function from the SWUS reference profile to the ATR profiles. The mean site-specific hazard curve and its fractiles for 10 Hz and 2 Hz are shown in Figures 10-121, 10-122, and 10-123 for soil thickness of 20, 40, and 60 ft, respectively.

a)

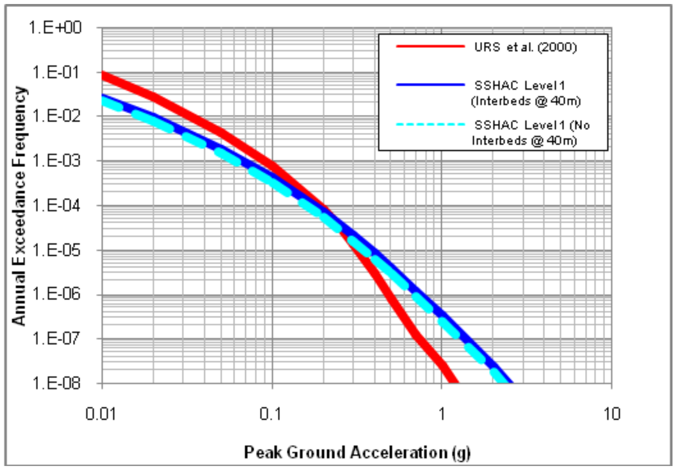

b)

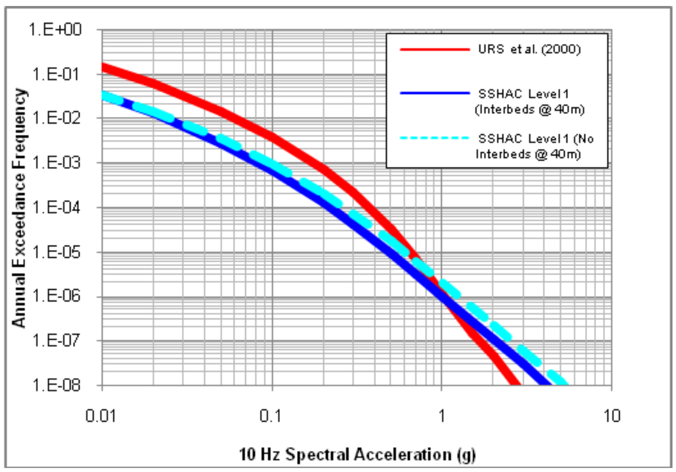

c)

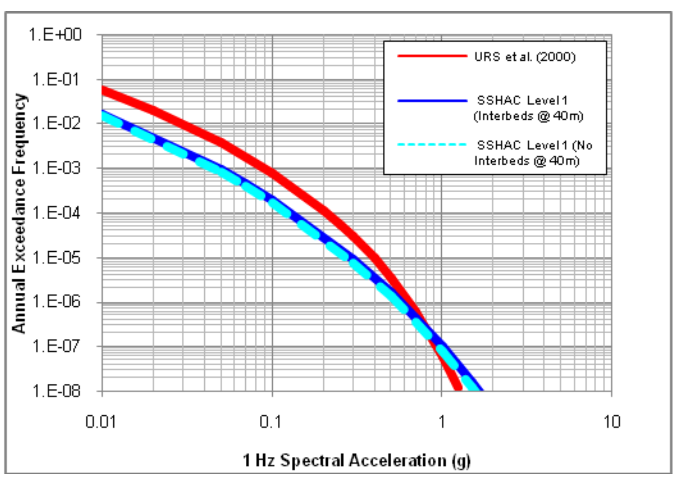

Figure 10-119. Comparison of the mean site-specific hazard curves at ATR for rock conditions obtained in this study (SSHAC Level 1) with the corresponding curves from URS Greiner Woodward Clyde Federal Services et al. (2000) for: a) PGA; b) 10 Hz spectral acceleration; and c) 1 Hz spectral acceleration.

a)

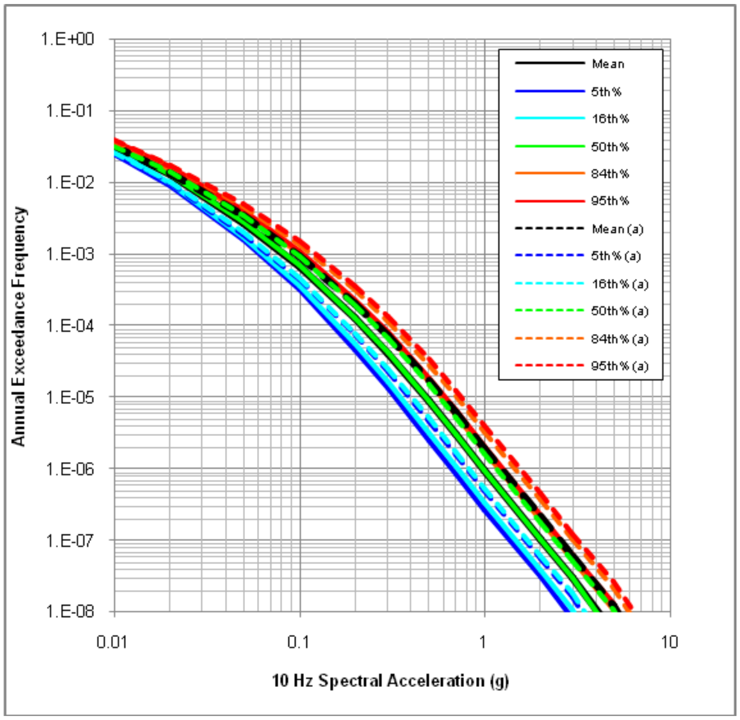

b)

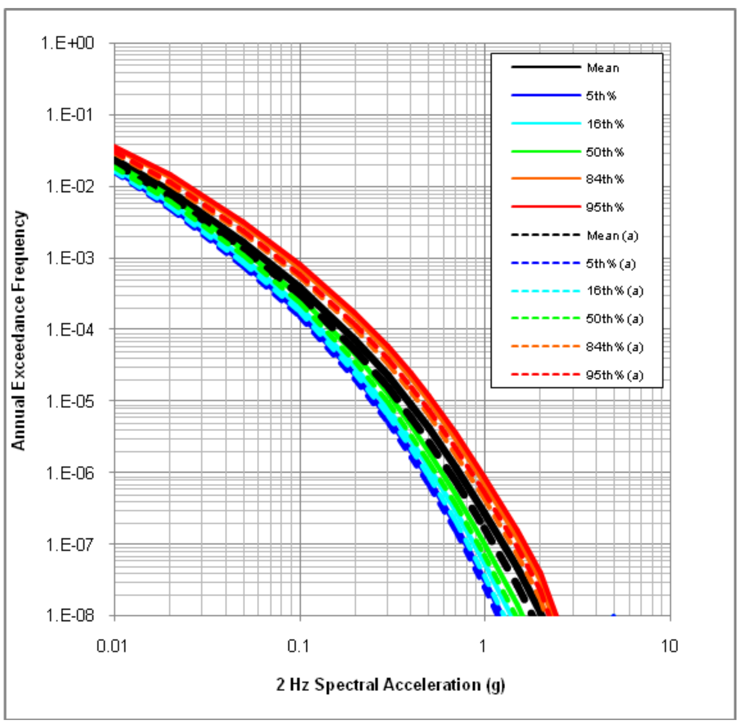

Figure 10-120. Total mean site-specific hazard and conditional fractiles at ATR for rock conditions for: a) 10 Hz spectral acceleration; and b) 2 Hz spectral acceleration. Solid curves represent hazard from profiles with basalt interbeds at ~40 m depth. Dashed curves, labeled (a), represent hazard from profiles without basalt interbeds at ~40 m depth.

Table 10-28. Mean site-specific hazard curves at ATR for rock conditions computed using profiles with basalt interbeds at depth ~ 40 m.

PGA	AEF	50 Hz SA	AEF	33.3 Hz SA	AEF	20 Hz SA	AEF	13.33 Hz SA	AEF	10 Hz SA	AEF	6.67 Hz SA	AEF
0.01	2.55E-02	0.01	2.73E-02	0.01	2.60E-02	0.01	3.64E-02	0.01	4.04E-02	0.01	3.31E-02	0.01	5.53E-02
0.02	9.39E-03	0.02	1.01E-02	0.02	1.04E-02	0.02	1.54E-02	0.02	1.67E-02	0.02	1.31E-02	0.02	2.44E-02
0.05	1.87E-03	0.05	2.10E-03	0.05	2.48E-03	0.05	4.03E-03	0.05	4.15E-03	0.05	2.77E-03	0.05	6.24E-03
0.1	4.19E-04	0.1	5.23E-04	0.1	7.01E-04	0.1	1.22E-03	0.1	1.20E-03	0.1	6.79E-04	0.1	1.71E-03
0.2	7.04E-05	0.2	1.07E-04	0.2	1.66E-04	0.2	3.02E-04	0.2	2.84E-04	0.2	1.28E-04	0.2	3.78E-04
0.3	2.11E-05	0.3	3.75E-05	0.3	6.51E-05	0.3	1.20E-04	0.3	1.09E-04	0.3	4.19E-05	0.3	1.35E-04
0.4	8.37E-06	0.4	1.68E-05	0.4	3.16E-05	0.4	5.83E-05	0.4	5.24E-05	0.5	8.97E-06	0.5	3.13E-05
0.5	3.95E-06	0.5	8.76E-06	0.5	1.74E-05	0.5	3.22E-05	0.5	2.86E-05	0.7	3.06E-06	0.7	1.07E-05
0.7	1.21E-06	0.7	3.09E-06	0.7	6.75E-06	0.7	1.24E-05	0.7	1.09E-05	1	9.67E-07	1	3.24E-06
1	3.24E-07	1	9.61E-07	1	2.31E-06	1	4.27E-06	1	3.66E-06	2	1.06E-07	2	3.11E-07
2	2.38E-08	2	8.52E-08	2	2.48E-07	2	4.87E-07	2	3.83E-07	3	3.03E-08	3	8.46E-08
5	4.74E-10	5	2.87E-09	5	1.12E-08	5	2.74E-08	5	1.98E-08	5	5.23E-09	5	1.92E-08
10	1.05E-11	10	1.13E-10	10	7.86E-10	10	2.58E-09	10	2.00E-09	10	1.07E-10	10	9.88E-10
5 Hz SA	AEF	3.33 Hz SA	AEF	2.50 Hz SA	AEF	2 Hz SA	AEF	1 Hz SA	AEF	0.5 Hz SA	AEF		
0.01	6.82E-02	0.01	5.79E-02	0.01	4.43E-02	0.01	2.48E-02	0.01	4.42E-01	0.0001	3.55E-01		
0.02	3.13E-02	0.02	2.58E-02	0.02	1.82E-02	0.02	8.73E-03	0.02	1.74E-01	0.001	8.88E-02		
0.05	8.46E-03	0.05	6.35E-03	0.05	4.01E-03	0.05	1.70E-03	0.05	1.68E-02	0.01	5.89E-03		
0.1	2.50E-03	0.1	1.77E-03	0.1	1.04E-03	0.1	4.03E-04	0.1	9.26E-04	0.05	2.51E-04		
0.2	6.07E-04	0.2	4.12E-04	0.2	2.23E-04	0.2	7.40E-05	0.2	4.54E-04	0.07	1.11E-04		
0.3	2.33E-04	0.3	1.56E-04	0.3	7.94E-05	0.3	2.29E-05	0.3	1.93E-04	0.1	4.18E-05		
0.5	5.87E-05	0.5	3.79E-05	0.5	3.51E-05	0.5	9.11E-06	0.4	9.09E-06	0.3	1.17E-06		
0.7	2.08E-05	0.7	1.31E-05	0.7	1.76E-05	0.7	4.22E-06	0.5	1.57E-06	0.5	1.66E-07		
1	6.17E-06	1	3.78E-06	1	5.69E-06	1	1.21E-06	0.7	4.33E-07	0.7	4.10E-08		
2	4.69E-07	2	2.46E-07	2	1.50E-06	2	2.85E-07	1	9.82E-08	1	8.36E-09		
3	1.02E-07	3	4.32E-08	3	7.78E-08	3	4.69E-08	1.5	1.56E-08	1.5	1.22E-09		
5	1.97E-08	5	4.84E-09	5	8.05E-10	5	1.12E-08	2	3.74E-09	2	2.89E-10		
10	1.22E-09	10	1.61E-10	10	7.43E-12	10	1.21E-11	5	1.72E-11	5	1.72E-12		

PGA- Peak Ground Acceleration (g); AEF – Annual Exceedance Frequency; SA – Spectral Acceleration (g).

Table 10-29. Mean site-specific hazard curves at ATR for rock conditions computed using profiles without basalt interbeds at depth ~ 40 m.

PGA	AEF	50 Hz SA	AEF	33.3 Hz SA	AEF	20 Hz SA	AEF	13.3 Hz SA	AEF	10 Hz SA	AEF	6.67 Hz SA	AEF
0.01	2.21E-02	0.01	2.38E-02	0.01	2.29E-02	0.01	3.24E-02	0.01	3.79E-02	0.01	3.30E-02	0.01	4.99E-02
0.02	7.78E-03	0.02	8.48E-03	0.02	8.95E-03	0.02	1.34E-02	0.02	1.61E-02	0.02	1.40E-02	0.02	2.15E-02
0.05	1.49E-03	0.05	1.71E-03	0.05	2.12E-03	0.05	3.50E-03	0.05	4.20E-03	0.05	3.47E-03	0.05	5.36E-03
0.1	3.25E-04	0.1	4.25E-04	0.1	6.08E-04	0.1	1.05E-03	0.1	1.23E-03	0.1	9.57E-04	0.1	1.45E-03
0.2	5.34E-05	0.2	8.68E-05	0.2	1.46E-04	0.2	2.55E-04	0.2	2.88E-04	0.2	2.08E-04	0.2	3.13E-04
0.3	1.58E-05	0.3	3.02E-05	0.3	5.74E-05	0.3	9.96E-05	0.3	1.08E-04	0.3	7.34E-05	0.3	1.10E-04
0.4	6.20E-06	0.4	1.35E-05	0.4	2.79E-05	0.4	4.77E-05	0.4	5.06E-05	0.5	1.72E-05	0.4	2.50E-05
0.5	2.91E-06	0.5	6.99E-06	0.5	1.54E-05	0.5	2.60E-05	0.5	2.70E-05	0.7	6.15E-06	0.5	8.49E-06
0.7	8.82E-07	0.7	2.44E-06	0.7	5.94E-06	0.7	9.88E-06	0.7	9.88E-06	1	1.98E-06	0.7	2.56E-06
1	2.36E-07	1	7.51E-07	1	2.03E-06	1	3.36E-06	1	3.18E-06	2	2.16E-07	1	2.47E-07
2	1.74E-08	2	6.53E-08	2	2.16E-07	2	3.78E-07	2	3.18E-07	3	6.07E-08	2	6.87E-08
5	3.15E-10	5	2.14E-09	5	9.74E-09	5	2.14E-08	5	1.79E-08	5	1.22E-08	5	1.54E-08
10	6.17E-12	10	7.43E-11	10	6.52E-10	10	1.85E-09	10	1.50E-09	10	5.71E-10	10	6.66E-10
5 Hz SA	AEF	3.33 Hz SA	AEF	2.5 Hz SA	AEF	2 Hz SA	AEF	1 Hz SA	AEF	0.5 Hz SA	AEF		
0.01	5.14E-02	0.01	4.43E-02	0.01	3.72E-02	0.01	2.16E-02	0.01	4.36E-01	0.0001	3.54E-01		
0.02	2.14E-02	0.02	1.76E-02	0.02	1.40E-02	0.02	7.33E-03	0.02	1.68E-01	0.001	8.85E-02		
0.05	5.15E-03	0.05	3.89E-03	0.05	2.88E-03	0.05	1.36E-03	0.05	1.57E-02	0.01	5.84E-03		
0.1	1.40E-03	0.1	1.01E-03	0.1	7.10E-04	0.1	3.09E-04	0.1	8.41E-04	0.05	2.45E-04		
0.2	3.07E-04	0.2	2.13E-04	0.2	1.43E-04	0.2	5.30E-05	0.2	4.08E-04	0.07	1.08E-04		
0.3	1.09E-04	0.3	7.42E-05	0.3	4.78E-05	0.3	1.57E-05	0.3	1.70E-04	0.1	4.04E-05		
0.5	2.45E-05	0.5	1.61E-05	0.4	2.01E-05	0.5	6.03E-06	0.4	7.70E-06	0.3	1.11E-06		
0.7	8.02E-06	0.7	5.15E-06	0.5	9.71E-06	0.7	2.72E-06	0.5	1.30E-06	0.5	1.58E-07		
1	2.23E-06	1	1.36E-06	0.7	2.94E-06	1	7.54E-07	0.7	3.52E-07	0.7	3.88E-08		
2	1.64E-07	2	8.05E-08	1	7.26E-07	2	1.71E-07	1	7.85E-08	1	7.88E-09		
3	3.99E-08	3	1.40E-08	2	3.31E-08	3	2.66E-08	1.5	1.21E-08	1.5	1.15E-09		
5	7.80E-09	5	1.58E-09	5	3.13E-10	5	5.98E-09	2	2.88E-09	2	2.70E-10		
10	2.08E-10	10	2.23E-11	10	1.07E-12	10	5.11E-12	5	1.25E-11	5	1.60E-12		

PGA- Peak Ground Acceleration (g); AEF – Annual Exceedance Frequency; SA – Spectral Acceleration (g).

Table 10-30. Site-specific hazard conditional fractiles at ATR for rock conditions computed using profiles with basalt interbeds at depth ~40 m for 2 Hz and 10 Hz.

Spectral Acceleration (g)	ATR Rock (with basalt interbeds at depth ~ 40m) Annual Exceedance Frequency at Fractiles				
	5th	16th	50th	84th	95th
10 Hz					
0.01	2.55E-02	2.84E-02	3.37E-02	3.76E-02	3.86E-02
0.02	9.04E-03	1.00E-02	1.33E-02	1.57E-02	1.67E-02
0.05	1.58E-03	1.72E-03	2.87E-03	3.85E-03	4.07E-03
0.10	3.26E-04	3.69E-04	7.14E-04	1.02E-03	1.12E-03
0.20	4.74E-05	5.71E-05	1.32E-04	2.12E-04	2.36E-04
0.30	1.35E-05	1.68E-05	4.30E-05	7.27E-05	8.22E-05
0.40	2.52E-06	3.24E-06	9.01E-06	1.64E-05	1.89E-05
0.50	8.52E-07	1.07E-06	3.01E-06	5.68E-06	6.65E-06
0.70	2.65E-07	3.39E-07	9.58E-07	1.79E-06	2.11E-06
1.00	3.19E-08	3.88E-08	1.04E-07	1.94E-07	2.29E-07
2.00	8.25E-09	1.07E-08	3.01E-08	5.48E-08	6.47E-08
5.00	6.14E-10	1.08E-09	4.65E-09	1.10E-08	1.35E-08
10.00	1.43E-20	1.62E-14	3.16E-11	2.53E-10	5.53E-10
2 Hz					
0.01	1.73E-02	1.88E-02	2.16E-02	3.54E-02	3.74E-02
0.02	5.35E-03	6.05E-03	7.26E-03	1.38E-02	1.49E-02
0.05	8.66E-04	1.03E-03	1.32E-03	2.94E-03	3.22E-03
0.10	1.77E-04	2.17E-04	2.94E-04	7.45E-04	8.28E-04
0.20	2.43E-05	3.14E-05	4.70E-05	1.52E-04	1.73E-04
0.30	6.01E-06	8.07E-06	1.29E-05	5.06E-05	5.87E-05
0.50	2.02E-06	2.78E-06	4.63E-06	2.10E-05	2.47E-05
0.70	8.17E-07	1.17E-06	1.98E-06	1.00E-05	1.19E-05
1.00	1.90E-07	2.88E-07	5.01E-07	2.98E-06	3.62E-06
2.00	3.32E-08	5.67E-08	1.05E-07	7.31E-07	9.06E-07
3.00	3.77E-09	7.04E-09	1.43E-08	1.26E-07	1.60E-07
5.00	8.52E-11	8.79E-10	2.76E-09	3.14E-08	4.08E-08
10.00	0.00E+00	0.00E+00	2.08E-14	2.21E-11	6.58E-11

Table 10-31. Site-specific hazard conditional fractiles at ATR for rock conditions computed using profiles without basalt interbeds at depth ~40 m for 2 Hz and 10 Hz.

Spectral Acceleration (g)	ATR Rock (without basalt interbeds at depth ~40 m) Annual Exceedance Frequency at Fractiles				
	5th	16th	50th	84th	95th
10 Hz					
0.01	2.56E-02	2.70E-02	3.31E-02	3.78E-02	3.99E-02
0.02	9.94E-03	1.02E-02	1.41E-02	1.72E-02	1.78E-02
0.05	1.90E-03	2.03E-03	3.53E-03	4.73E-03	5.05E-03
0.10	4.44E-04	4.73E-04	9.37E-04	1.37E-03	1.53E-03
0.20	7.54E-05	8.08E-05	1.96E-04	3.19E-04	3.69E-04
0.30	2.32E-05	2.52E-05	6.74E-05	1.17E-04	1.38E-04
0.40	4.67E-06	5.13E-06	1.51E-05	2.85E-05	3.44E-05
0.50	1.57E-06	1.72E-06	5.27E-06	1.04E-05	1.27E-05
0.70	5.01E-07	5.50E-07	1.66E-06	3.37E-06	4.15E-06
1.00	5.55E-08	6.18E-08	1.82E-07	3.70E-07	4.54E-07
2.00	1.61E-08	1.84E-08	5.24E-08	1.03E-07	1.25E-07
5.00	1.86E-09	2.35E-09	1.06E-08	2.22E-08	2.70E-08
10.00	2.92E-12	9.27E-12	3.22E-10	1.30E-09	1.81E-09
2 Hz					
0.01	1.60E-02	1.68E-02	1.93E-02	2.96E-02	3.13E-02
0.02	4.93E-03	5.35E-03	6.17E-03	1.09E-02	1.18E-02
0.05	7.76E-04	8.81E-04	1.10E-03	2.22E-03	2.44E-03
0.10	1.55E-04	1.83E-04	2.40E-04	5.41E-04	6.05E-04
0.20	2.04E-05	2.55E-05	3.63E-05	1.05E-04	1.20E-04
0.30	4.95E-06	6.40E-06	9.60E-06	3.34E-05	3.92E-05
0.50	1.64E-06	2.17E-06	3.38E-06	1.35E-05	1.60E-05
0.70	6.56E-07	8.87E-07	1.42E-06	6.32E-06	7.56E-06
1.00	1.50E-07	2.08E-07	3.62E-07	1.83E-06	2.22E-06
2.00	2.54E-08	3.74E-08	7.32E-08	4.35E-07	5.39E-07
3.00	2.60E-09	4.25E-09	9.07E-09	7.16E-08	9.13E-08
5.00	3.52E-11	2.04E-10	1.51E-09	1.74E-08	2.26E-08
10.00	0.00E+00	0.00E+00	4.62E-14	1.28E-11	2.45E-11

a)

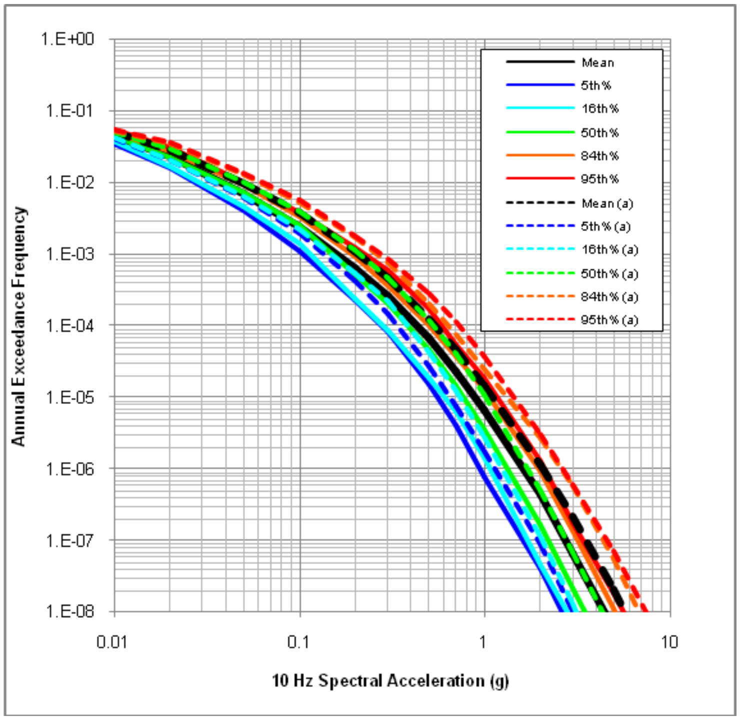

b)

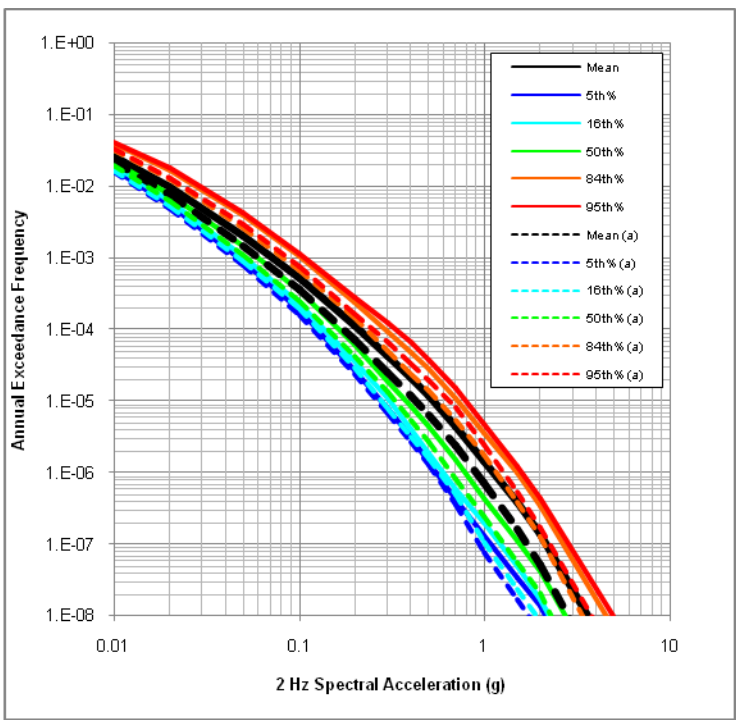

Figure 10-121. Total mean site-specific hazard and conditional fractiles at ATR, assuming a soil thickness of 20 ft, for: a) 10 Hz spectral acceleration; and b) 2 Hz spectral acceleration.Solid curves represent hazard from profiles with basalt interbeds at depth ~40 m. Dashed curves, labeled (a), represent hazard from profiles without basalt interbeds at depth ~40 m.

a)

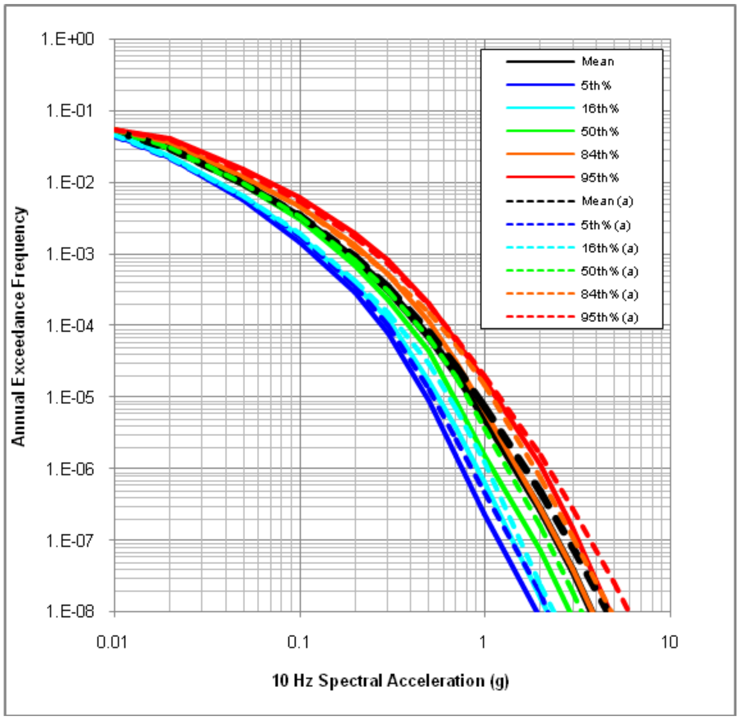

b)

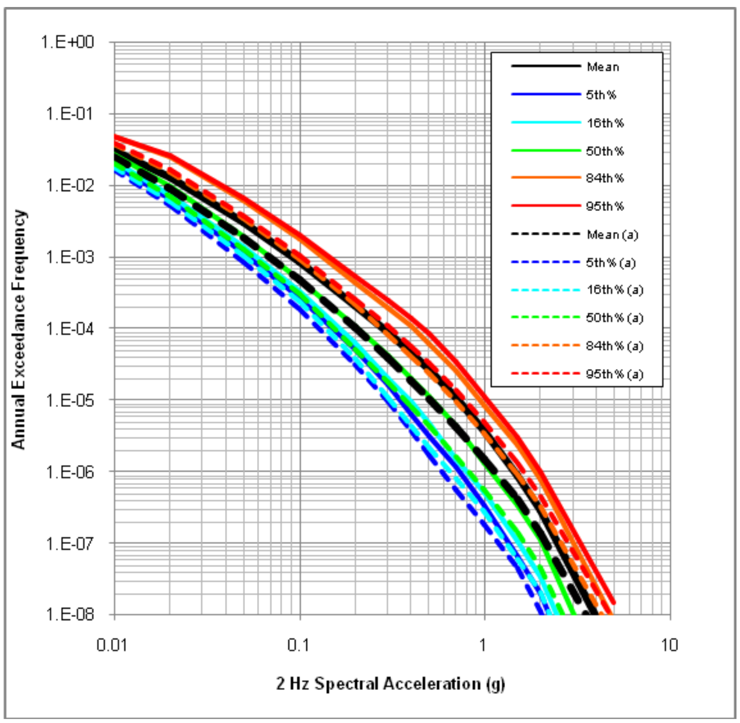

Figure 10-122. Total mean site-specific hazard and conditional fractiles at ATR, assuming a soil thickness of 40 ft, for: a) 10 Hz spectral acceleration; and b) 2 Hz spectral acceleration. Solid curves represent hazard from profiles with basalt interbeds at depth ~ 40 m. Dashed curves, labeled (a), represent hazard from profiles without basalt interbeds at depth ~ 40 m.

a)

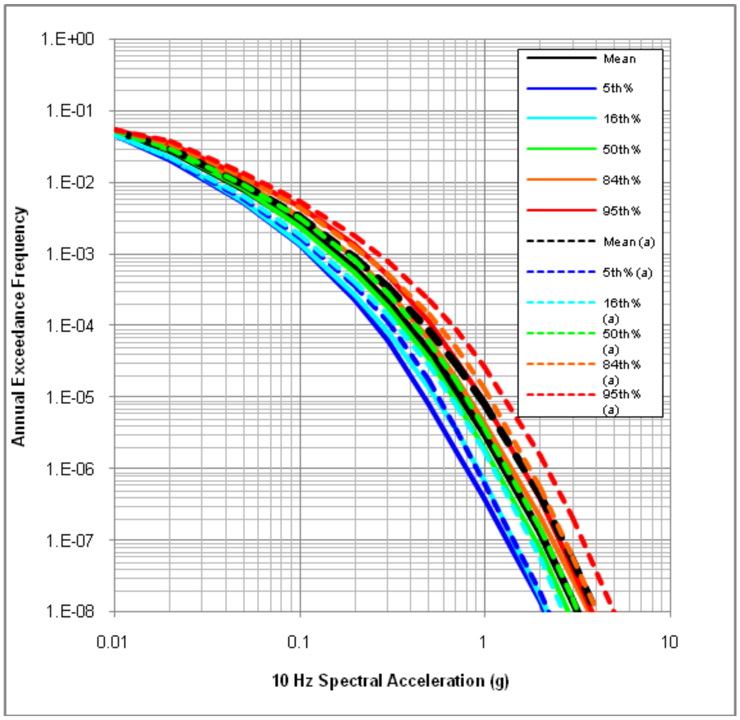

b)

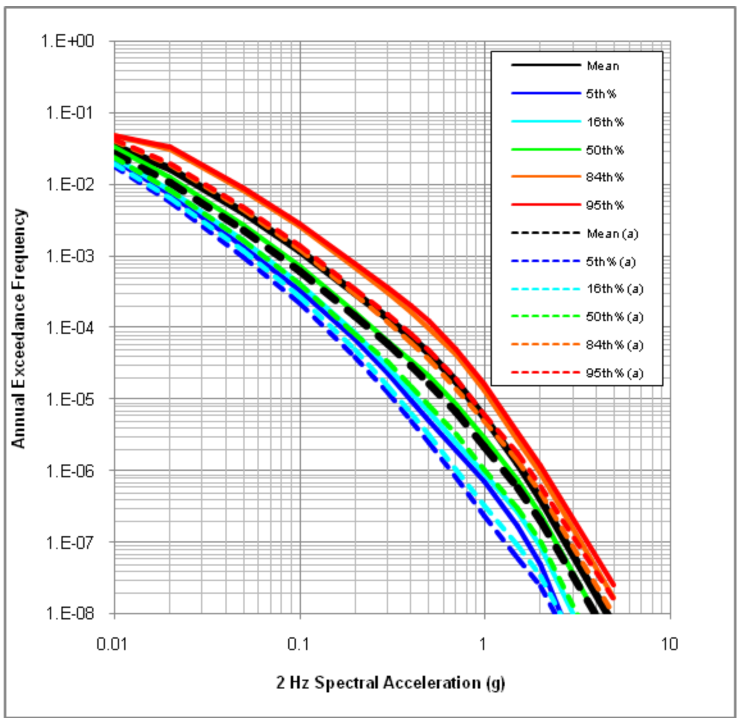

Figure 10-123. Total mean site-specific hazard and conditional fractiles at ATR, assuming a soil thickness of 60 ft, for: a) 10 Hz spectral acceleration; and b) 2 Hz spectral acceleration.Solid curves represent hazard from profiles with basalt interbeds at depth ~ 40 m. Dashed curves, labeled (a), represent hazard from profiles without basalt interbeds at depth ~ 40 m.

Table 10-32. Mean site-specific hazard curves at ATR assuming 20 ft soil thickness computed using profiles with basalt interbeds at depth ~ 40 m.

PGA	AEF	50 Hz SA	AEF	33.3 Hz SA	AEF	20 Hz SA	AEF	13.33 Hz SA	AEF	10 Hz SA	AEF	6.67 Hz SA	AEF
0.01	3.00E-02	0.01	3.22E-02	0.01	3.04E-02	0.01	4.27E-02	0.01	5.24E-02	0.01	4.58E-02	0.01	6.76E-02
0.02	1.27E-02	0.02	1.38E-02	0.02	1.38E-02	0.02	2.00E-02	0.02	2.68E-02	0.02	2.33E-02	0.02	3.41E-02
0.05	3.11E-03	0.05	3.46E-03	0.05	3.86E-03	0.05	5.94E-03	0.05	8.55E-03	0.05	7.22E-03	0.05	1.07E-02
0.1	8.15E-04	0.1	9.70E-04	0.1	1.22E-03	0.1	1.98E-03	0.1	2.99E-03	0.1	2.43E-03	0.1	3.63E-03
0.2	1.50E-04	0.2	2.01E-04	0.2	2.87E-04	0.2	4.80E-04	0.2	7.68E-04	0.2	6.46E-04	0.2	1.02E-03
0.3	4.53E-05	0.3	6.69E-05	0.3	1.02E-04	0.3	1.76E-04	0.3	2.84E-04	0.3	2.59E-04	0.3	4.31E-04
0.4	1.68E-05	0.4	2.65E-05	0.4	4.40E-05	0.4	7.87E-05	0.4	1.26E-04	0.5	6.61E-05	0.4	1.22E-04
0.5	7.30E-06	0.5	1.21E-05	0.5	2.10E-05	0.5	3.97E-05	0.5	6.32E-05	0.7	2.31E-05	0.5	4.71E-05
0.7	1.88E-06	0.7	3.37E-06	0.7	6.28E-06	0.7	1.28E-05	0.7	1.98E-05	1	6.77E-06	0.7	1.49E-05
1	3.88E-07	1	7.46E-07	1	1.54E-06	1	3.49E-06	1	5.05E-06	2	4.38E-07	1	1.13E-06
2	1.48E-08	2	2.91E-08	2	7.10E-08	2	2.20E-07	2	2.71E-07	3	6.58E-08	2	2.27E-07
5	1.57E-10	5	2.44E-10	5	6.31E-10	5	3.27E-09	5	3.14E-09	5	5.78E-09	5	2.57E-08
10	1.63E-12	10	3.01E-12	10	8.03E-12	10	5.89E-11	10	3.92E-11	10	1.25E-10	10	9.16E-10
5 Hz SA	AEF	3.33 Hz SA	AEF	2.5 Hz SA	AEF	2 Hz SA	AEF	1 Hz SA	AEF	0.5 Hz SA	AEF		
0.01	7.60E-02	0.01	6.31E-02	0.01	4.71E-02	0.01	2.68E-02	0.0001	4.43E-01	0.0001	3.55E-01		
0.02	3.80E-02	0.02	3.07E-02	0.02	2.04E-02	0.02	9.96E-03	0.001	1.75E-01	0.001	8.91E-02		
0.05	1.13E-02	0.05	8.09E-03	0.05	4.72E-03	0.05	2.06E-03	0.01	1.71E-02	0.01	5.92E-03		
0.1	3.74E-03	0.1	2.43E-03	0.1	1.29E-03	0.1	5.25E-04	0.05	9.57E-04	0.05	2.58E-04		
0.2	1.06E-03	0.2	6.30E-04	0.2	3.06E-04	0.2	1.14E-04	0.07	4.74E-04	0.07	1.15E-04		
0.3	4.61E-04	0.3	2.69E-04	0.3	1.23E-04	0.3	4.33E-05	0.1	2.05E-04	0.1	4.41E-05		
0.5	1.39E-04	0.5	8.02E-05	0.4	6.12E-05	0.4	2.11E-05	0.3	1.10E-05	0.3	1.43E-06		
0.7	5.70E-05	0.7	3.23E-05	0.5	3.45E-05	0.5	1.17E-05	0.5	2.43E-06	0.5	2.50E-07		
1	1.97E-05	1	1.08E-05	0.7	1.35E-05	0.7	4.50E-06	0.7	8.91E-07	0.7	7.49E-08		
2	1.64E-06	2	9.67E-07	1	4.35E-06	1	1.48E-06	1	3.06E-07	1	1.93E-08		
3	3.03E-07	3	1.91E-07	2	3.16E-07	1.5	3.90E-07	1.5	8.74E-08	1.5	3.69E-09		
5	3.09E-08	5	1.79E-08	5	5.58E-09	2	1.41E-07	2	3.36E-08	2	1.04E-09		
10	1.42E-09	10	4.74E-10	10	1.52E-10	5	2.44E-09	5	9.84E-10	5	1.05E-11		

PGA- Peak Ground Acceleration (g); AEF – Annual Exceedance Frequency; SA – Spectral Acceleration (g).

Table 10-33. Mean site-specific hazard curves at ATR assuming 20 ft soil thickness computed using profiles without basalt interbeds at depth ~40 m.

PGA	AEF	50 Hz SA	AEF	33.3 Hz SA	AEF	20 Hz SA	AEF	13.33 Hz SA	AEF	10 Hz SA	AEF	6.77 Hz SA	AEF
0.01	2.87E-02	0.01	3.09E-02	0.01	2.93E-02	0.01	4.16E-02	0.01	5.35E-02	0.01	5.02E-02	0.01	7.00E-02
0.02	1.24E-02	0.02	1.35E-02	0.02	1.35E-02	0.02	1.98E-02	0.02	2.86E-02	0.02	2.89E-02	0.02	3.69E-02
0.05	3.20E-03	0.05	3.57E-03	0.05	3.99E-03	0.05	6.09E-03	0.05	9.66E-03	0.05	1.00E-02	0.05	1.22E-02
0.1	8.66E-04	0.1	1.04E-03	0.1	1.31E-03	0.1	2.11E-03	0.1	3.57E-03	0.1	3.78E-03	0.1	4.43E-03
0.2	1.63E-04	0.2	2.23E-04	0.2	3.17E-04	0.2	5.37E-04	0.2	9.61E-04	0.2	1.11E-03	0.2	1.35E-03
0.3	4.91E-05	0.3	7.57E-05	0.3	1.14E-04	0.3	2.03E-04	0.3	3.68E-04	0.3	4.58E-04	0.3	5.92E-04
0.4	1.80E-05	0.4	3.02E-05	0.4	4.98E-05	0.4	9.18E-05	0.4	1.70E-04	0.5	1.24E-04	0.4	1.73E-04
0.5	7.56E-06	0.5	1.37E-05	0.5	2.40E-05	0.5	4.64E-05	0.5	8.72E-05	0.7	4.60E-05	0.5	6.81E-05
0.7	1.94E-06	0.7	3.73E-06	0.7	7.12E-06	0.7	1.47E-05	0.7	2.84E-05	1	1.45E-05	0.7	2.25E-05
1	4.32E-07	1	8.70E-07	1	1.78E-06	1	3.88E-06	1	7.39E-06	2	1.15E-06	1	2.07E-06
2	1.34E-08	2	3.35E-08	2	9.38E-08	2	2.56E-07	2	4.07E-07	3	2.16E-07	2	4.83E-07
5	1.03E-10	5	1.71E-10	5	7.71E-10	5	3.70E-09	5	4.90E-09	5	2.10E-08	5	6.51E-08
10	8.44E-13	10	1.82E-12	10	9.16E-12	10	6.24E-11	10	5.50E-11	10	5.42E-10	10	2.54E-09
5 Hz SA	AEF	3.33 Hz SA	AEF	2.5 Hz SA	AEF	2 Hz SA	AEF	1 Hz SA	AEF	0.5 Hz SA	AEF		
0.01	6.47E-02	0.01	5.15E-02	0.01	3.94E-02	0.01	2.25E-02	0.0001	4.40E-01	0.0001	3.52E-01		
0.02	2.98E-02	0.02	2.17E-02	0.02	1.51E-02	0.02	7.79E-03	0.001	1.72E-01	0.001	8.75E-02		
0.05	8.54E-03	0.05	5.26E-03	0.05	3.24E-03	0.05	1.50E-03	0.01	1.65E-02	0.01	5.74E-03		
0.1	2.75E-03	0.1	1.47E-03	0.1	8.35E-04	0.1	3.63E-04	0.05	9.11E-04	0.05	2.46E-04		
0.2	7.80E-04	0.2	3.63E-04	0.2	1.86E-04	0.2	7.21E-05	0.07	4.49E-04	0.07	1.09E-04		
0.3	3.51E-04	0.3	1.50E-04	0.3	7.09E-05	0.3	2.54E-05	0.1	1.92E-04	0.1	4.13E-05		
0.5	1.11E-04	0.5	4.42E-05	0.4	3.43E-05	0.4	1.18E-05	0.3	9.77E-06	0.3	1.27E-06		
0.7	4.55E-05	0.7	1.75E-05	0.5	1.91E-05	0.5	6.36E-06	0.5	2.03E-06	0.5	2.16E-07		
1	1.53E-05	1	5.54E-06	0.7	7.43E-06	0.7	2.36E-06	0.7	7.34E-07	0.7	6.27E-08		
2	1.28E-06	2	3.98E-07	1	2.18E-06	1	7.30E-07	1	2.53E-07	1	1.56E-08		
3	2.92E-07	3	8.28E-08	2	1.30E-07	1.5	1.64E-07	1.5	7.30E-08	1.5	2.90E-09		
5	3.71E-08	5	8.71E-09	5	2.62E-09	2	5.13E-08	2	2.93E-08	2	8.11E-10		
10	1.16E-09	10	2.31E-10	10	5.57E-11	5	7.28E-10	5	9.77E-10	5	7.78E-12		

PGA- Peak Ground Acceleration (g); AEF – Annual Exceedance Frequency; SA – Spectral Acceleration (g).

Table 10-34. Site-specific hazard conditional fractiles at ATR, assuming a soil thickness of 20 ft computed using profiles with basalt interbeds at depth ~ 40 m.

Spectral Acceleration (g)	ATR Soil 20 ft (with basalt interbeds at depth ~ 40 m) Annual Exceedance Frequency at Fractiles				
	5th	16th	50th	84th	95th
10 Hz					
0.01	3.60E-02	3.79E-02	4.55E-02	5.16E-02	5.44E-02
0.02	1.60E-02	1.66E-02	2.27E-02	2.76E-02	3.16E-02
0.05	4.06E-03	4.64E-03	7.49E-03	9.54E-03	1.04E-02
0.10	1.12E-03	1.40E-03	2.56E-03	3.44E-03	3.81E-03
0.20	2.36E-04	2.45E-04	5.39E-04	9.47E-04	1.25E-03
0.30	8.12E-05	8.47E-05	2.03E-04	3.70E-04	5.93E-04
0.40	1.50E-05	1.86E-05	4.71E-05	1.03E-04	1.76E-04
0.50	4.13E-06	6.46E-06	1.47E-05	3.78E-05	5.52E-05
0.70	8.00E-07	1.46E-06	3.67E-06	1.28E-05	1.88E-05
1.00	3.99E-08	4.62E-08	1.62E-07	9.46E-07	1.31E-06
2.00	5.14E-09	7.38E-09	2.22E-08	1.40E-07	1.82E-07
5.00	2.12E-10	4.70E-10	1.67E-09	1.14E-08	1.82E-08
10.00	3.94E-16	4.79E-14	3.27E-12	1.78E-10	6.00E-10
2 Hz					
0.01	1.75E-02	1.94E-02	2.28E-02	4.04E-02	4.20E-02
0.02	5.44E-03	6.17E-03	7.71E-03	1.71E-02	1.84E-02
0.05	8.94E-04	1.06E-03	1.49E-03	3.91E-03	4.27E-03
0.10	1.85E-04	2.29E-04	3.48E-04	1.06E-03	1.18E-03
0.20	2.69E-05	3.70E-05	6.09E-05	2.42E-04	2.85E-04
0.30	7.75E-06	1.08E-05	1.87E-05	9.53E-05	1.25E-04
0.50	3.17E-06	4.05E-06	8.58E-06	4.92E-05	6.62E-05
0.70	1.42E-06	1.85E-06	4.52E-06	2.81E-05	3.86E-05
1.00	4.26E-07	5.80E-07	1.50E-06	1.09E-05	1.50E-05
2.00	1.31E-07	2.03E-07	4.41E-07	3.59E-06	4.79E-06
3.00	3.48E-08	4.89E-08	1.12E-07	9.95E-07	1.25E-06
5.00	1.36E-08	1.69E-08	4.15E-08	3.47E-07	4.50E-07
10.00	1.48E-10	2.34E-10	6.48E-10	6.87E-09	9.92E-09

Table 10-35. Site-specific hazard conditional fractiles at ATR, assuming a soil thickness of 20 ft computed using profiles without basalt interbeds at depth ~ 40 m.

Spectral Acceleration (g)	ATR Soil 20 ft (without basalt interbeds at depth ~40 m) Annual Exceedance Frequency at Fractiles				
	5th	16th	50th	84th	95th
10 Hz					
0.01	4.18E-02	4.42E-02	5.14E-02	5.41E-02	5.55E-02
0.02	2.08E-02	2.10E-02	2.97E-02	3.54E-02	3.74E-02
0.05	6.27E-03	6.59E-03	1.02E-02	1.30E-02	1.38E-02
0.10	1.94E-03	2.23E-03	3.96E-03	5.37E-03	5.66E-03
0.20	4.34E-04	5.56E-04	1.18E-03	1.77E-03	1.85E-03
0.30	1.45E-04	2.18E-04	4.70E-04	7.59E-04	8.55E-04
0.40	2.73E-05	4.36E-05	1.18E-04	2.07E-04	2.84E-04
0.50	7.60E-06	1.25E-05	4.09E-05	7.54E-05	1.15E-04
0.70	1.83E-06	2.85E-06	1.10E-05	2.52E-05	3.71E-05
1.00	8.94E-08	1.14E-07	5.10E-07	2.71E-06	3.06E-06
2.00	1.03E-08	1.35E-08	7.06E-08	5.80E-07	6.06E-07
5.00	3.59E-10	5.59E-10	4.87E-09	5.73E-08	7.18E-08
10.00	1.60E-14	1.85E-13	4.94E-11	1.20E-09	2.35E-09
2 Hz					
0.01	1.60E-02	1.66E-02	1.94E-02	3.26E-02	3.45E-02
0.02	4.92E-03	5.28E-03	6.28E-03	1.24E-02	1.34E-02
0.05	7.88E-04	8.97E-04	1.11E-03	2.68E-03	2.94E-03
0.10	1.63E-04	1.95E-04	2.49E-04	6.84E-04	7.66E-04
0.20	2.43E-05	2.92E-05	4.34E-05	1.45E-04	1.67E-04
0.30	6.73E-06	7.92E-06	1.33E-05	5.05E-05	6.67E-05
0.50	2.70E-06	3.17E-06	5.46E-06	2.45E-05	3.41E-05
0.70	1.27E-06	1.60E-06	2.67E-06	1.40E-05	2.00E-05
1.00	3.64E-07	5.06E-07	8.30E-07	5.44E-06	8.18E-06
2.00	7.92E-08	1.09E-07	2.45E-07	1.80E-06	2.54E-06
3.00	1.70E-08	2.33E-08	5.66E-08	3.98E-07	5.35E-07
5.00	5.74E-09	8.60E-09	2.09E-08	1.27E-07	1.69E-07
10.00	2.73E-11	5.12E-11	1.46E-10	1.57E-09	3.00E-09

Table 10-36. Mean site-specific hazard curves at ATR assuming 40 ft soil thickness computed using profiles with basalt interbeds at depth ~ 40 m.

PGA	AEF	50 Hz SA	AEF	33.3 Hz SA	AEF	20 Hz SA	AEF	13.33 Hz SA	AEF	10 Hz SA	AEF	6.67 Hz SA	AEF
0.01	3.48E-02	0.01	3.74E-02	0.01	3.49E-02	0.01	4.77E-02	0.01	5.61E-02	0.01	5.36E-02	0.01	8.25E-02
0.02	1.71E-02	0.02	1.83E-02	0.02	1.77E-02	0.02	2.45E-02	0.02	3.03E-02	0.02	3.09E-02	0.02	5.82E-02
0.05	4.49E-03	0.05	4.82E-03	0.05	5.07E-03	0.05	7.04E-03	0.05	9.12E-03	0.05	9.77E-03	0.05	2.19E-02
0.1	1.23E-03	0.1	1.37E-03	0.1	1.58E-03	0.1	2.24E-03	0.1	2.94E-03	0.1	3.34E-03	0.1	8.23E-03
0.2	2.19E-04	0.2	2.59E-04	0.2	3.27E-04	0.2	4.81E-04	0.2	6.57E-04	0.2	8.54E-04	0.2	2.44E-03
0.3	6.24E-05	0.3	7.81E-05	0.3	1.03E-04	0.3	1.57E-04	0.3	2.17E-04	0.3	3.17E-04	0.3	1.01E-03
0.4	2.15E-05	0.4	2.82E-05	0.4	4.01E-05	0.4	6.32E-05	0.4	8.68E-05	0.5	6.97E-05	0.4	2.61E-04
0.5	8.56E-06	0.5	1.17E-05	0.5	1.74E-05	0.5	2.90E-05	0.5	3.93E-05	0.7	2.13E-05	0.5	9.16E-05
0.7	1.90E-06	0.7	2.71E-06	0.7	4.39E-06	0.7	7.79E-06	0.7	1.05E-05	1	5.31E-06	0.7	2.55E-05
1	3.26E-07	1	4.94E-07	1	8.76E-07	1	1.68E-06	1	2.14E-06	2	2.75E-07	1	1.42E-06
2	9.61E-09	2	1.42E-08	2	2.84E-08	2	7.01E-08	2	7.63E-08	3	3.88E-08	2	2.26E-07
5	9.11E-11	5	1.10E-10	5	1.75E-10	5	4.40E-10	5	6.00E-10	5	2.16E-09	5	1.85E-08
10	5.78E-13	10	5.98E-13	10	1.04E-12	10	2.94E-12	10	1.78E-12	10	1.17E-11	10	3.56E-10
5 Hz SA	AEF	3.33 Hz SA	AEF	2.5 Hz SA	AEF	2 Hz SA	AEF	1 Hz SA	AEF	0.5 Hz SA	AEF		
0.01	8.35E-02	0.01	6.73E-02	0.01	5.37E-02	0.01	3.17E-02	0.0001	4.47E-01	0.0001	3.60E-01		
0.02	5.44E-02	0.02	3.78E-02	0.02	2.64E-02	0.02	1.34E-02	0.001	1.79E-01	0.001	9.19E-02		
0.05	1.85E-02	0.05	1.08E-02	0.05	6.57E-03	0.05	3.05E-03	0.01	1.79E-02	0.01	6.26E-03		
0.1	6.82E-03	0.1	3.51E-03	0.1	1.94E-03	0.1	8.52E-04	0.05	1.04E-03	0.05	2.86E-04		
0.2	2.09E-03	0.2	9.84E-04	0.2	4.99E-04	0.2	2.12E-04	0.07	5.22E-04	0.07	1.30E-04		
0.3	9.43E-04	0.3	4.36E-04	0.3	2.16E-04	0.3	9.02E-05	0.1	2.32E-04	0.1	5.11E-05		
0.5	2.86E-04	0.5	1.35E-04	0.4	1.14E-04	0.4	4.69E-05	0.3	1.38E-05	0.3	1.88E-06		
0.7	1.11E-04	0.7	5.47E-05	0.5	6.77E-05	0.5	2.72E-05	0.5	3.36E-06	0.5	3.97E-07		
1	3.49E-05	1	1.76E-05	0.7	2.84E-05	0.7	1.10E-05	0.7	1.29E-06	0.7	1.42E-07		
2	1.94E-06	2	1.20E-06	1	9.65E-06	1	3.69E-06	1	4.72E-07	1	4.61E-08		
3	2.77E-07	3	2.00E-07	2	7.11E-07	1.5	9.08E-07	1.5	1.46E-07	1.5	1.20E-08		
5	2.21E-08	5	1.79E-08	5	8.62E-09	2	2.98E-07	2	6.08E-08	2	4.29E-09		
10	4.56E-10	10	4.55E-10	10	1.00E-10	5	3.30E-09	5	1.89E-09	5	8.40E-11		

PGA- Peak Ground Acceleration (g); AEF – Annual Exceedance Frequency; SA – Spectral Acceleration (g).

Table 10-37. Mean site-specific hazard curves at ATR assuming 40 ft soil thickness computed using profiles without basalt interbeds at depth ~ 40 m.

PGA	AEF	50 Hz SA	AEF	33.3 Hz SA	AEF	20 Hz SA	AEF	13.33 Hz SA	AEF	10 Hz SA	AEF	6.67 Hz SA	AEF
0.01	3.31E-02	0.01	3.55E-02	0.01	3.32E-02	0.01	4.58E-02	0.01	5.48E-02	0.01	5.29E-02	0.01	8.28E-02
0.02	1.56E-02	0.02	1.68E-02	0.02	1.63E-02	0.02	2.32E-02	0.02	2.90E-02	0.02	3.03E-02	0.02	5.93E-02
0.05	4.13E-03	0.05	4.48E-03	0.05	4.76E-03	0.05	6.95E-03	0.05	9.06E-03	0.05	9.91E-03	0.05	2.21E-02
0.1	1.11E-03	0.1	1.26E-03	0.1	1.49E-03	0.1	2.32E-03	0.1	3.06E-03	0.1	3.51E-03	0.1	8.45E-03
0.2	1.92E-04	0.2	2.39E-04	0.2	3.16E-04	0.2	5.30E-04	0.2	7.34E-04	0.2	9.25E-04	0.2	2.57E-03
0.3	5.45E-05	0.3	7.32E-05	0.3	1.03E-04	0.3	1.83E-04	0.3	2.61E-04	0.3	3.52E-04	0.3	1.10E-03
0.4	1.91E-05	0.4	2.71E-05	0.4	4.12E-05	0.4	7.71E-05	0.4	1.12E-04	0.5	8.28E-05	0.4	3.04E-04
0.5	7.91E-06	0.5	1.17E-05	0.5	1.86E-05	0.5	3.68E-05	0.5	5.44E-05	0.7	2.74E-05	0.5	1.11E-04
0.7	1.80E-06	0.7	2.82E-06	0.7	4.97E-06	0.7	1.08E-05	0.7	1.61E-05	1	7.55E-06	0.7	3.26E-05
1	3.13E-07	1	5.23E-07	1	1.03E-06	1	2.49E-06	1	3.79E-06	2	4.76E-07	1	1.92E-06
2	8.55E-09	2	1.47E-08	2	3.33E-08	2	1.01E-07	2	1.42E-07	3	8.05E-08	2	2.94E-07
5	7.47E-11	5	1.07E-10	5	2.14E-10	5	1.10E-09	5	1.26E-09	5	7.30E-09	5	2.57E-08
10	4.94E-13	10	9.61E-13	10	2.43E-12	10	1.61E-11	10	2.31E-11	10	1.76E-10	10	7.42E-10
5 Hz SA	AEF	3.33 Hz SA	AEF	2.5 Hz SA	AEF	2 Hz SA	AEF	1 Hz SA	AEF	0.5 Hz SA	AEF		
0.01	7.89E-02	0.01	5.75E-02	0.01	4.32E-02	0.01	2.52E-02	0.0001	4.41E-01	0.0001	3.57E-01		
0.02	4.96E-02	0.02	2.69E-02	0.02	1.75E-02	0.02	9.17E-03	0.001	1.72E-01	0.001	9.00E-02		
0.05	1.70E-02	0.05	7.08E-03	0.05	3.97E-03	0.05	1.89E-03	0.01	1.66E-02	0.01	6.03E-03		
0.1	6.21E-03	0.1	2.15E-03	0.1	1.07E-03	0.1	4.84E-04	0.05	9.34E-04	0.05	2.67E-04		
0.2	1.90E-03	0.2	5.68E-04	0.2	2.52E-04	0.2	1.05E-04	0.07	4.63E-04	0.07	1.20E-04		
0.3	8.52E-04	0.3	2.43E-04	0.3	9.97E-05	0.3	3.95E-05	0.1	1.99E-04	0.1	4.60E-05		
0.5	2.60E-04	0.5	7.34E-05	0.4	4.92E-05	0.4	1.91E-05	0.3	1.05E-05	0.3	1.52E-06		
0.7	1.03E-04	0.7	2.96E-05	0.5	2.76E-05	0.5	1.07E-05	0.5	2.28E-06	0.5	2.80E-07		
1	3.27E-05	1	9.69E-06	0.7	1.08E-05	0.7	4.29E-06	0.7	8.17E-07	0.7	9.34E-08		
2	2.08E-06	2	7.25E-07	1	3.71E-06	1	1.54E-06	1	2.79E-07	1	2.96E-08		
3	3.05E-07	3	1.22E-07	2	3.09E-07	1.5	4.16E-07	1.5	8.31E-08	1.5	7.82E-09		
5	2.33E-08	5	1.07E-08	5	4.30E-09	2	1.42E-07	2	3.41E-08	2	2.85E-09		
10	5.54E-10	10	2.54E-10	10	4.87E-11	5	2.09E-09	5	9.19E-10	5	5.76E-11		

PGA- Peak Ground Acceleration (g); AEF – Annual Exceedance Frequency; SA – Spectral Acceleration (g).

Table 10-38. Site-specific hazard conditional fractiles at ATR, assuming a soil thickness of 40 ft computed using profiles with basalt interbeds at depth ~ 40 m.

Spectral Acceleration (g)	ATR Soil 40 ft (with basalt interbeds at depth ~ 40m) Annual Exceedance Frequency at Fractiles				
	5th	16th	50th	84th	95th
10 Hz					
0.01	4.76E-02	4.95E-02	5.50E-02	5.63E-02	5.65E-02
0.02	2.22E-02	2.35E-02	3.03E-02	3.68E-02	4.17E-02
0.05	5.68E-03	6.42E-03	9.52E-03	1.22E-02	1.54E-02
0.10	1.50E-03	1.81E-03	3.13E-03	4.67E-03	6.16E-03
0.20	3.01E-04	3.81E-04	6.95E-04	1.38E-03	2.00E-03
0.30	7.93E-05	1.25E-04	2.29E-04	5.33E-04	8.31E-04
0.40	8.80E-06	1.66E-05	4.38E-05	1.15E-04	2.02E-04
0.50	1.54E-06	3.77E-06	8.85E-06	3.16E-05	6.17E-05
0.70	2.37E-07	6.57E-07	1.57E-06	6.81E-06	1.84E-05
1.00	8.27E-09	1.57E-08	7.20E-08	2.79E-07	1.13E-06
2.00	9.45E-10	2.06E-09	8.45E-09	3.99E-08	1.54E-07
5.00	1.88E-11	6.98E-11	4.82E-10	2.33E-09	7.94E-09
10.00	3.59E-17	1.22E-15	1.10E-13	1.99E-11	7.54E-11
2 Hz					
0.01	2.00E-02	2.21E-02	2.71E-02	4.86E-02	4.92E-02
0.02	6.42E-03	7.31E-03	9.66E-03	2.50E-02	2.67E-02
0.05	1.15E-03	1.39E-03	1.98E-03	6.17E-03	6.74E-03
0.10	2.72E-04	3.40E-04	4.89E-04	1.82E-03	2.02E-03
0.20	5.36E-05	6.37E-05	1.09E-04	4.54E-04	5.47E-04
0.30	1.63E-05	2.06E-05	4.24E-05	1.99E-04	2.55E-04
0.50	6.55E-06	9.56E-06	2.05E-05	1.09E-04	1.41E-04
0.70	3.22E-06	4.79E-06	1.14E-05	6.32E-05	8.53E-05
1.00	1.18E-06	1.54E-06	4.36E-06	2.66E-05	3.55E-05
2.00	3.41E-07	5.18E-07	1.36E-06	8.73E-06	1.13E-05
3.00	6.71E-08	1.08E-07	3.44E-07	2.41E-06	3.03E-06
5.00	2.01E-08	3.48E-08	1.14E-07	7.79E-07	1.02E-06
10.00	7.18E-11	1.50E-10	5.84E-10	8.56E-09	1.52E-08

Table 10-39. Site-specific hazard conditional fractiles at ATR, assuming a soil thickness of 40 ft. computed using profiles without basalt interbeds at depth ~ 40 m.

Spectral Acceleration (g)	ATR Soil 40 ft (without basalt interbeds at depth ~40 m) Annual Exceedance Frequency at Fractiles				
	5th	16th	50th	84th	95th
10 Hz					
0.01	4.55E-02	4.75E-02	5.46E-02	5.62E-02	5.65E-02
0.02	2.15E-02	2.27E-02	3.10E-02	3.61E-02	3.93E-02
0.05	6.25E-03	6.54E-03	9.78E-03	1.22E-02	1.41E-02
0.10	1.81E-03	1.96E-03	3.44E-03	4.60E-03	5.63E-03
0.20	3.68E-04	4.38E-04	8.27E-04	1.26E-03	1.77E-03
0.30	1.01E-04	1.51E-04	3.15E-04	5.35E-04	7.38E-04
0.40	1.30E-05	2.99E-05	6.81E-05	1.52E-04	1.97E-04
0.50	2.65E-06	7.07E-06	1.98E-05	5.51E-05	6.82E-05
0.70	4.86E-07	1.32E-06	3.78E-06	1.54E-05	2.01E-05
1.00	1.87E-08	2.37E-08	1.57E-07	7.57E-07	1.59E-06
2.00	1.24E-09	3.08E-09	1.95E-08	1.12E-07	2.82E-07
5.00	1.31E-11	1.32E-10	1.02E-09	8.72E-09	2.73E-08
10.00	2.78E-18	1.23E-15	5.31E-12	1.82E-10	7.36E-10
2 Hz					
0.01	1.70E-02	1.82E-02	2.07E-02	3.81E-02	3.99E-02
0.02	5.31E-03	5.93E-03	6.95E-03	1.56E-02	1.67E-02
0.05	8.80E-04	1.06E-03	1.33E-03	3.52E-03	3.88E-03
0.10	1.91E-04	2.39E-04	3.08E-04	9.57E-04	1.08E-03
0.20	3.16E-05	3.88E-05	5.36E-05	2.19E-04	2.60E-04
0.30	9.63E-06	1.12E-05	1.83E-05	8.29E-05	1.10E-04
0.50	3.70E-06	4.50E-06	8.14E-06	4.18E-05	5.73E-05
0.70	1.74E-06	2.24E-06	4.45E-06	2.40E-05	3.36E-05
1.00	5.75E-07	8.05E-07	1.68E-06	9.84E-06	1.41E-05
2.00	1.83E-07	2.76E-07	5.58E-07	3.54E-06	5.11E-06
3.00	4.54E-08	6.13E-08	1.48E-07	9.38E-07	1.37E-06
5.00	1.15E-08	2.07E-08	4.65E-08	3.32E-07	4.65E-07
10.00	2.68E-11	6.82E-11	3.24E-10	5.26E-09	8.56E-09

Table 10-40. Mean site-specific hazard curves at ATR assuming 60 ft soil thickness computed using profiles with basalt interbeds at depth ~ 40 m.

PGA	AEF	50 Hz SA	AEF	33.3 Hz SA	AEF	20 Hz SA	AEF	13.33 Hz SA	AEF	10 Hz SA	AEF	6.67 Hz SA	AEF
0.01	3.61E-02	0.01	3.88E-02	0.01	3.62E-02	0.01	4.92E-02	0.01	5.75E-02	0.01	5.28E-02	0.01	8.49E-02
0.02	1.84E-02	0.02	1.97E-02	0.02	1.88E-02	0.02	2.60E-02	0.02	3.17E-02	0.02	2.83E-02	0.02	5.89E-02
0.05	4.74E-03	0.05	5.06E-03	0.05	5.19E-03	0.05	7.28E-03	0.05	9.30E-03	0.05	8.39E-03	0.05	2.04E-02
0.1	1.27E-03	0.1	1.39E-03	0.1	1.54E-03	0.1	2.25E-03	0.1	2.92E-03	0.1	2.65E-03	0.1	7.38E-03
0.2	2.19E-04	0.2	2.54E-04	0.2	3.04E-04	0.2	4.68E-04	0.2	6.36E-04	0.2	6.17E-04	0.2	2.07E-03
0.3	6.06E-05	0.3	7.40E-05	0.3	9.22E-05	0.3	1.49E-04	0.3	2.06E-04	0.3	2.14E-04	0.3	8.46E-04
0.4	2.06E-05	0.4	2.61E-05	0.4	3.43E-05	0.4	5.85E-05	0.4	8.02E-05	0.5	4.40E-05	0.4	2.19E-04
0.5	8.20E-06	0.5	1.06E-05	0.5	1.46E-05	0.5	2.64E-05	0.5	3.55E-05	0.7	1.32E-05	0.5	7.63E-05
0.7	1.84E-06	0.7	2.45E-06	0.7	3.58E-06	0.7	7.15E-06	0.7	9.09E-06	1	3.16E-06	0.7	2.14E-05
1	3.32E-07	1	4.51E-07	1	7.00E-07	1	1.58E-06	1	1.87E-06	2	1.27E-07	1	1.14E-06
2	8.74E-09	2	1.14E-08	2	1.89E-08	2	5.79E-08	2	6.69E-08	3	1.42E-08	2	1.66E-07
5	9.76E-11	5	1.21E-10	5	1.83E-10	5	4.25E-10	5	5.57E-10	5	7.91E-10	5	1.22E-08
10	1.17E-12	10	1.46E-12	10	2.33E-12	10	5.73E-12	10	4.87E-12	10	8.27E-12	10	2.01E-10
5 Hz SA	AEF	3.33 Hz SA	AEF	2.5 Hz SA	AEF	2 Hz SA	AEF	1 Hz SA	AEF	0.5 Hz SA	AEF		
0.01	8.55E-02	0.01	7.29E-02	0.01	5.75E-02	0.01	3.51E-02	0.0001	4.49E-01	0.0001	3.59E-01		
0.02	5.92E-02	0.02	4.53E-02	0.02	3.25E-02	0.02	1.67E-02	0.001	1.82E-01	0.001	9.14E-02		
0.05	1.97E-02	0.05	1.34E-02	0.05	8.60E-03	0.05	4.09E-03	0.01	1.83E-02	0.01	6.20E-03		
0.1	7.00E-03	0.1	4.39E-03	0.1	2.64E-03	0.1	1.21E-03	0.05	1.08E-03	0.05	2.84E-04		
0.2	2.00E-03	0.2	1.21E-03	0.2	6.93E-04	0.2	3.15E-04	0.07	5.45E-04	0.07	1.29E-04		
0.3	8.49E-04	0.3	5.24E-04	0.3	2.98E-04	0.3	1.37E-04	0.1	2.44E-04	0.1	5.06E-05		
0.5	2.39E-04	0.5	1.58E-04	0.4	1.56E-04	0.4	7.38E-05	0.3	1.48E-05	0.3	1.85E-06		
0.7	8.83E-05	0.7	6.13E-05	0.5	9.11E-05	0.5	4.39E-05	0.5	3.64E-06	0.5	3.98E-07		
1	2.58E-05	1	1.90E-05	0.7	3.70E-05	0.7	1.79E-05	0.7	1.41E-06	0.7	1.45E-07		
2	1.53E-06	2	1.19E-06	1	1.23E-05	1	5.67E-06	1	4.94E-07	1	4.87E-08		
3	2.40E-07	3	1.99E-07	2	8.29E-07	1.5	1.27E-06	1.5	1.39E-07	1.5	1.32E-08		
5	1.72E-08	5	1.59E-08	5	1.30E-08	2	4.08E-07	2	5.46E-08	2	4.86E-09		
10	2.93E-10	10	3.04E-10	10	3.90E-10	5	7.26E-09	5	1.63E-09	5	1.02E-10		

PGA- Peak Ground Acceleration (g); AEF – Annual Exceedance Frequency; SA – Spectral Acceleration (g).

Table 10-41. Mean site-specific hazard curves at ATR assuming 60 ft soil thickness computed using profiles without basalt interbeds at depth ~ 40 m.

PGA	AEF	50 Hz SA	AEF	33.3 Hz SA	AEF	20 Hz SA	AEF	13.33 Hz SA	AEF	10 Hz SA	AEF	6.67 Hz SA	AEF
0.01	3.47E-02	0.01	3.74E-02	0.01	3.49E-02	0.01	4.78E-02	0.01	5.63E-02	0.01	5.27E-02	0.01	8.43E-02
0.02	1.67E-02	0.02	1.79E-02	0.02	1.72E-02	0.02	2.42E-02	0.02	3.03E-02	0.02	2.95E-02	0.02	5.60E-02
0.05	4.35E-03	0.05	4.68E-03	0.05	4.87E-03	0.05	7.05E-03	0.05	9.36E-03	0.05	9.57E-03	0.05	1.92E-02
0.1	1.17E-03	0.1	1.30E-03	0.1	1.48E-03	0.1	2.28E-03	0.1	3.12E-03	0.1	3.38E-03	0.1	7.07E-03
0.2	2.03E-04	0.2	2.45E-04	0.2	3.03E-04	0.2	5.11E-04	0.2	7.41E-04	0.2	9.11E-04	0.2	2.08E-03
0.3	5.77E-05	0.3	7.40E-05	0.3	9.59E-05	0.3	1.73E-04	0.3	2.59E-04	0.3	3.53E-04	0.3	8.93E-04
0.4	2.02E-05	0.4	2.71E-05	0.4	3.73E-05	0.4	7.06E-05	0.4	1.09E-04	0.5	8.61E-05	0.4	2.57E-04
0.5	8.17E-06	0.5	1.13E-05	0.5	1.65E-05	0.5	3.25E-05	0.5	5.14E-05	0.7	2.96E-05	0.5	9.95E-05
0.7	1.80E-06	0.7	2.61E-06	0.7	4.19E-06	0.7	8.78E-06	0.7	1.42E-05	1	8.31E-06	0.7	3.21E-05
1	3.11E-07	1	4.67E-07	1	8.18E-07	1	1.83E-06	1	3.01E-06	2	4.22E-07	1	2.30E-06
2	8.00E-09	2	1.14E-08	2	2.27E-08	2	6.32E-08	2	1.01E-07	3	5.41E-08	2	3.88E-07
5	8.32E-11	5	1.06E-10	5	1.69E-10	5	4.18E-10	5	6.35E-10	5	2.88E-09	5	3.14E-08
10	7.56E-13	10	1.01E-12	10	1.80E-12	10	4.97E-12	10	5.28E-12	10	3.08E-11	10	5.32E-10
5 Hz SA	AEF	3.33 Hz SA	AEF	2.5 Hz SA	AEF	2 Hz SA	AEF	1 Hz SA	AEF	0.5 Hz SA	AEF		
0.01	8.43E-02	0.01	6.54E-02	0.01	4.96E-02	0.01	2.81E-02	0.0001	4.44E-01	0.0001	3.55E-01		
0.02	5.99E-02	0.02	3.56E-02	0.02	2.25E-02	0.02	1.09E-02	0.001	1.76E-01	0.001	8.91E-02		
0.05	2.06E-02	0.05	1.02E-02	0.05	5.44E-03	0.05	2.36E-03	0.01	1.72E-02	0.01	5.94E-03		
0.1	7.36E-03	0.1	3.24E-03	0.1	1.56E-03	0.1	6.33E-04	0.05	9.89E-04	0.05	2.64E-04		
0.2	2.12E-03	0.2	8.64E-04	0.2	3.91E-04	0.2	1.48E-04	0.07	4.94E-04	0.07	1.19E-04		
0.3	9.02E-04	0.3	3.66E-04	0.3	1.63E-04	0.3	5.90E-05	0.1	2.16E-04	0.1	4.56E-05		
0.5	2.60E-04	0.5	1.07E-04	0.4	8.37E-05	0.4	2.96E-05	0.3	1.18E-05	0.3	1.54E-06		
0.7	9.96E-05	0.7	4.13E-05	0.5	4.80E-05	0.5	1.68E-05	0.5	2.68E-06	0.5	3.06E-07		
1	3.12E-05	1	1.31E-05	0.7	1.90E-05	0.7	6.60E-06	0.7	9.85E-07	0.7	1.06E-07		
2	1.93E-06	2	8.65E-07	1	6.14E-06	1	2.21E-06	1	3.38E-07	1	3.42E-08		
3	2.85E-07	3	1.54E-07	2	4.53E-07	1.5	5.78E-07	1.5	9.93E-08	1.5	9.00E-09		
5	1.96E-08	5	1.36E-08	5	6.97E-09	2	2.04E-07	2	4.08E-08	2	3.27E-09		
10	2.93E-10	10	2.72E-10	10	2.04E-10	5	3.78E-09	5	1.54E-09	5	6.20E-11		
PGA- Peak Ground Acceleration (g); AEF – Annual Exceedance Frequency; SA – Spectral Acceleration (g).													

Table 10-42. Site-specific hazard conditional fractiles at ATR, assuming a soil thickness of 60 ft computed using profiles with basalt interbeds at depth ~ 40 m.

Spectral Acceleration (g)	ATR Soil 60 ft (with basalt interbeds at depth ~ 40m) Annual Exceedance Frequency at Fractiles				
	5th	16th	50th	84th	95th
10 Hz					
0.01	4.65E-02	4.80E-02	5.44E-02	5.60E-02	5.63E-02
0.02	2.10E-02	2.23E-02	2.89E-02	3.30E-02	3.58E-02
0.05	5.31E-03	5.57E-03	8.18E-03	1.01E-02	1.22E-02
0.10	1.36E-03	1.42E-03	2.41E-03	3.42E-03	4.60E-03
0.20	2.33E-04	2.69E-04	5.45E-04	9.01E-04	1.34E-03
0.30	6.13E-05	8.12E-05	1.83E-04	3.12E-04	5.13E-04
0.40	8.01E-06	1.38E-05	3.47E-05	6.38E-05	1.14E-04
0.50	1.81E-06	3.65E-06	9.06E-06	1.86E-05	3.38E-05
0.70	3.92E-07	6.99E-07	1.94E-06	4.50E-06	8.87E-06
1.00	1.36E-08	1.64E-08	7.51E-08	2.07E-07	3.77E-07
2.00	1.03E-09	1.73E-09	7.53E-09	2.90E-08	4.00E-08
5.00	1.34E-11	2.60E-11	3.75E-10	2.08E-09	2.20E-09
10.00	8.44E-17	1.76E-15	4.67E-13	1.85E-11	3.26E-11
2 Hz					
0.01	2.20E-02	2.44E-02	3.33E-02	4.92E-02	4.95E-02
0.02	7.30E-03	8.34E-03	1.25E-02	3.14E-02	3.33E-02
0.05	1.39E-03	1.67E-03	2.75E-03	8.42E-03	9.16E-03
0.10	3.37E-04	4.18E-04	7.28E-04	2.64E-03	2.92E-03
0.20	6.99E-05	8.58E-05	1.64E-04	7.06E-04	7.95E-04
0.30	2.34E-05	2.82E-05	6.49E-05	3.08E-04	3.71E-04
0.50	9.90E-06	1.26E-05	3.53E-05	1.65E-04	2.07E-04
0.70	5.06E-06	6.77E-06	2.08E-05	9.88E-05	1.24E-04
1.00	1.97E-06	2.53E-06	8.62E-06	4.24E-05	5.02E-05
2.00	7.26E-07	9.45E-07	2.99E-06	1.36E-05	1.65E-05
3.00	1.70E-07	2.66E-07	7.45E-07	2.74E-06	3.43E-06
5.00	5.08E-08	8.91E-08	2.50E-07	9.19E-07	1.19E-06
10.00	1.60E-10	6.92E-10	3.53E-09	1.72E-08	2.54E-08

Table 10-43. Site-specific hazard conditional fractiles at ATR, assuming a soil thickness of 60 ft. computed using profiles without basalt interbeds at depth ~ 40 m.

Spectral Acceleration (g)	ATR Soil 60 ft (without basalt interbeds at depth ~40 m) Annual Exceedance Frequency at Fractiles				
	5th	16th	50th	84th	95th
10 Hz					
0.01	4.66E-02	4.77E-02	5.42E-02	5.57E-02	5.60E-02
0.02	2.17E-02	2.25E-02	3.01E-02	3.49E-02	3.76E-02
0.05	6.11E-03	6.40E-03	9.43E-03	1.19E-02	1.36E-02
0.10	1.73E-03	1.91E-03	3.30E-03	4.43E-03	5.48E-03
0.20	3.69E-04	4.14E-04	8.34E-04	1.27E-03	1.79E-03
0.30	1.14E-04	1.41E-04	2.88E-04	5.35E-04	7.88E-04
0.40	1.72E-05	2.80E-05	5.93E-05	1.46E-04	2.35E-04
0.50	3.68E-06	8.01E-06	1.72E-05	5.00E-05	9.17E-05
0.70	6.47E-07	1.82E-06	3.83E-06	1.37E-05	2.72E-05
1.00	1.82E-08	5.66E-08	1.46E-07	5.37E-07	1.49E-06
2.00	1.67E-09	5.16E-09	1.54E-08	5.91E-08	2.07E-07
5.00	4.71E-11	1.42E-10	5.07E-10	3.20E-09	1.06E-08
10.00	5.44E-15	4.15E-14	1.18E-12	2.07E-11	1.53E-10
2 Hz					
0.01	1.81E-02	2.02E-02	2.41E-02	4.24E-02	4.39E-02
0.02	5.76E-03	6.56E-03	8.42E-03	1.88E-02	2.02E-02
0.05	9.90E-04	1.19E-03	1.69E-03	4.44E-03	4.88E-03
0.10	2.20E-04	2.77E-04	4.14E-04	1.25E-03	1.40E-03
0.20	3.90E-05	5.11E-05	8.39E-05	3.01E-04	3.53E-04
0.30	1.24E-05	1.54E-05	3.34E-05	1.19E-04	1.54E-04
0.50	5.04E-06	6.47E-06	1.52E-05	6.22E-05	8.26E-05
0.70	2.54E-06	3.24E-06	8.23E-06	3.62E-05	4.89E-05
1.00	8.21E-07	1.07E-06	3.34E-06	1.42E-05	1.97E-05
2.00	2.41E-07	3.34E-07	1.06E-06	4.95E-06	6.10E-06
3.00	6.12E-08	9.23E-08	3.08E-07	1.43E-06	1.77E-06
5.00	2.46E-08	3.41E-08	1.04E-07	5.01E-07	6.24E-07
10.00	2.87E-10	3.86E-10	9.97E-10	1.00E-08	1.61E-08

10.8.2 Sensitivity Analyses

This section presents the hazard sensitivity at the ATR sites with respect to the various parameters used to generate alternative site-amplification functions. Additionally, this section presents hazard sensitivity with respect to the two alternative models for $\sigma_{\text{epistemic}}$ described in section 9.3.4. As described in section 10.2.2, for a particular node of the logic tree, the sensitivity analyses are conducted by assigning full weight alternatively to each of the branches that represent epistemic uncertainty.

10.8.2.1 ATR Rock Site

Alternatives of four different parameters (three alternative kappa values, three alternative velocity profiles, two alternative $\sigma_{\text{epistemic}}$ models, and two alternative earthquake source spectra) were used to capture the uncertainty in the site-amplification functions for the ATR rock site conditions, which provided 36 alternative hazard curves at each frequency of spectral acceleration.

Figure 10-124 compares the conditional-mean hazard for a given kappa (red curves) with the total mean hazard at 2 Hz and 10 Hz spectral acceleration for ATR Rock (blue curve); results for the individual 36 possible outcomes of the logic tree for ATR Rock are shown by the grey curves. Kappa has a non-negligible effect on the ground motion level at all AEF less than $1\text{x}10^{-2}$ for spectral acceleration at high frequencies. In the AEF range of interest ($4\text{x}10^{-4}$ to $4\text{x}10^{-5}$ for SDC-4) the ground motion level differs by approximately a factor of 1.5 between the upper and lower bounds of kappa (0.013-0.035 sec). For spectral acceleration at low frequencies kappa has small effect on the ground motion level at all levels of AEF. Further, kappa = 0.013 sec produces hazard curves above those of kappa = 0.021 sec and kappa = 0.035 sec consistently across all frequencies of spectral acceleration.

There are two sets of three alternative velocity profiles: one set with basalt interbeds at depth ~ 40 m, and the other without basalt interbeds at depth ~ 40 m. Alternatives within each set produce variation in the ground motion level at all levels of AEF. The degree to which they vary depends on frequencies of spectral acceleration. This is shown in Figure 10-125 (profiles with basalt interbeds at depth ~ 40 m) and 10-126 (profiles without basalt interbeds at depth ~ 40 m), where the conditional-mean hazard for a given profile (red curves) is compared with the total mean hazard at 2 Hz and 10 Hz spectral accelerations for ATR Rock (blue curve), and with the individual results of the 36 logic tree branches (grey curves). Between 0.04 and 20 Hz spectral acceleration, there is not one profile that consistently produces larger hazard relative to the remaining across all frequencies of spectral acceleration. These two observations are a result of the relative similarity in the amplitude of the amplification between the three profiles combined with slight phase shifts in the locations of resonant peaks. Above and below this frequency range P2 (and P5) produces the most amplification while P3 (and P6) produces the least.

The two alternative $\sigma_{\text{epistemic}}$ models, produce similar mean hazard at 2 Hz spectral acceleration and higher. At spectral accelerations lower than 2 Hz the conditional mean hazard of the alternatives begins to deviate, with the deviation increasing as frequency of spectral acceleration and AEF decrease. In the AEF range of interest ($4\text{x}10^{-4}$ to $4\text{x}10^{-5}$ for SDC-4) the two models differ by factors up to 1.2 for frequencies of spectral acceleration from 0.5-1.0 Hz (with Option B having a higher hazard for the given frequency range). The observations of hazard sensitivity are consistent with the difference in the two $\sigma_{\text{epistemic}}$ models. Figure 10-127 compares the conditional-mean hazard for a given $\sigma_{\text{epistemic}}$ model (red curves) with the total mean hazard at 2 Hz and 10 Hz spectral acceleration for ATR Rock (blue curve), and with the individual results of the 36 logic tree branches (grey curves).

The hazard at ATR Rock is not sensitive to the selection of the model for the earthquake source spectrum used in generating site-amplification functions.

10.8.2.2 ATR Soil Sites

Alternatives of five different parameters (the 4 sets of parameters used at ATR Rock with the addition of alternative soil material models) were used to capture the uncertainty in the site-amplification functions for ATR soil sites. For the soil material models, two alternatives were used. Set M1 used Darendeli/Menq dynamic material property curves for the gravel material present in the soil profiles and the Darendeli clay curves for the other materials present. Set M2 used Rollins dynamic material property curves for the gravel material and the Vucetic and Dobry clay curves for the other material present. This produces 72 alternative hazard curves at each frequency of spectral acceleration. In addition, amplification functions were computed for three soil thicknesses: 20 ft, 40 ft, and 60 ft.

The hazard for the ATR Soil sites is only slightly less sensitive to alternative kappa values than the ATR Rock site but follows the same trends. The sensitivity to velocity profile is shown on Figures: 10-128 and 10-129 for 20 ft soil thickness, 10-130 and 10-131 for 40 ft soil thickness, and 10-132 and 10-133 for 60 ft soil thickness. For both depths the higher range velocity profiles (P3 and P6) tend to produce higher 10 Hz hazard and the lower range velocity profiles (P2 and P5) tend to produce higher 2 Hz hazard. The hazard for all three soil depths show similar sensitivity with respect to $\sigma_{\text{epistemic}}$ models as is observed for the ATR Rock site.

The hazard at the ATR Soil sites is not sensitive to the selection of source spectrum used in generating site-amplification functions.

Figures 10-134 through 10-136 compare the conditional-mean hazard for a given material property model with the total mean hazard at 2 Hz and 10 Hz spectral accelerations for soil depths of 20 ft, 40 ft, and 60 ft, respectively. The M2 set of dynamic material properties is more linear than the M1 set and therefore produce higher motions at 10 Hz. At 2 Hz the motions are nearly identical between the two alternatives.

a)

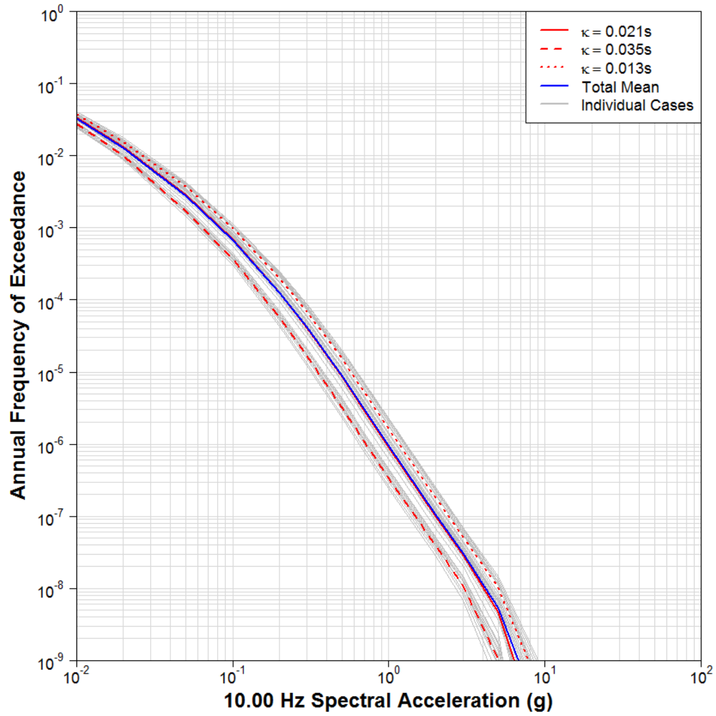

b)

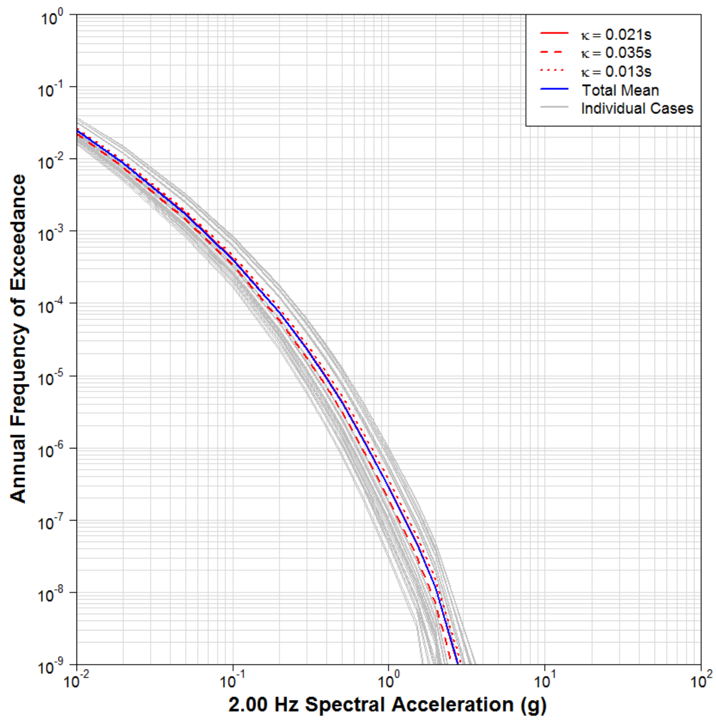

Figure 10-124. Sensitivity of hazard at ATR Rock with respect to kappa at: a) 10 Hz (0.1-sec); and b) 2 Hz (0.5-sec) spectral accelerations (k1 = 0.021s, k2=0.035s, k3=0.013s).

a)

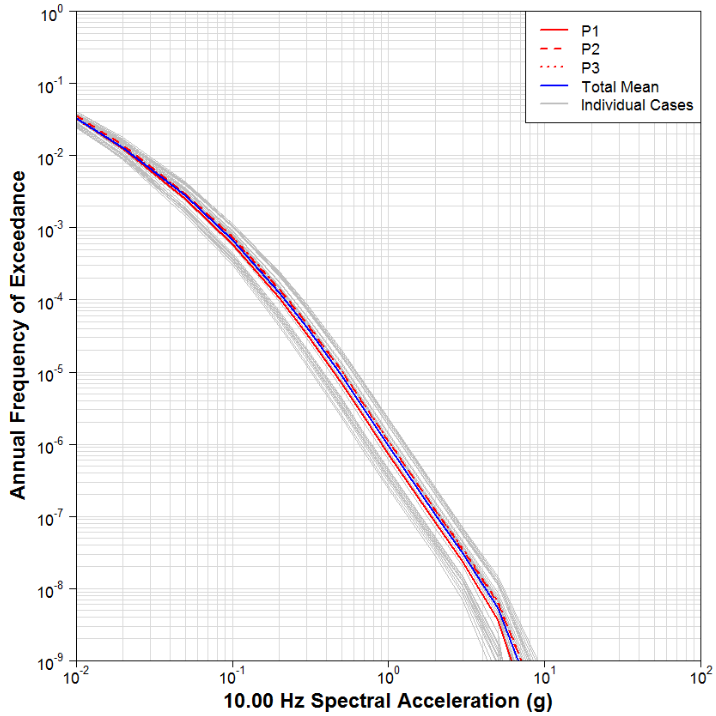

b)

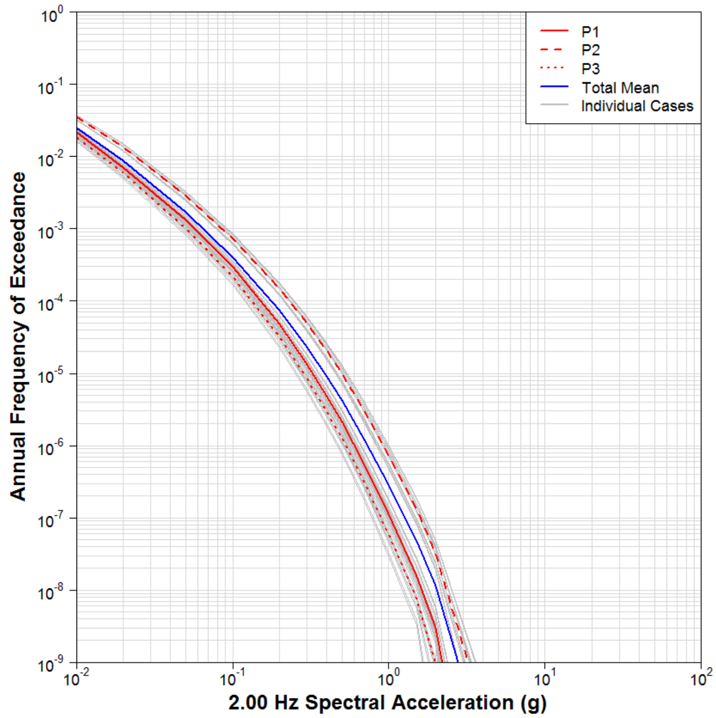

Figure 10-125. Sensitivity of hazard at ATR Rock with respect to velocity profile at: 10 Hz (0.1-sec); and b) 2 Hz (0.5-sec) spectral accelerations. Profiles P1 through P3 contain basalt interbeds at depth ~ 40 m.

a)

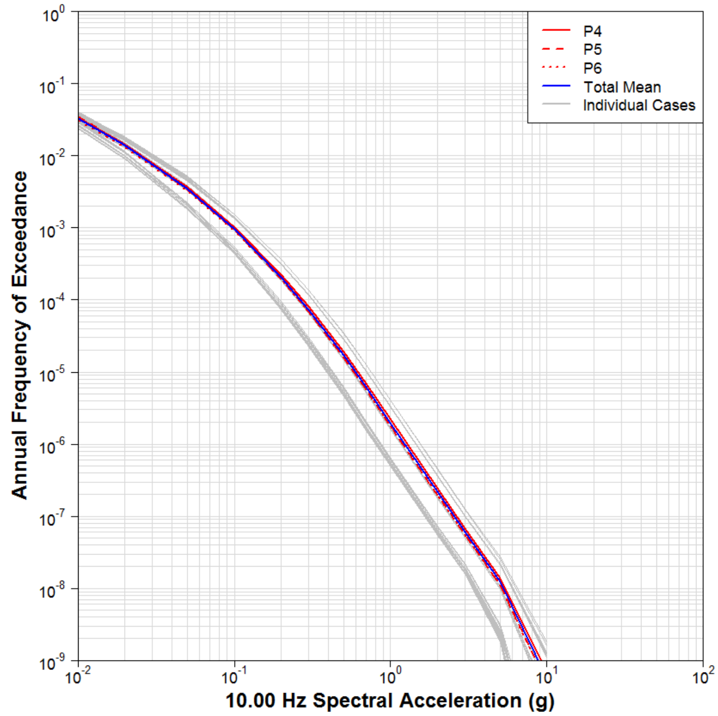

b)

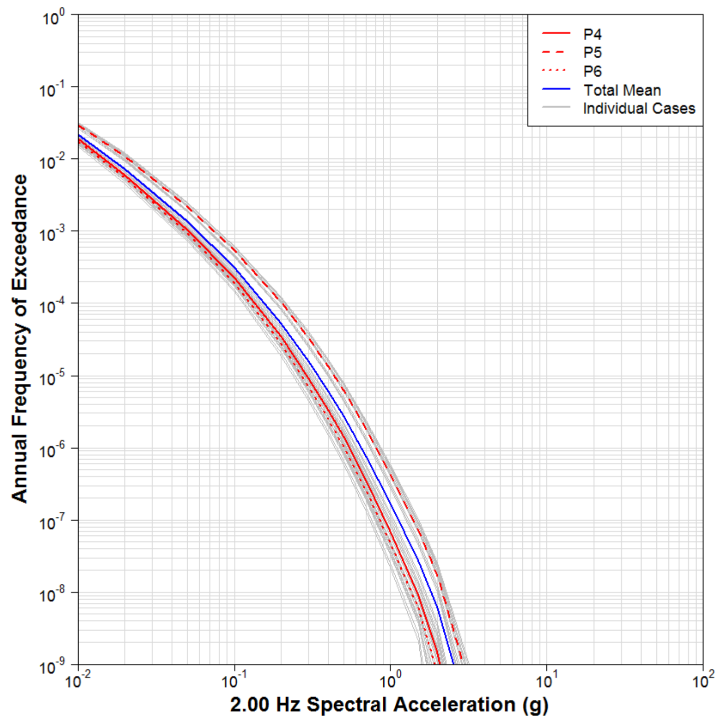

Figure 10-126. Sensitivity of hazard at ATR Rock with respect to velocity profile at: 10 Hz (0.1-sec); and b) 2 Hz (0.5-sec) spectral accelerations. Profiles P4 through P6 do not contain basalt interbeds at depth ~ 40 m.

a)

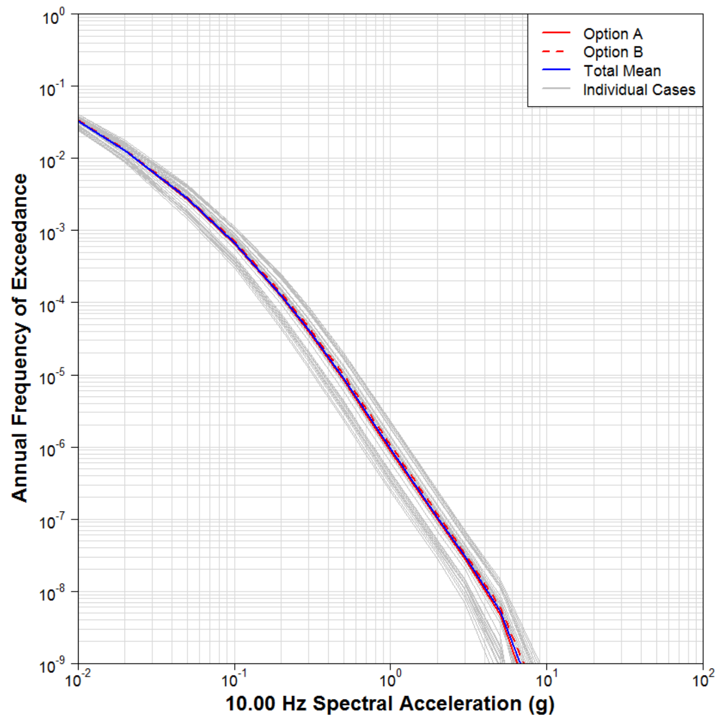

b)

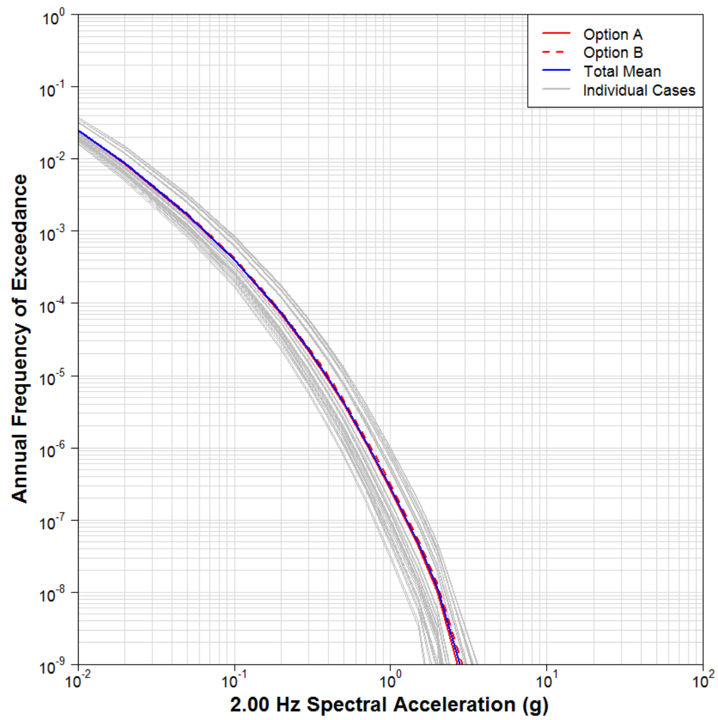

Figure 10-127. Sensitivity of hazard at ATR Rock with respect to $\sigma_{epistemic}$ model at: a) 10 Hz (0.1-sec); and b) 1 Hz (1-sec) spectral accelerations.

a)

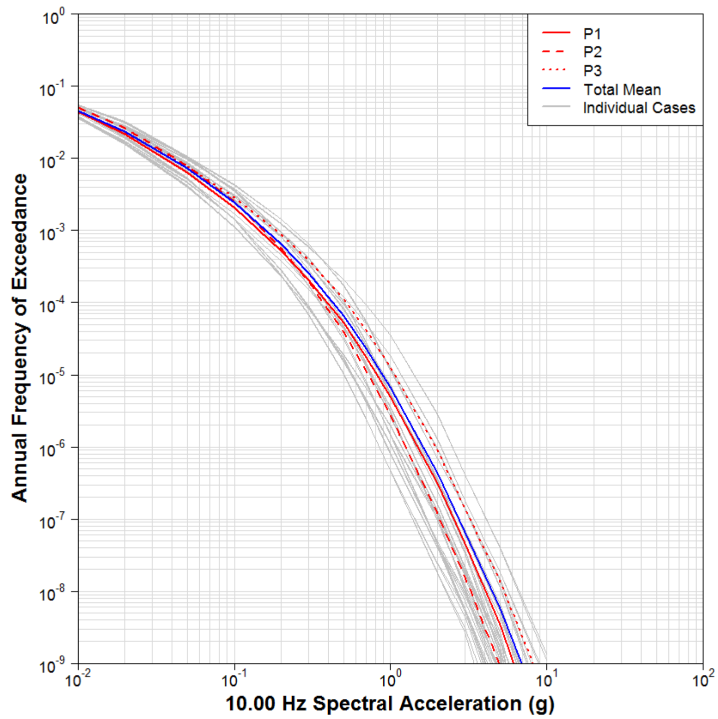

b)

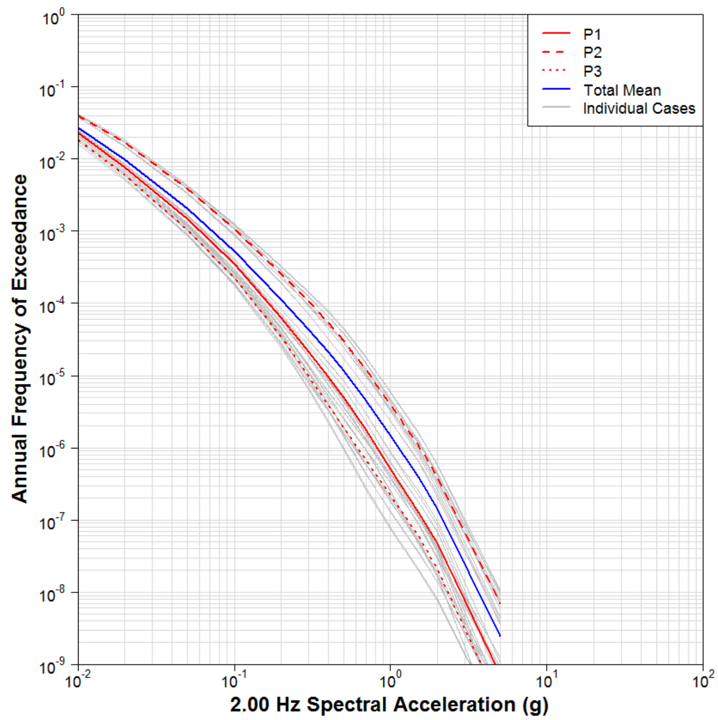

Figure 10-128. Sensitivity of the hazard at ATR for 20 ft of soil with respect to velocity profile at: 10 Hz (0.1-sec); and b) 2 Hz (0.5-sec) spectral accelerations. Profiles P1 through P3 contain basalt interbeds at depth ~ 40 m.

a)

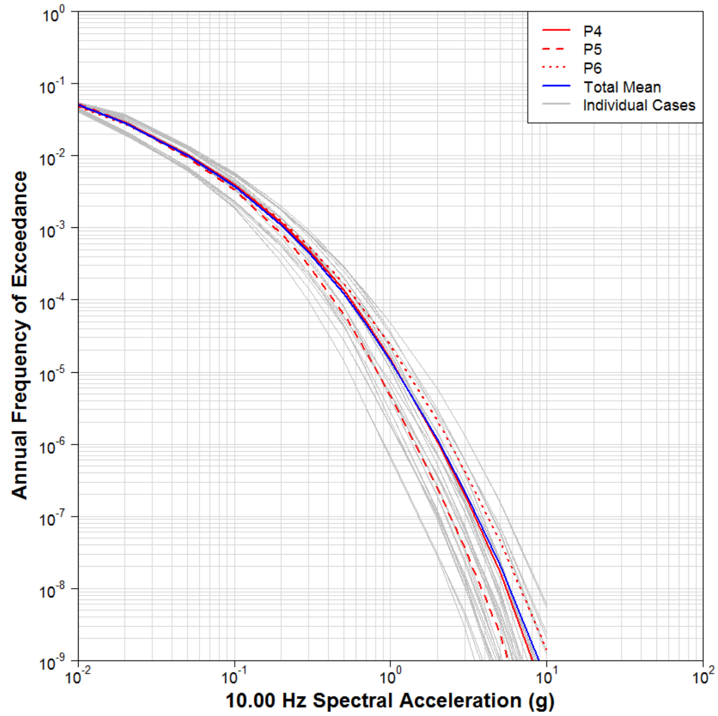

b)

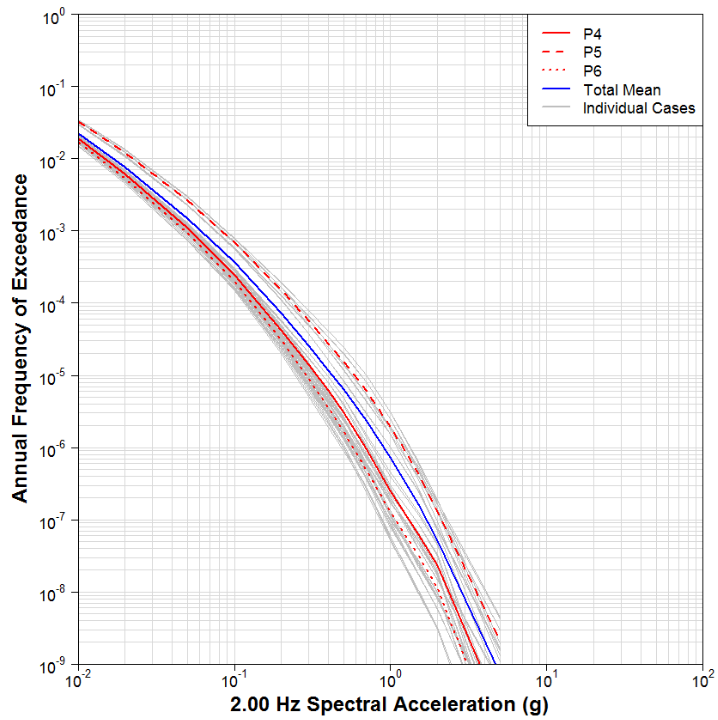

Figure 10-129. Sensitivity of the hazard at ATR for 20 ft of soil with respect to velocity profile at: 10 Hz (0.1-sec); and b) 2 Hz (0.5-sec) spectral accelerations. Profiles P4 through P6 do not contain basalt interbeds at depth ~ 40 m.

a)

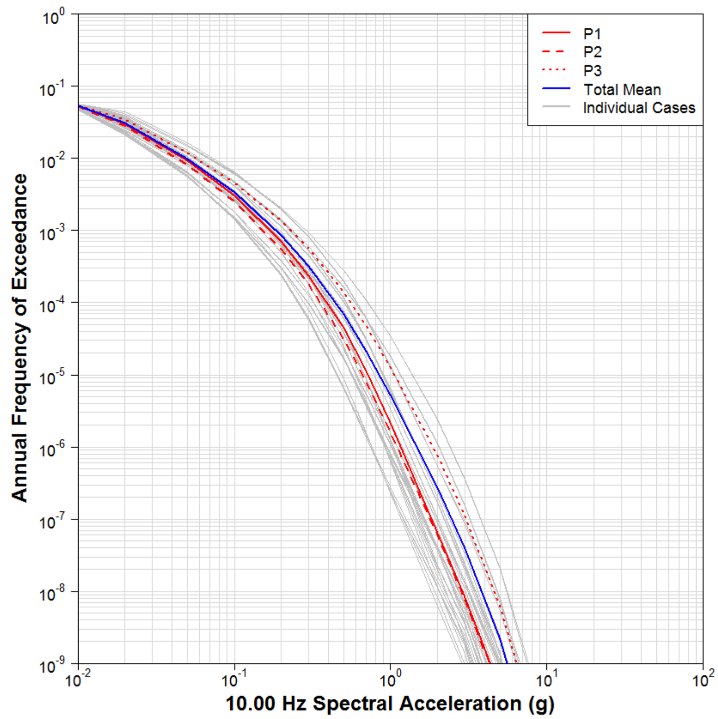

b)

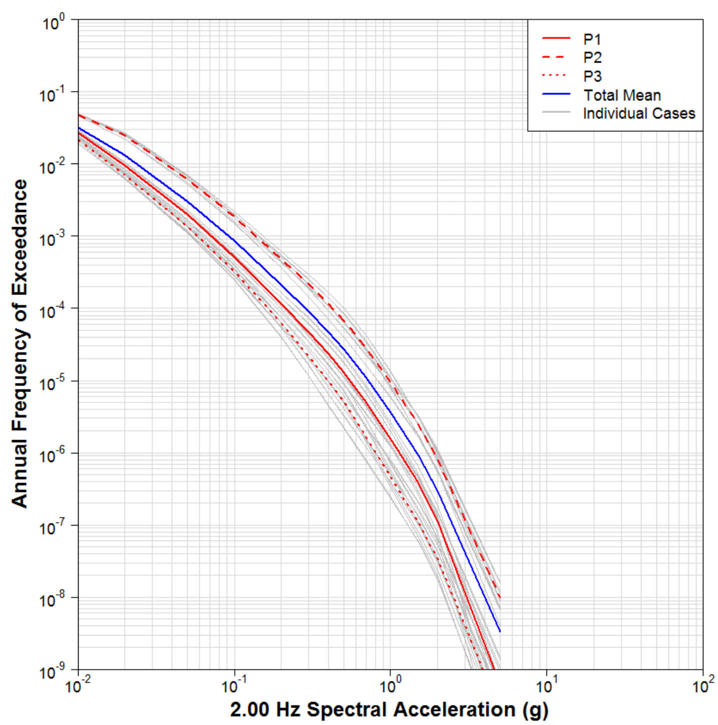

Figure 10-130. Sensitivity of the hazard at ATR for 40 ft of soil with respect to velocity profile at: 10 Hz (0.1-sec); and b) 2 Hz (0.5-sec) spectral accelerations. Profiles P1 through P3 contain basalt interbeds at depth ~ 40 m.

a)

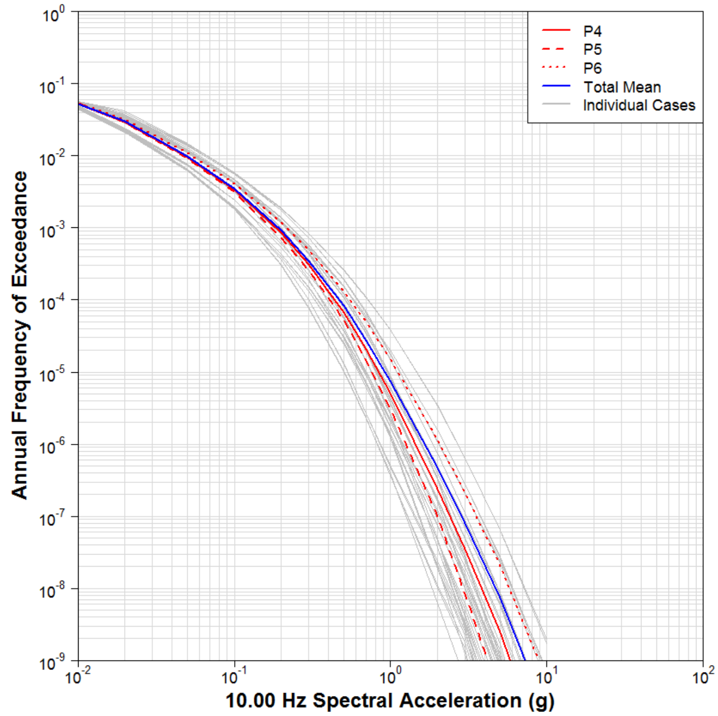

b)

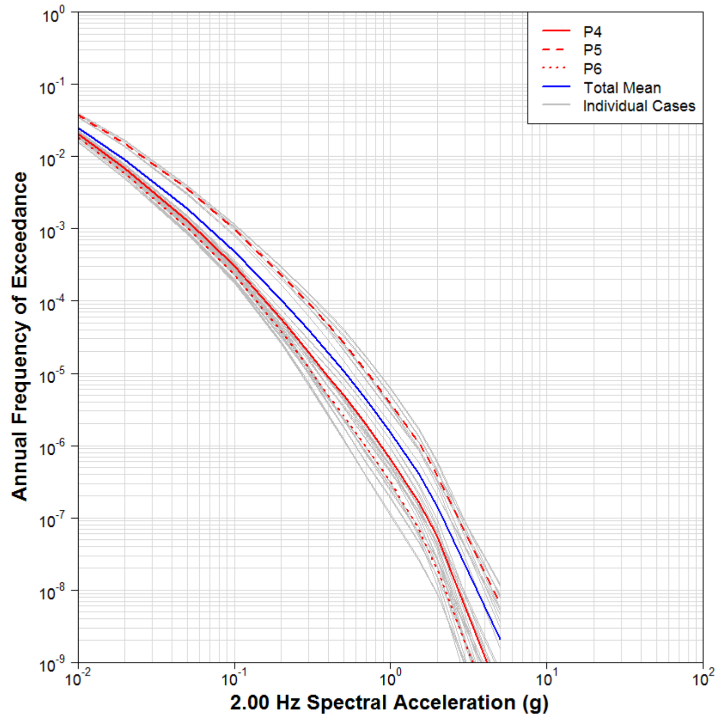

Figure 10-131. Sensitivity of the hazard at ATR for 40 ft of soil with respect to velocity profile at: 10 Hz (0.1-sec); and b) 2 Hz (0.5-sec) spectral accelerations. Profiles P4 through P6 do not contain basalt interbeds at depth ~ 40 m.

a)

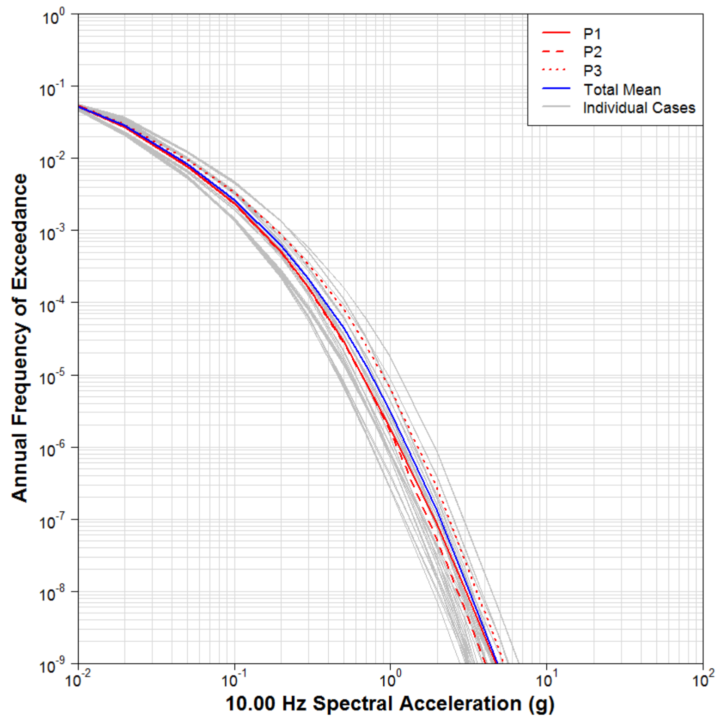

b)

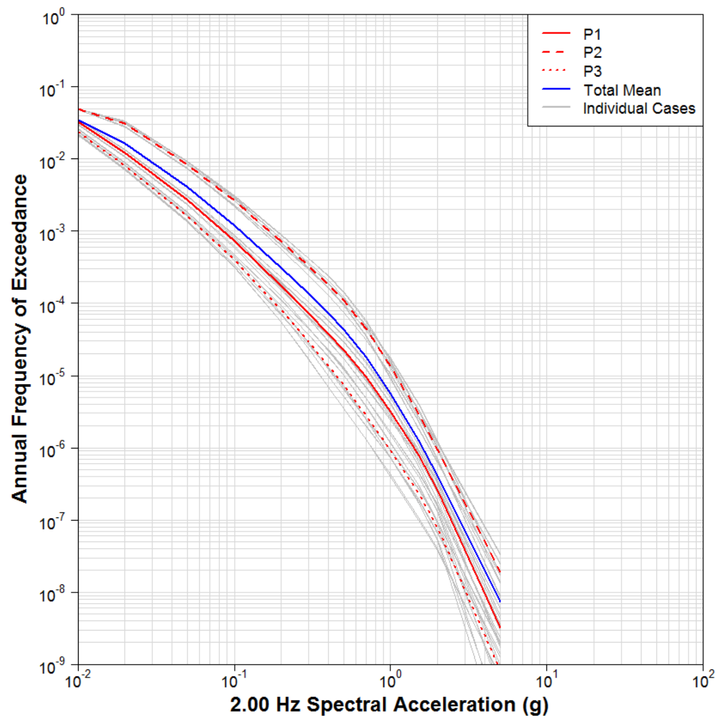

Figure 10-132. Sensitivity of the hazard at ATR for 60 ft of soil with respect to velocity profile at: 10 Hz (0.1-sec); and b) 2 Hz (0.5-sec) spectral accelerations. Profiles P1 through P3 contain basalt interbeds at depth ~ 40 m.

a)

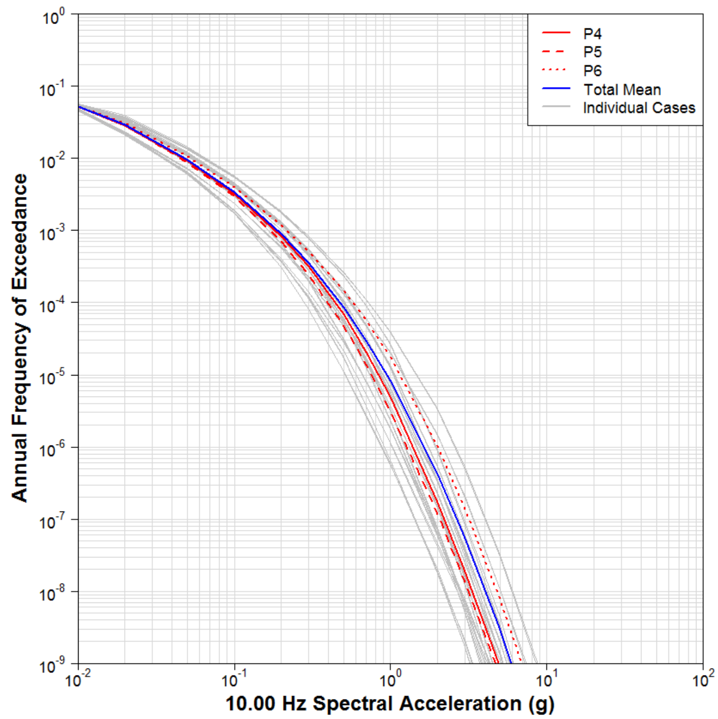

b)

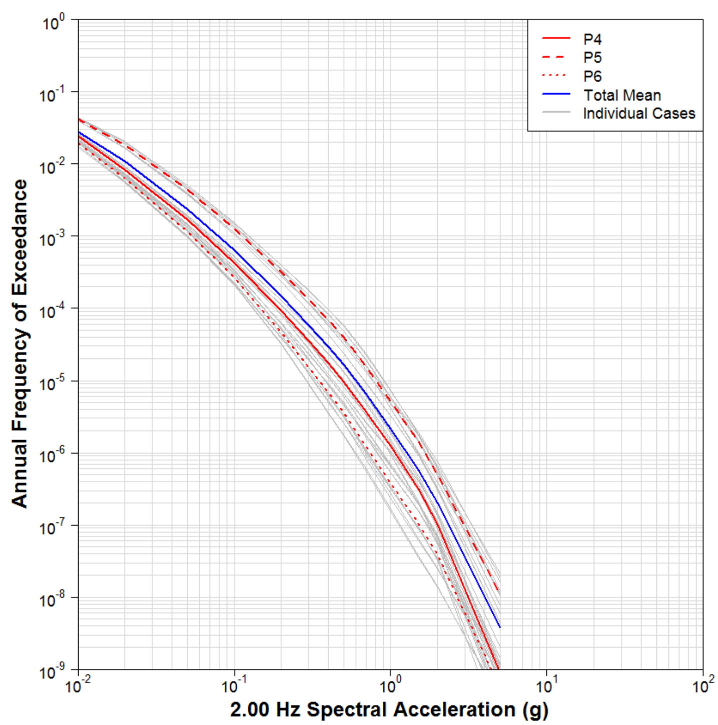

Figure 10-133. Sensitivity of the hazard at ATR for 60 ft of soil with respect to velocity profile at: 10 Hz (0.1-sec); and b) 2 Hz (0.5-sec) spectral accelerations. Profiles P4 through P6 do not contain basalt interbeds at depth ~ 40 m.

a)

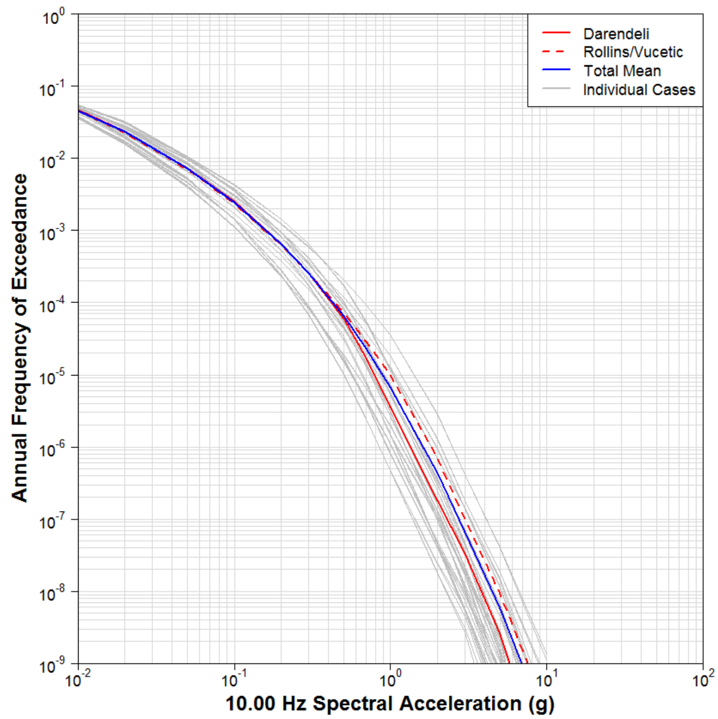

b)

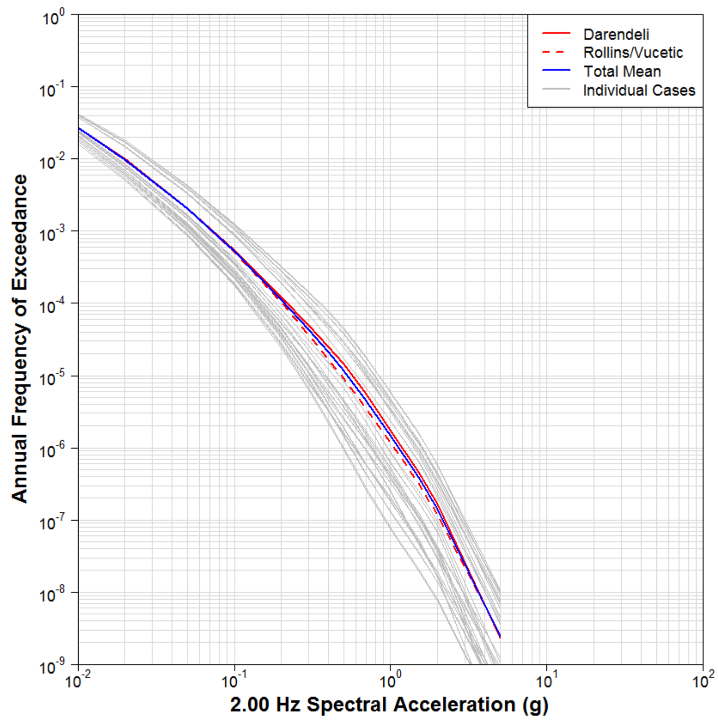

Figure 10-134. Sensitivity of the hazard at ATR for 20 ft of soil with respect to material properties at: 10 Hz (0.1-sec); and b) 2 Hz (0.5-sec) spectral accelerations.

a)

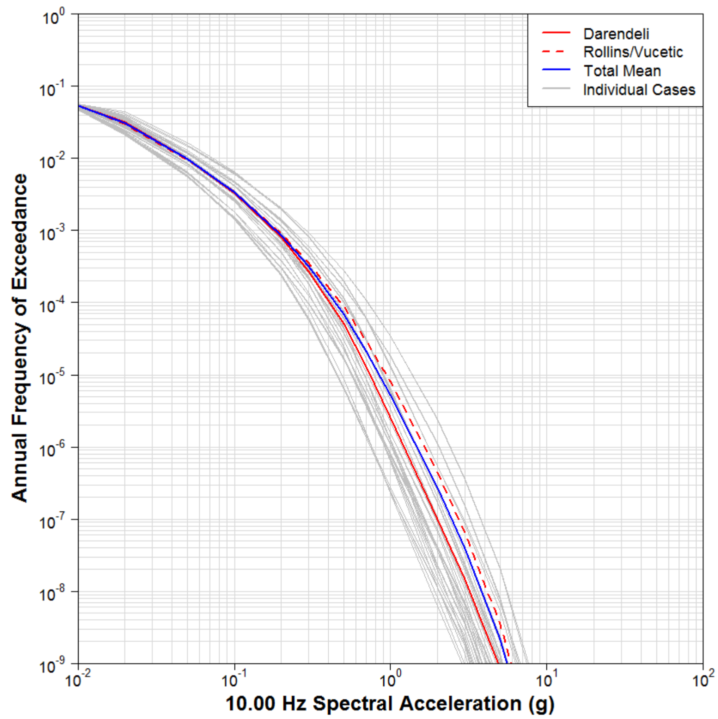

b)

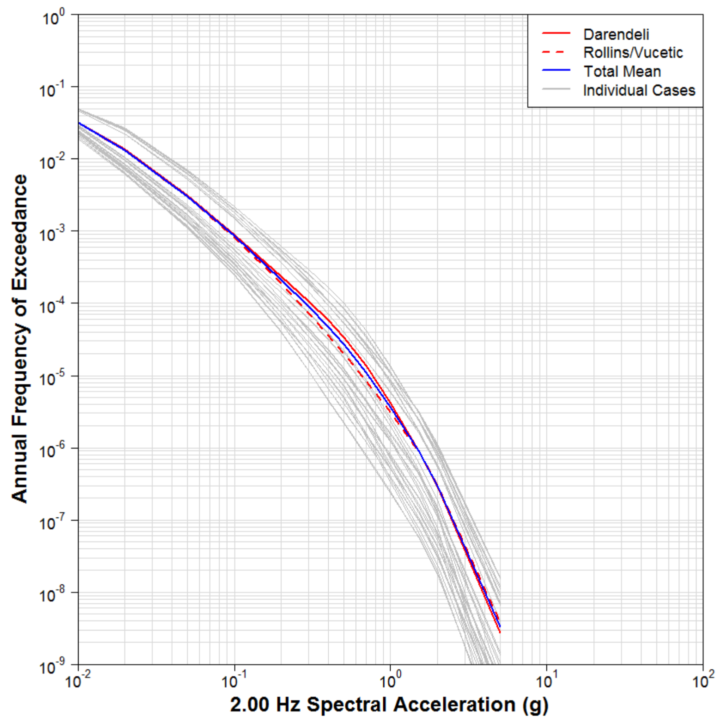

Figure 10-135. Sensitivity of the hazard at ATR for 40 ft of soil with respect to material properties at: 10 Hz (0.1-sec); and b) 2 Hz (0.5-sec) spectral accelerations.

a)

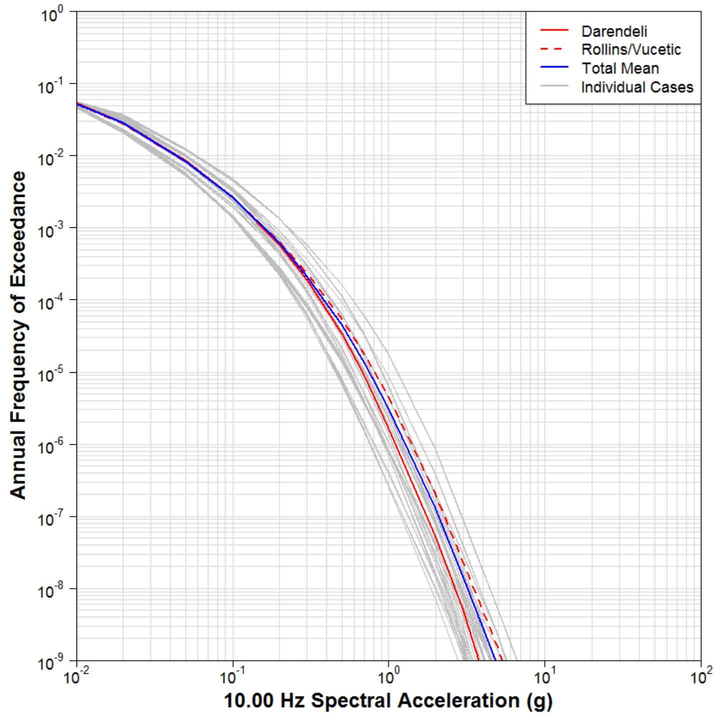

b)

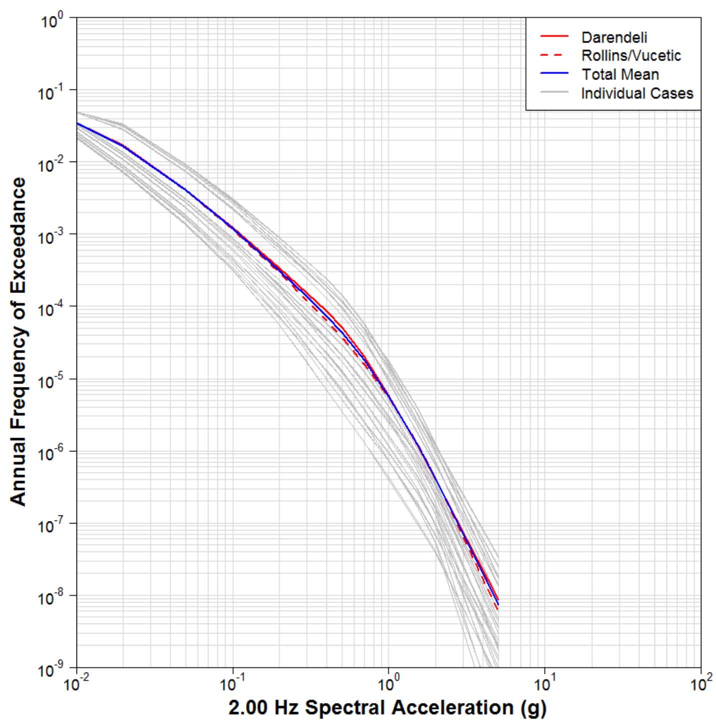

Figure 10-136. Sensitivity of the hazard at ATR for 60 ft of soil with respect to material properties at: 10 Hz (0.1-sec); and b) 2 Hz (0.5-sec) spectral accelerations.

10.8.3 UHRS and GMRS for ATR

This section presents the horizontal and vertical UHRS and GMRS for rock and soil sites, and compares the UHRS and GMRS to their respective DBGMs for ATR buildings and firewater piping areas per their rock and soil conditions. The horizontal GMRS are calculated first and then the vertical GMRS are calculated using the V/H ratios. The results in this section will be used as input to the SHPRM for Criteria 5 and 6 (Section 1.2.3). For ATR, the DBGMs are defined as the “2002 ATR Rock DBE” (Payne et al., 2002), and “2006 ATR Soil DBE” (Payne, 2006b) (Table 1-1); both at the 10,000-yr return period.

The horizontal UHRS are computed for the ATR sites by interpolating the mean hazard curves for the individual spectral frequencies. The hazard was computed using two shear wave velocity profiles, one with and one without interbeds at ~40 m depth, so the individual horizontal UHRS for rock and soil depths (20 ft, 40 ft, and 60 ft) are compared with their respective DBGMs for Evaluation Criterion 5. Following the approach in Section 10-3, the horizontal GMRS at SDC-4, which is associated with the return period of 2,500 yr (ASCE, 2005), is calculated using the UHRS. The GMRS for rock and each soil depth of 20 ft, 40 ft, and 60 ft is developed by enveloping the spectra for the two profiles (with and without interbeds at ~40 m depth). The site-specific horizontal GMRS for ATR buildings or firewater piping areas on soil sites are developed by enveloping the individual soil depth GMRS for the applicable combinations of soil depths listed in Table 7-11. For Evaluation Criterion 6, each horizontal GMRS is then compared with the respective horizontal DBGM for the ATR buildings and firewater piping areas per their rock and soil conditions.

The vertical GMRS is computed using V/H ratios and the horizontal GMRS for the rock and soil GMRS. Table 9-6 contains the V/H ratios recommended for use at ATR rock and soil sites. These ratios are applied to the horizontal GMRS for the four different site conditions of rock and 20 ft, 40 ft, and 60 ft soil depths to obtain corresponding vertical GMRS. The vertical GMRS for ATR buildings or firewater piping areas on soil sites are developed by enveloping the individual soil depth GMRS for the applicable combinations of soil depths (Table 7-11). The vertical GMRS is then compared with the vertical DBGM for the ATR buildings or firewater piping areas.

10.8.3.1 UHRS and GMRS for ATR Rock Sites

Horizontal UHRS for return periods of 2,500, 10,000, 25,000, and 100,000 yr for the ATR Rock site are shown in Figure 10-137. The solid curves are for the profiles with basalt interbeds at depth ~ 40 m and the dashed curves, labeled (a), are for profiles without basalt interbeds at depth ~ 40 m. This figure shows that the profiles with basalt interbeds at depth ~ 40 m produce UHRS with a more prominent bi-modal shape, resulting from greater deamplification of motions near 10 Hz and greater amplification of motions near 3Hz than profiles without basalt interbeds at depth ~ 40 m.

For rock sites at ATR, Figure 10-138 compares the horizontal UHRS at the 2,500-yr return period and the GMRS for SDC-4 with the DBGM, which is the 2002 ATR Rock DBE (Payne et al., 2002). Rock site conditions apply to the ATR reactor building (TRA-670). Figure 10-138a shows that the DBGM envelopes the UHRS for both profiles with and without the basalt interbeds at ~40 m depth. Figure 10-138b shows the GMRS for each profile with and without the basalt interbeds at ~40 m depth and the “2016 ATR Rock” GMRS, which is taken as the envelop of these two spectra in this study. The 2002 ATR Rock DBE spectrum completely envelops the 2016 ATR Rock GMRS because of the different return periods for the GMRS (2,500 yr) and DBGM (10,000 yr). Table 10-44 lists the horizontal GMRS for 2016 ATR Rock and profiles with and without basalt interbeds ~ 40 m depth.

The vertical SDC-4 GMRS for ATR Rock site for both profiles with and without the basalt interbeds at ~40 m depth and the envelope of the two spectra are shown in Figure 10-139. As was the case for the horizontal GMRS, the vertical 2016 ATR Rock GMRS falls well below the vertical rock DBGM at all frequencies. The vertical 2016 ATR Rock GMRS is listed in Table 10-44.

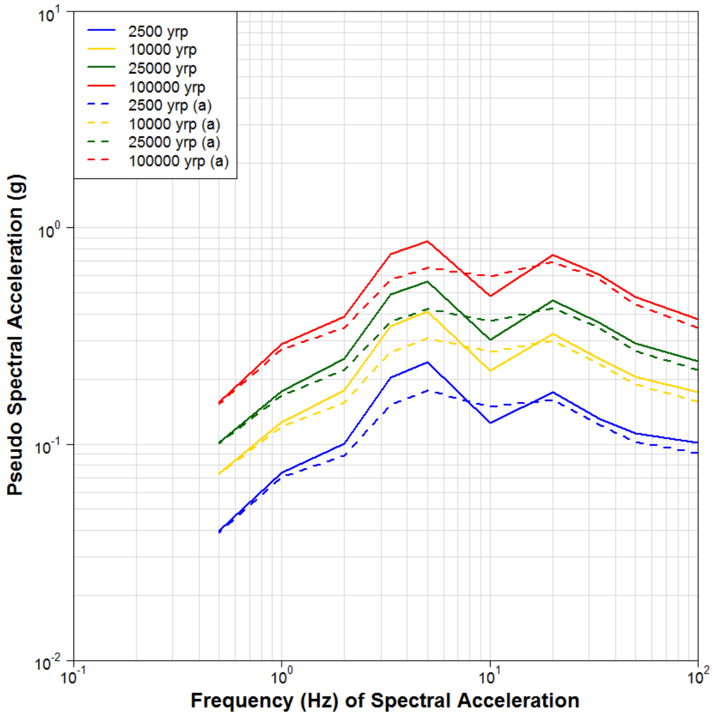

Figure 10-137. ATR rock horizontal UHRS for profiles with sediment interbeds at depth ~ 40 m (solid lines) and profiles without sediment interbeds at depth ~ 40 m (dashed lines labeled (a)) at 5% damping.

Table 10-44. SSHAC Level 1 horizontal and vertical SDC-4 GMRS for ATR Rock site conditions.

Period (sec)	Frequency (Hz)	ATR Rock Spectral Acceleration (g)			
		Profile With Sediment interbeds at depth ~ 40 m Horizontal GMRS	Profile Without Sediment interbeds at depth ~ 40 m Horizontal GMRS	Horizontal 2016 ATR Rock GMRS	Vertical 2016 ATR Rock GMRS
0.01	100	1.22E-01	1.11E-01	1.22E-01	7.93E-02
0.02	50	1.45E-01	1.33E-01	1.45E-01	9.86E-02
0.03	33.3	1.78E-01	1.69E-01	1.78E-01	1.26E-01
0.05	20	2.28E-01	2.11E-01	2.28E-01	1.68E-01
0.075	13.33	2.19E-01	2.16E-01	2.19E-01	1.51E-01
0.1	10	1.53E-01	1.86E-01	1.86E-01	1.11E-01
0.15	6.67	2.32E-01	2.15E-01	2.32E-01	1.46E-01
0.2	5	2.86E-01	2.13E-01	2.86E-01	1.94E-01
0.3	3.33	2.46E-01	1.85E-01	2.46E-01	1.80E-01
0.40	2.5	1.91E-01	1.59E-01	1.91E-01	1.47E-01
0.5	2	1.24E-01	1.10E-01	1.24E-01	9.54E-02
1	1	8.88E-02	8.44E-02	8.88E-02	6.84E-02
2	0.5	5.04E-02	4.98E-02	5.04E-02	3.88E-02

a)

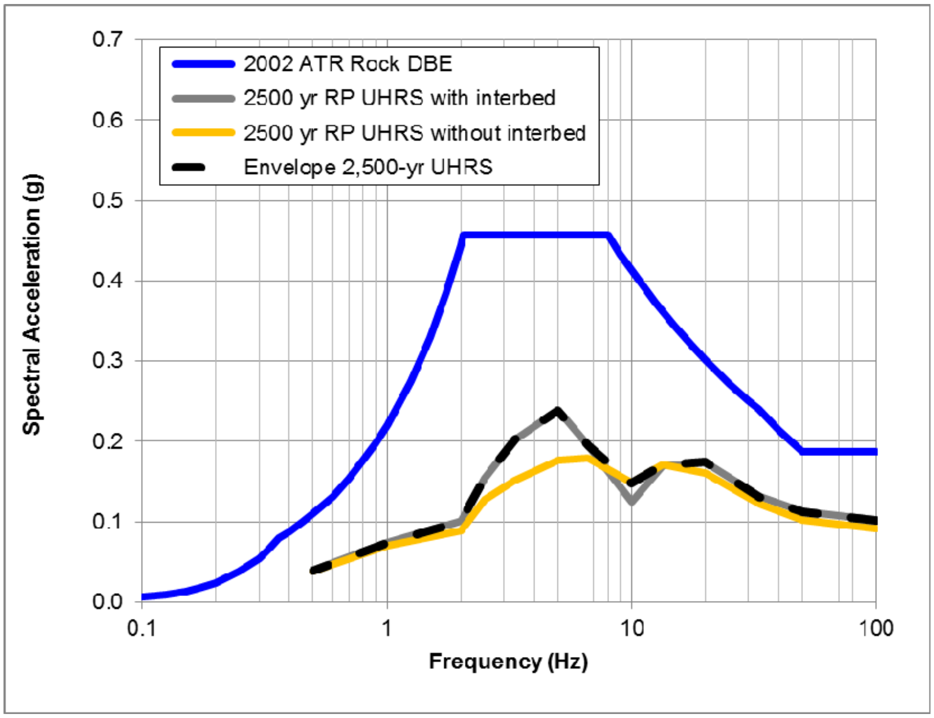

b)

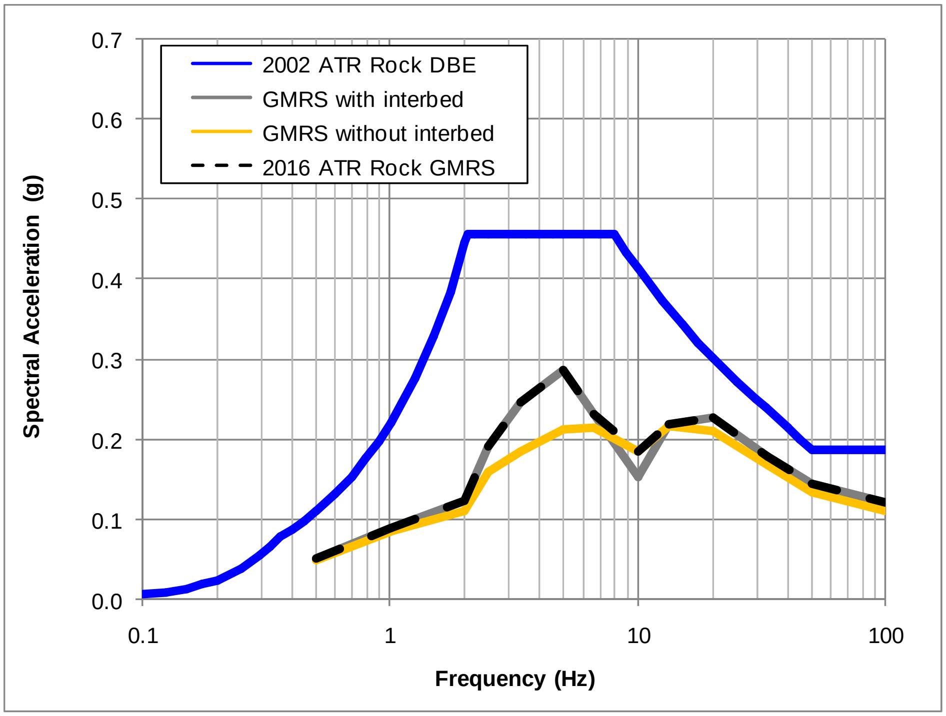

Figure 10-138. Comparisons of the 2002 ATR Rock DBE (blue line) with: a) UHRS at the 2,500 year return period (black dashed line); and b) 2016 ATR Rock GMRS (black dashed line). Both plots show the envelopes of the GMRS for profiles with (grey line) and without (gold line) sediment interbeds at depth ~ 40 m. All spectra are 5% damping.

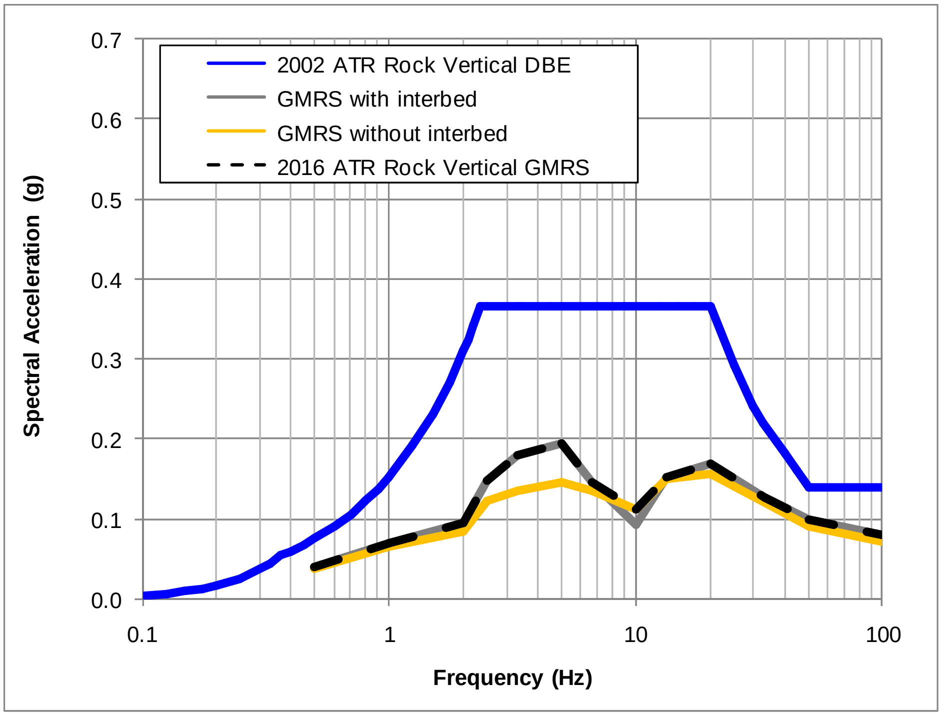

Figure 10-139. Comparison of the 2002 ATR Rock vertical DBE (blue line) with the 2016 ATR Rock vertical GMRS (black line), which is the envelope of the GMRS for profiles with (grey line) and without (gold line) sediment interbeds at depth ~ 40 m.

10.8.3.2 UHRS and GMRS for ATR Soil Sites

Horizontal UHRS for return periods of 2,500, 10,000, 25,000, and 100,000 yr for the ATR soil depths of 20 ft, 40 ft, and 60 ft are shown in Figure 10-140 a, b, and c, respectively. For each soil depth, the plots show the two sets of spectra computed using the velocity profiles with and without sediment interbeds at depth ~ 40 m. The UHRS for 20 ft soil depth show a slight shift in response peak between results with and without sediment interbeds at depth ~ 40 m, with the response peak for profiles with sediment interbeds occurring at slightly lower frequency (Figure 10-140a). However, the observed difference in spectral shape is not as drastic as was the case for the ATR Rock site. The differences in spectral shape become less prominent for the 40 ft (Figure 10-140b) and 60 ft (Figure 10-140c) soil depths.

The horizontal UHRS at 2,500 yr return period for all three soil depths are compared with the DBGM for soil conditions at ATR. Figure 10-141 shows that the 2006 ATR Soil DBE spectrum (Payne, 2006b) envelopes the six UHRS for the three soil depths which include the profiles with and without the sediment interbeds at ~40 m depth. The 2006 ATR Soil DBE spectrum was broadened to be applicable to soil depths that range from 20 to 65 ft at ATR (Payne, 2006b).

The horizontal 2006 ATR Soil DBE spectrum (Payne, 2006b) is compared with the 2016 SDC-4 GMRS for the three soil depths from this SSHAC Level 1 study. For each soil depth, an envelope was developed from the two profiles with and without sediment interbeds at ~40 m depth. Figure 10-142 a, b, and c shows that the 2006 ATR Soil DBE spectrum envelopes the 2016 SDC-4 GMRS for all three soil depths. Table 10-45 lists the horizontal 2016 SDC-4 GMRS spectra for the 20 ft, 40 ft, and 60 ft, respectively, for both profiles with and without sediment interbeds at depth ~ 40 m.

Site-specific 2016 Soil GMRS were developed for the soil depth variability underlying the ATR support buildings and firewater piping areas. The site-specific horizontal GMRS for ATR buildings and firewater piping areas on soil sites are developed by enveloping the individual soil depth GMRS for the applicable combinations of soil depths. Table 10-46 lists the sets of soil depths that were enveloped to produce the site-specific GMRS which are labeled as follows: 2016 Soil (20-40) GMRS, 2016 Soil (40-60) GMRS, and 2016 Soil (20-40-60) GMRS. Each of the site-specific GMRS is compared with the 2006 ATR Soil DBE spectrum. Figure 10-143 shows the comparison with the 2016 Soil (20-40) GMRS which applies to the range of soil depths from 20 to 40 ft that underlies ATR support buildings TRA-688, TRA-674, TRA-770, and TRA-781 and Firewater Piping Areas A1 and A3. Figure 10-144 shows the comparison with the 2016 Soil (40-60) GMRS for sites that have soil depths from 40 to 60 ft, which includes ATR buildings TRA-650 and TRA-786 and Firewater Piping Area A4. Figure 10-145 shows the comparison with 2016 Soil (20-40-60) GMRS for sites that have the largest range of soil depths from 20 to 60 ft which underlies Firewater Piping Area A2. In each figure the 2006 ATR Soil DBE spectrum (Payne, 2006b) envelops the site-specific 2016 GMRS primarily due to the different return periods of the GMRS (2,500 yr) and DBGM (10,000 yr). The spectral accelerations for the site-specific 2016 Soil GMRS are listed in Table 10-47.

The vertical site-specific SDC-4 GMRS are compared with the vertical 2006 ATR Soil DBE spectrum. Figures 10-146, 10-147, and 10-148 show the vertical Soil (20-40) GMRS, 2016 Soil (40-60) GMRS, and 2016 Soil (20-40-60) GMRS, respectively. Each of the vertical SDC-4 GMRS spectra is shown for the soil depths that produced the site-specific envelopes. All of the site-specific vertical 2016 soil GMRS fall well below the vertical 2006 ATR Soil DBE spectrum (Payne, 2006b) for the same reason as the horizontal spectra. Table 10-48 lists the vertical SDC-4 GMRS for each of the soil depths (20 ft, 40 ft, and 60 ft), and Table 10-49 lists the vertical 2016 Soil (20-40) GMRS, 2016 Soil (40-60) GMRS, and 2016 Soil (20-40-60) GMRS.

a)

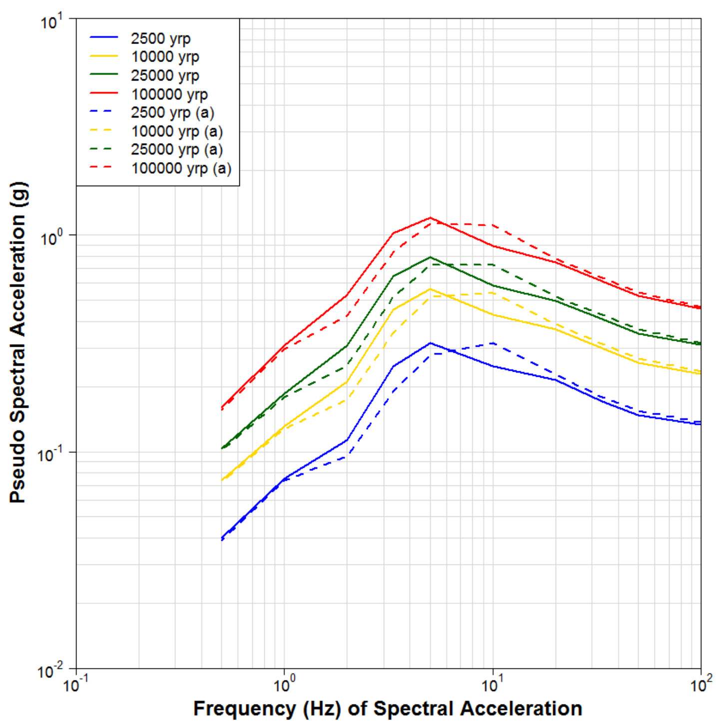

b)

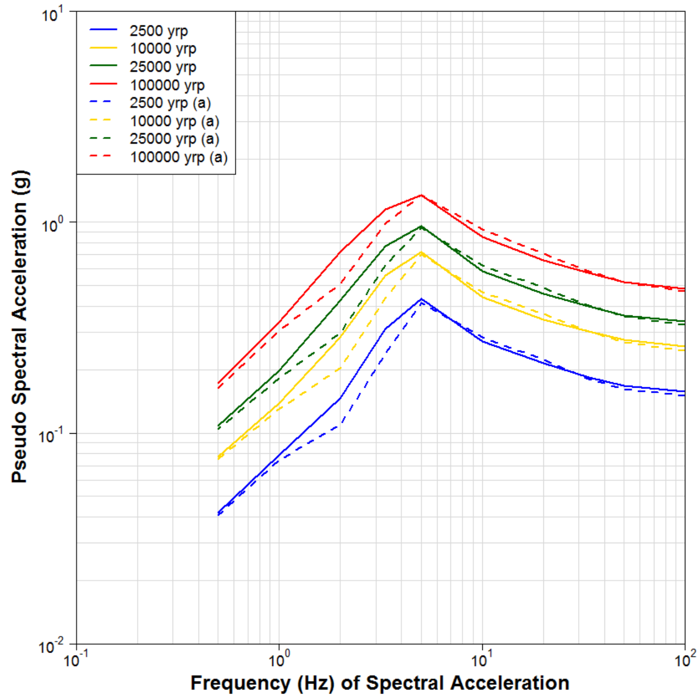

c)

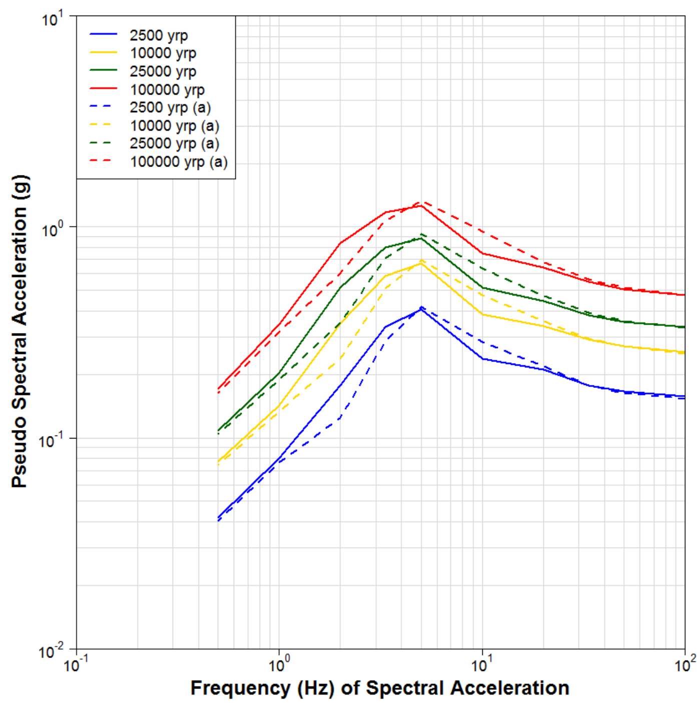

Figure 10-140. Horizontal UHRS for profiles with basalt interbeds at depth ~ 40 m (solid lines) and profiles without basalt interbeds at depth ~ 40 m (dashed lines labeled (a)) at 5% damping for soil depths of: a) 20 ft; b) 40 ft; and c) 60 ft.

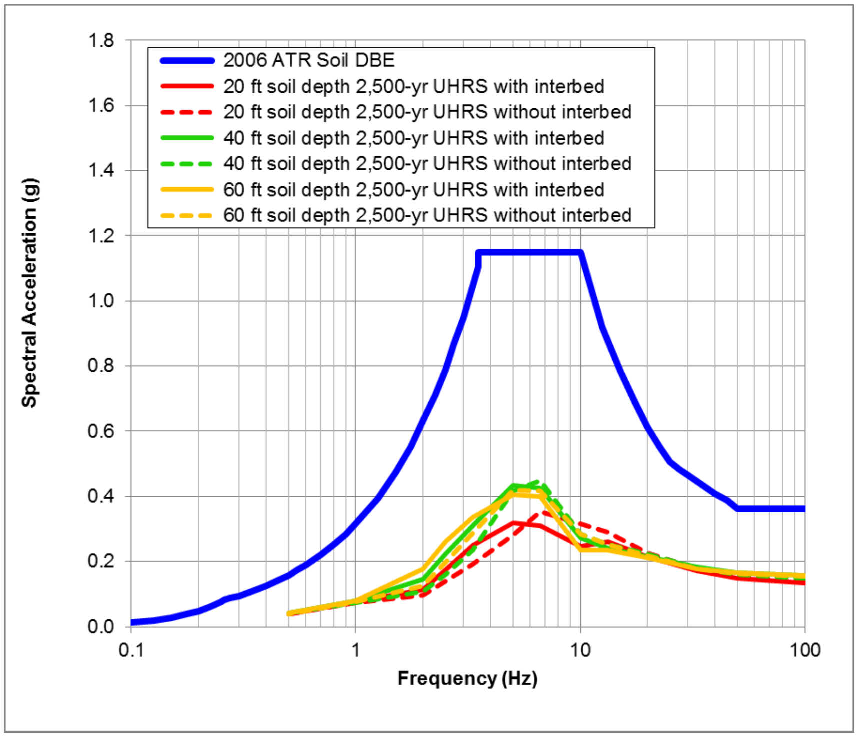

Figure 10-141. Comparisons of the 2006 ATR Soil DBE spectrum with the horizontal UHRS at 2,500 yr return period for profiles with (solid lines) and without (dashed lines) basalt interbeds at depth ~ 40 m at 5% damping for soil depths of 20 ft (red); 40 ft (green); 60 ft (yellow).

a)

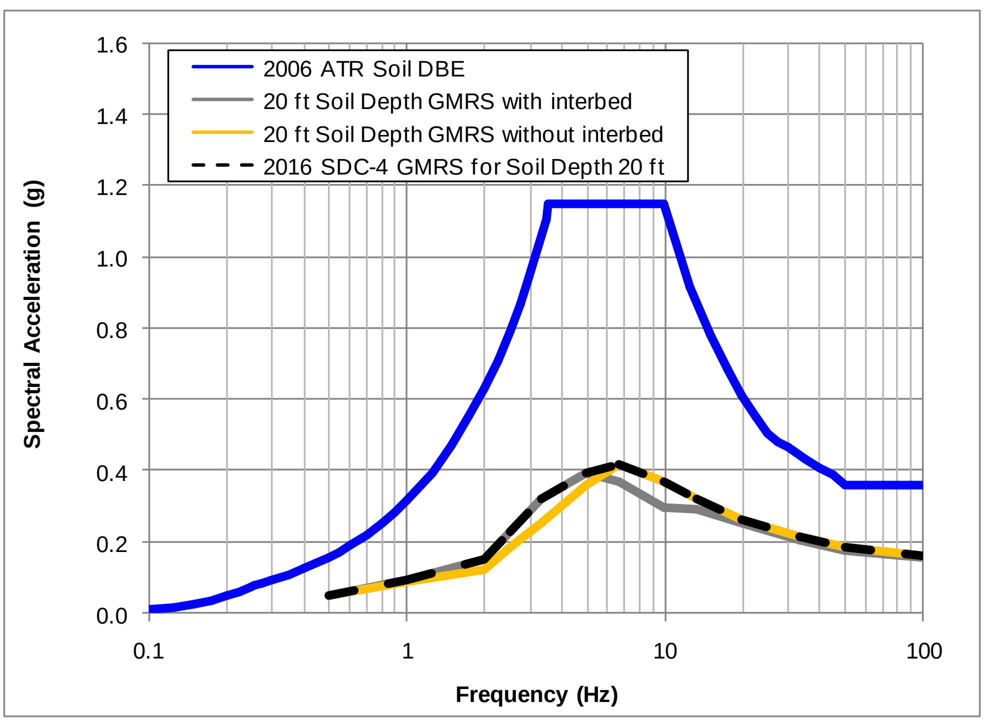

b)

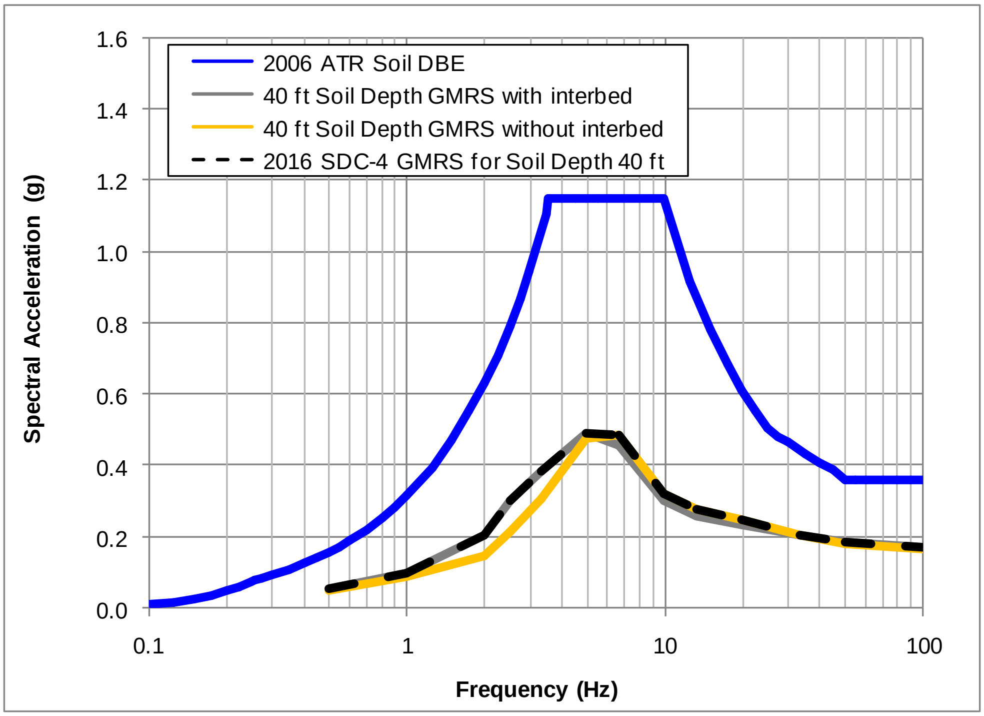

c)

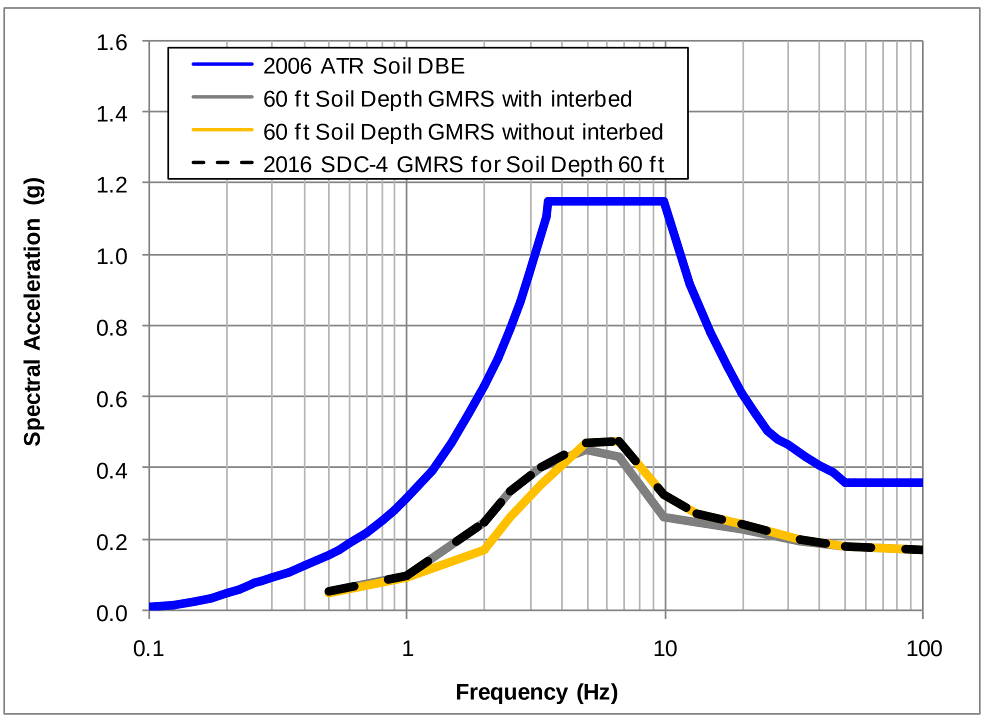

Figure 10-142. Comparisons of the 2006 ATR Soil DBE spectrum (blue line) and 2016 SDC-4 GMRS (dashed black lines) for soil depths: a) 20 ft; b) 40 ft; and 60 ft from this SSHAC Level 1 study. Each 2016 SDC-4 GRMS is produced by enveloping the spectra for the two profiles with (grey line) and without (gold line) basalt interbeds at depth ~ 40 m. All spectra are 5% damping.

Table 10-45. Horizontal SDC-4 GMRS for ATR soil depths of 20 ft, 40 ft, and 60 ft computed using the results of the SSHAC Level 1 study.

Period (sec)	Frequency (Hz)	ATR of Soil Spectral Acceleration (g)		
		Profile With Basalt Interbeds at depth ~ 40 m Horizontal GMRS	Profile Without Basalt Interbeds at depth ~ 40 m Horizontal GMRS	Envelop SDC-4 Soil GMRS
20 ft Soil Depth				
0.01	100	1.58E-01	1.61E-01	1.61E-01
0.02	50	1.78E-01	1.85E-01	1.85E-01
0.03	33.3	2.07E-01	2.16E-01	2.16E-01
0.05	20	2.53E-01	2.65E-01	2.65E-01
0.075	13.33	2.93E-01	3.24E-01	3.24E-01
0.1	10	2.96E-01	3.71E-01	3.71E-01
0.15	6.67	3.71E-01	4.20E-01	4.20E-01
0.2	5	3.95E-01	3.62E-01	3.95E-01
0.3	3.33	3.20E-01	2.55E-01	3.20E-01
0.40	2.5	2.32E-01	1.85E-01	2.32E-01
0.5	2	1.52E-01	1.24E-01	1.52E-01
1	1	9.26E-02	8.96E-02	9.26E-02
2	0.5	5.12E-02	5.01E-02	5.12E-02
40 ft Soil Depth				
0.01	100	1.74E-01	1.68E-01	1.74E-01
0.02	50	1.86E-01	1.83E-01	1.86E-01
0.03	33.3	2.05E-01	2.06E-01	2.06E-01
0.05	20	2.35E-01	2.50E-01	2.50E-01
0.075	13.33	2.58E-01	2.80E-01	2.80E-01
0.1	10	3.01E-01	3.20E-01	3.20E-01
0.15	6.67	4.58E-01	4.87E-01	4.87E-01
0.2	5	4.91E-01	4.79E-01	4.91E-01
0.3	3.33	3.86E-01	3.09E-01	3.86E-01
0.4	2.5	3.00E-01	2.13E-01	3.00E-01
0.5	2	2.07E-01	1.46E-01	2.07E-01
1	1	9.89E-02	9.14E-02	9.89E-02
2	0.5	5.38E-02	5.19E-02	5.38E-02

Table 10-45. Continued.

Period (sec)	Frequency (Hz)	ATR of Soil Spectral Acceleration (g)		
		Profile With Basalt Interbeds at depth ~ 40 m Horizontal GMRS	Profile Without Basalt Interbeds at depth ~ 40 m Horizontal GMRS	Envelop SDC-4 Soil GMRS
60 ft Soil Depth				
0.01	100	1.73E-01	1.70E-01	1.73E-01
0.02	50	1.83E-01	1.83E-01	1.83E-01
0.03	33.3	1.97E-01	2.00E-01	2.00E-01
0.05	20	2.30E-01	2.43E-01	2.43E-01
0.075	13.33	2.52E-01	2.76E-01	2.76E-01
0.1	10	2.64E-01	3.25E-01	3.25E-01
0.15	6.67	4.34E-01	4.76E-01	4.76E-01
0.2	5	4.53E-01	4.74E-01	4.74E-01
0.3	3.33	4.02E-01	3.54E-01	4.02E-01
0.40	2.5	3.37E-01	2.63E-01	3.37E-01
0.5	2	2.51E-01	1.72E-01	2.51E-01
1	1	1.01E-01	9.48E-02	1.01E-01
2	0.5	5.36E-02	5.18E-02	5.36E-02

Table 10-46. Envelop sets of soil depths used to produce site-specific GMRS for ATR buildings and piping areas, group names, and DBGM.

Building or Area	Enveloped Set of Soil Depths for Site-Specific Ground Motion Response Spectrum (GMRS)	Site-specific GMRS Name	Design Basis Ground Motion (DBGM)
TRA-688 TRA-674 TRA-770 TRA-781 Piping Area A1 Piping Area A3	20 ft and 40 ft	2016 Soil (20-40) GMRS	ATR/INTEC 10,000-yr Soil DBE (Payne, 2006b) referred to as “2006 ATR soil DBE” in this study
TRA-650 TRA-786 Piping Area A4	40 ft and 60 ft	2016 (40-60) Soil GMRS	
Piping Area A2	20 ft, 40 ft, and 60 ft	2016 (20-40-60) Soil GMRS	

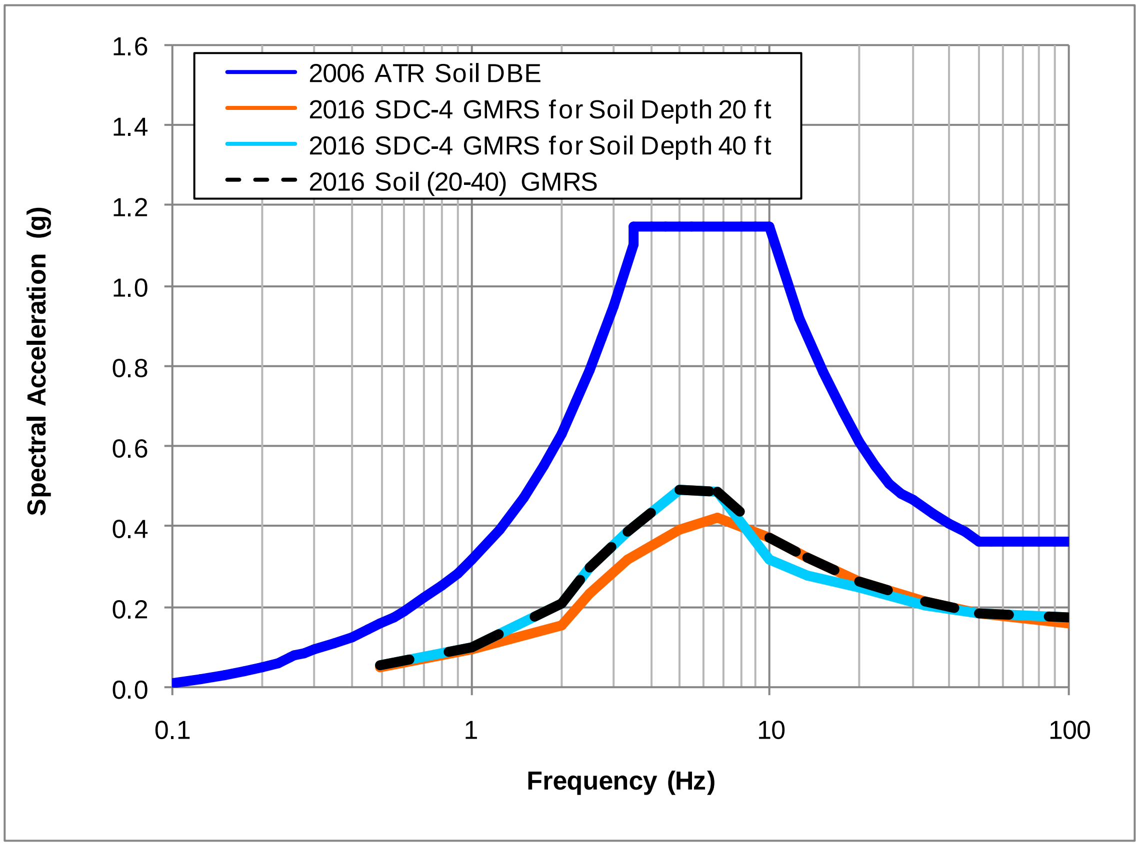

Figure 10-143. Comparison of the 2006 ATR Soil DBE (blue line) and the 2016 Soil (20-40) GRMS (black dashed line), which is the envelope of the SDC-4 GMRS for 20 ft (orange line) and 40 ft (light blue line). The 2016 Soil (20-40) GRMS is for ATR sites with soil depths that range from 20 to 40 ft including ATR support buildings, TRA-688, TRA-674, TRA-770, and TRA-781, and Firewater Piping Areas A1 and A3.

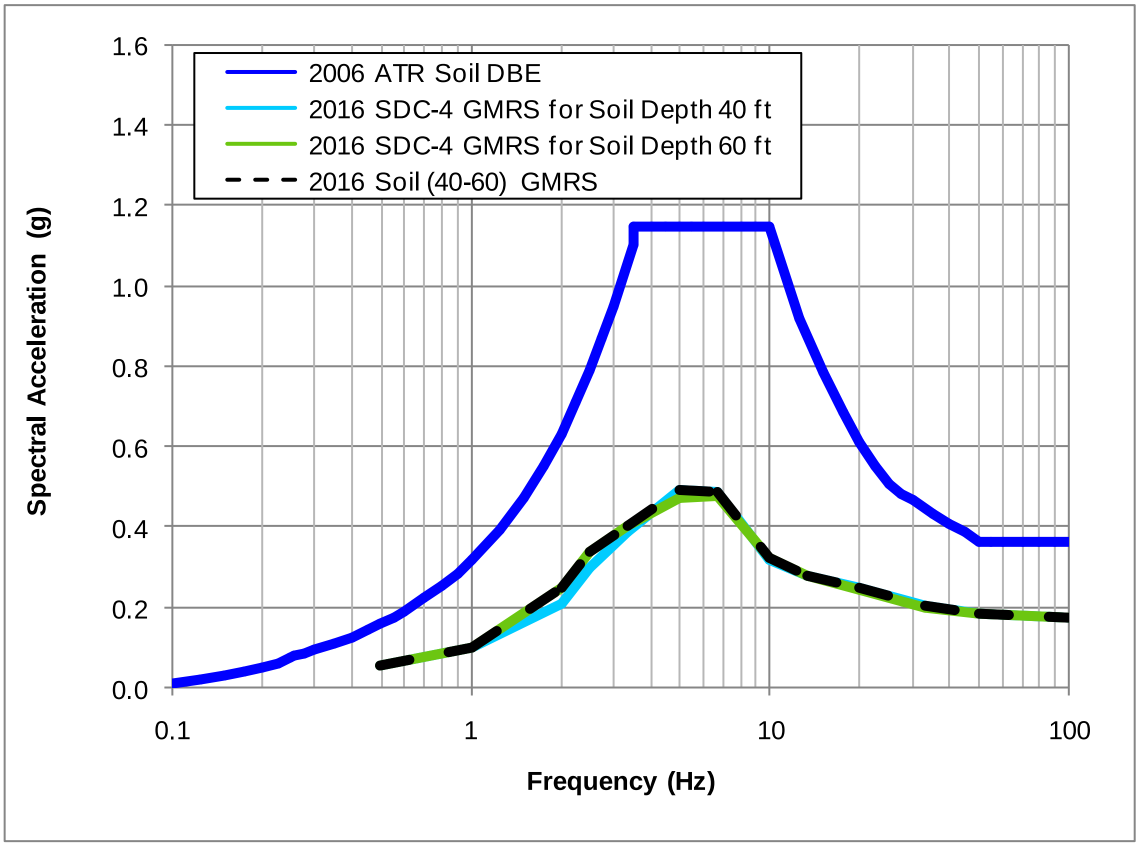

Figure 10-144. Comparison of the 2006 ATR Soil DBE (blue line) and the 2016 Soil (40-60) GRMS (black dashed line), which is the envelope of the SDC-4 GMRS for 40 ft (light blue line) and 60 ft (dark blue line). The 2016 Soil (40-60) GRMS is for ATR sites with soil depths that range from 40 to 60 ft including ATR support buildings, TRA-650 and TRA-786, and Firewater Piping Area A4.

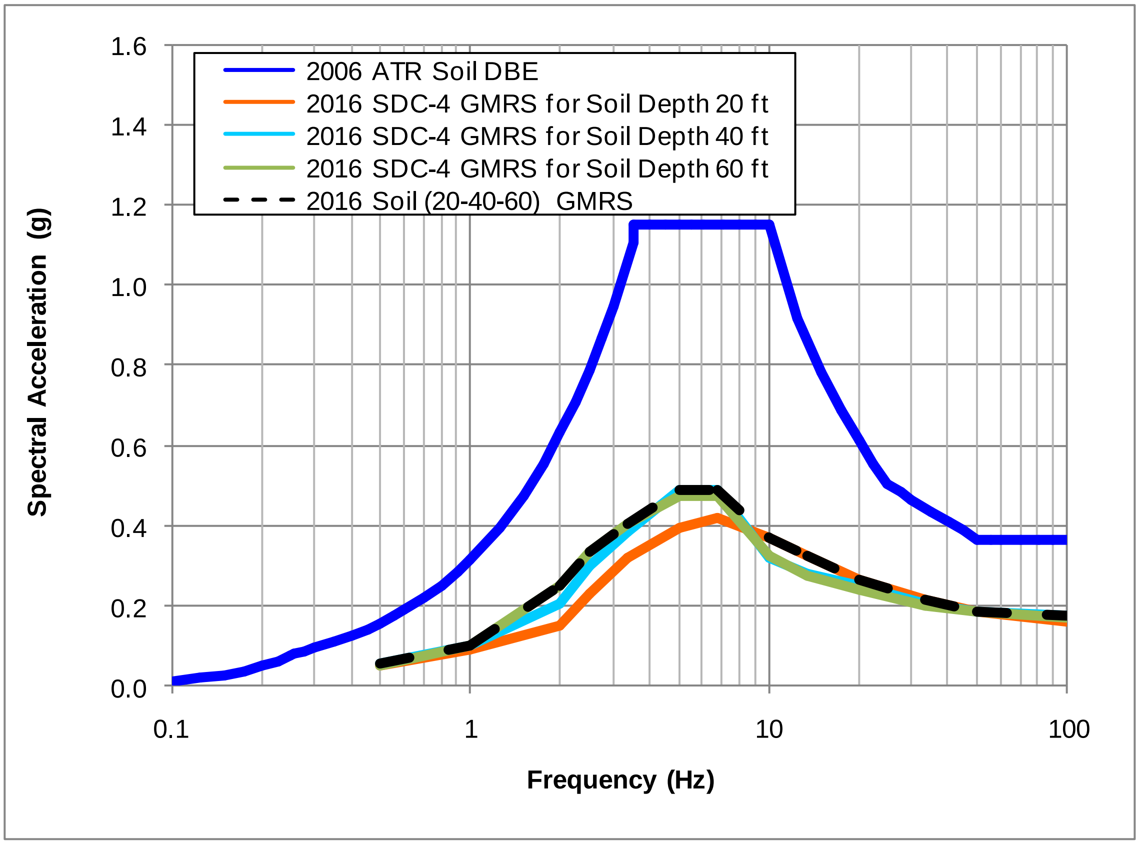

Figure 10-145. Comparison of the 2006 ATR Soil DBE (blue line) and the 2016 Soil (20-40-60) GRMS (black dashed line), which is the envelope of the SDC-4 GMRS for 20 ft (orange line), 40 ft (light blue line), and 60 ft (dark blue line). The 2016 Soil (20-40-60) GRMS is for ATR sites with soil depths that range from 20 to 60 ft including Firewater Piping Area A2.

Table 10-47. Horizontal 2016 GMRS at SDC-4 for ATR soil sites.

Period (sec)	Frequency (Hz)	Horizontal 2016 Soil ATR GMRS at SDC-4 Spectral Acceleration (g)		
		(20-40)	(40-60)	(20-40-60)
0.01	100	1.74E-01	1.74E-01	1.74E-01
0.02	50	1.86E-01	1.86E-01	1.86E-01
0.03	33.3	2.16E-01	2.06E-01	2.16E-01
0.05	20	2.65E-01	2.50E-01	2.65E-01
0.075	13.33	3.24E-01	2.80E-01	3.24E-01
0.1	10	3.71E-01	3.25E-01	3.71E-01
0.15	6.67	4.87E-01	4.87E-01	4.87E-01
0.2	5	4.91E-01	4.91E-01	4.91E-01
0.3	3.33	3.86E-01	4.02E-01	4.02E-01
0.40	2.5	3.00E-01	3.37E-01	3.37E-01
0.5	2	2.07E-01	2.51E-01	2.51E-01
1	1	9.89E-02	1.01E-01	1.01E-01
2	0.5	5.38E-02	5.38E-02	5.38E-02

a)

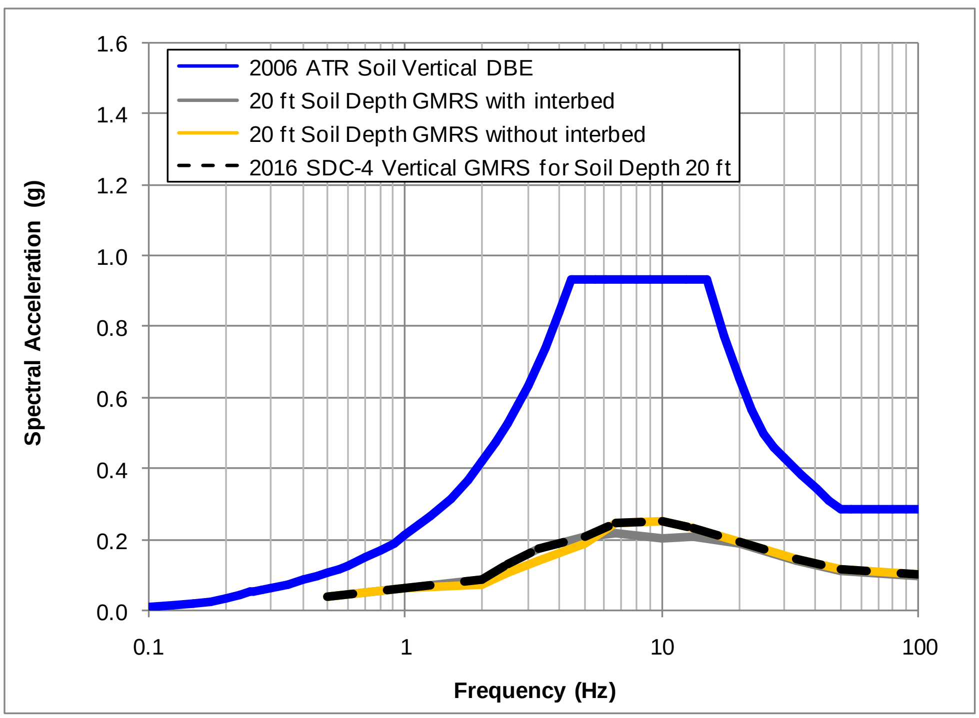

b)

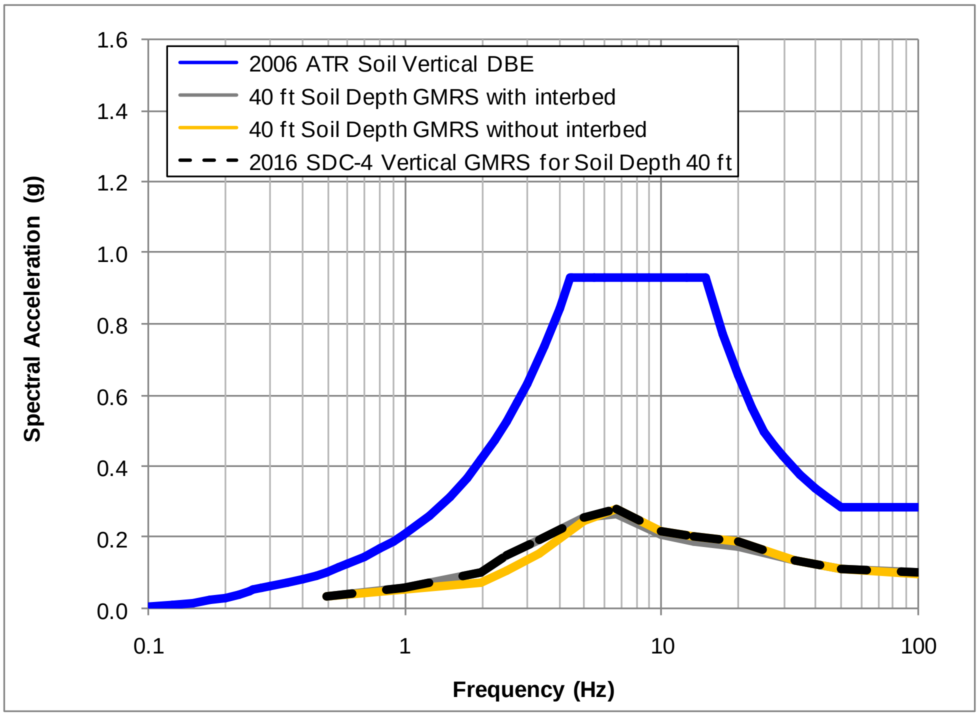

c)

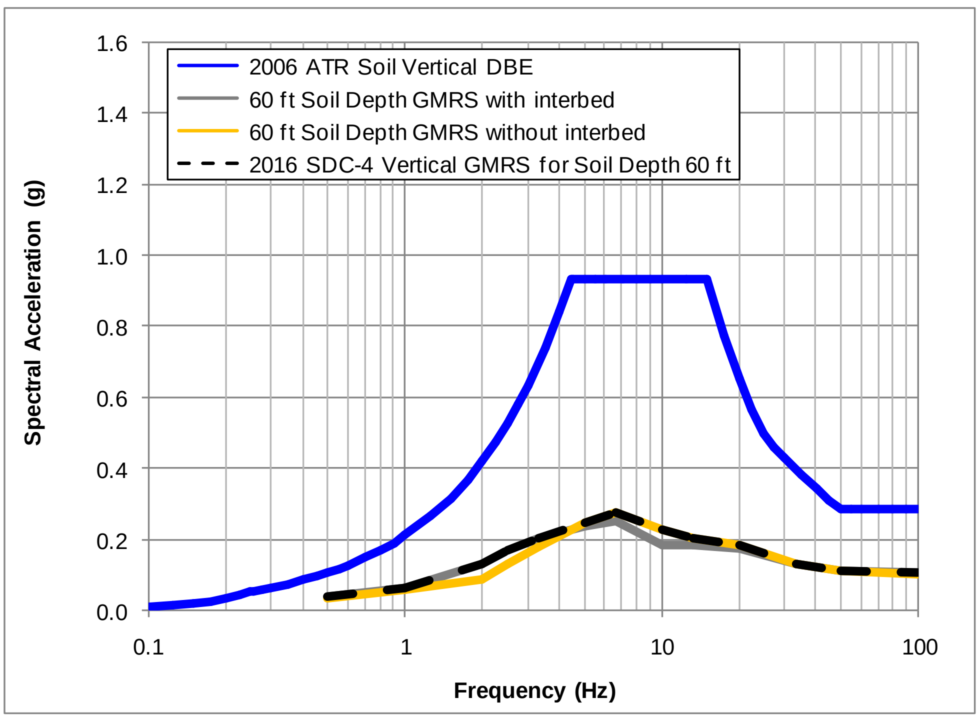

Figure 10-146. Comparisons of the 2006 ATR Soil Vertical DBE spectrum (blue line) and 2016 SDC-4 Vertical GMRS for soil depths: a) 20 ft; b) 40 ft; and c) 60 ft from this SSHAC Level 1 study. Dashed black line is the 2016 SDC-4 GRMS produced by enveloping the spectra for the two profiles with (grey line) and without (gold line) basalt interbeds at depth ~ 40 m. All spectra are 5% damping.

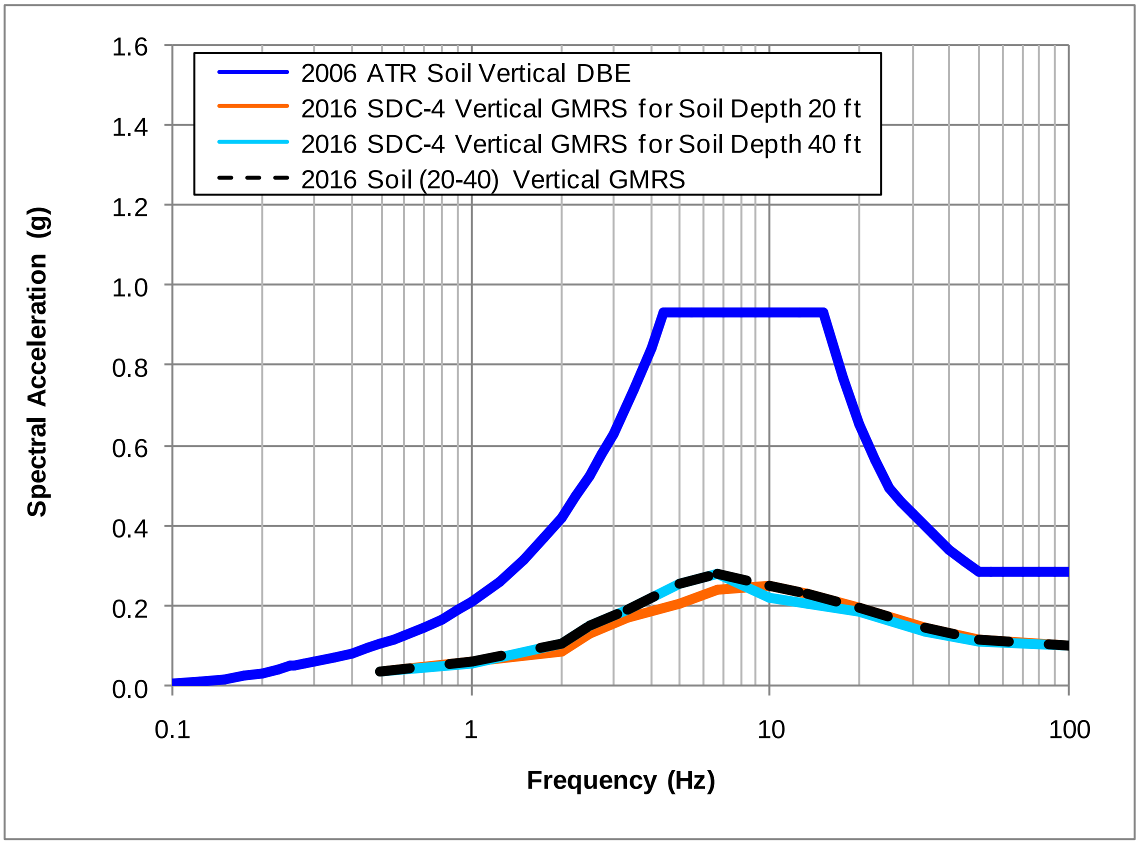

Figure 10-147. Comparison of the 2006 ATR Soil Vertical DBE (solid blue) to the enveloped SDC-4 Vertical GMRS ATR 20 ft soil site (solid red) and the enveloped SDC-4 Vertical GMRS ATR 40 ft soil site (solid cyan). The dashed black line is their envelope.

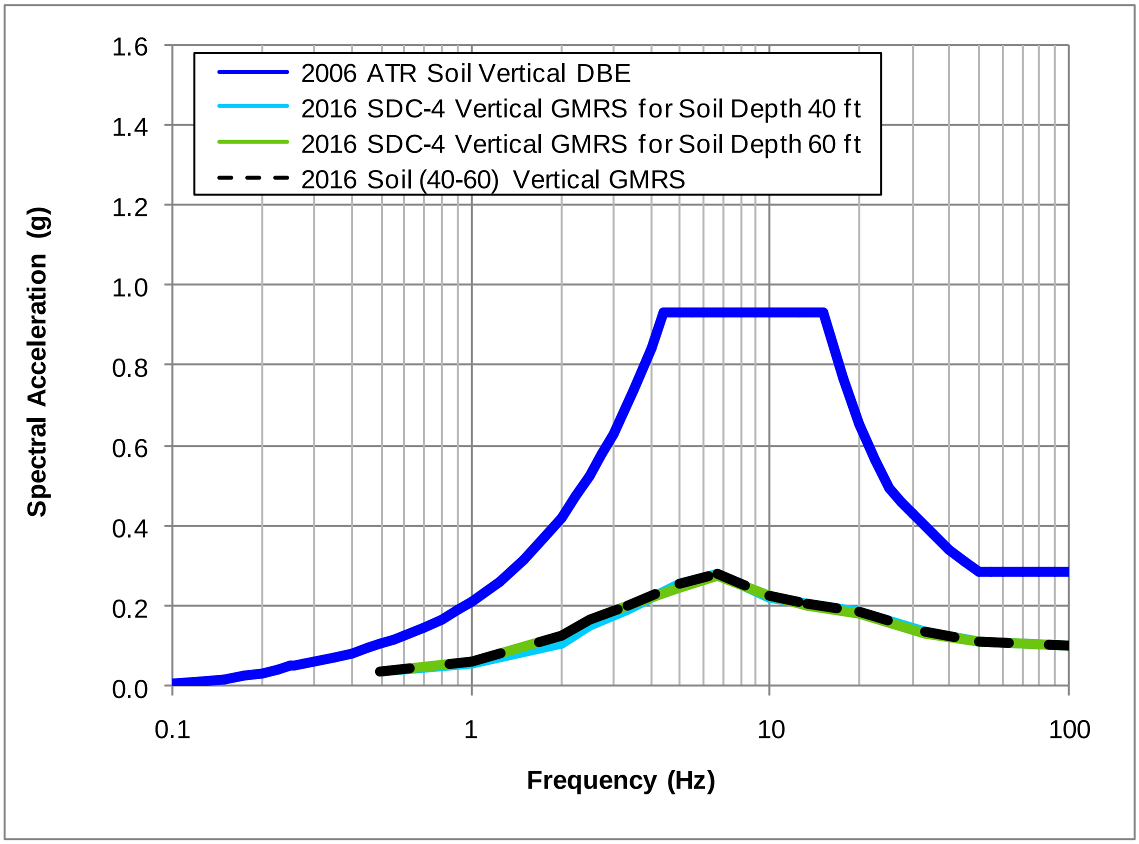

Figure 10-148. Comparison of the 2006 ATR Soil Vertical DBE (solid blue) to the enveloped SDC-4 Vertical GMRS ATR 40 ft soil site (solid cyan) and the enveloped SDC-4 Vertical GMRS ATR 60 ft soil site (solid green). The dashed black line is their envelope.

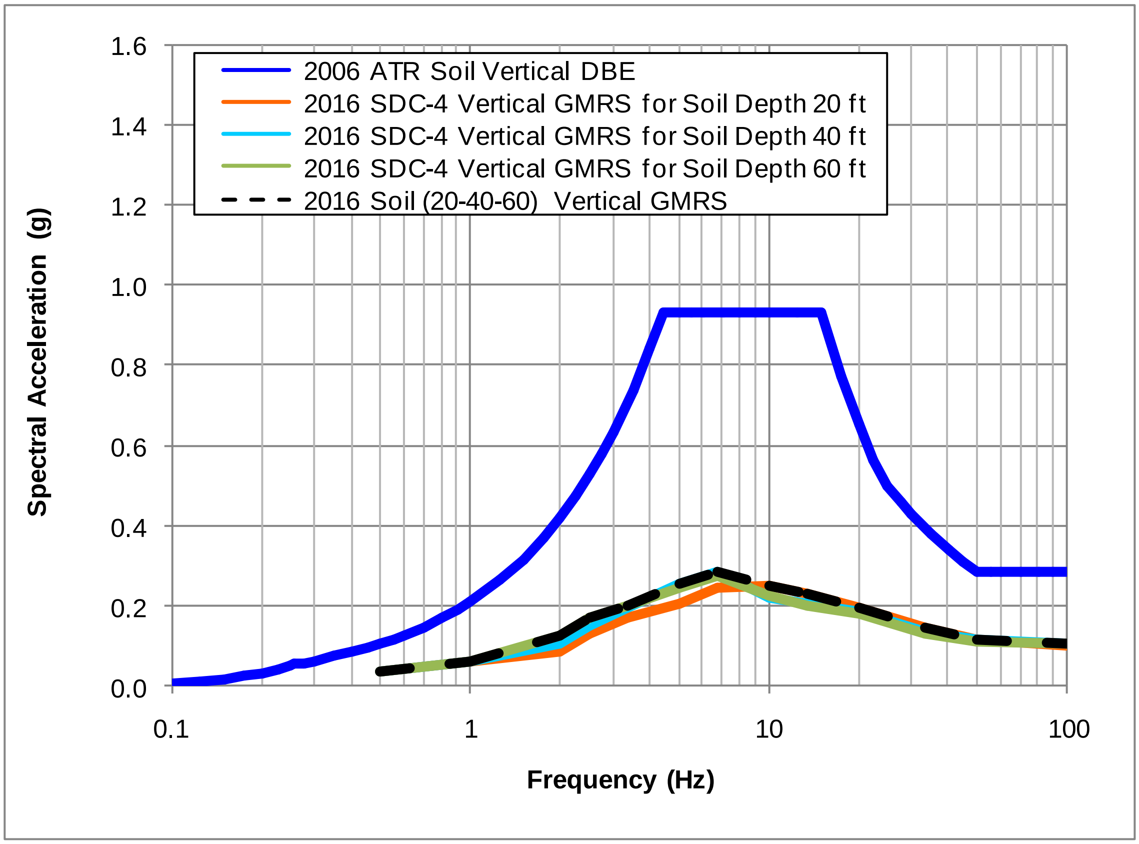

Figure 10-149. Comparison of the 2006 ATR Soil Vertical DBE (solid blue) to the enveloped SDC-4 Vertical GMRS ATR 20 ft soil site (solid red), the enveloped SDC-4 Vertical GMRS ATR40 ft soil site (solid cyan), and the enveloped SDC-4 Vertical GMRS ATR 60 ft. soil site (solid green). The dashed black line is their envelope.

Table 10-48. Vertical SDC-4 GMRS for ATR soil depths of 20 ft, 40 ft, and 60ft computed using the results of the SSHAC Level 1 study.

Period (sec)	Frequency (Hz)	Vertical SDC-4 GMRS Spectral Acceleration (g)		
		20 ft	40 ft	60 ft
0.01	100	1.00E-01	1.04E-01	1.04E-01
0.02	50	1.17E-01	1.14E-01	1.12E-01
0.03	33.3	1.47E-01	1.36E-01	1.32E-01
0.05	20	1.95E-01	1.88E-01	1.82E-01
0.075	13.33	2.30E-01	2.05E-01	2.02E-01
0.1	10	2.52E-01	2.21E-01	2.24E-01
0.15	6.67	2.44E-01	2.83E-01	2.76E-01
0.2	5	2.07E-01	2.55E-01	2.47E-01
0.3	3.33	1.73E-01	1.93E-01	2.01E-01
0.4	2.5	1.30E-01	1.50E-01	1.68E-01
0.5	2	8.73E-02	1.05E-01	1.28E-01
1	1	6.29E-02	5.93E-02	6.07E-02
2	0.5	3.79E-02	3.61E-02	3.59E-02

Table 10-49. Vertical 2016 GMRS at SDC-4 for ATR soil sites.

Period (sec)	Frequency (Hz)	Vertical 2016 Soil ATR GMRS at SDC-4 Spectral Acceleration (g)		
		(20-40)	(40-60)	(20-40-60)
0.01	100	1.04E-01	1.04E-01	1.04E-01
0.02	50	1.17E-01	1.14E-01	1.17E-01
0.03	33.3	1.47E-01	1.36E-01	1.47E-01
0.05	20	1.95E-01	1.88E-01	1.95E-01
0.075	13.33	2.30E-01	2.05E-01	2.30E-01
0.1	10	2.52E-01	2.24E-01	2.52E-01
0.15	6.67	2.83E-01	2.83E-01	2.83E-01
0.2	5	2.55E-01	2.55E-01	2.55E-01
0.3	3.33	1.93E-01	2.01E-01	2.01E-01
0.4	2.5	1.50E-01	1.68E-01	1.68E-01
0.5	2	1.05E-01	1.28E-01	1.28E-01
1	1	6.29E-02	6.07E-02	6.29E-02
2	0.5	3.79E-02	3.61E-02	3.79E-02

11. References

Abdallah, A., Courtillot, V., Kasser, M., Le Dain, A. Y., Lepine, J. C., Robineau, B., Ruegg, J. C., Tapponnier, P., and Tarantola, A., 1979, Relevance of Afar seismicity and volcanism to the mechanics of accreting plate boundaries, Nature (London), v. 282, p. 17-23.

Abrahamson, N.A., and Silva, W., 2008, Summary of the Abrahamson & Silva NGA Ground-Motion Relations, Earthquake Spectra, v. 24, p. 67-97.

Abrahamson, N.A., Silva, W.J., and Kamai, R., 2014, Summary of the AKS14 Ground-Motion Relation for Active Crustal Regions, Earthquake Spectra, v. 30, DOI: 10.1193/070913EQS198M.

Abrahamson, N.A., Gregor, N., and Addo, K., 2015, BC Hydro ground motion prediction equations for subduction earthquakes, Earthquake Spectra, in press, doi: http://dx.doi.org/10.1193/051712EQS188MR

AECOM, 2015, Current SDC-3, -4, and -5 Design Response Spectra at Rock, Memorandum from Dan Eggers to Leon McGovern, document 150212-M-005, dated 18 November.

Agbabian Associates Inc., 1995, Borehole velocity and damping measurements at Argonne National Laboratory West Borehole ANL-1; Report #9455-6554 prepared for ANL-W under contract 31-109-38-9410-W, Pasadena, California, 39 p.

Akkar, S. and Bommer, J.J., 2010, Empirical Equations for the Prediction of PGA, PGV, and Spectral Accelerations in Europe, the Mediterranean Region, and the Middle East, Seismological Research Letters, v. 81, p. 195-206.

Akkar, S. and Z. Çagnan, 2010, A local ground-motion predictive model for Turkey, and its comparison with other regional and global ground-motion models, Bulletin of the Seismological Society of America, v. 100, p. 2978-2995.

Akkar, S., Sandikkaya, M.A., and Bommer, J.J., 2014a, Empirical ground-motion models for point- and extended-source crustal earthquake scenarios in Europe and the Middle East, Bulletin of Earthquake Engineering, v. 12, p. 359-387.

Akkar, S., Sandikkaya, M.A., and Bommer, J.J., 2014b, Erratum to: Empirical ground-motion models for point- and extended-source crustal earthquake scenarios in Europe and the Middle East, Bulletin of Earthquake Engineering, v. 12, p. 389-390.

Akkar S., Sandıkkaya M.A., Şenyurt M., Azari Sisi A., Ay B.Ö., Traversa P., Douglas J., Cotton F., Luzi L., Hernandez B., Godey S., 2014c, Reference database for seismic ground-motion in Europe (RESORCE), Bulletin of Earthquake Engineering, v. 12, p. 311-339.

Al Atik, L., and Youngs, R.R., 2014, Epistemic Uncertainty for NGA-West2 Models, Earthquake Spectra, v. 30, p. 1301-1318.

AMEC, 2011, Probabilistic seismic hazard sensitivity analyses for the Naval Reactors Idaho Falls, Idaho, project 148899, December, 186 p.

AMEC 2013, Fault sources hazard sensitivity analyses for the Naval Reactors Facility, Addendum, project 148899, February, 103 p.

Ancheta, T.D, Darragh, R.B, Stewart, J.P., Seyhan, E., Silva, W.J, Chiou, B.S-J., Wooddell, K.E. Graves, R.W., Kottke, A.R., Boore, D.M., Kishida, T., and Donahue J.L., 2014, NGA-West 2 Database, Earthquake Spectra, DOI http://dx.doi.org/10.1193/070913EQS197M.

Anders, M.H., Geissman, J.W., Piety, L.A. and Sullivan, J.T., 1989, Parabolic distribution of circumeastern Snake River Plain seismicity and latest Quaternary faulting: Migratory pattern and association with the Yellowstone Hotspot, Journal of Geophysical Research, v. 94, p. 1589-1621.

Anders, M.H., Rodgers, D.W., Hemming, S.R., Saltzman, J., DiVenere, V.J., Hagstrum, J.T., Embree, G.F., and Walter, R.C., 2014, A fixed sublithospheric source for the late Neogene track of the Yellowstone hotspot: Implications of the Heise and Picabo volcanic fields, Journal of Geophysical Research, v. 119, p. 2871-2906, doi:10.1002/2013JB010483.

Anders, M.H., Saltzman, J., and Hemming, S.R., 2009, Neogene tephra correlations in eastern Idaho and Wyoming: Implications for Yellowstone hotspot-related volcanism and tectonic activity, Geological Society of America Bulletin, v. 121, p. 837–856.

Anders, M.H. and Sleep, N.H., 1992, Magmatism and extension: The thermal and mechanical effects of the Yellowstone hotspot, Journal of Geophysical Research, v. 97, p. 15379-15393.

Anderson, J.G., 2011, Seismicity and seismic hazard of northeastern Nevada, Nevada Bureau of Mines and Geology Special Publication 36, p. 43-50.

Anderson, J. G. and S. E. Hough, 1984, A model for the shape of the Fourier amplitude spectrum of acceleration at high frequencies, Bulletin of the Seismological Society of America, v. 74, p. 1969-1993.

ANS, 2004, Categorization of nuclear facility structures, systems, and components for seismic design, American Nuclear Society, ANSI/ANS-2.26-2004, 29 p.

ANS, 2008a, Probabilistic Seismic Hazard Analysis, American Nuclear Society, ANSI/ANS-2.29-2008, 33 p.

ANS, 2008b, Criteria for Investigations of Nuclear Facility Sites for Seismic Hazard Assessments, American Nuclear Society, ANSI/ANS-2.27-2008, 24 p.

Aoki, Y., Segall, P., Kato, T., Cervelli, P., and Shimada, S., 1999, Imaging magma transport during the 1997 seismic swarm off the Izu peninsula, Japan, Science, v. 286, p. 927-930.

Argonne National Laboratory, 1985, Fuel Manufacturing Facility underground rock plan, boring log, and gravel backfill, Battelle Energy Alliance, Drawing No. W7040-0016-ED-00.

ASCE, 2005, Seismic design criteria for structures, systems, and components in nuclear facilities, American Society of Civil Engineers, ASCE/SEI 43-05, 81 p.

ASME, 2009, Addendum, Quality Assurance Requirements for Nuclear Facilities Applications, American Society of Mechanical Engineers, ASME NQA-1 2008/2009.

Atkinson, G.M., and Silva, W.J., 2000, Stochastic modeling of California ground motions, Bulletin of the Seismological Society of America, v. 90, p. 255-274.

Ayele, A., Nyblade, A.A., Langston, C.A., Cara, M., and Lévêque, J.J., 2006, New evidence for Afro Arabian plate separation in southern Afar, Geological Society of America Special Publication 259, p. 133-141, doi:10.1144/GSL.SP.2006.259.01.12.

Baltzer, E.M., 1990, Quaternary surface displacements and segmentation of the northern Lemhi fault, Idaho, unpublished MS Thesis: State University of New York at Binghamton, N.Y. pp. 1-88 p.

Barrientos, S.E., Stein, R.S., and Ward, S.N., 1987, Comparison of the 1959 Hebgen Lake, Montana and the 1983 Borah Peak, Idaho earthquakes from geodetic observations, Bulletin Seismological Society of America, v. 77, p. 748-808.

BC Hydro, 2012, Probabilistic Seismic Hazard Analysis (PSHA) Model, Volume 2: Seismic Source Characterization (SSC) Model, BC Hydro Engineering (Vancouver, British Columbia) Report No. E658, v. 2, WPR-3030.

Bestland, E.A., Link, R.K., Lanphere, M.A., and Champion, D.E., 2002, Paleoenvironments of sedimentary interbeds in the Pliocene and Quaternary Big Lost Trough, eastern Snake River Plain, Idaho, *in* Link, P.K. and L.L. Mink, editors, Geology, Hydrogeology, and Environmental Remediation: Idaho National Engineering and Environmental Laboratory, Eastern Snake River Plain, Idaho, Boulder, Colorado, Geological Society of America Special Paper 353, p. 27-44.

Beukelman, S.G., 1997, Evidence of active faulting in the Halfway Gulch-Little Jacks Creek Area of the Western Snake River Plain, Idaho, unpublished M.S. Thesis, Boise State University, Boise Idaho, 138 p.

Bindi D., Massa M., Luzi L., Ameri G., Pacor F., Puglia R., and Augliera, P., 2014a, Pan-European Ground-Motion Prediction Equations for the Average Horizontal Component of PGA, PGV, and 5%-Damped PSA at Spectral Periods up to 3.0 s using the RESORCE dataset, Bulletin of Earthquake Engineering, v. 12, p. 391-430.

Bindi D., Massa M., Luzi L., Ameri G., Pacor F., Puglia R., and Augliera, P., 2014b, Erratum to: Pan-European Ground-Motion Prediction Equations for the Average Horizontal Component of PGA, PGV, and 5%-Damped PSA at Spectral Periods up to 3.0 s using the RESORCE dataset, Bulletin of Earthquake Engineering, v. 12, p. 432-448.

Bindi, D., Pacor, F., Luzi, L., Puglia, R., Massa, M., Ameri, G., and Paolucci, R., 2011, Ground motion prediction equations derived from the Italian strong motion database, Bulletin of Earthquake Engineering, v. 9, p. 1899-1920.

Blackwell, D.D. 1989, Regional implications of heat flow of the Snake River Plain, northwestern United States, Tectonophysics, v. 164, p. 323-343.

Blackwell, D.D. and Richards, M., 2004, Geothermal Map of North America, American Association of Petroleum Geologists, scale 1:6,500,000.

Blair, J. J., 2001, Sedimentology and stratigraphy of sediments of the Big Lost Trough subsurface from selected coreholes at the Idaho National Engineering and Environmental Laboratory, Idaho, unpublished MS Thesis, Idaho State University, Pocatello, Idaho, 148 p.

Bommer, J.J., Akkar, S., and Kale, Ö, 2011, A model for vertical-to-horizontal response spectral ratios for Europe and the Middle East, Bulletin of the Seismological Society of America, v. 101, p. 1783-1806.

Bond, J.G., Kauffman, J.D., Miller, D.A. and Venkatakrishnan, R., 1978, Geologic map of Idaho, Idaho Bureau of Mines and Geology, Scale 1:500000.

Bondre, N.R., 2006, Field and geochemical investigation of basaltic magmatism from the western United States and western India, unpublished M.S. Thesis, Miami University, Oxford, OH.

Bonnichsen, B., Leeman, W.P., Honjo, N., McIntosh, W.C. and Godchaux, M.M., 2008, Miocene silicic volcanism in southwestern Idaho: Geochronology, geochemistry, and evolution of the central Snake River Plain, Bulletin of Volcanology, v. 70, p. 315-342.

Boore, D.M., 1983, Stochastic simulation of high-frequency ground motions based on seismological models of the radiated spectra, Bulletin of the Seismological Society of America, v. 73, p. 1865-1894.

Boore, D. M., 1986, Short-period P- and S-wave radiation from large earthquakes: Implications for spectral scaling relations, Bulletin of the Seismological Society of America, v. 76, p. 43-64.

Boore, D.M., Stewart, J.P., Seyhan, E., and Atkinson, G.M., 2014, NGA-West 2 Equations for Predicting PGA, PGV, and 5%-Damped PSA for Shallow Crustal Earthquakes, Earthquake Spectra, DOI: 10.1193/070113EQS184M.

Bora, S.S., Scherbaum, F., Kuehn, N., and Stafford, P., 2013, Fourier spectral- and duration models for the generation of response spectra adjustable to different source-, propagation-, and site conditions, Bulletin of Earthquake Engineering, v. 12, p. 467-493.

Bozorgnia, Y., and Campbell, K.W., 2015, Vertical ground motion model for PGA, PGV, and linear response spectra using the NGA-West2 database, Earthquake Spectra, in-press, doi: http://dx.doi.org/10.1193/072814EQS121M.

Bozorgnia, Y., Abrahamson, N.A., Al Atik, L., Ancheta, T.D, Atkinson, G.M., Baker, J.W., Baltay, A., Boore, D.M., Campbell, K.W., Chiou, B.S.-J., Darragh, R., Day, S., Donahue, J., Graves, R.W., Gregor, N., Hanks. T., Idriss, I.M., Kamai, R., Kishida, T., Kottke, A., Mahin, S.A., Rezaeian, S., Rowshandel, B., Seyhan, S., Shahi, S., Shantz, T., Silva, W., Spudich, P., Stewart, J.P., Watson-Lamprey, J., Wooddell, K, and Youngs, R.R., 2014, NGA-West2 research project, Earthquake Spectra, v. 30, p. 973-987.

Bosher, R., and Duennebier, F. K., 1985, Seismicity associated with the Christmas 1965 event at Kilauea Volcano, Journal of Geophysical Research, v. 90**,** p. 4529-4536.

Bradley, B.A., 2013, A New Zealand-specific pseudospectral acceleration ground-motion prediction equation for active shallow crustal earthquakes based on foreign models, Bulletin of the Seismological Society of America, v. 103, p. 1801-1822.

Braile, L.W., Smith, R.B., Ansorge, J., Baker, M.R., Sparlin, M.A., Prodehl, C., Schilly, M.M., Healy, J.H., Mueller, S.T., and Olsen, K.H., 1982, The Yellowstone-Snake River Plain Seismic Profiling Experiment: Crustal Structure of the Eastern Snake River Plain, Journal of Geophysical Research, v. 87, p. 2597-2610.

Brandes, H.G., Robertson, N., and Johnson, G.P., 2011, Soil and Rock Properties in a Young Volcanic Deposit on the Island of Hawaii, American Society of Civil Engineers, ASCE Press, 14 pp.

Brandsdottir, B., and Einarsson, P., 1979, Seismic activity associated with the September 1977 deflation of the Krafla central volcano in northeastern Iceland, Journal of Volcanology and Geothermal Research, v. 6, p. 197-212.

Brott, C.A., Blackwell, D.D., and Ziagos, J.P, 1981, Thermal and tectonic implications of heat flow in the eastern Snake River Plain, Idaho; Journal of Geophysical Research, v. 86, p. 11709-11734.

Bruhn, R.L., Wu, D., and Lee, J-J., 1992, Final Report on the structure of the southern Lemhi and Arco fault zone, Idaho; EG&G Informal Report EGG-NPR-10680, 26 p.

Brune, J.N., 1970, Tectonic stress and the spectra of seismic shear waves from earthquakes, Journal of Geophysical Research, v. 75, p. 4997-5009.

Brune, J.N., 1971, Correction, Journal of Geophysical Research, v. 76, p. 5002.

Byrd, J.O.D., Smith, R.B., and Geissman, J.W., 1994, The Teton fault, Wyoming: Topographic signature, neotectonics, and mechanisms of deformation, Journal of Geophysical Research, v. 99, p. 20095-20122.

Campbell, K.W., and Bozorgnia, Y., 2008, NGA Ground Motion Model for the Geometric Mean Horizontal Component of PGA, PGV, PGD and 5% Damped Linear Elastic Response Spectra for Periods Ranging from 0.01 to 10 s, Earthquake Spectra, v. 24, p. 139-171.

Campbell, K.W., and Bozorgnia, Y., 2014, NGA-West2 Ground Motion Model for the Average Horizontal Components of PGA, PGV, and 5%-Damped Linear Acceleration Response Spectra, Earthquake Spectra, v. 30, DOI: 10.1193/062913EQS175M.

Carlton, B., and N. Abrahamson, 2014, Issues and approaches for implementing conditional mean spectra in practice. Bulletin of the Seismological Society of America, v. 104, p. 503-512.

Carpenter, N.S., 2010, Compilation of Earthquakes from 1850-2007 within 200 miles of the Idaho National Laboratory, Battelle Energy Alliance External Report, INL/EXT-10-19120, 65 pp.

Carpenter, N.S. and Payne, S.J., 2009, Deep, Long-period earthquakes in and around Craters of the Moon National Monument, Idaho, Seismological Research Letters, v. 80, p. 350-357.

Carpenter, N.S., Payne, S.J, and A.L. Schafer, 2012, Toward Reconciling Magnitude Discrepancies Estimated from Paleoearthquake Data, Seismological Research Letters, v. 83, p. 555-565.

Cervelli et al., 2002, The 12 September 1999 upper east rift zone dike intrusion at Kilauea volcano, Hawaii, Journal of Geophysical Research, v. 107, 2150, doi:10.1029/2001JB000602.

Chadwick, J.D., Rodgers, D.W., and Payne S.P., 2005, Contemporary tectonic motion of the eastern Snake River Plain, Idaho: A global positioning system study, 1995-2004: Tectonics, v. 26, TC6005, doi:10.1029/2005TC001914.

Chang, W.-L., Smith, R.B., Puskas, C.M., and Farrell, J.M., 2010, Kinematics and magmatic modeling of an extraordinary period of Yellowstone caldera uplift, 2004-2009, from GPS and InSAR observations, Geophysical Research Letters, v. 37, L23302, doi:10.1029/2010GL045451.

Chiou, B.S-J., and Youngs, R.R., 2014, Update of the Chiou and Youngs NGA Model for the Average Horizontal Component of Peak Ground Motion and Response Spectra, Earthquake Spectra, v. 30, DOI: 10.1193/072813EQS219M.

Chiou, B.J. and Youngs, R.R., 2008, An NGA model for the average horizontal component of peak ground motion and response spectra, Earthquake Spectra, v. 24, p. 173-215.

Chiou, B.S-J., Youngs, R.R., Abrahamson, N.A., and Addo, K., 2010, Ground-Motion Attenuation Model for Small-To-Moderate Shallow Crustal Earthquakes in California and Its Implications on Regionalization of Ground-Motion Prediction Models, Earthquake Spectra, v. 26, p. 907-926.

Christiansen, R.L., 2001, The Quaternary and Pliocene Yellowstone Plateau volcanic field of Wyoming, Idaho, and Montana, U.S. Geological Survey Professional Paper 729-G.

Cornell CA. 1971. Probabilistic analysis of damage to structures under seismic loads, in Howells, D.A., Haigh, I.P., and Taylor, C., editors, Dynamic Waves in Civil Engineering, John Wiley, London.

Cornell, C.A. and Van Marke, E.H., 1969, The major influences on seismic risk, Proceedings of the Third World Conference on Earthquake Engineering, Santiago Chile, A-1, p. 69-93.

Cox, C. M., Keller, G.R., and Harder, S.H., 2011, Integrated 2-D models of crustal structure in the High Lava Plains region of eastern Oregon, abstract, 2011 EarthScope National Meeting, May 17-20, 2011, Austin, Texas.

Cox, M., Henslee, P. and Coleman, J., 2016, INL 10 Year Seismic Re-evaluation for FMF and ZPPR, Battelle Energy Alliance External Report, INL/EXT-16-37751, 12 p., Appendix A.

Craig, T.J., Jackson, J.A. , Priestley, K., and McKenzie, D., 2011, Earthquake distribution patterns in Africa: their relationship to variations in lithospheric and geological structure, and their rheological implications, Geophysical Journal International, v. 185, p. 403-434, doi: 10.1111/j.1365-246X.2011.04950.x.

Crawford, C.C., 1994, Determination of Oceanic Crustal Shear Velocity Structure from Seafloor Compliance Measurements, PhD Dissertation, University of California, San Diego.

Crone, A.J. and Haller, K.M., 1991, Segmentation and coseismic behavior of basin-and-range normal faults: Examples from east-central Idaho and southwestern Montana, U.S.A.; Journal of Structural Geology, v. 13, p.151-164.

Crone, A.J., Machette, M.N., Bonilla, M.G., Lienkaemper, J.J., Pierce, K.L., Scott, W.E. and Bucknam, R.C., 1987, Surface faulting accompanying the Borah Peak earthquake and segmentation of the Lost River fault, central Idaho, Bulletin Seismological Society of America, v. 77, p. 739-770.

CRWMS M&O, 1998, Probabilistic Seismic Hazard Analysis for Ground Motions and Fault Displacement at Yucca Mountain, Nevada (Wong, I.G., and Stepp, J.C., coordinators), Civilian Radioactive Waste Management System, Management & Operation Contractor, unpublished report prepared for the U.S. Geological Survey, 3 volumes.

Cummings, M.L., Evans, J.G., Ferns, M.L. and Lees, K.R., 2000, Stratigraphic and structural evolution of the middle Miocene synvolcanic Oregon-Idaho graben, Geological Society of America Bulletin, v. 112, p. 668-682.

Dames and Moore, 1965, Report of foundation investigation proposed Zero Power Plutonium Reactor, National Reactor Testing Station, near Idaho Falls, Idaho, prepared for the U.S. Atomic Energy Commission, April 2.

Darendeli, M. B., 2001, Development of a new family of normalized modulus reduction and material damping curves, Ph.D. Dissertation, University of Texas at Austin, Texas.

Das, S. and Scholz, C.H., 1983, Why large earthquakes do not nucleate at shallow depths, Nature, v. 305, p. 621-623.

dePolo, C.M., 2011, An Introduction to the February 21, 2008, Mw 6.0 Wells Nevada Earthquake and the Earthquake Documentation Volume, Nevada Bureau of Mines and Geology Special Publication 36, p. 15-42.

DeNosaquo, K.R., R.B. Smith, and A.R. Lowry, 2009, Density and lithospheric strength models of the Yellowstone-Snake River Plain volcanic system from gravity and heat flow data, Journal of Volcanology and Geothermal Research, v. 188, p. 108-127.

Derras, B., Bard, P-Y, and Cotton, F., 2013, Towards fully data driven ground-motion prediction models for Europe, Bulletin of Earthquake Engineering, v. 12, p. 391-430.

Dewey, J.W., 1987, Instrumental seismicity of central Idaho, Bulletin of Seismological Society of America, v. 77, p. 819-836.

DOE, 2012a, Natural Phenomena Hazards Analysis and Design Criteria for DOE Facilities, U.S. Department of Energy, DOE-STD-1020-12, 90 p.

DOE, 2012b, Facility Safety, U.S. Department of Energy, DOE O 430.1C, 52 p.

Doherty, D.J., 1979, Drilling data from exploration well 1, NE 1/4, sec.22, T.2N., R. 32E., Bingham County, Idaho, U.S. Geological Survey Open-File Report 79-1225, 1 sheet.

Doser, D.I., 1985, Source parameters and faulting processes of the 1959 Hebgen Lake, Montana, earthquake sequence, Journal of Geophysical Research, v. 90, p. 4537-4555.

Doser, D.I., 1989a, Source parameters of Montana earthquakes (1925-1964) and tectonic deformation in the northern Intermountain Seismic Belt, Bulletin of Seismological Society of America, v. 79, p. 31-50.

Doser, D.I., 1989b, Extensional tectonics in northern Utah-southern Idaho, U.S.A., and the 1934 Hansel Valley sequence, Physics of the Earth and Planetary Interiors, v. 54, p. 12-134.

Doser, D.I., and Smith, R.B., 1989, An assessment of source parameters of earthquakes in the Cordillera of the western United States, Bulletin Seismological Society of America, v. 79, p. 1383-1409.

Draper, D.S., 1991, Late Cenozoic bimodal magmatism in the northern Basin and Range province of southeastern Oregon, Journal of Volcanology and Geothermal Research, v. 47, p. 299-328.

Dzurisin, D., Anderson, L.A., Eaton, G.P., Koyanagi, R.Y., Lipman, P.W., Lockwood, J.P., Okamura, R.T., Puniwai, G.S., Sato, M.K., and Yamashita, K.M., 1980, Geophysical observations of Kilauea volcano, Hawaii: 2. Constraints on the magma supply during November 1975-September 1977, Journal of Volcanology and Geothermal Research, v. 7, p. 241-269.

Ebasco Services, Inc., 1961a, ATR site foundation investigation, Drawing ATR-1075-MTR-104-1 and ATR-1075-MTR-104-2 (numbers 120007 and 120008, respectively).

Ebasco Services, Inc., 1961b, ATR Study No. 2 C-2 Foundation Investigation, AT(10-1)-1075, April 13, 1961, p. 230-262.

EG&G Idaho Inc., 1984, Report of the geotechnical investigation for the 7th Bin Set at the Chemical Processing Plant, INEL, August.

Einarsson, P., and Brandsdottir, B., 1980, Seismological evidence for lateral magma intrusion during the July 1978 deflation of the Krafla volcano in NE-Iceland, Journal of Geophysics, v. 47**,** p. 160-165.

Einarsson, P., and Bjornsson, A., 1979, Earthquakes in Iceland, Jokull, v. 29, p. 37-43.

Elbring, G.J., 1984, A method for inversion of two-dimensional seismic refraction data with applications to the Snake River Plain region Idaho: unpublished M.S. thesis, University of Utah, 123 p.

EPRI, 1993, Guidelines for determining design basis ground motions, Palo Alto, California, Electric Power Research Institute, v. 1-5, EPRI TR-102293.

EPRI, 2013, Seismic Evaluation Guidance Screening, Prioritization and Implementation Details (SPID) for the Resolution of Fukushima Near-Term Task Force Recommendation 2.1: Seismic, Electric Power Research Institute, Report 1025287, February.

EPRI/SOG, 1988, Seismic Hazard Methodology for the Central and Eastern United States, Electric Power Research Institute Seismic Owners Group Technical Report NP-4726-A, Volumes 1–10, EPRI, Palo Alto, California.

Erickson, D., D.E. McNamara, and M.B. Harley, 2004, Frequency-dependent Lg Q within the continental United States, Bulletin of the Seismological Society of America, v. 94, p. 1630-1643.

Faccioli, E., Bianchini, A., and Villani, M., 2010, New ground motion prediction equation for T > 1 s and their influence on seismic hazard assessment, *in*: Proceedings of the University of Tokyo Symposium on Long-Period Ground Motion and Urban Disaster Mitigation, March 17-18, 2010.

Fagereng, Å., and Toy, V.G., 2011, Geology of the earthquake source: an introduction. Geological Society, London, Special Publications 359, p. 1-16.

Farrell, J., Smith, R.B., Husen, S., and Diehl, T., 2014, Tomography from 26 years of seismicity revealing that the spatial extent of the Yellowstone crustal magma reservoir extends well beyond the Yellowstone caldera, Geophysical Research Letters, v. 41, doi:10.1002/2014GL059588.

Francis, T. J, and Shor, G.G., 1966, Seismic refraction measurements in the northwest Indian Ocean, Journal of Geophysical Research, v. 71, p. 427-449.

Fournier, R.O., 1989, Geochemistry and dynamics of the Yellowstone National Park hydrothermal system, Annual Reviews in Earth and Planetary Science, v. 17, p. 13- 53.

Gardine, M., West, M.E., and Cox, T., 2011, Dike emplacement near Parícutin volcano, Mexico in 2006, Bulletin of Volcanology, v. 73, p. 123-132.

Gardner, J.K., and Knopoff L., 1974, Is the sequence of earthquakes in Southern California, with aftershocks removed, Poissonian?, Bulletin of the Seismological Society of America, v. 64, p. 1363-1367.

Gaschnig, R.M., Vervoort, J.D., Lewis, R.S. and McClelland, W.C., 2009, Migrating magmatism in the northern US Cordillera: in situ U-Pb geochronology of the Idaho Batholith, Contrib. Mineral Petrol., doi:10.1007/s00410-009-0459-5.

Geist, D.J., Ellisor, R.A., Sims, E.N., and Hughes, S.S., 2002, Subsurface volcanology at Test Area North and controls on groundwater flow, *in* Link, P.K. and L.L. Mink, editors, Geology, Hydrogeology, and Environmental Remediation: Idaho National Engineering and Environmental Laboratory, Eastern Snake River Plain, Idaho, Boulder, Colorado, Geological Society of America Special Paper 353, p. 45-60.

Geist, D., and Richards M., 1993. Origin of the Columbia Plateau and Snake River Plain: Deflection of the Yellowstone plume, Geology, v. 21, p. 789-792.

GeoPentech, 2015, Southwestern United States Ground Motion Characterization SSHAC Level 3-Technical Report, Rev. 2, March 2015.

Geslin, J.K., Link, P.K., Riesterer, J.W., Kuntz, M.A., and Fanning, C.M., 2002, Pliocene to Quaternary stratigraphic architecture and drainage systems of the Big Lost Trough, northeastern Snake River Plain, Idaho, *in* Link, P.K. and L.L. Mink, editors, Geology, Hydrogeology, and Environmental Remediation: Idaho National Engineering and Environmental Laboratory, Eastern Snake River Plain, Idaho, Boulder, Colorado, Geological Society of America Special Paper 353, p. 11-26.

Gianniny, G.L.., Thackray, G.D., Kaufman, D.S., Forman, S.L., Sherbondy, M.J., and Findeisen, D., 2002, Late Quaternary highstands in the Mud Lake and Big Lost Trough subbasins of Lake Terreton, Idaho, *in* Link, P.K. and L.L. Mink, editors, Geology, Hydrogeology, and Environmental Remediation: Idaho National Engineering and Environmental Laboratory, Eastern Snake River Plain, Idaho, Boulder, Colorado, Geological Society of America Special Paper 353, p. 77-90.

Goulet, C. A., Kishida, T., Ancheta, T.D., Cramer, C. H. Darragh, R.B., Silva, W.J., Hashash, Y. M. A., Harmon, J., Stewart, J.P., Woodell, K.E., and Youngs, R. R., 2014, PEER NGA-East Database, PEER Report 2014/17, Pacific Earthquake Engineering Research Center, Berkeley, CA.

Grant, J.V. and Kattenhorn, S.A., 2004, Evolution of vertical faults at an extensional plate boundary, southwest Iceland, Journal of Structural Geology, v. 26, p. 537-557.

Graizer, V., 2014, Updated Graizer-Kalkan Ground-motion Prediction Equations for Western United States, Proceedings for the 10th U.S. National Conference on Earthquake Engineering Frontiers of Earthquake Engineering, July 21-25, 2014, Anchorage, Alaska, Paper ID 1097, 11 p.

Greely, R., 1982, The style of basaltic volcanism in the eastern Snake River Plain, Idaho, *in* Bonnichsen, B. and Breckenridge, R.M., editors, Cenozoic Geology of Idaho, Idaho Geological Survey Bulletin 26, p. 407-422.

Grindley, G.W., and Hull, A.G., 1986, Historical Taupo earthquakes and earth deformation, Bull. R. Soc. New Zealand, v. 24, p. 173-186.

Gülerce, Z., and Abrahamson, N.A., 2011, Site-specific design spectra for vertical ground motions. Earthquake Spectra, v. 27, no. 4, pp. 1023-1047.

Grünthal G., 1985, The up-dated earthquake catalogue for the German Democratic Republic and adjacent areas – statistical data characteristics and conclusions for hazard assessment, Proceedings 3rd International Symposium on the Analysis of Seismicity and Seismic Risk, Czech. Ac. Sc., Prague, p. 19-25.

Gudmundsson, A., Lecoeur, N., Mohajeri, N., and Thordarson, T., 2014, Dike emplacement at Bardarbunga, Iceland, induces unusual stress changes, caldera deformation, and earthquakes, J. Volcanology, v. 76, 868: DOI 10.1007/s00445-014-0869-8.

Gutenberg, B., and Richter, C., 1944, Frequency of earthquakes in California, Bulletin of the Seismological Society of America, v. 34, p. 185-188.

Gutenberg, B., and Richter, C.F., 1956, Earthquake magnitude, intensity, energy and acceleration, Bulletin of the Seismological Society of America, v. 46, p. 105-145.

Hackett, W.R. and Smith, R.P., 1994, Volcanic hazards of the Idaho National Engineering Laboratory and adjacent areas, Lockheed Idaho Technologies Company Technical Report, INEL-94/0276, 31p.

Hackett, W.R., Smith, R.P., and Khericha, S., 2002, Volcanic hazards of the Idaho National Engineering and Environmental Laboratory, southeast Idaho, *in* Bonnichsen, B., White, C.M., and McCurry, M., editors, Tectonic and Magmatic Evolution of the Snake River Plain Volcanic Province, Idaho; Idaho Geological Survey Bulletin 30, p. 461-482.

Haller, K.M., 1988, Segmentation of the Lemhi and Beaverhead faults, east-central Idaho, and Red Rock fault, southwest Montana, during the late Quaternary, M.S. Thesis: University of Colorado, Boulder, Colorado, 141 p.

Haller, K.M., and Wheeler, R.L., and Adema, G.W. (compilers), 2010a, Fault Number 601c, Lost River fault, Thousand Springs section, in Quaternary fault and fold database of the United States, U.S. Geological Survey, http://earthquake.usgs.gov/hazards/qfaults, accessed May, 2015.

Haller, K.M., and Wheeler, R.L., and Adema, G.W. (compilers), 2010b, Fault Number 603f, Beaverhead fault, Blue Dome section, in Quaternary fault and fold database of the United States, U.S. Geological Survey, http://earthquake.usgs.gov/hazards/qfaults, accessed May, 2015.

Hammond, W.C., Blewitt, G., and Kreemer. C., 2014, Steady contemporary deformation of the central Basin and Range Province, western United States, Journal of Geophysical Research, p. 5235-5253, 10.1002/2014JB011145.

Hanks, T.C. and Bakun, W.H., 2008, M − log A observations of recent large earthquakes, Bulletin of the Seismological Society of America, v. 98, p. 490-494.

Hanks, T.C., and Kanamori, H., 1979, A moment magnitude scale: Journal of Geophysical Research, v. 84, p. 2348-2350.

Hanks, T.C., and Schwartz, D.P., 1987, Morphologic Dating of the pre-1983 Fault Scarp on the Lost River Fault at Double Spring Pass Road, Custer County, Idaho, Bulletin of the Seismological Society of America, v. 77, p. 837-846.

Hart, W.K., Aronson, J.L. and Mertzman, S.A., 1984, Areal distribution and age of low-K, high alumina olivine tholeiite magmatism in the northwestern Great Basin, Geological Society of America Bulletin, v. 95, p. 185-195.

HCMT (Harvard Centroid Moment Tensor) catalog, 2015, available at: http://www.globalcmt.org/CMTsearch.html, accessed on April 30, 2015.

Hecker, S., Abrahamson, N.A., and Wooddell, K.E., 2013, Variability of Displacement at a Point: Implications for Earthquake-Size Distribution and Rupture Hazard on Faults., Bulletin of the Seismological Society of America, v. 103, p. 651-674.

Helm-Clark, C, Ansley, S., McLing, T., and Wood, T., 2006, Borehole and Well Middle-1823 and Its Relationship to the Stratigraphy of the South-Central Idaho National Laboratory, External Report for the Idaho Completion Project, Idaho National Laboratory, ICP/EXT-05-00790, 119 p.

Hemphill-Haley, M.A., Knuepher, P.L., Forman, S.L., and Smith, R.P., 1992, Paleoseismic investigations of the southern Lemhi Fault, Idaho, EG&G Informal Report EGG-GEO-10178, pp. 1-32.

Hermkes, M., Kuehn, N.M., and Riggelsen, C., 2013, Simultaneous quantification of epistemic and aleatory uncertainty in GMPEs using Gaussian process regression, Bulletin of Earthquake Engineering, DOI: 10.1007/s10518-013-9507-7.

Herrmann, R.B., 1985, An extension of random vibration theory estimates of strong ground motion to large distance, Bulletin of the Seismological Society of America, v. 75, p. 1447-1453.

Hodges, M.K.V., Link, P.K., and Fanning, C.M., 2009, The Pliocene Lost River found to west: Detrital zircon evidence of drainage disruption along a subsiding hotspot track, Journal of Volcanology and Geothermal Research, v. 188, p. 237-249.

Holmes, A.A,J., Rodgers, D.W. and Hughes, S.S., 2008, Kinematic analysis of fractures in the Great Rift, Idaho: Implications for subsurface dike geometry, crustal extension, and magma dynamics, Journal of Geophysical Research, v. 113, B04202, doi:10/1029/2006JB004782.

Huang, H-H. Lin, F-C., Schmandt, B., Farrell, J., Smith, R.B., and Tsai, V.C., 2015, The Yellowstone magmatic system from the mantle plume to the upper crust, Science Express, 23 April 2015, 8 p., doi: I 0.1126/science.aaa5648.

Hughes, G.R., 2011, Reinvestigation of the 1989 Mammoth Mountain, California seismic swarm and dike intrusion, Journal of Volcanology and Geothermal Research, v. 207, p. 106-112.

Hughes, S.S., Smith, R.P., Hackett, W.R., and Anderson, S.A., 1999, Mafic volcanism and environmental geology of the Eastern Snake River Plain, Idaho, *in* editors, Hughes, S.S., and Thackray, G.D., Guidebook to the Geology of Eastern Idaho: Idaho Museum of Natural History, p. 143-168.

Hurst, A. W., McGinty, P. J., 1999, Earthquake swarms to the west of Mt Ruapehu preceding its 1995 eruption, Journal of Volcanology and Geothermal Research, v. 90, p. 19-28.

Husen, S. and Smith, R.B., 2004, Probabilistic Earthquake Relocation in Three-Dimensional Velocity Models for the Yellowstone National Park Region, Wyoming, Bulletin of the Seismological Society of America, v. 94, p. 880-896.

Hyndman, R.D., 2013, Downdip landward limit of Cascadia great earthquake rupture, Journal of Geophysical Research, v. 118, p. 5530-5549.

Ida, Y., 2009, Dependence of volcanic systems on tectonic stress conditions as revealed by features of volcanoes near Izu peninsula, Japan, Journal of Volcanology and Geothermal Research, v. 181, p. 35-46.

Idriss, I.M., 2008, An NGA Empirical Model for Estimating the Horizontal Spectral Values Generated By Shallow Crustal Earthquakes, Earthquake Spectra, v. 24, p. 217-242.

Idriss, I.M, 2014, An NGA-West2 empirical model for estimating the horizontal spectral values generated by shallow crustal earthquakes, Earthquake Spectra, v. 30, p. 1155-1177.

ISRMIP (INL Seismic Risk-Informed Methodology Independent Panel), 2015, Proposed Risk Informed Seismic Hazard Periodic Reevaluation Methodology for Complying with DOE Order 420.1C, Battelle Energy Alliance, External Report INL/EXT-15-36510 (Revision 1), 27 p.

Jack Benjamin & Associates, URS Corporation Seismic Hazards Group, Geomatrix Consultants, Inc., and Shannon & Wilson, 2012, Probabilistic Seismic Hazard Analyses Project for the Mid-Columbia

Dams. Final Report prepared for the Public Utility Districts of Chelan, Douglas, and Grant Counties, Chelan County Public Utility District, Wenatchee, Washington.

Jackson, D.B., Swanson, D.A., Koyanagi, R.Y., and Wright, T.L., 1975, The August and October 1968 East Rift eruptions of Kilauea volcano, Hawaii. U.S. Geological Survey Professional Paper 890, p. 1-33.

Jackson, S.M., Carpenter, G.S., Smith, R.P., and Casper, J.L., 2006, Seismic reflection project near the southern terminations of the Lost River and Lemhi faults, eastern Snake River Plain, Idaho: Battelle Energy Alliance, Idaho Falls, Idaho, INL/EXT-06-11851, 16 pp.

Jackson, S.M., Wong, I.G., Carpenter, G.S., Anderson, D.M. and Martin, S.M., 1993, Contemporary seismicity in the eastern Snake River Plain, Idaho based on microearthquake monitoring, Bulletin of the Seismological Society of America, v. 83, p. 680-695.

Jackson, S.M. and Zollweg, J.E., 1988, Seismic studies of an earthquake sequence in the White Cloud Peaks, Idaho, Seismological Research Letters, v. 59, p. 6.

Jacobs Team, 2013, Spent Fuel Handling Recapitalization Project geotechnical investigation plan, prepared for Bechtel Marine Propulsion Corporation, Naval Reactors Facility report 110254-PL-01, March, 27 p.

Janecke, S.U., 1992, Kinematics and timing of three superimposed extensional systems, east central Idaho: Evidence for an Eocene tectonic transition, Tectonics, v. 11, p. 1121-1138.

Janecke, S.U., 2007, Cenozoic extensional processes and tectonics in the northern Rocky Mountains: southwest Montana and eastern Idaho, Northwest Geology, v. 36, p. 111-132.

Jayaram, N., and Baker, J.W., 2010, Considering spatial correlation in mixed-effects regression and the impact on ground-motion models, Bulletin of the Seismological Society of America, v. 100, p. 3295-3303.

Johnston, A.C., Coppersmith, K.J., Kanter, L.R., and Cornell, C.A., 1994, The Earthquakes of Stable Continental Regions, *in* Schneider, J.F., editor, final proprietary report for the Electric Power Research Institute, Palo Alto, California, EPRI TR-102261, five volumes.

Kanno, T., Narita, A., Morikawa, N., Fujiwara, H., and Fukushima, Y., 2006, A new attenuation relation for strong ground motion in Japan based on recorded data, Bulletin of the Seismological Society of America, v. 96, p. 879-897.

Karpin, T.L., and Thurber, C.H., 1987, The relationship between earthquakes swarms and magma transport. Kilauea Volcano, Hawaii, Pure and Applied Geophysics, v. 125, p. 971-991.

Kavotha, K. S., Mavonga, T., Durieux, J., and Mukambilwa, K., 2004, Towards a more detailed seismic picture of the January 17th, 2002 Nyiragongo eruption, Acta Vulcanologica, 14-15, p. 87-100.

Keir, D. Pagli, C. Bastow, I.D., and Ayele, A., 2011, The magma assisted removal of Arabia in Afar: Evidence from dike injection in the Ethiopian rift captured using InSAR and seismicity, Tectonics, v. 30, TC2008, doi:10.1029/2010TC002785

Kleinfelder, Inc., 2007, Geotechnical investigation Integrated Waste Treatment Unit (IWTU), Idaho National Laboratory, Kleinfelder Project No. 76388, Rev. 0. Prepared for CH2M Hill Washington Group, Idaho, LLC (CWI) Project Number 25051, June.

Kreemer, C., Blewitt, G., and Hammond, W.C., 2010, Evidence for an active shear zone in southern Nevada linking the Wasatch fault to the Eastern California shear zone, Geology, v. 38, p. 475-478, doi: 10.1130/G30477.1.

Kulkarni, R., Wong, I., Zachariasen, J., Goldfinger, C., and Lawrence, M., 2013, Statistical analyses of great earthquake recurrence along the Cascadia subduction zone, Bulletin of the Seismological Society of America, v. 103, p. 3205-3221.

Kuntz, M.A., 1992, A model-based perspective of basaltic volcanism, eastern Snake River Plain, Idaho, in Regional Geology of Eastern Idaho and Western Wyoming, *in* editors, Link, P. K., Kuntz, M. A., and Platt, L. B., Geological Society of America Memoir 179, p. 289-304.

Kuntz, M. A., Anderson, S.R., Champion, D.E., Lanphere, M.A., and Grunwald, D.J., 2002, Tension cracks, eruptive fissures, dike, and faults related to late Pleistocene – Holocene basaltic volcanism and implications for the distribution of hydraulic conductivity in the eastern Snake River Plain, Idaho, *in* Link, P.K. and L.L. Mink, editors, Geology, Hydrogeology, and Environmental Remediation: Idaho National Engineering and Environmental Laboratory, Eastern Snake River Plain, Idaho, Boulder, Colorado, Geological Society of America Special Paper 353, p. 111-133.

Kuntz, M.A., Champion, D.E., Lefebvre, R.H., and Covington, H.R., 1988, Geologic map of the Craters of the Moon, Kings Bowl, Wapi lava fields and the Great Rift volcanic rift zone, south-central Idaho; U. S. Geological Survey Miscellaneous Investigation Series Map I-1632, scale 1:100,000.

Kuntz, M.A., Covington, H.R., and Schorr, L.J., 1992, An overview of basaltic volcanism of the eastern Snake River Plain, Idaho, *in* Link, P. K., Kuntz, M. A. and Platt, L. B., eds., Regional Geology of Eastern Idaho and Western Wyoming, Geological Society of America Memoir, v. 179, p. 227-267.

Kuntz, M.A., Skipp, B., Champion, D.E., Gans, P.B., Van Sistine, D.P., Snyders, S.R., 2007, Geologic Map of the Craters of the Moon 30' x 60' Quadrangle, Idaho, U.S. Geological Survey Scientific Investigations Map 2969.

Kuntz, M.A., Skipp, B., Lanphere, M.A., Scott, W.E., Pierce, K.L., Dalrymple, G.B., Champion, D.E., Embree, G.F., Page, W.R., Morgan, L.A., Smith, R.P., Hackett, W.R., and Rodgers, D.W., 1994, Geologic map of the Idaho National Engineering Laboratory and adjoining areas, eastern Idaho, U.S. Geological Survey Miscellaneous Investigation Map, I-2330, 1:100,000 scale.

Kuntz, M.A., Spiker, E.C., Rubin, M., Champion, D.E. and Lefebvre, R.H., 1986, Radiocarbon studies of latest Pleistocene and Holocene Lava flows of the Snake River Plain, Idaho: Data, lessons, interpretations, Quaternary Res., v. 25, p. 163-176.

Laurendeau, A., F. Cotton, O.-J.Ktenidou, L.–F. Bonilla, and F. Hollender, 2013, Rock and stiff-soil site amplification: Dependency on VS30 and kappa, Bulletin of the Seismological Society of America, v. 103, p. 3131-3148.

Leeman, W.P., 1982, Development of the Snake River Plain-Yellowstone Plateau Province, Idaho and Wyoming: An overview and petrologic model, *in* Bonnichsen, B. and Breckenridge, R.M., editors, Cenozoic Geology of Idaho, Idaho Geological Survey Bulletin 26, p.155-178.

Leeman, W.P., Annen, C. and Dufek, J., 2008, Snake River Plain–Yellowstone silicic volcanism: Implications for magma genesis and magma fluxes, Special Publication of the Geological Society of London, v. 304, p. 235-259.

Lepine, J-C., and Hirn, A., 1992, Seismotectonics in the Republic of Djibouti, linking the Afar Depression and the Gulf of Aden, Tectonophysics, v. 209, p. 65-86.

Lewis, R.S., Link, P.K., Stanford, L.R., and Long, S.P., 2012, Geologic map of Idaho, Idaho Utah Geological Survey, Map 9, Moscow, Idaho, Scale 1:750,000.

Lin, P.-S., Chiou, B. S.-J., Abrahamson, N. A., Walling, M., Lee, C.-T., and Cheng, C.-T., 2011, Repeatable source, site, and path effects on the standard deviation for empirical ground-motion prediction models, Bulletin of the Seismological Society of America, v. 101, p. 2281-2295.

Link, P.K., Skipp, B., Hait, M.H., Janecke, S.U., and Burton, B.R., 1988, Structural and stratigraphic transect of south central Idaho: A field guide to the Lost River, White Knob, Pioneer, Boulder, and Smoky Mountains, Idaho Geological Survey Bulletin 27, p. 5-42.

Lippitsch, R., White, R.S., and Soosalu, H., 2005, Precise hypocentre relocation of microearthquakes in a high-temperature geothermal field: the Torfajokull central volcano, Iceland, Geophysical Journal International, v. 160, p. 371-388.

McCaffrey, R., King, R.W., Payne, S.J., and Lancaster, M., 2013, Active tectonics of northwestern U.S. inferred from GPS-derived surface velocities, Journal of Geophysical Research, v. 118, p. 1-15, doi:10.1029/2012JB009473.

McCalpin, J.P., 1993, Neotectonics of the northeastern Basin and Range margin, western USA: Zeitschrift fuer Geomorphologie N. Folge, v. 94, p. 137-157.

McCalpin, J.P., 2003, Neotectonics of Bear Lake Valley, Utah and Idaho; A preliminary assessment, Paleoseismology of Utah, Utah Geological Survey Miscellaneous Publication 03-4, 45 p.

McCalpin, J., 2009, Paleoseismology, Paleoseismology, San Diego, California, Academic Press.

McCurry, M., Hayden, K.P., Morse, L.H. and Mertzman, S., 2008, Genesis of post-hotspot, Atype rhyolite of the Eastern Snake River Plain volcanic field by extreme fractional crystallization of olivine tholeiite, Bulletin of Volcanology, v. 70, p. 361-383.

McIntyre, D.H., Ekrin, E.D., and Hardyman, R.F., 1982, Stratigraphic and structural framework of the Challis volcanics in the eastern half of the Challis 1° x 2° quadrangle, Idaho, *in* Bonnichsen, B. and Breckenridge, R.M., editors, Cenozoic Geology of Idaho, Idaho Geological Survey Bulletin 26, p.3-22.

McQuarrie, N. and Rodgers, D.W., 1998, Subsidence of a volcanic basin by flexure and lower crustal flow: The eastern Snake River Plain, Idaho, Tectonics, v. 17, p. 203-220.

McVerry, G.H., Zhao, J.X., Abrahamson, N.A., and Sommerville, P.G., 2006, New Zealand acceleration response spectrum attenuation relations for crustal and subduction zone earthquakes, Bulletin of the New Zealand Society for Earthquake Engineering, v. 39, p. 1-58.

Menq, F. Y., 2003, Dynamic properties of sandy and gravelly soils, Ph.D. Dissertation, University of Texas at Austin, Texas.

Moos, C. and Barton, C.A., 1990, In-situ stress and natural fracturing at the INEL site, Idaho, EG&G Informal Report EGG-NPR-10631, 49 p.

Morgan, L.A. and McIntosh, W.C., 2005, Timing and development of the Heise volcanic field, Snake River Plain, Idaho, western USA, Geological Society of America Bulletin, v. 117, p. 288-306.

Mori, J., and Abercrombie, R.E, 1997, Depth dependence of earthquake frequency-magnitude distributions in California: Implications for rupture initiation, Journal of Geophysical Research, v. 102, p. 15081-15090.

Musson, R.M.W., 2000, Evaluation of seismic hazard source models, *in* Lapajne, J.K., and Vidrih, R., editors, Seismicity Modeling in Seismic Hazard Mapping, Slovenian Geophysical Survey, Ljubljana, p. 53-66.

Myers, W.B. and Hamilton, W., 1964, Deformation accompanying the Hebgen Lake earthquake of August 17, 1959, U. S. Geological Survey Bulletin 435-I, p. 55-98.

Nakata, J.S., Tanigawa, W.R., and Klein, F.W., 1982 Hawaiian Volcano Observatory Summary 81. Part 1. Seismic data, January to December, 1981, U.S. Geological Survey Report.

Niewendorp, A., and Neuhaus, M.E., 2003, Map of selected earthquakes for Oregon, 1841 through 2003, State of Oregon Department of Geology and Mineral Industries Open-file Report 03-02.

Nishimura, T., 2001, Crustal deformation caused by magma migration in the northern Izu Islands, Japan, Geophysical Research Letters, v. 28, p. 3745-3748.

NWRC-RA (North Wind Resource Consulting, LLC and Rizzo Associates), 2015, Geotechnical report Spent Fuel Handling Recapitalization Project, Naval Reactors Facility, Idaho National Laboratory, prepared for Bechtel Marine Propulsion Corporation, Naval Reactors Facility report 30096-TR-01, April, 130 p., with Appendix A-J.

Nobile, A., Pagli, C., Keir, D., Wright, T.J., Ayele, A., Ruch, J. and Acocella, V., 2012, Dike-fault interaction during the 2004 Dallol intrusion at the northern edge of the Erta Ale Ridge (Afar, Ethiopia), Geophysical Research Letters, v. 39, L19305, doi:10.1029/2012GL053152.

NRC, 1997, SSHAC – Senior Seismic Hazard Analysis Committee, U.S. Nuclear Regulatory Commission, NUREG/CR-6372, 280 p.

NRC, 2001, Technical basis for revision of regulatory guidance on design ground motions: Hazard and risk-consistent ground motion spectra guidelines, U.S. Nuclear Regulatory Commission, NUREG/CR-6728.

NRC, 2007, Regulatory Guide 1.208: A performance-based approach to define the site-specific earthquake ground motions, U.S. Nuclear Regulatory Commission, March.

NRC, 2012a, Practical Implementation Guidelines for SSHAC Level 3 and 4 Hazard Studies, U.S. Nuclear Regulatory Commission, NUREG-2117, Rev. 1, 235 p.

NRC, 2012b, Central and Eastern United States Seismic Source Characterization for Nuclear Facilities, U.S. Nuclear Regulatory Commission, NUREG-2115, Washington, D.C.

NRC, 2013, Standard Review Plan, U.S. Nuclear Regulatory Commission, Section 3.7.2, NUREG-0800, Rev 4, ADAMS ML.13198A223.

Oaks, S.D., 1992, Historical seismicity investigation for the November 11, 1905 earthquake; EG&G Informal Report EGG GEO 10203, 106 p.

Okada, Y., and Yamamoto, E., 1991, Dyke intrusion model for the 1989 seismovolcanic activity off Ito, central Japan, Journal of Geophysical Research, v. 96, p. 10361-10376.

Oldow, J.S., Bally, A.W., Ave'Lallement, H.G., and Leeman, W.P., 1989, Phanerozoic evolution of the North American cordillera: United States and Canada, *in* Bally A.W., and Palmer, A.R., editors, The Geology of North America: An overview, Geological Society of America, Decade of North American Geology, v. A, p. 139-232.

Olig, S.S., 1997, Trench investigation of Butte City scarps, unpublished letter report prepared by Woodward-Clyde Federal Services for Lockheed Martin Idaho Technologies, 12 p.

Olig, S.S., Gorton, A.E., Bott, J.D., Wong, I.G., Knuepher, P.L.K., Forman, S. L., Smith, R.P., and Simpson, D., 1995, Paleseismic investigation of the southern Lost River fault zone, Idaho, Lockheed Idaho Technologies Company, Technical Report INEL-95/0508, 82 pp.

Olig, S.S., A.E. Gorton, R.P. Smith, and Forman, S. L., 1997, Additional geologic investigations of the southern Lost River Fault and northern Arco Volcanic Rift Zone, unpublished letter report to Lockheed Martin Idaho Technologies Company, dated September 30, 1997.

Pallister, J.S., McCausland, W.A., Jónsson, S., Lu, Z., Zahran, H.M., Hadidy, S.E., Aburukbah, A., Stewart, I.C.F., Lundgren, P.R., White, R.A., and Moufti, M.R.H., 2010, Broad accommodation of rift-related extension recorded by dyke intrusion in Saudi Arabia, Nature Geoscience, v. 3, DOI: 10.1038/NGEO966.

Pankow, K.L., and Pechmann, C., 2004, The SEA99 ground-motion predictive relations for extensional tectonic regimes: revisions and a new peak ground velocity relation, Bulletin of the Seismological Society of America, v. 94, p. 341-348.

Pankratz, L.W., and Ackerman, H.D., 1982, Structure along the northwest edge of the Snake River Plain interpreted from seismic refraction, Journal of Geophysical Research, v. 87, p. 2676-2682.

Parker, S.D. and Sears, J.W., 2016, Strain accommodation within emerging shear zones: Insights from the Centennial Shear Zone, Montana and Idaho, *in* Parker, S.D., Tectonic alteration of a major Neogene river drainage of the Basin and Range, unpublished M.S. Thesis, University of Montana, Missoula, p. 66-92.

Parsons, T., Thompson, G.A., and Smith, R.P., 1998, More than one way to stretch: a tectonic model for extension along the track of the Yellowstone hotspot and adjacent Basin and Range Province; Tectonics, v. 17, p. 221-234.

Payne, S. J., 2006a, Development of rock and soil Design Basis Earthquake (DBE) parameters for the Materials and Fuels Complex (MFC), Battelle Energy Alliance, External Report INEEL/EXT-05-00925, April, Revision 1.

Payne, S. J., 2006b, Development of soil Design Basis Earthquake (DBE) parameters for moderate and high hazard facilities at RTC, Battelle Energy Alliance, External Report INEEL/EXT-03-00942, April, Revision 2.

Payne, S.J., 2007, Modeling of the Sedimentary Interbedded Basalt Stratigraphy for the Idaho National Laboratory Probabilistic Seismic Hazard Analysis, Battelle Energy Alliance External Report, INL/EXT-05-01047, Rev 1, August, 68 pp.

Payne, S. J., 2008, Development of soil design basis earthquake (DBE) parameters for moderate and high hazard facilities for the Integrated Waste Treatment Unit (IWTU), Battelle Energy Alliance, External Report INL/EXT-07-12716, August, Revision 1.

Payne, S.J., V.W. Gorman, S.A. Jensen, M.E. Nitzel, M.J. Russell, and R.P. Smith, 2002, Development of probabilistic design basis earthquake (DBE) parameters for moderate and high hazard facilities at INEEL, Bechtel BWXT Idaho, LLC. External Report INEEL/EXT-99-000775, Final Report, Rev 2, June, 101 pp.

Payne, S.J., Hackett, W.R., and Smith, R.P., 2009, Paleoseismology of volcanic environments; *in* McCalpin, J.P., editor, Paleoseismology, San Deigo, CA: Academic Press, p. 271-314.

Payne, S.J., McCaffrey, R. and King, R.W., 2008, Strain rates and contemporary deformation in the Snake River Plain and surrounding Basin and Range from GPS and seismicity, Geology, v. 36, p. 647-650.

Payne, S.J., McCaffrey, R., King, R.W. and Kattenhorn, S.A., 2012, An new interpretation of deformation rates in the Snake River Plain and adjacent Basin and Range regions from GPS measurements, Geophysical Journal International, v. 189, p. 101-122.

Payne, S.J., McCaffrey, R. and Kattenhorn, S.A., 2013, Extension-driven Right-lateral Shear in the Centennial Shear Zone Adjacent to the Eastern Snake River Plain, Idaho, Lithosphere, v. 5, p. 407-419.

PC Exploration, Inc., 1995, Summary report of continuous core sampling and drilling of core hole 1 at the Argonne National Laboratory - West, 41 p.

Pelton, J.R., Vincent, R.J., and Anderson, N.J., 1990, Microearthquakes in the Middle Butte/East Butte area, eastern Snake River Plain, Idaho, Bulletin of Seismological Society of America, v. 80, p. 209-212.

Peng, X., and E.D. Humphreys, 1998, Crustal velocity structure across the eastern Snake River Plain and the Yellowstone swell, Journal of Geophysical Research, v. 103, p. 7171-7186.

Pennington, W.D., Smith, R.B. and Tremble, A.B., 1974, A microearthquake study of parts of the Snake River Plain and central Idaho, Bulletin of Seismological Society of America, v. 64, p. 307-312.

Petersen, M.D., Frankel, A.D., Harmsen, S.C., Mueller, C.S., Haller, K.M., Wheeler, R.L., Wesson, R.L., Zeng, Y., Boyd, O.S., Perkins, D.M., Luco, N., Field, E.H., Wills, C.J., and Rukstales, K.S., 2008, Documentation for the 2008 Update of the United States National Seismic Hazard Maps, U.S. Geological Survey Open-File Report 2008-1128.

Petrik, F.E., 2008, Scarp analysis of the Centennial normal fault, Beaverhead County, Montana and Fremont County, Idaho, unpublished M.S. thesis, Bozeman, Montana State University, 267 p.

Pezzopane, S.K. and Weldon, R. J., 1993, Tectonic role of active faulting in central Oregon, Tectonics, v. 12, p. 1140-1169.

Pierce, K.L., Chesley-Preston, T.L., and Sojda, R.L., 2014, Surficial geologic map of the Red Rock Lakes Area, Southwest Montana, U.S. Geological Survey Open-file Report 2014-1157, 26 p.

Pierce, K.L. and Morgan, L.A., 1992, The track of the Yellowstone hot spot: Volcanism, faulting, and uplift, *in* P.K. Link et al., editors, Regional Geology of Eastern Idaho and Western Wyoming: Geological Society of America Memoir 179, p. 1-54.

Pierce, K.L. and Morgan, L.A., 2009, Is the track of the Yellowstone hotspot driven by a deep mantle plume?-Review of volcanism, faulting, and uplift in light of new data, Journal of Volcanology and Geothermal Research, Vol. 188, pp. 1-25.

Piety, L.A., Wood, C.K., Gilbert, J.D., Sullivan, J.T., and Anders, M.H., 1986, Seismotectonic study for Palisades Dam and Reservoir, Palisades Project, U. S. Bureau of Reclamation, Engineering Research Center, Seismotectonic Division, Denver, Colorado, and Pacific Northwest Region Geology Branch, Boise Idaho, Seismotectonic Report 86-3, 198 pp.

Pitt, A.M., Weaver, C.S., and Spence, W., 1979, The Yellowstone Park earthquake of June 30, 1975, Bulletin of the Seismological Society of America, v. 69, p. 187 205.

PNNL, 2014, Hanford Sitewide Probabilistic Seismic Hazard Analysis, Pacific Northwest National Laboratory report PNNL-23361, November.

Power, M., Chiou, B., Abrahamson, N., Bozorgnia, Y., Shantz, T., and Roblee, C., 2008. An overview of the NGA Project, Earthquake Spectra, v. 24, p. 3-21.

Press, W.H., Flannery, B.P., Teukolsky, S.A., Vetterling, W.T., 1986, Numerical Recipes, Cambridge University Press, Cambridge, 818 p.

Ramelli, A.R., and dePolo, C.M., 2011, Quaternary faults in the 2008 Wells earthquake area, Nevada Bureau of Mines and Geology Special Publication 36, p. 79-88.

Redpath, 1997, Letter transmittal to B. Harris of downhole velocity measurements at ANL-W borehole, June.

Redpath Geophysics, 2001, Summary report of downhole velocity surveys at the Advanced Test Reactor Area, INEEL, May.

Richins, W.D., Pechmann, J.C., Smith, R.B., Langer, C.J., Goter, S.K., Zollweg, J.E. and King, J.J., 1987, The 1983 Borah Peak, Idaho earthquake and its aftershocks, Bulletin of the Seismological Society of America, v. 77, p. 694-723.

Rizzo (Paul C. Rizzo and Associates, Inc.), 2008, Field investigation for geotechnical and geophysical data collection and analysis: Comprehensive ECF water pit seismic evaluation, report prepared for Naval Reactors Facility, project number 93-1350, December.

Rizzo Associates, 1994, Geophysical testing program Expended Core Facility, INEL, report prepared for Naval Reactors Facility, project number 93-1350, June.

Rodgers, D.W., Hackett, W.R. and Ore, H.T., 1990, Extension of the Yellowstone Plateau, eastern Snake River Plain, and Owyhee plateau, Geology, v. 18, p. 1138-1141.

Rodgers, D.W., Ore, H.T., Bobo, R.T., McQuarrie, N. and Zentner, N., 2002, Extension and subsidence of the eastern Snake River Plain, Idaho, *in* Bonnichsen, B., White, C.M., and McCurry, M., editors, Tectonic and Magmatic Evolution of the Snake River Plain Volcanic Province, Idaho; Idaho Geological Survey Bulletin 30, p. 121-155.

Rodriguez-Marek, A., Montalva, G.A., Cotton, F., and Bonilla, F., 2011, Analysis of single-station standard deviation using the KiK-net data, Bulletin of the Seismological Society of America, v. 101, p. 1242-1258.

Rollins, K.M., Evans, M.D., Diehl, N.B, and Daily, W.D. III, 1998, Shear modulus and damping relationships for gravels. ASCE Journal of Geotechnical and Geoenvironmental Engineering, v. 124, n. 5, p. 396-405.

Rubin, A.M., 1992, Dike-induced faulting and graben subsidence in volcanic rift zones, Journal of Geophysical Research, v. 97**,** p. 1839-1858.

Saint Louis University, 2015, Catalog of Moment Tensors for Parts of North America, available at: http://www.eas.slu.edu/eqc/eqc_mt/MECH.NA/, accessed on May 1, 2015.

Sammon, J.W., 1969, A nonlinear mapping for data structure analysis, IEEE Transactions on Computers, C-18, p. 401-409.

Scherbaum, F., Kuehn, N.M., Ohrnberger, M., and Koehler, A., 2010, Exploring the proximity of ground-motion models using high-dimensional visualization techniques, Earthquake Spectra, v. 26, p. 1117-1138.

Schneider, J.F., Silva, W.J., and Stark, C.L., 1993, Ground motion model for the 1989 M 6.9 Loma Prieta earthquake including effects of source, path and site, Earthquake Spectra, v. 9, p. 251-287.

Scholz, C.H., 1998, Earthquakes and friction laws, Nature, v. 391, p. 37-42.

Schwartz, D.P., 1989, Paleoseismicity, persistence of segments, and temporal clustering of large earthquakes-examples from the San Andreas, Wasatch, and Lost River fault zones, in D.P. Schwartz and R.H. Sibson, editors, Proceedings of Conference XLV on Fault Segmentation and Controls of Rupture Initiation and Termination, Palm Springs, California, 1989, US. Geological Survey Open-File Report 89-315, p. 361-375.

Schwartz, D.P. and K.J. Coppersmith, 1984, Fault behavior and characteristic earthquakes: examples from the Wasatch and San Andreas faults, Journal of Geophysical Research, v. 89, p. 5681-5698.

Scott, W.E., 1982, Surficial Geologic Map of the Eastern Snake River Plain and Adjacent Areas, Idaho and Wyoming; U. S. Geological Survey Miscellaneous Investigation Map I-1372, scale 1:250,000; 2 sheets.

Seismic Evaluation Team, 2010, Evaluation of Idaho National Laboratory probabilistic seismic hazard analyses, Battelle Energy Alliance, External Report INL/EXT-10-19922, September.

Shahi K.S, Baker J.W., and Rodriguez-Marek, A., 2015, Effect of Spatial Correlation on the Model Standard Deviations of CY14 Model, Deliverable submitted to GeoPentech, January 2015, 9 p.

Sheriff, S.D. and Stickney, M.C., 1984, Crustal structure of southwestern Montana and east-central Idaho: Results of a reversed refraction line, Geophysical Research Letters, v. 11, p. 299-302.

Shervais, J.W. and Hanan, B.B., 2008, Lithospheric topography, tilted plumes, and the track of the Snake River–Yellowstone Hotspot, Tectonics, v. 27, TC5004, doi:10.1029/2007TC002181.

Shervais, J.W., Shroff, G., Vetter, S.K., Matthews, S., Hanan, B.B. and McGee, J.J., 2002, Origin and evolution of the western Snake River Plain: Implications from stratigraphy, faulting, and the geochemistry of basalts near Mountain Home, Idaho, *in* Bonnichsen, B., White, C.M., and McCurry, M., editors, Tectonic and Magmatic Evolution of the Snake River Plain Volcanic Province, Idaho; Idaho Geological Survey Bulletin 30, p. 343-361.

Shervais, J.W., S.K. Vetter, and B.B. Hanan, 2006, Layered mafic sill complex beneath the eastern Snake River Plain: Evidence from cyclic geochemical variations in basalt, Geology, v. 34; p. 365-368.

Shoemaker, K.A. and Hart, W.K., 2002, Temporal controls on basalt genesis and evolution on the Owyhee Plateau, Idaho and Oregon, *in* Bonnichsen, B., White, C.M., and McCurry, M., editors, Tectonic and Magmatic Evolution of the Snake River Plain Volcanic Province, Idaho; Idaho Geological Survey Bulletin 30, p. 313-328.

Silva, W., and Darragh, R.B., 1995, Engineering Characterization of Strong Ground Motion Records from Rock Sites, Electric Power Research Institute (EPRI) Report TR-102262, June.

Silva, W.J., N. Abrahamson, G. Toro, and C. Costantino, 1996, Description and validation of the stochastic ground motion model, Report Submitted to Brookhaven National Laboratory, Associated Universities, Inc. Upton, New York 11973, Contract No. 770573.

Silva, W.J. and Lee, K., 1987, WES RASCAL code for synthesizing earthquake ground motions, *in* State-of-the-Art for Assessing Earthquake Hazards in the United States, Report 24, U.S. Army Engineers Waterways Experiment Station, Miscellaneous Paper S-73-1.

Silverman, B.W., 1986, Density Estimation for Statistics and Data Analysis, Chapman and Hall, London, England.

Simoes, M., Chen, Y-G., Shinde, D.P., and Singhvi, A.K., 2014, Lateral variations in the long-term slip rate of the Chelungpu fault, Central Taiwan, from the analysis of deformed fluvial terraces, Journal of Geophysical Research, v. 119.

Sipkin, S.A., 2003, A correction to body-wave magnitude m_b based on moment magnitude Mw. Seismological Research Letters, v. 74, p. 739-742.

Skipp, B., 1985, Contraction and extension faults in the southern Beaverhead Mountains, Idaho and Montana, US. Geological Survey Open-File Report, 545.

Skipp, B. and Hait, M.H., 1977, Allochthons along the northeast margin of the Snake River Plain, Idaho, Wyoming Geological Association 29th Annual Field Conference Guidebook, p.499-515.

Smith, K.D., Pechmann, J., Meremonte, M., and Pankow, K., 2011, Preliminary Analysis of the Mw 6.0 Wells, Nevada, Earthquake Sequence, Nevada Bureau of Mines and Geology Special Publication 36, p. 127-146.

Smith, K.D., von Seggern, D.H., Blewitt, G., Preston, L., Anderson, J.G., Wernicke, B.P., and Davis, J.L., 2004, Evidence for Deep Magma Injection Beneath Lake Tahoe, Nevada-California, Science, v. 305, p. 1277-1280.

Smith, R.B. and Arabasz, W.J., 1991, Seismicity of the Intermountain Seismic Belt, *in* Slemmons, D.B., E.R. Engdahl, M.D. Zoback, and D.D. Blackwell, Eds., Neotectonics of North America, Geological Society of America Decade Map, Vol. 1, pp. 185-228.

Smith, R.B. and Braile, L.W., 1994, The Yellowstone hotspot, Journal of Volcanology and Geothermal Research, v. 61, p.121-187.

Smith, R.B., M. Jordan, B. Steinberger, C.M. Puskas, J. Farrell, G.P. Waite, S. Husen, W.L. Chang, and R. O'Connell, 2009, Geodynamics of the Yellowstone hotspot and mantle plume: Seismic and GPS imaging, kinematics, mantle flow, Journal of Volcanology and Geothermal Research, v. 188, p. 26-65.

Smith R.B. and Sbar, M.L., 1974, Contemporary tectonics and seismicity of the western United States with emphasis on the Intermountain Seismic Belt, Geological Society of America Bulletin, v. 85, p. 1205-1218.

Smith, R.P., Jackson, S.M., and Hackett, W.R., 1996, Paleoseismology and seismic hazards evaluations in extensional volcanic terrains, Journal of Geophysical Research, v. 101, p. 6277-6292.

Sparlin, M.A., Braile, L.W., and Smith, R.B., 1982, Crustal structure of the Eastern Snake River Plain determined from ray trace modeling of seismic refraction data, Journal of Geophysical Research, v. 87, p. 2619-2633.

Spudich, P., Joyner, W.B., Lindh, A.G., Boore, D.M., Margaris, B.M., and Fletcer, J.B., 1999, SEA99: A revised ground motion prediction relation for use in extensional tectonic regimes, Bulletin Seismological Society of Amertica, v. 89, p. 1156-1170.

Stachnik, J.C., K. Dueker, D.L. Schutt, and J. Yuan, 2008, Imaging Yellowstone plume-lithosphere interactions from inversion of ballistic and diffusive Rayleigh wave dispersion and crustal thickness data, Geochemistry Geophysics Geosystems, v. 9, p. 1-21.

Stanley, W.D., 1982, Magnetotelluric soundings of the Idaho National Engineering Laboratory Facility, Idaho, Journal of Geophysical Research, v. 87, p. 2683-2691.

Stepp, C.J., 1972, Analysis of the completeness of the earthquake sample in the Puget Sound Area and its effect on statistical estimates of earthquake hazard, *in* Proceedings of the International Conference on Microzonation, v. 2, p. 897-910.

Stepp, J.C, Wong, I., Whitney. J., Quittmeyer, R., Abrahamson, N., Toro, G., Youngs, R., Coppersmith, K., Savy, J., Sullivan, T., and Yucca Mountain PSHA Project Members, 2001, Probabilistic seismic hazard analysis for ground motions and fault displacement at Yucca Mountain, Nevada, Earthquake Spectra, v. 17, p. 113-151.

Stewart, J.P., Boore, D.M., Seyhan, E., and, Atkinson, G.M., 2015, NGA-West2 equations for predicting vertical-component PGA, PGV, and 5%-damped PSA from shallow crustal earthquakes, Earthquake Spectra, in press, doi: http://dx.doi.org/10.1193/072114EQS116M.

Stickney, M.C., 1997, Seismic source zones in southwestern Montana, Montana Bureau of Mines and Geology Open-File Report 366, 52 p.

Stickney, M.C., 2007, Historic earthquakes and seismicity in southwestern Montana, Northwest Geology, v. 36, p. 167-186.

Stickney, M.C. and Bartholomew, M.J., 1987, Seismicity and late Quaternary faulting of the northern basin and range province, Montana and Idaho: Bulletin of Seismological Society of America, v. 77, p. 1602-1625.

Stickney, M.C. and Lageson, D.R., 2002, Seismotectonics of the 20 August 1999 Red Rock Valley, Montana earthquake, Bulletin of the Seismological Society of America, v. 92, p. 2449-2464.

Stirling, M., Rhoades, D., and K. Berryman, 2002, Comparison of earthquake scaling derived from data of the instrumental and preinstrumental era, Bulletin of the Seismological Society of America, v. 92, p. 812-830.

Stock, C., and Smith, E.G.C., 2002, Adaptive kernel estimation and continuous probability representation of historical earthquake catalogs, Bulletin of the Seismological Society of America, v. 92, p. 913-922.

Stokoe, K. H., Menq, F-Y., Valle, C., and Choi, W. K., 2002, Dynamic properties of intact soil specimens from the Test Reactor Area Site, prepared for Idaho National Engineering and Environmental Laboratory, unpublished report, p. 250.

Stover, C., 1993, Seismicity of the United States, 1568-1989 (Revised), U.S. Geological Survey Professional Paper 1527, 427 pp.

STRATA Inc., 2011, Final Report geotechnical engineering evaluation Spent Fuel Handling Project facility, Naval Reactors Facility - INL, Butte County, Idaho, prepared for Michal Baker Jr. Inc (Naval Reactors Facility), 56 p.

Sutton, G. H., Maynard, G.L., and Hussong, D.M., 1971, Widespread occurrence of a high-velocity basal layer in the Pacific crust found with repetitive sources and sonobuoys, Geophysical Monograph, v. 14, p. 193-209.

Swanson, D.A., Jackson, D.B., Koyanagi, R.Y., and Wright, T.L., 1976, The February 1969 East Rift eruption of Kilauea volcano, Hawaii, U.S. Geological Survey Professional Paper 891, p. 1-30.

Tanaka, A., 2004, Geothermal gradient and heat flow data in and around Japan (II): Crustal thermal structure and its relationship to seismogenic layer, Earth, Planets, and Space, v. 56, p. 1195-1199.

Tanaka, A. and Ito, H., 2002, Temperature at the base of the seismogenic zone and its relationship to the focal depth of the western Nagano Prefecture area (in Japanese with English abstract), Journal of the Seismological Society of Japan, v. 55, p. 1-10.

Tanigawa, W.R., Nakata, J.S., and Klein, F.W., 1981, Hawaiian Volcano Observatory Summary 80. Part 1. Seismic data, January to December 1980, unpublished, U.S. Geological Survey Report, Hilo, HI.

Tanigawa, W.R., Nakata, J.S., and Klein, F.W., 1983, Hawaiian Volcano Observatory Summary 82. Part 1. Seismic data, January to December 1980, unpublished, U.S. Geological Survey Report, Hilo, HI.

Thackray, G.D., Rodgers, D.W., and Streutker, D., 2013, Holocene scarp on the Sawtooth fault, central Idaho, USA, documented through lidar topographic analysis, Geology, v. 41, p. 639-642.

Tinti, S., and Mulargia, F., 1985, Effects of magnitude uncertainties on estimating the parameters in the Gutenberg-Richter frequency-magnitude law, Bulletin of the Seismological Society of America, v. 74, p. 1681-1697.

Toppozada, T.R., 1975, Earthquake magnitude as a function of intensity data in California and western Nevada, Bulletin of the Seismological Society of America, v. 65, p.1223-1238.

TRA, 2000, Surficial sediments at TRA and INTEC: Comparison of particle size distributions and SPT results, unpublished report with INEL Materials Lab test results.

Turko, J.M. and P.K.L. Knuepfer, 1991, Late Quaternary fault segmentation from analysis of scarp morphology, Geology, v. 19, p. 718-721.

Twining, B.V., and Bartholomay, R.C., 2011, Geophysical logs and water-quality data collected for boreholes Kimama-1A and -1B, and a Kimama water supply well near Kimama, southern Idaho: U.S. Geological Survey Data Series 622 (DOE/ID 22215), 18 p.

Uhrhammer, R.A., 1986, Characteristics of northern and central California seismicity, abstract, Earthquake Notes, v. 57, p. 21.

URS Greiner Woodward-Clyde Federal Services, Geomatrix Consultants, and Pacific Engineering and Analysis, 1999, Final Report: Development of Design Basis Earthquake Parameters for TMI-2 Independent Spent Fuel Storage Installation at the INEEL, Bechtel BWXT Idaho, LLC. External Report INEEL/EXT-99-00619, November.

URS Greiner Woodward-Clyde Federal Services, Geomatrix Consultants, and Pacific Engineering and Analysis, 2000, Recomputation of the Seismic Hazard at the Idaho National Engineering and Environmental Laboratory, Bechtel BWXT Idaho, LLC. External Report INEEL/EXT-99-00786, February.

U.S. Geological Survey, 2013, Global earthquake search, http://earthquake.usgs.gov/earthquakes/eqarchives/epic/, accessed May 2013.

Veneziano, D., and Van Dyck, J., 1985, Analysis of earthquake catalogs for incompleteness and recurrence rates, Seismic Hazard Methodology for Nuclear Facilities in the Eastern United States, EPRI Research Projects N. P101-29, Electric Power Research Institute Seismic Owners Group Draft 85-1, v.2, Appendix A-6. Electric Power Research Institute, Palo Alto, California.

Vincent, K.R., 1985, Measurement of vertical tectonic offset using longitudinal profiles of faulted geomorphic surfaces near Borah Peak, Idaho, A preliminary report, *in* Stein, R.S., and Bucknam, R.C., editors, Proceedings of Conference XXVIII on the Borah Peak, Idaho, Earthquake, Sun Valley, Idaho, October 1985, U.S. Geological Survey Open File Report 85-290, p. 76-96.

von Seggern, D.H., Smith, K.D., and Preston, L.A, 2008, Seismic Spatial-Temporal Character and Effects of a Deep (25-30 km) Magma Intrusion below North Lake Tahoe, California-Nevada, Bulletin of the Seismological Society of America, v. 98, p.1508-1526.

Vucetic, M. and Dobry, R., 1991, Effect of soil plasticity on cyclic response, Journal of Geotechnical Engineering, v. 117, p. 89-107.

Waite, G.P. and Smith, R.B., 2002, Seismic evidence for fluid migration accompanying subsidence of the Yellowstone caldera, Journal of Geophysical Research, v. 107, 2177, doi: 10.1029/2001JB000586.

Waite, G.P., and Smith, R.B., 2004, Seismotectonic and stress field of the Yellowstone volcanic plateau from earthquake first-motions and other indicators, Journal of Geophysical Research, v. 109, p.1-14, doi:10.1029/2003JB002675.

Weichert, D.H., 1980, Estimation of the earthquake recurrence parameters for unequal observation periods for different magnitudes, Bulletin of the Seismological Society of America, v. 70, p. 1337-1346.

Wells, D.L. and K.J. Coppersmith, 1994, New empirical relationships among magnitude, rupture length, rupture area, and surface displacement, Bulletin of the Seismological Society of America, v. 84, p. 974-1002.

Wernicke, B.P., Christiansen, R.L., England, P.C. and Sonder, L.J., 1987, Tectonomagmatic evolution of Cenozoic extension in the North American Cordillera, *in* Coward, M.P., Dewey, J.F. and Hancock, P.L., editors, Continental Extensional Tectonics, Geological Society of America Special Publication, v. 28, p. 203-221.

Wesnousky, S.G., 1986, Earthquakes, Quaternary faults, and seismic hazard in California, Journal of Geophysical Research, v. 91, p. 12,587-12,631.

Wesnousky, S.G., 2008, Displacement and geometrical characteristics of earthquake surface ruptures–Issues and implications for seismic-hazard analysis and the process of earthquake rupture, Bulletin of the Seismological Society of America, v, 98, p. 1609-1632.

Witkind, I.J., 1964, Reactivated faults north of Hebgen Lake, U.S. Geological Survey Professional Paper 435, p. 37-50.

Witter, R.C., Zhang, Y., Wang, K., Goldfinger, C., Priest, G.R., and Allan, J.C., 2012, Coseismic slip on the southern Cascadia megathrust implied by tsunami deposits in an Oregon lake and earthquake-triggered marine turbidities, Journal of Geophysical Research, v. 117, B10303.

Wood S.H., and Clemens, T., 2002, Geologic and tectonic history of the Western Snake River Plain, *in* Bonnichsen, B., White, C.M., and McCurry, M., editors, Tectonic and Magmatic Evolution of the Snake River Plain Volcanic Province, Idaho; Idaho Geological Survey Bulletin 30, p. 69-103.

Wood, T.R., Helm-Clark, C.M., Huang, H., Magnuson, S., McLing, T., Orr, B., Podgorney, M.R., Plummer, M.A., Roddy, M.S., Rohe, M.J., and Whitmore, E., 2007, Operable Unit 10-08 Summary Report on the Idaho National Laboratory Sitewide three-dimensional aquifer model, Battelle Energy Alliance External Report INL/EXT-07-13337, September, pp. 276.

Woodward-Clyde Federal Services, 1998, Development of Design Basis Earthquake Parameters for the Argonne National Laboratory-West, Idaho National Engineering and Environmental Laboratory, Final Report, Argonne National Laboratory report, W7500-0587-ES-00, March.

Woodward-Clyde Federal Services, Geomatrix Consultants, and Pacific Engineering and Analysis, 1996, Site-specific Seismic Hazard Analyses for the Idaho National Engineering Laboratory, Volume I Final Report and Volume 2 Appendix, Lockheed Idaho Technologies Company Informal Report, INEL-95/0536, May.

Wong, I., Olig, S., Dober, M., Wright, D., Nemser, E., Lageson, D., Silva, W., Stickney, M., Lemieux, M., and Anderson, L., 2005, Probabilistic earthquake hazard maps for the state of Montana, Montana Bureau of Mines and Geology Special Publication 117, 72 pp.

Wong, I., Silva, W., Olig, S., Thomas, P., Wright, D., Ashland, F., Gregor, N., Pechmann, J., Dober, M., Christenson, G., and Gerth, R., 2002, Earthquake scenario and probabilistic ground shaking maps for the Salt Lake City, Utah, metropolitan area, Utah Geological Survey Miscellaneous Publication MP-02-05, 50 p.

Wong, I.G. and Bott, J.D.J., 1995, A look back at Oregon's earthquake history, 1841-1994, Oregon, Geology, v. 57, p. 125-139.

Wu, D. and Bruhn, R.L., 1994, Structural and rupture characteristics of the southern Lost River fault zone, Idaho, University of Utah, Report to Woodward-Clyde Federal Services, April, 33 p.

Yirgu, G., Ayele, A., and Ayalew, D., 2006, Recent seismovolcanic crisis in Northern Afar, Ethiopia, EOS, Transactions of the American Geophysics Union, v. 87, p. 325-329.

Young, R.A., and Lucas, J.E., 1988, Exploration beneath volcanics: Snake River Plain, Idaho, Geophysics, v. 53, p. 444-452.

Youngs, R.R., and Coppersmith, K.J., 1985, Implications of fault slip rates and earthquake recurrence models to probabilistic hazard estimates, Bulletin of the Seismological Society of America, v. 75, p. 939-964.

Youngs, R.R., Coppersmith, K.J., Taylor, C.L., Power, M.S., DiSilvestro, L.A., Angell, M.L., Hall, N.T., Wesling, J.R., and Mualchin, L., 1992, A comprehensive seismic hazard model for the San Francisco

Bay region, *in* Borchardt, G., Hirschfeld, S.E., Lienkaemper, J.J., McClellan, P., Williams, P.L., and Wong, I.G., editors, Proceedings of the Second Conference on Earthquake Hazards in the Eastern San Francisco Bay Area, , California Department of Conservation, Division of Mines and Geology, Sacramento, California, Special Publication 113, p. 431-441.

Yuan, H. and Dueker, K., 2005, Teleseismic P-wave tomogram of the Yellowstone plume, Geophysical Research Letters, v 32, 4 pp.

Zentner, N.C., 1989, Neogene normal faults related to the structural origin of the eastern Snake River Plain, Idaho; M.S. Thesis, Idaho State University, Pocatello, 48 p.

Zhao, J.X., and Lu, M., 2011, Magnitude-scaling rate in ground-motion prediction equations for response spectra from large, shallow crustal earthquakes, Bulletin of the Seismological Society of America, v. 11, p. 2643-2661.

Zhao, J.X., Zhang, J., Asano, A., Ohno, Y., Oouchi, T., Takahashi, T., Ogawa, H., Irikura, K., Thio, H.K., Somerville, P.G., Fukushima, Y., and Fukushima, Y., 2006, Attenuation Relations of Strong Ground Motion in Japan Using Site Classification Based on Predominate Period, Bulletin of the Seismological Society of America, v. 96, p. 898-913.

Zollweg, J.E., 2005, Long Term Seismic Hazard Assessment for Boise, Idaho: Moderate risk arising from a large number of low recurrence rate sources, in Lund, W. R., editor, Proceedings Volume, Basin and Range Province Seismic Hazards Summit II, abstract, Utah Geological Survey Miscellaneous Publications 05-2, p. 161-162.

Zollweg, J.E., and Richins, W.D., 1985, Later aftershocks of the 1983 Borah Peak, Idaho earthquake and related activity in central Idaho, *in* Stein, R.S., and Bucknam, R.C., editors, Proceedings of Conference XXVIII on the Borah Peak, Idaho, Earthquake, Sun Valley, Idaho, October 1985, U.S. Geological Survey Open-File Report, 85-290, p. 345-367.